



Ikuo Towhata

**Geotechnical**  
**Earthquake**  
**Engineering**

 Springer

# Springer Series in Geomechanics and Geoengineering

---

Editors: Wei Wu · Ronaldo I. Borja

Ikuo Towhata

---

# Geotechnical Earthquake Engineering

**Professor Wei Wu**, Institut für Geotechnik, Universität für Bodenkultur, Feistmantelstraße 4, 1180 Vienna, Austria.  
E-mail: wei.wu@boku.ac.at

**Professor Ronaldo I. Borja**, Department of Civil and Environmental Engineering, Stanford University, Stanford, California 94305-4020, USA. E-mail: borja@stanford.edu

## **Author**

Ikuo Towhata  
Professor of Geotechnical Engineering  
Department of Civil Engineering  
University of Tokyo  
7-3-1, Hongo, Bunkyo-Ku  
Tokyo 113-8656  
Japan  
Email:towhata@geot.t.u-tokyo.ac.jp

ISBN 978-3-540-35782-7

ISBN 978-3-540-35783-4 (eBook)

DOI 10.1007/ 978-3-540-35783-4

Springer Series in Geomechanics and Geoengineering

Library of Congress Control Number: 2008920290

© 2008 Springer-Verlag Berlin Heidelberg

This work is subject to copyright. All rights are reserved, whether the whole or part of the material is concerned, specifically the rights of translation, reprinting, reuse of illustrations, recitation, broadcasting, reproduction on microfilm or in any other way, and storage in data banks. Duplication of this publication or parts thereof is permitted only under the provisions of the German Copyright Law of September 9, 1965, in its current version, and permission for use must always be obtained from Springer. Violations are liable for prosecution under the German Copyright Law.

The use of general descriptive names, registered names, trademarks, etc. in this publication does not imply, even in the absence of a specific statement, that such names are exempt from the relevant protective laws and regulations and therefore free for general use.

Type setting by the authors and Scientific Publishing Services Pvt. Ltd.

Printed in acid-free paper

5 4 3 2 1 0

springer.com

地盤  
耐震  
工學



## Preface

This book is a product of my long-term activities in both education and research. Its publication was made possible by a financial support supplied by the Ministry of Education, Culture, Sports, Science and Technology. As for education, I was told for the first time in 1985 to teach soil dynamics in Asian Institute of Technology in Bangkok, Thailand. I collected experimental and field findings from many publications and made a small series of handouts. Since computer technologies were not well advanced in mid 80s, the handouts were products of cut-and-paste in the physical sense. Many pages were even handwritten. Afterwards, I started to teach the same subject in 1995 at University of Tokyo. Since then I have added more information from field investigation and laboratory tests as well as analyses. It has become possible to put all in an electronic media that makes teaching easier. Readers can find that this book includes Japanese writing among English text. This is because I use this text for teaching in Tokyo.

The main aim of this book is a collection of data which is useful in understanding the state-of-art technology and its application to new topics. Understanding the fundamental issues is important because practice makes use of many assumptions, hypotheses, and way of thinking. It has been my policy to show reasons why practice employs those ideas by showing experimental and field backgrounds. This idea does not change even today.

Collecting the background information is not very easy for an individual person. It is necessary to read many publications; some were published in the first half of the 20th Century, and others in domestic publications. Not being impossible, this information collection is firstly a time-consuming business. Secondly, the access to old publication may not be easy to everybody. I am therefore attempting in this book to collect information as much as possible so that the new generation of readers can save time in studying. Many figures were therefore reproduced from the original publications. Moreover, I tried to visit important sites and take photographs in order to show the ideas in practice to be meaningful. Although the result is not perfect, information in this book will be helpful when readers have to understand the meaning of present practice and improve it in future. This is particularly important because the development of our society generates new kinds of problems and new approach is continuously required.




One major problem in this book is the enormous amount of information. For very young readers who have just started geotechnical engineering and soil mechanics, it is more important to get the overall scope than learning details. The total number of pages and contents in this book may prevent their efforts. In this regard, I decided to classify the contents into three categories; elementary, advanced, and miscellaneous. Readers can pick up only pages of their interest in place of reading from the first page to the last. The miscellaneous content is not necessarily less important; sometimes many interesting topics are therein found. It is recommendable therefore that young readers take a quick look at those pages as well. On the other hand, it is not expected for readers to start reading from the first page and continue till the last.

I do hope that information in this book will help readers develop their knowledge and career in the discipline of geotechnical engineering. Certainly the contents of this book miss many important issue. I am going to show additions and modifications in my home page. Readers are advised to visit occasionally the site of Geotechnical Engineering Laboratory, Department of Civil Engineering, University of Tokyo (URL : <http://geotle.t.u-tokyo.ac.jp>).

Ikuo Towhata  
June, 2007.















# List of Contents

The following symbols indicate the types of respective chapters;

Chapters concerning elementary topics : ,  
advanced topics : , and  
miscellaneous topics : .




## PART 1 KNOWLEDGE OF SOIL MECHANICS

### Chapter 1 BASIC PRINCIPLES IN SOIL MECHANICS




Section 1.1	PHYSICAL PROPERTIES OF SOIL	4	
Section 1.2	WEIGHT AND DENSITY OF SOIL	6	
Section 1.3	EFFECTIVE STRESS AND PORE WATER PRESSURE	7	
Section 1.4	CONSIDERATION AND VOLUME CHANGE	10	
Section 1.5	SHEAR DEFORMATION AND STRENGTH OF SAND	12	
Section 1.6	DILATANCY OR SHEAR-INDUCED VOLUME CHANGE	13	
Section 1.7	UNDRAINED OR CONSTANT-VOLUME SHEAR TEST	15	
Section 1.8	EXCESS PORE WATER PRESSURE AND STRESS PATH DIAGRAM	16	
Section 1.9	TRIAXIAL SHEAR DEVICE	17	
Section 1.10	MEMBRANE PENETRATION	19	
Section 1.11	ELEMENTARY DYNAMICS	21	
Section 1.12	STANDARD PENETRATION TEST	22	
Section 1.13	FLOW OF GROUND WATER	24	
Section 1.14	SHEAR BAND	26	

## PART 2 PROBLEMS CONCERNING SHAKING OF SOFT GROUND UNDERGOING EARTHQUAKE LOADING




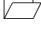
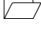
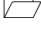






### Chapter 2 INTRODUCTION

Section 2.1	OBJECTIVES OF EARTHQUAKE GEOTECHNICAL ENGINEERING	32	
Section 2.2	GEOTECHNICAL PROBLEMS ENCOUNTERED DURING EARTHQUAKES	33	
Section 2.3	SCHEMATIC DIAGRAM TO SHOW RELATIONSHIP AMONG GEOTECHNICAL SEISMIC PROBLEMS	34	
















### Chapter 3 SEISMOLOGICAL KNOWLEDGE

Section 3.1	RUPTURE OF FAULT AS A CAUSE OF EARTHQUAKE	36	
Section 3.2	REGIONS WHERE BIG EARTHQUAKE IS LIKELY TO OCCUR	38	
Section 3.3	RESERVOIR-TRIGGERED SEISMICITY	40	









**Chapter 4 WAVE PROPAGATION IN ELASTIC MEDIUM**

Section 4.1	EARTHQUAKE WAVES : S WAVE	43	
Section 4.2	EARTHQUAKE WAVES : P WAVE	44	
Section 4.3	IDEALIZATION OF VERTICAL WAVE PROPAGATION	46	
Section 4.4	VERTICAL PROPAGATION OF “S” WAVE IN LEVEL GROUND	47	
Section 4.5	SOLUTION OF S-WAVE PROPAGATION IN REAL NUMBERS	48	
Section 4.6	<b>EXERCISE NO.1 ON AMPLIFICATIN OF GROUND MOTION</b>	50	
Section 4.7	EARTHQUAKE WAVES: RAYLEIGH WAVE	51	
Section 4.8	EARTHQUAKE WAVES: LOVE WAVE	53	
Section 4.9	RESPONSE OF ELASTIC GROUND TO SURFACE EXCITATION	54	
Section 4.10	WAVE TRANSMISSION AND REFLECTION AT INTERFACE	55	
Section 4.11	CALCULATION OF SEISMIC WAVE ENERGY	56	
Section 4.12	TRAFFIC-INDUCED GROUND VIBRATION	57	































**Chapter 5 EARTHQUAKE EFFECTS**

Section 5.1	INTENSITY OF EARTHQUAKE MOTION	60	
Section 5.2	REVISED EARTHQUAKE INTENSITY	62	
Section 5.3	INSTRUMENTAL DETERMINATION OF SEISMIC INTENSITY	63	
Section 5.4	EARTHQUAKE MAGNITUDES	65	
Section 5.5	TIME HISTORY OF GROUND MOTION	67	
Section 5.6	EFFECTS OF LOCAL SOIL CONDITIONS ON MAXIMUM ACCELERATION	68	
Section 5.7	SOME FAMOUS EARTHQUAKE MOTION RECORDS	69	
Section 5.8	GROUND MOTION DURING 1985 MEXICAN EARTHQUAKE	70	
Section 5.9	POWER OF ACCELERATION TIME HISTORY	72	
Section 5.10	DISTANCE FROM SOURCE OF EARTHQUAKE	73	
Section 5.11	ESTIMATION OF INTENSITY OF EARTHQUAKE MOTION	74	
Section 5.12	ESTIMATION OF DURATION OF EARTHQUAKE MOTION	75	
Section 5.13	DETERMINATION OF DESIGN EARTHQUAKE MOTION	76	
Section 5.14	SEISMIC DAMAGE IN TRADITIONAL HOUSES	78	
Section 5.15	RECONNAISSANCE STUDY OF EARTHQUAKE-INDUCED DAMAGE	83	












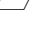
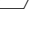
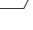
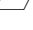
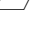
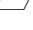
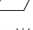




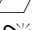

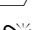


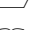






**Chapter 6 DYNAMIC RESPONSE ANALYSIS**

Section 6.1	RATE-DEPENDENT BEHAVIOUR OF CLAY	88	
Section 6.2	SIGNIFICANCE OF COMPLEX ANALYSIS	89	
Section 6.3	TRANSIENT RESPONSE	92	
Section 6.4	ANALYSES IN FREQUENCY DOMAIN AND TIME DOMAIN	93	
Section 6.5	NUMERICAL INTEGRATION OF EQUATION OF MOTION IN THE TIME DOMAIN	95	
Section 6.6	NEWMARK’S $\beta$ METHOD	97	
Section 6.7	INTRODUCTION TO SEISMIC RESPONSE ANALYSIS	100	
Section 6.8	AMPLIFICATION OF MOTION IN SURFACE ALLUVIUM	102	









Section 6.9	SIGNIFICANCE OF OUTCROP MOTION	104	
Section 6.10	SEISMIC RESPONSE OF MULTI-LAYERED GROUND	106	
Section 6.11	AMPLIFICATION OF MOTION AT THE TOP OF HILL	107	
Section 6.12	ANALYSIS ON HILL-INDUCED AMPLIFICATION	108	
Section 6.13	CALCULATED AMPLIFICATION EFFECTS OF HILLY TOPOGRAPHY	110	
Section 6.14	OBSERVED TOPOGRAPHIC EFFECTS	111	
Section 6.15	THEORY OF BESSEL FUNCTIONS	113	
Section 6.16	INFINITE BOUNDARY CONDITION	114	
Section 6.17	<b>EXERCISE NO.2 OF DYNAMIC RESPONSE ANALYSIS ON ELASTIC GROUND</b>	118	
 <b>Chapter 7 PSEUDOSTATIC LIMIT EQUILIBRIUM ANALYSIS</b>			
Section 7.1	SEISMIC COEFFICIENT	121	
Section 7.2	MODIFIED METHOD OF SEISMIC COEFFICIENT	124	
Section 7.3	VERTICAL MOTION	126	
Section 7.4	DIRECTION OF SEISMIC INERTIA FORCE IN DESIGN	127	
 <b>Chapter 8 FIELD INVESTIGATION</b>			
Section 8.1	FIELD INVESTIGATION ON SHEAR WAVE VELOCITY	130	
Section 8.2	SUSPENSION-TYPE DOWNHOLE SURVEY	131	
Section 8.3	CROSS-HOLE SURVEY	133	
Section 8.4	CORRELATION BETWEEN SPT- <i>N</i> AND $V_s$ OF ALLUVIAL SOILS	134	
Section 8.5	CORRELATION BETWEEN SPT- <i>N</i> AND $V_s$ OF GRAVELLY SOILS	136	
Section 8.6	CORRELATION BETWEEN SPT- <i>N</i> AND $V_s$ OF PLEISTOCENE SOILS	137	
Section 8.7	SEISMIC REFRACTION METHOD FOR SUBSURFACE EXPLORATION	138	
Section 8.8	STACKING TECHNIQUE TO REMOVE NOISE FROM SIGNAL	140	
Section 8.9	SWEDISH WEIGHT SOUNDING	142	
Section 8.10	MICROTREMOR	143	
Section 8.11	SUBSURFACE EXPLORATION BY SURFACE WAVE RECORDS	147	
 <b>Chapter 9 DYNAMIC RESPONSE OF COMPLEX-MODULUS MODEL</b>			
Section 9.1	COMPLEX STRESS-STRAIN MODELING	150	
Section 9.2	DAMPING RATIO IN SOIL DYNAMICS AND CRITICAL DAMPING RATIO	152	
Section 9.3	DAMPED OSCILLATION OF COMPLEX-MODULUS MODEL	153	
Section 9.4	FORCED OSCILLATION OF COMPLEX-MODULUS MODEL	155	
<b>EXERCISE</b>	<b>CALCULATION OF AMPLIFICATION FACTOR</b>	156	
Section 9.5	WAVE PROPAGATION IN COMPLEX-MODULUS MEDIUM	157	
Section 9.6	SOLUTION OF REAL NUMBERS IN COMPLEX-MODULUS GROUND	159	









## XII List of Contents

Section 9.7	OUTCROP AMPLIFICATION IN COMPLEX-MODULUS GROUND	160	
Section 9.8	<b>EXERCISE NO.4 RESPONSE ANALYSIS OF MULTILAYERED DEPOSITS</b>	162	
Section 9.9	VARIATION OF SHEAR MODULUS AT INTERFACE OF SOIL LAYERS	163	
Section 9.10	EQUIVALENT LINEAR MODELING	165	
Section 9.11	THEORY OF FOURIER SERIES	166	
Section 9.12	SPECTRUM ANALYSIS BY FOURIER SERIES	168	
Section 9.13	DYNAMIC ANALYSIS WITH EQUIVALENT LINEAR MODEL	171	
Section 9.14	EXAMPLE OF EQUIVALENT LINEAR ANALYSIS	172	
	<b>EXERCISE NO.5 EQUIVALENT LINEAR METHOD OF ANALYSIS</b>	173	
Section 9.15	DECONVOLUTION OF EARTHQUAKE MOTION	175	
Section 9.16	FURTHER REMARKS ON EQUIVALENT LINEAR MODEL	178	
 <b>Chapter 10 LABORATORY TESTS ON DYNAMIC PROPERTIES OF SOILS</b>			
Section 10.1	RESONANT COLUMN TEST OF SOILS	181	
Section 10.2	GENERAL PRINCIPLE IN INTERPRETATION OF STRAIN AMPLITUDE EFFECTS ON SHEAR MODULUS AND DAMPING RATIO	183	
Section 10.3	FACTORS THAT AFFECT MODULUS AND DAMPING OF SAND	184	
Section 10.4	FACTORS THAT AFFECT MODULUS AND DAMPING OF CLAY	185	
Section 10.5	SHEAR MODULUS OF SAND AT SMALL STRAIN AMPLITUDE	186	
Section 10.6	EFFECTS OF STRAIN AMPLITUDE ON SHEAR MODULUS	189	
Section 10.7	EFFECTS OF EFFECTIVE STRESS ON SHEAR MODULUS OF SAND	190	
Section 10.8	DAMPING RATIO OF SAND	191	
Section 10.9	RATE DEPENDENT NATURE OF CLAY	192	
Section 10.10	EFFECTS OF PLASTICITY ON CYCLIC BEHAVIOR OF CLAY	193	
Section 10.11	EFFECTS OF DENSITY ON SHEAR MODULUS OF CLAY	194	
Section 10.12	EFFECTS OF AGE ON SHEAR MODULUS OF CLAY	195	
Section 10.13	EFFECTS OF STRAIN AMPLITUDE ON SHEAR MODULUS OF CLAY	196	
Section 10.14	DEGRADATION OF SHEAR MODULUS OF CLAY	197	
Section 10.15	DAMPING RATIO OF CLAY	198	
Section 10.16	EFFECTS OF CONSOLIDATION TIME ON DAMPLING OF CLAY	199	
Section 10.17	G- $\gamma$ AND h- $\gamma$ CURVES OF UNDISTURBED SAMPLES	200	
Section 10.18	DYNAMIC DEFORMATION OF GRAVELLY SOILS	201	
Section 10.19	COLLECTING UNDISTURBED SOIL SAMPLES	202	
Section 10.20	FREEZING TECHNIQUE OF SAND SAMPLING	204	
Section 10.21	EXTENT OF SAMPLE DISTURBANCE	205	
Section 10.22	CORRELATION BETWEEN SURFACE VELOCITY AND STRAIN IN SUBSOIL	206	
Section 10.23	NONLINEAR CYCLIC BEHAVIOR OF SODIUM BENTONITE	208	
Section 10.24	NONLINEAR CYCLIC BEHAVIOR OF MUNICIPAL SOLID WASTE	210	









**Chapter 11 STRESS-STRAIN MODELS**

Section 11.1	HYPERBOLIC AND RAMBERG-OSGOOD STRESS-STRAIN MODELS	218	
Section 11.2	DILATANCY OF SAND SUBJECTED TO CYCLIC DRAINED SHEAR	221	
Section 11.3	THEORY OF ELASTOPLASTICITY	224	
Section 11.4	DILATANCY UNDER CYCLIC LOADING	228	
Section 11.5	MULTI-NONLINEAR SPRING MODEL	230	
Section 11.6	DISCRETE ELEMENT ANALYSIS	232	



**Chapter 12 APPLICATION OF SEISMIC INERTIA FORCE**

Section 12.1	CALCULATION OF EARTHQUAKE-INDUCED DISPLACEMENT	236	
Section 12.2	CORRELATION BETWEEN RESIDUAL DISPLACEMENT, BASE ACCELERATION AND BASE VELOCITY	238	
Section 12.3	RELATIONSHIP BETWEEN SEISMIC COEFFICIENT AND MAXIMUM ACCELERATION DURING EARTHQUAKES	239	
Section 12.4	BRIEF ANALYSIS ON SEISMIC COEFFICIENT EQUIVALENT TO MAXIMUM ACCELERATION	240	
Section 12.5	SEISMIC EARTH PRESSURE ON RETAINING WALL	241	
Section 12.6	SHAKING MODEL TEST ON SEISMIC EARTH PRESSURE	244	
Section 12.7	COMPARISON OF STATIC AND SEISMIC ACTIVE EARTH PRESSURES	247	
Section 12.8	MODIFIED MONONOBE-OKABE THEORY	248	




























**Chapter 13 SEISMIC FORCES EXERTED ON STRUCTURES**

Section 13.1	ANALYSIS ON SOIL-STRUCTURE INTERACTION	252	
Section 13.2	SEISMIC DESIGN OF EMBEDDED PIPELINE	255	
Section 13.3	AMPLIFICATION: SOIL COLUMN Vs SPRING-MASS MODEL	257	
Section 13.4	RIGOROUS COMPARISON OF SOIL COLUMN AND EQUIVALENT SPRING-MASS MODEL	259	
Section 13.5	SEISMIC WATER PRESSURE ON WALL	261	
Section 13.6	DYNAMIC EARTH PRESSURE EXERTED BY WATER SATURATED BACKFILL	263	
Section 13.7	DAMAGE IN TUNNELS CAUSED BY EARTHQUAKES	265	
Section 13.8	NODULAR PILE	267	









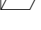
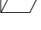





**Chapter 14 SEISMIC BEHAVIOR OF SLOPES AND EMBANKMENTS**

Section 14.1	CLASSIFICATION OF SEISMIC FAILURE OF ARTIFICIAL EMBANKMENT	271	
Section 14.2	EXAMPLE OF SLIDING FAILURE OF EMBANKMENT DUE TO EARTHQUAKES	273	



















## XIV List of Contents

Section 14.3	EXAMPLE OF SLUMPING OF EMBANKMENT DUE TO EARTHQUAKES	274	
Section 14.4	STATISTICS ON TYPES OF SUBSIDENCE OF EMBANKMENT DUE TO EARTHQUAKES	276	
Section 14.5	PERFORMANCE-BASED SEISMIC DESIGN	277	
Section 14.6	INQUIRY ON ALLOWABLE SEISMIC DISPLACEMENT	280	
Section 14.7	PRINCIPLE OF PERFORMANCE-BASED SEISMIC DESIGN AND LIFE CYCLE COST	282	
Section 14.8	RESTORATION OF DAMAGED FILL RESTING ON SOFT SOIL	288	
 <b>Chapter 15 LANDSLIDES</b>			
Section 15.1	EARTHQUAKE-INDUCED LANDSLIDES	291	
Section 15.2	YUNGAY CITY DESTROYED BY EARTHQUAKE-INDUCED DEBRIS FLOW	294	
Section 15.3	TSAOLING LANDSLIDE IN TAIWAN	296	
Section 15.4	SHEAR TESTS ON LANDSLIDE MECHANISM	298	
Section 15.5	OTHER LANDSLIDES CAUSED BY CHICHI EARTHQUAKE, TAIWAN	301	
Section 15.6	ASSESSMENT OF SEISMIC LANDSLIDE HAZARD	302	
Section 15.7	EARTHQUAKE-INDUCED SUBMARINE LANDSLIDES	306	
Section 15.8	NONSEISMIC SUBMARINE LANDSLIDES	308	
Section 15.9	DERIVATION OF FORMULA FOR APPARENT FRICTIONAL ANGLE	310	
 <b>Chapter 16 SEISMIC FAULTS</b>			
Section 16.1	TOPICS RELATED TO FAULT	315	
Section 16.2	EXAMPLE OF REVERSE FAULT	317	
Section 16.3	EXAMPLE OF NORMAL FAULT	319	
Section 16.4	EXAMPLE OF STRIKE-SLIP FAULT	320	
Section 16.5	EFFECTS OF FAULT MOVEMENT ON RUPTURE IN SURFACE SOIL	322	
Section 16.6	DISTORTION AT GROUND SURFACE PRODUCED BY SUBSURFACE FAULT	324	
Section 16.7	EFFECTS OF EARTHQUAKE FAULT ON TUNNELS	326	
Section 16.8	EFFECTS OF EARTHQUAKE FAULT ON EMBEDDED PIPELINES	328	
Section 16.9	FAULT-INDUCED SUBSIDENCE OF GROUND	330	
Section 16.10	TECTONICALLY INDUCED GROUND SUBSIDENCE INTO SEA DURING STRONG EARTHQUAKES IN KOHCHI, JAPAN	331	
Section 16.11	EARTHQUAKE-INDUCED SUBSIDENCE IN OTHER PARTS OF THE WORLD	333	
Section 16.12	GEOTECHNICAL ASPECTS OF TSUNAMI	335	













**PART 3 LIQUEFACTION****Chapter 17 FEATURES OF LIQUEFACTION-INDUCED DAMAGES**

Section 17.1	INTRODUCTION TO SEISMIC LIQUEFACTION	344	
Section 17.2	HISTORY OF PROBLEMS AND RESEARCH TOPICS CONCERNING LIQUEFACTION	346	
Section 17.3	LOSS OF BEARING CAPACITY CAUSED BY LIQUEFACTION	347	
Section 17.4	SUBSIDENCE OF EMBANKMENT DUE TO LIQUEFACTION	349	
Section 17.5	FLOATING OF EMBEDDED STRUCTURES	351	
Section 17.6	LATERAL DISPLACEMENT OF RETAINING WALL	352	
Section 17.7	LATERAL MOVEMENT OF LIQUEFIED SLOPE	353	
Section 17.8	GROUND SUBSIDENCE AFTER LIQUEFACTION	356	
Section 17.9	LIQUEFACTION-INDUCED SUBSIDENCE OF RIVER DIKES	357	
Section 17.10	LESSONS FROM 2000 TOTTORIKEN-SEIBU EARTHQUAKE	358	
Section 17.11	EARTHQUAKE INDUCED GROUND SUBSIDENCE	359	
Section 17.12	EARTHQUAKE MOTION RECORDED ON LIQUEFIED GROUND	360	
Section 17.13	SUBSIDENCE OF SHALLOW FOUNDATION DUE TO SUBSOIL LIQUEFACTION	361	
Section 17.14	LIQUEFACTION DAMAGE TO PRIVATE HOUSES	363	
Section 17.15	SUMMARY OF CASE HISTORIES	366	












**Chapter 18 MECHANISM OF ONSET OF LIQUEFACTION**

Section 18.1	MECHANISM OF LIQUEFACTION	370	
Section 18.2	SAND BOILING	372	
Section 18.3	DISSIPATION OF EXCESS PORE WATER PRESSURE	374	
Section 18.4	PALEOLIQUEFACTION	375	
Section 18.5	EXCAVATION OF BURIED SAND BOIL	376	
Section 18.6	HOT LIQUEFACTION; TRUE OR NOT TRUE	377	
Section 18.7	UNDRAINED SHEAR TESTS OF SAND	378	
Section 18.8	TORSION SHEAR DEVICE WITH HOLLOW CYLINDRICAL SPECIMEN	380	
Section 18.9	EFFECTS OF SUBSURFACE LIQUEFACTION ON INTENSITY OF ACCELERATION RESPONSE AT SURFACE	382	
Section 18.10	CONSOLIDATION AFTER LIQUEFACTION	383	
Section 18.11	LIQUEFACTION POTENTIAL AND SURFACE GEOLOGY	384	
Section 18.12	MAXIMUM DISTANCE OF LIQUEFACTION SITES FROM SOURCE AREA	386	
Section 18.13	EFFECTS OF AGEING ON LIQUEFACTION STRENGTH OF FILL	387	
Section 18.14	LIQUEFACTION IN NATURAL DEPOSIT OF LOOSE SAND	390	
Section 18.15	SIGNIFICANCE OF CYCLIC TRIAXIAL TESTS IN LIQUEFACTION PROBLEMS	391	
Section 18.16	SKEMPTON'S B VALUE	392	
Section 18.17	DEGREE OF SATURATION AND SKEMPTON'S B VALUE	394	
Section 18.18	EFFECTS OF SAMPLE PREPARATION METHODS ON RESISTANCE TO LIQUEFACTION IN LABORATORY SHEAR TESTS	396	

**Chapter 19 ASSESSMENT OF LIQUEFACTION POTENTIAL**























Section 19.1	SIGNIFICANCE OF STRESS RATIO	402	
Section 19.2	STRESS RATIO IN THE FIELD	404	
Section 19.3	LIQUEFACTION CURVE	406	
Section 19.4	FIELD AND LABORATORY STRESS RATIO	408	
Section 19.5	EFFECTS OF STATIC SHEAR STRESS ON RESISTANCE AGAINST LIQUEFACTION	410	
Section 19.6	IMPORTANCE OF TWO-WAY LOADING IN CYCLIC SHEAR WITH INITIAL STATIC STRESS	412	
Section 19.7	EFFECTS OF $K_0$ CONSOLIDATION ON LIQUEFACTION RESISTANCE OF SAND	414	
Section 19.8	LIQUEFACTION RESISTANCE OF SAND UNDER $K_0$ CONDITION AND OVER CONSOLIDATION	415	
Section 19.9	EFFECTS OF CONFINING PRESSURE ON LIQUEFACTION RESISTANCE	418	
Section 19.10	EFFECTS OF IRREGULAR LOADING ON RESISTANCE AGAINST LIQUEFACTION	420	
Section 19.11	CORRECTION OF STRESS RATIO WITH DEPTH	422	
Section 19.12	EFFECTS OF MULTI-DIRECTIONAL SHEAR ON LIQUEFACTION RESISTANCE	424	

**Chapter 20 BEHAVIOR OF SOIL UNDERGOING CYCLIC UNDRAINED LOADING**










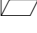




Section 20.1	LIQUEFACTION RESISTANCE OF DENSE SAND	430	
Section 20.2	CYCLIC UNDRAINED SHEAR OF GRAVEL	432	
Section 20.3	CYCLIC UNDRAINED SHEAR OF CLAY	433	
Section 20.4	DOES CLAY LIQUEFY?	435	
Section 20.5	LIQUEFACTION OF TAILING MATERIAL	437	
Section 20.6	EMPIRICAL RELATIONSHIP BETWEEN EXCESS PORE WATER PRESSURE AND NUMBER OF LOADING CYCLES	439	
Section 20.7	SIMPLE ASSESSMENTS OF PORE PRESSURE RISE	440	
Section 20.8	USE OF STRAIN ENERGY IN MODELLING OF SOIL UNDERGOING CYCLIC LOADING	441	
Section 20.9	CORRELATION BETWEEN SHEAR STRAIN ENERGY AND EXCESS PORE WATER PRESSURE	442	
Section 20.10	ENERGY CORRELATION OF PORE PRESSURE AT STATES OF SHEAR STRESS	444	
Section 20.11	STRESS–STRAIN BEHAVIOR REPRODUCED FROM ACCELERATION RECORDS	446	

**Chapter 21 IN-SITU TESTS ON LIQUEFACTION POTENTIAL OF SUBSOILS**


















Section 21.1	USE OF SPT FOR ASSESSING LIQUEFACTION POTENTIAL	450	
Section 21.2	SPT- $N$ OBSERVED IN NIIGATA CITY	452	

Section 21.3	ASSESSMENT OF LIQUEFACTION POTENTIAL	453	
Section 21.4	ASSESSMENT OF LIQUEFACTION POTENTIAL BY SPT-N BEFORE 1995	454	
Section 21.5	Exercise No.6: CALCULATION OF FACTOR OF SAFETY AGAINST LIQUEFACTION	456	
Section 21.6	ISSUES FOR FUTURE DEVELOPMENT OF CODE	457	
Section 21.7	REVISED DESIGN PREDICTION OF LIQUEFACTION AFTER 1995 (Part 1; Design load)	458	
Section 21.8	REVISED DESIGN PREDICTION OF LIQUEFACTION AFTER 1995 (Part 2; Resistance against liquefaction)	459	
Section 21.9	FACTOR OF SAFETY AGAINST LIQUEFACTION AND ITS CORRELATION WITH EXTENT OF DAMAGE	461	
Section 21.10	EFFECTS OF FREQUENCY ON LIQUEFACTION RESISTANCE	463	
Section 21.11	USE OF CONE PENETRATION TESTS FOR EARTHQUAKE GEOTECHNICAL SURVEY	464	
Section 21.12	USE OF S-WAVE VELOCITY FOR LIQUEFACTION INVESTIGATION	467	
<b>Chapter 22 POST-LIQUEFACTION BEHAVIOR OF SANDY GROUND</b>			
Section 22.1	GROUND SUBSIDENCE AFTER LIQUEFACTION	471	
Section 22.2	REPEATED LIQUEFACTION	473	
Section 22.3	EFFECTIVE STRESS ANALYSIS WITH HYPERBOLIC MODEL	475	
Section 22.4	EXAMPLE OF EFFECTIVE STRESS ANALYSIS	477	
Section 22.5	ASSESSMENT OF LIQUEFACTION RESISTANCE BY MEASURING SHEAR WAVE VELOCITY	481	
<b>Chapter 23 IMMEDIATE DETECTION OF LIQUEFACTION DAMAGE AND EMERGENCY ACTION</b>			
Section 23.1	RESPONSE SPECTRUM	484	
Section 23.2	SPECTRUM INTENSITY	485	
Section 23.3	IMMEDIATE DETECTION OF SUBSOIL LIQUEFACTION BY USING SPECTRUM INTENSITY (SI) - PRINCIPLE -	489	
Section 23.4	IMMEDIATE DETECTION OF SUBSOIL LIQUEFACTION BY USING SPECTRUM INTENSITY (SI) - EXAMPLE -	491	
<b>Chapter 24 PERMANENT DISPLACEMENT / DEFORMATION OF LIQUEFIED SUBSOIL</b>			
Section 24.1	LATERAL DISPLACEMENT OF LIQUEFIED SUBSOIL	494	
Section 24.2	LATERAL DISPLACEMENT OF QUAY WALL INDUCED BY SUBSURFACE LIQUEFACTION	496	
Section 24.3	STEADY STATE AND STATIC LIQUEFACTION	498	
























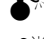




XVIII List of Contents

Section 24.4	SMALL SHAKING TABLE TESTS ON LATERAL DISPLACEMENT	501	
Section 24.5	ROLE PLAYED BY GRAVITY	502	
Section 24.6	BEHAVIOR OF SURFACE DRY CRUST	503	
Section 24.7	SHAKING TABLE TESTS ON LATERAL SOIL DISPLACEMENT	505	
Section 24.8	NEED FOR TESTS ON EXTREMELY LOOSE SANDY DEPOSITS	506	
Section 24.9	SHAKING TABLE TESTS ON EXTREMELY LOOSE DEPOSIT	508	
Section 24.10	SHAKING TABLE TESTS ON DISTORTION OF CAISSON QUAY WALL DURING EARTHQUAKES	509	
Section 24.11	GEOTECHNICAL CENTRIFUGE MODEL TESTS	511	
Section 24.12	LAW OF SIMILITUDE IN DYNAMIC CENTRIFUGE TESTS	513	
Section 24.13	1-G SHAKING TABLE TESTS	517	
Section 24.14	LAW OF SIMILITUDE FOR 1-G SHAKING TESTS	520	
Section 24.15	ONLINE TESTS	524	
Section 24.16	INTERACTION BETWEEN PILE AND LATERAL FLOW OF LIQUEFIED SAND	525	
Section 24.17	EARTH PRESSURE ON WALL EXERTED BY LIQUEFIED SUBSOIL	532	

**Chapter 25 PREDICTION OF PERMANENT DISPLACEMENT DUE TO LIQUEFACTION**

Section 25.1	MODE OF DISPLACEMENT	538	
Section 25.2	PRINCIPLE OF MINIMUM POTENTIAL ENERGY	540	
Section 25.3	PRINCIPLE OF LAGRANGEAN EQUATION OF MOTION	542	
Section 25.4	ENERGY THEORY ON FLOW OF LIQUEFIED SUBSOIL	544	
Section 25.5	VARIATIONAL PRINCIPLE AND ITS EULER'S DIFFERENTIAL EQUATION	546	
Section 25.6	PREDICTION OF LATERAL DISPLACEMENT	548	
Section 25.7	CLOSED FORM SOLUTION OF MAXIMUM POSSIBLE DISPLACEMENT	550	
Section 25.8	BOUNDARY CONDITIONS OF SOIL MASS UNDERGOING LATERAL FLOW	551	
Section 25.9	EXAMPLE PREDICTION OF LATERAL DISPLACEMENT	553	
Section 25.10	PARAMETRIC STUDIES ON LATERAL DISPLACEMENT	555	
Section 25.11	THREE DIMENSIONAL PREDICTION OF LATERAL DISPLACEMENT OF LIQUEFIED DEPOSIT	557	
Section 25.12	GLACIER AS SEEN FROM AIRCRAFT	559	
Section 25.13	DRAG FORCE OF EMBEDDED PIPE IN LIQUEFIED MODEL GROUND	560	
Section 25.14	RATE-DEPENDENCY OF LIQUEFIED SAND	561	
Section 25.15	EFFECTS OF CONTINUED SHAKING ON BEHAVIOR OF LIQUEFIED SAND	563	
Section 25.16	ATTEMPT TO MEASURE VISCOSITY OF LIQUEFIED SAND IN SHEAR TESTS	565	
Section 25.17	VISCOSITY OF LIQUEFIED SAND MEASURED IN LABORATORY TESTS	566	



Section 25.18	OBSERVED RATE OF STRAIN DURING LIQUEFACTION-INDUCED GROUND DEFORMATION	570	
Section 25.19	THREE-DIMENSIONAL DYNAMIC ANALYSIS ON LIQUEFACTION-INDUCED PERMANENT DEFORMATION OF GROUND	572	
Section 25.20	EXAMPLE OF THREE-DIMENSIONAL ANALYSIS ON LIQUEFACTION-INDUCED PERMANENT DEFORMATION OF GROUND	574	
Section 25.21	LATERAL LOAD ON PILE FOUNDATION EXERTED BY LATERAL DISPLACEMENT OF LIQUEFIED GROUND	576	
Section 25.22	PASSIVE EARTH PRESSURE EXERTED BY SURFACE UNLIQUEFIED SOIL ON FOUNDATION OF STRUCTURES	577	
Section 25.23	DEFORMATION ANALYSIS BASED ON STRAIN POTENTIAL	578	
Section 25.24	ANALYSIS ON SEISMIC DEFORMATION OF LIYUTAN DAM IN TAIWAN	580	
Section 25.25	ASSESSMENT OF SUBSIDENCE OF RIVER DIKES DUE TO SUBSURFACE LIQUEFACTION BY USING LIMIT EQUILIBRIUM ANALYSIS	582	
Section 25.26	WATER FILM	583	
 <b>Chapter 26 MITIGATION OF LIQUEFACTION-INDUCED DAMAGE</b>			
Section 26.1	PRINCIPLES IN MITIGATION OF LIQUEFACTION-INDUCED DAMAGE	589	
Section 26.2	PRINCIPLES IN PREVENTION OF LIQUEFACTION	592	
Section 26.3	MITIGATION OF LIQUEFACTION-INDUCED GROUND DISPLACEMENT	593	
Section 26.4	SAND COMPACTION PILE FOR DENSIFICATION OF LOOSE SAND	604	
Section 26.5	GROUND IMPROVEMENT BY COMPACTION	606	
Section 26.6	STATIC INSTALLATION OF SAND COMPACTION PILES	609	
Section 26.7	DYNAMIC CONSOLIDATION	610	
Section 26.8	VERIFICATION OF EFFECTS OF DYNAMIC CONSOLIDATION	612	
Section 26.9	RANGE OF SAND DENSIFICATION	613	
Section 26.10	COMPACTION GROUTING	614	
Section 26.11	DISSIPATION OF EXCESS PORE WATER PRESSURE	616	
Section 26.12	LOWERING OF GROUND WATER TABLE	621	
Section 26.13	GROUTING AND DEEP MIXING	622	
Section 26.14	SOLIDIFICATION BY COLLOIDAL SILICA GROUT	625	
Section 26.15	PREMIXING METHOD	631	
Section 26.16	SOIL DENSIFICATION BY BLASTING	633	
Section 26.17	BACKFILLING BY SHREDDED TIRE CHIPS	637	
 <b>Chapter 27 SEISMIC MICROZONATION</b>			
Section 27.1	MICROZONATION FOR INTENSITY OF EARTHQUAKE MOTION	644	
Section 27.2	MICROZONATION FOR LIQUEFACTION	647	

APPENDIX

APPENDIX 1	DERIVATION OF COULOMB'S ACTIVE EARTH PRESSURE FORMULA	652
APPENDIX 2	CONVENIENT EXPRESSIONS IN INTERNATIONAL CONVERSIONS	662
APPENDIX 3	APPLICATION OF VARIATIONAL PRINCIPLE OF MATHEMATICS TO DEFORMATION ANALYSIS	664

ANSWER TO EXERCISES	667
---------------------	-----

ACKNOWLEDGMENT	677
----------------	-----

INDEX	679
-------	-----

IMPORTANT MESSAGES

Since the total number of pages in this book is large, readers should pick up pages of their interest and not to read unnecessary pages.

Future correction and addition of the contents of this book will be announced in his website in the geotechnical engineering laboratory, Department of Civil Engineering, University of Tokyo. Try <http://geotle.t.u-tokyo.ac.jp>.

# PART 1

## Knowledge of Soil Mechanics



Machu Picchu, Peru

Machu Picchu is located at the top of a mountain which was far from the main transportation route at the bottom of a valley. Therefore, it was not found by modern people for a long time. This important cultural heritage is currently endangered by slope instability.

# Chapter 1




## Basic Principles in Soil Mechanics



Tomb of Li Yuanhao 李元昊

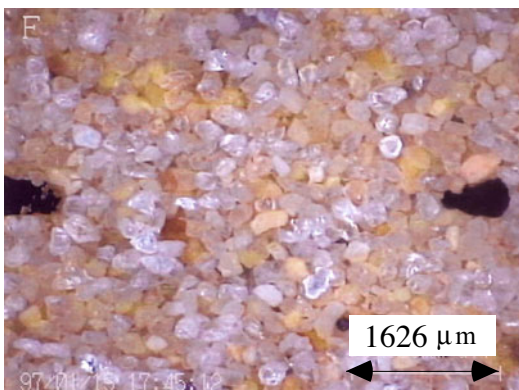
The Tangut people established their kingdom of Western Xia 西夏 in the present Ningxia 寧夏 Hui Autonomous Region, Northwest China. The first emperor, Li Yuanhao, started his reign in 1038 and his empire became prosperous with income from the silk road trading. His tomb near Yinchuan 銀川 City used to be covered by beautiful tile decoration.

The contents of this book are classified into three groups that concern

- Elementary topics with a symbol of 
- Advanced topics designated by 
- Miscellaneous topics accompanied by 

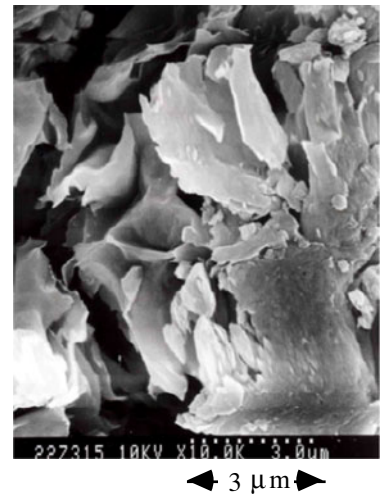
Readers can choose sections that are important and relevant to their personal interests. They do not have to spend a long time by reading all the pages.

 1.1 Physical Properties of Soil



Particle size is approximately 180 μm

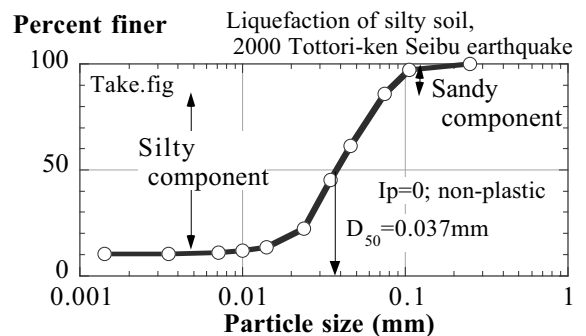
**Fig. 1.1** Microscopic photograph of Toyoura sand



**Fig. 1.2** Electronic microscopic photograph of bentonite clay (Towhata et al., 1993)

Soil is classified primarily into two categories; namely granular materials and cohesive soils. The former consists of gravel, sand, and cohesionless silts (Fig. 1.1), while the latter is clayey soil (Fig. 1.2). The mechanical properties of granular soils are governed by the grain-to-grain contact as well as friction. Hence, the magnitude of contact force and the geometrical nature of grain packing play major roles. It should be recalled that the magnitude of contact pressure per unit area of soil is called the effective stress, which is the most important concept in modern soil mechanics. In clayey soils, in contrast, chemical and electrical interactions among clay particles are important as well. Hence, shear strength is activated even at zero effective stress when the past stress-strain history allows it. Liquid limit (LL) and plastic limit (PL), which are called the Atterberg limits in combination, are two measures to evaluate the magnitudes of interparticle actions in addition to effective stress. The plasticity index, PI or  $I_p$ , is defined by  $PI = LL - PL$ . Generally speaking, PI of most clays lies in the range of 40–80 with such an exception of 400 or more of the sodium smectite (bentonite) group. As per 2006, the Japanese soil mechanic practice does not put “%” to the number of PI.

Another major difference between granular and cohesive soils lies in the grain size. The size affects the hydraulic conductivity (permeability or possibility of ground water to flow through soil). In conventional soil mechanics, grains larger than 75 μm are called



**Fig. 1.3** Particle size distribution curve of silty liquefied soil

sand and those larger than 2,000  $\mu\text{m}$  (2 mm) are gravel. On the other hand, particles smaller than 5  $\mu\text{m}$  are clay in which chemical and electrical forces (cohesion) are important. Silt is a name of particles between 5 and 75  $\mu\text{m}$ . Being called fine soils together with clay, silt has two groups. The first one is a plastic silt which includes clay minerals and has cohesion. The second group is nonplastic; being composed of small sand-like grains without cohesion. The difference of two silty soils should be borne in mind.

Figure 1.3 illustrates the particle size distribution of nonplastic silt, which liquefied during an earthquake (Sect. 17.10). The vertical coordinate denotes the accumulated (weight) percentage finer than the horizontal coordinate. Note that almost 80% of grains lies in the range of silt. The particle size at 50% is called the mean grain size,  $D_{50}$ . Hence, 50% of the total weight of soil is finer than  $D_{50}$ .

## 1.2 Weight and Density of Soil

The specific gravity, designated by  $G_s$ , stands for the mass density of minerals that compose grains divided by that of water. Hence, a unit volume of soil grain has a weight of  $G_s\gamma_w$ . Since most soil grains are made up similarly of silicate minerals,  $G_s$  of many soils, whether sandy or clayey, lies in the range of 2.6–2.75.

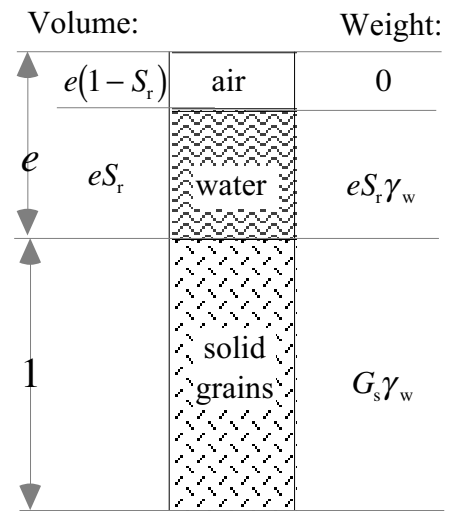
The weight of soil is important in calculating the earth pressure. When the weight of soil per unit volume,  $\gamma$ , is known, the overburden pressure (the vertical stress or the vertical compressional force per unit area) at the depth of  $z$  is given by  $\sigma_z = \gamma z$ . The range of  $\gamma$  is approximately around 15 (kN/m<sup>3</sup>) when soil is dry, and is 19–20 (kN/m<sup>3</sup>) or more under the ground water table. Soil is called water-saturated when the void space among solid particles is fully occupied by water, without air or gas bubbles. The extent of water-saturation is expressed by the degree of saturation,  $S_r$ .  $S_r = 1.0$  (100%) when soil is fully saturated, and  $S_r = 0.0$  when dry. Accordingly, the unit weight of soil is calculated by

$$\gamma = \frac{G_s\gamma_w + eS_r\gamma_w}{1 + e}, \quad (1.1)$$

where  $\gamma_w$  is the unit weight of water (9.8 kN/m<sup>3</sup>) and “ $e$ ” is called void ratio, which is the ratio of open void volume among solid grains against the volume of solid phase, see Fig. 1.4. Moreover, the water content is defined by means of weight ratio;

$$\begin{aligned} \text{Water content } w &= \text{ratio of weights of water and solid} \\ &= \frac{eS_r}{G_s}. \end{aligned} \quad (1.2)$$

In practice, soils under the ground water table is safely assumed to be 100 % saturated with water,  $S_r = 1.0$  in (1.2).



**Fig. 1.4** Definition of void ratio

Section 1.3 will deal with the effective stress, which stands for the magnitude of contact force between soil grains. The effective stress plays an extremely important role in soil mechanics because the behavior of soil is strongly affected by grain-to-grain contact force. In contrast, the conventional kind of stress, which is the extent of force per unit area of soil and is referred to as the total stress, is less important. The overburden pressure as mentioned above is one of the total stresses.

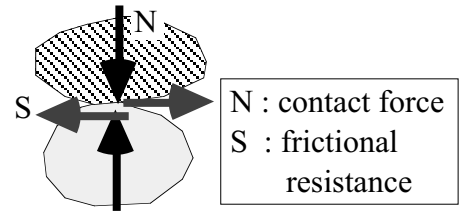
The mechanical behavior and, for example, liquefaction resistance of sand are deeply affected by the state of granular packing. Denser packing improves the behavior of sand. This feature cannot be fully accounted for by void ratio ( $e$ ) because the range of  $e$  taken by sand is varied by the grain shape and its surface roughness, and any sand is similarly weak at its maximum value of  $e$ . Therefore, a new parameter called the relative density ( $D_r$ ) was introduced.  $D_r = 0\%$  when sand is in the loosest state (void ratio  $e = e_{\max}$ ), and  $D_r = 100\%$  when sand is in the densest state ( $e = e_{\min}$ ).

$$D_r = \frac{e_{\max} - e}{e_{\max} - e_{\min}} \times 100(\%). \quad (1.3)$$

Values of  $e_{\max}$  and  $e_{\min}$  are determined by several specified methods under zero overburden pressure. For example, soft sedimentation of dry sand or sedimentation in water is employed for the loosest grain packing ( $e_{\max}$ ) and continued shaking for the densest state ( $e_{\min}$ ). Note that states of loosest and densest packing change under higher pressures.  $D_r = 0\%$  may be looser than the state of loosest packing under 100 kPa.

**1.3 Effective Stress and Pore Water Pressure**

Sand at a depth of 100 m has greater shear rigidity and shear strength than the same type of sand at the ground surface. Although this difference may be partly due to density and geological history, its major cause is the strong contact forces between sand particles. Since the slipping at particle-to-particle contacts is a frictional phenomenon (Fig. 1.5), the greater contact force makes slippage difficult to occur, and increases the overall shear rigidity and strength. Thus, sand at a deep elevation is reinforced by the generation of high contact forces due to the weight of overlying soils.



**Fig. 1.5** Illustration of role played by intergranular contact force

The difference between the effective stress and the conventional (total) stress is found in the consideration of pore pressures. Pore pressure means the pressure of air and water in the pore (void among solid grains). When soil is saturated with water, pore air pressure is not of concern, and pore water pressure is designated by “*u*.” Since pore water is one of the constituents of soil, the overburden pressure (vertical total stress) includes pore water pressure effects.

Pore water pressure does not affect the generation of frictional resistance at contact points as illustrated in Fig. 1.5. To understand this, compare the same sands, one is situated at the ground surface and the other upon the seabed at 10,000 m water depth. Clearly, the former has null total stress and the latter has 100 MPa. In spite of the high total stress, the seabed sand is soft due to null contact pressure. Note that pore water pressure at 10,000 m depth is 100 MPa, which is equal to the total vertical stress.

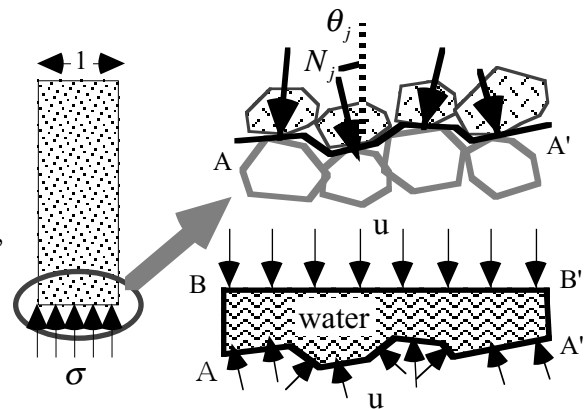
The idea of effective stress,  $\sigma'$ , was introduced to understand the above discussion. With “ $\sigma'$ ” as a symbol of effective stress,

$$\sigma' = \sigma - u. \tag{1.4}$$

For more information, refer to Fig. 18.2. At the seabed, therefore, the effective stress is

$$\sigma - u = 100 \text{ MPa} - 100 \text{ MPa} = 0 \text{ MPa}$$

and the behavior of seabed sand is similar to sand at the ground surface. Equation (1.4) is valid not only for the vertical stress but normal stresses in any directions. Shear stress in contrast does not have an idea of effective stress because pore water pressure does not have a shear component.



**Fig. 1.6** Interpretation of physical meaning of effective stress

To understand the significance of effective stress, Figure 1.6 studies the force equilibrium of a soil column. The weight of the column with a unit cross section is equal to the total stress,  $\sigma$ . This is in equilibrium with the vertical components of pore water pressure,  $\int_A^{A'} u \cos \theta ds$  and those of contact forces,  $\sum N_j \cos \theta_j$ , along  $AA'$ , in which  $N_j$  is the magnitude of contact force and  $\theta$  as well as  $\theta_j$  is the direction. The summation and integration are made along  $AA'$ , which is a curved bottom of the soil column that passes through pores and the granular contact points but never goes into grains. Another



force equilibrium shows that the integration of pore water along  $AA'$  is equal to the pore pressure,  $u$ , in a planar top of  $BB'$  ( $AB$  and  $A'B' \ll BB' = l$ ),

$$\sigma = u + \sum N_j \cos \theta_j. \quad (1.5)$$

By comparing (1.4) and (1.5),

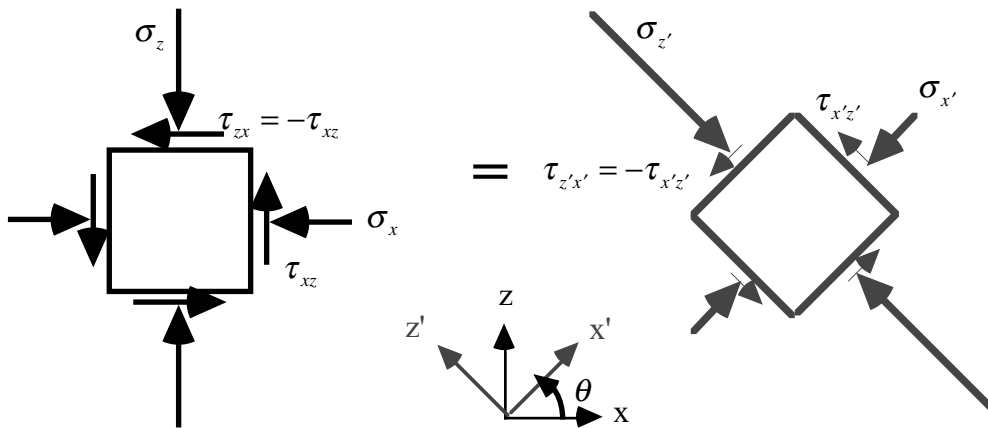
$$\sigma' = \sum N_j \cos \theta_j. \quad (1.6)$$

Thus, effective stress means a summation of granular contact forces per unit area in the direction of interest.

In a two-dimensional space in Fig. 1.7, there are three total stress components, and among them the normal stress components of  $\sigma_x$  and  $\sigma_z$  have effective stress components,  $\sigma'_x = \sigma_x - u$  and  $\sigma'_z = \sigma_z - u$ . Note that the stress difference or shear component is identical for both total and effective stresses,

$$\sigma_z - \sigma_x = \sigma'_z - \sigma'_x. \quad (1.7)$$

For any given stress state, the nominal values of stress components,  $\sigma_x$ ,  $\sigma_z$ , and  $\tau_{xz}$ , vary with the choice of coordinate system (direction of  $x$  and  $z$  axes). In Fig. 1.7, normal stress is positive in compression and shear stress is positive when it is oriented in counterclockwise direction. After rotation of the coordinate system by an angle of  $\theta$  in the counterclockwise direction from  $x-z$  to  $x'-z'$  system, the values of new stress components are calculated by using the theory of Mohr stress circle (Fig. 1.8).

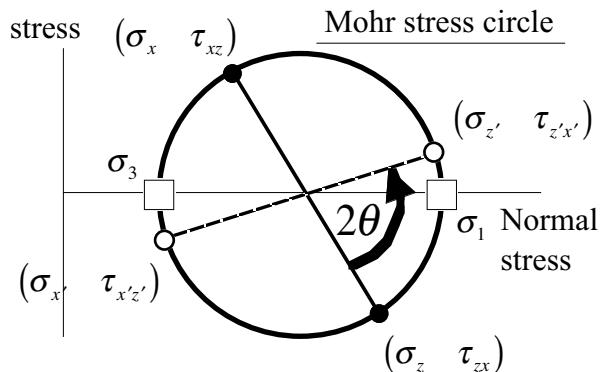


**Fig. 1.7** Stress components undergoing rotation of coordinate system  
Shear

By travelling along the Mohr stress circle in the counterclockwise direction by  $2 \times \theta$ ,

$$\begin{aligned} \sigma_{x'} &= \frac{\sigma_x + \sigma_z}{2} + \frac{\sigma_x - \sigma_z}{2} \cos 2\theta + \frac{\tau_{zx} - \tau_{xz}}{2} \sin 2\theta \\ \tau_{x'z'} &= \frac{\sigma_x - \sigma_z}{2} \sin 2\theta + \frac{\tau_{zx} + \tau_{xz}}{2} - \frac{\tau_{zx} - \tau_{xz}}{2} \cos 2\theta \end{aligned} \quad (1.8)$$

$$\begin{aligned} \sigma_{z'} &= \frac{\sigma_x + \sigma_z}{2} - \frac{\sigma_x - \sigma_z}{2} \cos 2\theta - \frac{\tau_{zx} - \tau_{xz}}{2} \sin 2\theta \\ \tau_{z'x'} &= -\frac{\sigma_x - \sigma_z}{2} \sin 2\theta + \frac{\tau_{zx} + \tau_{xz}}{2} + \frac{\tau_{zx} - \tau_{xz}}{2} \cos 2\theta \end{aligned}$$



**Fig. 1.8** Conversion of stress components after rotation of coordinate axes

Equation (1.8) is further simplified because  $\tau_{zx} = -\tau_{xz}$ . It is important that the mean value of normal stresses is independent of coordinate rotation,

$$\frac{\sigma_x + \sigma_z}{2} = \frac{\sigma_{x'} + \sigma_{z'}}{2}. \quad (1.9)$$

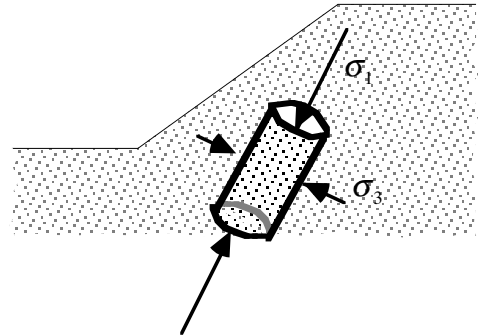
Figure 1.8 indicates that the stress circle crosses the horizontal axis at two points at which

$$\sigma = \frac{\sigma_x + \sigma_z}{2} \pm \sqrt{\left(\frac{\sigma_x - \sigma_z}{2}\right)^2 + \tau_{xz}^2}. \quad (1.10)$$

Since these points have zero vertical coordinate, it is found that any stress states have two special planes, which have only normal stress components (1.10) and zero shear stress. These stress components are called principal stresses: major principal stress,  $\sigma_1$ , > minor principal stress,  $\sigma_3$ . The orientation of principal stress components are obtained by the geometric relationship in Fig. 1.8.

Direction of  $\sigma_1$  plane is directed from the plane of  $\sigma_z$  at an angle of  $\beta$  in the counterclockwise direction;

$$\beta = -\frac{1}{2} \arctan \frac{2\tau_{zx}}{\sigma_z - \sigma_x}. \quad (1.11)$$



**Fig. 1.9** Reproduction of field stress state in triaxial specimen

One of the important aims of unconfined and triaxial compression tests of soil mechanics is to reproduce the principal stress states in a cylindrical soil specimens and measure the deformation, which is equivalent to the field condition (Fig. 1.9). Note moreover that the above discussion concerning total stress is exactly valid for effective stress components as well.

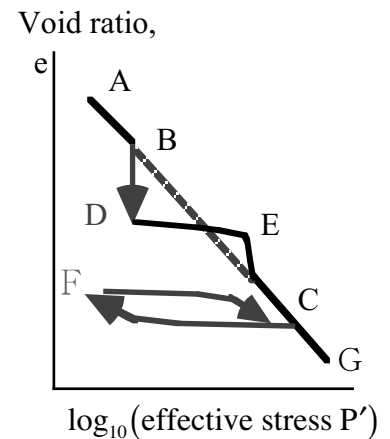
### 1.4 Consideration and Volume Change

Volume of soil varies with the effective stress. More accurately, the size of space (called void or pore) among solid grains decreases when the grain-to-grain contact forces increase. This is called primary consolidation. When the increment of effective stress,  $\Delta P'$ , is small, there is a proportionality between  $\Delta P'$  and the volumetric strain of soil,  $\Delta \epsilon_{\text{vol}}$ ,

$$\Delta \epsilon_{\text{vol}} = m_v \Delta P', \quad (1.12)$$

where  $m_v$  is called the volume compressibility of soil. The subsidence induced by consolidation has long been a problem in soft clayey deposits subjected to surcharge or pumping of water. Both kinds of human activity increases the effective stress and induces the ground subsidence.

Terzaghi's classic theory of consolidation hypothesized that the volume change of soil is proportional to the increase of the vertical effective stress. More precisely, however, linear proportionality is not true. A semilogarithmically linear relationship as AG in Fig. 1.10 is often used in practice.



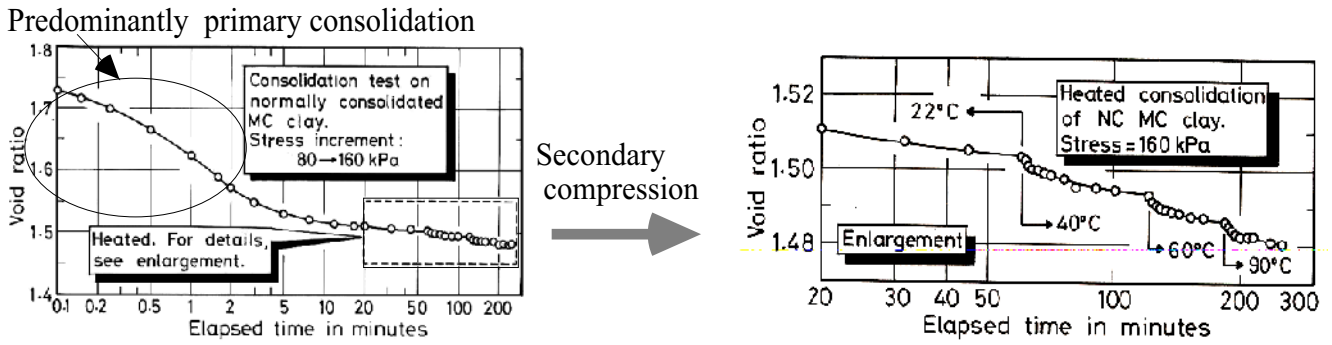
**Fig. 1.10** So called “ $e - \log P$ ” diagram on consolidation of soil

1. When consolidation starts from a state of slurry (mud) and the effective stress,  $P'$ , increases continuously, the state of soil follows a linear path, ABCG, in Fig. 1.10. Soil in this process is called normally consolidated; the current stress is the highest as so far experienced. This is the case in alluvial plane where sedimentation occurs continuously.
2. The diagram in Fig. 1.10 should be called “ $e - \log P$ ” diagram” but conventionally called  $e - \log P$  diagram. Anyway, the horizontal coordinate stands for either the effective vertical stress or the mean of three effective stresses in orthogonal directions (effective mean principal stress).
3. When the effective stress is held constant at B, the process of secondary compression occurs and the volume decreases with time. Then loading resumes at D and the clay follows the path of DEC. Until E, the volume change is relatively small; after yielding at E, soil becomes normally consolidated. It is often the case that the point E lies above the normal consolidation line (AG).
4. Decrease of stress on CF is called unloading. The void ratio (or soil volume) does not come back to the original level at A. Thus, deformation of soil is irreversible. Then, the reloading from F back towards C follows a path similar to CF; after C, normal consolidation starts again towards G.
5. Soil in CFC is called overconsolidated. Overconsolidated soil is thus characterized by minor volume change upon loading, The overconsolidation ratio is defined by

$$OCR \equiv (\text{Ever highest effective stress}) / (\text{Present effective stress}) = \frac{P'_{\text{at C}}}{P'}$$

6. The resemblance of DEC curve and FCG is noteworthy; significant volume contraction starts after an intermediate point. Note that this nature is induced by different mechanisms. Secondary compression or ageing (volume contraction under constant stress in BD) results are less volume change in DE, and the transfer of stress state from unloading (CF) / reloading (FC) to primary compression (CG) is important in FCG.

Primary consolidation is generated by compression of grain structure of soil due to change of effective stress. Little is known about secondary compression in contrast. Figure 1.11 shows that secondary compression in clay was accelerated by heating due possibly to thermal excitation of  $\text{H}_2\text{O}$  molecules that are electrically absorbed on surface of clay mineral.



**Fig. 1.11** Acceleration of secondary compression by heating of clay (Towhata et al. 1993)

The time required for the completion of consolidation settlement (completion of primary consolidation) is always important in practice. In principle, the consolidation time is governed by the amount of water that is drained out of ground (volume compressibility,  $m_v$ ), the thickness of soil deposit (more precisely, the length of water drainage,  $H$ ), and the easiness of water flow through clay (permeability,  $k$ , in Sec. 1.13). As illustrated in Fig. 1.12, the thickness of  $H$  stands for the length of water drainage. Many students, however, confuses this  $H$  with the thickness of clay deposits. When water is drained in both upward and downward directions due to good pervious layer at the bottom,  $H$  is half of the clay thickness.

Figure 1.13 illustrates the results of Terzaghi’s consolidation theory for a situation in which the ground surface is loaded by  $\Delta P$  at time = 0. The nondimensional time ( $T$ ) and the degree of consolidation ( $U$ ) are defined by

$$T = \frac{\left( \frac{k}{m_v \gamma_w} \right) \times \text{time}}{H^2} \text{ and}$$

$$U = \text{subsidence/ultimate subsidence, (1.13)}$$

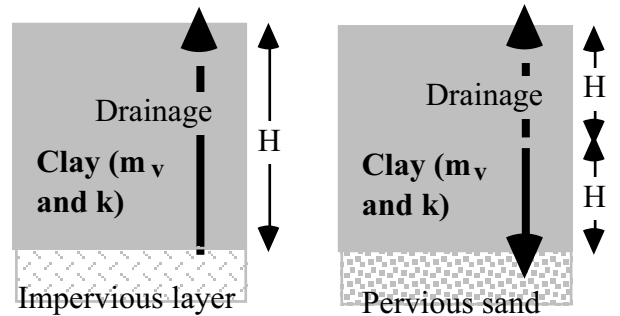
respectively, and  $\gamma_w = 9.8 \text{ kN/m}^3$  stands for the unit weight of water. Note that the ultimate subsidence is given by  $m_v \Delta P \times (\text{thickness of soil})$ . As mentioned before, this thickness of soil may be different from the drainage distance ( $H$ ). The curve in Fig. 1.13 never comes to  $U=100\%$ . In practice, therefore, the time for 90% consolidation ( $U=90\%$ ) is frequently referred to as an idea of time which is needed for consolidation

$$T=0.848 \text{ and}$$

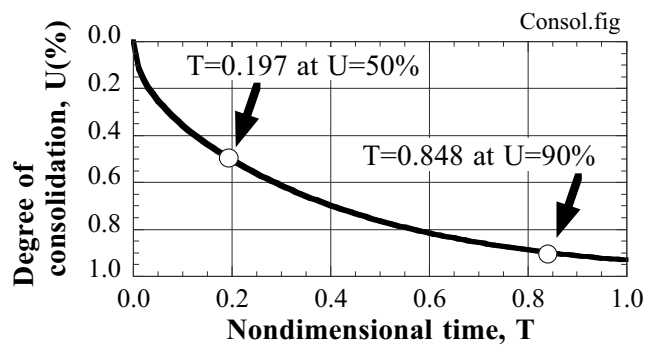
$$\text{Time needed for 90\% consolidation}$$

$$= 0.848 \times \frac{H^2}{k/m_v \gamma_w}. \quad (1.14)$$

Thus, the consolidation time increases in proportion to  $H^2$ . For shortening of consolidation time, it is essential to make the drainage length as short as possible.



**Fig. 1.12** Drainage of water from subsoil and consequent consolidation settlement



**Fig. 1.13** Terzaghi’s theoretical progress of consolidation settlement

1.5 Shear Deformation and Strength of Sand

The concept of “shear test” is understood by beginners more easily when a direct shear device is quoted than when a popular triaxial apparatus is. Figure 1.14 illustrates this device in which a sand specimen is placed between two rigid containers. After applying the effective (confining) stress in the vertical direction, the containers are forced to move laterally so that shear distortion occurs in the specimen. The shear stress is normally obtained by dividing the shear force by the cross section of the specimen. Since the strain in the specimen is not uniform, the extent of shear deformation is represented by the shear displacement. The vertical displacement of the upper container stands for the volume change of sand during shear (dilatancy).

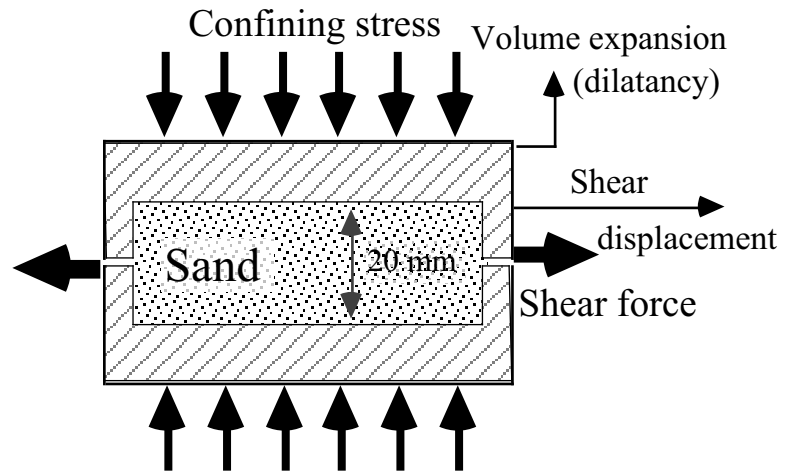


Fig. 1.14 Direct shear test

Figure 1.15 shows the relationship between shear stress and shear displacement. In the course of shear, the confining stress was maintained constant. This manner of test is called drained shear in soil mechanics because the volume of the specimen changes and causes flow (drainage) of pore water if sand is saturated with water. This figure demonstrates first that the stress-deformation relationship is not linear. Thus, the idea of linear elasticity has a limited significance in soil. Second, the peak shear stress increases with the effective stress. Thus, the shear strength of sand is interpreted by a frictional view point. Coulomb’s failure criterion states

$$\text{Shear strength} = \text{Effective stress} \times \tan \phi \quad (:\text{Coulomb’s failure criterion}), \quad (1.15)$$

where  $\tan \phi$  stands for the frictional coefficient and  $\phi$  is called the angle of internal friction. The slope of the curves stands for the shear rigidity of sand and increases with the confining stress. The stress level after large shear displacement is called the residual strength.

Figure 1.16 compares the stress–displacement behavior of medium dense sand (relative density=55%) and very loose sand ( $D_r = 0\%$ ). Note that the peak strength of loose sand is much lower, while the residual strength is similar.

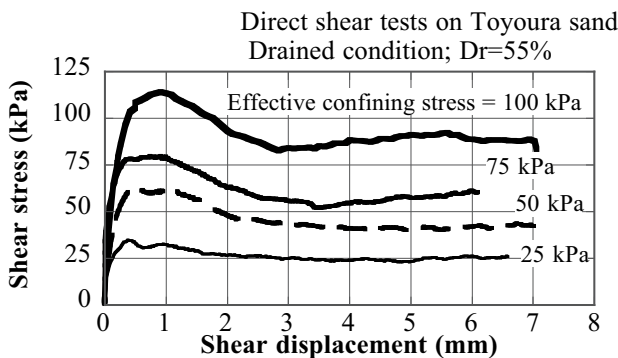


Fig. 1.15 Effects of confining stress level on drained stress-strain behavior of sand

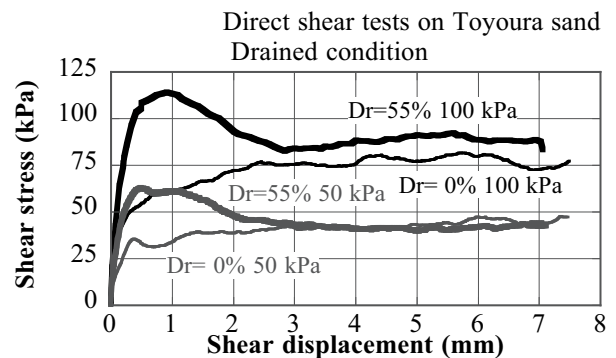


Fig. 1.16 Effects of density of sand on drained stress-strain behavior of sand

1.6 Dilatancy or Shear-Induced Volume Change

Figure 1.17 shows the relationship between shear displacement and vertical displacement (= volume expansion/contraction) during direct shear tests. Since the height of the sand sample was 20 mm at the beginning of shear, the 1 mm displacement stands for 5% expansive strain.

The shear-induced volume change occurs in a variety of materials. For example, concrete and rock develop cracking prior to failure, and the apparent overall volume increases.

The earth crust sometimes develops cracking before rupture (earthquake) and creates such earthquake precursors as small earthquakes and change of deep ground water level as well as chemical composition of water. For these materials, the volume increases and this behavior is called “dilatancy.”

In case of sandy materials, volume increases or decreases according to loading conditions. For example, Fig. 1.17 shows that the volume of medium dense sand (55% relative density) increases (dilatancy), while the volume decreases (contraction or negative dilatancy) for very loose sand.

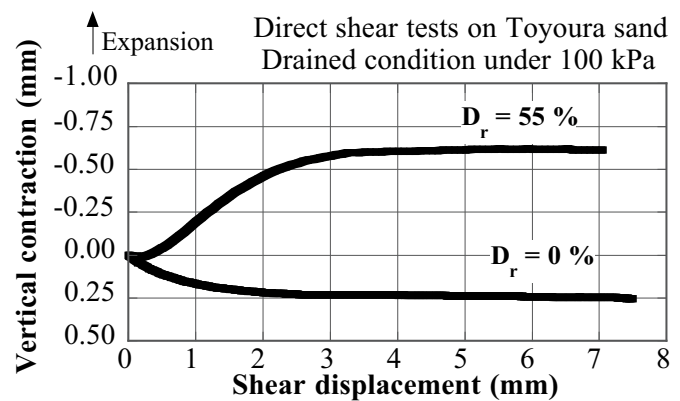


Fig. 1.17 Volume change of sand during direct shear test

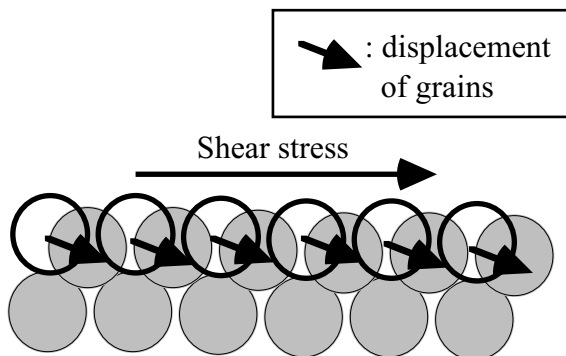


Fig. 1.18 Dilatancy of loose sand

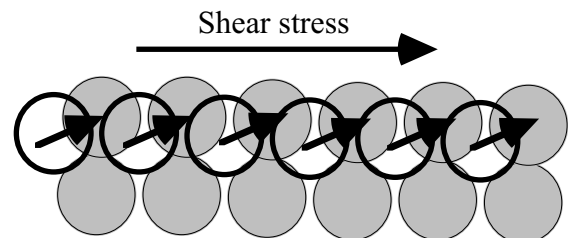


Fig. 1.19 Dilatancy of dense sand

The mechanism of dilatancy is illustrated in Figs. 1.18 and 1.19. When sand is loose (Fig. 1.18), the loading of shear force on sandy grains makes grains fall into large voids. Thus, the apparent height of the sandy deposit decreases. On the contrary, when sand is dense (Fig. 1.19), grains climb up adjacent grains. Thus, the overall volume increases. Note that this effect of density on nature of dilatancy is superimposed by the effect of confining stress; the volume expansion of dense sand under low effective stress may change to volume contraction under higher stress.

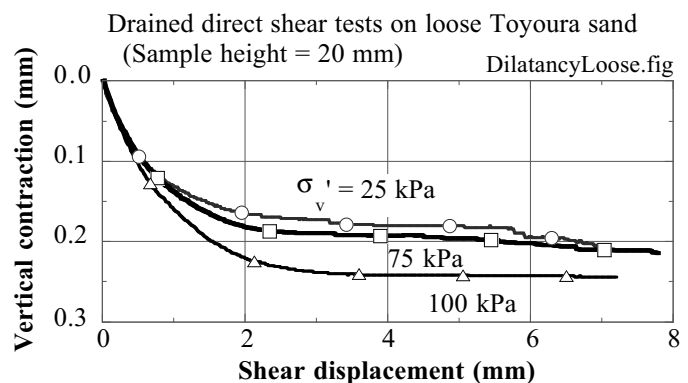
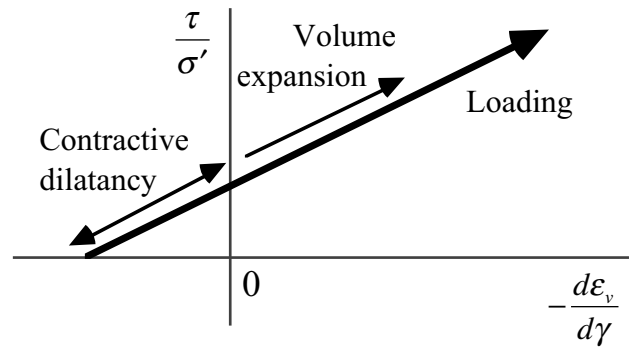


Fig. 1.20 Effects of stress level on extent of dilatancy

Thus, Fig. 1.20 illustrates that loose sand under 100 kPa is more contractive than the same sand under 25 kPa. Bishop (1950) discussed the effects of dilatancy on shear strength of sand, and Rowe (1962) proposed the idea of stress–dilatancy relationship for deformation theory of sandy soils

$$\frac{\tau}{\sigma'} = K \left( -\frac{d\varepsilon_v}{d\gamma} \right) + \text{constant}, \quad (1.16)$$

in which  $\tau$  and  $\sigma'$  are shear and effective normal stress, respectively,  $\gamma$  and  $\varepsilon_v$  are shear and volumetric (positive in contraction) strains, and  $K$  is a constant parameter. The nature of this equation is illustrated in Fig. 1.21.



**Fig. 1.21** Schematic illustration of stress–dilatancy equation

## 1.7 Undrained or Constant-Volume Shear Test

The shear tests as stated in Sects. 1.6 and 1.7 were subjected to volume change of sand. When tested sand is saturated with water ( $S_r=1.0$ ), this volume change is associated with migration of pore water into or out of sand. The direction of water migration depends upon the nature of dilatancy. Water flows into sand when sand is dense and dilatancy is positive (volume increase), while water comes out of sand when sand is loose and dilatancy is negative (volume contraction). Anyhow, shear associated with water migration is called drained shear.

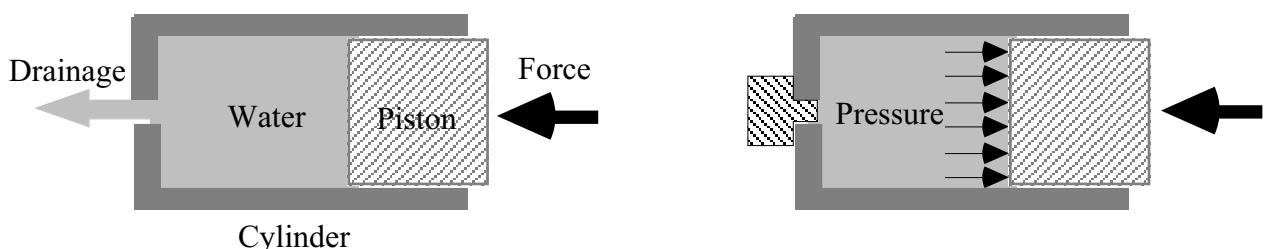
Since real alluvial ground in general has the thickness of meters or more, water migration and drainage take time to occur. Even in sandy ground in which the permeability coefficient is high, the needed time is often of the order of tens of minutes. Since this time is much longer than the earthquake duration time, it is reasonable that seismic loading on real ground, whether it is sandy or clayey, is associated with a negligible extent of drainage. In engineering practice, therefore, it is considered that no drainage occurs in sandy ground during seismic shaking. This situation is called undrained loading. When soil is fully saturated with water ( $S_r=1.0$ ), volume of soil does not change during undrained loading.

It is very important that volume change of soil during drained loading is converted to change of pore water pressure during undrained shear of water-saturated soil, and finally the rigidity and shear strength of soil are significantly affected. Figure 1.22 illustrates this mechanism. Figure 1.22a shows a drained condition in which a piston is pushed into a cylinder and water in it is easily drained out of a hole. In this situation the pressure of water in the cylinder does not change very much. In contrast when the drainage hole is closed in Fig. 1.22b, water cannot get out of the cylinder although the piston is pushed. Consequently, the pressure increases in the water and achieves equilibrium with the external force. Thus, volume contraction in loose sand undergoing drained shear is equivalent with pore water pressure increase in loose sand subjected to undrained shear. Similarly, the volume increase (positive dilatancy) in denser sand during drained shear is equivalent with pore pressure decrease in undrained shear.

Undrained shear is otherwise called constant-volume shear. Note that the effective stress principle of soil mechanics, (1.4), implies that the increase of pore water pressure ( $u$ ) in loose sand results in reduced effective stress ( $\sigma'$ ) if the total stress ( $\sigma$ ) is held constant.

(a) Drained condition

(b) Undrained condition



**Fig. 1.22** Simple illustration of drained and undrained conditions

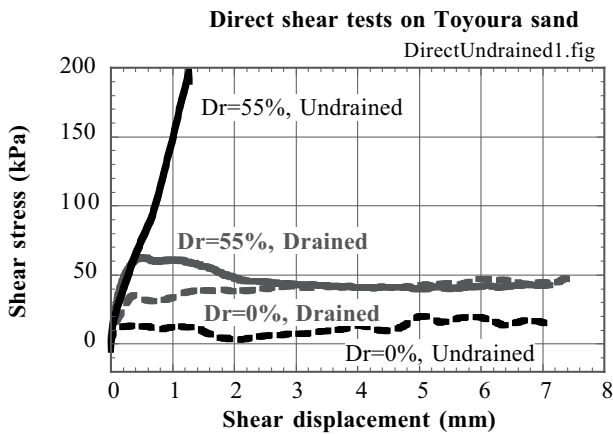


**1.8 Excess Pore Water Pressure and Stress Path Diagram**

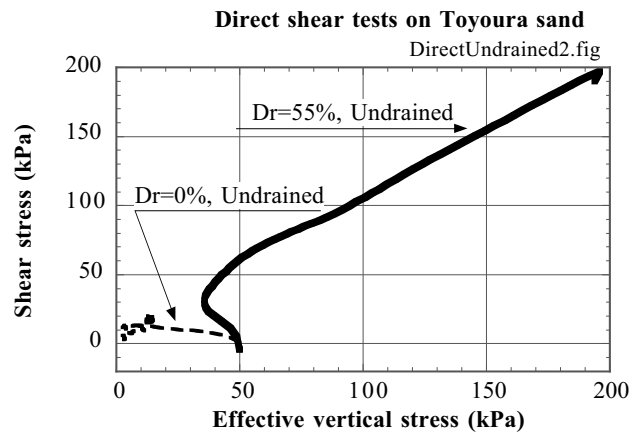
Figure 1.23 illustrates the results of direct shear tests as mentioned in Sect. 1.5. Since some tests were carried out by maintaining constant the volume of specimen (height) , it was possible to examine the effects of drainage condition on the shear behavior of sand. It is therein seen that the stress–displacement behaviors in drained and undrained tests are completely different. Moreover, the denser sand ( $D_r=55\%$ ) has the greater rigidity and strength in undrained shear than in drained shear, while conversely the loose sand ( $D_r=0\%$ ) has much lower strength during undrained shear. This difference was induced by the change of the effective stress.

Figure 1.24 shows the relationship between the effective stress and shear stress for two values of relative density (0% and 55%). A diagram of this type is called “stress path” and plays a very important role in interpretation of undrained behavior of soils. It is seen in this figure that the effective stress of denser sand increased drastically after a minor decrease. This increased stress level resulted in the greater stiffness and shear strength as seen in Fig. 1.23. In contrast, the effective stress in loose sand ( $D_r=0\%$ ) was reduced significantly and as a consequence the sand became very soft.

In soil mechanics, the change of effective stress is often induced by the change of pore water pressure (see (1.4)). The change of pore water pressure from its initial value is called excess pore water pressure.



**Fig. 1.23** Effects of drainage condition on stress-displacement relationship of sand



**Fig. 1.24** Stress path diagram for undrained shear tests

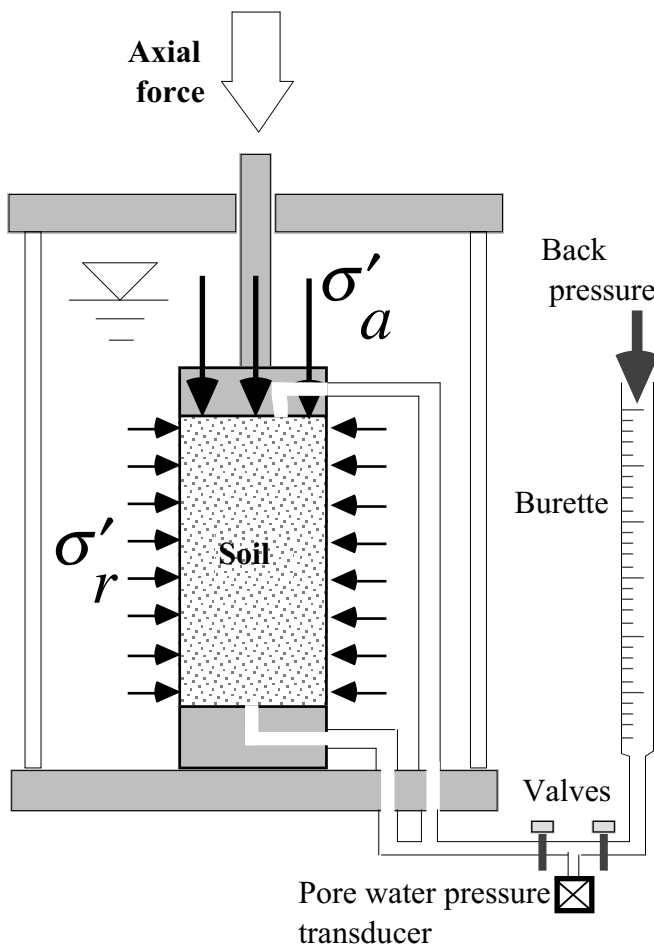
## 1.9 Triaxial Shear Device

Although the mechanical principle of direct shear in Sect. 1.5 is easy to understand, practical soil testing is more widely conducted by using a triaxial device. As illustrated in Fig. 1.25, a soil specimen of a columnar shape is covered by a rubber membrane, pressurized by equal pressure in both horizontal and vertical directions, and additional stress is loaded in the vertical direction. Although being called triaxial, this device controls only two stress components. The horizontal stress is often called the radial stress,  $\sigma'_r$ , and the vertical stress is called the axial stress,  $\sigma'_a$ .

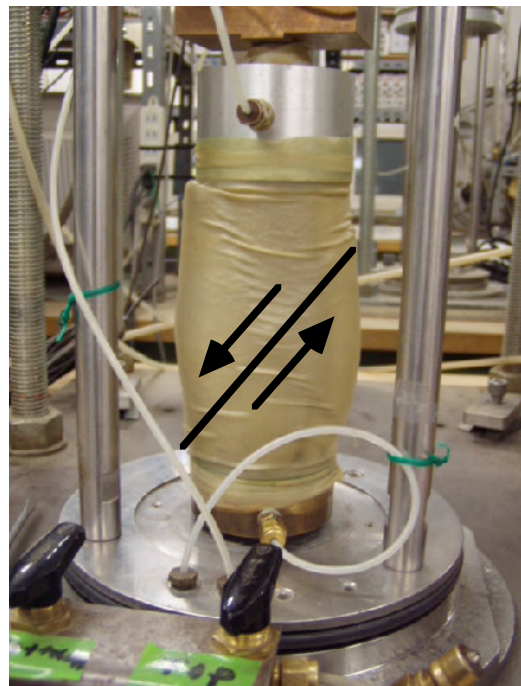
Some people ask questions why the loading of axial stress is not compression but shear. An answer to this question may be found in Fig. 1.26 where failure of a sand specimen was caused by the loading of axial stress. A development of shear failure along an inclined plane is evident.

The triaxial apparatus is more popular than a direct shear device or a similar simple shear machine because the cylindrical shape of a triaxial apparatus makes it easy to run tests on samples of a good quality collected from the site (undisturbed specimen which preserves the nature of soil in the field).

Figure 1.27 illustrates a schematic result of triaxial shear test in which the radial stress is held constant and the axial stress is increased. Note that shear deformation and failure are induced by the difference of  $\sigma'_a$  and  $\sigma'_r$ . Hence, the deviator stress of  $\sigma'_a - \sigma'_r$  plays a major role. The volume change of the sample is measured by using a burette that monitors the volume of pore water that comes out of the sample. To do this, the sample has to be saturated with water.



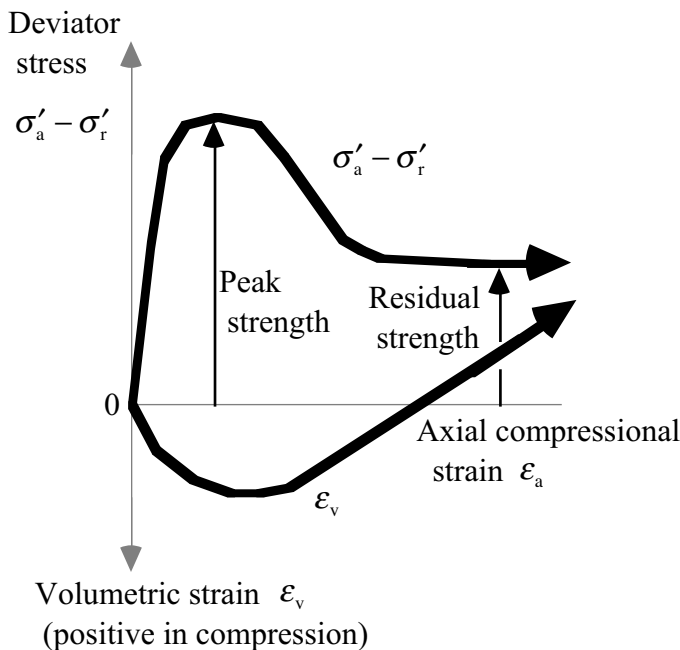
**Fig. 1.25** Stress condition in triaxial soil specimen



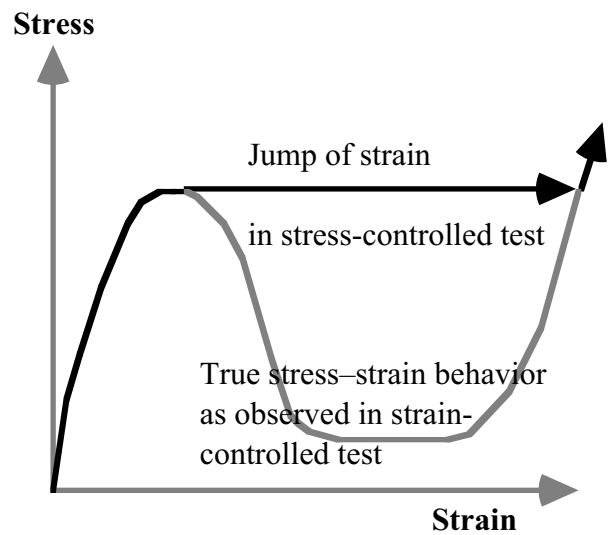
**Fig. 1.26** Development of shear failure due to loading of axial stress (Photo by M.Mizuhashi)

There are many variations in triaxial tests.

- Undrained tests (Sect. 1.7) are run by closing the right valve in Fig. 1.25. In place of volume change, pore water in the sample varies with shear deformation.
- Triaxial extension tests are run by either increasing  $\sigma'_r$  or decreasing  $\sigma'_a$  by which the sample is elongated in the axial direction.
- Strain-controlled tests are carried out by controlling the velocity of axial displacement. Upon softening after the peak stress (see Fig. 1.27), strain-controlled tests can follow the decreasing stress level. Note that this capability is achieved when the rigidity of the loading device is substantially greater than that of a specimen. Thus, a soil testing machine can record softening behavior of soft clay or liquefied sand. However, the same machine cannot record softening of hard rock or concrete.
- Stress-controlled tests are conducted by controlling the magnitude of the axial stress. Since the stress is directly applied by supplying air pressure into a belofram cylinder, the decrease in the stress level as in Fig. 1.27 cannot be recorded. In place of softening of stress, stress-controlled tests suddenly develop very large strain (Fig. 1.28).



**Fig. 1.27** Schematic idea of stress-strain behavior of soil in triaxial compression test



**Fig. 1.28** Missing stress softening behavior in stress-controlled tests

**1.10 Membrane Penetration**

The problem of membrane penetration, which is otherwise called membrane compliance, is important in undrained shear tests on coarse granular materials. Figures 1.29 and 1.30 show triaxial specimens of Chiba gravel undergoing negative pore pressures of  $-1$  kPa and  $-10$  kPa, respectively. It is clearly seen that the increase of the negative pressure from  $-1$  to  $-10$  kPa made the rubber membrane move into voids. This phenomenon is very significant in the illustrated case because the thickness of the employed membrane (approximately  $0.25$  mm) is much thinner than the size of the gravel that ranges between  $4.75$  and  $9.5$  mm. Note that the inward movement of the membrane upon increase of negative pressure (increase of effective stress) causes additional change in void volume, which is not related with the volume contraction of granular structure of soil.

The membrane penetration problem is significant in liquefaction tests on coarse grained soils as well, because the development of excess pore water pressure and decrease of effective stress lead to the outward movement of membrane (from Fig. 1.30 to Fig. 1.29, see Fig. 1.31). Thus, pore water migrates outwards from a tested specimen. Since this migration is equivalent with drainage of pore water, the measured excess pore water pressure is an underestimation in the test and, consequently, liquefaction resistance is overestimated.

Many attempts have been made to make correction of the membrane-penetration errors by evaluating the magnitude of membrane migration during change of effective stress. Experimentally, it is interesting to push water into a specimen in order to compensate for the penetration-induced drainage.

In principle, the experimental error in undrained tests due to membrane penetration can be reduced by either physically reducing the extent of penetration or injecting pore water into a specimen by the same amount as membrane penetration. As for the former idea, use of thick membrane might cause another problem: error in stress condition due to tensile force in the membrane. In this account, Towhata et al. (1998) pasted pieces of thin metal plates between membrane and gravelly soil.

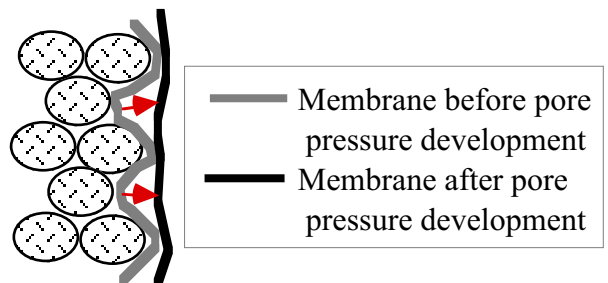
The amount of membrane penetration volume is a function of effective stress (difference between outer pressure and internal pore pressure). Thus, the penetration volume change has been experimentally evaluated by running a variety of drained tests. Newland and Allely (1957) assumed that difference between axial and radial strains during isotropic compression in triaxial tests is equal to the membrane penetration error. This idea, however, does not work because of anisotropic nature of sand. Roscoe (1970) and Raja and Sadasivan (1974) as well as Nicholson et al. (1993) embedded different volumes of brass rods and conducted isotropic compression. While the measured volume change varied with the amount of brass rods, the net



**Fig. 1.29** Appearance of Chiba gravel specimen undergoing  $1$  kPa of effective stress



**Fig. 1.30** Appearance of gravel specimen undergoing  $10$  kPa of effective stress



**Fig. 1.31** Drainage induced by membrane penetration

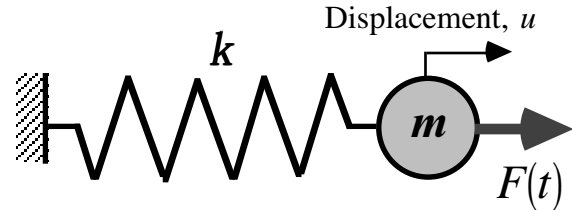
volume change in sand was assumed constant. By extrapolating the volume change to 100% volume of brass, the membrane penetration was evaluated. It is not clear whether or not interaction between brass and sand affected volume change of sand. Evans et al. (1992) filled void among gravel particles with loose fine sand, thus preventing penetration of membrane. Finally, Sivathayalan and Vaid (1998) proposed an idea for a hollow cylindrical specimen. In their idea, a hollow cylindrical specimen is subjected to drained isotropic consolidation, and a geometrical relationship in volumetric change of a tested specimen and the internal hollow space is used to assess the extent of membrane penetration as a function of effective stress. It is important for readers to fully understand the derivation of their equation prior to using it.

**1.11 Elementary Dynamics**

Basic knowledge on theory of vibration is very important in understanding ground response to earthquake excitation. Figure 1.32 illustrates a single-degree-of-freedom model in which a mass of  $m$  is subjected to oscillatory force of  $F(t)$ . The mass is connected to a fixed support by means of a linear elastic spring of  $k$ . By denoting the displacement of the mass by  $u$ , the equation of motion of this system is derived as

$$m \frac{d^2u}{dt^2} + ku = F(t), \quad (1.17)$$

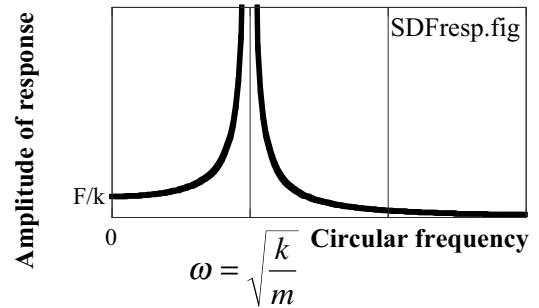
in which  $t$  stands for time.



When  $F(t)$  is a sinusoidal function of time,  $F = F_0 \sin \omega t$ , the solution of  $u$  is given by

$$u(t) = \frac{F_0}{k - m\omega^2} \sin \omega t. \quad (1.18)$$

This implies that the mass in Fig. 1.32 oscillates by a sinusoidal function with a period,  $T$ , of  $2\pi/\omega$ . The frequency (number of cycles per second,  $f$ ) is given by  $f = 1/T$ , while “ $\omega$ ” is called the circular frequency. Note that  $\omega = 2\pi f$ . The amplitude of the motion (1.18) changes with the shaking frequency ( $\omega$ ) as illustrated in Fig. 1.33. In particular, it becomes infinite when  $\omega = \omega_n = \sqrt{k/m}$ . This significant magnitude of motion is called resonance. The period of the force,  $T_n = \omega_n/(2\pi)$  is known as the natural period, while the frequency of  $f_n = 1/T_n$  is the natural frequency. When any structure is subjected to external force, the situation of resonance has to be avoided.



**Fig. 1.33** Amplification curve for single-degree-of-freedom model

The above discussion assumed that everything changes with a harmonic (sin) function of time. In reality, the motion starts at some time ( $t=0$ ). When  $u = 1.0$  and  $du/dt = 0.0$  at time  $t=0$  (initial conditions) under  $F(t) = 0.0$ , the solution of (1.17) is given by

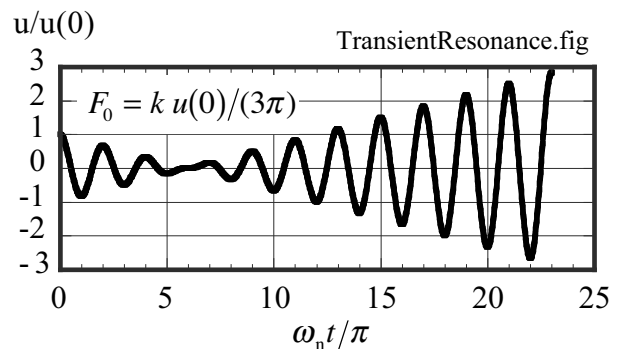
$$u(t) = \cos \omega_n t. \quad (1.19)$$

Thus, the motion without external force (free vibration) occurs with the natural period.

Moreover, the external force,  $F(t)$ , may start at  $t=0$ . Then, another solution under  $F = F_0 \sin \omega_n t$  at a resonant frequency while  $u = u(0)$  and  $du/dt = 0$  at  $t=0$  is derived

$$u(t) = \frac{F_0}{2k} (\sin \omega_n t - \omega_n t \cos \omega_n t) + u(0) \cos \omega_n t. \quad (1.20)$$

This implies that the amplitude of motion increases with time; see an example calculation in Fig. 1.34. This type of oscillation is called transient. Thus, the infinite amplitude of motion at resonance, as suggested by (1.18), takes infinite duration time of excitation to occur.



**Fig. 1.34** Transient solution of motion under resonance frequency

1.12 Standard Penetration Test

The soil investigation in the field aims at collecting information that helps to assess the mechanical properties of soils as well as stratification of the ground. On the other hand, such mechanical properties of soils as shear modulus and shear strength can be obtained by drilling a bore hole (boring), collecting soil samples of good quality, and running tests in the laboratory. However, this elaborate procedure is often more time consuming and expensive. Problem of sample disturbance error is another big issue. Thus, field tests that can be run in a bore hole is often preferred.

Standard penetration tests, which is abbreviated as SPT, have a long history (Fig. 1.35). A cylindrical tube of a specified size is penetrated into the bottom of a bore hole by repeating hammer impacts at the ground surface (Fig. 1.36). Since the mass of the hammer and the height of its free fall are specified as 63.5 kg and 76 cm, respectively, one blow produces impact energy of 0.467 kJ. With this specified energy, it is expected that the obtained results are of universal use. The number of hammer impacts (blows) is counted and the one which is needed to achieve 30 cm penetration is called SPT-*N*. This *N* value stands for the resistance of soil against penetration of a tube and most probably has a good correlation with shear modulus, shear strength, and density of soils.

The good points of SPT are as what follows:

- Equipment is mechanically simple
- Disturbed soil sample is collected by the penetrated tube (Fig. 1.37)
- Thus, types and physical properties of soils (Sect. 1.1) can be measured directly, although mechanical properties cannot be measured due to significant disturbance of soil
- There is a huge number of empirical correlations between SPT-*N* and mechanical properties of soils.

On the other hand, its shortcomings may be as what follows:

- State of maintenance of the equipment affects the measured *N* value
- The measured *N* value is affected by the effective stress in the ground,  $\sigma'_v$ , and does not represent the true nature of soil
- SPT-*N* is subjected to human errors such as insufficient height of free fall (<75 cm) and poor maintenance efforts
- The free-fall energy is not fully employed for penetration of the tube, making real impact energy to be, for example, 60–70 % of the ideal value of 0.467 kJ

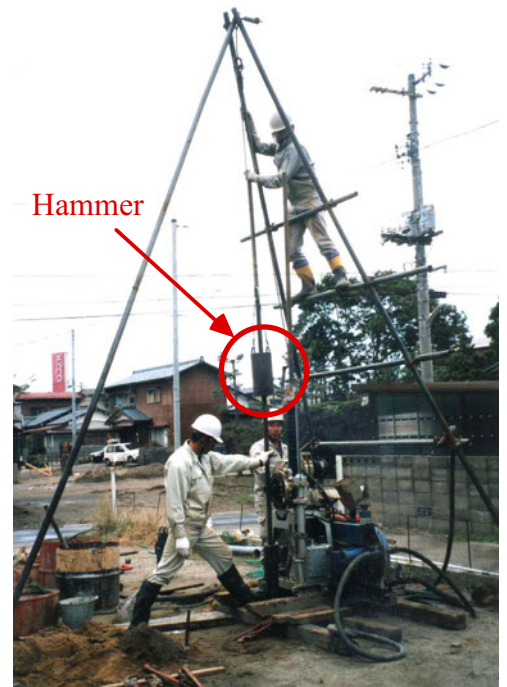


Fig. 1.35 Practice of standard penetration test

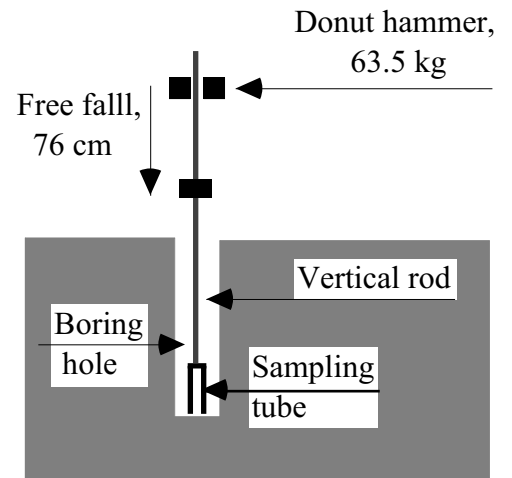


Fig. 1.36 Conceptual idea of standard penetration test



Fig. 1.37 Disturbed soil sample collected by tube

Seed et al. (1985) discussed the possible sources of errors in SPT such as insufficient impact energy, length of rod, and type of tip sampler. In this regard, attempts have been made to solve the problem of insufficient height and accordingly the insufficient free-fall energy. An example of such an attempt is the automatic free-fall device (Fig. 1.38). This device, however, needs more human load and makes the field operation less efficient. Effort for maintenance of this equipment is another problem. Thus, the precise achievement of the required free-fall energy is not yet universally achieved. Consequently, it has been practiced to correct measured  $N$  value to the one at 60% of the specified energy under effective stress of  $98 \text{ kN/m}^2$  ( $1 \text{ kgf/cm}^2$ ).

$$N_{1,60} = \frac{0.467 \times 0.6}{\text{Real impact energy}} \times \frac{1.7 \times (\text{Measured } N \text{ value})}{\sigma'_v (\text{kgf/cm}^2) + 0.7}. \quad (1.21)$$

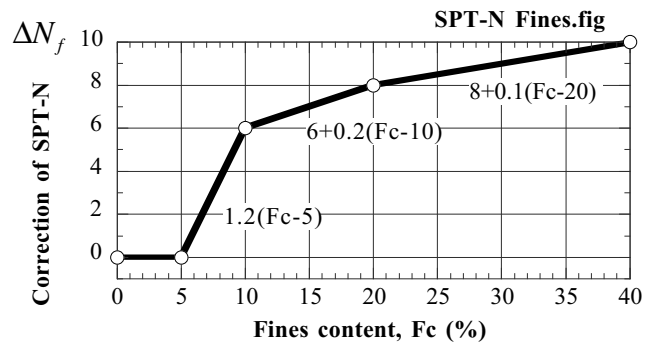
Moreover, it should be noted that fines content in soil (particles finer than  $75 \mu\text{m}$ ) makes the measured  $N$  value smaller. Meyerhof (1957) proposed an empirical relationship between SPT- $N$  and relative density of sand. Japanese Geotechnical Society (2004) employs its modification for sands with fines for design of soil improvement against liquefaction (Sect. 26.5);



**Fig. 1.38** Example of free-fall standard penetration equipment

$$D_r(\%) = 21 \sqrt{\frac{N}{0.7 + \sigma'_v/98} + \frac{\Delta N_f}{1.7}}, \quad (1.22)$$

in which  $\sigma'_v$  is the effective vertical stress ( $\text{kN/m}^2$ ) and  $\Delta N_f$  stands for the correction for fines content (finer than  $75 \mu\text{m}$ ), see Fig. 1.39.



**Fig. 1.39** Correction of SPT-N in terms of fines content (JGS, 2004)



1.13 Flow of Ground Water

It may be thought that the flow of ground water through soil is controlled by the water pressure difference. This is true in case of flow in the horizontal direction. Figure 1.40 illustrates the variation of water pressure indicated by height of water columns in imaginary pipes installed in ground. Note that water pressure is given by  $\gamma_w \times (\text{height of water column})$ . However, it should be recalled that the hydrostatic condition has no flow although pressure increases in the vertical direction (Fig. 1.41). Water flow is driven by any variation of water pressure from the hydrostatic condition. Thus, it is concluded that water flow is controlled by the change of water surface elevation along the direction of water flow. The elevation of water surface,  $Z$ , consists of the elevation at the point of pressure measurement,  $Z_m$ , and the contribution by water pressure,  $Z_p$

$$Z = Z_m + Z_p \tag{1.23}$$

Note that  $Z$  changes in the direction of water flow in Fig. 1.40, while it is constant in Fig. 1.41.

Figure 1.42 illustrates the significance of Darcy’s law on ground water flow. The elevation,  $Z$ , is measured from a fixed level, and the distance,  $s$ , is measured along the channel of water flow. The amount of water flow,  $v$ , per unit cross section of flow is given by

$$v = ki, \tag{1.24}$$

where the hydraulic gradient,  $i$ , is given by

$$i = dZ/ds. \tag{1.25}$$

The parameter of  $k$  is called the permeability coefficient, which is of the order of 0.001 to 0.01 m/s for sandy soil and less than, for example,  $10^{-8}$  m/s for clayey soils. Note that “ $v$ ” stands for the amount of water flow (flux) per unit cross section per second, and is different from the velocity of water flow. The velocity is equal to  $v \times (1 + e)/e$  where  $e$  is the void ratio of soil (Sect. 1.2).

Since water has some viscosity, water flow exerts force in the direction of flow. Being called seepage force, this force per unit volume of soil is given by

$$\text{Seepage force} = i\gamma_w,$$

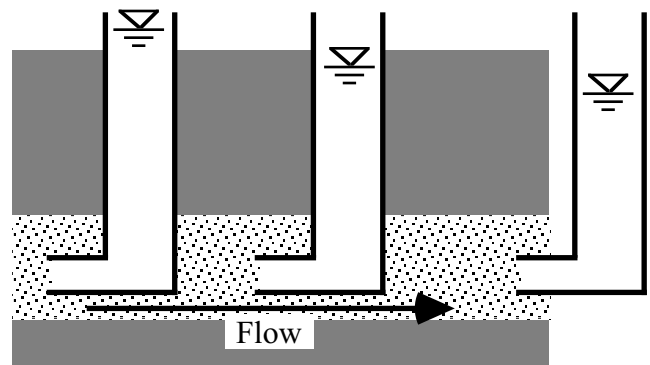


Fig. 1.40 Variation of water pressure in direction of horizontal water flow in soil

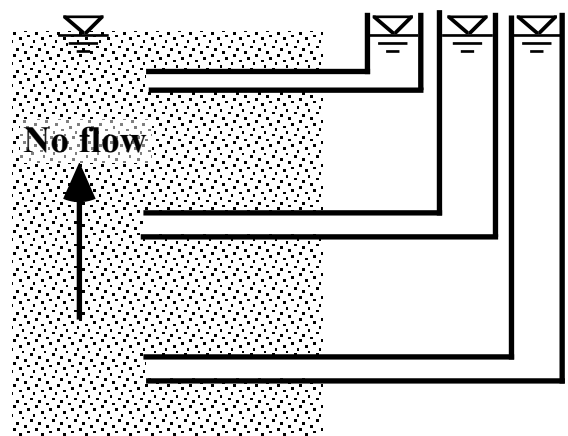


Fig. 1.41 Distribution of water pressure in hydrostatic condition

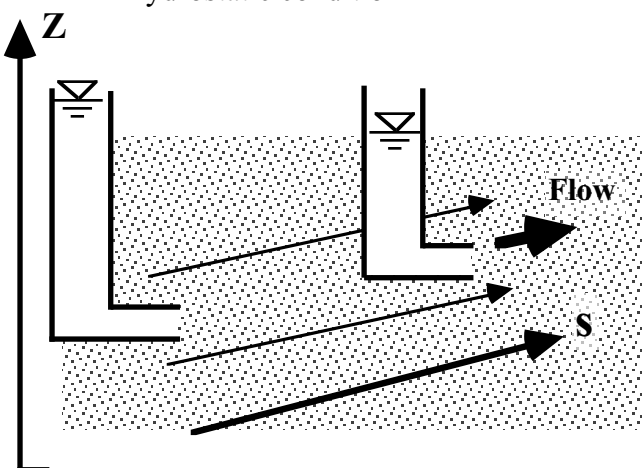
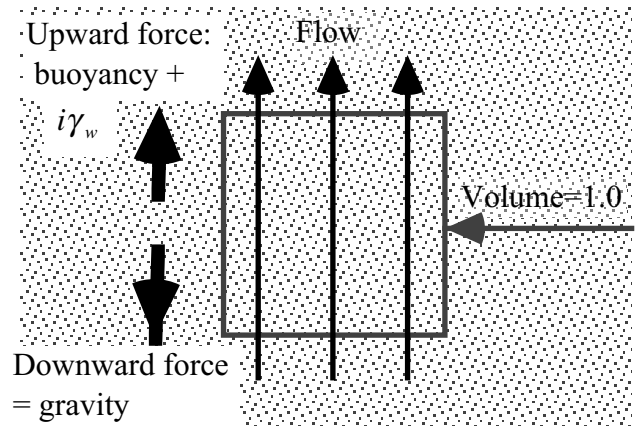


Fig. 1.42 Definition of hydraulic gradient

where  $\gamma_w (= \rho_w g)$  is the weight of water per unit volume. Figure 1.43 illustrates an extreme case in which a high rate of water flow towards the surface exerts significant force upon soil and this force is equal to the gravity force.

$$i\gamma_w = \gamma'$$

in which  $\gamma'$  is the buoyant weight of soil. Because of this force equilibrium, soil particles are floating in pore water and there is no effective stress any more. Consequently, soil loses shear strength (1.15). This extreme situation is called “boiling” and causes failure of earth structures such as river dike and earth dam among others. Liquefaction is another example of boiling (Sects. 18.2 and 18.3).



**Fig. 1.43** Hydraulic gradient at boiling

By using (1.1) on water saturated soil ( $S_r = 1.0$ ),

$$\begin{aligned} \gamma' &= \gamma - \gamma_w = \frac{G_s - 1}{1 + e} \gamma_w \quad \text{and} \\ i = i_{cr} &= \frac{\gamma'}{\gamma_w} = \frac{G_s - 1}{1 + e}. \end{aligned} \quad (1.26)$$

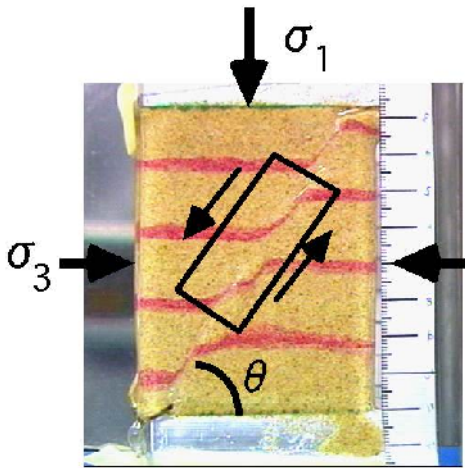
When  $G_s = 2.65$  and  $e = 0.8$  for example, the critical hydraulic gradient,  $i_{cr}$ , is approximately equal to 0.9.

## 1.14 Shear Band

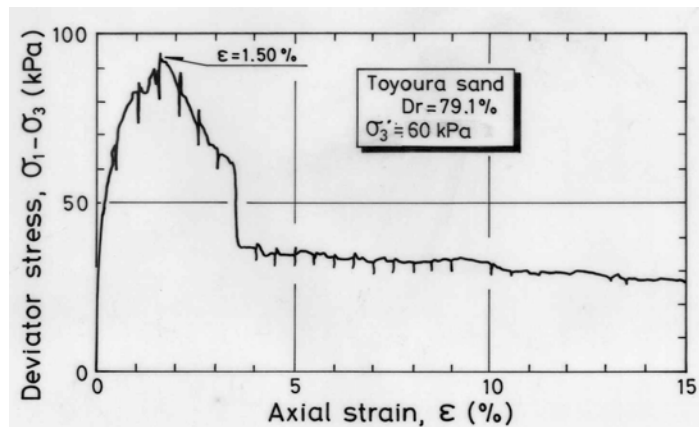
Classic soil mechanics hypothesized that shear failure and slip movement of soil occur along a plane: i.e., the boundary between stationary and moving soil masses had no thickness. Elaborate laboratory experiments in the recent times, however, found that shear failure occurs as a large shear strain that is localized (concentrated) within a narrow layer. This layer is called shear band.

Figure 1.44 demonstrates the appearance of shear band that was made visible through a transparent side wall of a special shear device. Shear failure occurred in a nearly plane-strain manner, and the movement of sand grains was recorded by a digital microscope (Furumoto et al., 1997; Towhata and Lin, 2003). Shear band developed in an oblique direction and its thickness in this postfailure photograph is approximately equal to 20 times sand grain size.

The observed shear stress–strain behavior (Fig. 1.45) shows the peak stress state that is followed by softening (decrease in stress level) and a residual state (constant stress). Note that the peak stress occurred at strain of 1.5 %.



**Fig. 1.44** Development of shear band in drained shear of dry Toyoura sand



**Fig. 1.45** Stress–strain behavior of medium dense sand in transparent shear device ( $D_r = 79\%$ )

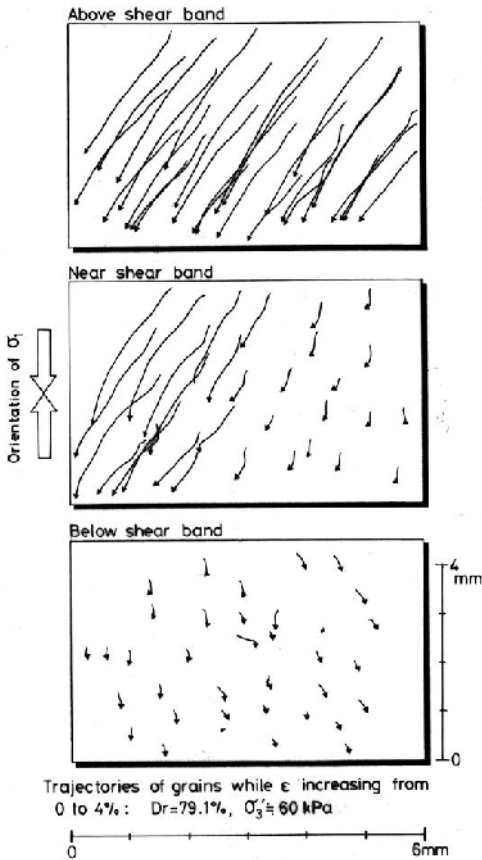
The grain movement was recorded by comparing two microscopic photographs at strains of 0 % and 4 % (Fig. 1.46). This strain range includes the occurrence of the peak stress state. As shown in this figure, all the grains in the upper portion of the specimen moved together, suggesting a rigid block movement, while grains in the bottom were stationary, implying again a stable block. In contrast, the middle part indicates discontinuity in displacement due to development of shear band or strain localization in a narrow band. According to this incremental grain movement, the thickness of the shear band is less than 10 times grain size. This thickness is smaller than the aforementioned shear band thickness (Fig. 1.44) probably because the location of temporary shear band (Fig. 1.46) translates with time and induced significant dislocation of grains in a bigger area (Fig. 1.44).

The orbit of grains (Fig. 1.47) shows that the volume of grain packing increased within a shear band. This dilatant behavior leads to softening and reduced shear strength after the peak stress.

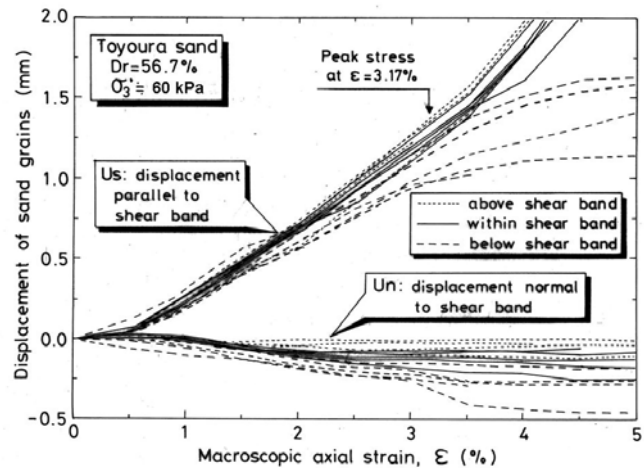
Figure 1.48 illustrates rotation of long axis of grains. It is noteworthy that significant rotation occurred within a shear band after the peak stress. Because rotational friction is lower than sliding friction, this finding may further account for the softening of stress level after the peak.

In the prepeak stage of tests, a microscopic motion picture showed that grains occasionally fall into nearby big voids. Figure 1.49 indicates the number of grain droppings that changes with the progress of shear deformation. Since dropping disappeared after the peak strength (strain = 1.5 %), it is inferred that

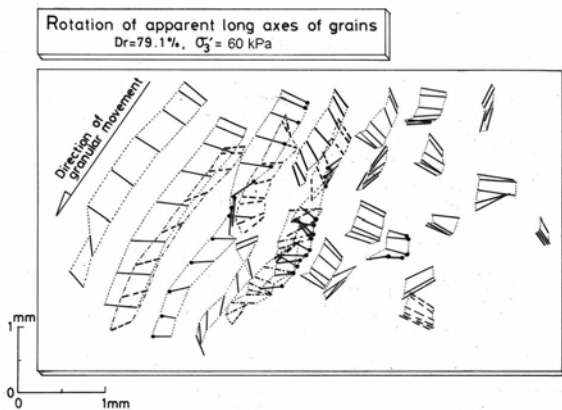
such dropping under increasing stress level erases large voids and improves the overall shear rigidity of sand. If this phenomenon continues for a longer time in the real subsoil, sandy ground will obtain greater rigidity and even higher liquefaction resistance. This mechanism may be a cause of ageing (Fig. 18.46) and a long-term increase in SPT-*N* (Fig. 26.59).



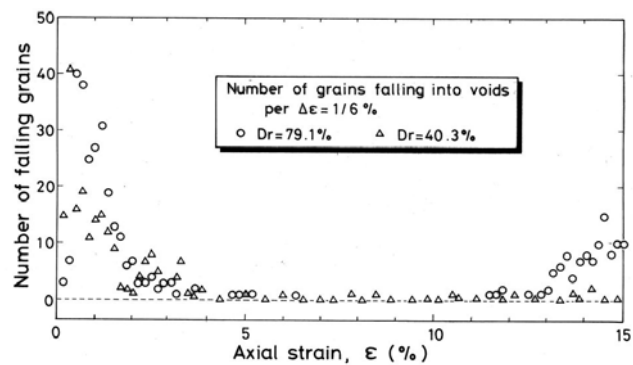
**Fig. 1.46** Microscopic observation of orbit of sand grains near shear band ( $D_r = 79\%$ )



**Fig. 1.47** Volume expansion in shear band ( $D_r = 57\%$ )



**Fig. 1.48** Rotation of grains in shear band ( $D_r = 79\%$ )



**Fig. 1.49** Histogram of grains dropping into large voids

**List of References in Chapter 1**

Bishop, A.W. (1950) Discussion, *Geotechnique*, Vol. 2, No. 2, pp. 113–116.  
 Evans, M.D., Seed, H.B. and Seed, R.B. (1992) Membrane compliance and liquefaction of sluiced gravel specimens, *J. Geotech. Eng., ASCE*, Vol. 118, No. 6, pp. 856–872.

- Furumoto, K., Towhata, I., and Yoshida, A. (1997) Microscopic observation of shear band in plane strain compression tests of sand, Proc. IS-Nagoya, pp. 235-240.
- Japanese Geotechnical Society (2004) Mitigation measures for liquefaction, pp. 238–240 (in Japanese).
- Meyerhof, G.G. (1957) Discussion of Session 1, Proc. 4th Int. Conf. Soil Mech. Found. Eng., Vol. 3, p. 110.
- Newland, P.L. and Allely, B.H. (1957) Volume change in drained triaxial tests on granular materials, *Geotechnique*, Vol. 7, No. 1, pp. 17–34.
- Nicholson, P.G., Seed, R.B. and Anwar, H.A. (1993) Elimination of membrane compliance in undrained triaxial testing, I. Measurement and evaluation, *Can. Geotech. J.*, Vol. 30, pp. 727–738.
- Raja, V.S. and Sadasivan, S.K. (1974) Membrane penetration in triaxial tests on sands, Proc. ASCE, Vol. 100, GT4, pp. 482–489.
- Rowe, P.W. (1962) The stress–dilatancy relation for static equilibrium of an assembly of particles in contact, *Proc. Royal Soc. Lond. A*, Vol. 269, pp. 500–527.
- Seed, H.B., Tokimatsu, K., Harder, L.F. and Chung (1985) Influence of SPT procedures in soil liquefaction resistance evaluations, Proc. ASCE, Vol. 111, GT12, pp. 1425–1445.
- Sivathayalan, S. and Vaid, Y.P. (1998) Truly undrained response of granular soils with no membrane-penetration effects, *Can. Geotech. J.*, Vol. 35, No. 5, pp. 730–739.
- Towhata, I., Chowdhury, F.K. and Vasantharajah, N. (1988) Cyclic undrained tests on gravel-like material using cubic triaxial apparatus, Proc. 9th World Conf. Earthq. Eng, Vol. III, pp. 53–58.
- Towhata, I., Kuntiwattanakul, P., Seko, I. and Ohishi, K. (1993) Volume change of clays induced by heating as observed in consolidation tests, *Soils Found.*, Vol. 33, No. 4, pp. 170–183.
- Towhata, I., Kuntiwattanakul, P. and Kobayashi, H. (1993) A preliminary study on heating of clays to examine possible effects of temperature on soil-mechanical properties, *Soils Found.*, Vol. 33, No. 4, pp. 184–190.
- Towhata, I. and Lin, C.-E. (2003) Microscopic observation of shear behavior of granular material, Proc. IS-Lyon, Lyon.

## **PART 2**

# **Problems Concerning Shaking of Soft Ground Undergoing Earthquake Loading**



Statue of Buddhism at Ajanta, India.

# Chapter 2

## Introduction



Chan Chan archaeological site in North Peru

## 2.1 Objectives of Earthquake Geotechnical Engineering

Earthquake geotechnical engineering is concerned with the following topics:

1. Prediction of ground motion during earthquakes
2. Prediction of residual deformation of ground and earth structures that remain after shaking
3. Study on stress–strain–strength characteristics of soils undergoing cyclic loading
4. Subsurface exploration by generating and observing propagation of ground vibration
5. Safety and/or satisfactory performance of structures during earthquakes
6. Application of knowledge to ground vibration caused by machine and traffic loading among others

In the past experiences, such earthquake-related damages as loss of human lives and properties as well as malfunctioning of facilities were induced by either a total collapse of structures or their unacceptably large deformation. Those collapse and deformation in turn were induced by either a strong shaking or a ground deformation that is not recovered after an earthquakes and remains permanently. Therefore, the topics (1) and (2) shown above are concerned with the prediction of the extent of damage.

It has been found that the ground shaking and the residual deformation that remains after shaking are strongly dependent on the stress–strain behavior of soils. Since soil is a nonlinear material, there is no proportionality between stress and strain. The deformation characteristics, and of course the strength, vary drastically with

- The magnitude of effective stress that stands for the contact forces among soil grains
- History of stress application in the past (normal or over consolidation)
- Age of soil
- Rate of loading (to some extent)
- Material strength of soil

among others. Thus, the basic understanding of soil behavior requires us to do much efforts experimentally. Consequently, many stress–strain models of soils have been proposed by a number of research people.

Even though an appropriate stress–strain model may be available for an analysis, identification of soil parameters at a specified site is further difficult. Practice runs tests in the field or collects soil specimens of good quality (this is already a big topic of study) for laboratory testing. The employed model may or may not be able to handle the complicated stress–strain behavior. The collected information may be representative of the whole ground (case of uniform ground) or indicates the behavior of a small specimen (case of heterogeneous ground).

To date, many computer codes have been developed that can calculate the earthquake shaking of ground and earth structures. They appear to be reasonable when the studied ground condition is relatively stiff. It means that the prediction is reasonable when the strain in soil is small and the nonlinearity is not significant. Conversely, computation on soft soil deposits is still difficult.

There is no general way to relate the predicted nature of ground shaking to the extent of damage. Many kinds of structures are of different causes of damages, which cannot be taken care of by a single or a limited number of seismic parameter(s).

In summary, there are still so many problems in earthquake geotechnical engineering that require further studies. It should be borne in mind that what are being discussed today at many occasions might be discarded in the next decade.



## 2.2 Geotechnical Problems Encountered During Earthquakes

Recent earthquake events have been studied in detail and many points have been made. Consequently, it has been found that two phenomena should be studied, namely amplification of shaking and liquefaction.

1. Problems induced by shaking include the following issues:

Amplification of motion in soft alluvial deposits 軟弱沖積層における地震動の増幅

Effects of local soil conditions and topography on amplification 地盤条件や地形が地震動増幅度に及ぼす影響

Permanent (residual) deformation of earth structures 土構造物の永久変形 (残留変形)

Landslide 地すべり

Different causes of seismic failure in different types of facilities 地震被害の原因は施設の種類によって異なる,

for instance, inertia force 慣性力, deformation of surrounding soil 周辺地盤の変形, etc.

Conventionally, earthquake engineering has been working on the intensity of acceleration 加速度 at the bottom of surface structures. This is because d’Lambert principle states the equivalence of the acceleration and the inertia force. It is, however, apparent that the acceleration does not account for the deformation/strain of the ground. Some people, therefore, prefer to use the earthquake velocity 速度 in place of acceleration for assessment of damage extent, although the physical significance of velocity is not clearly understood

Dynamic soil–structure interaction 地盤と構造物との動的相互作用

Fault movement 断層運動

2. Liquefaction causes the following problems and poses topics of study:

Effects of local geology on liquefaction potential 表層地質が液状化の可能性に及ぼす影響,  
type of soil 土の種類, age of soil 堆積後の年代

Loss of bearing capacity 支持力の喪失 and subsidence of surface structure 沈下・めり込み

Floating of embedded structure 埋設構造物の浮き上がり

Boiling of sand and water 噴砂と噴水

Consolidation and subsidence 圧密と地盤沈下

Liquefaction is the build-up of excess pore water pressure 過剰間隙水圧 due to cyclic shear loading.

When this pore pressure dissipates 消散する like consolidation of clayey deposits, the volume of sand decreases and ground subsidence 地盤沈下 occurs.

Lateral flow of ground 側方流動

Liquefied ground flows laterally and deforms in the meantime, causing damage to many underground facilities. This is the most recent topic of study and many people are trying to demonstrate the cause of lateral flow as well as to predict the amount of flow.

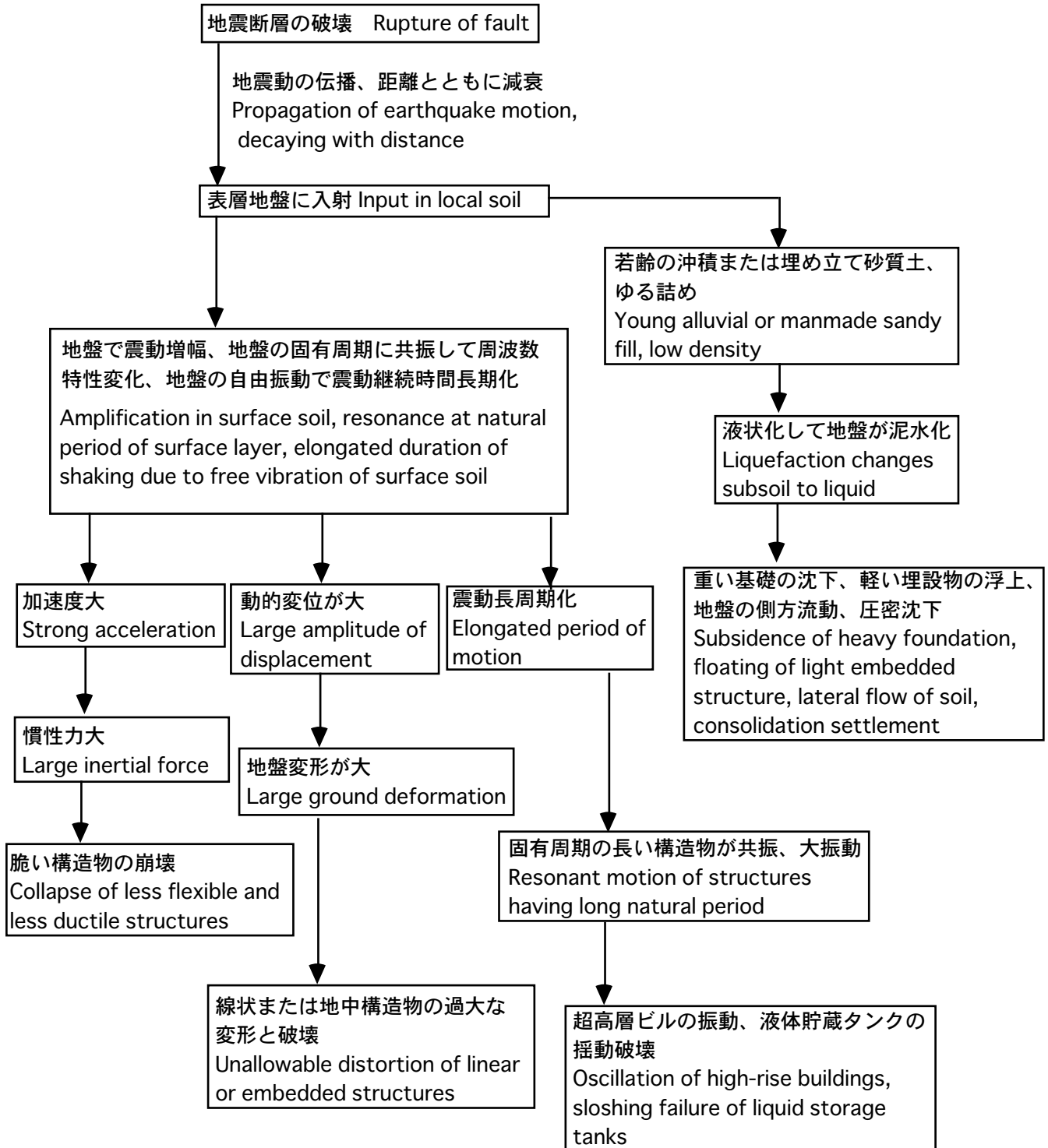
Soil–structure interaction 地盤と構造物との相互作用

Prevention of liquefaction 液状化の防止

Mitigation of liquefaction-induced damage 被害の軽減

It is still difficult to prevent liquefaction over a vast area where networks of lifelines are installed ライフライン網のような広大な施設全域で液状化を防止するのは不可能である. It is also expensive, or impossible in developed urban areas 都市域は建て込んですでに地盤を改良する余地がない. When this is the case, the bad consequences of liquefaction should be minimized by using several mitigation measures このような場合、液状化の発生はやむを得ないが、被害をなるべく少なくするような方策を考える.

2.3 Schematic Diagram to Show Relationship Among Geotechnical Seismic Problems



# Chapter 3

## Seismological Knowledge



Lion's gate at Hattusas, the ruin of the capital of ancient Hittite Empire, Anatolia, Turkey.

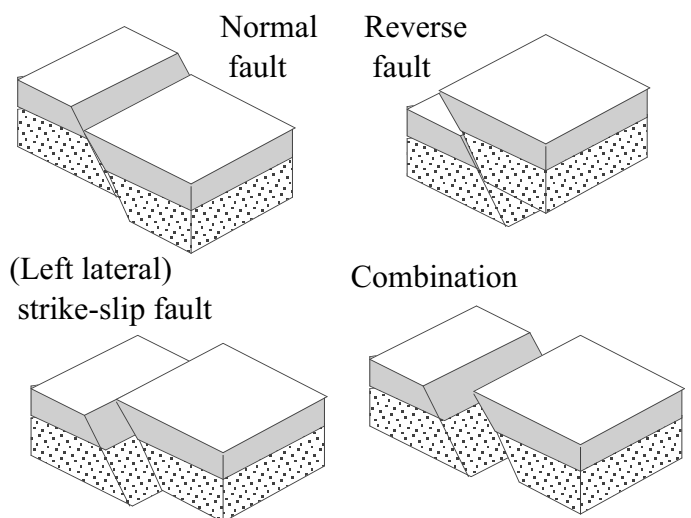
### 3.1 Rupture of Fault as Cause of Earthquake

Figure 3.1 illustrates a Japanese traditional idea on causative mechanism of earthquakes. Therein a cat fish (鯰) whose movement underground caused an earthquake and destroyed present Tokyo in the middle of nineteenth century are punished by angry people. The true understanding of the cause of earthquakes started in the second half of the twentieth century.



**Fig. 3.1** Stabilization of traditional earthquakes by punishing catfish

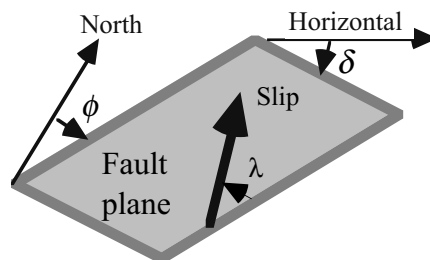
It is commonly understood today that an earthquake is caused by a rupture of a fault in the earth's crust. Figure 3.2 shows various fault movements: normal, reverse, and (left- or right-lateral) strike-slip. The normal fault is caused by tensile stress field because the two earth blocks in Fig. 3.2 are separated from each other. In contrast, the reverse fault is generated by compressional stress field. This is the case in the subduction zone where an ocean tectonic plate subsides under a continental plate.



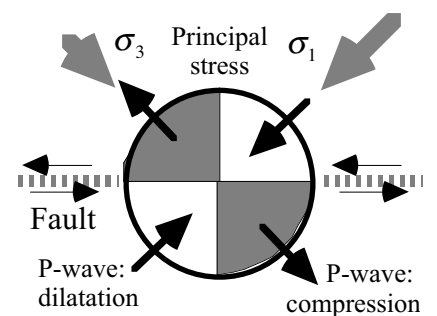
**Fig. 3.2** Types of faults

As for terminology, an earthquake hypocenter (震源) or focus stands for the place of the first rupture, whilst an epicenter (震央) is the place at the surface that lies just above the focus. See Sect. 5.10.

The geometric characteristics of a fault plane are expressed in terms of its direction ( $\phi$ ), inclination ( $\delta$ ), and the direction of displacement ( $\lambda$ ) in addition to the size. Three angular information is illustrated in Fig. 3.3. Moreover, the directions of tectonic stress and fault movement are related with the direction of ground motion. Generally, the direction of the principal stress (compressional stress) is related with the direction of the first ground movement (P wave in Sect. 4.2). Thus, the observed earthquake



**Fig. 3.3** Definition of geometric parameters of fault orientation



**Fig. 3.4** Example of motion in first part of P wave in strike-slip fault

motion is able to assess the nature of stress field and the mechanism of an earthquake causative fault. In Fig. 3.4, the white part implies the area of the first motion towards the fault (the center of fault rupture, or, more precisely, the epicenter at ground surface; see Sect. 5.10), while the shadowed part shows the first motion that is oriented away from the fault. Note that this type of diagram is in principle of a three-dimensional nature, although Figure 3.4 illustrates a simple two-dimensional situation.

The earth crust is continuously sheared or compressed by increasing tectonic forces. As the stress in rock increases with time, the strain energy is accumulated. Ultimately the crust is broken mechanically and the elastic energy is released (Fig. 3.5). Earthquake is the result. Thereafter, the accumulation of strain energy starts again towards a future earthquake.

The rock rupture is said to be associated with a generation of electric current. This may be related to many precursors (前兆). Measurement of electric current in Greece is making a success to some extent in prediction of earthquakes.

In reality, the whole fault does not rupture in a single event. The first breakage occurs at a place where the factor of safety is minimum. The working stress there is transferred to other portions of the fault, causing another rupture. Thus, the rupture propagates along the fault. Impact is generated from each rupture event and affects the ground surface. With all the impact combined, the ground motion is felt as an earthquake.

The number of possible earthquake occurrence in a concerned area is an important issue in assessing the regional seismic risk. Gutenberg and Richter (1944) reported a logarithmically linear relationship between seismic magnitude ( $M$ ) and the number of earthquakes ( $n$ ) that occurred in the California-Nevada region from 1921 to 1943

$$\log_{10} n(M) = a - bM. \quad (3.1)$$

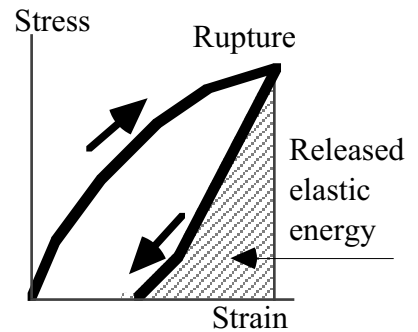


Fig. 3.5 Release of elastic energy after rupture

In this equation,  $n(M)$  stands for the number of earthquakes whose magnitude lies between  $M-1/2$  and  $M+1/2$ . Moreover,  $a$  and  $b$  are parameters that account for the local seismic activity. Since  $a$  and  $b$  were about 5 and 0.88 in their study, the above formula implies that the number of earthquakes decreases as illustrated in Fig. 3.6. Gutenberg and Richter (1944) then extended their studies to the entire world and validated the above empirical formula. Note, however, that the values of  $a$  and  $b$  parameters may vary from region to region. Moreover,  $a$  depends on the time period of concern.

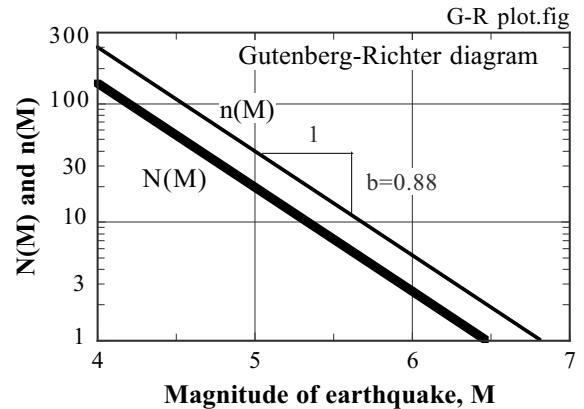


Fig. 3.6 Example illustration of Gutenberg-Richter relationship with  $a=5$  and  $b=0.88$

The number of earthquakes,  $N(M)$ , whose magnitude is greater than  $M$  can be calculated by integrating (3.1);

$$N(M) = \int_M^{\infty} n(M) dM.$$

Consequently,

$$\log_{10} N(M) = a - \log_{10}(b \log_e 10) - bM \quad (3.2)$$

Figure 3.6 illustrates both  $n(M)$  and  $N(M)$  changing with  $M$  by using  $a=5$  and  $b=0.88$ .

Recent studies in seismology revealed that the earthquake is not the only way to release the strain energy as illustrated in Fig. 3.5. The rebound may occur more slowly. This type of event is called slow earthquake, silent earthquake, or slow slip event (Kawasaki, 2006). Whatever may be the name, the rebound of the tectonic plate occurs over a long time, ranging from minutes to months, and accordingly the intensity of acceleration is very small. Noteworthy is that a slow earthquake can generate a big tsunami if the sea bed moves within a short time period. If this happens, it is possible that a disastrous tsunami attacks a coastal region despite that the associating seismic shaking is too weak to trigger any precaution.

### 3.2 Regions Where Big Earthquake Is Likely To Occur

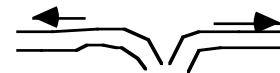
In modern seismology (for example, Bolt, 1973), the earth's surface is divided into many plates of crust which travel laterally. Figure 3.7 attempts to show major plates that are known so far. For latest information, refer to many literatures in this field. The mechanical interaction between plates, such as collision, friction, and separation, accumulates strain and strain energy that lead ultimately to rupture. Therefore, the number of earthquakes in the plate boundary regions is significantly greater than that inside plates.



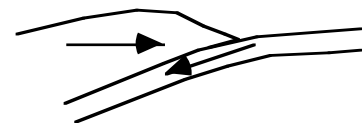
**Fig. 3.7** Earth surface divided into tectonic plates  
(drawn on the World Atlas by A. Ortelius, 1574: yellow lines show plate boundaries)

It is not true that all the plate boundaries generate strong earthquakes. For example, some parts of the San Andreas Fault in California, which is located along a boundary between North American and Pacific Ocean Plates, deform continuously and hence do not produce a sudden rupture. In opposition in the past, many big earthquakes occurred inside tectonic plates. A few of examples for this are the 1811–1812 New Madrid earthquake in south United States (magnitude being 8.0 or more) and the 1976 Tangshang (唐山) earthquake of magnitude=7.8 in North China. It seems that plate distortion occurs internally as well due to externally applied boundary stresses. Thus, there is virtually no earthquake-free region and the extent of earthquake risk is a matter of probability and local human population. In general, the time period until the next rupture is shorter in plate boundary earthquakes, and it is longer for internal rupture, although there are exceptions.

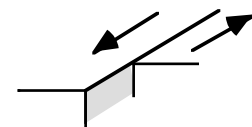
Separation undergoing tensile stress



Merging subject to compressive stress



Lateral slip and shear stress

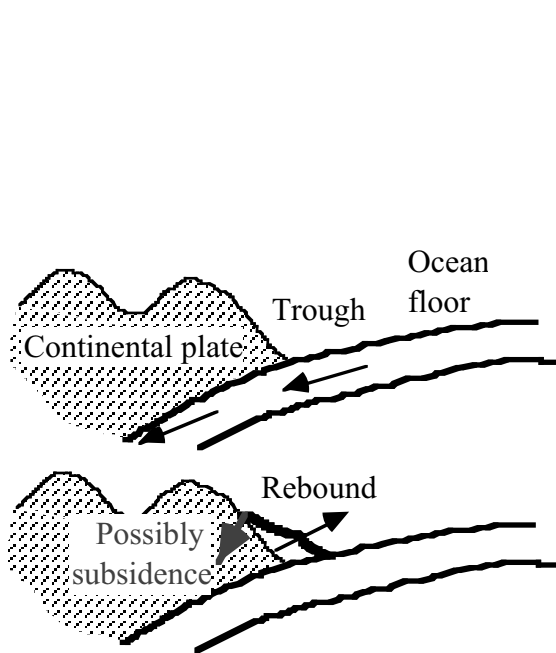


**Fig. 3.8** Types of plate boundaries

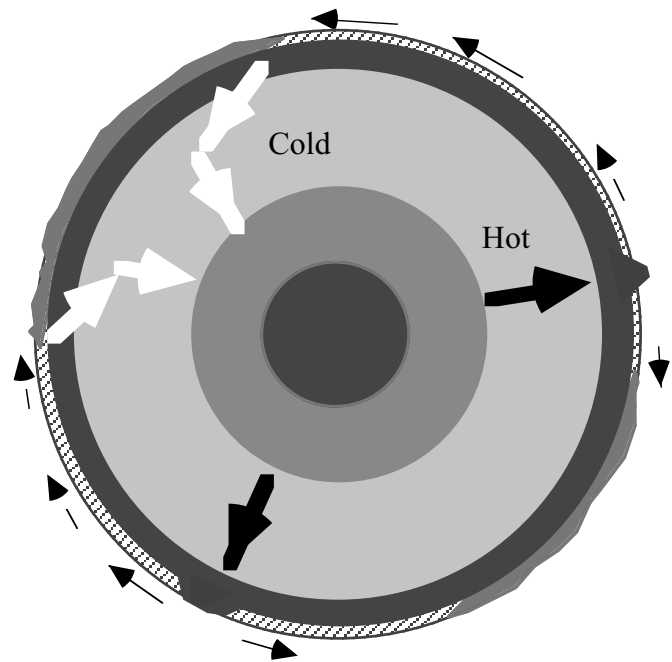
Figure 3.8 illustrates three kinds of plate boundaries where two plates are being separated (e.g. the Center of the Atlantic Ocean and the Rift Valley in East Africa), merging (subduction; Himalaya, Chile, and Japan), and being subjected to shear (California).

Figure 3.9 demonstrates a causative mechanism at a subduction zone where one of the colliding plates (mostly oceanic) is sinking down into the earth. The continental plate goes up as rebound and generates an “interplate” earthquake. This earthquake usually releases a huge elastic energy. This upward rebound action may trigger tsunami in the sea water. It is possible further that the part of the continental plate behind the rebound part may subside 1 m or so, leading to inundation by sea water, Kohchi in 1946 (Sect. 16.9) and Valdivia of Chile in 1960 (Sect. 16.10).

The modern theory of plume tectonics (Maruyama, 2002) states that the plate that is going down in Fig. 3.9 melts under high temperature and pressure, reaches the core part of the earth, and finally comes back to the surface again (Fig. 3.10). This procedure takes almost one billion years.



**Fig. 3.9** Rupture and rebound in a subduction zone



**Fig. 3.10** Conceptual illustration of plume tectonics

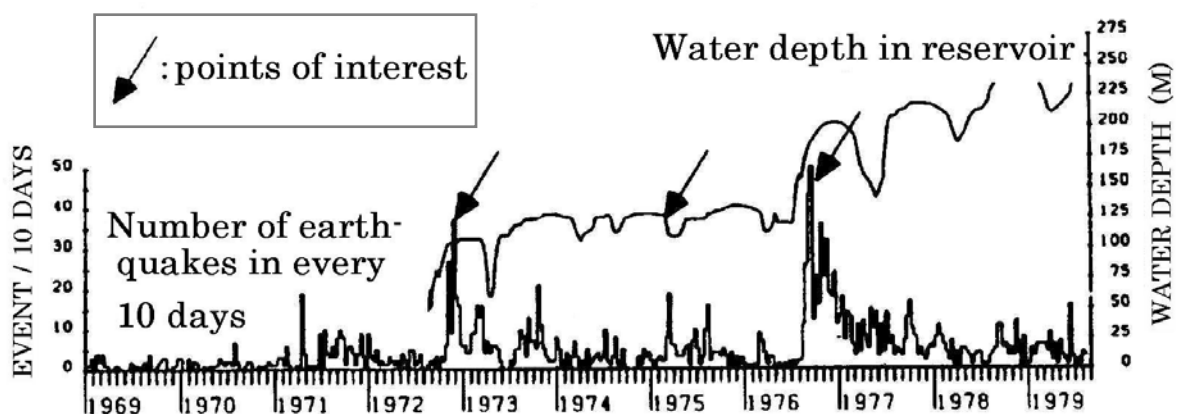
### 3.3 Reservoir-Triggered Seismicity

A unique type of earthquake triggering mechanism is found in the reservoir-triggered seismicity in which rising of water level in artificial lakes causes earthquakes. Gupta (1985) showed 44 quakes of this type among which four had magnitude greater than 6: Hsinfengkinan ( $M=6.0$ ; 1962 in China), Kariba ( $M=6.2$ ; 1963 in Zambia and Zimbabwe), Koyna ( $M=6.3$ ; 1967 in India), and Kremasta ( $M=6.3$ ; 1966 in Greece). The epicenters of reservoir-triggered earthquakes are scattered all over the world. When the Three-Gorge dam was constructed, the possibility of earthquake was discussed. Until 2007, no big earthquake has occurred in the reservoir area. It is noteworthy that the gigantic rock slide (275 million  $m^3$ ) at Vajont dam in Italy (1963) was preceded by not only minor slope failures but also small earthquakes upon reservoir filling (Nonveiller, 1987). Gupta (1985) pointed out that the Himalaya region does not have this kind of earthquake probably because of the thrust (reverse) kind of tectonic movement. He further mentioned that some reservoir decreased the local seismicity after water impounding. Thus, much is not yet known about the mechanism of reservoir-triggered seismicity.



**Fig. 3.11** Site of Three-Gorge Dam in China prior to construction

Simpson and Negmatullaev (1981) carried out a detailed investigation on the earthquakes in the area of Nurek reservoir in Tadjikistan, Central Asia. The Nurek dam is a 315 m high rockfill dam and formed a 40 km-long lake in one of the tributaries of the Amu Dary'a River. Figure 3.12 shows that earthquakes were induced when the reservoir level achieved new maximums. It was pointed out further that the very rapid draw-down of water level in early 1975 induced earthquakes. Thus, the reservoir-triggered earthquake is somehow related with the overburden pressure and pore pressure, which takes some time to propagate into rock mass and affects the rock stability. It was of further interest that the epicenters of the earthquakes migrated from the downstream area to the upstream area around the reservoir. This infers that seismicity is ceased when the strain energy is released and the earthquakes occurs in the newly impounded upstream area.



**Fig. 3.12** Correlation between number of earthquake events per 10 days and reservoir water depth at Nurek (Simpson and Negmatullaev, 1981)



**List of References in Chapter 3**

- Bolt, B.A. (1973) Earthquakes and Geological Discovery, Scientific American Library, ISBN 0-7167-5040-6.
- Gupta, H.K. (1985) The present status of reservoir induced seismicity investigations with special emphasis on earthquakes, Tectonophysics, Vol. 118, pp. 257–279.
- Gutenberg, B. and Richter, C.F. (1944) Frequency of earthquakes in California, Bull. Seismol. Soc. Am., Vol. 34, pp. 185–188.
- Kawasaki, K. (2006) Introduction to slow earthquake, NHK Books 1005, ISBN 4-14-091055-0 C1344 (in Japanese).
- Maruyama, S. (2002) Evolution of earth, Decoding the earth's evolution, Ed., Kumazawa, M., Ito, T. and Yoshida, S., University of Tokyo Press, ISBN 4-13-060741-3, pp. 18–54 (in Japanese).
- Nonveiller, E. (1987) The Vajont reservoir slope failure, Eng. Geol., Vol. 24, p. 499.
- Simpson, D.W. and Nagmatullaev, S.K. (1981) Induced seismicity at Nurek reservoir, Tadjikistan, USSR, Bull. Seismol. Soc. Am., Vol. 71, No. 5, pp. 1561–1586.

# Chapter 4

## Wave Propagation in Elastic Medium



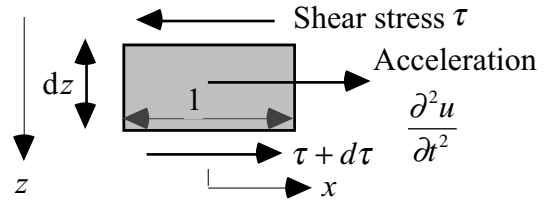
Buddhism statue at Longmen (龍門) in Luoyang (洛陽), China.

This was a place where rich people in the capital city of Luoyang donated statues for dead people. Descriptions on the life of the dead people were carved on rock and have been considered as the best calligraphy .

**4.1 Earthquake Waves: S Wave**

S wave (Secondary wave) is a propagation of shear deformation that arrives at earthquake observation stations after (second to) the Primary body wave (P wave, see Sect. 4.2). Since S wave generates a significant magnitude of horizontal motion at the ground surface, it is considered to be the most important cause of seismic damage.

Figure 4.1 illustrates the derivation of S-wave propagation equation for which a study is made of equation of motion of a small soil element in an semi-infinite level and elastic ground



**Fig. 4.1** Derivation of S-wave propagation equation

$$\rho \frac{\partial^2 u}{\partial t^2} = \frac{\partial \tau}{\partial z}, \tag{4.1}$$

where  $u$  is the horizontal displacement, and  $\rho$  stands for the mass density of soil (1.5–2 times that of water in most situations), while  $\tau$  is the shear stress in a horizontal plane at the top and bottom of the concerned soil element. Lateral normal stresses on the left and right sides of the element are not included in the equation. This is because the assumption of a homogeneous level ground subjected to horizontal shaking makes everything constant in the  $x$  direction and, consequently, the normal stresses on two sides are equal to and cancel each other.

Another assumption of linear elasticity correlates shear stress with shear strain and displacement

$$\tau = G \times (\text{shear strain}) = G \frac{\partial u}{\partial z}, \tag{4.2}$$

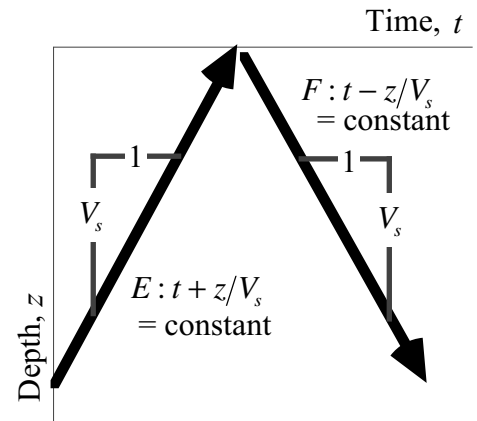
in which shear modulus of soil is designated by  $G$ . By substituting (4.2) in (4.1) and using a new notation of  $V_s = \sqrt{G/\rho}$ ,

$$\frac{\partial^2 u}{\partial t^2} = \frac{G}{\rho} \frac{\partial^2 u}{\partial z^2} = V_s^2 \frac{\partial^2 u}{\partial z^2}. \tag{4.3}$$

The general solution of (4.3) is given by

$$u(t, z) = E(t + z/V_s) + F(t - z/V_s), \tag{4.4}$$

in which  $E$  and  $F$  are arbitrary functions of  $t+z/V_s$  and  $t-z/V_s$ , respectively. They have to be arbitrary because the time history of earthquake motions are irregular.



**Fig. 4.2** Rate of wave propagation

Figure 4.2 shows that the motions represented by  $E$  and  $F$  travel upwards or downwards at the rate of  $V_s$  per second. For example, suppose that  $E = 1.2345$  when  $t+z/V_s = 2.00$ . There are many combinations of  $t$  and  $z$  for which  $t+z/V_s = 2.00$ . The only requirement for  $E = 1.2345$  is that  $z$  decreases by  $V_s$  when  $t$  increases by 1. Thus, the phenomenon of  $E = 1.2345$  moves upwards at the rate of  $V_s$  per second. Accordingly the horizontal shaking accounted for by  $E$  function travels upwards at the speed of  $V_s$ . Similarly, the  $F$  component of shaking propagates downwards at the rate of  $V_s$ . Hence,  $V_s$  is called the S-wave propagation velocity.

Thus, the horizontal shaking was decomposed into two parts: upward and downward propagations. Propagating inside a solid medium, S wave is one of what are called body waves. Typical  $V_s$  values are, approximately, 100 m/s for very soft soils, 300 m/s for stiff soils, and 3,000 m/s for hard intact rocks.

4.2 Earthquake Waves : P Wave

In addition to the S wave in Sect. 4.1, another kind of body wave that propagates in a homogeneous medium is called the P wave. P wave is a propagation of compression and extension (variation of pressure and volume change). Typical example of P wave is a propagation of sound, see Fig. 4.3.

The rate of P wave propagation is given by

$$V_p = \sqrt{\frac{E(1-\nu)}{\rho(1-2\nu)(1+\nu)}}, \quad (4.5)$$

where  $E$  is the modulus of elasticity and  $\nu$  the Poisson ratio. Note that the Poisson ratio is equal to 0.5 in an incompressible material and makes  $V_p$  infinite.

It is a common practice in geophysical exploration that P wave is generated artificially by any impact or explosion so that its rate of propagation,  $V_p$ , may be measured. The obtained  $V_p$  value is substituted in (4.5) to back-calculate the value of  $E$  while the Poisson ratio is assumed to be more or less 0.25–0.3. It is noteworthy that this technique of subsurface exploration is useful for very stiff soil and rock. When this technology is conducted in soft soil of an alluvial plane where the ground water table is high, the measured  $V_p$  is often 1,400–1,500 m/s. Since the pore of soil is saturated with water and the modulus of compressibility of water is greater than that of soft soil skeleton, the measured  $V_p$  is the velocity of sound propagation in water without much correlation with the engineering nature of soil. In contrast, the P wave velocity,  $V_p$ , is, for example, 5,000 m/s in an intact rock mass.

There is an interaction between P and S waves. Figure 4.4 illustrates two kinds of S waves. For SH, the direction of soil particle motion is antiplane and perpendicular to the cross section of subsoil, while SV moves soil particles inside the plane. After SH wave arrives at the boundary of two different soils, the motion is still SH, although the direction of wave propagation may change (refraction 屈折 into the next layer and reflection 反射 back into the first layer) in accordance with the nature of soil (Fig. 4.5a). On the contrary, SV wave upon arrival at a boundary generates both P and SV waves in refracted and reflected phases as well (Fig. 4.5b). Because of the simplicity, most seismic risk analyses of regions and municipalities assume SH waves assuming horizontally layered ground. On the contrary, dynamic response analyses on important structures (foundations, dams, etc.) are conducted on two-dimensional cross sections and hence work on SV (not SH) waves.

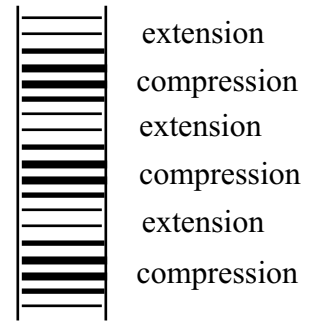


Fig. 4.3 Propagation of volume change in P wave propagation

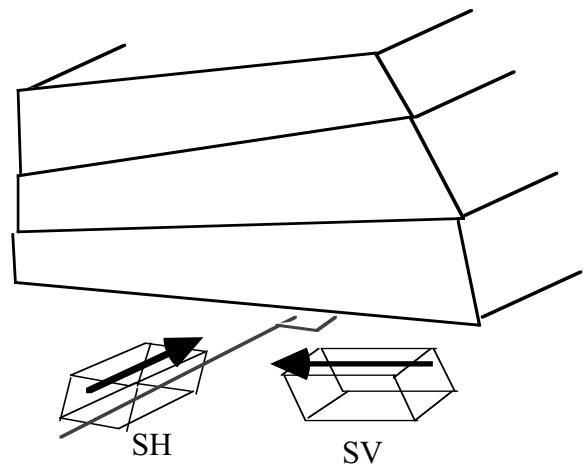


Fig. 4.4 Difference of SH and SV waves

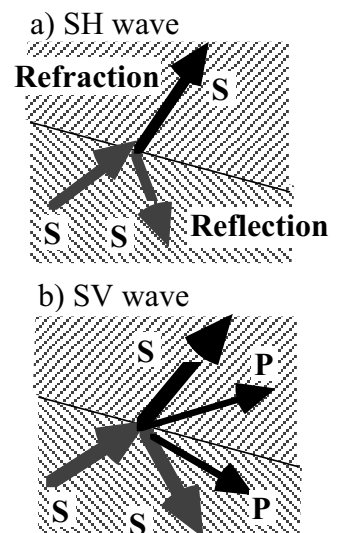


Fig. 4.5 Refraction and reflection of S waves at interface

An earthquake source generates both P and S waves simultaneously. At a focal distance of  $L$ , they arrive at different times because of different propagation velocities. The difference in arrival time is given by

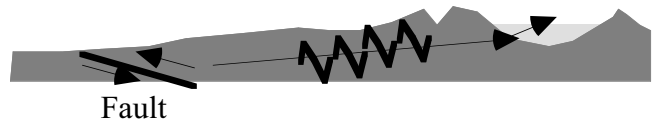
$$\Delta T = \frac{L}{V_s} - \frac{L}{V_p}. \quad (4.6)$$

This formula is used to assess the distance to the seismic source,  $L$ , by using the recorded time difference,  $\Delta T$ . For wave propagation in earth crust,  $V_p$  and  $V_s$  in intact rock mass are relevant,  $V_p = 5$  km/s and  $V_s = 3$  km/s. If  $L$  from three observation points are known, it is possible to determine the location of the wave source.

Hard rock has  $V_p$  of typically 5,000 m/s. In soft water-saturated soil, P wave propagation in pore water is predominant. Hence,  $V_p$  in such a soil condition is similar to the velocity of sound in water. For example, the sound velocity in water is 1,483 m/s at 20 °C and 1,433 m/s at 15 °C. The sound velocity in air is 343.5 m/s at 20 °C.

**4.3 Idealization of Vertical Wave Propagation**

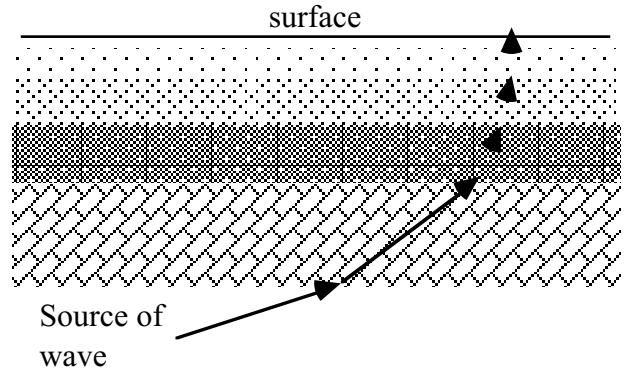
It is common that a (design) earthquake occurs at a distance of tens or hundreds of kilometers away from the site of concern while the depth of fault rupture is again tens of kilometers. Hence, the source of earthquake wave propagation is not below the site to be studied, see Fig. 4.6. Therefore, the idea of vertical wave propagation as discussed in Sect. 4.1 appears to be inappropriate.



**Fig. 4.6** Geometrical relationship between earthquake source and site of interest

Actually, the direction of wave propagation in an alluvial soft deposit should be studied in a more detailed scale (Fig. 4.7). For instance, the propagation velocity of S wave ( $V_s$ ) is a function of shear rigidity,  $G$

$$V_s = \sqrt{G/\rho} \tag{4.7}$$



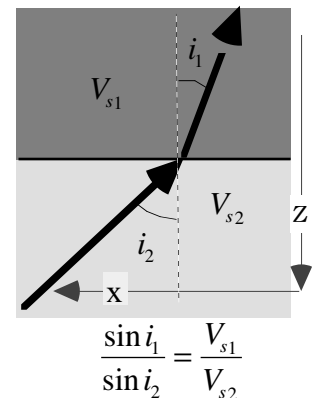
**Fig. 4.7** Wave path in alluvium

Since  $G$  of geomaterials is smaller at shallower depth,  $V_s$  decreases as well towards the ground surface. Hence, Snell’s law of wave refraction at an interface of two different wave velocities states that the wave propagation should change its direction to be more vertical, in general, as the ground surface is approached.

From Snell’s law in Fig. 4.8, using a proportionality parameter of  $\alpha$ ,

$$\sin i = \frac{dx}{\sqrt{dx^2 + dz^2}} = \alpha \times V_s \leq 1 \quad \text{or}$$

$$\frac{dx}{dz} = \frac{\alpha^2 V_s^2}{1 - \alpha^2 V_s^2} \tag{4.8}$$

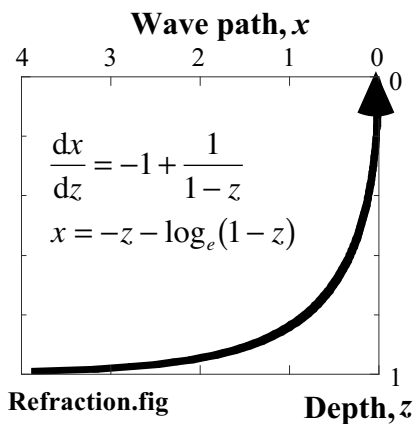


**Fig. 4.8** Snell’s law of wave refraction at interface

By assuming  $\alpha^2 V_s^2 = \alpha^2 G/\rho = z^n$  in which  $n$  accounts for the effects of depth ( or effective stress) on  $G$ ,

$$\frac{dx}{dz} = \frac{z^n}{1 - z^n} = -1 + \frac{1}{1 - z^n} \tag{4.9}$$

Figure 4.9 illustrates the integration of (4.9) that governs the change of direction of wave propagation. “ $n = 1$ ” was employed only for easy calculation;  $n < 1$  is more likely in reality. Note that Fig. 4.9 assumes a continuous variation of  $V_s$  with depth, while  $V_s$  in reality changes discontinuously at interfaces of materials of different geological ages. One of the important discontinuity occurs between alluvial and pleistocene deposits.



**Refraction.fig**

**Fig. 4.9** Example calculation of change of wave propagation direction due to continuous variation of  $G$  with depth

#### 4.4 Vertical Propagation of “S” Wave in Level Ground

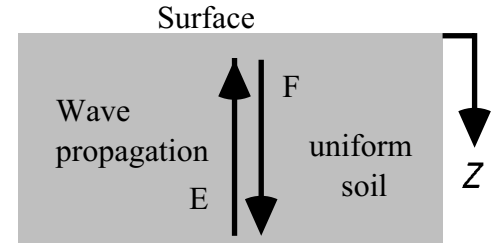
The most important type of earthquake shaking is conventionally, and most probably in future as well, the S wave that produces a ground motion in the horizontal direction. This direction of motion is substantially efficient in causing damage to surface structures.

As was already shown in Fig. 4.9, it is reasonable at a shallow depth to assume a vertical propagation of S wave. See Fig. 4.10 in this Section.

In what follows, the horizontal displacement of a soil grain is denoted by  $u$ . The equation of wave propagation is given by

$$\frac{\partial^2 u}{\partial t^2} = V_s^2 \frac{\partial^2 u}{\partial z^2}, \quad (4.10)$$

in which  $V_s = \sqrt{G/\rho}$ .



**Fig. 4.10** Vertical propagation of S wave in level subsoil

A harmonic solution (sinusoidal solution) of (4.10) is derived by assuming that  $u$  varies with time in accordance with  $\sin(\omega t)$  and  $\cos(\omega t)$  functions. The symbol of  $\omega$  denotes a circular frequency of shaking (円振動数), which is equivalent with a frequency of  $\omega/2\pi$ . It is, however, more efficient to use in this section a complex exponential function,

$$u(z, t) = A(z) \exp(i\omega t), \quad (4.11)$$

where  $i = \sqrt{-1}$  and  $A$  is an unknown function of  $z$ . In case this complex expression is not easy, it is acceptable for a reader to go to Sect. 4.5. In that section, it will be demonstrated that expressions in terms of complex number and real number are equivalent but that the complex number can save time. Note that the real and complex parts of the exponential function in (4.11) are  $\cos$  and  $\sin$  functions,

$$\exp(i\omega t) = \cos(\omega t) + i \sin(\omega t), \quad (4.12)$$

By substituting (4.11) in (4.10),

$$\frac{d^2 A}{dz^2} = -\left(\frac{\omega}{V_s}\right)^2 A \quad \text{and, accordingly,} \quad A = E \exp\left(\frac{i\omega z}{V_s}\right) + F \exp\left(-\frac{i\omega z}{V_s}\right), \quad (4.13)$$

where  $E$  and  $F$  are constant parameters that are determined by boundary conditions. The solution for “ $u$ ” is finally derived as

$$u(z, t) = \left\{ A = E \exp\left(\frac{i\omega z}{V_s}\right) + F \exp\left(-\frac{i\omega z}{V_s}\right) \right\} \exp(i\omega t) = E \exp\left\{ i\omega \left( t + \frac{z}{V_s} \right) \right\} + F \exp\left\{ i\omega \left( t - \frac{z}{V_s} \right) \right\}. \quad (4.14)$$

The  $E$  and  $F$  terms in (4.14) stand for an upward and downward wave propagations, respectively. See Fig. 4.10. Equation (4.14) states that “ $u$ ” varies with  $\exp(i\omega t)$  in terms of time. Hence, when  $\omega t$  increases by  $2\pi$ , the value of “ $u$ ” comes back to the original value. Hence,  $2\pi/\omega$  is the period of shaking. Similarly, “ $u$ ” varies with  $\exp(i\omega z/V_s)$  in terms of depth, and  $2\pi V_s/\omega$  stands for the wave length. Further,  $\omega/V_s$  is sometimes called the wave number. A further study will continue in Sect. 6.7.

Although a harmonic motion is not a reality, it is still very important in practice. This is because the real irregular ground motion can be divided into harmonic components of various frequencies, Fourier series (Sect. 9.11). Each component has a different intensity and it is further amplified to a different extent in the surface alluvium. This is called the local soil effect.

### 4.5 Solution of S-Wave Propagation in Real Numbers

The equation of S-wave propagation is given by

$$\frac{\partial^2 u}{\partial t^2} = V_s^2 \frac{\partial^2 u}{\partial z^2}. \quad (4.15)$$

By assuming its harmonic solution with real numbers,

$$u(z, t) = A(z) \sin(\omega t). \quad (4.16)$$

By substituting (4.16) in (4.15),

$$-\omega^2 A \sin \omega t = V_s^2 \frac{d^2 A}{dz^2} \sin \omega t. \quad (4.17)$$

Consequently,

$$\frac{d^2 A}{dz^2} = -\left(\frac{\omega}{V_s}\right)^2 A \quad (4.18)$$

whose solution is given by

$$A = A_1 \sin \frac{\omega z}{V_s} + A_2 \cos \frac{\omega z}{V_s}, \quad (4.19)$$

in which  $A_1$  and  $A_2$  are constant parameters to be determined by boundary conditions. Accordingly,

$$u(z, t) = \frac{A_1}{2} \left[ -\cos \left\{ \omega \left( \frac{z}{V_s} + t \right) \right\} + \cos \left\{ \omega \left( \frac{z}{V_s} - t \right) \right\} \right] + \frac{A_2}{2} \left[ \sin \left\{ \omega \left( \frac{z}{V_s} + t \right) \right\} - \sin \left\{ \omega \left( \frac{z}{V_s} - t \right) \right\} \right]. \quad (4.20)$$

Note thus that this solution consists of the upward  $\left(\frac{z}{V_s} + t\right)$  and downward  $\left(\frac{z}{V_s} - t\right)$  propagations of motion.

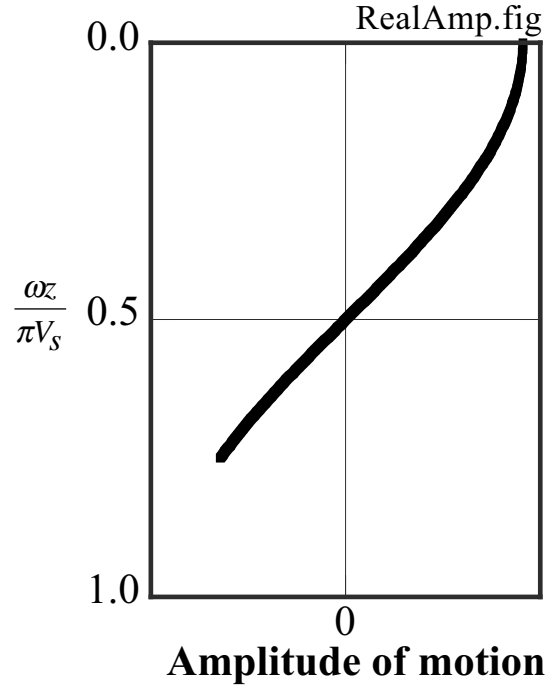
Since the ground surface is an interface of soil with air or water in which shear stress is zero, the boundary condition at the ground surface ( $z = 0$ ) specifies

$$\tau = G \times (\text{shear strain}) = G \frac{\partial u}{\partial z} = 0 \quad \text{or} \quad \frac{\partial u}{\partial z} = 0 \quad \text{and} \quad \frac{dA}{dz} = 0. \quad (4.21)$$

Accordingly,  $A_1 = 0$

$$A(z) = A_2 \cos \frac{\omega z}{V_s} \quad \text{and} \quad u(z, t) = A_2 \cos \frac{\omega z}{V_s} \sin \omega t. \quad (4.22)$$

Figure 4.11 illustrates the variation of the amplitude of motion,  $A(z)$ , in the vertical direction. Note that the sign of “ $A$ ” changes below  $\omega z/V_s = \pi/2$ . This implies that the ground surface and soil below some depth move in opposite directions. It is interesting that there is a special depth at which the amplitude is zero.



**Fig. 4.11** Variation of shaking amplitude in vertical direction



The simplest type of amplification of motion is defined by the ratio of motion at the surface and at the base (base stiff soil or rock) at  $z = H$ ;

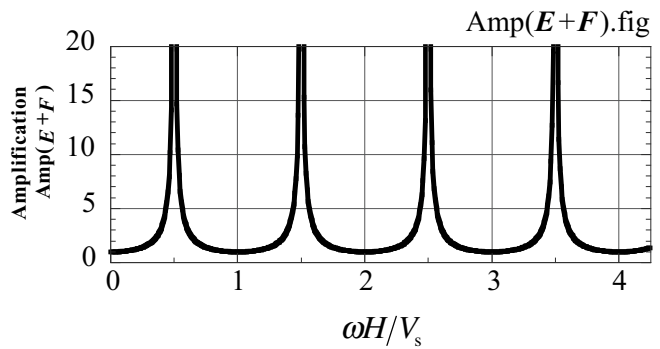
$$\text{Amp}(E + F) \equiv \frac{\text{Amplitude of motion at surface}}{\text{Amplitude of motion at base}} = \frac{|A(z = 0)|}{|A(z = H)|} = \frac{1}{\left| \cos \frac{\omega H}{V_s} \right|}. \quad (4.23)$$

Figure 4.12 demonstrates the variation of amplification with  $\omega H/V_s$ . The amplification thus varies with the frequency of motion (frequency =  $\omega/2\pi$ ) and the thickness of surface soil ( $H$ ). The maximum value of amplification (resonance) occurs when  $\omega H/V_s = \left(n - \frac{1}{2}\right) \times \pi$  in which  $n=1,2,3,\dots$ . When  $n = 1/2$  in particular,

$$\begin{aligned} \omega H/V_s = \frac{\pi}{2}, \quad \omega = \frac{\pi V_s}{2H}, \quad \text{frequency} = \frac{\omega}{2\pi} = \frac{V_s}{4H}, \quad \text{and} \\ \text{the period of motion} = \frac{1}{\text{frequency}} = \frac{4H_s}{V_s}, \end{aligned} \quad (4.24)$$

which is very important in seismic microzonation. The amplification means that the surface motion is  $\text{Amp}(E+F)$  times greater than the motion at the base.

Although Fig. 4.12 suggests an infinite value of amplification at resonance, the reality does not cause infinite intensity of surface motion upon (small) motion at the base. Real soil and ground have many kinds of energy loss and does not enable such a strong motion; see Sect. 9.6 and Chap 10.



**Fig. 4.12** Amplification of motion in ideally linearly elastic ground

 **4.6 Exercise No. 1 on Amplification of Ground Motion**

1. Take the real parts of (4.14) in Sect. 4.4. Determine the relationship between two unknown parameters,  $E$  and  $F$ , by using a boundary condition at the ground surface. Do not forget that “ $E$ ” and “ $F$ ” are complex numbers.

Boundary condition: Since the ground surface ( $z=0$ ) is a free surface, there is no shear stress,

$$G \frac{\partial u}{\partial z} = 0. \text{ Since } G \neq 0, \quad \frac{\partial u}{\partial z} = 0.$$

2. Remove “ $F$ ” from concerned formulae by using the relationship derived in [1]. Then, plot the relationship between the amplitude of shaking displacement “ $u$ ” and the depth. Use high and low values of frequency (high and low values of  $\omega$ ).
3. Calculate the amplification factor which is the ratio of the amplitudes of shaking motion “ $u$ ” at the surface and at the bottom of the surface soil ( $z = H$ ).
4. Calculate the amplification similarly for a situation where there is a rigid mass of “ $M$ ” per unit area at the ground surface.

For answers, see the end of this book.

**4.7 Earthquake Waves : Rayleigh Wave**

The Rayleigh wave travels along the ground surface (surface wave). It does not propagate into the earth. The displacements,  $u$  and  $w$  in Fig. 4.13, are analytically given in complex numbers

$$u = iAN \left[ -\exp\left\{-\frac{q}{N}(zN)\right\} + \frac{2\frac{q}{N}\frac{s}{N}}{\frac{s^2}{N^2} + 1} \exp\left\{-\frac{s}{N}(zN)\right\} \right] \exp\{i(\omega t)Nx\}$$

$$w = iAN \left[ \frac{2\frac{q}{N}}{\frac{s^2}{N^2} + 1} \exp\left\{-\frac{s}{N}(zN)\right\} - \frac{q}{N} \exp\left\{-\frac{q}{N}(zN)\right\} \right] \exp\{i(\omega t)Nx\},$$

in which  $i = \sqrt{-1}$ ,  $A$  is constant,  $N$  the wave number with the wave length =  $2\pi/N$ , and  $\omega$  the circular frequency. Moreover,

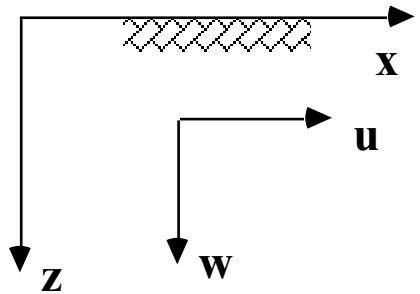
$$q = \sqrt{N^2 - \omega^2/V_p^2} \quad \text{and} \quad s = \sqrt{N^2 - \omega^2/V_s^2}$$

The wave number,  $N$ , is calculated by  $N = \omega/V_s K$  in which  $K$  is a solution of

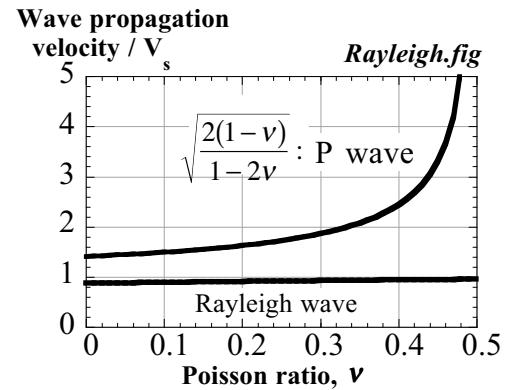
$$K^6 - 8K^4 + \left(24 - 8\frac{1-2\nu}{1-\nu}\right)K^2 - \frac{8}{1-\nu} = 0$$

and is given as

Poisson ratio $\nu$	0.0	0.1	0.2	0.3	0.333	0.4	0.5
$K = V_r / V_s$	0.874	0.893	0.911	0.927	0.933	0.942	0.955

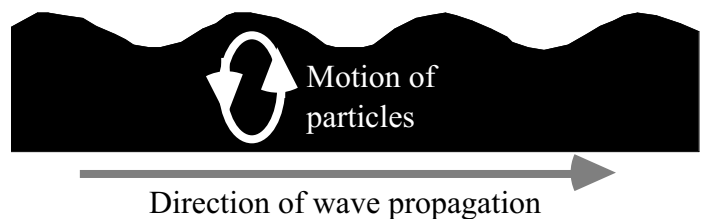


**Fig. 4.13** Positive direction of coordinates and displacements



**Fig. 4.14** Wave propagation velocities

The velocity of Rayleigh wave,  $V_r$ , is slightly smaller than  $V_s$ , see Fig. 4.14. Figure 4.15 illustrates the orbit of particle movement near the surface ( $z=0$ ). When the wave propagates towards the right, the particle rotates in a counterclockwise direction. Bolt (1993) drew a good illustration of the material movement in Rayleigh wave. The direction of the particle movement is reversed below some depth to be clockwise.



**Fig. 4.15** Form of Rayleigh-wave motion in elastic medium

When the subsoil is composed of soil layers that have different shear wave velocities ( $V_s$ ), the propagation velocity of Rayleigh wave is variable. Rayleigh wave of longer wave length (long period) is affected by nature of soils at greater depth where  $V_s$  is higher, and its propagation velocity is greater. On the contrary, Rayleigh wave of shorter wave length (high frequency) is controlled by soils at shallower elevation, and its propagation velocity is slower. This nature is applied to subsurface soil investigation in which the propagation velocity of many Rayleigh-wave components are measured and shear modulus of soils at corresponding depth is determined.

Seismologists are interested in Rayleigh wave traveling along the earth's perimeter. However, that wave causes a very small intensity of ground shaking without affecting engineering facilities. Earthquake geotechnical engineering is interested in Rayleigh waves that are generated when the incident P and S waves hit the surface irregularity and are reflected. A surface wave seems to decay quickly as it travels along the surface of soft deposits. It cannot reach a far distance. This is because the soft soil has a hysteresis stress-strain loop and the wave energy decays quickly during the propagation.

Application of Rayleigh wave to site investigation: Artificially generate Rayleigh wave (Sect. 4.9) and measure its propagation velocity  $V_r$ , at surface. Since  $V_r \cong V_s = \sqrt{G/\rho}$ , "G" of soil is obtained. " $\rho$ " is typically 1.8–2.0 ton/m<sup>3</sup>.

🌟 4.8 Earthquake Waves : Love Wave

There is another type of surface wave that is called Love wave. This wave occurs when an elastic halfspace is overlain by a softer surface layer (Fig. 4.16). Harmonic solution (sinusoidal function) is given by

$$u_1 = \{A \exp(is_1z) + B \exp(-is_1z)\} \exp(-iqy) \exp(i\omega t)$$

$$u_2 = C \exp(-is_2z) \exp(-iqy) \exp(i\omega t),$$

where  $u_1$  and  $u_2$  stand for displacement in  $x$  direction in the upper and lower layers, respectively.  $A$ ,  $B$ , and  $C$  are constants. Furthermore,  $\omega$  is the circular frequency, and

$$s_1 = \sqrt{k_1^2 - q^2}, \quad k_1 = \omega / V_{s1}, \quad V_{s1} = \sqrt{G_1 / \rho}$$

$$s_2 = \sqrt{k_2^2 - q^2}, \quad k_2 = \omega / V_{s2}, \quad V_{s2} = \sqrt{G_2 / \rho}$$

Since the particle motion is oriented in the  $x$  direction, Love wave is a type of SH wave. The above solution means that an upward and downward propagation of SH waves are superimposed (重複) in the upper layer; both propagating in  $y$  direction as well, whilst the lower layer has a horizontal propagation of a single SH wave (Fig. 4.17).

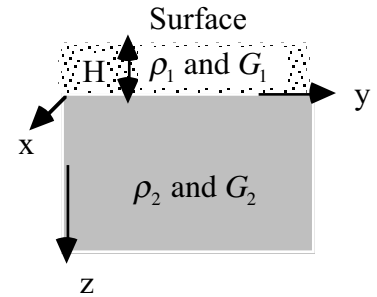


Fig. 4.16 Coordinates in Love-wave theory

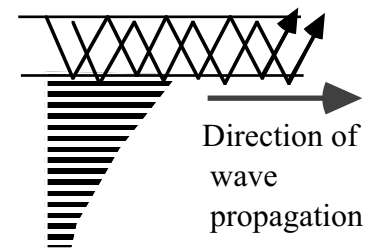


Fig. 4.17 Superimposed SH wave propagation

Figure 4.18 illustrates a view of ground deformation. The surface layer is sheared in both  $y$  and  $z$  directions. Bolt (1993) made a good illustration of particle movement in Love wave. Being SH wave, Love wave does not have a volume change.

$A$ ,  $B$ , and  $C$  parameters are determined by considering (1) shear stress = 0 at the ground surface ( $z=-H$ ), and (2) both stress and displacement are continuous at the interface ( $z=0$ ). The velocity of Love wave velocity,  $V_L$ , is given by

$$V_L = q/a = V_{s1} \sqrt{1 + s_1^2/q^2}$$

When the wave length seen along the surface,  $L=2p/q$ , varies,  $q$  value changes as well and  $V_L$  changes

High frequency  $\rightarrow$  short  $L \rightarrow V_L$  approaches  $V_{s1}$  and Low frequency  $\rightarrow$  long  $L \rightarrow V_L$  approaches  $V_{s2}$ .

Thus, the wave propagation velocity of Love wave depends on the frequency. This fact makes dispersion and group velocity ( $U$ , 群速度). Vibration of different frequency propagates at different  $U$ . The principle lying behind this is similar to beeping (うなり).

$$d(\omega t - qy)/dq = 0 \quad \therefore t(d\omega/dq) - y = 0 \quad U = y/t = d\omega/dq = d(V_L q)/dq$$

$$\therefore U = V_L + q(dV_L/dq) = V_L - L(dV_L/dL).$$

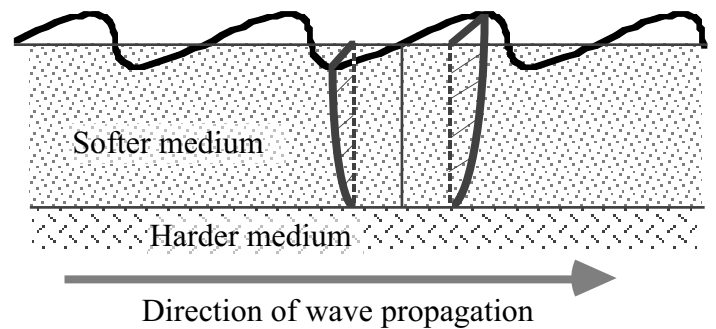


Fig. 4.18 Conceptual view of ground deformation in Love wave

**4.9 Response of Elastic Ground to Surface Excitation**

Figure 4.19 illustrates an elastic halfspace that is excited by a linear vertical loading. Solving the ground response under this situation is called Lamb’s problem. For details, see B ath (1968).

The solution of Lamb’s problem shows that the ground response to this linear loading consists of three components:

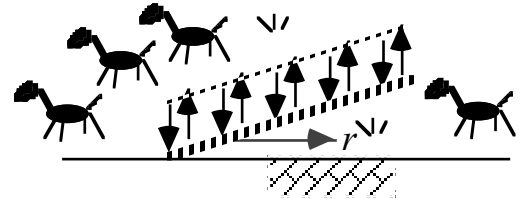
- P wave : decays with distance
- S wave : decays with distance
- Rayleigh wave : no decay

The first two are body waves and propagates into the infinite body of ground. Therefore, they become weaker (decay) as they travel farther. In contrast, the surface wave (Rayleigh wave) maintains its amplitude to the infinity, because it travels along the surface.

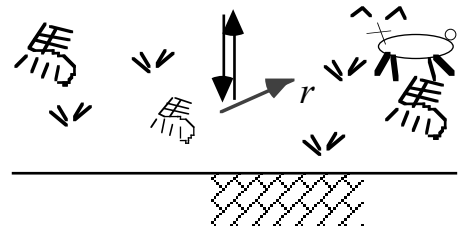
When the surface loading is applied at a point (Fig. 4.20), all the three components of motion decay with distance. Table 4.1 reveals the rate of decay with the distance.

**Table 4.1** Decrease of wave amplitude at surface with distance from the source (geometrical damping)

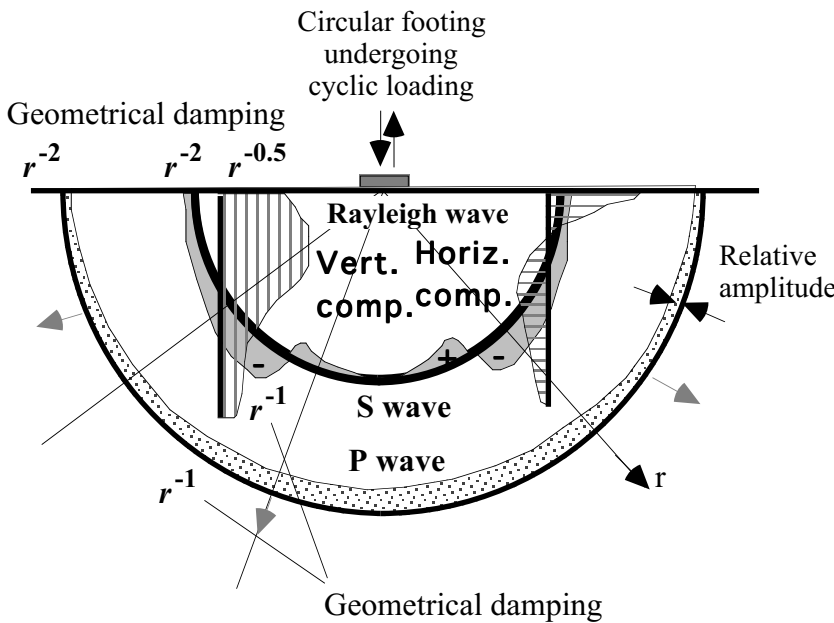
Source	Rayleigh	P	S	
Line	1	$r^{-3/2}$	$r^{-3/2}$	$r$ : surface distance from source
Point	$r^{-1/2}$	$r^{-2}$	$r^{-2}$	



**Fig. 4.19** Level ground excited by linear wave source at surface



**Fig. 4.20** Level ground excited by point wave source



Shear window is the direction in which S-wave energy is concentrated.

Wave type	Percent of total energy
Rayleigh	67
Shear	26
Compression	7

**Fig. 4.21** Distribution of displacement waves from a circular footing on a homogeneous, isotropic, elastic halfspace (after Woods, 1968)

Figure 4.21 indicates the variation of energy and wave type with the direction of propagation. Under a circular oscillating footing, similar to a point loading, the energy of P wave (compression wave) is more important in the vertical direction, S wave is important in the inclined directions, and Rayleigh wave is significant near the surface.

**4.10 Wave Transmission and Reflection at Interface**

Study is made of SH wave propagation across an interface of two elastic layers. An infinite medium is assumed here (Fig. 4.22), and attention is focussed on transmission and reflection at the interface. Being denoted as “a” and “b”, those two layers are of different impedance. An incident wave (入射波  $E_b$ ) arrives from the bottom and, at the interface, are partially transmitted into the next layer (透過波  $E_a$ ), while partially reflected back (反射波  $F_b$ ). Note that discussion in this section assumes infinite thickness of the upper layer without surface.

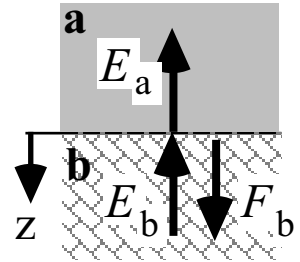
The displacement,  $u$ , and shear stress,  $\tau$ , under harmonic excitation are given by

$$u_a = E_a \exp\left\{i\omega\left(t + \frac{z}{V_{sa}}\right)\right\} \text{ and}$$

$$\tau_a = G_a \frac{\partial u_a}{\partial z} = i\omega\rho_a V_{sa} E_a \exp\left\{i\omega\left(t + \frac{z}{V_{sa}}\right)\right\} \text{ in layer "a"}$$

$$u_b = E_b \exp\left\{i\omega\left(t + \frac{z}{V_{sb}}\right)\right\} + F_b \exp\left\{i\omega\left(t - \frac{z}{V_{sb}}\right)\right\} \text{ and}$$

$$\tau_a = i\omega\rho_b V_{sb} \left[ E_b \exp\left\{i\omega\left(t + \frac{z}{V_{sb}}\right)\right\} - F_b \exp\left\{i\omega\left(t - \frac{z}{V_{sb}}\right)\right\} \right] \text{ in layer "b".}$$



**Fig. 4.22** Definition of incident and reflected waves near layer interface

Because of the continuity of displacement and shear stress at the interface ( $z=0$ ),

$$\begin{cases} E_a = E_b + F_b \\ R \times E_a = E_b - F_b \end{cases} \text{ in which } R = \frac{\rho_a V_{sa}}{\rho_b V_{sb}} \text{ being the impedance ratio.}$$

The ratio of transmitted and reflected amplitudes over the incident amplitude are

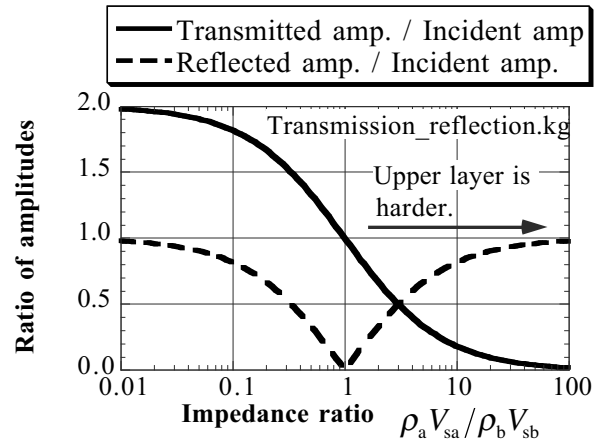
$$\frac{E_a}{E_b} = \frac{2}{1 + R} \text{ (transmitted) and}$$

$$\frac{F_b}{E_b} = \frac{1 - R}{1 + R} \text{ (reflected).}$$

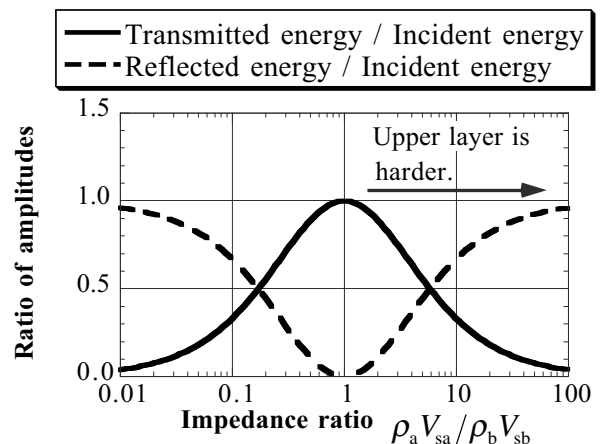
The wave energy per one wave length is proportional to  $\rho V_s E^2$  and  $\rho V_s F^2$  (see Sect. 4.11). Therefore, the ratio of energy is derived in a similar way

$$\frac{\rho_a V_{sa} E_a^2}{\rho_b V_{sb} E_b^2} = \frac{4R}{(1 + R)^2} \text{ and } \frac{\rho_b V_{sb} F_b^2}{\rho_b V_{sb} E_b^2} = \left(\frac{1 - R}{1 + R}\right)^2.$$

These results are graphically demonstrated in Figs. 4.23 and 4.24. When the impedance ratio is 1, the material property is uniform and there is no wave reflection.



**Fig. 4.23** Variation of wave amplitude at layer interface



**Fig. 4.24** Variation of wave energy at layer interface

**4.11 Calculation of Seismic Wave Energy**

Discussion here is made of S-wave propagation in the vertical direction. By assuming the displacement to be a cosine function of time, for example, displacement, velocity, and shear strain are derived

$$u = E \cos\left\{\omega\left(t + \frac{z}{V_s}\right)\right\}, \quad \frac{\partial u}{\partial t} = -\omega E \sin\left\{\omega\left(t + \frac{z}{V_s}\right)\right\}, \quad \frac{\partial u}{\partial z} = -\frac{\omega E}{V_s} \sin\left\{\omega\left(t + \frac{z}{V_s}\right)\right\}.$$

The wave energy per unit volume consists of kinetic and strain components

$$\begin{aligned} \frac{\rho}{2}\left(\frac{\partial u}{\partial t}\right)^2 + \frac{G}{2}\left(\frac{\partial u}{\partial z}\right)^2 &= \frac{\omega^2 E^2}{2} \left[ \rho \sin^2\left\{\omega\left(t + \frac{z}{V_s}\right)\right\} + \frac{G}{V_s^2} \sin^2\left\{\omega\left(t + \frac{z}{V_s}\right)\right\} \right] \\ &= \rho \omega^2 E^2 \sin^2\left\{\omega\left(t + \frac{z}{V_s}\right)\right\} = \frac{\rho \omega^2 E^2}{2} \left[ 1 - \cos\left\{2\omega\left(t + \frac{z}{V_s}\right)\right\} \right], \end{aligned}$$

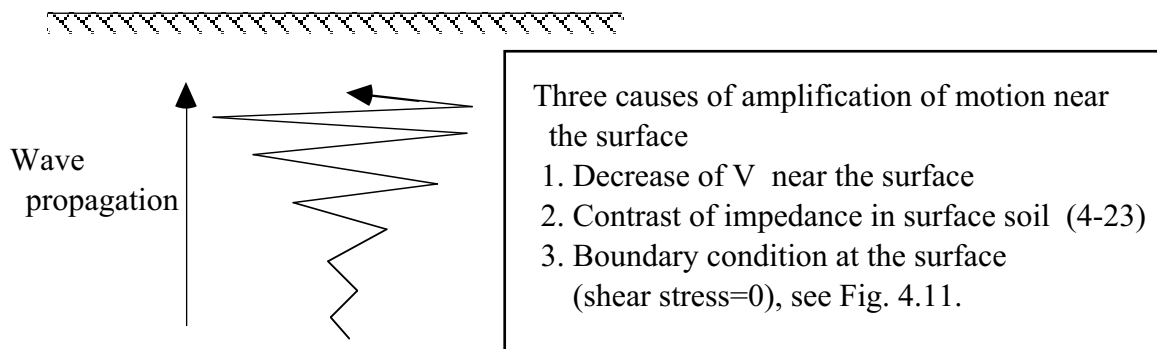
in which  $\rho$  stands for the mass density of soil. The wave energy in one wave length is derived by integrating this over the wave length ( $= 2\pi V_s/\omega$ );

$$\text{Energy per wave length} = \frac{\rho \omega^2 E^2}{2} \times \frac{2\pi V_s}{\omega} = \omega \pi (\rho V_s E^2).$$

Thus, the energy per wave length is proportional to the impedance  $\times$  amplitude<sup>2</sup>. Consequently, the energy conservation requires that the wave amplitude should increase as  $V_s$  in the medium decreases (Fig. 4.25). The amplitude is inversely proportional to the square root of wave impedance. As the wave approaches the ground surface,  $V_s$  normally decreases and the amplitude increases (Sect. 3.1). Similar to amplification of sea waves near the shore, this is one of the mechanisms of earthquake wave amplification.

The wave energy that passes through any “z” section in one period is same as above.

$$\text{Energy per one period} = (\text{Energy per volume}) \times \frac{dZ}{dt} \times \text{period} = \frac{\rho \omega^2 E^2}{2} \times \frac{2\pi V_s}{\omega} = \omega \pi (\rho V_s E^2)$$



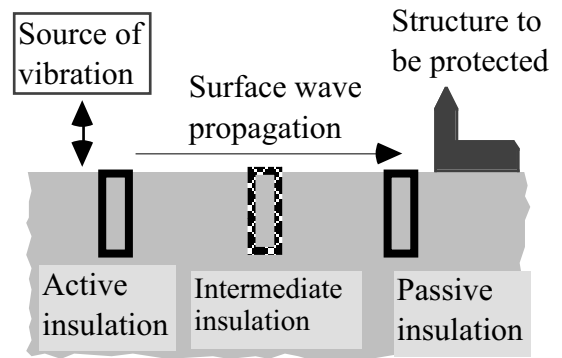
**Fig. 4.25** Increase of wave amplitude with decreasing wave propagation velocity



## 4.12 Traffic-Induced Ground Vibration

Figure 4.21 illustrated that the major energy of Rayleigh surface wave travels in a shallow depth. Since Rayleigh wave is the major component of ground vibration caused by traffics and such construction works as pile driving, it seems adequate to install a wave insulator near the ground surface in order to mitigate this environmental noise problem.

As shown in Fig. 4.26, there are three types of mitigation. The active insulation is installed near the source of ground vibration and the cost is most probably borne by the operator or the owner of the source. On the other hand, the passive insulation is installed near the structure to be protected: paid either by the source side or by the affected party. Moreover, installation of insulation in the middle is possible. However, the land is not necessarily owned by either the source or the affected sides, and the installation is more difficult than the other two locations.



**Fig. 4.26** Types of insulation against environmental ground vibration

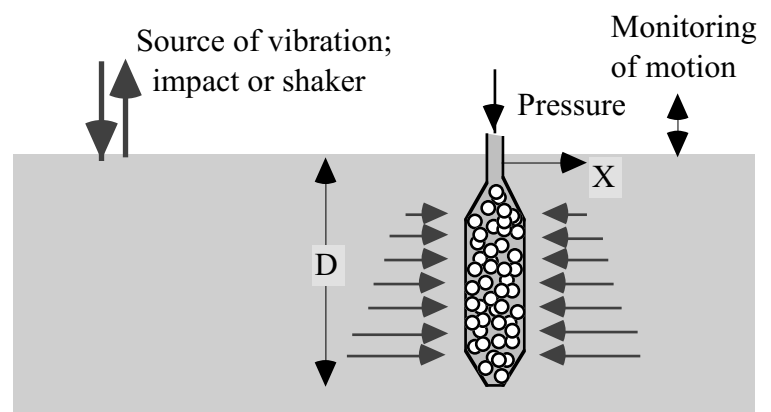
Section 4.10 discussed the energy reflection and transmission at an interface between hard and soft materials. It was shown in Fig. 4.24 that most wave energy is reflected backwards at an interface if the rigidity difference is significant. Therefore, two kinds of insulation are possible; being very rigid or very soft as compared with soil. The former is an embedded concrete wall, for example, and the latter is an open trench and embedding of other soft materials. For economical reasons, the latter appears to be more practical.

Haupt (1981) carried out model tests on an embedded rigid wall. Takemiya (2004) constructed a rigid honeycomb structure under road pavement in order to mitigate car-induced vibration.

Hayakawa et al. (1992) reduced the train-induced vibration by installing a mat under rails. The use of soft EPS can reduce the magnitude of vibration as well (Hayakawa et al. 1991). The use of gas cushion as a soft insulation was studied by De Cock and Legrand (1990) together with Massarsch (1991, 2004).

A design diagram was prepared by Woods (1968) for cut-off of surface wave propagation by a trench. The effects of a trench depend on the size of a trench and the wave length (frequency) of the concerned Rayleigh wave. The same diagram is valid for gas cushion because the same principle of cut-off is therein employed.

The author's group attempted to construct a similar diagram based on field tests. Ground vibration was caused either by a shaker or impact by hammer. The idea behind that study was as what follows:



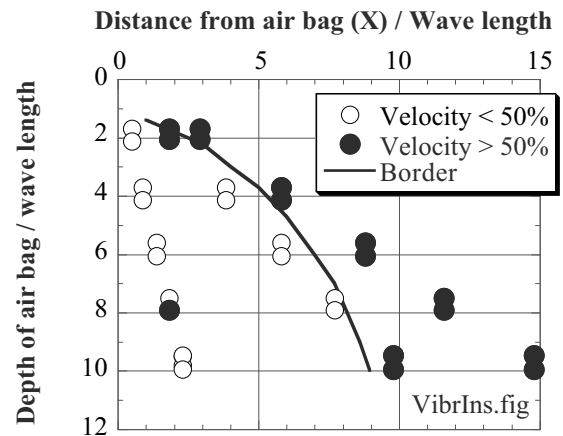
**Fig. 4.27** Generation of surface wave for study of mitigation of ground vibration

- An open trench is good for mitigation of vibration, but requires a retaining structure to maintain stability. This additional structure may reduce the mitigative effects.
- Cushion, which is called air bag by the author, with internal pressure is better in this sense.
- The stability of an embedded air bag should be further improved by placing light EPS beads in a bag so that lateral resistance against earth pressure may be improved.

Figure 4.27 shows the geometry of test conditions. An air bag with EPS beads was embedded (Sannomiya et al. 1993) in order to demonstrate a relationship between wave length, horizontal distance between the point of measurement and the air bag ( $X$ ), and the depth of the air bag ( $D$ ). The wave length was determined by measuring the wave propagation velocity ( $V_p$ ) and the shaking frequency ( $f$ );

$$\text{Wave length} = V_p / f.$$

The interpretation of the measured records considered that the air bag was effective when the intensity of vertical velocity was reduced to be less than 50%. Consequently, Fig. 4.28 was obtained. It is advised that the depth of an air bag is determined by referring to the curve in this figure. As the point of concern becomes further from the air bag (passive mitigation), a deeper air bag excavation is necessary.



**Fig. 4.28** Mitigative effects of embedded cushion under surface wave propagation (impact shaking)

#### List of References in Chapter 4

- Báth, M. (1968) *Mathematical Aspects of Seismology*, Chap. 12, Elsevier, New York.
- Bolt, B.A. (1993) *Earthquakes and Geological Discovery*, Scientific American Library, ISBN 0-7167-5040-6, p. 39.
- De Cock, F. and Legrand, C. (1990) Ground vibration isolation using gas cushions, Proc. Int. Conf. Geotextiles, Geomembranes, and Related Products, pp. 807–812.
- Haupt, W.A. (1981) Model tests on screening of surface waves, Proc. 10th Int. Conf. Soil Mech. Found. Eng., Stockholm, Vol. 3, pp. 215–222.
- Hayakawa, K., Takeshita, S. and Matsui, T. (1991) Reduction effect of EPS blocks on ground vibration caused by road Traffic and its evaluation, Soils Found., Vol. 31, No. 2, pp. 226–234 (in Japanese).
- Hayakawa, K., Takeshita, S. and Matsui, T. (1992) Ground vibration reduction due to vibration proof mats in railroad and its evaluation, Soils Found., Vol. 32, No. 1, pp. 249–259.
- Massarsch, K.R. (1991) Ground vibration isolation using gas cushions, Proc. 2nd Int. Conf. Recent Adv. Geotech. Earthq. Eng. and Soil Dyn., St. Louis, Vol. II, pp. 1461–1470.
- Massarsch, K.R. (2004) Mitigation of traffic-induced ground vibrations, Proc. 11th Int. Conf. Soil Dyn. Earthq. Eng. and the . Conf. Earthq. Geotech. Eng., Berkeley, Vol. 1, pp. 22–31.
- Sannomiya, T., Towhata, I. and Kinugawa, H. (1993) Field tests on mitigation methods of ground vibration, Proc. Annual Conv. Japan. Soc. Soil Mech. Found. Eng., Vol. 1, Kobe, pp. 1261–1262 (in Japanese).
- Takemiya, H. (2004) Field vibration mitigation by honeycomb WIB for pile foundations of a high-speed train viaduct, Soil Dyn. Earthq. Eng., Vol. 24, pp. 69–87.
- Woods, R.D. (1968) Screening the surface waves in soils, Proc. ASCE, Vol.94, SM4, pp.951–979.

# Chapter 5

## Earthquake Effects



Ruin of Sacsayhuaman fortress in Cuzco, Peru. Craftsmen of Inca Empire spent one third of their working time for God, another one third on duty for the emperor, and the remaining one third for themselves. With a long working time available, the stones in the photograph were cut into very complicated shapes so that they would make perfect contact with one another. This good quality of construction made structures survive for many years without distortion.

**5.1 Intensity of Earthquake Motion**

Traditionally, the intensity of earthquake motion was evaluated by human senses as well as damage extents. Examples of this kind of scale are JMA scale, Mercalli intensity scale, and the MSK scale in Fig. 5.1. Since the development of earthquake monitoring instruments in more recent times, the intensity of earthquake motion started to be expressed by the maximum acceleration, the maximum velocity, the maximum displacement, a response spectrum, etc. Although the maximum acceleration is the most popular and the maximum velocity is the second, there is no single parameter that can fully take into account the nature of complicated earthquake motion.

Whichever of the above-mentioned parameters may be concerned, the intensity of motion is affected by the following issues

1. The distance from the source of motion
2. The size of rupture zone (fault)
3. The released strain energy in rock
4. Type of geology between the source and the concerned site
5. Local topography (地形) and soil conditions (locality) among others

Note that the significance and the manner of effects of these issues are variable, depending upon the choice of measures: acceleration, velocity, displacement, or others. Moreover, it has been practiced to pay attention to the extent of damage that varies with

1. The earthquake resistant design of facilities
2. Its maintenance
3. Earthquake response of facilities (intensity of motion)
4. Importance of facilities (social impact) among others

The cause and mechanism of damage vary with the type of facilities. Hence, it is impossible to select any single parameter to describe the intensity of earthquake from the view point of observed damage. However, it has been practiced widely to use one type of intensity for convenience.

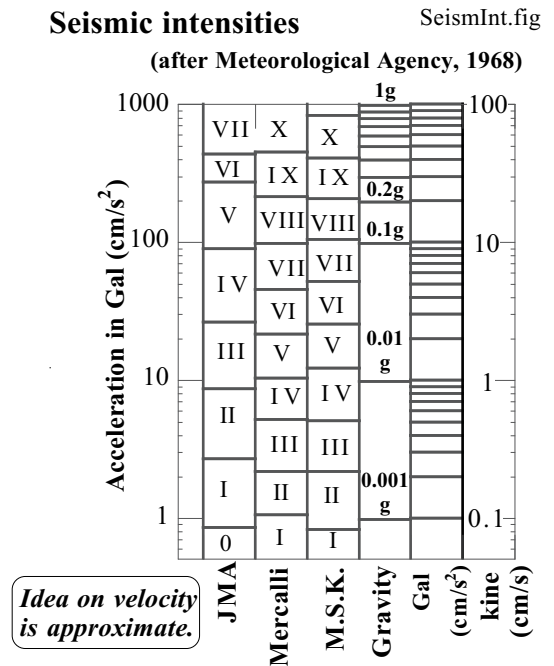
Seismic intensity is determined by taking into account

1. How strong the earthquake motion was FELT
2. Extent of structural damage
3. Extent of ground failure (cracking etc.)

Evidently, the intensity depends upon the locality.

Three kinds of seismic intensity scales are compared in Fig. 5.1: JMA scale (Japanese Meteorological Agency 気象庁震度), abridged modified Mercalli intensity scale (MM scale), and the MSK scale. They are roughly related to the maximum acceleration and velocity.

Any scale is affected by the local topography and geological conditions at earthquake observation stations. The determined intensity may not be related with the regional extent of damage.



**Fig. 5.1** Comparison of seismic intensity scales (Velocity value is approximate) (Meteorological Agency, 1968)

Recently a new seismic intensity scale has been developed in European countries. Being called EMS scale (European Macroseismic Scale), it has 12 divisions, each of which is defined based on human response and extent of damage. Thus, the basic principle is identical with those of classic scales. This scale is briefly summarized in what follows; for details, refer to the original definition (<http://geology.about.com/library/bl/blems.htm>).

**Table 5.1** Definition of European macroseismic scale

Scale	Rank	Brief description
1	Not felt	
2	Scarcely felt	Felt only by people at rest in house
3	Weak	Felt by a few people
4	Largely observed	Felt indoors by many people but not much felt outdoors. Swinging of objects is detected
5	Strong	Buildings shake; glasses clatter, and top heavy objects turn down
6	Slightly damaging	People are frightened and slight damage to many ordinary buildings such as fine cracks
7	Damaging	Most people are frightened, furniture move, and objects fall down. Moderate damage to ordinary buildings such as small cracks
8	Heavily damaging	Overturning of furniture. Buildings suffer large cracks and possibly collapse
9	Destructive	Partial collapse in many ordinary buildings and complete collapse in a few of them
10	Very destructive	Many ordinary buildings collapse
11	Devastating	Most ordinary buildings collapse
12	Completely devastating	Almost all structures, both above and below ground, are heavily damaged or destroyed

## 5.2 Revised Earthquake Intensity

The JMA scale in Sect. 5.1 was revised in 1996 from human observation of earthquake effects (shaking and damage extent) to instrumental observation. The new JMA scale 新しい気象庁震度 is determined by a specially developed equipment 震度計. This scale is, however, still correlated literally with observed phenomena as what follows.

Measured scale	Human effects	Effects on lifelines	Effects on ground and slope
0	Nothing felt		
1	Felt by some people, if staying indoor		
2	Felt by many indoor people. Some sleepers are awoken		
3	Felt by most indoor people; possible to be frightened		
4	Frightened. Some may try to escape		
Lower 5	Many try to escape, but not easy 身の安全を図ろうとしても一部の人は行動に支障	Gas supply is cut by a home safety system. Water supply and electricity may be lost	Possible cracking in soft soil. Stone fall and small landslide are possible in mountains
Higher 5	Substantially frightened. Cannot move easily 非常な恐怖、行動に支障	Minor gas pipes and major water pipes can be broken	ditto 上に同じ
Lower 6	Cannot stand upright 立っていることが困難	ditto	Cracks and landslides occur 亀裂と山崩れ
Higher 6	Can only crawl 這うのがやっと	Major gas pipelines and water treatment facilities are damaged	ditto
7	Cannot control one's body	Overall loss of electricity, gas, and water	Large cracks and landslides occur

This revised seismic intensity is determined by special instruments. Its details are described in Sect. 5.3. Thus, the human judgment of the scale was terminated.

**5.3 Instrumental Determination of Seismic Intensity**

The JMA (Japanese Meteorological Agency) scale of seismic intensity is today determined by electronic instruments that monitor on a real-time basis the seismic motion. A special attention was paid by JMA to maintain the consistency of the intensity between the former human and new instrumented procedures. Moreover, the quick determination of the seismic intensity immediately after the shaking is important.

The new procedure relies on a time history of acceleration, which probably best accounts for the damage extent. Figure 5.2 illustrates the schematic idea of the procedure. The three time histories in *NS*, *EW*, and *UD* directions are processed by digital filters. Figure 5.3 shows the effects of three digital filters and their combination, which remove both high- and low-frequency components from the acceleration records. The formulae of filters are;

Low-pass filter  $F_1 = \sqrt{1/f}$

High-cut filter

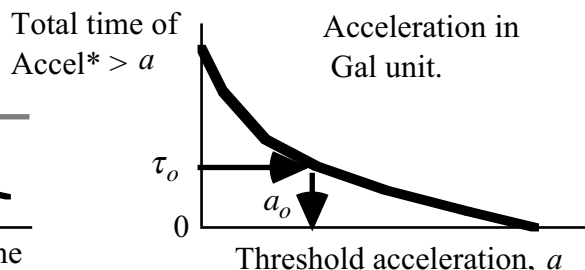
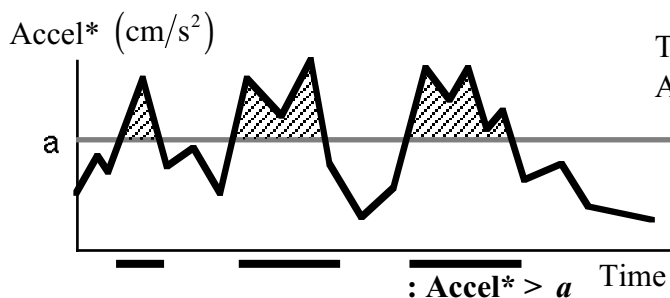
$$F_2 = 1 / \sqrt{1 + 0.694X^2 + 0.241X^4 + 0.0557X^6 + 0.009664X^8 + 0.00134X^{10} + 0.000155X^{12}}$$

Low-cut filter  $F_3 = \sqrt{1 - \exp\{-(f/f_0)^3\}}$ ,

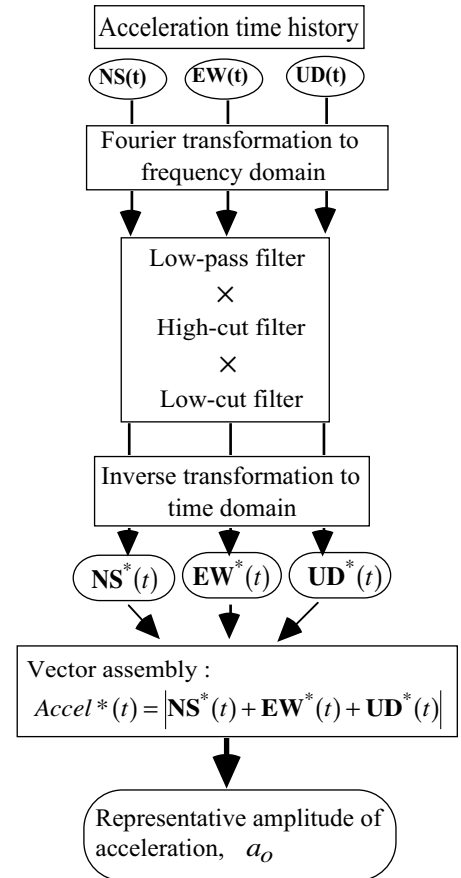
in which  $f$  is the frequency (Hz),  $X = f/f_c$ ,  $f_c = 10$  (Hz), and  $f_0 = 0.5$  (Hz). Hence, the total effects are given by  $F_1 \times F_2 \times F_3$ .

Then, three records are added in a vector manner to obtain a scalar (positive) time history,  $Accel^*(t)$ .

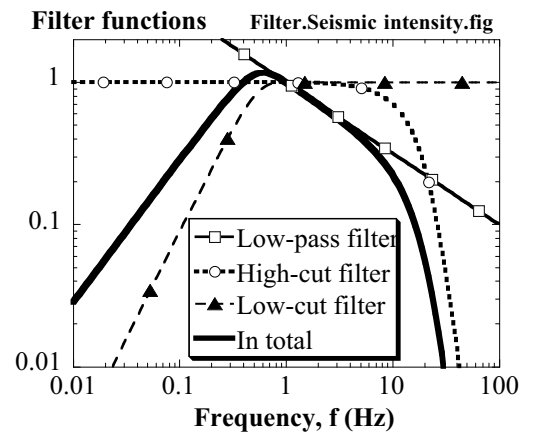
The representative amplitude of  $Accel^*$  is designated by  $a_0$  and is determined by the method in Fig. 5.4. The time in which  $Accel^*$  is greater than the threshold value,  $a$ , is shown by **—** in Fig. 5.4 and its total value is plotted against “ $a$ .” The total time decreases as “ $a$ ” increases, and  $a_0$  is the particular  $a$  value for which the total time is  $\tau_0 = 0.3$  s.



**Fig. 5.4** Determination of representative amplitude of irregular time history



**Fig. 5.2** Determination of instrumental seismic intensity



**Fig. 5.3** Effects of digital filters

This  $a_o$  (cm/s<sup>2</sup>) is finally substituted in

$$I = 2 \log_{10}(a_o) + K,$$

where  $I$  is the instrumental seismic intensity and  $K=0.94$ .

Although this instrumental seismic intensity was designed to be equivalent with the traditional one (Sect. 5.2), it is felt that the new one is greater than the conventional one by roughly 0.5; real damage is not so severe as suggested by the instrumental seismic intensity.



## 5.4 Earthquake Magnitudes

Since the seismic intensity highly depends on locality, it is not suitable to describe the size of an earthquake by this intensity. The size of earthquake is more appropriately evaluated by “earthquake magnitude  $M$ ,” which has several versions. One group of magnitudes depends on the intensity of earthquake shaking, in terms of energy or amplitude, as generated by the fault rupture zone, while the other group on the extent and size of distortion in the earth crust of the rupture zone (Utsu, 1999). Note that a detailed discussion on magnitudes is extremely complicated and difficult.

### 1. Local magnitude (Richter scale), $M_L$ (Richter, 1935)

This is the first idea of earthquake magnitude defined by

$$M_L = \log_{10} \{a(\Delta)/a_0(\Delta)\},$$

in which  $\Delta$  is the epicentral distance (km),  $a(\Delta)$  is the amplitude of record on paper obtained by a then available Wood-Anderson seismograph, and  $a_0(\Delta)$  is the amplitude of a standard earthquake (defined to have  $M_L=1.0$ ) at the same site. The standard earthquake is the one that gives  $a = 1$  mm at  $\Delta = 100$  km. Thus, the local magnitude is a ratio of a given and a standard earthquake intensity. By using a Californian empirical formula valid for  $\Delta < 600$  km :  $\log_{10} a_0 = 6.37 - 3 \log_{10} \Delta$ , together with the nature of the Wood-Anderson instrument  $a = 2800 \times A$  in which “ $A$ ” is the maximum ground displacement in mm unit,

$$M_L = \log_{10} A + 3 \log_{10} \Delta - 2.92.$$

This makes it possible to determine the Richter-scale magnitude in the Californian locality without a specified instrument. Empirically,  $M_L > 7$  is very rare (Utsu, 1999). In the recent times, the  $W-A$  instrument is not available, and media reports  $M_L$  as converted from other kinds of magnitude.

### 2. JMA (Japanese Meteorological Agency) magnitude, $M_{JMA}$

This magnitude is calculated by

$$M_{JMA} = \log_{10} A + 1.73 \log_{10} \Delta - 3.83$$

and is intended to be equivalent with the Richter scale. For the calculation of this magnitude, the single amplitude of displacement as recorded by an instrument is divided by the amplification of the instrument, and the amplitude of the ground displacement,  $A$  (mm unit), is obtained.

### 3. Kawasumi magnitude $M_k$ (Kawasumi, 1951)

Since the geological time scale is very long, the local seismic activity can be studied only by using historical earthquake information. Because of lack of measured intensity of seismic motion, Kawasumi (河角 1951) used the assessed JMA scale of seismic intensity (Sect. 5.2), which was determined by interpreting historical documents on damage. He defined the first version of his seismic magnitude,  $M_k$ , as the JMA scale at the epicentral distance of 100 km. He then found an empirical correlation between his magnitude and Richter magnitude ( $M_L$ ) as

$$M_L = 4.85 + 0.5 M_k .$$

In the recent times,  $4.85 + 0.5 M_k$  is called the (revised) Kawasumi magnitude and is widely referred to.

### 4. Surface wave magnitude $M_s$ (Richter, 1945a)

This magnitude suits a shallow earthquake, which is recorded at a far distance. The measured seismic motion record is dominated by surface wave propagation of a long period (about 20 s) (Sect. 4.7). This magnitude can hardly exceed the value of 8. Hence, it is not suitable for a gigantic earthquake.

5. Body wave magnitude,  $m_b$  (Richter, 1945b and 1945c)

This magnitude suits a deep earthquake. It is determined by using P and S waves (body waves, Sect. 4.2). These waves have predominant periods of about 1 s.

6. Earthquake energy  $E$  ( $\text{erg} = 10^{-7} \text{ J}$ )

$$\log_{10} E = 1.5M_{\text{JMA}} + 11.8 \quad \text{empirically.}$$

When  $M_{\text{JMA}}=6.5$ ,  $E=3.5 \times 10^{21}$  and when  $M_{\text{JMA}}=7.5$ ,  $E=1.1 \times 10^{23}$ . When the magnitude increases by 1, the energy increases 32 times. Utsu (1999) summarized many empirical relationships between earthquake energy and earthquake magnitudes.

7. Moment magnitude,  $M_w$ 

This magnitude is related with the earthquake moment,  $M_0$ . It considers the stress state in the fault before the breakage together with the fault size. The earthquake moment is defined by

$$M_0 = G_{\text{earth}} \times (\text{Fault displacement } D) \times (\text{Fault area}) \quad (\text{unit : dyne and cm})$$

in which  $G_{\text{earth}}$  stands for the shear modulus of earth crust. Accordingly,

$$M_w = (\log_{10} M_0 - 9.1) / 1.5 .$$

The moment magnitude is used to express the magnitude of gigantic earthquakes.

## 5.5 Time History of Ground Motion

It is a frequent practice for earthquake engineers to talk about the time history of acceleration and its maximum value. This comes from the principle of d'Alembert in mechanics, which states that a base acceleration is equivalent with an inertia force (Fig. 5.5). There are, however, different viewpoints in interpreting the significance of given seismic records.

In 1995, a velocity time history was recorded at University of Kobe on a rock outcrop (CEORKA: The Committee of Earthquake Observation and Research in the Kansai Area). A time-derivative of this record gave an acceleration history, while it was integrated with time to be a displacement record. Figure 5.6 compares the acceleration and displacement thus obtained. The maximum acceleration ( $A_{\max}$ ) was 270.3 Gal, Gal=cm/s<sup>2</sup>. It seems clear that the acceleration time history has a significantly shorter period or a higher frequency than the displacement record does. The reason for this is found in an example of a harmonic motion.

When a velocity record,  $v$ , is given by

$$v = v_0 \sin \omega t$$

the displacement ( $d$ ) and the acceleration ( $a$ ) records are expressed as

$$d = \int_0^t v_0 \sin \omega \tau \, d\tau = \frac{v_0}{\omega} (1 - \cos \omega t)$$

$$a = dv/dt = \omega v_0 \cos \omega t .$$

Note that the amplitude of the acceleration record is  $\omega^2$  times greater than that of the displacement. This ratio ( $\omega^2$ ) increases for a greater value of  $\omega$ , i.e. a higher frequency. Therefore, an acceleration record intensifies high frequency components, while low frequency components are predominant in a displacement record.

This feature is clearly seen in Fig. 5.6 where the original velocity record was differentiated and integrated with time to obtain acceleration and displacement, respectively. The predominant period of acceleration is much shorter than that of displacement.

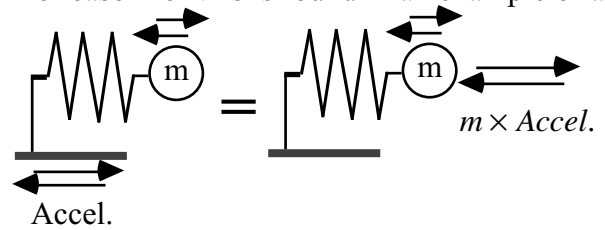


Fig. 5.5 d'Alembert's principle

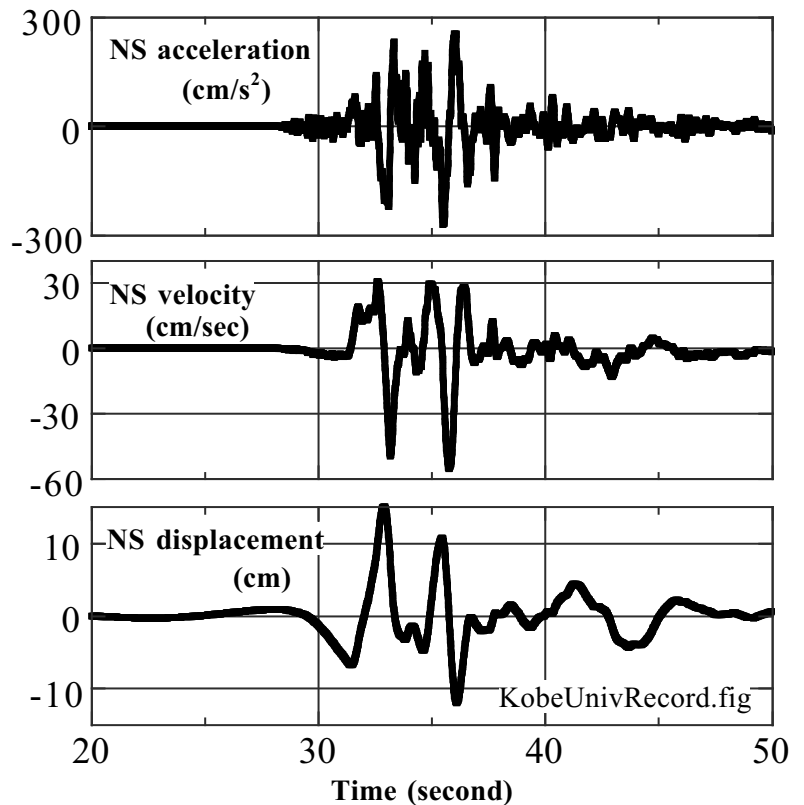


Fig. 5.6 Velocity time history of Kobe earthquake in Kobe University and its differentiation (acceleration) and integration (displacement) (CEORKA)

## 5.6 Effects of Local Soil Conditions on Maximum Acceleration

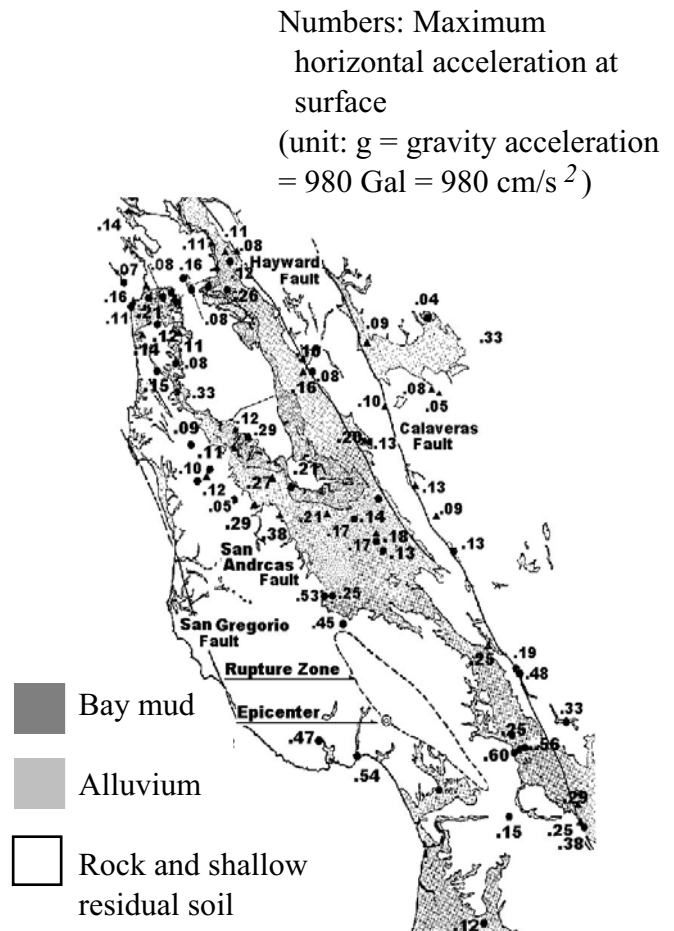
The intensity of earthquake motion depends on the following issues:

- Type of record; displacement, velocity, or acceleration
- Magnitude of earthquake (released energy)
- Direction and distance from the source fault
- Topography; plain, mountain, top and bottom of cliff, valley, etc.
- Local geology

With regards to the local geology, an alluvial deposit (沖積地盤) together with an artificial ground (人工島など) is generally associated with a stronger maximum acceleration. Figure 5.7 illustrates the maximum horizontal acceleration values recorded in the San Francisco Bay area, which was shaken by the 1989 Loma Prieta earthquake. The epicenter is located near the bottom of the figure, and the Bay area in the upper half of the figure is of more or less the same epicentral distance. With other things same, the area of softer subsoil along the bay coast had stronger acceleration than hilly and mountainous areas. It seems, therefore, that a softer deposit amplifies the earthquake motion.

The recent experience in Kobe in 1995 is not in line with San Francisco probably because the damaged area was above or very close to the causative fault, and the epicentral distance was more important than the local soil condition. Another reason is that the three-dimensional structure of base rock made a complicated propagation and reflection of seismic waves that could govern the intensity of surface motion.

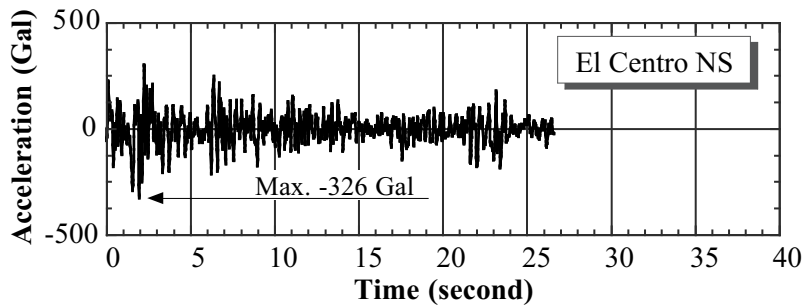
There is a case in which the surface soft soil deamplifies (makes weak) the earthquake motion. This occurs when the energy loss during the propagation of the earthquake wave towards the surface is very significant and the motion loses its amplitude; for example, the surface soil is a soft mud or a liquefied sand (Sect. 17.12). Another example is a propagation of very strong motion that produces a large amplitude of stress and strain; see Sect. 9.1 etc. for ideas on damping ratio.



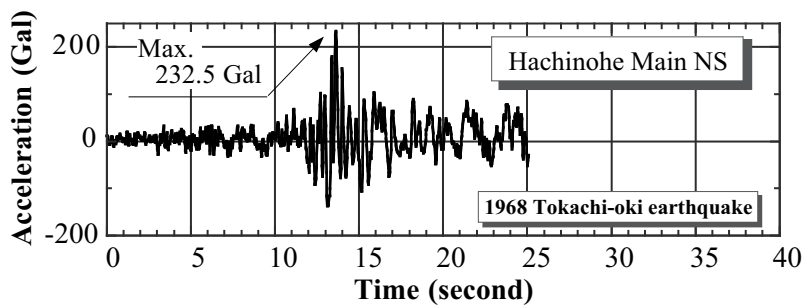
**Fig. 5.7** Maximum horizontal acceleration during 1989 Loma Prieta earthquake (original figure by Seed et al., 1991)

## 5.7 Some Famous Earthquake Motion Records

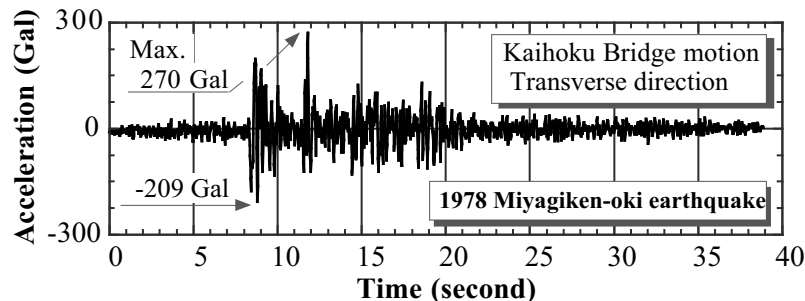
See Figs. 5.8–5.11 for several famous acceleration records.



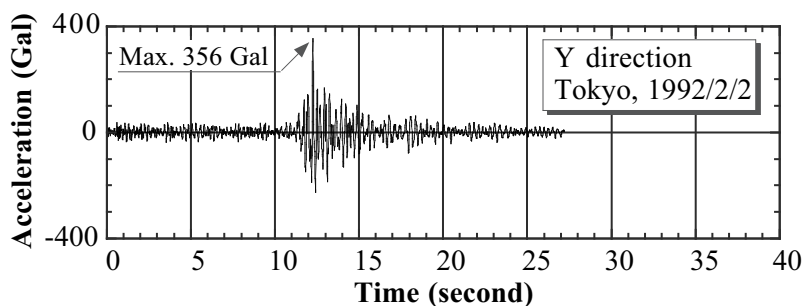
**Fig. 5.8** *El Centro* motion is the first-ever-recorded strong earthquake motion. This record has been widely used in earthquake-resistant design of structures



**Fig. 5.9** *Hachinohe* record during the 1968 Tokachi-oki earthquake is famous for its elongated period. This is an important input motion for analysis on structures that have a long natural period



**Fig. 5.10** *Kaihoku* (開北) motion during the 1978 Miyagiken-oki (宮城県沖) earthquake. This record has been considered to be a rock outcrop and has, therefore, been used as a typical input motion into surface deposits. Actually, the observation station for this record is close to a bridge pier and is situated on soil. For significance of outcrop motion, see Sect. 6.8



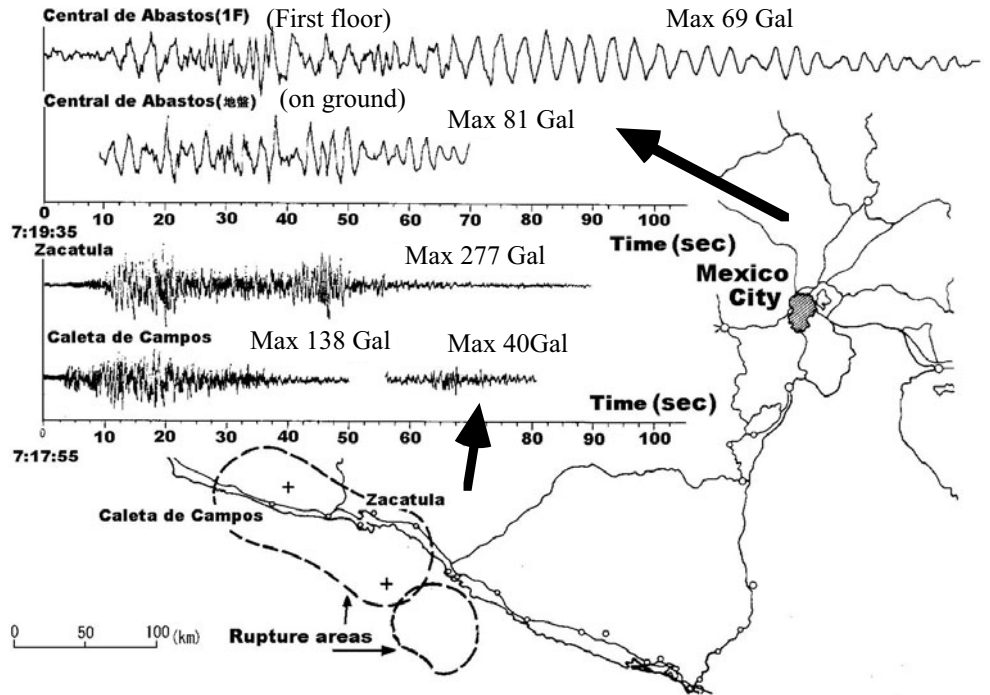
**Fig. 5.11** This record was obtained at a top of a *small hill in Tokyo* during a minor earthquake. No damage was caused by this. The maximum acceleration is, however, as large as 356 Gal ( $\text{cm/s}^2$ ) which is compatible with the maximum acceleration in other three records in this section. Thus, the intensity of maximum acceleration is not a fully-reliable damage parameter

**5.8 Ground Motion During 1985 Mexican Earthquake**

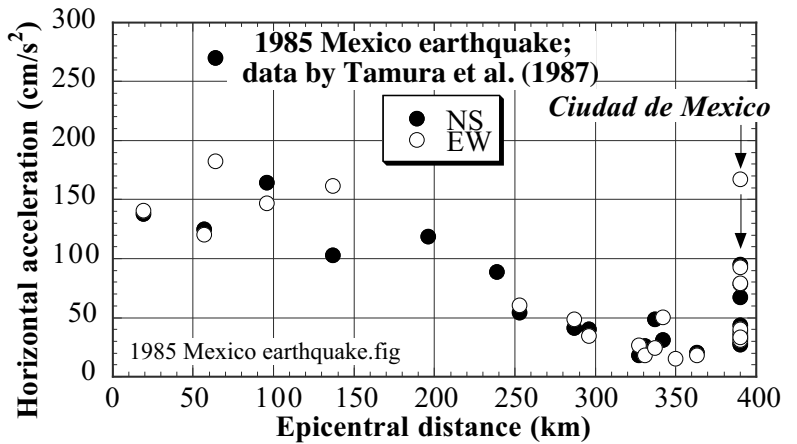
The 1985 Mexican earthquake is famous for heavy damages in buildings in the Mexico City. Although this city was located at 390 km from the fault area, the capital city suffered an unexpectedly significant damage. Figure 5.12 compares the acceleration records that were obtained in the Mexico City basin (Central de Abastos) and at the Pacific coast near the fault (Zacatula and Caleta de Campos). It is evident that the motion in the Mexico City had a longer period (approximately 3 s.) and an elongated duration time of shaking. Figure 5.13 shows that some sites in the Mexico City area were shaken by an extraordinarily strong magnitude of acceleration.

It is believed today that the locally strong ground motion was caused by the soft deposit of soil in the city. The Mexico City basin used to be a big lake, which was buried naturally and artificially after a long period of time. Being famous for big consolidation settlement, the Mexico City clay has a natural water content (Sect. 1.2) of 300–600% while its thickness is variable (Mendoza and Romo, 1998). In this respect, the following points are important.

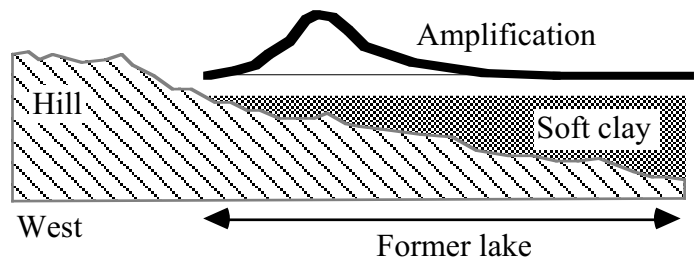
- The thickness of soft soil in Mexico City basin increases from zero at the western edge to tens of meters in the middle of the basin.
- The natural period of ground depends not only on the stiffness of soil but on the thickness of soft soil.
- The earthquake motion of the same period as the natural period of ground is amplified (made stronger).
- At the critical place where the natural period and the predominant period in the earthquake motion matched, a significant amplification occurred, leading to building damage, see Fig. 5.14.
- Earthquake energy was trapped by the soft deposit, leading to long duration of free shaking.



**Fig. 5.12** Ground motion records near the fault and the Mexico city basin (after Tamura et al., 1987)

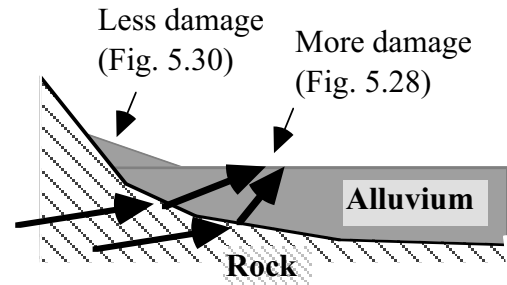


**Fig. 5.13** Strong motion in Mexico City at the longest distance



**Fig. 5.14** Schematic diagram on localized strong earthquake response in Mexico City

After the experience of Kobe earthquake in which location of damaged houses was localized (see Sect. 5.14), a different idea was proposed. Figure 5.15 illustrates a soft alluvial deposit staying on a concave interface with base rock. Since the wave propagation velocity is higher in the rock than in the upper soil, the direction of wave propagation is refracted at the interface (Snell's law) and the earthquake energy is focused on some point. Being called the edge effect, this situation induces damage concentration on a narrow area along the foot of a mountain.



**Fig. 5.15** Focusing of seismic energy due to concave underground structure

### 5.9 Power of Acceleration Time History

The destructiveness of an earthquake motion is most reasonably evaluated by its effects on residual deformation or energy dissipation within a given structure. Since real structures are substantially variable in the sense of size, shape, and rigidity, it is good to replace them by a single-degree-of-freedom model, see Fig. 5.16. Housner’s spectrum intensity (SI in Sect. 23.2; Housner, 1961) stands for the magnitude of relative velocity between the base and the top mass of this model and designates the extent of distortion and damage.

Arias (1970) stated that the energy dissipation,  $I$ , per unit weight of a single-degree-of-freedom model is given by

$$I = \frac{f(\mu)}{g} \int_{\text{beginning}}^{\text{end}} \text{acceleration}^2 dt = \frac{\arccos \mu}{g\sqrt{1-\mu^2}} \int_{\text{beginning}}^{\text{end}} \text{acceleration}^2 dt, \quad (5.1)$$

where  $\mu$  is the critical damping ratio of the model, and  $g$  is the gravity acceleration, while the integration is made from the beginning till the end of a given acceleration time history. Being called Arias intensity, this  $I$  has a unit of velocity. For practice, the value of  $f(\mu)$  is not much affected by the choice of the critical damping ratio (Fig. 5.17) and, hence, the type of a concerned structure. Since Arias did not present the derivation of (5.1), a detailed discussion on it is impossible. It is, however, subject to a question why an undamped model ( $\mu=0$ ) still makes  $f(\mu) > 0$  and energy is dissipated in the model.

A simplified version of (5.1) is called the power of acceleration time history

$$\text{Power} = \int_{\text{beginning}}^{\text{end}} \text{acceleration}^2 dt. \quad (5.2)$$

“Power” is more closely related with the destructiveness of an earthquake motion time history than the maximum acceleration because the duration time and probably the number of loading cycles are somehow taken into account. On the contrary, the power does not pay attention to the fact that soil (an elastoplastic material) develops the largest deformation during the first cycle if the amplitude of loading is uniform during a sequence of loading (Fig. 5.18). Thus, the order of loading is out of scope of the power.

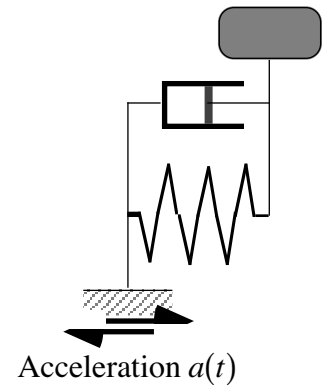


Fig. 5.16 Single-degree-of-freedom model

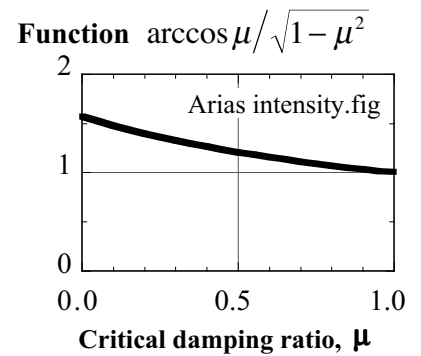


Fig. 5.17 Effects of critical damping ratio on Arias intensity

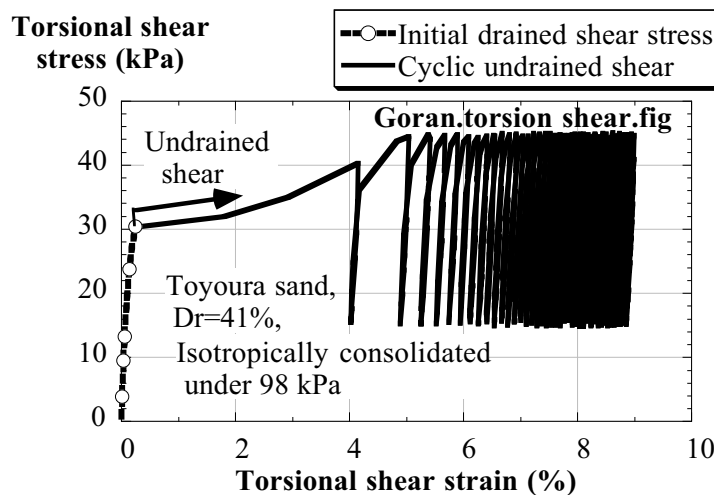


Fig. 5.18 Undrained cyclic loading on Toyoura sand with initial shear stress (Arangelovski and Towhata, 2004)



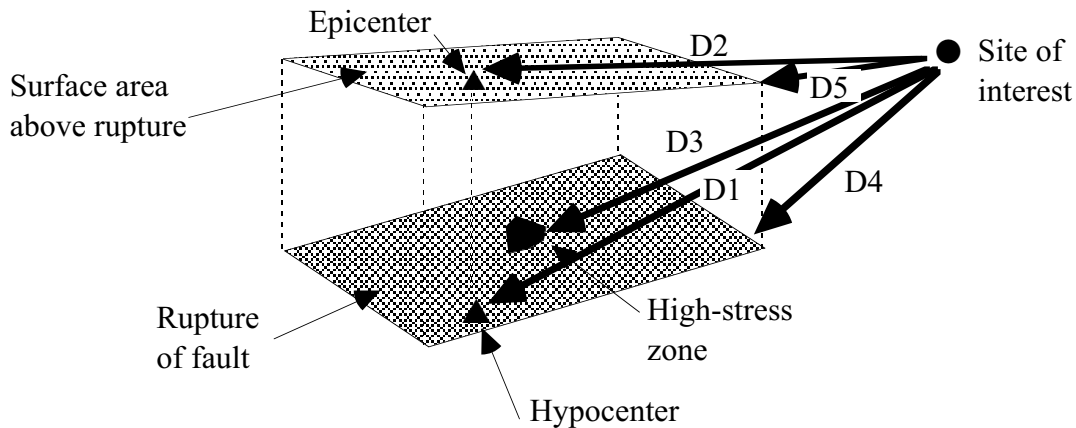
## 5.10 Distance From Source of Earthquake

It is well known that the intensity of shaking decreases as the distance increases from the seismic fault or the rupture of the earth where the earthquake shaking is generated. To quantitatively take into account the effects of distance into engineering practice, it is important to define the distance quantitatively. Figure 5.19 illustrates different ideas of distance parameters.

Definitions of terms:

Epicenter 震央: place at the earth's surface lying above the hypocenter.

Hypocenter 震源: part of fault where rupture starts.



D1: hypocentral distance.

D2: epicentral distance.

D3: closest distance to high-stress zone (possibly most seriously ruptured part of fault).

D4: closest distance to edge of fault rupture.

D5: closest distance to surface projection of rupture.

**Fig. 5.19** Illustration of parameters defining distance from an earthquake source to the place of interest (station) at the earth surface (original figure was drawn by Joyner and Boore, 1996)

Among five indices of distance, the epicentral distance (D2) has been used in many situations. Recently, however, the distance to the edge of a fault (D4) has been considered to be important; this is particularly the case at a short distance where the epicentral distance is large but the distance to the fault is short, leading to severe intensity of shaking.

### 5.11 Estimation of Intensity of Earthquake Motion

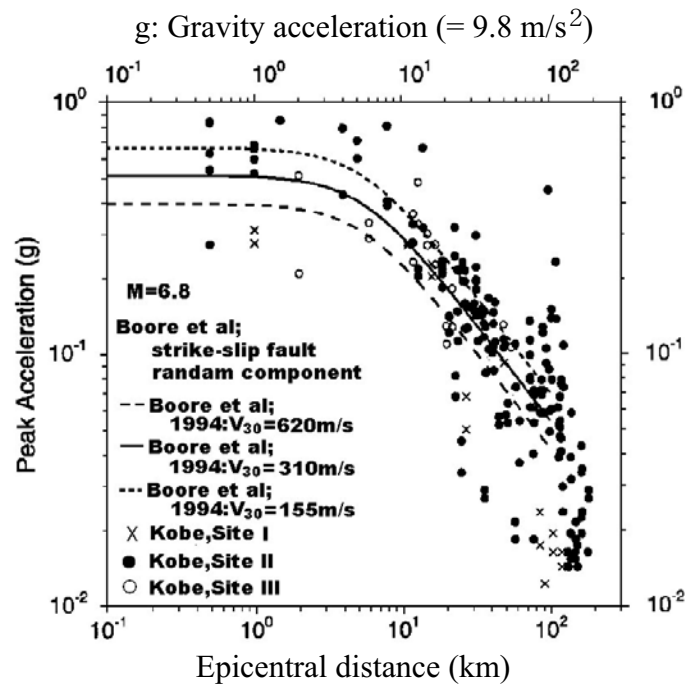
It is an interesting research to estimate the nature of future earthquakes by using information on potentially active seismic faults. One of the most rigorous approach to this goal is a use of fault rupture model combined with calculation of seismic wave propagation from the fault to the site of concern. This approach is, however, not able to assess acceleration for which higher frequency components are important for practice (Sect. 5.5).

Another approach is an empirical correlation between such a feature of earthquake motion as maximum velocity or acceleration and distance from the epicenter (or fault), while taking into account the seismic magnitude (Sect. 5.4). This issue stands for the decay of earthquake motion intensity and otherwise called attenuation curve (距離減衰). An early example was proposed by Kanai and Suzuki (1968) between maximum velocity and hypocentral distance (Fig. 5.19). Note that the concerned ground velocity was the one in the base rock underlying surface soil. Hence, the amplification in the surface soft soil was out of scope.

Figure 5.20 is another example correlation between epicentral distance and peak acceleration. It is important that the observed earthquake motion at the shortest distance from the fault of less than 3 km is included. Such a data became available since 1990s when many earthquake observation stations were deployed. Note that the acceleration near the fault is not affected by distance any more. Further, it should be borne in mind that the intensity of shaking and this type of correlation vary with the local soil types; normally soft soil deposits ( $V_s=155$  m/s in Fig. 5.20) exhibit greater intensity of shaking than harder soil deposits ( $V_s=620$  m/s in Fig. 5.20). Therefore, a suitable correlation should be chosen for practice. It is important that the surface acceleration is even reduced by subsurface liquefaction (Sect. 18.9).

Many empirical correlations have been proposed for response spectrum (Sect. 23.1) and maximum velocity among others; being improved today by adding recent data at short distance from faults. Since such an earthquake feature is affected by the amplification of ground motion in the surface geology, different surface soil conditions require different correlations to be used.

Because of the increasing number of earthquake observation stations, the above-mentioned correlation with the distance is being improved after every earthquake event. Therefore, it is necessary to use as recent as possible correlations for an earthquake hazard analysis.



**Fig. 5.20** Empirical correlation between observed maximum horizontal acceleration and distance from the surface area lying above the fault;  $V_{30}$  means the average  $V_s$  in the surface 30 m of deposit (Joyner and Boore, 1996)

## 5.12 Estimation of Duration of Earthquake Motion

Duration time of strong shaking plays an important role when the accumulated effects of shaking are of major concern. Some of the examples of this kind of phenomenon is a development of deformation of earth structure with the number of cycles or time. Another important example is liquefaction.

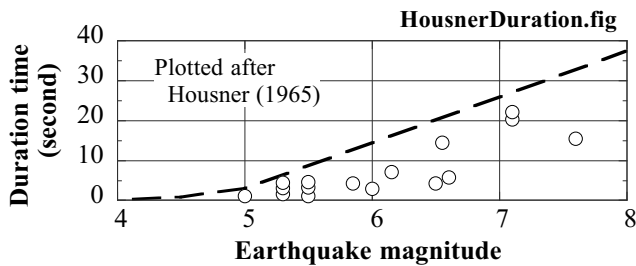


Fig. 5.21 Empirical estimation of duration time of strong motion (Housner, 1965)

Figure 5.21 by Housner (1965) exhibits the duration time of strong motion, although he did not clearly define what the strong motion stands for.

Figure 5.22 shows a correlation between duration time of strong shaking and the epicentral distance. Noteworthy is that Figure 5.22 concerns with the time period in which the amplitude of acceleration is greater than 0.3 times the maximum acceleration. Hence, no threshold acceleration level (e.g. 50 Gal) is intended. Also, the data was obtained upon relatively stiff soil.

Okada et al. (1999) analyzed many earthquake motion records to study the duration of horizontal acceleration greater than 50 Gal after the maximum acceleration (Fig. 5.23). It is in contrast with Housner (1965) as well as Lee and Chan

(1972) who were simply interested in duration of strong motion (>50 Gal in case of Lee and Chan). This study was particularly related to evaluation of liquefaction-induced ground flow. Noteworthy is the threshold acceleration of 50 Gal irrespective of the maximum acceleration. About 50 Gal was tentatively chosen because it is half of 100 Gal that is approximately the minimum acceleration needed to trigger liquefaction in loose sandy deposits. The obtained duration time depends upon the distance from the fault, which is not yet considered in the figure, as well as the magnitude in the horizontal coordinate. Hence, the upper bound of the data is used for practice.

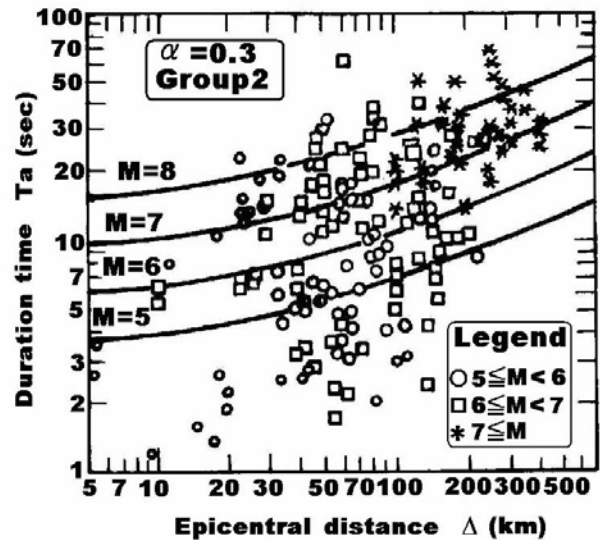


Fig. 5.22 Empirical correlation on relatively stiff ground between duration time of strong shaking and distance (Kawashima et al., 1985)

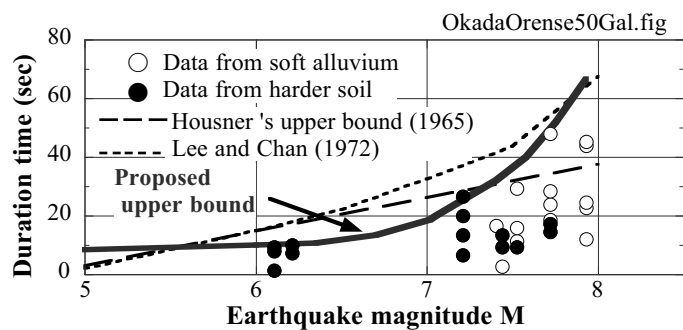


Fig. 5.23 Duration of acceleration greater than 50 Gal after maximum acceleration (Okada et al., 1999)

### 5.13 Determination of Design Earthquake Motion

In the tradition, design earthquake was simply specified by the seismic coefficient (Sect. 7.1), which is somewhat equivalent with the maximum acceleration during one shot of shaking. That practice was sufficient in the previous times because the engineering concern lay in the possibility of collapse: factor of safety greater or less than 1.0. In the recent times, however, the seismic performance of structures is very important (Sect. 14.5), and more detailed design earthquake such as time history of acceleration has to be prepared. Note that studies on time history of design earthquakes mostly concern with the motion on rock. Thus, the effects of surface soil has to be investigated separately.

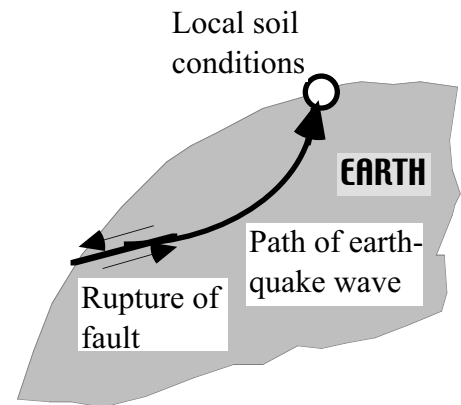
First of all, it should be stated that different kinds of design earthquakes are employed in practice. When safety against earthquakes that occur at least once during the life span of a concerned structure (probably once every fifty years or so), the employed design earthquake is not extremely strong. It is therein desired that a structure should maintain its function and nobody is injured by such an event. It is also important to pay attention to a very rare but extremely strong earthquake. Probably such an event occurs once every 500 or 1,000 years (return period = 500–1,000 years or longer). Under such an extreme situation, damage is allowed to some extent. However, a total collapse has to be avoided. To achieve this goal, the design earthquake is very strong as well. This topic will be discussed again in Sect. 14.7.

An earthquake motion is generated by rupture of a fault. This motion propagates in the earth, reaches its surface, and causes shaking. This surface shaking changes its intensity according to such local conditions as types of surface deposits, stiffness of soils, and the thickness of the surface soils. Figure 5.24 illustrates that the characteristics of the surface earthquake motion are composed of three factors: the fault characteristics, the nature and length of the intermediate path, and the local soil conditions. Thus, it has been an attractive idea to take into account these three components and predict the time history of earthquake motion at the earth's surface. In a mathematical form,

$$R(\omega) = F(\omega) \times P(\omega) \times L(\omega), \quad (5.3)$$

where  $R(\omega)$  designates the observed earthquake response at the surface which is a function of frequency or circular frequency ( $\omega = \text{frequency}/2\pi$ ).  $F(\omega)$  stands for the fault mechanism and varies with the seismic activity of the concerned fault.  $P(\omega)$  designates the effects of the intermediate path and reduces the intensity of motion as the distance from the fault becomes longer. Finally,  $L(\omega)$  is the effects of surface soil deposits (amplification effects). In principle, the surface earthquake motion can be predicted by taking into account three factors on the right-hand side of (5.3).

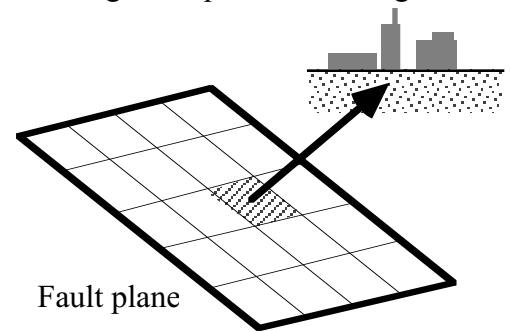
The identification of the local soil effects,  $L(\omega)$ , has been one of the major topics of soil dynamics. To date, this issue is understood to a substantial extent (Chaps 9 and 10). Remaining issues concern the technologies for in-situ soil investigation. The nature of  $P(\omega)$  has also been understood in detail by reasonably assuming that the earth is made of isotropically elastic media. In contrast, the nature of fault,  $F(\omega)$ , still has many to be studied. It appears to the author that the present understanding on  $F(\omega)$  is limited to a range of lower frequency. Above 1.0 or 1.5 Hz, the nature of the fault-generated earthquake



**Fig. 5.24** Relationship between causative fault, intermediate path, and local soil conditions

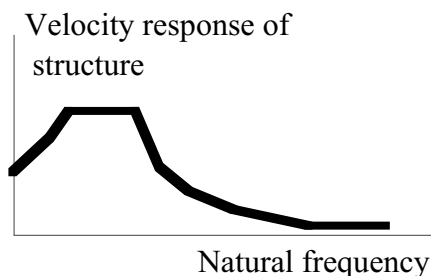
motion cannot be predicted. This implies that the acceleration cannot be predicted by (5-3), while displacement can be reproduced analytically by using a fault mechanism model. The research in this direction is still on-going for further development.

Since the practical use of (5.3) appears difficult, attempts have been made to propose alternative methods. One of them is an empirical determination of  $F(\omega) \times P(\omega)$  by observing earthquake motions generated by smaller but more frequent earthquakes in the same fault area (Fig. 5.25). Since a larger earthquake is produced by a bigger fault action with a greater rupture displacement, it is predicted by assembling motions that are produced by a number of small fault mechanisms. In the present engineering, the motion proposed by a small fault action is called Green's function (for example, Kobayashi and Midorikawa, 1982; Irikura, 1983, 1986). It is necessary not only to add the motion made by a small fault but also to consider the effects of greater fault displacement and the consequent elongated duration and the elongated period.

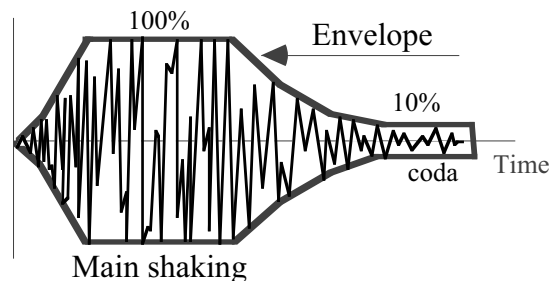


**Fig. 5.25** Individual effect of small fault rupture on earthquake motion

Another approach is the use of empirical relationships between the epicentral distance and the maximum acceleration, velocity, response spectra, and others (see Sects. 5.11 and 5.12). In this method, the initial time history, which is a white noise (all frequency components are equally but randomly included), is modified by trials and errors until the frequency components satisfy the desired response spectrum (Fig. 5.26; see Sect. 23.1). The obtained time history is further modified so that it may satisfy the desired time envelope (Fig. 5.27).



**Fig. 5.26** Concept of response spectrum of design earthquake motion



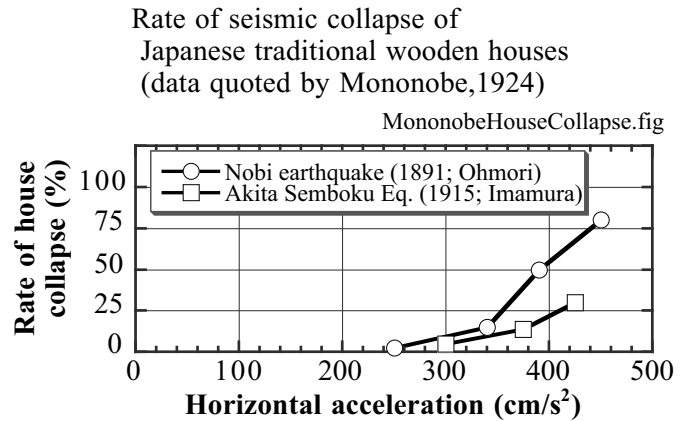
**Fig. 5.27** Concept of time envelope of design earthquake motion

**5.14 Seismic Damage in Traditional Houses**

Figure 5.28 shows a damaged shape of a Japanese traditional wooden house during the 1995 Kobe earthquake. Since the top roof was heavy as a stabilization against storm winds, while walls and columns did not have sufficient lateral resistance, the house was easily destroyed by the quake. Figure 5.29 by Mononobe (1924) summarizes data on damage rate of Japanese houses during two earthquakes. It is seen that there is a good correlation between the damage rate and the maximum acceleration, which justifies the use of inertia force as a design earthquake load (Sect. 7.1). Note, however, that the acceleration in this figure is not the observed acceleration. It was assessed many years later by using damage reports.



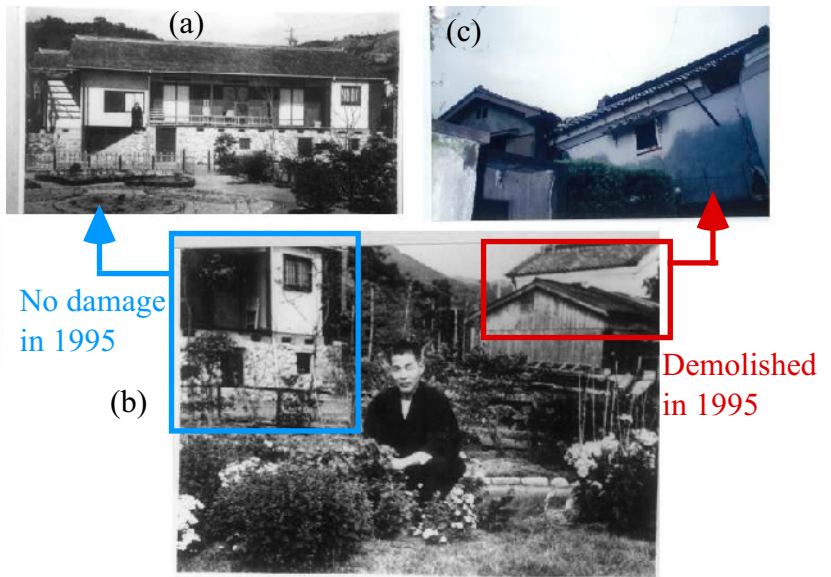
**Fig. 5.28** Damaged shape of Japanese traditional house in Kobe



**Fig. 5.29** Damage rate of Japanese traditional houses (Mononobe, 1924)



**Fig. 5.30** Undamaged wooden house in Kobe (1995)



**Fig. 5.31** Contrast in damage extent between soft wooden house and rigid ware house (1995 in Kobe; black-and-white photographs in 1948)

It may be pointed out that the damage rate is affected by local soil conditions. Figure 5.30 is a traditional house in Kobe as well which was not affected by the quake. Although the damage rate was low in the particular area of this house, a traditional ware house in the same area was significantly affected by horizontal shear failure near the bottom and was demolished. A traditional ware house is made of thick walls consisting of compacted earth (Fig. 5.31c) and wooden embedded reinforcement and it seems to have much greater shear rigidity than a wooden house. Figure 5.31b shows the same ware house to the right as well as another traditional wooden house on the left. In contrast to the heavily damaged ware house, the wooden house (Fig. 5.31a) was subject to very minor damage such as cracking in its earthen wall. This remarkable difference in damage extent may be attributed to structural difference because the distance between two structures was merely 30 m and the local soil condition together with the nature of input seismic motion was probably similar.

In spite of this rigidity, the ware house was damaged probably due to the following reasons.

- The area of Figs. 5.30 and 5.31 has a stiff soil condition, which is made of fluvial gravelly subsoil. Due to its rigidity, the natural period of the ground was short (Sect. 6.8). Hence, the shaking in this area had short predominant period of motion as well (resonance).
- The ware house was rigid and its natural period was short. Therefore, probably resonance and strong response occurred in the rigid ware house. In contrast, wooden houses are generally soft and their natural period is long. Therefore, resonance did not occur. The natural period was further elongated by the heavy roof, which is made heavy in the particular region in order to avoid typhoon wind effects.

Therefore, soil-structure interaction in the sense of matching between natural periods of ground and structure deserves engineering attention. Figure 5.32 illustrates the different extents of damage rate of wooden houses in Tokyo. It is therein seen that more houses were damaged in the east part of Tokyo where soil consists of soft young alluvium where ponds, rice field, and swamps were predominant until recent times (Figure 5.33). Conversely, damage was less significant in the west where pleistocene or tertiary hilly topography was predominant. This indicates clearly the importance of local soil conditions in damage extent of the community.

For practical assessment of the natural period of a building,  $T$ , Japanese building engineers uses an empirical formula of

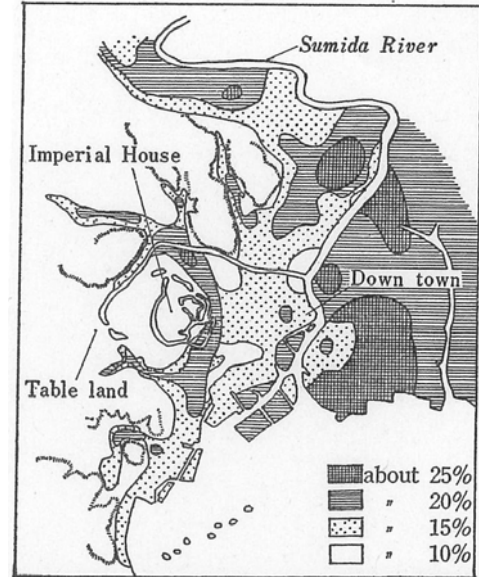
$$T(s) = H(0.02 + 0.01\alpha), \quad (5.4)$$

in which  $H$  is the height of a building (meter) and  $\alpha$  is the height ratio of floors in which columns and beams are made mainly of steel over the total building height. Housner (1961) proposed another formula of

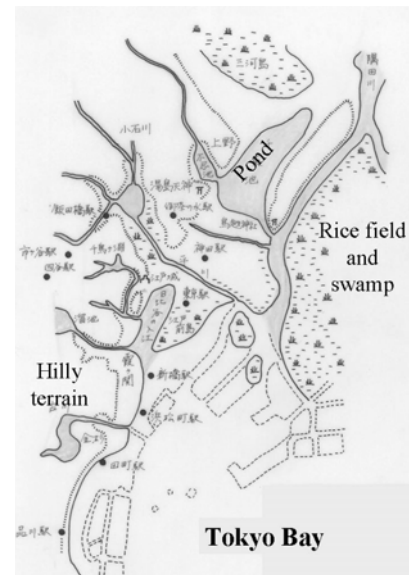
$$T(s) = 0.1n, \quad (5.5)$$

in which  $n$  stands for the number of storeys. For the natural period of ground, see (6.30).

Matsuda et al. (1978) proposed an interesting idea on the basis of information about collapse rate of Japanese wooden houses (Fig. 5.28 for example) during the 1923 Kanto earthquake. The data was collected from Yokohama City and was compared with the thickness of alluvial soils as well as the natural period of the ground. The natural period was determined by running dynamic analyses with a complex modulus approach (Sect. 9.6) and detecting the period at which the amplification was maximum. Thus, the natural period corresponds to the resonance period.

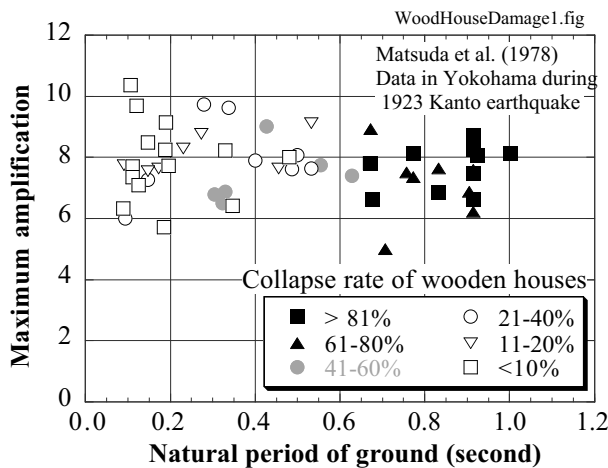


**Fig. 5.32** Damage distribution of traditional wooden houses in Tokyo during 1923 Kanto earthquake (Okamoto, 1973)

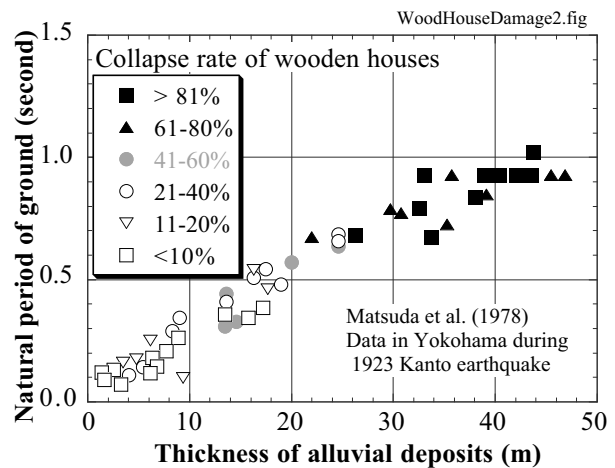


**Fig. 5.33** Topography of Edo (present Tokyo) before AD 1600 (after Murai, 1994)

Figure 5.34 shows the relationship between natural period of ground and the maximum amplification of earthquake motion. It is therein seen that the areas of greater collapse rate of houses had the longer natural period, approaching the natural period of houses. In contrast, the maximum amplification did not have much correlation with the collapse rate. Figure 5.35, moreover, indicates the relationship between the thickness of soft soil and the natural period of ground. It is seen that the area of higher collapse rate was associated with the greater thickness of soil and the longer natural period. Matsuda et al. (1978) consequently suggested that traditional houses were destroyed by strong response due to resonance and the amplification of seismic motion in the soil was less important. The importance of natural period of structures was already found in Fig. 5.31.



**Fig. 5.34** Relationship between natural period of ground and maximum amplification changing with collapse rate of traditional wooden houses (Matsuda et al., 1978)



**Fig. 5.35** Relationship between thickness of alluvium and natural period of ground changing with collapse rate of traditional wooden houses (Matsuda et al., 1978)



**Fig. 5.36** Collapsed adobe house in Bam, Iran, in 2004



**Fig. 5.37** Collapse of adobe house with heavy roof (Gilan, Iran, 1990)



**Fig. 5.38** Heavy roof of traditional house in Kerman, Iran



**Fig. 5.39** House of good maintenance which survived Bam earthquake in Iran



Traditional houses in Central Asia, which are made of masonry, have many problems as well. Figure 5.36 is the collapsed shape of a house that was made of adobe. Being a sun-baked brick, adobe can be easily made by using locally available materials and is widely used in arid countries. Since masonry walls made of adobe or other bricks cannot bear tensile force, bending failure is easy to occur, see Fig. 5.37.

The bending moment increases as the roof becomes heavier. Therefore, it may be desired to reduce the weight of the roof. However, local people tends to increase the weight by placing layers of bricks and mud. Consequently, many houses have very thick roofs (Fig. 5.38). This is because a heavy roof can avoid leakage of rain water and, together with thick walls, keep the inside temperature cool during hot daytime, while the stored sun heat maintains inside warm during cool night. Thus, seismic safety and daily convenience may conflict with each other. Note, however, that a house of good construction and maintenance in Bam (Fig. 5.39) was able to survive the devastating quake in 2004, and indicates the importance of the quality control in housing. The general principles in seismic safety of adobe or masonry houses are as what follows;

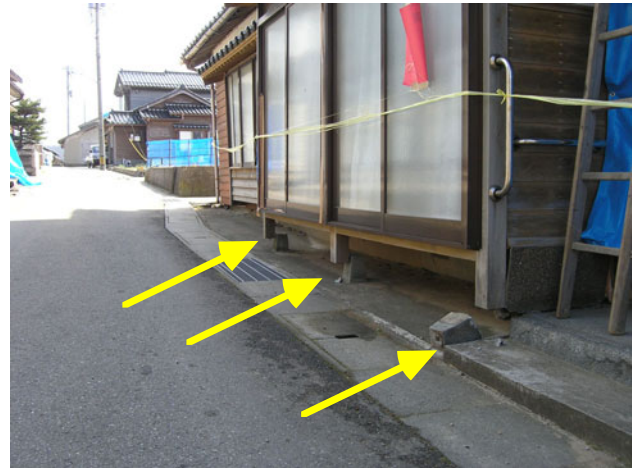


**Fig. 5.40** Total collapse of buildings in Balakot, Pakistan, in 2005

- Daily convenience should be sacrificed to some extent for seismic safety.
- Cost of seismic retrofitting (improvement of earthquake safety) has to be low.
- Technology of seismic retrofitting of existing houses is still being sought for.
- Both retrofitting and new construction of earthquake-safe houses have to be achieved by using cheap locally-available materials.
- Since houses are constructed by local contractors, technology transfer for seismic safety should be done on a local basis by using languages that local people can understand.

One should not imagine from the discussion above that reinforced concrete buildings have less number of problems. Figure 5.40 shows the entire collapse of Balakot in Pakistan in 2005, which was induced by inappropriate seismic resistance of local buildings.

The importance of technology transfer is often discussed in international engineering and disaster-mitigation occasions. In the author's opinion, highly educated engineers and designers in most countries in the world are doing good jobs. Engineered bridges and towers are able to survive strong earthquake motions. The real problem lies in the lack of technology transfer inside the country. In many countries, design codes and regulations are written in English because English is the common and official language when the nation is composed of many language groups. Although this idea is rational and lawful, many local contractors cannot read English documents. Moreover, the central government may not be able to control the quality of small constructions; codes are not respected. It therefore seems that domestic technology transfer is very important by publishing simplified translation / guidance of codes. Not only forcing contractors but also supplying incentives to contractors and customers is desired. Figure 5.39 showed that good quality of construction is able to improve the seismic resistance. Another issue is the maintenance. Decay of materials and dislocation of masonries reduces the seismic resistance. Again incentive to owners for better maintenance is needed.



**Fig. 5.41** Tilting towards direction of no wall rigidity    **Fig. 5.42** Dislocation of house from foundation

The problem of wall is important as well in Japanese traditional houses. Figure 5.41 shows a totally destroyed house in Douge of Wajima City (輪島市門前 道下地区) during the 2007 Noto earthquake. Significant tilting towards the direction without wall resistance is evident. Figure 5.42 reveals the problem of traditional foundation. Since the super structure was simply resting on small stones without mechanical connection, the strong inertia force (horizontal acceleration being more than 900 Gal probably) easily made the house separated from the foundation.

## 5.15 Reconnaissance Study of Earthquake-Induced Damage

This section is intended to supply some useful knowledge about damage investigation after a severe earthquake event. The special attention is focused on an international damage investigation out of one's home country.

### 1. Good health

All the efforts should be done to avoid local diseases, which one is not used to. It is a must to have preventive shot against tetanus, which comes from contaminated soils and might be fatal. A disinfectant should be always carried at hand. Rabies or hydrophobia is another important disease in some countries. Care should be taken of food poisoning. A very strong binding medicine is useful, if no bacteria is involved. However, a suitable antibiotic medicine should be prepared to stop diarrhea caused by bacteria. A good medical doctor is not always available in most parts of the world.

It is certainly important during a trip not to take suspicious food and drink. While food cooked by heat is mostly safe, raw food and those washed by tap water often cause troubles. Safe foods are such as baked meat and boiled food. Hot tea (called “*gyarm chai*” in Iran and Pakistan) as well as yogurt are generally safe and good. Banana is an ideal lunch because it is cheap and its inside is perfectly clean (Fig. 5.43). Recently, safe mineral water is supplied in bottles almost everywhere. To be more confident, however, bottled mineral water containing CO<sub>2</sub> gas (“*agua mineral con gas*”) is recommended. On the other hand, many people have bad stomach problems caused by cut fruits, fresh salad, and iced drinks. Local spicy food often causes diarrhea because your stomach is not used to it. It is advisable, therefore, to carry a role of toilet paper for an unexpected emergency situation.



**Fig. 5.43** Shopping banana in local market (Mansehra in Pakistan) (Abbotabad, Pakistan)



**Fig. 5.44** Ruin of building which collapsed suddenly upon minor aftershock

In addition to diseases, Fig. 5.44 shows a building in Abbotabad of Pakistan. This building was already damaged during an earthquake on October 8th, 2005, but managed to stand for more than one month. In the morning of November 20th, there was a minor aftershock, and this building suddenly collapsed as shown in the photograph. If anybody had entered this building at that moment for damage investigation, the situation could have been fatal. Another risk in a collapsed building is the nails in pieces of wooden walls and columns. To avoid injury due to walking upon nails, safety boots with steel plates inside are highly recommendable. Thus, entering damaged structures and buildings should be made very carefully on one's own risk. The author also experienced flooding of river in the center of a dry desert in Iran. Thus, one has to be prepared for a totally unexpected situation.

## 2. What should be brought

A topographical map of the affected area is very important. Your local counterpart researcher may prepare a detailed map. If it is not possible or if the local government does not publish a good map due to military reasons, air pilot's maps that are of the scale of 1:500,000 and are prepared by the Defense Mapping Agency Aerospace Center, St. Louis, Missouri, are available in major bookstores. Moreover, the exact location can be identified by a GPS equipment in any part of the world.

Taking pictures is absolutely important. The importance of pictures, however, deteriorates quickly after the excursion, because many researchers take similar photographs and people become familiar with them. It is important to take pictures that would support one's interpretation (theory) of the damage mechanism. Hence, some pictures should be taken of with some scenario in your mind. Note that a good photograph chance comes only one time during the trip and not twice. Therefore, do not postpone the chance until the next time.

It is essential to collect data/information other than photographs. Example data may be the size of a landslide mass, the width of ground cracks, the extent of ground movement, and damage distribution correlated with local geology. A local publication such as design code is important as well. Photographs of a damaged site prior to the quake may be found in a tourist book, which is available in a local bookstore. Moreover, subsoil investigation is possible by a portable cone penetrometer in clayey ground and a Swedish weight sounding in a loose sandy ground (Sect. 8.9). The equipment in Fig. 5.45 (developed by Dr. Sakai, the Kisojiban Consultants Inc., Tokyo) employs local soil as the 100- kg weight in place of metal weights so that the necessary equipments can be transported. In Fig. 5.44, sand is put in blue plastic bags which are hanging on the equipment.



**Fig. 5.45** Subsurface investigation by Swedish weight sounding supervised by Dr. Ilyas Suratman of Bandung Institute of Technology (Banda Aceh in Sumatra, Indonesia)

Although collecting samples of geomaterials for laboratory tests is important, quarantine regulations should be respected. Moreover, different practices in standard penetration tests and their effects on blow counts should be borne in mind, if boring profile is obtained.

## 3. Collaboration with local counterparts and people

International investigation is made easier and safer if one can work with local engineers and/or researchers. This is because they can make a detailed and reasonable travel plan and arrange transportations (4-wheel-drive vehicle is desirable) as well as accommodations. No complaint should be made to a possibly humble accommodation because the present trip is not sight-seeing. Moreover, those people may be able to obtain useful information. For example, inquiry to earthquake-affected people is made possible through their language-interpretation. To appreciate their collaboration, one should pay their travel expenses. It is another good idea to visit the counterpart's institution at the end of the trip in order to report and discuss about research findings. Coauthoring and submitting a report paper in an international journal is a very good idea.

The trip is made easier by learning a local language. Saying only “hello” and “thank you” with local people improves the situation significantly. It should not be insisted that English is an international language and that everybody should understand it. Such an idea never makes sense. See Appendix 2.

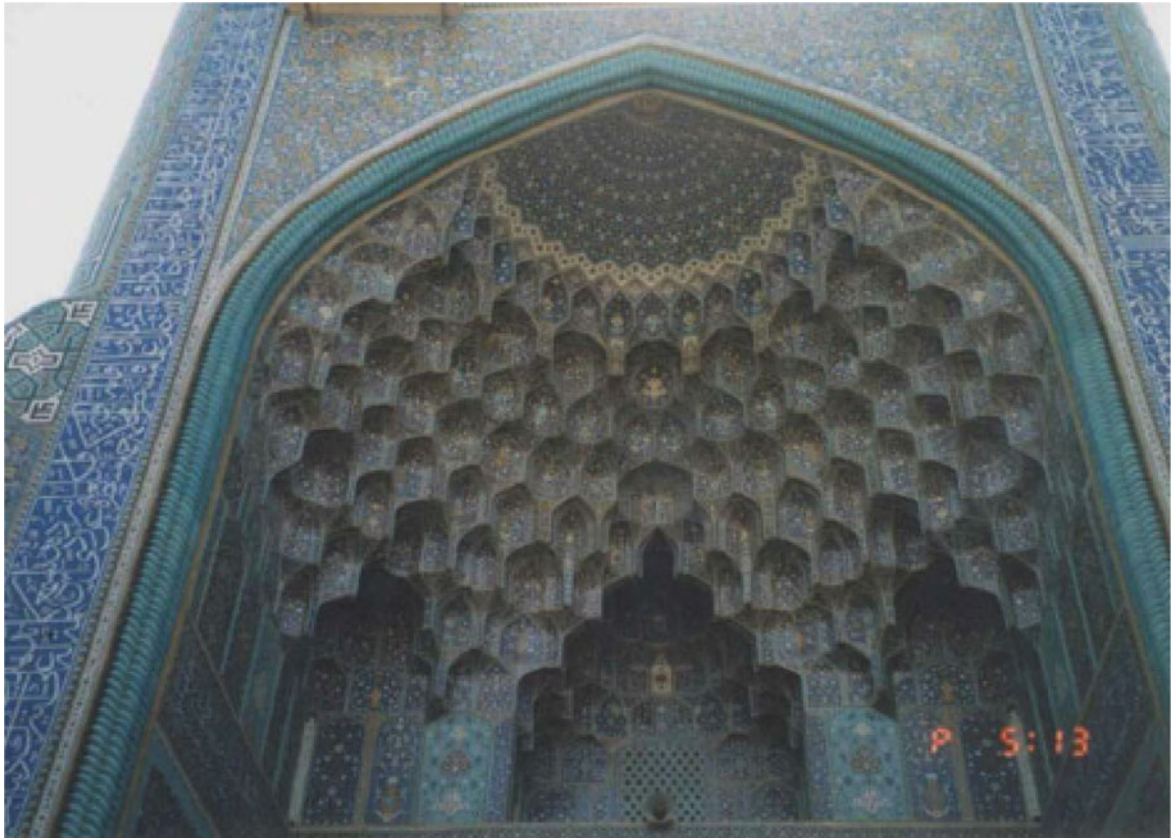
### List of References in Chapter 5

- Arangelovski, G. and Towhata, I. (2004) Accumulated deformation of sand with initial shear stress and effective stress state lying near failure conditions, *Soils and Foundations*, Vol. 44, No. 6, pp. 1–16.
- Arias, A. (1970) A measure of earthquake intensity, *Seismic Design for Nuclear Power Plants*, Hansen, R.J. Ed., MIT Press, pp. 438–483.
- Gutenberg, B. (1945a) Amplitude of surface waves and magnitudes of shallow earthquakes, *Bull. SeismoL. Soc. Am.*, Vol. 35, pp. 3–12.
- Gutenberg, B. (1945b) Amplitude of P, PP and magnitude of shallow earthquakes, *Bull. SeismoL. Soc. Am.*, Vol. 35, pp. 57–69.
- Gutenberg, B. (1945c) Magnitude determination for deep-focus earthquakes, *Bull. SeismoL. Soc. Am.*, Vol. 35, pp. 117–130.
- Housner, G. W. (1961) Vibration of structures induced by seismic waves, Part I. Earthquakes, *Shock and Vibration Handbook*, Harris, C.M. and Crede, C.E. Ed., McGraw-Hill, New York, pp. 50-1–50-32.
- Housner, G.W. (1965) Intensity of earthquake ground shaking near the causative fault, *Proc. 3rd World Conf. Earthq. Eng.*, Vol. 1, pp. III-94–III-115.
- Irikura, K. (1983) Semi-empirical estimation of strong ground motions during large earthquakes, *Bull. Disaster Prevention Res. Inst., Kyoto University*, pp. 63–104.
- Irikura, K. (1986) Prediction of strong acceleration motion using empirical Green's function, *7th Japan Earthq. Eng. Symp.*, pp. 151–156.
- Joyner, W.B. and Boore, D.M. (1996) Recent developments in strong-motion attenuation relationships, *Proc. UJNR 28th Joint Meeting of United States-Japan Panel on Wind and Seismic Effects*, NIST SP 904, Gaithersburg, pp. 101–115.
- Kanai, K. and Suzuki, T. (1968) Expectancy of the maximum velocity amplitude of earthquake ground motions at bedrock, *Bull. Earthq. Res. Inst., University of Tokyo*, Vol. 46, pp. 663–666.
- Kawashima, K., Aizawa, K. and Takahashi, K. (1985) Duration of strong motion acceleration records, *Proc. JSCE, Struct. Eng. Earthq. Eng.*, Vol. 2, No. 2, pp.161–168
- Kawasumi, H. (1951) Measures of earthquake danger and expectancy of maximum intensity throughout Japan as Inferred from the seismic activity, *Bull. Earthq. Res. Inst., University of Tokyo*, Vol. 29, pp. 469–482.
- Kobayashi, H. and Midorikawa, S. (1982) A semi-empirical method for estimating response spectra of near-field ground motions with regard to fault rupture, *Proc. 7th Eur. Conf. Earthq. Eng.*, Vol. 2, pp. 161–168.
- Lee, K.L. and Chan, K. (1972) Number of equivalent significant cycles in strong motion earthquakes, *Proc. Int. Conf. Microzonation Safer Construct. Res. Appl.*, pp. 609–627.
- Matsuda, I., Wada, S. and Miyano, M. (1978) The relation between subsoil condition and the collapse rate of wooden houses due to the Great Kanto earthquake of 1923 in Yokohama City, *J. Geography, Tokyo Geographical Society*, Vol. 87, No. 5, pp. 14–23 (in Japanese).
- Mendoza, M.J. and Romo, M.P. (1998) Performance of a friction pile-box foundation in Mexico City clay, *Soils Found.*, Vol. 38, No. 4, pp. 239–249.
- Meteorological Agency (1968) Guideline for earthquake observation, Appendix for reference information, p. 78 (in Japanese).
- Mononobe, N. (1924) Discussion and consideration on vertical earthquake motion and consideration, *Proc. JSCE*, Vol. 10, No. 5, pp. 1063–1095 (in Japanese).

- Murai, M. (1994) Edo castle and life of shogun family, Chuko Shinsho, No. 45, P. 5 (in Japanese).
- Okada, S., Orense, R., Kasahara, Y. and Towhata, I. (1999) Prediction of liquefaction-induced deformations of river embankments, Proc. Second Int. Conf. Earthq. Geotech. Eng., Vol. 2, pp. 543–548.
- Okamoto, S. (1973) Introduction of earthquake engineering, University of Tokyo Press, p. 62.
- Richter, C.F. (1935) An instrumental magnitude scale, Bull. SeismL. Soc. Am., Vol. 25, pp. 1–32.
- Seed, R.B., Dickenson, S.E. and Idriss, I.M. (1991) Principal geotechnical aspects of the 1989 Loma Prieta earthquake, Soils Found., Vol. 31, No. 1, pp. 1–26.
- Tamura, C., Hakuno, M., Abe, K., Iemura, H., Katada, T. and Takeuchi, M. (1987) Report on Mexico earthquake September 19, 1985, Nuclear Power Department, Report 006, Okumura Corporation (in Japanese).
- Utsu, T. 宇津徳治 (1999) 地震活動総説 Seismic studies: a comprehensive review, University of Tokyo Press, 東京大学出版会, ISBN 4-13-060728-6 (in Japanese).

# Chapter 6

## Dynamic Response Analysis



Masjid ye Imam, Isfahan, Iran.

Isfahan was a capital of the Safavid Dynasty of Iran since sixteenth Century. At the peak of its prosperity, this city was considered to be half of the world. The center of Isfahan was decorated by a beautiful garden and many marvellous buildings by monarchs of the dynasty mostly in the seventeenth Century. This city ended its time in 1722 upon invasion from north east.

### 6.1 Rate-Independent Behaviour of Clay

Clay has a creep behavior; its deformation develops slowly with time under constant magnitude of stress. Therefore, the stress–strain curve of clay varies with the rate of loading. When loaded faster, clay reveals greater modulus and higher strength. These observation suggests that clay is a viscous material.

On the other hand, the stress–strain–strength characteristics of clay is controlled by a grain-to-grain friction and chemical bonding as well as electric interaction. The magnitude of these forces are not much dependent of the rate of loading. Consequently, the stress–strain behavior of clay is partially rate-dependent but partially rate-independent.

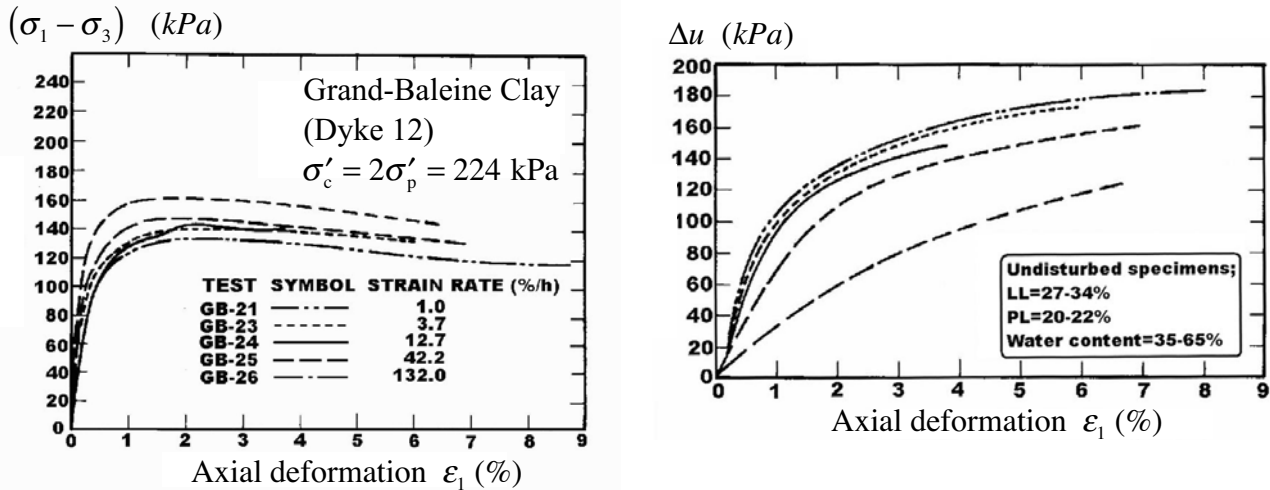


Fig. 6.1 Stress–strain and pore-water pressure behavior of normally consolidated Grande-Baleinee Clay (Lefebvre and LeBoeuf, 1987)

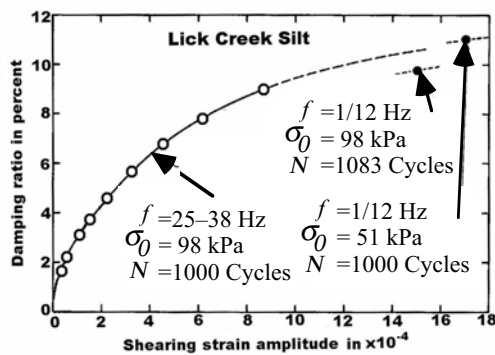


Fig. 6.2 Effect of frequency on damping ratio of silt (Hardin and Drnevich, 1972)

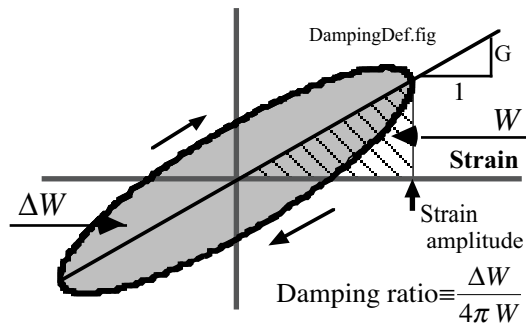


Fig. 6.3 Definition of damping ratio in soil dynamics

Figure 6.1 demonstrates undrained triaxial compression of clay with the axial strain rate varying between 1.0 %/hour and 132 %/hour. Evidently, the faster loading is associated with the greater strength and the less development of excess pore water pressure (the greater effective stress). In spite of the 132 times faster rate of loading, the maximum shear stress (strength) increased by about 25% only. The modulus increased by more or less the same amount as well. Thus, clay behavior is rate dependent to a limited extent.

Figure 6.2 illustrates a classic report on the damping ratio of Lick Creek Silt (liquid limit LL = 22–34%, plasticity limit PL= 20–27%). Damping ratio stands for the amount of energy loss in cycle due to a hysteretic nature of the loop (Fig. 6.3). A viscous material has a proportionality between damping ratio



and the rate of loading (frequency in Hz unit). Damping ratio has been known to increase as the amplitude of strain becomes larger. In Fig. 6.2, however, the relationship between damping ratio and the strain amplitude is independent of different frequencies of 25–38 and 1/12 Hz.

**6.2 Significance of Complex Analysis**

It may sound strange that many, although not all, dynamic analyses of ground make use of complex numbers: real and imaginary parts. Structural dynamics hardly do this. This practice has a reason in the simplicity in analysis and a use of complex-modulus modeling.

A discussion is initiated with a conventional single-degree-of-freedom model with mass, spring, and dashpot, which is called a Voigt model (Fig. 6.4a). The Voigt model can sustain a static force, while the other one in Fig. 6.4b (Maxwell model) cannot. Thus, the former model seems more similar to the real soil behavior.

When a Voigt model is excited by a harmonic force of  $F \cos \omega t$ , the equation of motion is given by

$$m \frac{d^2 u}{dt^2} + c \frac{du}{dt} + ku = F \cos \omega t. \tag{6.1}$$

Since the force is harmonic, the solution is assumed to be harmonic as well

$$u = A \sin \omega t + B \cos \omega t, \tag{6.2}$$

where  $A$  and  $B$  are unknown parameters. By substituting (6.2) in (6.1) and equating the coefficients of sin and cos terms,

$$\begin{cases} (k - m\omega^2)A - c\omega B = 0 \\ c\omega A + (k - m\omega^2)B = F \end{cases},$$

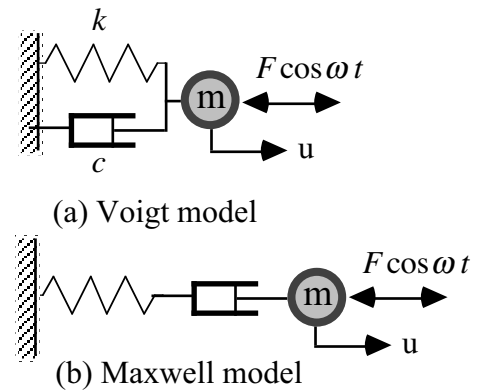
which is then easily solved;

$$\begin{Bmatrix} A \\ B \end{Bmatrix} = \frac{F}{(k - m\omega^2)^2 + (c\omega)^2} \begin{Bmatrix} c\omega \\ k - m\omega^2 \end{Bmatrix}. \tag{6.3}$$

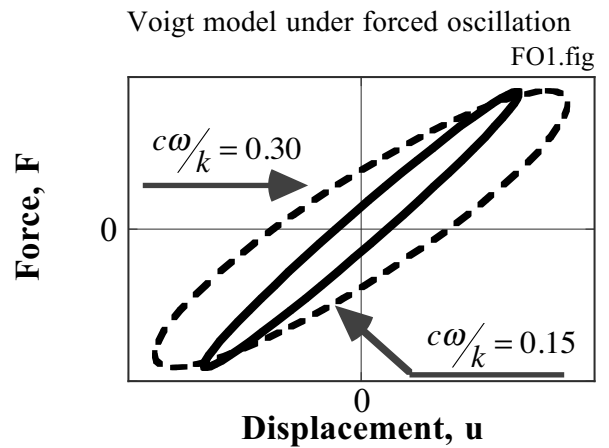
What follows employs a complex expression of force

$$m \frac{d^2 u}{dt^2} + c \frac{du}{dt} + ku = F \exp(i\omega t). \tag{6.4}$$

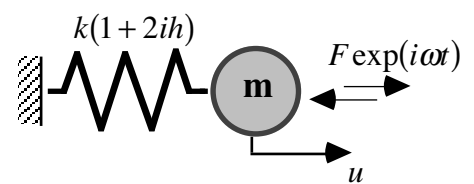
Equations (6.1) and (6.4) are equivalent when real parts of forces are compared. By assuming  $u = U \exp(i\omega t)$  in (6.4),



**Fig. 6.4** Single-degree-of-freedom models with real numbers



**Fig. 6.5** Rate effects in force-displacement relationship of Voigt model subjected to forced oscillation



**Fig. 6.6** Model of complex modulus

$$(-m\omega^2 + ic\omega + k)U = F$$

$$U = \frac{F}{(k - m\omega^2) + ic\omega} = \frac{F\{(k - m\omega^2) - ic\omega\}}{(k - m\omega^2)^2 + (c\omega)^2}.$$

By taking the real part of the solution  $U \exp(i\omega t)$ ,

$$\text{Re}(u) = \frac{F\{(k - m\omega^2) \cos\omega t + c\omega \sin\omega t\}}{(k - m\omega^2)^2 + (c\omega)^2} = A \sin\omega t + B \cos\omega t, \quad (6.5)$$

which is identical with (6.3). Thus, analyses with real and complex numbers are equivalent when real parts of complex numbers are used. However, the derivation of (6.5) is simpler.

The force–displacement relationship of a Voigt model thus derived is illustrated in Fig. 6.5. It is evident that the size of the loop, which stands for the energy loss per cycle, increases as the loading frequency is made higher. Note that real soil does not exhibit such rate dependency (Fig. 6.2 and Sect. 10.9).

The frequency independency of damping ratio (Sect. 6.1) can also be achieved by changing the dashpot parameter with the loading frequency (inverse proportionality:  $\propto 1/\text{frequency}$ ). This idea, however, is not acceptable from a mathematical viewpoint. When the input consists of harmonic motion of different frequencies, the equation of motion is given by

$$m \frac{d^2u}{dt^2} + c \frac{du}{dt} + ku = \sum_j (a_j \sin \omega t + b_j \cos \omega t). \quad (6.6)$$

It is then expected to derive the solution by superimposing individual solutions for respective frequency components

$$u(t) = \sum_j (A_j \sin \omega t + B_j \cos \omega t). \quad (6.7)$$

The practice of superposition is justified only when the given differential equation is linear. When the  $c$  value varies with  $\omega$ , however, the equation is not linear any more and, from the mathematical viewpoints, the superposition as (6.7) is not reasonable anymore. In other words, the earthquake response is irregular and its frequency varies with time in a random manner. Hence, it is difficult to determine any single number of  $c$  parameter. An alternative method of analysis is either a complex-modulus model (Sect. 9.1) or the use of nonlinear stress–strain model (e.g., hyperbolic stress–strain model in Sect. 11.1 or elastoplasticity in Sect. 11.3).

The Voigt model is often replaced in earthquake geotechnical engineering by a complex-modulus

Complex-modulus model under forced oscillation  
 $\omega/\omega_o = 0.3$  FO2.fig

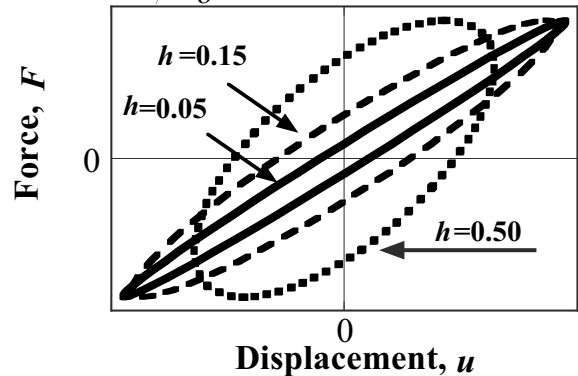


Fig. 6.7 Effects of  $h$  parameter on force–displacement loop of complex-modulus model

Complex-modulus model under forced oscillation  
FO3.fig

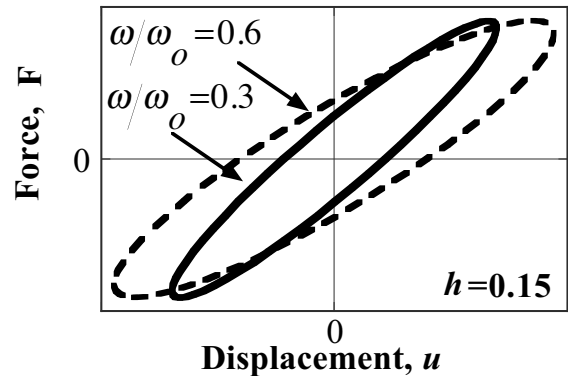


Fig. 6.8 Loading rate effects on force–displacement loop of complex-modulus model

model in which a spring parameter has an imaginary part (Fig. 6.6). As will be discussed later in Sect. 9.2, this imaginary part stands for an energy dissipation, eliminating the use of a rate-dependent dashpot in the model (Fig. 6.5). The equation of motion is

$$m \frac{d^2 u}{dt^2} + k(1 + 2ih)u = F \exp(i\omega t). \quad (6.8)$$

By assuming  $u = U \exp(i\omega t)$  again,

$$U = \frac{F_f(k - m\omega^2) - 2ikh\gamma}{(k - m\omega^2)^2 + 4k^2h^2} \quad \text{and} \quad \text{Re}(u) = \frac{F\{(k - m\omega^2) \cos\omega t + 2kh \sin\omega t\}}{(k - m\omega^2)^2 + 4k^2h^2}. \quad (6.9)$$

The energy dissipation in a complex-modulus model is governed by the “ $h$ ” parameter. Figure 6.7 demonstrates that the greater  $h$  value makes the loop bigger and increases the energy loss per cycle. In addition to this, Figure 6.8 reveals the effects of loading frequency. While the amplitude of displacement varies with the frequency, the damping ratio (Fig. 6.3) is not affected. This feature matches the nature of soil.

### 6.3 Transient Response

Transient response is a response starting from a state of stationary condition:  $displacement=velocity=0$ . The amplification during transient motion is different from what was obtained for a steady-state response in Sect. 6.2. A simple analysis is made in this section of a transient response of a rate-dependent single-degree-of-freedom model in Fig. 6.9. The equation of motion in terms of the relative displacement “ $u$ ” is given by

$$\frac{d^2u}{dt^2} + 2h\omega_0 \frac{du}{dt} + \omega_0^2 u = -\exp(i\omega t) \tag{6.10}$$

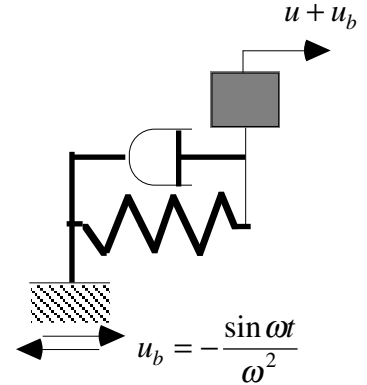


Fig. 6.9 Transient response of a simple model to harmonic shaking

Note that the base acceleration of  $\sin \omega t$  is replaced by  $\exp(i\omega t)$  for simplicity of calculation. Hence, the imaginary part of a complex solution to be derived will be adopted. By using the initial condition of  $u=du/dt=0$  at time = 0, a complex solution is given by

$$\frac{d^2(u + u_b)}{dt^2} = -\frac{(\lambda_1 + \lambda_2)i\omega - \lambda_1\lambda_2}{(\lambda_1 - i\omega)(\lambda_2 - i\omega)} \exp(i\omega t) - \frac{1}{\lambda_1 - \lambda_2} \left\{ \frac{\lambda_1^2 \exp(\lambda_1 t)}{\lambda_1 - i\omega} - \frac{\lambda_2^2 \exp(\lambda_2 t)}{\lambda_2 - i\omega} \right\} \text{ for } h < 1 \tag{6.11}$$

where  $\begin{cases} \lambda_1 \\ \lambda_2 \end{cases} = (-h \pm i\sqrt{1-h^2})\omega_0$ ,  $\omega_0$ =natural circular frequency, and  $h$  the critical damping ratio.

Figure 6.10 indicates the time history of response acceleration for a resonant input ( $\omega = \omega_0$ ), varying with the critical damping ratio. For a unit amplitude of input acceleration, the response acceleration does not immediately reach the steady-state amplitude of  $1/(2h)$ ; it takes a longer time for smaller critical damping ratio.

The electric power industries (変電所等における電気設備の耐震対策指針) have been employing such a resonant motion (only 2 or 3 cycles) for seismic design of transformers (変圧器), switches (開閉装置), etc. in place of real earthquake acceleration time histories. Figure 6.11 shows that the amplification of acceleration derived from 2 cycles (共振正弦2波) or 3 cycles (共振正弦3波) of harmonic resonant motion is comparative to those calculated for an irregular earthquake motion.

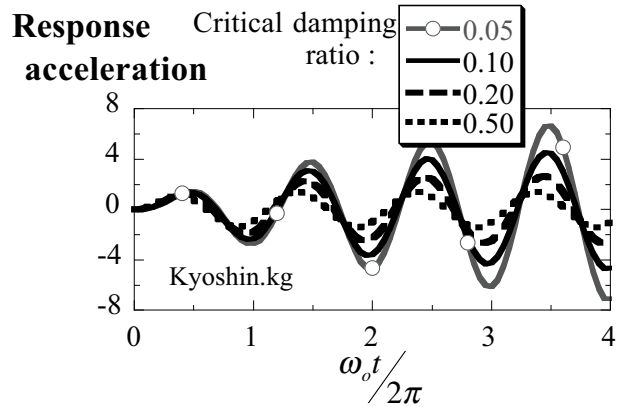


Fig. 6.10 Transient acceleration response to resonant input shaking

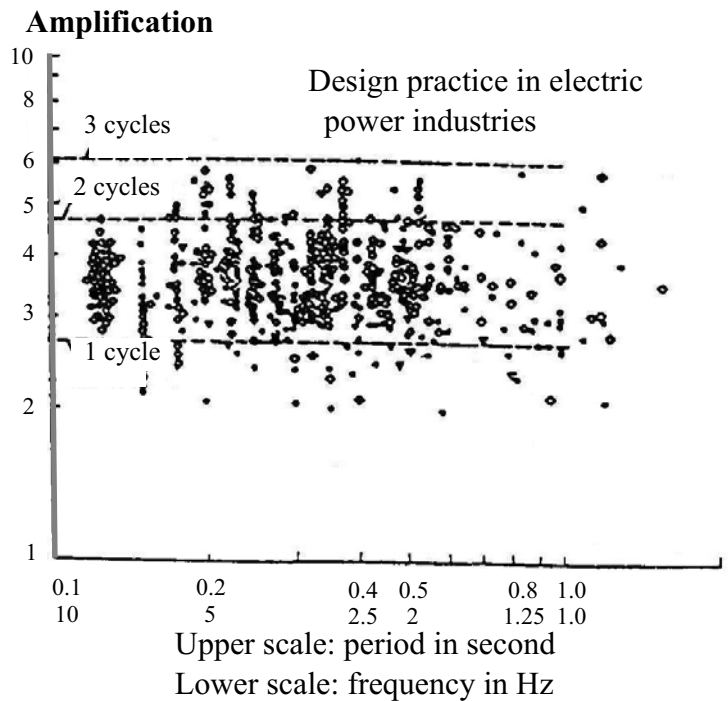


Fig. 6.11 Acceleration amplification for harmonic and irregular input motions (critical damping ratio = 0.05)

## 6.4 Analyses in Frequency Domain and Time Domain

Among two kinds of techniques of dynamic response analyses, the conventional analyses in soil dynamics have been conducted in the frequency domain (Sect. 4.4). The major features and shortcomings of the frequency-domain analyses are summarized below.

- The equation of motion,

$$m \frac{d^2 u}{dt^2} + k(1 + 2ih)u = f \exp(i\omega t)$$

in Sect. 9.4 is solved by assuming a harmonic response of  $u = U \exp(i\omega t)$ . Load amplitude,  $f$ , and material properties do not change with time (steady state response).

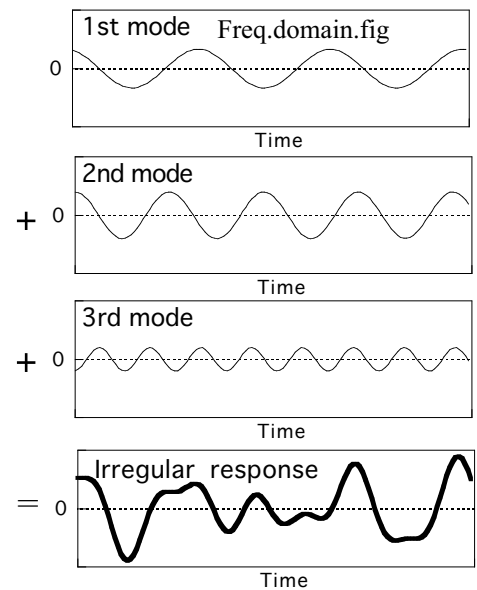
- Calculation of time history of shaking as well as the maximum acceleration and velocity is widely conducted by frequency-domain analyses.
- Response to irregular loading is calculated by summing up harmonic (sinusoidal) responses under different frequencies (theory of Fourier series expansion in Sect. 9.11), see Fig. 6.12.
- Since laboratory tests on behavior of soils under cyclic loading have been conducted by applying harmonic stress cycles to soil specimens, test results on nonlinear soil properties such as  $G/G_{\max}$  and damping ratio versus strain amplitude, can be directly used in the response analyses.
- Since the steady-state response analysis cannot take into account the variation of properties with time, degradation (softening) of clay and liquefaction of sand after excess pore water development are out of scope.
- Since the response is assumed to be harmonic, it comes back to the initial condition. Hence, residual deformation that remains after earthquake loading cannot be predicted.

On the other hand, time-domain analyses directly integrates the equation of motion of

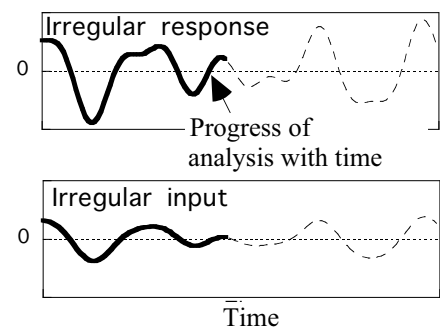
$$m \frac{d^2 u}{dt^2} + r\left(u, \frac{du}{dt}\right) = f(t)$$

in which  $r(u, du/dt)$  stands for the nonlinearly developed stress in soil, see Fig. 6.13. One of the famous techniques for direct integration is Newmark  $\beta$  method, see Sect. 6.6. Features of the time-domain analyses are described below.

- The nonlinearity of soil,  $r(u, du/dt)$ , is often modeled by elasto-plastic models. Being theoretically beautiful, those models require detailed laboratory tests on undisturbed soil samples.
- Previous test results on  $G/G_{\max}$  and damping ratio are not enough to determine parameters in elasto-plastic models.
- Irregularity of input motion does not make any computational problem.
- It is possible to take into account the change of soil properties with time.
- Residual deformation can be automatically calculated, although its accuracy is not clear.



**Fig. 6.12** Irregular response as summation of component harmonic modes



**Fig. 6.13** Principle of time-domain analysis

- Development of excess pore water pressure and consequent liquefaction can be handled only by the time-domain analysis (Sect. 22.3).
- Hence, demands for time-domain analyses are increasing today.

It is concluded, therefore, that the choice of the type of analyses depends upon what kind of calculation is being planned; e.g., time domain analysis suits studies on the development of excess pore water pressure, consequent softening of soil, and residual deformation. The frequency domain analysis is good at the assessment of maximum acceleration for example.

## 6.5 Numerical Integration of Equation of Motion in The Time Domain

Integration of equation of motion in the time domain is advantageous over the one in the frequency domain in that it can easily take into account the nonlinearity of material properties as well as the irregular time history of external load (transient analysis). On the other hand, being numerical, it cannot exhibit clearly the general scope of a concerned dynamic phenomenon, namely, the parameter effects. Moreover, nonlinearity of soil properties have been experimentally studied so far by using constant amplitudes of stress or strain. This situation directly fits an analysis on harmonic shaking. Therefore, most dynamic analysis of ground to date uses the idea of harmonic shaking. The irregularity of shaking is considered by using the theory of Fourier series (equivalent linear method in Sect. 9.10). It will be possible in future that a simple and useful plasticity theory is developed and becomes widely available.

This page illustrates a simple example of direct integration in the time domain. An example is taken of a simple equation of motion with a single-degree-of-freedom

$$m \frac{d^2u}{dt^2} + c \frac{du}{dt} + ku = R(t), \quad (6.12)$$

in which  $u$  stands for the displacement,  $du/dt$  and  $d^2u/dt^2$  the velocity and acceleration, respectively, and  $R(t)$  the external load that changes with time. It is assumed that the response is already known up to time  $T$ , while the response at  $T + \Delta t$  after a short time increment of  $\Delta t$  is going to be calculated.

All the numerical techniques for solution of (6.12) requires some assumption about time change of response. One of the assumptions is that the acceleration varies linearly with time within a short increment of  $\Delta t$

$$\frac{d^2u(t)}{dt^2} = \frac{d^2u(T)}{dt^2} + \frac{\frac{d^2u(T+\Delta t)}{dt^2} - \frac{d^2u(T)}{dt^2}}{\Delta t} (t - T), \quad (6.13)$$

where  $d^2u(T)/dt^2$  is the known acceleration at  $T$ , while  $d^2u(T + \Delta t)/dt^2$  is the unknown acceleration at  $T + \Delta t$ . By integrating (6.13) with time,

$$\begin{aligned} \frac{du(T + \Delta t)}{dt} &= \frac{du(T)}{dt} + \frac{d^2u(T)}{dt^2} \Delta t + \frac{1}{2} \left\{ \frac{d^2u(T + \Delta t)}{dt^2} - \frac{d^2u(T)}{dt^2} \right\} \Delta t \\ &= \frac{du(T)}{dt} + \frac{1}{2} \left\{ \frac{d^2u(T + \Delta t)}{dt^2} + \frac{d^2u(T)}{dt^2} \right\} \Delta t \end{aligned} \quad (6.14)$$

$$\begin{aligned} u(T + \Delta t) &= u(T) + \frac{du(T)}{dt} \Delta t + \frac{1}{2} \frac{d^2u(T)}{dt^2} \Delta t^2 + \frac{1}{6} \left\{ \frac{d^2u(T + \Delta t)}{dt^2} - \frac{d^2u(T)}{dt^2} \right\} \Delta t^2 \\ &= u(T) + \frac{du(T)}{dt} \Delta t + \Delta t^2 \left\{ \frac{1}{6} \frac{d^2u(T + \Delta t)}{dt^2} + \frac{1}{3} \frac{d^2u(T)}{dt^2} \right\} \end{aligned}$$

Substituting (6.14) in the equation of motion (6.12) at  $T + \Delta t$ ,

$$\left(m + \frac{\Delta t}{2}c + \frac{\Delta t^2}{6}k\right) \frac{d^2u(T + \Delta t)}{dt^2} = R(T + \Delta t) - c \left\{ \frac{du(T)}{dt} + \frac{\Delta t}{2} \frac{d^2u(T)}{dt^2} \right\} - k \left\{ u(T) + \Delta t \frac{du(T)}{dt} + \frac{\Delta t^2}{3} \frac{d^2u(T)}{dt^2} \right\} \quad (6.15)$$

$$\frac{d^2u(T + \Delta t)}{dt^2} = \frac{R(T + \Delta t) - c \left\{ \frac{du(T)}{dt} + \frac{\Delta t}{2} \frac{d^2u(T)}{dt^2} \right\} - k \left\{ u_T + \Delta t \frac{du(T)}{dt} + \frac{\Delta t^2}{3} \frac{d^2u(T)}{dt^2} \right\}}{\left(m + \frac{\Delta t}{2}c + \frac{\Delta t^2}{6}k\right)}. \quad (6.16)$$

Thus, the acceleration at  $T + \Delta t$  is obtained. By substituting it in (6.14), the velocity and displacement are obtained as well. Then, the calculation proceeds towards the next time increment.

Unfortunately, the numerical method as described above is nothing more than being conceptual. When the time increment is greater than a certain fraction of the natural period of (6.12), the calculated response erroneously grows without limit. This nature is called “conditionally stable.” The author prefers some other methods that are unconditionally stable. For example, see Sects. 6.6 and 9.8.



## 6.6 Newmark's $\beta$ Method

Newmark proposed a popular method for direct integration of equation of motion

$$m \frac{d^2 u}{dt^2} + c \frac{du}{dt} + ku = R(t). \quad (6.17)$$

Newmark employed the following relationships

$$\begin{aligned} \frac{du(T + \Delta t)}{dt} &= \frac{du(T)}{dt} + \left\{ (1 - \gamma) \frac{d^2 u(T)}{dt^2} + \gamma \frac{d^2 u(T + \Delta t)}{dt^2} \right\} \Delta t \\ u(T + \Delta t) &= u(T) + \frac{du(T)}{dt} \Delta t + \left\{ \left( \frac{1}{2} - \beta \right) \frac{d^2 u(T)}{dt^2} + \beta \frac{d^2 u(T + \Delta t)}{dt^2} \right\} \Delta t^2. \end{aligned} \quad (6.18)$$

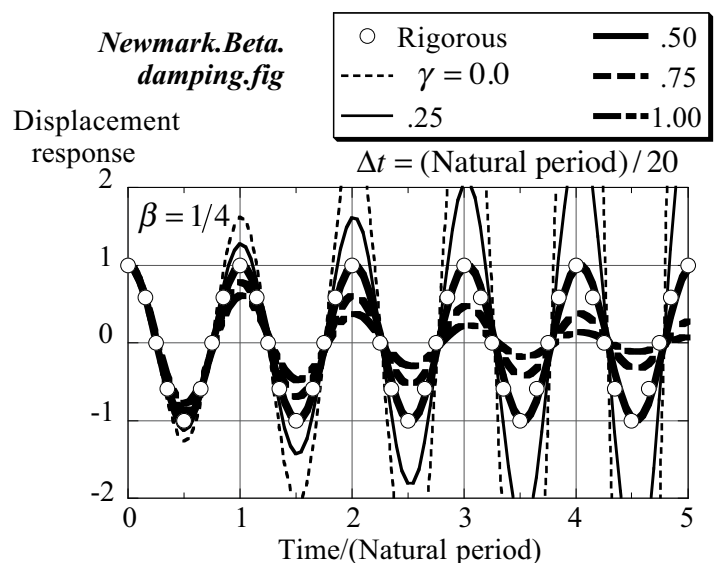
By comparing (6.18) with (6.14), it is found that a combination of  $\beta = 1/6$  and  $\gamma = 1/2$  represents a linear variation of acceleration within a short time increment. Certainly, other combinations stand for different variation of acceleration with time. By substituting (6.18) in (6.17),

$$\begin{aligned} (m + \gamma \Delta t c + \beta \Delta t^2 k) \frac{d^2 u(T + \Delta t)}{dt^2} &= R(T + \Delta t) - c \left\{ \frac{du(T)}{dt} + \Delta t (1 - \gamma) \frac{d^2 u(T)}{dt^2} \right\} \\ &\quad - k \left\{ u(T) + \Delta t \frac{du(T)}{dt} + \Delta t^2 \left( \frac{1}{2} - \beta \right) \frac{d^2 u(T)}{dt^2} \right\}. \end{aligned} \quad (6.19)$$

Thus,  $d^2 u(T + \Delta t)/dt^2$  is obtained. It is then substituted in (6.18) to calculate  $du(T + \Delta t)/dt$  and  $u(T + \Delta t)$ . The analysis then proceeds to the response at  $T + 2\Delta t$ .

The author prefers to use a combination of  $\beta = 1/4$  and  $\gamma = 1/2$ , which makes the analysis unconditionally stable (see Sect. 6.5). A constant acceleration of  $d^2 u(t)/dt^2 = \{d^2 u(T)/dt^2 + d^2 u(T + \Delta t)/dt^2\}/2$  is represented for by  $\beta = 1/4$ , while  $\gamma = 1/2$  does not generate numerical damping. Figure 6.14 illustrates the calculated response for  $c = 0$  and  $R = 0$  with the initial condition of  $u = 1$ ,  $du/dt = 0$ , and  $d^2 u/dt^2 = k/m$ . As compared with the rigorous solution of  $u = \cos(\sqrt{k/m} \times t)$ ,  $\gamma < 0.5$  produces erroneous increase of amplitude,  $\gamma = 0.5$  successfully reproduces the response, and  $\gamma > 0.5$  makes decay of response. This decay is called numerical damping. Although the numerical damping is a kind of error, it is often used to erase erroneous impulse that is numerically generated when nonlinear response of structure is analyzed. For detailed mechanism of unconditional stability and numerical damping, refer to Sect. 9.8.

It is certainly possible to solve the equation of motion in terms of displacement, in contrast to the use of acceleration in (6.19), and then to calculate velocity and acceleration.



**Fig. 6.14** Free vibration calculated by Newmark  $\beta$  method

Newmark's method is one of the direct integration methods for equation of motion. The following section addresses the mechanism of numerical damping and unconditional stability (Sect. 6.6) by applying the method to a simple undamped (viscosity = 0) equation of free vibration without damping

$$\frac{d^2u}{dt^2} + \omega_0^2 u = 0, \quad (6.20)$$

in which  $\omega_0$  stands for the natural circular frequency of this model.

The present calculation follows the original one made by Togawa (1975) with  $\gamma = 1/2$ . In Newmark's method, the variation of velocity and displacement over a short time interval of  $\Delta t$  is approximated by

$$\begin{aligned} \left(\frac{du}{dt}\right)_{T+\Delta t} &= \left(\frac{du}{dt}\right)_T + \Delta t \left\{ (1-\gamma) \left(\frac{d^2u}{dt^2}\right)_T + \gamma \left(\frac{d^2u}{dt^2}\right)_{T+\Delta t} \right\} \\ u_{T+\Delta t} &= u_T + \Delta t \left(\frac{du}{dt}\right)_T + \Delta t^2 \left\{ \left(\frac{1}{2} - \beta\right) \left(\frac{d^2u}{dt^2}\right)_T + \beta \left(\frac{d^2u}{dt^2}\right)_{T+\Delta t} \right\}. \end{aligned} \quad (6.21)$$

By substituting (6.21) in (6.20),

$$\begin{bmatrix} 1 & \omega_0^2 \gamma \Delta t \\ 0 & 1 + \omega_0^2 \beta (\Delta t)^2 \end{bmatrix} \begin{Bmatrix} \frac{du}{dt} \\ u \end{Bmatrix}_{T+\Delta t} = \begin{bmatrix} 1 & -\omega_0^2 \gamma \Delta t \\ \Delta t & 1 - \omega_0^2 \left(\frac{1}{2} - \beta\right) (\Delta t)^2 \end{bmatrix} \begin{Bmatrix} \frac{du}{dt} \\ u \end{Bmatrix}_T. \quad (6.22)$$

By introducing an eigen value problem of this equation

$$\lambda \begin{bmatrix} 1 & \omega_0^2 \gamma \Delta t \\ 0 & 1 + \omega_0^2 \beta (\Delta t)^2 \end{bmatrix} \begin{Bmatrix} \frac{du}{dt} \\ u \end{Bmatrix} = \begin{bmatrix} 1 & -\omega_0^2 \gamma \Delta t \\ \Delta t & 1 - \omega_0^2 \left(\frac{1}{2} - \beta\right) (\Delta t)^2 \end{bmatrix} \begin{Bmatrix} \frac{du}{dt} \\ u \end{Bmatrix}, \quad (6.23)$$

in which the eigen value,  $\lambda$ , is complex. Note that

$$\left(\frac{du}{dt}\right)_{T+\Delta t} = \lambda \left(\frac{du}{dt}\right)_T \text{ and } u(T + \Delta t) = \lambda u(T) \quad (6.24)$$

are implied here in complex numbers. When the numerical calculation maintains stability (calculated response does not increase towards infinity, see Fig. 6.14),  $|\lambda| \leq 1$ . When no numerical damping occurs, furthermore,  $|\lambda| = 1$ . Thus, the eigen value has to be calculated. Because (6.23) has a nontrivial solution of  $\vec{u}$  (not zero), the value of determinant is equal to zero

$$\begin{vmatrix} \lambda - 1 & \omega_0^2 \gamma \Delta t (\lambda + 1) \\ -\Delta t & \lambda \left\{ 1 + \omega_0^2 \beta (\Delta t)^2 \right\} - 1 + \omega_0^2 \left(\frac{1}{2} - \beta\right) (\Delta t)^2 \end{vmatrix} = 0 \quad (6.25)$$

$$\lambda^2 + \frac{-2 + \omega_0^2(\Delta t)^2\left(\frac{1}{2} + \gamma - 2\beta\right)}{1 + \omega_0^2\beta(\Delta t)^2}\lambda + \frac{1 + \omega_0^2\left(\beta + \gamma - \frac{1}{2}\right)(\Delta t)^2}{1 + \omega_0^2\beta(\Delta t)^2} = 0. \quad (6.26)$$

By denoting two solutions of  $\lambda$  by  $\lambda = \lambda_1$  and  $\lambda = \lambda_2$ , which are either real or complex,

$$\begin{aligned} \lambda_1 + \lambda_2 &= \frac{2 - \omega_0^2(\Delta t)^2\left(\frac{1}{2} + \gamma - 2\beta\right)}{1 + \omega_0^2\beta(\Delta t)^2} \quad \text{and} \\ \lambda_1\lambda_2 &= \frac{1 + \omega_0^2\left(\beta + \gamma - \frac{1}{2}\right)(\Delta t)^2}{1 + \omega_0^2\beta(\Delta t)^2} = 1 + \frac{\omega_0^2\left(\gamma - \frac{1}{2}\right)(\Delta t)^2}{1 + \omega_0^2\beta(\Delta t)^2}. \end{aligned} \quad (6.27)$$

The type of solutions, real or complex, depends on the sign (positive or negative) of

$$\begin{aligned} D &= \left\{ \frac{2 - \omega_0^2(\Delta t)^2\left(\frac{1}{2} + \gamma - 2\beta\right)}{1 + \omega_0^2\beta(\Delta t)^2} \right\}^2 - 4 \left\{ \frac{1 + \omega_0^2\left(\beta + \gamma - \frac{1}{2}\right)(\Delta t)^2}{1 + \omega_0^2\beta(\Delta t)^2} \right\} \\ &= \frac{\omega_0^2(\Delta t)^2}{1 + \omega_0^2\beta(\Delta t)^2} \left[ \omega_0^2(\Delta t)^2 \left\{ \left(\gamma + \frac{1}{2}\right)^2 - 8\beta\gamma \right\} - 8\gamma \right]. \end{aligned} \quad (6.28)$$

To achieve stability in analysis,

$$\text{both } |\lambda_1| \leq 1 \text{ and } |\lambda_2| \leq 1 \quad (6.29)$$

are needed.

Equation (6.27) is used to understand the mechanism of numerical damping.

(1) When  $\gamma = 1/2$ , for example,

$$\lambda_1\lambda_2 = 1 \text{ and } D = \frac{\omega_0^2(\Delta t)^2}{1 + \omega_0^2\beta(\Delta t)^2} \left\{ \omega_0^2(\Delta t)^2(1 - 4\beta) - 4 \right\}.$$

It is implied by  $\lambda_1\lambda_2 = 1$  that, if solutions of  $\lambda$  take two real and different numbers, one of them is greater than 1 and violates the requirement for stability (6.29). Hence, solutions of  $\lambda$  have to be real, equal to each other, or complex numbers. The requirement of  $D \leq 0$  leads to

$$\omega_0^2(\Delta t)^2(1 - 4\beta) \leq 4.$$

Consequently, the dynamic analysis with  $\gamma = 1/2$  is

- Unconditionally stable when  $\beta \geq 1/4$
- Stable when  $\beta < 1/4$  but  $\Delta t \leq 2/(\omega_0\sqrt{1 - 4\beta})$
- Unstable if  $\beta < 1/4$  and  $\Delta t > 2/(\omega_0\sqrt{1 - 4\beta})$

(2) When  $\gamma < 1/2$ , (6.27) implies  $\lambda_1\lambda_2 < 1$ . The solution of the equation of motion decays with time when  $D$  in (6.28) is less than or equal to zero. This is called numerical damping.

## 6.7 Introduction to Seismic Response Analysis

An elementary analysis is made of a two-layered elastic horizontal deposit (Fig. 6.15). The surface layer is equivalent to an alluvium (沖積層), whilst the lower layer is an older deposit or sometimes a base rock. In reality, there is often a stiff gravelly layer at the bottom of alluvium with SPT- $N$  ( $N$ 値)  $> 40$ . The age of two layers is discontinuous (unconformity 不整合) due to geological history.

It is reasonable to assume a vertical propagation of S wave near the surface (see Fig. 4.7). With reference to Sect. 4.4, the equation of S-wave propagation is solved

$$\frac{\partial^2 u}{\partial t^2} = V_s^2 \frac{\partial^2 u}{\partial z^2}.$$

When a harmonic shaking is the case, the horizontal displacement,  $u$ , is derived as

$$u_1 = E_1 \exp\left\{i\omega\left(t + \frac{z}{V_{s1}}\right)\right\} + F_1 \exp\left\{i\omega\left(t - \frac{z}{V_{s1}}\right)\right\} \quad \text{in the top layer } (0 \leq z \leq H \text{ in Fig. 6.15})$$

$$u_2 = E_2 \exp\left\{i\omega\left(t + \frac{z-H}{V_{s2}}\right)\right\} + F_2 \exp\left\{i\omega\left(t - \frac{z-H}{V_{s2}}\right)\right\} \quad \text{in the base layer } (H \leq z),$$

where  $E_1$  to  $F_2$  are constants. Note that the real parts of these solutions are used in practice. When this complex expression is not preferred, describe the solution as a sum of sin and cos functions. Shear stress is given by  $\tau = G \partial u / \partial z = \rho V_s^2 \partial u / \partial z$ ,

$$\tau_1 = i\omega\rho_1 V_{s1} \left[ E_1 \exp\left\{i\omega\left(t + \frac{z}{V_{s1}}\right)\right\} - F_1 \exp\left\{i\omega\left(t - \frac{z}{V_{s1}}\right)\right\} \right]$$

$$\tau_2 = i\omega\rho_2 V_{s2} \left[ E_2 \exp\left\{i\omega\left(t + \frac{z-H}{V_{s2}}\right)\right\} - F_2 \exp\left\{i\omega\left(t - \frac{z-H}{V_{s2}}\right)\right\} \right].$$

Because the shear stress is zero at any  $t$  at the surface ( $z = 0$ ), unless there is no structure,  $F_1 = E_1$ . Moreover, both displacement and shear stress are continuous at the interface ( $z = H$ ).

$$2E_1 \cos \frac{\omega H}{V_{s1}} = E_2 + F_2 \quad \text{and} \quad 2E_1 i \frac{\rho_1 V_{s1}}{\rho_2 V_{s2}} \sin \frac{\omega H}{V_{s1}} = E_2 - F_2.$$

Thus, all the constants are determined in terms of  $E_1$ .

$$\begin{Bmatrix} E_2 \\ F_2 \end{Bmatrix} = E_1 \begin{pmatrix} \cos \frac{\omega H}{V_{s1}} \pm i \frac{\rho_1 V_{s1}}{\rho_2 V_{s2}} \sin \frac{\omega H}{V_{s1}} \end{pmatrix}$$

- The amplitude of ground surface motion is  $2E_1$ .
- The free boundary condition at the surface (stress = 0) make the upward ( $E_1$ ) and the downward ( $F_1 = E_1$ ) propagations equal to each other in their intensity.
- The amplitude of upward propagation in the base rock is  $E_2$ . If the base rock is directly exposed to the air (rock outcrop),  $2E_2$  is the surface motion. Hence,  $2E_2$  is called the outcrop motion.

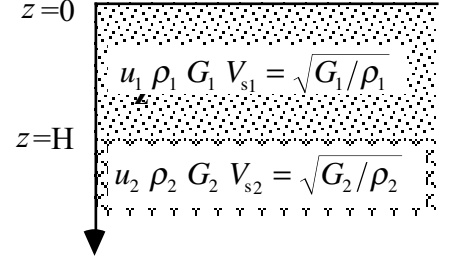


Fig. 6.15 Model of two-layered deposit

- $E_2$  is produced by the earthquake source and the travel path of the earthquake wave. It is the true input motion to the site of concern.
- The baserock motion of  $E_2+F_2$  has  $F_2$  which is the result of wave reflection at  $z = H$  and  $z = 0$ .  $F_2$  is affected by the nature of the surface layer and therefore is not the true INPUT to the site.
- Therefore,  $E_2$  has a more essential meaning than  $E_2+F_2$ .

The baserock here may not be a real rock. Being called “the engineering baserock,” in reality it is often a pleistocene soil (更新世、冰河期堆積物) or a soft rock.

6.8 Amplification of Motion in Surface Alluvium

The amplitude of motion in a horizontal layer,  $U_1$ , is given by

$$U_1 = |u_1| = 2E_1 \cos \frac{\omega z}{V_{s1}}$$

The variation of  $U_1$  with depth is illustrated in Fig. 6.16.  $U_1$  is equal to  $E_2 + F_2$  at the baserock ( $z = H$ ), and the ratio of  $U_1$  at the surface and at the base is conventionally called the amplification in terms of  $E + F$ , denoted by  $\text{Amp}(E + F)$  below.

$$\text{Amp}(E + F) = 1 / \cos \frac{\omega H}{V_{s1}}$$

This amplification is greater than or equal to 1 and takes an infinite value when  $\omega H / V_{s1} = (n - 1/2)\pi$  where  $n = 1, 2, 3, \dots$ . The state of this infinite amplification is called *resonance*. Theoretically, the base amplitude is zero at resonance.

At the fundamental mode of resonance ( $n = 1$ ) with  $\text{Amp}(E + F) \rightarrow \infty$ , the period of motion is obtained by

$$T = \frac{2\pi}{\omega} = \frac{4\pi H}{\pi V_{s1}} = \frac{4H}{V_{s1}} \tag{6.30}$$

This particular natural period is denoted by  $T_G$  which is the time that S wave needs to make 2 return trips between the surface and the base (21.4). See Table 21.2 for classification of subsoil by  $T_G$ .

$\text{Amp}(E + F)$  does not directly indicate the ability of shaking amplification of the surface soil. To show this ability, it is more suitable to use the ratio of surface shaking and the input shaking signal. This goal is achieved by another definition of amplification factor in what follows.

Another type of amplification is defined by the ratio of surface motion to the true input motion  $E_2$ . It is denoted by  $\text{Amp}(2E)$  here as conventionally practiced.

$$\begin{aligned} \text{Amp}(2E) &= \left| \frac{2E_1}{2E_2} \right| = 1 / \left| \cos \frac{\omega H}{V_{s1}} + i \frac{\rho_1 V_{s1}}{\rho_2 V_{s2}} \sin \frac{\omega H}{V_{s1}} \right| \\ &= 1 / \sqrt{\cos^2 \frac{\omega H}{V_{s1}} + \left( \frac{\rho_1 V_{s1}}{\rho_2 V_{s2}} \sin \frac{\omega H}{V_{s1}} \right)^2} \end{aligned} \tag{6.31}$$

At resonance when  $\omega H / V_{s1} = (n - 1/2)\pi$ ,

$$\text{Amp}(2E) = \frac{\rho_2 V_{s2}}{\rho_1 V_{s1}} \tag{6.32}$$

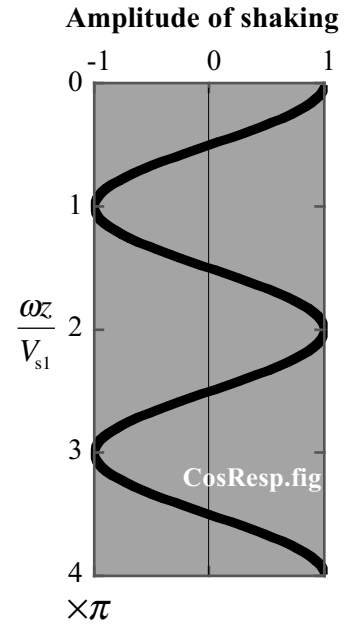


Fig. 6.16 Variation of amplitude with depth

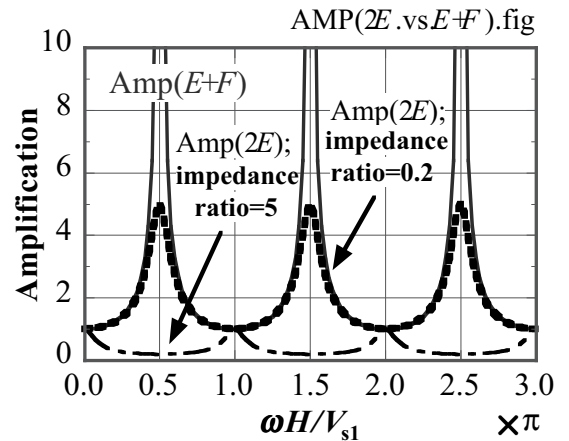


Fig. 6.17 Amplification of two types

Figure 6.17 compares  $\text{Amp}(E + F)$  and  $\text{Amp}(2E)$  for the case of impedance ratio  $\rho_1 V_{s1} / \rho_2 V_{s2} = 0.2$  and 5. Note that  $\text{Amp}(2E) > 1$  (large surface motion) occurs only when the surface layer is softer (*impedance ratio*  $< 1$ ). When the surface is harder, the ground motion is reduced.

When the impedance ratio = 1,  $\text{Amp}(2E) = 1.0$  for any value of  $\omega$  and hence  $E_1 = E_2$ . This is a situation of rock outcrop in which the surface motion is given by  $2E_2$  (Fig. 6.18). It is therefore true that  $\text{Amp}(2E)$  is the ratio of motions at the surface of soil and at a rock outcrop (Fig. 6.18). It is important that resonance, i.e. infinite amplification of  $\text{Amp}(E+F)$ , is possible only when there is a vertical variation (gap) in impedance.  $\text{Amp}(2E)$  does not take an infinite value even at the resonance frequency. Hence, an infinite surface response does not occur in reality.

6.9 Significance of Outcrop Motion

The amplification in terms of “2E” strictly means the increase in the intensity of the incident wave amplitude

$$\text{Amp}(2E) = \frac{2 \times (\text{Amplitude of surface incident motion})}{2 \times (\text{Amplitude of incident motion in base rock})} = \frac{2E_1}{2E_R} = \frac{\text{Amplitude of surface motion}}{\text{Amplitude of rock outcrop motion}},$$

which is the exact amplification in the surface soil.

In contrast,  $\text{Amp}(E + F)$  simply compares the amplitudes of the surface motion and the motion at the bottom. The bottom motion includes the downward propagation of wave, which is the result of the response of the surface soil, and, therefore,  $\text{Amp}(E + F)$  does not directly mean the amplification made by local soil conditions.

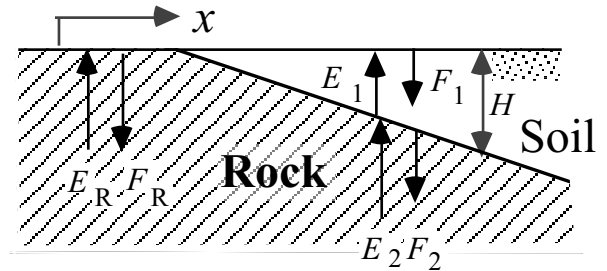


Fig. 6.18 Significance of outcrop motion

When the baserock appears at the surface, it is called a rock outcrop (露頭). Since a rock mass is considered to be uniform and elastic, the nature of the incident motion is identical at both the outcrop and base rock under alluvium, see Fig. 6.18;

$$E_R = E_2,$$

which is assumed to be real and positive without losing generality.

Since the shear stress is zero at the surface of both the outcrop and the soil

$$E_R = F_R \text{ and } E_1 = F_1.$$

The surface motion at the outcrop site is given by

$$u_R = 2E_R \exp(i\omega t)$$

Hence,  $\text{Amp}(2E)$  upon rock outcrop is equal to 1.0.

The surface motion at the surface of soft alluvial soil has an amplitude of

$$|2E_1| = \frac{2E_2}{\sqrt{\cos^2 \frac{\omega H}{V_{s1}} + \left(\frac{\rho_1 V_{s1}}{\rho_2 V_{s2}}\right)^2 \sin^2 \frac{\omega H}{V_{s1}}}} = \frac{2E_R}{\sqrt{\cos^2 \frac{\omega H}{V_{s1}} + \left(\frac{\rho_1 V_{s1}}{\rho_2 V_{s2}}\right)^2 \sin^2 \frac{\omega H}{V_{s1}}}},$$

where  $\rho_1 V_{s1} / \rho_2 V_{s2}$  is called the impedance ratio. Consequently,  $\text{Amp}(2E)$  at a soil site is given by

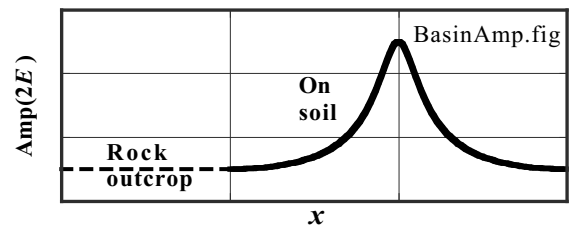


Fig. 6.19 Variation of amplification with local soil conditions

What is recorded upon a rock outcrop is a  $2E_R$  motion. Since  $E_R = E_2$ , the observed rock-outcrop motion can be directly used as an input motion at the bottom of a soil site.



$$\text{Amp}(2E) = \frac{1}{\sqrt{\cos^2 \frac{\omega H}{V_{s1}} + \left( \frac{\rho_1 V_{s1}}{\rho_2 V_{s2}} \right)^2 \sin^2 \frac{\omega H}{V_{s1}}}}, \quad (6.33)$$

as shown by (6.31). Figure 6.19 indicates the variation of  $\text{Amp}(2E)$  along the  $x$  axis. Since  $H$  varies with  $x$ ,  $\text{Amp}(2E)$  changes in the horizontal direction as well. The maximum amplification occurs at some distance from the edge of a soft alluvial plane where the condition of resonance is satisfied. According to (6.33), this maximum amplification is governed by the impedance ratio. Thus, the softer deposit of soil is subjected to the greater amplification and the more seismic risk.

6.10 Seismic Response of Multi-Layered Ground

It is not uncommon that a studied ground consists of many different types of soils. The surface fill is underlain by clayey and sandy soils possibly together with gravel. When this is the case, it is a common practice to assume a horizontally layered stratification (Fig. 6.20) in which layers of different soils are stacked in the horizontal direction.

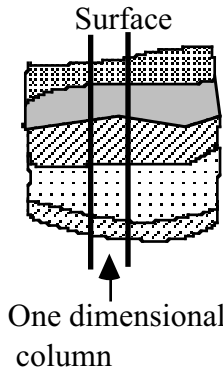


Fig. 6.20 Horizontally layered stratification

In reality, there is a variation of soil type in the horizontal direction. Figure 6.21 compares boring logs from two drilled holes that are only 4 m apart. Although the difference in logs depends on the personal interpretation of the engineer in charge, the two logs do not appear identical. It means that a two-dimensional analysis with this variation taken into account may be required. However, it is practically difficult to run many field investigation (drilling bore holes) and to precisely understand the horizontal variation. Thus, a one-dimensional analysis on a vertical soil column (Fig. 6.22) is commonly practiced today.

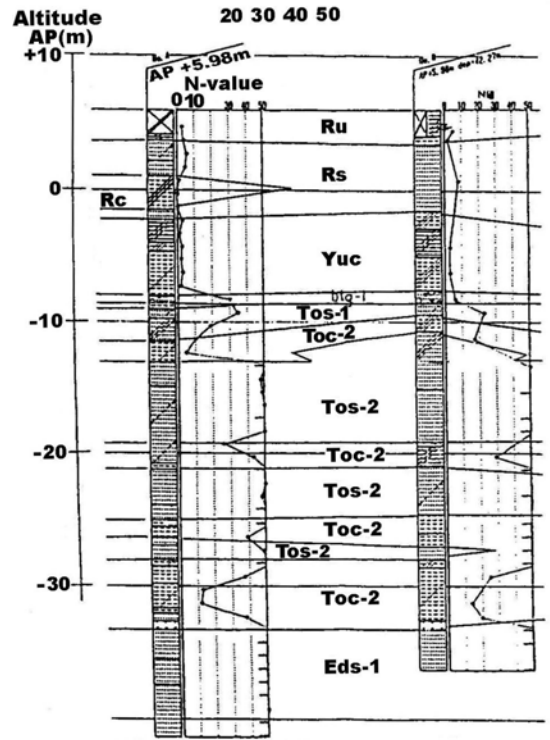


Fig. 6.21 Two boring logs at Shin-Ohta site in Tokyo (by ADEP)

When a harmonic shaking is assumed, each layer has a closed-form solution of displacement and shear stress. In the layer “j” with an elastic property of  $G = \rho V_s^2$ ,

$$u_j = E_j \exp\left\{i\omega\left(t + \frac{z - z_j}{V_{sj}}\right)\right\} + F_j \exp\left\{i\omega\left(t - \frac{z - z_j}{V_{sj}}\right)\right\}$$

$$\tau_j = i\omega\rho_j V_{sj} \left[ E_j \exp\left\{i\omega\left(t + \frac{z - z_j}{V_{sj}}\right)\right\} - F_j \exp\left\{i\omega\left(t - \frac{z - z_j}{V_{sj}}\right)\right\} \right],$$

in which  $z_j$  is the depth at the top of this layer (Fig. 6.22). An elastic formula of  $G = \rho V_s^2$  was used. Since both displacement “u” and shear stress “τ” are continuous at a layer interface,

$$E_j \exp\left(i\omega \frac{z_{j+1} - z_j}{V_{sj}}\right) + F_j \exp\left(-i\omega \frac{z_{j+1} - z_j}{V_{sj}}\right) = E_{j+1} + F_{j+1}$$

$$\rho_j V_{sj} \left\{ E_j \exp\left(i\omega \frac{z_{j+1} - z_j}{V_{sj}}\right) - F_j \exp\left(-i\omega \frac{z_{j+1} - z_j}{V_{sj}}\right) \right\} = \rho_{j+1} V_{sj+1} (E_{j+1} - F_{j+1}) \tag{6.34}$$

Note that  $z_{j+1} - z_j$  stands for the thickness of layer “j”. This set of equation makes it possible to describe  $E_{j+1}$  and  $F_{j+1}$  in terms of  $E_j$  and  $F_j$ . Moreover, since the shear stress is zero at the ground surface,  $E_1 = F_1$ . Consequently, all the  $E_j$  and  $F_j$ , including those in the baserock, are described in terms of  $E_1$ . Thus, it becomes possible to calculate the amplification in a multilayered ground.

Many boring logs show a thin soft layer of clay. A one-dimensional analysis that precisely considers this soft layer gives very small surface motion; wave energy is reflected back into the earth by this layer. Is this calculated motion reliable? Yes, it is, if the layer extends to a wide range. In practice, however, a thin layer (<50 cm, e.g.) is eliminated from analysis because it is probably a local clay pocket (deposit).

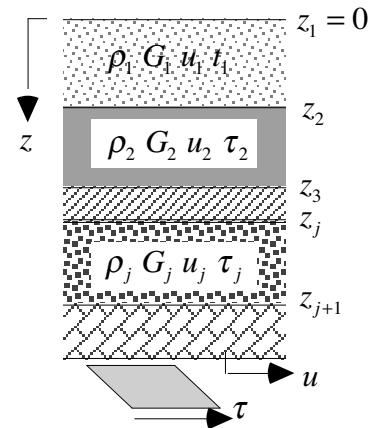


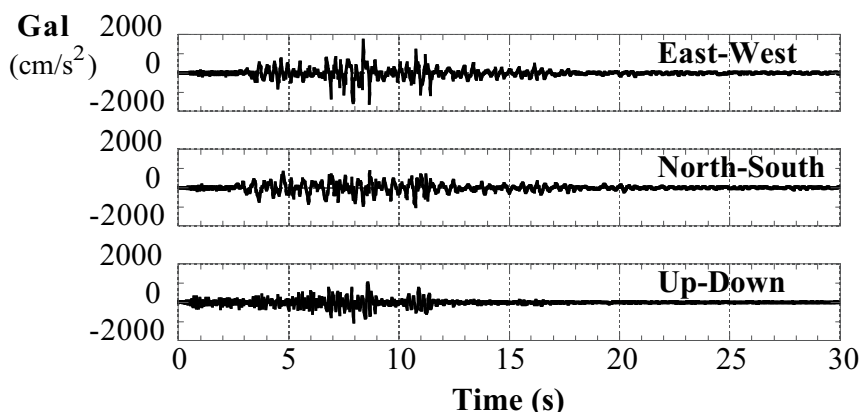
Fig. 6.22 Idealized ground for one-dimensional analysis

## 6.11 Amplification of Motion at the Top of Hill

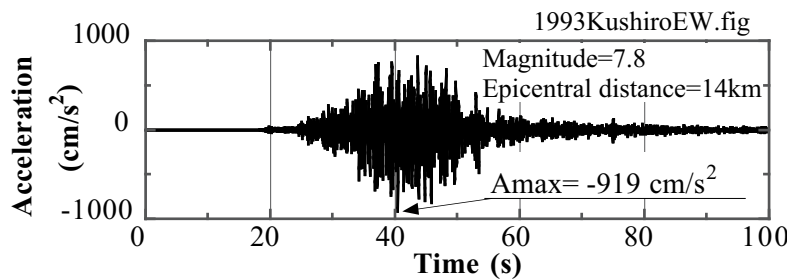
At the time of 1993 Kushiro-Oki earthquake (釧路沖地震), the maximum acceleration exceeded 900 Gal ( $=\text{cm/s}^2$ ) at the Kushiro Meteorological Observatory (釧路気象台), which was located at the top of a hill (Fig. 6.23). Although this record was surprisingly strong among previous records so-far measured at the ground surface (not inside high buildings), it did not cause structural damage to the observatory building except that shelves and other objects inside fell down to the floor. The reduced damage in the structure was probably because the maximum acceleration continued for a very short time (spiky impact). After this quake, many accelerometers were installed in the Kushiro City and the 1994 Hokkaido-Toho-Oki earthquake (北海道東方沖地震) was recorded. Again the acceleration at the observatory was the greatest (Fig. 6.24), greater than those in the alluvial plane.

It is noteworthy that a spiky strong acceleration is not a big problem to structures. This is because it does not give a sufficient time to cause large deformation/displacement (see Sects. 12.1 and 12.2).

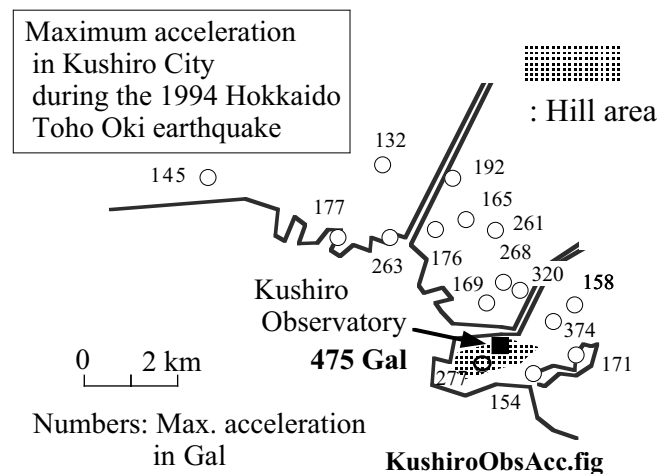
Another striking record was the one greater than 1,800 Gal (1.8 times *gravity*) at Tarzana near Los Angeles during the 1994 Northridge earthquake (Fig. 6.25). Although this motion was not spiky, the damage was still relatively light, see Fig. 7.4. During the 1995 Kobe earthquake, the Kobe Meteorological Observatory, which was located at the top of a small hill, recorded 818 Gal in the NS direction that was greater than what were recorded at other stations (Table 7.1). Onishi et al. (1999) collected many records observed at the Kushiro Observatory to show that this site is of greater acceleration than other sites. It is very interesting that both the Kushiro Observatory and the Tarzana sites are located at the top of a small hill (Fig. 6.26). This suggests a topographical amplification of earthquake motion (地形による地震動の増幅).



**Fig. 6.25** Acceleration at Tarzana during the 1994 Northridge earthquake (epicentral distance = 7km)



**Fig. 6.23** EW acceleration record at Kushiro Meteorological Observatory in 1993 (JSSMFE, 1994)



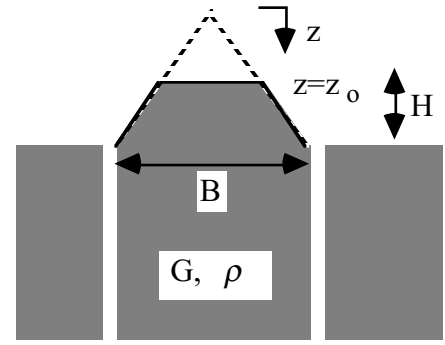
**Fig. 6.24** Distribution of the maximum acceleration in Kushiro City recorded in 1994 (WCEE, 1996)



**Fig. 6.26** Landscape from top of small hill at Tarzana site

### 6.12 Analysis on Hill-Induced Amplification

It seems that the shape of a hill concentrates the energy of an earthquake motion to its top because the width of a hill decreases at higher elevations. Bear in mind, however, that thus amplified motion does not necessarily induce a heavy damage to structures, although the acceleration is strong. To account for the hill effects, an analysis is made of propagation of SH wave (Sect. 4.2) in a simplified model of two-dimensional topography in Fig. 6.27. Since the attention is focused on the topography, the material properties are uniform.



**Fig. 6.27** 2-D simplified model of hill subjected to horizontal shaking

The model consists of a hill that rests on a vertical column of base rock.  $G$  and  $\rho$  stand for the elastic shear modulus and the mass density in both hill and base. The geometry of the hill gives the following expressions,

Width of hill =  $Bz/(z_0+H)$  and Shear force =  $Bz/(z_0+H) \times \tau$  for  $z_0 \leq z \leq z_0+H$  in which  $\tau$  is the shear stress. When “ $u$ ” designates the horizontal displacement, the equation of motion of horizontal shaking is derived as

$$\rho B \frac{z}{z_0+H} \frac{\partial^2 u}{\partial t^2} = \frac{\partial}{\partial z} \left( B \frac{z}{z_0+H} \tau \right) = \frac{\partial}{\partial z} \left( B \frac{z}{z_0+H} G \frac{\partial u}{\partial z} \right) \quad \text{and therefore,} \quad z \frac{\partial^2 u}{\partial t^2} = V_s^2 \frac{\partial}{\partial z} \left( z \frac{\partial u}{\partial z} \right),$$

where  $V_s = \sqrt{G/\rho}$ . By assuming a harmonic oscillation,  $u(z,t) = U(z) \exp(i\omega t)$ ,

$$V_s^2 z \frac{d^2 U}{dz^2} + V_s^2 \frac{dU}{dz} + \omega^2 z U = 0 \quad \text{and, hence,} \quad U = C_1 J_0 \left( \frac{\omega z}{V_s} \right) + C_2 Y_0 \left( \frac{\omega z}{V_s} \right),$$

in which  $J_0$  and  $Y_0$  are Bessel functions of the first and second kinds. Theories of Bessel functions are briefly described in Sect. 6.15. Accordingly, the shear stress at the bottom of the hill ( $z = H$ ) is given by

$$\tau = G \left( \frac{dU}{dz} \right) \exp(i\omega t) = -\omega \sqrt{\rho G} \left[ C_1 J_1 \left\{ \frac{\omega(z_0+H)}{V_s} \right\} + C_2 Y_1 \left\{ \frac{\omega(z_0+H)}{V_s} \right\} \right] \exp(i\omega t)$$

for which a formula of  $dJ_0(x)/dx = -J_1(x)$  was used.

In the elastic base, the conventional solution of S-wave propagation is valid

$$u = E \exp \left\{ i\omega \left( t + \frac{z-z_0-H}{V_s} \right) \right\} + F \exp \left\{ i\omega \left( t - \frac{z-z_0-H}{V_s} \right) \right\}$$

At the top of the base,  $u = (E+F) \exp(i\omega t)$  and  $\tau = i\omega \sqrt{\rho G} (E-F) \exp(i\omega t)$ . By considering the continuity of “ $u$ ” and “ $\tau$ ” between the hill and the base ( $z = z_0+H$ ) together with the boundary condition of  $\tau = 0$  at the top of the hill ( $z = z_0$ ),

$$\begin{aligned} \begin{Bmatrix} C_1 \\ C_2 \end{Bmatrix} &= \frac{2iE \begin{Bmatrix} Y_1(\omega z_0/V_s) \\ -J_1(\omega z_0/V_s) \end{Bmatrix}}{\left[ J_0 \left\{ \frac{\omega(z_0+H)}{V_s} \right\} Y_1 \left( \frac{\omega z_0}{V_s} \right) - J_1 \left( \frac{\omega z_0}{V_s} \right) Y_0 \left\{ \frac{\omega(z_0+H)}{V_s} \right\} \right]} \\ &\quad - i \left[ J_1 \left\{ \frac{\omega(z_0+H)}{V_s} \right\} Y_1 \left( \frac{\omega z_0}{V_s} \right) - J_1 \left( \frac{\omega z_0}{V_s} \right) Y_1 \left\{ \frac{\omega(z_0+H)}{V_s} \right\} \right] \\ F &= -E + C_1 J_0 \left\{ \frac{\omega(z_0+H)}{V_s} \right\} + C_2 Y_0 \left\{ \frac{\omega(z_0+H)}{V_s} \right\}. \end{aligned}$$

Consequently, amplifications produced by a hill topography are derived as

$$\text{Amp}(2E) = \left| \frac{U(z_0)}{2E} \right| = \frac{2V_s / \pi \omega z_0}{\sqrt{\left[ J_0 \left\{ \frac{\omega(z_0+H)}{V_s} \right\} Y_1 \left( \frac{\omega z_0}{V_s} \right) - J_1 \left( \frac{\omega z_0}{V_s} \right) Y_0 \left\{ \frac{\omega(z_0+H)}{V_s} \right\} \right]^2 + \left[ J_1 \left\{ \frac{\omega(z_0+H)}{V_s} \right\} Y_1 \left( \frac{\omega z_0}{V_s} \right) - J_1 \left( \frac{\omega z_0}{V_s} \right) Y_1 \left\{ \frac{\omega(z_0+H)}{V_s} \right\} \right]^2}}$$

$$\text{Amp}(E+F) = \left| \frac{U(z_0)}{U(z_0+H)} \right| = \frac{2V_s / \pi \omega z_0}{\left| J_0 \left\{ \frac{\omega(z_0+H)}{V_s} \right\} Y_1 \left( \frac{\omega z_0}{V_s} \right) - J_1 \left( \frac{\omega z_0}{V_s} \right) Y_0 \left\{ \frac{\omega(z_0+H)}{V_s} \right\} \right|}$$

for which the *Lommel's* formula,  $Y_v(x)J_{v+1}(x) - J_v(x)Y_{v+1}(x) = 2/\pi x$ , was employed.

6.13 Calculated Amplification Effects of Hilly Topography

The amplification effects of a hill,  $Amp(2E)$  and  $Amp(E+F)$ , are calculated by using the theory as developed in Sect. 6.12. In this section, five types of the hill shape are employed as illustrated in Fig. 6.28. Among them,  $Amp(2E)=1$  and  $Amp(E+F)=|1/\cos(\omega H/V_s)|$  are known for the case of “Top width = Base width,  $B$ ” at the far right.

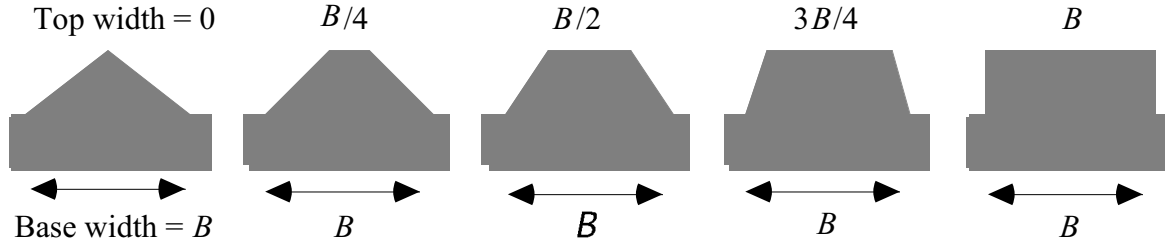


Fig. 6.28 Shapes of the analyzed hill

The calculated amplification,  $Amp(2E)$ , is illustrated in Fig. 6.29. When the top width is shorter than the bottom width, the amplification is always greater than unity irrespective of the shaking frequency. This amplification is equal to the amplitude ratio between the hill top and the surface of low land (Fig. 6.29). It is evident that the triangular hill with the top width = 0 achieves the greatest amplification at all the frequencies. In contrast, the top width =  $B$  is of  $Amp(2E)=1$  at any frequency as the theory of uniform elastic medium states. It seems that the assumption of uniform elasticity is not too bad because real hills are made of relatively harder materials than soft alluvium.

The calculated large amplification for the case of *top width = 0* is reasonable. The seismic energy that is incident at the base travels upwards. As the width of the hill decreases at higher elevations, the energy is concentrated within a limited hill width. Since the greater energy density makes the larger magnitude of shaking (see Sect. 4.11), the case of the zero width at the top demonstrates the largest amplification. Note that  $Amp(2E)$  in Fig. 6.29 approaches the theoretical value of  $\sqrt{\text{width ratio}}$  at higher frequencies. When the top width =  $B/4$  for example, the width ratio = 1:4 and the shaking energy density = 4:1. Hence, the amplitude ratio is 2:1.

Figure 6.30 shows  $Amp(E+F)$  of a hill topography. It is interesting that the resonance in a triangular hill (top width = 0) occurs at a frequency higher than those of more trapezoidal or rectangular topographies.

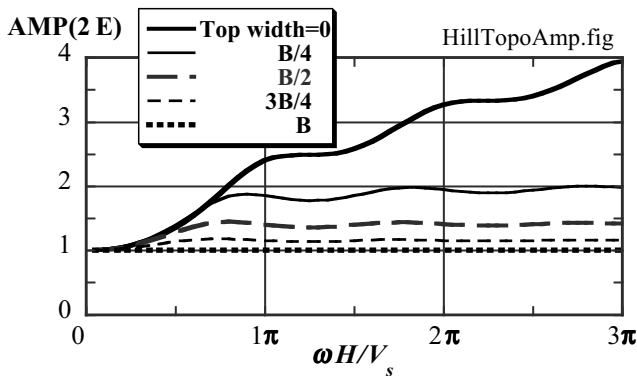


Fig. 6.29 Calculated amplification,  $Amp(2E)$  at the top of a hill

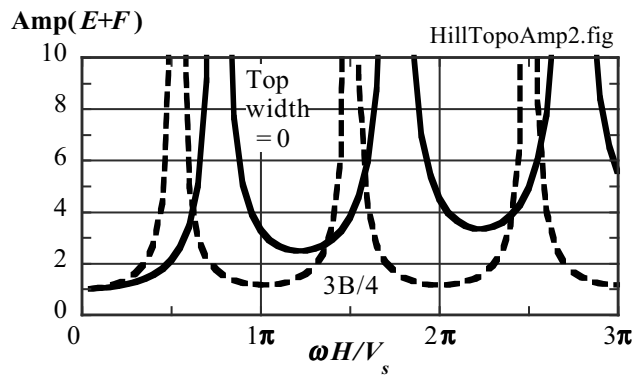


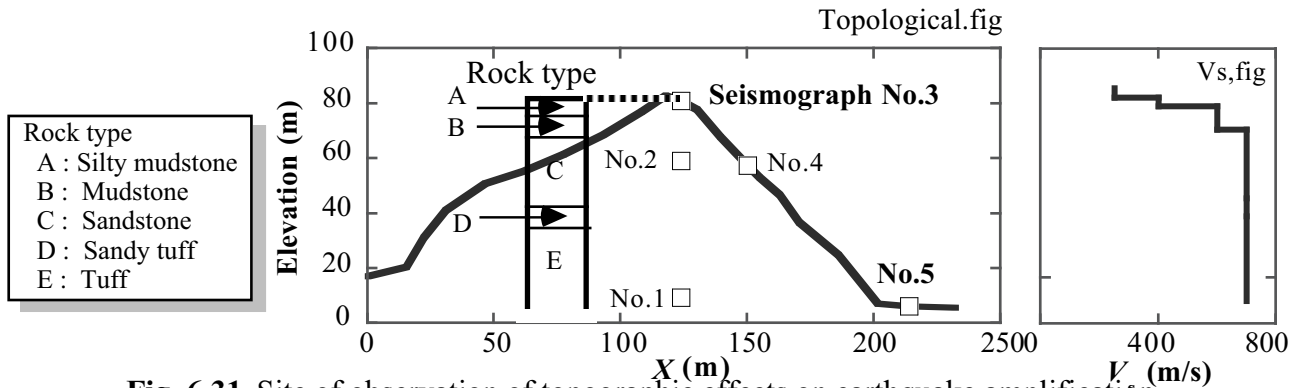
Fig. 6.30 Calculated amplification,  $Amp(E+F)$ , at the top of a hill

Further note that the resonance in  $Amp(E+F)$  in Fig. 6.30 does not affect  $Amp(2E)$  in Fig. 6.29.

Because of numerical reasons in a computer, the width of the top = 0.000999, 0.24999998, 0.500000, 0.750000, and 0.999001 times  $B$  were employed in the analysis.

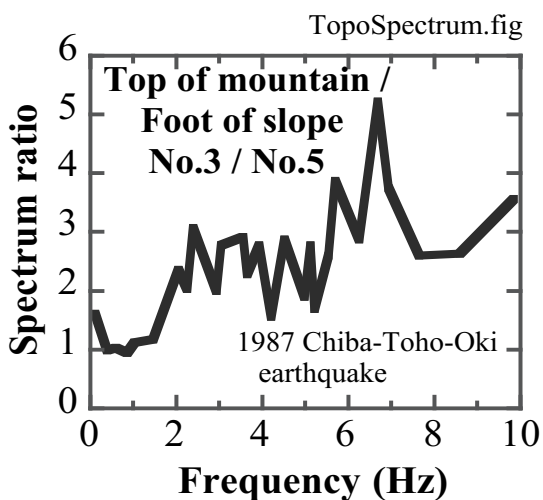
## 6.14 Observed Topographic Effects

After the experience of strong acceleration in Kushiro (Fig. 6.23), earthquake motion has been observed at the site in Kushiro at the surface and bottom of the hill (vertical array observation). In addition to Ohta (1995) who showed amplification between the surface and the foot of the hill slope [ $\text{Amp}(2E)$ ], Kanda and Motosaka (1995) as well as Ishida et al. (1996) showed increased acceleration at the surface as compared with that in the bottom layer of the hill. It seems that the amplification between the surface and the bottom includes not only the topographic amplification but also the one due to surface softer material that occurs even in a level topography.



**Fig. 6.31** Site of observation of topographic effects on earthquake amplification (after Kurita et al. 2005)

The topographic amplification as calculated in Sect. 6.15 is validated more clearly by another set of observed acceleration time histories during the 1985 Chiba-Toho-Oki earthquake. Kurita et al. (2005) recorded acceleration histories in and on a small hill as shown in Fig. 6.31. The Fourier spectra of acceleration records at two stations, No. 3 at the top and No. 5 at the foot, were calculated and their ratio was obtained as shown in Fig. 6.32. It is seen therein that the spectrum ratio that stands for the amplification of  $\text{Amp}(2E)$  increases with the shaking frequency. This finding is consistent with the findings in Fig. 6.29. The total collapse of houses on a terrace hill in Balakot of Pakistan during the 2005 North Pakistan earthquake (Fig. 6.33) may be the results of this topographic amplification.



**Fig. 6.32** Observed topographic effects on seismic amplification (after Kurita et al., 2005)



**Fig. 6.33** Completely destroyed houses on terrace hill in Balakot of Pakistan during 2005 earthquake

Suppose a topography in Fig. 6.34 where the crest angle is given by  $v\pi$ . Midorikawa (1999) presented an empirical knowledge that the hill-top motion is amplified by  $1/v$ , irrespective of shaking frequency, as compared with the motion on a free field. Kurita et al. (2005) presented the maximum horizontal accelerations that were observed at the top and the foot of a mountain. With reference to the topography

of the mountain in Fig. 6.31, the value of  $\nu$  is 0.57. This value suggests the amplification of 1.75. The real amplification in Fig. 6.35, however, is greater than  $1/\nu$ .

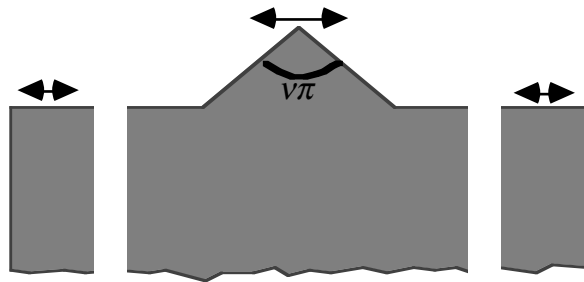


Fig. 6.34 Schematic topography of hill

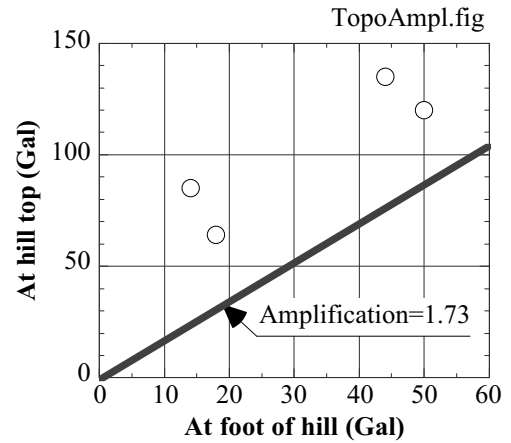


Fig. 6.35 Comparison of observed and assessed amplification of maximum acceleration

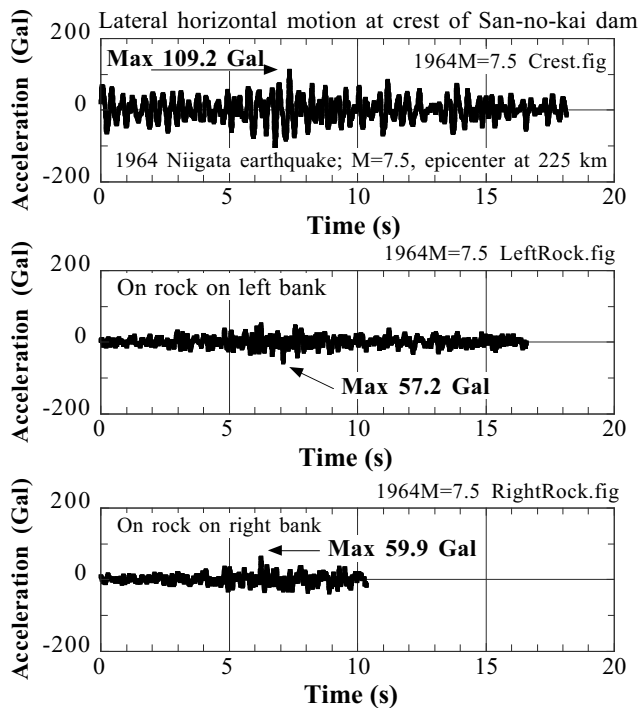


Fig. 6.36 Response of San-no-kai dam during the 1964 Niigata earthquake (data by Tamura, 1996)

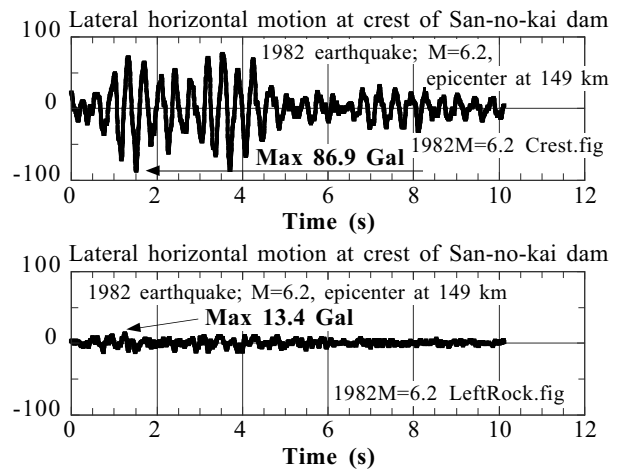


Fig. 6.37 Response of San-no-kai dam during a minor seismic event (data by Tamura, 1996)

It is interesting to discuss seismic response and amplification in a dam. San-no-kai Dam (山王海ダム) is an earth-fill dam which measures 37 m in height and 145 m in length. Its earthquake response has been monitored since 1960s (Tamura, 1996) and records of two quakes are compared in what follows.

Figure 6.36 compares the acceleration records during the 1964 Niigata earthquake (Magnitude = 7.3). In the top of this figure, the motion in the transverse direction (in the direction of valley) at the crest (top) of the dam is indicated. The maximum acceleration is 109 Gal. In the rock abutment on the left bank, the motion was smaller (57.2 and 59.9 Gal). By considering this rock motion as the outcrop motion, the amplification of  $Amp(2E)$  is derived as  $109.2/57.2 = 1.91$  and  $109.2/59.9 = 1.82$ . In contrast, Figure 6.37 presents the record during a minor earthquake in 1982 (Magnitude = 6.2). The maximum accelerations at the crest and at the left abutment are 86.9 Gal and 13.4 Gal, respectively, making  $Amp(2E) = 6.49$ . Thus, the amplification during these two earthquakes are completely different due probably to nonlinear stress-strain nature of soil (Chap. 9). More in detail, the stronger earthquake developed larger shear strain in soil and made the shear modulus smaller, while damping ratio was made greater. Hence, the amplification was reduced. The amplification thus depends on the shear strain during shaking.



## 6.15 Theory of Bessel Functions

The theory of Bessel functions (e.g., Wylie, 1975) states that a Bessel's differential equation of order  $\nu$ ;

$$x^2 \frac{d^2 y}{dx^2} + x \frac{dy}{dx} + (x^2 - \nu^2)y = 0 \quad (6.35)$$

has a solution of

$$y = C_1 J_\nu(x) + C_2 Y_\nu(x),$$

where  $J$  and  $Y$  are Bessel's functions of the first and the second types, respectively, while two constants of  $C_1$  and  $C_2$  are determined so that boundary or initial conditions may be satisfied. Thus, Bessel functions of  $J$  and  $Y$  in (6.35) play such roles that are similar to those of sin and cos functions in a harmonic differential equation.

When  $x$  is sufficiently large, the following approximate relationships hold true

$$J_\nu(x) \approx \sqrt{\frac{2}{\pi x}} \cos\left(x - \frac{\pi}{4} - \frac{\nu\pi}{2}\right) \quad \text{and} \quad Y_\nu(x) \approx \sqrt{\frac{2}{\pi x}} \sin\left(x - \frac{\pi}{4} - \frac{\nu\pi}{2}\right).$$

When  $x$  is very small, conversely, and  $\nu$  is not zero, the series solution of (6.35) suggests

$$J_\nu(x) \approx \frac{1}{\Gamma(1+\nu)} \left(\frac{x}{2}\right)^\nu \quad \text{and} \quad Y_\nu(x) \approx \frac{-1}{\sin \nu\pi \Gamma(1-\nu)} \left(\frac{2}{x}\right)^\nu,$$

where  $\Gamma$  stands for a Gamma function and  $\Gamma(n) = (n-1)! = (n-1)(n-2)(n-3)\cdots 2 \cdot 1$  when  $n = 1, 2, 3, 4, \dots$ .

Bessel functions give a set of general solutions for a differential equation that takes the form of

$$x^2 \frac{d^2 y}{dx^2} + x(a + 2bx^p) \frac{dy}{dx} + \{c + dx^{2q} + b(a+p-1)x^p + b^2 x^{2p}\}y = 0.$$

The solution is given by

$$y = x^\alpha \exp(-\beta x^p) \{C_1 J_\nu(\lambda x^q) + C_2 Y_\nu(\lambda x^q)\},$$

in which

$$\alpha = (1-a)/2, \quad \beta = b/p, \quad \lambda = \sqrt{|d|} q, \quad \text{and} \quad \nu = \sqrt{(1-a)^2 - 4c}/(2q),$$

Differentiation of Bessel functions is made possible by

$$\frac{dJ_\nu(x)}{dx} = \frac{\nu}{x} J_\nu(x) - J_{\nu+1}(x) \quad \text{and} \quad \frac{dY_\nu(x)}{dx} = \frac{\nu}{x} Y_\nu(x) - Y_{\nu+1}(x).$$

Finally, the Lommel's formula is important

$$Y_\nu(x) J_{\nu+1}(x) - J_\nu(x) Y_{\nu+1}(x) = \frac{2}{\pi x}.$$

6.16 Infinite Boundary Condition

Numerical analysis on seismic response of two-dimensional or three-dimensional shape (embankment, foundation of structure, etc.) is often conducted by finite element or finite difference formulations. It is commonly the case that those numerical methods work on a limited part of ground although the real ground has an infinite size (Fig. 6.38). This discrepancy may cause such a problem that the downward propagation of seismic motion is reflected at an artificial boundary of the domain of analysis while in reality the motion goes back into the infinite half space (see one-dimensional example in Fig. 6.39).

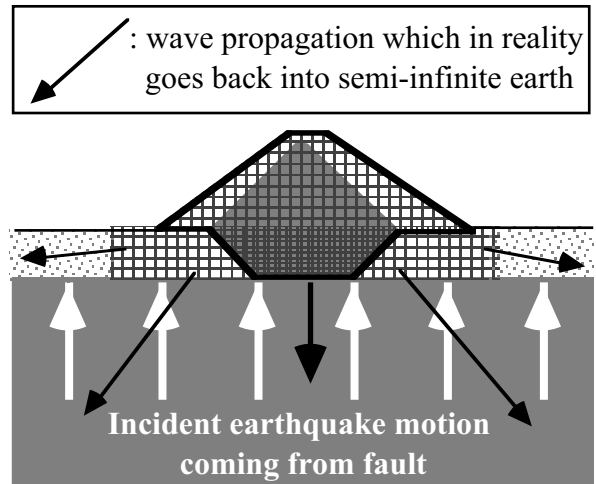


Fig. 6.38 Numerical analysis on limited size of model out of infinite halfspace

To remove the seismic wave energy that is reflected at the artificial boundary, a special boundary condition is needed, which accounts for an infinite size of the real ground. Without making reflection of wave, this kind of boundary condition is called energy absorbing boundary, energy transmitting boundary, silent boundary, transparent boundary, infinite boundary, etc.

The simplest energy absorbing boundary was proposed by Joyner (1975). Fig. 6.40 illustrates that a boundary is placed in an engineering base rock, which is actually not necessarily a real rock layer but possibly pleistocene or tertiary hard soil ( $V_s=500$  m/s for example). It is a convention to treat this base as an elastic medium. In a one-dimensional vertical wave propagation, the S-wave propagation at the base is expressed by an elastic model

$$u = E\left(t + \frac{z}{V_s}\right) + F\left(t - \frac{z}{V_s}\right), \quad (6.36)$$

in which  $E$  and  $F$  are arbitrary functions,  $u$  stands for lateral displacement and  $V_s$  is the S-wave velocity in the base rock. Note that S wave consists of superposition of incident and reflected waves (Sect. 4.4), and it is aimed by an infinite boundary to erase the  $F$  component (Fig. 6.40). Accordingly, velocity,  $v$ , and shear stress produced by S-wave motion are given by

$$v = \frac{\partial u}{\partial t} = E'\left(t + \frac{z}{V_s}\right) + F'\left(t - \frac{z}{V_s}\right) \quad \text{and}$$

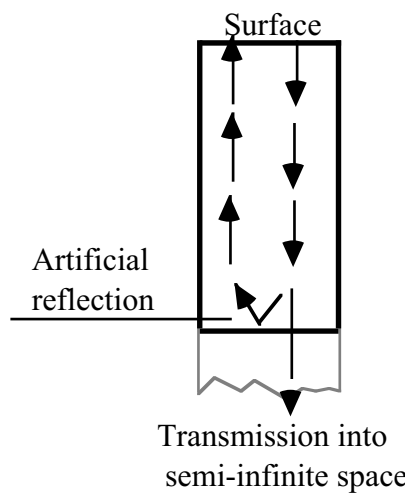


Fig. 6.39 Artificial reflection of seismic energy at boundary of numerical model

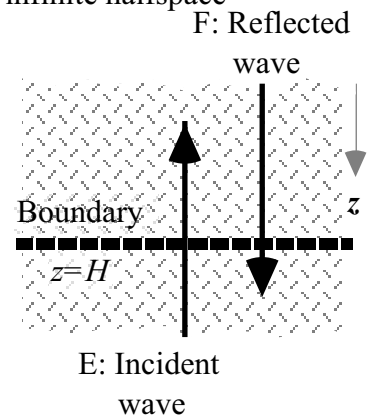


Fig. 6.40 Vertical wave propagation at engineering base rock of one-dimensional model

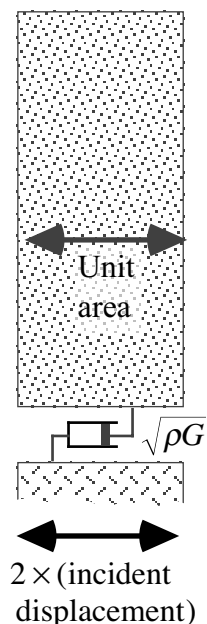


Fig. 6.41 Mechanism of viscous boundary condition

$$\tau = G \frac{\partial u}{\partial z} = \sqrt{\rho G} \left[ E' \left( t + \frac{z}{V_s} \right) - F' \left( t - \frac{z}{V_s} \right) \right], \quad (6.37)$$

where  $E'$  stands for a derivative of  $E$ . Note that the first term of the velocity formula gives the velocity induced by the incident wave,  $v_1$ , which is produced by fault mechanism and wave propagation in the elastic earth

$$v_1 = E' \left( t + \frac{z}{V_s} \right). \quad (6.38)$$

It is then interesting that shear stress and velocity are related with each other by

$$\tau = \sqrt{\rho G} (2v_1 - v). \quad (6.39)$$

This implies that the soil mass above the boundary is shaken by shear stress (6.39) in the base which is equal to a velocity difference,  $2v_1 - v$ , multiplied by  $\sqrt{\rho G}$ . This idea as proposed by Joyner (1975) is illustrated in Fig. 6.41 to show that the effects of elastic infinite medium is numerically reproduced by connecting the surface soil layer with  $2 \times$  (the incident soil motion) by means of a dashpot of  $\sqrt{\rho G}$ . Thus, the energy of incident wave is transmitted through the dashpot into the surface soil, while the energy of the reflected wave is absorbed.

The viscous boundary condition in Fig. 6.41 is able to absorb the reflected S wave perfectly in a one-dimensional case. For P wave, furthermore, a similar dashpot is installed in the vertical direction, for which  $G$  is replaced by (Young's modulus)  $\times (1 - \nu) / \{(1 + \nu)(1 - 2\nu)\}$ ; lateral distortion being confined ( $K_0$  condition) as is the case in an infinite level ground.

The viscous boundary perfectly absorbs wave energy when P and S waves propagate perpendicular to the boundary. When the wave propagation direction is oblique, which is often the case in a two (or three)-dimensional analysis (Fig. 6.42), the efficiency decreases (Lysmer and Kuhlemeyer, 1969; Lysmer and Waas, 1972). In this regard, White et al. (1977) attempted to optimize the dashpot coefficients for the minimal reflection of wave energy.

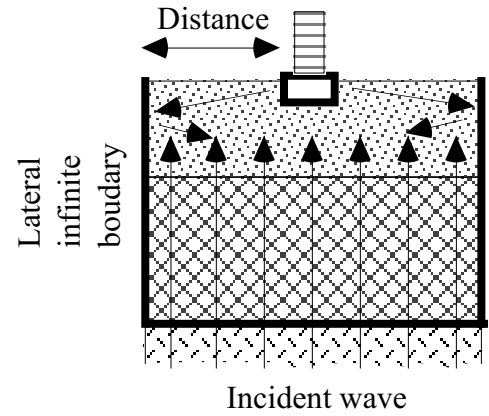
There are many more techniques of infinite boundary. Clayton and Engquist (1977) used what is called a paraxial equation in place of the conventional wave propagation equation. When displacement is designated by  $u$ , a paraxial equation of S wave propagation is written as

$$\frac{\partial^2 u}{\partial t^2} = V_s \frac{\partial^2 u}{\partial x \partial t}. \quad (6.40)$$

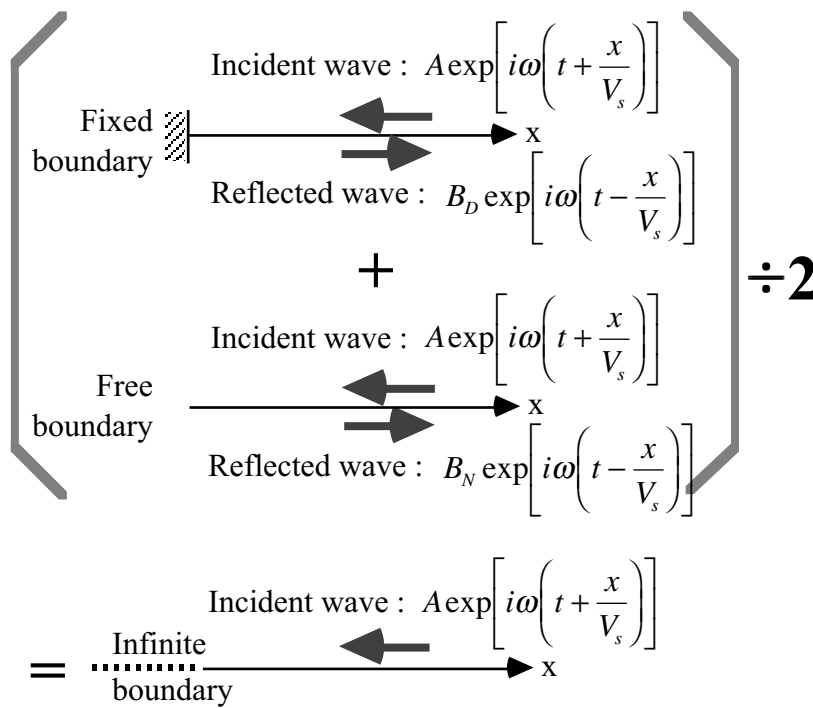
The solution of this paraxial equation is evidently given by

$$u = E \left( t + \frac{x}{V_s} \right), \quad (6.41)$$

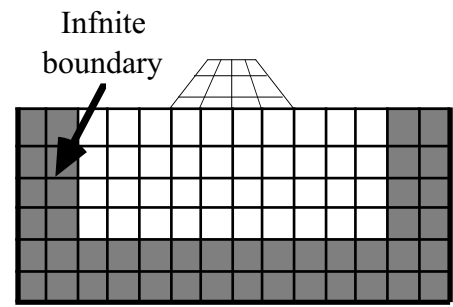
which implies that wave propagates only in the negative direction of  $x$  coordinate.



**Fig. 6.42** Two-dimensional idea of viscous boundary condition



**Fig. 6.43** Superposition of fixed (Dirichlet) and free (Neumann) boundary conditions for infinite boundary condition



**Fig. 6.44** Infinite boundary zone for superposition boundary in two-dimensional analysis

In contrast to the conventional wave propagation equation (solution is (6.36)), which allows wave propagation in both positive and negative directions of spatial coordinate, the paraxial equation allows wave propagation only in one direction. Thus, waves can propagate only in the outward direction at the infinite boundary, and no reflection is possible. This idea was used by Ak-

iyoshi et al. (1994) as well. Cohen and Jennings (1983) demonstrated its application to a simple one-dimensional wave propagation. Note that both viscous and paraxial boundaries assume the infinite space to be linearly elastic.

Smith (1974) developed a different infinite boundary technique in which solutions from two different but conventional boundary conditions are superimposed. When the wave that arrives at the boundary is specified by a harmonic function, for example, of  $A \exp\left[i\omega\left(t + \frac{x}{V_s}\right)\right]$  (Fig. 6.43), the fixed boundary (zero displacement at  $x = 0$ ) gives a reflected wave such as

$$\text{Reflected wave at fixed boundary} = B_D \exp\left[i\omega\left(t - \frac{x}{V_s}\right)\right] = -A \exp\left[i\omega\left(t - \frac{x}{V_s}\right)\right]. \quad (6.42)$$

In contrast when the boundary is free (zero shear stress),

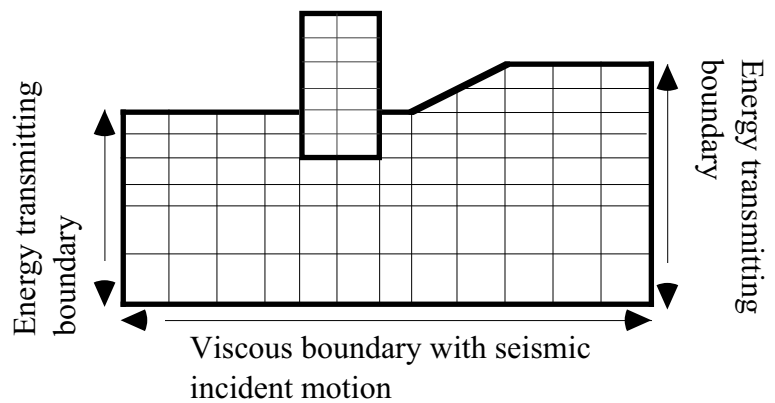
$$\text{Reflected wave at free boundary} = B_N \exp\left[i\omega\left(t - \frac{x}{V_s}\right)\right] = A \exp\left[i\omega\left(t - \frac{x}{V_s}\right)\right]. \quad (6.43)$$

By superposing (6.42) and (6.43) and then dividing by 2, the reflected wave is made null, while maintaining the incident wave unchanged. In practice of analysis, calculation is conducted twice with different boundary conditions and the solutions are added and divided by two. This superposition boundary has been used by Cundall et al. (1978), Kausel and Tassoulas (1981), Kunar and Rodriguez-Ovejero (1980), and Kunar (1982). This boundary condition works in a time-domain analysis in which an equation of motion is integrated along the time axis.

In practice of two-dimensional analysis, the reflected wave may hit another boundary and is reflected again. This multiple reflection makes superposition very complicated. To avoid this, the superposition is

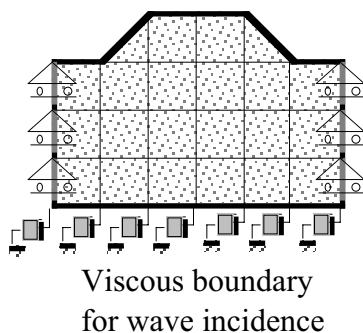
conducted periodically after a short specified time interval. Figure 6.44 illustrates an infinite boundary zone and the superposition is conducted before the reflected wave comes out of this zone.

In contrast to the foregoing boundaries that work in time-domain analyses, the energy transmitting boundary by Lysmer and Drake (1971, 1972) as well as Lysmer and Waas (1972) works in frequency-domain analyses, which assume seismic shaking as being superimposed harmonic motions. By considering the ground response to be Rayleigh and Love waves, harmonic stress response near the lateral boundary (Fig. 6.45) is calculated and employed as a lateral boundary condition, thus eliminating artificial wave reflection. This method has been used in combination with viscous boundary at the bottom (Fig. 6.45).

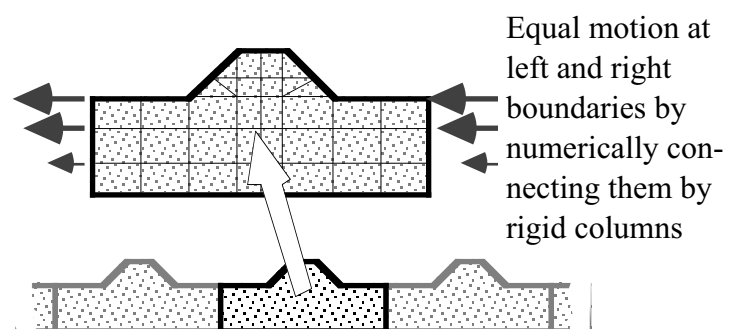


**Fig. 6.45** Combination of energy transmitting and viscous boundaries for analyses in frequency domain

The infinite boundaries so far described consist of special mathematical considerations. In spite of this, they have a limitation that nonlinear stress–strain behavior cannot be easily handled. This shortcoming may be significant in analyses of soft ground undergoing strong motion and liquefaction in which soil nonlinearity becomes substantial. Under such situations, elementary and primitive methods may be useful. The simplest method is to locate boundaries at a far distance from the area of interest; making “distance” in Fig. 6.42 large enough. This implies that energy dissipation due to nonlinearity (stress–strain loop) makes waves decay during propagation and the unfavorably reflected wave does not affect the calculated response in the interested zone. The lateral boundary may be (1) free horizontal motion and zero vertical motion (Fig. 6.46), or (2) repeated boundary (Fig. 6.47) for a symmetric geometry. Note that static active failure of a vertical lateral boundary has to be prevented by, for example, applying  $K_0$  static earth pressure in Fig. 6.46. Fixing the vertical displacement prevents ground subsidence during shaking and may not be appropriate. On the other hand, the repeated boundary makes horizontal motions at both right and left sides equal to each other and implies that identical model is repeated in the horizontal direction. This situation is similar to that in a laminar box (Sect. 24.13) in shaking model tests. Note again that lateral boundaries should be located at a sufficiently far distance so that the reflected wave may be too weak to affect the calculated response in the central part.



**Fig. 6.46** Horizontally free boundary.



**Fig. 6.47** Repeated lateral boundary

There are more attempts so far made to produce infinite boundary conditions. For example, Akao and Hakuno (1983) predicted the displacement at an infinite boundary by using previous boundary displacement together with displacement inside the domain of analysis. In 1980s the author and Dr. O.Al-Hunaidi tried to develop an energy absorbing boundary for 2- or 3-dimensional nonlinear analysis in the time domain. The idea was to remove numerically the kinematic energy near the boundary while fixing the strain energy therein. This was however difficult and the attempt was incomplete.

6.17 Exercise No. 2 of Dynamic Response Analysis on Elastic Ground

Figure 6.48 illustrates a topography of a horizontal free field and rock outcrop. Material properties and elastic and parameters are supplied in the figure.

1. Assume harmonic motion ( $\sin \omega t$  and  $\cos \omega t$ ) and express the amplitudes of  $F_1, E_2, F_2, E_1',$  and  $F_1'$  as functions of  $E_1$ .
2. Plot  $\text{Amp}(E+F)$  and  $\text{Amp}(2E)$  against  $\omega H/V_{s1}$  in which  $\omega$  is the circular frequency of motion. You can assume two kinds of the impedance ratio  $(\rho_1 V_{s1}/\rho_2 V_{s2})$ .
3. Suppose that the earthquake displacement at the surface of outcrop is expressed by

$$u_{\text{outcrop}}(t) = 0.02 \sin 2\pi t + 0.01 \cos 6\pi t + 0.002 \sin 20\pi t \quad (6.44)$$

as plotted in Fig. 6.49. Calculate and plot the function of the acceleration time history at the top of the outcrop.

4. Suppose  $H=12$  m,  $V_{s1}=150$  m/s, and  $V_{s2}=800$  m/s. Assume any realistic values for mass density of soils. Calculate and plot the time history of displacement at the surface of the alluvial deposit.
5. Calculate and plot the acceleration time history at the surface of the alluvial deposit.
6. Compare maximum values of displacement and acceleration at the surface of alluvium and the outcrop.

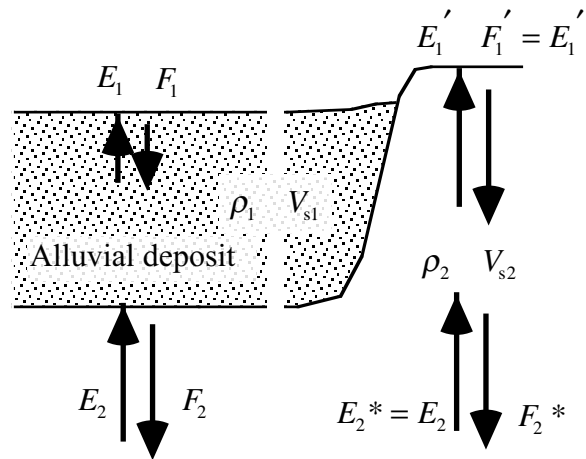


Fig. 6.48 Model of free field and rock outcrop

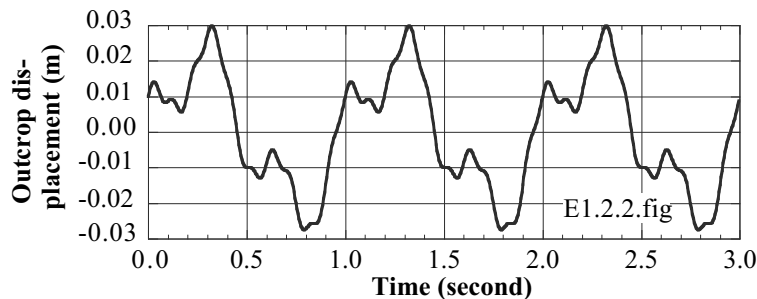


Fig. 6.49 Displacement time history at outcrop

List of References in Chapter 6

Akao, Y. and Hakuno, M. (1983) Dynamic analysis of wave propagation procedure on the infinite boundary, Proc. JSCE, No, 336, pp. 21–29 (in Japanese).

Akiyoshi, T., Fuchida, K. and Fang, H.L. (1994) Absorbing boundary condition for dynamic analysis of fluid-saturated porous media, Soil Dynam. Earthq. Eng., Vol. 13, pp. 387–397.

Clayton, R. and Engquist, B. (1977) Absorbing boundary conditions for acoustic and elastic wave equations, Bull. Seism. Soc. Am., Vol. 67, No. 6, pp. 1529–1540.

Cohen, M. and Jennings, P.C. (1983) Silent boundary methods for transient analysis, Computational Methods for Transient Analysis, Vol. 2, Computational Methods in Mechanics, Elsevier, New York, Chap. 7, pp. 301–360.

Cundall, P.A., Kunar, R.R., Carpenter, P.C. and Marti, J. (1978) Solution of infinite dynamic problems by finite modelling in the time domain, Proc. 2nd Int. Conf. Appl. Num. Modelling, pp. 339–351.

Hardin, B.O. and Drnevich, V.P. (1972) Shear modulus and damping in soils : measurement and parameter effects, Proc. ASCE, Vol. 98, SM6, pp. 603–624.

- Ishida, H., Sasaki, T., Niwa, M., Kitagawa, Y. and Kashima, T. (1996) Amplification characteristics of surface layers obtained from earthquake observation records of vertical instrument arrays at Kushiro local meteorological observatory, *J. Struct. Construct. Eng., Architectural Inst. Japan*, Vol. 490, pp. 91–100 (in Japanese).
- Joyner, W.B. (1975) Method for calculating nonlinear seismic response in two dimensions, *Bull. Seismol. Soc. Am.*, Vol. 65, No. 5, pp. 1337–1357.
- JSSMFE (1994) Damage investigation report of the 1993 Kushiro-oki and Noto-Hanto-oki earthquakes, p. 25 (in Japanese).
- Kanda, K. and Motosaka, M. (1995) The evaluation of effects of spatial variability of soil properties, surface topography and spatial coherency of incident wave on ground motion amplification – The case of Kushiro J.M.A. site, *J. Struct. Construct. Eng., Architectural Inst. Japan*, Vol. 476, pp. 85–94 (in Japanese).
- Kausel, E. and Tassoulas, J.L. (1981) Transmitting boundaries; a closed-form comparison, *Bull. Seismol. Soc. Am.*, Vol. 71, No. 1, pp. 143–159.
- Kunar, R.R. (1982) A mixed implicit/explicit procedure for soil-structure interaction, *Nucl. Eng. Des.*, Vol. 69, No. 1, pp. 87–93.
- Kunar, R.R. and Rodriguez-Ovejero, L. (1980) A model with non-reflecting boundaries for use in explicit soil-structure interaction analyses, *Earthq. Eng. Struct. Dynam.*, Vol. 8, pp. 361–374.
- Kurita, T., Annaka, T., Takahashi, S., Shimada, M. and Suehiro, T. (2005) Effects of irregular topography on strong ground motion amplification, *Proc. Japan Assoc. Earthq. Eng.*, Vol. 5, No. 3 (electronic journal in Japanese).
- Lefebvre, G. and LeBoeuf, D. (1987) Rate effects and cyclic loading of sensitive clays, *J. Geotech. Eng., ASCE*, Vol. 113, No. 5, pp. 476–489.
- Lysmer, J. and Drake, L.A. (1971) The propagation of Love waves across nonhorizontally layered structures, *Bull. Seismol. Soc. Am.*, Vol. 61, No. 5, pp. 1233–1251.
- Lysmer, J. and Drake, L.A. (1972) A finite element method for seismology, *Methods Comput. Phys.*, Vol. 11, Academic Press, New York, pp. 181–216.
- Lysmer, J. and Kuhlemeyer, R.L. (1969) Finite dynamic model for infinite media, *Proc. ASCE*, Vol. 95, EM4, pp. 859–877.
- Lysmer, J. and Waas, G. (1972) Shear waves in plane infinite structures, *Proc. ASCE*, Vol. 98, EM1, pp. 85–105.
- Midorikawa, S. (1999) Nature of seismic ground motion, *Earthquake Motion, Geotech-Notebook No. 9, Japan. Geotech. Soc.*, pp. 37–64 (in Japanese).
- Ohta, T. (1995) Strong ground motions at Kushiro observatory and vibration characteristics of ground and structures, *J. Struct. Construct. Eng., Architectural Inst. Japan*, Vol. 474, pp. 77–85 (in Japanese).
- Onishi, J., Yamazaki, F. and Wakamatsu, K. (1999) Relationship between geomorphological land classification and amplification ratio based on JMA strong motion records, *Proc. JSCE*, 626/I-48, pp. 79–91 (in Japanese).
- Proc. Special Theme Session on ‘Test-Sites’ (STS-16) (1996) 11th World Conf. Earthq. Eng., Acapulco, p. 30.
- Smith, W.D. (1974) A nonreflecting plane boundary for wave propagation problems, *J. Comput. Phys.*, Vol. 15, pp. 492–503.
- Tamura, C. (1996) Seismic damage and geosphere, publ. Sankai-Do, attached floppy disk (in Japanese).
- Togawa, H. (1975) Vibration analysis by FEM, Science Publication, pp. 46–47 (in Japanese).
- WCEE (1996) Special Theme Session on TEST-SITES of 11th world Conf. Earthq. Eng., Acapulco, pp.30.
- White, W., Valliappan, S. and Lee, I.K. (1977) Unified boundary for finite dynamic models, *Proc. ASCE*, Vol. 103, EM5, pp. 949–964.
- Wylie, C.R. (1975) *Advanced Engineering Mathematics*, International Student Editions, McGraw-Hill, New York, ISBN 0-07-072180-7, pp.388-440.

# Chapter 7

## Pseudostatic

### Limit Equilibrium Analysis



Turfan 高昌故城 in silk-road China was an independent trading city in early seventeenth Century. Being ruled by a Chinese royal family, Turfan warmly hosted a Chinese monk, Xuánzang, 唐之玄奘, who traveled to India on foot for studying true Buddhism. This city had been destroyed by war, however, when the monk visited it again 17 years later on his way back to China.



## 7.1 Seismic Coefficient

Strong earthquake motion used to destroy many brick structures and killed many people. Figure 7.1 illustrates an example in Tokyo in which a brick tower of 12 storeys was destroyed in the middle. In those days there was no clear idea to design structures against earthquake effects. The same mechanism of collapse is still seen widely in many nonengineered structures in the world and the number of victims is substantial.

The method of seismic coefficient (震度法) is the first measure to design facilities against earthquake effects. This method statically applies a force to a designed facility (pseudostatic or quasi-static method). The magnitude of this force is specified to be  $K \times W$  in which  $K$  is called the seismic coefficient and  $W$  is the weight of the facility. Before this idea, there was no design method against earthquake effects. Since this method works easily with static calculation, it is still widely used. Figure 7.2 is an example of slope stability analysis.

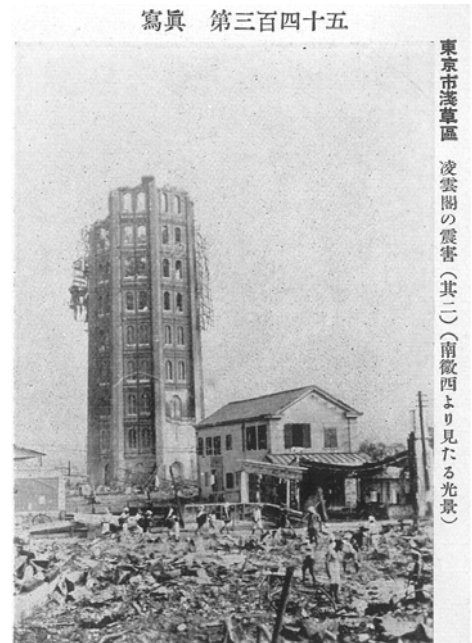
A theoretical background of seismic coefficient lies in the *d'Alembert's principle* (ダランベールの原理) of mechanics. When a base of a structure has an acceleration of  $A$ , the effects of this shaking to the overlying structure is equivalent to a force of  $(A/g)W$  in the opposite direction from the acceleration (Fig. 7.3); “ $g$ ” stands for the gravity acceleration. Thus, the seismic coefficient of “ $K$ ” appears to be equivalent to  $A/g$ .

The value of  $K$  today in Japan is 0.15–0.2 or greater. There is a variation in  $K$ , depending upon the local seismic activity, the importance of facilities, and the local geology or soil conditions.

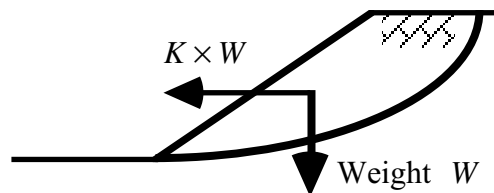
The method of seismic coefficient is good because it is simple and the factor of safety can be calculated by the same way as the conventional static stress calculation. No advanced analysis is therein necessary. It made a great contribution to the improvement of seismic safety.

Problems lying in the seismic coefficient are as follows:

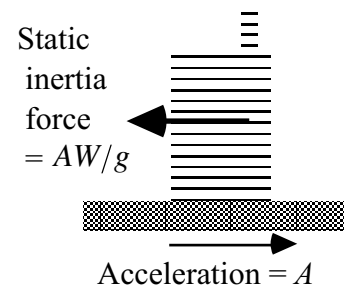
1. The real seismic force is cyclic, changing direction with time, and its duration time is



**Fig. 7.1** Destroyed tower in Tokyo during 1923 Kanto earthquake (photograph from JSCE report)



**Fig. 7.2** Example of elementary seismic slope stability analysis



**Fig. 7.3** d'Alembert's principle of mechanics.



**Fig. 7.4** A small hut that survived the 1994 Northridge earthquake

limited. In contrast, the seismic coefficient method applies a force in a static manner. This seismic force overestimates the risk of earthquake failure.

- 2) At the time of 1994 Northridge earthquake near Los Angeles, the maximum horizontal acceleration of 1.8 G or possibly 1.9 G was recorded at Tarzana site (Fig. 6.25). Within tens of meters from the accelerometer here, a small hut did not suffer a damage (Fig. 7.4). Was this structure well designed against a horizontal static force as intense as 1.8 times its weight?
- 3) Thus, the relation between  $K$  and the maximum ground acceleration is not clear. 1.9 G acceleration does not mean  $K = 1.9$ . Study on seismic damage of quay walls led Noda et al. (1975) to propose

$$K = (A_{\max}/g)^{1/3} / 3, \quad (7.1)$$

in which  $A_{\max}$  is the maximum horizontal acceleration (Sect. 12.3).

- 4) Many structures exhibit dynamic deformation during earthquake shaking. The intensity of shaking is normally greater in the upper portion than in the lower level. Therefore, a greater inertia force seems more appropriate near the top than near the bottom. This idea, called the modified seismic coefficient method, is already practiced in many situations; for example fill-type dams (Sect. 7.2).

The pioneer of seismic coefficient method of design in a modern sense was Prof. Toshikata Sano (1916 佐野利器博士; Fig. 7.5). He got an idea to apply horizontal force in design after his damage investigation on Great San Francisco earthquake (Sano, 1906). Since then, this method has been used at many places of the world. This method was further combined with the Coulomb active earth pressure theory (Appendix 1) to be the famous Mononobe-Okabe seismic (active) earth pressure theory (Sect. 12.5).



**Fig. 7.5** Prof. T.Sano (from Memorial book of Dr. Toshikata Sano owned by Civil Engineering Library, University of Tokyo)

The idea of earthquake resistant design based on the seismic coefficient is written as

$$\text{Factor of safety} = \text{Resistance} / (\text{Static} + \text{seismic force}) > 1. \quad (7.2)$$

Housner (1984) stated that the method of seismic coefficient was adopted in a design regulation in Italy after the 1908 Messina earthquake; Prof. M. Panetti proposed to design the first floor of a building with the seismic coefficient of 1/12, while upper stories with 1/8. The increased seismic coefficient in upper floors stands for the dynamic response of a building. This idea is equivalent with the modified seismic coefficient in Fig. 7.9.

Nakamura (2005) carried out dynamic centrifugal tests on distortion of a gravity retaining wall (refer to Fig. 12.25). He considered that  $A_{\max} = 670$  Gal of his seismic shaking was equivalent to the results of pseudostatic analysis in which  $K=0.39$  made the factor of safety = 1. This is because  $A_{\max} = 670$  Gal triggered lateral translation of 1.5% of the wall height which seems to be equivalent with factor of safety = 1. Note that  $A_{\max} = 670$  Gal as substituted in (7.1) gives  $K = 0.29$ .

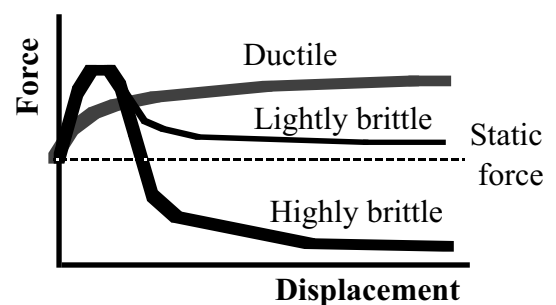
The method of seismic coefficient has drastically reduced the extent of damage and the number of casualties (victims) when it is “properly applied” to design and construction practice. It seems that this design principle was most effective for such brittle structures as the one in Fig. 7.1 which were made of bricks and a single big impact was enough to completely destroy them. See the highly brittle relationship between force and displacement in Fig. 7.6.

It seems that traditional (brick, adobe, and wooden) structures have had such a highly brittle nature (Fig. 7.6) that the resistance force drops significantly after the peak resistance. According to the method of seismic coefficient, seismic safety is achieved if the peak resistance is greater than the force (*static+ seismic*). A catastrophic failure is possible, however, if the force level after the peak is lower than the static force. This was the case in the tower in Fig. 7.1. Another example of this type was Arg-e-Bam in Fig. 7.7. Being constructed before 500 BC, Arg-e-Bam was a miraculous ruin of an old fortress or citadel and a town where all the structures were made of adobe bricks. Upon the earthquake in 2003, however, those marvelous brick structures were destroyed instantaneously by strong shaking.

Recent developments of reinforced concrete and steel structures as well as geotechnical structures have changed the force–displacement relationship from a highly brittle one to a lightly brittle or ductile one. Since the force level after large displacement (deformation) is still held greater than the static force, a catastrophic failure is not so likely. In such a situation, it may not be necessary to maintain the factor of safety greater than 1 by making very elaborate design and spending money on high resistance. For more economical construction, the design requirement may be relaxed to some extent by allowing for the seismic factor of safety  $< 1$  and still keeping the resultant displacement small enough (within an allowable extent). This is the aim of recent performance-based seismic design (Sect. 14.7).

Since the performance-based design focuses mainly residual displacement, a large value of acceleration,  $A_{\max}$ , is not necessarily taken seriously. In case the duration of  $A_{\max}$  is short (Fig. 5.11), an equation of motion does not give large displacement. The nature of earthquake motion will be more reasonably considered by performance-based design than the conventional seismic coefficient method, which is influenced unduly by the magnitude of  $A_{\max}$ . Since displacement analysis is conducted, on the other hand, the performance-based design requires more detailed understanding of soil behavior (more than strength) and hence more precise soil investigation.

Note that well-designed structures may be ductile during a strong earthquake, but furniture in rooms may fall down (highly brittle behavior) to injure residents.



**Fig. 7.6** Conceptual illustration of force-displacement relationships

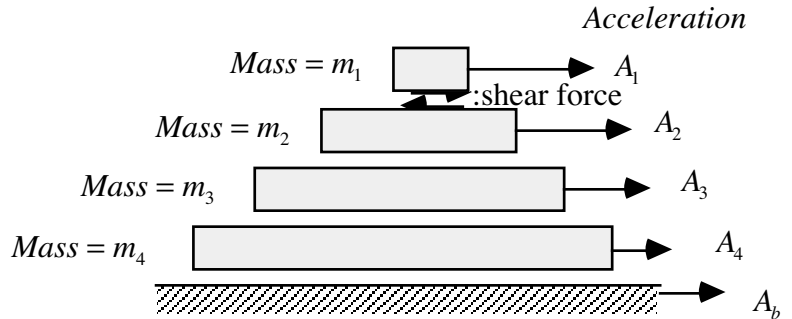


**Fig. 7.7** Damage of brittle structure (Arg-e-Bam Castle after 2003 Bam earthquake, Iran)

**7.2 Modified Method of Seismic Coefficient**

The idea of uniform acceleration from the top to the bottom of a structure (Fig. 7.2) is not necessarily correct. It is often the case that the top exhibits a greater magnitude of motion than the bottom; amplification in flexible structures. One of the examples of this situation is found in an earth dam of which the trapezoidal shape increases the top motion significantly (see Sect. 6.13).

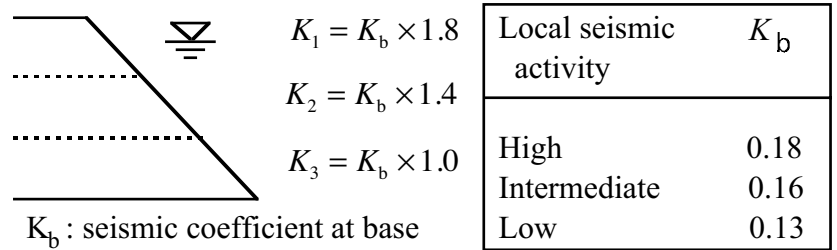
Figure 7.8 illustrates a situation in which a fill is subjected to an amplified shaking. The shear force between the top and the second blocks is given by  $\tau_1 = m_1 A_1$ . Since the acceleration varies in the vertical direction, the shear force at lower elevations is calculated by summation



**Fig. 7.8** Modified method of seismic coefficient

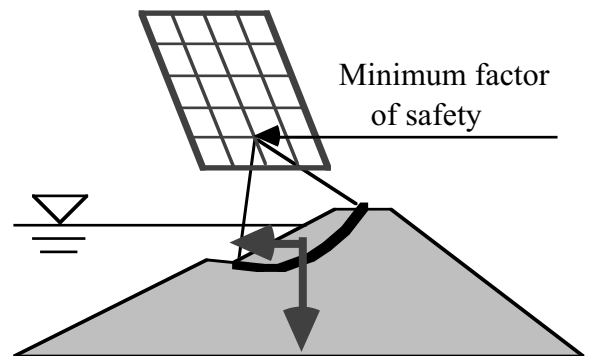
$$(\text{Shear force})_k = \sum_{i=1}^k m_i A_i = \sum_{i=1}^k (m_i g) \frac{A_i}{g},$$

where  $g$  stands for the gravitational acceleration,  $m_i g$  is the weight of a block and  $A_i / g = K_i$  is the seismic coefficient relevant for the  $i$ th block. It is evident that  $A_i$  is different from the base acceleration,  $A_b$ . The use of different values of  $K_i = A_i / g$  in the vertical direction is called the modified method of seismic coefficient (修正震度法).

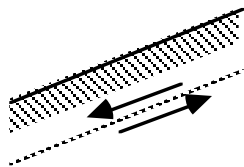


**Fig. 7.9** Modified seismic coefficient in rockfill dam design

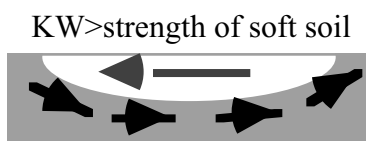
Figure 7.9 is an example idea of the modified seismic coefficients which is currently practiced for a seismic design of rockfill dams. Figure 7.10 is an example analysis on seismic limit equilibrium in which the critical slip plane is detected. In addition to this, consideration on a surface slip is necessary (Fig. 7.11).



**Fig. 7.10** Seismic analysis on earthdam by using limit equilibrium analysis



**Fig. 7.11** Shallow slip failure



**Fig. 7.12** Unrealistically predicted failure of level soft ground



**Fig. 7.13** Gentle slope of super river dike in Tokyo

The upstream slope of a fill dam is more gentle than the downstream slope. This is because the upstream soil is submerged in water and is heavier, generating a greater seismic inertia force. Moreover, the buoyancy force reduces the effective stress in the upstream side and makes the shear strength smaller. Possible development of excess pore water pressure and decrease in effective stress are important as well (Chap. 17).

One of the most ironical examples of the seismic coefficient method of analysis is that it predicts an overall failure of soft level subsoil (Fig. 7.12), although a level ground is unlikely to fail. This problem occurs because the method assumes a static one-way earthquake load despite that it is cyclic in reality. A symmetric loading in positive and negative directions does not accumulate deformation in a level subsoil. This shortcoming became a problem when a super river dike was designed in Tokyo (Fig. 7.13). The super river dike has a slope gradient of merely 1/30 and buildings were placed on it. Hence, seismic stability of the dike slope was considered essentially important and a stability analysis was conducted. Since the dike was underlain by soft alluvial clay, the calculated factor of safety was less than unity in spite of the gentle slope. This case implies the importance of assessment of residual displacement by using, for example, the method in Sect. 12.1.

### 7.3 Vertical Motion

Conventionally, the horizontal motion has been attracting more attention than the vertical component. There are two reasons for this. First, any facility has some resistance against the vertical motion. The inertia force in the vertical downward direction increases the static force by, for instance, 20–50%. This increased load is often still within the static safety margin. Most failures in masonry structures are caused by the horizontal inertia force (Fig. 7.14).



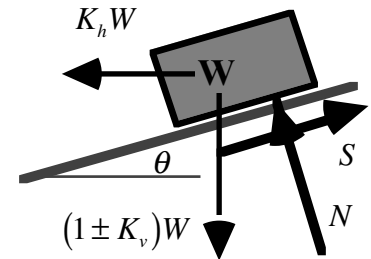
**Fig. 7.14** Collapse of adobe house in Bam, Iran, in 2003

When a slope stability is maintained by the frictional law (Fig. 7.15), the normal and the tangential reactions,  $N$  and  $S$ , are

$$N = (1 \pm K_v)W \cos\theta - K_h W \sin\theta \quad \text{and}$$

$$S = (1 \pm K_v)W \sin\theta + K_h W \cos\theta ,$$

where  $K_v$  and  $K_h$  stand for the vertical and horizontal seismic coefficients, respectively. Accordingly, the factor of safety,  $F_s$ , is derived as



**Fig. 7.15** Stability of block resting on frictional slope

$$F_s = \frac{\mu(1 \pm K_v - K_h \tan\theta)}{(1 \pm K_v) \tan\theta + K_h} ,$$

in which  $\mu$  denotes the coefficient of friction. Although  $1 \pm K_v$  does not vary substantially with  $K_v$  within a realistic range of variation, an increase in  $K_h$  directly reduces the factor of safety. Once the stability is lost, the block in Fig. 7.15 starts to slide down-slope and its displacement is (may be?) calculated by solving its equation of motion.

In the example above, the increase in the normal force ( $N$ ) directly increases the frictional resistance ( $\mu N$ ). From the soil-mechanic viewpoint, this means that the slope is dry or under drained conditions. Conversely when the slope is undrained, which is more realistic under rapid loading, the increase in  $N$  is transferred to excess pore water pressure. Hence, the effective stress and consequently the frictional resistance do not change. The factor of safety is then given by

$$F_s = \frac{\mu N_{\text{initial}}}{S} = \frac{\mu}{(1 \pm K_v) \tan\theta + K_h} .$$

Again the horizontal inertia force,  $K_h$ , reduces the factor of safety.

Empirically it is known that the vertical acceleration is weaker than the horizontal acceleration. Table 7.1 compares the maximum acceleration in vertical and horizontal directions recorded during the major earthquake in Kobe (1995). Generally, the vertical acceleration is half of the horizontal acceleration.

**Table 7.1** Maximum earthquake motion data (National Research Institute of Earth Science and Disaster Prevention, 1995)

Sites	Acceleration (Gal=cm/s <sup>2</sup> )		
	NS	EW	Up-Down
Kobe meteorological observatory <sup>a</sup>	818	617	332
Kobe port const. office	502	205	283
NTT Kobe building (B3F)	331	153	169
New Kobe station	530	267	344
Kobe port 8th pier <sup>b</sup>	683	394	334
Takatori station	635	553	175
Nishi Akashi station	397	381	319
Factory in Amagasaki	321	472	311
	Velocity (kine=cm/s)		
Univ. Kobe	55.1	31.0	33.2
Fukushima, Osaka	31.0	29.8	9.6
Chihaya-Akasaka	5.2	4.9	2.5

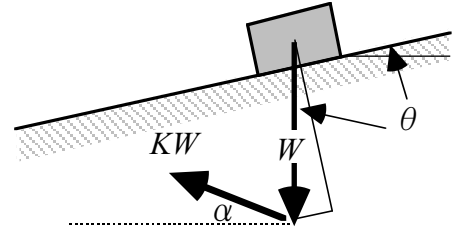
a Recorded at the top of a small hill.

b Recorded upon a quay structure, not on soil.

## 7.4 Direction of Seismic Inertia Force in Design

In many cases the seismic inertia force for design has been applied in the horizontal direction because the vertical acceleration in the observed records is weaker than the horizontal component. It might be interesting, however, to make a brief discussion on the appropriate direction of the design inertia force. It should be borne in mind that the following discussion is not very practical because the existing design values of seismic coefficient have been determined on the basis of the idea of horizontal inertia force, whether the idea is appropriate or not.

Figure 7.16 illustrates a situation in which a rigid body of weight =  $W$  is resting on a frictional slope. The inclination of the slope is  $\theta$ , while the frictional angle between the slope floor and the rigid body is  $\phi$ . Note that the inertia force of  $KW$  is inclined by an angle of  $\alpha$  from the horizontal direction. It is aimed at in what follows to detect a particular  $\alpha$  that minimizes the calculated factor of safety.



**Fig. 7.16** Inclined direction of inertia force

The factor of safety,  $F_s$ , is calculated as the ratio of the frictional resistance and the driving force

$$F_s = \frac{(\text{Normal force}) \times \tan \phi}{\text{Driving force}} = \frac{\{W \cos \theta - KW \sin(\theta + \alpha)\} \tan \phi}{W \sin \theta + KW \cos(\theta + \alpha)}$$

$$= \frac{\{\cos \theta - K \sin(\theta + \alpha)\} \tan \phi}{\sin \theta + K \cos(\theta + \alpha)} \quad (7.3)$$

The minimum factor of safety for varying  $\alpha$  is detected by

$$\frac{\partial F_s}{\partial \alpha} = \frac{-K \cos(\theta + \alpha) \{\sin \theta + K \cos(\theta + \alpha)\} + K \sin(\theta + \alpha) \{\cos \theta - K \sin(\theta + \alpha)\}}{\{\sin \theta + K \cos(\theta + \alpha)\}^2} \tan \phi = 0.$$

Accordingly,

$$\sin \alpha = K \text{ and } \cos \alpha = \sqrt{1 - K^2} \text{ for } K < 1$$

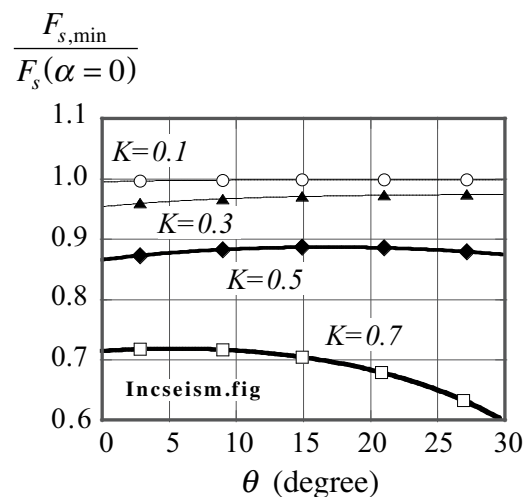
as is practiced commonly.

The minimum factor of safety,  $F_{s,\min}$ , is obtained by substituting this special  $\alpha$  in (7.3)

$$F_{s,\min} = \frac{\cos \theta - K \{\sin \theta \cos \alpha + \cos \theta \sin \alpha\}}{\sin \theta + K \{\cos \theta \cos \alpha - \sin \theta \sin \alpha\}} \tan \phi$$

$$= \frac{\cos \theta - K \{\sqrt{1 - K^2} \sin \theta + K \cos \theta\}}{\sin \theta + K \{\sqrt{1 - K^2} \cos \theta - K \sin \theta\}} \tan \phi$$

$$= \frac{\sqrt{1 - K^2} \cos \theta - K \sin \theta}{\sqrt{1 - K^2} \sin \theta + K \cos \theta} \tan \phi. \quad (7.4)$$



**Fig. 7.17** Significance of inclined seismic inertia force

The conventional factor of safety, on the other hand, is derived by substituting  $\alpha = 0$  in (7.3);

$$F_s = \frac{\cos\theta - K \sin\theta}{\sin\theta + K \cos\theta} \tan\phi. \quad (7.5)$$

Finally, the significance of the inclined inertia force is illustrated by using the ratio of (7.4) and (7.5), see Fig. 7.17. It is found that the inclined direction of the inertia force reduces the calculated factor of safety to some extent. It is not very important, however, unless the employed seismic coefficient,  $K$ , is very large.

### List of References in Chapter 7

- Housner, G.W. (1984) Keynote lecture, 8th World Conf. Earthq. Eng., San Francisco, Post Conference Volume, pp. 25–39.
- JSCE : Damage report on 1923 Kanto earthquake, Vol. 3.
- Nakamura, S. (2005) Clarification of seismic behavior of gravity retaining wall by using centrifugal model tests and a proposal for rationalization of the seismic coefficient method, Proc. JSCE, Vol. 785/III-70, pp. 107–122 (in Japanese).
- National Research Institute of Earth Science and Disaster Prevention (1995) Prompt report on strong-motion accelerograms No. 46 January 17, 1995 Southern Hyogo Prefecture, Feb.
- Noda, S., Uwabe, T. and Chiba, T. (1975) Relation between seismic coefficient and ground acceleration for gravity quaywall, Report of the Port and Harbor Research Institute, Vol. 14, No. 4 (in Japanese).
- Sano, T. (1906). Report on earthquake damage in California, USA 米國加州震災談, Journal of Architecture and Building Science 建築雜誌, Vol. 238, pp. 646–656 (in Japanese).
- Sano, T. (1916) Aseismic design of buildings (I) 家屋耐震構造論 (上), No. 83A 甲, 震災豫防調査會 (Research Institute for Mitigation of Earthquake Disasters), p. 2 (in Japanese).



# Chapter 8

## Field Investigation



Dharmarajika Stupa at Taxila of Pakistan; Taxila, which is close to the capital of Islamabad, is one of the sites of Gandhara civilization in which Greek and Indian Buddhism influences interacted.

8.1 Field Investigation on Shear Wave Velocity

The most reliable methods to determine the shear modulus of soil are those conducted in the field. This is because laboratory soil testing of undisturbed soil samples is often subjected to errors due to sample disturbance. Even if the disturbance is minor in advanced technique of sampling, time and expense may be substantial.

In the field, S wave is generated artificially and the wave propagation is recorded. The distance divided by wave travel time is the S-wave velocity,  $V_s$  (Fig. 8.1).  $G$  is then calculated;  $G = \rho V_s^2$ . It is important that an artificial source of wave has a limited power and the strain amplitude in the traveling wave is very small (of order of  $10^{-6}$  or less). Hence, the obtained  $V_s$  corresponds to the modulus at small strain,  $G_{max}$  (Fig. 8.2). At this small strain, soil behaves in a nearly elastic manner, and this  $G_{max}$  is an elastic property of soil.

Figure 8.3 illustrates a practice in S wave generation. The dead weight, as produced by the weight of a motor vehicle, should be as large as 9.8 kN (1 ton). Otherwise, the generated wave may not be a good S wave. Hence, the weight of a human body is not sufficient. Note that shear modulus at larger strain amplitude is much smaller than  $G_{max}$ . For example, 50%, 20%, and <10% of  $G_{max}$  (Sect. 10.6).

(Example) Typically,  $V_s = 100$  m/s in soft soil and 300–500 m/s in harder soils. An intact rock mass has  $V_s =$  approximately 3,000 m/s. The mass density of soil “ $\rho$ ” is of less variation;  $1.4\text{--}1.5 \times 1,000$  kg/m<sup>3</sup> for dry soil and  $1.8\text{--}2.0 \times 1,000$  kg/m<sup>3</sup> when water-saturated. Therefore, a water-saturated soft soil has  $G_{max} = \rho V_s^2 = 1.8 \times 10^7$  N/m<sup>2</sup> =  $1.8 \times 10^4$  kN/m<sup>2</sup> or 180 kgf/cm<sup>2</sup>.

In principle, it is possible to determine the P-wave velocity,  $V_p$ , by similarly generating P wave and monitoring its propagation. This is practiced in geophysical exploration for mining and oil production. However, this P-wave survey is difficult in alluvial soft soil, because the generated P wave propagates through pore water in which  $V_p$  is about 1,400 m/s, which is faster than propagation through soil skeleton. Thus, the property of soil skeleton is erased by the behavior of pore water. In contrast, P-wave survey works in harder rock media in which  $V_p$  in solid skeleton is faster than 1,500 m/s.

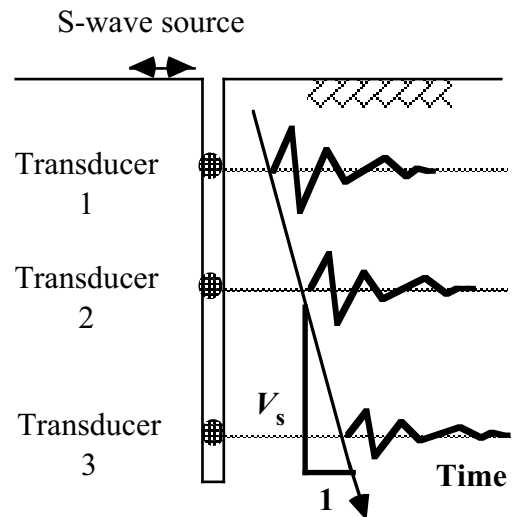


Fig. 8.1 Principle of downhole survey

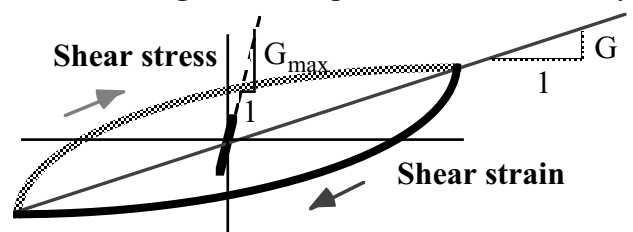


Fig. 8.2 Variation of shear modulus with Dead weight

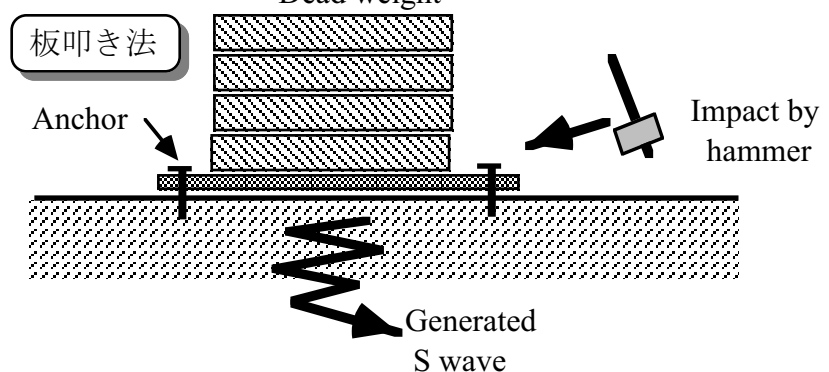


Fig. 8.3 Practice of downhole PS exploration

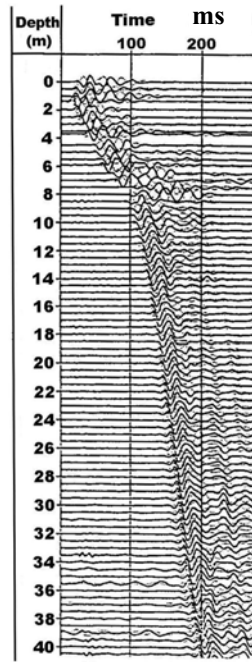
**8.2 Suspension-Type Downhole Survey**

Figure 8.4 reveals the practice of downhole survey data as described in Sect. 8.1. The inclination of travel time lines changes with depth, suggesting the increase of  $V_s$  at lower elevations. This figure suggests, however, that  $V_s$  is constant over a substantial distance in  $z$  directions. Actually, the conventional downhole survey is not so sensible to detect minor change of  $V_s$  in  $z$  direction. To overcome this problem, a suspension-type (漂遊式) downhole survey was developed (Kitsunezaki, 1978a,b).

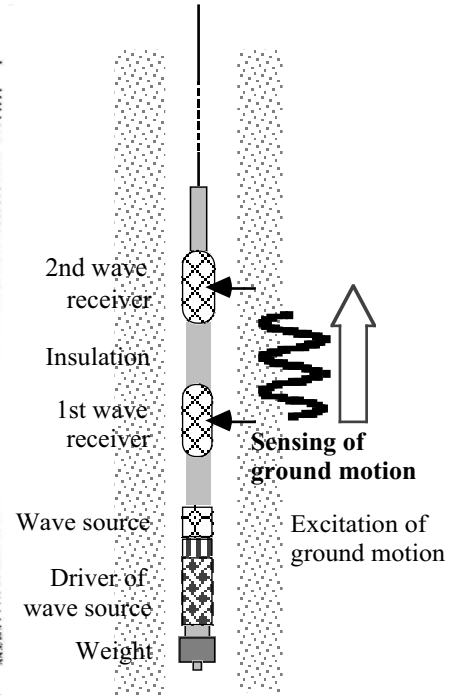
A suspension-type device has both the source and two receivers inside a bore-hole equipment (Fig. 8.5). The device measures the local travel time over the interval between two receivers. Therefore, the obtained  $V_s$  is local as well over the 1-m interval. The device is placed at the bottom of a bore hole first. Repeating the measurement, the device goes up with a prescribed interval, and finally reaches the ground surface. Figure 8.6 shows a photograph of this equipment.



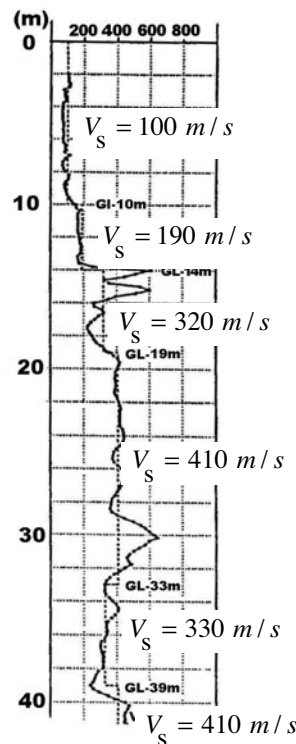
**Fig. 8.6** Suspension survey equipment on site



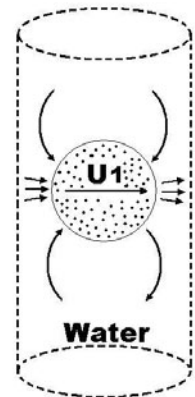
**Fig. 8.4** Conventional downhole survey at Shin Ohta Site (ADEP)



**Fig. 8.5** Suspension-survey in bore hole



**Fig. 8.7** Suspension-type survey at Shin Ohta Site (ADEP)



**Fig. 8.8** Detail of wave source in suspension-type instrument (Kitsunezaki, 1978a)

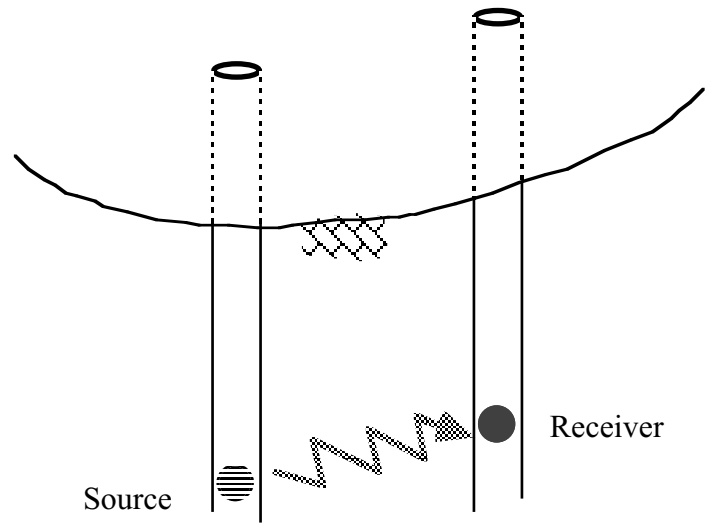
Figure 8.7 illustrates the detailed  $V_s$  profile at the same Shin Ohta site in Tokyo Bay. This was obtained by the suspension-type device, and the detailed variation of  $V_s$  with depth and soil type can be seen. It appears to the author that  $V_s$  varies continuously with depth.

Figure 8.5 shows the detailed structure of a wave source. This source is submerged in bore-hole water upon survey. A rigid mass installed in the equipment is driven laterally by an electromagnetic mechanism, and creates increased water pressure on one side of a bore-hole wall and reduced pressure on the other side. Accordingly, the ground around the bore hole is sheared laterally and S wave starts to propagate in the vertical direction. The travel time of this wave is monitored by receivers, which are of similar mechanism as the source and detects the lateral movement of bore-hole wall and water in the hole. Note that S wave does not propagate in the bore-hole fluid.

### 8.3 Cross-Hole Survey

A cross-hole survey requires at least two bore holes. A source is placed in one hole and a receiver is installed in the other, both at the same elevation. The monitored S wave travels in the horizontal direction from the source to the receiver. When a horizontal layer is the case, the measured wave velocity,  $V_s$ , is the local wave velocity, equivalent to the results of suspension-type survey (Fig. 8.9).

The cross-hole survey is more expensive than the down-hole survey because it needs drilling at least two bore holes. On the other hand, three, four, or more holes can be drilled and wave propagation can be monitored at various distances from the source. This makes it possible to measure not only the travel times and  $V_s$  but the decay of wave amplitude with distance. This decay is directly related to the damping ratio of soil.



**Fig. 8.9** Cross-hole survey

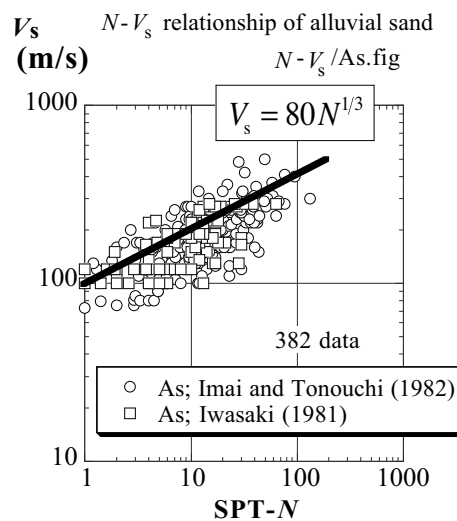
### 8.4 Correlation Between SPT- $N$ and $V_s$ of Alluvial Soils

It is a dream to carry out shear tests in a bore hole, because the obtained stress–strain data would exhibit nonlinear behavior of soil without bad effects of sample disturbance. Although such an attempt has been made by a limited people (for example, Henke and Henke, 1993), its development is not yet satisfactory. Note further that undrained shear is very difficult in bore holes. Hence, the present technology in the field still relies on sounding and measurement of soil resistance against penetration of objects.

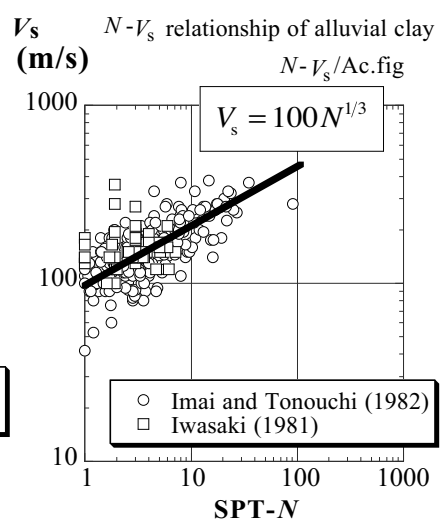
Standard penetration test (SPT in Sect. 1.12) is a popular method of subsoil investigation in which a sampler tube is hit into the bottom of a bored hole by an impact made by a hammer of 622.3 N (=63.5 kg) falling 75 cm (Fig. 8.10). The number of impacts needed for 30 cm penetration of a tube is designated by SPT- $N$ . Although it is widely used in the world, there are negative discussion about it concerning whether or not its practice is standardized. Despite that,  $N$  value has been correlated with many engineering soil parameters and the S wave velocity,  $V_s$ , is not an exception.



**Fig. 8.10** Practice of standard penetration test



**Fig. 8.11** SPT-  $V_s$  correlation for alluvial sandy soils

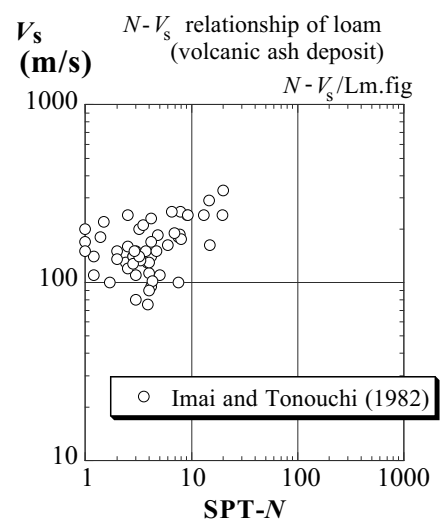


**Fig. 8.12** SPT-  $V_s$  correlation for alluvial clayey soils

The penetration of SPT sampler is resisted by soil. When denser and more compacted, soil can produce more resistance and a greater value of  $N$ . Soils of this type at the same time has a greater shear modulus and  $V_s$ . Therefore, there is a correlation between  $N$  and  $V_s$ .

Many empirical formulae have been proposed by compiling  $N$  and  $V_s$  values, which are measured at the same site and the same depth (Figs. 8.11 and 8.12 for sandy and clayey soils, respectively). Among them, those employed by the Japanese Highway Bridge Design Code appear the easiest to memorize

$$\begin{aligned}
 V_s &= 80N^{1/3} \text{ (m/s) for sand} && \text{and} \\
 V_s &= 100N^{1/3} \text{ (m/s) for clay,} && (8.1)
 \end{aligned}$$



**Fig. 8.13** SPT-  $V_s$  correlation for loam (volcanic ash deposits)

which are illustrated in Fig. 8.11 and Fig. 8.12. It is not meant here that other formulae are less reliable.

Figure 8.13 shows a similar correlation for  $V_s$  of loam (volcanic ash deposit), which is widely seen in Tokyo area. Furthermore, for soft organic soils,  $V_s = 50\text{--}60$  m/s appears to be appropriate.

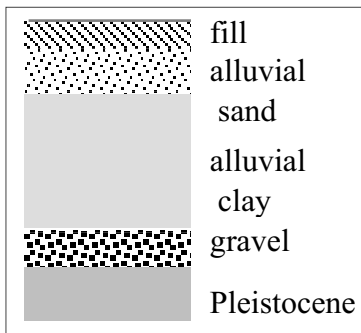
One of the problems lying in the correlation is the due scattering of data. Figure 8.11–8.13 demonstrate the data base collected by two literatures. For each type of soil, the observed  $V_s$  is roughly between 1/2 and 2 times of the correlation. The scattering occurs due to (1) spatial variation of soil type between SPT and  $V_s$  sites, (2) errors in field investigation, and (3) fuzzy nature of soil that does not exactly follow any equation. It is very important that the specified impact energy (622.3 N and 75 cm falling) is precisely produced. Moreover, reasonable maintenance of the SPT equipment is essential.

SPT device collects disturbed sample upon its impact penetration into subsoil at the bottom of a bore hole. Being disturbed (Fig. 1.37), this sample does not suit mechanical testing, but still is useful for physical properties such as particle size distribution and plasticity index. Liquefaction study by means of SPT will be described in Sect. 21.1.

**8.5 Correlation Between SPT-*N* and *V<sub>s</sub>* of Gravelly Soils**

The quaternary geology of alluvial deposits states that alluvial sandy and clayey deposits are underlain by gravels. This gravel layer was formed when the sea water level was still lower than today during the last (Ulm) glacier period. The sea water level achieved the highest level around 6,000 years before present and thereafter dropped slightly (Fig. 8.14). Consequently, the Japanese alluvial planes consist of such a stratification as illustrated in Fig. 8.15; gravel, clay, and sand from the bottom to the top; overlain by recent surface fills in urban areas.

The gravelly layer at the bottom of alluvial deposits is frequently employed as the bearing layer of building foundations. Its SPT-*N* is often greater than 50. Since the sea level change was repeated during the Pleistocene periods, there are more gravelly layers in the Pleistocene strata.

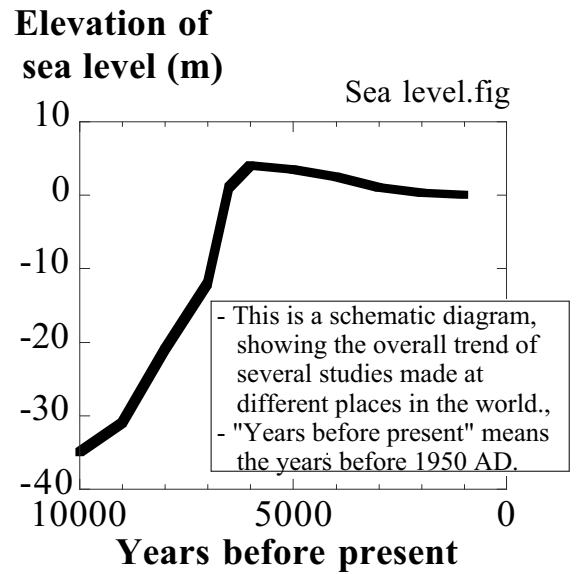


**Fig. 8.15** Schematic stratification of alluvial plane in Japan

Figure 8.16 indicates the relationship between SPT-*N* and *V<sub>s</sub>* of both alluvial (Holocene) and Pleistocene gravelly deposits. Generally, the Pleistocene gravel has greater penetration resistances and *V<sub>s</sub>* values than the younger alluvial (Holocene) materials. However, the correlation between SPT-*N* and *V<sub>s</sub>* is similar in those two gravels.

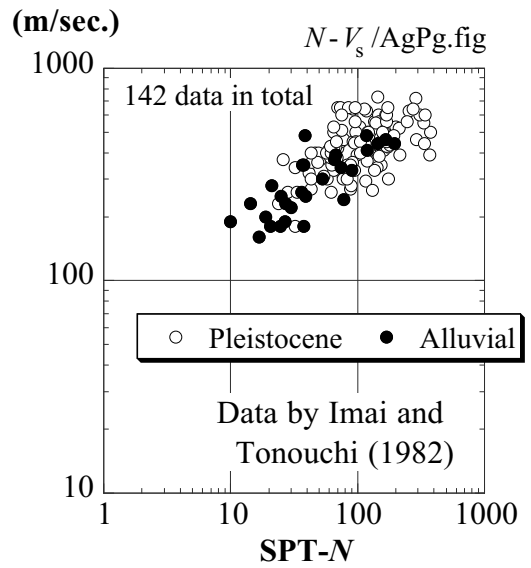
Figure 8.16 gives an impression that SPT-*N* > 300 was obtained by repeating the impact procedure as many as 300 times. It may not be true. It is a common practice that the penetration procedure is terminated after some number of blows when the achieved penetration is far less than the required 30 cm. If this is the case, SPT-*N* is obtained by extrapolation. For example,

$$(SPT - N) = (\text{Number of blows}) \times \frac{30 \text{ cm}}{\text{Achieved penetration}}$$



**Fig. 8.14** Sea level rising after last glacier period

*N* - *V<sub>s</sub>* relationship of alluvial gravel



**Fig. 8.16** SPT-*V<sub>s</sub>* correlation of Pleistocene and Holocene gravels



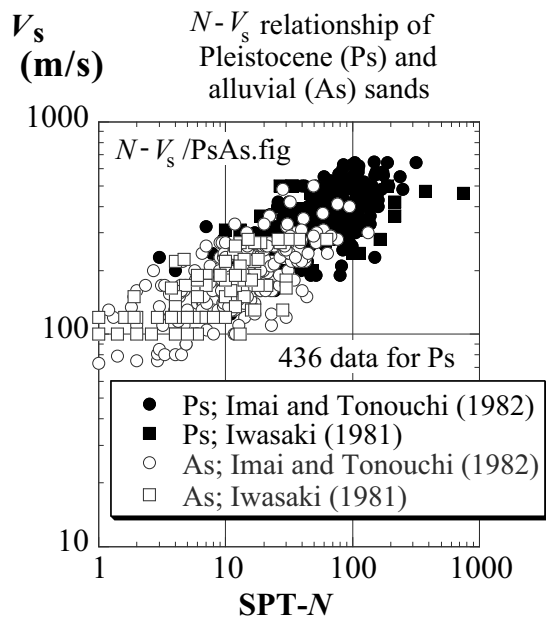
## 8.6 Correlation Between SPT- $N$ and $V_s$ of Pleistocene Soils

For construction of heavy structures, investigation on Pleistocene deposits is important. Figure 8.17 and Figure 8.18 plot SPT- $N$  versus S-wave-velocity ( $V_s$ ) relationships on Pleistocene sands and clays. Comparison is also made with similar data on alluvial soils which were presented in Sect. 8.4.

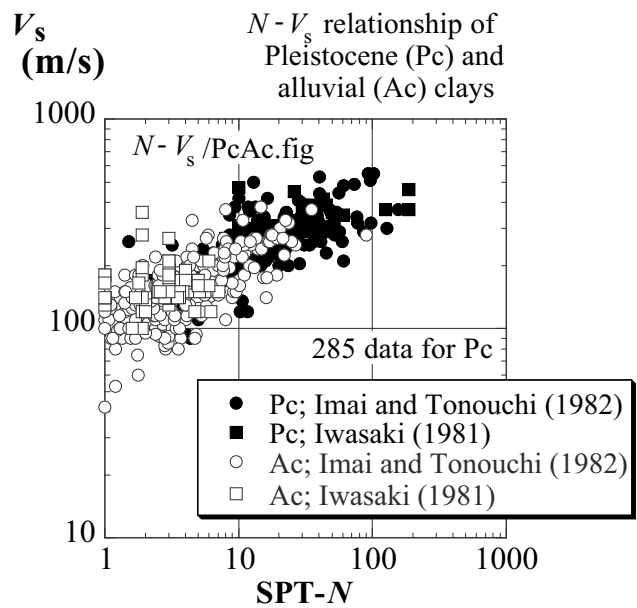
Pleistocene sands and clays certainly have greater SPT- $N$  and S wave velocity. It is interesting that the average correlations for Pleistocene materials are consistent with those for alluvial soils.

Since the measured  $V_s$  values are still less than 1,000 m/s, it is reasonable to state that Pleistocene soils are softer than sedimentary rocks, which, if free of weathering and joints, have  $V_s$  of 1–3 km/sec.

Some people prefer to use a terminology of “diluvial” in place of Pleistocene. The meaning of this word is related to flooding. Since the gravelly deposits of the last glacier period used to be considered to be a product of flooding, this word has been used. Recently, quaternary geologists consider that the deposits during the glacier period are not necessarily a product of flooding, and state that “diluvial” is not a relevant terminology. Hence, the present text uses the word of Pleistocene. Moreover, “Holocene” is an alternative word for “alluvial” for more recent deposits. There is not, however, a situation against the use of “alluvial.”



**Fig. 8.17** SPT- $V_s$  correlation of Pleistocene sands as compared with alluvial sands



**Fig. 8.18** SPT- $V_s$  correlation of Pleistocene clays as compared with alluvial clays

### 8.7 Seismic Refraction Method for Subsurface Exploration

One of the famous applications of wave propagation to the subsurface investigation is the seismic refraction method (屈折法地盤探査). In this method, the wave propagation velocity,  $V_p$  or  $V_s$ , is measured and the shear modulus of soil at small strain amplitude,  $G_{max}$ , is determined by using  $V_s$

$$G_{max} = \rho V_s^2. \tag{8.2}$$

Note that  $\rho$  is the mass density of soil and can be safely assessed to lie between 1.5–2.0 t/m<sup>3</sup>, depending on density and water content. In practice, P wave is more often investigated than S wave.

Figure 8.19 illustrates the principle of the method. Wave is generated by a source at the surface and propagates into the ground as well as along the surface.

1. Near the source, the first arrival of ground vibration is associated with the surface propagation. The travel time,  $T$ , from the source to the stations are given by

$$T = x/V_{s1}, \tag{8.3}$$

where  $x$  is the distance from the source and  $V_{s1}$  the wave velocity in the surface soft medium. Those waves reflected (反射) at the bottom of the layer arrive later.

2. Beyond some distance, in contrast, the wave propagation along the harder underlying deposit arrives first. Its travel time is given by

$$T = \frac{2H}{\cos\theta_{cr} V_{s1}} + \frac{x - 2H \tan\theta_{cr}}{V_{s2}}. \tag{8.4}$$

This wave propagation is achieved by the generated wave whose incident angle at the layer interface satisfies a special requirement of  $\theta_1 = \theta_{cr}$  from the Snell's law (Fig. 8.20).

3. In (8.3) and (8.4),  $V_{s1}$ ,  $V_{s2}$ , and  $H$  are unknown, while  $\theta_{cr}$  is a function of  $V_{s1}$  and  $V_{s2}$  (Fig. 8.20).
4. Figure 8.21 is a schematic relationship between  $x$  and the observed travel time,  $T$ . When there are two layers, the data points are approximated by a bilinear relationship.
5. The slopes of the bilinear relationship give the value of  $V_{s1}$  and  $V_{s2}$  as well as  $\theta_{cr} = \arcsin(V_{s1}/V_{s2})$ . The layer thickness,  $H$ , is determined from the observed intersection of two lines,  $x_{cr}$ , which is derived by equating (8.3) and (8.4)

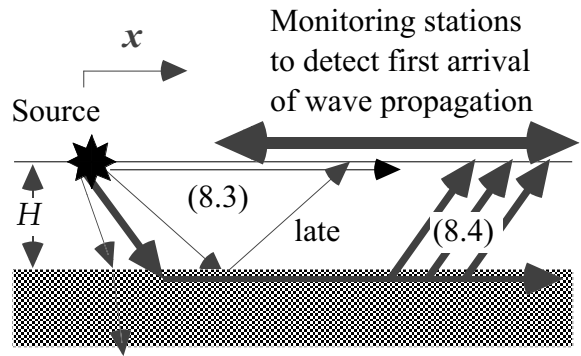


Fig. 8.19 Basic principle of seismic refraction method in horizontally layered deposits

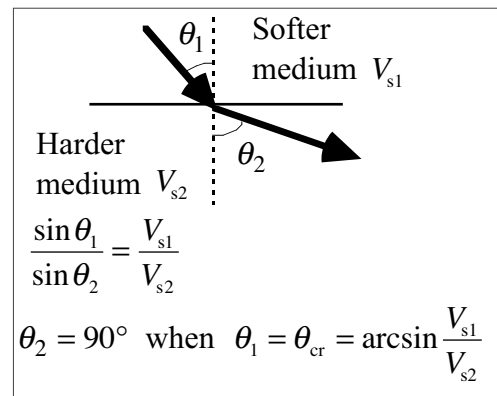


Fig. 8.20 Snell's law of wave refraction at interface of two different media

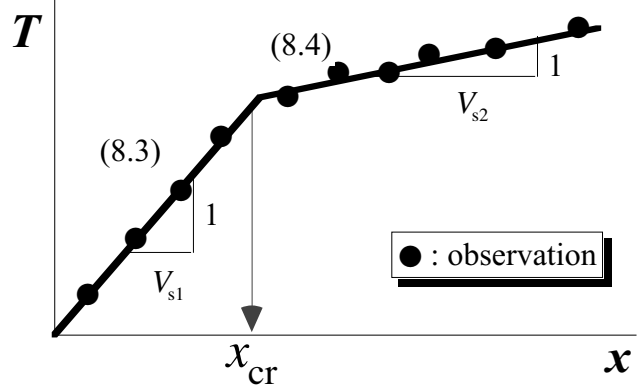


Fig. 8.21 Interpretation of seismic refraction data on horizontally deposited two layers

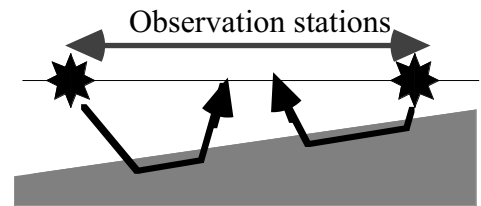


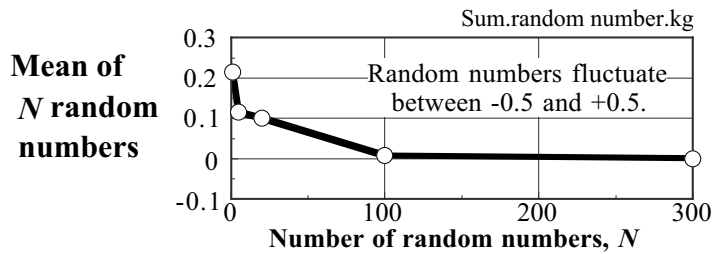
Fig. 8.22 Seismic refraction survey as provision for inclined layer boundary

$$x_{\text{cr}} = 2H \sqrt{\frac{V_{s1} + V_{s2}}{V_{s1} - V_{s2}}}. \quad (8.5)$$

Note that this method works when the underlying layer has a greater stiffness than the surface soil. Furthermore, it is often the case that the layer interface is inclined (Fig. 8.22). Hence, the seismic refraction survey is repeated in positive and negative  $x$  directions and the inclination angle is assessed as well.

### 8.8 Stacking Technique to Remove Noise from Signal

It is not uncommon that a geophysical survey such as seismic refraction is disturbed by environmental noises, which include typically traffic-induced vibrations in urban areas. Electromagnetic record of geophysical survey is disturbed as well by such a noise as ground electric current produced by trains and the existence of buried metal pipes.



**Fig. 8.23** Mean value of random numbers approaching zero as the total number of data increases

To remove noise and obtain a meaningful signal, a technique called stacking is useful. Since the noise is more or less of a randomly positive / negative nature, the stacking technique is based on the fact that the mean value of random numbers converges to zero when the total number of data is large as demonstrated in Fig. 8.23

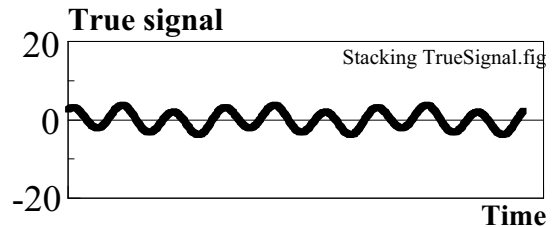
$$\frac{1}{N} \sum_{i=1}^N (\text{random number})_i \rightarrow 0 \quad \text{when } N \rightarrow \text{infinity.} \quad (8.6)$$

Figure 8.24 is a time history of a signal that is intended to be recorded. Being masked by a significant intensity of a noise in Fig. 8.25, the observed signal in Fig. 8.26 is totally different from the desired one in Fig. 8.24.

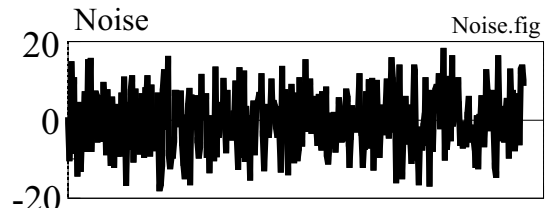
To overcome this problem by the stacking technique, monitoring is repeated  $K$  times, records are added (stacked) together, and the average is calculated

$$\text{Stacked record} = \frac{1}{K} \sum_{j=1}^K (\text{Recorded signal})_j \quad (8.7)$$

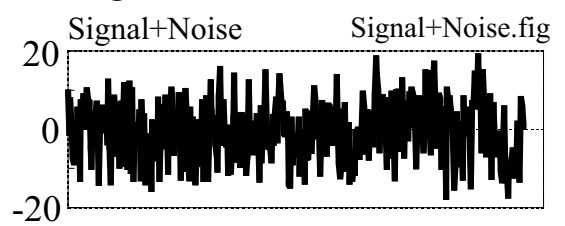
Figure 8.27–8.29 illustrate the results of stacking after numerically repeating the monitoring 5, 20, and 100 times, respectively. The signal–noise ratio ( $S/N$ ) was improved as the number of stacking increased. Consequently, the time history after 100 times stacking (Fig. 8.29) is more meaningful than a single shot of recording in Fig. 8.26. In practice, the stacking procedure is often conducted by adding data in the frequency–intensity diagram in place of the time domain as illustrated above.



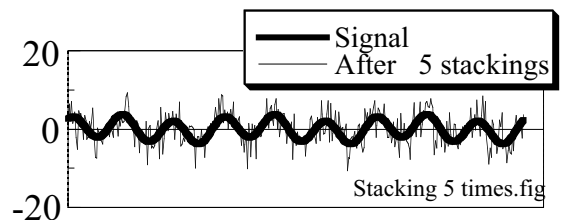
**Fig. 8.24** True time history of record



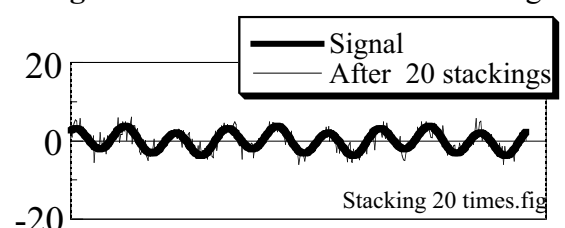
**Fig. 8.25** Intensity of noise



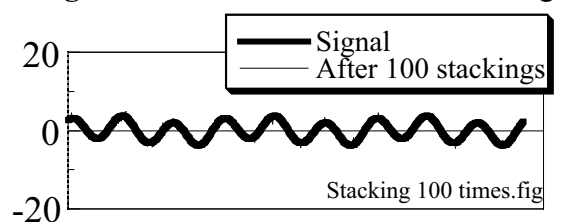
**Fig. 8.26** Superposition of signal and noise in actual observation



**Fig. 8.27** Record after 5 times stacking



**Fig. 8.28** Record after 20 times stacking



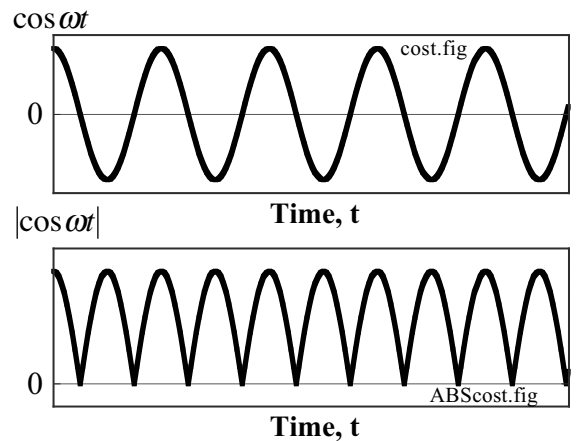
**Fig. 8.29** Record after 100 times stacking

The stacking as described above is carried out in the time domain: the added records stand for variation with time. One of the difficulties in the stacking in the time domain is the determination of the common zero time in many records. If this determination is difficult, an alternative choice is found in stacking in the frequency domain (Miyashita, 2006). First, the recorded signals,  $u_j(t)$ , are converted to absolute values,  $|u_j(t)|$ . This procedure converts negative signals to positive ones (Fig. 8.30), making the frequency doubled (horizontal axis of Fig. 8.31). Then the Fourier transformation (Sect. 9.12) is conducted on the absolute values

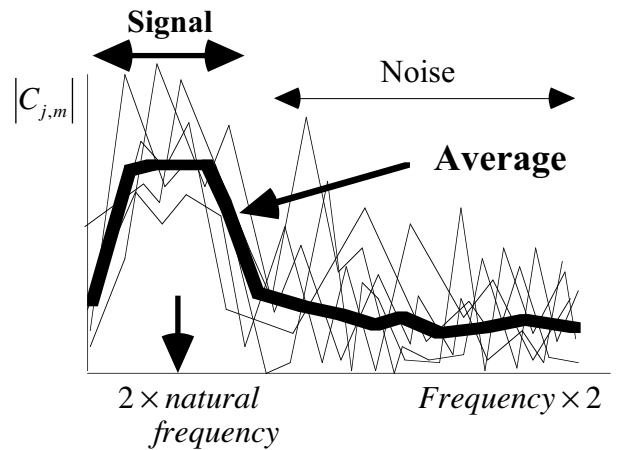
$$|u_j(t = k\Delta t)| = \sum_{m=0}^{N/2} C_{j,m} \exp\left(\frac{2\pi mk}{N} i\right), \quad (8.8)$$

in which  $k = 0, 1, 2, \dots, N/2$  and  $N$  is the number of the entire data. Thus,  $C_{j,m}$  stands for the intensity of records at different frequencies.

The same procedure is repeated for many data sets,  $j=1, 2, \dots$ . Figure 8.31 illustrates the schematic variation of Fourier amplitudes,  $|C_{j,m}|$ . Note that  $|C_{j,m}|$  is more or less similar in the range of true signal, because the signal is equally included in all the sets of data ( $j=1,2,3 \dots$ ). In contrast,  $|C_{j,m}|$  in the high frequency range, which stands for noise, is random. Thus, after stacking (adding) and averaging, the peak value can be detected more clearly. The predominant frequency (resonance frequency in a structural response) can be determined easily. Since the absolute values of  $|C_{j,m}|$  are employed in the analysis, information on phase of signal is lost.



**Fig. 8.30** Time history which is squared to erase negative parts



**Fig. 8.31** Stacking in frequency domain

### 8.9 Swedish Weight Sounding

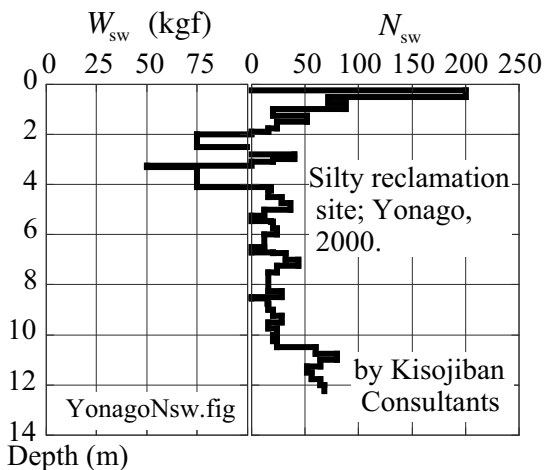
Swedish weight sounding is a portable method of ground investigation and is convenient for earthquake damage investigation when a motor vehicle and electricity are not available. This equipment consists of a screw point at the tip, steel rods of 1 m in length, dead weight of 0.98 kN (100 kgf), and a top handle.

Figure 8.32 shows engineers who are investigating the subsoil condition at a site of liquefaction of silty sand after the 2000 Tottori-Ken Seibu earthquake, Japan. Since no bore-hole drilling is necessary, the investigation is quick and cheap. The added dead weight of  $W_{sw} = 0.98 \text{ kN}$  makes penetration easy. The equipment is rotated, and the number of half rotations (180-degree rotations) needed for 1m penetration is counted and called  $N_{sw}$ . Certainly, the harder soil creates the greater value of  $N_{sw}$ . When soil is extremely soft, penetration occurs without any rotation; the dead weight of the equipment and the additional weight at the top ( $W_{sw} \leq 100 \text{ kgf}$ ) are sufficient to cause self-weight penetration.

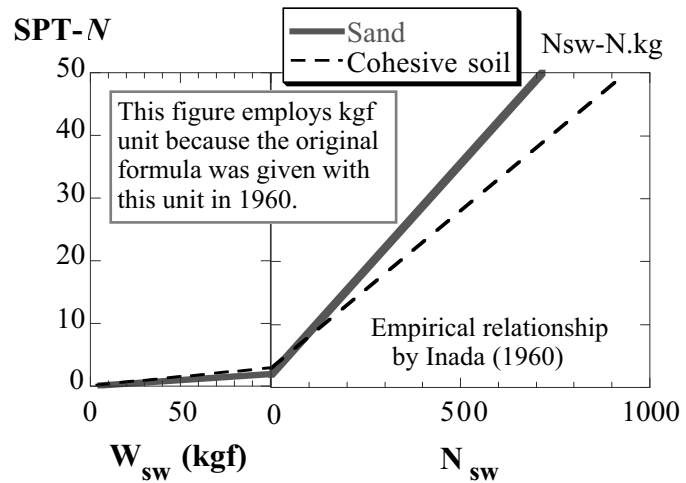


**Fig. 8.32** Rotating Swedish weight sounding device (100 kgf=0.98 kN)

The results at the site of Fig. 8.32 is presented in Fig. 8.33. The value of  $N_{sw}$  is very low in the young reclaimed sand, which came from a dredging project of a nearby harbor.



**Fig. 8.33**  $N_{sw}$  profile at the site of Fig. 8.32



**Fig. 8.34** Empirical correlations between  $N_{sw}$  and SPT- $N$  (Inada, 1960)

Inada (1960) proposed empirical correlations between  $N_{sw}$  and SPT- $N$  (Fig. 8.34);

For sand,  $N = 0.02W_{sw} \text{ (kgf)}$  and  $N = 2 + 0.067N_{sw}$

for cohesive soil,  $N = 0.03W_{sw} \text{ (kgf)}$  and  $N = 3 + 0.05N_{sw}$ .

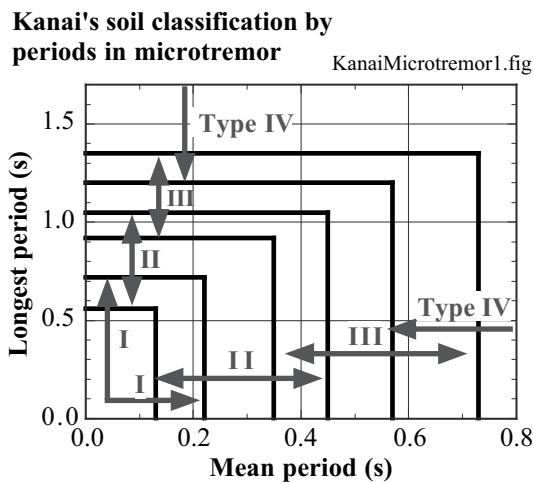
He stated that the correlation depends upon the types of soil and other factors and that a possible range of error is  $\Delta N = \pm 1.5-4$  for sandy soils and  $\pm 3$  for cohesive materials. Thus, the soil profile in Fig. 8.33 has an equivalent  $N$  less than 5.

When an extremely soft soil is encountered by this device, the whole machine drops suddenly into the ground. In such a situation, caution is necessary not to have your foot injured by the heavy weight of the equipment. Kisojiban Consultants Co. Ltd. of Tokyo developed a portable version of Swedish weight sounding machine in which the 100 kgf weight is produced by sand, which is collected at sites (Fig. 5.45). Thus, there is no need to carry the heavy iron weight.

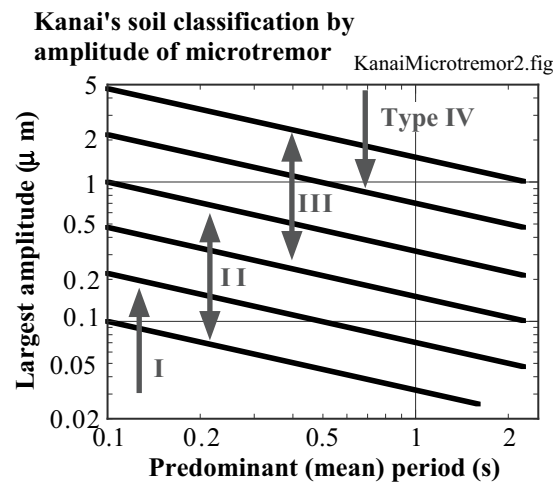
## 8.10 Microtremor

Microtremor (常時微動) is a very weak ground motion that is recorded at the ground surface. It is produced by a variety of excitation such as wind, traffics, sea wave, etc. It has been expected that the period of microtremor has a reasonable relationship with the nature of local soil deposit and dynamic characteristics of subsoil.

Kanai and Tanaka (1961) proposed to classify the type of ground on the basis of microtremor records. In their first proposal (Fig. 8.35), the subsoil classification was made on the basis of the period of motion. Moreover, they proposed the second classification on the basis of amplification of motion. Since the microtremor amplitude was varied by ambient noise in the daytime and night, they used the mean value of large amplitudes that often appear.



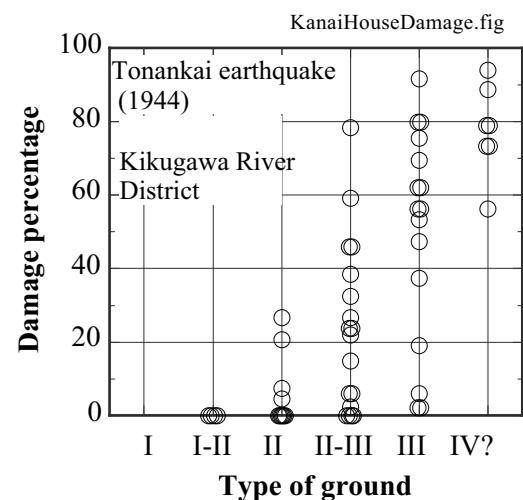
**Fig. 8.35** Subsoil classification based on period of microtremor (drawn after Kanai and Tanaka, 1961).



**Fig. 8.36** Subsoil classification based on period of microtremor (drawn after Kanai and Tanaka, 1961)

Kanai and Tanaka (1961) showed a good correlation between the subsoil classification (combination of two classifications in Figs 8.35 and 8.36) and damage rate of Japanese traditional wooden houses (1944 Tonankai earthquake, Kikugawa River District), see Fig. 8.37. This seems to be one of the earliest attempts of seismic microzonation which is based on local soil conditions.

Nakamura (2000) described his idea on use of microtremor records for more detailed classification of subsoil conditions. To the author's understanding, Nakamura's  $H/V$  spectrum method postulates that the shape of the Fourier spectrum (Sects. 6.4 and 9.11) of the vertical motion is identical between the base rock and the ground surface (Fig. 8.38), while the horizontal motion is subject to significant amplification (Sect. 6.7). Hence the amplification ratio,  $AMP(E+F)$ , is evaluated briefly by the following formula



**Fig. 8.37** Correlation between Kanai's subsoil classification and damage rate in Japanese traditional houses

$$AMP(E + F) \equiv \frac{\text{Spectrum of surface horizontal motion}}{\text{Spectrum of horizontal motion at baserock}} \propto \frac{\text{Spectrum of surface horizontal motion}}{\text{Spectrum of surface vertical motion}} \quad (8.9)$$

This equation enables to determine the natural frequency of the surface deposit by simply using the surface records of microtremor. Thus, it is expected that the surface deposit is classified from the viewpoint of earthquake response.

The author measured the microtremor at several places around the Kushiro Swamp of Hokkaido (Fig. 8.39). The amplitude of the measured records increased as the point of measurement proceeded towards the center of the swamp (Fig. 8.40). Moreover, The H/V study of the measured records showed that the predominant period of microtremor became longer in the inner part of the swamp (Fig. 8.41). Thus, the above-mentioned expectation seems reasonable. This measurement was conducted from 4 AM to 6 AM after which construction works started and microtremor

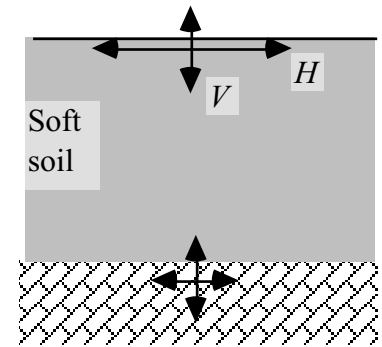


Fig. 8.38 Principle of H/V spectrum method

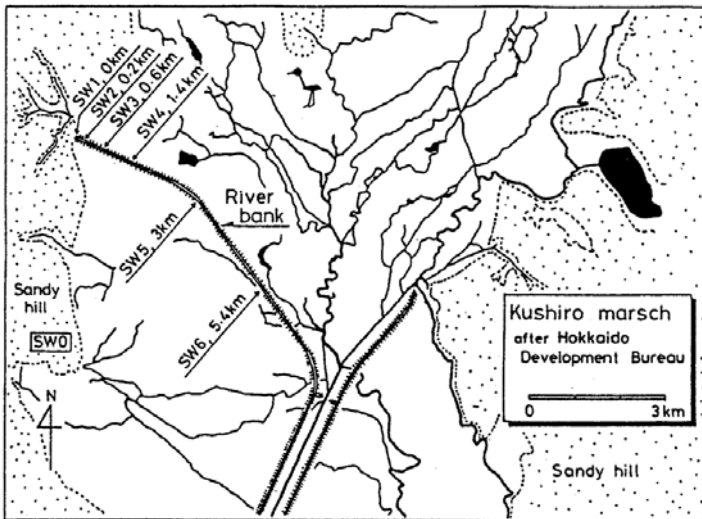


Fig. 8.39 Variation of predominant period with increasing thickness of peaty subsoil

erased by noise.

Because of its simplicity, Nakamura’s method is widely used and many good performances have been reported. However, it is yet to be known whether or not the shape of the Fourier spectrum of the vertical motion is unchanged between the bottom and the surface. Thus, the use of this method needs care. Note that the strain level caused by microtremor is extremely small (for example less than  $10^{-8}$ ) and the concerned soil rigidity is  $G_{max}$ . Soil behavior during strong shaking is associated with  $G$ , which is smaller than  $G$  due to stress–strain nonlinearity (Chap. 10).

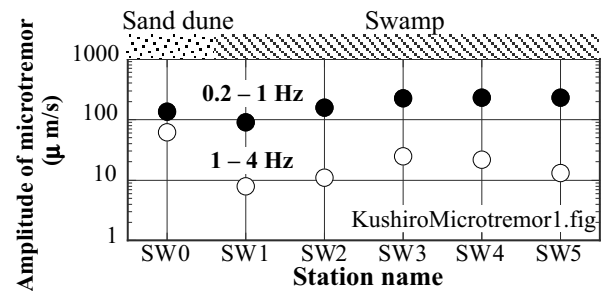


Fig. 8.40 Variation of microtremor amplitude in Kushiro Swamp

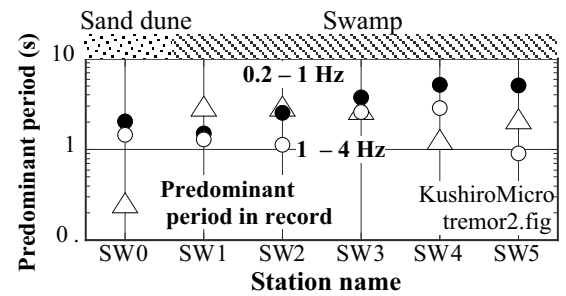
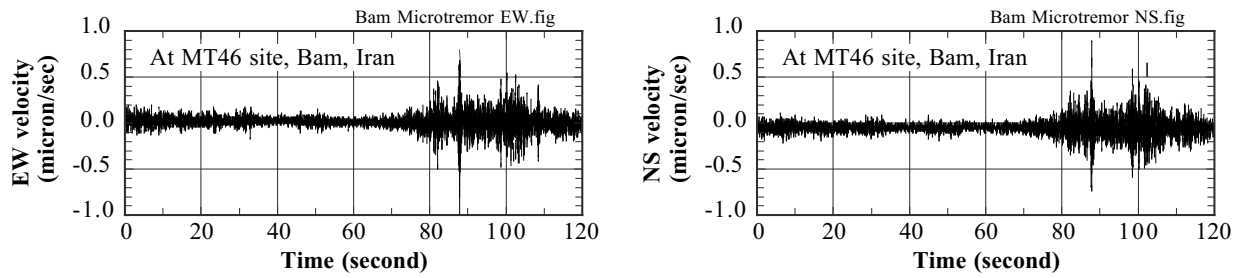


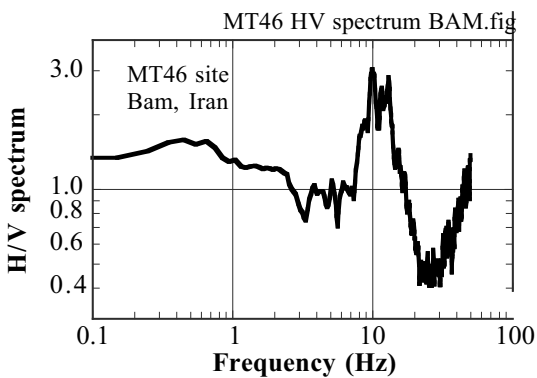
Fig. 8.41 Variation of predominant and H/V period in Kushiro Swamp



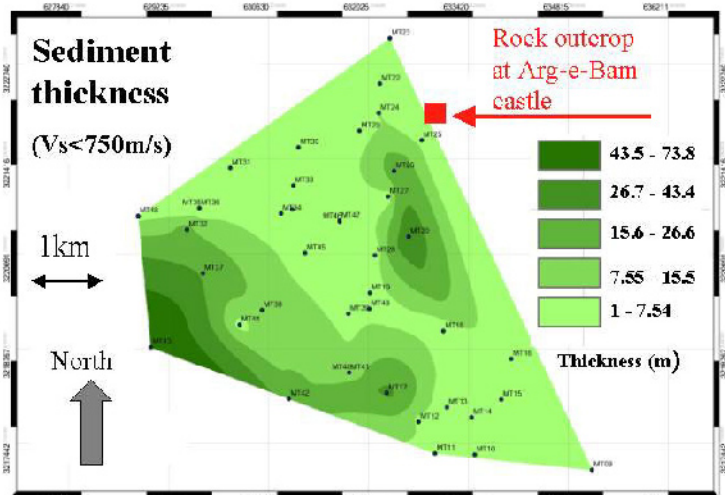


**Fig. 8.42** Example of microtremor records (Motamed et al. 2007)

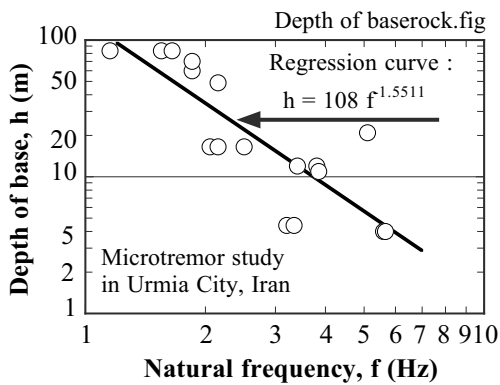
The following section demonstrates one successful use of the Nakamura’s method that was conducted in the city of Bam after a devastating earthquake in 2003 (Motamed et al. 2006). Figure 8.42 indicates the recording of microtremor. Care is certainly needed to avoid disturbance in the signal due to ambient heavy traffic or construction noise. Microtremor is usually recorded in terms of velocity. Figure 8.42 illustrates an example; see the very small intensity of motion and the associating soil strain. The spectral components of the recorded motions were obtained by Fourier Transformation Technique and then the ratio of horizontal spectrum over the vertical one was obtained. This ratio is called the *H/V* spectrum and has no dimension. The obtained *H/V* spectrum in Fig. 8.43 exhibits the greatest amplification at around 10 Hz. This frequency is considered to be the natural (resonance) frequency under small shear strain and is closely related with the nature of subsoil.



**Fig. 8.43** Example of *H/V* spectrum (Motamed et al., 2007)



**Fig. 8.45** Assessed depth of baserock in Bam City (Motamed et al., 2007)



**Fig. 8.44** Empirical correlation between assessed natural frequency and depth of baserock in Urmia City (Ghalandarzadeh., 2006)



**Fig. 8.46** Ongoing monitoring of microtremor in Kushiro City

Fig. 8.44 indicates an example of empirical correlation that was obtained in Urmia City of Iran between the obtained natural frequency and the depth of baserock as detected by nearby boring profiles. Note that the baserock is defined by S-wave velocity exceeding 750 m/s as specified by the Iranian code for earthquake-resistant design of buildings. Since there is a reasonable correlation in this figure, it was applied to the natural frequency in Bam city and the thickness of surface soil (= depth of baserock) was determined as illustrated in Fig. 8.45.

Microtremor can be recorded by a convenient portable instruments. However, the recording is easily disturbed by such an environmental noise as caused by traffics and construction works. It is therefore desirable to conduct it during quiet night times (Fig. 8.46).

**8.11 Subsurface Exploration by Surface Wave Records**

The use of microtremor as described in Sect. 8.10 is good because of its simplicity. It is important as well that no drilling of bore hole is required. It is, however, difficult to assess more detailed stratification of subsoils as usually required by geotechnical engineering. In contrast, the recent developments of advanced interpretation of microtremors have made it possible to draw such a stratification.

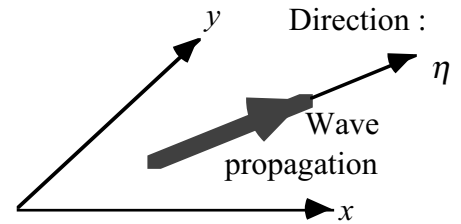
The new methodology is called SASW (spectral analysis of surface waves) and considers the measured ground vibration as Rayleigh wave (Stokoe et al. 1994), which is a wave that travels along the ground surface (Sect. 4.7). Figure 4.14 illustrated that the propagation velocity of Rayleigh wave is nearly equal to the S-wave velocity ( $V_s = \sqrt{G/\rho}$ ).

Tokimatsu et al. (1991, 1992a,b) classified SASW into passive and active types. The passive type monitors natural microtremors whose source is unknown and the direction of propagation is unknown either. Hence, transducers (geophones) have to be deployed on the ground surface in a two-dimensional manner. On the contrary, the active survey hits the ground surface and monitors the wave propagation along a known path. Thus, the transducers are placed along the same path in a one-dimensional manner. They also stated that the natural microtremor is more advantageous because components of longer wave length are included, which enable us to study soils at deeper elevations.

Figure 8.47 illustrates a situation in which motion “u” propagates in the x–y plane. The solution for this wave propagation is generally given by

$$u = F(\omega t - k_x x - k_y y), \tag{8.10}$$

where  $\omega$  stands for the circular frequency, while  $k_x$  and  $k_y$  are two-dimensional wave numbers. Since the direction of wave propagation ( $\eta$ ) is not known, the values of those wave numbers are unknown.



**Fig. 8.47** Propagation of wave in x–y horizontal plane

The subsurface exploration technology deploys many transducers at the ground surface and determines the direction of wave propagation. Hence,

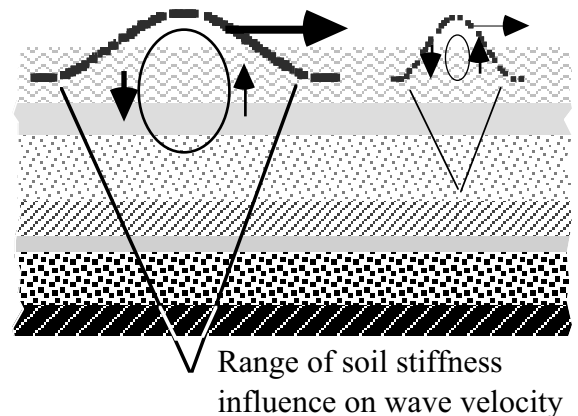
$$u = F(\omega t - k\eta), \tag{8.11}$$

in which  $k(\omega)$  is the wave number in the direction of wave propagation and varies with  $\omega$  when subsoil consists of many layers. The wave length,  $L$ , is then given by

$$L(\omega) = 2\pi/k,$$

which is a function of  $\omega$  as well.

The analysis of records from transducers makes it possible to determine the wave propagation velocities at many circular frequencies



**Fig. 8.48** Effects of wave length on propagation velocity of Rayleigh wave

$$\text{Velocity of Rayleigh wave propagation } V^R(\omega) \approx V^s \text{ and } V^R(\omega) = \omega/k. \quad (8.12)$$

Consequently,  $k$  and wave length,  $L$ , are determined as

$$k = \omega/V_R \text{ and } L = 2\pi V_R/\omega. \quad (8.13)$$

Thus, a correlation between  $L$  and  $V_s = \sqrt{G/\rho} \approx V_R$  is obtained. Usually,  $V_R$  increases as the wave length,  $L$ , becomes longer, because Rayleigh waves of longer wave length involve effects of deeper and stiffer (greater  $G$ ) soils (Fig. 8.48).

What has to be done is a back calculation of subsoil profile (variation of  $V_s$  with depth) that gives the best fitting between analytical and observed  $L - V_s$  relationships. Tokimatsu et al. (1991) introduced a mathematical procedure for this procedure. However, the most primitive method for this is to consider that the obtained  $V_R \approx \sqrt{G/\rho}$  occurs at  $L/2$ . Note that the obtained  $G$  is the modulus at small strain, and nonlinearity is out of scope.

### List of References in Chapter 8

- Ghalandarzadeh, A. (2006) Personal communication on comprehensive subsoil investigation in Urmia City, Iran.
- Henke, W. and Henke, R. (1993) Laboratory evaluation of in situ geotechnical torsional cylindrical impulse shear test for earthquake resistant design, *Bull. Seismol. Soc. Am.*, Vol. 83, No. 1, pp. 245–263.
- Imai, T. and Tonouchi, K. (1982) Correlation of  $N$  value with S-wave velocity and shear modulus, *Proc. 2nd Eur. Symp. Penetration Testing*, pp. 67–72.
- Inada, M. (1960) Interpretation of Swedish weight sounding, *Tsuchi-to-Kiso*, Japan. Soc. Soil Mech. and Found. Eng. (present Japan. Geotech. Soc.) Vol. 8, No. 1, pp. 13–18 (in Japanese).
- Iwasaki, T. (1981) Seismic design of highway bridges, Ph.D. Thesis, Kyushu University (in Japanese).
- Kanai, K. and Tanaka, T. (1961) On Microtremors. VIII, *Bull. Earthq. Res. Inst.*, University of Tokyo. Vol. 39, pp. 97–114.
- Kitsunezaki, C. (1978a) Indirect excitation type source for shear wave logging (1), *Geophysical Exploration*, Vol. 31, No. 6, pp. 329–337.
- Kitsunezaki, C. (1978b) Indirect excitation type source for shear wave logging (2), *Geophysical Exploration*, Vol. 31, No. 6, pp. 338–346.
- Miyashita, T. (2006) Personal communication.
- Motamed, R., Ghalandarzadeh, A. and Towhata, I. (2007) Seismic microzonation and damage assessment of Bam City, southeast of Iran, *J. Earthq. Eng.*, Vol. 11, No. 1, pp. 110–132.
- Nakamura, Y. (2000) Clear identification of fundamental idea of Nakamura's technique and its applications, *Proc. 12th World Conf. Earthq. Eng.*, Auckland, Paper number = 2656 in CD ROM proceedings.
- Stokoe, K.H., II, Wright, S.G., Bay, J.A. and Roësset, J.M. (1994) Characterization of geotechnical sites by SASW method, R.D. Woods, eds., *Geophysical Characterization of Sites*, Publication of Technical Committee 10, *Int. Soc. Soil Mech. Found. Eng.*, Oxford & IBH Publishers, pp. 15–25.
- Tokimatsu, K., Kuwayama, S., Tamura, S. and Miyadera, Y. (1991)  $V_s$  determination from steady state Rayleigh wave method, *Soils and Foundations*, Vol. 31, No. 2, pp. 153–163.
- Tokimatsu, K., Tamura, S. and Kojima, H. (1992a) Effects of multiple modes on Rayleigh wave dispersion characteristics, *J. Geotech. Eng.*, ASCE, Vol. 118, No. 10, pp. 1529–1543.
- Tokimatsu, K., Shinzawa, K. and Kuwayama, S. (1992b) Use of short-period microtremors for  $V_s$  profiling, *J. Geotech. Eng.*, ASCE, Vol. 118, No. 10, pp. 1544–1558.

# Chapter 9

## Dynamic Response of Complex-Modulus Model



Tomb mound of the fifth emperor of Han Dynasty, Xi'an, China.

This powerful monarch expanded his territory to Korea, Vietnam, and Central Asia. Even today, his strong spirit still punishes those who do not respect his tomb.

9.1 Complex Stress-Strain Modeling

The stress–strain relationship in complex numbers is given by

$$\tau^* = G(1 + 2ih)\gamma^*$$

in which  $G$  and  $h$  are real numbers, while  $i = \sqrt{-1}$  (Fig. 9.1).  $G$  is the elastic shear modulus and  $h$  is called the damping ratio. When the complex strain varies with time in a harmonic manner,

$$\gamma^* = \gamma_o \exp(i\omega t) = \gamma_o(\cos\omega t + i \sin\omega t)$$

the complex stress varies in a harmonic manner as well

$$\tau^* = G\gamma_o(\cos\omega t + i \sin\omega t)(1 + 2ih) = G\gamma_o\{(\cos\omega t - 2h \sin\omega t) + i(\sin\omega t + 2h \cos\omega t)\}.$$

Taking real parts of stress and strain,

$$\begin{aligned} \gamma &= \gamma_o \cos\omega t \\ \tau &= G\gamma_o(\cos\omega t - 2h \sin\omega t). \end{aligned}$$

The first term of stress is in phase with strain and stands for an elastic component. The second one is  $90^\circ$  earlier than strain, revealing the plastic component. See Fig. 9.2. According to Fig. 9.3,

$$\begin{aligned} \Delta W &= \oint \tau \, d\gamma = \oint \tau \frac{d\gamma}{dt} \, dt \\ &= -\omega G\gamma_o^2 \int_0^{2\pi} (\cos\omega t - 2h \sin\omega t)\sin\omega t \, dt = 2\pi h G\gamma_o^2 \\ W &= \frac{G}{2}\gamma_o^2. \end{aligned}$$

Note that  $\Delta W$  is independent of loading frequency, which is consistent with real soil behavior (Sect. 6.2). Accordingly,

$$\frac{\Delta W}{4\pi W} = \frac{2\pi h G\gamma_o^2}{2\pi G\gamma_o^2} = h!$$

Thus, damping ratio is constant, equal to  $h$ , independent of frequency,  $\omega/(2\pi)$ .

The damping ratio in soil dynamics is defined by using the area of a stress–strain loop. When the area of the loop is  $\Delta W$ , while the elastic energy is  $W$  (Fig. 9.3), the damping ratio,  $h$ , is defined by

$$h = \frac{\Delta W}{4\pi W}.$$

This definition should not be confused with the structural-dynamic definition of “critical damping ratio.”

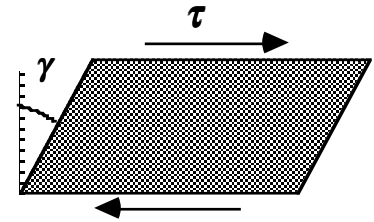


Fig. 9.1 Stress and strain in simple shear

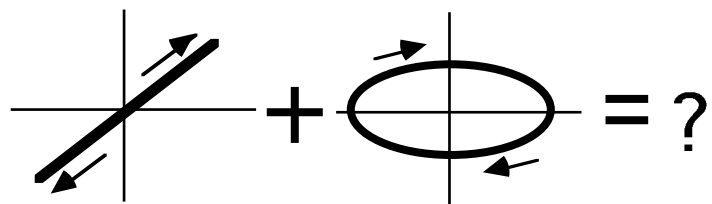


Fig. 9.2 Elastic and plastic components in complex stress–strain model

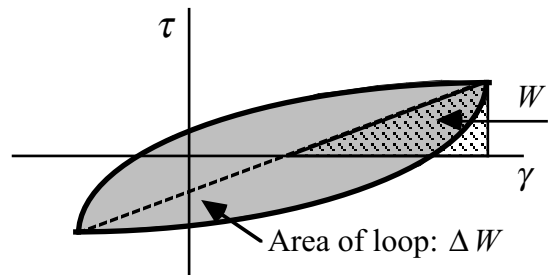


Fig. 9.3 Soil-dynamic definition of damping ratio

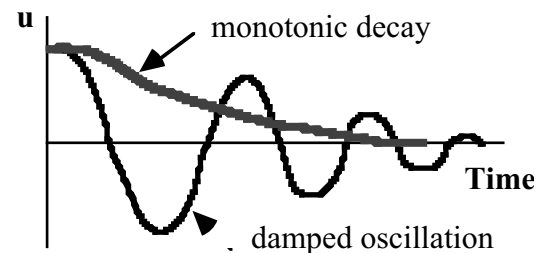


Fig. 9.4 Two types of free movements

Critical damping ratio: The equation of motion of a single-degree-of-freedom Voigt model

$$m \frac{d^2 u}{dt^2} + c \frac{du}{dt} + ku = 0,$$

reveals that the nature of free vibration varies with the magnitude of  $c$ ; damped oscillation when the critical damping ratio  $c/(2\sqrt{mk}) < 1$  and monotonic decay when  $c/(2\sqrt{mk}) \geq 1$ . See Fig. 9.4. Thus, the critical damping ratio should not be confused with damping ratio,  $h$ , in soil dynamics.

### 9.2 Damping Ratio in Soil Dynamics and Critical Damping Ratio

This section compares the damping ratio in soil dynamics and the critical damping ratio in structural dynamics. They are equal to each other when a Voigt model in structural dynamics (Fig. 9.5) is excited at a special frequency, as shown in what follows.

The area of hysteresis loop developed by a Voigt model increases in proportion to the frequency. It is interesting, however, that  $\Delta W/(4\pi W)$  of a Voigt model is equal to the critical damping ratio, when it is subjected to a forced vibration under a certain circular frequency of  $\omega$ . The equation of motion is

$$m \frac{d^2 u}{dt^2} + c \frac{du}{dt} + ku = F \exp(i\omega t),$$

where  $F$  is a real number. By safely employing a harmonic solution for “ $u$ ”,

$$u = U \exp(i\omega t) = U(\cos \omega t + i \sin \omega t),$$

where  $U$  is a real number. Hence,

$$\text{Force[in the Voigt Model]} = c \frac{du}{dt} + ku = U(ic\omega + k)\exp(i\omega t).$$

Taking the real parts,

$$\text{Re}(u) = U \cos \omega t \text{ and } \text{Re}(\text{Force}) = U(k \cos \omega t - c\omega \sin \omega t).$$

The elastic energy and the energy loss per cycle are obtained as (Fig. 9.6)

$$\begin{aligned} W &= \frac{k}{2} U^2 \\ \Delta W &= \oint \text{Re}(\text{Force}) d\{\text{Re}(u)\} = U \int_0^{2\pi/\omega} (k \cos \omega t - c\omega \sin \omega t) \frac{d\{\text{Re}(u)\}}{dt} dt \\ &= -U^2 \omega \int_0^{2\pi/\omega} \left\{ \frac{k}{2} \sin 2\omega t - \frac{c\omega}{2} (1 - \cos 2\omega t) \right\} dt = \pi c \omega U^2. \end{aligned}$$

Thus, the energy loss per cycle in a Voigt model depends on the loading frequency. Consequently,

$$\frac{\Delta W}{4\pi W} = \frac{c\omega}{2k}. \tag{9.1}$$

When the loading frequency is identical with the natural frequency,

$$\omega = \omega_0 = \sqrt{k/m} \text{ and } \frac{\Delta W}{4\pi W} = \frac{c}{2\sqrt{mk}},$$

which is identical with the structural-mechanic definition of critical damping ratio (Sect. 9.1).

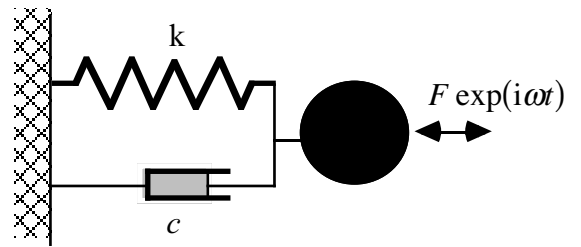


Fig. 9.5 Voigt model undergoing forced excitation

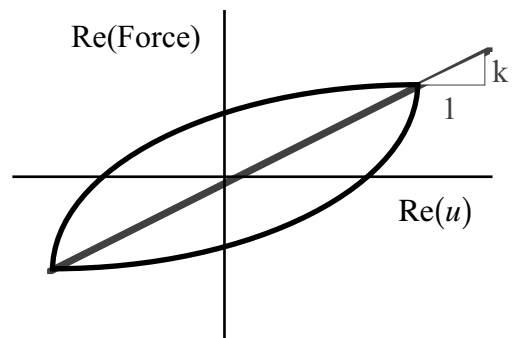


Fig. 9.6 Force vs. displacement relationship



**9.3 Damped Oscillation of Complex-Modulus Model**

The idea of complex modulus is used in a single-degree-of-freedom model (Fig. 9.7). The equation of motion in the course of free vibration is

$$m \frac{d^2u}{dt^2} + k(1 + 2ih)u = 0.$$

To derive its solution,  $u = U \exp(\lambda t)$  is assumed. Then,

$$m\lambda^2 + k(1 + 2ih) = 0$$

$$\lambda^2 = -\frac{k}{m}(1 + 2ih) = -\frac{k}{m}\sqrt{1 + 4h^2} \exp(i\delta),$$

in which  $\tan \delta \equiv 2h$ . Therefore,

$$\lambda = \pm i \sqrt{\frac{k}{m}\sqrt{1 + 4h^2}} \left( \cos \frac{\delta}{2} + i \sin \frac{\delta}{2} \right) = \pm \sqrt{\frac{k}{m}\sqrt{1 + 4h^2}} \left( -\sin \frac{\delta}{2} + i \cos \frac{\delta}{2} \right).$$

Since a positive value in the real part of the solution of  $\lambda$  gives an infinitely large displacement at an infinite time, only the negative solution is used. Therefore,

$$u = U \exp\left(-\sqrt{\frac{k}{m}\sqrt{1 + 4h^2}} \sin \frac{\delta}{2} \times t\right) \exp\left(i \sqrt{\frac{k}{m}\sqrt{1 + 4h^2}} \cos \frac{\delta}{2} \times t\right).$$

Thus, a damped oscillation occurs, whatever the damping ratio ( $h$ ) may be; the critical damping ratio < 1. The decay of amplitude during one period of free vibration

$$\text{Period} = \frac{2\pi}{\sqrt{\frac{k\sqrt{1 + 4h^2}}{m} \cos \frac{\delta}{2}}}$$

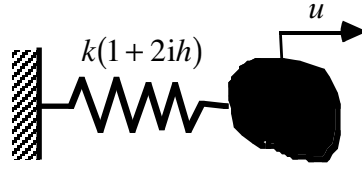
is derived as (see Fig. 9.8)

$$\frac{U_i}{U_{i+1}} = \exp\left(2\pi \tan \frac{\delta}{2}\right).$$

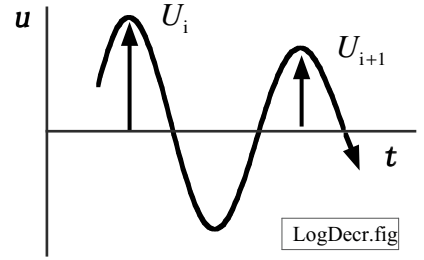
The logarithmic decrement is defined by  $\log_e(U_i/U_{i+1})$

$$\log_e \frac{U_i}{U_{i+1}} = 2\pi \tan \frac{\delta}{2} \approx \pi \tan \delta = 2\pi h.$$

The logarithmic decrement is approximately proportional to “ $h$ ” when damping is reasonably small. Upon forced vibration, in contrast,

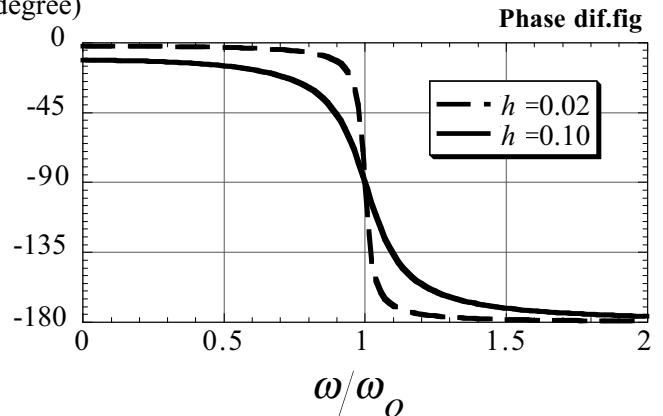


**Fig. 9.7** Free vibration of complex-modulus model



**Fig. 9.8** Definition of logarithmic decrement in free vibration

Phase delay in displacement response (degree)



**Fig. 9.9** Phase delay of displacement in complex-modulus model

$$m \frac{d^2 u}{dt^2} + c \frac{du}{dt} + ku = F_0 \exp(i\omega t)$$

The solution is derived by assuming  $u = U \exp(i\omega t)$ ,

$$u = \frac{F_0}{(k - m\omega^2)^2 + (2kh)^2} (k - m\omega^2 - 2khi) \exp(i\omega t),$$

This means that the phase angle of displacement is behind the phase of force ( $\omega t$ ) due to “ $-2khi$ ”. The delay angle is given by

$$-\arctan \frac{2kh}{k - m\omega^2} = -\arctan \frac{2h}{1 - (\omega/\omega_0)^2},$$

which is illustrated in Fig. 9.9. At resonance, the delay is  $90^\circ$ .

## 9.4 Forced Oscillation of Complex-Modulus Model

Knowledge about dynamic response is useful in experimentally identifying material parameters. When a complex modulus model in Fig. 9.7 is subjected to a harmonic force, the equation of motion is given by

$$m \frac{d^2 u}{dt^2} + k(1 + 2ih)u = F \exp(i\omega t)$$

where  $F > 0$  is a real number. The solution is derived as

$$u = \frac{F}{(k - m\omega^2) + 2khi} \exp(i\omega t)$$

and the amplitude of displacement is found to be

$$U = |u| = \frac{F}{\sqrt{(k - m\omega^2)^2 + 4k^2 h^2}} = \frac{1}{2h} \times \frac{F}{k} \times \frac{1}{\sqrt{1 + \left(\frac{1 - \omega^2/\omega_o^2}{2h}\right)^2}},$$

where  $F/k$  is the displacement under a static force. This equation shows that

1. The resonance occurs at  $\omega = \omega_o = \sqrt{k/m}$  for which the amplitude of motion is  $(1/2h)$  times the static displacement ( $F/k$ ). Thus, the value of “ $h$ ” is experimentally determined by comparing the resonant amplitude with the static displacement. When the static displacement cannot be measured, use the second method as below.
2. The circular frequencies at which the amplitude of motion is  $1/\sqrt{2}$  times the resonance amplitude are denoted by  $\omega_-$  and  $\omega_+$

$$\left\{ \begin{array}{l} \omega_+ \\ \omega_- \end{array} \right\} = \omega_o \sqrt{1 \pm 2h}.$$

By detecting experimentally these two special frequencies, the damping ratio of any structure can be determined

$$h = \left\{ \left( \frac{\omega_+}{\omega_o} \right)^2 - \left( \frac{\omega_-}{\omega_o} \right)^2 \right\} / 4.$$

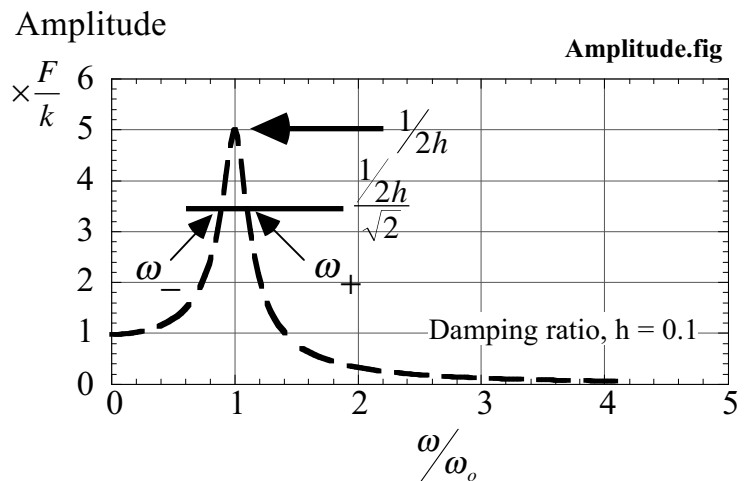


Fig. 9.10 Amplitude of complex-modulus model

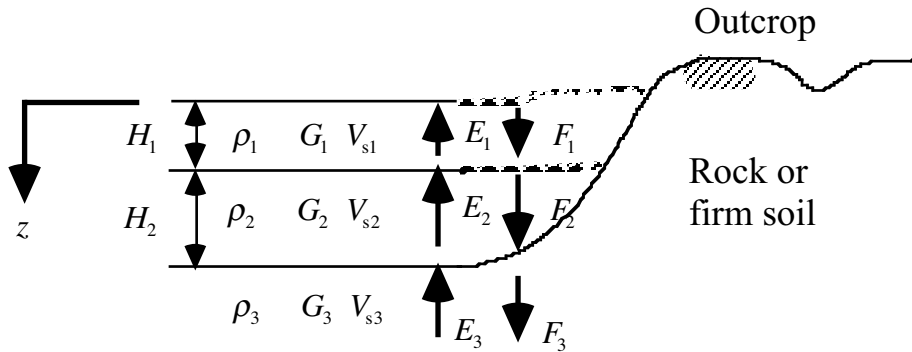
See Fig. 9.10. The idea described in this page is used in the interpretation of resonant column tests of soils in which unknown soil parameters of shear modulus and damping ratio are determined.

The complex-modulus model concerns only dynamic phenomena. For example, substitute  $\omega = 0$  into the above equations to see the amplitude of motion not being equal to the static displacement of  $F/k$ .

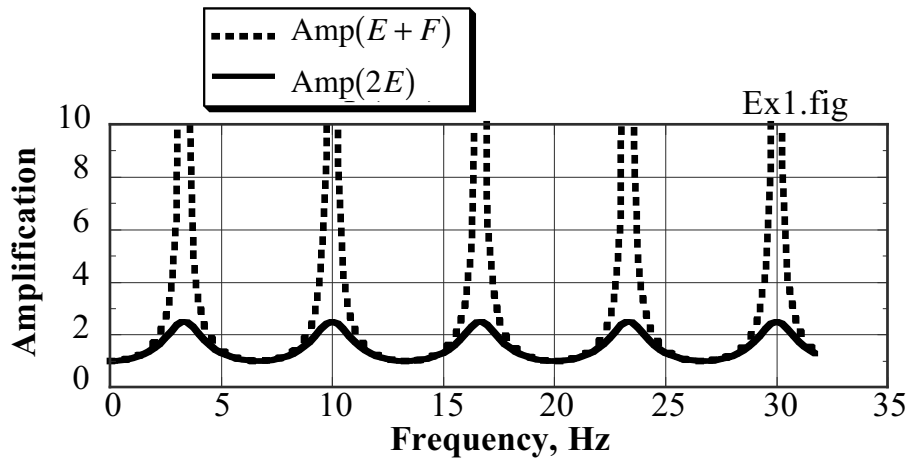
### Exercise 3 Calculation of Amplification Factor

See a three-layered ground in the figure.

1. Calculate the amplification of  $\text{Amp}(2E)$  and  $\text{Amp}(E+F)$ .
2. What is the ground motion at the rock outcrop (露頭)?



Answer! →



### 9.5 Wave Propagation in Complex-Modulus Medium

The equation of wave propagation is going to be solved here for a case of complex-modulus material. When the modulus is given by  $G(1+2ih)$ , which is uniform in a ground,

$$\frac{\partial^2 u}{\partial t^2} = V_s^2(1+2ih)\frac{\partial^2 u}{\partial z^2}$$

where  $V_s = \sqrt{G/\rho}$  and  $\delta = \arctan(2h)$ . Hence,

$$\frac{\partial^2 u}{\partial t^2} = V_s^2(1+4h^2)^{1/2} \exp(i\delta)\frac{\partial^2 u}{\partial z^2}.$$

The harmonic solution for this is symbolically described as

$$u = E \exp\left\{i\omega\left(t + \frac{z}{V_s^*}\right)\right\} + F \exp\left\{i\omega\left(t - \frac{z}{V_s^*}\right)\right\}, \quad (9.2)$$

in which  $V_s^* = V_s(1+4h^2)^{1/4} \exp(i\delta/2)$  and  $\exp(i\delta/2) = \cos\frac{\delta}{2} + i \sin\frac{\delta}{2}$ . The “E” and “F” terms stand for the upward and downward wave propagations, respectively. Then, more in detail, the “E” term is described as

$$u = E \exp\left[ i\omega\left\{t + \frac{\left(\cos\frac{\delta}{2} - i \sin\frac{\delta}{2}\right)z}{V_s(1+4h^2)^{1/4}}\right\}\right] = E \exp\left\{\frac{\omega\left(\sin\frac{\delta}{2}\right)z}{V_s(1+4h^2)^{1/4}}\right\} \exp\left[ i\omega\left\{t + \frac{\left(\cos\frac{\delta}{2}\right)z}{V_s(1+4h^2)^{1/4}}\right\}\right]. \quad (9.3)$$

The associating shear stress of “E” component is given by

$$\begin{aligned} \tau &= G(1+2ih)\frac{\partial u}{\partial z} \\ &= E \frac{i\omega\rho V_s(1+4h^2)^{1/2} \exp(i\delta)\left(\cos\frac{\delta}{2} - i \sin\frac{\delta}{2}\right)}{(1+4h^2)^{1/4}} \exp\left\{\frac{\left(\omega \sin\frac{\delta}{2}\right)z}{V_s(1+4h^2)^{1/4}}\right\} \exp\left[ i\omega\left\{t + \frac{\left(\cos\frac{\delta}{2}\right)z}{V_s(1+4h^2)^{1/4}}\right\}\right] \\ &= E \times i\omega\rho V_s(1+4h^2)^{1/4} \exp\left(i\frac{\delta}{2}\right) \exp\left\{\frac{\left(\omega \sin\frac{\delta}{2}\right)z}{V_s(1+4h^2)^{1/4}}\right\} \exp\left[ i\omega\left\{t + \frac{\left(\cos\frac{\delta}{2}\right)z}{V_s(1+4h^2)^{1/4}}\right\}\right]. \end{aligned} \quad (9.4)$$

The wave length,  $L$ , is determined by

$$\omega \frac{\left(\cos\frac{\delta}{2}\right)L}{V_s(1+4h^2)^{1/4}} = 2\pi \quad \text{and} \quad L = \frac{2\pi V_s(1+4h^2)^{1/4}}{\omega \cos\frac{\delta}{2}}. \quad (9.5)$$

For the “F” term of shear stress, “z” above is replaced by “-z” By using the boundary condition of zero shear stress at the surface (z = 0),

$$\tau(z = 0) = (E - F) \times i\omega\rho V_s (1 + 4h^2)^{1/4} \exp(i\delta/2) \text{ and, consequently, } E = F.$$

Thus, the solution of wave propagation equation is obtained

$$u = E \left[ \exp \left\{ \frac{\omega \left( \sin \frac{\delta}{2} \right) z}{V_s (1 + 4h^2)^{1/4}} \right\} \exp \left[ i\omega \left\{ t + \frac{\left( \cos \frac{\delta}{2} \right) z}{V_s (1 + 4h^2)^{1/4}} \right\} \right] + \exp \left\{ \frac{-\omega \left( \sin \frac{\delta}{2} \right) z}{V_s (1 + 4h^2)^{1/4}} \right\} \exp \left[ i\omega \left\{ t - \frac{\left( \cos \frac{\delta}{2} \right) z}{V_s (1 + 4h^2)^{1/4}} \right\} \right] \right].$$

Both components on the right-hand side have exponential multipliers (indicated by dashed underlines). They stand for the decay of wave with a propagation distance. It means that the amplitude is reduced at a rate of  $\exp\{-2\pi \tan(\delta/2)\}$  per one wave length,  $L$ .

The velocity of wave propagation is consequently derived

$$\text{Velocity} = \frac{\text{Wave length } L}{\text{Period } (= 2\pi/\omega)} = V_s \frac{(1 + 4h^2)^{1/4}}{\cos \frac{\delta}{2}} = V_s \frac{(1 + \tan^2 \delta)^{1/4}}{\cos \frac{\delta}{2}} = \frac{V_s}{\sqrt{\cos \delta} \cos \frac{\delta}{2}}. \tag{9.6}$$

9.6 Solution of Real Numbers in Complex-Modulus Ground

The solution in Sect. 9.5 is further studied. Figure 9.11 illustrates the concept of a two-layered soil deposit. The surface soil is soft, while the bottom one is a rigid material such as base rock, tertiary deposit, or pleistocene material.

$$u = 2E_1 \left[ \cosh \left\{ \frac{\omega \sin \frac{\delta}{2} \times z}{V_s(1+4h^2)^{1/4}} \right\} \cos \left\{ \frac{\omega \cos \frac{\delta}{2} \times z}{V_s(1+4h^2)^{1/4}} \right\} + i \sinh \left\{ \frac{\omega \sin \frac{\delta}{2} \times z}{V_s(1+4h^2)^{1/4}} \right\} \sin \left\{ \frac{\omega \cos \frac{\delta}{2} \times z}{V_s(1+4h^2)^{1/4}} \right\} \right] \exp(i\omega t)$$

$$\tau = 2E_1 \rho V_s (1+4h^2)^{1/4} \exp \frac{i\delta}{2} \times \left[ \sinh \left\{ \frac{\omega \sin \frac{\delta}{2} \times z}{V_s(1+4h^2)^{1/4}} \right\} \cos \left\{ \frac{\omega \cos \frac{\delta}{2} \times z}{V_s(1+4h^2)^{1/4}} \right\} + i \cosh \left\{ \frac{\omega \sin \frac{\delta}{2} \times z}{V_s(1+4h^2)^{1/4}} \right\} \sin \left\{ \frac{\omega \cos \frac{\delta}{2} \times z}{V_s(1+4h^2)^{1/4}} \right\} \right] \exp(i\omega t)$$

The amplification of Amp(E+F) is given by the ratio

$$\text{Amp}(E + F) \equiv \frac{|u(z = 0)|}{|u(z = H)|}$$

and is illustrated in Fig. 9.12. Note that the amplification is smaller at higher frequency. This is because the wave length is shorter, the number of cycles during wave propagation is greater, and, in accordance with the number of cycles in the course of wave propagation, the amount of energy loss is increased. This disappearance of high-frequency components is in good contrast with the elastic solution in Sect. 6.8.

For plotting time histories of displacement or stress, the real parts of the above equations are employed.

Note that Amp(E+F) simply indicates the dynamic behavior of the surface deposit; it does not account for the local geology in which there is a harder base layer underneath. Use Amp(2E) in Sect. 9.7 when effects of such a local geological structure has to be investigated.

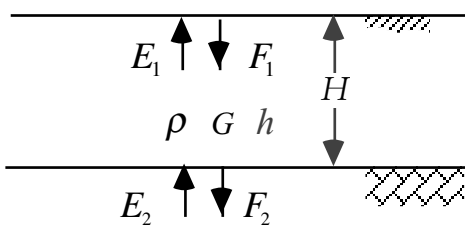


Fig. 9.11 Model of level ground with complex modulus

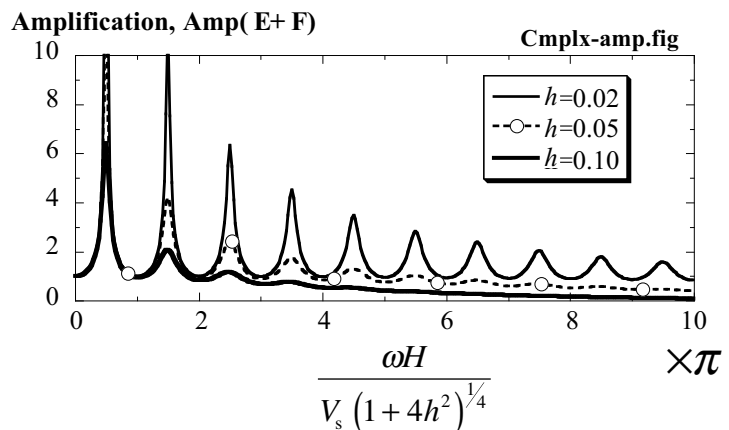


Fig. 9.12 Amplification in complex-modulus ground

### 9.7 Outcrop Amplification in Complex-Modulus Ground

Study is made of the propagation of SH wave (Sect. 4.2) in a two-layered complex-modulus subsoil; see Fig. 9.13 for notation. The amplitudes of motion at the outcrop and at the surface of soft alluvium are compared. When a harmonic motion is considered, the motion in the alluvium is given by

$$u_1 = E_1 \left[ \exp \left\{ i\omega \left( t + \frac{z}{V_{s1}^*} \right) \right\} + \exp \left\{ i\omega \left( t - \frac{z}{V_{s1}^*} \right) \right\} \right], \quad (9.7)$$

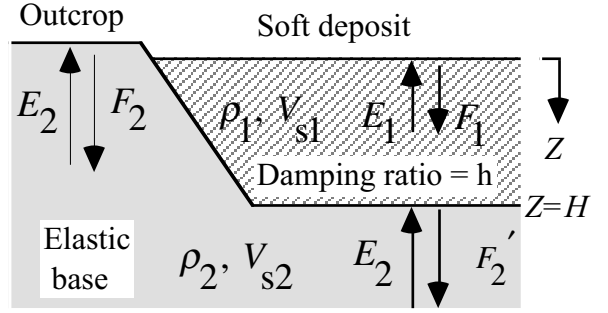


Fig. 9.13 Two-layered alluvium

where  $V_{s1}^* = V_{s1} (1 + 4h^2)^{1/4} \exp(i\delta/2)$  and  $\delta = \arctan(2h)$ ,

Sect. 9.5. See that the amplitude of  $u$  is  $2E_1$  at the surface ( $z = 0$ ). Furthermore, the shear stress is given by

$$\tau_1 = G_1(1 + 2ih) \frac{\partial u_1}{\partial z} = G_1(1 + 2ih) \frac{i\omega}{V_{s1}^*} E_1 \left[ \exp \left\{ i\omega \left( t + \frac{z}{V_{s1}^*} \right) \right\} - \exp \left\{ i\omega \left( t - \frac{z}{V_{s1}^*} \right) \right\} \right], \quad (9.8)$$

in which the boundary condition at the surface (*shear stress = 0*) is accounted for. Similarly, the solution in the elastic base beneath the alluvium is given by

*Amp(2E) is a more direct index than Amp(E+F) of the effects of local geology.*

$$u_2 = E_2 \exp \left\{ i\omega \left( t + \frac{z-H}{V_{s2}} \right) \right\} + F_2' \exp \left\{ i\omega \left( t - \frac{z-H}{V_{s2}} \right) \right\} \quad (9.9)$$

$$\tau_2 = G_2 \frac{i\omega}{V_{s2}} \left[ E_2 \exp \left\{ i\omega \left( t + \frac{z-H}{V_{s2}} \right) \right\} - F_2' \exp \left\{ i\omega \left( t - \frac{z-H}{V_{s2}} \right) \right\} \right]. \quad (9.10)$$

Since both displacement and shear stress are continuous at  $z = H$ , (9.7) = (9.9) and (9.8) = (9.10),  $E_2$  and  $F_2'$  are solved in terms of  $E_1$ . Consequently,

$$\left\{ \frac{1}{\text{Amp}(2E)} \right\}^2 = \left| \frac{2E_2}{2E_1} \right|^2 = \frac{1}{2} \left\{ \cosh \left( 2x \sin \frac{\delta}{2} \right) + \cos \left( 2x \cos \frac{\delta}{2} \right) \right\} + \frac{\rho_1 V_{s1}}{\rho_2 V_{s2}} (1 + 4h^2)^{1/4} \left\{ \cos \frac{\delta}{2} \sinh \left( 2x \sin \frac{\delta}{2} \right) - \sin \frac{\delta}{2} \sin \left( 2x \cos \frac{\delta}{2} \right) + \frac{1}{2} \left( \frac{\rho_1 V_{s1}}{\rho_2 V_{s2}} \right)^2 (1 + 4h^2)^{1/2} \left\{ \cosh \left( 2x \sin \frac{\delta}{2} \right) - \cos \left( 2x \cos \frac{\delta}{2} \right) \right\} \right\}, \quad (9.11)$$

where  $x = (\omega H) / \left\{ V_{s1} (1 + 4h^2)^{1/4} \right\}$ . The outcrop amplification is obtained by  $\text{Amp}(2E) = |2E_1 / 2E_2|$ , which is demonstrated in Fig. 9.14 for two values of the impedance ratio,  $\rho_1 V_{s1} / \rho_2 V_{s2}$ . The amplification is greater when the alluvium is softer (impedance ratio = 0.1) and the damping ratio is smaller.

It is interesting that very soft ground with a small value of  $V_s$  has a large value of  $\omega H / V_s$  and consequently low amplification. When the intensity of shaking is very strong, moreover, the induced



shear strain is large and consequently the damping ratio,  $h$ , becomes substantial (nonlinearity in Sect. 10.8 and Sect. 10.15). This situation leads to the amplification, that may be less than 1.0. Idriss (1990) combined dynamic analyses and measured earthquake records to suggest that this idea may be the reality (Fig. 9.15).

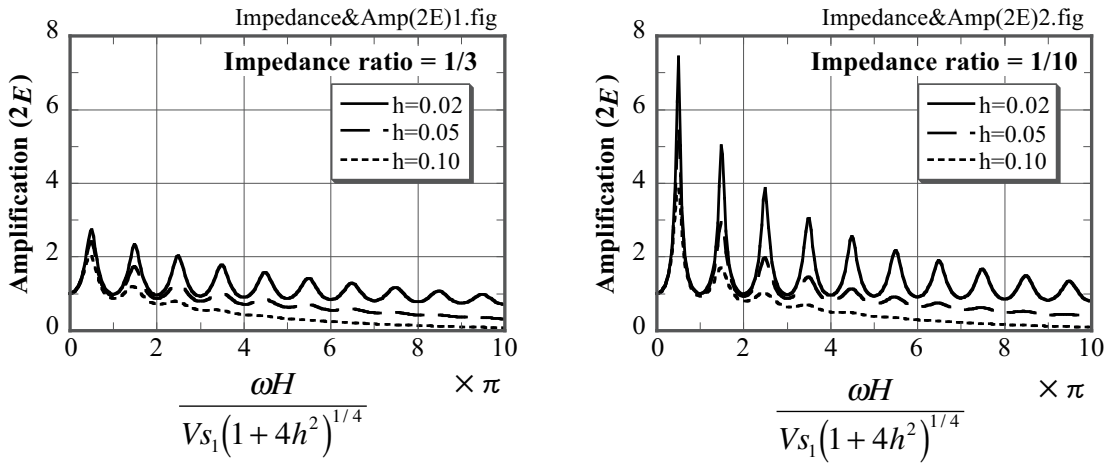


Fig. 9.14 Effects of impedance ratio on amplification in surface deposit

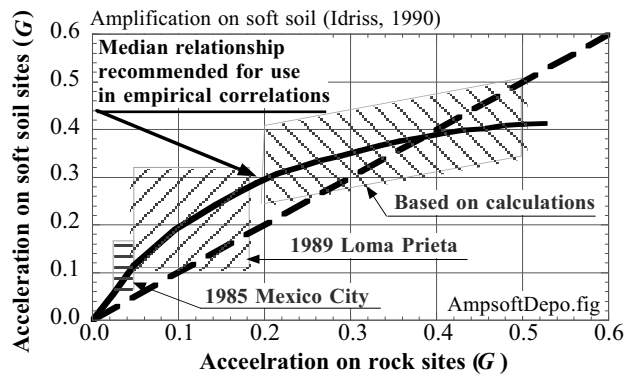
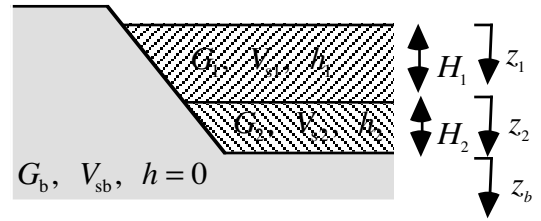


Fig. 9.15 Amplification of soft ground changing with intensity of outcrop excitation (drawn after Idriss, 1990)

### 9.8 Exercise No. 4 Response Analysis on Multilayered Deposits

First develop a computer program that can solve a linear equation

$$\begin{bmatrix} C_{11} & C_{12} \\ C_{21} & C_{22} \end{bmatrix} \begin{Bmatrix} x_1 \\ x_2 \end{Bmatrix} = \begin{Bmatrix} q_1 \\ q_2 \end{Bmatrix},$$



in which all numbers are complex 複素数. Use the conventional Gaussian elimination ガウスの消去法 and do not be afraid of a singular matrix,  $C_{11}C_{22} - C_{12}C_{21} = 0$ .

Assume then a stratification of soil with two alluvial layers resting on an engineering base rock (see the illustration above). The nonlinear stress–strain relationship of soils is expressed by a complex-modulus model  $G^* = G(1 + 2ih)$ . The base is made of an elastic medium.

1. Calculate the amplification  $\text{Amp}(2E)$  of the surface motion against the outcrop motion by taking into account the continuity of displacement and shear stress at the interfaces. For convenience of calculation use vertical coordinates of  $z_1$ ,  $z_2$ , and  $z_b$  in respective layers.
2. Plot  $\text{Amp}(2E)$  then over a range of normalized frequency of  $\omega H_1 / V_{s1} = 0-10$ , for a special case of
  - constant  $\rho$  of soils from the surface to the base
  - $V_{s1}/V_{s2} = 1/3$  and  $V_{s2}/V_{sb} = 1/3$
  - Damping ratio :  $h_1 = 0.10$  and  $h_2 = 0.03$
  - $H_1 = H_2$

It is recommended to run all the calculations by using complex numbers. Keep the computer program for this assignment, and if you make any, for a later assignment.

### 9.9 Variation of Shear Modulus at Interface of Soil Layers

It is a common practice in current dynamic analyses to divide subsoil into homogeneous layers (or finite elements). Consequently, material properties are discontinuous at layer interfaces, see Fig. 9.16. Section 4.10 indicated that discontinuity in material properties generates wave reflection.

Material properties of artificially reclaimed soil and natural alluvial deposits were studied in Tokyo Bay area by the Association for Development of Earthquake Prediction, Tokyo. Undisturbed soil samples were collected to measure shear modulus,  $G_{max}$ , as well as gradation (粒度分布) and they were compared with  $V_s$  which was measured insitu by a suspension technique (Sect. 8.2).

Upon artificial reclamation, the reclaimed soil and the existing seabed soil are different. This point is evidenced by the drastic variation of fines content at around 9 m depth (Fig. 9.17). The in-situ measured  $V_s$  is continuous, in contrast, at this depth (Fig. 9.18) probably because the effective stress is continuous in the vertical direction. Hence, the discontinuous modeling as illustrated in Fig. 9.16 at the interface may not be very realistic and reflects earthquake energy back into the lower strata, reducing shaking energy in the surface soil.

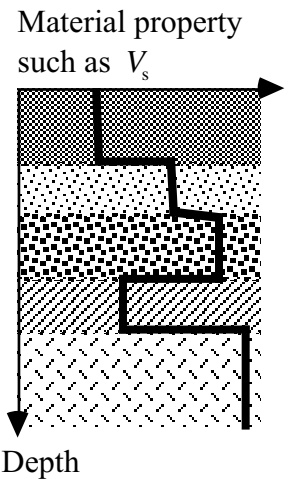


Fig. 9.16 Modelling of subsoil by uniform layers

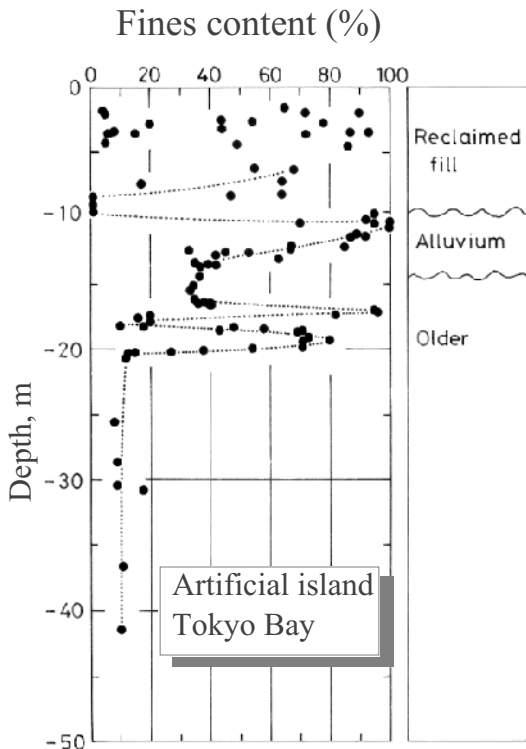


Fig. 9.17 Change of fines content at interface of natural deposit and artificial fill

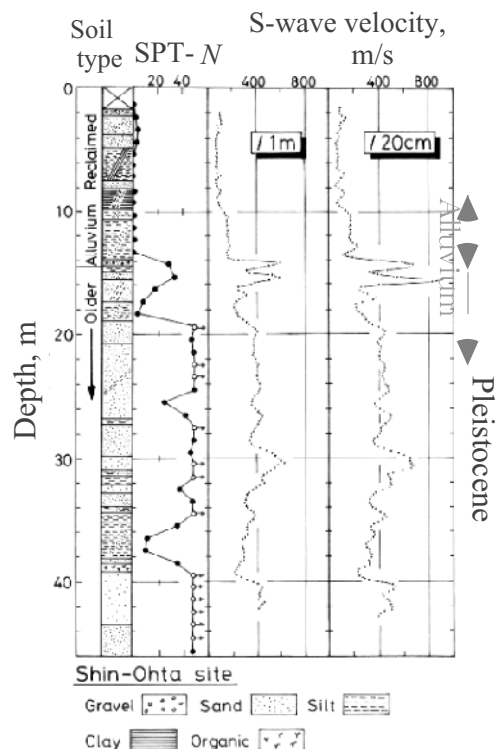


Fig. 9.18 Discontinuity of shear wave velocity at interface of natural deposit and artificial fill

The alluvial layer exhibits continuous variation in both fines content and S wave velocity. This seems consistent with the continuity of age of soil as well as the continuity of effective stress. Thus, the discontinuous modelling in Fig. 9.16 is not realistic.

The interface between the alluvium and the pleistocene deposit (15 m below surface) demonstrates a remarkable change in fines content due to discontinuity in age and material type (unconformity 不整合); older deposit was eroded while the sea level was low and then new material started to deposit. The associating variation of S wave velocity ( $V_s$ ) is so significant as well, and may be modeled by a discontinuity (Fig. 9.11) for practice.

The underlying pleistocene deposits has some significant change in fines content due probably to the variation of sedimentary environment. However,  $V_s$  is still continuous, although it varies with depth.

From these observations, it seems reasonable to state that the real natural ground has a continuous variation of S wave velocity and, in general, the discontinuous modelling may not be appropriate. Discontinuous modelling seems reasonable only at unconformity where both age and type of soil vary suddenly. The effects of continuous and discontinuous modellings were studied in dynamic analyses by the author (Towhata, 1996).

## 9.10 Equivalent Linear Modeling

The major nonlinearity in stress–strain behavior of soil is detected in two points

1. Shear modulus,  $G$  (more precisely, secant shear modulus) that decreases as the strain amplitude increases.
2. A hysteresis loop in shear stress–strain relationship and the damping ratio that increases with the strain amplitude.

The nonlinearity is taken into account in analysis in several ways. First, the stress–strain behavior can be modeled in detail by elastoplasticity (Chap. 10) possibly combined with viscosity. This approach requires many input parameters, which are determined by elaborate laboratory soil testing on specimens of good quality. Therefore, there is a general impression that this approach is good but time consuming. Moreover, it is common that many elastoplastic models give different results.

The second method is the equivalent linear method for which a closed-form solution of motion is available (Sect. 9.5). Although there are many limitations, this approach has been widely used because of its easy use. Therefore, two types of soil data have to be prepared:

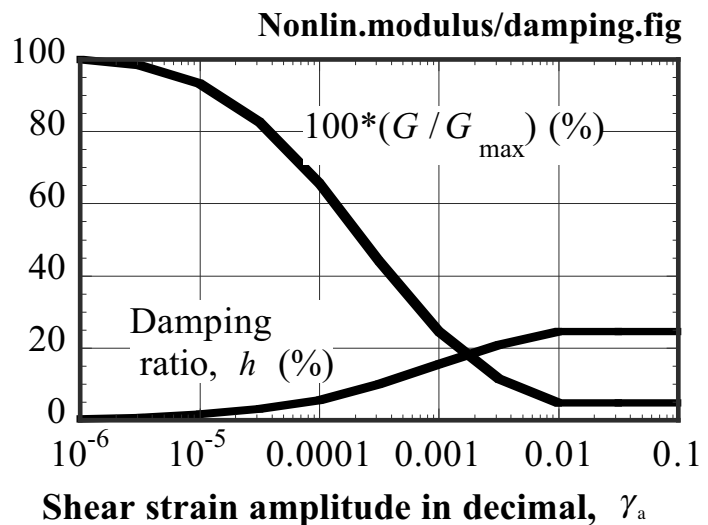
1. Shear modulus at small strain amplitude that is typically  $10^{-6}$  ( $=10^{-4}\%$ ) or less. Most field investigation technologies (downhole survey, PS logging, etc. in Chap. 7) generate this magnitude of strain. Hence,  $V_s$  measured insitu directly gives this small-strain modulus. This modulus is denoted by  $G_{\max}$  or  $G_0 = \rho V_s^2$ .
2. Nonlinearity of soil expressed by variation of  $G$  and  $h$  (damping ratio) with the strain amplitude  $\gamma_a$  during cyclic loading. Since  $G_{\max}$  is already known above, test data on variation of  $G/G_{\max}$  and  $h$  against  $\log_{10}(\gamma_a)$  is widely used. See Fig. 9.19.

Although the real soil behavior under cyclic loading is much more complicated than expressed by  $G$  and  $h$ , the dynamic response of ground is most strongly affected by these two parameters.

Many laboratory tests have been carried out to measure the data in such a manner as shown in Fig. 9.19. In this sense, the

equivalent linear modeling in terms of  $\tau = G(1 + 2ih)\gamma$  is a standard approach to soil dynamics. It is fortunate that  $G/G_{\max}$  and  $h$  vs. strain curves are not much affected by most soil conditions, e.g., effective stress level, fines content, overconsolidation, etc. The effects of these factors appear in  $G_{\max}$  itself. Therefore, only  $G_{\max}$  should be determined with reference to insitu investigation (原位置試験). Only soil types, sand or clay, affect the shape of curves (later topic).

In practice, the curves in Fig. 9.19 are seldom measured directly. They are obtained from literatures reported on soils that are similar to the concerned one.



**Fig. 9.19** Example of soil data on nonlinear stress-strain behaviour (0.01 strain = 1% strain)

### 9.11 Theory of Fourier Series

Although the time history of a real earthquake motion is irregular, the equivalent linear technique of dynamic response analysis makes use of a harmonic base motion (Sect. 9.1). This is because any irregular time history can be divided into harmonic components by using the theory of Fourier series. Response analysis is made of harmonic components and the calculated responses are added together to obtain an irregular response.

Discussion is made of a Fourier series expansion of 16 data in Fig. 9.20;  $u(k)$ ,  $k = 0-15$ . Note that an identical time history is repeated before  $k = 0$  and after  $k = 16$  due to the nature of harmonic functions (*sin* and *cos*). The Fourier series of this time history is given by summation of the following terms,

	$u(k) = -0.25$	Series 0
+	$(1.22 + 0.24i) \exp\left(\frac{2\pi i}{16} k\right)$	1
+	$(-0.08 - 1.20i) \exp\left(\frac{4\pi i}{16} k\right)$	2
+	$(0.14 - 0.39i) \exp\left(\frac{6\pi i}{16} k\right)$	3
+	$(-0.94 - 0.06i) \exp\left(\frac{8\pi i}{16} k\right)$	4
+	$(0.50 - 0.34i) \exp\left(\frac{10\pi i}{16} k\right)$	5
+	$(-1.05 + 0.05i) \exp\left(\frac{12\pi i}{16} k\right)$	6
+	$(0.13 + 0.54i) \exp\left(\frac{14\pi i}{16} k\right)$	7
+	$0.38 \exp\left(\frac{16\pi i}{16} k\right)$	Nyquist, 8
+	$(0.13 - 0.54i) \exp\left(\frac{-14\pi i}{16} k\right)$	9
+	$(-1.05 - 0.05i) \exp\left(\frac{-12\pi i}{16} k\right)$	10
+	$(0.50 + 0.34i) \exp\left(\frac{-10\pi i}{16} k\right)$	11
+	$(-0.94 + 0.06i) \exp\left(\frac{-8\pi i}{16} k\right)$	12
+	$(0.14 + 0.39i) \exp\left(\frac{-6\pi i}{16} k\right)$	13
+	$(-0.08 + 1.20i) \exp\left(\frac{-4\pi i}{16} k\right)$	14
+	$(1.22 - 0.24i) \exp\left(\frac{-2\pi i}{16} k\right)$	15

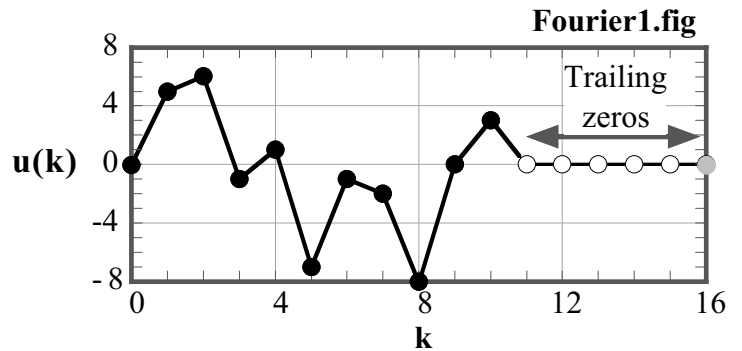


Fig. 9.20 Example of time history of ground motion,  $u(k)$

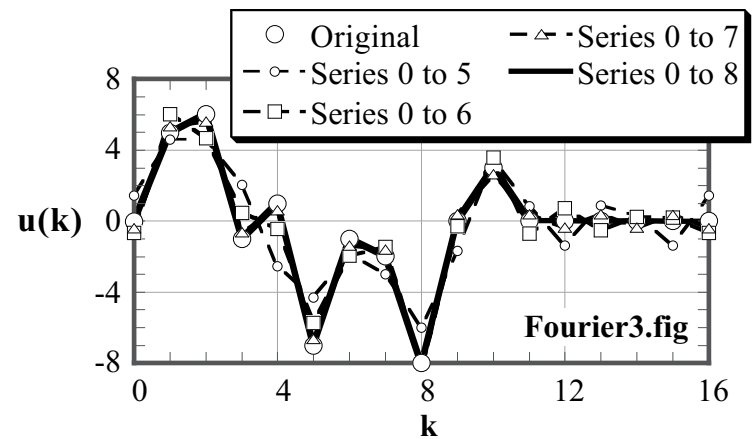
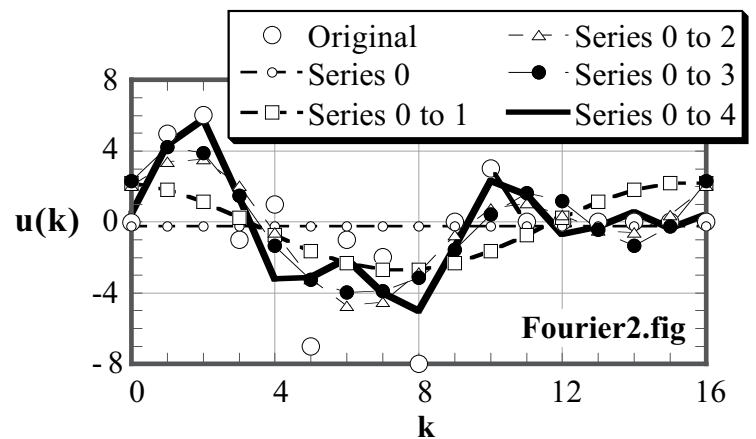


Fig. 9.21 Convergence of Fourier series

See the conjugate (複素共役) relationships of complex coefficients. The middle of the above series (Series 8) has the highest frequency. The frequency of this component is called the Nyquist frequency. Figure 9.21 shows that the Fourier series expansion approaches the original function as components of higher frequencies are added. Trailing zeros in Fig. 9.20 is added to the original time history of earthquake motion in order (1) to account for the fact that the earthquake motion ceases after some time and (2) to make the total number of data a power of 2 (2のべき) such as 256, 512, and 1,024 that make easy the fast Fourier transformation (FFT).

In principle, a Fourier series consists of *sin* and *cos* functions.

$$\begin{aligned}
 u(k) &= \sum_{m=0}^{N-1} C_m \exp\left(\frac{2\pi mk}{N} i\right) \\
 &= \sum_{m=0}^{N-1} C_m \left( \cos \frac{2\pi mk}{N} + i \sin \frac{2\pi mk}{N} \right), \tag{9.12}
 \end{aligned}$$

where  $k = 0, 1, 2 \dots N-1$  and  $C_{N-m} = C_m^*$ : conjugate relationship.

Note that each component with “k” in (9.12) has a period of

$$\begin{aligned}
 \frac{2\pi m \times \text{Period}}{N} &= 2\pi \\
 \text{Period} &= \frac{N}{m}. \tag{9.13}
 \end{aligned}$$

if  $m \leq N/2$ .

Being a combination of periodical *sin* and *cos* functions, (9.12) means that exactly identical  $u(k)$ s appear after a certain number. Figure 9.22 illustrates this nature. Note that the trailing zeros effectively separate two neighboring time histories. Without zeros, the earthquake motion in the analysis is repeated without a stationary period and consequently the calculated response would be an overestimation. Those zeros erase the influence of the previous cycle of the imaginary earthquake (from  $k = -16$  to  $-1$  in Fig. 9.22).

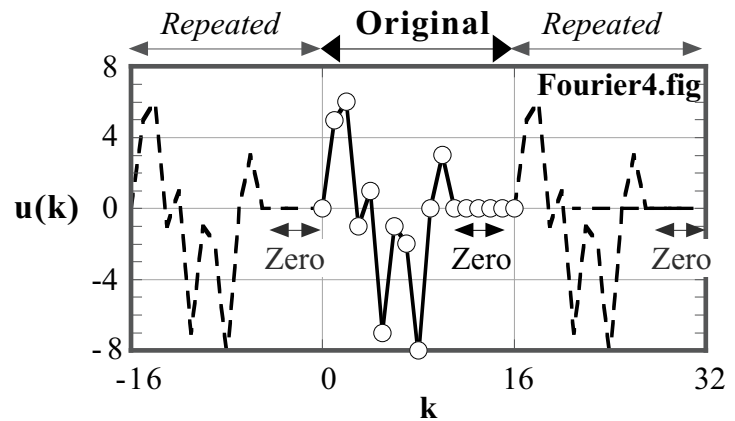


Fig. 9.22 Repeated nature of Fourier series

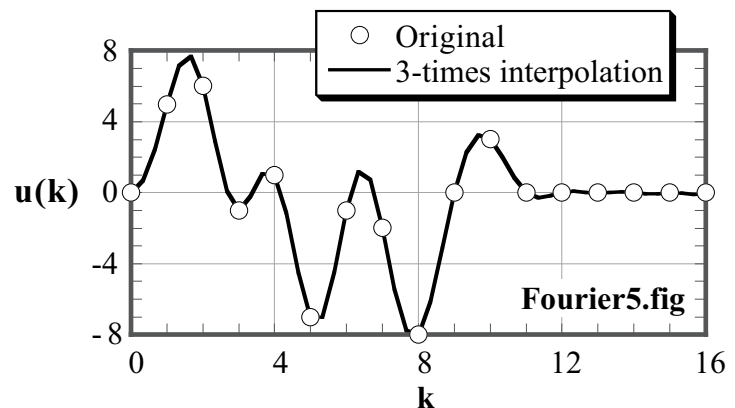


Fig. 9.23 Interpolated time history of Fourier series

Therefore, a sufficient number of trailing zeros should be added to the input motion data. Moreover, the technique of “fast Fourier transformation,” which accelerates the equivalent linear analysis, needs to make the total number of motion data equal to any power of 2, e.g., 512, 1,024, 2,048, etc. Since the number of given earthquake motion data is not necessarily a power of 2, the trailing zeros are used to satisfy the requirement from FFT.

In Fig. 9.23, the values of the Fourier series expansion were calculated at interpolated points of  $k = 1/3, 2/3, 4/3, 5/3$ , etc. By comparing the interpolated values with the original time history, it is found that the new magnitude of the interpolated motion is somewhat greater than the original one. Therefore, the use of the equivalent linear analysis with Fourier series expansion may overestimate the magnitude of input motion and, accordingly, the response of the surface subsoil during earthquakes.

**9.12 Spectrum Analysis by Fourier Series**

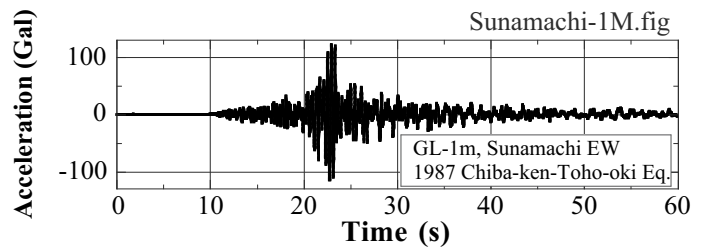
The theory of Fourier series has been applied to interpretation of earthquake motion records. Figure 9.24 shows the time history of acceleration at the top of an alluvial deposit (depth being GL -1m) in Tokyo during the 1987 Chiba-ken-Toho-oki (千葉県東方沖地震) earthquake. It may be seen that this motion has a predominant period of around 1.0 s. This surface motion is compared with the motion at the bottom of the alluvial layer (at the depth of GL -89 m) in Fig. 9.25. While the intensity of motion is much weaker in the bottom motion (Fig. 9.25), the predominant period of around 1.0 s is not evident. It seems that the motion of 1.0 s period was produced by the amplification in the alluvial soil (Sect. 6.8).

The time history of an earthquake motion record is expressed by means of Fourier series

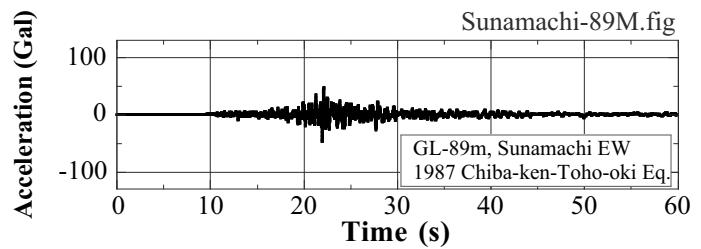
$$u(t) = \sum_{m=0}^{N-1} C_m \left( \cos \frac{2\pi mt}{T} + i \sin \frac{2\pi mt}{T} \right) \text{ or } u(k\Delta t) = \sum_{m=0}^{N-1} C_m \left( \cos \frac{2\pi mk\Delta t}{T} + i \sin \frac{2\pi mk\Delta t}{T} \right), \quad (9.14)$$

in which the time interval of the original digital data is  $\Delta t$  and the total number of data is  $N$ ; hence, the entire duration time of the record is  $T = N\Delta t$ . Therefore, each of the component with “m” has its own period of  $T/m$  and the frequency of  $m/T$  (Hz). On the other hand, the absolute value of  $C_m$  in (9.14) stands for the intensity of each frequency component.

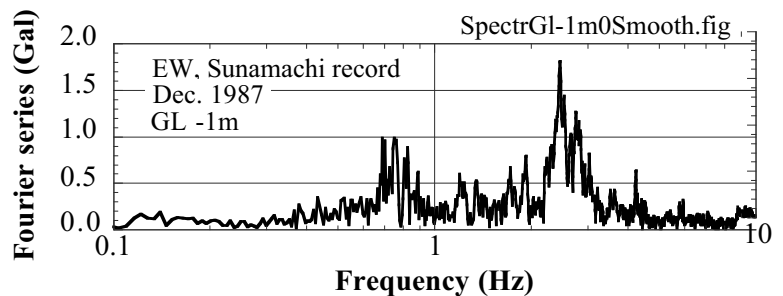
Figure 9.26 illustrates the relationship between  $|C_m|$  and  $m/T$ , and is called the Fourier spectrum in this text. Figure 9.26 indicates that the motion is intense at the frequency of 0.8 Hz and 2.4 Hz; the former being the predominant component, which was mentioned above. In contrast, the Fourier spectrum of the base motion (Fig. 9.27) does not have a peak spectrum value at 0.8 Hz. This implies that the alluvial



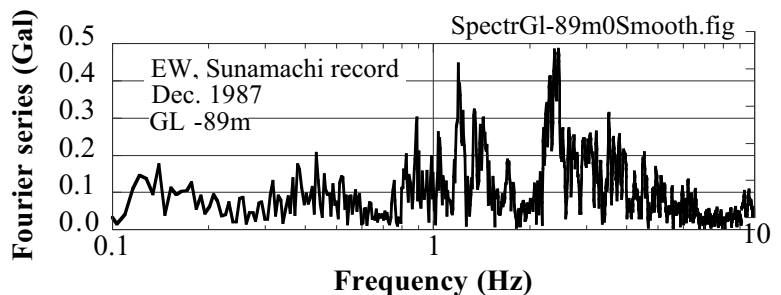
**Fig. 9.24** Time history of surface acceleration at Sunamachi site in Tokyo during the 1987 Chiba-ken-Toho-oki earthquake



**Fig. 9.25** Time history of acceleration at the bottom of Sunamachi site in Tokyo during the 1987 Chiba-ken-Toho-oki earthquake



**Fig. 9.26** Fourier spectrum of Sunamachi surface acceleration record



**Fig. 9.27** Fourier spectrum of Sunamachi base acceleration record



soil made this frequency component stronger, which is called amplification. Note further that both spectra (Figs. 9.26 and 9.27) have peaks at 2.4 Hz. It seems therefore that this particular predominant component of acceleration was produced in the deeper deposit or the source mechanism of earthquake. Note moreover that the strong component at around 1.3 Hz in the base motion (Fig. 9.27) disappeared in the surface motion (Fig. 9.26).

A possible draw-back of the spectra shown above is that the variation of the spectrum value fluctuates significantly, making it difficult to exactly determine the predominant frequency, frequency at which the spectrum is maximum. To solve this problem, smoothing technique was developed. Figure 9.28 demonstrates an example of smoothing in which the spectrum valued prior to smoothing is modified by

$$\text{new } S_k = 0.25S_{k-1} + 0.50S_k + 0.25S_{k+1} \quad (9.15)$$

to be a smoothed spectrum. Equation (9.15) is called Hanning Window, and another formula of

$$\text{new } S_k = 0.23S_{k-1} + 0.54S_k + 0.23S_{k+1} \quad (9.16)$$

is called Hamming Window. Since

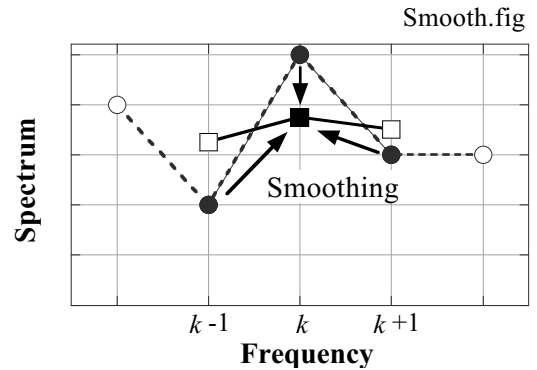
$$0.25+0.50+0.25=1.0 \quad \text{and} \\ 0.23+0.54+0.23=1.0,$$

the use of these smoothing does not artificially reduce the energy of an acceleration record.

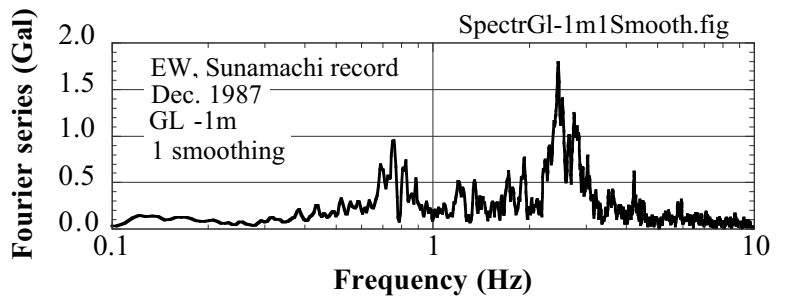
Figure 9.29 reveals the smoothing of the Sunamachi surface motion. It is found here that the spectrum still has a significant extent of fluctuation. Thus, one time of smoothing is not sufficient. Consequently, the Hanning Window was repeated up to 100 times: Figure 9.30 after 10 times of smoothing may not be sufficient. Figure 9.31 after 100 times of smoothing appears good. Thus, smoothing has to be repeated so many times until a good smoothed spectrum is obtained.

The amplification of motion,  $AMP(E+F)$  in Sects. 6.8 and 9.6 is calculated by taking the ratio of Fourier spectra at two depths

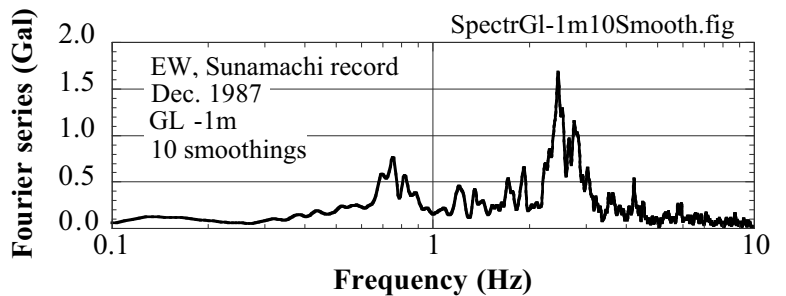
$$Amp(E + F) = \frac{\text{Spectrum at surface}}{\text{Spectrum at base}} \quad (9.17)$$



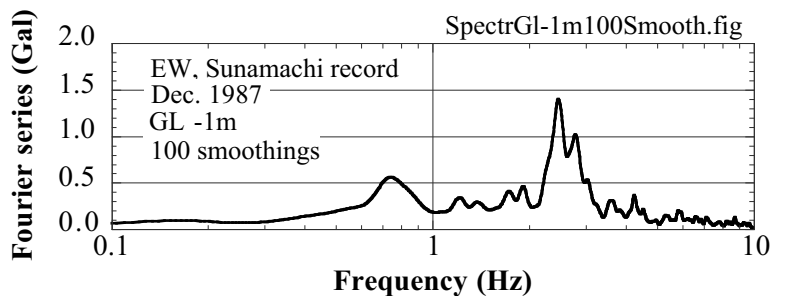
**Fig. 9.28** Example of spectrum smoothing



**Fig. 9.29** Fourier spectrum of Sunamachi surface motion after one time of Hanning Window



**Fig. 9.30** Fourier spectrum of Sunamachi surface motion after ten times of Hanning Window



**Fig. 9.31** Fourier spectrum of Sunamachi surface motion after 100 times of Hanning Window

It is certainly necessary to do smoothing for this ratio as well. Figure 9.32 presents the amplification thus obtained. Clearly, the amplification factor is very large at 0.8 Hz. It is reasonable, therefore, to say that the natural frequency of the Sunamachi site is 0.8 Hz and a design of a structure should avoid its natural period near 0.8 Hz in order not be troubled by resonance and significant earthquake response.

One common mistake made by unexperienced programmers in smoothing is a use of

$$S(K)=0.25*S(K-1)+0.5*S(K)+0.25*S(K+1).$$

This program changes the value of  $S(K)$  and the next step of smoothing

$$S(K+1)=0.25*S(K)+0.5*S(K+1)+0.25*S(K+2)$$

is made erroneous. One should do as what follows:

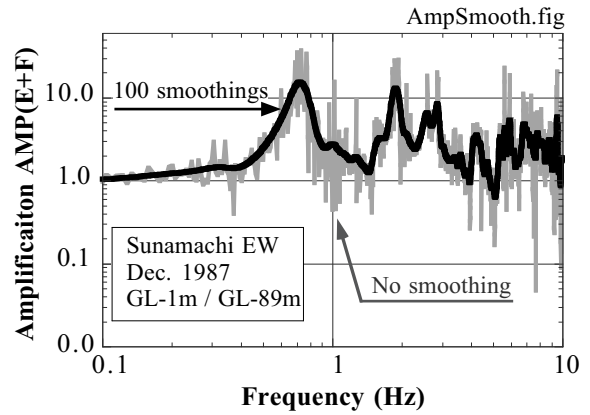
$$SK=0.25*S(K-1)+0.5*S(K)+0.25*S(K+1)$$

.....

$$SKP1=0.25*S(K)+0.5*S(K+1)+0.25*S(K+2)$$

$$S(K)=SK$$

$$SK=SKP1 \quad (\text{repeated for increasing } K)$$



**Fig. 9.32** Amplification of motion before and after 100 times of Hanning Window

### 9.13 Dynamic Analysis with Equivalent Linear Model

In practice, the equivalent linear modeling ( $G/G_{\max}$  and  $h$  vs.  $\gamma_a$ ) is combined with a harmonic base motion to analyze the dynamic response of ground. Since the real base motion during earthquakes is not harmonic, its irregular time history is deconvoluted (divided) into harmonic components (Fourier series expansion), individual response to a harmonic component is calculated, and all the responses are combined to obtain the irregular response.

Since  $G$  and  $h$  vary with the strain amplitude, it is necessary to determine the representative strain amplitude out of an irregular time history so that strain compatible modulus and damping may be determined. Since this is possible only after analysis, the analysis has to be repeated with trials and errors on selection of strain. The flow chart is demonstrated in Fig. 9.33. A level ground with horizontal layers is assumed.

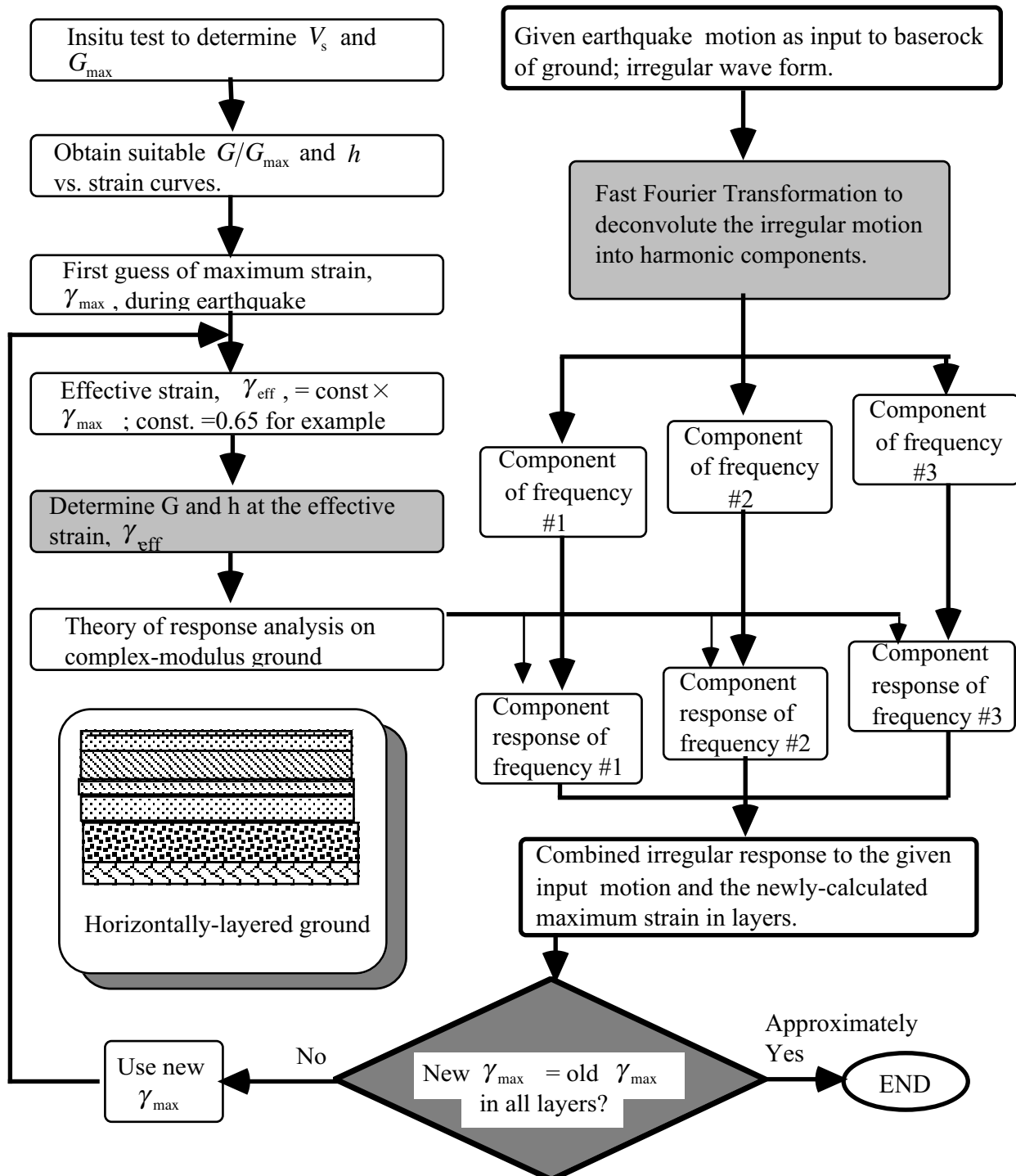
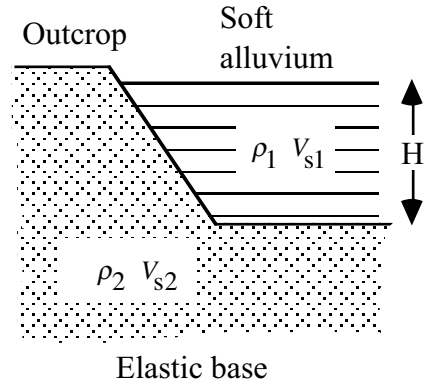


Fig. 9.33 Flow chart of equivalent linear analysis

**9.14 Example of Equivalent Linear Analysis**

A brief example of an equivalent linear analysis is presented here. Figure 9.34 illustrates a model of ground that has a 7 m soft alluvium at the surface together with an elastic base. Such a field exploration as down-hole investigation has presented  $V_s = 150$  m/s in the alluvium and  $V_s = 500$  m/s in the base, respectively. Since the field exploration can generate only a small amplitude of shear strain (for example, of the order of  $10^{-7}$ ), the dynamic analysis has to pay further attention to strain amplitude effects.



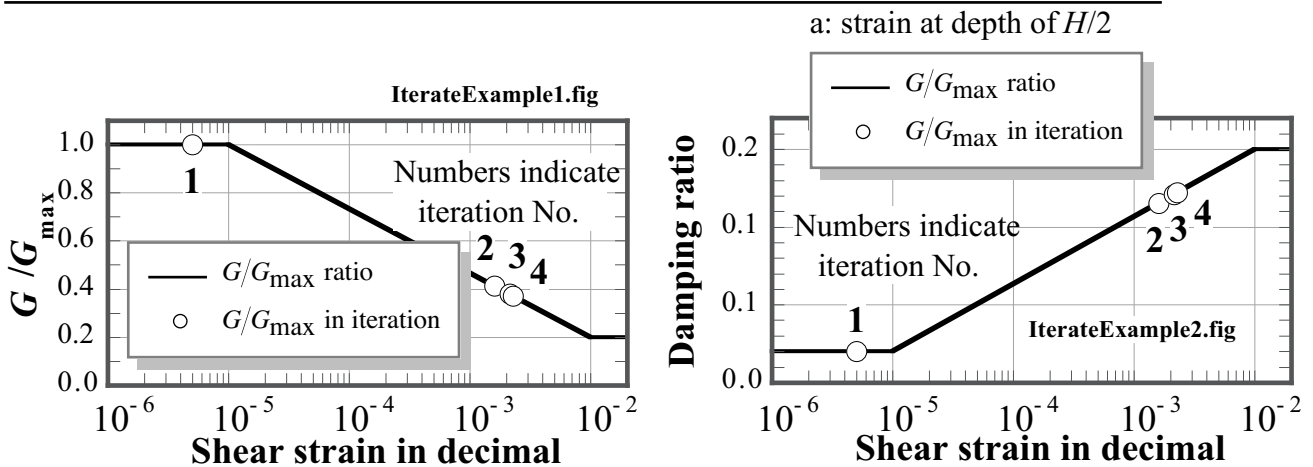
**Fig. 9.34** Model of subsoil

Laboratory tests on undisturbed soil specimens revealed the degradation of shear modulus and the variation of damping ratio with the amplitude of shear strain, which are illustrated by solid curves in Fig. 9.35. The modulus or  $V_s$  as well as the damping ratio is modified in accordance with the estimated shear strain until a good convergence 収束 is obtained.

The present analysis assumes a harmonic shaking of 3 Hz and the outcrop amplitude of acceleration to be  $4 \text{ m/s}^2$  ( $2E\omega^2 = 400$  Gal in the surface deposit). Table 9.1 indicates the procedure of iteration 繰り返し計算. Note that, since the shaking is harmonic, the shear strain amplitude ( $\gamma_{\text{max}}$ ) obtained by a previous iteration is directly used as the estimated strain ( $\gamma_{\text{eff}}$ ) in the next iteration without multiplying by 0.65 (Sect. 9.13). The modulus and damping ratio at this strain are employed in the next dynamic analysis.

**Table 9.1** Sequence of iteration

No. of iteration	Assumed shear strain amplitude <sup>a</sup>	$G/G_{\text{max}}$	Damping ratio	Obtained surface acceleration	Obtained shear strain
1	$5 \times 10^{-6}$ : initial guess	1.0000	0.0200	4.72 m/s <sup>2</sup>	$1.59 \times 10^{-3}$
2	$1.59 \times 10^{-3}$	0.4132	0.1154	4.05	$2.14 \times 10^{-3}$
3	$2.14 \times 10^{-3}$	0.3795	0.1208	4.27	$2.28 \times 10^{-3}$
4	$2.28 \times 10^{-3}$	0.3714	0.1222	4.33	-----



**Fig. 9.35** Variation of material properties with the progress of iteration

Since the difference between the 3rd and 4th iterations is negligible, a good convergence was obtained and the results of the 4th iteration are reported as final. Figure 9.35 indicates the variation of  $G/G_{\text{max}}$  and the damping ratio with the progress of iteration.

**Exercise No. 5 Equivalent Linear Method of Analysis**

The nonlinear stress–strain relationship of soils is replaced by an equivalent complex modulus model and, thereby, the equation of wave propagation is made linear. In this exercise, the soil property is specified by a hyperbolic model by Hardin and Drnevich (1972) (see Fig. 9.36) in which the skeleton curve that connects two ends of hysteresis loops is defined by

$$\tau = \frac{G_{\max}\gamma}{1 + |\gamma/\gamma_r|} \tag{9.18}$$

where  $\gamma_r$  is called the reference strain. Equation (9.18) gives the secant modulus,  $G \equiv \tau/\gamma$

$$\frac{G}{G_{\max}} = \frac{\tau}{G_{\max}\gamma} = \frac{1}{1 + |\gamma/\gamma_r|} \tag{9.19}$$

Moreover, the damping ratio,  $h$ , is modeled by

$$h = h_{\max} \left( 1 - \frac{G}{G_{\max}} \right) \tag{9.20}$$

which fits the experimental knowledge.

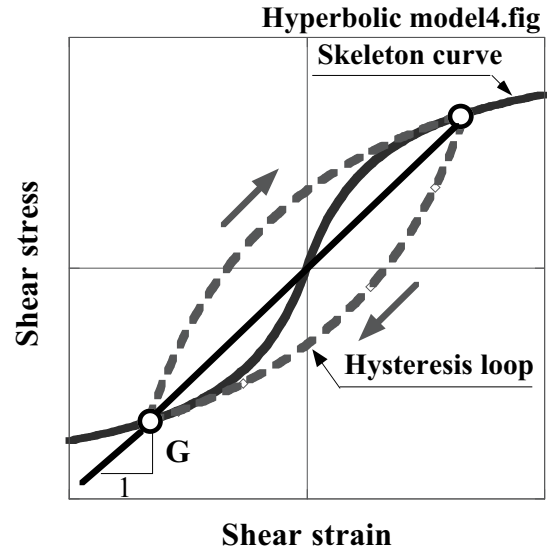
Run an equivalent linear analysis on a two-layered ground in Fig. 9.37 with a harmonic outcrop motion (正弦波) of  $2E = 0.2 \text{ m/s}^2$  and  $2 \text{ m/s}^2$ . The frequency is set equal to  $5 \text{ Hz}$ . The material properties are indicated in Table 9.2.

**Table 9.2** Material properties

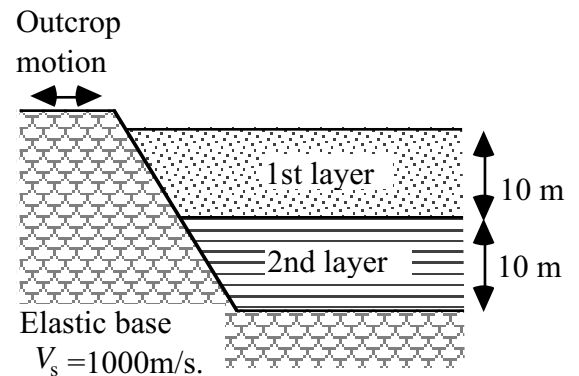
Layer	Mass density, $\rho$	$V_s$	$\gamma_r$	$h_{\max}$
1	2 g/cm <sup>3</sup>	150 m/s	$1.1 \times 10^{-3}$	0.20
2	2 g/cm <sup>3</sup>	350 m/s	$3.0 \times 10^{-3}$	0.15
Base	2 g/cm <sup>3</sup>	1,000 m/s	----	----

0.00

Summarize the procedure of trial-and-error and convergence in a table as shown below. The strain-consistent  $G/G_{\max}$  and damping ratio are calculated by using  $\gamma_{\text{eff}} = 1.00 \times \gamma_{\max}$  at the middle depth of each layer. Do be careful of unit conversion!



**Fig. 9.36** Model of stress–strain behaviour



**Fig. 9.37** Soil profile

To avoid common mistakes of students

- In layer 1,  $G_{\max} = 2 \times 150^2 \text{ kPa}$ .  
 $\rho$  is not  $2 \times 9.8$  but 2.
- $E_b$  of the outcrop motion is not  $2 \text{ m/s}^2$   
It is  $2 \div 2 \div \omega^2 \text{ m}$  because  $E_b$  is the amplitude of displacement.

The answer will be as what follows; see the answer of exercises at the end of this book.

Base acceleration	Surface acceleration	Amplification Amp( $E+F$ )
0.20	0.32	1.6
2.0	2.653	1.3

The amplification was made different by the nonlinear behavior of soil. The greater acceleration increased the shear strain in the soil, and reduced the shear modulus, while increasing the damping ratio. Consequently, the natural period of ground changed, and more energy was lost due to damping. Thus, the amplification during strong earthquakes is smaller than amplification during minor shaking.

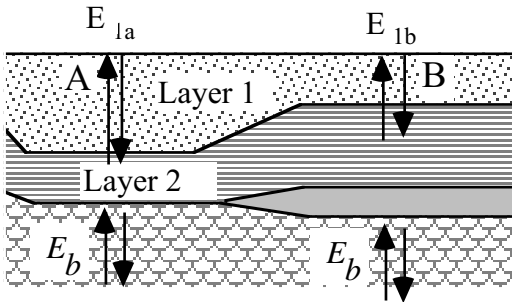
Example: Outcrop motion is of  $5 \text{ m/s}^2$  in amplitude and 1 Hz in frequency

Iteration	1st Layer				2nd layer				Surface acc.
	Assessed strain	Shear modulus	Damping ratio	Obtained strain	Assessed strain	Shear modulus	Damping ratio	Obtained strain	
1	0.0020	16,000 kPa	0.129	0.0041	0.0010	184,000 kPa	0.037	0.0010	6.811
2	0.0041	9,610	0.157	0.0078	0.0010	185,000	0.037	0.0010	8.071
3	0.0078	5,580	0.175	0.0180	0.0010	182,000	0.039	0.0013	11.257
4	0.0180	2,590	0.189	0.0449	0.0013	172,000	0.044	0.0010	13.908
5	0.0449	1,080	0.195	0.0334	0.0010	184,000	0.037	0.0002	5.087
6	0.0334	1,440	0.194	0.0347	0.0002	227,000	0.011	0.0002	6.572
7	0.0347	1,380	0.194	0.0344	0.0002	229,000	0.010	0.0002	6.312

**9.15 Deconvolution of Earthquake Motion**

The equivalent linear technique is further useful when the base incident motion has to be assessed by using the measured surface motion. This procedure is called “deconvolution.” Figure 9.38 illustrates a situation in which the surface motion at site “A” ( $E_{1a}$ ) is known and the incident motion in the base ( $E_b$ ) is desired. The assessed  $E_b$  will later be put in at the base of another site “B” in order to calculate the surface motion ( $E_{1b}$ ). Although  $E_{1a} \neq E_{1b}$ ,  $E_b$  at two sites are identical.

In the following example, the subsoil condition as in Table 9.3 is employed at the site A.



**Table 9.3** Material properties in the example

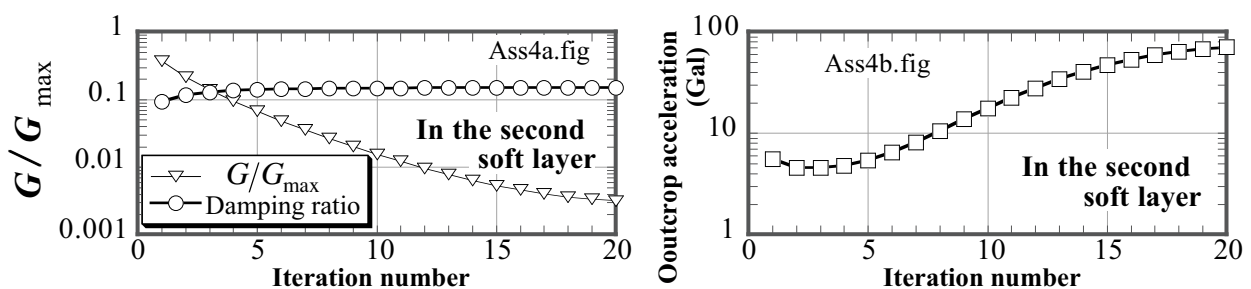
Layer	Thick-ness	Mass density	$V_s$	$\gamma_r$	$h_{max}$
1	10 m	2 g/cm <sup>3</sup>	150 m/s	$1.1 \times 10^{-3}$	0.20
2	10 m	2 g/cm <sup>3</sup>	350 m/s	$3.0 \times 10^{-3}$	0.15
Base		2 g/cm <sup>3</sup>	1,000 m/s		0.00

**Fig. 9.38** Deconvolution

Assuming that the surface motion at “A” is specified by  $2E_{1a} = 2.653 \text{ m/s}^2$  and 5 Hz, the deconvolution procedure of iteration is shown in what follows. Note that the solved situation at “A” is same as the one in Exercise 3 with the outcrop motion of  $2 \text{ m/s}^2$ . The outcrop acceleration ( $2E_b$ ) converged to  $2 \text{ m/s}^2$  as expected.

Iteration	Layer 1				Layer 2				Surface accel. ( $\text{m/s}^2$ ) ( $2E_b$ )
	Estimated strain	Shear modulus (kPa)	Damping ratio	Obtained strain	Estimated strain	Shear modulus (kPa)	Damping ratio	Obtained strain	
1	0.0100	4,460	0.180	$1.02e-3$	0.0050	91900	0.094	$4.67e-4$	2.431
2	$1.02e-3$	23,400	0.096	$7.74e-4$	$4.67e-4$	222000	0.020	$1.05e-5$	1.976
3	$7.74e-4$	26,400	0.083	$7.17e4$	$1.05e-5$	237000	0.005	$7.52e-5$	2.010
4	$7.17e-4$	27,200	0.079	$7.03e-4$	$7.52e-5$	239000	0.004	$6.93e-5$	2.002
5	$7.03e-4$	27,500	0.078	$7.00e-4$	$6.93e-5$	239000	0.003	$6.79e-5$	1.999
end	$7.00e-4$	27,500	0.078	$7.00e-4$	$6.79e-5$	240000	0.003	$6.80e-5$	

The second example uses  $2E_{1a} = 5 \text{ m/s}^2$  and 2 Hz while making the second layer *very thin* (0.5 m thick) and *very soft* ( $V_s = 80 \text{ m/s}$ ), while making the first layer thick (19.5 m) with  $V_s = 150 \text{ m/s}$ . The material properties in the second soft layer as well as the assessed outcrop motion did not converge (see Fig. 9.39). Such a problematic situation is often encountered in practice where the observed surface motion is too strong when a subsoil appears to be very soft. In reality, most probably the soft thin layer is nothing more than a local small deposit and does not extend to infinity as assumed in analysis. Such a local clay pocket should be ignored in practical analysis, although a single boring data cannot reveal its lateral size.



**Fig. 9.39** Example deconvolution without reaching convergence

It is meaningful to herewith introduce an example of unsuccessful deconvolution, because a similar problem is not uncommon in practice. Figure 9.40 shows the site where a deconvolution was attempted. This area was once a sea thousands of years ago when the sea level was higher than the present level. Sediments from several big rivers deposited here, and those rivers have been flooding frequently during the human period when the sea level retreated a few meters. Consequently, there remained many ponds and swamps until recent times. In the past decades, this area has been developed as a residential area.

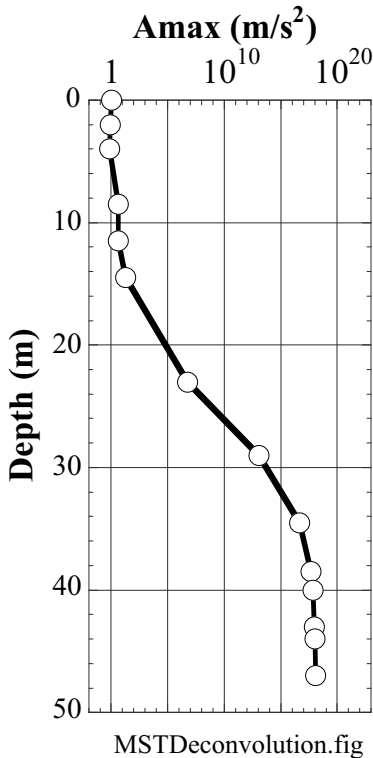
Figure 9.41 illustrates the outside of a building where an earthquake motion was recorded. Note the differential settlement around the building due to the ongoing consolidation of the soft subsoil. Many cracks have occurred inside this building as well. The convolution of this surface motion was the aim of the analysis.



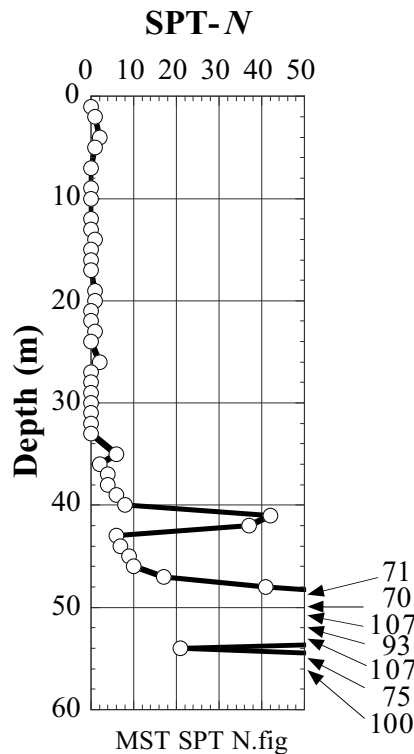
**Fig. 9.40** Soft ground condition at site of deconvolution



**Fig. 9.41** Differential settlement around building



**Fig. 9.42** Poor results of deconvolution



**Fig. 9.43** Soil profile at site of deconvolution

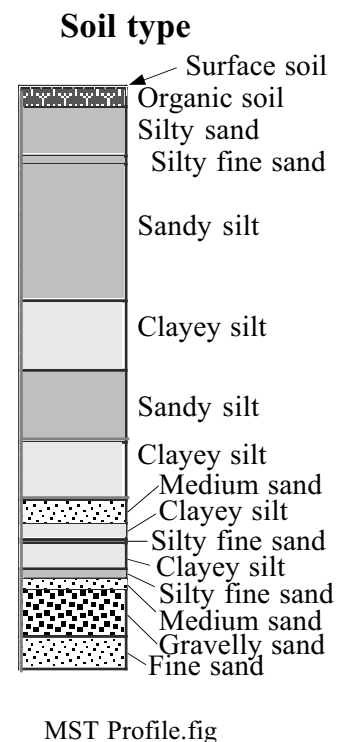


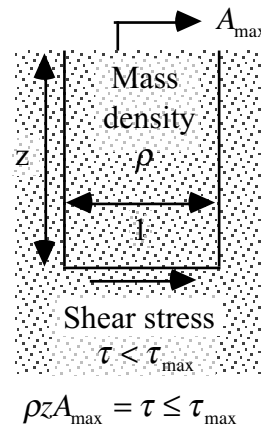


Figure 9.42 demonstrates an unsuccessful result in which the surface recorded acceleration was  $1.01 \text{ m/s}^2$  while the calculated bottom motion became as large as  $10^{18} \text{ m/s}^2$ . This result is certainly nonsense. The reason for this problem lies in the extremely soft soil condition. As illustrated in Fig. 9.43, there is a very thick deposit of silty materials in which SPT- $N$  value is 0 or 1. This low value of SPT- $N$  made  $G_{\text{max}}$  very small in the analysis (8.10), and created low  $G = G_{\text{max}}(G/G_{\text{max}})$  as well. Consequently, the shear stress level in the soft subsoil was not high enough to account for the recorded acceleration of  $A_{\text{max}} = 1 \text{ m/s}^2$  in the top soil;

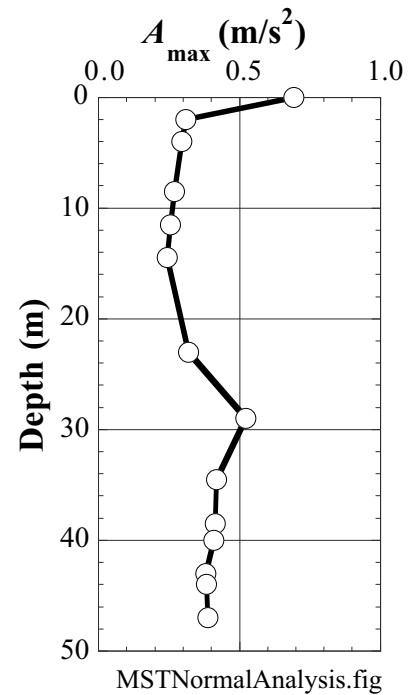
The equation of motion of the top soil (Fig. 9.44) states that the maximum acceleration,  $A_{\text{max}}$ , in the surface soil is limited by the shear strength in the subsoil,  $\tau_{\text{max}}$ , if the assumption of one-dimensional stratification is acceptable.

Moreover, many analyses were run on the same profile, while changing the intensity of input acceleration at the bottom. As shown in Fig. 9.45, it was not possible to reproduce the surface acceleration of  $1 \text{ m/s}^2$ . The reduction of acceleration above the level of 30 m below the ground surface is evident.

Thus, it seems that the surface acceleration of  $1 \text{ m/s}^2$  was not caused solely by the vertical propagation of S wave. Most probably, the subsoil condition was of two- or three-dimensional configuration, the seismograph in the building recorded a very local dynamic phenomenon in the building, or else. The effect of surface waves (Sects 4.7 and 4.8) is unlikely because the thick deposit of soft soil induces significant energy dissipation and would not allow the propagation of surface waves over a long distance.



**Fig. 9.44** Equation of motion for surface soil undergoing S wave propagation in vertical direction



**Fig. 9.45** Normal analysis with specified acceleration amplitude at the bottom

### 9.16 Further Remarks on Equivalent Linear Model

- The equivalent linear model of  $\tau = G(1 + 2ih)\gamma$  is combined with (1) the theory of wave propagation in complex-modulus media and (2) the assumption of harmonic shaking. Therefore, dividing an irregular motion into harmonic components is necessary.
- The highest frequency employed in analysis is normally 10–15 Hz. For important rigid facilities, for example, nuclear power plants, 30 Hz may be the case.
- The comparison of old and new maximum strains are made by using  $G/G_{\max}$  and  $h$ . Those calculated by new and old maximum strains should be reasonably close to each other. When the difference is less than 1–5 %, the analysis is terminated (end).
- The number of iterations (trials and errors) is usually about 5–10, depending upon the required level of difference between new and old  $G$  and  $h$ .

#### Advantages of the method:

- The equation of wave propagation is rigorously solved from the mathematical viewpoint (厳密解). Therefore, a large thickness of layers does not make a serious error in computation. Hence, the computation time can be saved by using large thickness and reduced number of layers. This is in contrast with errors in finite element method and others that are generated by unacceptably large size of layers.
- There are many experimental  $G/G_{\max}$  and  $h$  data in literatures. Therefore, the preparation of input data is possible without running laboratory tests.

#### Disadvantages of the method:

- In real earthquakes,  $G$  and  $h$  are not constant from the beginning till the end of shaking, although the method assumes that they are constant.

Even in a single earthquake event, there is a stage in which the shaking and strain are small, whilst in other stage they are large (Fig. 9.46). Hence, it is more appropriate to use different values of  $G$  and  $h$  in different stages of shaking.

Dry sand subjected to cyclic loading of constant stress amplitude increases its  $G$  and decreases its  $h$  as the number of cycles increases (see Sect. 10.3).

Loose deposit of water-saturated sand undergoing heavy shaking, which is one of the most important subject of dynamic analysis, increases the excess pore water pressure with the number of cycles. Accordingly, the effective stress decreases with time. Since  $G$  of sand highly depends on the level of effective stress, it decreases with time. Therefore, the equivalent linear method combined with the theory of harmonic shaking should not be used on the strong earthquake response of loose sandy deposits.

It is empirically known, however, that the method of analysis is acceptable unless a complete loss of effective stress (liquefaction) occurs.

- The effective strain is calculated by  $\gamma_{\text{eff}} = 0.65 \times \gamma_{\max}$ . The parameter of 0.65 is just empirical and there is no theoretical background. It is maybe related to the electric theory of AC current. When the strain time history is exactly harmonic, in contrast, the parameter should be 1.0.

- The maximum acceleration in response is produced by harmonic components of high frequency. The strain amplitude of those

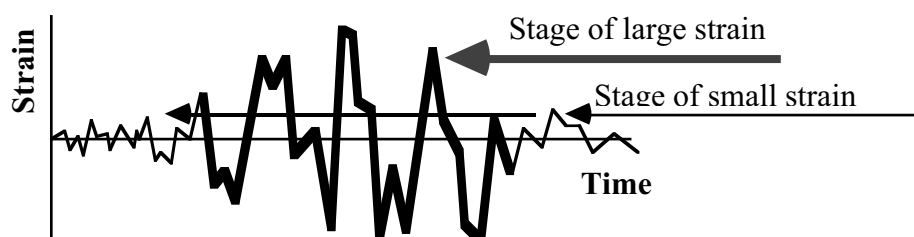


Fig. 9.46 Conceptual time history of strain with varying magnitude

components is normally small because their displacement amplitude is small, and hence large  $G$  and small  $h$  should be assigned to them. Since the method uses for all the frequency components common values of  $G$  and  $h$ , which are actually relevant for a larger strain amplitude, the high-frequency components are overdamped (過減衰) and the maximum acceleration is underestimated. Sugito et al. (1994) and Sugito (1995) improved this point by allocating different values of  $G$  and  $h$  to different frequency components in accordance with their respective strain amplitudes.

### List of References in Chapter 9

- Hardin, B.O. and Drnevich, V.P. (1972) Shear modulus and damping in soils; design equation and curves, Proc. ASCE, Vol. 98, SM7, 667–692.
- Idriss, I.M. (1990) Response of soft soil sites during earthquakes, Proc. H. Bolton Seed Memorial Symposium, pp. 273–290.
- Sugito, M. (1995) Frequency dependent equivalent strain for equi-linearized technique, Proc. First Int. Conf. Earthq. Geotech. Eng., Tokyo, Vol. 2, pp. 655–660.
- Sugito, M., Goda, H. and Masuda, T. (1994) Frequency dependent equi-linearized technique for seismic response analysis of multi-layered ground, Proc. JSCE, Vol. 493/III-27, pp. 49-58.
- Towhata, I. (1996) Seismic wave propagation in elastic soil with continuous variation of shear modulus in the vertical direction, Soils Found., Vol. 36, No. 1, pp. 61–72.

# Chapter 10

## Laboratory Tests on Dynamic Properties of Soils



Nirvana, the dying shape of Buddha in Boronnaruwa, Sri Lanka.

Bhuddism in its earliest stage was accepted in Sri Lanka and was then transferred to South East Asia. A legend states that Bhuddha's mother came down from the heaven to see him after his death, and Bhudda revived for a short time.

## 10.1 Resonant Column Tests of Soils

Laboratory testing skills have been needed to determine  $G/G_{\max}$  and  $h$  in a small strain range of  $10^{-6}$ – $10^{-2}$  (0.0001%–1%). It was, however, difficult in 1960s and 70s to precisely measure the stress–strain behavior in the small strain range ( $<10^{-4}$  approximately). The solution to this problem was the resonant column test (共振法試験).

The method of resonant column test was developed by K. Iida in 1930s. It became popular worldwide since 1950s. Firstly, Ishimoto and Iida (1936, 1937) developed both a theory and a device for resonant column tests on soils, in which the loading frequency at the maximum response was employed to determine elastic properties of soils. Since no confining pressure was able to be applied to consolidate specimens at their times, soil samples with fines and moisture, that could maintain shape without pressure application, were tested. Later, Iida (1938) carried out tests on dry sand which was supported by cellophane sheets. Since no effective stress was applied in these tests, the measured  $V_s$ , ranging from  $V_s = 50$  m/s to  $V_s = 200$  m/s, appears to be low.

This testing technique applies cyclic force to a soil specimen at various frequencies. The dynamic response of a specimen to this force is measured in terms of velocity and/or acceleration. While a precise measurement of small displacement (deformation) is difficult, velocity and acceleration at a high frequency are large enough to be measured. By varying the loading frequency, the variation of amplification in amplitude of response is plotted against the frequency. Fig. 10.1 illustrates the testing method conceptually and Fig. 10.2 is an idea of test results.

The soil specimen in Fig. 10.1 is fixed at the bottom and is subjected to torsion at the top. By applying the idea of wave propagation to torsion of a solid cylinder with a top mass, a theoretical value of resonant (natural) frequency is detected. By equating the theoretical and experimental resonant frequencies (Fig. 10.2), the shear modulus,  $G$ , is obtained.

For example, when there is no top mass in Fig. 10.1, the natural period of soil column,  $T_n$ , in torsional shear is given by

$$T_n = 4H/V_s$$

When the resonance or the maximum response occurs at the loading frequency of  $T_n^*$  (or the frequency of  $1/T_n^*$ ) in the test, this experimental value and the theoretical value are equated. Hence,

$$T_n^* = 4H/V_s, \quad V_s = \sqrt{G/\rho} = 4H/T_n^*, \quad \text{and} \quad G = \rho(4H/T_n^*)^2.$$

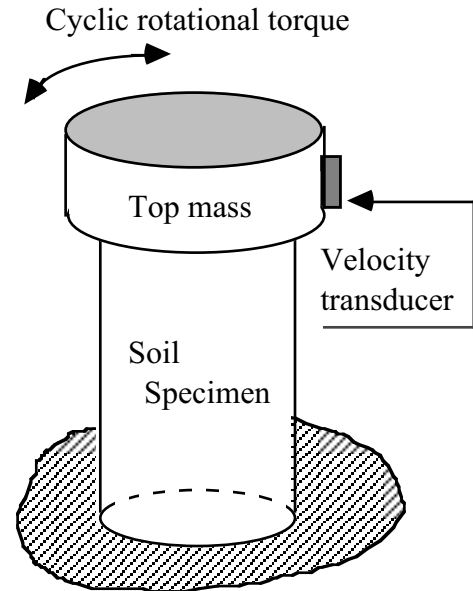


Fig. 10.1 Cylindrical specimen undergoing resonant column test

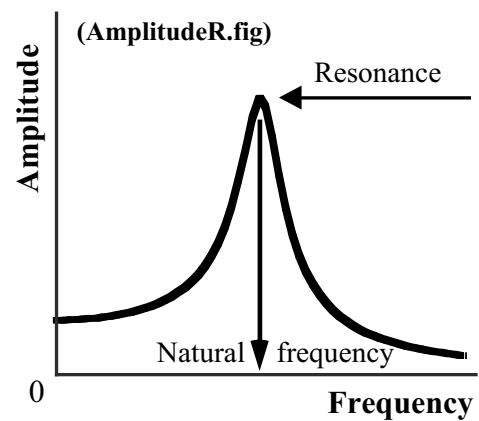


Fig. 10.2 Interpretation of resonant column test

The shear strain in a specimen (= top displacement/specimen height ) varies in the radial direction: zero at the center and maximum at the perimeter (円周). Hence, the average value is employed in interpretation. The damping ratio is obtained by using the logarithmic decrement (Fig. 9.8) or the maximum response of  $1/(2h)$  or  $1/\sqrt{2}$  of amplification (Sect. 9.4). It is noteworthy that resonant column tests give  $G$  and  $h$  after repeating more number of cycles of loading than what occurs in most earthquake events.

One of the limitations of resonant column tests is the number of loading cycles that a soil specimen experiences during tests. Since the number is significantly greater than that in real earthquakes, the obtained modulus and damping ratio correspond to those after many cycles. Note that earthquakes of magnitude = 7 or less have only a few significant shaking cycles (see Fig. 5.6 and Table 19.1). Another shortcoming is that resonant column tests on water saturated specimens under large strain amplitudes cause liquefaction (Ellis et al. 2000). This is because high frequency shaking makes free drainage of pore water impossible.

Recent developments in laboratory testing technique have made resonant column tests less important than before. This is because stress-strain data at small strain amplitude can be precisely measured today, which was impossible in and before 1970s. For example, a local displacement transducer (LDT) in Fig. 10.3 is able to record a very small displacement of  $0.25 \mu\text{m}$  (Goto et al. 1991). This sensitivity is equivalent with strain of  $1.25 \times 10^{-6}$  for a sample size of 20 cm.



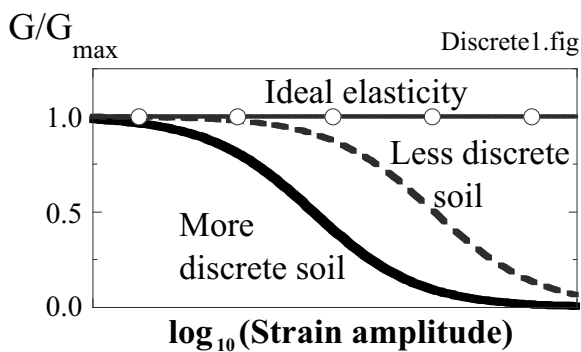
**Fig. 10.3** Local displacement transducer attached on triaxial shear specimen

## 10.2 General Principle in Interpretation of Strain Amplitude Effects on Shear Modulus and Damping Ratio

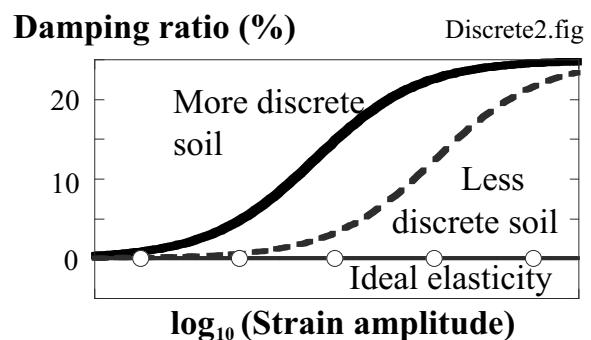
In 1970s and early 80s a plenty of experimental studies were made of nonlinearity of soil undergoing cyclic loading. They are summarized and presented in this chapter. It will be shown therein that such factors as particle size, effective stress level, plasticity of clays, and many others affect the variation of shear modulus and damping ratio with the strain amplitude. Since there are so many studies made so far, they may cause confusion among readers. To avoid this situation, one basic principle that governs the nonlinearity is briefly described in this section.

Shear modulus of an ideally elastic material is never affected by the strain amplitude. Damping ratio of an elastic material is null. This is an extreme situation on one hand. On the other hand, sand and, in particular, gravelly soils have a significant nonlinearity; shear modulus and damping ratio change with the strain amplitude. It is inferred therefore that the extent of nonlinearity varies with the discreteness of the concerned material. Discreteness means how the constituent particles of soil are separated from one another. This idea is schematically illustrated in Fig. 10.4 and Fig. 10.5. In more details,

1. In sand and gravels without fines, particles are not bonded. They simply maintain contact and friction. This situation is called highly discrete. Test results on sand and gravel, which will be presented later, exhibit more significant nonlinearity than those on clay (Sect. 10.6).
2. Moreover, the magnitude of effective stress in sand and gravel affects the nonlinearity. Higher stress generates more interaction among grains and reduces the discreteness. Consequently, the nonlinearity decreases. Conversely, sand and gravel under lower effective stress exhibit more nonlinearity. See Sects. 10.6 and 10.8.
3. Clays with greater plasticity index ( $PI=LL-PL$  in Sect. 1.1) have more connection among grains than less plastic clays. This connection is generated not only by the grain-to-grain contact forces (effective stress) but also by the increased electric and chemical interactions. Thus, more plastic clays are not so discrete as less plastic clays and sands. Consequently, the nonlinearity of plastic clays is not so significant as compared with other kinds of soils (Sects. 10.6 and 10.13).



**Fig. 10.4** Effects of discreteness of soils on nonlinearity in terms of variation of shear modulus with strain amplitude



**Fig. 10.5** Effects of discreteness of soils on nonlinearity in terms of variation of damping ratio with strain amplitude

### 10.3 Factors That Affect Modulus and Damping of Sand

There are many test results that studied the cyclic deformation of soils. It is known today that the following factors affect the shear modulus and damping ratio.

For shear modulus of sandy soils, first,

(1) strain amplitude, (2) effective stress, (3) density or void ratio, and (4) anisotropic consolidation.

On the contrary, the degree of overconsolidation (overconsolidation ratio, OCR) does not significantly affect the shear modulus of sand. The effects of grain size is less important. For details, see the following sections.

The damping ratio of sand varies with

(1) strain amplitude and (2) effective stress level.

Damping ratio of soil is independent of loading frequency (Sect. 10.9). Therefore, laboratory test to determine damping of sand can be carried out at a relatively low frequency (e.g., 0.1 Hz) by using a pneumatic-controlled device. This device is cheaper than hydraulic ones that can work at such a higher frequency as encountered during earthquakes. Further, void ratio and anisotropic consolidation do not significantly affect damping ratio of sand. Overconsolidation is not important either.

Cyclic drained test on Toyoura sand in Fig. 10.6 shows that modulus increases and energy damping (area of stress–strain loop) decreases with the number of cycles. Although the effective stress and the isotropic consolidation state did not change with the number of cycles and the void ratio decreased only slightly, the modulus and damping varied drastically. Because such a variation is often encountered during laboratory testing, most reported  $G$  and  $h$  come from the 10th or 15th cycles. Accordingly, those reported values may not be appropriate for the first few cycles or analysis on earthquakes of smaller magnitude (less number of cycles). Note that resonant column tests (Sect. 10.1) report values after thousands of cycles of loading.

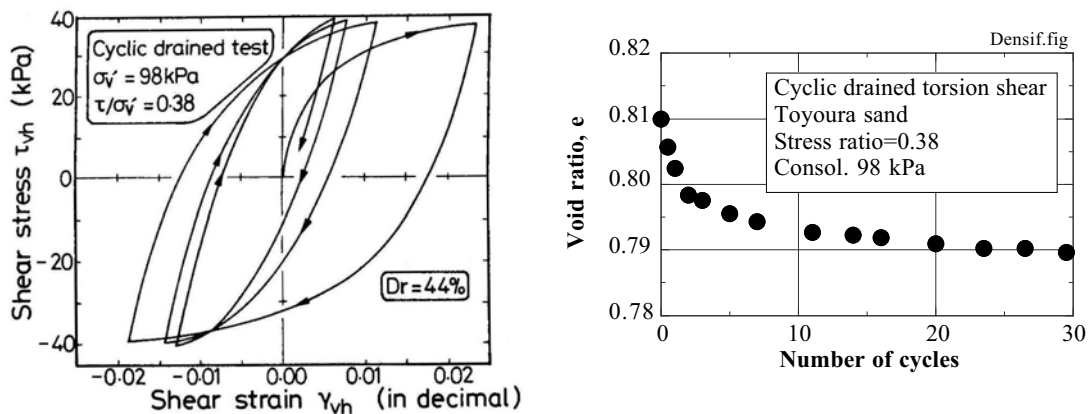


Fig. 10.6 Cyclic deformation of sand in drained test (Towhata et al. 1985)

#### Difference between sand and clay

Sand and clay are called cohesionless and cohesive soils. They are different in the following points.

1. Particle size of clay is much smaller than the size of sand grains. This smaller grain size makes water seepage more difficult in clay.
2. Clay particles have electric charges. They can attract water around them. Therefore, the water content of clay can be high. When compressed, consequently, clay reveals large consolidation settlement.
3. Cemented sand has bonding between grains. But, bonding that develops with age is more significant in clay. Cohesion that is the shear strength under zero effective stress is a product of bonding.



**10.4 Factors That Affect Modulus and Damping of Clay**

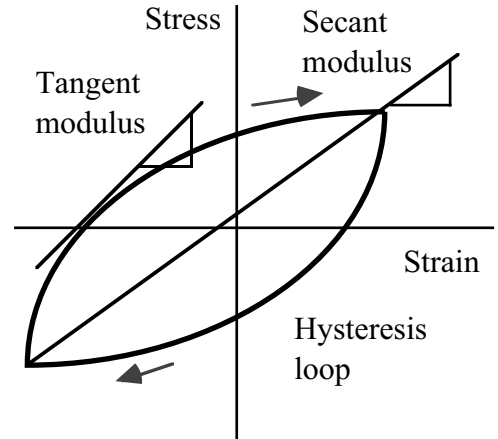
Secant shear modulus of clay (Fig. 10.7) is affected by

- (1) strain amplitude, (2) density or void ratio or water content (when saturated with water), (3) effective stress, (4) overconsolidation, (5) consolidation time, and (6) prestraining (previous cyclic loading). Among these, (1)–(3) are more important.

Shear modulus of clay is not much affected by loading frequency (Sect. 6.1). It is affected by strain amplitude.

Damping ratio of clay is not affected by

- (1) loading frequency and (2) effective stress. The effects of consolidation time seems less important.



**Fig. 10.7** Definition of secant and tangent shear moduli

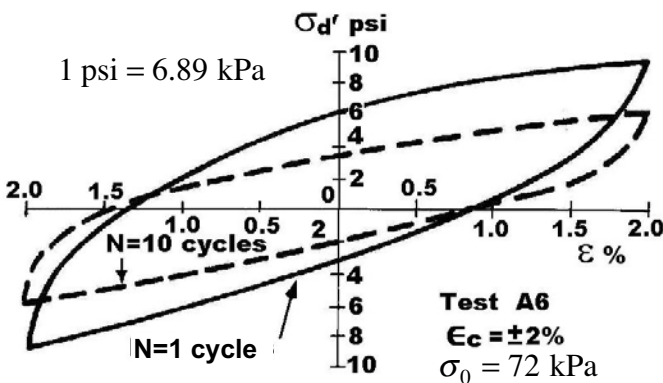
Similar to sand, the modulus and damping ratio of clay vary with

the number of loading cycles. Figure 10.8 compares the stress–strain loops that were observed during the first and the tenth cycles of loading. In contrast to sand that underwent drained cyclic loading and became stiffer with the number of cycles (Sect. 10.3), clay in Fig. 10.8 became softer with the number of cycles. This seems to be because

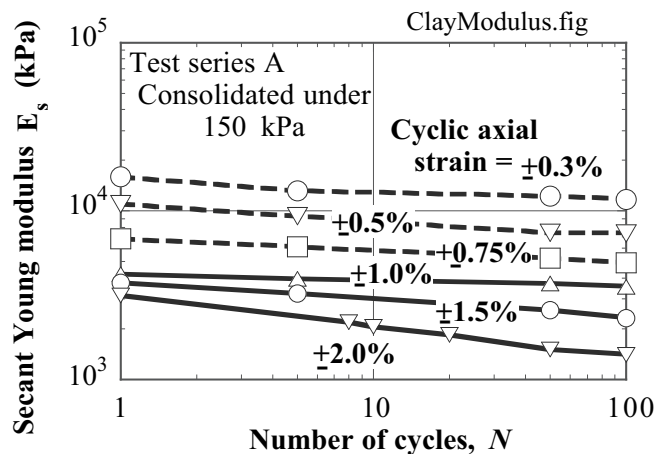
- excess pore water pressure increased and consequently the effective stress decreased with the number of cycles, reducing the frictional resistance between clay grains, and
- bonding between grains were destroyed and clay became softer.

The second mechanism is widely experienced during determination of sensitivity by unconfined compression tests (一軸圧縮試験による鋭敏比の決定).

The softening of clay during cyclic loading (Fig. 10.8 and Fig. 10.9) is called degradation. This is important in the problem of offshore platforms subjected to storm-wave loading. Note that storm loading exerts thousands of cycles of loading that is much greater than the number of cycles included in earthquake motions.



**Fig. 10.8** Hysteresis loops measured during first and tenth cycles (Idriss et al. 1978)



**Fig. 10.9** Variation of secant modulus with number of cycles in clay (after Idriss et al. 1978)

**10.5 Shear Modulus of Sand at Small Strain Amplitude**

The shear modulus,  $G = G_{\max}$ , at small strain amplitude, which is typically  $10^{-6}$  (=0.0001%) or less, is considered as one of the basic soil parameters. This modulus is most adequately determined from shear wave velocity ( $V_s$ ), which is measured directly in-situ (原位置観測);  $V_s = \sqrt{G_{\max}/\rho}$ . When this is not possible, a use of SPT- $N$  ( $N$ 値; for example, see Sect. 8.4) is commonly practiced. Field investigation on  $V_s$  or  $N$  is not possible when a studied earth structure is not yet constructed. This is a case of a planned dam and a planned land reclamation. Then, a study of dynamic response of a planned structure requires  $V_s$  or  $G_{\max}$  to be determined by the following methods:

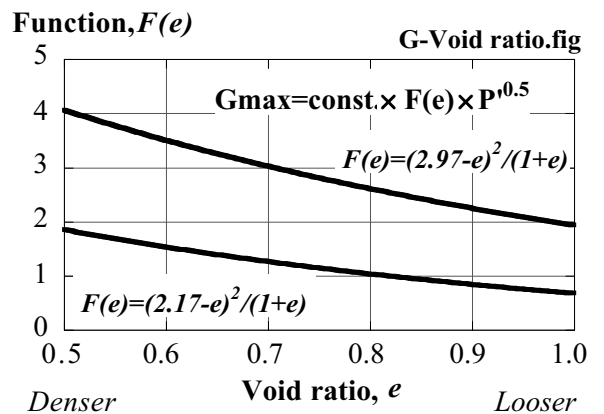
1. Disturbed soil specimen is collected at a borrow area and consolidated in a laboratory at a planned density (土取場で乱した土を採取し、実験室で所要の密度で圧密する). Cyclic tests are run on reconstituted specimens (実験室で調製された試料) and “shear modulus  $G$ ” as well as “ $h$ ” is determined over a range of strain amplitude.  $G$  at a very small strain gives  $G_{\max}$ .
2. Use is made of an empirical formula such as

kgf = kg as force  
 1 kgf/cm<sup>2</sup> = 98 kN/m<sup>2</sup>  
 = 98 kPa

$$G_{\max} = 700 \frac{(2.17 - e)^2}{1 + e} (P')^{0.5} \text{ (kgf/cm}^2\text{) (for round sand)}$$

$$G_{\max} = 330 \frac{(2.97 - e)^2}{1 + e} (P')^{0.5} \text{ (kgf/cm}^2\text{) (for angular sand)}$$

by Richart et al. (1970) in which “ $e$ ” stands for the void ratio of sand and the effective mean principal stress of  $P'$  is defined by  $P' = (\sigma'_1 + \sigma'_2 + \sigma'_3)/3$ . Note-worthy is that empirical formulae do not care the specific nature of a concerned soil. It should be used only for preliminary purposes.

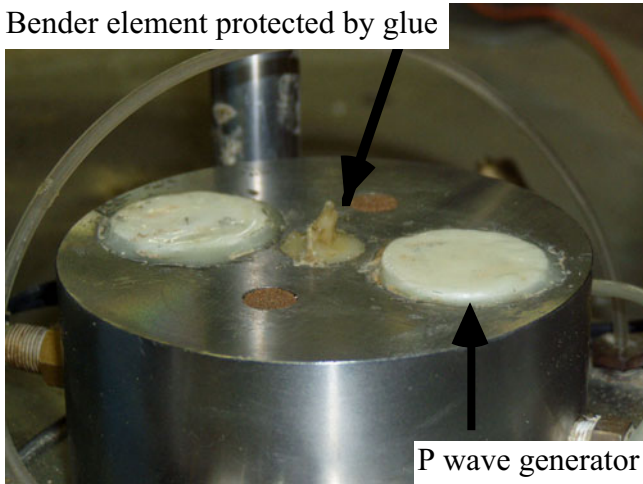


**Fig. 10.10** Empirical relationship between void ratio and shear modulus,  $G_{\max}$

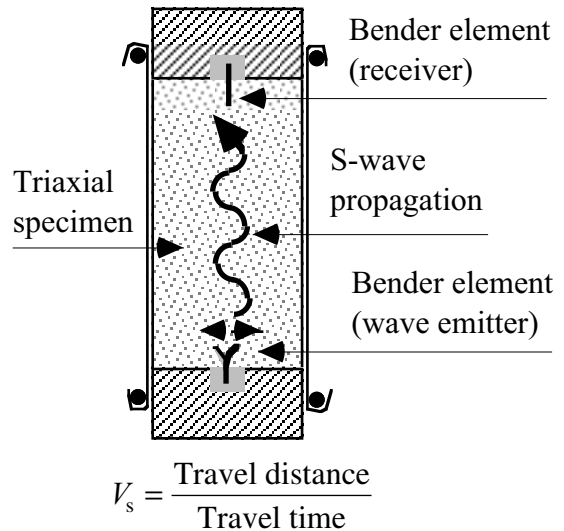
The formulae shown above indicate two important points:

- The effects of void ratio on shear modulus are taken into account by an empirical function of  $F(e) = (2.17 - e)^2 / (1 + e)$  or  $(2.97 - e)^2 / (1 + e)$ . Since denser sand has a greater value of modulus,  $F(e)$  increases as “ $e$ ” decreases (see Fig. 10.10).
- Shear modulus increases in proportion to the square root of the effective stress. In a level ground,  $P' = \frac{1 + 2K_o}{3} \sigma'_v$ , where  $K_o$  is the lateral earth pressure coefficient and  $\sigma'_v$  is the effective vertical stress. Accordingly,  $V_s = \sqrt{G_{\max}/\rho}$  increases in proportion to  $(P')^{1/4}$ .
- Constant parameters of 700 and 330 stand for the effects of all other factors. They are nothing but average values of data from many types of sand. Hence, they may not be appropriate for any specified sand.
- At such a very small strain amplitude as  $10^{-6}$  (0.0001%), any soil is said to be elastic. Hence,  $G_{\max}$  at such a small strain amplitude seems to be an elastic shear modulus. There may be no hysteresis loop, making  $h = 0\%$ . There is an opinion, however, that there is a small damping ratio such as  $h = 2\%$  even at a very small strain amplitude. Otherwise, there may be an infinite amplification at a resonance frequency of subsoil, which is not very realistic.

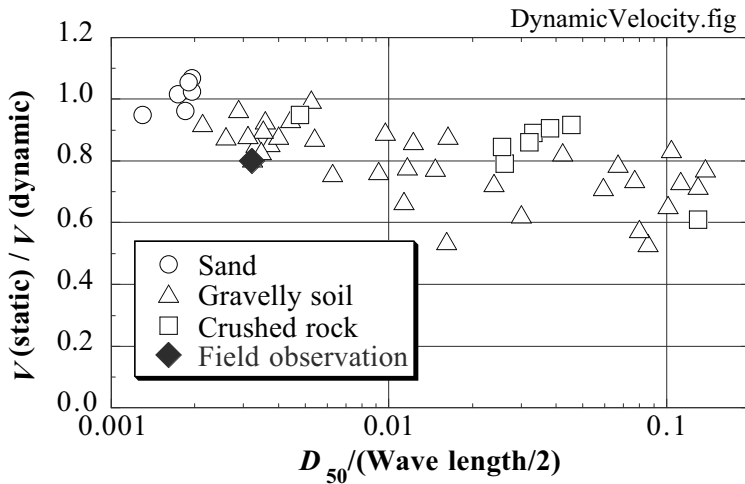
Deformation modulus ( $G$  or  $E$ ) of soil at small strain is determined by two different ways in laboratories. One is the measurement of wave propagation velocity (Fig. 10.11;  $G_{\max} = \rho V_s^2$  for example). The obtained modulus is called dynamic modulus. The other method is the very precise laboratory measurement of stress and strain in soil samples (Fig. 10.3). The modulus thus obtained is called static modulus.



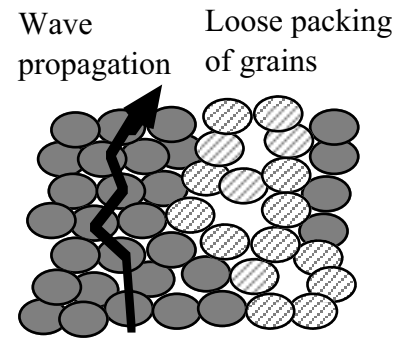
**Fig. 10.11** Bender element attached to bottom of triaxial device



**Fig. 10.12** Measurement of wave propagation velocity by bender elements



**Fig. 10.13** Comparison of dynamic and static moduli at small strain (data by Tanaka et al. 2000 and Maqbool and Koseki, 2006)



**Fig. 10.14** Different mechanisms of dynamic and static moduli

A bender element in Fig. 10.11 is a device that shakes at high frequencies in the horizontal direction and generates S-wave propagation from one end towards the other end of a soil specimen (Fig. 10.12). The S-wave velocity is determined by using the travel distance and the travel time (Viggiani and Atkinson, 1995). In spite of this simple concept, there are some uncertainties. First, it is not clear whether the travel distance is the distance between two ends of the sample, the distance between tips of bender elements, or else. Moreover, the travel time is supposed to be the time difference between wave emission and wave arrival. The wave arrival cannot be clearly defined. The arrival of initial shaking or the arrival of the peak give different times. This uncertainty is because the wave field is not one-dimensional but is subjected to more complicated near-field effects (Brignoli et al. 1996). For P-wave generation, a piezo electric device is available.

Conceptually, the small strain moduli should be identical whether measured dynamically or statically. In reality, however, the dynamic modulus is greater than the static modulus as shown in Fig. 10.13 in which experimental and field data by Tanaka et al. (2000) and Maqbool and Koseki (2007) are illustrated. Note

that data of both  $V_p$  and  $V_s$  are plotted together in this figure. Although two kinds of modulus (wave velocity) are similar in fine sand (small grain size,  $D_{50}$ ), the wave velocity as calculated from static modulus ( $\sqrt{G_{\max}/\rho}$ ) becomes smaller than the dynamically measured wave velocity (static modulus < dynamic modulus) as the grain size becomes greater.

The main reason for the difference between two moduli is probably that wave propagates along rigid particles and the obtained modulus stands for the rigidity of stable grain packing, while the static modulus represents the overall deformation of a soil specimen and is affected particularly by loose and soft parts in it. This point is conceptually demonstrated in Fig. 10.14.

**10.6 Effects of Strain Amplitude on Shear Modulus**

At small strain ( $<10^{-5}$ ), a stress-strain loop is reduced to a nearly straight line: an elastic behavior. The secant modulus of  $G = \tau/\gamma$  decreases as the strain amplitude increases. It is a convention to study separately the effects of strain-nonlinearity from such factors as the effective stress and density:

$$G = G_{\max} (\text{function of } \sigma', e, \text{ etc.}) \times (G/G_{\max}). \tag{10.1}$$

Thus, the effect of strain is indicated by  $G/G_{\max}$ .

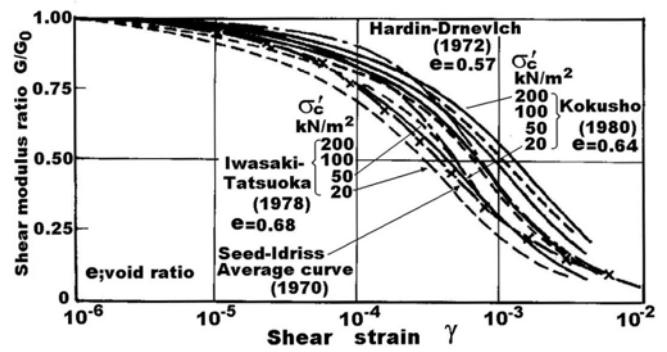
$G_{\max}$  is frequently designated by  $G_0$ . Fig. 10.15 (Kokusho, 1987) compares  $G/G_{\max}$  measured on laboratory-reconstituted samples of clean sand under *drained* conditions. The importance of undrained shear tests on undisturbed samples will be discussed in Sect. 10.17. Since  $G$  varies with the number of cycles (Sect. 10.3), the data in Fig. 10.15 shows  $G$  in the 10th–20th cycles. Figure 10.15 indicates the following:

1.  $G/G_{\max}$  decreases as the strain amplitude increases
2. The reduction of  $G/G_{\max}$  is less significant when the effective stress is higher
3. Nevertheless, most sands exhibit similar  $G/G_{\max}$  curves irrespective of different testing conditions

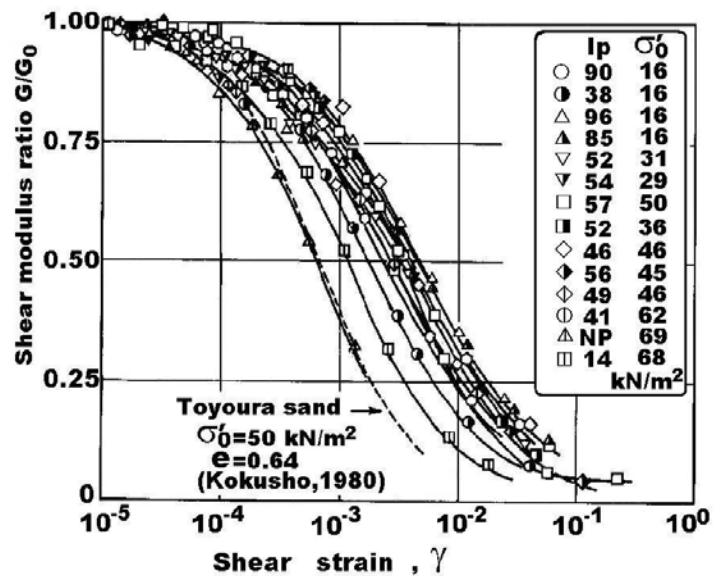
Figure 10.16 shows data obtained from cohesive soils. It may be seen that those soils with larger  $I_p$  (plasticity index, Sect. 1.1) indicate greater  $G/G_{\max}$ , suggesting that a greater cohesion keeps  $G/G_{\max}$  large up to a large strain amplitude. Kokusho (1987) then quoted a summary of many data by Imazu and Fukutake (1986) to confirm this point. Figure 10.17 clearly indicates that  $G/G_{\max}$  is greater for clay and smaller for sand and gravel.

It should be noted therefore that the effects of strain amplitude (i.e., decrease in  $G/G_{\max}$ ) is more significant when the soil grains are separated or discrete from each other more substantially. Discreteness is the case when grains have no cohesion and when the effective stress is low.

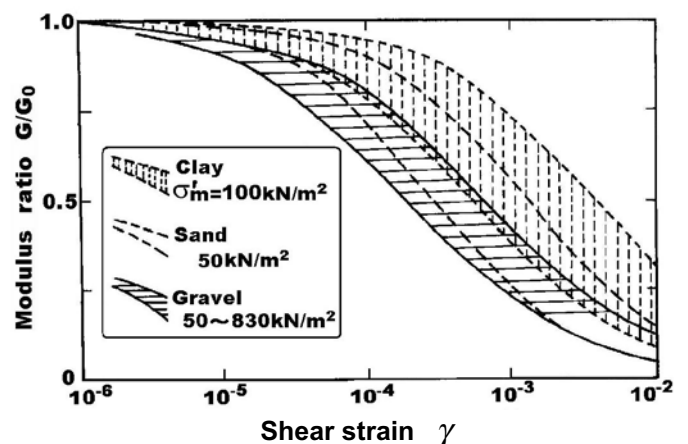
The amplitude of strain stands for the single amplitude. When the shear strain varies between  $-\gamma_a$  and  $\gamma_a$ , the single amplitude is  $\gamma_a$ . The double amplitude stands for  $2 \times \gamma_a$ .



**Fig. 10.15**  $G/G_{\max}$  of reconstituted clean sands (Kokusho, 1987)



**Fig. 10.16**  $G/G_{\max}$  of clays with different  $I_p$  (Kokusho, 1987)



**Fig. 10.17** Effects of soil type on  $G/G_{\max}$  (summary made by Imazu and Fukutake, 1986)

10.7 Effects of Effective Stress on Shear Modulus of Sand

Figure 10.15 already showed that  $G/G_{max}$  is affected by the effective stress to some extent. However, the more important effects of the effective stress occurs in  $G_{max}$  at small strain amplitude.

Chung et al. (1984) carried out resonant column tests (see Sect. 10.1) on clean sand. Their specimens were isotropically consolidated under an effective stress of  $\sigma'_3$ . The following natures of resonant column tests should be borne in mind:

1. Test is possible in relatively small strain range
2. The number of loading cycles prior to measurement is very large; possibly thousands
3. The loading frequency is high, being of order of 100 Hz

Figure 10.18 indicates the variation of  $G$  with the strain amplitude between  $10^{-4}$  and  $10^{-1}$  % (from  $10^{-6}$ – $10^{-3}$  in decimal). The higher effective stress is associated with the greater shear modulus.

Figure 10.19 illustrates the variation of  $G_{max}$  with the effective stress. This figure shows that

1.  $G_{max}$  increases in proportion to  $\sigma'^{0.5}_3$
2. The effects of void ratio,  $e$ , on  $G_{max}$  is approximated by an empirical formula of  $(2.97 - e)^2 / (1 + e)$

It is a common practice today in equivalent-linear dynamic analyses to

1. First, determine  $G_{max}$  at small strain amplitude by running in-situ tests (downhole survey etc.) or by using a rough empirical formula by means of SPT- $N$ :  $V_s = 80N^{1/3}$  for sand (Sect. 8.4)
2. Second, find out an appropriate  $G/G_{max}$  vs.  $\gamma$  correlation
3. Finally,  $G = G_{max} \times (G/G_{max})$  gives the shear modulus at any strain amplitude

This practice means that  $G_{max}$  takes into account site-specific conditions: type of soil, the effective stress, age, over-consolidation, fines content, etc., while  $G/G_{max}$  is rather independent of those factors as repeatedly shown in this chapter.

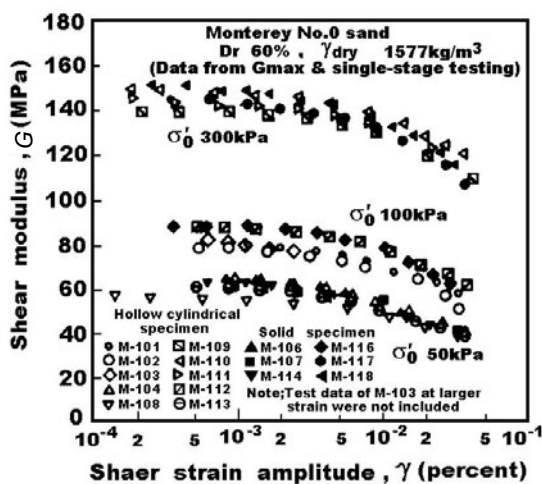


Fig. 10.18 Effects of effective stress on  $G$  (Chung et al. 1984)

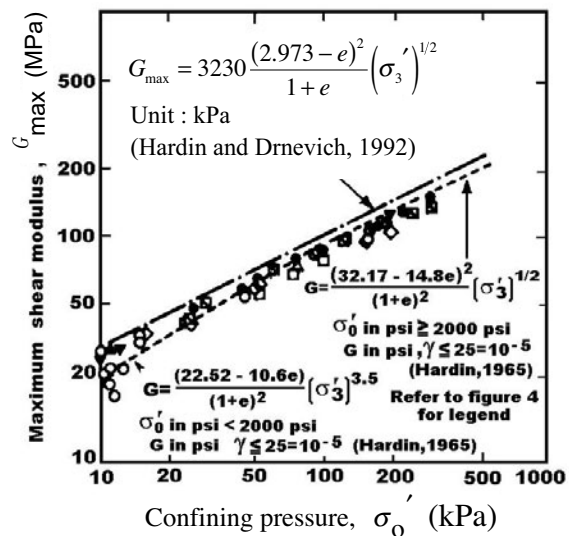


Fig. 10.19 Variation of  $G_{max}$  with effective stress (drawn after Chung et al. 1984)

10.8 Damping Ratio of Sand

As was shown in Sect. 10.3, the shape of a hysteresis stress–strain loop of sand undergoing drained cyclic shear changes with the number of loading cycles. The secant shear modulus increases with the cycles while the area of loops decreases. Consequently, the damping ratio decreases with the progress of the cyclic loading. Therefore, most laboratory tests report the damping ratio in the 10th–20th cycles without paying attention to the first few cycles.

Figure 10.20 by Kokusho (1987) indicates the effects of soil type on damping ratio. Since sand and gravel have a greater damping ratio than clay, it may be said that the more discrete material has the greater energy damping than more continuous soils.

The damping ratio of sand in Fig. 10.20, however, is larger than that for gravel probably because the sand was tested under lower effective stress (50 kPa). If correction is made for this point, the damping ratio of sand will be smaller than that for gravel.

The resonant column tests by Chung et al. (1984) indicate the influence of the effective stress level on damping ratio of sand. Figure 10.21 compares three series of tests that were conducted under the effective stress of 50, 100, and 300 kPa. The damping ratio is greater when the pressure is lower. This observation is consistent with the idea in Sect. 10.6 that  $G$  decreases more rapidly under lower pressures, indicating a more nonlinear behavior.

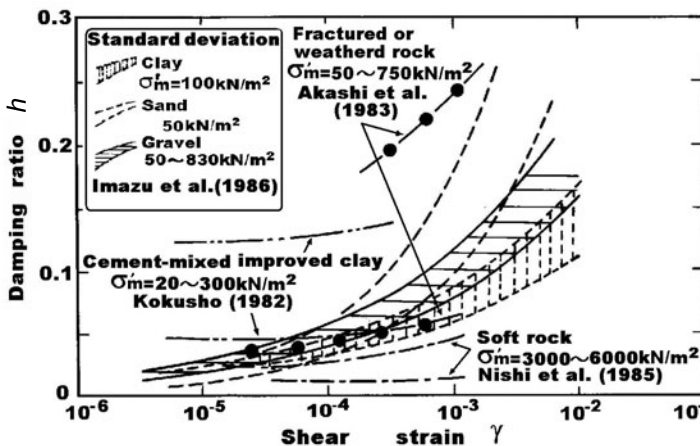


Fig. 10.20 Damping ratio of different types of soils (Kokusho, 1987)

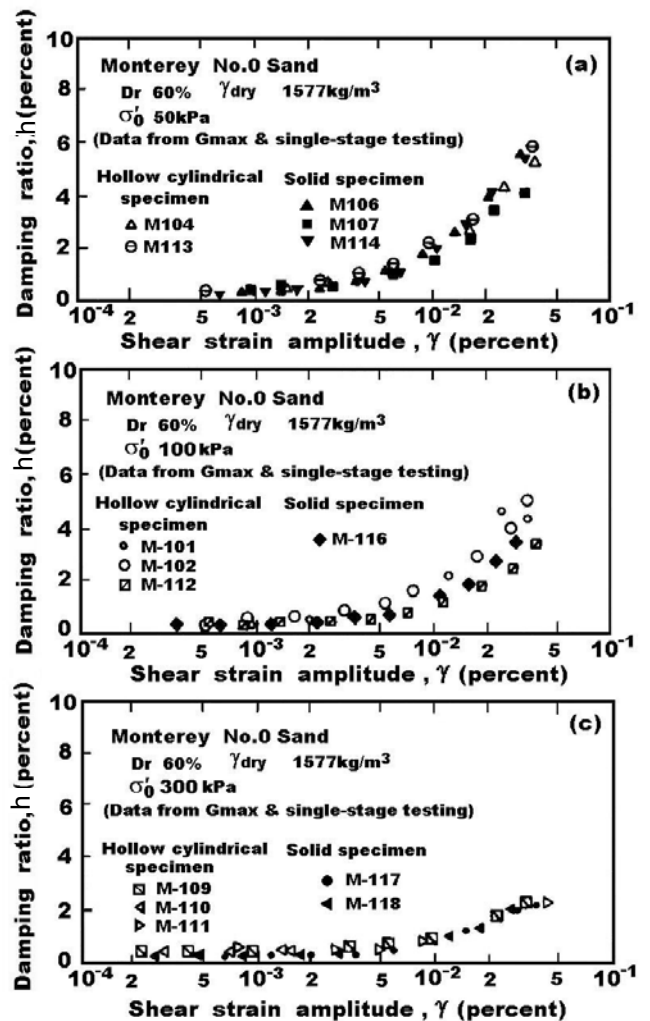


Fig. 10.21 Damping ratio of different effective stress level (Chung et al. 1984)

The energy damping described here may not account for all the energy dissipation. A recent discussion is made of wave reflection inside a sandy layer. The heterogeneous  $V_s$  in sandy layer due to increase of the effective stress in the vertical direction causes complex transmission and reflection and disperses the wave energy. Much is not known about this effects.

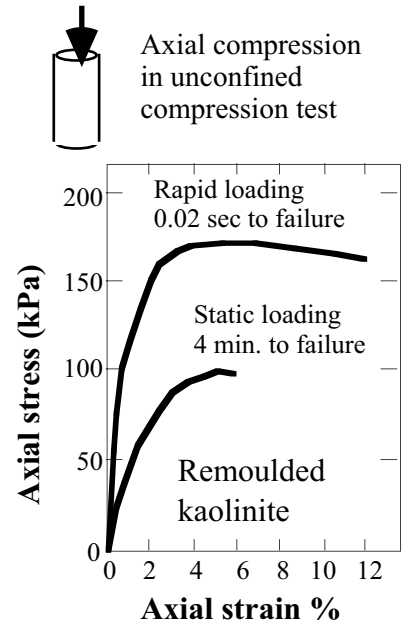
### 10.9 Rate Dependent Nature of Clay

This section addresses the effects of loading rate on the stress–strain behavior of clay. Casagrande and Shannon (1948a,b) performed unconfined compression tests on clays at different speeds. The rate of strain varied thousands of times and in case of remoulded kaolinite, the peak strength increased about 70% (Fig. 10.22). Lefebvre and LeBoeuf (1987) conducted monotonic shear tests on clay to find greater rigidity and strength when the rate of loading was faster.

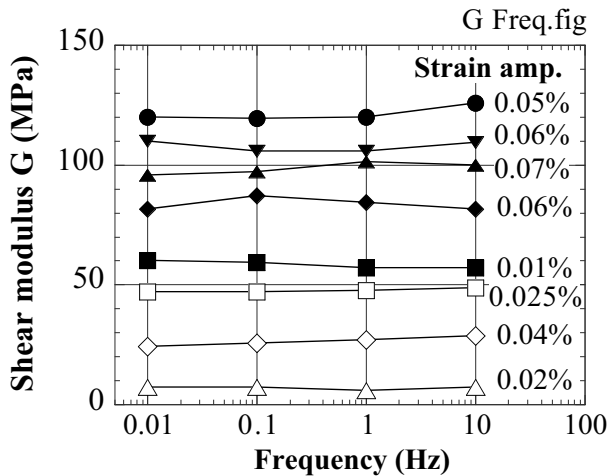
One of the difficulties in testing clays is the drainage condition and heterogeneous deformation of a specimen. Since the permeability is low in clay, the nonuniformity in strain induces different excess pore water pressure in a specimen, making the stress–strain behavior dependent on the nonuniformity. This problem appears to be more significant when the rate of loading is faster, because the excess pore water pressure has even a shorter and less sufficient time to adjust the nonuniform pressure distribution.

Hara (1973) conducted cyclic loading on a variety of clays. His strain amplitude seems relatively small. His results in Fig. 10.23 do not suggest significant rate dependency.

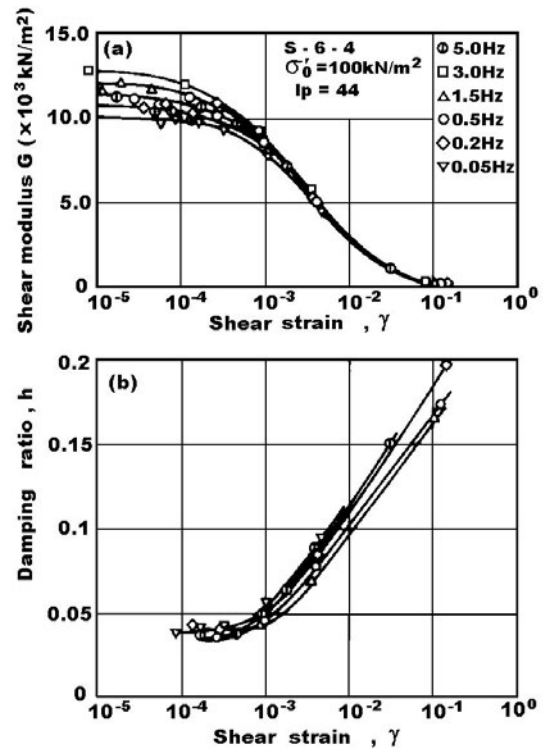
Kokusho (1982) presents in Fig. 10.24 the effects of loading frequency on  $G$  and damping ratio of clay. It seems that  $G$  increases with the increase of frequency. The damping ratio is larger under lower frequency than under higher frequency. According to constant-volume cyclic tests, which is equivalent with undrained shear, by Lefebvre and Pfendler (1996), 12% increase in strength occurred per one log cycle of rate of deformation.



**Fig. 10.22** Effects of loading rate on shear deformation of clay (Casagrande and Shannon, 1948a)



**Fig. 10.23** Effects of loading frequency on modulus of clays (after Hara, 1973)



**Fig. 10.24** Effects of loading frequency on dynamic properties of clays (Kokusho, 1982)

Thus, there are some effects of loading frequency on the cyclic stress–strain behavior of clays. However, these rate effects are not seriously taken in practice because other factors are more influential. Ellis et al. (2000) conducted resonant column tests to examine the effects of viscosity of pore fluid on damping ratio. Damping ratio increases by a few percent when viscosity increased by tens of times.



☀ 10.10 Effects of Plasticity on Cyclic Behavior of Clay

Clay has a thixotropic nature. Its shear rigidity and strength increase with time, because the cementation and bonding develop with time between particles. It is reasonable, therefore, that clays with a greater plasticity index ( $I_p$ ) is more thixotropic than less plastic materials. Further, the bonding may be destroyed by cyclic loading with a relatively large strain amplitude. Hence, clay becomes softer with the number of cycles. This phenomenon is called “*degradation*,” which is important in behavior of offshore structures resting on clayey seabed during storms. The development of bonding is more substantial when clay is overconsolidated. An empirical formula is available for  $G_{max}$  of clay:

$$G_{max} = 625 \frac{OCR^k}{0.3 + 0.7e^2} \sqrt{P_a P'}, \quad (10.2)$$

in which  $P'$  stands for the effective mean principal stress of  $(\sigma'_1 + \sigma'_2 + \sigma'_3)/3$ ,  $P_a$  is the atmospheric pressure (大気圧  $\approx 98$  kPa) and  $OCR$  designates the overconsolidation ratio (Sect. 1.4). This formula works with any unit system. For the value of parameter  $k$ , see Fig. 10.25.

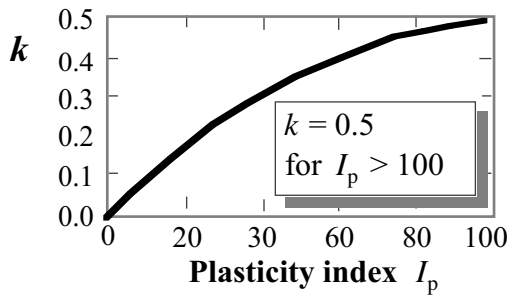


Fig. 10.25 Effects of OCR on  $G_{max}$  of clay (Hardin, 1978)

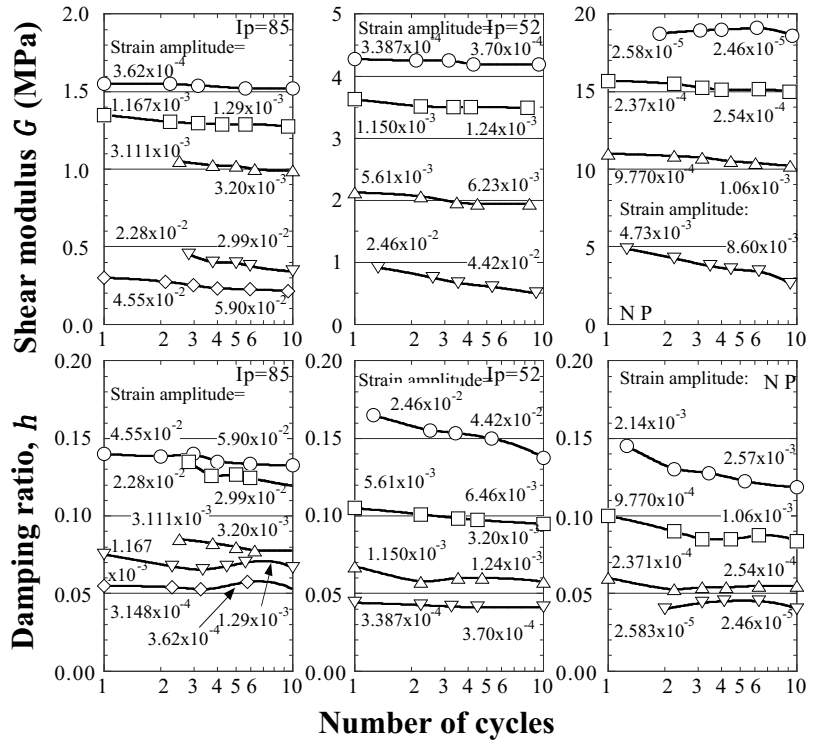


Fig. 10.26 Effects of plasticity on cyclic behavior of clay (Kokusho, 1982)

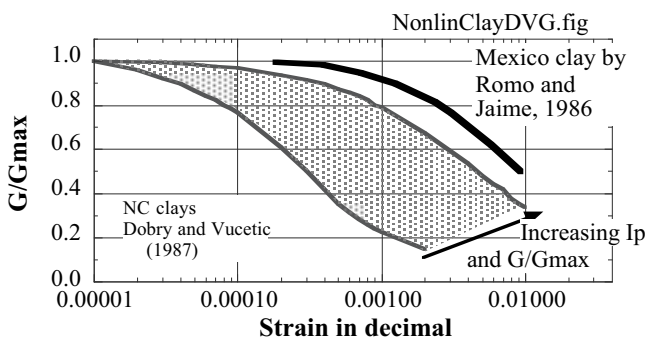


Fig. 10.27 Effects of  $I_p$  on  $G/G_{max}$  of clay (Dobry and Vucetic, 1987)

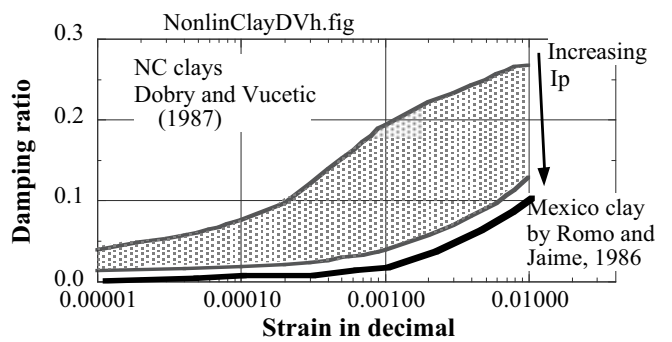


Fig. 10.28 Effects of  $I_p$  on damping ratio of clay (Dobry and Vucetic, 1987)

Kokusho (1982) studied that  $G$  and  $h$  (damping ratio) of Teganuma (手賀沼) clay decrease with the number of cycles (Fig. 10.26). It is more interesting in Fig. 10.26 that the specimens with greater  $I_p$  have smaller  $G$  and  $h$ ; the smaller  $h$  suggests more elastic behavior. Dobry and Vucetic (1987) summarized this data and others to obtain Fig. 10.27 and Fig. 10.28, which indicate that the greater  $I_p$  is associated with less reduction of  $G/G_{max}$  and smaller damping ratio. The greater  $I_p$  is thus associated with more linear elastic behavior, suggesting less discrete nature of soil (Sect. 10.2). Note that  $I_p = 150\text{--}250$  for Mexico City Clay, while  $I_p = 20\text{--}100$  for other clays.

10.11 Effects of Density on Shear Modulus of Clay

Hardin and Black (1968) studied the variation of  $G$  of NC (normally consolidated) clay with void ratio. Figure 10.29 indicates that  $G_{max}$  varies in proportion to  $(2.973-e)^2/(1+e)$  and the square root of the isotropic consolidation pressure,  $\sqrt{\sigma'_0}$ . Note, however, that the parameter of 2.973 varies with type of clay. Figure 10.30 and Fig. 10.31 compare the variation of  $G_{max}$  of overconsolidated (OC) kaolinite (LL = 65.9% and  $I_p = 35\%$ ) and calcium-bentonite (LL = 120% and  $I_p = 60\%$ ). See that  $e$ -log  $P$  behavior of kaolinite is more elastic than that of bentonite during unloading and reloading. This difference seems consistent with the recoverable change of  $G_{max}$  of OC kaolinite.

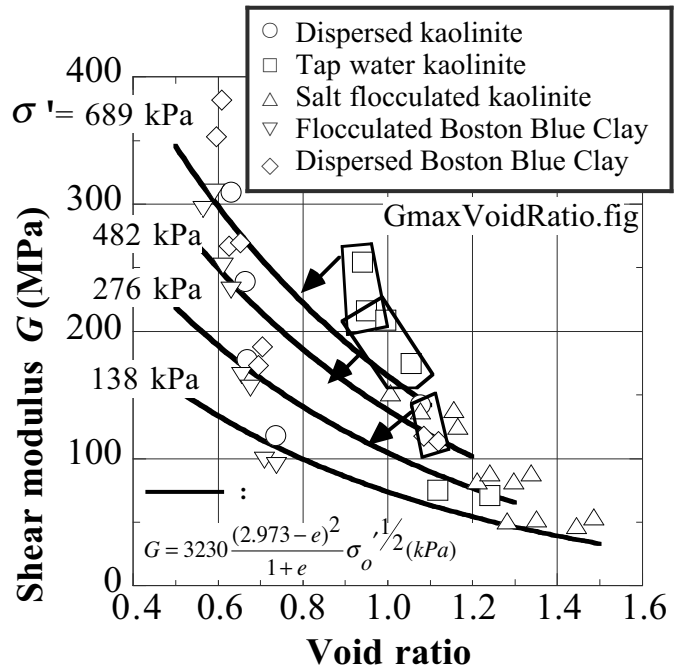


Fig. 10.29 Variation of  $G_{max}$  of clay with void ratio

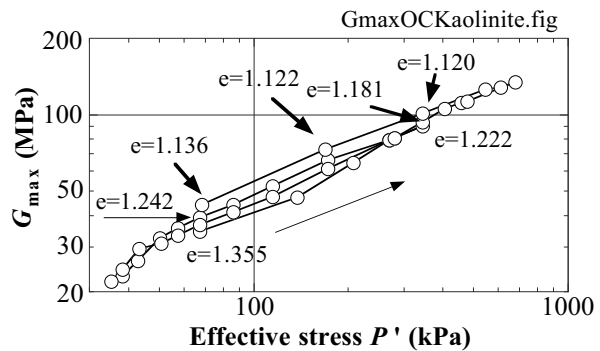
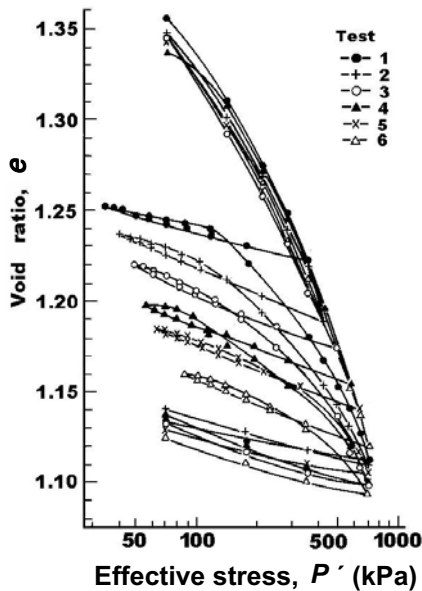


Fig. 10.30  $G_{max}$  of overconsolidated kaolinite (Humphries and Wahls, 1968)

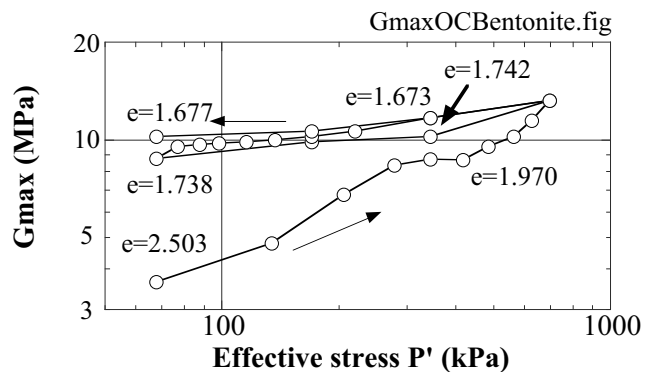
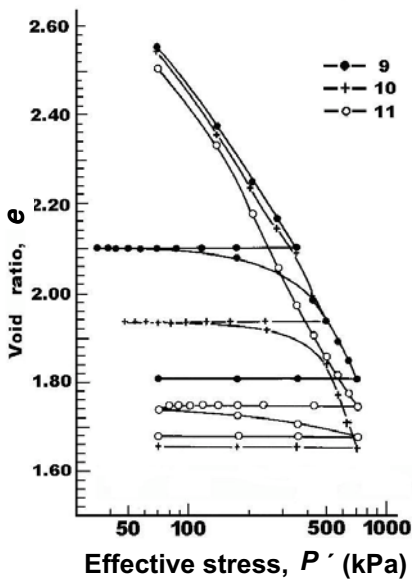


Fig. 10.31  $G_{max}$  of overconsolidated bentonite (after Humphries and Wahls, 1968)

10.12 Effects of Age on Shear Modulus of Clay

Bonding between clay particles develops gradually with time. This seems to increase  $G_{max}$  of clay with time as well. Afifi and Richart (1973) studied this time effect by running resonant column tests. Figure 10.32 indicates the stress history in which loading and unloading/reloading were carried out. The primary consolidation ceased at about 100 min. Figure 10.33 illustrates the time increase of  $G_{max}$  of NC samples. Although the primary consolidation was completed at 100 min,  $G_{max}$  kept increasing after 100 min without further densification. This suggests the effects of particle bonding together with possible minor rearrangement of particles, which can be called ageing.

Kokusho (1982) compared  $\Delta G/G_{1000}$  in his own tests with those by Afifi and Richart (1973) and Anderson and Woods (1976); Fig. 10.34.  $G_{1000}$  stands for  $G_{max}$  at 1,000 min and  $\Delta G$  is the increase of  $G_{max}$  per one logarithmic cycle of time (e.g. from 1,000 to 10,000 min). The finer soils (smaller  $D_{50}$ ; Fig. 1.3) show greater rate of increase in  $G_{max}$  probably due to ageing of clay contents. Finally, a good correlation was demonstrated between  $\Delta G/G_{1000}$  and plasticity index ( $I_p$ ); Fig. 10.35.

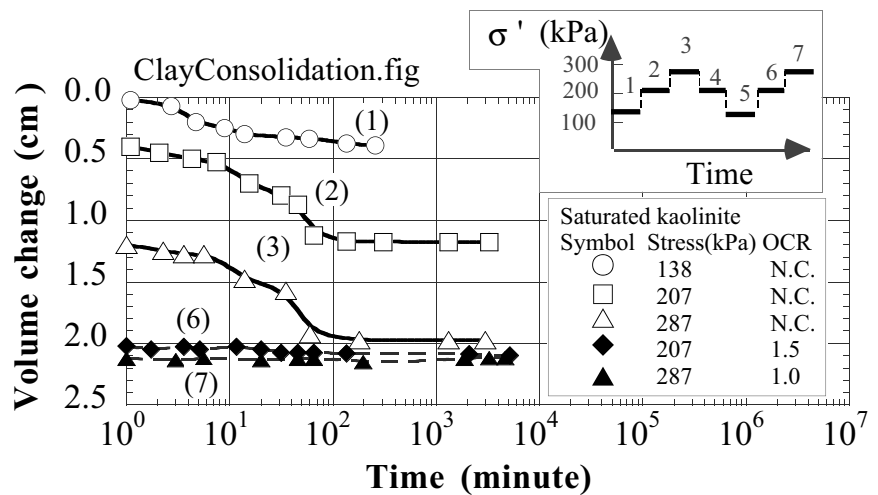


Fig. 10.32 Consolidation data of tested clay (Afifi and Richart, 1973)

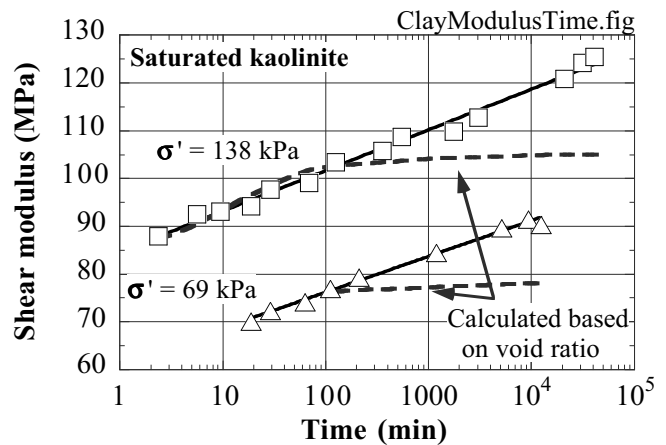


Fig. 10.33 Increase of  $G_{max}$  of clay with time (drawn after Afifi and Richart, 1973)

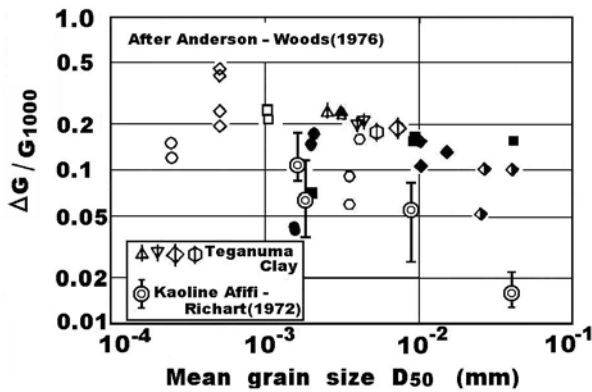


Fig. 10.34 Increase rate of  $G_{max}$  (Kokusho, 1982)

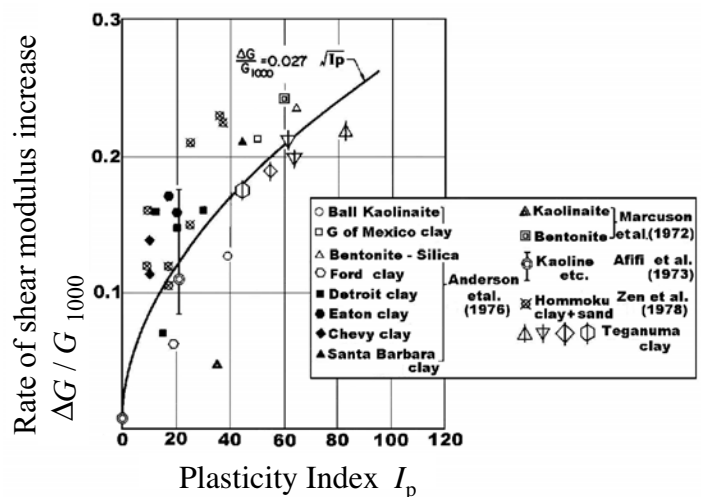


Fig. 10.35 Rate of increase in  $G_{max}$  changing with plasticity index (Kokusho, 1982)

The use of  $D_{50}$  in study of clay and silt has caused a problem in which true clay and silt with cohesion were confused with such a cohesionless fine material as mine tailing materials (Sect. 20.5). Information about clay and silt were often applied to tailings because the latter had a small value of  $D_{50}$  as well. Study in terms of plasticity index can solve this problem because the tailing material is non plastic.

10.13 Effects of Strain Amplitude on Shear Modulus of Clay

Since the modulus of clay decreases with the number of cycles (degradation; Sect. 10.14),  $G$  at a specified number of cycles has been studied by many people. The employed number is 10–20 depending upon researchers.

Figure 10.36 indicates the variation of  $G$  with the single amplitude of strain. The nonlinearity in clay is less significant than that in coarser materials. Figure 10.37 shows that the effects of  $I_p$  (plasticity index; Sect. 1.1) and OCR (overconsolidation ratio) on  $G/G_{max}$  vs.  $\gamma$  curve is not very important, although smaller OCR appears to be associated with more nonlinearity. A more detailed study in Fig. 10.38, however, suggests that a fixed  $G/G_{max}$  occurs at a larger strain amplitude when  $I_p$  increases; greater  $I_p$  reduces nonlinearity of clay. Finally, Fig. 10.39 shows that  $G/G_{max}$  is independent of the effective stress level.

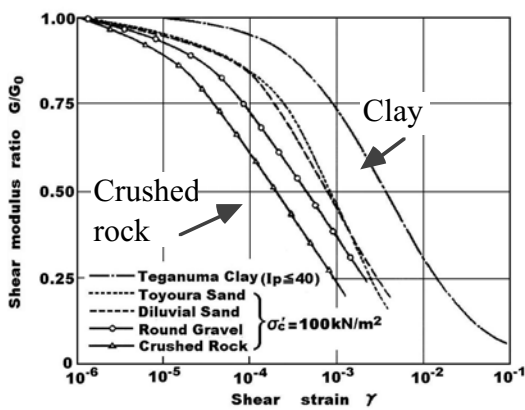


Fig. 10.36 Variation of  $G$  with strain amplitude (Kokusho, 1982)

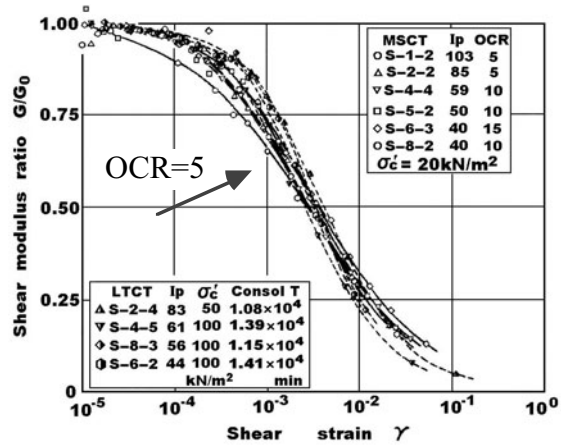


Fig. 10.37 Effects of  $I_p$  and OCR on  $G$  of clay (Kokusho et al. 1982)

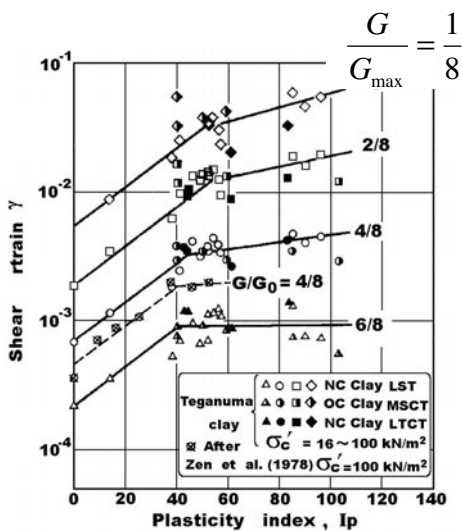


Fig. 10.38 Effects of  $I_p$  on nonlinearity of clay (Kokusho, 1982)

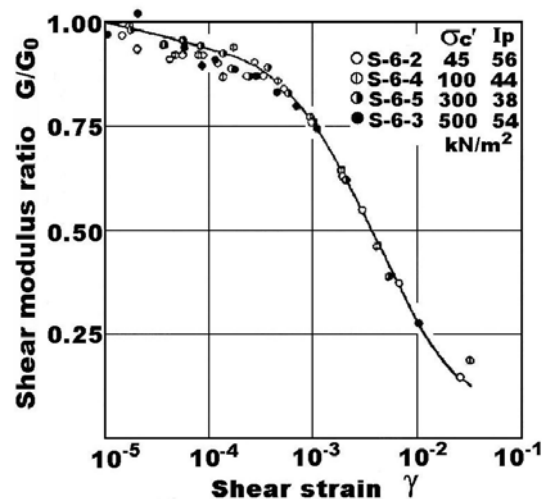


Fig. 10.39 Effects of confining pressure on  $G$  of clay (Kokusho et al. 1982)

### 10.14 Degradation of Shear Modulus of Clay

Degradation is a phenomenon in which shear modulus (rigidity) of clay decreases with the number of loading cycles (Dobry and Vucetic, 1987). An example of degradation is illustrated in Fig. 10.40 (see Fig. 10.8 as well). The decrease of shear modulus is important in the stability of foundation of offshore structures that are subjected to thousands of cycles of wave loads during heavy storms. Degradation is caused probably by (1) the accumulation of excess pore water pressure and decrease of effective stress, and (2) breakage of bonding between clay particles. Osipov et al. (2005) took an electron-microscopic photograph of a clay bridge connecting sand grains. Practical engineers may consider degradation in such a manner as

$$\delta \equiv \frac{G(\text{Nth cycle})}{G(\text{1st cycle})} = N^{-t}, \quad (10.3)$$

in which  $N$  is the number of cycles while  $t$  is called the degradation parameter.

Dobry and Vucetic (1987) reported values of  $\delta$  at a variety of OCR (overconsolidation ratio) and strain amplitude. Figure 10.41 indicates that the shear modulus is possible to decrease to 70 or 80% of the initial value when a substantial amplitude of strain is repeated 100 times or more. The greater values of  $t$  suggests that the pore pressure increase and the breakage of bonding are substantial when the strain amplitude is large in young clay with smaller values of OCR (Fig. 10.42).

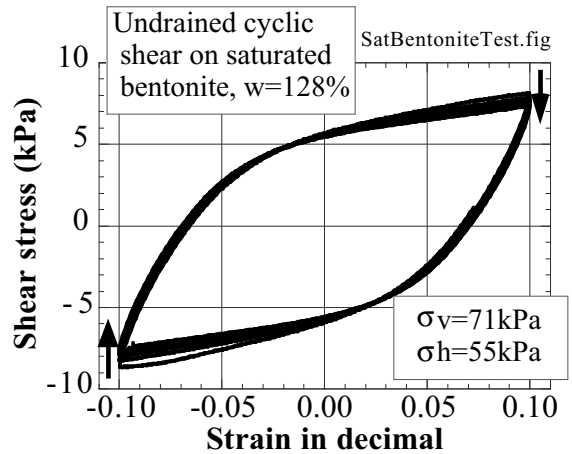


Fig. 10.40 Example of degradation in undrained cyclic shear of bentonite clay

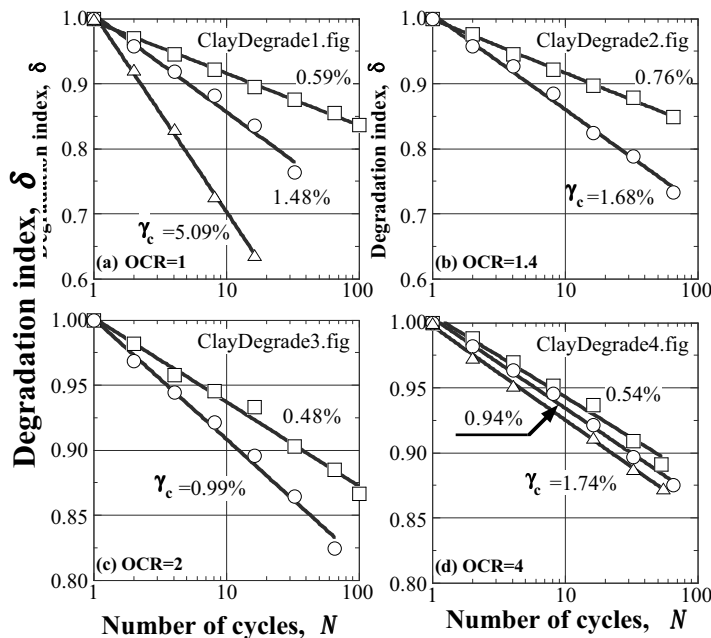


Fig. 10.41 Observed degradation (Dobry and Vucetic, 1987)

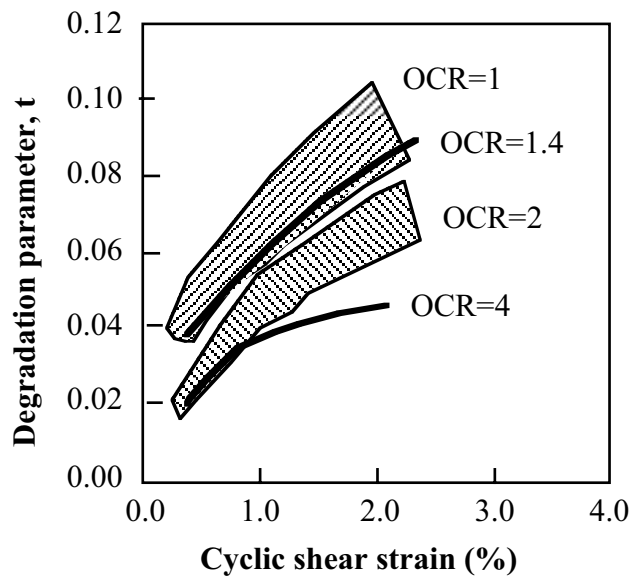


Fig.10.42 Variation of degradation parameter with OCR and strain amplitude (drawn after Dobry and Vucetic, 1987)

10.15 Damping Ratio of Clay

Damping ratio seems to be less affected by many factors than shear modulus. A limited rate-dependency was indicated in Sect. 10.9. The type of soil, however, appears relatively important as Fig. 10.43 reveals that the damping ratio of clay is smaller than that of coarser materials. This is probably because clay is more continuous than sand and gravel.

Figure 10.44 by Kokusho et al. (1982) indicates test results on undisturbed clay specimens that the damping ratio is not significantly affected by the effective stress level. What is peculiar in this figure is that the higher effective stress caused slightly larger damping ratio, opposite from what was found for sand (Fig. 10.21). Although not clearly known, one of the possible reasons for this may be that the greater amount of consolidation volume change under the higher stress destroyed the interparticle bonding of clay.

Figure 10.45 demonstrates that NC and OC clays are of more or less similar magnitude of damping ratio.

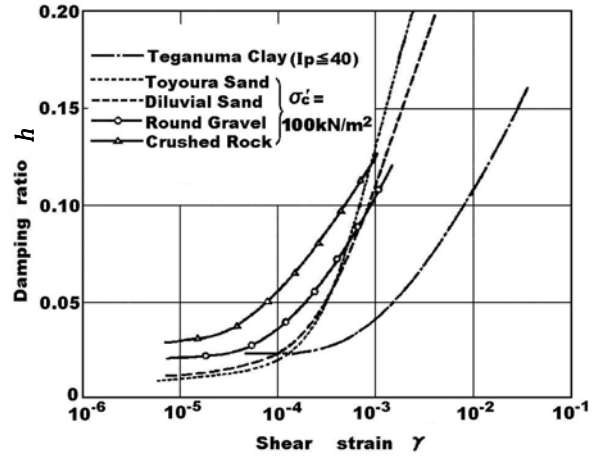


Fig. 10.43 Damping ratio of clay, sand, and gravel (Kokusho, 1982)

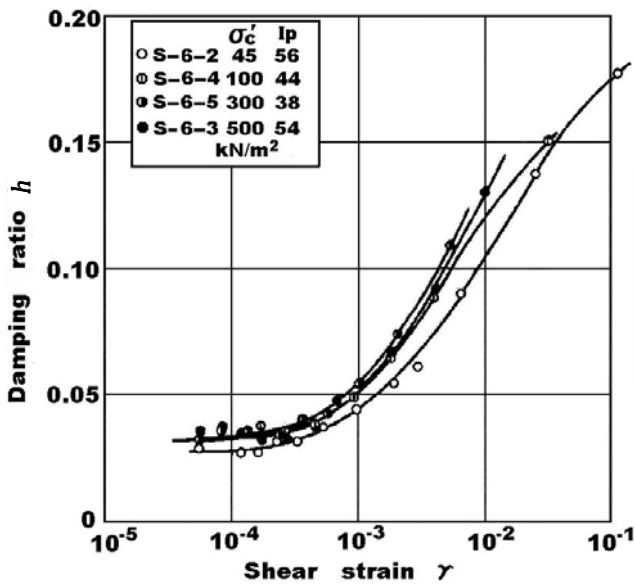


Fig. 10.44 Effects of confining pressure on damping ratio of clay (Kokusho, Yoshida and Esashi, 1982)

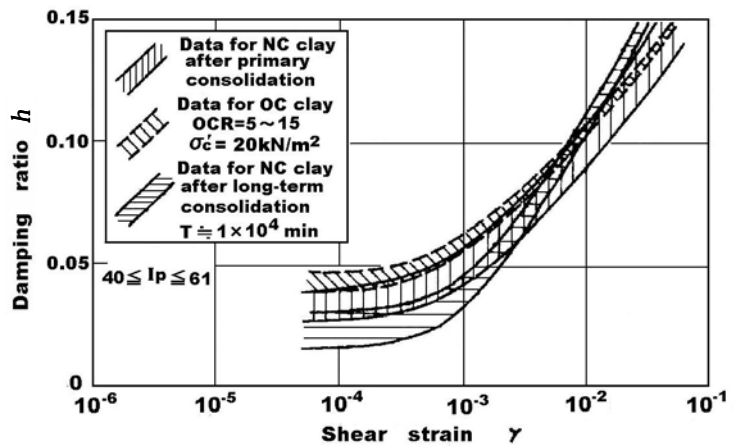


Fig. 10.45 Damping ratio of NC (Normally Consolidated) and OC (Overconsolidated) clays (Kokusho et al. 1982)

10.16 Effects of Consolidation Time on Damping of Clay

Marcuson and Wahls (1978) studied the damping ratio at a small strain range ( $\gamma=0.0012-0.0048\%$ ). Both drained and undrained tests were run on kaolinite specimens as well as more plastic bentonite samples. It was shown by all tests in Figs. 10.46–10.49 that the damping ratio decreases as the consolidation time becomes longer. This may suggest that particle bonding is built as time passes and that clay becomes a more continuous material. In the figures, the *T* ratio is defined by

$$T \text{ ratio} = \frac{\text{Consolidation time}}{\text{Time for 100\% primary consolidation}}$$

Note further that damping ratio is greater under lower effective stress.

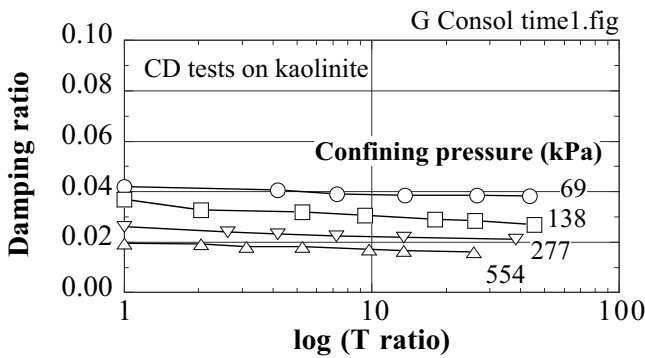


Fig. 10.46 Change in damping ratio of kaolin with time in drained tests (Marcuson and Wahls, 1978)

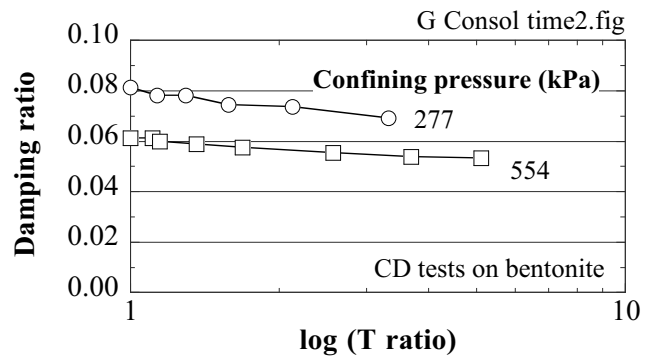


Fig. 10.47 Change in damping ratio of bentonite with time in drained tests (Marcuson and Wahls, 1978)

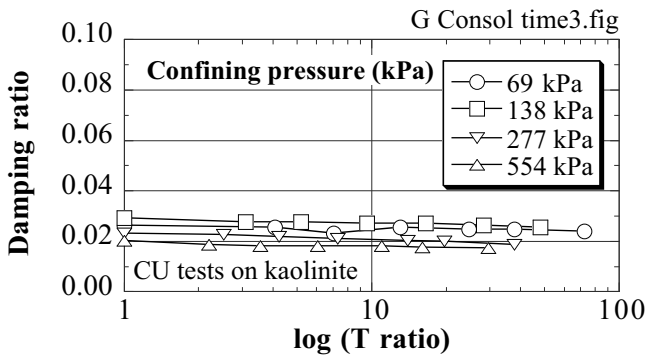


Fig. 10.48 Change in damping ratio of kaolin with time in undrained tests (Marcuson and Wahls, 1978)

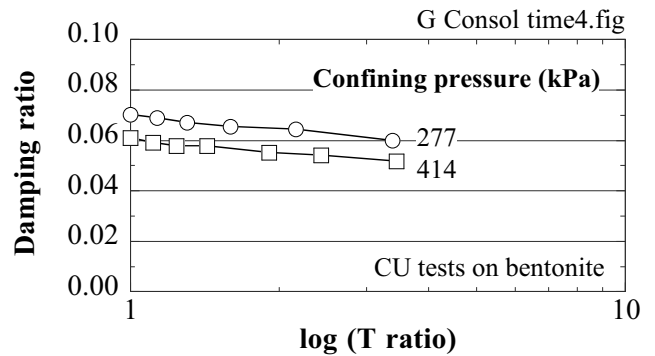


Fig. 10.49 Change in damping ratio of bentonite with time in undrained tests (Marcuson and Wahls, 1978)

**10.17  $G - \gamma$  and  $h - \gamma$  Curves of Undisturbed Samples**

Many data on nonlinear dynamic deformation characteristics of soils were obtained from drained tests on laboratory-reconstituted specimens. Since the effects of age and drainage are not negligible in real ground, however, nonlinearity data obtained from more realistic test conditions have been desired. In this regard, Yasuda and Yamaguchi (1985) summarized those data obtained from undrained tests on undisturbed samples and proposed an empirical rule:

$$\frac{G}{G_{\max}} = (A_1 + A_2 \log_{10} D_{50}) \times P'^{(B_1 + B_2 \log_{10} D_{50})} \quad \text{and} \quad h = (C_1 + C_2 \log_{10} D_{50}) \times P'^{(D_1 + D_2 \log_{10} D_{50})},$$

where  $D_{50}$  is the mean particle size of sand (mm) and  $P'$  the effective mean principal stress (kgf/cm<sup>2</sup>);

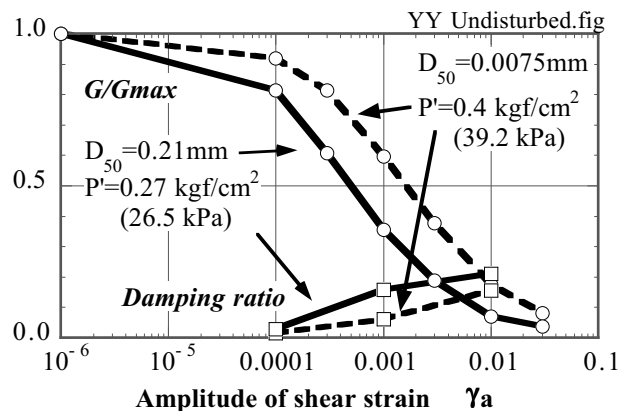
$$P' = (\sigma'_1 + \sigma'_2 + \sigma'_3) / 3 = (1 + 2K_0) \sigma'_{\text{vertical}} / 3 \quad \text{for in-situ } K_0 \text{ consolidation.}$$

The parameters of  $A_1$  to  $D_2$  were determined empirically as shown in Table 10.1. Consequently,

**Table 10.1** Parameters in Yasuda–Yamaguchi empirical formulae

Shear strain $\gamma_a$	$A_1$	$A_2$	$B_1$	$B_2$	$C_1$	$C_2$	$D_1$	$D_2$
$10^{-4}$	0.827	-0.044	0.056	0.026	0.035	0.005	-0.0559	-0.258
$3 \times 10^{-4}$	0.670	-0.068	0.184	0.086				
$10^{-3}$	0.387	-0.099	0.277	0.130	0.136	0.036	-0.375	-0.173
$3 \times 10^{-3}$	0.189	-0.089	0.315	0.147				
$10^{-2}$	0.061	-0.054	0.365	0.167	0.234	0.037	0.000	0.000
$3 \times 10^{-2}$	0.041	-0.019	0.403	0.183				

- $G_{\max}$  in their study is the shear modulus at a strain amplitude of  $10^{-6}$  (=0.0001%).
- $B_1=B_2=D_1=D_2=0$  when  $D_{50} < 0.007$  mm.
- The original database for this study was obtained for a limited condition of  $0.2 \leq P' \leq 3$  kgf/cm<sup>2</sup> ( $19.6 \leq P' \leq 294$  kPa) and  $0.002 \leq D_{50} \leq 1.0$  mm.
- Predicted  $G$  and damping ratio are indicated in Fig. 10.50. Both sandy and clayey materials were studied.
- When  $D_{50}$  is unknown in practice, its rough estimate may be given below:  
 0.4 mm for coarse gravelly sand, 0.3 mm for medium sand, 0.2 mm for fine sand, 0.1 mm for silty sand, 0.04 mm for sandy silt, 0.03 mm for clayey sand, 0.007 mm for silt, and 0.005 mm for clayey silt.
- All the ideas given in this section may include significant error due to their approximate nature.
- $B_1+B_2 \log_{10}(D_{50})$  is positive, indicating that  $G/G_{\max}$  is greater when  $P'$  increases.
- Similarly,  $D_1+D_2 \log_{10}(D_{50})$  is negative, suggesting that the damping ratio decreases as  $P'$  increases.
- Examine that  $G/G_{\max}$  decreases and damping ratio increases for coarser materials (greater  $D_{50}$ ).



**Fig. 10.50** Example of predicted characteristics of undisturbed samples



10.18 Dynamic Deformation of Gravelly Soils

Although gravelly subsoils are highly stable and their shear strength is hardly discussed, the seismic behavior of nuclear power plant facilities has been a problem. While buildings of power plants to date are situated on a base rock, such important facilities as intake channels of emergency cooling water may be placed on a relatively softer layer. A gravelly layer is preferred to less stable sand and clay.

The safety of a nuclear power plant is absolutely important. Therefore, a seismic response analysis of important facilities has been conducted intensely by using an equivalent linear technique. Because of this reason, the dynamic deformation characteristics of gravelly soils have been studied in detail. Another important application of this study is the seismic behavior of rock-fill dams (Fig. 10.51).

- Kokusho (1982) carried out a series of cyclic shear tests on gravelly materials by using a large triaxial device that measured 30 cm in sample diameter.
- Figure 10.52 reveals test results on crushed rock (碎石) with  $D_{50}$  about 30 mm.  $G_{max}$  varies with  $(2.17 - e)^2 / (1 + e)$  and  $\sigma'_c{}^{0.55}$ ;  $\sigma'_c$  being the isotropic consolidation pressure.
- Figures 10.53 and 10.54 compare the crushed rock with finer Toyoura sand ( $D_{50}$  being about 0.18 mm). See that the coarser material has smaller  $G/G_{max}$  and greater damping ratio, which imply more nonlinearity.
- Since a gravelly layer is normally dense, the effects of excess pore water pressure is neglected.



Fig. 10.51 Construction of rock fill dam

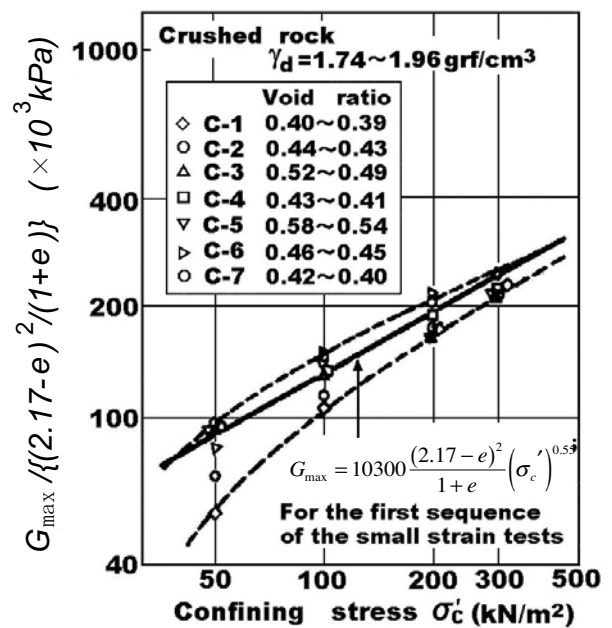


Fig. 10.52 Variation of  $G_{max}$  at small strain with void ratio and effective confining pressure (Kokusho, 1982)

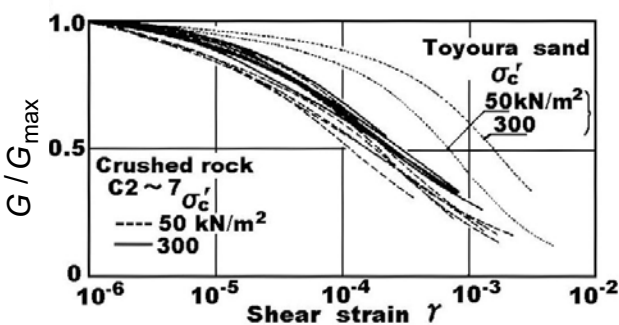


Fig. 10.53  $G/G_{max}$  of crushed rock (Kokusho, 1982)

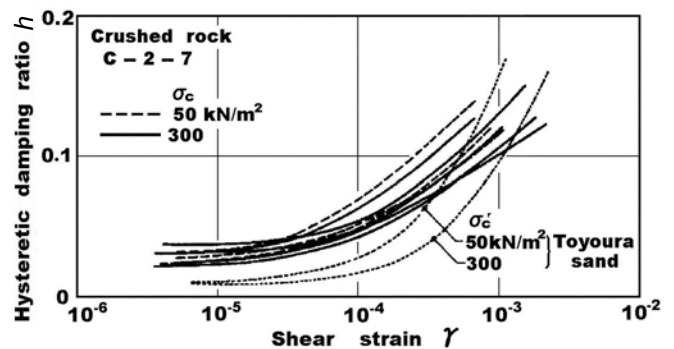
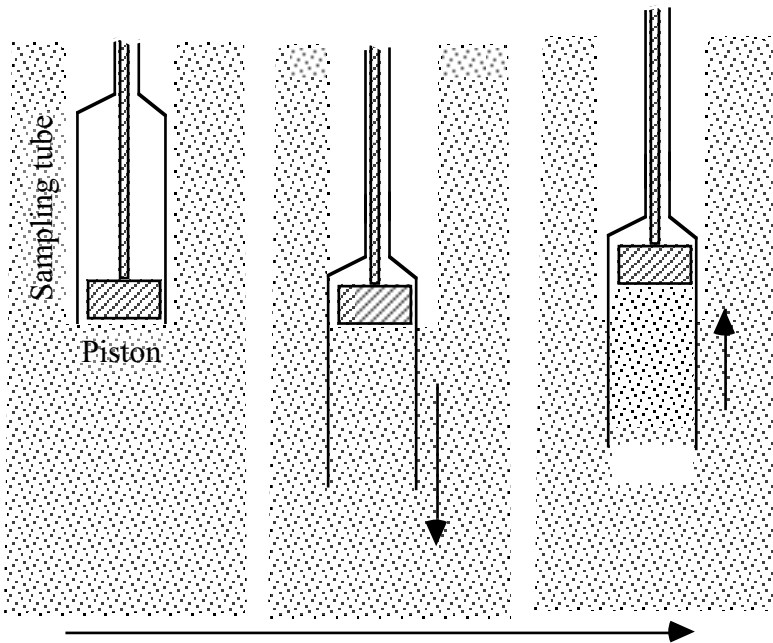


Fig. 10.54 Damping ratio of crushed rock (Kokusho, 1982)

**10.19 Collecting Undisturbed Soil Samples**

The nonlinear stress–strain behavior is measured precisely by running triaxial or other shear tests on undisturbed specimens that are collected in situ. The quality of collected samples is affected by stress history that occurs in samples. Although it is desirable that the stress-state in the field is kept unchanged during sampling, transportation to laboratory, and preparation of testing, it is impossible in practice. Among major sources of sample disturbance are the change of stress state from the anisotropic one in the ground to the isotropic one at the surface (Fig. 10.55) and the undesired force generated by penetration of a sampling machine into soil. Change of stress as illustrated in Fig. 10.55 is inevitable.

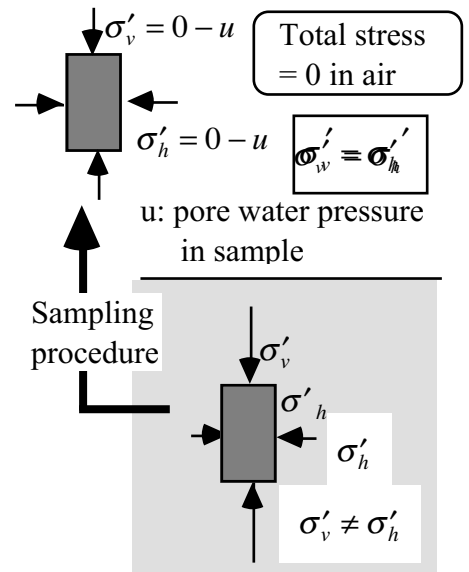
Figure 10.56 illustrates the mechanism of a soil sampler. At the bottom of a bore hole, the piston is fixed to a facility at the ground surface, and the sampling tube is pushed into soil.



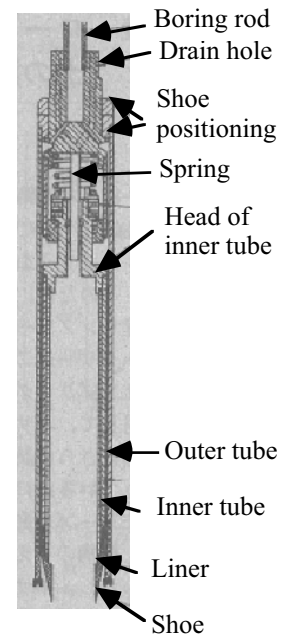
**Fig. 10.56** Mechanism of soil sampling at bottom of bore hole

Efforts have been made to reduce the effects of penetration of a sampling tube into ground. In a triple-tube sampler for loose sandy soils (Fig. 10.57), the outer tube removes unnecessary soil in order to make easy the penetration of the inner tube: less force and less disturbance. The inner tube has a liner inside (third tube made of vinyl chloride or acryl), which contains a collected sample. This device is, however, not able to collect samples of extremely loose sand ( $SPT-N < 2$ , for example). Sand falls down from the tube. It seems necessary to hold sand by closing the bottom of the tube. Figure 10.58 shows extrusion of an undisturbed soil sample from a tube (Fig. 10.58).

Collecting blocks of specimen is a cheap method of sampling if it is possible to approach the target soil layer at the bottom of an excavation work (Fig. 10.59). Collected sandy samples are frozen in an insulated container by using dry ice and are transported without additional disturbance. Make sure that unfrozen pore water is drained out of a specimen because freezing increases the volume of water. Otherwise, ice pushes sand grains, disturbs the granular structure, and makes sand softer. Fig. 10.60 shows a block sampling of a large size. The collected specimen was later used for centrifugal model tests (Sect. 24.11).

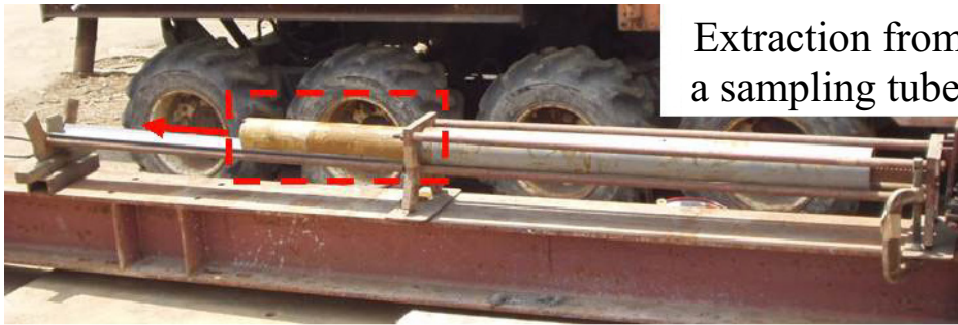


**Fig. 10.55** Change of underground effective stress state to subaerial state



**Fig. 10.57** Triple-tube sampler for sand (Japanese Geotechnical Society, 1995)

Clay sample ( $SPT-N > 4$ ) is often collected by a thin wall sampler (Fig. 10.61). This device has a very thin (approx. 2 mm) sampling tube, which minimizes the soil particle movement during penetration. A tightly fixed piston is important to avoid sample disturbance.



Extraction from a sampling tube

A sampling tube is pushed downward softly.

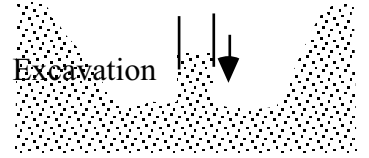


Fig. 10.59 Block sampling



Fig. 10.58 Collected undisturbed soil sample by tube sampling method



Fig. 10.60 Large block sampling of Yurakucho sand in Tokyo by Fujiwara et al. (2005)

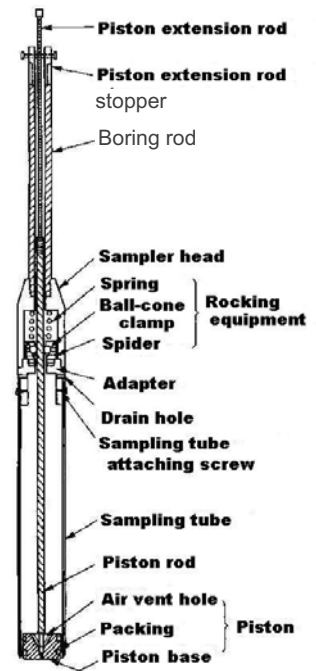


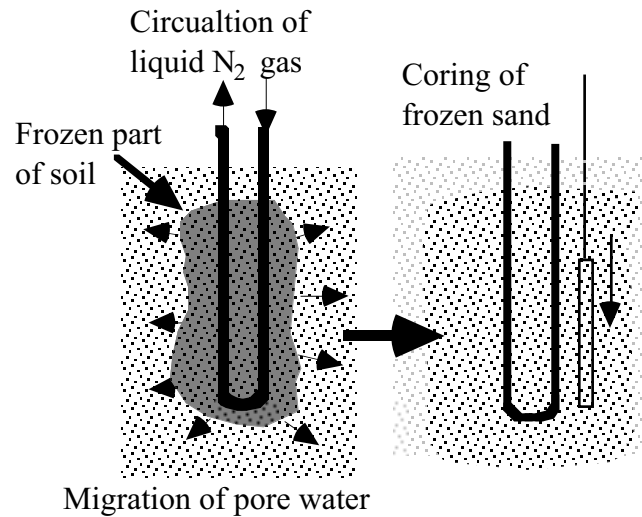
Fig. 10.61 Thin-wall sampler for clay with fixed piston (Japanese Geotechnical Society, 1995)

A recent development in undisturbed sampling is found in freezing technique. For its details, refer to Sect. 10.20. Another achievement is the use of polymer liquid during cutting soil core (Tani and Kaneko, 2006). This liquid solidifies around a sample and produces a confining effect so that disturbance is minimized. This method was successfully applied to sampling of alluvial gravelly sand with  $SPT = 15-30$  with a large size of 160 mm in diameter and 1,600 mm in length.

For the quality of undisturbed samples, refer to Sect. 10.21.

## 10.20 Freezing Technique of Sand Sampling

A better sample quality of loose sand is achieved by the technique of in-situ freezing (Yoshimi et al. 1985, 1994, 1996); Fig. 10.62. This technique is, therefore, employed for investigation of liquefaction hazard. The frozen pore water (ice) prevents any mechanical disturbance in granular structure (粒子構造) of sand. Care should be taken to start freezing from one end of soil mass and pushing the freezing front to proceed to the other end. Thus, unfrozen water is drained out. Otherwise, volume increase of ice pushes sand particles outwards and changes the granular structure, leading to disturbance in mechanical nature of sand. For the same reason, freezing of impervious clayey ground is not advisable.



**Fig. 10.62** In-situ freezing of sandy ground

The practice of freezing of gravelly sandy ground and the appearance of collected sample are demonstrated in Fig. 10.63 and Fig. 10.64. See the section of a large grain that was cut smoothly by a diamond bit of a coring device. This ideal technique of sand sampling is more expensive than thin-wall sampling, and, therefore, is employed in relatively important projects.

Freezing technique is frequently used for investigation of liquefaction potential in important projects.

It seems that less attention has been paid to the thawing process of a frozen specimen. Free flow and sufficient supply of pore water are needed in thawing parts of a specimen. Otherwise, an open space with air may be formed in a specimen or the specimen volume may contract due to volume contraction during melting of ice to water.



**Fig. 10.63** Practice of in-situ freezing (in Uozaki)

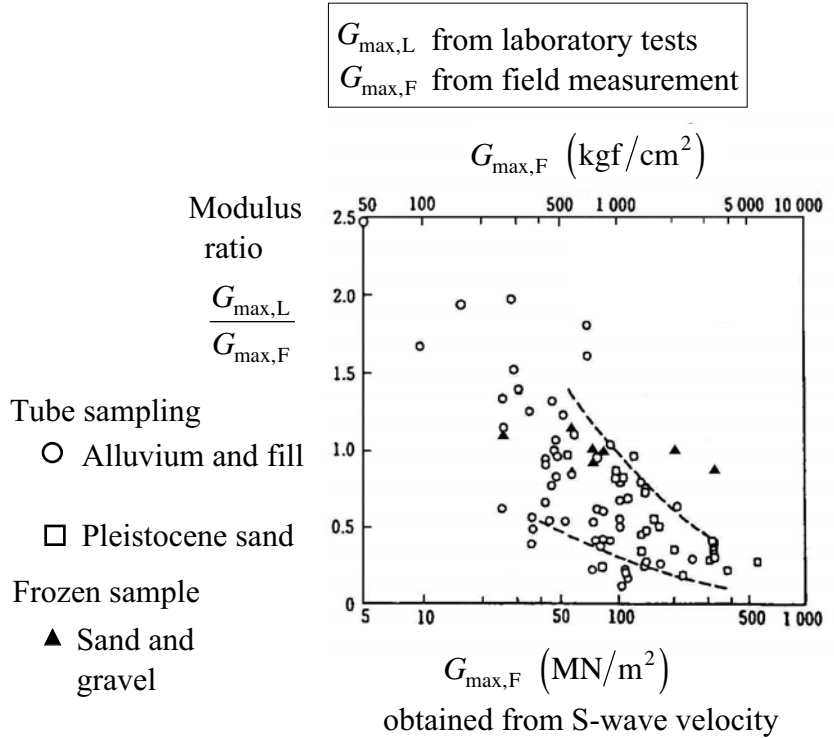


**Fig. 10.64** Gravel particles at the surface of collected frozen specimen

10.21 Extent of Sample Disturbance

It is important to assess the extent of sample disturbance caused by the present state of “undisturbed sand sampling.” At present, comparison of  $G_{max}$  at small strain obtained from laboratory tests on “undisturbed” specimen and the in-situ  $G/G_{max}$  obtained from  $V_s$  (down-hole or suspension survey) meets this requirement. Figure 10.65 compares  $G_{max,L}$  from laboratory tests on undisturbed specimens and  $G_{max,F}$  from in-situ measurement of S-wave velocity ( $V_s = \sqrt{G_{max}/\rho}$ ). Unfortunately, they are not necessarily equal to each other.

Symbols of  $\circ$  and  $\square$  in Fig. 10.65 compares values of laboratory  $G_{max}$  values and those determined from S-wave velocity. The former was obtained from laboratory tests on samples collected by so-called “undrained” tube sampling (Sect. 10.19) and is possibly subject to sample disturbance, while the latter is free of such an error. It is illustrated therein that laboratory  $G_{max}$  ( $G_{max,L}$ ) is greater than field  $G_{max}$  ( $G_{max,F}$ ) when they are relatively small. This is probably because the concerned soil was loose and is subject to densification caused by sample disturbance.  $G_{max}$  of densified soil ( $G_{max,L}$ ) is greater than the original  $G_{max,F}$ . Conversely, dense insitu soil is subjected to loosening induced by disturbance. Therefore, the relatively greater  $G_{max}$  of in-situ soil is reduced after loosening. Thus, the quality of what is called undisturbed sampling is not yet fully reliable.



**Fig. 10.65** Comparison of shear modulus at small strain obtained from laboratory tests on undisturbed samples and from in-situ downhole survey (Tokimatsu, 1995; data was added to the original figure by Yasuda and Yamaguchi, 1984)

It is advisable, therefore, to determine  $G_{max}$  from field investigation (direct measurement of  $V_s$ ). On the other hand, the nonlinearity (change of  $G$  with strain amplitude and damping ratio) is assessed by laboratory testing of undisturbed samples because those data appears less sensitive to many factors as have been shown so far.

It is interesting in Fig. 10.65 that  $G_{max}$  of undisturbed samples collected by freezing technique ( $\blacktriangle$ ) is in good agreement with the field data ( $G_{max,F}$ ). It appears that freezing technique of sampling can avoid efficiently the bad effects of sample disturbance.

Hatanaka et al. (1995) compared liquefaction resistance of frozen samples and that of conventional samples (triple tube sampler in Fig. 10.60). It was found that tube sampling generally densifies the collected sand and decreases its liquefaction resistance.

🌟 10.22 Correlation Between Surface Velocity and Strain in Subsoil

The propagation of S wave is governed by the following equation:

$$\frac{\partial^2 u}{\partial t^2} = V_s^2 \frac{\partial^2 u}{\partial z^2}, \tag{10.4}$$

in which  $u$  is the displacement and  $V_s$  is the wave propagation velocity. First when the wave propagates in one direction (positive direction of  $z$  coordinate), the solution of (10.4) is given by

$$u = F(t - z/V_s), \tag{10.5}$$

where  $F$  is an arbitrary function of  $t - z/V_s$ . Hence, velocity,  $v$ , and shear strain,  $\gamma$ , are given by

$$v = \frac{\partial F}{\partial t} = F'(t - z/V_s) \quad \text{and} \quad \gamma = \frac{\partial F}{\partial z} = -F'(t - z/V_s)/V_s = -v/V_s \tag{10.6}$$

where “ $F'$ ” denotes derivative of  $F$ . Therefore, it is possible to assess the magnitude of strain by monitoring the velocity time history and somehow measuring independently the value of  $V_s$  (soil investigation).

In a horizontal soil deposit subjected to horizontal shaking, there are always two components (i.e., upward and downward propagations) of soil displacement as discussed in Sect. 4.1. Hence, the assessment of subsurface strain is not very simple. In the simplest case when harmonic shaking occurs,

$$u(t, z) = U_0 \cos \frac{\omega z}{V_s} e^{i\omega t} \text{ (Sect. 4.6),} \quad v(t, z) = \frac{\partial u}{\partial t} = i\omega U_0 \cos \frac{\omega z}{V_s} e^{i\omega t}, \quad \text{and} \\ \gamma(t, z) = \frac{\omega}{V_s} U_0 \sin \frac{\omega z}{V_s} e^{i\omega t}. \tag{10.7}$$

Hence, the surface velocity amplitude and the subsurface strain amplitude maintain a simple proportionality.

$$\left| \frac{\gamma(t, z)}{v(t, z=0)} \right| = \frac{\tan \frac{\omega z}{V_s}}{V_s}. \tag{10.8}$$

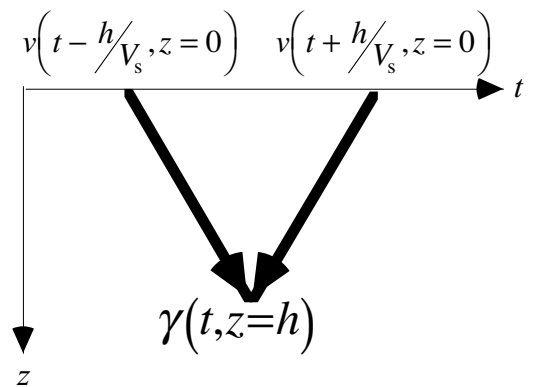
Therefore, the greater velocity implies the larger strain in soil and probably the more significant damages in different facilities.

More generally, the solution of wave propagation is given by

$$u = E(t + z/V_s) + F(t - z/V_s) \\ v(t, z) = E'(t + z/V_s) + F'(t - z/V_s) \tag{10.9} \\ \gamma(t, z) = \{E'(t + z/V_s) - F'(t - z/V_s)\}/V_s.$$

Since the strain is zero at the free ground surface ( $z = 0$ ),

$$E' = F'. \tag{10.10}$$



**Fig. 10.66** Assessment of strain in subsoil by using surface velocity records (idea by Tokimatsu et al., 1989)

According to Tokimatsu et al. (1989), therefore, the strain at the depth of  $z = h$  can be assessed by using the record of surface velocity as well as (10.10):

$$\begin{aligned}
 \gamma(t, z = h) &= \{E'(t + h/V_s) - F'(t - h/V_s)\}/V_s \\
 &= \{E'(t + h/V_s) + F'(t + h/V_s) - E'(t - h/V_s) - F'(t - h/V_s)\}/(2V_s) \\
 &= \{v(t + h/V_s, z = 0) - v(t - h/V_s, z = 0)\}/(2V_s).
 \end{aligned}
 \tag{10.11}$$

This idea was practiced by Tokimatsu et al. (1989) and is illustrated in Fig. 10.66. Moreover,  $V_s$  and, consequently, the shear modulus ( $G = \rho V_s^2$ ) were determined separately by depicting the predominant period of surface motion records,  $T$ . Assuming that this  $T$  is equal to the natural period of the surface deposit,  $V_s = 4h/T$  (Sect. 4.5 Exercise 1). Thus, it became possible to study  $G$  vs. *strain* relationship from the field observation. A good agreement in strain effects was obtained, consequently, between the field investigation and laboratory tests.

### 10.23 Nonlinear Cyclic Behavior of Sodium Bentonite

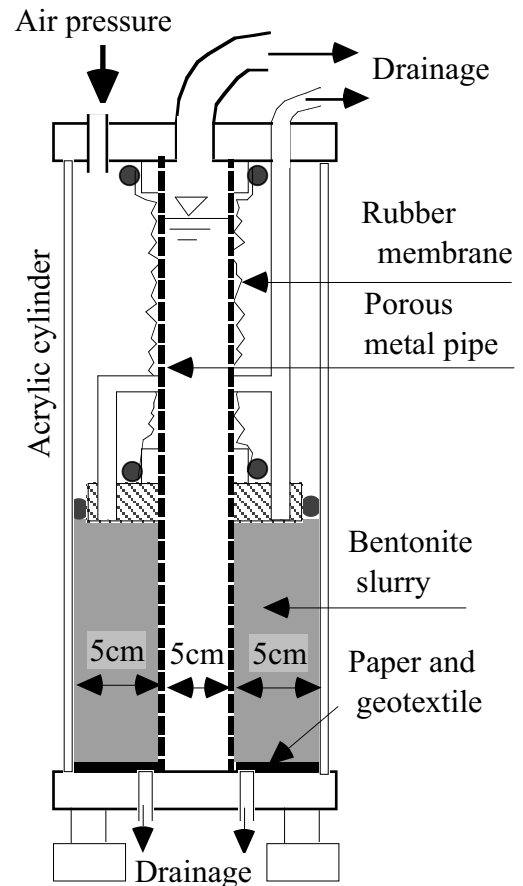
Bentonite clay is used widely as a buffer material in municipal waste landfill and probably in a repository of nuclear waste in future. Although its seismic behavior is important, there are few experimental information (see  $G_{\max}$  data on Ca-bentonite in Fig. 10.31). In particular, much has not been known about the behavior of water-saturated Na-bentonite (sodium bentonite) that swells significantly upon water submergence. This is because of difficulties in experiments in which water saturated bentonite has to be produced from a slurry and consolidation time could be as long as 10 years for a laboratory specimen due to the low permeability and significant volume compression.

In literatures, Chijimatsu et al. (1999) produced water-saturated bentonite samples for permeability tests. The sample height in their study was, however, only 10 mm, which is not sufficient for triaxial tests. Noteworthy is the extremely patient studies by Mesri and Olson (1970) as well as Olson (1974) in which montmorillonite (bentonite) samples were consolidated from slurry. Consolidation time was longer than 1 year and triaxial tests lasted for more than 13 years.

Specimens of water-saturated Na bentonite was produced recently by Nakamura et al. (2007). They produced a new consolidation tank for highly compressible bentonite slurry in which drainage occurs in a radial direction of a hollow cylindrical specimen towards the drainage pipe at the center (Fig. 10.67). Since this drainage path is merely 5 cm in length and is much shorter than the 1-m maximum thickness of the bentonite slurry, the consolidation time is drastically reduced. The consolidation theory states that the time required for the completion of consolidation is proportional to the square of the size (1.14).

Figure 10.68 indicates the shape of a hollow cylindrical bentonite specimen after 3-month consolidation in the tank. This specimen was further trimmed to fit a torsion shear device (Sect. 18.8), consolidated again in the device for several days and tested under cyclic shear loading.

Figure 10.69 indicates the variation of  $G/G_{\max}$  and damping ratio of water-saturated bentonite specimen. Since this study was related with nuclear waste problems, the original Na bentonite was mixed with 30% of silica sand. Hence, the plasticity index of the tested material was reduced to 251 %, which was lower than that of the original bentonite (more than 400 %). By comparing the values in this figure with data of other soils (Figs. 10.27 and 10.28), it is found that  $G/G_{\max}$  of bentonite is greater than those of other soils, and



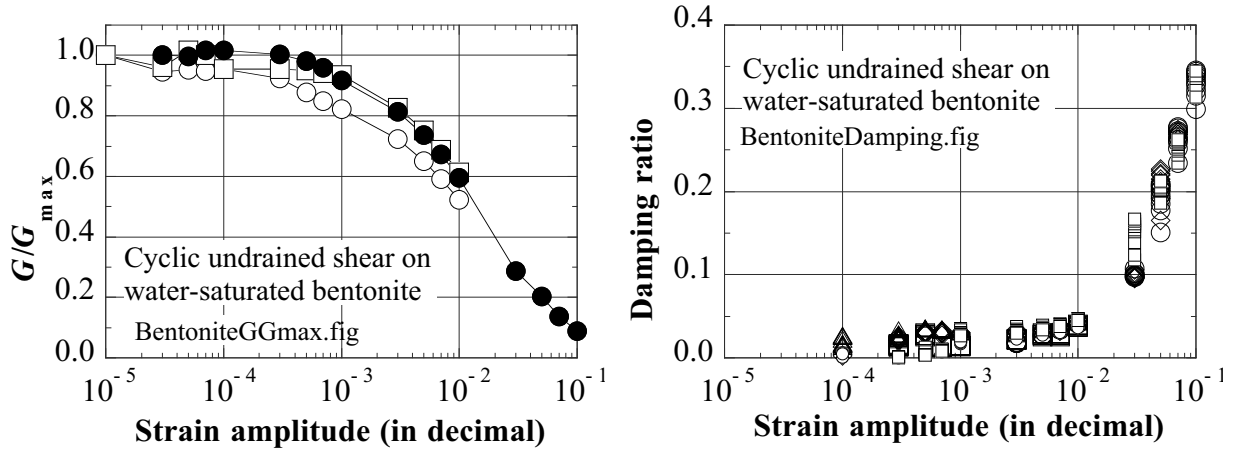
**Fig. 10.67** Consolidation tank for preparation of hollow cylindrical specimen of water-saturated bentonite (Nakamura et al., 2007)



**Fig. 10.68** Appearance of bentonite specimen after preconsolidation under 98 kPa



the damping ratio is lower. Thus, more plastic soils have less extent of nonlinearity as stated in Sect. 10.2.



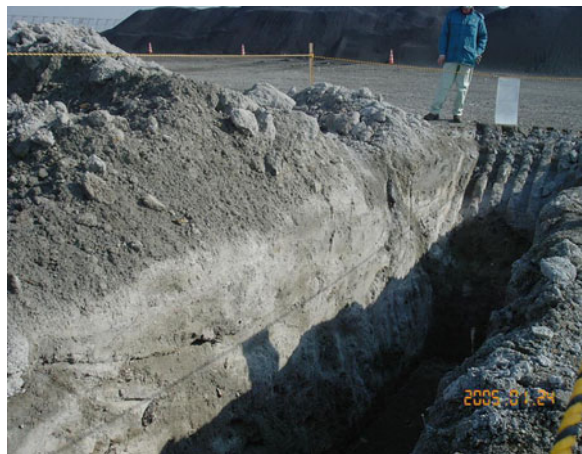
**Fig. 10.69** Variation of  $G/G_{max}$  and damping ratio of water-saturated Na-bentonite

### 10.24 Nonlinear Cyclic Behavior of Municipal Solid Waste

A recent target of geotechnical engineering is a landfill that is composed of municipal solid waste. In principle, there are three kinds of waste, which are unprocessed wastes, incinerated ash, and incombustible wastes, that are composed of plastics, metals, soil, ceramics, etc. Such unprocessed wastes as food and other organic materials are either dumped directly in landfills to be subjected to bio-disintegration or incinerated (burnt) to be ash. Figure 10.70 shows a landfill in Delaware of USA where wastes are directly dumped. Figure 10.71 is indicative of an incinerated ash ground near Tokyo. The appearance of this material is similar to sand. Figure 10.72 reveals a dumping site of plastic wastes. The original plastics are shredded into small pieces prior to dumping. It is important that the incombustible wastes include organic waste as well because of the inclusion of unfinished lunch boxes etc. In many municipalities, organic and incombustible wastes are separated in families prior to dumping. In contrast, a recent technology has made it possible to incinerate all the family wastes under higher temperatures, and the produced slug waste looks similar to clean gravel (Fig. 10.73).



**Fig. 10.70** Unprocessed waste landfill in Wilmington of Delaware



**Fig. 10.71** Trench cut in landfill of incinerated ash in Tokyo



**Fig. 10.72** Landfill of plastic waste in Tokyo



**Fig. 10.73** Landfill of incinerated slugs in Yokohama

Many people imagine that municipal waste is a very soft and unstable material. This idea is supported by failure accidents of landfills such as the Payatas landfill near Manila, the Philippines, in 2000 (Merry et al. 2005), and another one in Bandung of Indonesia (2005, Fig. 10.74). Most of these failures were induced by heavy rainfalls and the lack of compaction of the waste. Vincential Missionaries (1998) reported the pre-failure situation of the Payatas landfill. There are, however, examples in which nearly vertical cliffs of municipal waste have been stable for many years (Figs. 10.75 and 10.76). As is clearly seen in Fig. 10.75, these stable cliffs are stabilized by such fibrous materials as paper, clothes, strings, etc. This stabilizing mechanism is identical with those employed in modern reinforced soils. Noteworthy

is that the reinforcement by fibers is destroyed by fires, making the landfill less unstable. Both Payatas and Bandung landfills had fire prior to failure (Merry et al. 2005, Kölsch et al. 2005).

A series of triaxial drained compression tests were conducted on bio-treated waste that was collected at the Yever landfill near Wilhelmshafen, Germany (Fig. 10.77) (Towhata et al. 2004 and Itoh et al. 2005). Figure 10.78 illustrates test results. It is interesting that tested samples revealed approximately linear stress–strain relationships and did not yield within the range of the test (within the strain capacity of a triaxial device). By comparing these results with the behavior of densified Toyoura sand in the same figure, it may be said that the tested waste has better shear resistance. The deformation modulus of waste is, on the contrary, much lower than that of sand, implying that waste is significantly softer than sand.



**Fig. 10.74** Failure of Leuwigajah landfill near Bandung, Indonesia



**Fig. 10.75** Vertical and stable cliff in landfill near Göttingen, Germany



**Fig. 10.76** Stable waste cliff in Tokyo  
(Photo by Y. Imai)



**Fig. 10.77** Ongoing field bio-treatment in Yever landfill in Germany

An important feature in Fig. 10.78 is the behavior of the organic waste from which the reinforcing fibrous materials were removed. As expected, the stress–strain curve reveals yielding followed by

softening of the stress level. Note further that the incombustible waste from Tokyo site is extremely soft, but still exhibits stress level higher than that of sand in a large strain range.

More recently, a large triaxial shear device was constructed for waste tests (Towhata et al. 2007). Since the grain size of incombustible waste reaches several centimeters, at maximum, a specimen size of 30 cm in diameter and 60 cm in height was considered necessary. After obtaining approximately linear stress-strain behavior (similar to Fig. 10.78), cyclic triaxial tests were conducted to measure shear modulus and damping ratio of Tokyo's incombustible waste (Fig. 10.79). In this study, shear stress and shear strain were defined by

$$\tau \equiv (\sigma_a - \sigma_r)/2 \text{ and } \gamma \equiv \epsilon_a - \epsilon_r$$

by using triaxial stress and strain data.

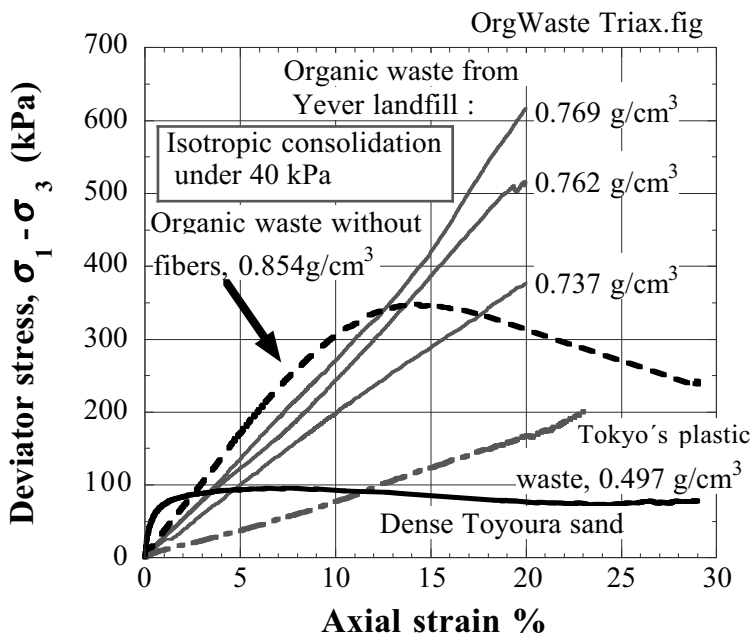


Fig. 10.78 Triaxial shear tests on waste



Fig. 10.79 Incombustible waste collected from Tokyo landfill

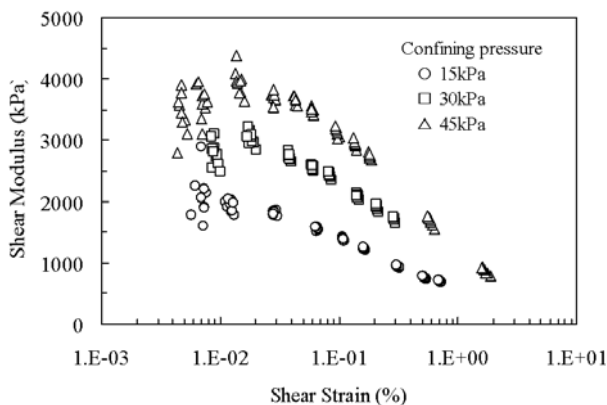


Fig. 10.80 Variation of shear modulus of Tokyo incombustible waste with strain amplitude

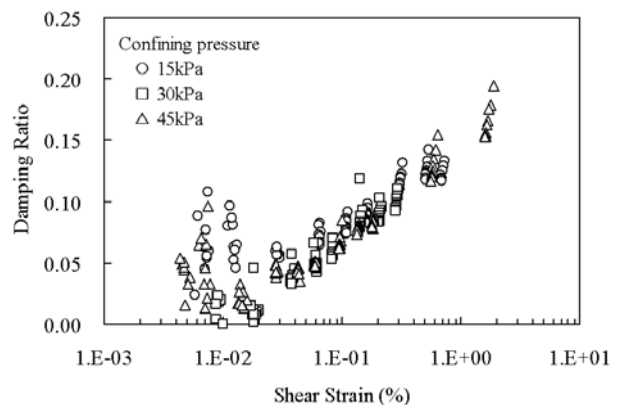


Fig. 10.81 Variation of damping ratio of Tokyo incombustible waste with strain amplitude

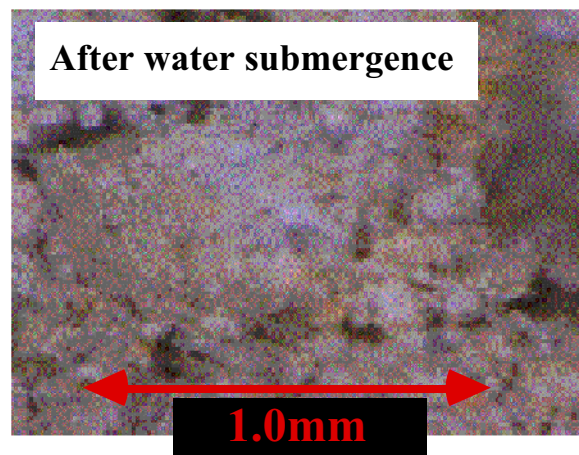
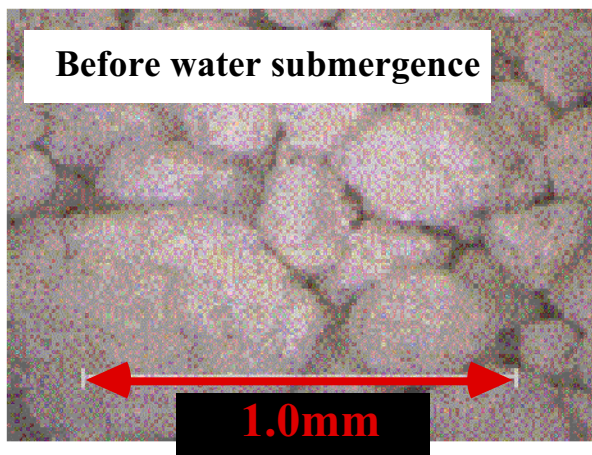
Figures 10.80 and 10.81 illustrate the nonlinear properties of incombustible waste. Although there is some uncertainty in the strain range of 0.01% or less (due probably to large grain size), the nonlinearity

in the greater strain range is consistent with what have been known on other soils. The values of shear modulus (Fig. 10.80) is somewhat lower than modulus of soils under similar stress. Thus, the natural period of a landfill of incombustible wastes is longer than in soil deposits.

Incinerated ash appears similar to gravelly sand (Fig. 10.82). It is important that this ash reacts with water and gains intergranular bonding; Fig. 10.83 shows that surface of grains are covered by cementing materials after water submergence. Consequently, a deposit of incinerated ash comes to exhibit a very high rigidity. Figure 10.84 illustrates the results of a triaxial compression test in which loading was paused for 1–6 h after large strain. It is evident that the stress level increased while loading stopped and the mechanical damage (yielding) during previous loading was cured in the meantime (self curing).



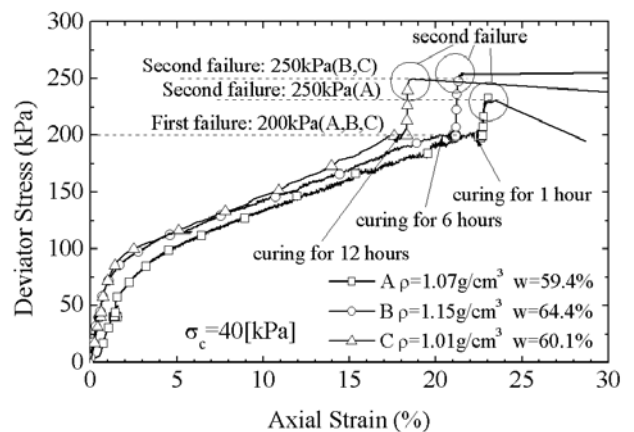
**Fig. 10.82** Incinerated ash collected from Tokyo Bay landfill



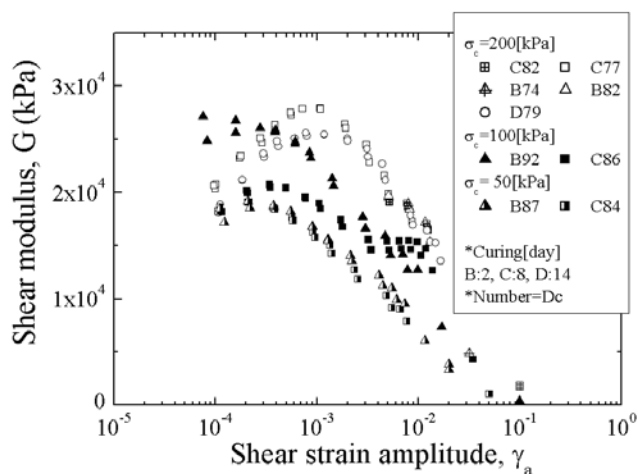
**Fig. 10.83** Appearance of incinerated ash before and after water submergence

The cyclic properties of incinerated ash were studied by torsion shear tests. Figures 10.85 and 10.86 demonstrate that the modulus becomes small at a strain of 10% (0.1). The significant increase in damping ratio beyond this strain value may be due to shear failure. In general, the behavior of incinerated ash is similar to what have been know for other soils.

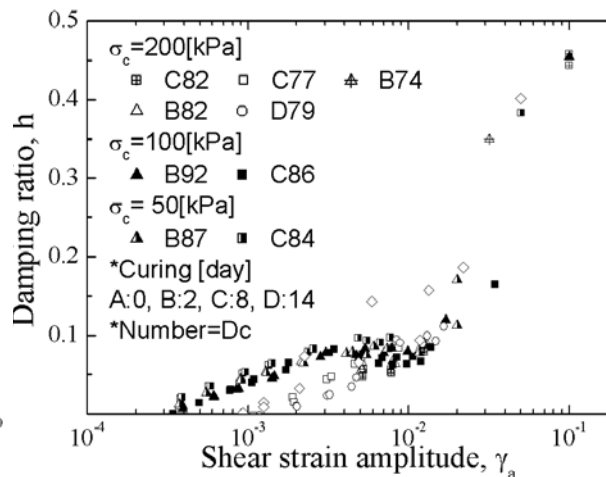
As may be known, one of the significant problems in municipal waste landfill is the long-term consolidation. Uno et al. (2007) found experimentally that this problem can be solved by preloading in which the stress level in landfill is temporarily increased by additional soil filling and, after several months when substantial subsidence has occurred, the soil is removed.



**Fig. 10.84** Development of cementation and its effect on stress–strain behavior of incinerated ash



**Fig. 10.85** Variation of shear modulus of incinerated ash with shear strain amplitude



**Fig. 10.86** Variation of damping ratio of incinerated ash with shear strain amplitude

### List of References in Chapter 10

- Afifi, S.S. and Richart Jr., F.E. (1973) Stress-history effects on shear modulus of soils, *Soils Found.*, Vol. 13, No. 1, pp. 77–95.
- Anderson, D.G. and Woods, R.D. (1976) Time-dependent increase in shear modulus of clay, *J. Geotech. Eng.*, ASCE, Vol. 102, pp. 525–537.
- Brignoli, E.G.M., Gotti, M. and Stokoe, K.H.I. (1996) Measurement of shear waves in laboratory specimens by means of piezoelectric transducers, *Geotech. Test. J.*, Vol. 19, No. 4, pp. 384–397.
- Casagrande, A. and Shannon, W.L. (1948a) Research on stress-deformation and strength characteristics of soils and rocks under transient loading, *Harvard University Soil Mechanics Series*, No. 31.
- Casagrande, A. and Shannon, W.L. (1948b) Strength of soils under dynamic loads, *Proc. ASCE*, Vol. 74, No. 4, pp. 591–608.
- Chijimatsu, M., Fujita, T., Suzuki, H. and Matsumoto, K. (1999) Hydraulic properties of buffer material, *Bulletin of Japan Nuclear Cycle Development Institute*, No. 5.
- Chung, R.M., Yokel, F.Y. and Drnevich, V.P. (1984) Evaluation of dynamic properties of sands by resonant column testing, *Geotech. Test. J.*, Vol. 7, No. 2, pp. 60–69.
- Dobry, R. and Vucetic, M. (1987) Dynamic properties and seismic response of soft clay deposits, *Proc. Intern. Symp. Geotech. Eng. Soft Soils*, Vol. 2, pp. 51–87.
- Ellis, E.A., Soga, K., Bransby, M.F. and Sato, M. (2000) Resonant column testing of sands with different viscosity pore fluids, *J. Geotech. Geoenviron. Eng.*, ASCE, Vol. 126, No. 4, pp. 10–17.
- Fujiwara, T., Horikoshi, K. and Sakai, K. (2005) Development of a sampler designed for laminar box and its application to dynamic centrifuge modeling of footing settlement due to liquefaction, *Proc. 16th Int. Conf. Soil Mech. Geotech. Eng.*, Vol. 4, pp. 2645–2648.
- Goto, S., Tatsuoka, F., Shibuya, S., Kim, Y.S. and Sato, T. (1991) A simple gauge for local small strain measurements in the laboratory, *Soil Found.*, Vol. 31, No. 1, pp. 169–180.
- Hara, A. (1973) Dynamic nature of ground and its application in practice 地盤の動力学的性質とその応用, *Proc. 2nd Symp. on Dynamic Behavior of Ground 第2回地盤振動シンポジウム*, AIJ 建築学会, pp. 33–39 (in Japanese).
- Hardin, B.O. (1978) The nature of stress-strain behavior for soils, *ASCE Geotech. Engg. Div. Specialty Conf. Earthq. Eng. Soil Dynam.*, Vol. I, pp. 3–90.
- Hardin, B.O. and Black, W.L. (1968) Vibration modulus of normally consolidated clay, *Proc. ASCE*, Vol. 94, SM2, pp. 353–369.

- Hatanaka, M., Uchida, A. and Oh-oka, H. (1995) Correlation between the liquefaction strengths of saturated sands obtained by in-situ freezing method and rotary-type triple tube method, *Soils Found.*, Vol. 35, No. 2, pp. 67-75.
- Humphries, W.K. and Wahls, H.E. (1968) Stress history effects on dynamic modulus of clay, *Proc. ASCE*, Vol. 94, SM2, pp. 371-389.
- Idriss, I.M., Dobry, R. and Singh, R.D. (1978) Nonlinear behaviour of soft clays during cyclic loading, *Proc. ASCE*, Vol. 104, GT12, pp. 1427-1447.
- Iida, K. (1938) The velocity of elastic waves in sand, *Bulletin of Earthquake Research Institute, University of Tokyo*, Vol. 16, pp. 131-145.
- Imazu, M. and Fukutake, K. (1986) Dynamic shear modulus and damping ratio of gravel materials, *Proc. 21st Annual Convention of JSSMFE*, pp. 509-512.
- Ishimoto, M. and Iida, K. (1936) Determination of elastic constants of soils by means of vibration methods, Part 1. Young's modulus, *Bulletin of Earthquake Research Institute, University of Tokyo*, Vol. 14, pp. 632-657.
- Ishimoto, M. and Iida, K. (1937) Determination of elastic constants of soils by means of vibration methods, Part 2. Modulus of rigidity and Poisson's ratio, *Bulletin of Earthquake Research Institute, University of Tokyo*, Vol. 15, pp. 67-85.
- Itoh, T., Towhata, I., Kawano, Y., Kameda, M., Fukui, S., Kölsch, F. and Yonai, Y. (2005) Mechanical properties of municipal waste deposits and ground improvement, *Proc. XVIth International Conference on Soil Mechanics and Geotechnical Engineering, Osaka* Vol. 4, pp. 2273-2276.
- Japanese Geotechnical Society (1995) Field soil investigation, p. 154 and p. 164 (in Japanese).
- Kölsch, F., Fricke, K., Mahler, C. and Damanhuri, E. (2005) Stability of landfills – The Bandung dumpsite disaster, *Proceedings of the 10th Int. Landfill Symposium, Cagliari*.
- Kokusho, T. (1982) Dynamic deformation characteristics of soils and nonlinear seismic response of ground, *Doctoral Thesis, University of Tokyo* (in Japanese).
- Kokusho, T. (1982) Dynamic soil properties and nonlinear seismic response of ground, *Doctoral Thesis, University of Tokyo* (in Japanese).
- Kokusho, T., Yoshida, Y. and Esashi, Y. (1982) Dynamic properties of soft clay for wide strain range, *Soil Found.*, Vol. 22, No. 4, pp. 1-18.
- Kokusho, T. (1987) In-situ dynamic soil properties and their evaluations, *Proc. 8th Asian Regional Conf. Soil Mech. Found. Engg.*, Vol. 2, pp. 215-240.
- Lefebvre, G. and Pfendler, P. (1996) Strain rate and preshear effects in cyclic resistance of soft clay, *J. Geotech. Geoenviron. Eng.*, ASCE, Vol. 122, No. 1, pp. 21-26.
- Lefebvre, G. and LeBoeuf, D. (1987) Rate effects and cyclic loading of sensitive clays, *J. Geotech. Eng.*, ASCE, Vol. 113, No. 5, pp. 476-489.
- Maqbool, S. and Koseki, J. (2006) Effects of compaction on dynamically and statically measured small strain stiffness of gravel, *Proceedings of International Conference on Earthquake Engineering (ICEE), Lahore, Pakistan*, pp. 161-175.
- Marcuson III, W.F. and Wahls, H.E. (1978) Effects of time on damping ratio of clays, *ASTM STP 654 Dynamic Geotechnical Testing*, pp. 126-147.
- Merry, S.M., Kavazanjian, E. and Fritz, W.U. (2005) Reconnaissance of the July 10, 2000, Payatas Landfill Failure, *J. Performance Construct. Facilities*, ASCE, Vol. 19, No. 2, pp. 100-107.
- Mesri, G. and Olson, R.E. (1970) Shear strength of montmorillonite, *Geotechnique*, Vol. 20, No. 3, pp. 261-270.
- Nakamura, M., Thuan, B.T., Uchimura, T., Sugo, K. and Towhata, I. (2007) Torsional shear tests on water-saturated bentonite samples and method of sample preparation, to be submitted to *Soils and Foundations*.
- Olson, R.E. (1974) Shearing strengths of kaolinite, illite and montmorillonite, *Proc. ASCE*, Vol. 100, GT11, pp. 1215-1229.

- Osipov, V.I., Gratchev, I.B. and Sassa, K. (2005) The mechanism of liquefaction of clayey soils (M124), Chap. 15, *Landslides: Risk Analysis and Sustainable Disaster Management*, pp. 127–131, Springer, Berlin, Heidelberg, New York.
- Richart Jr., F.E., Hall, J.R. and Woods, R.D. (1970) *Vibrations of soils and foundations*, Prentice-Hall, Japanese translation : 土と基礎の振動、岩崎・嶋津訳、鹿島出版会.
- Tanaka, Y., Kudo, K., Nishi, K., Okamoto, T., Kataoka, T. and Ueshima, T. (2000) Small strain characteristics of soils in Hualien, Taiwan, *Soils Found.*, Vol. 40, No. 3, pp. 111–125.
- Tani, K. and Kaneko, S. (2006) Undisturbed sampling method using thick waste-soluble polymer solution, *Tsuchi-to-Kiso: Monthly Magazine of Japan. Geotech. Soc.*, Vol. 54, No. 4, pp. 19-21 (in Japanese).
- Tokimatsu, K. (1995) Quality of undisturbed samples, *Field soil investigation*, Japanese Geotechnical Society, p. 150.
- Tokimatsu, K., Midorikawa, S. and Yoshimi, Y. (1989) Dynamic soil properties obtained from strong motion records, *Proc. 12th Int. Conf. Soil Mech. Found. Eng.*, Vol. 3, pp. 2015–2018.
- Towhata, I., Haga, K. and Nakamura, S. (1985) Effects of cyclic drained shear or rigidity of sand, *Proc. 20th Nat. Conf. Soil Mech. Found. Eng.*, Vol. 1, pp. 591–592.
- Towhata, I., Kawano, Y., Yonai, Y. and Kölsch, F. (2004) Laboratory tests on dynamic properties of municipal waste, *Proc. the 11th Int. Conf Soil Dynamics and Earthquake Engineering and the 3rd International Conference on Earthquake Geotechnical Engineering, Berkeley*, Vol. 1, pp. 688–693.
- Towhata, I., Uno, M., Kawano, Y., Kameda, M., Kita, Y. and Yonai, Y. (2007) Laboratory tests on mechanical properties of municipal waste solid waste, to be submitted to *Proc. JSCE* (in Japanese).
- Uno, M., Itoh, T., Imai, Y., Tsujimura, T., Towhata, I., Fukui, S., Kita, Y. and Watanabe, Y. (2007) Laboratory tests on improvement of mechanical properties of municipal solid waste, to be submitted to *Proc. JSCE* (in Japanese).
- Viggiani, J. and Atkinson, J.H. (1995) Interpretation of bender element tests. *Geotech.*, Vol. 45, No. 1, pp. 149–154.
- Vincentian Missionaries (1998) The Payatas environment programme: micro-enterprise promotion and involvement in solid waste management in Quezon City, *Environment and Urbanization*, Vol. 10, No. 2, pp. 55–68.
- Yasuda, S. and Yamaguchi, I. (1984) Dynamic shear modulus of sand obtained from laboratory and in-situ tests, *Symp. Monitoring Deformation and Strength of Sand and Sandy Ground, JSSMFE*, pp. 115–118.
- Yasuda, S. and Yamaguchi, I. (1985) Dynamic soil properties of undisturbed samples, *20th Ann. Conv. JSSMFE*, pp. 539–542, Nagoya.
- Yoshimi, Y. and Goto, S. (1996) Liquefaction resistance of silty sand based on in situ frozen samples, *Geotech.*, Vol. 46, pp. 153–156.
- Yoshimi, Y., Hatanaka, M., Oh-Oka, H. and Makihara, Y. (1985) Liquefaction of sands sampled by in situ freezing, *Proc. 11th ICSMFE*, Vol. 4, pp. 1927–1930.
- Yoshimi, Y., Tokimatsu, K. and Ohara, J. (1994) In situ liquefaction resistance of clean sands over a wide density range, *Geotech.*, Vol. 44, No. 3, pp. 479–494.



# Chapter 11

## Stress–Strain Models

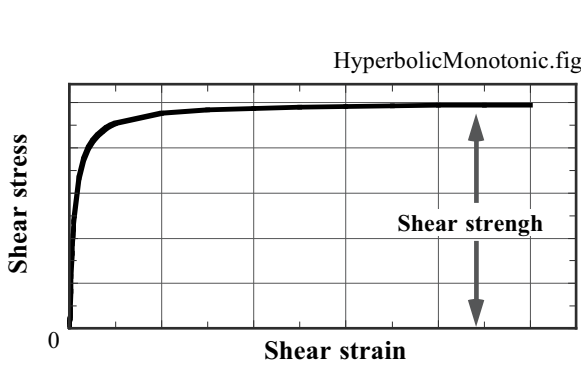


Buddhism statue in Sukhothai, Thailand.

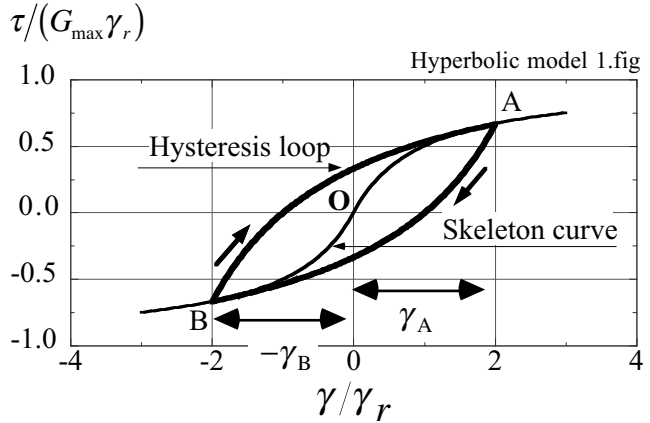
Sukhothai was the capital of the first Thai kingdom within the present territory of Thailand. Buddhism flourished in this capital. Sukhothai Kingdom reached its peak in late thirteenth Century under the reign of King Ramkhamhaeng. After him, however, Sukhothai declined quickly and came under control of Ayutthaya Dynasty in late fourteenth Century.

**11.1 Hyperbolic and Ramberg–Osgood Stress–Strain Models**

Stress–strain relationship of soil is characterized by the rigidity when strain is small as well as the shear strength at large strains, which is the upper bound of the stress level. This fundamental nature of soil behavior has often been modeled by a hyperbolic curve (Fig. 11.1); refer to Kondner (1963) together with Kondner and Zelasko (1963).



**Fig. 11.1** Hyperbolic modeling of stress–strain behavior subjected to monotonic shear



**Fig. 11.2** Hyperbolic stress–strain model for cyclic loading

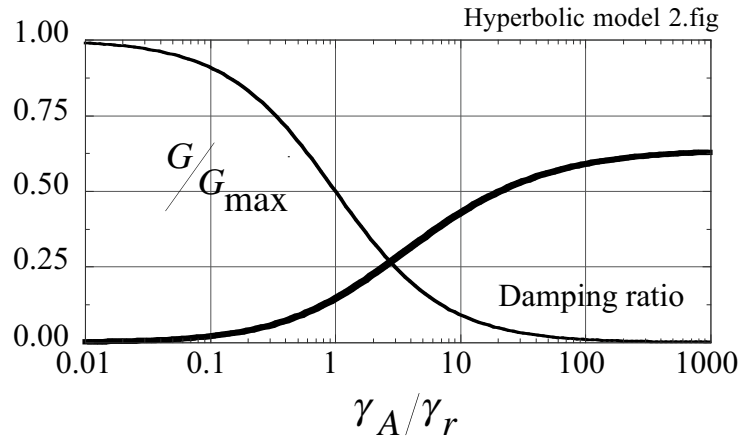
It is possible to model a cyclic stress–strain curve by a hyperbola as well. This model is used for dynamic analyses in the time domain. In case of an analysis on a one-dimensional (level) ground subjected to horizontal shaking,

$$\tau = \frac{G_{\max} \gamma}{1 + |\gamma/\gamma_r|}, \quad (11.1)$$

in which  $G_{\max}$  is the shear modulus at a very small strain amplitude, while a parameter of  $\gamma_r$  is called the reference strain. Since

$$\tau \rightarrow G_{\max} \gamma_r \text{ when } \gamma \rightarrow \infty,$$

$\gamma_r$  stands somehow for shear strength property.



**Fig. 11.3**  $G$  and  $h$  of hyperbolic model

The hyperbolic equation (11.1) models the skeleton curve BOA in Fig. 11.2. The skeleton curve is the one that passes through the ends of hysteresis loop with a variety of strain amplitude  $\pm\gamma_A$  (Fig. 11.2). Equation (11.2) gives a formula for secant modulus,  $G$ , varying with the strain amplitude,

$$\frac{G}{G_{\max}} = \frac{\tau/\gamma}{G_{\max}} = \frac{1}{1 + |\gamma_A/\gamma_r|}. \quad (11.2)$$

The hysteresis loop,  $A \Rightarrow B \Rightarrow A$  in Fig. 11.2, is often modeled by enlarging the skeleton curve two times (Masing rule: Masing, 1926);

$$\frac{\tau - \tau_A}{2} = \frac{G_{\max} \frac{\gamma - \gamma_A}{2}}{1 + |(\gamma - \gamma_A)/(2\gamma_r)|} \quad \text{for } A \Rightarrow B \quad \text{and} \quad \frac{\tau - \tau_B}{2} = \frac{G_{\max} \frac{\gamma - \gamma_B}{2}}{1 + |(\gamma - \gamma_B)/(2\gamma_r)|} \quad \text{for } B \Rightarrow A,$$

where  $\gamma_B = -\gamma_A$  and  $\tau_B = -\tau_A$  as shown by (11.1). The damping ratio is obtained by calculating  $W$  and

$\Delta W$  (area of loop):

$$W = \frac{G\gamma_A^2}{2} = \frac{G_{\max}\gamma_A^2}{2(1+\gamma_A/\gamma_r)} \quad (11.3)$$

$$\Delta W = 2 \int_{-\gamma_A}^{\gamma_A} (\text{Hysteresis loop } B \Rightarrow A) d\gamma = 2 \int_{-\gamma_A}^{\gamma_A} \left\{ \tau_B + \frac{G_{\max}(\gamma - \gamma_B)}{1 + |(\gamma - \gamma_B)/(2\gamma_r)|} \right\} d\gamma \quad (11.4)$$

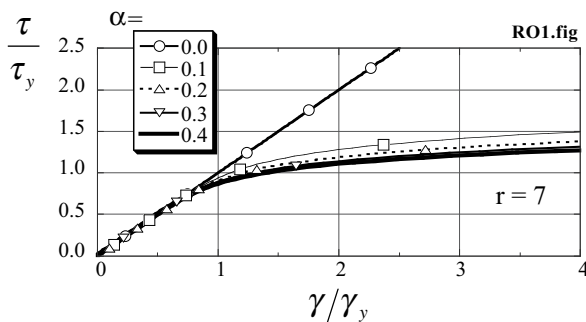
$$= 2 \int_{-\gamma_A}^{\gamma_A} \left\{ -\frac{G_{\max}\gamma_A}{1 + \gamma_A/\gamma_r} + \frac{G_{\max}(\gamma + \gamma_A)}{1 + (\gamma + \gamma_A)/(2\gamma_r)} \right\} d\gamma = \frac{4G_{\max}}{1 + \gamma_A/\gamma_r} \frac{\gamma_A}{\gamma_r} \left( \frac{\gamma_A}{\gamma_r} + 2 \right) - 8G_{\max}\gamma_r^2 \log_e \left( 1 + \frac{\gamma_A}{\gamma_r} \right) \quad (11.5)$$

$$\text{Damping ratio, } h = \frac{2}{\pi} \left\{ \left( 1 + \frac{2}{\gamma_A/\gamma_r} \right) - 2 \frac{1 + \frac{\gamma_A}{\gamma_r}}{(\gamma_A/\gamma_r)^2} \log_e \left( 1 + \frac{\gamma_A}{\gamma_r} \right) \right\} \quad (11.6)$$

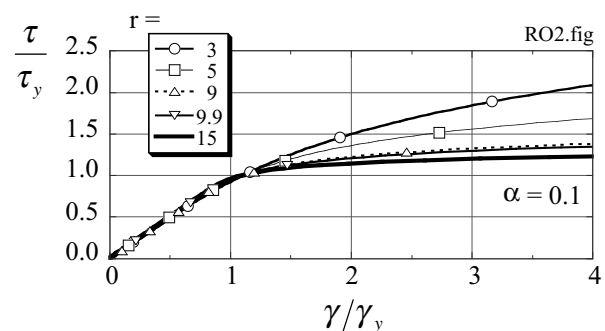
Figure 11.3 demonstrates the relationship of  $G/G_{\max}$  and  $h$  with the strain amplitude. It should be noted that the reference strain is the strain amplitude at which  $G/G_{\max} = 0.5$ . The damping ratio at a very large strain amplitude approaches  $2/\pi = 0.637$ , which is much larger than what is reported by experiments (Chap. 10). Thus, the hyperbolic model should not be used in a large-strain range. Although its idea is clear, the hyperbolic model cannot freely adjust the shape of curves. Hence, experimental results cannot be fully considered. This problem is avoided in an equivalent-linear approach (Sect. 9.10) by using a model by Hardin and Drnevich (1972):

$$\text{Damping ratio, } h = \text{Maximum damping ratio at large strain} \times \left( 1 - G/G_{\max} \right)$$

in which  $G/G_{\max}$  at a given strain amplitude is derived from (11.2).



**Fig. 11.4** Variation of skeleton curve with  $\alpha$



**Fig. 11.5** Variation of skeleton curve with changing  $r$ .

The Ramberg–Osgood model is another kind of idea that reproduces the one-dimensional stress–strain behavior in the course of cyclic shear. Jennings (1964) used this model in terms of force and displacement. This text, however, describes the skeleton curve of this model by means of stress and strain:

$$\frac{\gamma}{\gamma_y} = \frac{\tau}{\tau_y} \left\{ 1 + \alpha \left( \frac{\tau}{\tau_y} \right)^{r-1} \right\} \quad (11.7)$$

in which a subscript “y” means characteristic values, while  $\alpha$  and  $r$  are soil parameters to be determined by soil testing. Figures 11.4 and 11.5 illustrate the variation of curves by (11.7) with changing parameters:

The major features of this model as compared with the hyperbolic model are as what follows.

1. There is no upper bound in shear stress; i.e.,  $\lim_{\gamma \rightarrow \infty} \tau$  is infinite. Therefore, shear strength is not considered. As an alternative, soil parameters in the model are adjusted to make shear stress at 1% strain, for example, equal to an appropriate value.
2. Since there are three parameters, there is more freedom to take into account the complex soil behavior; for example, shear modulus at small strain, damping ratio at large strain, and shear stress at large strain.
3. Equation (11.7) helps calculate the strain value from a given value of stress. Shear stress, conversely, cannot be directly calculated from strain. This may make a nonlinear analysis more time consuming because stress determination needs iteration.

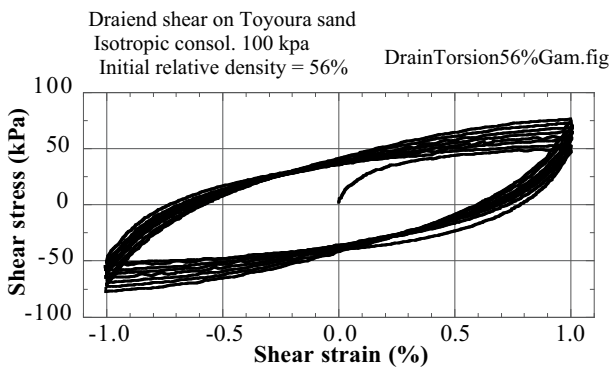
Both hyperbolic and Ramberg–Osgood models are intended to be used for a single-degree-of-freedom situation. Therefore, horizontal shaking of a level ground is their major target. Extension to a multi-dimensional situation needs more elaborate modeling.

**11.2 Dilatancy of Sand Subjected to Cyclic Drained Shear**

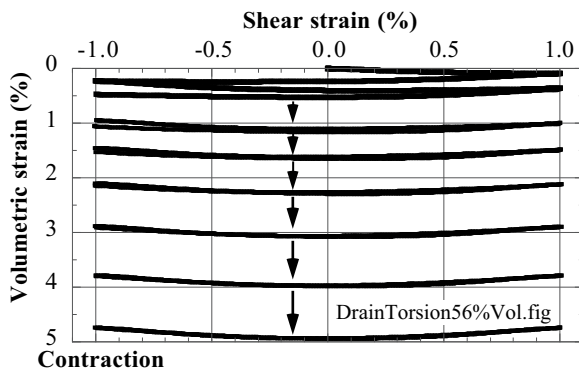
Deformation of soil is characterized by dilatancy, which is the volume change induced by shear deformation (Sect. 1.6). Under cyclic loading, the volume change occurs as contraction, which means subsidence of ground surface after an earthquake event (Sect. 17.11). It will be shown later that the volume contraction in drained condition is equivalent with the development of excess pore water pressure in undrained conditions (Sect. 18.1). This is the cause of liquefaction and extensive damage.

Figure 11.6 illustrates an example of a drained cyclic shear test with a constant amplitude of strain conducted by a torsion shear apparatus (Sect. 18.8). The density of the tested sand was medium (relative density = 56%). It is first observed that the stress amplitude increases as the number of cyclic loading increases (see Fig. 10.6 as well). This implies that stiffness of soil increases with the progress of drained cyclic loading. Second, the net volumetric strain is contractive, accumulating toward 5% or more, although dilatant behavior is still observed when the shear strain exceeds 0.7%. Figure 11.7 illustrates more detailed variation of volumetric strain in one cycle in which both contraction and dilation occur in different phases of deformation.

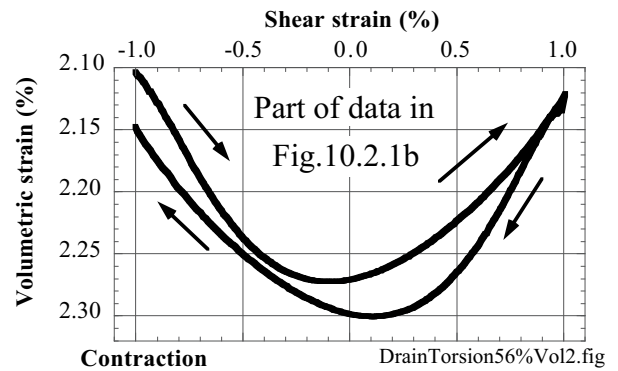
(a) Stress–strain behavior



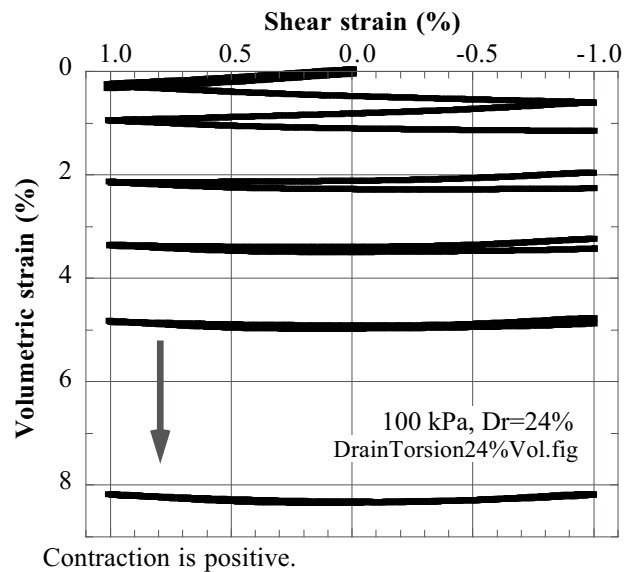
(b) Development of volume contraction



**Fig. 11.6** Drained cyclic shear test ( $D_r = 56\%$ ) (Shahnazari and Towhata, 2002)



**Fig. 11.7** Accumulation of volumetric strain in one cycle of loading (data from Shahnazari and Towhata, 2002)



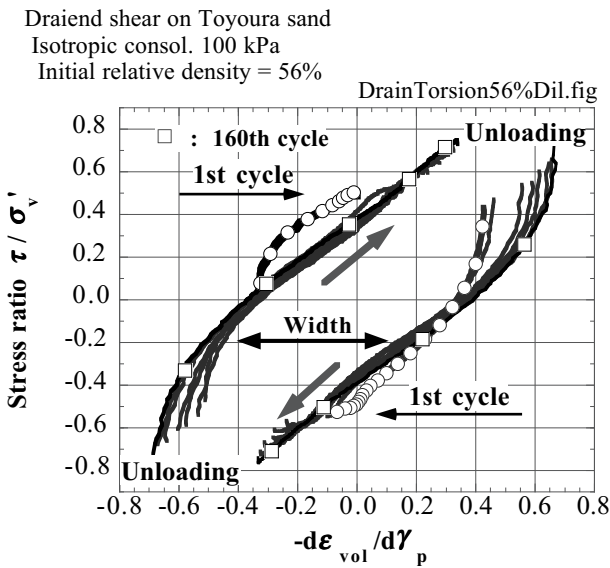
**Fig. 11.8** Volume change of very loose sand ( $D_r = 24\%$ ) (Shahnazari and Towhata, 2002)

Figure 11.8 indicates the volume contraction of looser sand. Although the consolidation stress and strain amplitude are identical with the data in Fig. 11.6, the accumulation of volume change occurred faster.

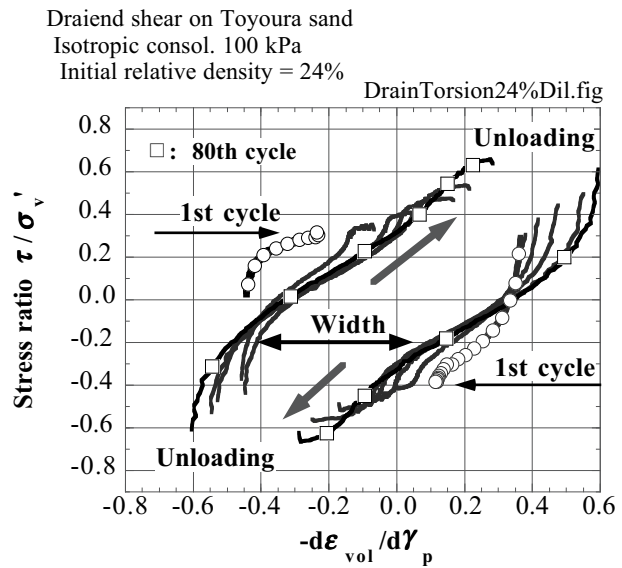
As mentioned in Sect. 1.6, the dilatant behavior of sand has been investigated by many people by using the so-called stress-dilatancy relationship:

$$\frac{\tau}{\sigma'} = K \left( -\frac{d\varepsilon_v}{d\gamma_p} \right) + \text{constant} \quad (11.8)$$

in which  $\varepsilon_v$  designates the volumetric strain (positive in compression). Positive and negative dilatancy is reproduced in accordance with positive and negative values of  $d\varepsilon_v/d\gamma_p$ . Moreover, the present section employs  $\gamma_p$ , which is the plastic (irrecoverable) component of shear strain. The stress dilatancy relationship of sand undergoing cyclic loading was studied by Pradhan et al. (1989) and later by Hinokio et al. (2001). The present study, in contrast, attempts to indicate the stress-dilatancy behavior of sand subjected to more number of cycles.

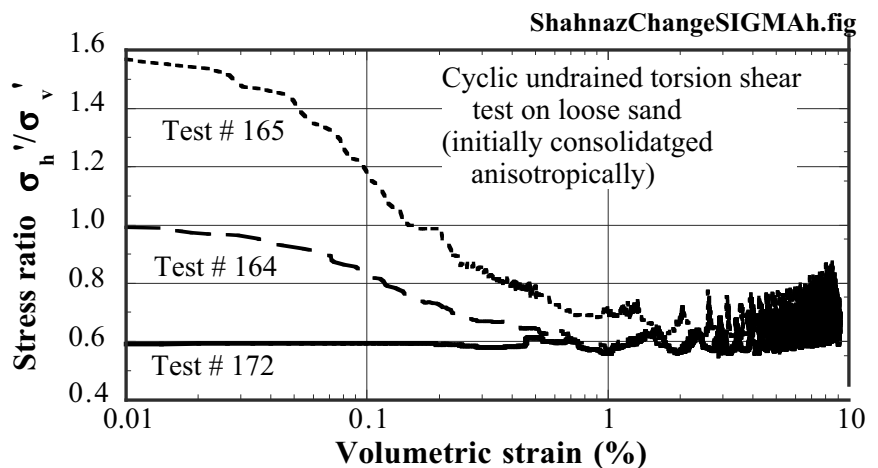


**Fig. 11.9** Stress-dilatancy relationship of sand with relative density = 56% (Shahnazari and Towhata, 2002)



**Fig. 11.10** Stress-dilatancy relationship of sand with relative density = 24% (Shahnazari and Towhata, 2002)

Figures 11.9 and 11.10 reveal two stress-dilatancy diagrams that were obtained by tests with relative densities of 56% and 24%, respectively. The employed number of loading cycles was 160 and 80, and the relative density was increased by cyclic loading to 80% and 69%, respectively. Only data from selected cycles was plotted in the figures. Note that  $-d\varepsilon_{vol}/d\gamma_p < 0$  means volume contraction when the stress ratio,  $\tau/\sigma'$ , is increasing and vice versa. From these diagrams, the following points may be made:



**Fig. 11.11** Reduction of lateral earth pressure coefficient due to cyclic drained loading (Shahnazari and Towhata, 2002)

1. Although the density of sand affects the range of mobilized (activated) stress level, the range of dilatancy ratio,  $-d\varepsilon_{vol}/d\gamma_p$ , is not much affected.
2. There is an approximate linearity in the stress–dilatancy relationship.
3.  $-d\varepsilon_{vol}/d\gamma_p$  jumps upon the initiation of unloading as reported by Pradhan et al. (1989).
4. The first cycle of loading exhibits greater values of  $|-d\varepsilon_{vol}/d\gamma_p|$ , which imply greater tendency for volume contraction.
5. Immediately after the onset of unloading (change of loading direction),  $-d\varepsilon_{vol}/d\gamma_p$  exhibits volume contraction. This tendency increases as the number of loading cycles increases.
6. Conversely towards the end of loading (before unloading),  $-d\varepsilon_{vol}/d\gamma_p$  shows greater values (more dilatancy), making the width of stress–dilatancy loop smaller; for definition of “width”, see the figures.

Volume contraction as a consequence of cyclic shear results not only in ground subsidence but also in lateral contraction. In a horizontal ground where lateral strain is confined to zero, the potential contraction in the horizontal direction causes reduction of lateral earth pressure. Figure 11.11 is an experimental evidence of this phenomenon, which was obtained by torsion shear tests. This finding implies reduction of lateral earth pressure coefficient at rest ( $K_0$ ).

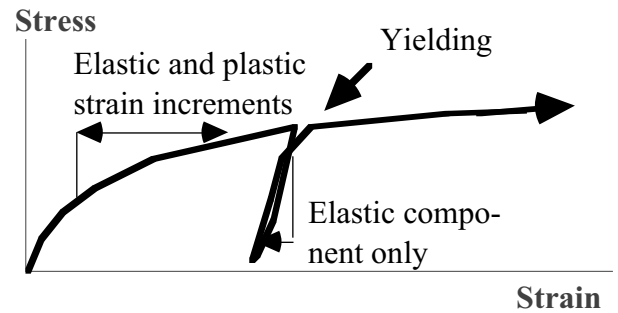
### 11.3 Theory of Elastoplasticity

Hyperbolic and Ramberg–Osgood models in Sect. 11.1 presented relationships between shear stress and strain, which are useful in dynamic analyses on horizontal ground. Since only one component of stress and one component of strain are therein studied, however, those models cannot be applied to two- or three-dimensional analyses in which many components of stress and strain are involved.

The elastoplastic modeling is one of the widely employed approaches to multi-dimensional modeling in which an increment of strain,  $d\epsilon$ , induced by stress increments is decomposed into elastic and plastic components;

$$d\epsilon = d\epsilon^e + d\epsilon^p \tag{11.9}$$

where the prefix of “e” and the prefix of “p” designate elastic and plastic components, respectively. In the elastoplastic terminology, the elastic component is the one which is recovered upon removal of the loaded stress increments, while the plastic component remains unchanged (irreversible) upon unloading and reloading (Fig. 11.12). The elastic strain increments are calculated by a conventional elasticity framework. In a three-dimensional case, the isotropic theory of elasticity states



**Fig. 11.12** Definition of elastic and plastic strain components

$$\begin{Bmatrix} d\epsilon_{xx} \\ d\epsilon_{yy} \\ d\epsilon_{zz} \\ d\gamma_{xy} \\ d\gamma_{yz} \\ d\gamma_{zx} \end{Bmatrix}^e = \frac{1}{E} \begin{bmatrix} 1 & -\nu & -\nu & 0 & 0 & 0 \\ -\nu & 1 & -\nu & 0 & 0 & 0 \\ -\nu & -\nu & 1 & 0 & 0 & 0 \\ 0 & 0 & 0 & 2(1+\nu) & 0 & 0 \\ 0 & 0 & 0 & 0 & 2(1+\nu) & 0 \\ 0 & 0 & 0 & 0 & 0 & 2(1+\nu) \end{bmatrix} \begin{Bmatrix} d\sigma_{xx} \\ d\sigma_{yy} \\ d\sigma_{zz} \\ d\tau_{xy} \\ d\tau_{yz} \\ d\tau_{zx} \end{Bmatrix}^e \tag{11.10}$$

in which  $E$  is the Young's modulus (modulus of elasticity),  $\nu$  is the Poisson ratio, and  $E/\{2(1+\nu)\}$  is often called the shear modulus,  $G$ . In case that stress–strain relationship is nonlinear, these soil parameters are defined by tangent values and change with the magnitudes of stress components, void ratio, and possibly other soil parameters.

The theory of plasticity prefers to use the tensor way of designation for stress and strain. The relationships between the tensor designation and the engineering designation (11.10) are given by

$$\begin{Bmatrix} \epsilon_{11} & \epsilon_{22} & \epsilon_{33} & \epsilon_{12} & \epsilon_{21} & \epsilon_{23} & \epsilon_{32} & \epsilon_{31} & \epsilon_{13} \end{Bmatrix} = \begin{Bmatrix} \epsilon_{xx} & \epsilon_{yy} & \epsilon_{zz} & \gamma_{xy}/2 & \gamma_{xy}/2 & \gamma_{yz}/2 & \gamma_{yz}/2 & \gamma_{zx}/2 & \gamma_{zx}/2 \end{Bmatrix}, \tag{11.11}$$

$$\begin{Bmatrix} \sigma_{11} & \sigma_{22} & \sigma_{33} & \sigma_{12} & \sigma_{21} & \sigma_{23} & \sigma_{32} & \sigma_{31} & \sigma_{13} \end{Bmatrix} = \begin{Bmatrix} \sigma_{xx} & \sigma_{yy} & \sigma_{zz} & \tau_{xy} & \tau_{xy} & \tau_{yz} & \tau_{yz} & \tau_{zx} & \tau_{zx} \end{Bmatrix}. \tag{11.12}$$

By using the tensor designations, the theory of plasticity (Hill, 1983) expresses increments of plastic strain as

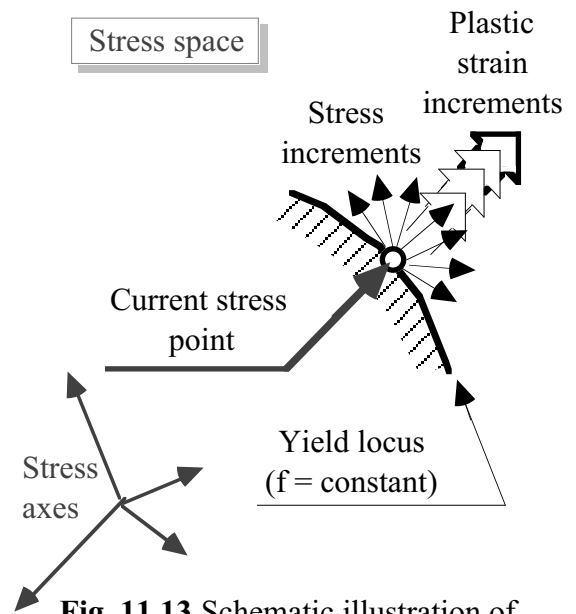


$$d\varepsilon_{ij}^p = h \frac{\partial g}{\partial \sigma_{ij}} df \quad (i, j = 1, 2, 3) \quad (11.13)$$

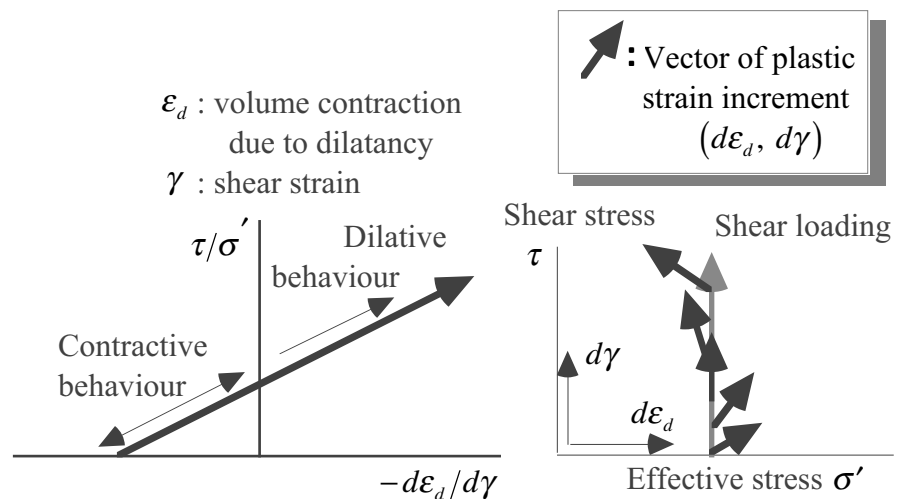
in which  $h$ ,  $g$ , and  $f$  are called hardening function, plastic potential, and yield function, which are functions of stress components and soil density possibly together with other soil parameters.

The theory of plasticity has several hypotheses. First, the plastic deformation occurs only when the yield function,  $f$ , increases. In other words, plastic deformation occurs only after yielding (Fig. 11.12) and no plastic deformation occurs when the current stress level is lower than the previous maximum value. In the extreme case where deformation is large close to failure, the yield function becomes similar to a failure criterion (Sect. 1.5).

Second, the ratio of components in a plastic strain increment (11.13) is independent of the magnitude and direction of stress increment. In other words, the orientation of the vector of plastic strain increment in Fig. 11.13 is independent of the direction and magnitude of the stress increment. This orientation is determined (flow rule) by partial derivative of the plastic potential function,  $\partial g / \partial \sigma_{ij}$ . Hence, this orientation is normal to the plane of constant  $g$  function. The stress–dilatancy relationship (Sect. 1.6) that is widely observed in soil testing determines the ratio of shear and volumetric strains and therefore is a kind of flow rule (Fig. 11.14).



**Fig. 11.13** Schematic illustration of plastic strain increments



**Fig. 11.14** Use of stress-dilatancy relationship as flow rule of plasticity

Some theories employ  $g$  that is equal to  $f$  (associated flow rule). In this situation, the vector of plastic strain increment is normal to the yield locus (Fig. 11.13). This feature is called normality. On the contrary, the nonassociated flow rule employs different  $f$  and  $g$  functions.

The magnitude of the plastic strain increment vector is determined by the increment of the yield function,  $df = (\partial f / \partial \sigma_{ij}) d\sigma_{ij}$ , in (11.13).

Principal stresses (Sect. 1.3) play a major role in plasticity theory. The requirement of objectivity states that the ground deformation as calculated by the plasticity theory has to be independent of the choice of coordinate directions ( $x$ - $y$ - $z$  system or  $x'$ - $y'$ - $z'$  system). Therefore,  $h$ ,  $g$ , and  $f$  functions in (11.13) are functions of principal stresses that are independent of the coordinate system. In other words, they are functions of stress invariants such as

$$(\sigma'_1 + \sigma'_2 + \sigma'_3)/3, (\sigma'_1 - \sigma'_2)^2 + (\sigma'_2 - \sigma'_3)^2 + (\sigma'_3 - \sigma'_1)^2, \text{ and } \sigma'_1 \times \sigma'_2 \times \sigma'_3.$$

Effective stress components are used in the above expression because soil behavior is governed not by the total stress but by the effective stress. The third hypothesis of plasticity theory is called coaxiality, which states that the principal axes of stress and plastic strain increments are parallel to each other (Fig. 11.15).

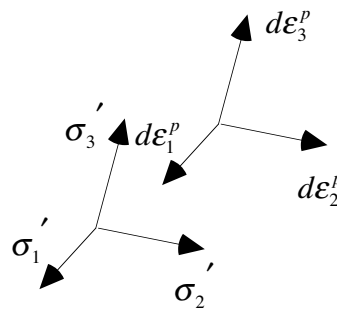


Fig. 11.15 Conceptual drawing of coaxiality

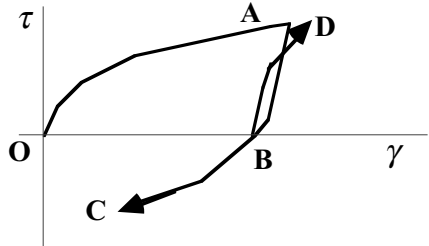


Fig. 11.16 Two variations of shear stress with different consequences

The use of principal stresses or stress invariants in functions  $h$ ,  $g$ , and  $f$  causes one significant problem in application of plasticity theory to cyclic stress history. Figure 11.16 compares two kinds of shear stress history: OABC and OABD. Since the principal stress formulation cannot recognize the different direction of shear stress after B, continued soft behavior in BC and elastic reloading in BD cannot be reproduced. This problem is significant in the popular  $P'$ - $q$  formulation [ $P' = (\sigma'_1 + \sigma'_2 + \sigma'_3)/3$  and  $q = \sigma'_1 - \sigma'_3$ ] as well.

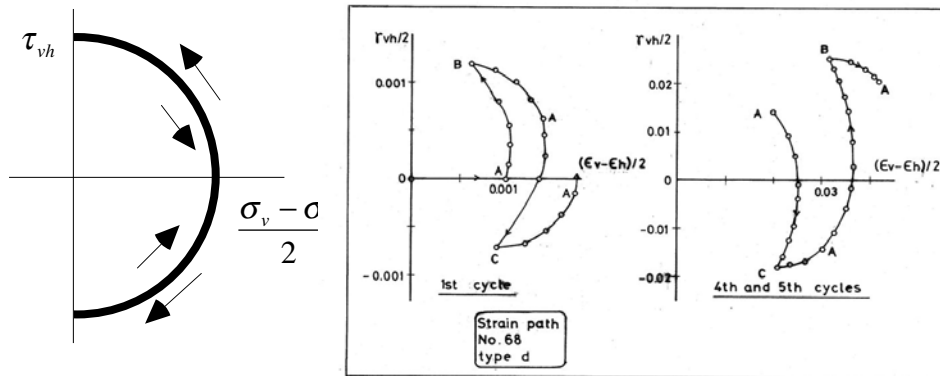
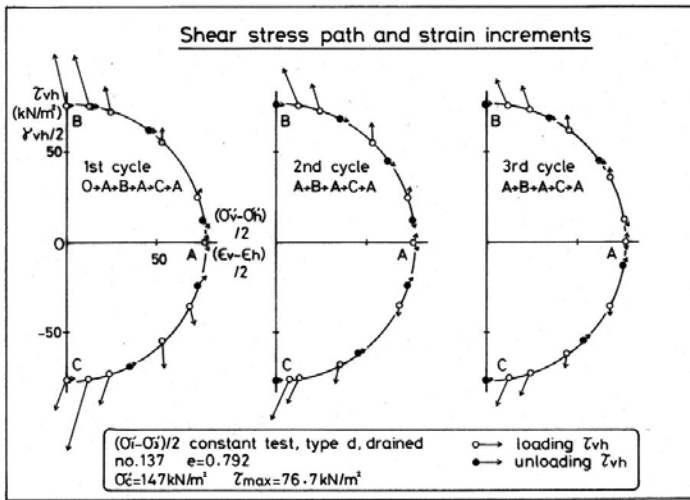


Fig. 11.17 Development of plastic shear strain under continuous rotation of principal stress axes

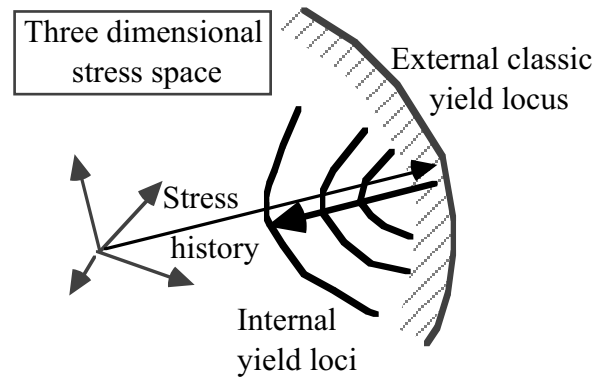
It is physically possible that principal stress axes rotate significantly while maintaining the magnitudes of  $\sigma'_1$ ,  $\sigma'_2$ , and  $\sigma'_3$  constant. Since  $f$ ,  $g$ , and  $h$  functions are held constant under constant values of principal stresses, the theory of plasticity does not give plastic stress increments;  $df = 0$  in (11.13). In reality, on the contrary, such stress components as  $\tau_{xz}$  can still vary, and changes corresponding strain components ( $\gamma_{xz}$  for example). Consequently, plastic strain of  $\gamma_{xz}^p$  can develop (Ishihara and Towhata, 1983). Figure 11.17 illustrates the development of shear strains,  $(\epsilon_v - \epsilon_h)/2$  and  $\gamma_{vh}$ , undergoing cyclic rotation of principal stress axes while maintaining  $\sigma_1 - \sigma_3$  constant. Figure 11.18 shows vectors of strain increments along another circular stress path. As the stress state approached failure in the third cycle, the vector became greater and more perpendicular to the circular stress path. Thus, the strain increment vector became overwhelmed by plastic components that were coaxial with the principal stress.

Consequently, it is reasonable to state that elastoplasticity theory for, in particular, complex cyclic loading should be formulated with special provisions for stress axes rotation; simple use of stress invariants is not appropriate. An example of such a provision is the use of stress difference tensor,

$\sigma_{ij} - \sigma_{ij}^*$ , in which  $\sigma_{ij}^*$  stands for the stress state at the beginning of unloading (Point A in Fig. 11.16). This kind of modeling produces plasticity mechanism even when the stress level decreases from the previous maximum value (inside the yield locus in the classical sense) as schematically illustrated in Fig. 11.19. Mroz et al. (1978) developed such a theory.



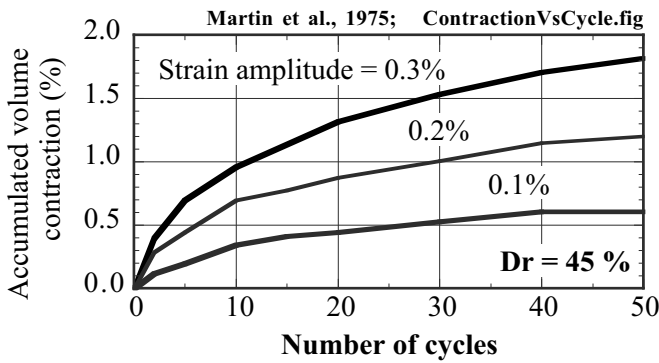
**Fig. 11.18** Development of strain increments during continuous rotation of principal stress axes



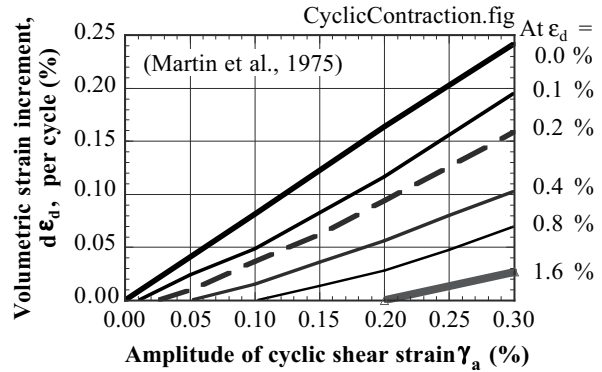
**Fig. 11.19** Idea of multiple yield mechanisms of plasticity

### 11.4 Dilatancy under Cyclic Loading

Dilatancy is a phenomenon of volume change caused by shear deformation of discrete material (Sects. 1.2 and 1.6). In earthquake engineering practice, volume contraction due to dilatancy (negative dilatancy) is important because it stands for ground subsidence induced by strong shaking. Dilatancy plays an extremely important role in liquefaction analysis (Chap. 2) as well, because the major cause of liquefaction and large ground deformation is the development of high pore water pressure caused by dilatancy (Sect. 18.1).



**Fig. 11.20** Volume contraction of sand due to cyclic shear (Martin et al., 1975)



**Fig. 11.21** Increment of volumetric strain per cycle of shear strain (Martin et al., 1975)

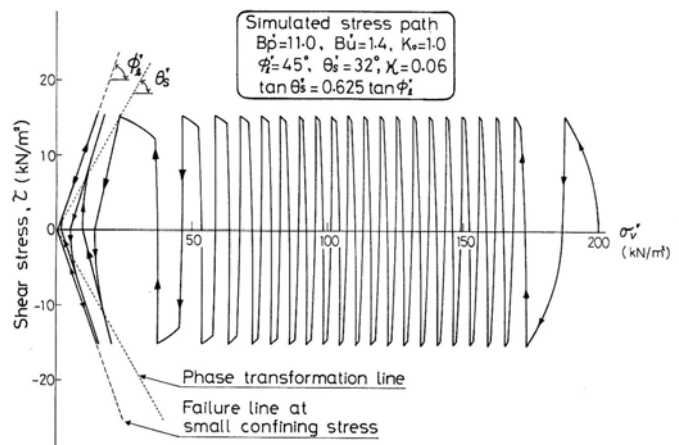
This section concerns modeling of dilatancy under one-dimensional cyclic shear loading. There are two kinds of approach for modeling of dilatancy. One is modeling of volume change, which is measured in cyclic drained shear of sand. Martin et al. (1975) conducted drained cyclic simple shear tests and reported that the volumetric strain due to dilatancy is proportional to shear strain amplitude; see Fig. 11.20. They studied the increment of volumetric strain per cycle (Fig. 11.21) and proposed an empirical formula,

$$d\epsilon_d = C_1(\gamma_a - C_2\epsilon_d) + \frac{C_3\epsilon_d^2}{\gamma_a + C_4\epsilon_d}, \quad (11.14)$$

where  $d\epsilon_d$  is the increment of volumetric strain per cycle of strain amplitude  $\gamma_a$ . If cyclic loading occurs in a drained manner (dry sand for example), this  $\epsilon_d$  is equal to the real volume compression. If loading is undrained as is the case of liquefaction, this potential volume contraction is converted to the decrease in effective stress under constant volume by

$$d\sigma' = K(d\epsilon_v - d\epsilon_d), \quad (11.15)$$

where  $\epsilon_v$  is the volumetric strain that does occur in reality. Note that  $\epsilon_v = 0$  under perfectly undrained conditions. Moreover,  $K$  is called bulk modulus of soil and is equivalent with  $1/m_v$  ( $m_v$  being volume compressibility in (1.12)) in consolidation theory. The determination of soil parameters in (11.14) requires cyclic drained loading on undisturbed soil specimens.



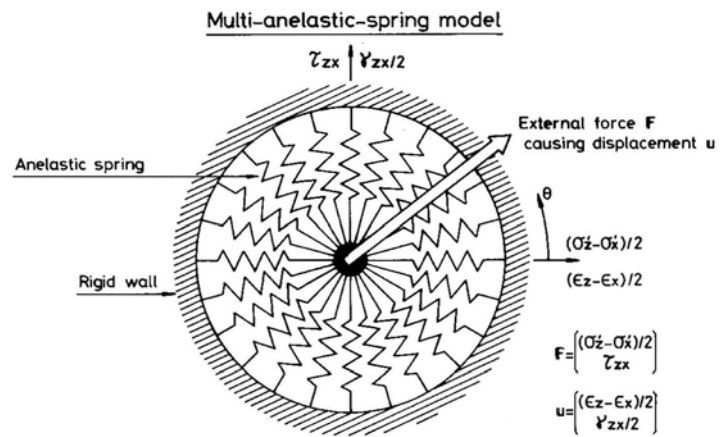
**Fig. 11.22** Stress-path model of dilatancy and excess pore water pressure (see Set. 22.4)

The other approach to modeling of dilatancy is that of excess pore water pressure that develops during undrained cyclic loading. Apparently, this approach is related with liquefaction tests on sand. Figure 11.22 (Ishihara and Towhata, 1982) indicates a modeled relationship between decrease in effective stress (increase in pore water pressure) and cyclic change in shear stress. This stress path model consists of three parts: under loading (increase of shear stress), unloading (decrease of shear stress), and that near perfect liquefaction.

Both approaches as described above concern one-dimensional cyclic loading (case of horizontal ground subjected to one direction, EW or NS, of shaking). For more complicated situations, those models have to be significantly revised, or more complicated models such as stress–dilatancy approach of plasticity (Sects. 1.6 and 11.3) for volume change or energy correlation of pore water pressure (Sect. 20.8–20.10) are employed.

**11.5 Multi-Nonlinear Spring Model**

Figure 11.23 illustrates an example of multi-nonlinear spring model for a two-dimensional situation in which simultaneous loading of  $(\sigma_v - \sigma_h)/2$  and  $\tau_{vh}$  associated with continuous rotation of principal stress axes is taken into account (Towhata and Ishihara, 1985). The big arrow in the figure stands for the above-mentioned shear stress components and its variation induces the displacement of the point of action at the center. This displacement stands for the shear strain of soil;  $(\epsilon_v - \epsilon_h)/2$  and  $\gamma_{vh}/2$ . Note that the ratio of two stress components (direction of the arrow) indicates the orientation of principal stresses. When this orientation rotates, the direction of the arrow changes and component springs are subjected to nonlinear deformation. Consequently, plastic deformation is produced. This model was combined with the energy correlation of excess pore water pressure (Sects. 20.8–20.10) to reproduce the undrained cyclic behavior of loose sand. It was applied by Iai et al. (1992a,b) to develop a seismic design code of harbor structures.



**Fig. 11.23** Multi-spring model for two-dimensional shear deformation

The relationship between the nature of springs and the reproduced soil properties are as what follows. In an ideal case where the number of springs is infinite, the shear modulus of soil at small strain,  $G_{max}$ , and the spring modulus at small deformation,  $k_{max} d\theta$ , are related to each other by supposing a loading in the direction of  $\pi/2$  in Fig. 11.23;

$$G_{max} = \int_{\pi/2}^{5\pi/2} k_{max} \left\{ \cos\left(\theta - \frac{\pi}{2}\right) \right\}^2 d\theta = \pi k_{max}. \quad (11.16)$$

When the deformation of springs is extremely large, all the springs develop their full strength;  $F_f d\theta$ . Accordingly, the magnitude of shear strength of modeled soil is given by

$$\text{Shear strength of soil} = 2 \int_0^\pi F_f \cos\left(\theta - \frac{\pi}{2}\right) d\theta = 4F_f. \quad (11.17)$$

These simple calculations assumed that all the springs have identical properties of  $k_{max}$  and  $F_f$ . By changing these parameters with the direction of springs,  $\theta$ , it is possible to model anisotropic soil properties.

Since a two-dimensional condition has two independent shear stress components such as  $(\epsilon_z - \epsilon_x)/2$  and  $\gamma_{zx}$  or  $\gamma_x$  and  $\gamma_y$ , the two-dimensional model illustrated in Fig. 11.23 is useful. In a three-dimensional condition, there are five independent shear stresses (six stresses minus mean effective stress) and its modeling by a multi-spring model is not easy. Simple expansion of the circle in the figure to a three-dimensional sphere is not sufficient because a sphere can handle only three degrees of freedom. Nishimura and Towhata (2004) solved this problem by allocating many circle models on the surface of a sphere; two degrees of freedom from a circle and three more degrees from the sphere.

It seems promising to extend the stress–dilatancy relationship (Fig. 11.14) to a multi-dimensional conditions. This goal may be achieved by employing the generalized shear stress of  $\tau \equiv$

$$\sqrt{\frac{3}{2}(\sigma'_{ij} - \delta_{ij}\sigma'_m)(\sigma'_{ij} - \delta_{ij}\sigma'_m)}$$

and the generalized shear strain of  $\gamma \equiv \sqrt{\frac{2}{3}\left(\epsilon_{ij} - \frac{\delta_{ij}\epsilon_v}{3}\right)\left(\epsilon_{ij} - \frac{\delta_{ij}\epsilon_v}{3}\right)}$ . In

these expressions,  $i$  and  $j$  are 1, 2, or 3, while  $\delta_{ij}$  stands for the Kronecke's delta;

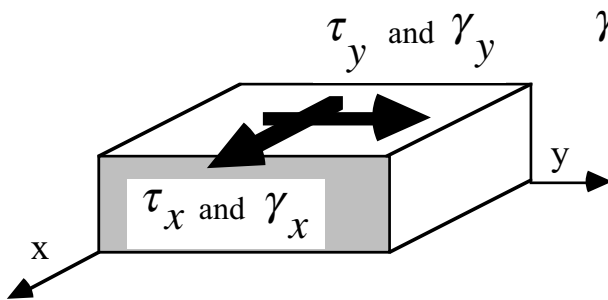
$$\delta_{ij} = 1 \text{ if } i = j \text{ and } \delta_{ij} = 0 \text{ if } i \neq j.$$

Moreover,  $\sigma'_m \equiv (\sigma'_1 + \sigma'_2 + \sigma'_3)/3$  designates the effective mean principal stress, and  $\epsilon_v$  is the volumetric strain. Note that the above definitions of  $\tau$  and  $\gamma$  follow the tensor abbreviation;

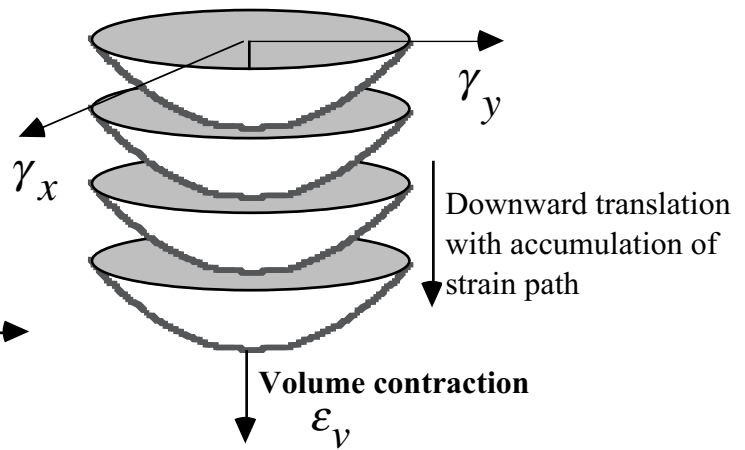
$$A_k B_k \equiv \sum_k A_k B_k \text{ and, in particular, } \tau_{ij} \tau_{ij} \equiv \sum_i \sum_j \tau_{ij} \tau_{ij}$$

The problem lying in the stress–dilatancy formulation is that no volumetric strain occurs if cyclic loading occurs with a constant value of  $\gamma$ ; if  $d\gamma = 0$ ,  $d\epsilon_v$  has to be zero in order to avoid an infinite value of  $d\epsilon_v/d\gamma$ .

The bowl model was proposed by Fukutake and Matsuoka (1989) with a scope to predict volume contraction of sand undergoing multi-dimensional cyclic shear. For illustration, this section studies a situation of Fig. 11.24 where soil is sheared by two components of shear stress:  $\tau_x$  and  $\tau_y$ . The associating shear strains,  $\gamma_x$  and  $\gamma_y$ , are substituted in the dilatancy model in Fig. 11.25 where a bowl-like curved surface stands for the relationship between volume change and shear strain. The concave shape stands for the fact that volume expands when shear strain is large. See its similarity with the experimental curve in Fig. 11.8.



**Fig. 11.24** Soil subjected to two-dimensional shear



**Fig. 11.25** Conceptual illustration of bowl model of dilatancy

Since the volume of soil further continues to contract with the number of shear cycles, the bowl surface moves down in Fig. 11.25, thus representing the accumulated volumetric contraction during cyclic loading. This downward translation is a function of the shear strain path;

$$\text{Length of shear strain path} \equiv \int \left[ (d\gamma_x)^2 + (d\gamma_y)^2 \right].$$

### 11.6 Discrete Element Analysis

Although the finite element analysis has been proved to be a powerful tool to calculate deformation of a continuous medium, there have been different attempts that consider materials discontinuous. This attempt is appropriate for such situations as post-failure behavior of rock slopes in which blocks of breached rock move and collide independently (Cundall, 1971; Kawai and Takeuchi, 1981).

Deformation analysis on an assembly of circular or spherical objects started in 1950s (Deresiewicz, 1958a,b). Since sand consists of grains, this approach is attractive; particularly being so when displacement is large. Hence, a method of analysis called distinct element analysis or discrete element analysis (DEM) has been developed in which particles move and collide with each other (Cundall and Strack, 1979). However, the limited capacity of computers has not allowed to analyze behavior of real individual grains in either two-dimensional or three-dimensional manners; the number of real grains is too many for any computer memory. Hence, the existing DEM works in a two-dimensional manner on imaginary grains, which are much bigger than real grains. The two-dimensional analysis employs void ratio, which is smaller than the well-known void ratio range in real sandy deposit. For example, a regular packing of round grains in Fig. 11.26 has void ratio of  $1 - \pi/4 = 0.273$ .

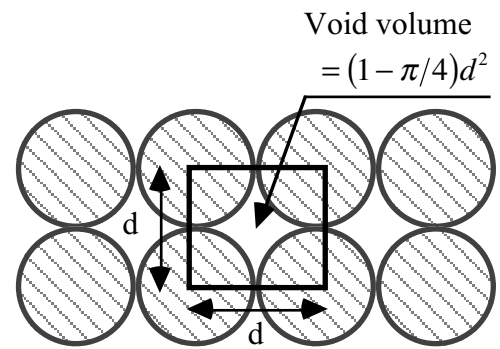


Fig. 11.26 Regular packing of two-dimensional circular grains

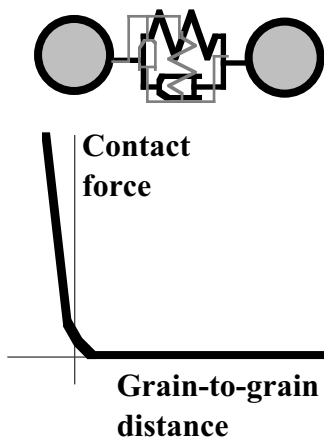


Fig. 11.27 Contact mechanism in normal direction

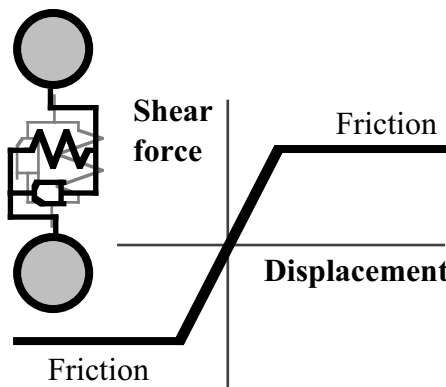


Fig. 11.28 Contact mechanism in shear direction

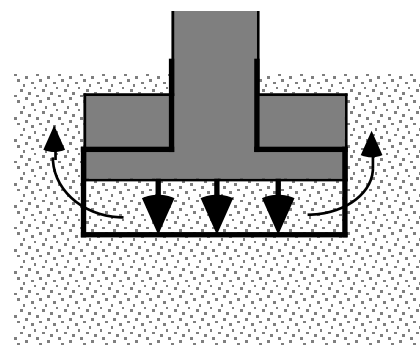


Fig. 11.29 Grains turning around corner

In DEM, the grain-to-grain interaction is modeled by nonlinear springs and dashpots, which are illustrated in Figs. 11.27 and 11.28. When the grain-to-grain distance is short, a particle contact occurs, and a normal mechanism (Fig. 11.27) is activated to resist against compression. At the same time, a shear resistant mechanism (Fig. 11.28) is generated that stands for friction between grains. The magnitude of friction in Fig. 11.28 varies with the extent of contact force in Fig. 11.27. DEM analysis is more advantageous than FEM when displacement and deformation are large. For example, DEM can calculate grain movements that turn around a corner of sinking foundation (Fig. 11.29), while such an analysis is very difficult in FEM.

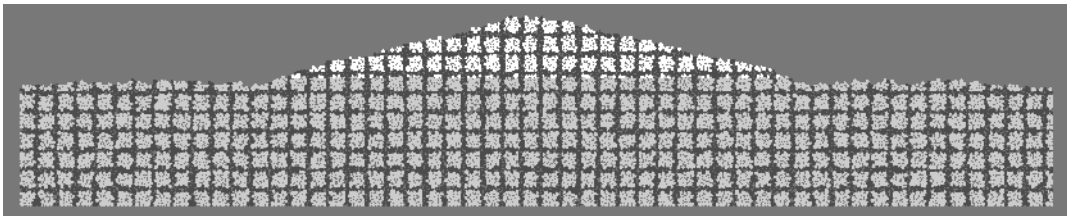
In a dynamic analysis, the grain-to-grain distance has to be examined for pairs of extremely many particles at every time increment. To make ease this procedure, most DEM analyses employ circular or spherical grains. Moreover, previous DEM assumed only such two types of mechanisms as compression and shear at contact points. This idea is reasonable when the real contact occurs at a single point. If the real contact occurs by a plane or two points, the transfer of moment becomes important. Iwashita and Oda (1998) installed bending moment mechanism at contacts of imaginary spherical particles.



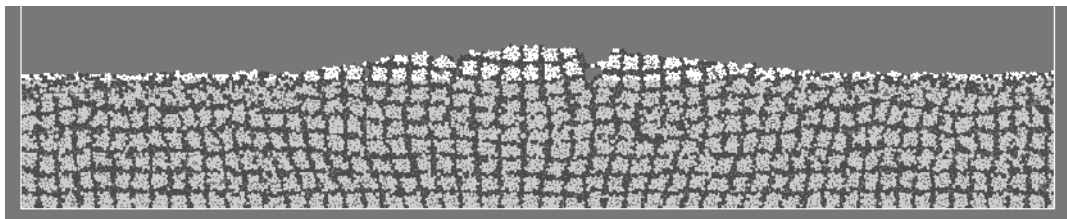
For an application to geotechnical earthquake problems, Kanatani et al. (2001) combined FEM and DEM in which FEM was applied to a more continuous soil deposit, while DEM to an accumulation of big concrete pieces. Furthermore, Hakuno and Tarumi (1988) as well as Nakase et al. (1998) showed how to calculate excess pore water pressure and seepage flow in a water-saturated model. Figure 11.30 illustrates an example calculation of liquefaction-induced deformation in a 30g centrifuge test. The number of spherical elements are 14,000 with the diameter of 0.4 mm. Shaking of 300 Gal with 2 Hz was applied. It is seen in this figure that the subsidence was terminated after some subsidence at which the buoyancy and gravity forces achieved equilibrium. Note that the force equilibrium after some displacement can be reproduced by FEM only if a large-displacement formulation is employed.

A three-dimensional DEM analysis is very interesting but evidently difficult because of the heavy computation load. Harada and Gotoh (2006) conducted this type of analysis on the transportation of river bed grains, taking simply into account the water effects. They employed 9,350 grains.

(a) Initial configuration prior to shaking.



(b) Configuration after subsidence into liquefied subsoil.



**Fig. 11.30** DEM calculation on subsidence of embankment into liquefied subsoil  
(Honda and Towhata, 2006)

### List of References in Chapter 11

- Cundall, P.A. (1971) A computer model for simulating progressive, large-scale movements in blocky rock systems, Proc. Symp. Int. Soc. Rock Mech., Nancy, p. II-8.
- Cundall, P.A. and Strack, O.D.L. (1979) A discrete numerical model for granular assemblies, Geotech., Vol. 29, No. 1, pp. 47–65.
- Deresiewicz, H. (1958a) Mechanics of granular matter, Advances in Applied Mechanics, Academic Press, New York, pp. 233–306.
- Deresiewicz, H. (1958b) Stress–strain relations for a simple model of a granular medium, J. Appl. Mech., Vol. 25, pp. 402–406.
- Fukutake, K. and Matsuoka, H. (1989) A unified law for dilatancy under multi-directional simple shearing, Proc. JSCE, No. 412/III-12, pp. 240–248 (in Japanese).
- Hakuno, M. and Tarumi, Y. (1988) A granular assembly simulation for the seismic liquefaction, Struct. Eng. / Earthq. Eng., Vol. 5, No. 2 (Proc. JSCE, No.398/I-10), pp. 333–342.
- Harada, E. and Gotoh, H. (2006) Numerical simulation of sediment sorting in sheetflow regime by 3D granular material model, Proc. JSCE B, Vol. 62, No. 1, pp. 128–138 (in Japanese).
- Hardin, B.O. and Drnevich, V.P. (1972) Shear modulus and damping in soils design equation and curves, Proc. ASCE, Vol. 98, SM7, pp. 667–692.

- Hill, R. (1983) *The mathematical theory of plasticity*, The Oxford Engineering Science Series, pp. 14–69 (first edition in 1950).
- Hinokio, M., Nakai, T., Hoshikawa, T. and Yoshida, H. (2001) Dilatancy characteristics and anisotropy of sand under monotonic and cyclic loading, *Soils Found.*, Vol. 41, No. 3, pp. 107-124.
- Honda, T. and Towhata, I. (2006) Factors influencing ground deformation of river dike due to liquefaction by distinct element analysis, *Proceedings of IS-Yamaguchi 06 on Geomechanics and Geotechniques of Particulate Media*, Ube, Yamaguchi, Japan, pp. 225–232.
- Iai, S., Matsunaga, Y. and Kameoka, T. (1992a) Strain space plasticity model for cyclic mobility, *Soils Found.*, Vol. 32, No. 2, pp. 1–15.
- Iai, S., Matsunaga, Y. and Kameoka, T. (1992b) Analysis of undrained cyclic behavior of sand under anisotropic consolidation, *Soils Found.*, Vol. 32, No. 2, pp. 16–20.
- Ishihara, K. and Towhata, I. (1982) Dynamic response analysis of level ground based on the effective stress method, *Soil Mechanics – Transient and Cyclic Loads*, Wiley, New York, pp. 133–172.
- Ishihara, K. and Towhata, I. (1983) Sand response to cyclic rotation of principal stress directions as induced by wave loads, *Soils Found.*, Vol. 23, No. 4, pp. 11–26.
- Iwashita, K. and Oda, M. (1998) Rolling resistance at contacts in simulation of shear band development by DEM, *J. Eng. Mech., ASCE*, Vol. 124, No. 3, pp. 285–292.
- Jennings, P.C. (1964) Periodic response of a general yielding structure, *Proc. ASCE*, Vol. 90, EM2, pp. 131–166.
- Kanatani, M., Kawai, T. and Tochigi, H. (2001) Prediction method on deformation behavior of caisson-type seawalls covered with armored embankment on man-made islands during earthquakes, *Soils Found.*, Vol. 41, No. 6, pp. 79–96.
- Kawai, T. and Takeuchi, N. (1981) A discrete method of limit analysis with simplified elements, *Proc. 1st Int. Conf. Computing in Civil Eng.*, pp. 27–42.
- Kondner, R.L. (1963) A hyperbolic stress–strain response: Cohesive soils, *Proc. ASCE*, Vol. 89, SM1, pp. 115–143.
- Kondner, R.L. and Zelasko, J.S. (1963) A hyperbolic stress–strain formulation for sands, *Proc. 2nd Pan-American Conf. Soil Mech. Found. Eng.*, Vol. I, pp. 289–324.
- Martin, G.R., Finn, W.D.L. and Seed, H.B. (1975) Fundamental of liquefaction under cyclic loading, *Proc. ASCE*, Vol. 101, GT5, pp. 423–38.
- Masing, G. (1926) Eigenspannungen und Verfestigung beim Messing, *Proc. 2nd Int. Cong. Applied Mechanics*, pp. 332–335.
- Mroz, Z., Norris, V.A. and Zienkiewicz, O.C. (1978) An anisotropic hardening model for soils and its application to cyclic loading, *Int. J. Nume. Anal. Methods Geomech.*, Vol. 2, pp. 203–221.
- Nakase, H. (1999) A simulation study on liquefaction using DEM, *Mechanics of Granular Materials*, an Introduction, ed. M. Oda and K. Iwashita, publ. A.A.Balkema, The Netherlands, pp. 183–187.
- Nishimura, S. and Towhata, I. (2004) A three-dimensional stress–strain model of sand undergoing cyclic rotation of principal stress axes, *Soils Found.*, Vol. 44, No. 2, pp. 103–116.
- Pradhan, T.B.S., Tatsuoka, F. and Sato, Y. (1989) Experimental stress–dilatancy relations of sand subjected to cyclic loading, *Soils Found.*, Vol. 29, No. 1, pp. 45-64.
- Shahnazari, H. and Towhata, I. (2002) Torsion shear tests on cyclic stress–dilatancy relationship of sand, *Soils Found.*, Vol. 42, No. 1, pp. 105-119.
- Towhata, I. and Ishihara, K. (1985) Modelling soil behaviour under principal stress axes rotation, *Proc. of 5th International Conference on Numerical Methods in Geomechanics*, Nagoya, Japan, Vol. 1, pp. 523–530.

# Chapter 12

## Application of Seismic Inertia Force



The five-storeyed Buddhism pagoda in Horyu-ji Temple (法隆寺), Nara, Japan. This temple, inclusive of this pagoda, was first constructed in A.D. 607. It is said that the original temple was destroyed by fire in 670 and reconstructed later. There is a recent archaeological finding that supports this story. Whether this story of fire is true or not, Horyu-ji is the world oldest wooden building.

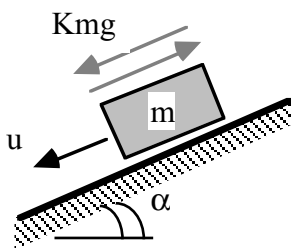
**12.1 Calculation of Earthquake-Induced Displacement**

In the recent times, except those caused by soil liquefaction, there has been few failure of dam due to earthquakes. An important issue, therefore, is the prevention of unallowable deformation of a dam embankment. This need has led to a study on the residual displacement of a soil body that remains after the end of shaking.

Newmark (1965) proposed an analogy between the seismic slope movement and the motion of a rigid block on a frictional slope (Fig. 12.1). When the rigid block of mass “*m*” is subjected to a cyclic base acceleration parallel to the floor, an inertia force of *Kmg* is loaded on. Note that *K* is a function of time. Accordingly, (1) the block starts to move downwards when the exciting force plus the gravity effects exceed the frictional resistance, and (2) it decelerates its velocity when the friction exceeds the cyclic plus the gravity forces. The equation of motion of the rigid block is given by

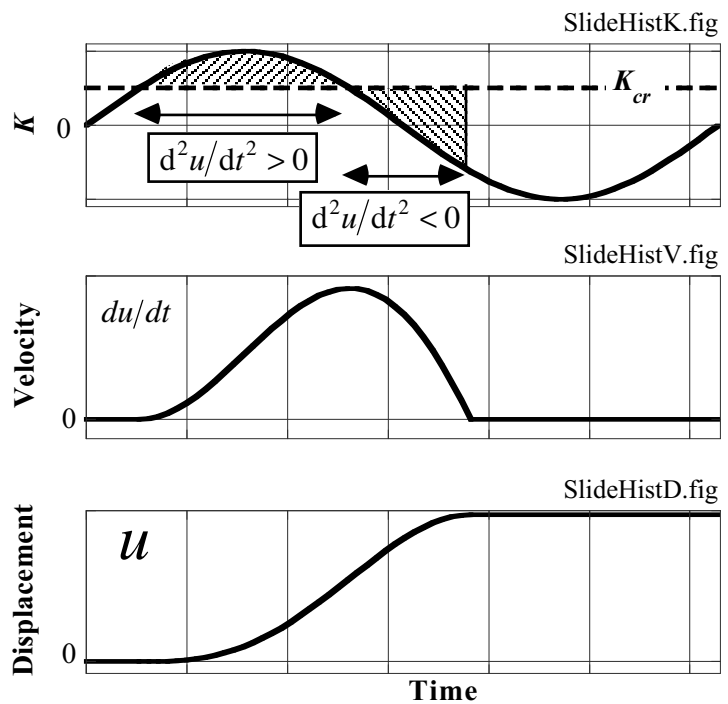
$$\frac{d^2u}{dt^2} = g(\sin \alpha + K - \mu \cos \alpha) = g(K - K_{cr}) \tag{12.1}$$

in which  $\alpha$  is the slope angle and  $\mu$  the frictional coefficient. Under a preearthquake static condition, the factor of safety is given by  $F_s = \mu/\tan \alpha$ . The downward motion starts when *K* exceeds  $K_{cr} = \mu \cos \alpha - \sin \alpha$ . The upward motion is ignored for conservatism (安全側の考え方) in many practical studies, although it is possible to start when *negative K* exceeds  $-(\mu \cos \alpha + \sin \alpha)$ .



**Fig. 12.1** Newmark’s analogy of sliding rigid block of frictional floor

Since the Newmark analogy relies on shear failure mechanism, no elastic component is taken into account. Figure 12.2 illustrates the initiation and termination of slip movement. First, the movement starts when *K* exceeds  $K_{cr}$ , making the acceleration greater than zero and velocity increases with time. This situation continues until *K* becomes less than  $K_{cr}$  after which  $d^2u/dt^2$  becomes negative and velocity decreases. As shown in the time history of displacement, the displacement continues to increase without fluctuation and ceases to increase any more when the velocity becomes zero.



**Fig. 12.2** Initiation and termination of sliding movement in Newmark analogy

An example analysis is presented below by using a harmonic excitation;

$$K = K_{max} \sin \omega t. \tag{12.2}$$

Although this *K* is similar to the static inertia force employed in conventional seismic designs (Sect. 7.1), it is different in a sense that this *K* changes with time. Hence, *K* is equivalent with a base acceleration.

The motion starts at  $t_0 = \arcsin(K_{cr}/K_{max})/\omega$  at which  $K = K_{cr}$ . By substituting (12.2) in (12.1) and integrating with time,

$$\frac{\omega}{gK_{cr}} \frac{du}{dt} = -\frac{K_{max}}{K_{cr}} (\cos \omega t - \cos \omega t_0) - (\omega t - \omega t_0). \tag{12.3}$$

The end of sliding,  $t = t_1$ , is detected by making the right-hand side of (12.3) equal to zero (velocity = 0). The solution for this is obtained by Newtonian iterative method;  $x_{i+1} = x_i - F(x_i)/\{dF(x_i)/dx\}$ ; with the initial assessment of  $\omega t_1 = 1.5\pi$ . Finally by integrating (12.3) once more with time from  $t_0$  to  $t_1$ , the development of displacement per cycle, denoted by  $U_1$ , is calculated. See Fig. 12.3 for the duration time of sliding and Fig. 12.4 for  $U_1$ . Note that sliding starts early and lasts for a longer time when  $K_{max}$  value is greater. Consequently, the magnitude of sliding displacement is greater as well.

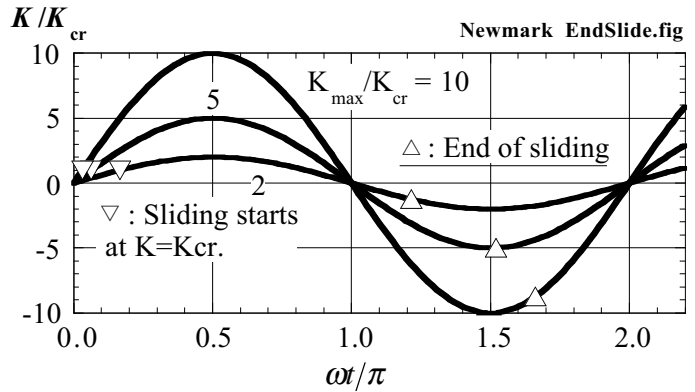


Fig. 12.3 Duration time of sliding under different intensity of inertia force

*Exercise: Study the effects of shaking frequency on the residual displacement per cycle and per second by using Fig. 12.4 and Table 12.1.*

*A typical result is illustrated in Fig. 12.5 where frequency was varied 5 times over a range of the static factor of safety. Evidently, the higher shaking frequency causes significantly less magnitude of residual displacement. This implies that such an earthquake input motion with high acceleration but high frequency is not necessarily harmful to structures.*

In practice, the rigid block in Fig. 12.1 is a replacement of a sliding soil mass, while the frictional floor is equivalent with a slip plane with  $\mu = \tan \phi$ .

Since the Newmark method was originally intended for a dam analysis, it basically concerns with a good compacted material. Therefore, it does not pay attention to excess pore water pressure development and the consequent loss of resistance.

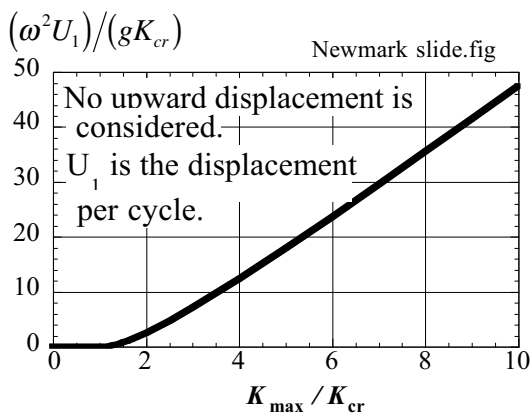


Fig. 12.4 Residual displacement per cycle predicted by Newmark analysis

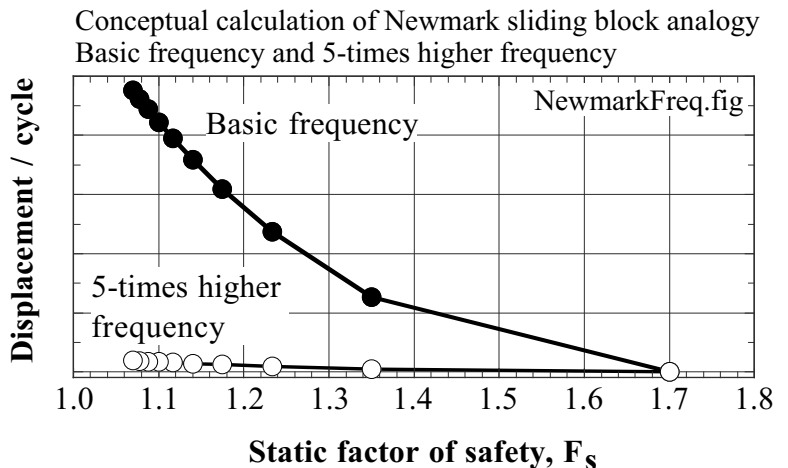


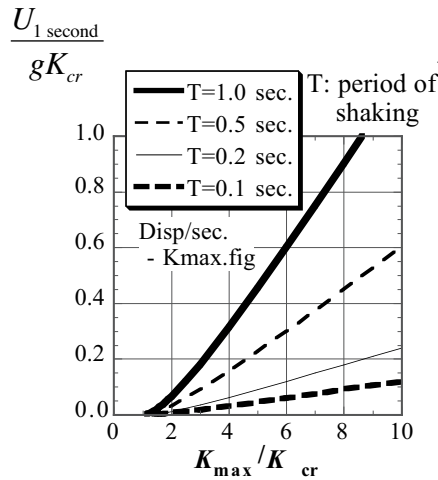
Fig. 12.5 Effects of shaking frequency on residual displacement as calculated by Newmark analogy

### 12.2 Correlation Between Residual Displacement, Base Acceleration and Base Velocity

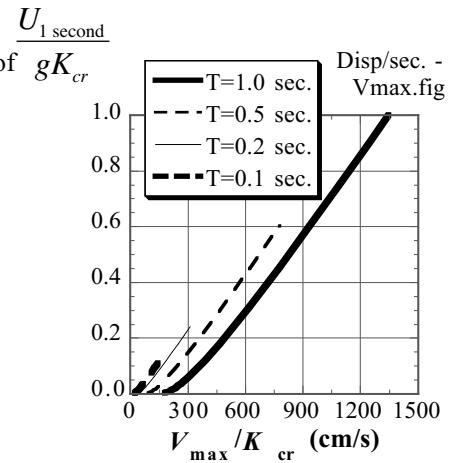
It should be recalled that one of the essences of geotechnical earthquake damage is the displacement which remains after an earthquake. This displacement is called the residual or permanent displacement. To study this aspect, the data in Fig. 12.4 is tabulated in Table 12.1.

**Table 12.1** Relationship between intensity of dynamic inertia force and accumulation of residual displacement per cycle (see Fig. 12.2)

$K_{max}/K_{cr}$	$\omega^2 U_1/gK_{cr}$
1.0	0.00
2.0	2.53
3.0	7.11
4.0	12.36
5.0	17.94
6.0	23.70
7.0	29.57
8.0	35.52
9.0	41.53
10.0	47.57



**Fig. 12.6** Correlation between residual displacement and intensity of base acceleration

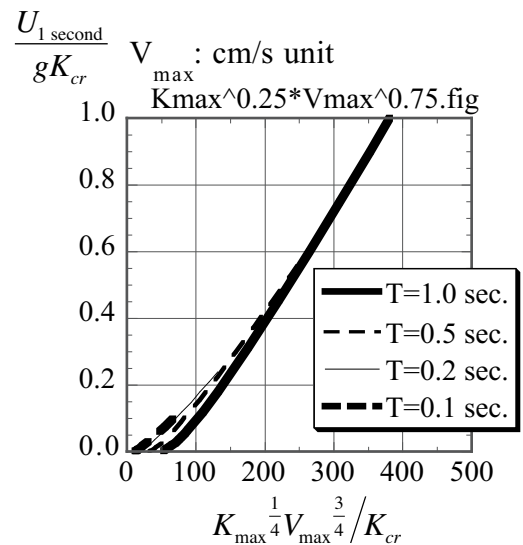


**Fig. 12.7** Correlation between residual displacement and intensity of base velocity

Because  $U_1$  above is a residual displacement per cycle, it does not carry much practical sense. It seems better to use the residual displacement per second, which is derived as  $U_{1\text{ second}} = U_1 \times \text{frequency}$ . In reality, what is reported as the residual displacement (of foundations and slopes) is equal to  $U_1 \times \text{frequency} \times (\text{Duration time of strong earthquake motion})$ .

Figures 12.6 and 12.7 plot  $U_{1\text{ second}}/(gK_{cr})$  against the intensity of base acceleration ( $K_{max}$ ; Fig. 12.6) and the amplitude of velocity at base ( $V_{max} = gK_{max}/\omega$ ; Fig. 12.7). Although the residual displacement increases with these two typical earthquake motion parameters, there is not seen a good unique correlation. This is the reason why there is yet no agreement about the suitable earthquake intensity parameter to be used in practice.

Since the correlation in terms of velocity in Fig. 12.7 is more promising than that of  $K_{max}$ , it seems reasonable that seismic damage estimation is better carried out by velocity than the maximum acceleration. To further improve this, a new parameter of  $K_{max}^{1/4} V_{max}^{3/4}$  was attempted in Fig. 12.8. Its correlation with the residual displacement per second appears reliable.



**Fig. 12.8** Correlation between residual displacement and combined effects of base acceleration and velocity

Ohmachi et al. (1990) proposed an idea of sliding response spectrum that indicates the power of a real earthquake motion to cause a sliding block displacement. The residual displacement after the whole earthquake changed with the slope angle and the frictional coefficient of the floor ( $\alpha$  and  $\mu$  in Sect. 12.1).

### 12.3 Relationship Between Seismic Coefficient and maximum Acceleration During Earthquakes

The seismic coefficient,  $K$ , that is applied in a static manner in design (Sect. 7.1) and the magnitude of acceleration,  $A_{\max}$ , during earthquakes are not equivalent to each other in reality in spite of the d'Alembert principle. Surface acceleration with the maximum value of  $A_{\max} = 980 \times 0.7$  Gal is not so destructive as  $K = 0.7$ . This is because the duration of acceleration is limited and may not give structures time to move significantly, while the static seismic inertia force with  $K = 0.7$  is hypothesized to last forever in design.

Noda et al. (1975) analyzed past earthquake damages in quay walls at harbors. Limit equilibrium analyses with a static seismic inertia force gave the critical  $K$  values, denoted as  $K_{cr}$ , which were required to induce failure. The real values of  $K$  was probably greater than  $K_{cr}$  at sites with damage, while  $K$  was less than  $K_{cr}$  when there was no damage. Thus, a range of possible  $K$  values were obtained.

At the same time, they estimated the maximum horizontal acceleration,  $A_{\max}$ , by using the acceleration records obtained at nearby sites, or by using fault models, attenuation with the epicentral distance, and response analysis on local subsoil models.

By combining these all, the range of realistic  $K$  was plotted against  $A_{\max}$  (Fig. 12.9). An empirical formula of  $K = (A_{\max}/g)^{1/3}/3$  was proposed. Figure 12.9 was a unique attempt to physically correlate  $K$  and  $A_{\max}$ . Note that there are many uncertainties in this study, probably including the determination of appropriate soil strength in the limit equilibrium analysis.

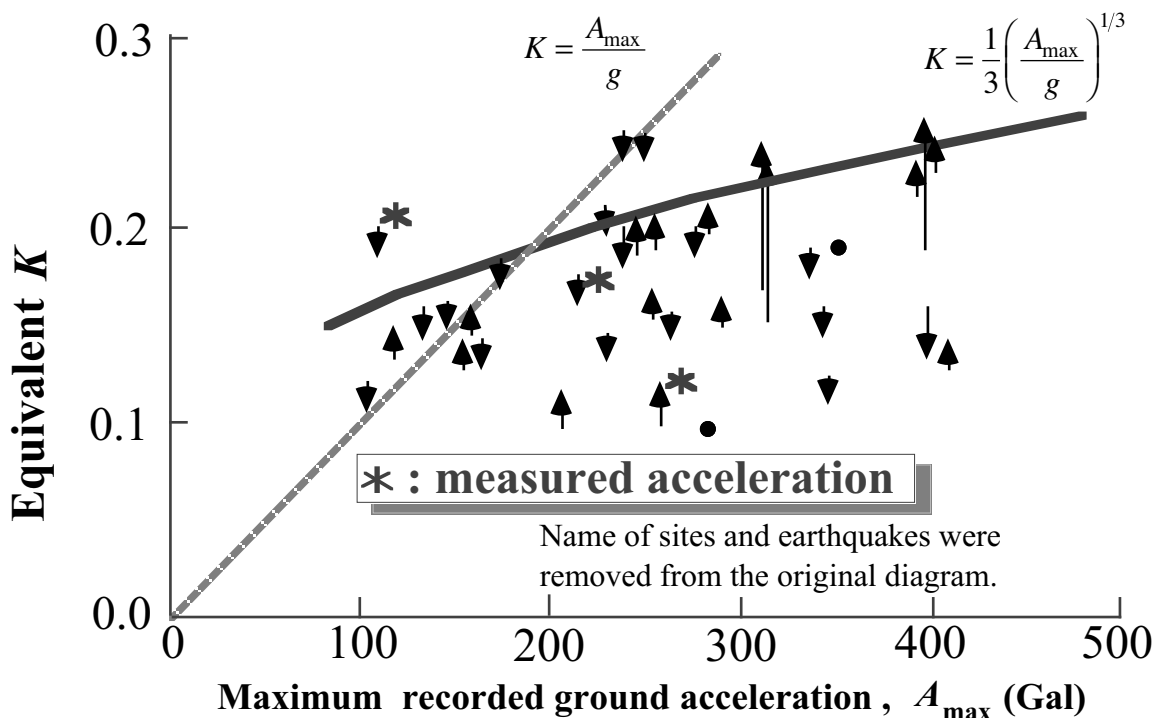


Fig. 12.9 Correlation between maximum acceleration and seismic coefficient  
(drawn after Noda et al. 1975)

12.4 Brief Analysis on Seismic Coefficient Equivalent to Maximum Acceleration

An attempt was made to determine the pseudo-static seismic coefficient that is equivalent with a given seismic loading. Figure 12.10 shows a simple time history of acceleration in which the wave shape is rectangular with a period of  $T$  and the amplitude equal to  $A_{max}$ . When a rigid mass resting on a level frictional floor (Fig. 12.11) is subjected to this acceleration history, the equation of motion is given by

$$m \frac{d^2u}{dt^2} = mA_{max} - \mu mg \quad \text{for } 0 \leq t \leq \frac{T}{2}$$

$$m \frac{d^2u}{dt^2} = -mA_{max} - \mu mg \quad \text{for } \frac{T}{2} \leq t \leq T,$$

which is easily integrated with the initial conditions of  $u = du/dt = 0$  at  $t = 0$ . Consequently, it is found that the motion stops at  $t = A_{max}T / (A_{max} + \mu g)$  in which  $g$  stands for the gravitational acceleration. By assuming that the mass does not move back towards the original position after this time, the residual displacement per one cycle of shaking is derived;

$$u_{/cycle} = \frac{A_{max}T^2(A_{max} - \mu g)}{4(A_{max} + \mu g)}.$$

When the hypothetical earthquake has  $N$  cycles of shaking, the ultimate residual displacement at the time of  $NT$  is derived as

$$u_{ult} = \frac{NA_{max}T^2(A_{max} - \mu g)}{4(A_{max} + \mu g)} \tag{12.4}$$

Second, a static seismic force of  $Kmg$  is applied to the mass in Fig. 12.11. By integrating the equation of motion with this constant (pseudostatic) force, the residual displacement,  $u_{inertia}$ , at  $t = NT$  is easily derived as

$$u_{inertia} = \frac{(K - \mu)g(NT)^2}{2} \tag{12.5}$$

By equating (12.4) and (12.5), a value of  $K = K_{eq}$  that is equivalent with the acceleration in Fig. 12.10 is determined;

$$\frac{K_{eq}}{\mu} = 1 + \frac{A_{max} \left( \frac{A_{max}}{\mu g} - 1 \right)}{2N \left( \frac{A_{max}}{\mu g} + 1 \right)} \tag{12.6}$$

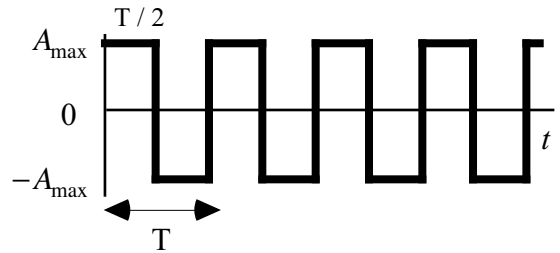


Fig. 12.10 Rectangular history of acceleration

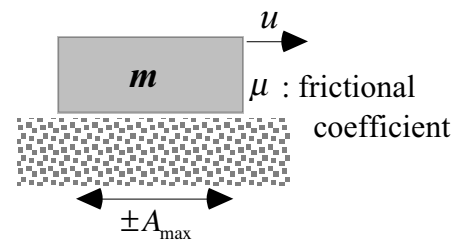


Fig. 12.11 Rigid mass resting on frictional level floor, which is subjected to motion

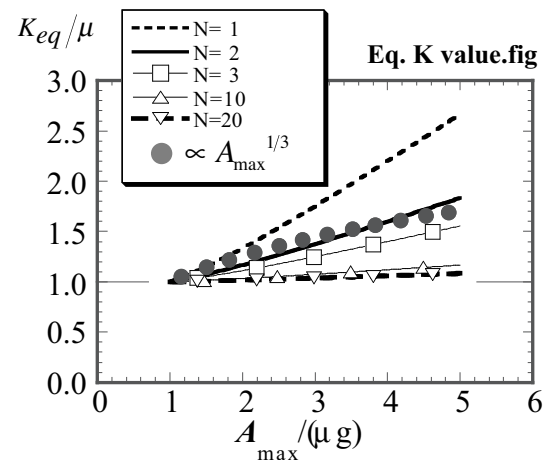


Fig. 12.12 Equivalent seismic coefficient

$K_{eq}$  here is equivalent with the given acceleration history in the sense that both develops the same magnitude of residual displacement after the same time.

Figure 12.12 plots  $K_{eq}$  thus calculated against  $A_{max}/\mu g$ . Note that  $K_{eq}$  decreases as  $N$  increases. The proportionality to  $(A_{max}/g)^{1/3}$  as proposed by Noda et al. (1975) (Sect. 12.3) agrees with the case of  $N = 2$ . When more than two cycles occur, even a smaller  $K_{eq}$  is appropriate.



**12.5 Seismic Earth Pressure on Retaining Wall**

Calculation of seismic earth pressure on a retaining wall is one of the important applications of the pseudo-static (quasi-static) seismic inertial force. Figure 12.13 indicates the real failure of a wall. Not only lateral sliding but also rotation occurs in reality.



**Fig. 12.13** Overturning of retaining wall during 1995 Kobe earthquake (near Hanshin Ishiyagawa Station)

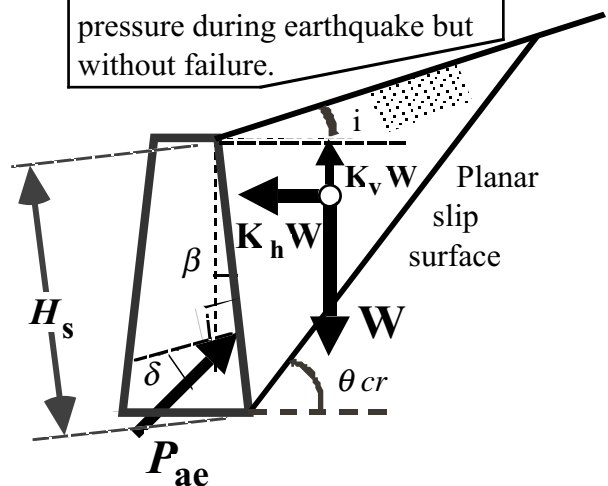


**Fig. 12.14** Prof. N. Mononobe around 1930



**Fig. 12.15** Dr. S. Okabe in 1926

Mononobe-Okabe pressure is a pressure at limit equilibrium. Do not confuse it with the real earth pressure during earthquake but without failure.

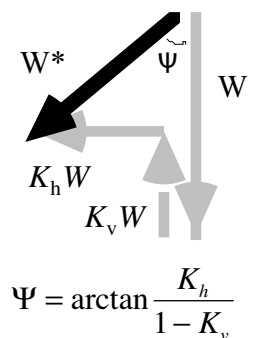


**Fig. 12.16** Failure mechanism assumed in Mononobe-Okabe formula

Mononobe and Okabe (Figs. 12.14 and 12.15) developed a theory of seismic earth pressure by modifying the Coulomb theory on (static) active earth pressure (Mononobe, 1924, Okabe, 1924, 1929; Mononobe and Matsuo, 1929). The Mononobe-Okabe theory is still in practical use all over the world.

Figure 12.16 illustrates the situation in which Mononobe-Okabe theory was developed. A soil wedge (楔くさび) behind a rigid wall is subjected to inertial forces in both horizontal and vertical directions. Since an active pressure is going to be studied, the horizontal inertia force is oriented outwards. The rear face of the wall is inclined by  $\beta$ , having a frictional angle of  $\delta$  with soil.

The gravity force,  $W$ , is a static force that is oriented vertically and acting on the soil wedge. Under seismic conditions, inertia forces of  $K_v W$  and  $K_h W$  are added to  $W$ , composing a total load of  $W^*$ , which is inclined by  $\psi$  (Fig. 12.17).



$$\psi = \arctan \frac{K_h}{1 - K_v}$$

**Fig. 12.17** Total force acting on soil wedge

By examining Figs. 12.16 and 12.17, it is found that Mononobe-Okabe theory is different from Coulomb's active-earth-pressure theory (Fig. 12.18) only in the direction of force  $W^*$ . Hence, the Mononobe-Okabe's Fig. 12.16 is rotated by  $\psi$  to obtain Fig. 12.19 where the force of  $W^*$  is vertical. By applying the original Coulomb theory to Fig. 12.19, the seismic active earth pressure,  $P_{ac}^*$ , is derived.

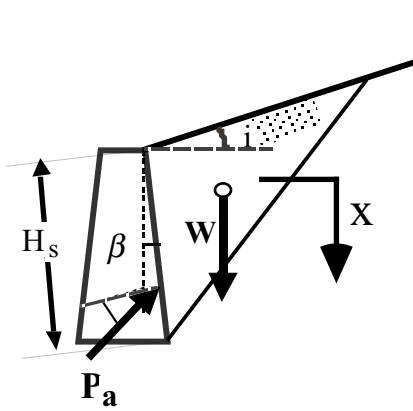
The original Coulomb active pressure was given by

$$P_a = \frac{\gamma H_s^2}{2} \frac{\cos^2(\phi - \beta)}{\cos(\delta + \beta) \left\{ 1 + \sqrt{\frac{\sin(\phi + \delta) \sin(\phi - i)}{\cos(\delta + \beta) \cos(i - \beta)}} \right\}^2} \quad (12.7)$$

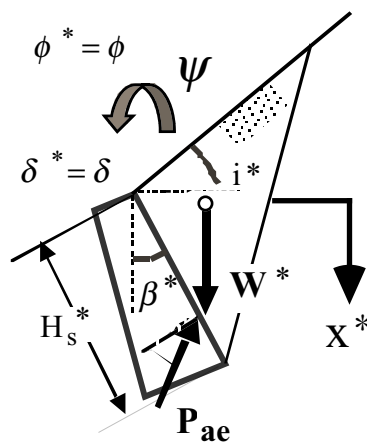
and the direction of the slip plane by

$$\cot(\theta_{cr} - i) = -\tan(\beta - i + \delta + \phi) + \frac{1}{\cos(\beta - i + \delta + \phi)} \sqrt{\frac{\sin(\phi + \delta) \cos(\beta + \delta)}{\cos(\beta - i) \sin(\phi - i)}}, \quad (12.8)$$

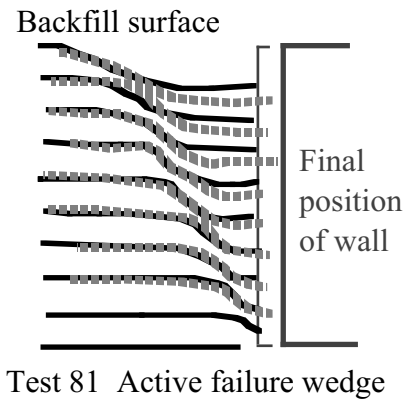
where  $H_s$  is the length of the face of the wall. For detailed derivation of (12.7) and (12.8), refer to Appendix 1.



**Fig. 12.18** Coulomb coordinate before rotation



**Fig. 12.19** Mononobe-Okabe coordinate after rotation



**Fig. 12.20** Displacement of backfill soil in centrifuge tests on retaining wall (after Bolton and Steedman, 1985)

After rotating Fig. 12.16, symbols in (12.7) are replaced by new ones with “\*”,

$$P_{ae} = \frac{\gamma^* H_s^{*2}}{2} \frac{\cos^2(\phi - \beta^*)}{\cos(\delta + \beta^*) \left\{ 1 + \sqrt{\frac{\sin(\phi + \delta) \sin(\phi - i^*)}{\cos(\delta + \beta^*) \cos(i^* - \beta^*)}} \right\}^2} \quad (12.9)$$

in which  $\beta^* = \beta + \psi$ ,  $i^* = i + \psi$ ,  $\theta_{cr}^* = \theta_{cr} + \psi$ ,  $H_s^* = H_s$ , and  $\gamma^* = \frac{W^*}{W} \gamma = \frac{1 - K_v}{\cos \psi} \gamma$ . Consequently,

$$P_{ae} = \frac{\gamma H_s^2}{2} \frac{(1 - K_v) \cos^2(\phi - \beta - \psi)}{\cos \psi \cos(\delta + \beta + \psi) \left\{ 1 + \sqrt{\frac{\sin(\phi + \delta) \sin(\phi - i - \psi)}{\cos(\delta + \beta + \psi) \cos(i - \beta)}} \right\}^2} \quad (12.10)$$

and the direction of slip plane as measured from the horizontal direction is given by

$$\cot(\theta_{\text{cr,e}} - i) = -\tan(\beta - i + \delta + \phi) + \frac{1}{\cos(\beta - i + \delta + \phi)} \sqrt{\frac{\sin(\phi + \delta)\cos(\beta + \psi + \delta)}{\cos(\beta - i)\sin(\phi - i - \psi)}}. \quad (12.11)$$

The Mononobe–Okabe seismic active pressure acts at the elevation of 1/3 from the bottom. Recent studies recommend, however, 0.45 to 2/3 (e.g., Seed and Whitman, 1970). Figure 12.20 supports a planar slip plane as assumed by the Mononobe–Okabe theory.

Problems and further developments of the Mononobe–Okabe theory will be described in Sect. 12.8.

### 12.6 Shaking Model Test on Seismic Earth Pressure

The Mononobe–Okabe theory is simply a product of theoretical consideration and does not have an experimental back ground. Further, there are strange attempts in which the theory is applied to situation without failure despite that the theory is a limit equilibrium one which is valid only when soil fails. With these in mind, shaking table tests were conducted on seismic earth pressure on a model of retaining wall (Watanabe et al. 1999).

Figure 12.21 illustrates a model in 1-G field in which a retaining wall is supported by an air spring and can rotate around its base. The backfill is made of air-dry (気乾) dense Toyoura sand that has 90% relative density.

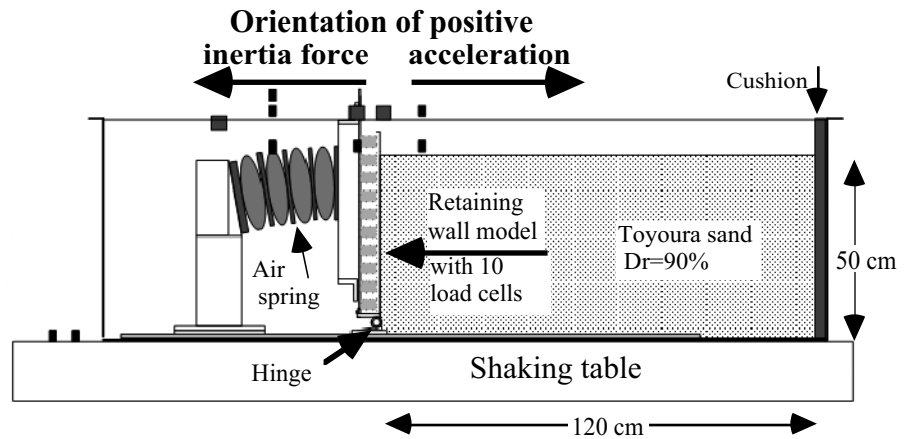


Fig. 12.21 Model of retaining wall

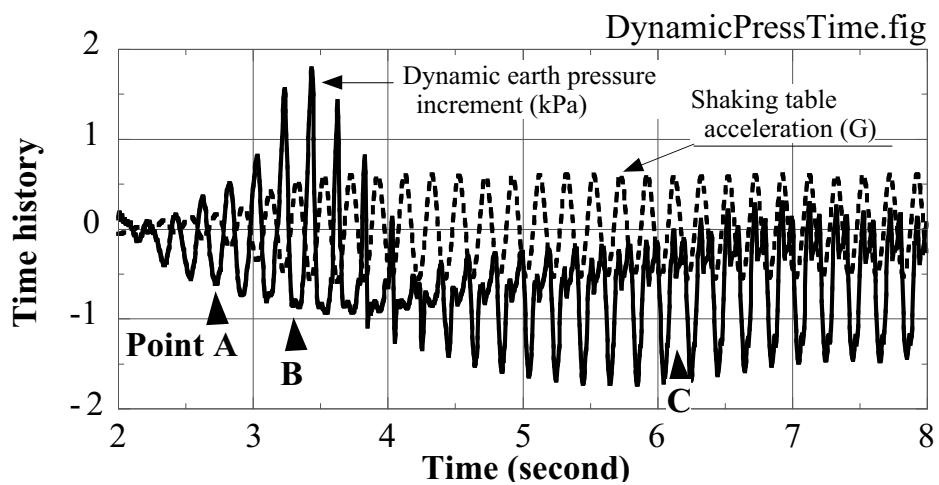


Fig. 12.22 Time history of shaking and earth pressure

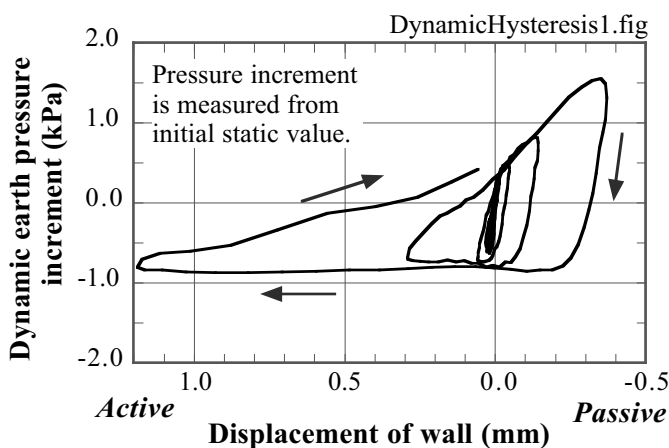


Fig. 12.23 Variation of earth pressure before failure

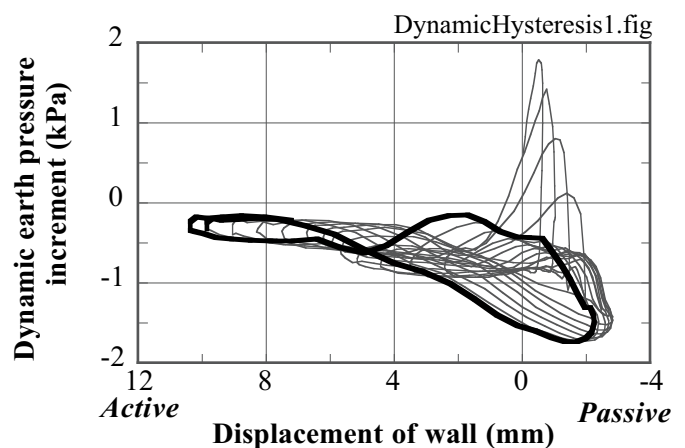


Fig. 12.24 Variation of earth pressure after failure

Figure 12.22 manifests the time history of base shaking and the dynamic increment of earth pressure. When the shaking was weak in the initial stage, the shaking and the earth pressure are 180° out of phase (逆位相 : point A). This means that the induced inertia force moved the wall outwards more than the backfill soil, leading to reduced earth pressure. This situation starts to change at around point B and, in the latest stage of point C undergoing stronger shaking, the acceleration and the earth pressure are in phase with each other (同位相). This is because the increased magnitude of shaking increased the strain amplitude, and accordingly reduced the stiffness of backfill soil (nonlinearity). Thus the soil was made

easier to move than the wall. Consequently, the inertia force in the outward direction made “collision” between soil and wall, resulting in the increased earth pressure.

Figures 12.23 and 12.24 show the relationship between the displacement of wall and the earth pressure increment during shaking. Before failure (Fig. 12.23), the earth pressure takes the maximum value when the wall moves towards the soil (positive displacement : passive state). Since the Mononobe–Okabe theory is concerned with the active state, this maximum earth pressure is out of scope of the theory. After failure (Fig. 12.24), in contrast, there is another peak earth pressure in the active state that agrees with the idea of the theory. It is noteworthy, therefore, that the Mononobe–Okabe theory assumes the wall to be more stable than the backfill soil.

Nakamura (2005) carried out centrifugal model tests (Sect. 24.11) under 30G field on dynamic earth pressure on a gravity-type retaining wall. The data hereinafter is presented in the equivalent prototype scale. Constructed models were first shaken under relatively weak intensity of motion prior to strong excitation. Figure 12.25 shows the distribution of earth pressure after this preliminary shaking. It is seen that the earth pressure had decreased to be close to the static active earth pressure probably because of minor displacement of the wall.

Strong shaking with the maximum acceleration of 600 Gal occurred thereafter. Figure 12.26 illustrates the relationship between the inertia force and the dynamic earth pressure when harmonic shaking occurred with 600 Gal at maximum and 2 Hz. The inertial force is taken positive when it is oriented outwards in the active direction, and the dynamic earth pressure stands for the increment of earth pressure after the initial pressure.

It is shown in Fig. 12.26 that the dynamic earth pressure increment is negative when the inertial force takes the maximum value in the active direction. Thus, it may be reasonable to take the design seismic pressure equal to the initial pressure, which is equal to the static active pressure (Fig. 12.25). Furthermore in Fig. 12.27, the point of application of the earth pressure during shaking is around 25% of the wall height as shown by the data when the inertial force takes the maximum active value.

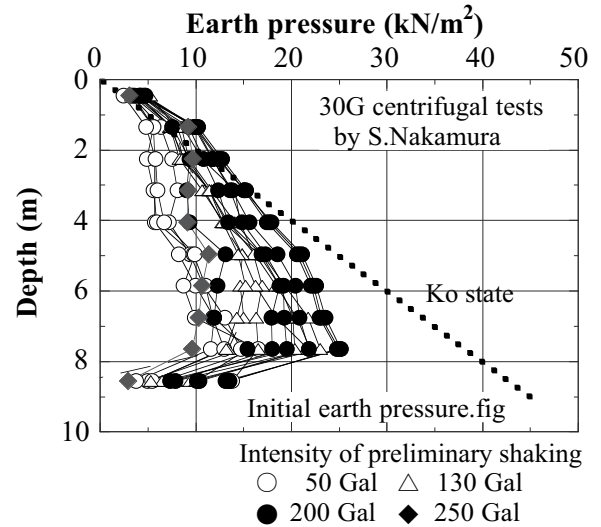


Fig. 12.25 Earth pressure distribution prior to strong shaking (after Nakamura, 2005)

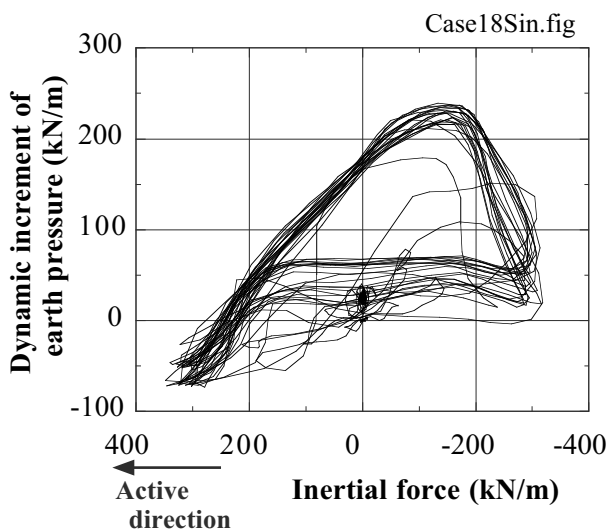


Fig. 12.26 Relationship between inertia force and earth pressure under harmonic shaking

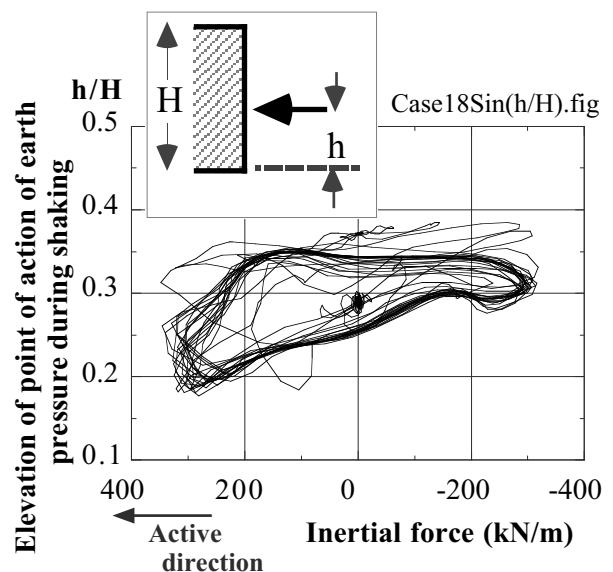
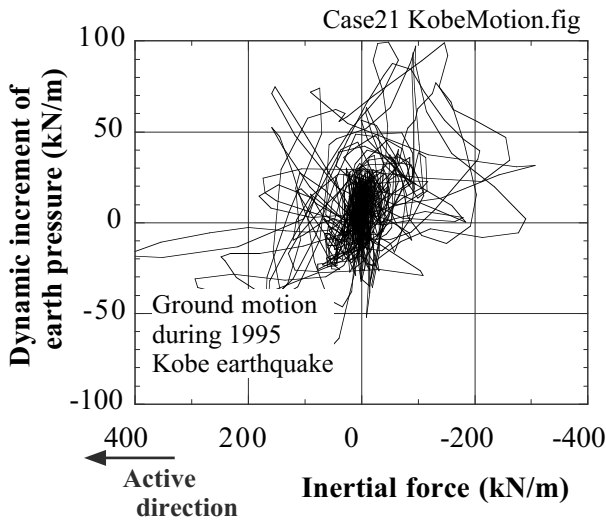


Fig. 12.27 Time change of the point of application of earth pressure during harmonic shaking

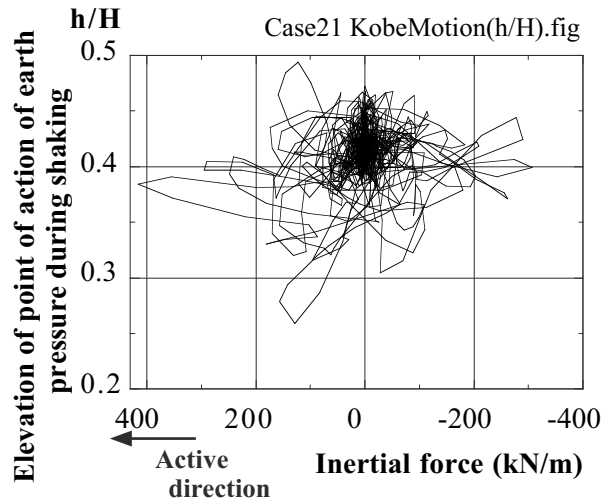
(600 Gal and 2 Hz) (data by Nakamura, 2005)

(600 Gal and 2 Hz) (data by Nakamura, 2005)

The same points can be made in Figs. 12.28 and 12.29 in which an irregular shaking of maximum 600 Gal and the predominant period of 2 Hz are employed. Thus, in contrast to the implication of Mononobe–Okabe pseudo-static theory, the static active earth pressure may be employed as the design dynamic earth pressure.



**Fig. 12.28** Relationship between inertia force and earth pressure under irregular shaking (600 Gal and 2 Hz) (data by Nakamura, 2005)



**Fig. 12.29** Time change of the point of application of earth pressure during irregular shaking (600 Gal and 2 Hz) (data by Nakamura, 2005)

## 12.7 Comparison of Static and Seismic Active Earth Pressures

It is intended here to compare the seismic active earth pressure as derived by the *Mononobe–Okabe* formula with the *Coulomb* static active earth pressure. Fig. 12.30 illustrates the concerned situation in which the face of a wall is smooth ( $\delta = 0$ ) and vertical ( $\beta = 0$ ), while the surface of the backfill is level ( $i = 0$ ). The *Mononobe–Okabe* seismic active earth pressure is then given by

$$P_{ae} = \frac{K_{ae}}{2} \gamma H^2, \quad (12.12)$$

where the earth pressure coefficient,  $K_{ae}$ , is given by

$$K_{ae} = \frac{\cos^2(\phi - \psi)}{\cos \psi \left\{ 1 + \sqrt{\frac{\sin \phi \sin(\phi - \psi)}{\cos \psi}} \right\}^2}. \quad (12.13)$$

The static active earth pressure, on the other hand, is given by

$$P_a = \frac{K_a}{2} \gamma H^2 \quad (12.14)$$

wherein

$$K_a = \tan^2 \left( 45^\circ - \frac{\phi}{2} \right). \quad (12.15)$$

Moreover, the coefficients of static earth pressure at rest ( $K_0$ ) and of passive earth pressure,  $K_p = \tan^2 \left( 45^\circ + \frac{\phi}{2} \right)$ , are going to be studied.

Figure 12.31 compares three kinds of static earth pressure coefficients,  $K_a$ ,  $K_0$ , and  $K_p$ , with  $K_{ae}$ , which varies with the seismic coefficient of  $K_h$ . The friction angle of  $40^\circ$  is assumed in the backfill soil. In Fig. 12.31, following points are made:

1.  $K_a$  is less than  $K_0$  that is around 0.5 for normally consolidated soils.
2.  $K_{ae}$  increases from  $K_a$  as  $K_h$  increases. However,  $K_{ae}$  is still less than  $K_0$  when  $K_h$  is relatively small.
3. Since small values of  $K_h$  cannot induce a state of limit equilibrium, the calculated  $K_{ae}$  with small  $K_h$  is not meaningful. Hence, a dashed curve is employed in the figure.

Seed and Whitman (1970) used  $\phi = 35^\circ$  and proposed an approximate expression of

$$K_{ae} = K_a + \frac{3}{4} K_h. \quad (12.16)$$

This approximation is shown also in Fig. 12.31 by a symbol of  $\square$ . Its matching with the original Mononobe–Okabe formula is good in spite of different friction angles of  $35^\circ$  and  $40^\circ$  employed.

Fig. 12.30 Illustration of studied retaining wall model

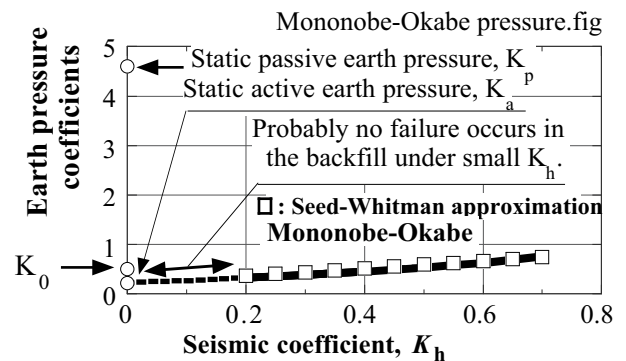
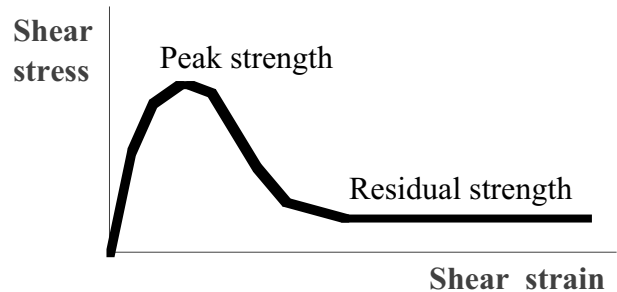


Fig. 12.31 Comparison of Mononobe–Okabe seismic active earth pressure coefficient with static earth pressure coefficients

**12.8 Modified Mononobe–Okabe Theory**

Since 1990s, there has been a strong trend to increase the design seismic coefficient due to experiences of strong earthquake motions (see Fig. 14.20) and importance of structures. Consequently, the seismic coefficient is increasing from former levels of, for example,  $K_h = 0.20$  to stronger levels such as 0.5 or more. Another issue is the use of friction angle at the residual deformation,  $\phi_{residual}$ , rather than that at the peak strength,  $\phi_{peak}$ . As Fig. 12.32 illustrates conceptually, the residual friction angle is smaller than the peak friction angle and gives a conservative (higher) earth pressure coefficient. For experimental data, see Fig. 1.15.

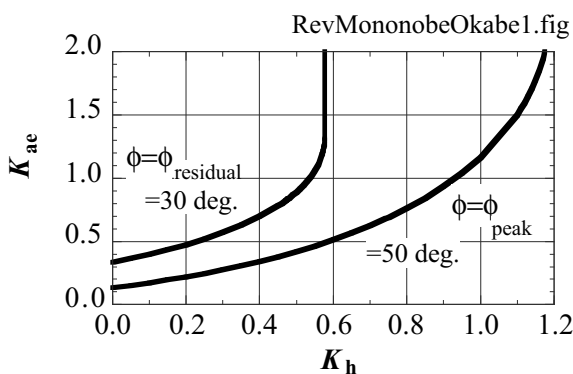


**Fig. 12.32** Schematic illustration of peak and residual shear strength

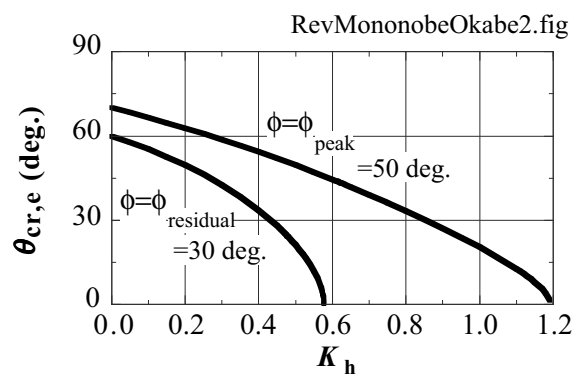
Those greater values of  $K_h$  were substituted in (12.10) and (12.11) to calculate the seismic earth pressure coefficient,  $K_{ae}$ , and the direction of the slip plane,  $\theta_{cr,e}$ . The direction of the slip plane is measured from the horizontal direction; see (12.17) and (12.18).

$$K_{ae} = \frac{(1 - K_v) \cos^2(\phi - \beta - \psi)}{\cos \psi \cos(\delta + \beta + \psi) \left\{ 1 + \sqrt{\frac{\sin(\phi + \delta) \sin(\phi - i - \psi)}{\cos(\delta + \beta + \psi) \cos(i - \beta)}} \right\}^2}, \tag{12.17}$$

$$\cot(\theta_{cr,e} - i) = -\tan(\beta - i + \delta + \phi) + \frac{1}{\cos(\beta - i + \delta + \phi)} \sqrt{\frac{\sin(\phi + \delta) \cos(\beta + \psi + \delta)}{\cos(\beta - i) \sin(\phi - i - \psi)}}. \tag{12.18}$$



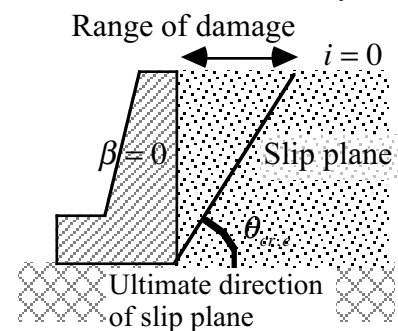
**Fig. 12.33** Seismic earth pressure coefficient by conventional Mononobe–Okabe theory



**Fig. 12.34** Direction of seismic slip plane calculated by conventional Mononobe–Okabe theory

In this calculation,  $\psi = \arctan\{K_h / (1 - K_v)\}$ , while  $K_v = 0$  and  $\beta = i = \delta = 0$  is assumed for simplicity. The calculated results in Figs. 12.33 and 12.34 employed  $\phi_{peak}$  and  $\phi_{residual}$  being  $50^\circ$  and  $30^\circ$  respectively. Accordingly,

1. The earth pressure that was increased by the residual strength is conservative but makes retaining walls more costly,
2. When  $K_h$  exceed 0.6, the earth pressure with  $\phi_{residual}$  becomes infinite and design calculation is made impossible, and
3. This problem is accompanied by the direction of slip plane, which becomes nearly horizontal (Fig. 12.35).

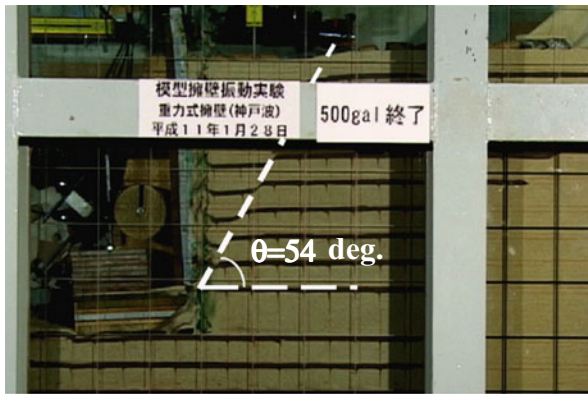


**Fig. 12.35** Negative orientation of slip plane calculated by conventional Mononobe–Okabe theory

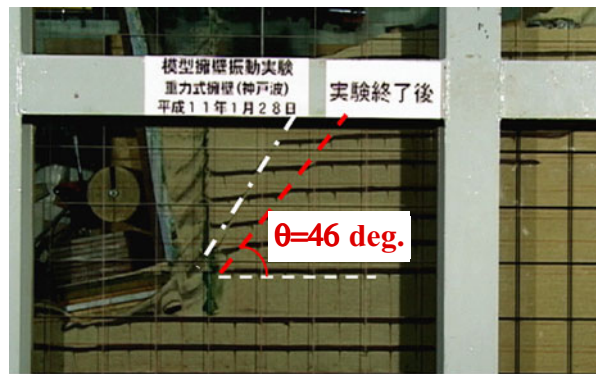
To overcome this problem and to assess a reasonable magnitude of seismic earth pressure under strong design earthquake and  $\phi_{residual}$ , Koseki et al. (1998) proposed a modified Mononobe–Okabe theory. They



conducted 1-G shaking tests on a model of a gravity-type quay wall with dense sandy backfill (Toyoura sand of relative density = 80%). Shaking was conducted by using the motion that was recorded at Kobe Meteorological Observatory in 1995. This shaking was repeated several times by increasing the amplitude.



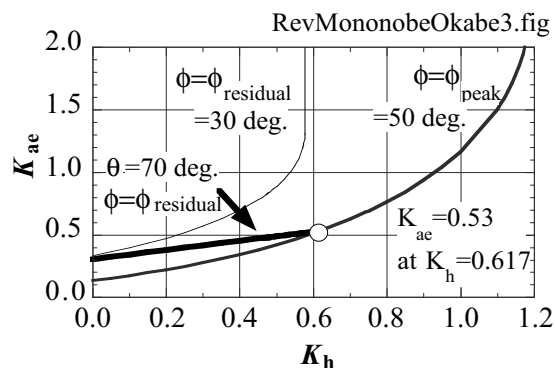
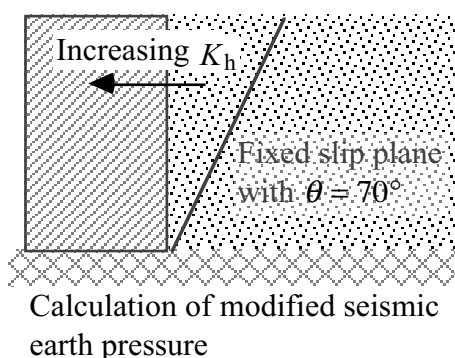
**Fig. 12.36** Development of first slip plane after shaking with maximum acceleration = 513 Gal (Photo by K. Watanabe)



**Fig. 12.37** Development of second slip plane after shaking with maximum acceleration = 919 Gal (Photo by K. Watanabe)

Figure 12.36 illustrates the appearance of a model after shaking with the maximum acceleration of 513 Gal. The orientation of the developed slip plane was 54°. Shaking was further conducted on the same model, while maintaining the first slip plane unchanged. After shaking at 919 Gal (Fig. 12.37), the second slip plane developed in the direction of 46°. Consequently, the new earth pressure theory was constructed as what follows:

1. The first failure mechanism (slip plane) is determined by  $\phi_{peak}$  under minor magnitude of seismic coefficient ( $K_h = 0.0$  or 0.2 for design practice);  
 in case of  $\phi_{peak} = 50^\circ$  and  $K_h = 0$  together with  $\beta = i = \delta = K_v = 0$ , for example,  $K_{ae} = 0.132$  and  $\theta_{cr,e} = 70^\circ$ .
2. Under stronger seismic loads ( $K_h > 0$ ), the seismic active earth pressure is produced by this mechanism ( $\theta = 70^\circ$ ), but the friction angle along this plane is reduced to  $\phi_{residual}$ . Because of this reduced friction angle, the earth pressure is increased. Note that the friction angle in other parts of the backfill is still kept at  $\phi_{peak}$ . Figure 12.38 compares earth pressure coefficients obtained by the conventional Mononobe–Okabe theory and this modified idea. The increased earth pressure is still less than the pressure calculated by Mononobe–Okabe theory with  $\phi_{residual}$ .



**Fig. 12.38** Comparison of conventional Mononobe–Okabe seismic earth pressure and the pressure obtained by fixed slip plane under increasing  $K_h$

3. As Fig. 12.38 indicates, the modified theory and the conventional Mononobe–Okabe theory with  $\phi_{peak} = 50^\circ$  give the same results at  $K_h = 0.617$ . This implies that the entire backfill is subject to failure again. The conventional Mononobe–Okabe theory with  $\phi_{peak} = 50^\circ$  and  $K_h = 0.617$  gives  $\theta_{cr,e} = 43.6^\circ$

4. After  $K_h = 0.617$ , the second failure mechanism plays a chief role in the direction of  $\theta = 43.6^\circ$  together with  $\phi_{\text{residual}} = 30^\circ$ . This feature is illustrated in Fig. 12.39.

The modified Mononobe–Okabe theory maintains  $\theta$  angle at a constant value while  $K_h$  value increases. This is in a good contrast with the conventional theory in which  $\theta$  decreases with increasing  $K_h$  (Fig. 12.34). Thus, the range of damage in Fig. 12.35 ( $H/\tan\theta$ ) is made smaller by the modified theory. This is a good advantage because the need for soil improvement in the backfill is reduced.

Note that the earth pressure calculation in the modified theory depends on the initial determination of the slip plane orientation. In the example above, this orientation was determined at  $K_h = 0$ . There is no definite reason, however, to support this practice, and engineering judgement is required in this respect.

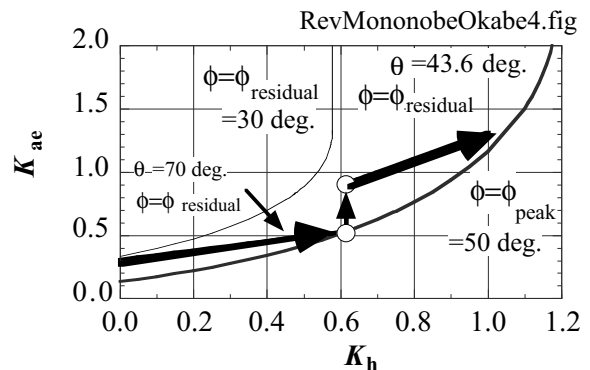


Fig. 12.39 Seismic earth pressure activated after second development of slip plane

### List of References in Chapter 12

- Bolton, M.D. and Steedman, R.S. (1985) Modelling the seismic resistance of retaining structures, Proc. 11th Int. Conf. Soil Mech. Found. Eng., Vol. 4, pp. 1845–1848.
- Koseki, J., Tatsuoka, F., Munaf, Y., Tateyama, M. and Kojima, K. (1998) A modified procedure to evaluate active earth pressure at high seismic loads, Soils and Foundations, Special Issue No.2 on Geotechnical Aspects of the January 17 1995 Hyogoken-Nambu earthquake, pp. 209–216.
- Mononobe, N. (1924) Discussion and consideration on vertical earthquake motion and consideration, Proc. JSCE, Vol. 10, No. 5, pp. 1063–1095 (in Japanese).
- Mononobe, N. and Matsuo, H. (1929) On the determination of earth pressure during earthquakes, Proc. World Engineering Conference, Vol. 9, pp. 177–185.
- Nakamura, S. (2005) Clarification of seismic behavior of gravity retaining wall by using centrifugal model tests and a proposal for rationalization of the seismic coefficient method. Proc. JSCE, 785/III-70, pp. 107–122 (in Japanese).
- Newmark, N.M. (1965) Effects of earthquakes on dams and embankments, Geotech., Vol. 5, No. 2, pp. 137–160.
- Noda, S., Uwabe, T. and Chiba, T. (1975) Relation between seismic coefficient and ground acceleration for gravity quaywall 重力式岸壁の震度と地盤加速度, Report of the Port and Harbor Research Institute 港湾技術研究所報告, Vol. 14, No. 4, pp. 67–111 (in Japanese).
- Ohmachi, T., Toshinawa, T. and Yasuhara, M. (1990) Earthquake sliding response spectrum and its application, Proc. 8th Jpn. Earthq. Eng. Symp., pp. 981–986, Tokyo (in Japanese).
- Okabe, S. (1924) General theory on earth pressure and seismic stability of retaining wall and dam. Proc. JSCE, Vol. 10, No. 6, pp. 1277–1330 (in Japanese).
- Okabe, S. (1926). General theory of earth pressure and laboratory testings on seismic stability of retaining walls, Proc. JSCE, Vol. 12, No. 1, pp. 123–134 (in Japanese).
- Seed, H.B. and Whitman, R.V. (1970) Design of earth retaining structures for dynamic Loads, Lateral Stresses in the Ground and Design of Earth-Retaining Structures, ASCE, pp. 103–147.
- Watanabe, K., Maeda, T., Kobayashi, Y. and Towhata, I. (1999) Shaking table tests on seismic earth pressure exerted on retaining wall model, Proc. 2nd International Conference on Earthquake Geotechnical Engineering, Vol. 1, Lisbon, pp. 297–302.

# Chapter 13

## Seismic Force Exerted on Structures



Sigiriya means Singha (lion) giri (mountain) in Sanskrit language. King Kasyapa of Sri Lanka who was afraid of his enemy's attack located his palace at the top of this rock. Water was supplied from big pools which were excavated at the top of the rock as well.

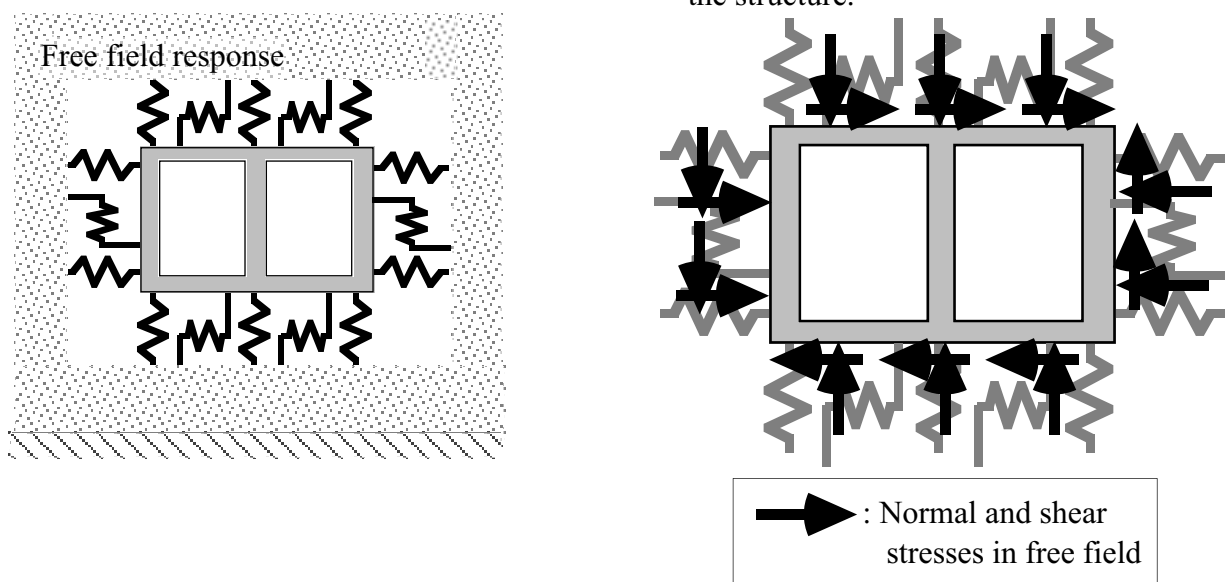
**13.1 Analysis on Soil–Structure Interaction**

Effects of ground shaking on underground structures such as tunnels and basements are often analyzed by connecting structures with free field of ground (1D soil columns without effects of embedded structures) by means of (nonlinear) springs, see Fig. 13.1a. Springs are classified into those concerning normal earth pressure and those transmitting shear force. This method of analysis is called the method of seismic displacement, the method of subgrade reaction, or the method of Winkler foundation. The modulus of springs has long been studied in the fields of, for example, pile foundation (nonlinear subgrade reaction modulus). The horizontal response (time history of displacement) of a one-dimensional soil column is first calculated by using wave propagation theory in a level ground (Sect. 4.1 and Chap. 8). The calculated motion is then substituted at the support of springs, which generate dynamic response of the structure.

Strictly speaking, the method in Fig. 13.1a is not sufficient. Suppose a soil mass embedded in a free field consisting of the same type of soil. Since no relative displacement occurs between the soil mass and the free field, because of the same material type, spring mechanisms are not activated, causing no motion in the soil mass in the analysis. This problem is solved by superimposing stress components in the free field (Fig. 13.1b). Thus, a strict analysis requires a free-field calculation of both displacement time history and the stress time history, which are then substituted in a soil-structure interaction analysis (Fig. 13.1b). In most practical cases, the magnitude of free-field stress is less significant than the spring forces and the stress superposition is ignored.

(a) Structures connected to free field by springs

(b) Rigorous method of seismic displacement with superimposed free-field stress around the structure.



**Fig. 13.1** Method of seismic displacement

An example of an elaborate method of analysis is illustrated in Fig. 13.2 in which a dynamic finite element analysis was conducted on nonlinear soil models and elastic model of a Daikai subway station in Kobe which collapsed during the 1995 Kobe earthquake. Conventionally, it had been believed that tunnel was safe during earthquakes because shaking at depth is weaker and the surrounding stiff ground prevents large deformation of tunnels in mountains (Sect. 13.7). Such an idea did not hold true when shaking was extremely strong and the surrounding soil was not very stiff; Daikai station was constructed in an excavated pit and then backfilled.

One of the limitations of the dynamic analysis in Fig. 13.2 was that the complicated nonlinear behavior of the structural members (columns and slabs) was not taken into account. This was because the employed computer code could not handle nonlinear deformation characteristics of both soil and concrete at the same time.

To overcome this problem, the maximum calculated forces exerted by surrounding soil elements upon the structural elements were applied statically on the nonlinear model of the subway station (Fig. 13.3). Nonlinear springs at connection of columns and slabs stand for the nonlinearity of the structure. This analysis was able to reproduce the failure of central columns (Fig. 13.4), which consequently caused the significant subsidence at the ground surface (Fig. 13.5). This lesson triggered reinforcement of central columns in many other subway stations. See examples in Tokyo (Figs. 13.6 and 13.7).

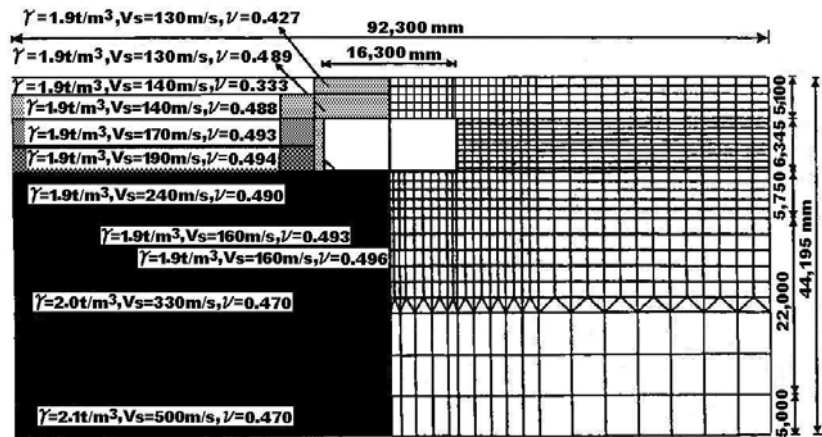


Fig. 13.2 FE model of failed subway station (Nakamura et al., 1996)

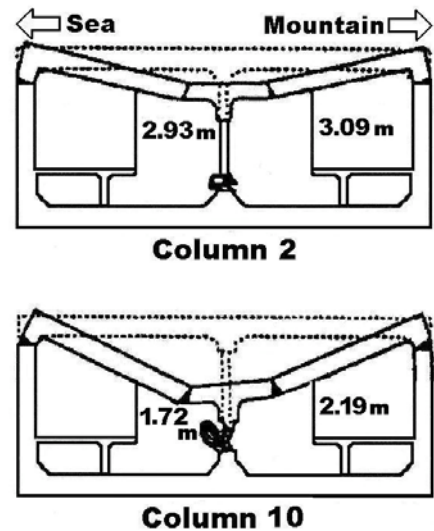


Fig. 13.4 Collapse of columns at the center of station (Nakamura et al., 1996)

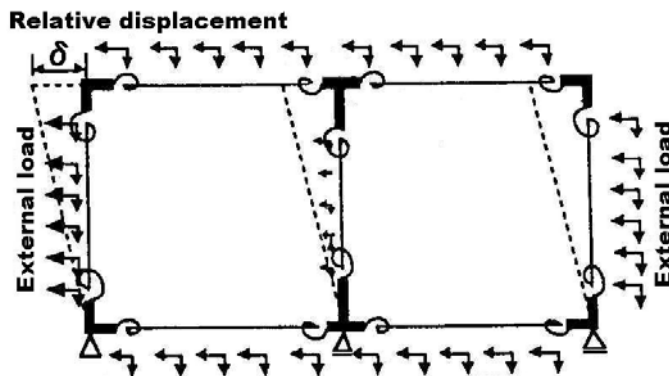


Fig. 13.3 Static nonlinear analysis of subway station. (Nakamura et al., 1996)

Theoretically the dynamic soil–structure interaction is often decomposed into the inertial and kinetic interaction; Fig. 13.8 illustrates an example of a structure supported by a single pile. The inertial interaction means the force which is the mass of the super structure  $\times$  its acceleration and is exerted on the foundation. The kinetic interaction is the force that is caused by the differential displacement between soil and the foundation. Springs in Fig. 13.1 stand for the kinetic interaction. Both kinds of force induce dynamic deformation and possibly failure.



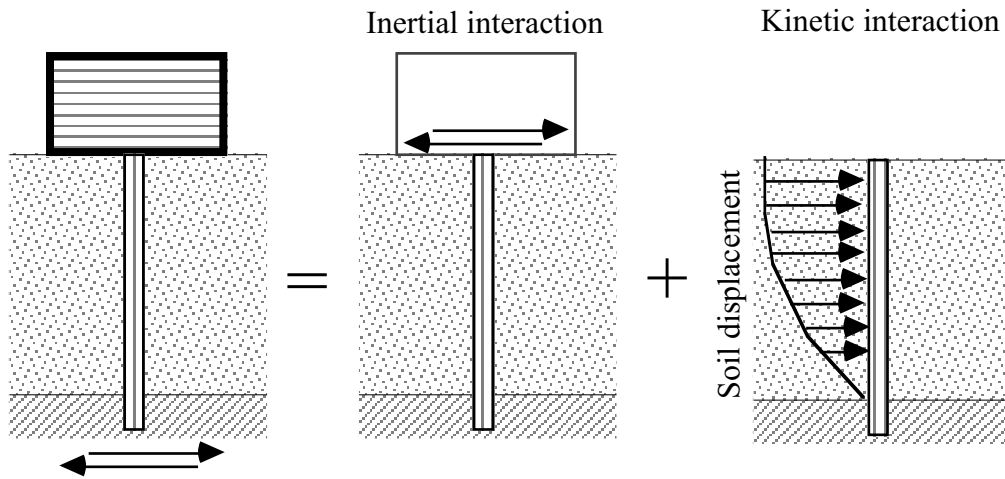
Fig. 13.5 Ground subsidence above Daikai subway station (by Nozomu Yoshida)



**Fig. 13.6** Reinforced central columns in Kasuga Station of Tokyo Metropolitan Subway



**Fig. 13.7** Reinforced central columns in Daimon Station of Tokyo Metropolitan Subway

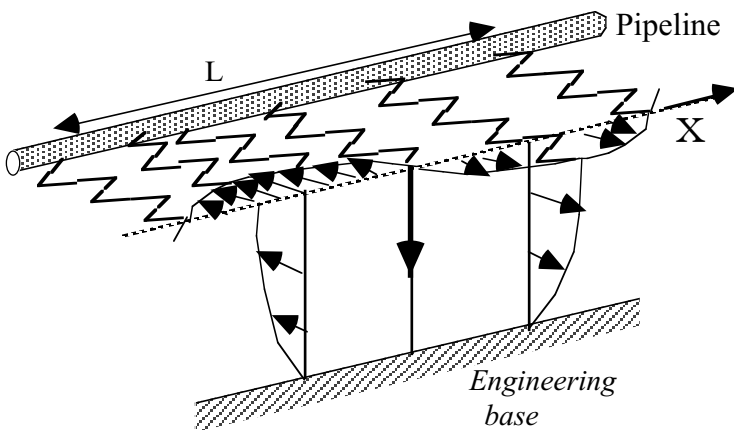


**Fig. 13.8** Schematic illustration of dynamic soil–structure interaction

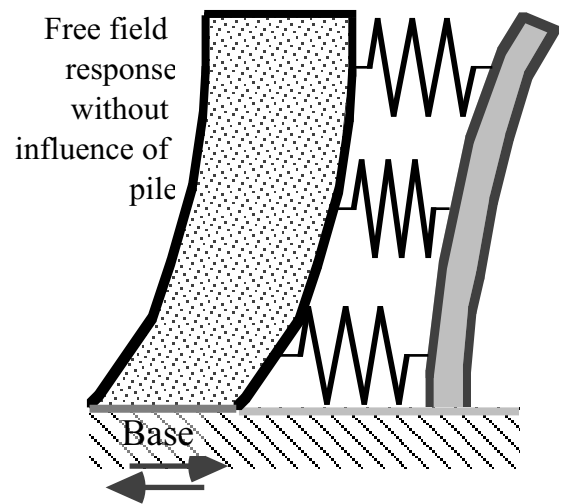
**13.2 Seismic Design of Embedded Pipeline**

Embedded pipelines for gas, water, electricity, and communications are subjected to earthquake effects such as buckling, bending failure, and separation at joints. Since these seismic effects are caused by distortion of ground, the seismic design of embedded pipelines puts emphasis on soil–structure interaction; the seismic inertia force is therein less important.

Figure 13.9 illustrates the concept of seismic design in which the ground consists of two layers, a soft surface deposit and a stiff engineering base. In this figure a pipeline is connected with the surface soil by springs (elastic beam resting on Winkler foundation). This figure concerns only with bending of a pipe because the springs are perpendicular to the axis of the pipe. Figure 13.10 illustrates another application of the method to lateral response of a pile. The use of (linear or nonlinear) springs between an embedded structure and free ground motion is called the method of seismic displacement and is widely practiced in design of piles as well.



**Fig. 13.9** Analysis on soil–pipeline interaction

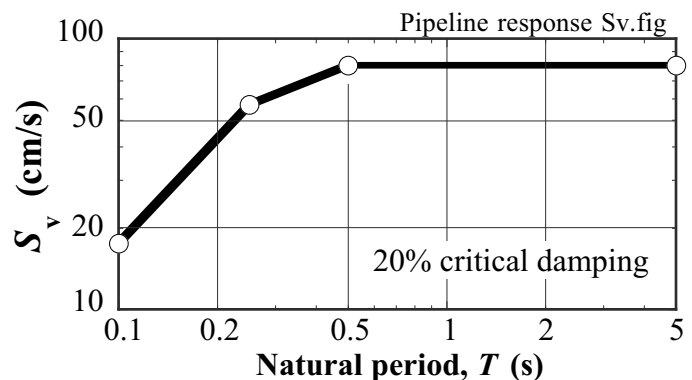


**Fig. 13.10** Method of seismic displacement as applied to lateral response of pile

The seismic input is given by the amplitude of soil displacement,  $u$ , which is idealized by

$$u(z) = U \cos \frac{\pi z}{2H} \sin \frac{2\pi x}{L} \quad (13.1)$$

where  $z$  is the depth below surface,  $U$  is the surface displacement amplitude, and  $L$  is the wave length of surface displacement. The displacement varies in a harmonic manner in both  $x$  and  $z$  directions. This ground displacement exerts lateral forces on the pipeline through spring connections. Since the magnitudes of ground displacement and spring forces vary in the  $x$  direction, the pipeline is subjected to bending.



**Fig. 13.11** Example of design velocity response spectrum

The surface displacement,  $U$ , in (13.1) is given for design purposes by the following procedure.

1. The seismic coefficient (Sect. 7.1) in the engineering base is specified as  $K_H$ .
2. The (relative) velocity response spectrum (Sect. 23.1) of a design earthquake motion in the base is normalized by the seismic coefficient and is designated by  $S_v$ . Hence,  $K_H S_v$  is the design velocity response of the surface soil, which is idealized by a single-degree-of-freedom model as the theory of response spectrum states. See Fig. 13.11 for example of  $S_v$ , while  $K_H$  is 0.65 for example. Note in this figure that the response spectrum,  $S_v$ , is a function of natural period,  $T$ .
3. The natural period of the surface deposit,  $T$ , is calculated by  $T = 4H/V_s$  where  $V_s$  is the S-wave velocity of soil (6.30). It is assumed that the surface shaking occurs in a harmonic manner under this natural period.
4. Since the amplitude of velocity in the surface soil is  $K_H S_v(T)$ , the displacement amplitude is given by

$$\begin{aligned} \text{Displacement amplitude} &= \text{Velocity amplitude/ Circular frequency} \\ &= [K_H S_v(T)] / (2\pi/T). \end{aligned} \tag{13.2}$$

5. Since the displacement,  $U$ , at the surface of a soil column is  $4/\pi$  times greater than that of a single-degree-of-freedom model, (13.1) is modified to be

$$u(z) = \frac{4}{\pi} \times \frac{T}{2\pi} K_H S_v(T) \cos \frac{\pi z}{2H} \sin \frac{2\pi x}{L} = \frac{2T}{\pi^2} K_H S_v(T) \cos \frac{\pi z}{2H} \sin \frac{2\pi x}{L}. \tag{13.3}$$

For derivation of  $4/\pi$  parameter, refer to Sect. 13.3.

6. The wave length,  $L$ , for design is determined in practice as the harmonic mean of two wave lengths

$$L = 2L_1 L_2 / (L_1 + L_2), \tag{13.4}$$

where  $L_1 = V_s T = 4H$ ,  $V_s$  the S-wave length in the surface soil, and  $L_2 = (V_s \text{ in the engineering base}) \times T$ .



### 13.3 Amplification: Soil Column Vs. Spring–Mass Model

A comparison is going to be made of seismic amplifications of a realistic soil column and its equivalent single-degree-of-freedom model, see Fig. 13.12. The properties of the soil column are uniform while the single-degree-of-freedom model consists of a lumped mass and an elastic spring. They are called equivalent when their natural periods are identical. The response of these two models to the base acceleration of  $A \sin \omega t$  is going to be studied.

The response of the lumped mass model is governed by

$$\frac{d^2U}{dt^2} + \omega_0^2 U = -A \sin \omega t, \quad (13.5)$$

where  $U$  is the displacement relative to the base,  $d^2U/dt^2$  its second time derivative, and  $\omega_0$  the natural circular frequency of the model.

Similar to the discussion on lifeline earthquake engineering (Fig. 13.9), the displacement of a soil column,  $u$ , is approximated by the fundamental harmonic mode of response

$$u(z,t) = U(t) \cos \frac{\pi z}{2H}, \quad (13.6)$$

in which  $U(t)$  is the unknown time history of surface displacement. The governing equation of motion for  $U(t)$  in (13.6) is derived by using the theory of Lagrangean equation of motion (Sect .25.3). First, the kinetic energy of the soil column,  $K$ , is expressed in terms of  $U$

$$K = \frac{\rho}{2} \int_0^H \left( \frac{du}{dt} \right)^2 dz = \frac{\rho}{2} \int_0^H \cos^2 \frac{\pi z}{2H} dz \times \left( \frac{dU}{dt} \right)^2 = \frac{\rho H}{4} \left( \frac{dU}{dt} \right)^2. \quad (13.7)$$

The potential energy due to strain of the soil column is denoted by  $Q$

$$Q = \frac{G}{2} \int_0^H \left( \frac{du}{dz} \right)^2 dz = \frac{G}{2} \int_0^H \left\{ \frac{d}{dz} \left( \cos \frac{\pi z}{2H} \right) \right\}^2 dz \times U^2 = \frac{GH}{4} \left( \frac{\pi}{2H} \right)^2 U^2. \quad (13.8)$$

The potential energy due to the inertia force is denoted by  $I$

$$I = \rho \int_0^H U \cos \frac{\pi z}{2H} A \sin \omega t dz = \rho A \frac{2H}{\pi} \sin \omega t \times U. \quad (13.9)$$

Equations (13.6)–(13.8) are substituted in the Lagrangean equation of motion

$$\frac{d}{dt} \left\{ \frac{\partial(K-Q-I)}{\partial(dU/dt)} \right\} - \frac{\partial(K-Q-I)}{\partial U} = 0. \quad (13.10)$$

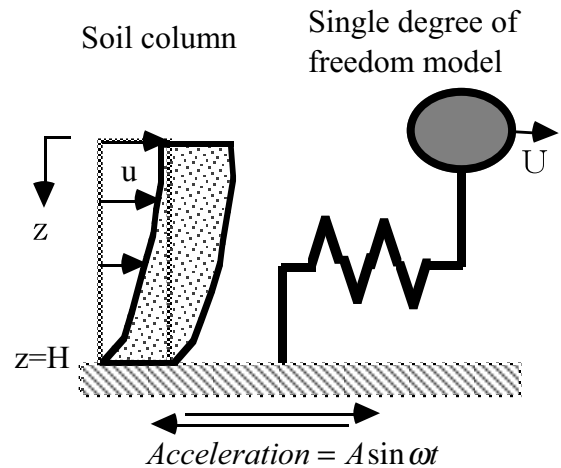


Fig. 13.12 Soil column and spring–mass model

Consequently,

$$\frac{\rho H}{2} \frac{d^2 U}{dt^2} + \frac{GH}{2} \left( \frac{\pi}{2H} \right)^2 U = -\rho A \frac{2H}{\pi} \sin \omega t \quad \text{or} \quad \frac{d^2 U}{dt^2} + \frac{G}{\rho} \left( \frac{\pi}{2H} \right)^2 U = -A \frac{4}{\pi} \sin \omega t. \quad (13.11)$$

Accordingly, the natural circular frequency of the soil column is given by

$$\omega_o = \frac{2\pi}{\text{Natural period}} = \frac{2\pi}{4H/V_s} = \frac{\pi}{2H} \sqrt{\frac{G}{\rho}}. \quad (13.12)$$

Equation (13.11) is simplified to be

$$\frac{d^2 U}{dt^2} + \omega_o^2 U = -\frac{4}{\pi} \times A \sin \omega t \quad (13.13)$$

By comparing (13.5) and (13.13), which are of a similar appearance, it is found that the surface motion of a soil column (13.13) is  $4/\pi$  times greater than the response of a spring-mass model when their natural periods are made identical. This finding was used in derivation of (13.3). The factor of  $4/\pi$  is called the participation factor (刺激係数).

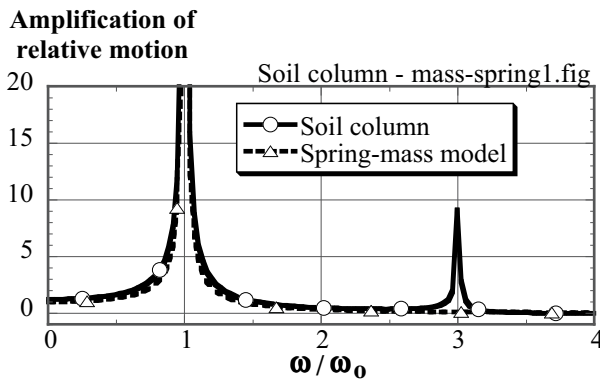
### 13.4 Rigorous Compaction of Soil Column and Equivalent Spring-Mass Model

The assumption of harmonic variation of displacement along a soil column ( $z$  direction) is removed from the discussion in the preceding Sect. 13.3. The harmonic response of a spring-mass model is obtained by solving

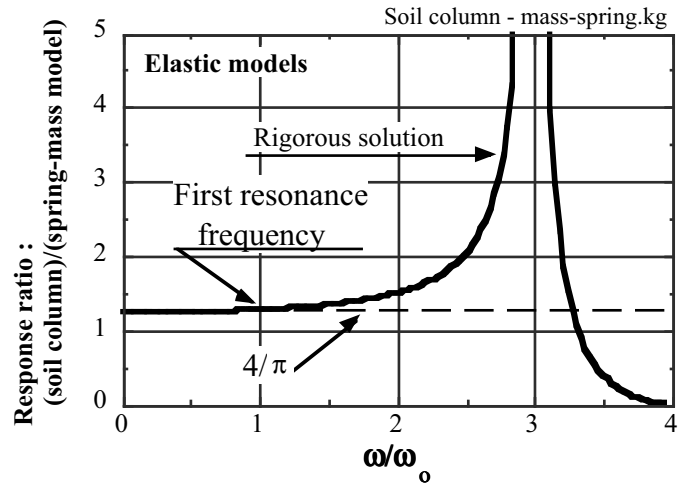
$$\frac{d^2U}{dt^2} + \omega_o^2 U = -A \sin \omega t. \quad (13.14)$$

Hence,

$$U = \frac{A}{\omega^2 - \omega_o^2} \sin \omega t = \frac{A}{\omega^2} \frac{1}{1 - (\omega_o/\omega)^2} \sin \omega t. \quad (13.15)$$



**Fig. 13.13** Amplification of relative displacement in uniform soil column and equivalent mass-spring model



**Fig. 13.14** Comparison of response of soil column and equivalent spring-mass model

The response of a uniform soil column is obtained by considering the wave propagation. By paying attention to the fact that the concerned displacement,  $u(z,t)$ , is a relative displacement to the base displacement of  $-A \sin \omega t / \omega^2$ ,

$$u(z,t) = \frac{A}{\omega^2} \left\{ 1 - \frac{\cos \frac{\omega z}{V_s}}{\cos \frac{\omega H}{V_s}} \right\} \sin \omega t. \quad (13.16)$$

At the ground surface,  $z = 0$ , in particular,

$$u(z=0,t) = \frac{A}{\omega^2} \left\{ 1 - \frac{1}{\cos \frac{\omega H}{V_s}} \right\} \sin \omega t = \frac{A}{\omega^2} \left\{ 1 - \frac{1}{\cos \left( \frac{\pi}{2} \frac{\omega}{\omega_o} \right)} \right\} \sin \omega t, \quad (13.17)$$

in which  $\omega_o = (\pi V_s)/2H$  was taken into account. Note again that this  $u(z=0,t)$  is the surface displacement relative to the base.

The behaviors of a soil column and its equivalent spring-mass model are compared by using a common value of  $\omega_0$ . Figure 13.13 illustrates that the amplification curves of two models look similar except that the spring-mass model does not have the second resonance peak due certainly to its single degree of freedom. The ratio of the amplification, however, reveals that two models are different:

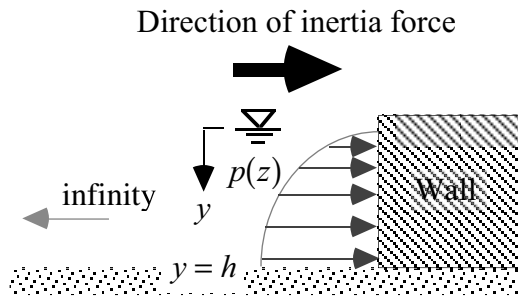
$$\begin{aligned} \text{Ratio of amplitude} &= \frac{\text{Amplitude at surface of soil column}}{\text{Amplitude of spring - mass model}} \\ &= \left\{ 1 - \left( \frac{\omega_0}{\omega} \right)^2 \right\} \left[ 1 - \frac{1}{\cos \left\{ \frac{\pi}{2} \left( \frac{\omega}{\omega_0} \right) \right\}} \right] \end{aligned} \quad (13.18)$$

Figure 13.14 compares (13.18) against the simplified solution of  $4/\pi$  that was derived in Sect. 13.3. It is found therein that the approximate solution is acceptable in the lower frequency range; being valid at least up to the first resonance frequency.

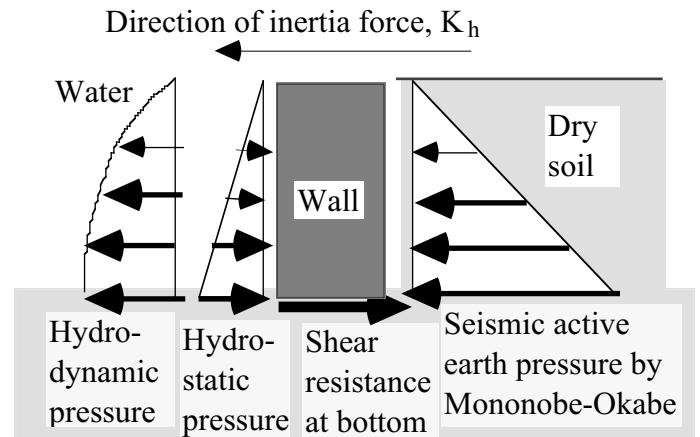
### 13.5 Seismic Water Pressure on Wall

Dam engineering has been interested in the water pressure exerted by a reservoir (貯水池, 水庫) subjected to a seismic inertia force. Westergaard (1931) developed a theory that can calculate this dynamic pressure by assuming a semi-infinite reservoir water facing a vertical quay wall (Fig. 13.5). The total water pressure acting on a wall is given by

Water pressure = Hydrostatic pressure + Westergaard pressure



**Fig. 13.15** Westergaard's dynamic reservoir pressure



**Fig. 13.16** Forces acting on water-front wall of gravity type

Westergaard derived a series solution (級数解) of the dynamic water pressure. The distribution of this pressure was reasonably approximated by a parabola (see Fig. 13.15),

$$p = \frac{7}{8} K_h \gamma_w \sqrt{hy}, \quad (13.19)$$

where  $p$  is the hydrodynamic pressure at a water depth of  $y$ ,  $K_h$  the horizontal seismic coefficient,  $\gamma_w$ , the unit weight of water, and  $h$  the depth of reservoir. By integrating (13.19) from  $y = 0$  to  $y = h$ ,

$$\text{Total hydrodynamic force} = \frac{7}{12} K_h \gamma_w h^2. \quad (13.20)$$

The point of action of the Westergaard pressure is found as

$$y = \frac{\int_0^h \frac{7}{8} K_h \gamma_w \sqrt{hy} \times y \, dy}{\frac{7}{12} K_h \gamma_w h^2} = \frac{3}{5} h, \quad (13.21)$$

while the hydrostatic pressure has a triangular distribution and acts at  $1/3$  from the bottom.

Figure 13.16 illustrates the lateral forces acting on a revetment wall at a water front. Note that the hydrodynamic pressure decreases the water pressure because the inertial force is oriented towards the reservoir water. Accordingly, the lateral stability of the wall is lost when

- (Seismic active earth pressure calculated by Mononobe–Okabe theory)
- (Hydrostatic water pressure) + (Westergaard hydrodynamic pressure)
- (Shear resistance at the bottom)

is positive. Note further that the direction of the hydrodynamic pressure is identical with the direction of the inertia force, consequently decreasing the total water pressure. The above calculation does not care the moment equilibrium that concerns the rotation of the wall.

The backfill soil in Fig. 13.16 is dry and unrealistic for simplicity. When this soil is water-saturated, (1) accumulation of excess pore water pressure due to dilatancy, and (2) dynamic fluctuation (動的変動) of pore water pressure due to inertia force have to be taken into account. The accumulation of excess pore water pressure will be discussed after Sect. 17.1 concerning liquefaction. Section 24.17 will address the application of Westergaard theory to dynamic earth pressure in liquefied subsoil.

Matsuo and O-Hara (1965) developed a theory on the amplitude of pore pressure fluctuation in pervious soil. This amplitude is about 70% of the Westergaard pressure, oriented in the direction of  $K_h$ . They reported their shaking table tests to show a good agreement between prediction and observation.

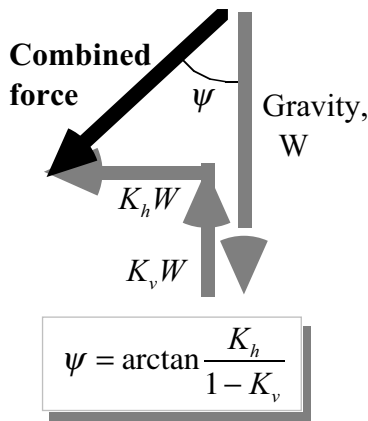
### 13.6 Dynamic Earth Pressure Exerted by Water Saturated Backfill

In most design practice, the seismic earth pressure exerted by water-saturated back fill is calculated by simply modifying the Mononobe–Okabe active earth pressure formula (Sects. 12.5 and 12.7);

$$P_{ae} = \frac{K_{ae}}{2} \gamma H^2, \quad (13.22)$$

in which the seismic earth pressure coefficient,  $K_{ae}$ , changes with the seismic coefficient,  $K_h$ , in terms of the angle,  $\psi$  (Fig. 13.17).

The Mononobe–Okabe formula consists of two mechanisms. The one is a mechanism of shear resistance. Since shear strength is governed by the effective stress, the unit weight as employed in the earth pressure formula has to be the buoyant unit weight,  $\gamma' = \gamma - \gamma_w$ . The problem is that the mass of existing pore water is removed from the analysis.



**Fig. 13.17** Definition of orientation of combined force



**Fig. 13.18** Active seismic failure of quay wall and tilting of building behind the wall

The use of  $\gamma'$  in place of  $\gamma$  in (13.22) is not sufficient. This is because the seismic force is exerted on mass of both soil grains and pore water. Unless the permeability of soil is extremely high, soil grains and pore water move together. Thus, the inertia force is given by  $K_h \gamma$  and  $K_v \gamma$ ; note that  $\gamma$  is used here and not  $\gamma'$ . Therefore, the calculation of seismic earth pressure should employ both  $\gamma$  for inertia force and  $\gamma'$  for shear resistance. Equation (13.17), however, can make use of only one kind of unit weight.

In practice, (13.22) should use  $\gamma'$ ,

$$P_{ae} = \frac{K_{ae}}{2} \gamma' H^2. \quad (13.23)$$

However, the seismic coefficient in the horizontal direction has to be modified in order to take into account the horizontal inertia force. Therefore, the seismic coefficient,  $K'_h$ , is defined by

$$K'_h \equiv \frac{\gamma}{\gamma'} K_h. \quad (13.24)$$

Accordingly,

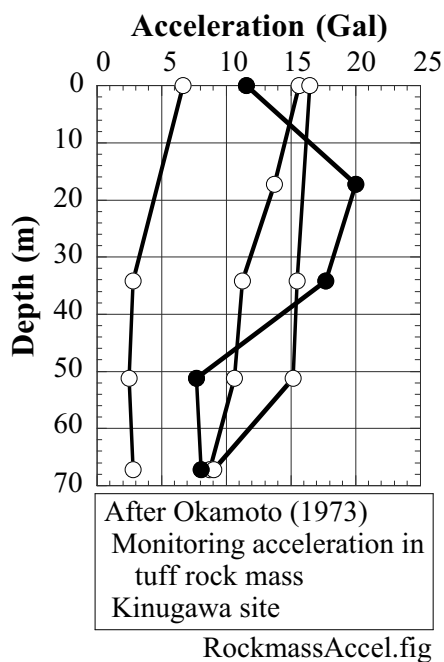
$$\psi' = \arctan \frac{K'_h}{1 - K_v} = \arctan \left( \frac{K_h}{1 - K_v} \frac{\gamma}{\gamma'} \right) \quad (13.25)$$

The new seismic earth pressure coefficient,  $K_{ac}$ , is calculated by using (13.25). For an example of seismic active earth pressure exerted by water-saturated backfill, see Fig. 13.18. This wall moved towards the sea and the backfill moved together. Consequently, a pile foundation of a building on the left side was destroyed and the building tilted towards the sea.



**13.7 Damage in Tunnels Caused by Earthquakes**

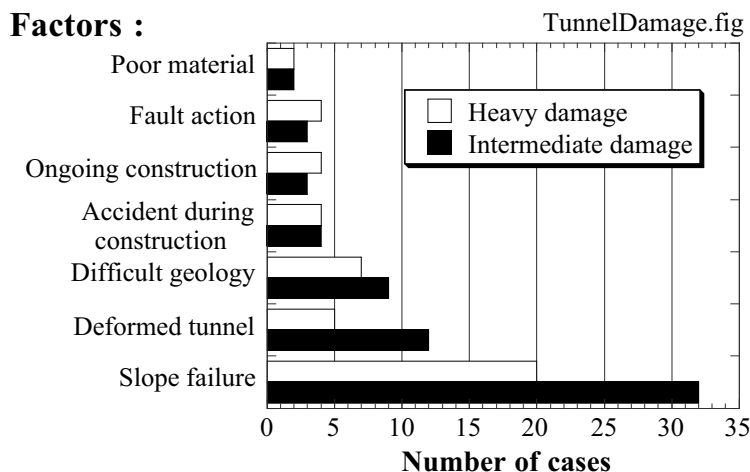
It has been conventionally believed that tunnels have good resistance against shaking, most probably. The first reason for this is that the intensity of shaking in rock under the ground is weaker than the surface acceleration (Fig. 13.14). The second reason is because the rock mass around a tunnel has sufficient rigidity to keep the shape of the tunnel unchanged. Even when tunnels are intersected with causative faults, no fatal collapse occurred (Sect. 16.7). This traditional idea is not always correct, however, as illustrated by the following examples. Remarks on subway tunnels were made in Sect. 13.1.



**Fig. 13.19** Acceleration recorded in rock mass

**Fig. 13.21** Collapsed Kinoura tunnel during the 1992 Noto-Hanto-Oki earthquake

Figure 13.20 is a summary of earthquake-induced problems in tunnels. The number of events related with seven situations are illustrated therein. It is noteworthy that the majority of problems were caused by slope instability at the entrance. The second majority is related with difficult geology and deformation that had been going on prior to earthquakes. In contrast, the number of cases is small concerning poor tunnel materials such as deterioration, fault action, ongoing construction, and tunnels that experienced collapse or other accident during construction.



**Fig. 13.20** Factors concerning seismic damage of tunnels (JR TT, 1996)



**Fig. 13.22** Mountain behind entrance of Kinoura tunnel



**Fig. 13.23** Slope failure at the entrance of tunnel (五龍隧道 Taiwan, 1999)

Figure 13.21 illustrates collapse of a tunnel during the 1992 Noto-Hanto-Oki earthquake (能登半島沖地震). This Kinoura (木の浦) tunnel had a overburden soil of only 22 m (Fig. 13.22), which collapsed into the tunnel. It was possible at the time of inspection to see the sun light through the collapsed tunnel from inside the tunnel. One of the common problems caused by earthquakes in tunnels is the slope failure near the entrance (Fig. 13.23). Slope reinforcement or construction of a protective structure is thus important. Another source of problem lies in a fault (Sect. 16.7).

The dynamic shaking and ground pressure may affect tunnels. Figure 13.24 indicates the significant distortion of Haguro Tunnel during the 2004 Niigata-Chuetsu earthquake. While the weak bottom of the tunnel (road pavement) buckled due to lateral compression, the top part developed longitudinal cracks due to superposition of bending and compression (Fig. 13.25). The distortion of Haguro Tunnel is related to the following two issues. First, the rock around the tunnel is young and soft as evidenced by a large landslide that occurred immediately next to the tunnel entrance (Fig. 13.26). The shortage in rigidity made it difficult for the tunnel to maintain its shape. Second, the bottom part of the tunnel (invert) did not develop arching action and was not very rigid, thus being vulnerable to compression and buckling failure. The compression in the bottom easily resulted in extension in the top (Fig. 13.27). Since the Haguro Tunnel was very important in a local road network, it was restored within six months by replacing the damaged concrete by new one. Note that a similar damage and collapse were experienced in a subway tunnel in Kobe (Sect. 13.1).

Tunnel damages due to fault action will be discussed in Sect. 16.7.



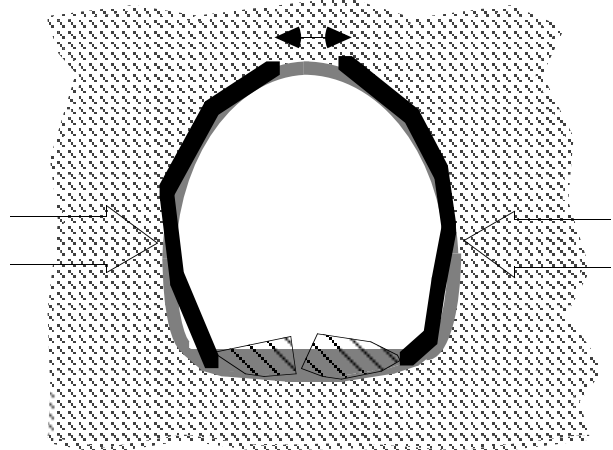
**Fig. 13.24** Distorted shape and buckling of pavement in Haguro Tunnel, Niigata-Chuetsu



**Fig. 13.25** Tension crack in top part of Haguro Tunnel



**Fig. 13.26** Landslide near the western entrance of Haguro Tunnel



**Fig. 13.27** Schematic illustration of deformation mechanism of Haguro Tunnel

## 13.8 Nodular Pile

Pile foundation is often damaged by strong earthquake motion. One reason for the damage is the inertial action due to mass of a super structure, and the other is the kinematic action induced by shaking ground. Figure 13.28 illustrates an example of pile damage due to inertial effects.

Past experiences showed good performance of a type of pile, which is called a nodular pile. Being a prefabricated prestressed concrete pile, a nodular pile has an irregular shape and develops increased skin friction. Figure 13.29 indicates a nodular-pile foundation in Kobe Port Island after the quake in 1995. Although it was located immediately behind a damaged quay wall, the foundation was able to survive the significant soil displacement. Moreover, Fig. 17.39 shows a building that was supported by nodular piles and survived the subsoil liquefaction. More precisely, the columns and roofs that were supported by nodular piles had no damage, while the concrete block floors suffered significant distortion because they simply rested on ground and were not connected to the stable structural members.



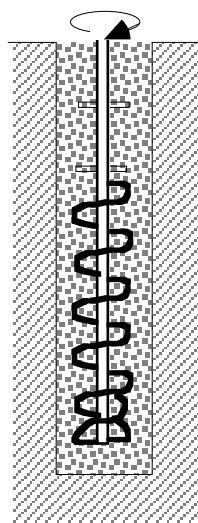
**Fig. 13.28** Damaged pile in Navrakhi Harbor, Gujarat Province, India, in 2001



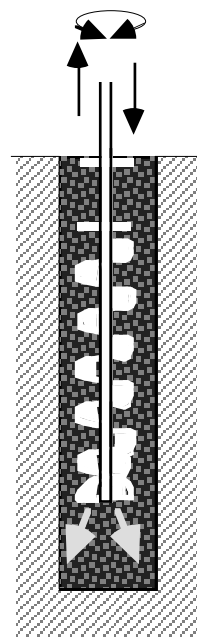
**Fig. 13.29** Nodular pile foundation in Kobe Rokko Island in 1995 (Japan Pile Inc., 2007)

A nodular pile is an embedded pile whose installation process is illustrated in Fig. 13.30. First, a hole is bored by an auger (Fig. 13.30a), and then the auger moves back and forth in the hole, while jetting grout and mixing it with soil (Fig. 13.30b). After sufficient mixing, a nodular pile is pushed downwards from the surface (Fig. 13.30c). After curing time, the pile and the surrounding cement-mixed soil forms a body of pile. Since the injected grout has high w/c ratio (water/cement being typically 100%), the pile has much higher rigidity than the soil.

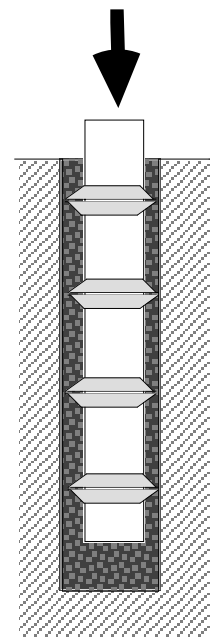
(a) Auger boring



(b) Grouting and mixing with soil



(c) Installation of nodular pile



**Fig. 13.30** Installation of nodular pile

Figure 13.31 shows nodular piles prior to installation. The diameter of the main shaft is 300 mm or more and the minimum diameter of nodes is 440 mm. The spacing between nodes is 1 m. It is possible to connect two or more piles for deeper installation. Figure 13.32 indicates two stages during pile installation; auger boring and pushing of a pile.

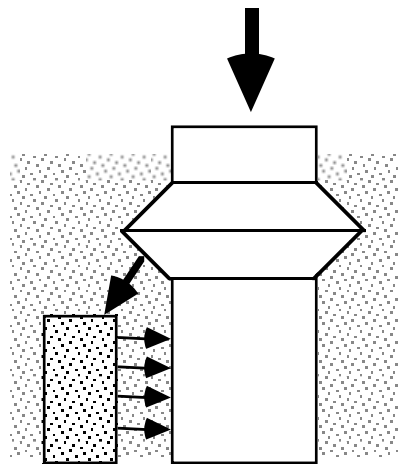


**Fig. 13.31** Nodular piles prior to installation

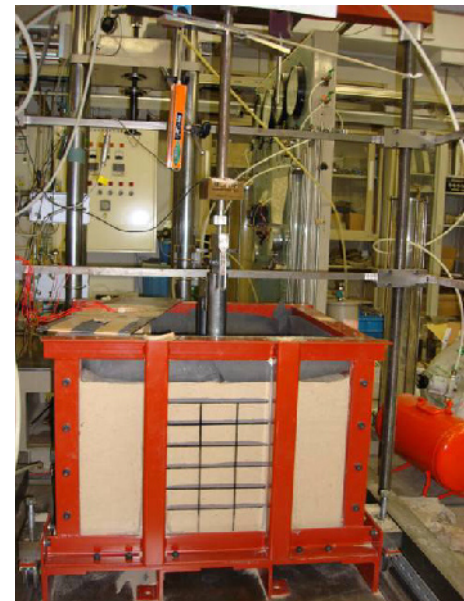


**Fig. 13.32** Installation of nodular pile

In the current design practice, the increased bearing capacity of a nodular pile is attributed to the pile diameter, which is increased by the enlarged nodules and the surrounding cement-mixed soil. In reality, the bearing capacity is increased by the force transfer from the pile axis to the surrounding soil by means of nodules (Yabuuchi, 2007). It seems that the compressed soil under a node expands laterally, increases the horizontal effective stress along the pile shaft, and further increases the skin friction, see Fig. 13.33.



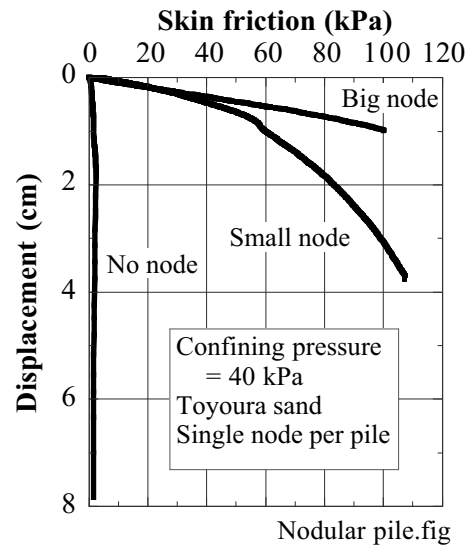
**Fig. 13.33** Probable mechanism of increased skin friction of nodular pile



**Fig. 13.34** Soil container for model tests on vertical bearing capacity of nodular pile



**Fig. 13.35** Model of nodular pile for bearing capacity tests



**Fig. 13.36** Displacement vs. skin friction curves for model piles with and without node

To further study this issue, model tests were conducted (Borda et al., 2007) in a container (Fig. 13.34) that has air bags at the ground surface so that overburden pressure would be applied for better reproduction of in-situ stress conditions. Figure 13.35 reveals an employed model pile that measures 4.0 cm in diameter and is of one or a few simplified node. The diameter of the node measured either 6.4 cm (small node) or 7.1 cm (big node). The measured relationship between skin friction and vertical displacement of a pile is presented in Fig. 13.36 for the case of single node. It is therein seen that a plain pile without node achieved the ultimate but negligible skin friction after a small displacement and this friction was maintained constant under larger displacement. In contrast when a node was attached to a pile, the skin friction increased gradually with displacement and finally the magnitude of friction was remarkably greater than that of a plain pile. Note, however, that the behavior of a nodular pile undergoing lateral load is yet to be known.

### List of References in Chapter 13

- Borda, O., Uno, M. and Towhata, I. (2007) Shaft capacity of nodular piles in loose sand, Proc. 49th Nat. Conf. Japan. Geotech. Soc., Vol. 2, pp. 1175-1176.
- Japan Pile Corporation (2007) Behavior of nodular piles during 1995 Kobe earthquake, Internal Report (in Japanese).
- JRRT (Japan Railway Construction, Transport, and Technology Agency) (1996) Guideline for Design and Construction of NATM Tunnels, p. 49 (in Japanese).
- Matsuo, H. and O-Hara, S. (1965) Dynamic pore water pressure acting on quay walls during earthquakes, Proc. 3rd World Conf. Earthq. Eng., Vol. 1, pp. 130-141.
- Nakamura, S., Yoshida, N. and Iwatate, T. (1996) Damage to Daikai subway station during the 1995 Hyogoken Nanbu earthquake and its investigation, The 1995 Hyogoken-Nanbu Earthquake, JSCE Committee of Earthquake Engineering, pp. 287-295.
- Okamoto, S. (1973) Introduction to earthquake engineering, Univ. Tokyo Press, p. 62.
- Westergaard, H.M. (1931) Water pressure on dams during earthquakes, Transactions of ASCE, Paper, No. 1835, pp. 418-433.
- Yabuuchi, S. (2007) The behavior of nodular piles in sand: calibration research on cylindrical and nodular piles packed with gravel or slag, accepted by Soils Found.

# Chapter 14

## Seismic Behavior of Slopes and Embankments

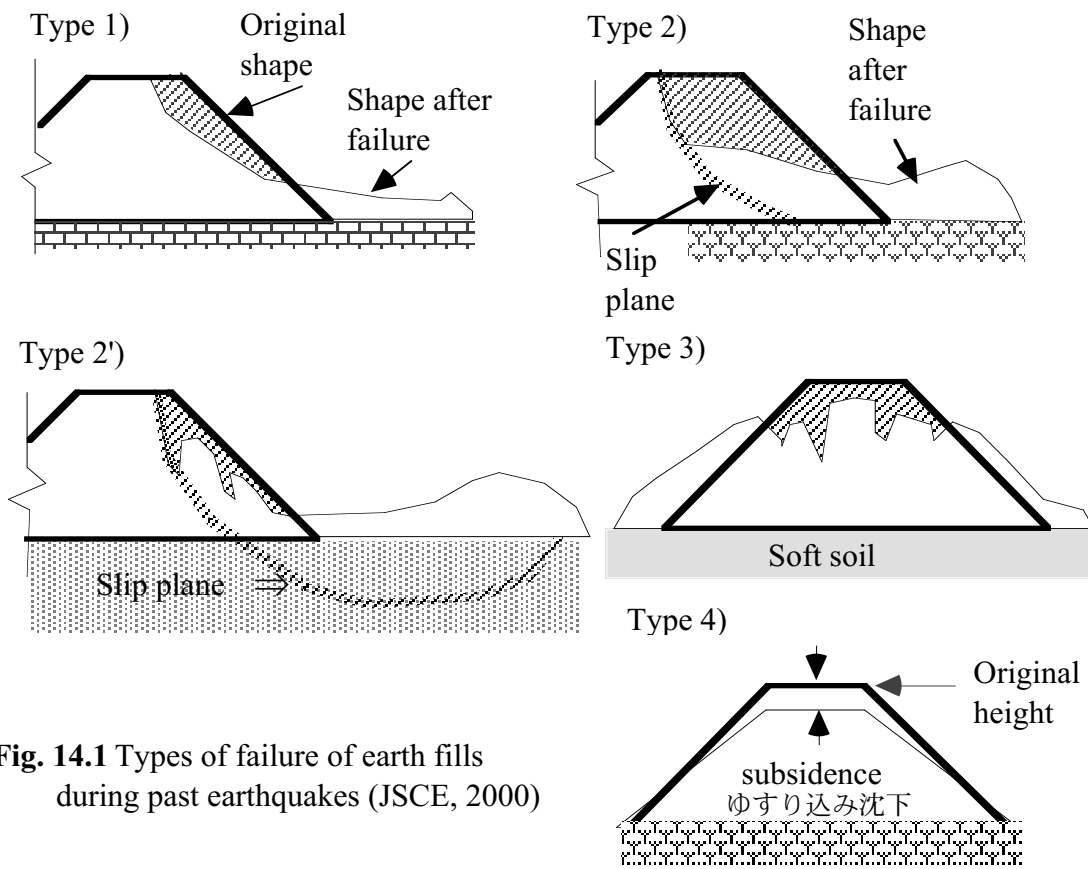


Pyramid in Mexico was a place to worship God.

**14.1 Classification of Seismic Failure of Artificial Embankment**

Embankments such as river dikes as well as road and railway fills have been affected to different extents by earthquakes in the past. Since an earth embankment can be easily repaired, when compared with steel and concrete structures, it is important that the induced deformation is less than the allowable limit so that the damage is quickly restored.

Figure 14.1 illustrates a variety of residual deformation of earth fills which were experienced during past earthquakes. They are classified as 1) shallow surface sliding of slope, 2) development of slip surface within the body of embankment, 2') development of slip surface reaching the soft foundation soil, 3) slumping, and 4) densification. Another type of damage of fill is the one caused by fault action. A river-dike fill resting directly upon a fault was deformed as shown in Fig. 14.2 (Wufeng 霧峰 in Taiwan). This dike was quickly repaired as shown in Fig. 14.3.



**Fig. 14.1** Types of failure of earth fills during past earthquakes (JSCE, 2000)



**Fig. 14.2** River dike distorted by fault action at Wufeng in Taiwan



**Fig. 14.3** Repaired shape of dike in Wufeng

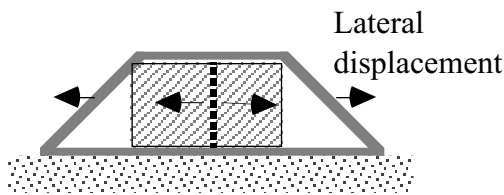
The quick restoration in Fig. 14.3 makes an important point that the restoration of earth structure is much easier and quick than that of steel or concrete structures. This issue will play an important role in the

discussion on allowable seismic displacement in the performance-based design principle (Sect. 14.4 and Sect. 14.5).

Failure of an embankment may trigger additional problems. Fig. 14.4 shows a case of road embankment during the 2004 Niigata-Chuetsu earthquake (see Fig. 14.24 as well). The large displacement of a road fill destroyed many embedded pipelines. It is important that this site was situated upon a small valley, suggesting the potential instability of embankment upon such a small geology; see also Fig. 14.43.



**Fig. 14.4** Effects of collapse of road embankment on embedded lifelines



**Fig. 14.5** Distortion of embedded structure due to deformation of highway embankment

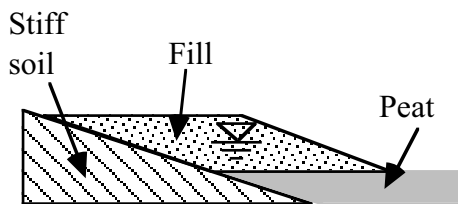
Another example is demonstrated in Fig. 14.5. A highway embankment deformed in the horizontal direction and an embedded underpass concrete structure (culvert) was separated into two pieces. The separation was restored by placing steel plates. Thus, the stability of an embankment has to be discussed from the viewpoint of interaction with embedded facilities.



## 14.2 Example of Sliding Failure of Embankment Due to Earthquakes

Figure 14.6 manifests a development of a shallow slip plane (Type-1 failure in Sect. 14.1). Placed upon a small stream channel, this fill failed during the 1994 Hokkaido-Toho-Oki earthquake.

A deeper slip plane inside a fill (Type-2 and 2') can generate a more significant damage. Fig. 14.7 shows a damaged shape of a fill at Kayanuma site (茅沼) which was constructed upon a small stream facing a peaty marsh deposit; 1993 Kushiro-Oki earthquake. It is possible that ground water flowed into the fill in place of flowing into the stream, raising the ground water table in the fill and increasing the weight. The increased seismic inertia force was not resisted by the peaty soil at the bottom (Fig. 14.8). Thus, the fill collapsed. This fill was reconstructed after the quake to the exactly same shape and failed once more during the 1994 Hokkaido-Toho-Oki earthquake.

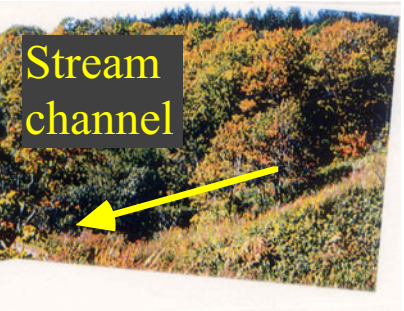


**Fig. 14.8** Mechanism of failure of Kayanuma fill

Figure 14.9 illustrates a failure of a road embankment during the 2004 Niigata-Chuetsu earthquake. Situated upon a small valley, the failed earth is overtopped by stream water. This failure was probably caused by a combination of two reasons, which are elevated water table in the fill as well as the weak stream deposit



**Fig. 14.9** Failure of road embankment during the 2004 Niigata-Chuetsu earthquake



**Fig. 14.6** Surface sliding of road embankment at Nakachambetsu site in 1994



**Fig. 14.7** Failure of residential development site in Kayanuma in 1993



**Fig. 14.10** Slip failure of fill part in cut-and-fill area (Midoriga-oka in Kushiro)

that was not fully removed during construction. Thus, an embankment constructed upon a stream (集水地形) needs special care such as drainage and reinforcement at the toe of a slope.

Many land development projects in hilly areas employ cut-and-fill construction to achieve a level ground surface. The interface between cut and fill can form a slip plane. Figure 14.10 indicates a sliding failure of this kind. During the 1993 Kushiro-Oki earthquake, only the bathroom of this house, which was situated upon a fill fell down, while the remaining part of the same house was intact.

### 14.3 Example of Slumping of Embankment Due to Earthquakes

Slumping (Type 3 in Sect. 14.1) is another important kind of failure of an embankment. The 1983 Nihonkai-Chubu earthquake caused liquefaction in subsoil under Gomyoko Bridge (五明光橋) site on the western side of Hachiro-gata (八郎潟) Lake. Figure 14.11 shows that slumping of the fill resting upon soft lake deposit produced many cracks at the surface pavement. These longitudinal cracks suggest that the fill spread laterally. Figure 14.12 demonstrates an example failure of a road embankment at Chiebunnai Bridge (智恵文内橋) during the 1994 Hokkaido-Toho-Oki earthquake. This fill was constructed on a deposit of a small stream. Thus, an embankment resting upon soft soil deposit is vulnerable to earthquake-induced failure.



**Fig. 14.11** Slump failure of road embankment due to subsoil liquefaction (Akita Sakigake Newspaper)



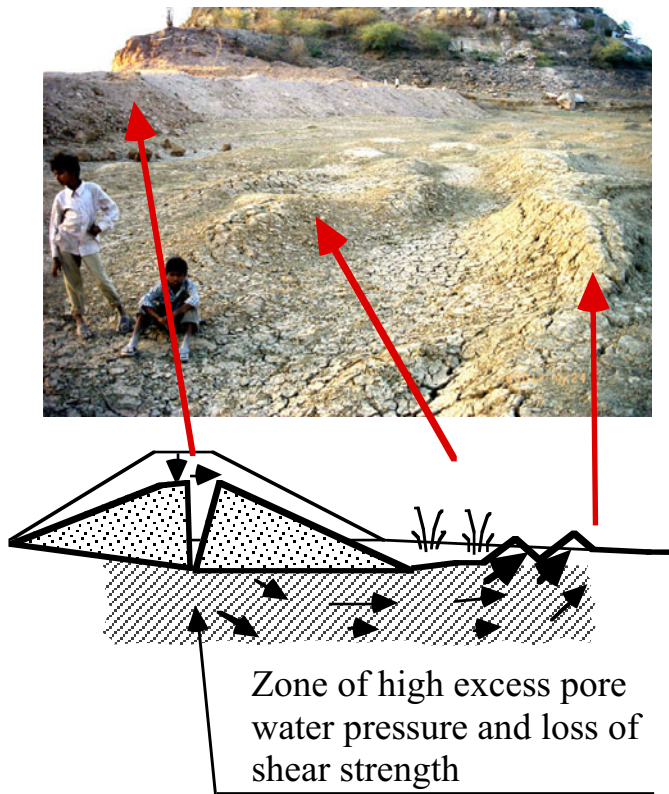
**Fig. 14.12** Failure of road embankment at Chiebunnai Bridge in 1994



**Fig. 14.13** Damaged shape of Tokachi riverdike in 1993 (Ministry of Construction)



**Fig. 14.14** Cracks at the top of Nagara River dike caused by 1891 Nobi earthquake (Photo supplied by Ministry of Construciton)



**Fig. 14.15** Ground distortion in soft foundation of Chan Dam (2001 Gujarat earthquake in India; Towhata et al., 2002)



**Fig. 14.16** Bridge out of service due to subsidence of approach embankment (Minami Yamabe Bridge of Ojiya City, 2004 Niigata-Chuetsu earthquake)

Figure 14.13 illustrates a damaged shape of the Tokachi river dike (十勝川堤防) during the 1993 Kushiro-Oki earthquake. Note that the center of the dike subsided more than the lateral slopes. Since an evidence of liquefaction (sand boil) was found here although the foundation soil was unliquefiable peat, the source of liquefaction was discussed. Sasaki (1998) stated that the original sandy body of the dike subsided into peat, expanded in its volume (loosening) and became liquefiable. For more details, refer to Sect. 17.4. Since this site took five months to repair, the conventional philosophy of quick repair before flooding comes did not function. Hence, a need of seismic resistance of important river dikes was recognized for the first time. Figure 14.14 shows a classical record of Nagara River dike which was destroyed by the 1891 Nobi earthquake. The longitudinal cracks suggest the tensile deformation of the dike in the lateral direction (Type 3 in Fig. 14.1). See in this figure the falling of railway bridge (Kansai Line) as well. It is very important that the stability of foundation soil significantly affects the stability of an overlying embankment. Figure 14.15 illustrates a case of Chan Dam in Gujarat Province of India which was destroyed by an earthquake in 2001. Although the dam body was compacted in accordance with the regulation, not much attention was paid to the natural deposit under the dam body. The subsoil liquefied when earthquake occurred, and its large distortion destroyed the dam body. It is interesting that the heaving at the end of the distortion zone was visible at the time of the author's site visit.

Densification of road embankment due to strong shaking results in subsidence. If this occurs near an abutment of a bridge, the road transportation is stopped (Fig. 14.16) and even an emergency traffic is prevented. Thus, although the main body of a bridge is of good seismic design, its function is stopped by the soil part.

### 14.4 Statistics on Types of Subsidence of Embankment Due to Earthquakes

The JSCE committee on earthquake engineering studied 47 cases of earthquake-induced distortion of fills. The number of cases belonging to each of four mechanisms as stated in Sect 14.1 is shown below:

5 cases of type 1, 23 cases of type 2, 12 cases of type 3, and 7 cases of type 4.

Although the cases were chosen in an as-random-as-possible way, the failure type 2 (development of a slip plane inside a fill) is the majority. It was reported further that all the failures of type 3 (slumping) were associated with development of high excess pore water pressure either in the fill body or in the foundation.

Figure 14.17 illustrates the ratio of subsidence/height in each case. It is shown therein that Type 2 (slip plane) and Type 3 (slumping) can generate larger subsidence/height ratio than other types. It is interesting that the maximum subsidence / height ratio is less than 0.7 which is consistent with the finding from river dike damage (Fig. 17.36).

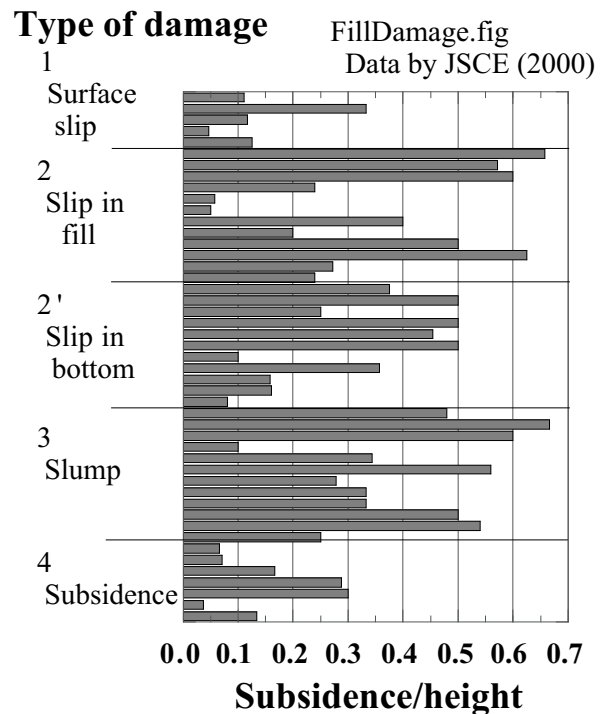


Fig. 14.17 Subsidence/height ratio of damaged fills (JSCE, 2000)

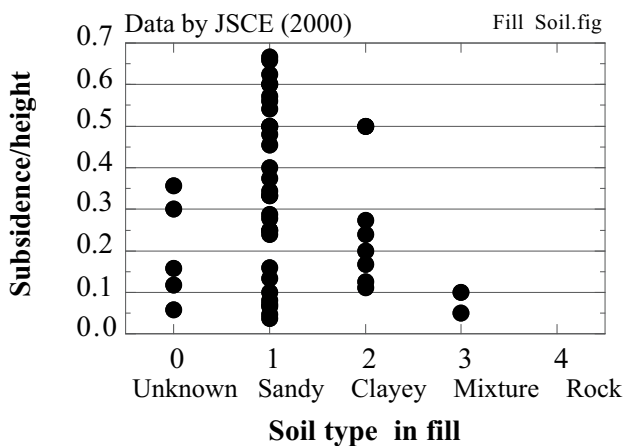


Fig. 14.18 Effects of soil type in embankment on extent of subsidence (JSCE, 2000)

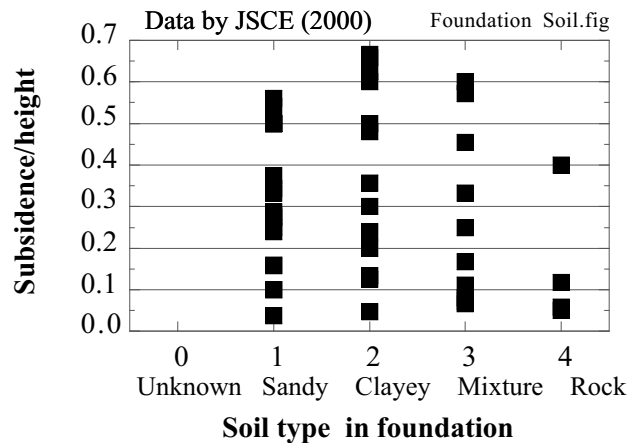


Fig. 14.19 Effects of soil type in foundation on extent of subsidence (JSCE, 2000)

Figure 14.18 illustrates the magnitude of subsidence (subsidence/height ratio) changing with the type of soil in the embankment. It is found that sandy fill material can induce significant subsidence. Furthermore, Fig. 14.19 examines the effects of soil type in foundation on the extent of subsidence. Again, sandy foundation can cause large subsidence. These findings are probably related to excess pore water pressure development and consequent liquefaction either in fill or in foundation. It is important in Fig. 14.19 that clayey (or peaty) foundation soil might generate significant subsidence as well.

## 14.5 Performance-Based Seismic Design

The conventional principle in seismic design of geotechnical structures has been based on the allowable stress concept. Therein the factor of safety,  $F_s$ , is calculated by

$$F_s = \frac{\text{Resistance}}{\text{Static Load} + \text{Seismic Load}} \quad (14.1)$$

and should be greater than unity. The seismic load in (14.1) is related to the expected intensity of earthquake. Figure 14.20 illustrates the variation of maximum acceleration which has been recorded during earthquakes. It is noteworthy that the intensity of acceleration increased suddenly after 1990. For examples, see the 1993 Kushiro record in Fig. 6.23 and the 1994 Tarzana record in Fig. 6.25. This situation led to the increased intensity of design earthquakes and the magnitude of seismic load in (14.1).

Figure 14.20 does not mean that the seismic activity of the earth planet changed after 1990. Actually, since earthquake observation network was installed in many countries, the probability of obtaining very strong motions increased.

One of the problems in geotechnical engineering caused by the increased seismic load is that it is hence difficult to maintain the factor of safety in (14.1) greater than unity. This is certainly because the shear resistance of soil is limited. Thus, an alternative idea is desired. Evidently, it is not good to replace all the earth structures by reinforced concrete.

Maximum acceleration (Gal)

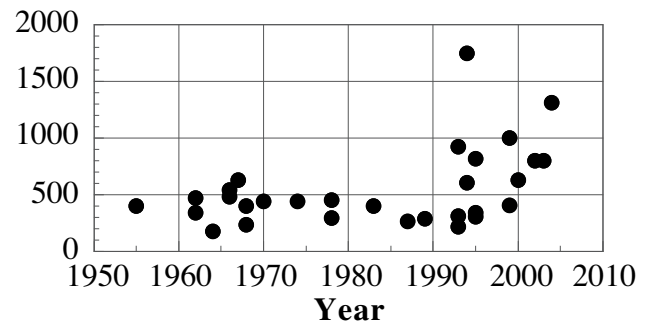


Fig. 14.20 Variation of maximum acceleration in recent earthquakes



Fig. 14.21 Total collapse of road bridge in Taiwan, 1999 (after 1999 ChiChi earthquake in Taiwan)



Fig. 14.22 Quick construction of temporary road embankment after collapse of bridge (1999, Taiwan)

It should be stressed that performance of geotechnical structures is different from those of steel and concrete structures. Even if the factor of safety is far less than unity, the situation may still be different from what is called total collapse. The most important feature is the quick restoration. A typical example was presented in the restoration of damaged dike in Taiwan (Fig. 14.3). Figure 14.21 illustrates a total collapse of an important bridge in Taiwan at the time of the 1999 ChiChi earthquake. When the author visited the site two weeks after the quake, a temporary road had already been constructed by earth fill (Fig. 14.22). Figure 14.23 manifests a similar example of river dike restoration after the 2003 Tokachi-oki earthquake.



**Fig. 14.23** Quick restoration in dike of Ushishubetsu River in Hokkaido



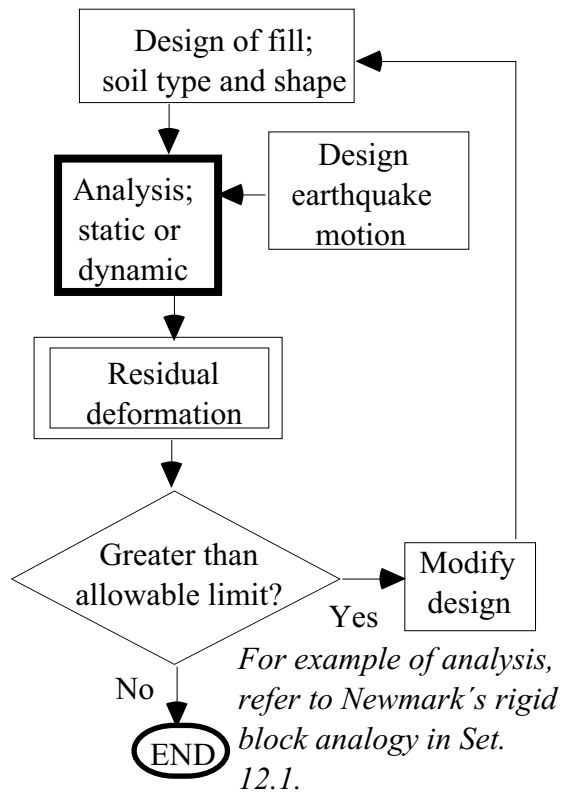
**Fig. 14.24** Significant subsidence of road embankment resting on small valley topography caused by 2004 Niigata-Chuetsu earthquake



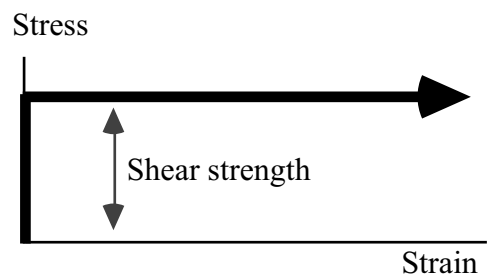
**Fig. 14.25** Quick construction of temporary road next to the site of Fig.14.24

Quick restoration and construction are important and unique feature of geotechnical structures. The total collapse of a road embankment in Fig. 14.24 appears to be too significant to be allowed. The seismic stability of this part of road embankment was bad because it was placed many decades ago on soft valley deposits. From the viewpoint of oil pipeline and communication lifelines which were embedded in this embankment, this collapse was certainly not allowable. From the viewpoint of road, in contrast, this case may still be allowable. Fig. 14.25 shows the reason; a detour road was constructed next to this collapsed fill within a few days after the quake. Hence, the road traffic was not stopped for many days.

The future principle in seismic design will allow the factor of safety to be less than unity and maintain the residual deformation within an allowable extent (Fig. 14.26). Since the seismic load is not of a static nature as (14.1) hypothesizes, its effect lasts for a short time (Sect. 5.12), and does not cause an infinite magnitude of deformation even if the factor of safety is less than unity.



**Fig. 14.26** Flow of seismic design based on allowable deformation



**Fig. 14.27** Rigid perfectly plastic model of soil

The performance-based design evaluates the residual deformation/displacement of an earth structure undergoing a design earthquake motion. Thereinafter, the calculated residual deformation/displacement at the end of the earthquake is compared with a prescribed allowable value. If the calculated value is greater than the allowable limit, the original design has to be modified. Figure 14.24 illustrates a conceptual flow of this principle. This new principle and the conventional one based on the static seismic coefficient and the factor of safety are compared in Table 14.1.

In spite of the simple idea as above, the new design principle is not yet fully in practice because of the following reasons:

1. Prediction of residual deformation which remains after earthquake is not easy. It is difficult even with an advanced nonlinear finite element analysis. For most of earth structures, an advanced elastoplastic analysis is not feasible because ordinary earth structures do not afford expensive insitu investigations and laboratory tests. Soil parameters have to be determined only by SPT- $N$ , cone penetration, and likes.
2. In this respect, the Newmark's rigid block analogy (Sect. 12.1; Newmark, 1965) is one of the good choices because it assumes a very simple, rigid, perfectly plastic constitutive relationship (Fig. 14.27). It should be borne in mind, however, that the determination of appropriate strength parameters (drained, undrained, static, or dynamic) is still disputable. Furthermore, the Newmark method is not appropriate when deformation of soil is less than failure strain because the method assumes the development of failure mechanism (rigid and perfectly plastic behavior). Liquefaction-induced large deformation is out of scope as well, because liquefaction-induced displacement is a consequence of large strain in place of shear failure mechanism (slip plane) as Newmark assumed.
3. There is not a clear idea on how to determine the allowable deformation. From the viewpoint of limit state design, it is not evident what kind of limit state is appropriate for geotechnical earthquake design; serviceability, restoration, or ultimate failure. If somebody says that 50 cm is the allowable limit, what about 55cm? What is the reason to insist on 50 cm? Most probably, the allowable limit is related to risk to human life, damage cost, pause period of expected service, influence to region/nation, time for restoration, and others. It is important to take into account the situations in Figs. 14.22, 14.23, and 14.25.

**Table 14.1** Features of seismic design principle based on allowable deformation

	New design principle based on allowable deformation	Conventional principle based on factor of safety
Input earthquake effects	Time history of acceleration	Static inertia force
Nature of soil	Rigid perfectly plastic (Fig. 14.24) or nonlinear stress-strain model	Rigid perfectly plastic
Method of calculation	Dynamic analysis to solve equation of motion	Static calculation on limit equilibrium
Criteria of design	Residual deformation < Allowable limit	Seismic factor of safety >1.0 (maybe >1.05?)

### 14.6 Inquiry on Allowable Seismic Displacement

Since there are many uncertainties in determination of allowable limit of seismic residual deformation and/or displacement, inquiries were made by JSCE (2000) to engineers and officers who were involved in restoration of damaged geotechnical structures after major earthquakes in 1990s (earthquakes in Hokkaido and Kobe). The author was a chairman of a committee in charge of this study (Towhata, 2005).

The inquired people were involved in restoration in such manners as taking the initiative of reconstruction at sites, design of reconstructed structures, administration, and others; see Fig. 14.28. It was expected that the difficult experiences gave people reasonable ideas about the extent of allowable displacement. Note that their answers are personal and do not represent any official view of their institutes and/or companies. On the contrary, those who simply use the facilities (e.g., passengers of trains) were not included because they often demand too much safety. Moreover, the concerned structures include harbor quay walls, river dikes, irrigation dams, roads, and embedded lifelines.

The first question addressed the key issue in determination of allowable displacement. As shown in Table 14.2, human life was chosen as the absolutely most important issue. This issue, however, was eliminated from further discussion because seismic failure of geotechnical structures does not affect human life significantly; most victims are killed by collapse of houses or failure of natural slopes. Among the remaining choices of negative effects to the public (社会的迷惑), difficulty in restoration, and cost of restoration, 12 out of 14 answers chose the negative effects as the second important issue (Table 14.2). Thus, the following discussion will focus on measures to reduce the negative effects. Being contrary to the initial expectation, the restoration cost was not chosen probably because the inquired people belonged to public sectors.

The next question was asked to whether or not the people allow the geotechnical damage that they experienced. Figure 14.29 plots the observed displacement values by using two different symbols depending on whether the displacement is allowed or not. Here, “to allow” means to consider the results of the quake as what should be restored without need for seismic reinforcement. Conversely, “not to allow” means that measures should have been taken in order to mitigate the damage prior to the quake.

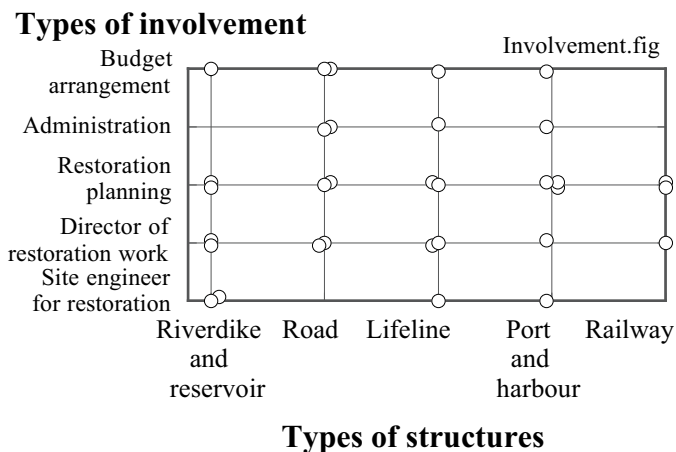


Fig. 14.28 Types of involvement of inquired people

Table 14.2 Factors that affect the allowable displacement

Importance	Factors			
	Human life	Negative effects to public	Difficulty in restoration	Cost of restoration
1	14	3	0	1
2	1	12	0	1
3	1	0	4	7
4	0	0	7	5

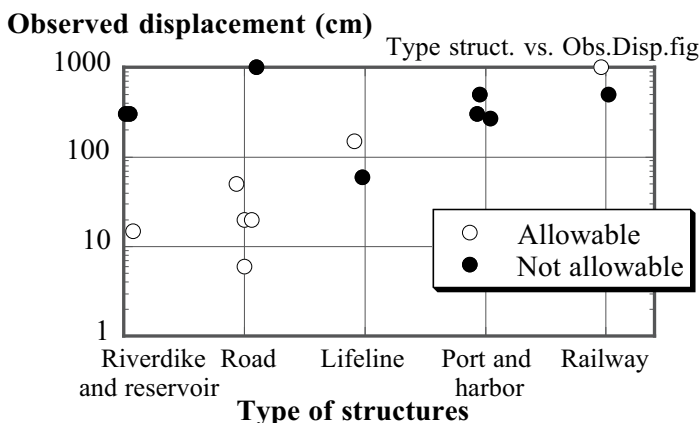
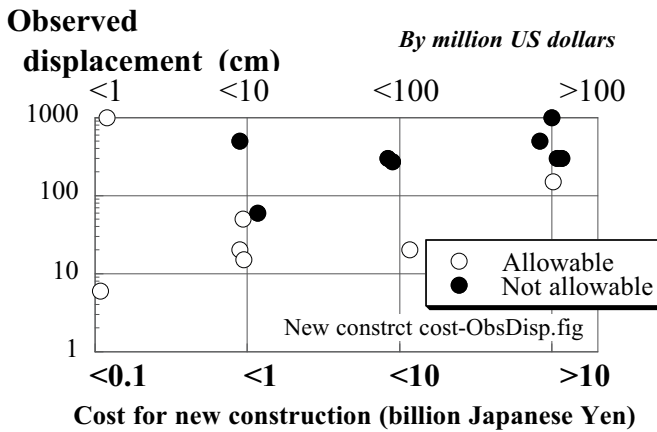


Fig. 14.29 Relationship between magnitude of displacement and people’s attitude

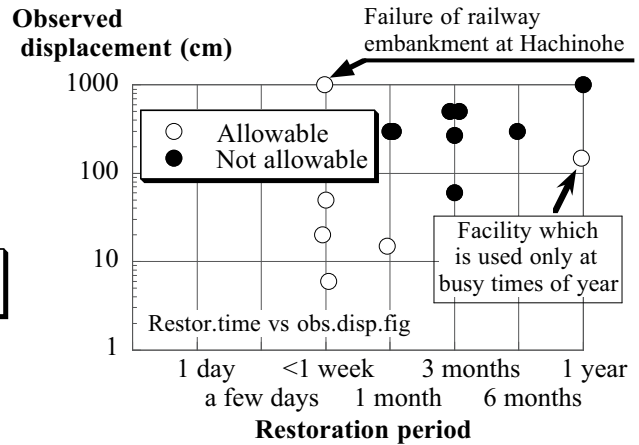


Moreover, the displacement in this section is the biggest one in each structure whether it is vertical or horizontal. Figure 14.29 gives a simple idea that displacement greater than 200 cm is not allowed, although the 1000-cm displacement of a railway embankment was considered allowable.

Costs for restoration and reconstruction do not affect the idea on allowability as shown in Fig. 14.30. This is consistent with the opinions shown in Table 14.2.



**Fig. 14.30** Relationship between observed displacement and cost for restoration

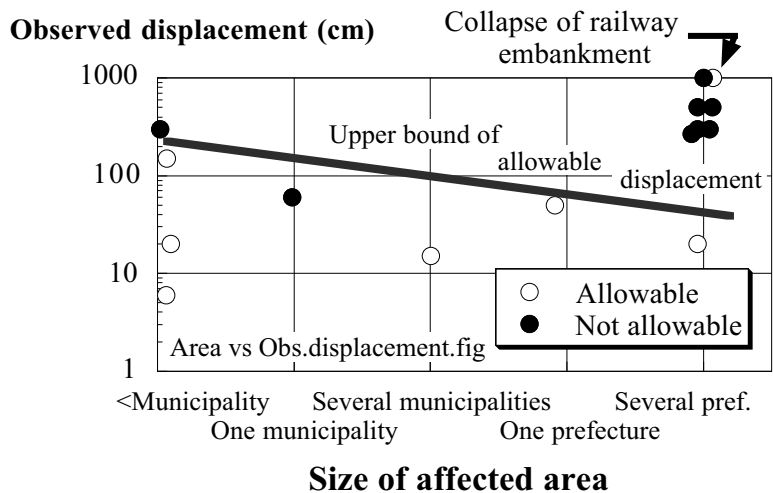


**Fig. 14.31** Relationship between observed displacement and time needed for restoration

Since the negative effects to the public is a very important issue, efforts were made to understand the details. First, it is easy to understand that railway customers are in trouble if train service stops for a long time. In this regard, the time needed for restoration was studied. Figure 14.31 illustrates that the restoration period longer than one month is taken seriously. People on the contrary allow period without service until one month after big earthquakes.

The second component of the negative effects to the public lies in the size of the affected public. The effects to the whole nation are certainly more significant than those to a small village. In this regard, the present study inquired people about “the size of the affected area” as the simplest parameter that was easy to answer, although the size of the affected population or the size of the affected economy are more suitable for further studies. To make the answering even easier, the inquired people were

requested to answer in terms of the municipal units. In Fig. 14.32, one municipality stands for a city, for example, with a population of tens of thousand to a few million. As for the prefecture, it is a good instruction to state that Japan has 47 prefectures in total. It appears reasonable to state that less extent of displacement is allowed when the affected area is greater.



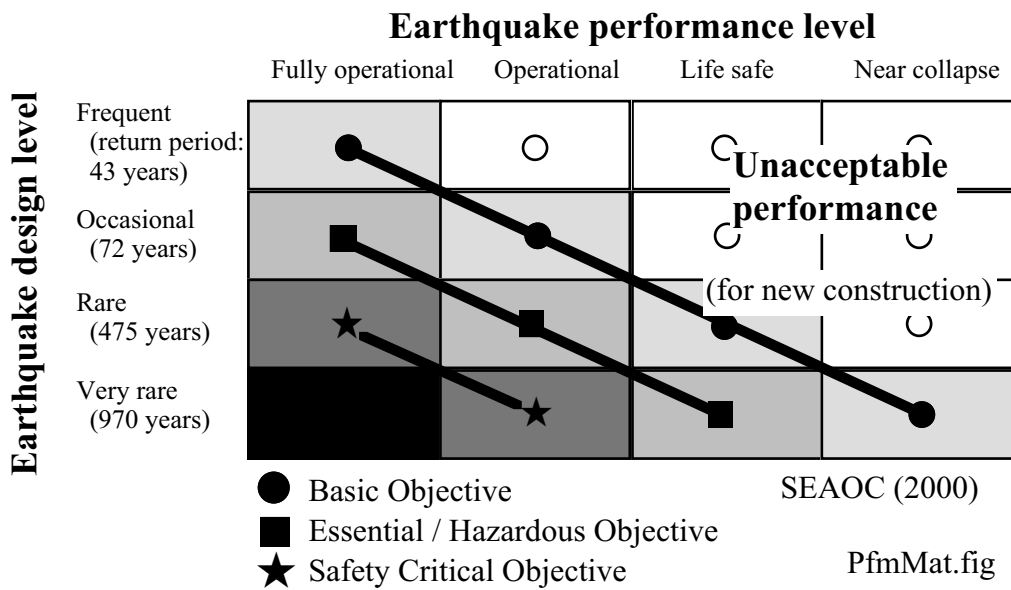
**Fig. 14.32** Relationship between size of affected area and observed displacement

In summary, experienced engineers and officers wish to mitigate the negative effects to the public and the negative effects consist of two factors that are the time without service (restoration time) and the size of the affected public.

14.7 Principle of Performance-Based Seismic Design and Life Cycle Cost

Experiences of strong acceleration, typically greater than 700 Gal, during the earthquakes in 1990s urged the seismic coefficients in conventional seismic design principle to be raised substantially. Consequently, design procedure found that soil cannot resist the increased seismic inertia force as specified by the revised design requirement. This is the reason why a displacement-based design principle is desired, which allows a conventional factor of safety less than unity. It is therein desired that the consequence of seismic factor of safety which is less than unity still remains within an allowable extent. The allowable extent varies with different seismic performance requirements. Since the design relies on the earthquake-induced displacement/ deformation which is a seismic performance of a structure, the design procedure is called performance-based design.

Table 14.3 Example of performance matrix (redrawn after SEAOC, 2000)



A similar approach has been investigated widely in other fields of earthquake engineering. An example of *performance matrix* is shown in Table 14.3 where the consequence of earthquake response in a building is classified into four performance levels, and this level varies with the importance of structure (basic, essential/hazardous, and safety critical) and the intensity or rareness of design earthquake. Even in the worst case, it is required that a total collapse which would claim many casualties should be avoided. Each performance in the table may be related to different kinds of limit states (serviceability, restorability, and ultimate state) in design principles.

The recent discussion on performance-based seismic design takes into consideration the universal idea in Table 14.3. What is special in geotechnical engineering is (1) the extent of allowable damage is evaluated by the magnitude of *allowable displacement*, and (2) the importance of structure is represented by the size of affected area combined with time accepted for restoration (Sect. 14.6). These ideas account for the engineer’s opinion obtained by the aforementioned inquiry.

The results of inquiries in Sect. 14.6 are further introduced in what follows. Discussion here is focused on the allowable displacement in place of the observed (real) displacement in Sect. 14.6. Since the allowable displacement is the one in the mind of those who had difficult times in restoration after big earthquakes, there is a reasonable thinking behind.

First, Fig. 14.33 shows the relationship between the allowable restoration time and the allowable displacement. When those people allowed longer restoration time probably due to very strong shaking or reduced importance, the greater residual displacement is allowed. Second, the upper bound in Fig. 14.34 illustrates that the allowable restoration time becomes shorter when the affected area (affected population

and economy) becomes larger. This certainly implies that important structures have to be restored more quickly. Further note in these figures that the idea of allowable displacement is significantly variable, suggesting that direct decision on the magnitude of allowable displacement is not an easy task; if 30 cm is allowed, why 35 cm is not allowed?

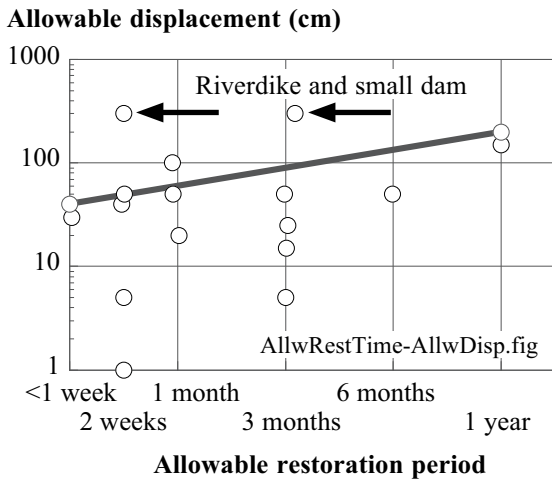


Fig. 14.33 Relationship between allowable restoration time and allowable displacement

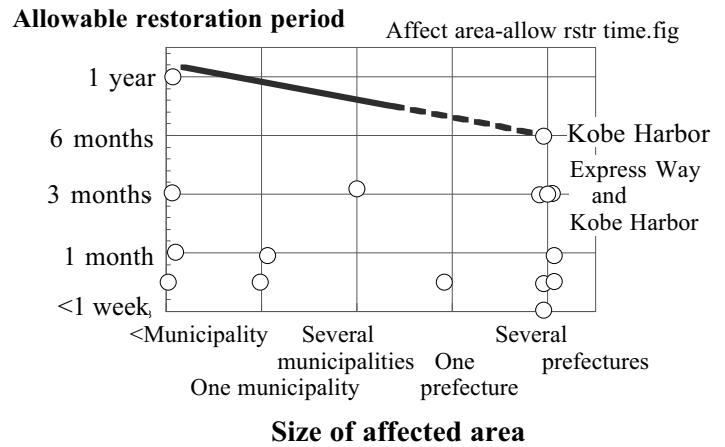


Fig. 14.34 Relationship between size of affected area and allowable restoration period

Table 14.4 Concept of matrix of allowable displacement

Importance of structures	Intensity of design earthquake	
	Strong	Rare and extremely strong
More	Not damaged	Restorable damage
Less	Restorable damage	Avoid collapse

It is aimed that the performance-based design principle for geotechnical structures under seismic effects follows the idea in Table 14.4 which is a revision of more universal Table 14.3. Emphasis is therein placed on importance of structure and time needed for restoration. Note that the negative effects to the public caused by seismic damage consist of the size of affected area and the duration of time without service; both are taken into account in Table 14.4 by “importance” and “restoration.”

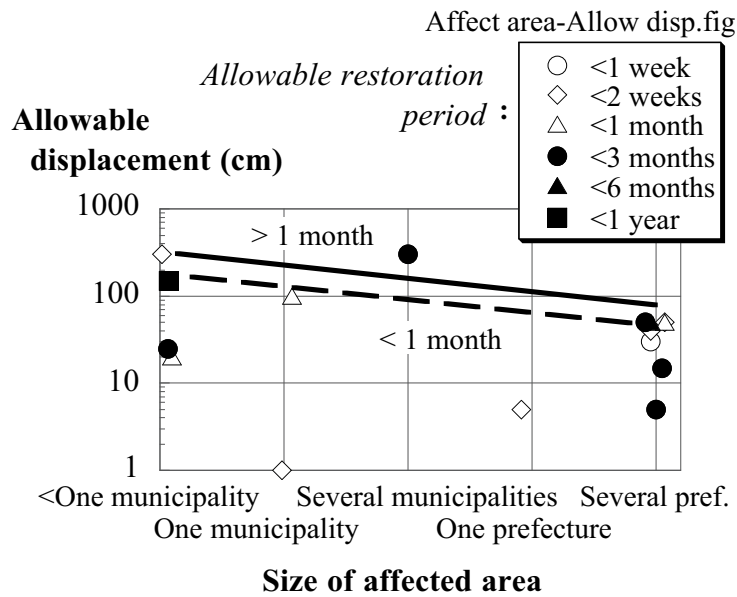
To make the idea more realistic, Fig. 14.35 summarizes the opinions in Figs. 14.33 and 14.34. It is therein proposed to first decide the size of the affected area. It is a single village if a small bridge is the target structure. Conversely, the whole nation is the affected area if a nation’s No.1 highway is the target. This decision seems easy. The second decision is then made of the allowable restoration time: only a few days or several months, etc. This decision is easier than that on allowable displacement. Based on these two decisions, the magnitude of the allowable displacement is determined by this figure.

According to Fig. 14.35, a structure which affects several prefectures is an important structure. Hence, smaller displacement is allowed. However, when a design earthquake is a very rare one whose recurrence period is hundreds of years, a longer restoration period should be allowed. Then the allowable displacement should be increased to some extent. Once the allowable displacement is thus determined, design and prediction of displacement are made. Thus there are three important components in performance-based seismic design of geotechnical structures which are

1. Determination of allowable displacement
2. Design and construction
3. Practical but reliable prediction of earthquake-induced displacement

Note that prediction has to be reasonably cheap and easy. Advanced numerical analysis is not appropriate for ordinary bridge abutment etc. It is evident that the reliability of prediction relies on the quality of soil investigation in which accuracy as well as detection of spatial variation of soil properties is important.

There have been several attempts to determine the allowable displacement. Their consequences are tabulated in Table 14.5.



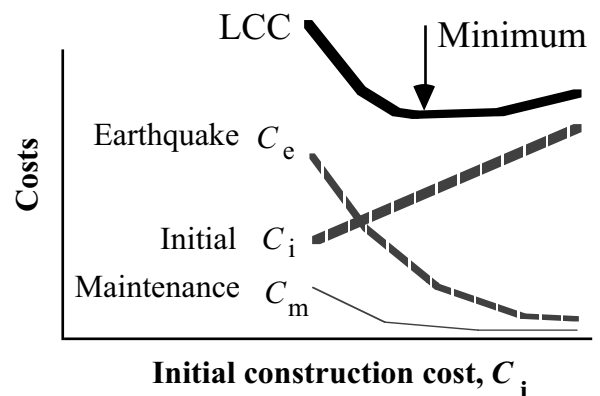
**Fig. 14.35** Relationship between allowable displacement and size of affected area in terms of allowable restoration time

**Table 14.5** Examples of allowable displacement of geotechnical structures in Japan

Railway	River dike
No damage : negligible displacement	Top and river side : displacement < 50 cm
Minor damage : subsidence < 20 cm	Super river dike (Fig. 7.13) with urban development: < 20 cm
Quick restoration : 20–50 cm	
Longer restoration : >50 cm	

The performance-based design principle will be extended in future to the idea of minimization of life cycle cost. The life cycle cost (*LCC*) of a geotechnical structure stands for the combination of the initial construction cost ( $C_i$ ), the maintenance cost ( $C_m$ ) during the service period (life cycle of  $N$  years) of a concerned structure, and the cost caused by a natural disaster ( $C_e$ ) such as an earthquake:

$$LCC = C_i + C_m + \sum_{k=1}^N P_k C_{e,k}, \quad (14.2)$$



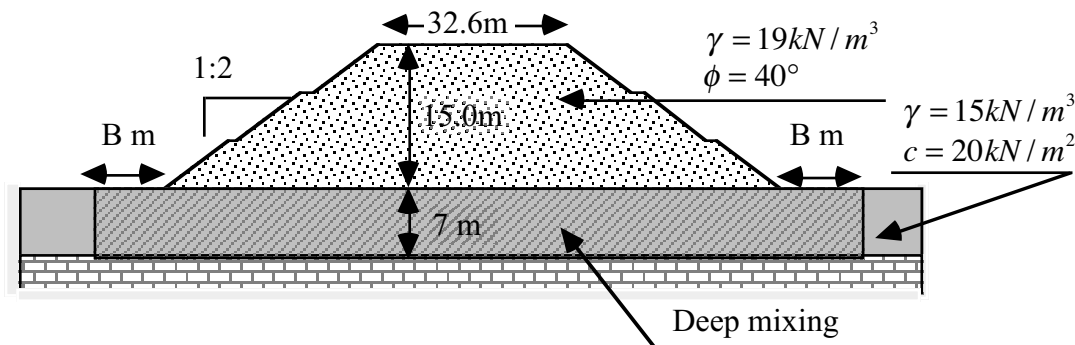
**Fig. 14.36** Conceptual illustration of minimization of life cycle cost (LCC)

in which the third term on the right-hand side calculates the earthquake damage cost for the  $k$ th year from  $k = 1$  to  $N$ . This cost is calculated by using the probability of damage,  $P_k$ , and the induced cost,  $C_{e,k}$ , in the respective year. It is expected that the initial construction at a reasonable cost (not too expensive but not too cheap) can keep the maintenance and disaster costs at reasonably low levels and the entire LCC would be minimized (optimization); see Fig. 14.36.

The problems to be overcome may be as follows:

1. For geotechnical structures, the length of life ( $N$  years) is not clear; river dikes of more than 1,000 years old are still used today.
2. Maintenance becomes necessary not only because of the quality deterioration of a constructed earth structure but also because of the underlying natural soil condition (consolidation).
3. Seismically induced cost consists of the direct cost (restoration) and the indirect cost (economic loss). The latter is particularly difficult to evaluate. For example, the entire economic loss due to a big earthquake can be evaluated, but how much of that loss is caused by a single particular failure of a highway embankment?

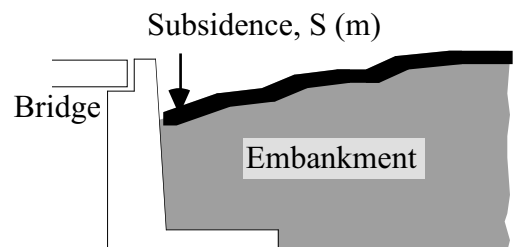
An example calculation of LCC was conducted on an expressway embankment (Ishihara et al. 2007). Figure 14.37 shows a cross section of an embankment studied which is underlain by very soft clay. It is possible upon a strong earthquake, therefore, that a shear failure mechanism is activated through the embankment and the soft subsoil, resulting in subsidence of the road pavement and cars may crash into it. Consequently, passengers in those cars are killed in such an accident. Moreover, the restoration of the expressway takes time, and the function of the expressway stops for a long time, thus causing economic loss in regional and even national economy. During the period of restoration, many vehicles come into local small roads and the number of traffic accidents may increase.



**Fig. 14.37** Cross section of expressway embankment with soft subsoil (Ishihara et al. 2007)

The present study employed deep mixing (mixing clay with cement; Sect. 26.13) of clay as a mitigation of soft clay. The size of deep mixing and the ratio of improved soil mass were variables. For definition of the size of deep mixing ( $B$ ), see Fig. 14.37 The types of cost which were included in the LCC calculation are as follows:

1. Initial construction cost in which the expense for deep mixing increases as the range and quality of soil improvement increase
2. Direct damage cost upon earthquake:
  - Restoration of embankment
  - Human life due to car crush into subsidence ( $S$  in Fig. 14.38)



**Fig. 14.38** Subsidence of road pavement as a cause of car crush

3. Indirect damage cost after earthquake;

- Elongated travel time (due to shifting from expressway to local roads)
- Missing toll fee income
- Increased traffic accidents in local roads
- Reduced air pollution along expressway (environmental issue)

By referring to many practices in both public and private sectors, the number of days needed for restoration was determined (Fig. 14.39). The restoration time is totally different for  $S$  greater than or smaller than 15 cm because of different types of restoration. On the basis of this  $S$ , the costs were determined as second-order functions of  $S$ . See Fig. 14.40 for details.

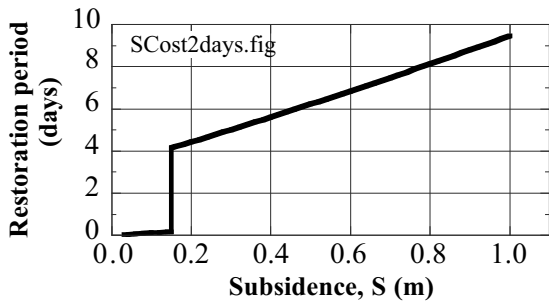


Fig. 14.39 Number of days for restoration



Fig. 14.41 Good condition of ancient irrigation dam in Sri Lanka

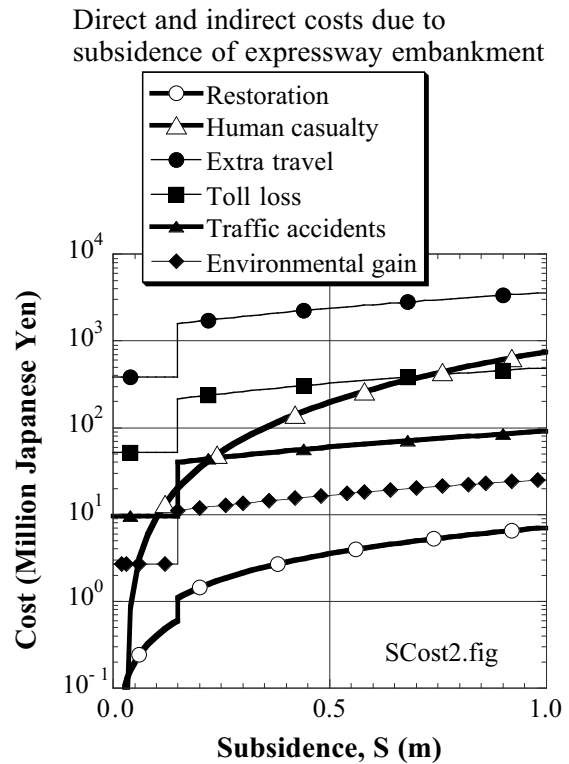


Fig. 14.40 Damage costs in express way as functions of subsidence

(a) Variation of LCC with extent of soil improvement

(b) Change of LCC with initial construction cost

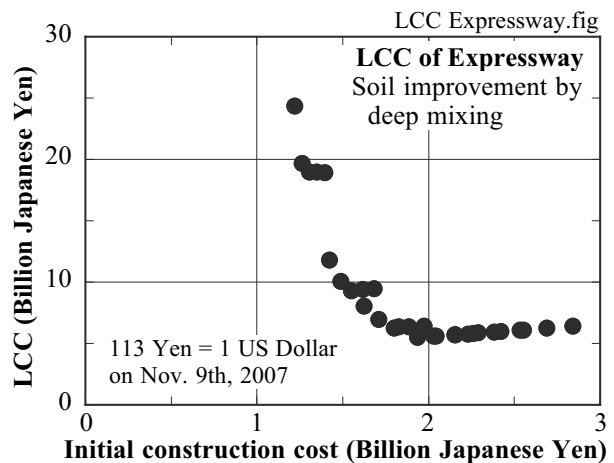
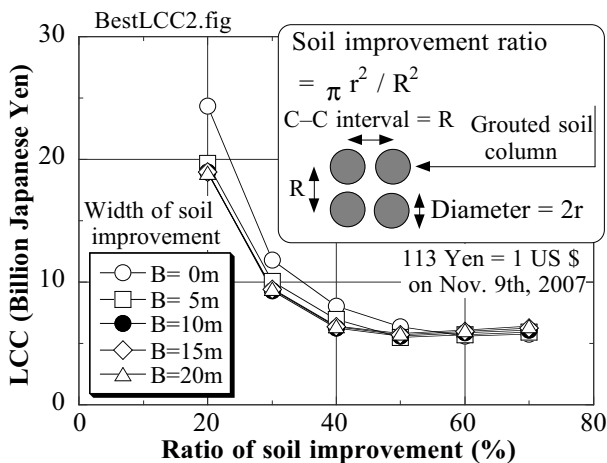


Fig. 14.42 Minimum LCC of expressway embankment

Note here that the aforementioned economic cost (negative effects to economic activity) is not considered explicitly here. This is because of an advice from a socioeconomic specialist that this cost is already and somehow taken into account by the missing toll fee cost. Although there may be different opinions on this issue, there is no unanimous idea at this moment.

Another point in the list of considered cost is that maintenance cost is not included. Although the authors expected that maintenance cost is reduced by a better construction effort, the reality was found different. Interviews with officers of government and other authorities revealed that maintenance of embankment consists mainly of regular cleaning and cutting grasses, which are not affected by the quality of construction. This implies that the maintenance cost is constant, independent of the construction cost. Hence, maintenance was removed from further study.

There are many uncertainties in geotechnical evaluation of LCC. Firstly, geotechnical materials do not decay with time in such a manner as steel and concrete. Therefore, it is difficult to define explicitly the life of a geotechnical structure. For example, there are many ancient earth dams (irrigation reservoirs) which are still in use (Fig. 14.41). After discussion, the life of geotechnical structures was set equal to 80 years, similar to practice in other types to structures. The second question concerned the cost of human life, which was an extremely difficult and sensitive issue. Certainly there are a wide range of opinions and practices in evaluation of human life in monetary units, namely missing income or annual economic products. It may be advisable to refer to travel insurance in which the loss of life due to accidents is evaluated in terms of money. In case of the author, the maximum insurance money is 100 million Japanese Yen in 2006.

**Table 14.6** Comparison of conventional seismic design and LCC-based design

	Conventional design	LCC design
Soil improvement	CDM	CDM
<i>B</i>	0 m	10 m
Ratio of improvement	30%	40%
Seismic safety factor	1.12	1.58
Probability of damage (subside. 0.15 m) / year	$5.02 \times 10^{-3}$	$2.30 \times 10^{-3}$
Initial construction cost	1.42	1.80
Seismic risk	10.36	4.47
LCC	11.78	6.27

Unit of cost : Billion Japanese Yen,  
113 Yen = 1 US \$ on Nov 9th, 2007

The intensity of future earthquakes were given in a probabilistic manner. Many earthquake records were put in an embankment model (Fig. 14.37) and the subsidence, *S*, was calculated by repeating the Newmark rigid block analogy (Sect. 12.1). Finally, the seismic costs were evaluated by substituting many *S* values in the empirical formulae (Fig. 14.40) in a probabilistic manner and added together. Thus, the conducted analysis was a Monte Carlo probabilistic simulation.

The variation of LCC with the quality of soil improvement is illustrated in Fig. 14.42. The better quality of deep mixing (grouting for solidification of soft soil, Sect. 26.13) increases the initial construction cost but reduces the subsidence (*S*) and the seismic cost. Consequently, the optimum (least) LCC was achieved by the *B* value of 10 m and the soil improvement ratio = 50%. Further efforts of soil improvement do not reduce LCC anymore.

Table 14.6 compares details of the road embankment designed either by a conventional approach (seismic factor of safety = 1.12) or the LCC approach (mean factor of safety = 1.58, but varying probabilistically). Although the latter requires more initial construction cost, the overall cost in its life cycle is smaller.

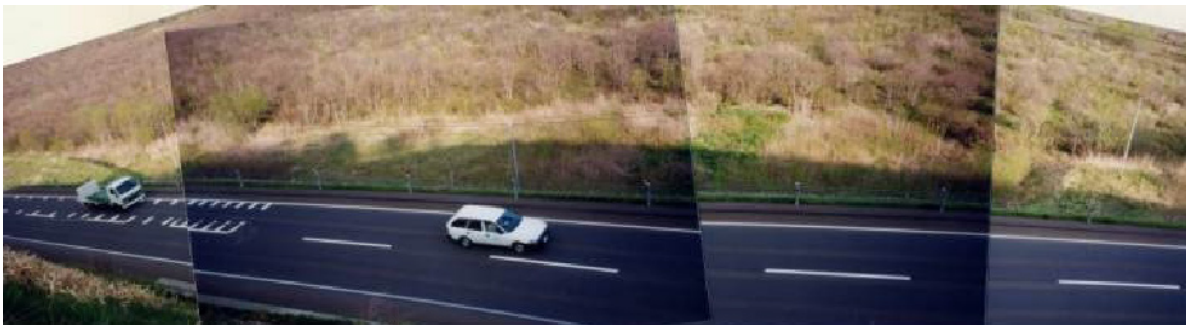
**14.8 Restoration of Damaged Fill Resting on Soft Soil**



**Fig. 14.43** Failed shape of Itoizawa road embankment in 1993



**Fig. 14.44** Small creek at the place of embankment failure (Photo taken by T. Honda in May, 2000)



**Fig. 14.45** Overall view of Itoizawa embankment in year 2000 (photo by T. Honda)

The 1993 Kushiro-Oki earthquake triggered a failure of an important road embankment at Itoizawa site (糸魚沢) between Akkeshi (厚岸) and Nemuro (根室) in Hokkaido. This road was situated along the foot of hills which faced a marsh (swamp) of soft stream deposit. Figure 14.43 indicates the failed shape of the road embankment. This failure occurred at a place where the road crossed the exit of a small stream into the marsh (Fig. 14.44). Thus, an embankment resting on soft soil collected much water from a valley behind and failed easily upon shaking. The slope stability of the embankment had been improved before the quake by placing berms (腹付け盛土 on left and right sides of Fig. 14.45) at the bottom of the fill. This was however insufficient on the embankment resting on softer subsoil.



**Fig. 14.46** Repaired toe of road embankment in Itoizawa (photo by T. Honda)

The damaged fill was restored by constructing reinforced earth fill (soil with geogrids, plastic sheets, geotextiles, etc) while installing more water drainage pipes and replacing the base soft soil by gravels. Gravel gabions were placed at the toe of the slope for better shear strength and drainage (Fig. 14.46).



Note that the slope toe is the place where stress concentrates and shear strain becomes greater than in other part of the fill. Together with the effects of drainage from inside the new embankment, consequently, no damage occurred here upon the 1994 Hokkaido-Toho-Oki earthquake.

In addition to reinforcement, the type of fill materials has to be considered. Asada (2005) compared SPT- $N$  values in residential fills which were affected during the 1978 Miyagiken-oki earthquake around Sendai City. While  $N$  values exhibit substantial variation within each site, the mean value in Fig. 14.47 clearly decreases with years after completion of filling. This infers that the filled geomaterials were affected by ground water and disintegrated with time (slaking of such materials as mudstone). This is in contrast with a common idea that soil increases its rigidity with time (ageing: Sect. 10.12).

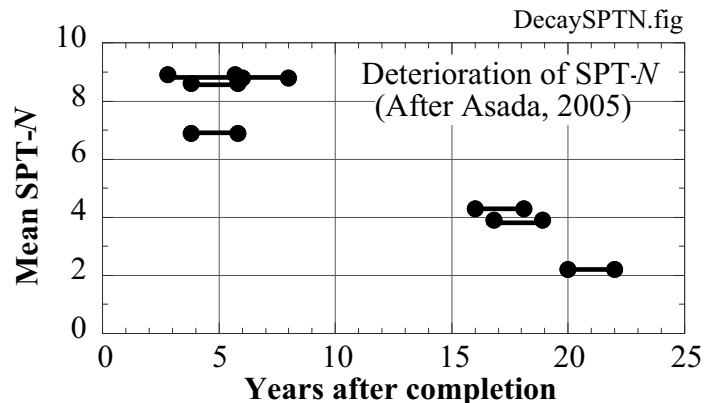


Fig. 14.47 Deterioration of fill material with time (after Asada, 2005)

#### List of References in Chapter 14

- Akita Sakigake Newspaper 秋田魁新報社 (1983) Record of M7.7 earthquake 秋田沖大地震M7.7恐怖の記録, p. 27 (in Japanese).
- Asada, A. (2005) Assessment of seismic risk in residential areas under future Miyagi-ken-Oki earthquake and its mitigation, Draft report, p. 112.
- Ishihara, Y., Yoshida, I., Suzuki, S., Okada, K. and Towhata, I. (2007) Evaluation of life cycle cost of express highway from viewpoint of seismic damage, Symposium on Prediction of Seismic Performance and Residual Deformation of Geotechnical Structures, July, Jpn. Geotech. Soc. (in Japanese).
- JSCE (2000) Research report on seismic design of earth structures undergoing strong earthquake motion, Research Committee on Earthquake Engineering, Jpn. Soc. Civil Eng., pp. 38–54 (in Japanese).
- JSCE (2000) Subcommittee activity on behavior of earth structures undergoing strong earthquake motion, Research Committee on Earthquake Engineering, Jpn. Soc. Civil Eng. (in Japanese).
- Newmark, N.M. (1965) Effects of earthquakes on dams and embankments, *Geotech.*, Vol. 5, No. 2, pp. 137-160.
- Sasaki, Y. (1998) Seismic damage to river dikes, Proc. Symp. Flow Failure and Permanent Displacement of Ground and Earth Structures Induced by Earthquakes, Jpn. Geotech. Soc., pp. 293–298.
- SEAOC: Structural Engineers Association of California (2000) Vision 2000, Performance based seismic engineering of buildings.
- Towhata, I. (2005) Development of Geotechnical Earthquake Engineering in Japan, Heritage Lecture, 16th Int. Conf. Soil Mech. Geotech. Eng., Osaka, Vol. 1, pp. 251–291.
- Towhata, I., Prasad, S.K., Honda, T. and Chandradhara, G.P. (2002) Geotechnical reconnaissance study on damage caused by 2001 Gujarat earthquake of India, *Soils Found.*, Vol. 42, No. 4, pp. 77–88.

# Chapter 15

## Landslides



Hawa Mahal in Jaipur, Rajasthan, India. This was a place for ladies of Maharaja's court to look at a parade in the street. This is a very thin building in contrast with its width as seen here.

## 15.1 Earthquake-Induced Landslides

Earthquake is one of the major causes of landslides. Keefer (1984) summarized past records to classify them and also to show the maximum distance to landslides for varying seismic magnitudes. He also showed that the minimum earthquake magnitude to cause landslides is  $M_L = 4.0$  according to US records. It seems, however, that this number depends on local geology as well as the annual rainfall.

Figure 15.1 shows an overall view of a large landslide which occurred near Galdian village during the 1990 Manjil earthquake ( $M = 7.3$ ) in Iran (Ishihara et al. 1992). The soil type in the slip plane was clayey as indicated by the exposed slip plane (Fig. 15.2). Some part of the sliding soil was mixed with water and formed a mud flow (Fig. 15.3). It is not uncommon that sliding mass is significantly fluidized and reaches an unexpectedly long distance.



**Fig. 15.1** Galdian landslide in Iran during the 1990 Manjil earthquake



**Fig. 15.2** Exposed slip plane in Galdian landslide



**Fig. 15.3** Deposit of fluidized material near landslide in Fig. 15.1



**Fig. 15.4** Seismic collapse of Mt. Ontake (photo by Prof. K. Ishihara)

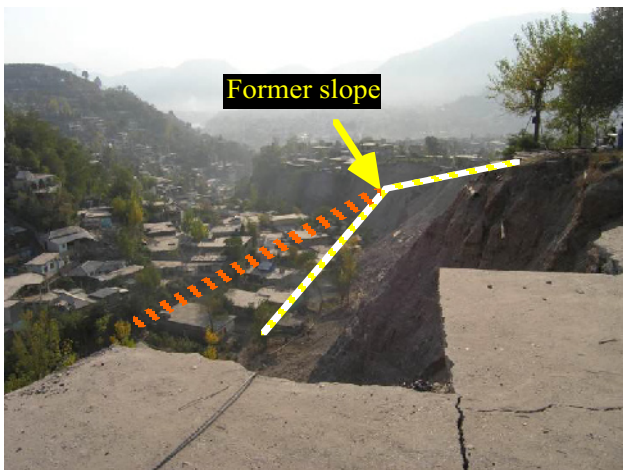
Figure 15.4 shows the collapse in a slope Mt. Ontake during the 1984 Nagano-ken Seibu earthquake. Being a volcano, the body of this mountain was made of debris with water. Thus, it collapsed easily upon shaking, got fluidized, and flowed downstream along a valley. Note further that volcanic slopes are subjected to nonseismic failures as well which are induced by slope steepening due to magma intrusion and hydrothermal excess pore water pressure caused by magma intrusion (Voight and Elsworth, 1997).

It is interesting that the risk of fluidization depends on moisture content of soil. Figure 15.5 indicates a slope failure in the town of Muzaffarabad which was triggered by an earthquake in 2005 that hit North

Kashmir of Pakistan. It is important that the soil of the collapsed slope did not travel laterally and many houses in the small valley were not affected by the soil flow. It seems that this fortunate situation was produced by the dry state of soil. Since the earthquake occurred in dry season (early October), there was not much water in the slope. There is water in subsoil, however, if water is supplied from leaking canal, pipeline, irrigation channel, or reservoir.

The 2005 earthquake in Pakistan showed several interesting features of seismic slope failure. Figure 15.6 demonstrates an example which occurred to the north of Muzaffarabad. The surface of limestone slope was significantly weathered due to temperature change and heavy sunshine, in particular, because of the lack of vegetation and repeated wetting and drying together with freezing in winter. The state of weathering is evidenced in detail by Fig. 15.7.

Failure of surface material may not be so significant in volume as those in Figs. 15.1 and 15.4. It is, however, able to stop local transportation if the fallen debris close a mountain road. Figure 15.6 is an example. The time needed to open the road again is shorter than the case of failure of road embankments (Figs. 14.12, 14.43 and 15.8), because removal of fallen debris is much easier than reconstruction of a fill. Modern construction of highway tries to make a short cut by crossing valleys by means of embankments and bridges. Consequently, a failure of embankment seriously affects the operation of transportation. Conversely, such roads located along slope surface are constructed by cutting slopes and are more stable during earthquakes, although such roads are curved and not good for high-speed transportation.



**Fig. 15.5** Collapse of dry slope in Muzaffarabad, Pakistan



**Fig. 15.6** Surface failure of weathered limestone slope near Muzaffarabad, Pakistan, in 2005



**Fig. 15.7** Weathered rock surface in Pakistan, 2005



**Fig. 15.8** Collapse of slope surface and road shoulder near Barakot of Pakistan

Ohya slide (大谷崩れ, Fig. 15.9) in Shizuoka Prefecture, Japan, is said to have been caused by the 1707 Hiei (宝永) gigantic earthquake. Since then, the destabilized slope (Fig. 15.10) has been producing debris flow at heavy rainfall frequently (Imaizumi et al. 2006). Consequently, the bed of the Abe River (安倍川) is filled with cobbles and stones, rising continuously due to sediments (Fig. 15.11). To mitigate this situation, many erosion control dams have been constructed (Fig. 15.12). However, the problem has not yet been solved. Effort is also made to plant trees in the unstable slope (Fig. 15.13). It is noteworthy that decreased discharge of sediment from rivers into the sea has recently resulted in erosion of beaches, making coastal structures less unstable than before. The same problem is found in downstream area of rivers as well where the foundation of bridges is scoured.



**Fig. 15.9** Ohya slide in Shizuoka



**Fig. 15.10** Unstable mountain slope



**Fig. 15.11** Valley of Abe River



**Fig. 15.12** Erosion control dams in Abe river channel



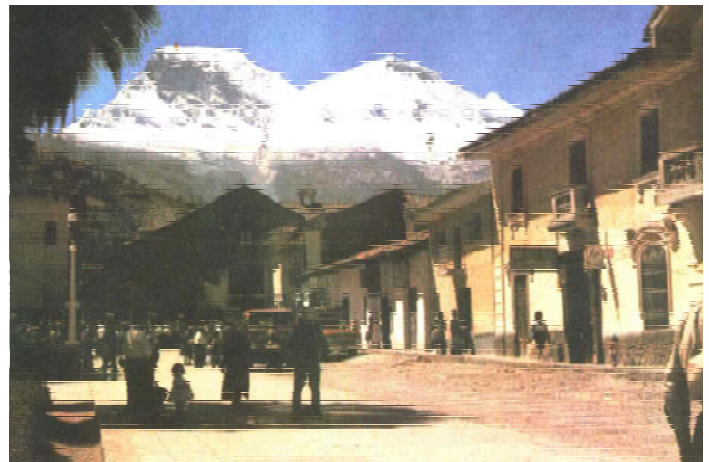
**Fig. 15.13** Tree planting in unstable Ohya slope

**15.2 Yungay City Destroyed by Earthquake-Induced Debris Flow**

An earthquake-induced collapse of Snowy Huascarán Mountain (Nevados Huascarán; Fig. 15.14) in Peru in 1970 was characterized by debris which was fluidized when the falling rock and ice were mixed with water and stream deposits. A debris flow thus developed flowed over a small hill and buried the whole city of Yungay, killing over 30,000 people. Figure 15.15 shows the city prior to the disaster; the hill and Mt. Huascarán are seen behind. This debris flow traveled hundreds of kilometers along the channel of Río Santa to finally reach the Pacific Ocean. The total volume of this debris avalanche is assessed to be 50 million m<sup>3</sup> (Plafker et al. 1971). The soil deposit at the ruins of Yungay includes much amount of fines (Fig. 15.16), suggesting that original rocky material was ground into small particles.



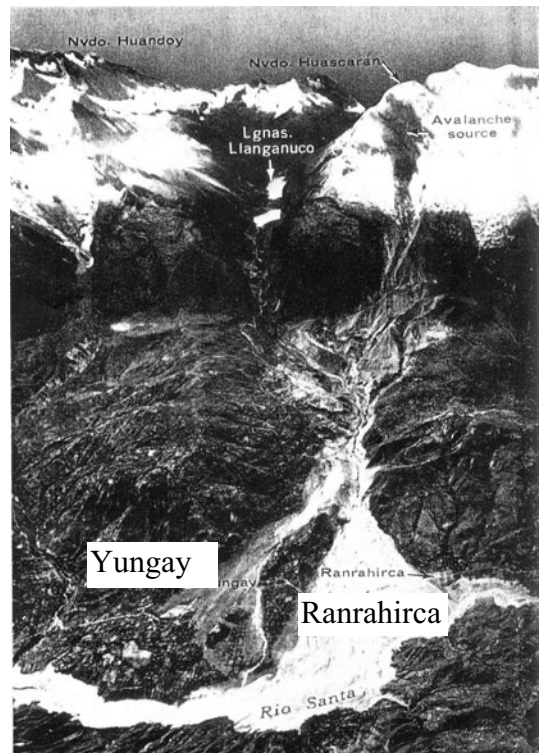
**Fig. 15.14** Slope of Huascarán Mountain (August, 1989)



**Fig. 15.15** Mt. Huascarán and Yungay City in July, 1965 (Hayakawa, 1967)



**Fig. 15.16** Soil at ruin of former Yungay City



**Fig. 15.17** Aerial view of Yungay-Ranrahirca area (Town names were added to original photograph by Plafker et al. 1971)

Figure 15.17 shows the aerial view of the concerned area. The town of Ranrahirca was attacked in 1960 by another flow, while Yungay was protected by a hill. This experience gave the Yungay residents a wrong idea that their town was well protected from such a geohazard. This idea did not work in 1970 when another flow had a greater size.

After this tragedy, the city of Yungay was reconstructed at a safer place. Relocation is the best solution for avoiding natural disasters. It has to be borne in mind, however, that relocated people have to survive by finding new source of income. It is not good that they have to rely on governmental aids forever. Farmers need new agricultural land and fishermen need to go to the sea. This requirement is not always satisfied in relocation programs. Figure 15.18 and 15.19 show a life-aid activity by NGO (Non Governmental Organization) for those who were evacuated from home villages after eruption of Pinatubo volcano and resultant lahar flow (flooding of rain water with volcanic ash deposit); Figs. 15.20 and 15.21 in the Philippines.



**Fig. 15.18** Production of hand crafts by Pinatubo refugee people



**Fig. 15.19** Aid for self support of Pinatubo refugee people



**Fig. 15.20** River bed filled with flooding of lahar from Pinatubo Volcano, the Philippines



**Fig. 15.21** Church which was 50% buried by lahar after Pinatubo eruption in the Philippines

### 15.3 Tsaoling Landslide in Taiwan

The 1999 ChiChi (集集) earthquake in Taiwan triggered many landslides in this geologically young island which was produced by tectonic interaction between Eurasia and Philippine sea plates. Being of the tertiary origin (新世代第三紀), the young rock of the island has not yet developed a stable geological structure. Moreover, the tectonic motion has distorted the rock significantly, developing fractured rock conditions. The high rate of rainfall and erosion have made steep mountain slopes which are prone to instability.



Fig. 15.22 Overall view of Tsaoling landslide



Fig. 15.23 Slip plane after the 1999 quake

Figure 15.22 illustrates the overall view of the Tsaoling (草嶺) slide which included the total volume of sliding mass greater than 100 million m<sup>3</sup>. Of 4 km in width, this amount of sliding mass appears to be one of the greatest seismically induced landslides in the twentieth century. Similar to other landslides during the same earthquake, the Tsaoling slide occurred in an interbedded slope of shale and mud stone. Figure 15.23 shows the slip plane which was seen after the quake (December, 1999). It is important that this slide had developed failure two times during the past earthquakes; the first one in 1862 and the second in 1941 (Fig. 15.24). Another big sliding occurred due to rainfall in

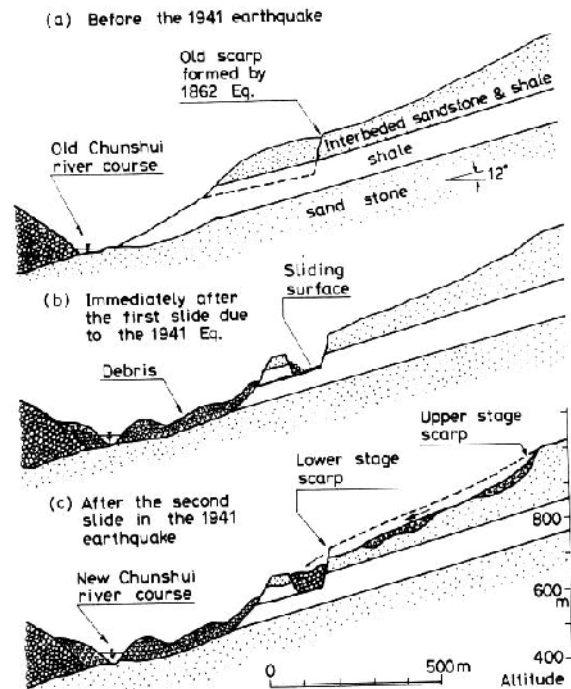


Fig. 15.24 Repeated instability of Tsaoling slope (Ishihara, 1985)



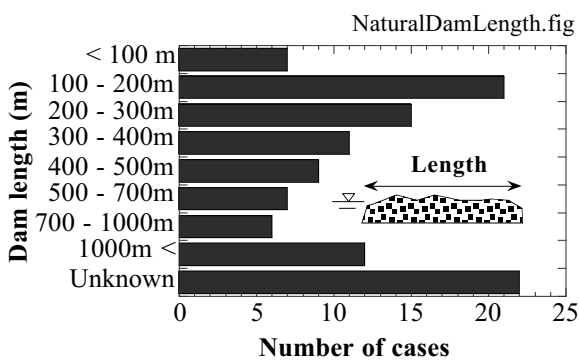
Fig. 15.25 Natural dam after 1999 event



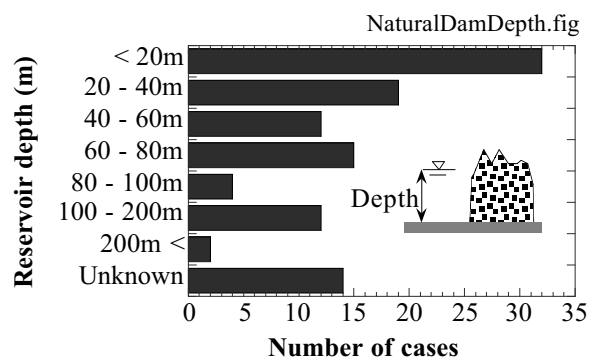
1942 and stopped the flow of river (Kawata, 1943). Being the biggest in the scale, the failure in 1999 was simply a failure of the remaining rock mass.

A big landslide often generates a natural dam. In 1999, the dam lake in Fig. 15.25 was produced. If the natural dam body is narrow, its erosion during high water level and a possible failure may lead to flooding and debris flow. Tabata et al. (2002) made a statistic analysis on landslide-induced natural dams in Japan. The size (length of dam in the direction of river channel) and depth information in Figs. 15.26 and 15.27 may be useful. Noteworthy is that most natural dams in the past failed due to overtopping of water, which led to erosion, and the number of failures due to piping of seepage water (seepage of water removing debris from the body of dam) is small (Fig. 15.28).

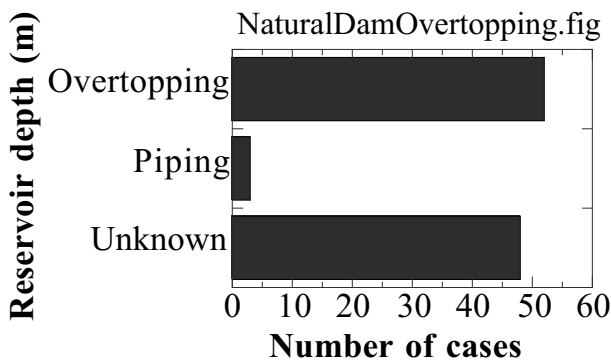
Figure 15.29 demonstrates a water channel which was excavated across a natural dam (Terano natural dam, 2004 Niigata-Chuetsu earthquake).



**Fig. 15.26** Statistics on length of natural dam in the direction of river channel (after Tabata et al. 2002)



**Fig. 15.27** Statistics on depth of reservoir dam produced by natural dam (after Tabata et al. 2002)



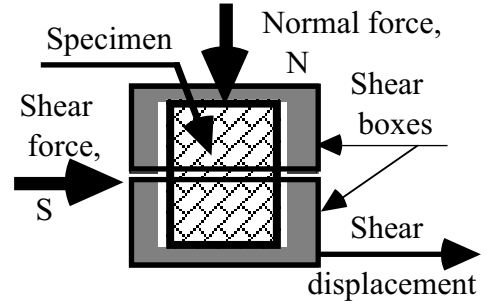
**Fig. 15.28** Statistics on cause of failure of natural dams (after Tabata et al. 2002)



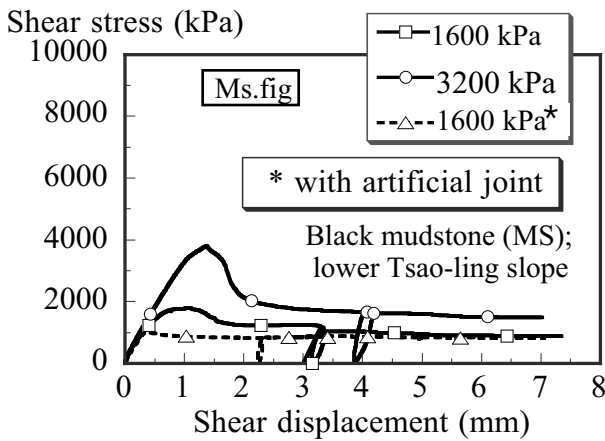
**Fig. 15.29** Water drainage channel in Terano natural dam in Niigata

**15.4 Shear Tests on Landslide Mechanism**

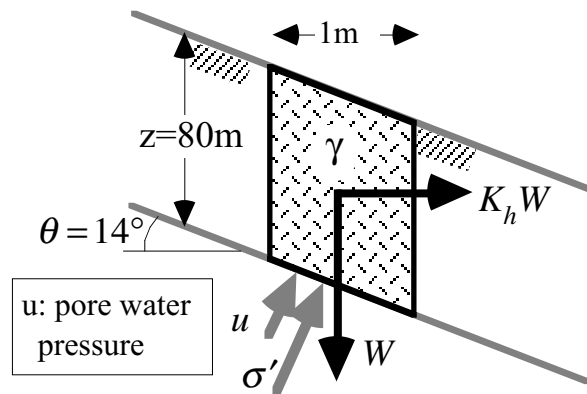
Sampling, laboratory shear tests, and stability analyses were performed to understand the Tsaoling landslide triggered by the 1999 Chi-Chi earthquake of Taiwan. Samples were collected from the slip plane (Fig. 15.23) and debris deposits. Figure 15.24 showed the stratification of local geology which is parallel to the slope. Attention was therefore focused on the possibility of a weak layer and a weak interface between two different rocks. The problem was that the slope had already collapsed, making sampling of weak intact materials impossible. It was decided consequently to collect samples from debris deposits of broken rocks as well as the remaining slickenside slip plane (Fig. 15.23). Shear tests were carried out at CRIEPI (Central Research Institute of Electric Power Industry) by using its direct shear device, see Fig. 15.30. When the lower shear box moves laterally, shear failure of a rock specimen occurred along a small spacing between two rigid boxes.



**Fig. 15.30** Illustration of direct shear test



**Fig. 15.31** Shear stress vs. shear displacement relationship of Tsaoling black mud stone



**Fig. 15.32** Idea of quasistatic stability analysis

Figure 15.31 presents the drained direct shear results of black mud stone specimens collected from the slip plane. Two intact specimens under different confining pressures developed peak strengths which were then followed by softening and a state of residual strength (constant stress level). Cracking and shear failure occurred at and after the peak strength. One cycle of unloading and reloading in the residual state did not develop a peak strength again because the specimen with cracks had already lost the peak strength. Effects of existing cracks were considered significant in the slope failure in 1999 because the earthquakes in 1862 and 1941 not only caused slope failure but also probably produced cracks in the remaining part which failed in 1999. In this respect, a third test was run by combining two separate rock specimens with a smooth interface in between. The dashed curve in Fig. 15.31 indicates that there is no peak strength and that the residual strength is more or less similar to that of an intact specimen under the same pressure of 1600 kPa. Thus, the residual strength stands for the strength of cracks and weak interfaces.

A pseudostatic stability analysis was conducted by using the idea of an infinite slope subjected to static lateral force (Fig. 15.32). The seismic coefficient,  $K_h = 0.305$ , was obtained by substituting  $A_{max} = 748 \text{ Gal}$  at a nearby CHY028 station (8 km from Tsaoling, Seismology Center of Central Weather Bureau) in an empirical formula (Sect. 12.3):

$$K_h = \sqrt[3]{A_{\max}/g/3}. \tag{15.1}$$

For the residual strength,  $c = 417 \text{ kPa}$  and  $\phi = 19.4^\circ$  were used. The derived safety factors were 1.01 for the peak strength and 0.73 for the residual strength.

A risk assessment of seismic slope failure requires evaluation of not only the factor of safety but also the travel distance of failed debris (Fig. 15.57). The latter issue certainly needs understanding of soil behavior in the course of rapid sliding movement. A unique idea on mechanism of long-traveling landslide was proposed by Sassa et al. (2004). This idea supposes that grains are crushed extensively in a thin layer (slip plane) during slope failure. Consequently, the granular structure of soil loses its capability to bear the overburden (loss of effective stress) and excess pore water pressure develops. This mechanism is called sliding surface liquefaction. This idea may also be applicable to a fault action if a fault is filled with soil.

The role of sliding surface liquefaction has been studied experimentally by using a ring shear device. This device houses a hollow cylindrical soil specimen within upper and lower containers and applies torsional shear load. Since the specimen has a cylindrical shape, there is no limitation in shear displacement (Fig. 15.33). This feature is suitable in experimental reproduction of sliding surface mechanism in which slip displacement may be as large as tens of meters or more. Note that this device can measure shear displacement of a ring but cannot determine shear strain because strain is concentrated (localized) within a narrow sliding surface.

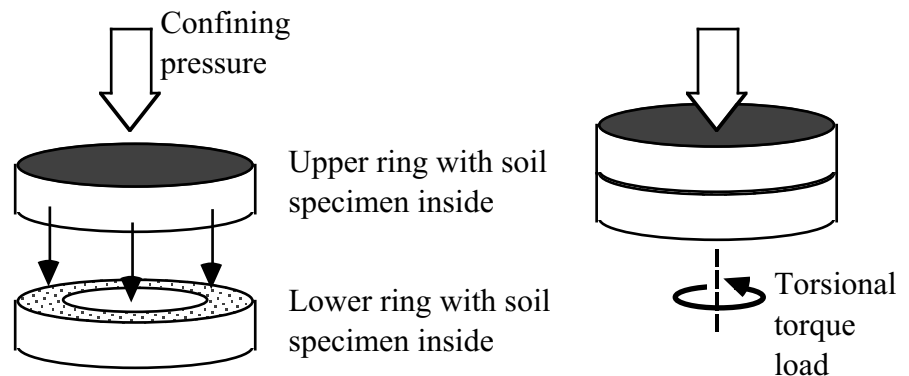


Fig. 15.33 Illustration of ring shear test

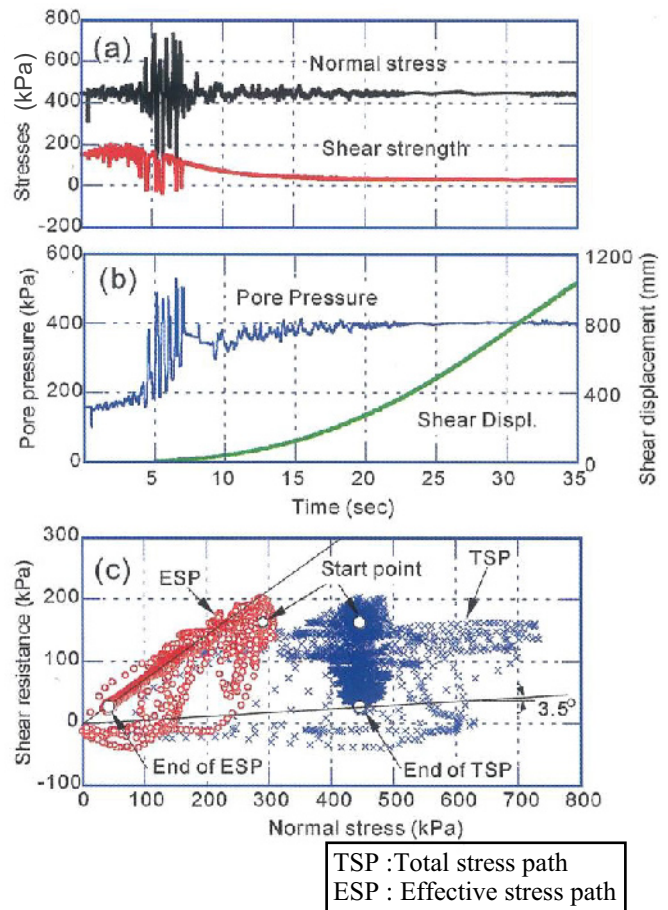


Fig. 15.34 Experimental reproduction of sliding surface liquefaction by means of ring shear device (after Sassa et al., 2004)

Figure 15.34 illustrates a typical test result in which the sliding displacement was induced in sand to be as large as 1,100 mm at a rate of about 50 mm/s. This rate corresponds to a real velocity of landslide mass. It is seen that cyclic loading of both shear and normal stresses increased the pore water pressure (Fig. 15.34b), and accordingly the shear strength decreased to a level of about 20 kPa (Fig. 15.34a). Since this strength was lower than the applied shear stress (vertical coordinate of Fig. 15.34c as well as the initial static shear stress of about 170 kPa), soil movement was accelerated and the displacement became as large as 1,100 mm. Note that

the effective stress path (red symbols in Fig. 15.34c) shows that the stress path reached the failure line. Therefore, the development of large displacement is understandable. Nigawa landslide which was triggered by the 1995 Kobe earthquake was studied by running a similar ring shear test (Sassa et al. 1996).

Crushing of sand grains was verified by observing the soil behavior through a transparent side wall. In Fig. 15.35a, individual grains were visible prior to shear. Once shear displacement started, the initial high effective stress (300 kPa) caused crushing and lots of sand powders emerged within the specimen (Fig. 15.35b).

(a) Prior to undrained shear



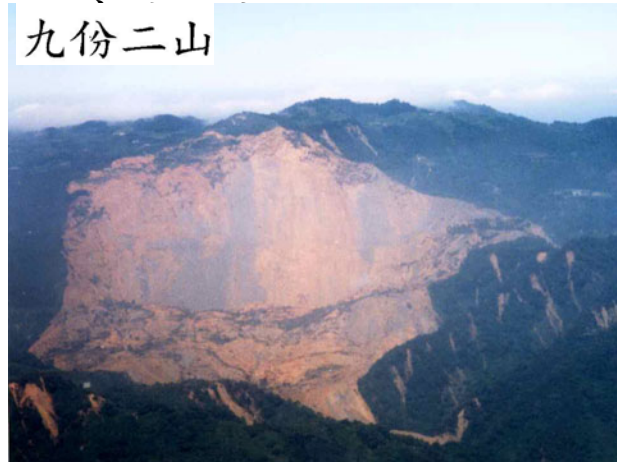
(b) After shear displacement of 30 m



**Fig. 15.35** Ring shear test with visual observation of grain behavior (Sassa et al., 2004)

### ☀ 15.5 Other Landslides Caused by Chichi Earthquake, Taiwan

Among many landslides in Taiwan, 1999, the second most gigantic one, second to the Tzaoling (Sect. 15.3), was the one at Jiu-Feng-Er-Shan. Its view from a helicopter is shown in Fig. 15.36. The exposed layer of gray color is probably made of shale stone which formed a slip plane (Fig. 15.37), similar to the slide at Tsaoling. Figure 15.38 shows a plantation of betel palm trees (檳榔樹) near the top of this slide. It is interesting that the tree and its root were separated from the ground, suggesting that the tree jumped out of the ground due to strong (but probably less than 980 Gal) vertical acceleration. Residents near the top of this slide say that they heard a roaring and explosive sounds during the slide. They also saw the sky had pink color during shaking in midnight.



**Fig. 15.36** Aerial view of Jiu-Feng-Er-Shan landslide



**Fig. 15.37** View of Jiu-Feng-Er-Shan landslide



**Fig. 15.38** Palm tree separated from ground



**Fig. 15.39** Appearance of 99 peaks after the quake (Sino Geotechnology Inc., 1999)

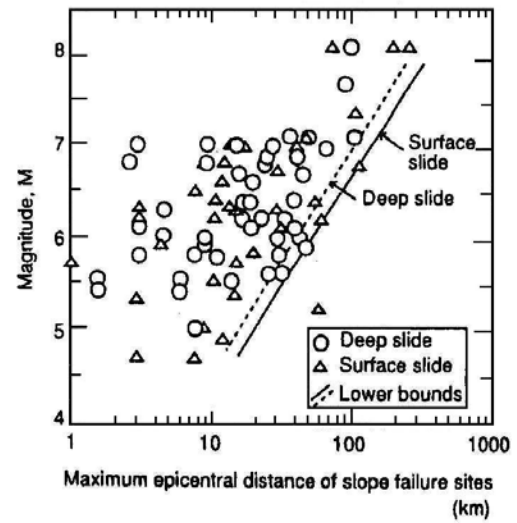


**Fig. 15.40** Gravelly material composing 99 peaks

Ninety-nine peaks (九九峰) developed many surface slides as well and lost vegetation (Fig. 15.39). This mountain was made of gravelly sand and was vulnerable to earthquake-induced falling down of the material. Figure 15.40 indicates the gravelly material at the top of one of the failed slope.

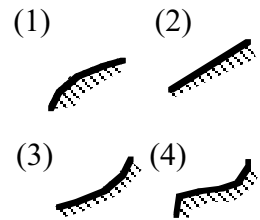
**15.6 Assessment of Seismic Landslide Hazard**

Seismic failure of natural slopes is a significant problem to human societies. It is therefore desired to inspect the stability of slopes near human habitations as much as possible. The stability analysis has to take into account the expected intensity of earthquake motion, topography of the studied slope, and material properties of the rock/soil. This process requires a time-consuming site investigation, and, therefore, it is costly and unlikely to be practiced everywhere. To avoid complexity, Fig. 15.41 shows relationship between the earthquake magnitude and the maximum epicentral distance of failed slopes during past earthquakes. Beyond this distance, slope failure is unlikely. Although significantly simplified, it can do some help to risk assessment.



**Fig. 15.41** Maximum possible epicentral distance to failed slopes during past earthquakes (Yasuda, 1993)

A slightly more detailed but time-consuming method has been proposed by the Kanagawa Prefectural Government (1986). This method counts points in accordance with site conditions, adds the points together, and assesses the magnitude of landslide risk of localities. Table 15.1 shows the counting of points, and Table 15.2 indicates the number of possible slope failures in a 500 m × 500 m square grid of localities. This type of work is called zoning and hazard assessment. The numbers in Table 15.1 were obtained by statistic analyses of past case studies. In particular, the small value of  $W_4$  for soil may appear strange because it implies that soft soil slopes is more stable than hard rock slopes. This strange situation is due to the fact that failure of soil slopes is rare during earthquakes; slopes of softer materials are already destroyed prior to earthquakes by heavy rainfall etc.



**Fig. 15.42** Vertical cross section of slopes

This method is useful in quick assessment of local/regional risk of seismic landslides. It, therefore, does not show safety factor of any individual slope.

**Table 15.1** Weighting for factors related to slope instability (Kanagawa Prefectural Government, 1986)

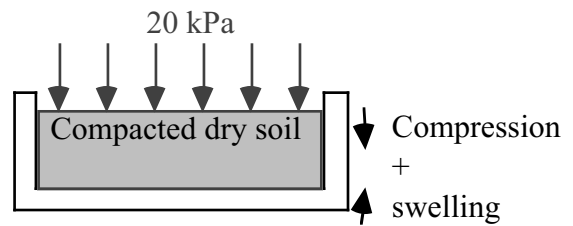
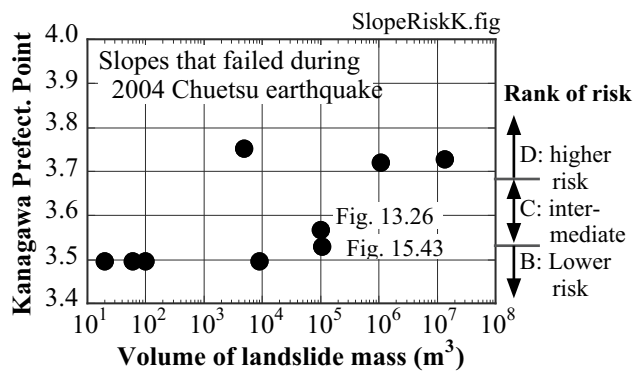
Factor	Category	Weight	Factor	Category	Weight
Maximum surface acceleration (Gal), $W_1$	0–200	0.0	Hardness of rock, $W_4$	Soil	0.0
	200–300	1.004		Soft rock	0.169
	300–400	2.306		Hard rock	0.191
	>400	2.754	Length of faults (m), $W_5$	No fault	0.0
Length of a contour line at mean elevation (m), $W_2$	0–1000	0.0		0–200	0.238
	1000–1500	0.071		>200	0.710
	1500–2000	0.320	Length of artificial slopes (m), $W_6$	0–100	0.0
>2000	0.696	100–200		0.539	
Difference between highest site and lowest site (m), $W_3$	0–50	0.0		>200	0.845
	50–100	0.550	Shape of slope, $W_7$ (see Fig. 15.42)	(1)	0.0
	100–200	0.591		(2)	0.151
	200–300	0.814		(3)	0.184
>300	1.431	(4)		0.207	

**Table 15.2** Assessed number of slope instabilities (Kanagawa Prefectural Government, 1986)

$W = W_1 + W_2 + W_3 + W_4 + W_5 + W_6 + W_7$	2.93		3.53		3.68	
Rank	A		B		C	
Number of slope failures within 500 m×500 m grid	0		1–3		4–8	
					D	
					>9	



**Fig. 15.43** Different extents of lateral movement of debris due to different volumes at Naraki after 2004 Chuetsu earthquake



**Fig. 15.45** Method of swelling test

**Fig. 15.44** Assessment of seismic risk of slopes by Kanagawa Prefecture method

As shown above, concerning the  $W_4$  factor, the Kanagawa method does not fully account for local soil conditions. Moreover, the experience of many landslides during the 2004 Niigata Chuetsu earthquake revealed that the size of slope failure affected the extent of risk. Figure 15.43, for example, demonstrates two slope failures which occurred at a short distance from each other. The bigger one caused the debris to translate significantly in the lateral direction and stopped the stream flow, forming a natural dam (Sect. 15.3). The other one was merely falling of the surface weathered soil and the fallen material did not move laterally very much. Thus, it was thought necessary to add an assessment of “size” in the risk assessment. Another issue was the effect of water on slope instability because the Chuetsu earthquake was preceded by heavy rainfall three days before.

First, Fig. 15.44 plots the Kanagawa method’s point against the volume of landslide mass for many slope failures during the Chuetsu earthquake. Generally, there is a good consistency between the volume of landslide and the calculated point. There are, however, two slopes (Figs. 13.26 and 15.43) that received relatively low points in spite of their damage extent.

Effort was made to improve the method by paying attention to the effects of water on properties of local soils (Mizuhashi et al. 2006). It was, however, considered difficult in practice to collect undisturbed soil samples and to run laboratory shear tests, because it was too elaborate for the present purpose of damage assessment. Therefore, disturbed soils were collected from the surface of failed slopes in the Chuetsu area and, in addition to measurement of liquid limits and plastic limits (Sect. 1.1), volume change upon water submergence was measured.

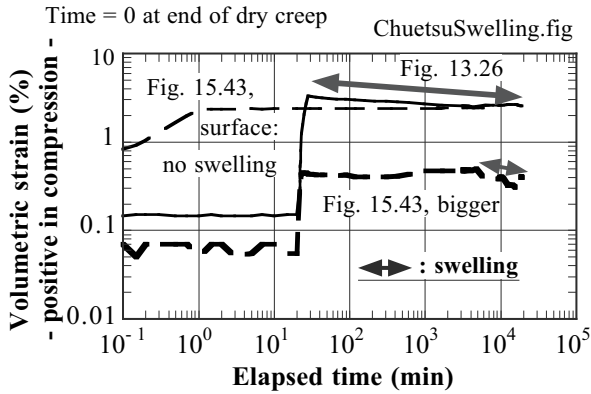


Fig. 15.46 Example of swelling tests (volume change after water submergence)

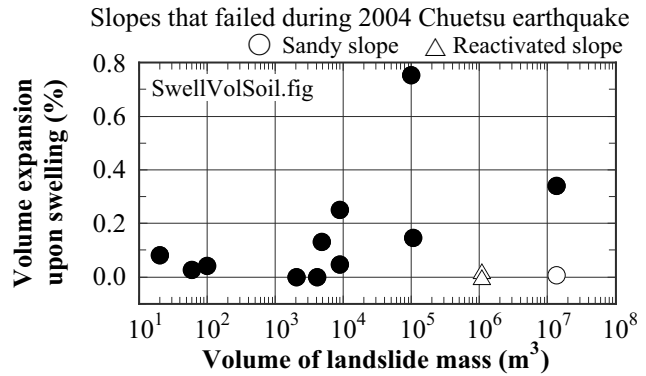


Fig. 15.47 Relationship between volume of slope failure and extent of soil swelling

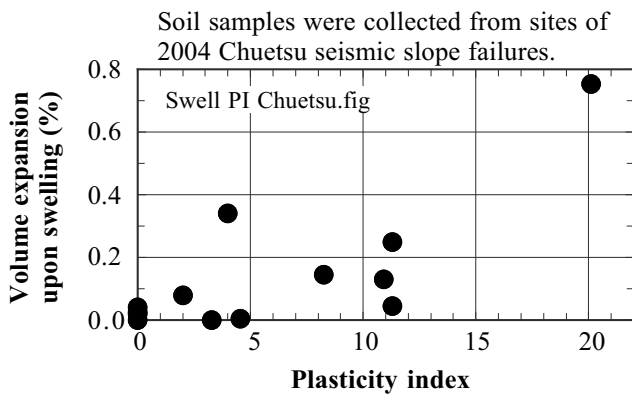


Fig. 15.48 Correlation between plasticity index and swelling strain

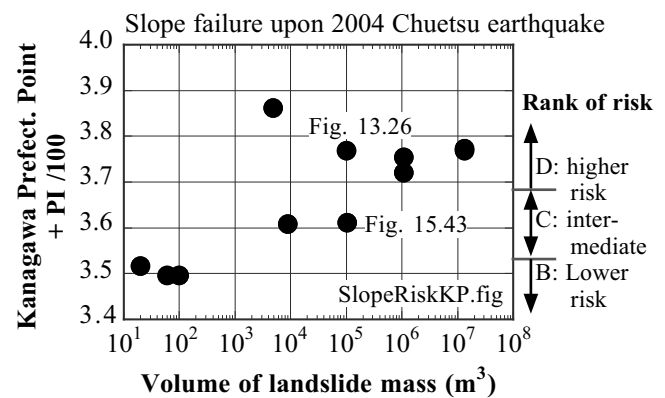


Fig. 15.49 Revisal of seismic risk assessment of slopes by means of plasticity index

Figure 15.45 illustrates the method of testing. First, an air-dry soil sample was prepared in a conventional oedometer (consolidation testing device) by compacting with a hammer with a constant and specified energy. After loading under 20 kPa and allowing for creep deformation in a dry state, water was introduced into the sample quickly. This water submergence caused subsidence, and thereafter, some soils exhibited swelling. It is supposed in this study that swelling is caused by interaction of clay mineral and water and leads to loss of shear strength. Figure 15.46 shows the time history of volume change of three specimens which are those in Fig. 13.26 and Fig. 15.43 (both bigger and surface ones). It is therein seen that the extent of swelling varies with soil types; the surface material in Fig. 15.43 did not have swelling.

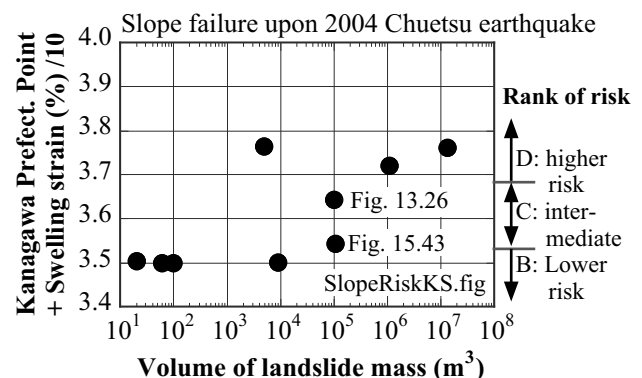


Fig. 15.50 Revisal of seismic risk assessment of slopes by means of swelling strain



Figure 15.47 shows a positive correlation between the volume of landslide mass and the measured volumetric strain during swelling. There are, however, exceptional cases where the material was sandy or the landslide was a reactivation of an existing unstable mass. These cases do not affect the significance of the swelling strain in practice.

One of the shortcomings in the use of swelling is the long time needed for the test (Fig. 15.45). To avoid this, a correlation between swelling strain and plasticity index was plotted in Fig. 15.48. There is certainly some relationship between them, and probably the plasticity index can be used as an alternative parameter which does not require much time for testing.

Figures 15.49 and 15.50 examine two types of revisal of the original Kanagawa Prefecture method. The original points were modified by adding either (plasticity index)/100 or (swelling strain, %)/10. It may be seen that points for the cases of Figs. 13.26 and 15.43 were increased to more reasonable values. This is particularly significant in the case of Fig. 15.49 wherein the plasticity index was employed for improvement.

15.7 Earthquake-Induced Submarine Landslides

Heezen and Ewing (1952) stated that a sequential breakage of submarine telegraph cables immediately after the 1929 Grand Banks earthquake in the continental slope to the south of New Foundland was caused by a turbidity current of water and mud. Figure 15.51 by Heezen et al. (1954) indicates that the slope inclination was as small as 1/500 or less in the area of submarine cable breaks, while the velocity of the turbidity current was on average 20 knots (=39 km/h); the highest velocity probably exceeded 90 km/h. It is remarkable that the fluidized debris traveled more than 700 km over a very small inclination of sea bed. Note, however, that Hasegawa and Kanamori (1987) stated that the ground shaking which was recorded at the time of the sliding was not of an earthquake origin, but was the consequence of huge submarine sliding. If this is correct, one should understand that the Grand Banks Sliding was caused by nonseismic causes (Sect. 15.8).

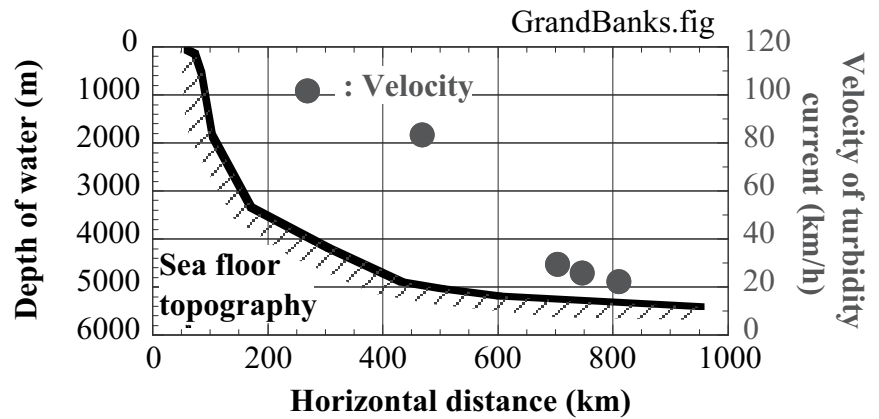


Fig. 15.51 Velocity of turbidity current after Grand Banks earthquake (drawn after Heezen et al., 1954)



Fig. 15.52 Conceptual sketch of Valdez submarine landslide (Drawn by David Laneville; after Coulter and Migliaccio, 1966)



Fig. 15.53 Aerial photograph of former site of Valdez (taken by K.Horikoshi)

A submarine landslide occurred in a gigantic scale at Valdez, Alaska, in March, 1964, when the great Alaska earthquake affected the area. Figure 15.52 illustrates the loss of sea slope, and the harbor facilities disappeared. The total volume of landslide was estimated to be around 100 million m<sup>3</sup> (Coulter and Migliaccio, 1966). Consequently, a large tsunami was produced and washed Valdez town. Figure 15.53 shows the aerial view of the present Valdez delta in 2002. The subsoil in this deltaic deposit consists of fine-grained cohesionless soil. This material was produced by scraping of mountain rock by glacier. Moreover, the small particle size makes the velocity of grain sedimentation very slow in water, and therefore the density becomes low.

When the gigantic earthquake occurred in Alaska in 1964, this submarine slope failed easily, most probably accompanied by development of excess pore water pressure. This feature of glacier deposit is similar to that of tailing material (Sect. 20.5).

The Alaska earthquake also destroyed the sea-front ground in the town of Seward. Most probably, the shaking effect was superimposed by tsunami action (Lemke, 1971) which caused rapid drop of water level and loss of buoyancy force in soil.

Most probably, submarine landslides have been repeated in the past, although they were not detected because they were hidden by the sea-water coverage.

Another earthquake of magnitude = 6.7 induced a submarine landslide in the Mediterranean Sea off the coast of Orléansville (later called El Asnam and further renamed as Ech Cheliff), Argeria, in 1954. This slide traveled more than 70 km toward the deep sea (Heezen and Ewing, 1955) at a rate of, roughly, 40 km/h.

The body of a volcano is often affected by seismic motion. Figure 15.54 reveals an example in which a submerged wall of the Tohya (洞爺湖) caldera lake fell down at the time of the 1993 Hokkaido-Nansei-Oki earthquake and affected the shore line.



**Fig. 15.54** Earthquake-induced failure of caldera wall (Tohya Lake, 1993)

## 15.8 Nonseismic Submarine Landslides

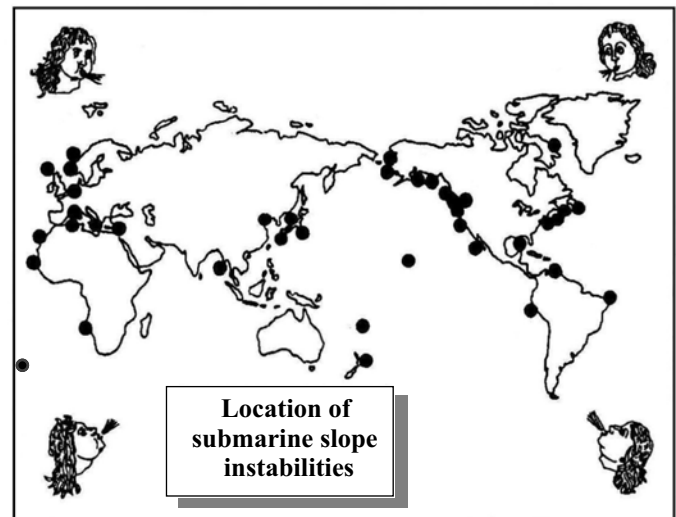
Submarine landslides have occurred at many places in the past. Terzaghi (1956) as well as Andresen and Bjerrum (1967) reported very unstable nature of submarine slopes and the typical example was taken of fjord deposits. An event at shore of Skagway in Alaska (1994) is one of the examples (Kulikov et al. 1996). Figure 15.55 illustrates their locations, inclusive of historic and prehistoric ones. Three important nonseismic causes of the submarine landslides are described below:

1. *Rapid sedimentation*: This is a major problem at mouths of big rivers where the rate of sedimentation is very rapid. Although the shear stress increases quickly together with sedimentation, the effective stress and shear strength take time for development due to delayed consolidation. Thus, the factor of safety decreases with time and minor impacts such as wave action or small earthquake suddenly trigger the total failure. An oil production platform was destroyed by this mechanism off the Mississippi River mouth (Sterling and Strohbeck, 1973). More detailed study is going on off the Fraser River delta, Canada (McKenna et al. 1992; Chillarige et al. 1997). Figure 15.56 is a small example of submarine landslide which was triggered by rapid sedimentation of sand in the sea bed off this beach.

2. *Wave action*: Wave pressure on seabed is not uniform. Therefore, it can create cyclic shear stress in the seabed (Henkel, 1970). The consequent pore pressure increase can lead to loss of shear strength and slope failure (Okusa, 1985). This mechanism of loading can be fatal in a slope of rapid sedimentation as discussed above.

3. *Tsunami*: Slope instability may be induced by a rapid draw-down of water level in front of its face. This is because of the loss of buoyancy force which used to support the slope when the water level was higher. A typical example is the failure of the ongoing reclamation site of Nice Airport, France, where a tsunami was triggered by the massive movement of seabed sediment after its rapid deposition and the sea water level dropped (Seed et al. 1988).

A gigantic submarine landslide and a sudden change of submarine topography may trigger tsunami. Kulikov et al. (1998) pointed out that several nonseismic tsunami had occurred at the time of low tide. This is consistent with a well-known fact that rapid draw-down of reservoir water can trigger instability in shore slope. This instability is caused by the disappearance of buoyancy force after lowering of water level and the weight of the soil which still contains much pore water.



**Fig. 15.55** Location of submarine landslides, historic and prehistoric



**Fig. 15.56** Small submarine landslide and missing beach due to rapid sedimentation (Naruto, Japan)

In addition to the aforementioned causes, Locat and Lee (2002) mentioned such causes as gas charging, explosion of gas hydrate, low tides, seepage, glacial loading, and volcanic island growth. Among these, methane gas hydrate is an icy material which is buried in the soil of the ocean sea bottom (Matsumoto, 1997; Cruickshank and Masutani, 1999). It maintains stability under high pressure and/or low temperature. It is said that the seabed methane hydrate was less stable during the last glacier period when the sea level was lower than today by more than 100 m and the hydrate underwent lower pressure. A possible explosion of this material could have triggered submarine landslides of a huge scale (Ashi, 1999; Rothwell et al. 1998). One of the biggest submarine landslides in the prehistoric times is the Storegga Slide which occurred 30,000–50,000 years ago in the North Sea off Trondheim of Norway (Bugge et al. 1988). Its volume is estimated to be  $3.88 \times 10^{12} \text{ m}^3$ . This event was probably triggered by unstable hydrate upon an earthquake (Bugge et al. 1988). Holcomb and Searle (1991) described several gigantic submarine landslides around volcanic islands such as Hawaii, Tristan da Cunha, and Canary.

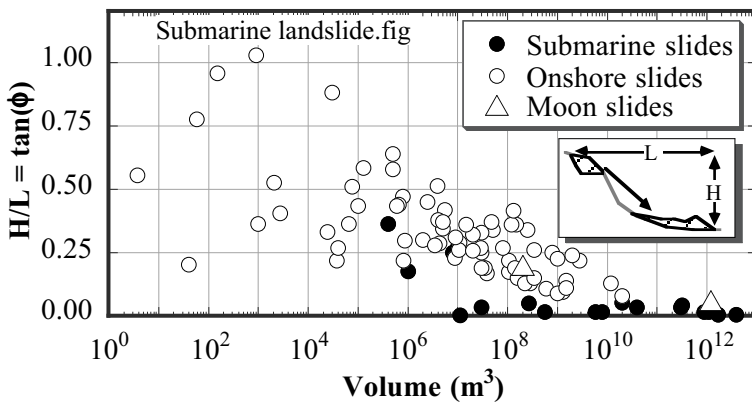


Fig. 15.57 Apparent frictional coefficient of landslides; subaerial and submarine

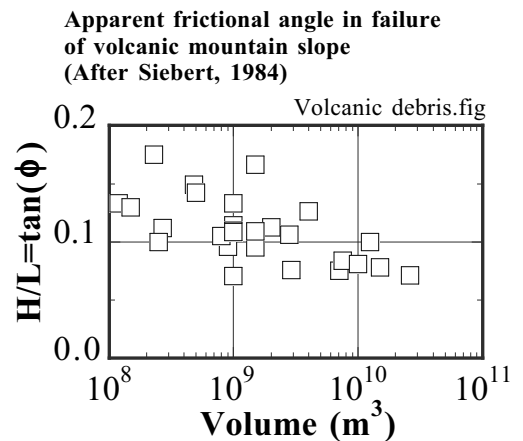


Fig. 15.58 Apparent frictional coefficient in failure of volcanic mountains (data by Siebert, 1984)

Upon submarine landslides, the energy dissipation of moving soil mass is approximately evaluated by using the height of fall,  $H$ , and the horizontal distance of flow,  $L$ . Consequently,

$$\phi = \arctan(H/L) \tag{15.2}$$

is supposed to be the frictional angle of the flowing debris (Hsü, 1975); for its mathematical derivation, refer to Sect. 15.9. Figure 15.57, wherein data was collected from such literatures as Scheidegger (1973), Howard (1973), Moriwaki (1987) and Okuda (1984) as well as the author’s own study, indicates the frictional parameter,  $\phi$ , thus obtained. Note that, first, the subaerial (on-shore) landslides have a greater friction than the submarine ones, and second that the greater volume of flowing soil mass is associated with smaller friction. Therefore, the greater landslide can reach a longer distance. Noteworthy is that the apparent frictional angle is significantly small in large submarine slides probably because of the high degree of water saturation and pore pressure development (liquefaction).

Figure 15.57 suggests that typically  $H/L = \tan 30^\circ \approx 0.6$  for the cases of smaller debris volume which often occurs. This information is frequently used for assessment of area which is vulnerable to potential risk of landslide (hazard mapping). Note, however, that there are cases where  $H/L$  is very small possibly due to high water content and development of excess pore water pressure in the soil mass. It is empirically known, furthermore, that debris flow in volcanic slopes (Fig. 15.4 for example) has smaller  $H/L$  and greater travel distance than other onshore events (Siebert, 1984); compare Fig. 15.58 with Fig. 15.57.

**15.9 Derivation of Formula for Apparent Frictional Angle**

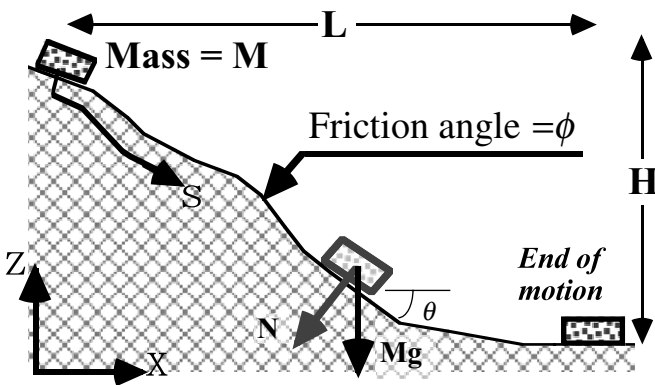
This section presents the mathematical derivation of the formula on friction angle (15.2) which was proposed by Hsü (1975). Figure 15.59 illustrates a slope and a moving mass at its surface. This mass is an idealization of debris and the frictional angle between this mass and the slope surface is designated by  $\phi$ . Note that the present discussion is based on a total stress approach of soil mechanics. Hence, the shear force,  $S$ , is related to the normal force,  $N$ , without paying attention to effective stress or pore water pressure;

$$\text{Friction } S = N \tan \phi = mg \cos \theta \tan \phi, \quad (15.3)$$

where  $\theta$  stands for the slope angle at the current location of the moving mass. The energy dissipation per unit time due to friction is expressed as

$$\frac{dD}{dt} = S \times \text{velocity} = mg \cos \theta \tan \phi \times \frac{ds}{dt}, \quad (15.4)$$

where  $s$  is the location of the moving mass measured along the slope surface (Fig. 15.59).



**Fig. 15.59** Motion of mass along slope surface

**Fig. 15.60** Changed flow direction of debris at bottom of slope (rainfall-induced slope failure in Shikoku, Japan, in 2004)

By integrating (15.4) from the beginning to the end of motion, the total energy dissipation is obtained and it is equal to the loss of gravity potential energy. Hence,

$$mgH = \int \frac{dD}{dt} dt = \int S \times \text{velocity} dt = \int mg \cos \theta \tan \phi \times \frac{ds}{dt} dt. \quad (15.5)$$

Since  $\cos \theta = \frac{dx}{ds}$ ,

$$H = \tan \phi \times \int \frac{dx}{ds} \frac{ds}{dt} dt = \tan \phi \times \int \frac{dx}{ds} ds = \tan \phi \times \int dx = \tan \phi \times L. \quad (15.6)$$

Consequently,

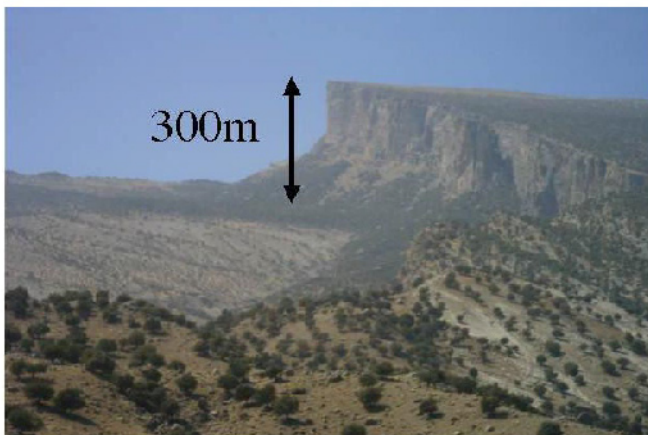
$$\frac{H}{L} = \tan \phi. \quad (15.7)$$

Theoretically, this formula assumes a two-dimensional straight channel of flow. When the flow channel in a valley is bent and three-dimensional (Fig. 15.60), energy is dissipated by collision between soil mass and valley wall. Also, it is difficult to define  $L$ .

Figure 15.61 demonstrates the biggest onshore landslide that can be seen today (Harrison and Falcon, 1938). The width and the length of this Seimareh, Iran, landslide are 16 km and 5 km, respectively, while the thickness of the failed rock mass is 300 m (Fig. 15.62). Thus, the total volume of the debris was around 24 billion  $m^3$ . A  $C_{14}$  dating (Watson and Wright, 1969) by using sediment of a lake in this area suggests that this landslide occurred 10,000 years ago. Since the annual precipitation is very low (500–600 mm/year; van Zeist and Bottema, 1977), erosion is not significant and it is possible to see the slip plane (Fig. 15.63). This slide was probably caused by erosion by river at the foot of the slope (Oberlander, 1965). It is however possible that the unstable slope was finally destroyed by shaking. As Fig. 15.57 implied, this huge volume of debris makes H/L value very small; the travel distance was as long as 20 km which is evidenced by the debris deposit which is still visible today (Fig. 15.64).



**Fig. 15.61** Total view of Seimareh landslide seen from nearby town of Pol-e-Doghtar



**Fig. 15.62** Side cliff of Seimareh landslide



**Fig. 15.63** Smooth slip plane of Seimareh landslide



**Fig. 15.64** Debris deposit of Seimareh landslide

**List of References in Chapter 15**

- Andresen, A. and Bjerrum, L. (1967) Slides in subaqueous slopes in loose sand and silt, *Marine Geotechnique*, Ed. A.F. Richards, Univ. Illinois Press, pp. 221-239.
- Ashi, J. (1999) Large submarine landslides associated with decomposition of gas hydrate, *Landslide News*, Vol. 12, pp. 17-20.
- Bugge, T., Belderson, R.H. and Kenyon, N.H. (1988) The Stregga Slide, *Phil. Trans. Roy. Soc. London*, A. 325, pp. 357-388.
- Chillarige, A.V., Morgenstern, N.R., Robertson, P.K. and Christian, H.A. (1997) Seabed instability due to flow liquefaction in the Fraser River delta, *Can. Geotech. J.*, Vol. 34, pp. 520-533.
- Coulter, H.W. and Migliaccio, R.R. (1966) Effects of the earthquake of March 27, 1964 at Valdez, Alaska, Professional Report 542-C, US Geological Survey.
- Cruickshank, M.J. and Masutani, S.M. (1999) Methane hydrate research & development, *Sea-Technology*, Vol. 40, No. 8, pp. 69-74.
- Harrison, J.V. and Falcon, N.L. (1938) An ancient landslip at Saidmarreh in southwestern Iran. *J. Geol.*, Vol. 46, pp. 296-309.
- Hasegawa, H.S. and Kanamori, H. (1987) Source mechanism of the magnitude 7.2 Grand Banks earthquake of November 1929: double couple or submarine landslide?, *Seismol. Soc. Am. Bull.*, Vol. 77, pp. 1984-2004.
- Hayakawa, A. (1967) Photograph of Mt. Huascaran, *Mountains of the World, YAMAKEI Color Guide* 8, p. 177 (in Japanese) (早川滉 撮影 山溪カラーガイド 8, 山と溪谷社).
- Heezen, B.C. and Ewing, M. (1952) Turbidity currents and submarine slumps, and the 1929 Grand Banks Earthquake, *Am. J. Sci.*, No. 250, pp. 849-873.
- Heezen, B.C. and Ewing, M. (1955) Orleansville earthquake and turbidity currents, *Bull. Am. Assoc. Petroleum Geologists*, Vol. 39, No. 12, pp. 2505-2514.
- Heezen, B.C., Ericson, D.B. and Ewing, M. (1954) Further evidence for a turbidity current following the 1929 Grand Banks earthquake, *Deep-Sea Research*, Vol. 1, pp. 193-202.
- Henkel, D.J. (1970) The role of waves in causing submarine landslides, *Geotechnique*, Vol. 20, No. 1, pp. 75-80.
- Holcomb, R.T. and Searle, R.C. (1991) Large landslides from oceanic volcanoes, *Marine Geotechnol.*, Vol. 10, pp. 19-32.
- Howard, K.A. (1973) Avalanche mode of motion: Implication from Lunar examples, *Science*, Vol. 180, pp. 1052-1055.
- Hsü, K.J. (1975) Catastrophic debris streams (Sturzstroms) generated by rockfalls, *Geol. Soc. Am. Bull.*, Vol. 86, pp. 129-140.
- Imaizumi, F., Tsuchiya, S. and Ohsaka, O. (2005) Behaviour of debris flows located in a mountainous torrent on the Ohya landslide, Japan, *Can. Geotech. J.*, Vol. 42, pp. 919-931.
- Ishihara, K. (1985) Stability of natural deposits during earthquakes, Theme Lecture, 11th ICSMFE, San Francisco, Vol. 1, pp. 321-376.
- Ishihara, K., Haeri, S.M., Moinfar, A.A., Towhata, I. and Tsujino, S. (1992) Geotechnical aspects of the June 20, 1990 Manjil Earthquake in Iran, *Soils Found.*, Vol. 32, No. 3, pp. 61-78.
- Kanagawa Prefectural Government (1986) Prediction of seismic damage in Kanagawa Prefecture, pp. 13-63 (in Japanese).
- Kawata, S. (川田三郎) (1943) Study of new lake created by the earthquake in 1941 in Taiwan 台南州斗六郡草嶺震生湖, *Bulletin of the Earthquake Research Institute, University of Tokyo*, 東京大学地震研究所彙報, Vol. 21, pp. 317-325 (in Japanese).
- Keefer, D.K. (1984) Landslides caused by earthquakes, *Geol. Soc. Am. Bull.*, Vol. 95, pp. 406-421.
- Kulikov, E.A., Rabinovich, A.B., Thompson, R.E. and Bornhold, B. (1996) The landslide tsunami of November 3, 1994, Skagway Harbour, Alaska, *J. Geophys. Res.*, Vol. 101, No. C3, pp. 6609-6615.
- Kulikov, E.A., Rabinovich, A.B., Fine, I.V., Bornhold, B. and Thompson, R.E. (1998) Tsunami generation by landslides at the Pacific coast of North America and the role of tides, *Oceanology*, Vol. 38, No. 3, pp. 323-328.



- Lemke, R.W. (1971) Effects at Seward, In *The Great Alaska Earthquake of 1964, Chapter on Geology*, National Academy of Sciences, Washington, D.C., pp. 395–437.
- Locat, J. and Lee, H.J. (2002) Submarine landslides: advances and challenges, *Can. Geotech. J.*, Vol. 39, pp. 198-212.
- Matsumoto, R. (1997) Perspective of methane hydrate science, *J. Jpn. Inst. Energy*, Vol. 76, No. 841, pp. 354-361.
- McKenna, G.T., Luternauer, J.L. and Kostaschuk, R.A. (1992) Large-scale mass-wasting event on the Fraser River, British Columbia, *Can. Geotech. J.*, Vol. 29, pp. 151-156.
- Mizuhashi, M., Towhata, I., Sato, J. and Tsujimura, T. (2006) Examination of slope hazard assessment by using case studies of earthquake- and rainfall-induced landslides, *Soils Found.*, Vol. 46, No. 6, pp. 843–853.
- Moriwaki, H. (1987) A prediction of the runout distance of a debris, *J. Jpn. Landslide Soc.*, Vol. 24, No. 2, pp. 10-16 (in Japanese).
- Oberlander, T. (1965) *The Zagros Streams*, Syracuse Geographical Series, No. 1, Syracuse University Press.
- Okuda, S. (1984) Features of debris deposits of large slope failures investigated from historical records, Report of Disaster Prevention Research Institute, Kyoto University, No. 27B-1 (in Japanese).
- Okusa, S. (1985) Wave-induced stresses in unsaturated submarine sediments, *Geotechnique*, Vol. 35, No. 4, pp. 517-532.
- Plafker, G., Ericksen, G.E. and Fernández Concha, J. (1971) Geological aspects of the May 31, 1970, Peru Earthquake, *Bull. Seismol. Soc. Am.*, Vol. 61, No. 3, pp. 543–578.
- Rothwell, R.G., Thompson, J. and Kähler, G. (1998) Low-sea-level emplacement of a very large late Pleistocene 'megaturbidite' in the western Mediterranean Sea, *Nature*, Vol. 392, pp. 377-380.
- Sassa, K., Fukuoka, H., Scarascia-Mugnozza, G. and Evans, S. (1996) Earthquake-induced-landslides: distribution, motion and mechanisms, *Soils Found.*, Special Issue on Geotechnical Aspects of the January 17 1995 Hyogoken-Nambu earthquake, pp. 53–64.
- Sassa, K., Fukuoka, H., Wang, G.-H. and Ishikawa, N. (2004) Undrained dynamic-loading ring-shear apparatus and its application to landslide dynamics, *Landslides*, Vol. 1, No. 1, pp. 7–19.
- Scheidegger, A.E. (1973) On the prediction of the reach and velocity of catastrophic landslides, *Rock Mech.*, Vol. 5, pp. 211-236.
- Seed, H.B., Seed, R.B., Schlosser, F., Blondeau, F. and Juran, I. (1988) *The Landslide at the Port of Nice on October 16 1979*, EERC Report 88-10, University of California, Berkeley.
- Siebert, L. (1984) Large volcanic debris avalanches: characteristics of source areas, deposits, and associated eruptions, *J. Volcanol. Geothermal Res.*, Vol. 22, pp. 163-197.
- Sino Geotechnology Inc. (1999) *Taiwan Chi-Chi earthquake 9.21. 1999*, ISBN 957-99763-2-5.
- Sterling, G.H. and Strohbeck, E.E. (1973) The Failure of the South Pass 70 Platform B in Hurricane Camill, *Proc. Offshore Technology Conf.*, Vol. 2, pp. 719-729.
- Tabata, S., Mizuyama, T. and Inoue, K. (2002) Natural dam and disasters, *Kokin Shoin Publ.*, ISBN4-7722-5065-4 C3051, pp. 50–53 (in Japanese).
- Terzaghi, K. (1956) *Varieties of submarine slope failures*, Harvard Soil Mechanics Series, No. 52.
- Towhata, I., Yamazaki, H., Kanatani, M., Ling, C.-E. and Oyama, T. (2002) Laboratory shear tests of rock specimens collected from site of Tsao-ling earthquake-induced landslide, *Tamkang J. Science Eng.*, Vol. 4, No. 3, pp. 209–219.
- van Zeist, W. and Bottema, S. (1977) Palynological investigations in Western Iran, *Palaeohistoria*, Vol. 19, pp. 20–85.
- Voight, B. and Elsworth, D. (1997) Failure of volcano slopes, *Geotechnique*, Vol. 47, No. 1, pp. 1–31.
- Watson, R.A. and Wright Jr., H.E. (1969) *The Saidmarreh landslide, Iran*, Geological Society of America Special Paper 123, pp. 115–139.
- Yasuda, S. (1993) Zoning for slope instability, *Manual for zonation on seismic geotechnical hazards*, Technical Committee 4, Int. Soc. Soil Mech. Found. Eng., p. 49.

# Chapter 16

## Seismic Faults

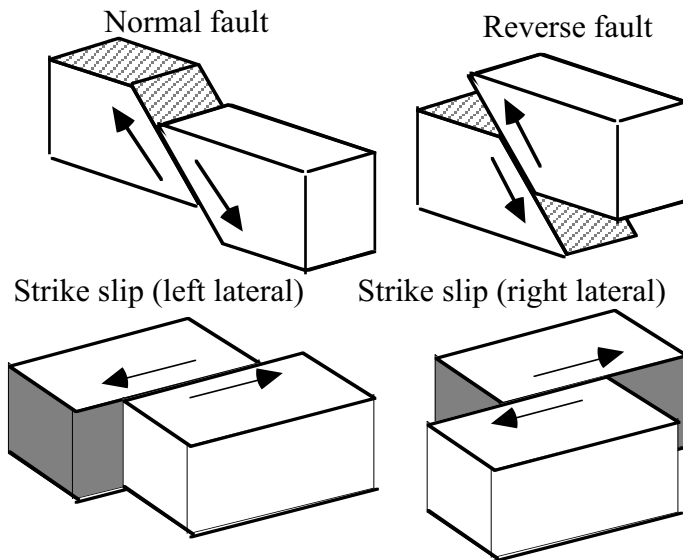


Ayutaya, Thailand. This former capital was destroyed upon invasion from outside.

## 16.1 Topics Related to Fault

One of the new problems in geotechnical earthquake engineering is related to a fault action. This situation was triggered by the 1995 earthquake in Kobe area as well as the 1999 ChiChi earthquake in Taiwan. The effects of fault movement in the underlying rock mass may or may not affect structures at the ground surface.

Fault is a kind of discontinuity in rock movement, which is associated with relative displacement between two blocks of rock mass. Figure 16.1 illustrates four types of fault movement (Sect. 3.1). Real faults are combination of those four movements. Some people use a terminology of “thrust fault” when the slip plane of a reverse fault is close to horizontal (angle being less than  $45^\circ$  for example).

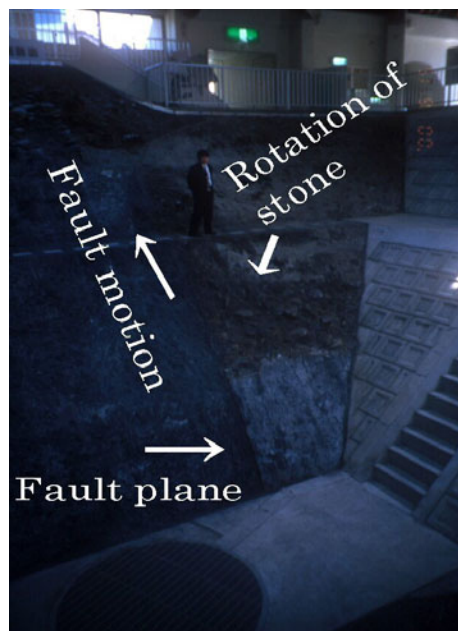


**Fig. 16.1** Classification of fault movements



**Fig. 16.2** Midori fault after the 1891 Nobi earthquake (Koto 古藤文次郎, 1893)

Figure 16.2 indicates the appearance of the Midori (水鳥) fault in Neo-dani (根尾谷) area near Nagoya, which was detected by a trench excavation. Produced by the 1891 Nobi (濃尾) earthquake, the vertical displacement was as large as 6 m at maximum. It is possible to see the cross section of this fault in an excavated trench (Fig. 16.3). It was found therein that this fault moved many times during past earthquakes. It was further found that (i) a thin clay layer (斷層粘土) is sandwiched in the fault plane, see Fig. 16.4, (ii) big gravel particles near the fault plane rotated during the fault movement and are oriented parallel to the fault motion, and (iii) the rock mass next to the fault is fractured (斷層破碎帶). Sect. 5.11 discussed the intensity of acceleration on and near the fault.



**Fig. 16.3** Cross section of excavated Midori fault in Neodani, Gifu



**Fig. 16.4** Clay in fault plane

Fault clay (Fig. 16.4) often caused a big problem in tunneling. The ruptured part of a fault behind clay is pervious and contain a huge amount of water. When tunneling breaks the impervious clay, this water flows out and floods tunnel which has so far been excavated. A famous example of this trouble is the Tanna Tunnel (丹那トンネル Fig. 16.35). Geological investigation prior to and drainage during construction are two important keys.

The assessment of the risk caused by future fault movement is a difficult task. Active faults are defined as those that moved one time in the past, for example, 50 thousand years, or several times in the past, for example, 300 thousand years. Thus, the definition of an active fault has variations. Although they moved in the recent times in a geological sense, it is not clear whether or not they will move again during the life time of our structures (50 years or so only). The effects of an earthquake would be extremely significant, if it is induced by a hidden fault immediately below or very close to a structure.

Active faults are classified based on its recent activities. For example, the extent of fault displacement averaged over the recent 1,000 years,  $S$ , is a good parameter (Matsuda, 1975, see Table 16.1). Different types of fault classification are possible based on the time of its most recent movement (in the historical era, Quaternary period, or pre-Quaternary), frequency of its movement (number of fault action in the past thousands of years or so), or certainty of being an active fault (linearment that appears similar to a fault-induced topography, however, may be formed due to river erosion and geological conditions).

**Table 16.1** Classification of active faults based on rate of displacement (after Matsuda, 1975)

Class	$S$ (=Displacement/1,000 years)
AA	$100 \text{ m} > S \geq 10 \text{ m}$
A	$10 \text{ m} > S \geq 1 \text{ m}$
B	$100 \text{ cm} > S \geq 10 \text{ cm}$
C	$10 \text{ cm} > S \geq 1 \text{ cm}$
D	$1 \text{ cm} > S \geq 0.1 \text{ cm}$

Note: Class AA was added later to the original idea by Matsuda.

Active faults have been detected by topographical studies as well as excavation of trenches in order to find such features as shown in Figs. 16.3 and 16.4. Figure 16.5 reveals a part of Tachikawa fault to the west of Tokyo (Class B in Table 16.1). This fault has moved with an interval of several thousand years. The gentle slope in the photograph was created by the fault movements in the past. Since erosion effects are superimposed on the fault-induced cliff, it is now difficult to recognize this slope as a product of fault action.



**Fig. 16.5** Slope produced by Tachikawa fault in Tokyo

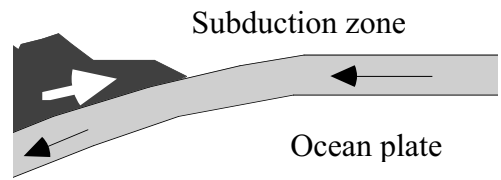
**16.2 Example of Reverse Fault**

Reverse fault is a cause of big earthquakes in a subduction zone of an ocean tectonic plate where the plate is sinking beneath a continental plate (Fig. 16.6).

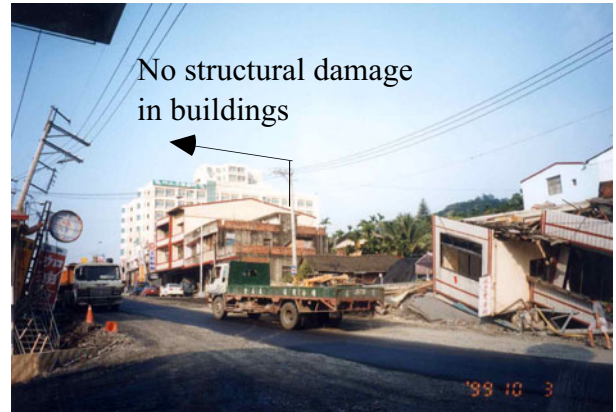
Figure 16.7 manifests the surface deformation in Taiwan, which was generated by an underlying reverse fault in 1999. Noteworthy is that the damage of buildings was concentrated only near the fault. It should be borne in mind that fault in general is a phenomenon in the earth crust rock and that, therefore, such a distortion in the surface soil is not a fault itself. Examples such as shown in Fig. 16.7 imply that the magnitude of acceleration near the faults is less destructive than permanent displacement of ground.

Another important issue in a reverse fault is that the extent of damage is more significant on the upper tectonic plate (hanging wall) than on the lower one (foot wall area) (Fig. 16.8). This is because the distance from the fault (or from the hypocenter) to surface structures is shorter on the upper plate than on the lower plate.

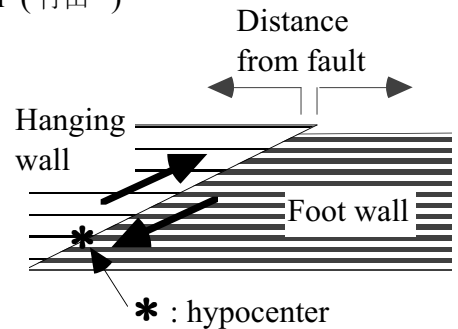
Figure 16.9 shows the consequence of large fault action at the Shi-kang (石岡) dam. The differential vertical motion of 10 m completely destroyed the massive concrete dam. The same fault created a water fall near this dam (Fig. 16.10).



**Fig. 16.6** Mechanism of reverse fault



**Fig. 16.7** Reverse fault influence in Taiwan (竹山)



**Fig. 16.8** Different seismic effects in upper and lower plates



**Fig. 16.9** Destroyed Shih-kang Dam



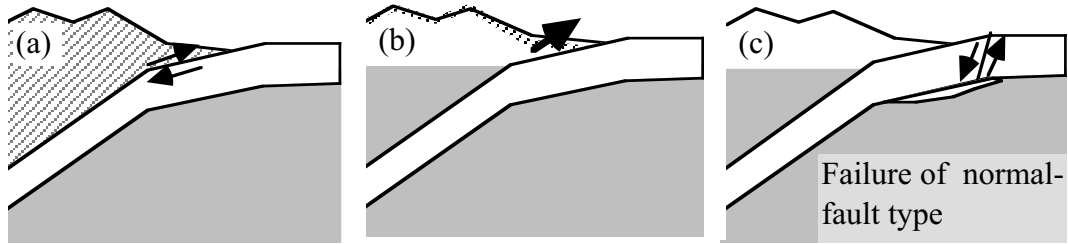
**Fig. 16.10** New water fall produced by reverse fault



**Fig. 16.11** Building resting immediately on fault (水源路 ChiChi earthquake in Taiwan, 1999)

Effects of subsoil deformation such as the one induced by a fault action are significant. The conventional principle of seismic design of buildings, however, does not account for subsoil deformation. The fault action is a big problem to lifelines (pipelines) as well. Figure 16.11 depicts an inclined building that still survived fault displacement beneath its foundation. This good performance was achieved by its rigidity.

Figure 16.12 illustrates a mechanism of normal fault that occurs in an ocean plate in a subduction area. Initially, the ocean plate is going down under a continental plate (Fig. 16.12a). Then shear failure or earthquake occurs at the plate interface as described already (see Fig. 16.6). It is sometimes possible, further, that a second shear failure occurs inside the ocean plate (Fig. 16.12c) due to a void that was produced under the plate at the time of the first failure event.



**Fig. 16.12** Mechanism of earthquake of normal-fault type in subduction zone

### 16.3 Example of Normal Fault

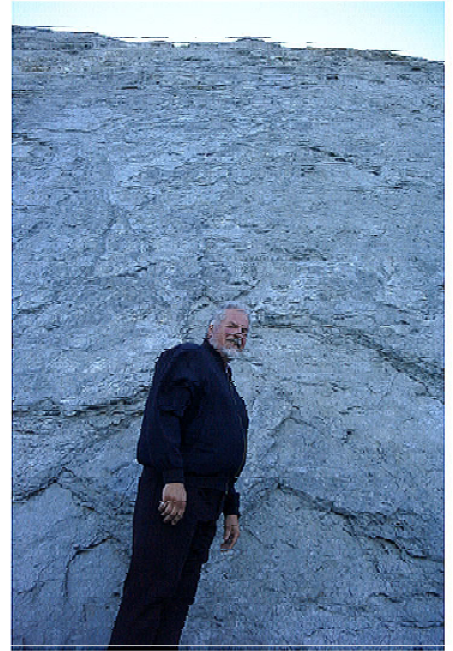
Normal fault is produced by tensile tectonic forces in the earth's crust. An example of a normal fault is found in the Genoa fault in Nevada, Reno. This fault forms a boundary between a mountain range to the west and a basin to the east where the present city of Reno is located. This fault moved 500 to 650 and 2,100 to 2,300 years ago, causing earthquakes in this area (Purkey and Garside, 1995).

A normal fault is produced when the tectonic stress field is tensile, making the upper earth block slide down (Fig. 16.1).

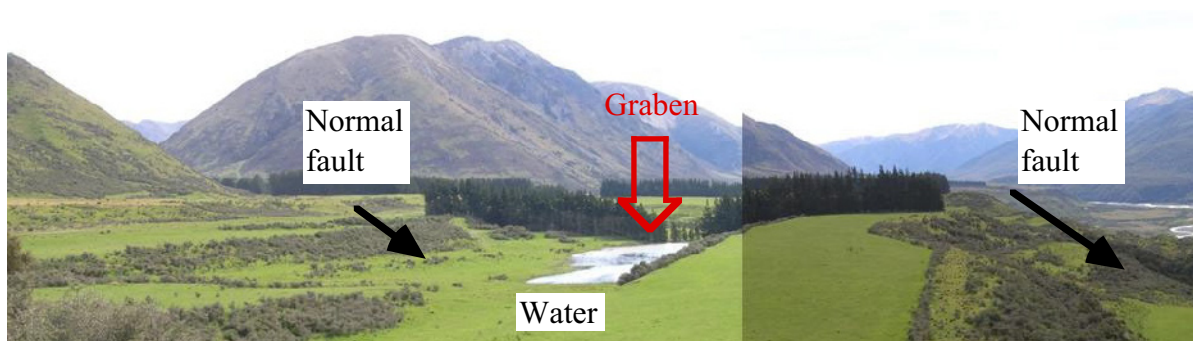
Figure 16.13 illustrates the appearance of the Genoa fault. The total height of the fault-induced cliff is hundreds of meters, which accumulated during geological periods with occasional earthquakes. Figure 16.14 shows a slickenside face of the fault plane that is very smooth due to scraping effects between rock blocks. Figure 16.15 indicates a subsidence (graben) induced by normal fault action. Being adjacent to a greater strike slip fault, this area is subject to enlargement of valley width, which induces normal faults as well.



**Fig. 16.13** Genoa normal fault near Reno, Nevada



**Fig. 16.14** Slickenside face of Genoa fault with Prof. G. M. Norris of University of Nevada, Reno



**Fig. 16.15** Subsidence or graben induced by normal fault action (along Hope Fault in New Zealand)

### 16.4 Example of Strike-Slip Fault

A strike-slip fault is characterized by relative displacement in the horizontal direction. Figure 16.16 shows an example that was observed after the Tangshan earthquake, North China. One of the most remarkable earthquake induced by a strike-slip earthquake was the one in Kobe and Awaji Island, 1995. Figure 16.17 shows the surface manifestation of the causative fault (Nojima fault). This distortion at the surface is not the fault action itself and was not so destructive as might be imagined; it was produced in the surface soil by the action of the underlying fault movement. The well-engineered house in the figure did not suffer a structural problem. The foundation of the house was rigid enough to resist the deformation and stress in the soft soil under the foundation.



**Fig. 16.16** Lateral displacement difference caused by Tangshan earthquake in China (Photo by Building Research Institute of China)

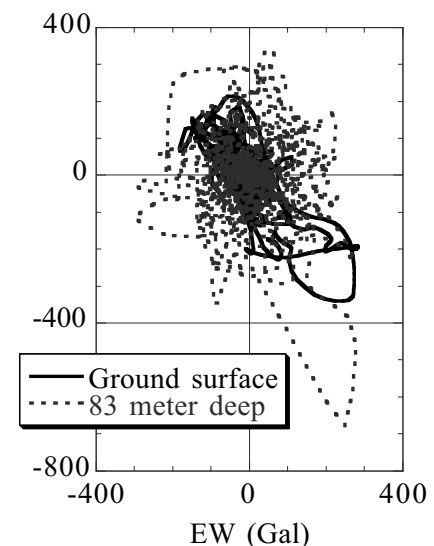


**Fig. 16.17** Strike-slip fault passing under house (in Awaji Island, 1995)

It deserves a special attention that the earthquake motion induced by a strike-slip fault and recorded at a short distance (near-fault motion) has a specified direction of strong shaking. Figure 16.18 illustrates the history of accelerations that were recorded at the surface and in the Pleistocene base (83 m deep) of Port Island in Kobe, 1995. While the surface motion was weaker than the base motion due to liquefaction in the artificial deposit (Sect. 18.9), both records reveal preferred orientation of strong motion. This special direction of motion is perpendicular to the direction of the nearest causative strike-slip fault (NE-SW direction). In Fig. 16.18, the directions of the maximum acceleration are different between the surface and the base records. Sekiguchi et al. (1996) pointed out that the orientation of the base motion in Fig. 16.18 should be corrected by rotating  $22.5^\circ$  in the counterclockwise direction.

Figure 16.19 illustrates the stress field that triggers failure of a strike-slip fault. When rupture propagates along the fault (Fig. 16.20), a double-couple mechanism of shear failure generates the direction of shaking perpendicular to the fault. Since the propagation rates of rupture and generated S waves are similar in rock, being about 3 km/s, those motions from all the ruptures are superimposed at a place near the fault and produce a predominantly perpendicular motion (directivity), refer to Bray and Rodriguez (2006).

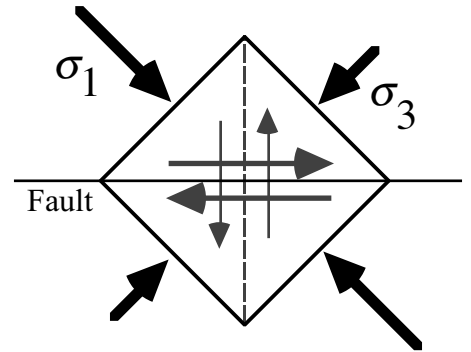
*Port Island acceleration records*  
NS (Gal) *PI.fig*



**Fig. 16.18** Orbit of acceleration records at the surface and in Pleistocene layer under Port Island, 1995 (data by Development Bureau of Kobe City Government)



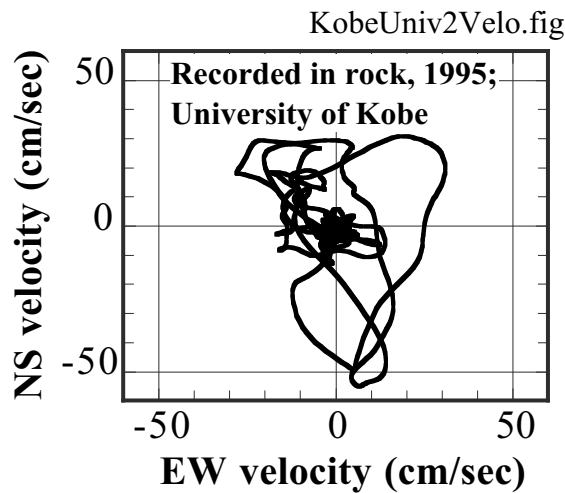
Figure 16.21 shows another orbit of ground velocities that were recorded in rock in the campus of Kobe University in 1995. This site is located within 1 km from the causative fault of the 1995 Kobe earthquake. There is again a directivity in the direction perpendicular to the fault orientation. Bray and Rodriguez (2004) examined many near-fault velocity records to show that the number of significant shaking cycles that have velocity amplitudes greater than 50% of the maximum velocity (PGV) is not more than three. This small number of loading is important in consideration of the effects to failure of structures and subsoil liquefaction. Somerville et al. (1997) stated that directivity is produced not only by strike-slip faults but also by reverse faults.



**Fig. 16.19** Double-couple mechanism of stress that generates strike-slip fault



**Fig. 16.20** Schematic illustration of preferred orientation of strong motion caused by strike-slip fault action



**Fig. 16.21** Orbit of velocity records in shallow rock in Kobe University Campus (The Committee of Earthquake Observation and Research in the Kansai Area)

## 16.5 Effects of Fault Movement on Rupture in Surface Soil

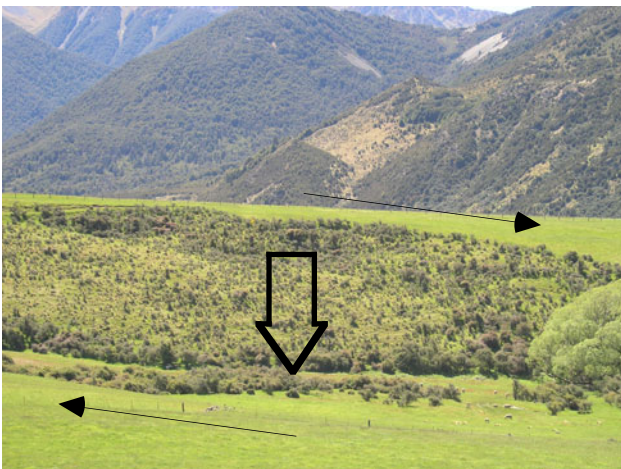
One of the important problems concerning faults is the prediction of the location and magnitude of surface rupture (large deformation) induced by fault action in the base rock. This is very important in seismic safety of lifelines. In a small scale, Fig. 16.22 shows a group of surface rupture (crack) that occurred at the ground surface above an underlying strike-slip fault. The orientation of ruptures is oblique to the direction of a fault as the orientation of tensile minor principal stress,  $\sigma_3$ , infers.

In a larger scale, Tchalenko and Ambraseys (1970) showed many surface shear failures, which were observed after an Iranian earthquake in 1968. Moreover, Fig. 16.23 illustrates subsidence as well as uplifting at a place where the strike-slip fault diverts into two lines at the surface. Thus, a strike-slip action of an embedded fault induces significant deformation over a substantial area at the ground surface. If an important facility is situated in this area, its damage is serious. A hint for mitigation may be seen in Fig. 16.17 where a house lying on the deforming ground was supported by a rigid concrete slab.



**Fig. 16.22** Surface rupture at ground surface above fault (1997 Qayen-Birjand earthquake, Iran)

(a) Subsidence



(b) Uplifting

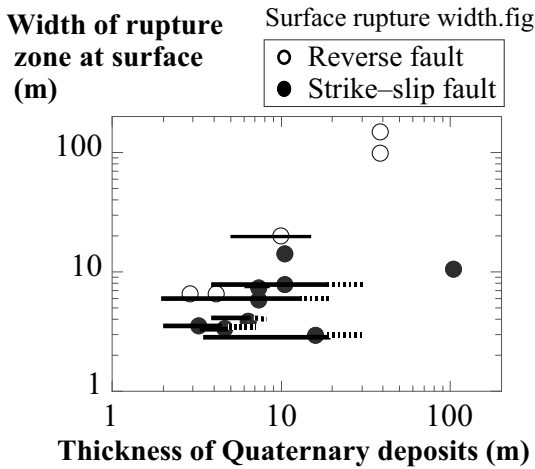


**Fig. 16.23** Distortion at ground surface caused by interaction between two diverting surface ruptures (Hope fault, South Island of New Zealand)

Ueta (1993) assembled results of fault excavations to obtain Fig. 16.24 where the width of the affected area increases with the thickness of surface soil. Thus, the thicker soil deposits may lead to damages in the greater range of area. It should be noted, however, that the fault-induced rupture may disappear within the surface soil and may not generate any influence at the ground surface. This point will be discussed in Sect. 16.6.

It is interesting that the Alaska oil pipeline was safe when an underlying fault moved laterally in 2002, although support structures were damaged to some extent. The pipeline was originally designed not to be affected by foundation movement due to possible melting of permafrost. It has a zigzag configuration and is supported freely on a beam without rigid fixing (Fig. 16.25); thus ground movement was absorbed.

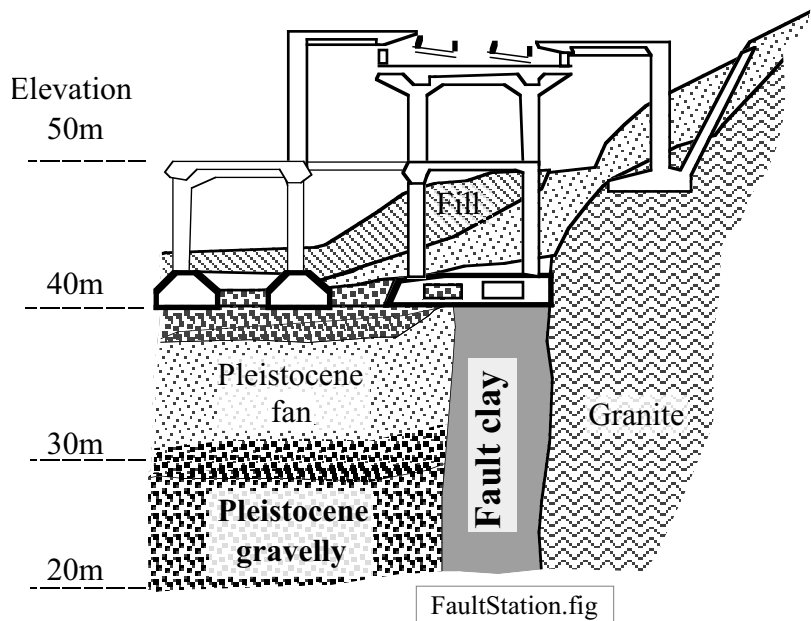
The best idea to avoid hazard due to future movement of an underlying fault is “not to construct upon the fault.” For example, a 20-m distance from an identified fault is recommended in New Zealand, while 50 feet (15.25 m) in California.



**Fig. 16.24** Empirical relationship between thickness of surface soil and width of surface rupture zone (modification of figure by Ueta, 1993)

**Fig. 16.25** Alaska pipeline which is simply sitting on lateral bar without fixing (Photo by M. Yoshimine)

There is, however, a special situation in which such a measure is not possible. For example, the New Kobe Railway Station had to be constructed upon the Suwayama Fault due to space limitations. Since this fault has been moving in the geologically recent times, a special structural arrangement was made (Okada et al. 2000). The geological condition under the station is illustrated in Fig. 16.26. The right part of the station building rests on a stable granite layer, while the left part on gravelly fan deposits. Between them, there is a fault clay which is 5 m in width and this part of the ground supports the railway track. If the fault should move during a future earthquake, the three parts of the station would be subjected to differential movement. Thus, as shown in the figure, the three parts of the station are supported by separated foundations and are lightly connected with one another by nonstructural members. Moreover, a possible rotation of the railway-track part is allowed by arranging a special space. The 1995 Kobe earthquake did not move this particular fault and the station was not damaged.



**Fig. 16.26** Cross section of New Kobe Station located across active fault (drawn after Okada et al., 2000)

16.6 Distortion at Ground Surface Produced by Subsurface Fault

Cole and Lade (1984) and Bray et al. (1993) carried out model tests on fault influence on an overlying soil deposit. It was revealed that the locations of a slip plane and rupture in the surface soil are affected significantly by the type of fault: normal or reverse. Figures 16.27 and 16.28 illustrate the test results on clean and dry Toyoura sand in 1-G field (Ueta and Tani, 1999). The direction of fault movement (motion of the base of the model) is illustrated by arrows. It is seen therein that a reverse fault causes fracture in an oblique location while a normal fault affects soils directly above the fault at the bottom. Figure 16.27 illustrates that shear deformation caused by a reverse fault is concentrated or localized rather along a single plane. For more details, refer to Tani et al. (1997) as well. Taniyama and Watanabe (1998) conducted model tests as well to make a similar finding.

Figure 16.29 indicates the location of the surface appearance of a slip plane ( $W$ ) when compared with the thickness of the sand deposit ( $H$ ). The difference between normal and reverse faults is evident.

It is noteworthy that a minor fault motion decays in the surface soil and does not reach the surface. Figure 16.30 manifests the minimum fault displacement ( $D$ ) that is needed to affect the surface.  $D/H$  decreases as the sense of fault changes from reverse to normal. Thus, a normal fault affects the surface more easily.

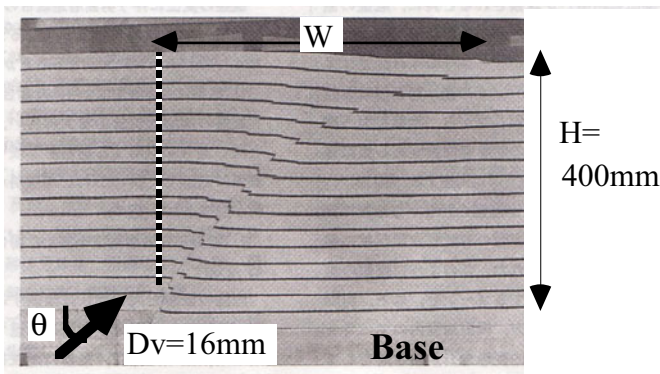


Fig. 16.27 Distortion of sandy ground due to embedded reverse fault; thickness of sand = 400 mm (Ueta and Tani, 1999)

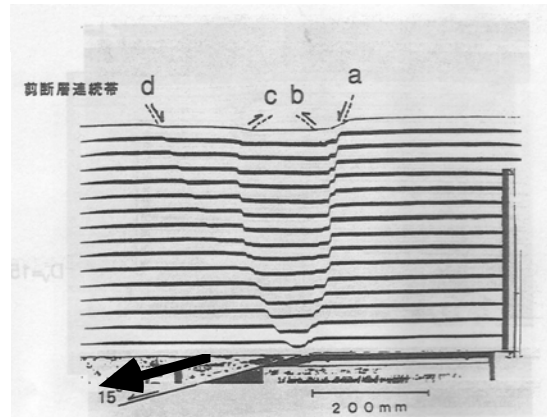


Fig. 16.28 Distortion of sandy ground due to embedded normal fault (Ueta and Tani, 1999)

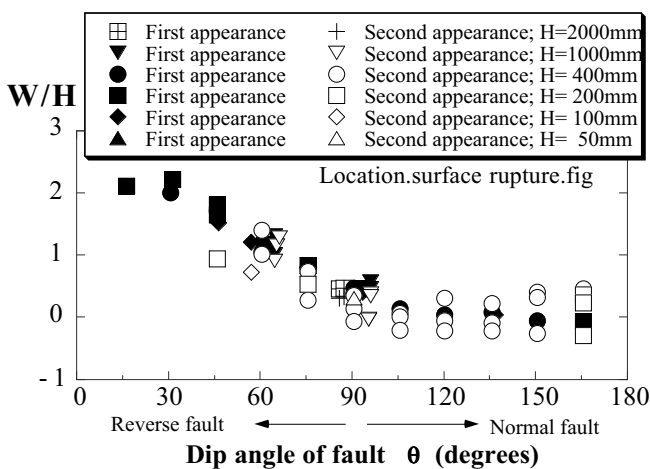


Fig. 16.29 Location of surface rupture as compared with thickness of surface soil (after Ueta and Tani, 1999)

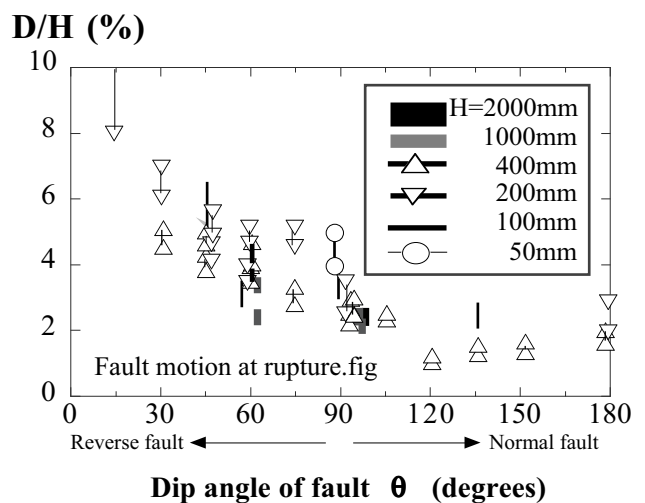
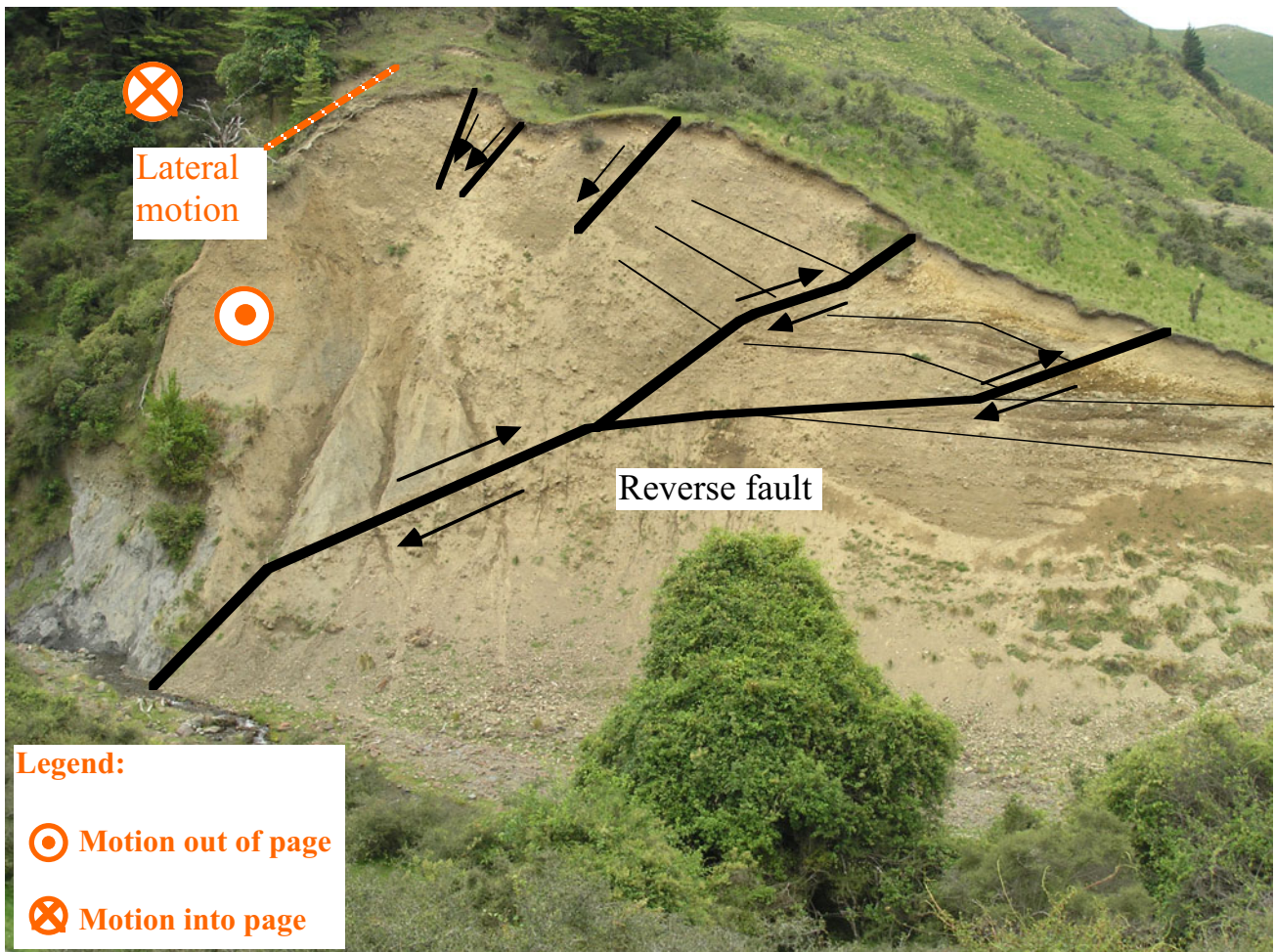


Fig. 16.30 Variation of minimum fault displacement ( $D$ ) that affects surface (after Ueta and Tani, 1999)

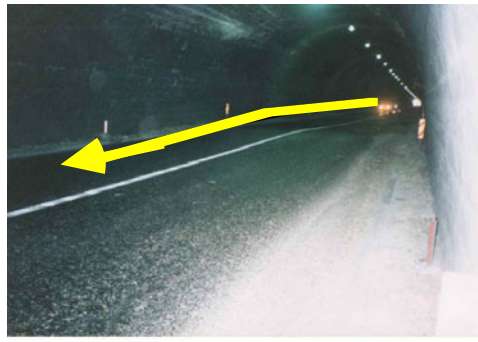
The distortion of ground in a real reverse (thrust) fault movement is shown in Fig. 16.31. It deserves attention therein that situation is more complicated than that in the model (Fig. 16.27) and is sometimes called flower structure (Sect. 16.8). Moreover, note that the fault motion in Fig. 16.31 is a combination of a right-lateral strike-slip and a reverse (thrust) movements.



**Fig. 16.31** Cross section of ground distortion adjacent to Hope Fault, South Island of New Zealand (drawn with reference to Pettinga, 2006).

## 16.7 Effects of Earthquake Fault on Tunnels

Tunnels have experienced few earthquake-induced damages. The collapse of Kinoura Tunnel in Fig. 13.22 was an exceptional case in which the tunnel was situated in a relatively soft material. Several tunnels in Niigata-Chuetsu area were affected as well due to soft-rock geology (Sect. 13.7). It appears conversely that tunnels in hard rock have a good resistance against earthquakes. For example, Fig. 16.32 shows the post-earthquake shape of a tunnel between Manjil and Rasht in Iran. Although this tunnel crossed a seismic fault and the pavement became wavy, road traffic was still possible. However, the internal brick lining of the tunnel was distorted and the width of the tunnel was reduced (Fig. 16.33). The entrance was damaged by shaking (Fig. 16.34).



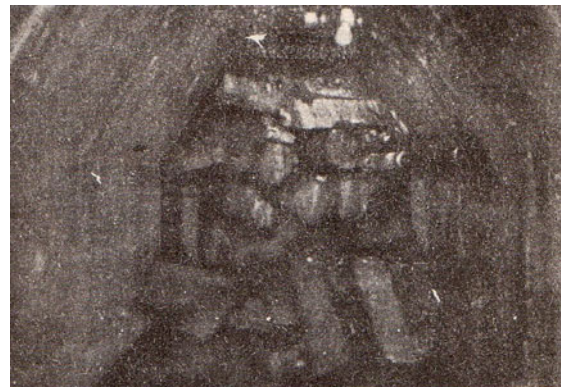
**Fig. 16.32** Wave-like distortion of tunnel pavement during the 1990 Manjil earthquake in Iran



**Fig. 16.33** Distortion of cover stone of drainage trench due to reduced width (Manjil earthquake)



**Fig. 16.34** Damage at entrance of tunnel (Manjil earthquake)



**Fig. 16.35** Fault plane which crossed Tanna tunnel (JSCE, 1936)



**Fig. 16.36** Compressed arch of tunnel in Taiwan (1999)



**Fig. 16.37** Water tunnel distorted by crossing fault (by N. Yoshida)

Upon the 1930 Kita-Izu earthquake (北伊豆地震), the fault crossed the Tanna tunnel (丹那トンネル) of Tokaido railway line, which was under construction then. The strike-slip movement of rock mass distorted the tunnel's axis by 2.5 m approximately (Fig. 16.35). No fatal collapse happened to the tunnel.

Figure 16.36 shows the blocks of arch of 五龍 tunnel in Taiwan, 1999. The arch was compressed and survived the strong earthquake, although surface of mountain slope fell down near this tunnel. Finally, Fig. 16.37 indicates the failed shape of a water tunnel of Kakkonda (葛根田) No. 2 hydraulic power plant after the 1998 Iwate-Ken Hokubu (岩手県北部) earthquake. In spite of the caving-in of soil, this tunnel survived the quake.

In summary, a tunnel in good soil/rock conditions has a remarkable resistance against earthquake. The safety of its entrance, however, depends upon the structural resistance or the slope stability of the mountain.

16.8 Effects of Earthquake Fault on Embedded Pipelines

Figure 16.38 illustrates a buckling failure of water pipeline that crossed a seismic fault upon the 1990 Manjil earthquake in Iran. The compressive tectonic movement across the fault exerted superposition of compression and bending (Fig. 16.39). This type of loading as occurs in a reverse fault (Fig. 16.1) can cause failure of a pipe easily. In contrast, tensile deformation due to a normal fault is not so important because flexibility of modern pipes can catch up with this movement. Thus, engineering concerns have been focused on a reverse fault.

When a softer soil layer rests on a harder base layer in which fault action occurs, the soil deformation at the pipe depth is not so concentrated (discontinuous) as Fig. 16.39 suggests. Figure 16.40 illustrates what is called flower structure in the surface soil. Since the displacement of soil is distributed over a certain range, the damage to a pipeline is reduced. Refer to Sect. 16.6 for experimental and field findings on the geometry of this flower structure. Seismic design of a pipeline is carried out by assessing the displacement of soil and then connecting a pipeline with the surrounding soil by means of springs (Fig. 16.41). The pipeline is considered safe if the bending angle of the pipe is less than a critical value. The critical angle is typically around  $40^\circ$ , which changes depending on the material and geometry of the pipe. Note that the assessment of fault-induced displacement is not an easy task yet.



Fig. 16.38 Buckling of pipeline due to fault action (Manjil earthquake, Iran, 1990)

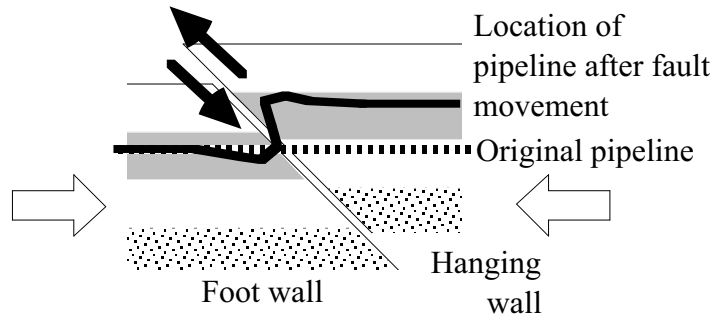


Fig. 16.39 Superposition of compression and bending around reverse fault

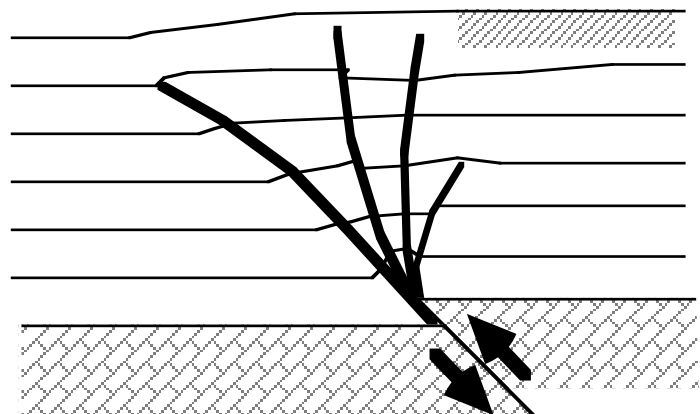


Fig. 16.40 Flower structure of distortion in surface soft soil produced by reverse fault action

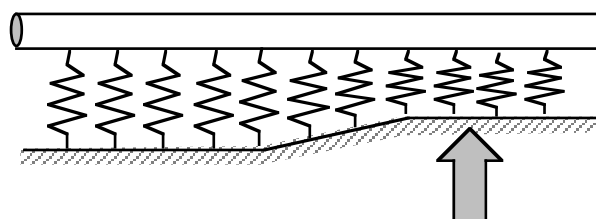


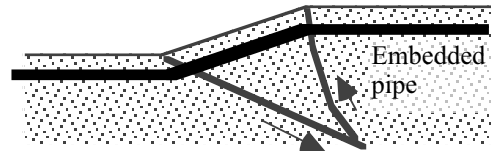
Fig. 16.41 Analytical model of pipeline undergoing reverse fault action



Figure 16.42 shows the surface geometry of Tachikawa fault to the west of Tokyo. This place is close to the site in Fig. 16.5. The road in this photograph comes up towards the hanging wall side of the fault. This fault moved most probably more than 10,000 years ago and the time of the next action is attracting concerns from the disaster mitigation business. When a pipeline is installed across the fault, the pipe is bent from the beginning (Fig. 16.43). This initial bending increases the buckling resistance of the pipe (Fig. 16.25), although people may imagine that this initial bending reduces the safety margin to the critical angle (Suzuki, 2006). Yasuda and Hori (2006) proposed a design principle for an embedded pipeline crossing an active fault.



**Fig. 16.42** Tachikawa fault in Tokyo



**Fig. 16.43** Initial shape of pipeline embedded in existing fault slope

**16.9 Fault-Induced Subsidence of Ground**

The 1999 Kocaeli earthquake in Turkey was characterized by subsidence of ground along the south coast of Izmit Bay (Fig. 16.44). Figure 16.45 illustrates the postearthquake appearance of a coast in Ihsaniye in which light poles and a small house were inundated under water without tilting. It seems therefore that the subsoil did not fail, but simply sank during the quake.

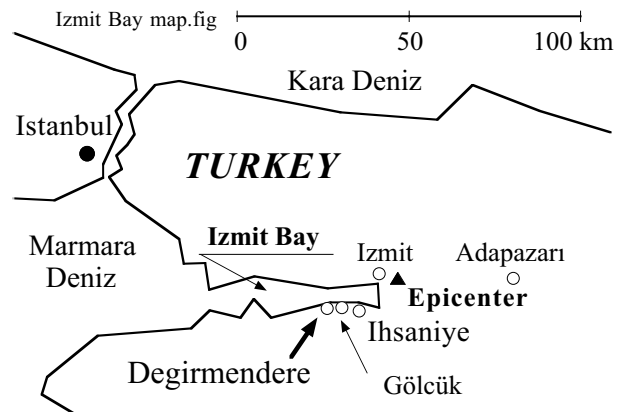
Figure 16.46 compares the bathymetry (sea depth) before and after the quake, in which the preearthquake depth was obtained from a bathymetric map (海図), while the postearthquake water depth was measured by a reconnaissance team organized by the Japanese Geotechnical Society. Off Ihsaniye, for example, two sea depth curves are parallel to each other, suggesting again a vertical subsidence of the sea floor.



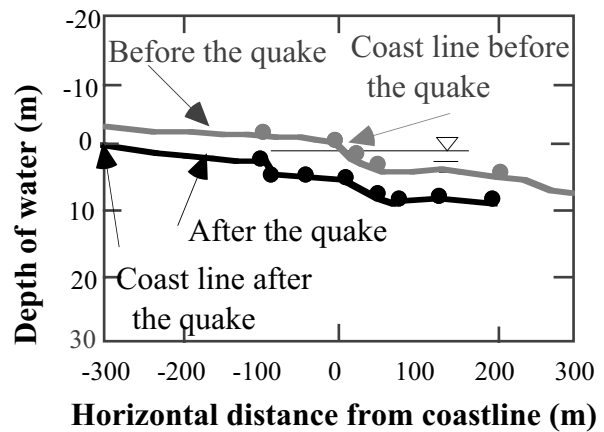
**Fig. 16.45** Inundation of ground at coast of Ihsaniye



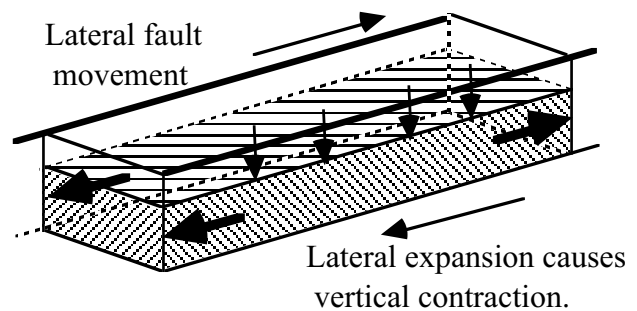
**Fig. 16.47** Fault action at surface of Gölcük



**Fig. 16.44** Map of Izmit Bay area in Turkey



**Fig. 16.46** Change of sea depth during the earthquake at Ihsaniye (Towhata et al., 2001)



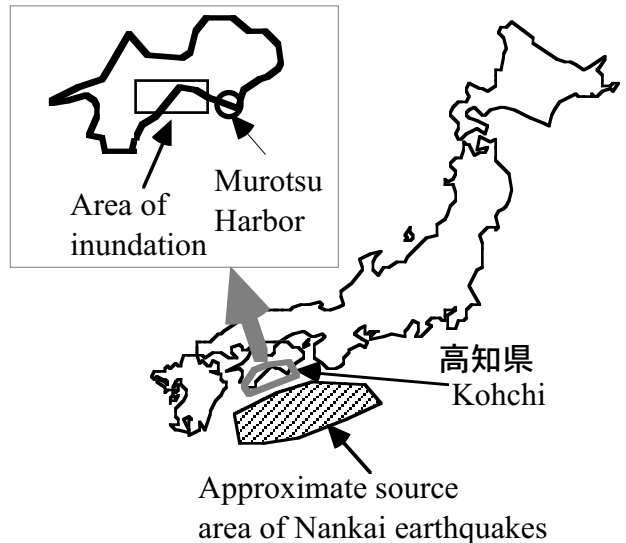
**Fig. 16.48** Mechanism of pull-apart action and ground subsidence

It is inferred that the subsidence was caused by what is called a Pull-Apart action of a seismic fault. The fault of this earthquake was of a lateral-slip type, and the slip motion reached the surface along two lines. Figure 16.47 shows one of them, which appeared on shore. The vertical step is a part of the concerned subsidence. Another fault action is supposed to be in the bottom of the Izmit Bay. When a lateral slip takes place along two lines as illustrated in Fig. 16.48, the soil mass between lines is elongated laterally and a vertical compression (subsidence) occurs for the balance of volume. Note that the subsidence of the coast line at Degirmendere during the same earthquake was probably a consequence of a submarine slope failure; destroying a hotel building which used to be located on shore.

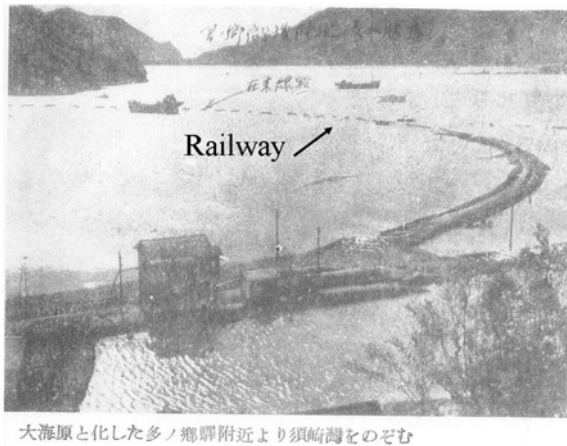
**16.10 Tectonically Induced Ground Subsidence into Sea During Strong Earthquakes in Kohchi, Japan**

Figure 16.49 indicates the location of Kohchi Prefecture of Japan, which is situated close to the source of Nankai gigantic earthquakes. Being repeated at every 150 years or so (Fig. 18.11), the Nankai earthquakes in the past caused tectonic subsidence of the area repeatedly.

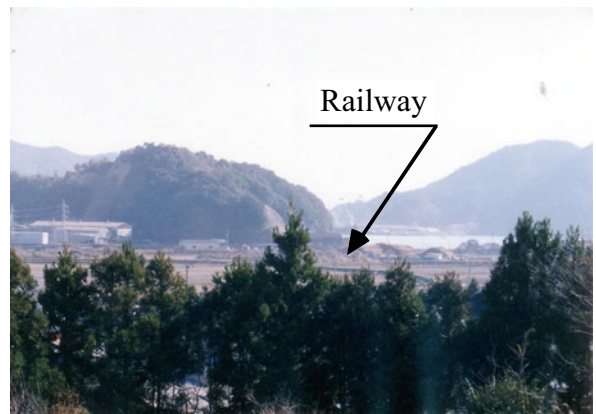
Table 16.2 shows the subsidence history in the area that was recorded during past earthquakes. It is interesting that the area of water submergence is similar in all the events. The most recent experience in 1946 showed that the water submergence finished after several months due possibly to the tectonic uplift of the region. Figure 16.50 illustrates water submergence of Suzaki City. When the author visited this place in 1990s (Fig. 16.51), the ground was already above water. Kishigami together with Kawasumi and Sato showed the change of sea level after the quake to demonstrate that the water level went down relative to the shore, which is actually an evidence of slow uplift of the ground towards the original level (Figs. 16.52 and 16.53).



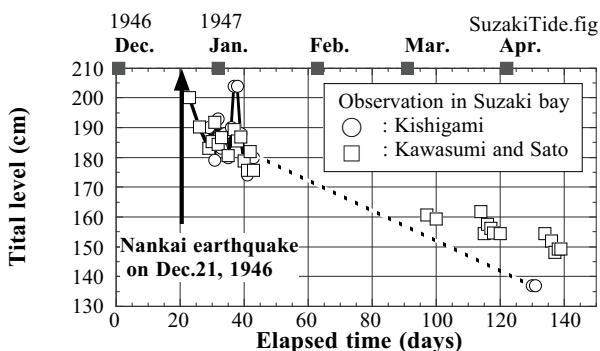
**Fig. 16.49** Location of Kohchi Prefecture of Japan



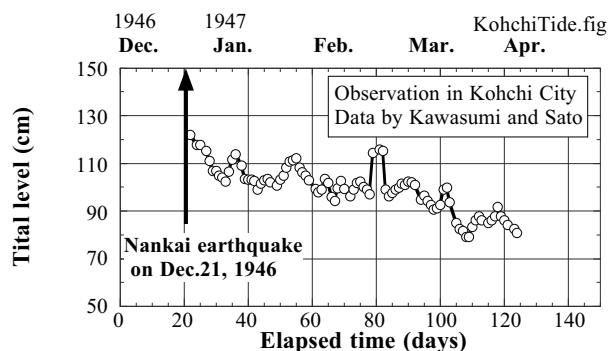
**Fig. 16.50** Inundation in Suzaki in 1946 (Kohchi Prefectural Government)



**Fig. 16.51** Suzaki city in 1990s



**Fig. 16.52** Recovery of tidal level in Suzaki Bay of Kohchi Prefecture



**Fig. 16.53** Recovery of tidal level in Kohchi City

Table 16.2 shows only five events of regional subsidence during the period of more than 1,100 years. Particularly, the interval between two events in 684 and 1099 is very long. This does not mean that no

subsidence occurred during that interval. This lack of event is simply due to disappearance of written records. Figure 18.11 is a product of studies that verified the occurrence of unknown big earthquakes in the Kohchi region. Most probably, those events were accompanied by regional inundation as well.

**Table 16.2** Written history of land submergence in Kohchi area during past earthquakes (data collected from Usami, 1996, and Archives of Historical Records of Earthquakes)

Japanese calendar	yy/mm/dd	Area of submergence	Remarks
天武Ten-mu 13	684/11/29	10 km <sup>2</sup>	白鳳大地震 $M=8+1/4$ , 水没50余萬頃と伝える。Hakuho earthquake; approx. 10 km <sup>2</sup> of rice field inundated <sup>a</sup> .
承德Shotoku 3	1099/2/22	10 km <sup>2</sup>	$M=8.0-8.3$ , 田の水没千余町と伝える <sup>b</sup> Inundation > 10 km <sup>2</sup>
宝永Ho-ei 4	1707/10/28	20 km <sup>2</sup>	宝永大地震 Ho-ei big earthquake $M=8.4^c$
安政Ansei 元1	1854/12/24	15 km <sup>2</sup>	安政南海地震 Ansei-Nankai earthquake $M=8.4^d$ , Inundation in similar area as in 1946
昭和Showa 21	1946/12/21	15.3 km <sup>2</sup>	南海地震 Nankai earthquake <sup>e</sup> $M=8.0$ ; Inundation over 9.3 km <sup>2</sup> in Kohchi 高知 City, 3.0 km <sup>2</sup> in Suzaki 須崎, and 3.0 km <sup>2</sup> in Sukumo 宿毛

- a (天武天皇)十三年十月巳卯朔 (中略) 土佐國田苑五十餘萬頃没為海 古老曰若是地動未曾有也(日本書紀) : “In AD 684, approximately 10 km<sup>2</sup> of rice field was inundated under sea. Local people had never experienced this type of disaster.” The official history book of Japanese Government (eighth Century).
- b According to Archives of Historical Records of Earthquakes (日本地震史料), Vol. 1, p. 54, 國內作田千餘町皆以成海底畢 (廣橋本兼仲卿記): “>10 km<sup>2</sup> of rice field was inundated.” Sir Kanenaka’s diary. Note that “diary” in those days was not the one in the modern sense. Court people made personal records of the ceremonial procedures and many occasions in the Imperial Court so that they would precisely follow the traditions if a similar situation occurs again. Such records were called diary. It is peculiar that Sir Kanenaka lived in the second half of the thirteenth Century, which is almost 200 years later than this earthquake. Did he know much about the earthquake damage precisely? One possibility is that Sir Kanenaka studied historical documents in the court and described it in his diary. Another story is that, in late eleventh century, there was another Kanenaka in the ruling Fujiwara family who was a great-grand son of Michikane, the second elder brother of famous Michinaga, and that two Kanenakas were confused. The author could not clarify this point.
- c 南海志 日本地震史料, 第三卷別卷 (Archives of Historical Records of Earthquakes Separate Volume of Vol. 3) pp. 428–435; 土佐古今大震記, 日本地震史料 第三卷別卷 (Ditto) pp. 448–452.
- d 室津湊の潮四尺許りも足り申さざる様に相成りて (室戸町誌) The sea level in Murotsu Harbor (Fig. 16.49) appeared to be 1.2 m lower than before. History of Muroto Town, 日本地震史料 第五卷別卷五一二 (Archives of Historical Records of Earthquakes Separate Volume 5–2 of Vol. 5), p. 2309. (Note: the lower sea level actually meant uplift of earth crust.)  
History of Ohkata Township quoted Mr. N. Miyaji as saying “Rice field near beach of Nishi-Hijiri was inundated under sea for two years and became land again after 7–10 years” (ditto, p. 2339).  
A stone monument in Irino-Kamo shrine has a description that rice field became sea as had occurred during the Ho-ei earthquake (ditto, p. 2339).
- e Many records were assembled by Kohchi Prefectural Government.

## 16.11 Earthquake-Induced Subsidence in Other Parts of the World

Valdivia is a city in the south part of Chile (Fig. 16.54). It was shaken by an extremely strong earthquake in 1960. According to eyewitness reports, *El terreno bajó entre 1,50 y 2 metros* (the ground sank between 1.5 and 2 m; Rodríguez, 1998). This subsidence, however, did not result directly in water submergence. The problem was a natural dam (Sect. 15.3) formed by many landslides in the upstream area of a river. Since the dam appeared to collapse soon, people intentionally opened a water channel and discharged water downstream. Consequently, the river water level was raised in Valdivia City, and, since the ground level was lower than before, the entire city was submerged under water. Figure 16.55 shows that many streets were submerged under water depth of about 2 m (Alvarez, 1963; Housner, 1963; Thomas et al. 1963; Weischet, 1963).

*Al descender el terreno, las calles y los edificios de las orillas del río fueron cubiertos por el agua;* upon the subsidence of ground, streets and buildings along the river shores were covered by water (Castedo, 2000).

Cisternas (2005) investigated the geological evidences of past tsunamis and inundations to show that the previous significant subsidence occurred in 1575. Figure 16.56 presents the recent (Dec, 2001) view of Haverbeck Island in the city. Seed and Idriss (1982) mentioned that this island subsided into water due to combination of tectonic action and densification of sand. Since the island is again above the water today, it seems that the tectonic movement was the major cause of the vertical motion. Densification is an irreversible process and cannot be restored as actually occurred.



Fig. 16.54 Location of Valdivia.



Fig. 16.55 Inundation of Valdivia City (Soto Melo)



Fig. 16.56 Present view of Haverbeck Island

Similar tectonic subsidence occurred in other parts of the world. For example, Atwater (1987), Atwater and Yamaguchi (1991), and Atwater (1992) examined the date of dead trees and grasses as well as buried liquefaction to find that the coastal area of the Washington State, USA, subsided suddenly by

0.5–2.0 m several times in the past 2,000 years. Nelson (1992) studied the estuary deposit in Oregon to show localized coseismic subsidence as well. Moreover, Ota and Umitsu (1995) together with Ota et al. (1995) studied diatom fossils in subsoil to show that subsidence occurred once every hundreds of years and that each event was accompanied by subsidence of 0.5 m.

At the time of the great earthquake in Alaska, 1964, significant tectonic movement, which consisted of both subsidence and uplift, was reported (Plafker, 1969). A typical example of this subsidence occurred in the township of Portage (Reported by Cohen). Being threatened by water submergence upon high water table, people had to move their residences to higher places. Being different from those in Kohchi (Sect. 16.9) and Valdivia, the subsidence in the Pacific coast area of North America did not recover. Finally, the great earthquake of magnitude exceeding 9.0 in the Indian Ocean caused tectonic subsidence in the west coast of Sumatra (Fig. 16.57) as well as in the Andaman Islands (at the maximum 3 m of subsidence, EERI, 2005; Malik and Murty, 2005).

The cover of this book presents the landscape of Kisagata (象潟) where many islands in a calm lagoon used to produce a beautiful scenery. There is a folklore that those islands were created by seismic subsidence and inundation upon an earthquake in AD 850 (嘉祥3年).

More local subsidence occurs due to densification of subsoil. Examples of this kind of subsidence, such as the case in Luzon Island of the Philippines in 1990 (Fig. 16.58; also refer to Sect. 18.14), will be addressed in Sects. 17.8 and 17.11.



**Fig. 16.57** Disappearance of beach over 100 meters in Lepung of Aceh Province, Sumatra, Indonesia



**Fig. 16.58** Subsidence of Narbakan Peninsula due probably to densification of loose and young sandy deposit

## 16.12 Geotechnical Aspects of Tsunami

Sections 15.7 and 15.8 addressed a tsunami-generated slope failure at Seward, Alaska, and Nice, France. The more widely-known effects of tsunami is characterized by its significant drag force. The drag force is stronger when the water goes back to the sea than when the wave comes to the land (Fig. 16.59). This is because the coming water is rather uniformly distributed along a coast line, while the retreating water is concentrated in a limited size of channel (Fig. 16.60). When water flows over a dike or an embankment, erosion or scouring is possible (Fig. 16.61). Also, the ground surface is covered by deposits of sea-bed sand, which is transported by the tsunami propagation. When a sea dike is destroyed by such a mechanism, a lowland behind a dike may be inundated. Damages caused by such mechanisms are illustrated in figures in this section. In case of Fig. 16.62, a former quay wall remains in the sea, while the backfill ground was eroded into the sea. In Fig. 16.63, the house that faced the sea was destroyed by tsunami, while the other one behind was not. This was probably because the wave effects were reduced by the first house.



**Fig. 16.59** Sea wall destroyed by retreating tsunami water (1993 Hokkaido Nansei-oki earthquake)



**Fig. 16.60** Village destroyed by tsunami, Mindro Island, the Philippines



**Fig. 16.61** Scoured ground behind road embankment (Banda Aceh, Indonesia)



**Fig. 16.62** Former quay wall and eroded backfill area (Banda Aceh, Indonesia)



**Fig. 16.63** Destroyed and intact houses after tsunami effects (Samalanga, Sumatra, Indonesia)

It is widely believed that the attack of tsunami is preceded by retreating of sea water. However, this is not necessarily true. It is sometimes possible that the sea bed rises due to fault rupture and tsunami attack begins with sudden high water level. In this light, a global tsunami warning network is needed. Since tsunami is a rare event, it is important to continue maintaining efforts for a warning network for many decades. Construction of emergency refugee places (high buildings etc.) is another way to mitigate damages.

The significance of tsunami can be evaluated by using a recently developed tsunami intensity scale (Papadopoulos and Imamura, 2001). It is briefly described in what follows. Being based on people's response and extent of damage at respective localities, the tsunami intensity scale is of similar nature as seismic intensity scale (Sect. 5.1). Hence, it does not account for the entire tsunami energy. For more information, visit <http://geology.about.com/library/bl/bltsunamiscalenew.htm> or refer to Yalçiner et al. (2004).

**Table 16.3** Definition of tsunami intensity scale by Papadopoulos and Imamura (2001)

Scale	Rank	Brief description (tsunami height is a rough idea.)
<b>I</b>	Not felt.	
<b>II</b>	Scarcely felt	Few people on board small vessels feel it. There occurs no damage
<b>III</b>	Weak	Observed by a few people on the coast, but no damage
<b>IV</b>	Largely observed	Observed by most people on the coast
<b>V</b>	Strong	Few people are frightened and try to escape. Minor effects of wave on the coast
<b>VI</b>	Slightly damaging	Tsunami height may be 2 m. Damage and flooding to some extent
<b>VII</b>	Damaging	4 m high tsunami. Many people are frightened and try to escape. Objects overturn and drift, and many wooden structures are damaged
<b>VIII</b>	Heavily damaging	4 m high wave. All people escape but a few are washed away. Few large ships are moved towards the shore. Most wooded buildings are washed away or destroyed
<b>IX</b>	Destructive	8 m high tsunami. Many people are washed away. Many large ships are moved significantly, and sand beach is eroded remarkably. Light damage in reinforced concrete buildings
<b>X</b>	Very destructive	8 m high tsunami. Most people are washed away. Buildings are damaged
<b>XI</b>	Devastating	16 m high tsunami. Flooding makes many objects drift and transport them into the sea. Buildings are damaged.
<b>XII</b>	Completely devastating	32 m high tsunami. Most reinforced-concrete buildings are damaged

Tsunami is generated not only by seismic shaking or tectonic movement but also landslides. For example, the tsunami that destroyed Valdez of Alaska was caused by a submarine landslide which was triggered by an earthquake (Sect. 15.7). Another example is a prehistoric one which was caused by the gigantic Storegga Slide in the Norwegian Sea of the North Atlantic Ocean (Jansen et al. 1987; Bugge et al. 1988; Nisbet and Piper, 1998) and an induced tsunami attacked Scotland as evidenced by a sandy

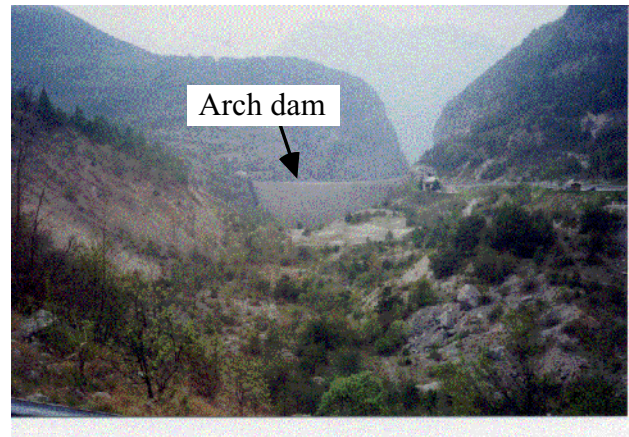


layer, which was transported from the sea bed to land (Dawson et al. 1988; Long et al. 1989). The highest tsunami so far known is the one that occurred in Lituya Bay of Alaska in 1958 and hit trees at an elevation of 520 m above the water level. When an earthquake of magnitude = 8.3 occurred in the south east part of Alaska, a rock slope above a narrow Lituya Fjord fell down into water and generated this tsunami (Miller, 1960). A similarly generated tsunami is the one at Vajont Dam in 1963 (Nonveiller, 1987). The first filling of water in a newly constructed dam lake caused a gigantic rock slide of 200 million m<sup>3</sup> in volume (Müller-Salzburg, 1987) into reservoir and triggered a tsunami. This tsunami overtopped the Vajont arch dam by more than 200 m and caused significant flooding in the downstream area. The dam body itself, however, was not destroyed by this overtopping; see Fig. 16.64 for present situation of the Vajont dam site.

(a) Slip plane of rock mass fall.



(b) Remaining earth dam body and fallen rock mass (seen from upstream side).



**Fig. 16.64** Present landscape of former Vajont dam site (photograph by Mr. Z. Athanasios)

### List of References in Chapter 16

- Alvarez, S.L. (1963) Studies made between Arauco and Valdivia with respect to the earthquake of 21 and 22 May 1960, *Bull. Seismol. Soc. Am.*, Vol. 53, No. 6, pp. 1315–1330.
- Atwater, B.F. (1987) Evidence for great Holocene earthquakes along the outer coast of Washington State, *Science*, Vol. 236, pp. 942–944.
- Atwater, B.F. (1992) Geologic evidence for earthquakes during the past 2000 Years along the Copalis River, Southern Coastal Washington. *J. Geophys. Res.*, Vol. 97, B2, pp. 1901–1919.
- Atwater, B.F. and Yamaguchi, D.K. (1991) Sudden, probably coseismic submergence of Holocene trees and grass in coastal Washington State, *Geology*, Vol. 19, pp. 706–709.
- Bray, J.D. and Rodriguez-Marek, A. (2004) Characterization of forward-directivity ground motions in the near-fault region, *Soil Dyn. Earthq. Eng.*, Vol. 24, pp. 815–828.
- Bray, J.D. and Rodriguez-Marek, A. (2006) Design ground motions near active faults, *Proc. New Zealand Workshop Geotech. Earthq. Eng.*, Christchurch, pp. 19–31.
- Bray, J.D., Seed, R.B. and Seed, H.B. (1993) 1 g small-scale modelling of saturated cohesive soils, *Geotech. Test. J.*, ASTM, Vol. 16, No. 1, pp. 46–53.
- Bugge, T., Belderson, R.H. and Kenyon, N.H. (1988) The Storegga Slide, *Phil. Trans. Roy. Soc. Lond.*, A. 325, pp. 357–388.
- Castedo, Leopoldo (2000) Hazaña del Riñihue, El terremoto de 1960 y la resurrección de Valdivia, p. 37.
- Cisternas, M., Atwater, B.F., Torrejon, F., Sawai, Y., Machuca, G., Lagos, M., Eipert, A., Youlton, C., Salgado, I., Kamataki, T., Shishikura, M., Rajendran, C.P., Malik, J.K., Rizal, Y. and Husni, M. (2005) Predecessors of the giant 1960 Chile earthquake, *Nature, Letters*, Vol. 437, pp. 404–407.

- Cohen, S. The Great Alaska earthquake, p. 40.
- Cole, D.A.J. and Lade, P.V. (1984) Influence zones in alluvium over dip-slip faults, *J. Geotech. Eng., ASCE*, Vol. 110, No. 5, pp. 599–625.
- Doyel, W.W. and Moraga B., A. (1963) Relation between the geology of Valdivia, Chile, and the damage produced by the earthquake of 22 May 1960, *Bull. Seismol. Soc. Am.*, Vol. 53, No. 2, pp. 1331–1345.
- EERI (2005) The Great Sumatra earthquake and Indian Ocean tsunami of December 26, 2004, Special Earthquake Report, pp. 1–12.
- Gonzaro Soto Melo “Valdivia 1960,” Imprenta Gráfica Sur, Valdivia, Chile.
- Housner, G.W. (1963) An engineering report on the Chilean earthquakes of May 1960. *Bull. Seismol. Soc. Am.*, Vol. 53, No. 2, pp. 219–223.
- Jansen, E., Befring, S., Bugge, T., Eidvin, T., Holtedahl, H. and Sejrup, H.P. (1987) Large submarine slides on the Norwegian continental margin: Sediments, transport and timing. *Marine Geol.*, Vol. 78, pp. 77–107.
- JSCE (1936) Record of Tanna Tunnel construction, ed. Atami Railway Construction Office, Ministry of Railway, p. 427.
- Kawasumi, H. and Sato, Y. Geodetic effects, tsunami, and intensity of motion during the Nankai earthquake, Appendix, Nankai Earthquake Report, Kohchi Prefectural Government (in Japanese).
- Kishigami, F. Recovery of tectonic uplift/subsidence after gigantic earthquake in Tosa (Kohchi), Appendix, Nankai Earthquake Report, Kohchi Prefectural Government (in Japanese).
- Kohchi Prefectural Government: Nankai Earthquake Report (in Japanese).
- Malik, J.N. and Murty, C.V.R. (2005) Landscape changes in Andaman and Nicobar Islands (India) due to Mw 9.3 tsunamigenic Sumatra earthquake of 26 December 2004, *Current Science*, Vol. 88, No. 9 and 10, pp. 1384–1386.
- Matsuda, T. (1975) Magnitude and recurrence interval of earthquakes from a fault, *J. Seismol. Soc. Jpn.*, Vol. 28, pp. 269–283 (in Japanese).
- Miller, D.J. (1960) Giant Waves in Lituya Bay Alaska, USGS Professional Paper, 354-C, Shorter Contributions to General Geology.
- Müller-Salzburg, L. (1987) The Vajont catastrophe – A personal review, *Eng. Geol.*, Vol. 24, pp. 423–444.
- Nelson, A.R. (1992) Holocene tidal-marsh stratigraphy in south-central Oregon – Evidence for localized sudden submergence in the Cascadia subduction zone, *Quaternary Coasts of the United States, Marine and Lacustrine Systems*, SEPM Special Publication No. 48, pp. 282–301.
- Nisbet, E.G. and Piper, D.J.W. (1998) Giant submarine landslides, *Nature*, No. 392, pp. 329–331.
- Nonveiller, E. (1987) The Vajont reservoir slope failure, *Eng. Geol.*, Vol. 24, pp. 493–512.
- Okada, K., Ikeda, K. and Hasegawa, T. (2000) Active faults from site investigation to design, *Kajima Publ.*, ISBN 4-306-02339-7, p. 182 (in Japanese).
- Ota, Y. and Umitsu, M. (1995) Stratigraphic, radiocarbon and diatom indicators of sudden submergence along the Nessel River mouth, Washington, USA, *J. Geogr.*, Vol. 104, No. 1, pp. 107–112 (in Japanese).
- Ota, Y., Nelson, A.R., Umitsu, M., Kashima, K. and Matsushima, Y. (1995) Interpreting an earthquake history from the stratigraphy of late Holocene intertidal deposits in South Slough, Coos Bay, Oregon, USA, *J. Geogr.*, Vol. 104, No. 1, pp. 94–106 (in Japanese).
- Papadopoulos, G.A. and Imamura, F. (2001) A proposal for a new tsunami intensity scale, *Proc. Int. Tsunami Symp. 2001*, Seattle.
- Pettinga, J.R. (2006) Active tectonics of Northeastern South Island – NZ: Earthquake-driven landscape evolution in the plate boundary transfer zone, *Proc. New Zealand Workshop Geotech. Earthq. Eng.*, Christchurch, pp. 351–393.
- Plafker, G. (1969) Tectonics of the March 27, 1964, Alaska earthquake, *The Alaska Earthquake, March 27, 1964: Regional effects*, US Geological Survey Professional Report, 543-I.

- Purkey, B.W. and Garside, L.J. (1995) Geologic and natural history tours in the Reno area, Nevada Bureau of Mines and Geology Special Publication 19.
- Rodríguez Lamas, Digna (1998) Acuarela en el Rio II “La Ciudad Sumergida,” p. 12.
- Seed, H.B. and Idriss, I.M. (1982) Ground motions and soil liquefaction during earthquakes, Engineering Monograph on Earthquake Criteria, Structural Design, and Strong Motion Records, Earthq. Eng. Res. Inst., University of California, Berkeley, p. 12.
- Sekiguchi, K., Sugito, M., Oka, F., Yashima, A., Taguchi, Y. and Kato, Y. (1996) Non-linear amplification characteristics of ground motions and examinations of analyses methods based on the borehole strong motion array records obtained during the south Hyogo Earthquake, Proc. Special Conf. Kobe Earthq., JSCE (in Japanese).
- Somerville, P.G., Smith, N.F., Graves, R.W. and Abrahamson, N.A. (1997) Modification of empirical strong ground motion attenuation relations to include the amplitude and duration effects of rupture directivity, *Seismol. Res. Lett.*, Vol. 68, No. 1, pp. 199–222.
- Suzuki, Nobuhisa (2006) Personal communication.
- Tani, K., Ueda, K., Abe, S., Nakata, H. and Hayashi, H. (1997) Deformation structure of surface unconsolidated layer along the Nojima earthquake, Proc. JSCE, No. 568/III-39, pp. 21–39 (in Japanese).
- Taniyama, H. and Watanabe, H. (1998) Deformation of sandy deposit by reverse faulting, Proc. JSCE, 591/I-43, pp. 313–325.
- Tchalenko, J.S. and Ambraseys, N.N. (1970) Structural analysis of the Dasht-e Bayāz (Iran) earthquake fractures, *Bull. Geol. Soc. Am.*, Vol. 81, pp. 41–60.
- Thomas, H., Bowes, W. and Bravo S., N. (1963) Field observations made between Puerto Montt and Maullin, *Bull. Seismol. Soc. Am.*, Vol. 53, No. 2, pp. 1353–1356.
- Towhata, I., Ishihara, K., Kiku, H., Shimizu, Y., Horie, Y. and Irisawa, T. (2001) Submarine slides and land settlements in coastal areas during Kocaeli earthquake, Satellite Conf. Earth. Geotech., 16th Int. Conf. Soil Mech. Geotech. Eng., Istanbul, pp. 71–76.
- Ueta, K. (1993) Deformation of Quaternary deposits and ground surface caused by bedrock fault movements – Field surveys of active faults, Abiko Research Laboratory Report U893007, Central Research Institute of Electric Power Industry.
- Ueta, K. and Tani, K. (1999) Deformation of quaternary deposits and ground surface caused by bedrock fault movements, Part 2, - Normal and reverse fault model tests, Report of Central Research Institute of Electric Power Industries.
- Usami, T. (1996) Comprehensive list of destructive earthquakes in Japan [Revised and Enlarged Edition], University of Tokyo Press, ISBN4-13-060712-X (in Japanese) (宇佐美龍夫著 新編日本被害地震総覧[増補改定版]、東京大学出版会).
- Weischet, W. (1963) The distribution of the damage caused by the earthquake in Valdivia in relation to the form of the terrane, *Bull. Seismol. Soc. Am.*, Vol. 53, No. 6, pp. 1259–1262.
- Yalçiner, A., Pelinovsky, E., Talipova, T., Kurkin, A., Kozelkov, A. and Zaitsev, A. (2004) Tsunamis in the Black Sea: comparison of the historical, instrumental, and numerical data, *J. Geophys. Res.*, Vol. 109, C12023.
- Yasuda, S. and Hori, M. (2006) Framework of design procedures of pipeline structures against surface earthquake faulting, Proc. 2nd Japan–Taiwan Joint Workshop, Nagaoka, ATC 3 domestic Committee of Japanese Geotechnical Society (JGS), pp. 232–235.

# PART 3

## Liquefaction



Hindu temple in Kajaraho, India, which is famous for realistic sculptures.

# Chapter 17

## Features of Liquefaction-Induced Damages



This is a ruin of the main entrance to Troy, which is situated in present Turkey.

## 17.1 Introduction to Seismic Liquefaction

Seismic liquefaction occurs in loose sandy ground that is saturated with water. When pore water pressure rises during shaking, the effective stress decreases with time (1.4);

$$\text{Effective stress} = \text{Total stress (weight of overburden soil)} - \text{pore water pressure} \quad (17.1)$$

有効応力 = 全応力 (土かぶり圧、土の重さ) - 間隙水圧

Shear modulus of sand decreases as the effective stress decreases. Shear strength of sand decreases with  $(\text{effective stress})\tan\phi$ . Thus, sandy ground becomes softer with time.

*In the extreme case, the effective stress becomes zero.* Since the effective stress stands for the contact force at grain-to-grain contacts in sand, the zero effective stress suggests that there is *no effective contact between grains*. Hence, grains are actually floating in pore water without constraint from surrounding sand particles. Now sand is similar to mud water; grains are in suspension in water.

After complete loss of effective stress, sand has neither shear modulus nor shear strength, and consequently develops large deformation even under minor shear stress (Figs. 17.1 and 17.2).



**Fig. 17.1** Distortion of quay wall along Shinano River and falling of Showa Bridge in Niigata, 1964 (Department of Civil Engineering, University of Tokyo)



**Fig. 17.2** Subsidence and tilting of building in Niigata (Department of Civil Engineering, University of Tokyo)

It was not until 1964 when liquefaction came to be considered seriously by engineers. In early days, collapse of buildings and failure of slopes were more important and more harmful than liquefaction, because those conventional types of seismic damage caused more human casualties. In contrast, liquefaction does not kill people, although it is hazardous to modern structures.

Further, liquefaction occurs in loose sandy deposits that are found in abandoned river channels, young alluvial planes, and human reclamations. These areas of high liquefaction potential were not used by human activity before. Therefore, liquefaction used to be nothing but a geological phenomenon, and it was not a threatening to our society.

In recent times, urban development has spread into those areas that were not made use of before. Areas of soft soil used to be agricultural areas, and in particular, rice field: people lived on more

stable ground. In many cases, these newly urbanized areas have loose sandy deposit with high ground water level; hence, the liquefaction potential is high as well. Since land reclamation became popular, liquefaction-susceptible ground has been produced. In summary, liquefaction as a natural hazard is a consequence of spreading of urbanization into unsuitable ground conditions.

In 1964, Niigata in June and Anchorage, Alaska, in March were hit by earthquakes. Both earthquakes caused serious liquefaction and damage. In this particular year, studies on mechanism and prediction of liquefaction as well as remedial measures (対策) were commenced.

Engineering topics concerning liquefaction are indicated below:

Case history 事例研究: liquefaction-prone soil conditions and topography, type of damage and its causative mechanism, intensity of earthquake motion needed to trigger liquefaction, etc.

Assessment of liquefaction potential 液状化の危険度評価: field investigation, laboratory testing on liquefaction resistance of soil, undisturbed sampling of loose sand, etc.

Consequence of liquefaction 液状化の結果: permanent deformation and displacement caused by liquefaction

Dynamic response analysis 動的解析: prediction of amplification, acceleration, etc. together with development of excess pore water pressure and decrease in effective stress; shear modulus and strength decreasing with time and affecting the modulus, stiffness, and characteristics of amplification

## 17.2 History of Problems and Research Topics Concerning Liquefaction

Since the problem of liquefaction became important in 1960s, many topics have attracted engineering concerns. The following information may be useful for better understanding of the history of efforts so far made.

**Table 17.1** Historical change of important topics in study of liquefaction

Topics	Years	Remarks
Mechanism of liquefaction	1960s	Niigata and Alaska earthquakes in 1964
Assessment of liquefaction potential	1970s–1980s	Minimum SPT- <i>N</i> , Factor of safety, Low liquefaction potential of gravel and fine silt Ground subsidence after liquefaction
Prevention of liquefaction	1970s–now	Soil improvement (compaction, gravel drain, grouting, mitigation under existing structures etc.)
Consequence of liquefaction	1983–2000	Even gravels and cohesionless silt liquefy Permanent displacement; cause and prediction of displacement
Mitigation of permanent displacement	1995–now	Reliability of lifeline / river dike Use of underground wall Protection of existing structures
Real-time earthquake engineering	1990s–now	Quick detection of liquefaction (within one hour and starting emergency action as quickly as possible)
Methods of study		
Case history		Investigation at earthquake damage sites
Laboratory shear tests		Undrained cyclic loading or undrained monotonic loading up to large deformation
Shaking model tests		Understanding of behavior of earth structures
Numerical analysis		Development of numerical tool to predict earthquake response and large deformation of liquefied ground



### 17.3 Loss of Bearing Capacity Caused by Liquefaction

Since effective stress disappears in sandy ground after liquefaction, bearing capacity disappears as well and significant subsidence occurs in foundation of surface structures. Figure 17.3 was taken in Dagupan City, the Philippines. An RC building subsided into liquefied ground due to loss of bearing capacity. Figure 17.4 reveals a flat annex behind this building. The extent of subsidence was smaller for this light flat than the main building. Roofs and windows in the annex were affected by human activities after the quake. Except this, no structural damage such as cracking of walls and columns or breakage of window glasses occurred.

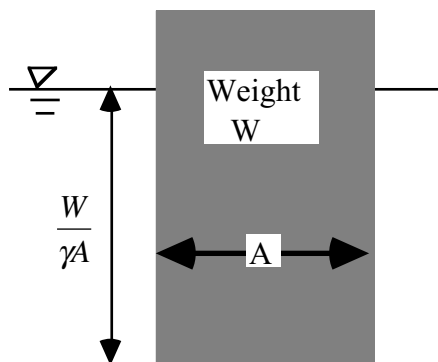
There is a correlation between the differential subsidence of buildings and buoyancy (浮力). In Fig. 17.5 a block of weight “W” and cross section “A” is floating in liquid of unit weight “ $\gamma$ .” At force equilibrium, the depth of the bottom of the object below the surface of liquid is  $W/(\gamma A)$ . This depth increases with the weight of the block. This simple analogy suggests that the subsidence of buildings resting on liquefied ground is at least qualitatively governed by the gravity and buoyancy.



**Fig. 17.3** Subsidence of building in Dagupan City



**Fig. 17.4** Reduced subsidence of lighter annex



**Fig. 17.5** Analogy of buoyancy force



**Fig. 17.6** Inclined apartment buildings in Niigata (Niigata Nippo Newspaper, 1964); arrows added by the author show direction of tilting

Figure 17.6 demonstrates inclined apartment buildings at Kawagishi-cho (川岸町) in Niigata. Arrows in the photograph indicate the direction of tilting. One of the buildings totally fell down. This falling took minutes of time and did not kill people inside. It is further interesting that, except the building at top right of Fig. 17.6 that was supported by a piled foundation, the direction of tilting of other buildings is consistent with the direction of eccentricity of gravity force caused by the roof structure. This is consistent with Fig. 24.25, which will later show that the direction of permanent displacement such as tilting is governed by the gravity force. Figure 17.7 illustrates the foundation in one of the apartment buildings. No pile foundation is seen therein. Before this earthquake, it was believed that sandy ground was a good bearing layer because consolidation settlement in sand was small and bearing capacity was high. Hence, no pile was considered necessary. This traditional idea was abandoned after this earthquake. Finally note that apartment buildings did not have a structural damage due to liquefaction.



**Fig. 17.7** Base of Kawagishi-cho apartment building after falling (Department of Civil Engineering, University of Tokyo)



**Fig. 17.8** Map of Niigata City in 1849

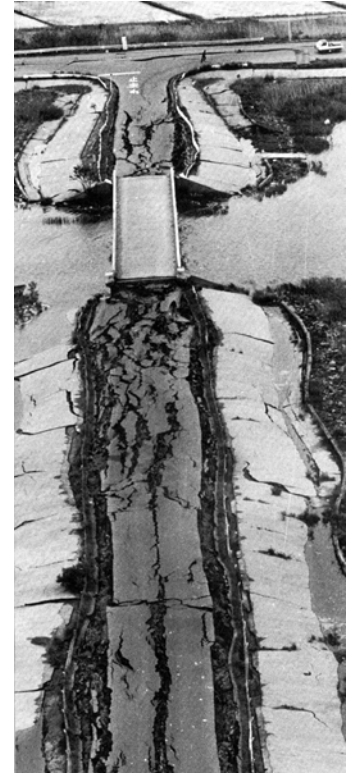
Figure 17.8 illustrates the City of Niigata in 1849. The big water cove along the Shinano River is the site of the apartment buildings. In 1920s, this water inlet was reclaimed by using clean and fine beach sand without densification. Being repeated in Dagupan City as well, reclamation of water by clean beach sand is a typical way to construct liquefaction-prone land.

It is interesting that buildings in Fig. 17.6 have a pent-house at the top (階段の屋上出口). Inclination occurred to the direction of this roof structure. Probably, there was an eccentricity of gravity center due to this added structure. Gravity and buoyancy generated a rotational moment in these buildings and tilting in this special direction resulted.

Figure 17.33 will present subsidence of an oil storage tank into liquefied subsoil.

## 17.4 Subsidence of Embankment due to Liquefaction

Embankment is often constructed on liquefaction-susceptible loose sandy deposits. Figure 17.9 indicates the distortion of road embankment at Gomyoko Bridge, Hachirogata Lake, Akita after the 1983 Nihonkai-Chubu earthquake (日本海中部地震、八郎潟の五明光橋; also see Fig. 14.11). Since the foundation soil lost its bearing capacity, the embankment sank down and at the same time spread laterally. See that many cracks opened in the road pavement in the longitudinal direction of the embankment. This indicates that the embankment spread laterally in the direction of the slope. Tensile deformation occurred in the soil.

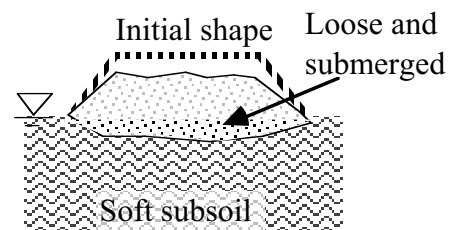


**Fig. 17.9** Liquefaction at Gomyoko Bridge (Akita Sakigake Shinpo Inc.; JSCE, 1986)

Figure 14.13 showed a collapse of Tokachi-River dike, Hokkaido, during the 1993 Kushiro-oki earthquake. This river dike was constructed by stages during the past decades on a peat deposit. Since the peaty soil has an extremely high compressibility (water content = 200%), much amount of embankment soils has subsided into peat. After the earthquake damage, the damaged dike was excavated to study the cause of damage (Fig. 17.10). It is inferred today (Sasaki, 1994) that the former body of the embankment was loosened during the subsidence and lateral expansion (Fig. 17.11). Staying under the ground water table, the dike got water-saturated and liquefied during the earthquake. Similar collapse occurred at the Kushiro-river dike as well. The collapse of the Yodo River dike in Osaka (Fig. 17.35) in 1995 is also similar. Furthermore, Fig. 17.12 indicates a development of multiple shear plane in the harbor embankment in Navrakhi during the 2001 Gujarat earthquake of India (Towhata et al. 2002). This fill was constructed on very soft marine deposit. Thus, gravity force governs the direction of deformation in embankment.



**Fig. 17.10** Excavation of damaged Tokachi-river dike



**Fig. 17.11** Mechanism of loosening of compacted river dike (Prof. Y. Sasaki)

From 2009 on, the seismic design of Japanese river dikes is going to be conducted without taking into account the inertial force (seismic coefficient). This is because liquefaction is the cause of severe damage that may affect the function of dikes (Oshiki and Sasaki, 2001, 2006); minor distortion due to inertial force is able to be restored quickly and is not a serious problem.



**Fig. 17.12** Shear failure of harbor fill in Navrakhi harbor of India

Few reinforcement against earthquake and liquefaction had been practiced in river dikes before 1995. The basic philosophies behind this were (1) embankment made of soil should quickly be repaired (within 2 weeks typically) even if it collapses, and (2) the probability of earthquake and flooding occurring at the same time is very low. When the land elevation behind the embankment is low (<high tidal level + 2 m) and urbanized, seismic provision is performed now. Empirically, the subsidence of embankment is <75% of height (see Fig. 17.36).

Figure 17.13 indicates minor liquefaction at the foot of Tokachi River dike. A limited extent of cracks occurred in the slope as well. There is no need to prevent such minor problems and the philosophy of quick restoration (Fig. 17.14) is still reasonable.



**Fig. 17.13** Minor liquefaction near Tokachi River dike in 2003



**Fig. 17.14** Quick restoration after 2003 Tokachi earthquake

## 17.5 Floating of Embedded Structures

Liquefied sand behaves like liquid that has neither shear stiffness nor shear strength. Its unit weight is about 1.8–2.0 times that of water. When the weight of an embedded structure is less than the buoyancy exerted by the liquefied surrounding sand, the structure floats upwards.

Figure 17.15 indicates the floating of a buried fuel tank in Dagupan City of the Philippines in 1990. The tank contained gasoline, and its apparent unit weight was at the maximum about 1.0 times that of water. Since this unit weight was less than that of liquefied soil, the tank floated.

Figure 17.16 demonstrates a floated sewage tank (浄化槽) in Dagupan City as well. The cause of this floating is similar: buoyancy exceeded gravity. Figure 17.17 shows the floating of manhole in Tokachi River area during the 2003 earthquake. Many manholes floated in this area, which was a land reclamation by using sand. There was a controversy after the earthquake whether this floating was caused by the liquefaction of original ground or liquefaction of backfill soil (poorly compacted?) of sewage pipes (下水管の埋め戻し土).

Figure 17.18 indicates floating of manholes in Shibetsu (標津), Hokkaido, at the time of 1994 Hokkaido-Toho-Oki earthquake. Clearly, the ground surface above the embedded water channel subsided (沈下). This seems to suggest the liquefaction and re-consolidation of the backfill soil (埋め戻し土). Mitigation of floating of buried lifelines is attracting concern today.



**Fig. 17.15** Floating of buried gasoline tank (by Dr. A.A. Acacio)



**Fig. 17.16** Floating of sewage tank



**Fig. 17.17** Floating of manhole in Ohtsu of Hokkaido



**Fig. 17.18** Floating of manhole in Shibetsu

17.6 Lateral Displacement of Retaining Wall

Earth retaining structures are pushed outwards by the increased pressure exerted by the liquefied backfill (Fig. 17.19). Figure 17.20 indicates the situation in Niigata after the 1964 earthquake. The wall here was made of steel sheet piles (鋼矢板) with anchorage. The wall moved towards the sea, and the ground surface in backfill, subjected to lateral extension, cracked. It is important that significant distortion of quay wall in Kobe Port Island (Sect. 24.2) stopped the service of the harbor for a long time and consequently the harbor lost many clients. Negative effects to local economy and public are very important.

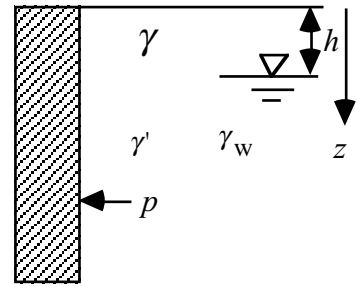


Fig. 17.19 Static lateral earth pressure on retaining wall

Figure 17.21 shows the displacement of a gravity quay wall at Hanasaki Harbor (花咲港) after 1994 Hokkaido-Toho-Oki earthquake. The wall moved outwards and the ground surface sank. For the tremendous wall deformation in Port Island of Kobe Harbor, see Sect. 24.2.



Fig. 17.20 Sheet pile wall near Showa Bridge in Niigata, 1964 (Dept. Civil Engineering, University of Tokyo)



Fig. 17.21 Liquefaction damage at Hanasaki

The lateral earth pressure acting on a retaining structure (Fig. 17.19) is normally calculated by

$$p = K\{\gamma h + \gamma'(z - h)\} + \gamma_w(z - h), \tag{17.2}$$

under static conditions (Fig. 17.19). The vertical effective stress is denoted by  $\gamma h + \gamma'(z - h)$ , while the pore water pressure is given by  $\gamma_w(z - h)$ . The earth-pressure coefficient,  $K$ , lies between the active and passive extremes:  $K_A \leq K \leq K_P$ . The pore pressure term above does not have an earth pressure coefficient because liquid pressure is isotropic. When the effective stress is lost upon liquefaction, the effective stress in  $\{\}$  becomes excess pore water pressure, and the total lateral earth pressure becomes 100% pore water pressure;

$$p = \gamma h + (\gamma' + \gamma_w)(z - h), \tag{17.3}$$

which is equal to the total vertical stress. This increased pressure, together with the dynamic earth pressure, may overcome the lateral resistance of a wall.

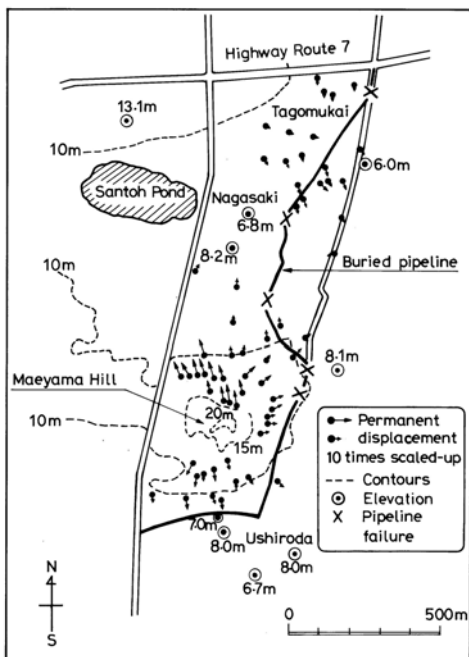
When dynamic components of effective earth pressure and pore water pressure are required for design, the Mennonite-Okabe (Mononobe and Matsuo, 1929; Okabe, 1924) and Westergaard (1931) theories are commonly employed. For more details, see Sects. 12.5 and 13.5. Moreover, Sect. 24.17 presents the dynamic earth pressure exerted by liquefied sand on a flexible wall.

**17.7 Lateral Movement of Liquefied Slope**

Section 17.5 stated that gravity and buoyancy control the subsidence and floating of surface structures. The movement of slope is also related to the gravity. Figure 17.22 indicates the lateral movement of a gentle liquefied slope in Noshiro City 能代, which was detected by air photo surveys by Hamada et al. (1986a, 1986) after the 1983 Nihonkai-Chubu earthquake. Although the slope gradient was merely 1–2 %, the lateral movement reached at maximum 4 m. The direction of displacement was downwards.

In Hamada’s study, two air photos were compared; one taken before and the other after the earthquake. After stationary points 不動点 were selected, the ground movement in the entire surveyed area was determined.

Figure 17.23 reveals the displacement of a river bank in Dagupan where liquefaction was intense during the earthquake in 1990. The river bank moved down into water.



**Fig. 17.23** Lateral movement of embankment in Dagupan

**Fig. 17.22** Permanent ground displacement due to liquefaction in Noshiro



**Fig. 17.24** Buckling of buried pipe in Dagupan City, the Philippines



**Fig. 17.25** Broken piles in Niigata (Kawamura et al. 1985)

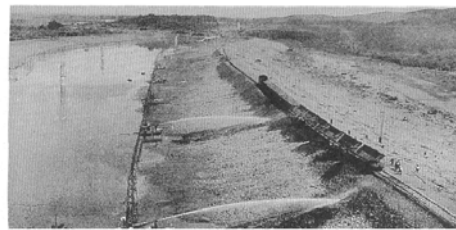
The lateral movement of ground is important in two senses. First, buried lifelines are distorted and broken at bents (see Fig. 17.22). When the ground deformation is tensile, pipes are separated at joints. When ground is compressed, pipelines are compressed as well and buckling may occur (Fig. 17.24). For information in the area of this buckling, see Fig. 24.4.

Second, the lateral displacement of ground moves foundation of buildings laterally. This induces bending failure of piles, because piles are penetrated into stable bearing layers at their tips and cannot move together with the flowing ground. One example of this type of damage is illustrated in Fig. 17.25 in which the damage caused by the 1964 Niigata earthquake was found in 1984 when the building was demolished. Note therefore that the particular building had been in use for 20 years after the damage in pile in spite of minor inclination.

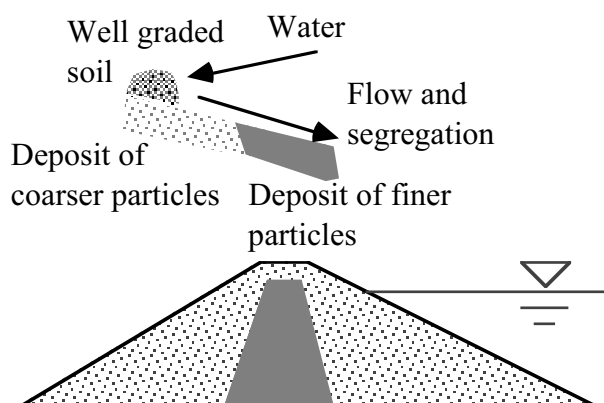
A significant slope failure occurred in the Lower San Fernando Dam in California in 1971. The upstream slope developed high excess pore water pressure and shear failure was induced (Seed et al. 1975). After failure, a merely few meter of free board remained above the reservoir water and flooding in the residential area was avoided (Fig. 17.26).



**Fig. 17.26** Lower San Fernando Dam after failure (reconnaissance team, Univ. Tokyo)



**Fig. 17.27** Semi-hydraulic filling for dam construction around 1925 in Taiwan (Furukawa, 1989)



**Fig. 17.28** Conceptual cross-section of earth-fill dam of zone type



**Fig. 17.29** Soil compaction for dam construction

In the first half of the twentieth Century, many earth fill dams were constructed by what is called the semi-hydraulic filling method (Fig. 17.27). In this method, the dam material is damped on the ground surface and water is jetted to it. The induced water flow transports the soil, and the segregation of particles during flow makes different grain size distribution at different places of planned dam section (Fig. 17.28). Thus, the central core has finer particles, while the outer parts have coarser materials, producing a zoned cross-section of a dam (Hazen, 1920). Although this method was easy, its problem was the insufficient densification. Consequently, earthquake loading was able to cause pore pressure rise and, in the extreme case, liquefaction failure. Today, more



powerful compaction methods are available (Fig. 17.29) and hydraulic filling is seldom conducted. As for an exception of tailing dam construction, refer to Sect. 20.5.

In contrast with the above-mentioned semi-hydraulic filling, the “hydraulic filling” mixes fine grains of soil with water and then transports together to the site of dumping. It is practiced in treatment of tailing materials (Sect. 20.5).

## 17.8 Ground Subsidence after Liquefaction

Liquefaction of sand is caused by an intense development of excess pore water pressure. This high water pressure dissipates later, which is a consolidation procedure. In the meantime, water and sand are ejected out and the ground surface sinks. Figure 17.30 shows the Lingayen Bay Area of the Philippines. A school and a village sank about 1 m after liquefaction. Figure 17.31 shows a differential elevation between the ground surface and a structure supported by a pile. When an abandoned pile foundation rests on a stable unliquefied layer, an elevation difference 抜け上がり results (Fig. 17.32).



**Fig. 17.30** Subsidence in Narbakan Village, Philippines



**Fig. 17.31** Ground subsidence after liquefaction in Port Island, Kobe, 1995



**Fig. 17.32** Pile head appearing above subsided ground surface (by K. Ishihara)



**Fig. 17.33** Flexible joint of oil storage tank that absorbed heavily subsidence of tank

The differential settlement between a building and the surrounding ground can be harmful to lifelines. The joint of lifeline pipes to a building is strongly distorted and could possibly be broken. A leakage of gas could be fatal. This problem is efficiently solved by using a flexible joint that can absorb, for example, 50 cm differential settlement (Fig. 17.33). Figure 17.34 demonstrates a differential subsidence in Dagupan, the Philippines, between areas of liquefaction (front) and no liquefaction (back). Pipeline failure is likely in such a circumstance.



**Fig. 17.34** Boundary between areas of liquefaction and no liquefaction

Negative skin friction is not a problem in subsidence of liquefied sand. This is because sedimentation of sand grains occurs under very low effective stress, and, therefore, the skin friction is small.

17.9 Liquefaction-Induced Subsidence of River Dikes

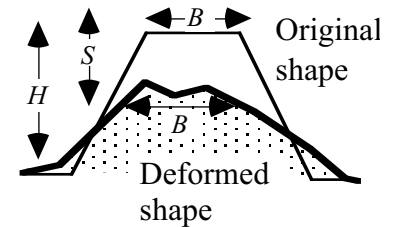
Figure 17.35 indicates the subsidence of Yodo-River dike caused by the subsoil liquefaction during the 1995 Kobe earthquake. This event, together with the ones in Fig. 17.10, changed the policy on the seismic design of river dikes.



Fig. 17.35 Collapse of Yodo River dike in 1995 (Fudo Tetra Corp.)

Former policy: Since flooding is unlikely to occur at the same time as a big earthquake, seismic design was not important. Although a dike may deform significantly during an earthquake, it should be repaired quickly within, for example, two weeks before a flooding may come.

New policy: River dikes and sea walls with low lands behind should not subside very much, because water can overtop the dike and easily inundate the low back area. The top of the dike should be higher than the design highest water level plus 2 m (provision for wave height).



When there is a low and developed area behind, the river dikes need to have an earthquake resistance. At the same time, however, unnecessarily strong resistance against earthquakes should not be given to the dikes. Therefore, the dikes may subside but the height should be still higher than the allowable level as stated above.

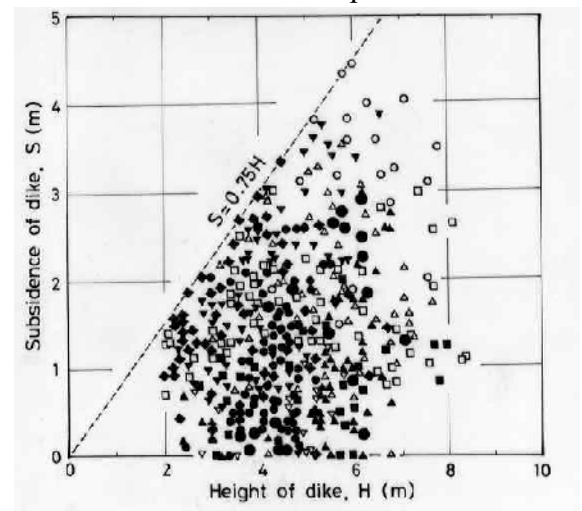


Fig. 17.36 Empirical relationship between height and subsidence of river dikes (TC-ERDRS)

There are two problems today. How can we predict the subsidence and what is the maximum possible subsidence? Figure 17.36 is an answer to the second question that was obtained by summarizing the history of seismic damages (with and without liquefaction) since late nineteenth century. The horizontal coordinate is the original height,  $H$ . The vertical coordinate stands for the subsidence,  $S$ , which was determined by the elevation where the width is equal to the original width at the top. See the inset figure in Fig. 17.36. Thus,  $H-S$  is the residual height. Note that  $S < 0.75H$  and at least 25% of the original height remains after the strongest earthquake.

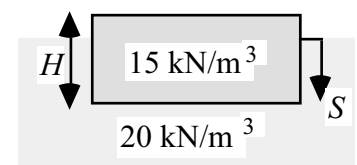


Fig. 17.37 Balance of gravity and buoyancy

*Earthquakes studied in Fig. 17.36: Nobi 濃尾, 1891; Kanto, 1923; Fukui, 1948; Tokachi-oki, 1968; Niigata, 1964; Miyagiken-oki, 1978; Nihonkai-chubu, 1984; Kushiro-oki, 1992; Hokkaido-nansei-oki, 1993; Kobe, 1995.*

This empirical rule of  $S < 0.75H$  can be understood by considering a dike of unit weight =  $15 \text{ kN/m}^3$  floating in liquefied sand of  $20 \text{ kN/m}^3$  (Fig. 17.37). The equilibrium between the gravity and buoyancy forces is achieved at the subsidence of  $S = 0.75H$ .

☛ 17.10 Lessons from 2000 Tottoriken-Seibu Earthquake

The 2000 Tottoriken-Seibu earthquake (鳥取県西部地震) on 6th of October registered the JMA magnitude of 7.3. This earthquake caused sand liquefaction in young artificial land around the Nakaumi lake; see Fig. 17.38.

The Takenouchi Industrial Park was situated on a reclaimed island that was constructed not later than 1988; probably in early 80s. The filled material was a seabed soil dredged from the nearby Sakai-Minato strait. Figure 17.39 illustrates sand boil that caused significant subsidence of the floor slab of the building. In contrast the building structure survived liquefaction due probably to good behavior of nodular pile foundation (Sect. 13.8). Swedish weight sounding (Sect. 8.9) revealed that there is a soft soil deposit (equivalent  $SPT-N < 5$ ) down to 10–11m depth, which is the original sea depth in this area. Figure 17.40 shows the grain size distribution of boiled sand, which is basically silt. Being nonplastic (liquid and plastic limits are not measurable), even fine silty material liquefies. The sand boiling continued for 7.5 h, which was much longer than former experiences in sandy deposit in Niigata. Note that fine grain size of silt reduces permeability and more undrained conditions, which leads to higher pore pressure and longer duration of liquefaction.

Figure 17.41 shows on-going liquefaction in Yonago. This site was situated on a young artificial land. Actually, all the liquefied sites in Fig. 17.38 were on artificial ground. Older natural deposit did not liquefy for unknown reasons; refer to Sect. 18.13. One idea is that all the old loose deposit liquefied many times in the past and now has a sufficient density and resistance. Finally, boiled material at both sites of Figs. 17.39 and 17.41 was *not* hot according to eyewitnesses (Sect. 18.6).

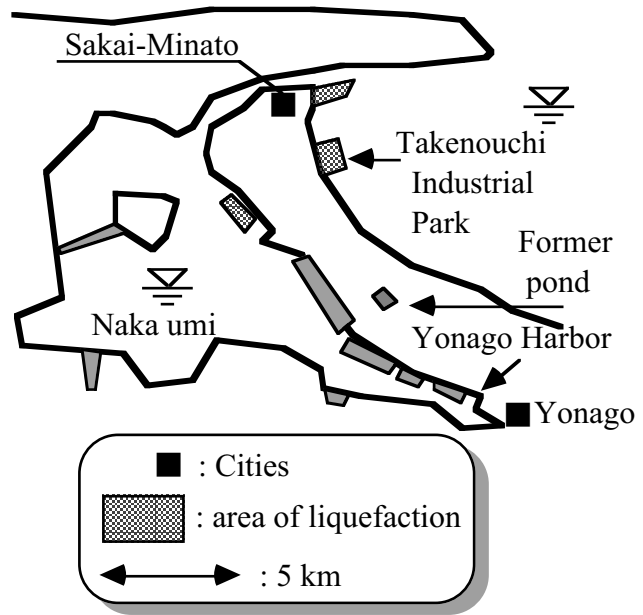


Fig. 17.38 Geotechnical damage caused by the 2000 Tottoriken-Seibu earthquake



Fig. 17.39 Boiled sand in Takenouchi Industrial Park

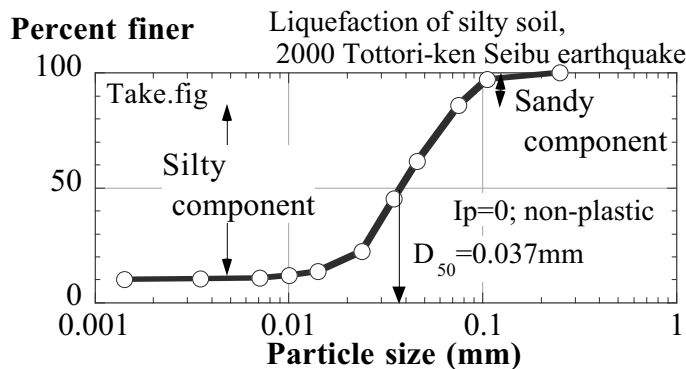


Fig. 17.40 Grain size distribution of liquefied sand in Takenouchi Industrial Park



Fig. 17.41 On-going liquefaction and sand boiling in Yonago City (Photo by Mr. Naoki Higuchi)

## 17.11 Earthquake Induced Ground Subsidence

Apart from liquefaction-induced subsidence, there are examples of seismically-triggered subsidence of clayey subsoils. Figure 17.42 shows an example reported in Mexico City after an earthquake in 1957. The basin of Mexico City is famous for its continuous consolidation settlement in the clayey subsoil. Although this type of clay does not liquefy, its subsidence is affected by earthquake shaking. This is probably because some amount of excess pore water pressure developed during the shaking and its dissipation induced volume contraction (体積収縮). Another possibility is softening of clay due to disturbance during shaking. Note that some of the subsidence observed after an earthquake may have been induced by slope instability movement as can occur along a circular slip plane.

The second example in Fig. 17.43 comes from Nagoya City in the Nobi Plain (濃尾平野). This area was shaken twice by gigantic earthquakes; the 1891 Nobi earthquake ( $M = 8.0$ ) and the 1944 Tohankai (東南海) earthquake ( $M = 7.9$ ). The three records of subsidence at the ground surface indicate that abnormally large subsidence occurred between 1890 and 1895 and between 1932 and 1948. The exact times of the subsidence were most probably coincident with the earthquakes. Since the amount of water pumping (shown by a dashed curve) was negligible until 1940s, earthquakes is the most likely cause. After 1950, ground water pumping was so significant that consolidation settlement became large; this kind of settlement stopped after 1970 because pumping was banned.

The 1978 Miyagi-ken-oki earthquake induced subsidence in a clayey Holocene subsoil (完新統). Figure 17.44 indicates the time history of volume contraction in each individual layer. The subsidence in the most recent holocene layer is more significant than in others.

The negative friction on pile shafts placed in a sinking soft subsoil reduces the bearing capacity. This adverse situation may lead to a collapse of pile foundation when an earthquake shaking exerts a horizontal force to the superstructure which in turn increases the axial force in a pile.

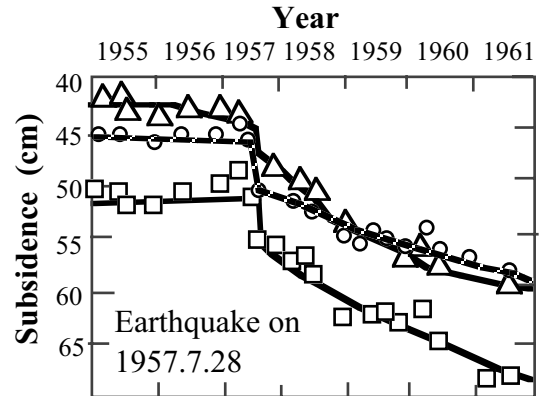


Fig. 17.42 Subsidence of building foundation triggered by earthquake (after Zeevaert, 1972)

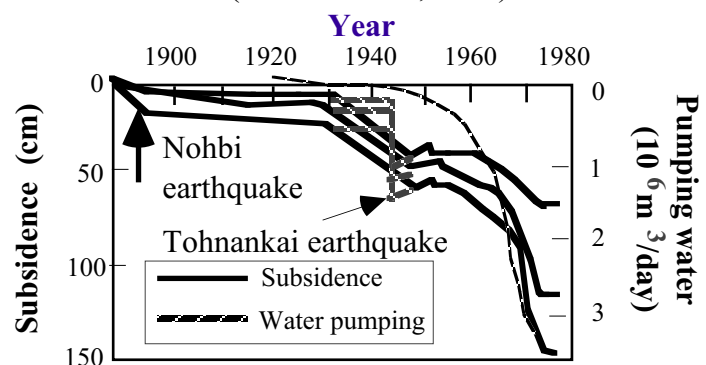


Fig. 17.43 Time history of subsidence and water pumping in Nobi plain (drawn after Iida et al., 1976, as quoted by Kuwahara et al, 1977)

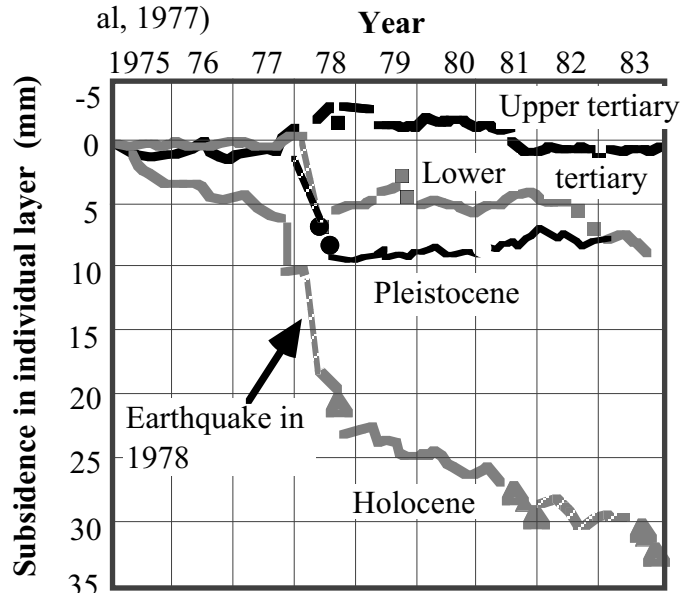


Fig. 17.44 Earthquake-induced subsidence in Sendai City (after Touno, 1993; Data by Miyagi Government)

17.12 Earthquake Motion Recorded on Liquefied Ground

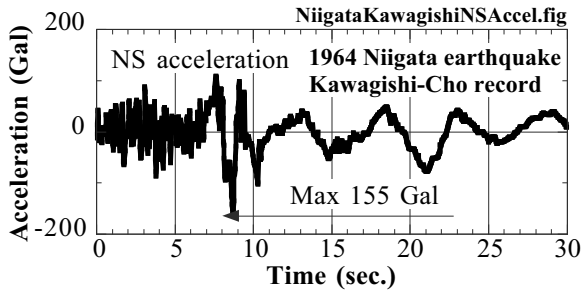


Fig. 17.45 Niigata Kawagishi-cho NS motion

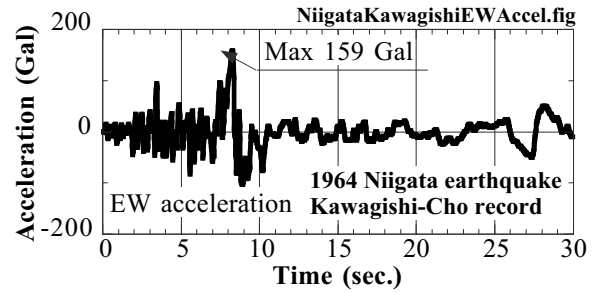


Fig. 17.46 Niigata Kawagishi-cho EW motion

Figures 17.45 and 17.46 illustrate acceleration records at the basement of Kawagishi-cho apartment building in Niigata (Sect. 17.3). The maximum acceleration occurred at about 8 s, after which the amplitude decreased and the shaking period was elongated. When the excess pore water pressure increased with time, the effective stress dropped. This resulted in the reduced shear modulus (dependent on effective stress) and S-wave velocity ( $V_s = \sqrt{G/\rho}$ ). A rough estimate of the natural period of a ground (thickness  $H$ ) is given by  $T_g = 4H/V_s$  (Sect. 6.8). Hence, the natural period increased with time. Probably, at about 8 s the natural period matched with the predominant period 卓越周期 of input earthquake motion and resonance occurred. This is why the maximum acceleration occurred around this time. Thereafter, the natural period became even longer, and the ground amplified the component of input motion that had even longer period.

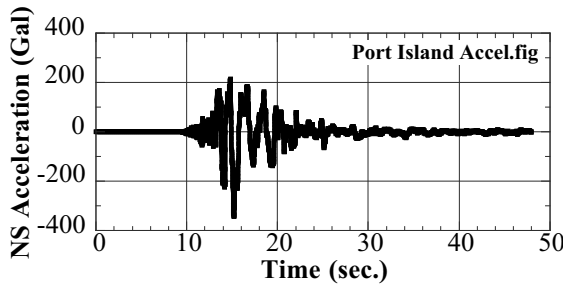


Fig. 17.47 Acceleration time history in Kobe Port Island (Kobe City Development Bureau)

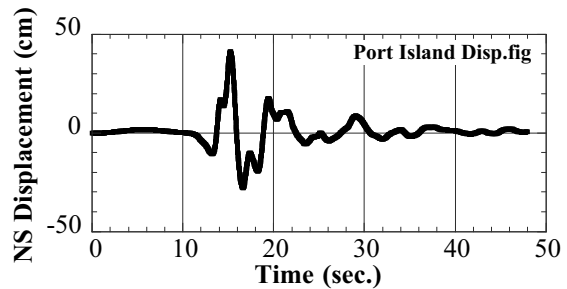


Fig. 17.48 Displacement time history in Kobe Port Island

Figures 17.47 and 17.48 show the acceleration and displacement time histories of Port Island motion that occurred at a liquefied site. The displacement history was obtained by double integration of the acceleration. Note that the elongated period is obvious in the displacement history. As will be shown in Sect. 18.9, liquefied subsoil reduces the acceleration at the surface, while it increases the surface displacement amplitude. Thus, displacement seems to be a more appropriate index of subsurface liquefaction.

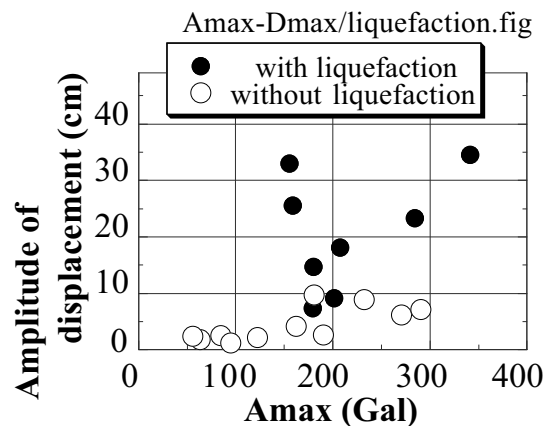


Fig. 17.49 Amplitude of displacement in recorded earthquake motion

Figure 17.49 demonstrates the displacement amplitudes during many past earthquakes, which are plotted against the maximum acceleration. The displacement was obtained by analytically (FFT) integrating the original motion twice with time, picking up components with period shorter than 10 s. See that the acceleration at liquefied sites is not much different from others, while the displacement amplitude is much bigger.

17.13 Subsidence of Shallow Foundation due to Subsoil Liquefaction

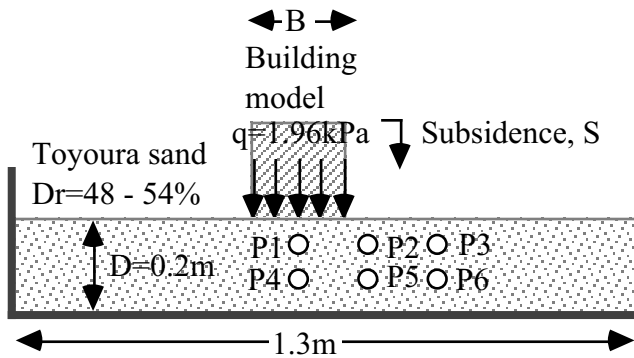
Subsidence of building supported by shallow foundations (footing or slab) is frequently seen in liquefaction areas (Figs. 17.50, 17.51, 17.2 and Sect. 17.3). This phenomenon is obviously caused by shortage of rigidity and bearing capacity in the subsoil immediately below the structure.



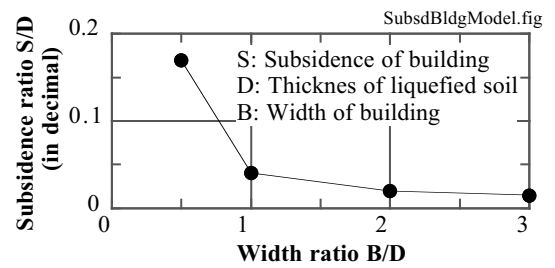
**Fig. 17.50** Subsidence of building in liquefied area in Niigata, 1964 (Department of Civil Engineering, University of Tokyo)



**Fig. 17.51** Tilting of building in liquefied area in Niigata, 1964 (Department of Civil Engineering, University of Tokyo)



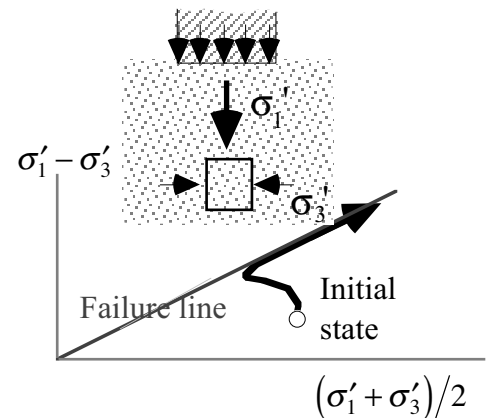
**Fig. 17.52** 1-G model tests on liquefaction-induced subsidence of building resting on shallow foundation (tests by Yoshimi and Tokimatsu, 1977)



**Fig. 17.53** Experimental relationship between width and subsidence of building resting on shallow foundation (drawn after Yoshimi and Tokimatsu, 1977)

Yoshimi and Tokimatsu (1977) studied the subsidence of buildings. Their 1-G shaking model tests (Fig. 17.52 with 100 Gal and 3 Hz shaking for a long time; Toyoura sand sedimentation in Glycerin liquid) revealed that the ratio of (subsidence,  $S$ )/(thickness of liquefied soil,  $D$ ) is greater when the ratio of (building width  $B$ )/ $D$  is smaller (Fig. 17.53). This implies that wider buildings are less susceptible to liquefaction-induced subsidence.

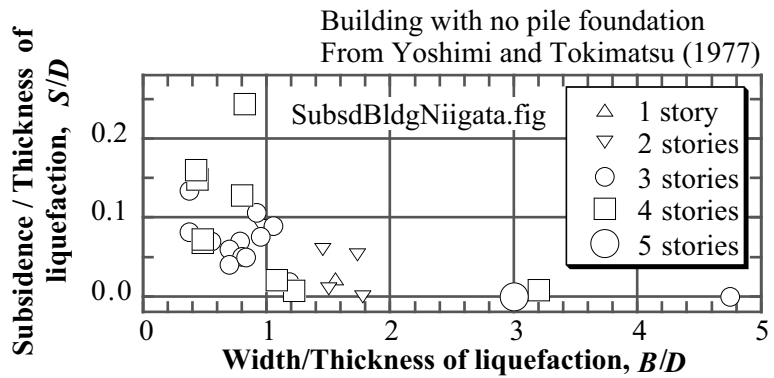
Their model tests also revealed that excess pore water pressure under the building model ( $P1$  and  $P2$  in Fig. 17.52) became lower than the hydrostatic level when the building subsidence



**Fig. 17.54** Possible stress state under sinking buildings

became significant. This is because of large shear deformation and dilatancy (volume trying to expand) of subsoil under the building. The stress path in this situation is illustrated in Fig. 17.54 where the effective stress state reaches the failure line and develops large shear deformation. Thus, the building subsidence is caused not by liquefaction of subsoil but undrained shear failure. The magnitude of shear stress,  $\sigma_1' - \sigma_3'$ , in the subsoil increases because the lateral effective stress,  $\sigma_3'$ , decreases due to liquefaction in the free field (away from foundation).

Yoshimi and Tokimatsu (1977) further examined the effects of building width on the extent of subsidence (Fig. 17.55) by collecting data from the 1964 Niigata earthquake. Figure 17.55 was drawn by using their data from buildings without pile foundation. It may be seen that the extent of subsidence ( $S/D$ ) is more significant when the width ( $B/D$ ) is smaller. Thus, there is consistency between model tests



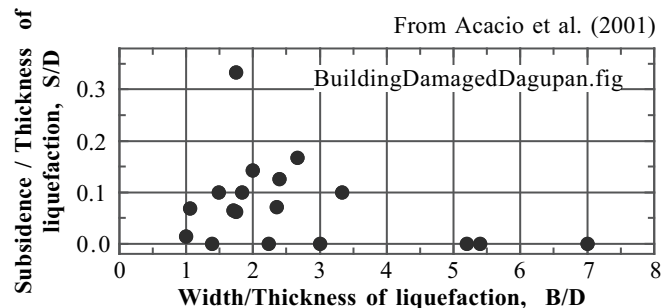
**Fig. 17.55** Effects of building width on extent of subsidence due to liquefaction (after Yoshimi and Tokimatsu, 1977)

and field data. It is noteworthy in Fig. 17.55 that the height of buildings (number of stories and contact pressure of buildings) does not affect the magnitude of subsidence. Note further, however, that Fig. 17.55 may simply suggest that  $B/D > 2$  prevents subsidence. In this respect, it seems interesting to study the stress distribution in the foundation.



**Fig. 17.56** Subsidence and tilting of building in Dagupan, Luzon, in 1990

Similar studies were made in Dagupan of the Philippines (Fig. 17.56) after the quake in 1990. Adachi et al. (1992) demonstrated that buildings of greater width suffered less extent of subsidence and tilting. Acacio et al. (2001) presented Fig. 17.57 where significant subsidence occurred only when  $B/D$  was less than 3. Thus there is similarity between Dagupan and Niigata (Fig. 17.55), although the concerned range of  $B/D$  is different.



**Fig. 17.57** Subsidence of buildings in Dagupan, the Philippines (Acacio et al. 2001)



## 17.14 Liquefaction Damage to Private Houses

Protection of private houses from natural disasters is different from that of bigger structures such as bridges and buildings. In the case of Fig. 17.58, subsoil liquefaction caused differential settlement between the main part of the house and the lighter entrance. The major issue is the limited income and budget that are available for mitigation measures. In spite of this, the effects of liquefaction are significant; even minor differential settlement (Fig. 17.59; tilting) of 1/700 made residents uncomfortable. Asada (1998) studied the damage extents of houses in Akita Prefecture of Japan when the 1983 Nihonkai-chubu earthquake ( $M_{JMA} = 7.7$ ) caused significant liquefaction and damage to houses.



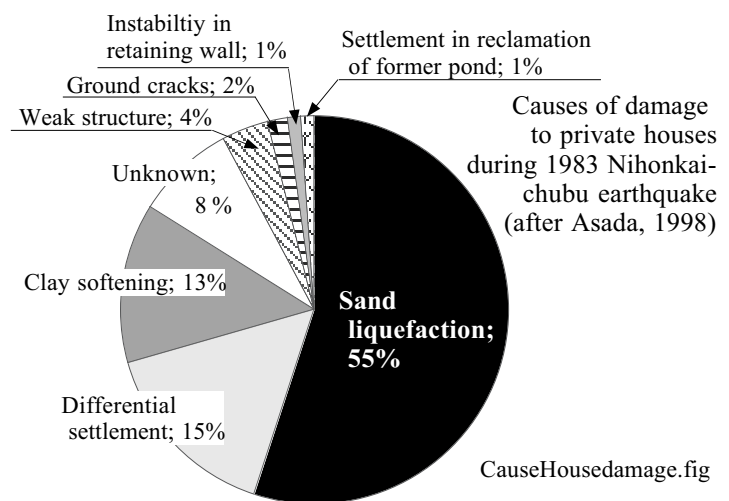
**Fig. 17.58** Liquefaction under private house (Gilan, Iran in 1990)



**Fig. 17.59** Minor tilting of private house due to subsoil liquefaction (in Yonago City, 2000 Tottoriken Seibu earthquake)



**Fig. 17.60** Distortion of retaining wall due to subsurface liquefaction (Noshiro City in Akita, Japan)



Data from 938 houses with damage extent > 50%

**Fig. 17.61** Causative mechanisms of damage to studied houses (data by Asada, 1998)

Most house damages that were studied by Asada were caused by subsoil liquefaction, while differential settlement and instability of retaining walls are often detected in liquefaction area (Figs. 17.60 and 17.61).

Such topics as deformation of clay and reclamation of former ponds are important but should be discussed elsewhere. In Asada's study, it was firstly found that the thickness of surface unliquefied

soil (above ground water table),  $H_1$ , (Fig. 17.62) has a remarkable effect to mitigate damage. According to Fig. 17.63, when  $H_1$  was greater than 2 m, there was no such evidences of liquefaction as cracking and sand boiling at the ground surface. When  $H_1$  was less than 2 m, the possibility of such evidences depended upon  $H_1$  and  $H_2$ ;  $H_2$  stands for the thickness of liquefied layer that was judged by  $SPT-N < 15$ . This finding is consistent with Ishihara (1985) in Sect. 21.9.

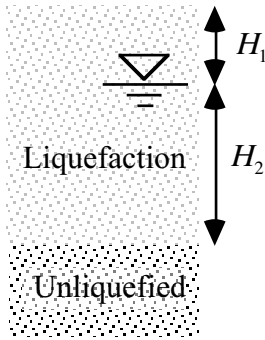


Fig. 17.62 Definition of  $H_1$  and  $H_2$

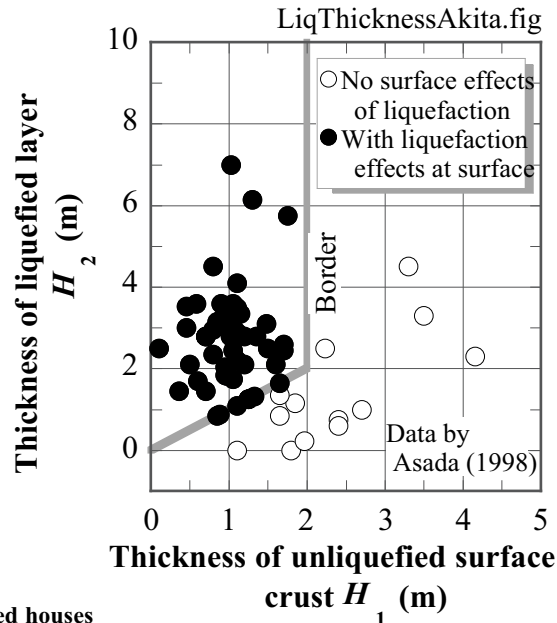


Fig. 17.63 Relationship between thicknesses of liquefied layer and unliquefied layer at damaged and undamaged sites (data by Asada, 1998)

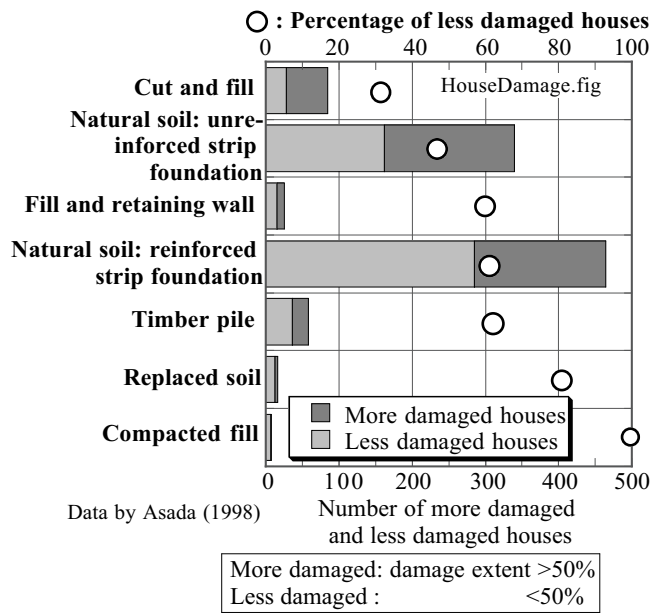


Fig. 17.64 Damage rate and type of foundation (data by Asada, 1998)



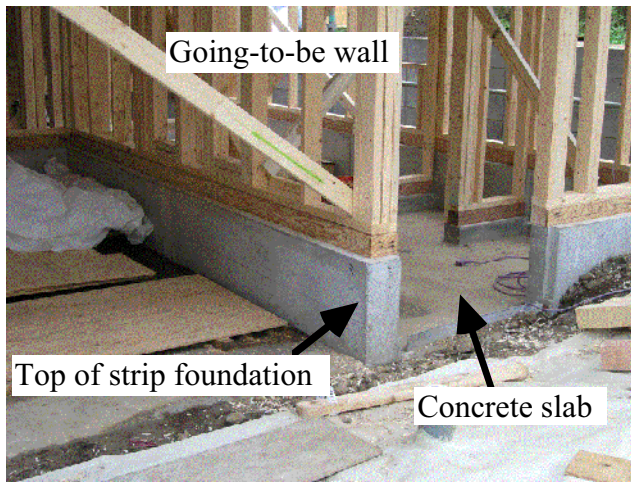
Fig. 17.65 Ongoing jacking up of house foundation (in Taiwan)

Second, the damage extent of houses were examined against types of subsoil as well as kinds of house foundations (Fig. 17.64). Although there were many uncertainties in the details of soil and foundation conditions, it was found that following kinds of foundation behaved in a good way during subsoil liquefaction;

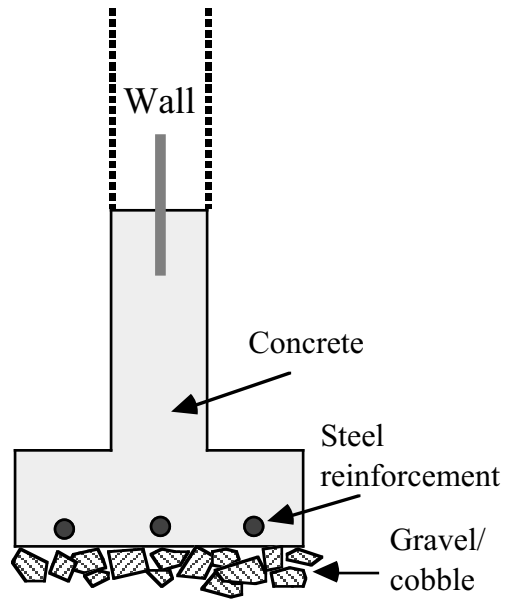
1. Resting on compacted thick fill
2. Replaced good soil
3. Good number of piles
4. Reinforcement of commonly-used strip foundation (布基礎 Figs. 17.66 and 17.67)

Furthermore, a rigid foundation slab is recommendable because it helps maintain the integrity of the entire house, although tilting is possible to a certain extent. These measures avoid large deformation in the foundation of houses and prevent fatal structural damage. Minor tilting and subsidence can be restored by jacking up the foundation (Fig. 17.65) or compaction grouting (Sect. 26.10) in the subsoil.

In addition, the risk of liquefaction-induced damage is very small when the ground water table is deeper than 2 m (Fig, 17.63). Since the ground water table is subject to seasonal variation, it is important to monitor the depth for several months before making decision.



**Fig. 17.66** Strip foundation of Japanese house under construction



**Fig. 17.67** Strip foundation for ordinary Japanese house

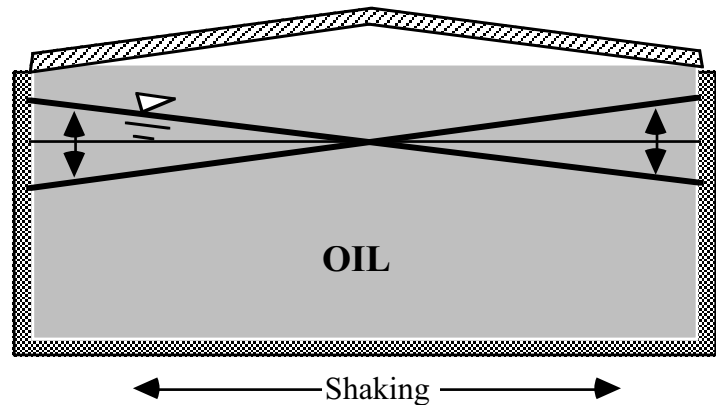
### 17.15 Summary of Case Histories

The studies on case histories of liquefaction stated in Sects. 17.3–17.12 may be summarized as below:

1. Damage related to liquefaction is one or combination of subsidence, floating, and lateral displacement.

Whatever the direction may be, displacement and deformation are the causes of damage. Such structural damages as cracking, collapse of columns, breakage of window glasses are unlikely.

2. The period of motion at the surface of a liquefied ground is elongated. This long period may match the long natural period of such structures as oil-storage tanks. Upon resonance, oil in a tank moves substantially, which is called sloshing (Fig. 17.68). Because of heavy oil-wave pressure, wall and top plate of a tank could be strongly damaged. When a lid of a floating type is employed, a heavy motion of the metal lid may induce friction with the side wall of the tank, leading possibly to a spark and fire of the stored oil.

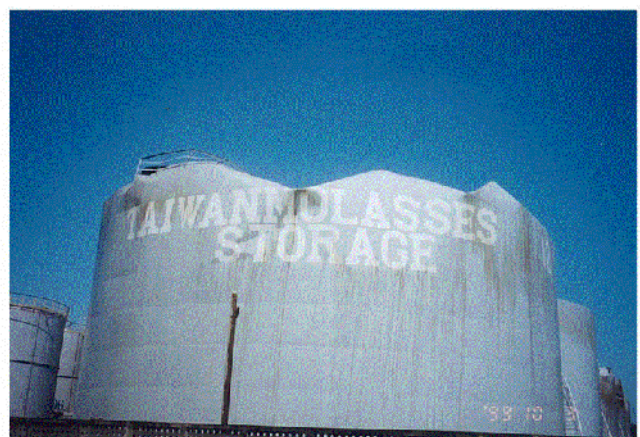


**Fig. 17.68** Conceptual view of oil sloshing in storage tank

Figures 17.69 and 17.70 illustrate earthquake problems of tanks during past earthquakes, although they may not have been directly related with subsoil liquefaction. Another possible problem to a tank is the effects of differential subsidence in the foundation, which may be caused by liquefaction and induces buckling failure of the tank structure that leads to leakage.



**Fig. 17.69** Fire in oil refinery in Niigata (Photograph by Mr. F. Yuminamochi, JGS, 1999)



**Fig. 17.70** Buckling of liquid storage tank in Taiwan after 1999 ChiChi earthquake

3. Acceleration at liquefied site is not very strong. Note that the recent developments of the accuracy of accelerometers and their dense deployment pick up surprisingly big motion. About 900 Gal at Kushiro, 1992, and almost 1,900 Gal at Tarzana during the 1994 Northridge earthquake (Sect. 6.11). At these sites no significant damage occurred.
4. Liquefaction is threatening to buried lifelines, water-front facilities, and artificial reclamation. It, however, does not kill people.

Therefore, it seems that there are two approaches that mitigate liquefaction disaster. They are prevention of liquefaction (pore pressure rise), and reduction of ground deformation although pore pressure may rise.

### List of References in Chapter 17

- Acacio, A.A., Kobayashi, Y., Towhata, I., Bautista, R.T. and Ishihara, K. (2001) Subsidence of building resting upon liquefied subsoil; case studies and assessment, *Soils Found.*, Vol. 41, No. 6, pp. 111–128.
- Adachi, T., Iwai, S., Yasui, M. and Sato, Y. (1992) Settlement and inclination of reinforced concrete buildings in Dagupan City due to liquefaction during 1990 Philippine earthquake, *Proc. 10th World Conf. Earthq. Eng.*, Madrid, Vol. 2, pp. 147-152.
- Asada, A. (1998) Simplified prediction of liquefaction-induced damage to individual houses and its mitigation, 15-year anniversary of 1983 Nihonkai-chubu earthquake, Chap. 9 (in Japanese).
- Furukawa, K. (1989) Engineer Yoichi Hatta, a Japanese who loved Taiwan, Aoba Books, Matsuyama, ISBN 4-90024-04-X, p. 185 (in Japanese).
- Hamada, M., Yasuda, S., Isoyama, R. and Emoto, K. (1986a) Generation of permanent ground displacements induced by soil liquefaction, *Proc. JSCE*, Vol. 376/III-6, pp. 211–220 (in Japanese).
- Hamada, M., Yasuda, S., Isoyama, R. and Emoto, K. (1986b) Study on liquefaction-induced permanent ground displacements and earthquake damage, *Proc. JSCE*, Vol. 376/III-6, pp. 221–229 (in Japanese).
- Hazen, A. (1920) Hydraulic-fill dams, *Transactions of ASCE*, Paper No. 1458, pp. 1713–1745.
- Iida, K., Sazanami, T., Kuwahara, T. and Ueshita, K. (1976) Subsidence of the Nobi Plain, *Proc. 2nd Int. Symp. Land Subsidence* (in Japanese).
- Ishihara, K. (1985) Stability of natural deposits during earthquakes, Theme Lecture at 11th ICSMFE, San Francisco, Vol. 1, pp. 321–376.
- Japanese Geotechnical Society (1999) 液状化災害発生直後の新潟市街地航空写真集 Air photographs of the Niigata city immediately after the earthquake in 1964, ISBN 4-88644-054-1.
- JSCE (1986) Report on the 1983 Nihonkai-Chubu earthquake.
- Kawamura, S., Nishizawa, T. and Wada (1985) Seismic damage in piles detected by excavation 20 years after earthquake, *Nikkei Architecture*, July 29th Issue, pp. 130–134 (in Japanese).
- Kuwahara, T., Ueshita, K. and Itabashi, K. (1977) Consolidation settlement in Nobi Plane, *Monthly Magazine of Japanese Geotechnical Society*, Vol. 25, No. 6, pp. 53 –60 (in Japanese).
- Mononobe, N. and Matsuo, H. (1929) On determination of earth pressure during earthquakes, *Proc. World Engineering Congress*, Tokyo, pp. 177–185.
- Niigata Nippo Newspaper (1964) Records of Niigata Earthquake, p. 27.
- Okabe, S. (1924) General theory on earth pressure and seismic stability of retaining walls during earthquakes, *Proc. JSCE*, Vol. 10, No. 6, pp. 1277–1330.
- Oshiki, H. and Sasaki, Y. (2001) Restoration works of seismically damaged river dikes using remedial treatment of liquefiable layer, *Proc. JSCE*, Vol. 686/VI-52, pp. 15–29 (in Japanese).

- Oshiki, H. and Sasaki, Y. (2006) Damage of the Shinano River dike due to the Niigata-ken Chuetsu earthquake, Proc. 2nd Japan-Taiwan Joint Workshop on Geotechnical Hazards from Large Earthquakes and Heavy Rainfall, Nagaoka, pp. 262–269.
- Sasaki, Y. (1994) River dike failure due to the Kushiro-Oki Earthquake of January 15, 1993, Proc. International Workshop on Remedial Treatment of Liquefiable Soils, Public Works Research Institute, Tsukuba.
- Seed, H.B., Lee, K.L., Idriss, I.M. and Makdisi, F.I. (1975) The Slides in the San Fernando Dams during the Earthquake of February 9, 1971, J. Geotech. Eng., ASCE, Vol. 101, GT7, pp. 651–688.
- TC-ERDRS (1996) Report of Technical Committee for Earthquake Resistant Design of River Structures (河川構造物地震対策技術検討委員会報告書), 1996.
- Touno, I. (1993) History and present situation of ground subsidence, Handbook of Soft Ground Engineering, p. 319 (in Japanese).
- Towhata, I., Prasad, S.K., Honda, T. and Chandradhara, G.P. (2002) Geotechnical reconnaissance study on damage caused by 2001 Gujarat earthquake of India, Soils Found., Vol. 42, No. 4, pp. 77–88.
- Westergaard, H.M. (1931) Water pressure on dams during earthquakes, Transaction of ASCE, paper No. 1835, pp. 418–433.
- Yoshimi, Y. and Tokimatsu, K. (1977) Settlement of buildings on saturated sand during earthquakes, Soils Found., Vol. 17, No. 1, pp. 23–38.
- Zeevaert, L. (1972) Foundation Engineering for Difficult Subsoil Conditions, van Nostrand Reinhold, p. 523.

# Chapter 18

## Mechanism of Onset of Liquefaction



The Badshahi Masjid in Lahore of Pakistan, which was constructed by Shah Jahan, the fifth Mughal Emperor.

18.1 Mechanism of Liquefaction

Studies on causative mechanisms of liquefaction were initiated by shaking water-saturated model ground (Maslov, 1957; Florin and Ivanov, 1961; Yoshimi 1967). Although much was found by them, more quantitative study became possible after introducing laboratory shear tests.

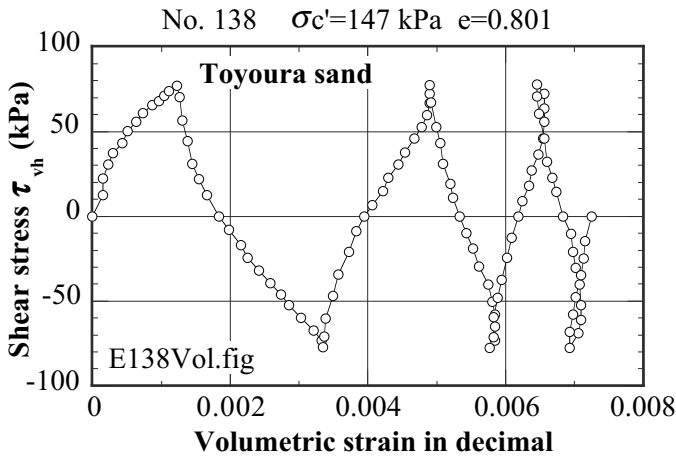


Fig. 18.1 Volume decrease of loose sand during cyclic drained shear

Figure 18.1 indicates the volume contraction 体積収縮 of loose Toyoura sand undergoing cyclic drained shear. This volume change induced by shear is called negative dilatancy (Sect. 1.6). If sand is saturated, pore water is drained out of sand upon this cyclic volume contraction.

In real earthquake loading, drained cyclic shear and immediate volume contraction are unlikely. When a sand deposit is of several meters in thickness, the time required for drainage is 10–30 min (see Sect. 17.3), which is much longer than the duration time of earthquake loading (10–20 s, approximately). It is thus reasonable to consider real sandy ground to be undrained during earthquake shaking. When there is a thin clayey impervious layer, furthermore, it prevents seepage and drainage from underlying deposits toward the surface.

When shear occurs under undrained conditions, pore water cannot be drained out, and develops pressure. This pressure is called the excess pore water pressure 過剰間隙水圧 and is defined as the pore water pressure minus the hydrostatic pressure that existed before earthquake;

$$\text{Excess pore water pressure} = \text{Pore water pressure} - \text{Hydrostatic pressure}, \quad (18.1)$$

which is identical with (1.4). The contact force between sand grains is called the effective stress and controls the rigidity and shear strength of soil (Sects. 1.3 and 1.5). The effective stress is calculated by

$$\text{Effective stress} = \text{Total stress} - \text{Pore water pressure} \quad (18.2)$$

Since the total stress is equal to the weight of soil above the concerned elevation, it does not change with time (Fig. 18.2). Accordingly, the effective stress decreases when pore water pressure increases.

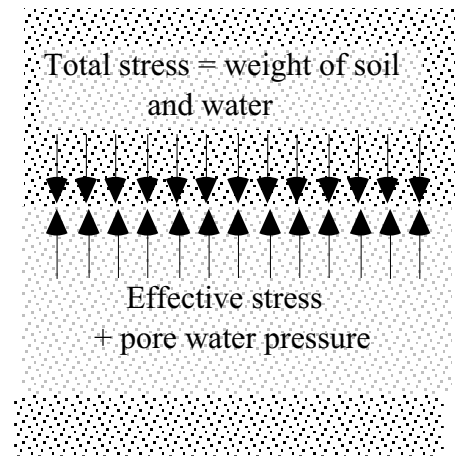


Fig. 18.2 Calculation of effective stress

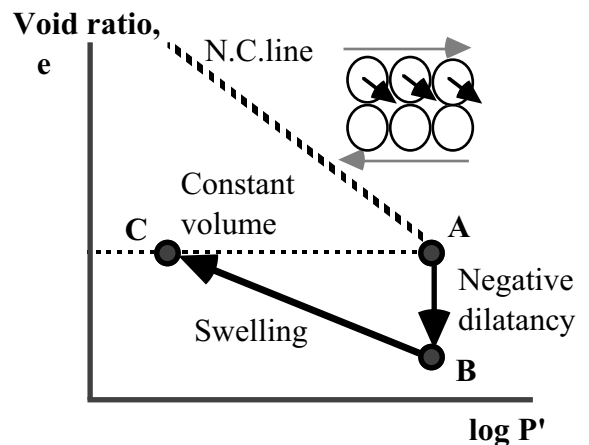


Fig. 18.3 Negative dilatancy



Consequently, sand becomes softer. When the effective stress reaches zero, there is no more shear strength in sand (Coulomb's failure criterion, 1.14), sand behaves similar to liquid, and large ground deformation occurs. The high excess pore water pressure is dissipated after tens of minutes. This consolidation procedure results in subsidence of ground (settlement 压密沈下).

Figure 18.3 illustrates an “ $e$  vs.  $\log P'$ ” diagram, as originally drawn by Seed (1979), that demonstrates the mechanism of pore pressure rise. Initially, the state of *water-saturated sand* 飽和砂 is at **A** upon a normal-consolidation line. When sheared, sand tries to contract its volume toward **B**. Since no drainage is allowed, however, the volume and void ratio have to be held constant. Thus, unloading of effective stress is needed to cancel the volume contraction (**AB**) by swelling (**BC**). In reality, the volume contraction (**AB**) and swelling (**BC**) are superimposed, and the state of soil moves directly from **A** to **C**. The volume contraction of **AB** becomes reality after dissipation of developed excess pore water pressure (consolidation settlement; Sects. 17.8 and 18.3).

When the extent of negative dilatancy is more significant, the point **B** is located further below, and the effective stress at **C** becomes very small. This is called liquefaction. This occurs when sand is very loose or when the magnitude of cyclic shear is substantial.

When sand is not saturated with water 不飽和砂, pore air is compressed or solves into water. Hence, volume can contract and swelling is not required very much. Hence, effective stress does not decrease very much.

The discussion above suggests not only the mechanism of liquefaction but also the following principles of mitigative measures against liquefaction:

- Densification or compaction of sand in order to reduce negative dilatancy (**AB**)
- Installation of gravel drains to accelerate the rate of drainage
- Grouting to bond grains to each other and prevent particle movement as well as negative dilatancy (Fig. 18.2)
- Preventing large shear strain that leads to high excess pore water pressure
- Lowering of ground water to introduce air into pore space (volume change is allowed)

**18.2 Sand Boiling**

When the vertical effective stress is zero, the excess pore water pressure at depth  $z$  is  $(\gamma - \gamma_w)z$ . The hydraulic gradient, 動水勾配, is  $i = (\gamma/\gamma_w) - 1 = i_{cr}$ , which is known as the critical gradient. Consequently, a mixture of sand grain and water is ejected out of ground. In Fig. 18.4, the sand boiling reached the height of 2 m above the surface and the ejected sand is seen on the wall. In the Shinano River, Niigata, and the small inlet in the Lingayen Bay area, the Philippines, many water boilings were observed out of river/sea water (Wakamatsu, 1993). It seems that the energy of ejected water in river/sea beds is stronger than those onshore.



**Fig. 18.4** Ejected sand on wall (Dagupan, 1990)



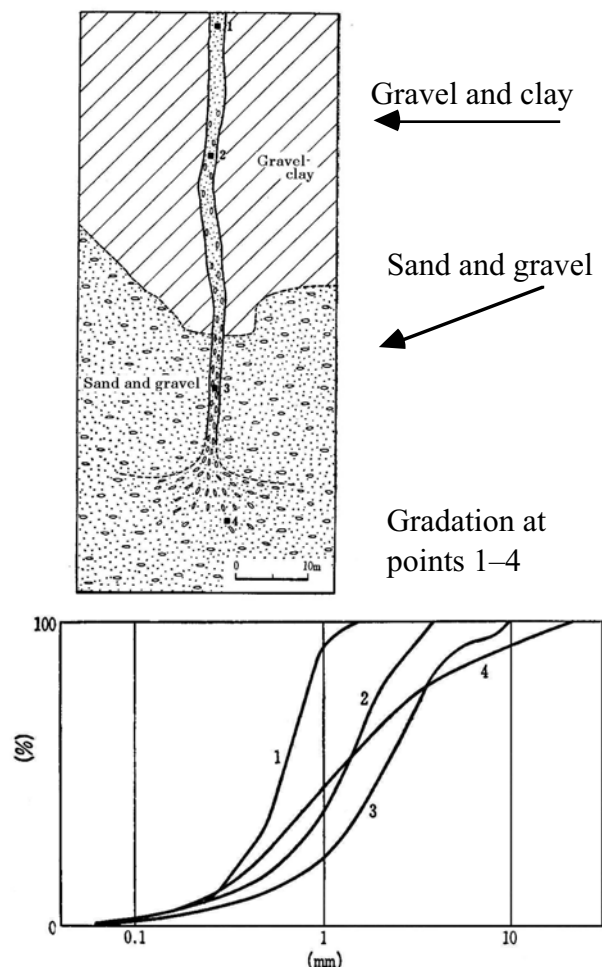
**Fig. 18.5** Sand crater after Liquefaction (1994 Hokkaido Nansei-oki earthquake, Hakodate Harbor)

Boiling of water and sand leaves a crater on the ground surface (Fig. 18.5). The ejected sand deposits around the hole of ejection, while water flows away, transporting fine particles together. Coarse grains cannot be transported to the ground surface (Stokes law). Therefore, the grain size in the crater is uniform and fine (100–300  $\mu m$ ), although there are some exceptions. This observation led to an idea in early days that fine uniform sand is most likely to liquefy. In recent years, however, liquefaction of gravelly soils (Sect. 20.2) as well as fine cohesionless soils (Sect. 20.5) attracts concern.

The color of ejected sand is blue to gray, because the sand has been submerged in water until liquefaction, and is not oxidized.

Sangawa (1992) excavated an archaeological site of liquefaction and showed that coarse material was not transported to the ground surface (Fig. 18.6).

Boiling is possible to occur in submarine ground if sand is loose. After the May 25 Noto Peninsula



**Fig. 18.6** Excavated boiling channel (Sangawa, 1992)

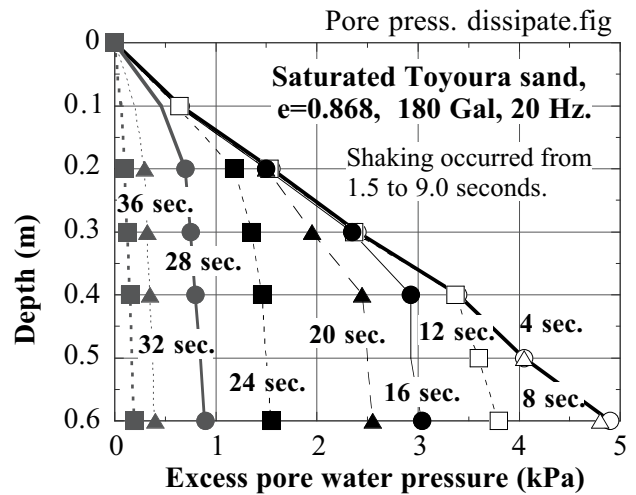
earthquake in Japan (magnitude = 6.9), the Japan Coast Guard conducted detailed surveys on the seabed topography along the submarine seismic fault and detected more than ten topographies that appeared similar to boiling of sand.

**18.3 Dissipation of Excess Pore Water Pressure**

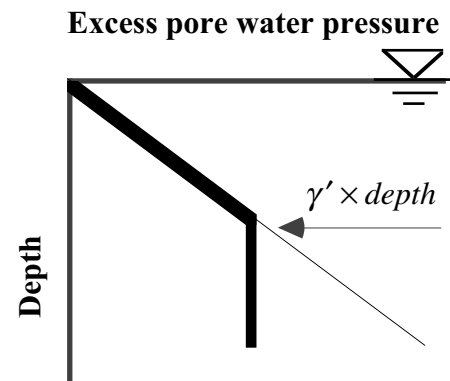
Figure 18.7 reveals the distribution of excess pore water pressure (not including hydrostatic pressure) observed in a shaking table test. When dissipation is going on, the pressure distribution is bilinear, conformed of  $\gamma' \times depth$  in the upper portion, and the constant pressure in the lower part (Fig. 18.8). This point is different from what Terzaghi consolidation theory demonstrated for clay. Dissipation started at the bottom and the range of constant pressure expanded upward with time. It is important that the hydraulic gradient at the surface is equal to the critical gradient  $i_{cr}$  (Sect. 1.12) until 28 s (Fig. 18.8) which is most part of the period of dissipation. The duration time of dissipation can be calculated by Darcy's law (Sect. 1.12);

$$Time = (Volume\ of\ drained\ water) / (Rate\ of\ water\ flow) = (\epsilon_v H) / (k i_{cr}) \tag{18.3}$$

where  $\epsilon_v$  is the volumetric strain after liquefaction (e.g., 0.05 or 5% for loose sand),  $H$  the thickness of liquefied sand (60 cm here),  $k$  the permeability (0.1 cm/s here), and  $i_{cr} = 0.8$  in this text; for definition of  $i_{cr}$ , see (1.26). Consequently, the calculated duration time is 37.5 s, which is in good agreement with the observation of around 40 s. Upon Niigata earthquake, sand boiling started at a few minutes after shaking and continued for roughly 20 min (Fig. 18.9 by Mr. Yutaka Takeuchi). The duration time is proportional to  $H$ , in contrast to  $H^2$  proportionality in Terzaghi theory. Consequently, the insitu duration time can be as long as 1 h.

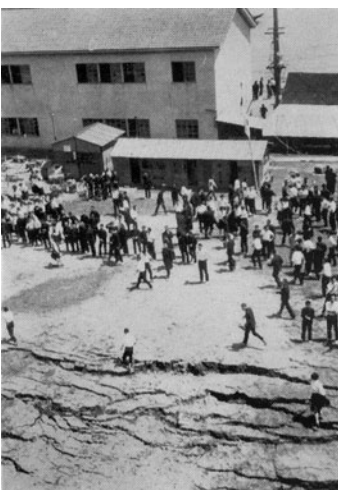


**Fig. 18.7** Distribution of pore pressure in 1-G model test (Sundarraaj,1996).

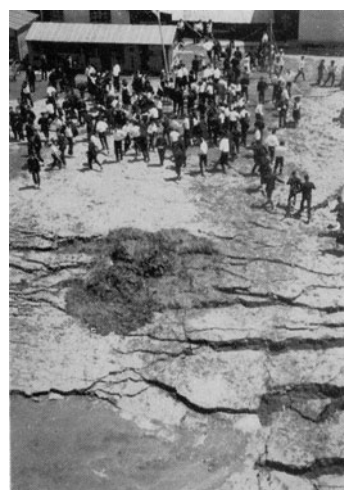


**Fig. 18.8** Bilinear idealization of excess pore water variation in vertical direction

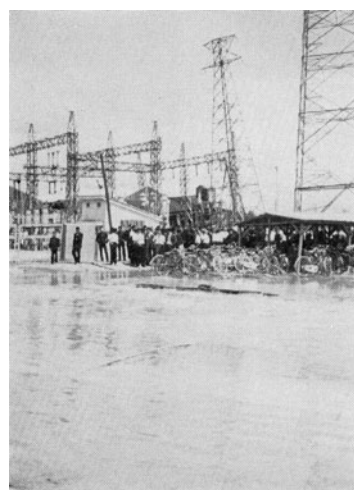
1:05 pm



1:10 pm



1:22 pm



**Fig. 18.9** Pictures taken during the 1964 Niigata earthquake (1:02 pm) (Photographs taken by Mr. Yutaka Takeuchi; JSSMFE, 1966)

Sand has a large volume contraction when the effective stress increases slightly from the state of complete liquefaction (Sect. 19.10). This is the reason for the difference from the Terzaghi's theory (1.12).

### 18.4 Paleoliquefaction

Liquefaction is an evidence that an earthquake of substantial intensity occurred. A detected sand boil (Sect. 18.2) indicates that a strong earthquake occurred in the particular region at a certain time. Liquefaction is thus a reliable evidence to find ancient earthquakes that are missing in written history or that occurred in prehistoric times (See also Sect. 18.5).

Figure 18.10 illustrates the idea. The excavated sand boil penetrates through soils of third and fifth centuries. Therefore, this liquefaction and the causative earthquake occurred in or after the 5th century. On the other hand, the sand boil is covered by a flood deposit of sixth century. Hence, the earthquake occurred before this flooding. Consequently, it is concluded that a big earthquake took place in fifth or sixth century. The age of soil is identified by using archaeological objects (考古学資料), carbon isotope ( $C_{14}$ ), tefra chronology (volcanic ash), and others.

By performing this kind of study nationwide, Sangawa (1997) detected many gigantic earthquakes, which had been missing in history. Figure 18.11 summarizes the history of big earthquakes that rocked the western part of Japan in the past more than 1,300 years. Those earthquakes with ● were identified by excavated sand boils and are consistent with known ones in written history. In contrast, those earthquakes with ○ were newly discovered by liquefaction studies. It is important that the newly detected earthquakes such as those in the B zone in 1498 fill the blank of earthquake histories between 1361 and 1605 and indicates more clearly the regular return period of gigantic earthquakes in the subduction zone. Accordingly, it is somehow possible to imagine the time of the next catastrophic earthquake.

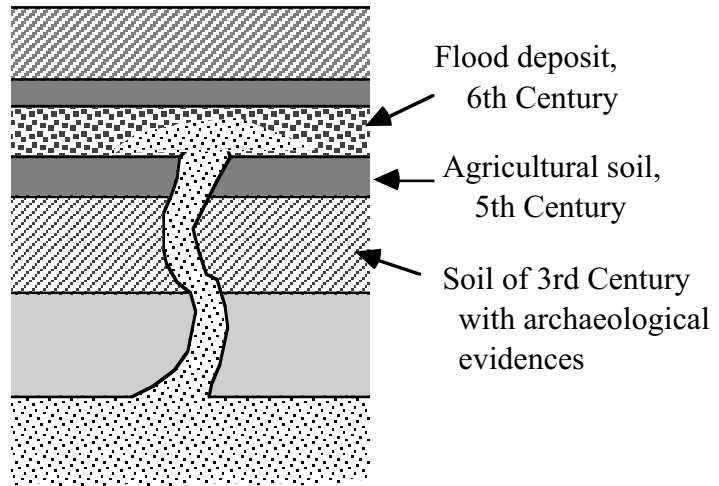


Fig. 18.10 Identification of age of ancient liquefaction

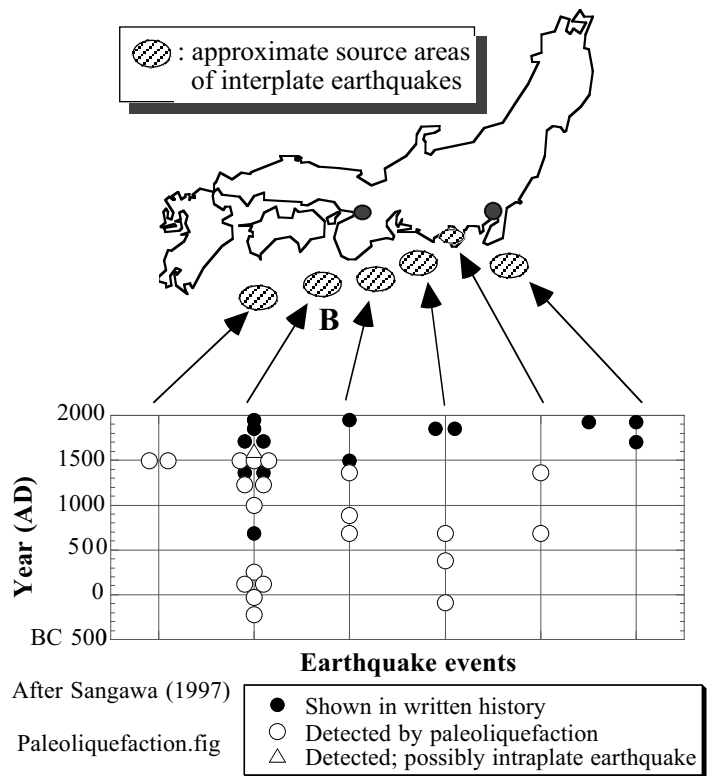


Fig. 18.11 History of gigantic earthquakes in subduction zone of Philippine Sea plate (drawn after Sangawa, 1997)

Paleoliquefaction study is a useful tool to investigate the local seismic activity when no written historical document is available (Elton and Hamou, 1990; Obermeier et al., 1985; Talwani and Cox, 1985; Talwani and Schaeffer, 2001). The paleoliquefaction approach to detect gigantic earthquake has been taken as well in the coastal area of, for example, Washington state of USA (Atwater, 1992).

### 18.5 Excavation of Buried Sand Boil

Embedded sand boiling is excavated at many places in the recent times. The aim of the excavation is to investigate the history of unrecorded strong earthquakes in the past, to understand the relationship between particle sizes of ejected sand at the surface and those in the original sand layer, and to observe the geometry of sand boiling.

Figure 18.12 is the view of excavation in a river bed in Sekiyado Town of Saitama, Japan, which was carried out by Tobishima Corporation. Figure 18.13 shows the cross section of the excavated ground in which sand boil was detected. The channel of boiled sand is not straight. Tuttle et al. (1990) found an extremely complicated shape of a boiling channel in their excavation study.



**Fig. 18.12** Overall view of excavation at liquefaction site in Sekiyado



**Fig. 18.13** Channel of boiled sand (Sekiyado)

## ☀ 18.6 Hot Liquefaction; True or Not True

Several past earthquakes were associated with something hot. For example, when Eginitis (1895) reported a big earthquake of 1894 in the Marmara Sea area of Turkey, he quoted eyewitness reports on warm sea water in St. Stephanos, warm well water in Makrikeuy, and rising of ground temperature at Galata. When the same area was hit by the 1999 Kocaeli earthquake, Mr. Beytullah Emen of Degirmendere City had his back injured by something hot when he fell down into the sea upon tsunami attack (Towhata et al. 2001). Tsukuda (1995) cited an eyewitness report that boiling water from liquefaction (Sect. 18.2) was as warm as 50°C during the 1990 Manjil earthquake, Iran. Wakamatsu (1993) reported that boiled sand and water were warm in Ago area of the Philippines after the Luzon earthquake in 1990 (Sect. 18.14). As for the same earthquake, Hamada et al. (1995) and Tsukuda (1995) mentioned that fish was boiled in a pond when the bottom soil liquefied in the Narbakan area. The author heard about hot liquefaction after the Qayen-Birjand earthquake of Iran in 1997. Finally, the ejected water was as hot as coffee according to local people, when the fill of Navlakhi Harbour liquefied (Fig. 17.12) during the 2001 Gujarat earthquake of India (Towhata et al. 2002).

In contrast to those *hot* events in Turkey, Iran, India, and the Philippines, no such event has been known in Taiwan, Japan, and California. When Mr. F. Yuminamochi was taking a motion picture of boiling water in Niigata (Fig. 25.59) in June, 1964, he never felt anything warm although his feet were under ejected water. No shaking model test and cyclic undrained tests reported warm liquefaction. The only one exception is Jouanna et al. (2000) who elevated the ground temperature by merely 2°C after artificially shaking ground for 1 h at 10 Hz with the acceleration level of 200 Gal.

To throw light on this topic, the author measured the temperature of boiled water when artificial liquefaction was generated by subsurface explosion at Tokachi Harbour, Nov. 2001 (Port and Harbour Research Institute; Fig. 18.14). Prior to the test, the air and ground water temperatures were 10 and 3.8°C, respectively. After shaking, the temperature in the ejected water ranged from 4–10°C. Similarly, in-situ liquefaction tests were carried out by the Zenitaka Corporation using mechanical shaking (Fig. 18.15). The temperature of the ejected water was 16°C, while the air and ground water temperatures prior to shaking were 9 and 16°C. Thus, no hot liquefaction was detected. It seems quite likely that the hot liquefied water in the past was made hot by surface soil that was heated by sunshine in the daytime and through which pore water was ejected at the time of liquefaction.



**Fig. 18.14** Explosion to trigger liquefaction



**Fig. 18.15** Field shaking test for verification of drain pipe technology

18.7 Undrained Shear Tests of Sand

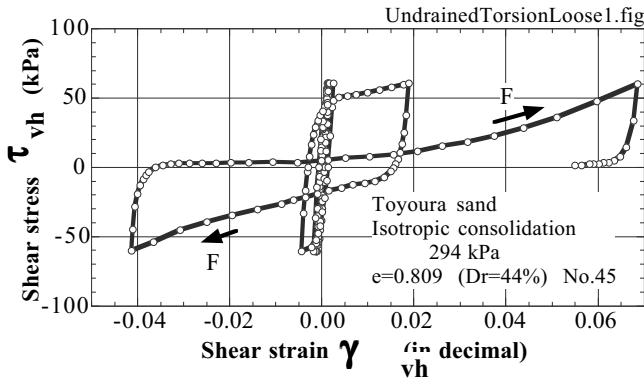


Fig. 18.16 Undrained stress–strain behavior of loose sand

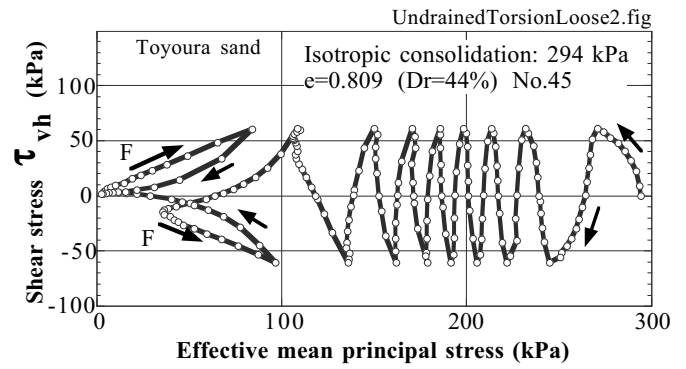


Fig. 18.17 Stress path of loose sand

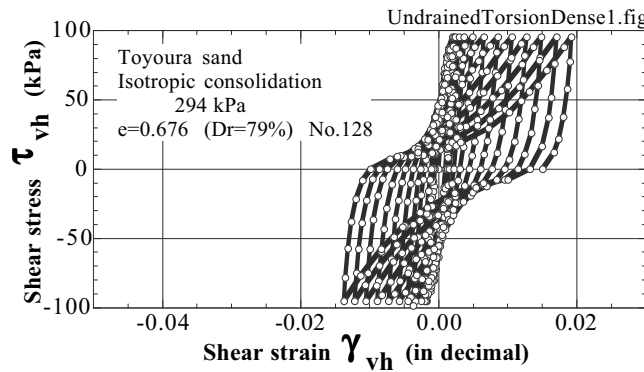


Fig. 18.18 Undrained stress–strain behavior of dense sand

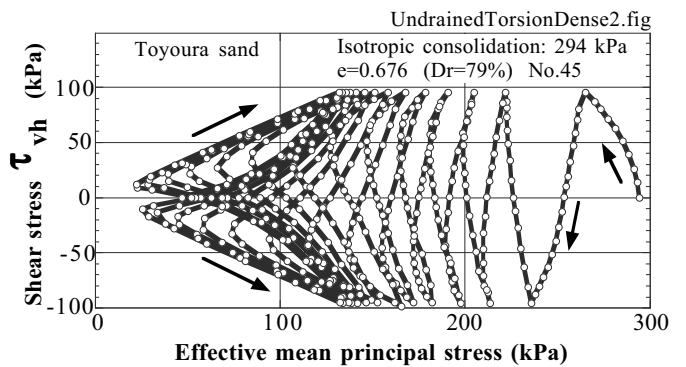


Fig. 18.19 Stress path of dense sand

Figures 18.16 and 18.17 illustrate the stress–strain and the stress-path diagrams of loose Toyoura sand. A hollow-cylindrical specimen was isotropically consolidated and then sheared by a torsion shear apparatus (Set. 18.8). It is seen that

1. The strain amplitude starts to increase drastically after some number of loading cycles
2. This strain increase seems to be associated with 50% pore pressure rise (excess pore water pressure = 50% of initial effective stress)
3. After 50% pore pressure rise, a few cycles of loading is sufficient to induce large deformation and zero effective stress (liquefaction)
4. In the final stage (shown by “F” in Fig. 18.17), the effective stress state moves along the failure line (dilative behavior), increasing effective stress as shear stress is loaded
5. In the meantime, the tangent modulus increases due to the increased effective stress (Fig. 18.16)
6. In the final stage of loading, pore pressure increases during unloading shear stress, while pore pressure drops in the course of loading [as stated in 3]; opposite from what was observed in early stages

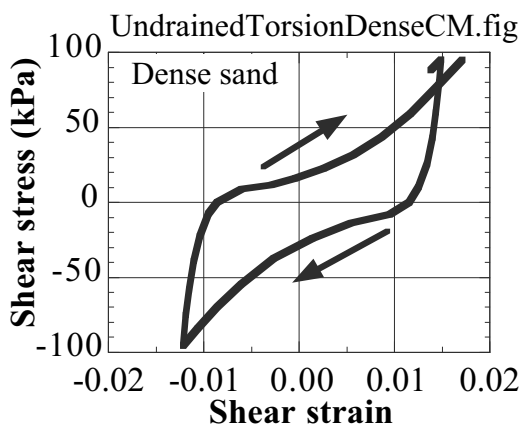


Fig. 18.20 Cyclic mobility

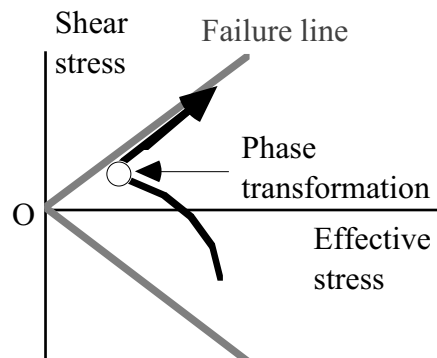


Fig. 18.21 Phase transformation in undrained stress path of sand



Figures 18.18 and 18.19 show similar test results obtained from dense Toyoura sand. The shear strain does not increase so rapidly as in Fig. 18.16. One part of the stress strain curve is depicted in Fig. 18.20. The slope (tangent modulus) increases as the shear stress is loaded because of increasing effective stress (Fig. 18.19 and Fig. 18.21). This behavior is called cyclic mobility and prevents development of large shear strain. Moreover, the effective stress does not reach zero. Thus, dense and compacted sand has a good resistance against liquefaction. Therefore, densification of sand (compaction) is the most important remedial measure 対策 against liquefaction (Sect. 26.4). It is good that the effect of densification is permanent without maintenance. Dense sand is unlikely to liquefy because its void ratio is close to the minimum void ratio ( $e_{\min}$  in Sect. 1.2) and there is not much volume contraction any more.

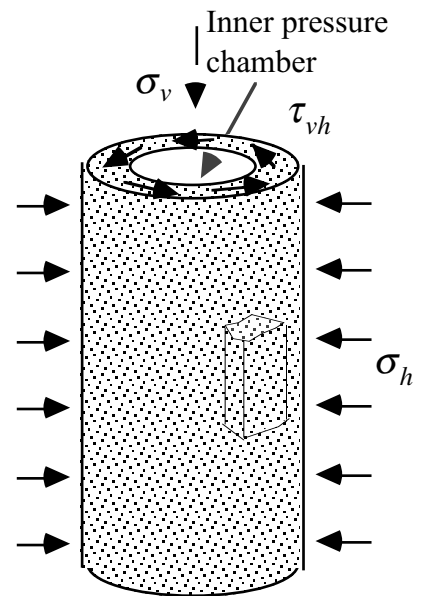
The transition from contractive behavior to dilatant one (decreasing effective stress to increasing) is called phase transformation (Fig. 18.21).

**18.8 Torsion Shear Device with Hollow Cylindrical Specimen**

In spite of its convenience, the triaxial shear device (Sect. 1.9) has several limitations. For example,

- It has only two independent stress components, while reality has three components in two-dimensional situation or six in three-dimensional conditions
- The orientations of principal stress axes ( $\sigma_v$  and  $\sigma_h$ ) are fixed in vertical and horizontal directions, whereas those axes rotate in real loading conditions

These limitations have been overcome by a torsion shear device that tests a hollow cylindrical specimen (Fig. 18.22). Similar to a conventional triaxial machine, this torsion shear device shears a specimen that is covered by rubber membranes and consolidated under cell water pressure (Fig. 18.23). Since the outer and inner cell pressures in the horizontal direction are equal in many cases, there are three degrees of freedom in stress control ( $\sigma_v$ ,  $\sigma_h$ , and  $\tau_{vh}$  in Fig. 18.22), and the radial and tangentially horizontal stresses are considered equal to each other ( $= \sigma_h$ ). Consequently, the effective mean principal stress,  $P'$ , is defined by



**Fig. 18.22** Stress application on hollow cylindrical specimen

$$P' = (\sigma_1' + \sigma_2' + \sigma_3')/3 = (\sigma_v' + 2\sigma_h')/3 \quad (18.4)$$

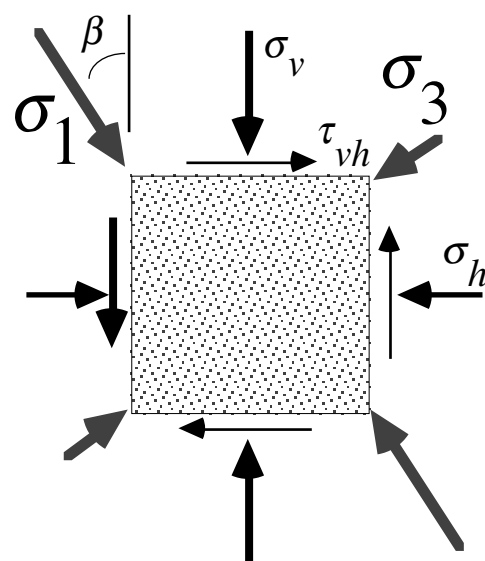
These components of stress are loaded on a hollow cylindrical specimen and the field stress condition is reproduced. Many tests have been conducted on liquefaction problems by using this apparatus.

The orientation of the major principal stress axes measured from the vertical direction (Fig. 18.24) is given by

$$\beta = \left\{ \arctan \left( \frac{2\tau_{vh}}{\sigma_v - \sigma_h} \right) \right\} / 2. \quad (18.5)$$



**Fig. 18.23** Hollow cylindrical specimen undergoing consolidation (by G. Arangelovski)

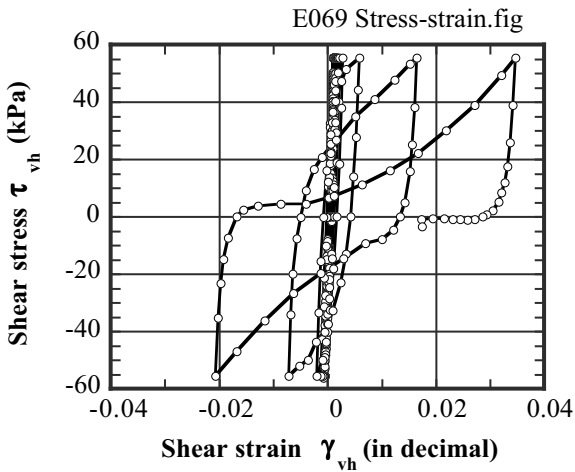


**Fig. 18.24** Definition of orientation of major principal stress

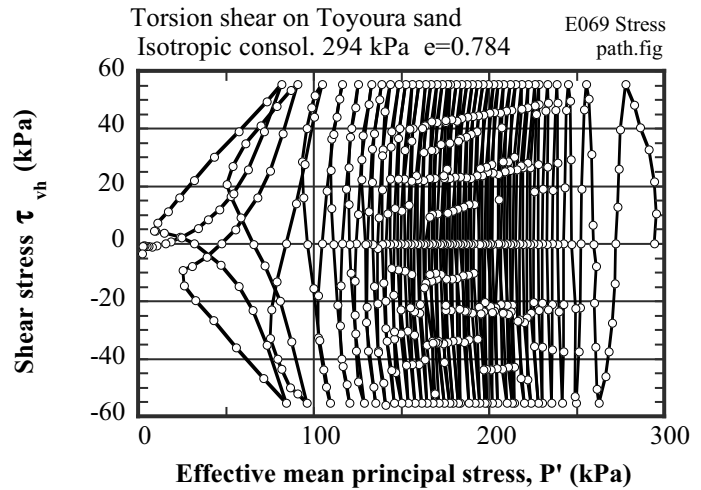
Another advantage of this device is that there is no end in the peripheral direction. Therefore, this device avoids the problem of nonuniform stress that is caused by end effects.

When undrained shear is conducted with lateral confinement (zero lateral strain) in the radial direction, the drainage valve of a specimen and another water inlet to the inner cell that is completely filled with water (see Fig. 18.22) are closed. This situation is equivalent with cyclic loading of level ground undergoing  $K_0$  condition.

It is sometimes stated that the torsion shear device cannot test an undisturbed soil specimen. It is not correct, actually. When the outer diameter of a tested specimen is 10 cm, a large undisturbed sample of at least 10 cm in diameter is trimmed to a hollow cylindrical shape so that it fits the employed size.



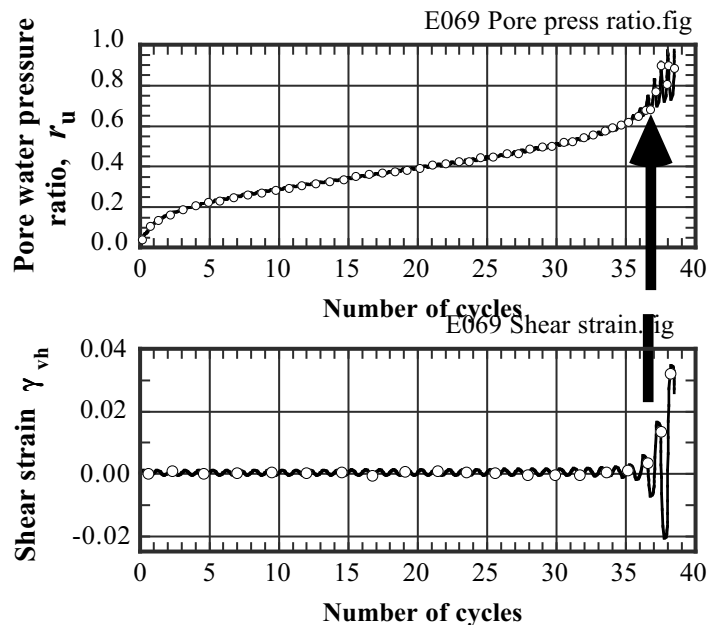
**Fig. 18.25** Stress–strain diagram in cyclic undrained torsion shear test



**Fig. 18.26** Stress-path diagram in cyclic undrained torsion shear test

An attempt has been made to increase the degree of stress freedom to four by applying different horizontal pressures in inner and outer chambers. This measure generates different horizontal stress in the radial and circumferential directions of a specimen. Although this is an attractive idea, care should be taken of heterogeneity of stress. The different horizontal pressures vary the radial stress in the specimen from its inner face to the outer face.

Similar to Figures in Sect. 18.7, Figs. 18.25 and 18.26 present undrained cyclic shear data. The number of cycles here is much greater than those in Sect. 18.7. This set of data was replotted in Fig. 18.27 where the variation of excess pore water pressure ratio ( $r_u = \text{excess pore water pressure} / \text{initial consolidation stress}$ ) is compared with the variation of shear strain amplitude. It is seen that sand becomes significantly soft and the shear strain amplitude starts to increase when the pore water pressure development exceeds approximately 60% of the initial consolidation pressure.



**Fig. 18.27** Comparison of pore pressure ratio and shear strain amplitude in undrained cyclic torsion shear

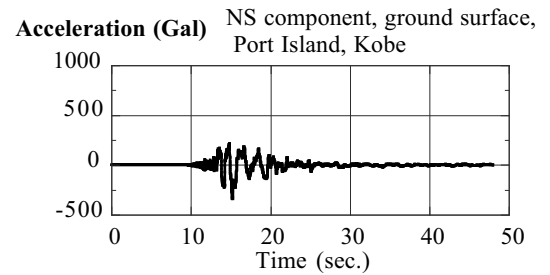
**18.9 Effects of Subsurface Liquefaction on Intensity of Acceleration Response at Surface**

The seismic isolation technology of modern buildings employs a very soft material in the foundation to avoid strong base-shear force that generates high acceleration in the super structure. The same principle holds true in a liquefied deposit where shear modulus is reduced drastically and high shear stress is not transmitted to the ground surface. This phenomenon is interpreted by the Newtonian equation of motion;

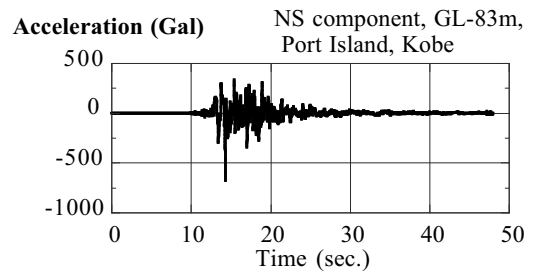
$$\text{Acceleration at surface} = \frac{\text{Shear stress in liquefied subsoil}}{\text{Mass of surface soil.}}$$

Figures 18.28 and 18.29 compare the acceleration time histories in the NS direction which was recorded in Port Island of Kobe in 1995 by a seismic vertical array deployed by the Development Bureau of Kobe City Government. It is evident that the maximum acceleration at the surface was weaker than the one at the depth of 83 m far below the liquefied deposit. It is important as well that the surface acceleration had a longer predominant period than the bottom motion, which is the consequence of softening of liquefied subsoil and the elongation of the natural period (resonance). Accordingly, Fig. 18.30 shows the variation of maximum acceleration in all the three directions. The reduction of accelerations in the top 20 m is evident. The assessment by SI (Set. 23.4) suggests that the same range of soil liquefied; *MASA* soil that is a decomposed granite used for reclamation in 1960s and 1970s.

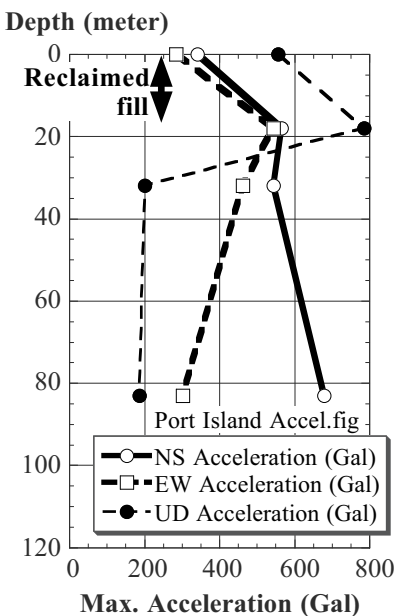
The elongated shaking period in Fig. 18.28 affected the velocity and displacement responses in Figs. 18.31 and 18.32. After time integration, the surface response became “greater” than the subsurface ones. Thus, although the reduced acceleration is probably less hazardous for superstructures above the surface, the increased displacement is hazardous to embedded lifelines and other facilities that are vulnerable to displacement-induced damages.



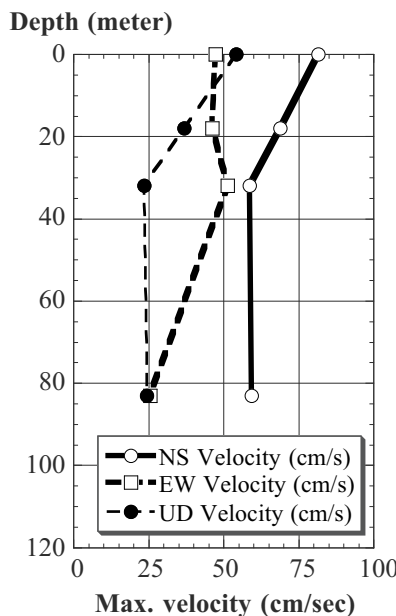
**Fig. 18.28** Acceleration record at surface of Port Island



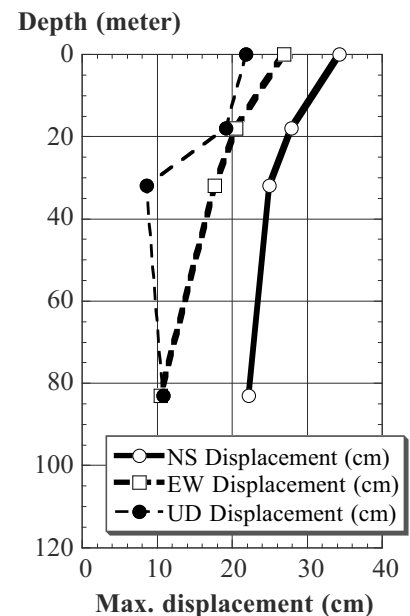
**Fig. 18.29** Acceleration record at GL-83m of Port Island



**Fig. 18.30** Variation of maximum acceleration with depth in Port Island



**Fig. 18.31** Variation of maximum velocity with depth in Port Island



**Fig. 18.32** Variation of displacement amplitude with depth in Port Island

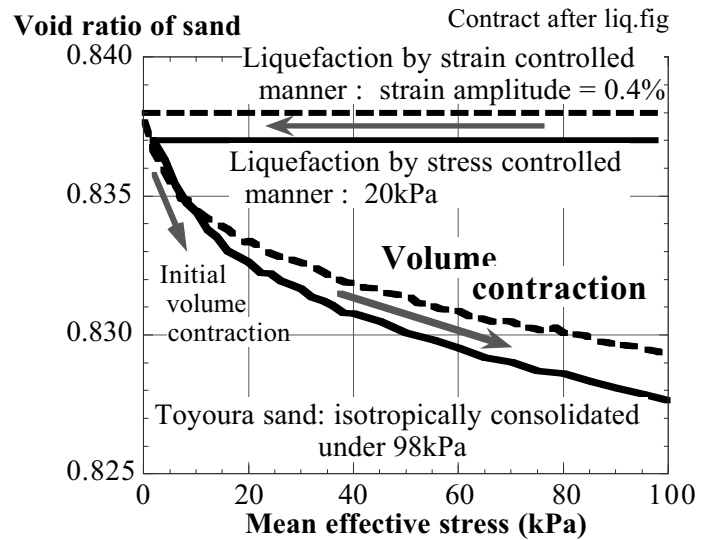
**18.10 Consolidation after Liquefaction**

The bilinear distribution of excess pore water pressure during dissipation/consolidation (Sect. 18.3) means that the critical hydraulic gradient continues for a long time near the surface until dissipation is completed. It is noteworthy that the conventional theory of consolidation by Terzaghi cannot predict such a bilinear pore pressure distribution. Therefore, a numerical analysis on the procedure of pore-pressure dissipation after liquefaction, as is often conducted for design of gravel drain (Sect. 26.11), should not employ Terzaghi theory.

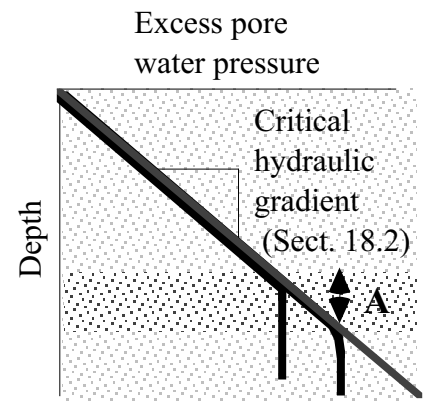
It is important that the volume change behavior of liquefied sand during dissipation of pore pressure is different from what Terzaghi theory assumes. Terzaghi theory employs a constant value of volume compressibility,  $m_v$ , which supposes a linear relationship between effective stress and volume change. Liquefied sand, conversely, does not exhibit such a linear behavior.

Figure 18.33 illustrates the variation of effective stress and void ratio of Toyoura sand specimen during undrained cyclic loading and the following dissipation/consolidation. Errors due to membrane penetration (Sect. 1.9) was corrected for by using the method by Sivathayalan and Vaid (1998). Liquefaction was induced by two manners, namely stress-controlled (constant stress amplitude) and strain-controlled (constant strain amplitude) manners. When effective stress started to increase again due to reconsolidation, void ratio did not respond in a linear way. As shown in Fig. 18.33, the stage of initial volume contraction (Fig. 18.33) generated greater volume compressibility than in the following stages. This suggests that sand grains that are floating in pore water during 100% liquefaction (Sect. 18.1) deposit quickly in the first stage of effective stress increase.

From the viewpoint of seepage flow, the substantial amount of pore water that is drained out from the lower layer (initial volume contraction in layer A, Fig. 18.34) is used to maintain high pore water pressure and the critical hydraulic gradient in the upper layers. In conclusion, it is necessary to take into account the large volume compressibility of sand undergoing the initial volume contraction to make a reasonable prediction of excess pore water pressure change during its dissipation process.



**Fig. 18.33** Volume contraction of Toyoura sand after liquefaction



**Fig. 18.34** Bilinear distribution of excess pore water pressure during dissipation and reconsolidation

18.11 Liquefaction Potential and Surface Geology

The possibility of liquefaction (liquefaction potential) is high in loose deposits of sand. In contrast, liquefaction is unlikely in dense sandy deposits. Liquefaction is not possible when there is no ground water. In a gigantic slope failure, furthermore, pore air may play the same role as pore water in liquefaction;

$$effective\ stress = total\ stress - pore\ air\ pressure \rightarrow zero.$$

Figure 17.8 demonstrated that the Shinano River in Niigata City was wider in previous times, and the area that was reclaimed in the twentieth century (Kawagishi-Cho) developed substantial liquefaction in 1964 (Fig. 17.6). Figure 18.35 is a map of Niigata City, which was published in early twentieth century. The Shinano River is drawn in the center. This river channel was twice wider in those days. By the middle of twentieth century, two flood channels were constructed in the upstream area, directly connecting this river and the sea, and it thereby became possible to reduce the river width in Niigata City for urban development. The land reclamation project was carried out by transporting fine uniform sand from the dune along the beach and throwing sand into the big inlet of the river. No densification was undertaken because sand was considered to be a good foundation soil (without consolidation settlement) in those days. Consequently, loose water-saturated young deposit of sand was formed. This is the place where liquefaction occurred intensely and apartment buildings tilted or fell down in 1964 (Fig. 17.6). Dagupan City of the Philippines where liquefaction occurred substantially in 1990 (Sect. 17.5) has a similar history of development; in the middle of the twentieth century, rice fields and fish ponds were reclaimed by throwing beach sand into water (Fig. 18.36). No liquefaction occurred in older ground of the city (Fig. 18.41).

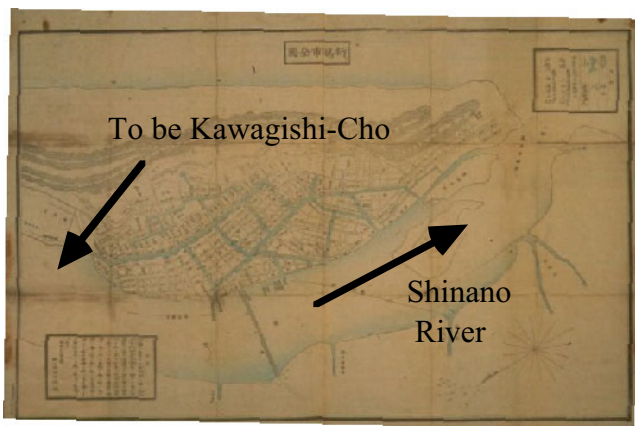


Fig. 18.35 Niigata City in early twentieth century

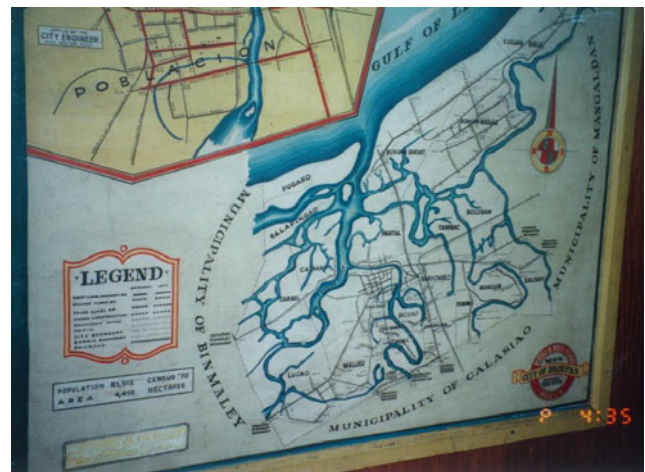


Fig. 18.36 Waters in Dagupan City

Loose sandy deposit with high ground water table is found in the following geological settings.

Land reclamation 埋立地: sedimentation in water makes loose sand packing (relative density being around 40%), young age of sand means no significant cementation, and few experience of strong earthquake shaking.

Abandoned river channels 旧河道: abandoned channels are often filled with natural sand deposit that is not compacted naturally.

Low land between sand dunes and near edge of dune hill 砂丘間低地: Dune sand has good resistance against liquefaction because it is dense due to wind action and water table is low. However, dune sand is transported downwards and deposits softly in low places where there is normally much water

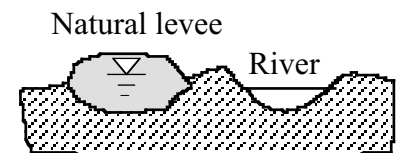
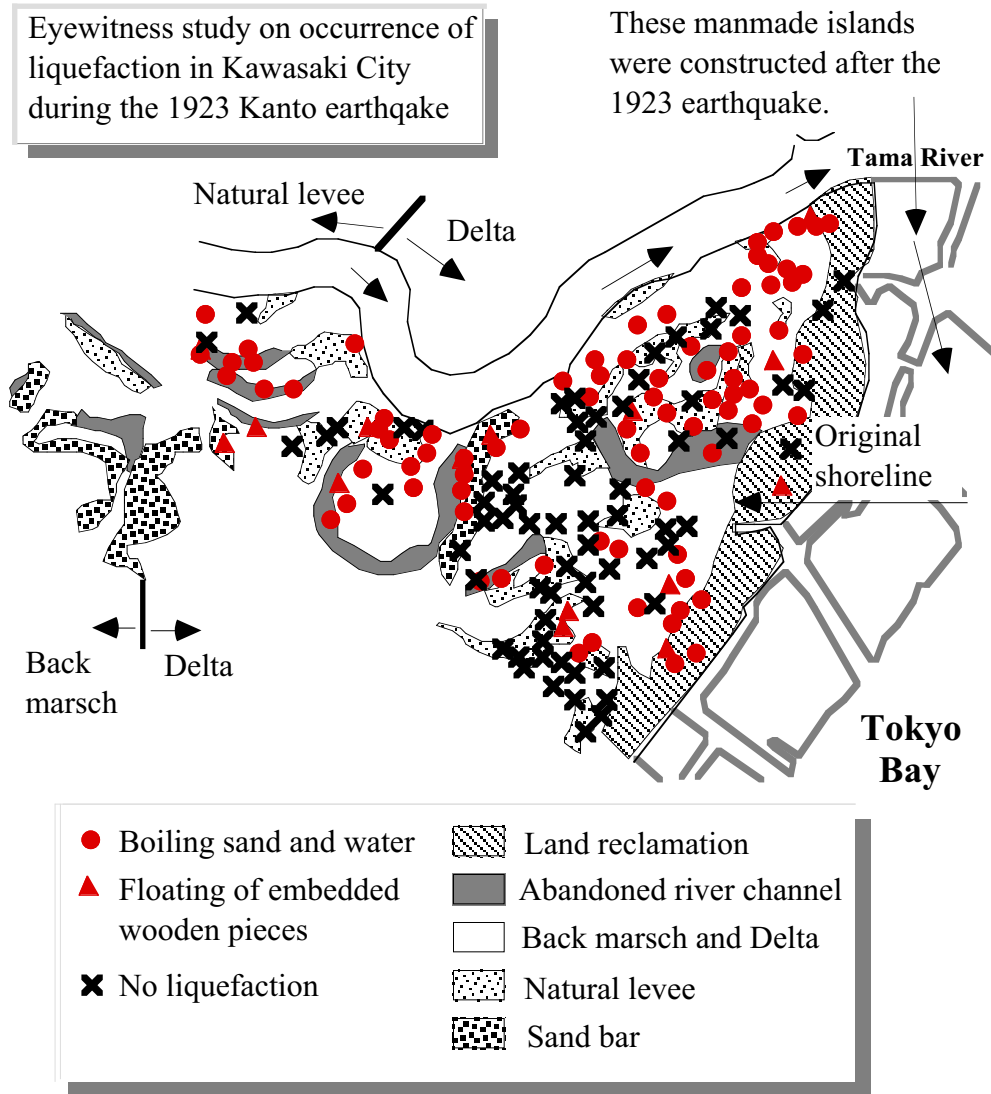


Fig. 18.37 Natural levee

Minor natural levee 自然堤防 : flooding leaves a natural embankment of sandy materials (Fig. 18.37); a natural levee itself is dry and good to live, but ground water table is high and sand may not be dense.

Liquefaction is not possible in terrace, hill, and mountains where neither loose young deposit of sand nor ground water is there. Those liquefaction-vulnerable soil conditions are usually accompanied by low SPT-*N* and cone penetration resistance.



**Fig. 18.38** Sites of liquefaction in Kawasaki, 1923 (Kubo et al. 1979)

Figure 18.38 is a case history study of liquefaction in the Kawasaki City during the Kanto earthquake in 1923. When an eyewitness mentions boiling of sand or floating of embedded wooden objects, it is judged that liquefaction occurred at the particular place. Note that area without any symbol in Fig. 18.38 may have developed liquefaction; missing of symbols simply means that there is no eyewitness.

Liquefaction mostly occurred along the abandoned channels of the Tama River and in its alluvial plain. The marine reclamation was not there in 1923. On the contrary, it is empirically known that beach sand has higher liquefaction resistance probably because it was densified by cyclic wave action.

Wakamatsu (1991) compiled an enormous amount of documents and eye-witness reports, which were mostly collected by herself, to identify the location of sand boiling and other liquefaction evidences all over Japan during past earthquakes. It is very useful to learn from her achievements that abandoned river channel is highly vulnerable to liquefaction.

**18.12 Maximum Distance of Liquefaction Sites from Source Area**

It is important from the perspective of seismic hazard assessment to predict the size of area where liquefaction is quite likely to occur. Basic data for this was assembled by using documented liquefaction during past earthquakes. Since people in old days did not use the term of “liquefaction,” alternative expressions such as boiling of sand and water, ejection, surface depression, subsidence of buildings, floating of embedded structures and likes had to be detected in literatures and interpreted.

Kuribayashi and Tatsuoka (1975) collected informations in Japanese earthquakes and did this job. The upper bound of the epicentral distance,  $R_e$  (Set. 5.10), at sites of liquefaction was taken for respective seismic magnitude. Since no magnitude of modern sense was known for historical earthquakes, the Kawasumi magnitude (Set. 5.4), which relies on the documented extents of damage, was used in place of  $M_{JMA}$  (magnitude determined by the Japanese Meteorological Agency in Set. 5.4). Consequently,

$$\log_{10}(R_e) = 0.77M_{JMA} - 3.6 \tag{18.6}$$

was derived; the unit of the epicentral distance,  $R_e$ , is kilometer. Ambraseys (1988) stated that Kuribayashi reduced the assessed Kawasumi magnitude by 0.5 for historical earthquakes before 1922. Accordingly, a revised formula was proposed;

$$\log_{10}(R_e) = 0.88M_{JMA} - 4.4 \tag{18.7}$$

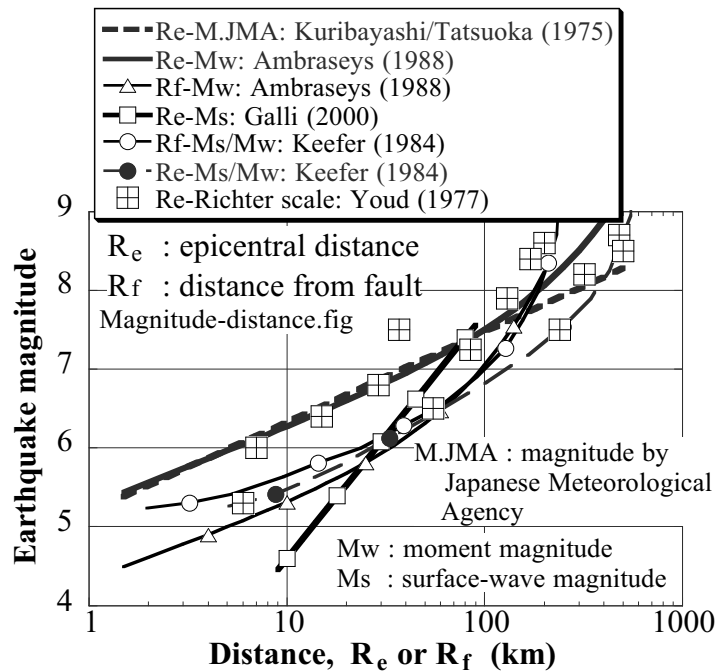
Afterwards, several studies of a similar type have been performed by using case histories in different parts of the world. For example, Ambraseys (1988) obtained

$$\begin{aligned} M_w &= -0.31 + 2.65 \times 10^{-8} R_e + 0.99 \log_{10}(R_e) \\ M_w &= 0.18 + 9.2 \times 10^{-8} R_e + 0.90 \log_{10}(R_f) \end{aligned} \tag{18.8}$$

in which  $R_e$  and  $R_f$  (distance from fault) are given in “cm” unit. Moreover, Galli (2000) obtained

$$M_s = 1.5 + 3.1 \times \log_{10}(R_e) \tag{18.9}$$

where  $R_e$  is in *km* unit. In summarizing liquefaction-induced soil flow, Keefer (1984) used  $M_s$  when it is less than 7.5 and  $M_w$  when it is greater than 7.5. Youd (1977) added data from many parts of the world. Although not clearly mentioned, his magnitude is probably the Richter magnitude. All the empirical formulae and data as mentioned earlier are summarized in Fig. 18.39. Note that liquefaction at the greatest distance is likely to be associated with the most liquefaction-prone soil conditions such as very loose young sandy deposit, amplification of motion by basin structure (Sect. 5.8) etc.



**Fig. 18.39** Maximum distance to liquefaction sites varying with seismic magnitude



### 18.13 Effects of Ageing on Liquefaction Strength of Fill

Figure 17.34 indicated the totally different behaviors of ground in Dagupan City, the Philippines. Although the younger ground subsided upon the 1990 Luzon earthquake due to liquefaction, the older natural-levee ground did not. A similar contrast is found between Figs. 18.40 and 18.41. While the former illustrates subsidence of building into liquefied ground, the latter shows the situation in the area of natural levee where no liquefaction occurred. Dagupan City was founded in this area by the Spanish people, and was expanded to the water area of rice field and fish pond in the twentieth century (Sect. 18.11). The new city area was made by placing beach sand in water, resulting thus in young loose water-saturated ground, which is highly vulnerable to liquefaction.



**Fig. 18.40** Subsidence of building in Dagupan City due to liquefaction

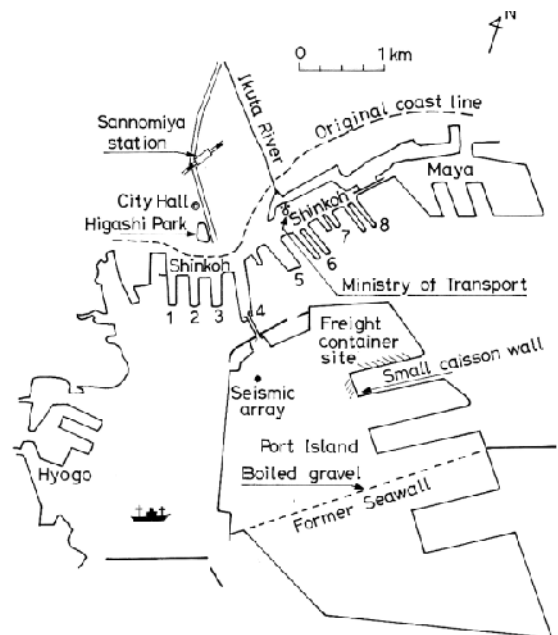


**Fig. 18.41** Area without liquefaction in Dagupan City



**Fig. 18.42** Kobe Harbor in 1868

Kobe harbor was constructed by filling soil in the sea. Figure 18.42 indicates the Kobe Harbor in 1868 before modern harbor construction was initiated. Figure 18.43 shows the area of Kobe Harbor in 1995. It is seen therein that Port Island, which suffered significant liquefaction, (Sects. 17.8, 20.2, 26.1) is located to the south of the original coast line. It means that liquefaction was substantial in young reclamation. In contrast, to the north of the original coast line, only very minor liquefaction was seen; for example in the Higashi Park as shown in Fig. 18.44. A similar contrast in liquefaction resistance was found in the coastal area of Nishinomiya, which is located to the east of Kobe. Figure 18.45 shows that no liquefaction occurred to the right hand side of an original sea wall because the soil condition here was a natural and aged sand. Conversely, beyond the sea wall, the subsoil was a product of very recent (after 1970) reclamation and liquefaction occurred significantly.



**Fig. 18.43** Location of liquefaction in coastal area of Kobe, 1995



**Fig. 18.44** Minor liquefaction in Higashi Park on inland side of original coast line in Kobe



Significant liquefaction on the other side of sea wall

Former sea wall and coast

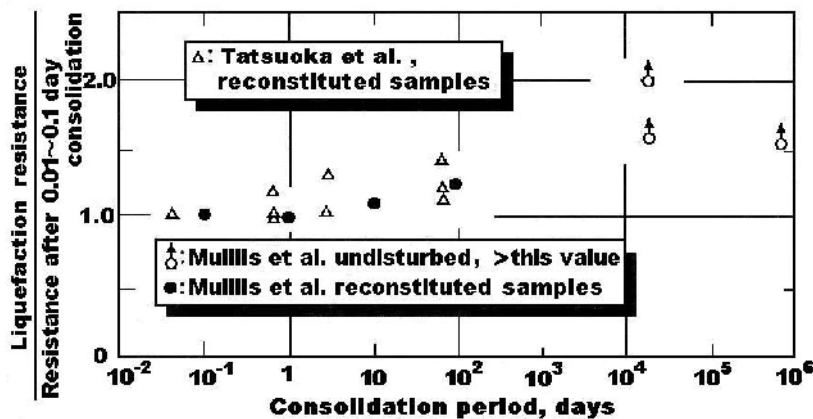


No liquefaction in aged soil

**Fig. 18.45** Contrast in liquefaction resistance due to age difference

Thus, there is a significant difference in possibility of liquefaction due to the age of soil. Although volume compression after liquefaction (Sect. 18.10) increases the density of sand, its resistance against liquefaction does not increase so much as may be expected; see repeated liquefaction in Sect. 22.2.

Most probably the liquefaction resistance of sand is increased by age. Although the details of ageing effects are not yet known, the first issue may be the accumulated densification effects because of historically repeated strong earthquakes. For example, Japanese sandy ground that is probably a few thousand years old hardly liquefies because of active seismicity, while aged pleistocene sand in the New Madrid area, Central USA, liquefied during the 1811–1812 New Madrid earthquake. Probably, low seismic activity in this area did not densify natural sand and liquefaction resistance was still low.

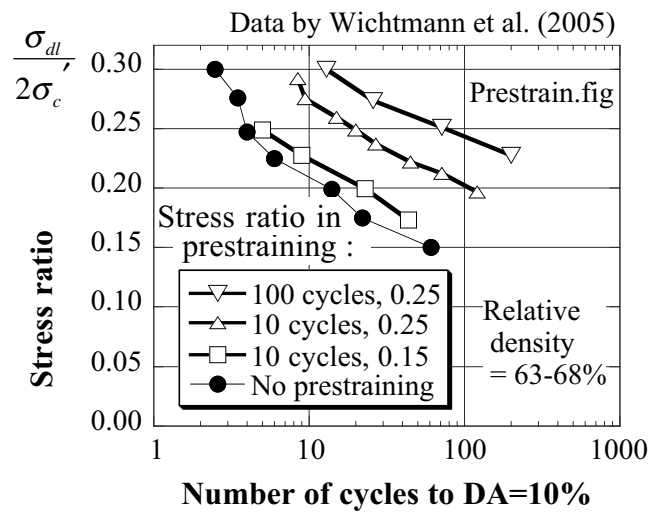


**Fig. 18.46** Effects of consolidation time on liquefaction resistance

The ageing effects have been reported from laboratory tests as well (Fig. 18.46). In this figure, the data by Tatsuoka et al. (1988) comes from laboratory shear tests, which show that sand after longer consolidation has greater resistance, although no earthquake loading occurred to the specimen. Mullis et al. (1977) compared laboratory measured strength against assessed behavior of aged sand to show the increase of strength with age. Moreover, Seki et al. (1992) collected undisturbed sand samples from a site in Kamakura where sand boil evidences the liquefaction (Sect. 18.2) 700 years ago. The cyclic triaxial tests on undisturbed and laboratory-reconstituted specimens revealed that the undisturbed samples, which

were 700 years old since the previous earthquake, is 1.3–1.4 times more resistant. Note that the relative density of the undisturbed samples were 73–82%, while the reconstituted samples were looser (67–72%). Finally, Fig. 18.47 illustrates the effects of minor cyclic (drained) shear (prestraining) on liquefaction resistance of sand of medium density. The prestraining was intended to reproduce effects of minor past earthquakes. Although prestraining with the stress ratio of 0.25 with 100 cycles induced only 0.3% of volumetric contraction, the increase in the liquefaction resistance was remarkable. In summary, it seems that ageing is induced by two agents: repeated compaction due to minor earthquakes and grains dropping into big voids (Sect. 1.14).

It seems that these findings on ageing suggests very low potential of liquefaction in natural deposits of sand that are at least hundreds of years old and have experienced several strong earthquakes. Possibly repeated liquefaction (Sect. 22.2) finally results in sufficiently high density and resistance of sand and also minor shaking generates the prestraining effects. This idea is consistent with the empirical knowledge that most significant liquefaction has occurred in young artificial deposits or backfill of sand (Chap. 17). It may be, therefore, said that liquefaction risk in sea bed is high only in special environments where the rate of sedimentations is very high, for example, near a mouth of a big river (Fraser River mouth in Chillarige et al. 1997; Valdez Harbor in Fig. 15.52). In contrast, the submarine ground in a continental shelf where the rate of sedimentation is, for example, 0.1 cm/y or less (Saito, 1993) is not susceptible to liquefaction except in the top 1 m. This suggests that a destructive lateral flow of liquefied soil (Chap. 24) is quite unlikely in sea bed except in a special environment such as that off a river mouth. This idea is beneficial to submarine development in seismically active region of the world, although further geological evidence and soil investigation, such as submarine CPT, are needed.



**Fig. 18.47** Effects of prestraining on liquefaction resistance of sand (data by Wichtmann et al. 2005)

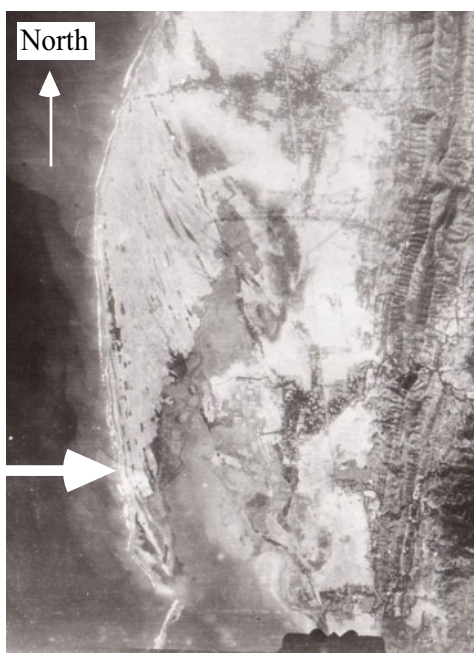
**18.14 Liquefaction in Natural Deposit of Loose Sand**

Section 18.13 revealed that liquefaction in older natural deposits is less likely than in recent artificial fill. The experience in Kobe, 1995, agrees with this idea. The Kawagishi-cho site in Niigata was filled artificially by using clean sand in about 1930 (Fig. 18.35). The Marina district in San Francisco where liquefaction occurred in 1989 Loma Prieta earthquake was filled in 1900s. The liquefaction in fill of Dagupan City is in line with these experiences. The good resistance of natural and more aged sandy deposit against liquefaction comes probably from the ageing (Sect. 18.13), the densification by repeated shaking during past earthquakes, and possibly another densification by wave action.

The heavy liquefaction in the Narbakan Village (Fig. 17.30) occurred in a natural deposit of sand. This may appear exceptional. Figure 18.48 shows the Luzon Island of the Philippines in which the Lingayen Gulf is seen on the north-west part of the Island. The Narbakan village is located on a small sandy peninsula to the north of Dagupan. The important feature of this sandy subsoil is the rapid sedimentation of sand. Figure 18.49 was taken around 1940 of the peninsula. The rapid growth of the peninsula in consequence of sedimentation is evidenced by the laminar structure of the surface. Inside the inland sea between the peninsula and the mainland (Fig. 18.50) there is only weak wave action, which exerts limited cyclic loading and densification. The young sandy deposit without sufficient ageing had not experienced seismic densification in the past. Consequently, the sand in the peninsula had low resistance against liquefaction at the time of the earthquake in 1990.



**Fig. 18.48** Map of the Luzon Island, the Philippines



**Fig. 18.49** Narbakan peninsula in air photo (National Archives, Washington D.C.)



**Fig. 18.50** Inland sea between mainland and peninsula of Narbakan

## 18.15 Significance of Cyclic Triaxial Tests in Liquefaction Problems

Although shaking model tests can provide important information about mechanism of liquefaction, it cannot assess the liquefaction potential of specified sites. This assessment is done by running cyclic triaxial tests on undisturbed soil samples (Sect. 10.19) collected at sites.

Figure 18.51 illustrates an idealized stress state during earthquakes in a level ground. Prior to earthquakes, the effective stress has a  $K_0$  state ( $\sigma'_{hc} = K_0 \sigma'_{vc}$ ; anisotropic consolidation; 異方圧密) and there is no shear stress in the horizontal plane. The vertical propagation of  $S$  wave produces in the horizontal plane a cyclic shear stress, which alternates in positive and negative directions and induces negative dilatancy of sand fabric (砂の粒子構造) as well as build-up of excess pore water pressure. The amplitude of the cyclic shear stress is denoted by  $\tau$ . Although there is a need to reproduce this stress state in a laboratory, an appropriate testing machine (cyclic simple shear or torsion shear device) is not widely available. More important is that a soil specimen of rectangular (直方体) or hollow cylindrical (中空円筒) shape, which is required by those testing machines, does not suit the use of undisturbed soil specimens collected by insitu soil samplers.

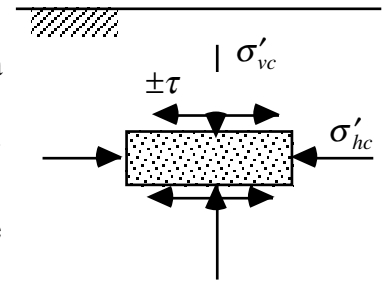


Fig. 18.51 Seismic stress state in level ground

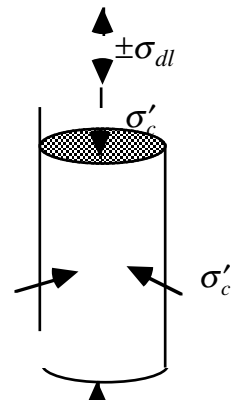


Fig. 18.52 Stress state in cyclic triaxial tests

Consequently, cyclic triaxial testing on *undisturbed soil samples* (Sects. 10.17 and 10.19) is widely practiced. Figure 18.52 indicates the stress state in this testing. A soil specimen is isotropically consolidated under the effective stress of  $\sigma'_c$ , which is normally set equal to the insitu effective vertical stress. After consolidation, a cyclic axial stress,  $\pm\sigma_{dl}$ , is loaded in undrained manners until large deformation occurs. Note that  $\pm\tau$  in the horizontal plane in the field is replaced by  $\pm\sigma_{dl}$  in the axial direction in the laboratory.

Stress states in Figs. 18.51 and 18.52 are different in the following points: (1) plane strain and axial symmetry, (2) anisotropic and isotropic consolidations, (3) rotation and fixed directions of principal stress, etc. Thus, perfect agreement between the field and the laboratory conditions is not possible. However, there is some similarity in stress states between Fig. 18.51 and the one in the  $45^\circ$  plane of a triaxial specimen (Fig. 18.53).

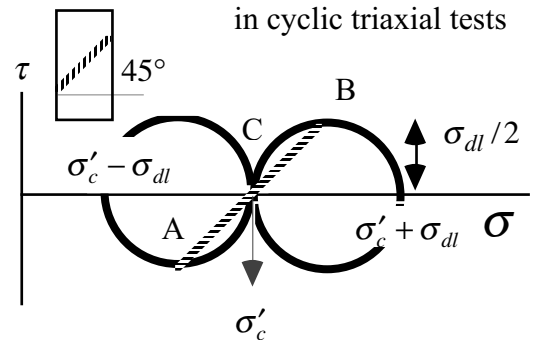


Fig. 18.53 Mohr's stress circle during cyclic triaxial test

Figure 18.53 indicates a Mohr's stress circle of a cyclically loaded triaxial specimen. The  $45^\circ$  plane is initially consolidated under  $\sigma'_c$  without initial shear stress (point C). Upon cyclic loading, its normal and shear stress vary in the range of  $\sigma'_c \pm \sigma_{dl}/2$  and  $\pm\sigma_{dl}/2$  (points A and B). Since the specimen is fully saturated with water, the variation of normal stress is 100% transferred to pore water pressure (Skempton's  $B = 1$ ; Sect. 18.16), and does not affect the specimen. Thus, the normal stress variation is ignored and the following relation is found between the field and the laboratory;  $\sigma'_{vc} \Leftrightarrow \sigma'_c$ ,  $\pm\tau \Leftrightarrow \pm\sigma_{dl}/2$ , and stress ratio  $\tau/\sigma'_{vc} \Leftrightarrow \sigma_{dl}/(2\sigma'_c)$ .

One may imagine that the normal stress upon the  $45^\circ$  plane can be maintained constant by varying both the axial stress by  $\sigma_{dl}/2$  and the lateral cell pressure by  $-\sigma_{dl}/2$ . This is difficult in practice, because the cell pressure is controlled by pneumatic system (air pressure) that is slow in response and cannot operate in phase with the axial loading.

### 18.16 Skempton's B Value

Cyclic triaxial tests on sand in the laboratory are performed by using water-saturated samples, because unsaturated sand is significantly less liquefiable than saturated insitu sand (Sect. 18.1).

The extent of water saturation of tested specimens is evaluated by using Skempton's  $B$  value. Skempton (1954) described the increment of pore water pressure in soil undergoing undrained stress increments by

$$\Delta u = B\{\Delta\sigma_3 + A(\Delta\sigma_1 - \Delta\sigma_3)\} \quad (18.10)$$

where  $\Delta u$  is the increment of pore water pressure, while  $\Delta\sigma_1$  and  $\Delta\sigma_3$  are the increments of major and minor total principal stresses, respectively; they are not effective stresses. The first term in  $\{\}$  stands for the contribution by the isotropic stress increment, while the latter designates the component made by shear-induced dilatancy.

$B$  is 1.0 when sand is ideally and fully saturated. Hence,

$$\Delta u = \Delta\sigma_3 \quad (18.11)$$

when stress increment is isotropic ( $\Delta\sigma_1 = \Delta\sigma_3$ ).

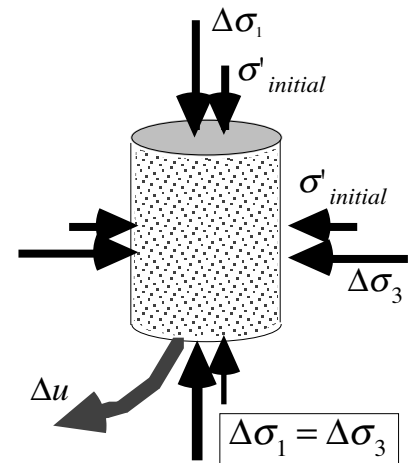
In the practice of laboratory tests, the following procedure is made for good saturation.

1. A sand specimen is supported by low isotropic effective stress of  $\sigma'_{initial}$  in an assembled pressure chamber
2. To help achieve high extent of saturation, the pore air in the sample is removed either by using vacuum or circulating carbon-dioxide ( $\text{CO}_2$ ) gas slowly through the specimen from its bottom to the top. Note that, when vacuum is employed, the applied external pressure has to be reduced as well so that the effective stress of  $\sigma'_{initial}$  may be maintained
3. De-aired water (distilled water without solved air) is then circulated slowly from the bottom to the top. The rate of circulation of gas and water has to be sufficiently slow; otherwise grain packing of sand would be disturbed by the flow
4. To examine the extent of saturation, the drainage valve of a triaxial device is closed and isotropic undrained compression is made; equal total stress increments are applied to the specimen;  $\Delta\sigma_1 = \Delta\sigma_3$ ; see Fig. 18.54. The increment of pore water pressure,  $\Delta u$ , during this loading is measured
5. The extent of saturation is evaluated by comparing the measured pore pressure increment with the theoretical value of fully saturated sand (18.11).

$$B = \Delta u / \Delta\sigma_3 \quad (18.12)$$

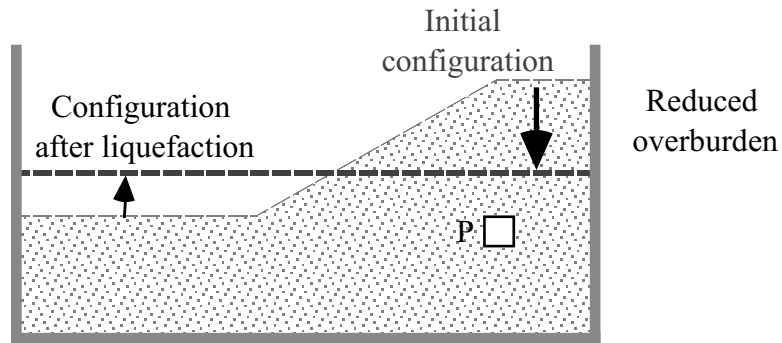
6.  $B$  greater than 0.95 (or 0.97, for example) is considered satisfactory. The water pressure in the pore water circuit of a testing machine is raised to the same level as the measured pore water pressure, the drainage valve is opened, and the consolidation stage is resumed
7. If saturation is not satisfactory, the drainage valve is opened in the same way as stated earlier, de-aired water is circulated again, and the  $B$  value is measured once more. Since the pore water pressure during this second attempt is higher than during the previous attempt, pore gas is solved in water, and improved saturation is very likely

Note that  $B$  value is still low even if the conventional degree of saturation,  $S_r$ , is close to 100%. Thus, the  $B$  value is a more sensitive index of saturation.



**Fig. 18.54** Undrained isotropic loading of total stress for examining extent of saturation

In shaking model tests on large deformation of liquefied slope (Chap. 23), it is possible that the recorded excess pore water pressure does not reach the initial effective stress level (what is called 100% development of excess pore water pressure), although the sand exhibits very soft behavior. While one of the reasons for this is the positive dilatancy and drop of pore water pressure due to large shear deformation ( $A < 0$ ), the other reason is the decrease of  $\Delta\sigma_3$  (the disappearance of overburden pressure);  $B\Delta\sigma_3 < 0$  at point P in Fig. 18.55. Because of the reduced overburden, the 100% development of excess pore water pressure is achieved under lower magnitude of pressure.



**Fig. 18.55** Full development of liquefaction in model test at excess pore pressure lower than initial effective stress

**18.17 Degree of Saturation and Skempton’s B Value**

Since liquefiable subsoil is considered to be water-saturated, laboratory liquefaction tests make a lot of efforts to attain high extent of saturation in a specimen. The extent of saturation is evaluated by Skempton’s  $B$  value in place of the degree of saturation,  $S_r$ , because the  $B$  value is a more sensitive index when a specimen is near the complete saturation. The relationship between  $B$  value and  $S_r$  is going to be derived in this section.

Suppose an undrained isotropic loading of stress increment,  $\Delta\sigma$ , on a soil sample with pore water and minor amount of air bubbles (Fig. 18.56). The effective stress and pore water pressure increase by  $\Delta\sigma'$  and  $\Delta u$ , respectively. The volume contraction of the soil skeleton (fabric of grains) is given by

$$\Delta\varepsilon_{\text{skeleton}} = m_v \Delta\sigma'$$

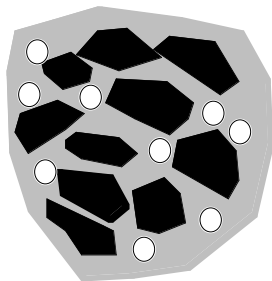
where  $m_v$  is the volume compressibility of soil skeleton (1.12).

The volume change of pore space is calculated by assembling contributions from pore water and pore air bubbles. The volume contraction of water is derived as

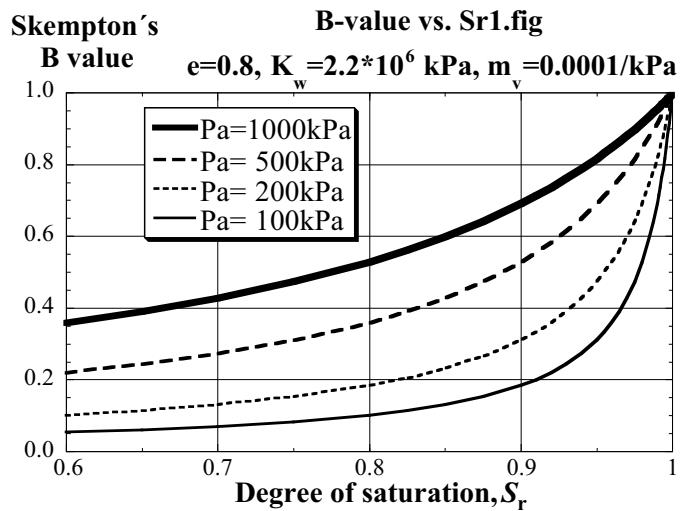
$$\Delta\varepsilon_{\text{water}} = \frac{e S_r \Delta u}{1 + e K_w}$$

in which “ $e$ ” stands for the void ratio,  $e S_r / (1 + e)$  the volume of water per unit volume of soil, and  $K_w$  the bulk modulus of water.

When the effects of surface tension at the interface of water and air are ignored for simplicity, the pore air pressure increment is equal to that of pore water pressure,  $\Delta u$ . The volume of pore air changes from the initial value of  $e(1 - S_r) / (1 + e)$  under the absolute pressure of  $P_a$  to a new volume of  $e(1 - S_r) / (1 + e) - \Delta\varepsilon_{\text{air}}$  when the pressure increases from the absolute pressure of  $P_a$  to  $P_a + \Delta u$ . The absolute pressure starts from zero under perfect vacuum. Since the Boyle’s law states that  $Pressure \times Volume$  is maintained constant,



**Fig. 18.56** Soil element consisting of particles, pore water, and air bubbles



**Fig. 18.57** Example calculation of Skempton’s B value varying with degree of saturation



$$P_a \frac{e(1-S_r)}{1+e} = (P_a + \Delta u) \left\{ \frac{e(1-S_r)}{1+e} - \Delta \epsilon_{\text{air}} \right\}$$

Accordingly,

$$\Delta \epsilon_{\text{air}} = \frac{e(1-S_r)}{1+e} \frac{\Delta u}{P_a + \Delta u} \approx \frac{e(1-S_r)}{1+e} \frac{\Delta u}{P_a}$$

when  $\Delta u$  is small. Note that solving of pore air into pore water is ignored.

No drainage is allowed upon undrained loading, and, therefore, the volume change of soil skeleton is equal to the volume change of pore;

$$\begin{aligned} \Delta \epsilon_{\text{skeleton}} &= m_v \Delta \sigma' = \Delta \epsilon_{\text{water}} + \Delta \epsilon_{\text{air}} \\ m_v (\Delta \sigma - \Delta u) &= \frac{e S_r}{1+e} \frac{\Delta u}{K_w} + \frac{e(1-S_r)}{1+e} \frac{\Delta u}{P_a} = \frac{e}{1+e} \left( \frac{S_r}{K_w} + \frac{1-S_r}{P_a} \right) \Delta u \\ B &\equiv \frac{\Delta u}{\Delta \sigma} = \frac{1}{1 + \frac{e}{1+e} \left( \frac{S_r}{K_w} + \frac{1-S_r}{P_a} \right) / m_v} \end{aligned}$$

Figure 18.57 illustrates an example calculation in which  $e=0.8$ ,  $K_w=2.2 \times 10^6$  kPa, and  $m_v = 10^{-4}$  kPa. The  $B$  value suddenly increases toward 1.0 when  $S_r$  exceeds 0.9. The minimum acceptable value of  $B$  in laboratory tests is 0.95–0.97. When saturation is not satisfactory, the back pressure,  $P_a$ , is raised to higher values so that pore gas solves into water and the remaining size of bubbles is compressed and decreases further.

### 18.18 Effects of Sample Preparation Methods on Resistance to Liquefaction in Laboratory Shear Tests

The liquefaction resistance of insitu ground is evaluated by collecting undisturbed soil samples (Sects. 10.19 and 10.20) and running undrained cyclic shear tests. Although this measure is useful, different approach is needed for planning of earth fill dam and more basic studies on effects of a variety of soil properties on liquefaction phenomenon. If latter is the case, soil samples are prepared in a laboratory.

There are several methods of sample preparation. For example, Fig. 18.58 illustrates the method of air pluviation in which air-dry sand falls through a funnel with the height of fall maintained constant. The prepared sample is made denser by increasing the height of fall (gravity energy) or reducing the rate of fall (less grain-to-grain collision and energy loss) as Kolbuszewski (1948a, b) reported.

The density is controlled also by vibration or impacts (Fig. 18.59). This densification is performed by placing sand by layers (for example, 10 layers) and each layer is densified as illustrated in Fig. 18.59 to the desired relative density (Sect. 1.2). Usually, the number of hammer impacts or tamping is held constant for all the layers. It is sometimes the case that less efforts are made for bottom layers because the bottom layers are somehow densified further when upper ones are compacted. The particular number of impacts for each layer is determined by trials-and-errors. Among these methods, the author prefers air pluviation with controlled height of sand fall because this method gives the most stable results (repeatability in test results).

Since shear tests assume uniform stress and strain states within a specimen, efforts are needed to achieve uniform density and uniform packing of sand grains as well. When sand is densified layer by layer as in Fig. 18.59, it is possible that lower layers are subject to more number and more extent of compaction than upper layers. To avoid this, Ladd (1978) proposed to carry out less extent of compaction for lower layers (undercompaction). Although some index was proposed by Ladd (1978) to achieve the best uniformity, its meaning is not clear. Anyhow, the variation in extent of compaction between lower and upper layers should be determined by trials-and-errors.

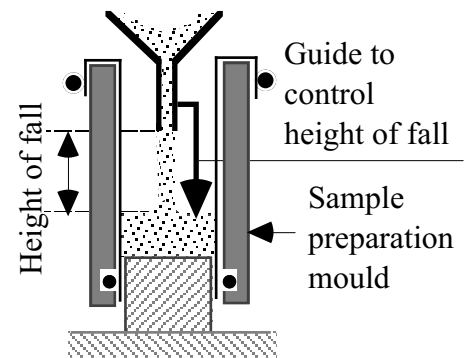


Fig. 18.58 Air pluviation technique of sample preparation

Another important issue in sample preparation is the extent of water saturation. In early days, a reasonably high extent of saturation was achieved by water-pluviation in which a sample preparation mould (Fig. 18.58) was filled with deaired water, and then sand, which was submerged in water, was slowly poured into the mould

(Fig. 18.60a). Deaired water means distilled water (pure water without solution of gas) that is placed under vacuum for at least several hours so that dissolved gas may be removed. Deaired water is expected to have less risk to generate air bubble in the pore of a soil sample.

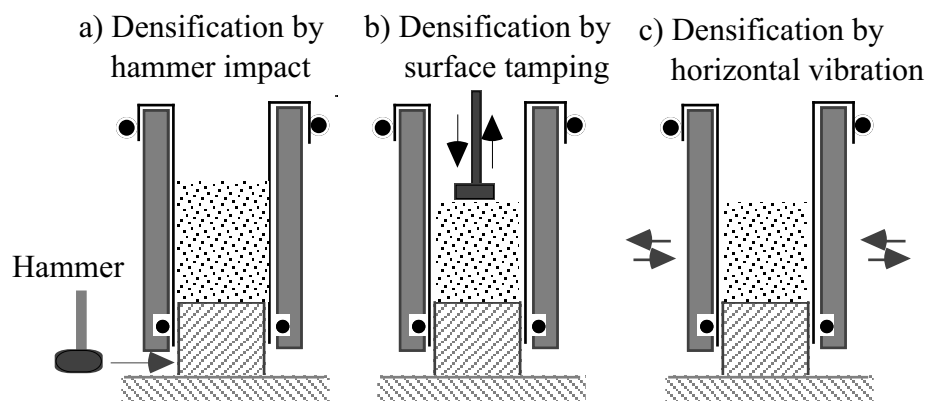
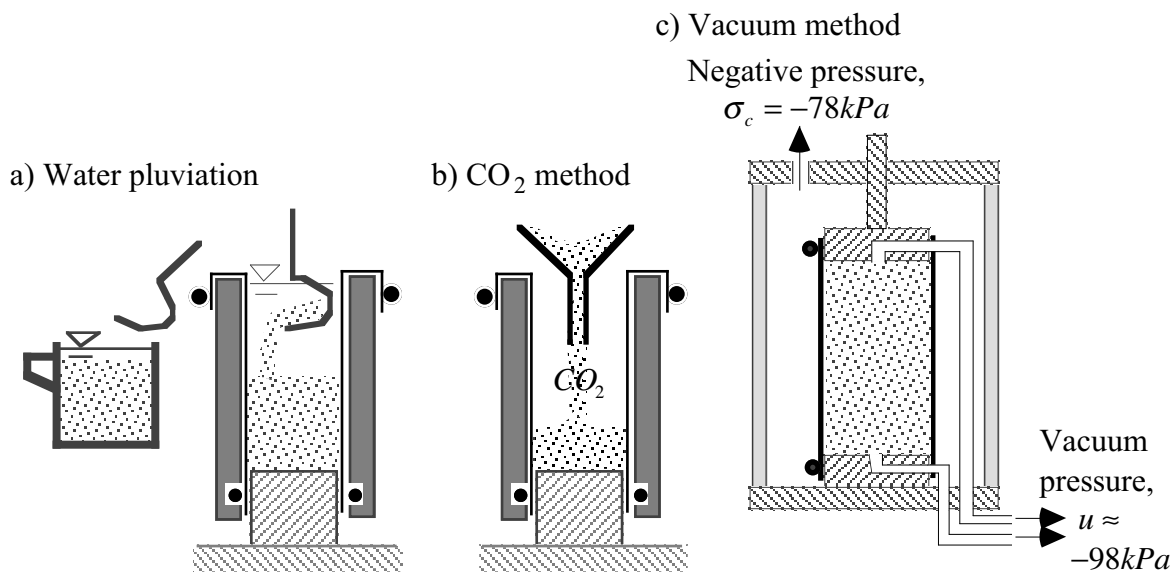


Fig. 18.59 Densification of sand sample

Another problem to affect water saturation is the migration of molecules of pressurized air ( $N_2$  and  $O_2$ ) through the pressurized water in the triaxial chamber and then through molecular holes of a rubber membrane. Since the water in the chamber is under higher pressure, no bubble occurs. Once the gas

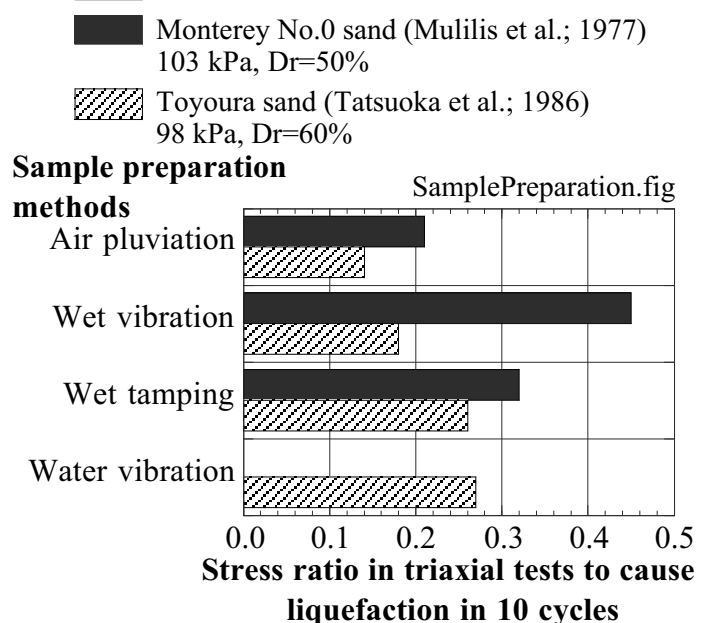
molecules come into a soil specimen, the pore water is subject to lower pressure, and the dissolved gas is turned to bubbles. This is a problem during long-term consolidation (maybe longer than ten days). To avoid this, it is necessary to pressurize the chamber water by balloons, which prevents any contact of water and air. Use of mercury as the chamber liquid is useful. However, mercury may give health problems to experimentalists.

More recently, the degree of saturation has been improved either by (1) pluviation of CO<sub>2</sub> gas (during sample preparation) (Fig. 18.60b) and circulating CO<sub>2</sub> gas from bottom to top of a sample followed by deaired water or by (2) removal of pore air by vacuum (Fig. 18.60c). In the vacuum method, the pore pressure is made approximately equal to -98 kPa. To maintain the effective stress at a low level in this stage of sample preparation, the external pressure (total stress or chamber pressure) is reduced as well to, for example, -78 kPa, so that the effective stress is maintained at -78 kPa - (-98 kPa) = 20 kPa. Skempton's B value (Sect. 18.16) is desired to be not less than 0.95 as a criterion of water-saturation. It is, however, easy to achieve  $B > 0.98$  after some experiences.



**Fig. 18.60** Measures to help achieve high degree of water saturation

Different methods of sample preparation give different resistance to liquefaction. Mulilis et al. (1977) prepared sand samples by vibration of wet sand, tamping of wet sand, and pluviation of dry sand, and conducted liquefaction tests in order to find different liquefaction resistance. They further conducted microscopic studies on grain-to-grain contacts and discussed their statistic nature. It was also shown that sample preparation by layers results in layered structure in a sample. This is not a very good situation because uniformity within a sample body is always desired. In this regard, Miura and Toki (1982) proposed multiple sieve pluviation technique in which dry sand falls continuously through several sieves prior to deposition in a sample preparation mould.



**Fig. 18.61** Effects of sample preparation methods on liquefaction resistance of sand specimens

Tatsuoka et al. (1986) carried out experimental studies as well. Their results together with those by Mulilis et al. (1977) are shown in Fig. 18.61. It is seen therein that air pluviation produces the least liquefaction resistance (Chap. 19), while vibration or tamping leads to higher resistance. Air pluviation reproduces grain-to-grain contacts (microscopic granular structure) under gravity field. This condition is similar to what happens in real sedimentation process. More recently, Ghionna and Porcino (2006) obtained similar liquefaction resistance from frozen undisturbed samples (Sect. 10.20) and water-pluviation samples.

The effects of stress state during consolidation of a sand specimen was investigated by Yamashita et al. (1990). Thus, many studies have been made on the effects of sample preparation method on measured liquefaction resistance. Note, however, that no sample preparation method can precisely reproduce the natural geological procedure that consists not only of sedimentation process but also stress history and ageing effects (Sect. 18.13). This is the reason why collecting undisturbed soil samples is always important.

### List of References in Chapter 18

- Ambraseys, N.N. (1988) *Engineering Seismology, Earthq. Eng. Struct. Dynam.*, Vol. 17, No. 1, pp. 1–105.
- Atwater, B.F. (1992) Geologic evidence for earthquakes during the past 2000 Years along the Copalis River, Southern Coastal Washington, *J. Geophys. Res.*, Vol. 97, B2, pp. 1901–1919.
- Chillarige, A.V., Morgenstern, N.R., Robertson, P.K. and Christian, H.A. (1997) Seabed instability due to flow liquefaction in the Fraser River delta, *Canadian Geotechnical Journal*, Vol. 34, pp. 520–533.
- Eginitis, D. (1895) Le tremblement de terre de Constantinople du 10 juillet 1894, *Annales de Geographie*, Vol. 4, pp. 151–165 (in French).
- Elton, D.J. and Hamou, T.H. (1990) Liquefaction potential for Charleston, South Carolina, *J. Geotech. Eng., ASCE*, Vol. 116, No. 2, pp. 244–265.
- Florin, V.A. and Ivanov, P.L. (1961) Liquefaction of saturated sandy soils, *Proc. 5th Int. Conf. Soil Mech. Found. Eng.*, Vol. 1, pp. 107–111.
- Galli, P. (2000) New empirical relationships between magnitude and distance for liquefaction, *Tectonophysics*, No. 324, pp. 169–187.
- Ghionna, V.N. and Porcino, D. (2006) Liquefaction resistance of undisturbed and reconstituted samples of a natural coarse sand from undrained cyclic triaxial tests, *J. Geotech. Geoenv. Eng., ASCE*, Vol. 132, No. 2, pp. 194–201.
- Hamada, M., Wakamatsu, K., Tazoh, T. and Yoshida, N. (1991) Soil liquefaction and resulting damage to structures during the July 16, 1990 Philippine earthquake, *Tsuchi-to-Kiso, Month. Magazine, Jpn. Geotech. Soc.*, Vol. 39, No. 2, pp. 51–56 (in Japanese).
- Jouanna, P., Mabssout, M. and Abellan, M.-A. (2000) Thermal signature of in situ soil damping under severe seismic actions, *Soil Dynam. Earthq. Eng.*, Vol. 19, pp. 55–64.
- JSSMFE (1966) Brief explanation on pictures taken at the moment of Niigata Earthquake, *Soils Found.*, Vol. 6, No. 1, pp. i–vi.
- Keefer, D.K. (1984) Landslides caused by earthquakes, *Geol. Soc. Am. Bull.*, Vol. 95, pp. 406–421.
- Kolbuszewski, J.J. (1948a) General investigation of the fundamental factors controlling loose packing of sands, *Proc. 2nd Int. Conf. Soil Mech. Found. Eng.*, Vol. 1, pp. 47–49.
- Kolbuszewski, J.J. (1948b) An experimental study of the maximum and minimum porosities of sands, *Proc. 2nd Int. Conf. Soil Mech. Found. Eng.*, Vol. 1, pp. 158–165.
- Kubo, K., Sugiyama, T. and Yasuda, S. (1979) Sites of liquefaction in Kawasaki City during 1923 Kanto earthquake 関東地震時の川崎市における液状化地点, *Proc. 14th National Conf., Jpn Soc. Soil Mech. Found. Eng.*, pp. 1289–1292 (in Japanese).

- Kuribayashi, E. and Tatsuoka, F. (1975) Brief review of liquefaction during earthquake in Japan, *Soils Found.*, Vol. 15, No. 4, pp. 81–92.
- Ladd, R.S. (1978) Preparing test specimens using undercompaction, *Geotech. Test. J.*, Vol. 1, No. 1, pp. 16–23.
- Maslov, N.N. (1957) Questions of seismic stability of submerged sandy foundations and structures, *Proc. 4th Int. Conf. Soil Mech. Found. Eng.*, Vol. 1, pp. 368–372.
- Miura, S. and Toki, S. (1982). A sample preparation method and its effect on static and cyclic deformation -strength properties of sand, *Soils Found.*, Vol. 22, No. 1, pp. 61–77.
- Mulilis, J.P., Mori, K., Seed, H.B. and Chan, C.K. (1977) Resistance to Liquefaction due to Sustained Pressure, *Proc. ASCE*, Vol. 103, GT7, pp. 793–797.
- Mulilis, J.P., Seed, H.B., Chan, C.K., Mitchell, J.K. and Arulanandan, K. (1977) Effects of sample preparation on sand liquefaction, *Proc. ASCE*, Vol. 103, GT2, pp. 91–107.
- Obermeier, S.F., Gohn, G.S., Weems, R.E., Gelinas, R.L. and Rubin, M. (1985) Geologic evidence for recurrent moderate to large earthquakes near Charleston, South Carolina. *Science*, Vol. 227, pp. 408–411.
- Saito, Y. (1993) Sequence in continental shelf in Pacific Ocean off North East Japan, *Chikyu Monthly, Special Issue 8 on Symposium on Events, Rhythm, and Their Records*, pp. 80-85 (in Japanese).
- Sangawa, A. (1992) Paleoliquefaction detected in archaeological sites, *Tsuchi-to-Kiso Month. Magazine, Jpn. Geotech. Soc.*, Vol. 40, No. 1, pp. 13–18 (in Japanese).
- Sangawa, A (1997) Shaking ground - seismic history of Japanese Archipelago, *Doubou-Sha*, ISBN4-8104-2363-8 C0021, p. 20 (in Japanese) (寒川旭 : 揺れる大地—日本列島の地震史—、同朋舎).
- Seed, H.B. (1979) Soil liquefaction and cyclic mobility evaluation for level ground during earthquakes, *Proc. ASCE*, Vol. 105, GT2, pp. 201–255.
- Seki, S., Mori, S. and Tachibana, H. (1992) Study on liquefaction and ageing effects in archaeological sites at Yuhigahama of Kamakura, *Proc. 47th Ann. Conv. JSCE*, Vol. 3 (in Japanese).
- Shahnazari, H. and Towhata, I. (2002) Torsion shear tests on cyclic stress-dilatancy relationship of sand, *Soils Found.*, Vol. 42, No. 1, pp. 105–119.
- Sivathayalan, S. and Vaid, Y.P. (1998) Truly undrained response of granular soils with no membrane-penetration effects, *Can. Geotech. J.*, Vol. 35, No. 5, pp. 730–739.
- Skempton, A.W. (1954) The pore pressure coefficients A and B, *Geotech.*, Vol. 4, No. 4, pp. 143–147.
- Sundarraj, K. Prasad (1996) Evaluation of deformation characteristics of 1-G model ground during shaking using a laminar box, *Doctoral thesis, University of Tokyo*, p. 238.
- Talwani, P. and Cox, J. (1985) Paleoseismic evidence for recurrence of earthquake near Charleston, South Carolina. *Science*, Vol. 229, pp. 379–381.
- Talwani, P. and Schaeffer, W.T. (2001) Recurrence rates of large earthquakes in the South Carolina coastal plain based on paleoliquefaction data, *J. Geophys. Res.*, Vol. 106, pp. 6621–6642.
- Tatsuoka, F., Kimura, H., Pradhan, T.B.S. (1988) Liquefaction strength of sands subjected to sustained pressure, *Soils Found.*, Vol. 28, No. 1, pp. 119–131.
- Tatsuoka, F., Ochi, K., Fujii, S. and Okamoto, M. (1986) Cyclic undrained triaxial and torsional shear strength of sands for different sample preparation methods, *Soils Found.*, Vol. 26, No. 3, pp. 23–41.
- Towhata, I., Ishihara, K., Kiku, H., Shimizu, Y. and Irisawa, T. (2001) Submarine slides and land settlements in coastal areas during Kocaeli earthquake, *Proc. Earthq. Geotech. Eng. Satellite Conf., XVth Int. Conf. Soil Mech. Geotech. Eng.*, Istanbul, Turkey, pp. 71–76.
- Towhata, I., Prasad, S.K., Honda, T. and Chandradhara, G.P. (2001) Geotechnical reconnaissance study on damage caused by 2001 Gujarat earthquake of India, *Soils Found.*, Vol. 42, No. 4, pp. 77–88.
- Tsukuda, T. (1995) Precursor and Prediction of Big Earthquake, *Asahi News Shop series*, p. 46.
- Tuttle, M., Law, K.T., Seeber, L. and Jacob, K. (1990) Liquefaction and ground failure induced by the 1988 Saguenay Quebec Earthquake, *Can. Geotech. J.*, Vol. 27, pp. 580–589.

- Wakamatsu, K. (1993) In Report on the July 16, 1990, Luzon earthquake, the Philippines, JSCE, pp. 170–173.
- Wakamatsu, K. (1991) Map of historical liquefactions in Japan, University of Tokai Press (in Japanese).
- Wakamatsu, K. (1993) In Report on the July 16, 1990, Luzon earthquake, the Philippines, JSCE, pp. 170–173.
- Wichtmann, T., Niemunis, A., Triantafyllidis, Th. and Poblete, M. (2005) Correlation of cyclic preloading with the liquefaction resistance, *Soil Dynam. Earthq. Eng.*, Vol. 25, pp. 923–932.
- Yamashita, S., Toki, S. and Miura, M. (1990) Change of liquefaction behaviour in sand with anisotropic fabric due to anisotropic consolidation history, *Soils Found.*, Vol. 30, No. 2, pp. 167–178 (in Japanese).
- Yoshimi, Y. (1967) An experimental study of liquefaction of saturated sands, *Soils Found.*, Vol. 7, No. 2, pp. 20–32.
- Youd, T.L. (1977) Discussion of "Brief review of liquefaction during earthquakes in Japan," *Soils Found.*, Vol. 17, No. 1, pp. 82–85.

# Chapter 19

## Assessment of Liquefaction Potential



The castle of Gwalior, India.

Many lords or Maha Raja maintained their political status during the British period.

19.1 Significance of Stress Ratio

Resistance of sand against liquefaction is determined by running undrained cyclic triaxial tests on undisturbed soil specimens (Sect. 18.15). Cyclic stress with a constant amplitude is loaded repeatedly (similar to torsion shear tests in Sect. 18.8), and the number of cycles are counted until 1) excess pore water pressure equal to the initial effective stress ( $\sigma'_c$ ) and (2) peak-to-peak (i.e., double amplitude) axial strain equal to 2.5%, 5%, 10%, etc. The 100% development of excess pore water pressure is called “initial liquefaction” and the strain upon initial liquefaction may not yet be as large as those mentioned above. Thus, liquefaction in laboratory tests are defined in different ways; by pore pressure rise or development of strain. When sand is loose, the number of cycles needed for pore pressure rise and large strain amplitude are not much different.

Lee and Seed (1967) reported the cyclic stress amplitude that causes liquefaction in 10 or 100 cycles. In Fig. 19.1, liquefaction is defined by 100% pore pressure rise and 20% axial strain in double amplitude (peak-to-peak amplitude). For any void ratio of sand, the cyclic stress amplitude needed to cause liquefaction increases with the initial confining pressure (consolidation stress). Noteworthy is that the required shear stress amplitude increases as sand becomes denser as well. In Fig. 19.2, the cyclic stress amplitude again increases with the confining pressure. See that liquefaction defined by large strain requires greater stress amplitude than the initial liquefaction defined by pore pressure rise equal to the initial consolidation pressure (initial liquefaction). This means that the strain is not yet large at the moment of initial liquefaction. This is particularly the case of dense sand; see Fig. 19.26.

Since the cyclic shear stress increases with the initial confining pressure in these figures, the idea of stress ratio was developed;  $\sigma_{dl}/(2\sigma'_c)$ . Since the stress ratio thus measured stands for the resistance of sand against cyclic undrained loading, it may be called the cyclic resistance ratio (CRR). However, there can be seen in figures some curvature in data. This means that stress ratio needed to trigger liquefaction slightly decreases as effective

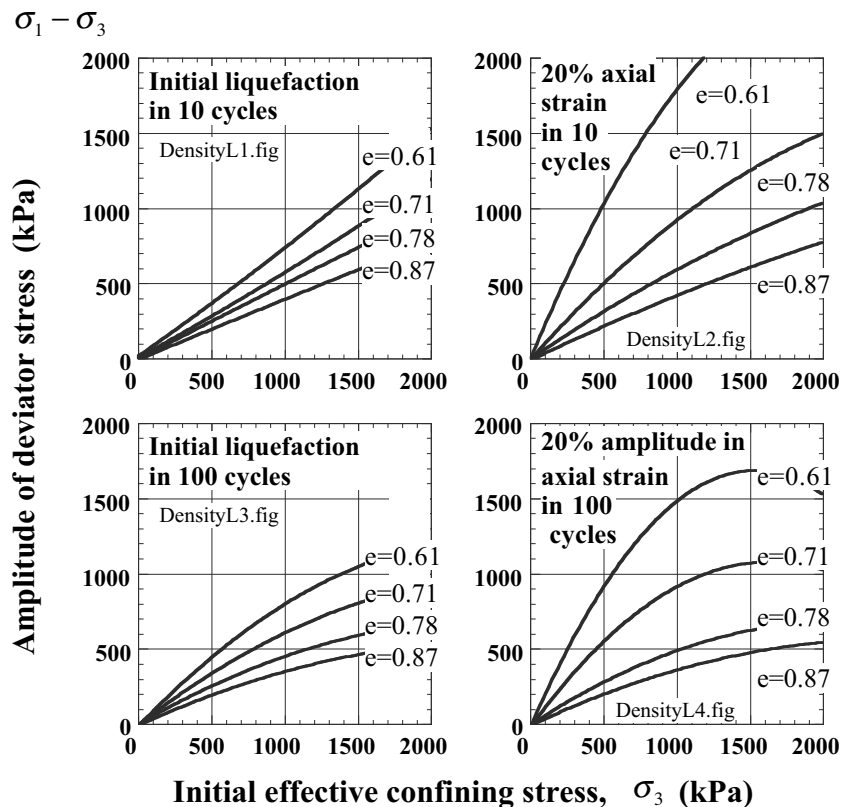


Fig. 19.1 Effects of sand density on stress state to cause liquefaction (Lee and Seed, 1967)

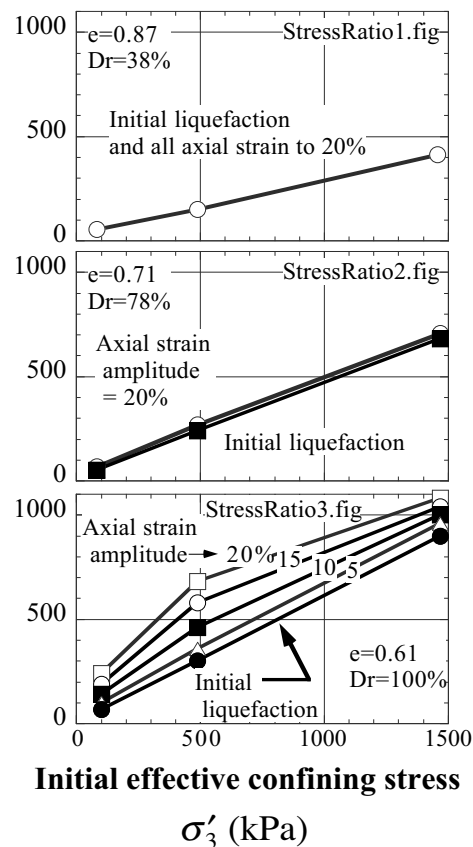


Fig. 19.2 Stress state to cause liquefaction as defined in different ways (Lee and Seed, 1967)



stress increases. This is due to negative dilatancy of sand that is more profound under higher pressure (Figs. 1.20 and 1.24). Hence, the resistance of sand against liquefaction, as defined by a cyclic stress ratio, decreases as the overburden pressure (depth) increases, even if other conditions are kept identical.

19.2 Stress Ratio in the Field

Section 19.1 showed that the resistance of soil against liquefaction is expressed by stress ratio, which is measured experimentally by cyclic triaxial tests. In contrast, there is a need to determine the stress ratio that may occur in the field during an expected (design) earthquake. To date, there are two ways to determine this field stress ratio:

1. Use of computer analysis : The wave propagation theory in horizontally layered ground is employed. The design earthquake is specified at the base and an equivalent linear analysis is carried out. The maximum shear stress as calculated is divided by the initial effective vertical stress to obtain  $\tau/\sigma'_{vc}$ .

Problem : The equivalent linear analysis does not take into account the softening of soil due to pore pressure build-up. This shortcoming could cause errors in analysis of liquefaction. It is thought today that the equivalent linear analysis is acceptable until apore pressure develops 50%. During this phase, the maximum shear stress is quite likely to occur. Hence, *the field stress that causes liquefaction is able to be predicted by an equivalent linear analysis, but postliquefaction stress and shaking cannot be analyzed.*

2. Use of rigid block analogy : The idea (Seed and Idriss, 1971) is shown in Fig. 19.3. The maximum horizontal acceleration at the ground surface,  $A_{max}$ , is directly specified by design codes (for instance,  $A_{max} = 0.15 G$ ). When the soil column in Fig. 19.3 is ideally rigid, it does not deform and the acceleration is uniformly distributed from the surface to the bottom of the column. By designating the unit weight of soil by  $\gamma$ , the maximum shear stress at the bottom of the column, depth =  $z$ , is give by the Newtonian equation of motion 運動方程式;

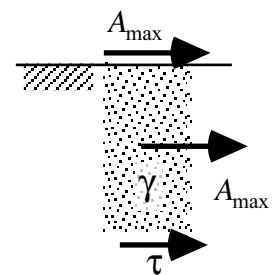


Fig. 19.3 Simple calculation of insitu shear stress

$$\tau = \text{mass of soil column} \times \text{acceleration} = \int_0^z \frac{\gamma}{g} dz \times A_{max} = \sigma_v \frac{A_{max}}{g} \quad (19.1)$$

in which  $g$  stands for the gravity acceleration 重力加速度 = 1 G and  $\sigma_v$  is the total vertical stress. Since a level ground is assumed, the lateral earth pressures on the right and left sides of the column are equal to each other and are canceled in the equation of motion. Moreover, the initial effective vertical stress is given by

A typical value of  $A_{max}$  is 15–25 % of gravity acceleration.

$$\sigma'_{vc} = \int_0^z \gamma' dz. \quad (19.2)$$

Before taking the ratio of shear stress and effective stress as above, a correction for the rigid idealization has to be made. Since the real liquefiable soil is not rigid, shear deformation occurs therein and the acceleration in the soil column is smaller than  $A_{max}$  at the surface. Hence, the shear stress at the base of a soil column is smaller than what was calculated as shown earlier. Many dynamic analyses were conducted on a variety of soil conditions and a correction factor of  $r_d$  was obtained;

$$r_d = \frac{\text{(maximum shear stress obtained by analysis)}}{\text{(shear stress in rigid column)}}$$

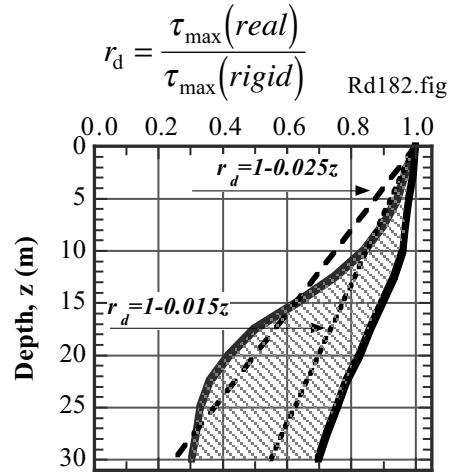
Figure 19.4 is one of the examples of the calculated range of  $r_d$ . In design codes,

$$r_d = 1 - 0.015z \quad \text{or} \quad 1 - 0.025z \quad (19.3)$$

where  $z$  is the depth in meter unit (see Sect. 19.11). See also Fig. 19.32. Consequently, the cyclic stress ratio in the field (CSR) is given by

$$\frac{\tau}{\sigma'_{vc}} = r_d \frac{\sigma_v}{\sigma'_{vc}} \frac{A_{max}}{g} \quad (19.4)$$

It is evident that this stress ratio stands for the seismic load, which is in contrast with the resistance of sand against liquefaction (CRR in Sect. 19.1). Note that this stress ratio does not take into account the number of loading cycles and the irregularity of an earthquake motion. In reality,  $A_{max}$  which is equivalent with the earthquake loading may be repeated many times if the earthquake magnitude is 7.5 or more, while only a few times when the earthquake magnitude is smaller (see Port Island record, Fig. 18.28). A correction for this shortcoming will be described in Sect. 19.10.



**Fig. 19.4** Correction for rigid idealization (original figure by Seed and Idriss, 1971, was revised)

19.3 Liquefaction Curve

The number of loading cycles to liquefaction depends on the amplitude of stress ratio. Therefore, laboratory tests should be run with a variety of stress amplitude, and the varying stress ratio is plotted against the respective number of cycles needed for liquefaction. Liquefaction here is defined by one of the 100% pore pressure development (initial liquefaction), 5%, or greater double (peak-to-peak) amplitudes of axial strain in cyclic triaxial tests. The test data plotted as in Fig. 19.5 is called a liquefaction curve (液化化曲線).

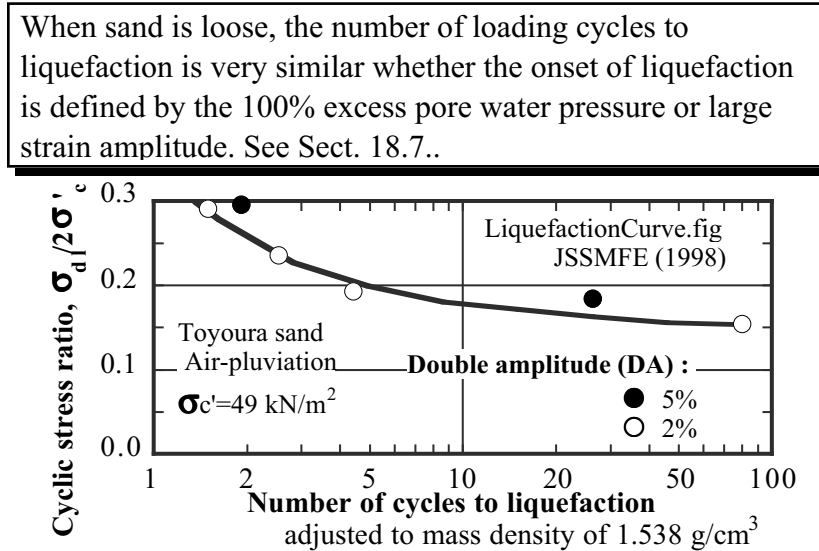


Fig. 19.5 Liquefaction curve of loose Toyoura sand in large triaxial sample;  $D_r = 65\%$  diameter = 30cm (JSSMFE, 1988)

Figure 19.5 apparently shows that the resistance of sand against liquefaction depends on the number of stress cycles during an expected earthquake. Table 19.1 shows the idea of Seed and Idriss (1982) who replaced an irregular time history of earthquake loading by an equivalent stress history with a constant amplitude. The equivalent stress amplitude is defined by 65% of the maximum shear stress in the irregular history. After this consideration, the number of cycles changing with the earthquake magnitude is taken into account by reducing the soil resistance for quakes of greater magnitude. When an earthquake includes only a few cycles (a case of smaller earthquake magnitude), the soil can resist a greater stress ratio.

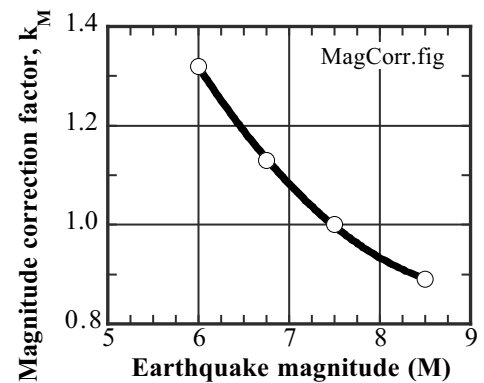
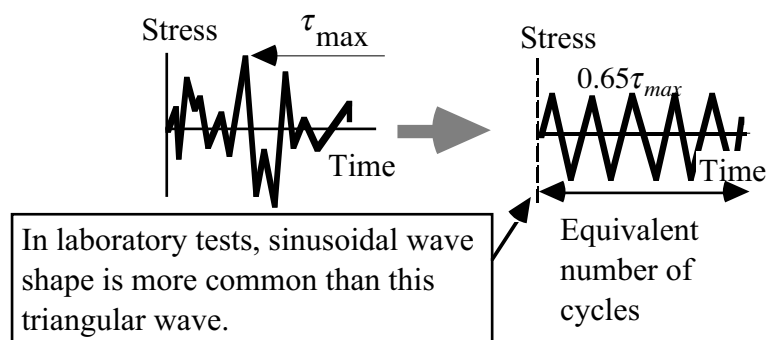


Fig. 19.6 Earthquake magnitude correction of liquefaction resistance (drawn by using Fig. 12 by Seed et al., 1983)

Table 19.1 Equivalent number of cycles (Seed and Idriss, 1982)

Richter scale of earthquake magnitude ( $M$ )	Equivalent number of stress cycles (This is a rough estimate.)
8.5	26
7.5	15
6.75	10
6	5-6
5.25	2-3



In contrast, when the expected number of cycles is large (an earthquake of larger magnitude), the soil can resist a smaller stress ratio. See the magnitude correction factor,  $k_M$ , in Fig. 19.6. Arango (1996) stated that the greater magnitude reduces the minimum acceleration needed for liquefaction because the number of loading cycles is increased.

In today's practice, the number of equivalent cycles is specified as equal to 20 in most design codes. The seismically induced stress ratio (load) is compared with the stress ratio at 20 cycles in Fig. 19.5 (resistance of soil). Thus, the factor of safety ( $F_D$ ) is calculated.

The liquefaction curve is drawn on a semilogarithmic plot. Some people prefer to use a log-log plot, because, they insist, the liquefaction curve becomes linear and its analytical expression is easy.

**19.4 Field and Laboratory Stress Ratio**

When the number of cycles is specified as, for example, 20 (Table 19.1), it is important to compare the resistance of soil against 20 cycles of loading (laboratory stress ratio) and the field stress ratio that is expected to occur during real irregular earthquake loadings.

Factor of safety against liquefaction;  $F_L = (\text{Resistance: laboratory stress ratio})/(\text{Load: field stress ratio})$

These two types of stress ratio include many differences in its nature. Hence, it may not be appropriate to compare them directly and to calculate the factor of safety. A detailed discussion is needed on difference between the laboratory and the field. See Table 19.2 for the idea as well as Fig. 19.7 for definition of stresses. Moreover, the following sections will describe details of the correction parameters.

**Table 19.2** Correction of laboratory-measured liquefaction resistance to resistance in field

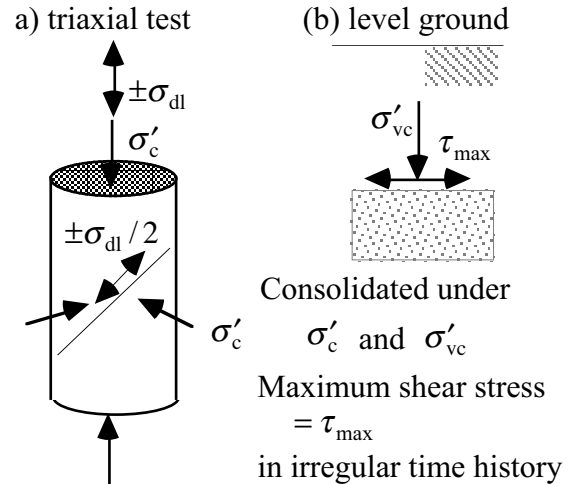
Issues	Laboratory tri-axial tests	Field conditions	Typical correction factor = Field/Triaxial (reference)
Stress ratio	$\sigma_{dl} / 2\sigma'_c$	$\tau_{max} / \sigma'_{vc}$	-----
Drainage	Undrained	Negligible drainage	Not in practice
Consolidation stress	Isotropic	$K_0$ consolidation	Use $\tau_{max} / (C_1 \sigma'_{vc})$ and $C_1 = (1 + 2K_0) / 3$ (Ishihara and Li, 1972)
Number of cycles	Use stress ratio at 20 cycles.	20 is assumed for design	Triaxial sample that can resist 20 cycles of $\sigma_{dl} / \sigma'_c$ can resist an irregular loading
Dynamic loading	Mostly sinusoidal	Irregular	with max. $C_2 \times (\sigma_{dl} / \sigma'_c)$ where $C_2 = 1/0.65$ or $1/(0.55-0.7)$ . (Ishihara and Yasuda, 1975)
Sheared plane	Inclined $45^\circ$ , cone shaped	Horizontal and planar	Not in practice; anisotropy may affect
Stress axes	Fixed vertical axis	Rotation around	Not in practice; anisotropy may affect
Sample disturbance	Resistance is underestimated		Use $C_3 \times (\sigma_{dl} / 2\sigma'_c)$ and $C_3 > 1$ but not clearly understood yet
Sand density	Densified during handling	Weaker than laboratory tests	Use $C_4 \times (\sigma_{dl} / 2\sigma'_c)$ and $C_4 < 1$ but not clearly understood yet
Cyclic change of stress	Only axial stress: overestimation of strength	At least 2 components; EW and NS.	Use $C_5 \times (\sigma_{dl} / 2\sigma'_c)$ and $C_5 = 0.8-0.9$ or more (Ishihara and Yamazaki, 1980)
Saturation	Saturated; $B > 0.95$	Not saturated? difficult to know	Not in practice; probably $C < 1$

The Japanese Design Code of Highway Bridge 道路橋示方書 V 耐震設計篇, which is one of the most important codes concerning liquefaction, states that, when  $K_0=0.5$ ,  $C_1 \times C_2$  is approximately equal to one. Moreover,  $C_3 \times C_4 = 1$  is assumed, although the quality of samples is unpredictable. By further assuming  $C_5 = 1$ , accordingly,  $C_1 C_2 C_3 C_4 C_5 \cong 1$  and

$$F_L = \frac{\text{Triaxial strength}}{\text{Field stress ratio}} = \frac{C_2 C_3 C_4 C_5 \left\{ \frac{\sigma_{dl}}{2\sigma'_c} \right\}_{\text{triaxial}}}{\left( \frac{\tau_{\max}}{C_1 \sigma'_{vc}} \right)_{\text{field}}} = \frac{\left\{ \frac{\sigma_{dl}}{2\sigma'_c} \right\}_{\text{triaxial}}}{\left( \frac{\tau_{\max}}{\sigma'_{vc}} \right)_{\text{field}}} \quad (19.5)$$

Thus, the laboratory stress ratio obtained by cyclic triaxial test is directly compared with the field stress ratio. Note that this  $F_L$  indicates the liquefaction potential of a single soil layer from which the tested sample was collected. It does not indicate the risk of liquefaction damage of a site. The liquefaction damage risk depends on the total thickness of liquefied layer as well.

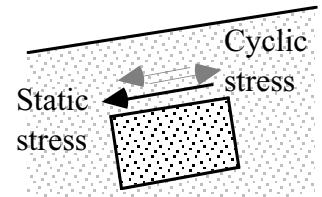
Commonly encountered questions addresses the effects of initial static shear stress, that may cause large distortion of subsoil, the effects of different earthquake magnitudes that may produce different number of loading cycles, and the level of confining pressure (depth). For these issues, refer to Sects. 19.6, 19.3, and 19.9, respectively.



**Fig. 19.7** Stress states in triaxial tests and horizontal shaking of level ground

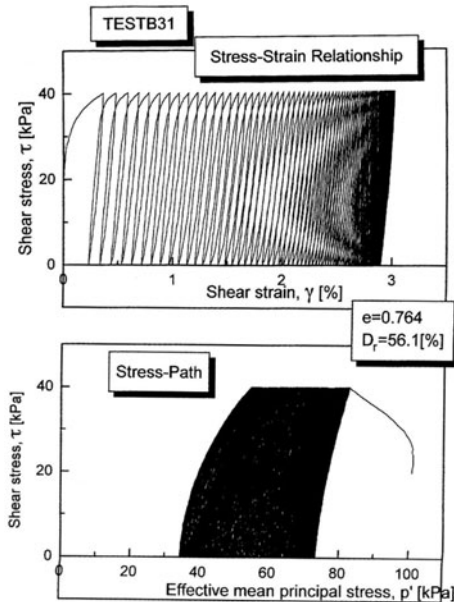
**19.5 Effects of Static Shear Stress on Resistance Against Liquefaction**

Cyclic triaxial tests on liquefaction resistance of sand (Sect. 18.15) are carried out on isotropically consolidated samples in which there is no static shear stress. This means that liquefaction in level ground is studied. Then a question arises; what is the liquefaction potential of slopes where there is an initial static shear stress and it is superimposed by cyclic shear stress (Fig. 19.8).

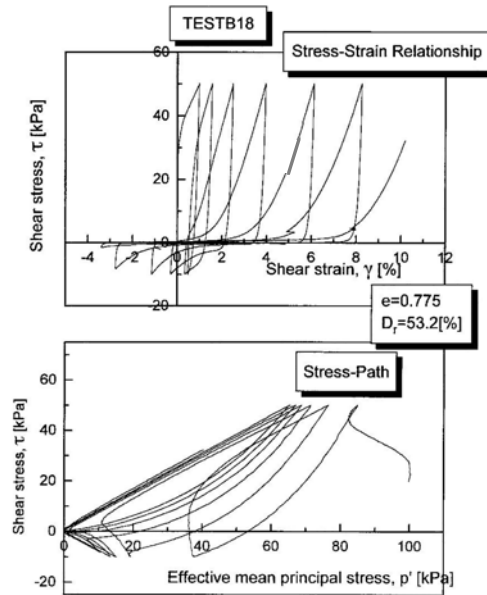


**Fig. 19.8** Initial shear stress in a slope

The effects of the static shear stress on undrained behavior of sand are illustrated in Figs. 19.9 and 19.10. In Fig. 19.9, the static shear stress of 20 kPa was applied in a drained manner and was then superimposed by a cyclic component of  $\pm 20$  kPa in a torsion shear apparatus (Sect. 18.8). Hence, the combined shear stress (static + cyclic) changed between 0 and +40 kPa. Since the stress was always positive (or zero), this type of loading was called one-way (片振り). Although so many cycles of shear stress were loaded, the sample maintained its stability. In Fig. 19.10, in contrast, the cyclic component had a greater amplitude of  $\pm 30$  kPa, making the combined stress vary between  $-10$  and  $+50$  kPa. This type of loading was called two-way (両振り). The specimen easily liquefied and developed large shear deformation. Note that two-way loading is very important in causing liquefaction under effects of static shear stress.



**Fig. 19.9** One-way test loading on sample with the relative density of 56.1% (Yokouchi, 1997)



**Fig. 19.10** Two-way loading on sample with the relative density of 53.2% (Yokouchi, 1997)

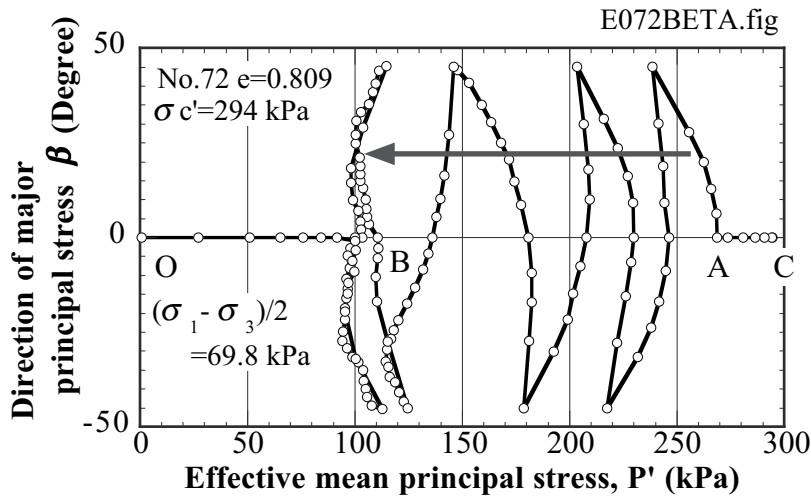
When the static shear stress is substantial, the combined stress (static + cyclic) is unlikely to be zero (one-way loading). Therefore, liquefaction (effective stress = 0, shear stress = 0) is difficult to occur. This, however, does not mean that sand is very resistant against seismic loading. A significant magnitude of combined shear stress may cause shear failure. It is, therefore, important to watch whether or not the effective stress state comes close to the failure criterion ( $\tau = \sigma' \tan \phi$ ). If the failure criterion is nearly satisfied, shear strain of a few % or more is possible to occur. This point is particularly important in very loose sand, which is subjected to a disastrous flow failure (see, for example, Sect. 24.3).

In another undrained torsion shear test in Fig. 19.11(a), (1) the deviator stress ( $\sigma_1 - \sigma_3$ ) was loaded to a specified value (C→A), (2) orientations of  $\sigma_1$  and  $\sigma_3$  rotated over  $\pm 45^\circ$  with constant  $\sigma_1 - \sigma_3$  until large shear deformation occurred (A→B), and then (3)  $\sigma_1 - \sigma_3$  was unloaded to zero (B→O). Although  $P'$  and pore water pressure stopped its variation at the end of Stage 2 (Point B), they started to change again in



the unloading phase (Stage 3 after B). The variation and motion of Mohr stress circle is illustrated in Fig. 19.12. At B, Mohr effective stress circle touched the failure envelope and large strain started to develop, Fig. 19.11(b). Thereinafter,  $\sigma_1 - \sigma_3$  was reduced and the excess pore water pressure increased quickly; the specimen liquefied. It is reasonable, therefore, that shear stress near failure prevents further pore pressure rise with the aid of positive dilatancy. In other words, the Mohr stress circle at B is in contact with the failure line and cannot translate toward the left any more. When this effect disappears, liquefaction is quite likely (Stage 3).

(a) Decrease of effective stress with rotation of stress axis



(b) Development of strain with rotation of stress axis

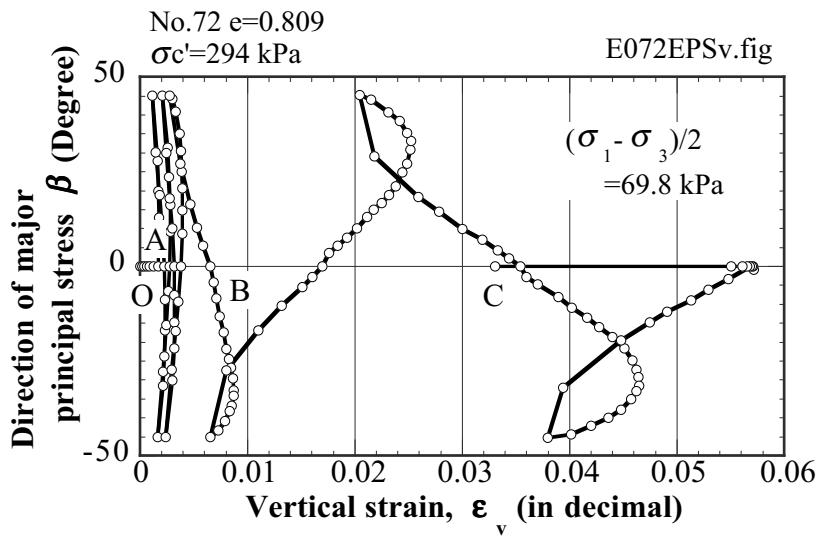


Fig. 19.11 Undrained torsion shear with constant deviator stress

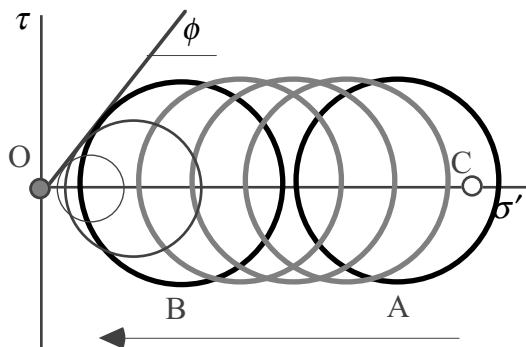
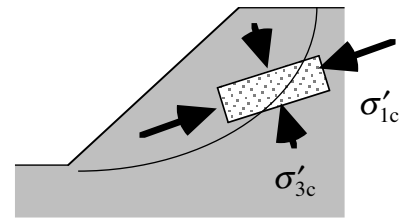


Fig. 19.12 Behavior of Mohr effective stress circle during test in Fig. 19.11

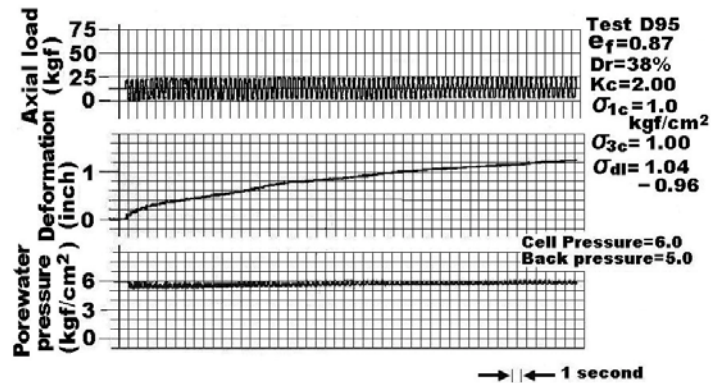
**19.6 Importance of Two-Way Loading in Cyclic Shear with Initial Static Stress**

The study on initial static shear started from an interest in seismic stability of slopes and embankments. By assuming that a slip plane coincides with the 45° plane in a triaxial specimen (Fig. 19.13), triaxial shear tests on anisotropically consolidated specimen (3.5 in. high) were conducted. After consolidation under  $K_c = \sigma'_{1c} / \sigma'_{3c}$ , a cyclic deviator stress,  $\pm\sigma_{dl}$ , was loaded (Lee and Seed, 1967).

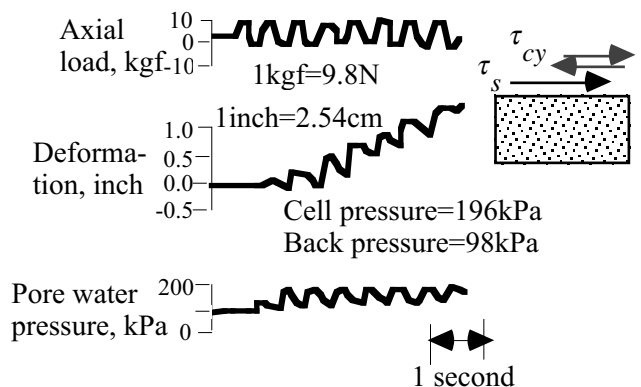


**Fig. 19.13** Modelling seismic failure of slope by triaxial test

In the test of Fig. 19.14, a specimen of Sacramento River sand with  $D_r = 38\%$  was loaded under  $\sigma'_{1c} = 196 \text{ kN/m}^2$  and  $\sigma'_{3c} = 98 \text{ kN/m}^2$ , while the cyclic deviator stress varied between  $\sigma_{dl} = 102$  and  $-94 \text{ kN/m}^2$ . Hence, the combined axial stress was between 298 and 102  $\text{kN/m}^2$  and was always greater than the lateral stress. This one-way test is also called nonreversal. Figure 19.14 shows that the axial deformation increased very slowly and the excess pore water pressure never reached  $\sigma'_{3c}$ . On the contrary in Fig. 19.15, the amplitude of the deviator stress was  $\pm 102 \text{ kN/m}^2$ . Although the maximum combined shear stress was same as in Fig. 19.14, the minimum stress was  $-4 \text{ kN/m}^2$ . This slight reversal of shear stress direction (negative deviator stress) made a drastic difference in soil behavior. Figure 19.15 reveals that the sample liquefied quickly.

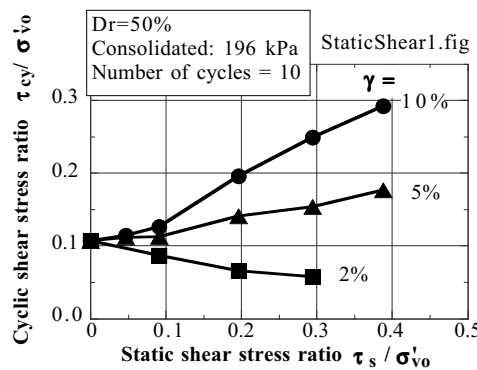


**Fig. 19.14** Cyclic undrained shear without stress reversal (Seed and Lee, 1967)

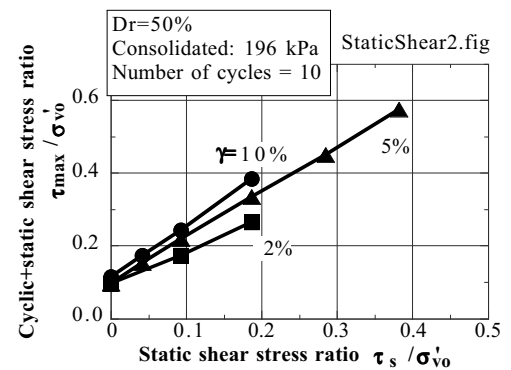


**Fig. 19.15** Cyclic undrained shear with stress reversal (after Seed and Lee, 1967)

Vaid and Finn (1967) carried out simple shear tests (as schematically shown in inset figure in Fig. 19.15) on Ottawa sand, which was of  $D_r = 50\%$  and was consolidated under  $\sigma'_{vo} = 196 \text{ kN/m}^2$ . Figure 19.16 shows that the cyclic stress ratio,  $\tau_{cy} / \sigma'_{vo}$ , needed to develop strain of  $\gamma = 2\%$  at 10th cycle decreased as the static stress ratio  $\tau_{max} / \sigma'_{vo}$  increased. It seems that static shear makes small strain easy to develop. Conversely,  $\tau_{cy} / \sigma'_{vo}$  required for  $\gamma = 10\%$  increased. More significant positive dilatancy due to greater static shear prevents a large



**Fig. 19.16** Effects of static shear on cyclic component of strength (after Vaid and Finn, 1979)



**Fig. 19.17** Effects of static shear on combined strength of sand (after Vaid and Finn, 1979)

strain to develop. The combined stress ratio in Fig. 19.17,  $(\tau_{\max} = \tau_s + \tau_{cy})/\sigma'_{vo}$  increases as the initial static stress increases. This means that the cyclic strength of sand is increased by the static shear. The correction factor for the initial static shear stress,  $k_a$ , was proposed to take this issue into account and increase the liquefaction resistance obtained experimentally without static shear stress (Federal Highway Administration, 1997). Note that the discussion so far made is based on strain amplitude induced by cyclic loading. In case of very loose sand subjected to static shear, large residual deformation and flow failure are more important issue; see Chap. 24.

**19.7 Effects of  $K_0$  Consolidation on Liquefaction Resistance of Sand**

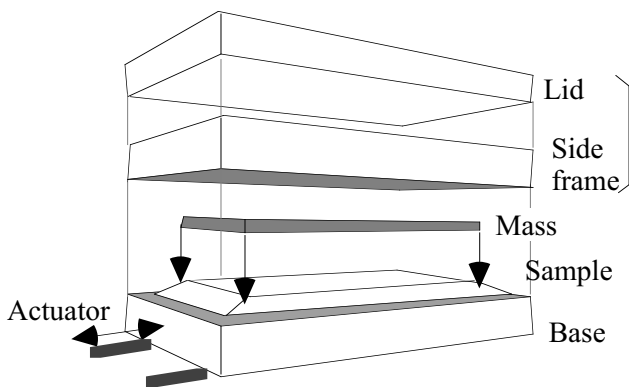
Cyclic triaxial test is useful in practice because it can test undisturbed soil samples. Conversely, one of its drawbacks is the different stress states during consolidation; isotropic consolidation in triaxial tests and  $K_0$  consolidation in real subsoil.  $K_0$  consolidation in level ground is characterized by (see Fig. 18.51)

1. The different effective stress in the horizontal and vertical directions;  $\sigma'_h = K_0 \sigma'_v$
2. Lateral deformation is not allowed during consolidation and during cyclic shear

In the sense of (2),  $K_0$  consolidation is discriminated from anisotropic consolidation which is the case under shallow foundation, embankments, etc. Simple shear of a box-shape specimen can best reproduce the state of  $K_0$  consolidation, although it cannot test undisturbed specimens and produces a nonuniform stress state within a specimen (Cole, 1967).

Finn et al. (1971) compared stress ratio obtained by triaxial and simple shear tests (Fig. 19.18). They concluded that two types of stress ratio are related with each other by

$$\frac{\sigma_{dl}}{2\sigma'_{co}} = \frac{\text{Cyclic shear stress}}{\text{Mean consolidation stress}} = \frac{\tau_{cy}}{1 + K_0 \sigma'_{vo} / 2}$$

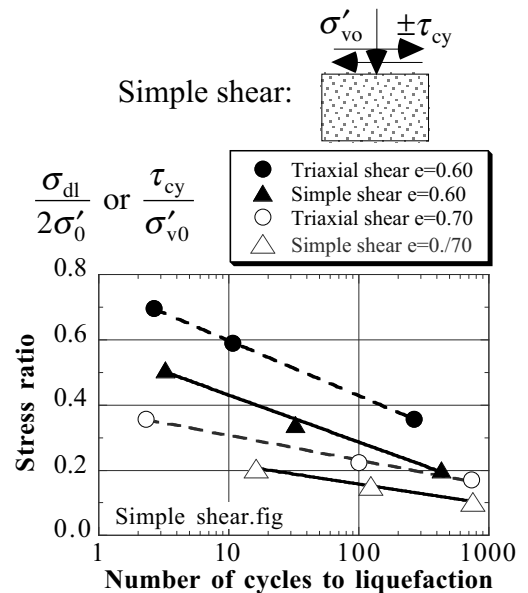


**Fig. 19.19** Large simple shear device excited on shaking table (after De Alba et al., 1976)

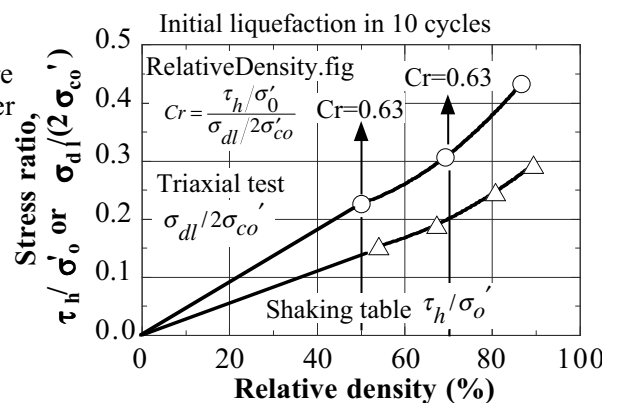
De Alba et al. (1976) carried out shaking table tests (Fig. 19.19) in which a layer of sand covered by a rubber sheet was consolidated by air pressure and sheared by force generated by a shaking top mass (shear force = mass × acceleration). The liquefaction resistance (stress ratio required for initial liquefaction at 10th cycle, in which initial liquefaction means the excess pore pressure reaching the consolidation pressure) obtained by triaxial tests and this simple shear is examined in Fig. 19.20. Eventually, a conversion formula of

$$\frac{\sigma_{dl}}{2\sigma'_{co}} = \frac{\tau_{cy}}{C_1 \sigma'_{vo}} \text{ where } C_1 \approx 0.63$$

was proposed between two kinds of stress state.



**Fig. 19.18** Different liquefaction resistances obtained by simple shear and triaxial shear (Finn et al., 1971)



**Fig. 19.20** Comparison of liquefaction resistance of sand obtained by triaxial and simple shear tests (after De Alba et al., 1976)

**19.8 Liquefaction Resistance of Sand Under  $K_0$  Condition and Overconsolidation**

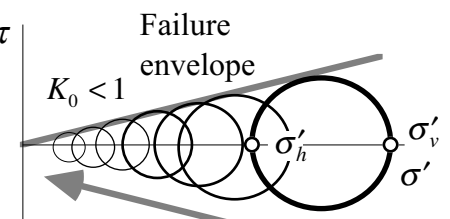
The  $K_0$  condition of a level ground is characterized by the lateral confinement in which the horizontal strain,  $\epsilon_h$ , is held zero during shaking. This means that no horizontal extension or contraction occurs in the subsoil, although horizontal displacement is excited by shaking. Since a level ground is idealized by an infinite size, even the smallest  $\epsilon_h$  gives an infinite displacement when it is multiplied by an infinite size. Therefore, the strain has to be zero.

The idea of earth pressure at rest states that the ratio of horizontal and vertical effective stresses are kept equal to  $K_0$  when  $\epsilon_h$  is zero. By denoting the hydrostatic pore pressure and excess pore water pressure by  $u_s$  and  $\Delta u$ , respectively, the ratio of total stress is derived:

$$\frac{\sigma_h}{\sigma_v} = \frac{\sigma'_h + u_s + \Delta u}{\sigma'_v + u_s + \Delta u} = \frac{K_0 \sigma'_v + u_s + \Delta u}{\sigma'_v + u_s + \Delta u} \tag{19.6}$$

This means that, when  $\sigma'_v$  is reduced to zero upon liquefaction, the total stress ratio becomes equal to one, which stands for an isotropic stress state.

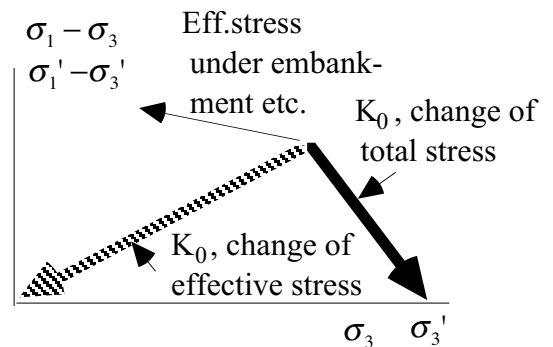
Table 19.3 indicates the change of stress components and Fig. 19.21 illustrates the variation of Mohr's effective stress circle during liquefaction procedure, while Fig. 19.22 reveals the variation of total and effective stress states. Note that the stress difference,  $\Delta\sigma_1 - \Delta\sigma_3$  decreases.



**Fig. 19.21** Effective stress circle during liquefaction process

**Table 19.3** Change of stress components during liquefaction process

	Total stress		Effective stress	
	$\sigma_1 = \sigma_v$	$\sigma_1 = \sigma_h$	$\sigma'_v$	$\sigma'_h$
Initial	$\sigma_1 = \sigma_{vo}$	$\sigma_3 = K_0 \sigma'_{vo} + u_s$	$\sigma'_{vo}$	$K_0 \sigma'_{vo}$
Upon liquefaction	$\sigma_1 = \sigma_{vo}$	$\sigma_3 = \sigma_{vo} = \sigma'_{vo} + u_s$	0	0



**Fig. 19.22** Change of total stress state during liquefaction process

The excess pore water pressure is generated not only by cyclic shear but by the total stress change. The latter component may be given by modifying Skempton's formula:

$$\Delta u_t = B \Delta \left( \frac{\sigma_1 + 2\sigma_3}{3} \right) + A (\Delta\sigma_1 - \Delta\sigma_3) \tag{19.7}$$

Since  $\Delta\sigma_1 - \Delta\sigma_3$  is unloaded (decrease) during the process of liquefaction (Table 19.3), it does not develop much pore pressure; see the stress path of unloading phase in Fig. 18.17. Hence,  $A = 0$  is reasonable. Moreover,  $B = 1$  in water saturated sand. Therefore,

$$\Delta u_t = \frac{2}{3} (1 - K_0) \sigma'_{vo} \tag{19.8}$$

Ishihara and Li (1972) stated that stress ratio should be defined as the ratio of cyclic shear stress

amplitude over excess pore water pressure generated by cyclic loading, while excluding  $\Delta u_t$  (19.7). In  $K_0$  condition, therefore,

$$\text{Stress ratio} = \frac{\tau_{cy}}{\sigma'_{vo} - \Delta u_t} = \frac{\tau_{cy}}{\sigma'_{vo} - \frac{2}{3}(1 - K_0)\sigma'_{vo}} = \frac{\tau_{cy}}{\frac{1 + 2K_0}{3}\sigma'_{vo}} \quad (19.9)$$

which is equivalent with the stress ratio of triaxial test;

$$\frac{\sigma_{dl}}{2\sigma'_{co}} = \frac{\tau_{cy}}{\frac{1 + 2K_0}{3}\sigma'_{vo}} \quad \text{and hence,} \quad C_1 = \frac{1 + 2K_0}{3} \quad (19.10)$$

in Sect. 19.4.  $C_1$  is 0.67 for a typical value of  $K_0 = 0.5$ .

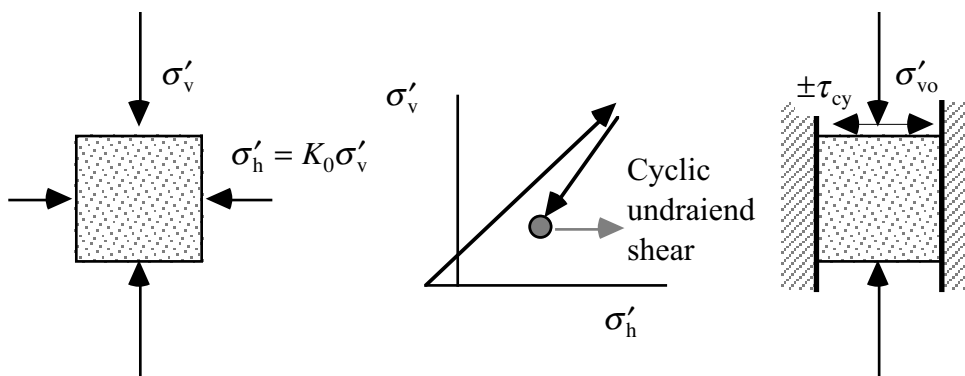


Fig. 19.23 Stress history in torsional shear tests on overconsolidated sand

Overconsolidated stress state increases liquefaction resistance of sand in two manners. First, overconsolidated level ground is of greater  $K_0$  value (earth pressure coefficient at rest), which is defined by (horizontal effective stress)/(vertical effective stress,  $\sigma'_v$ ) (19.23). This is due to plastic deformation of sand in the horizontal direction during the preceding high vertical stress. To reduce the horizontal expansion, the horizontal effective stress has to be maintained high after unloading of  $\sigma'_v$ , leading to greater  $K_0$ . Second, the stress history of overconsolidation makes sand less contractive (or more dilative) during cyclic shear. Hence, excess pore water pressure develops less during cyclic undrained shear.

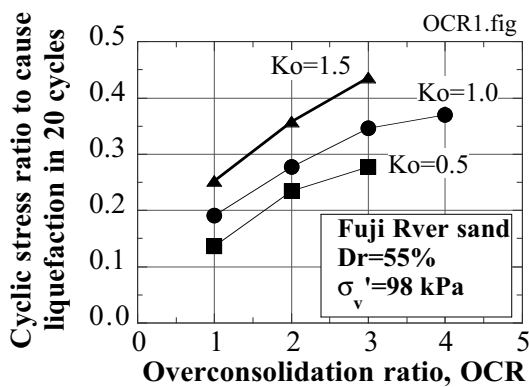


Fig. 19.24 Increase of liquefaction resistance of sand due to overconsolidation (Ishihara and Takatsu, 1979)

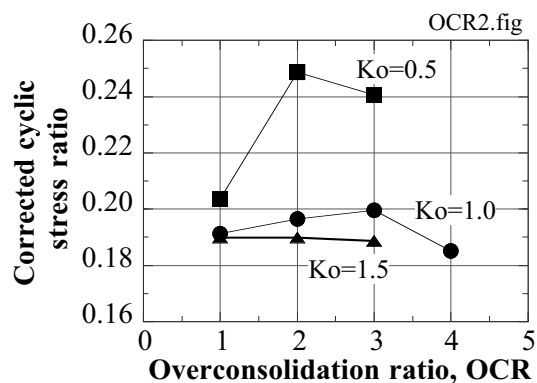


Fig. 19.25 Normalized cyclic stress ratio to cause liquefaction in 20 cycles (data by Ishihara and Takatsu, 1979)

Ishihara and Takatsu (1979) carried out undrained torsional shear (Fig. 19.24) to study the overconsolidation effects on liquefaction. The stress state in this device is illustrated in Fig. 19.23. Specimens were subjected to stress history of loading and unloading so that the desired overconsolidation ratio ( $OCR$ ) was produced. In this stage, the ratio of  $K_0$  was maintained constant. Thereinafter, cyclic shear stress,  $\tau$ , was loaded in an undrained manner, while preventing lateral deformation from occurring. This situation is similar to what happens in real level ground.

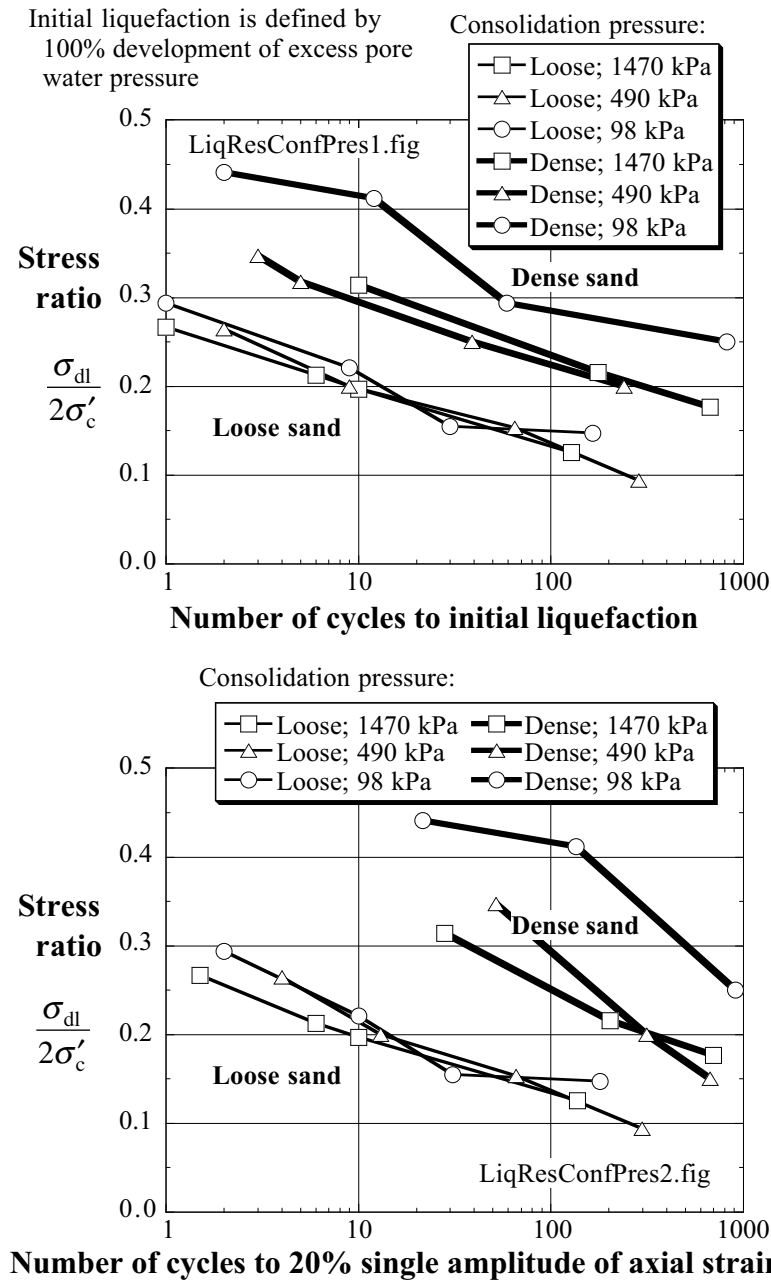
Figure 19.24 compares stress ratio,  $(\tau_{cy}/\sigma'_{vo})$ , which was needed to cause liquefaction in 20 cycles. Evidently, the stress ratio (resistance of sand against liquefaction) increases with both  $K_0$  and overconsolidation ratio. It was then attempted to express the effects of these parameters by using such an empirical formula as

$$\left(\frac{\tau_1}{\sigma'_{vo}}\right)_{OC, K_0} = \frac{1+2K_0}{3} \sqrt{OCR} \left(\frac{\tau_1}{\sigma'_{vo}}\right)_{NC, K_0=1} \quad (19.11)$$

The stress ratio thus corrected is plotted in Fig. 19.25. Although some data are still different, there is a general consistency. On the basis of these findings, it may be reasonable to state that liquefaction resistance of sand is improved by producing overconsolidated stress state by means of preloading.

**19.9 Effects of Confining Pressure on Liquefaction Resistance**

Monotonic shear of sand under different consolidation pressures reveal that higher pressures make sand more contractive during shear than lower pressures (Fig. 1.17). The same is true of liquefaction because the development of excess pore water pressure is a consequence of (negative) dilatancy; see Sects. 18.1 or 20.1. Hence, liquefaction is more likely under higher consolidation stresses.



**Fig. 19.26** Cyclic triaxial test data on liquefaction resistance of sand under different stress levels (reproduced from data by Seed and Lee, 1967)

Figure 19.26 was drawn by the author by using a pioneering data set by Lee and Seed (1967). The employed sand was uniform Sacramento River sand with  $e_{max}$  and  $e_{min} = 1.03$  and  $0.63$ , respectively. The relative density of loose and dense sands were 30% and 78%. The amplitude of cyclic axial stress in the original paper was converted to the cyclic stress ratio according to the present convention.

It appears evident, particularly for dense sand, that higher consolidation pressure,  $\sigma'_c$ , reduces the stress ratio needed for liquefaction, whether liquefaction is defined by 100% pore pressure rise or large axial



strain. Similar finding was reported later by Vaid and Chern (1985). This issue is taken into account by what is called the correction factor for stress levels,  $k_{\sigma}$  (Federal Highway Administration of USA, 1997).

From such a discussion, some people imagine that insitu sand at greater depth is more vulnerable to liquefaction than sand near the surface, because the greater depth means higher consolidation pressure. It is not true, however, because sand at a greater depth is more aged and the liquefaction resistance of sand increases with the number of years after deposition. This is called ageing effects. See Sect. 18.13.

**19.10 Effects of Irregular Loading on Resistance Against Liquefaction**

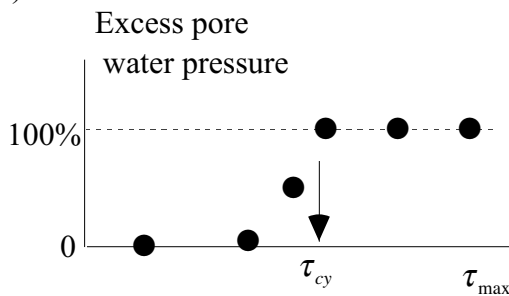
Resistance of sand against liquefaction is conventionally indicated by the stress ratio that causes liquefaction (Sect. 19.3), whether 100% pore pressure development or significant strain amplitude, at 20 cycles of constant amplitude. The real earthquake loading, however, has never a constant stress amplitude or 20 cycles. It seems that the idea of “20” cycles empirically comes from a rule of thumb shown in Table 19.4.

**Table 19.4** Equivalent number of cycles (after Seed and Idriss, 1971).

Earthquake magnitude (Richter scale)	Number of significant stress cycles
7	10
7.5	20
8	30

The effect of irregular loading was studied by running torsion shear tests on isotropically consolidated specimens with  $D_r = 55\%$  (Ishihara and Yasuda, 1975). Figure 19.27 illustrates results of a test in which a time history of Hachinohe NS record during the 1968 Tokachi-oki earthquake (Fig. 5.9) was loaded. Note that this record has a few stress cycles with relatively large stress amplitudes, while other cycles are of minor magnitudes. Hence, this record is classified as “a shock type (衝撃型).” By varying the maximum stress,  $\tau_{max}$ , while maintaining the wave shape unchanged, the minimum value of  $\tau_{max}$  needed for liquefaction was determined. This amplitude is called  $\tau_{cy}$  in this section. See Fig. 19.28 for illustration.

Similar tests were conducted on Aomori record in Fig. 19.29. This record is characterized by many cycles of stress, which are of major magnitudes. Hence, this type of record is called “vibratory type (振動型).”



**Fig. 19.28** Idea of liquefaction resistance under irregular loading

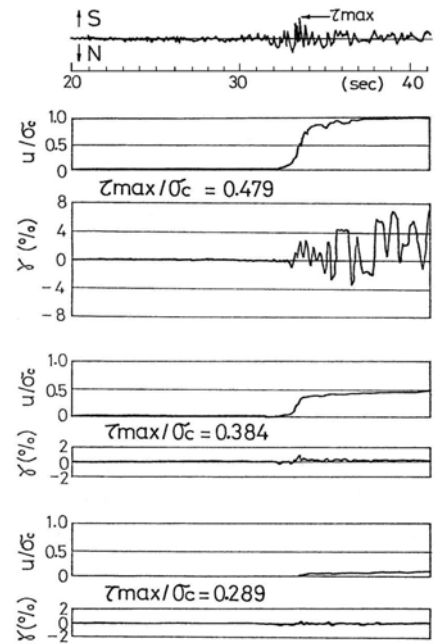
Similar tests were further conducted with four more records so that the liquefaction resistance under irregular loading thus determined,  $\tau_{cy}$ , was compared with the liquefaction resistance in triaxial tests on isotropically consolidated specimens. The correction factor,  $C$  in Sect. 19.4, for irregularity was obtained as manifested below;

$$\frac{\tau_{cy}}{\sigma'_{vo}} = C_2 \frac{\sigma_{dl}}{2\sigma'_{co}} \quad \text{and}$$

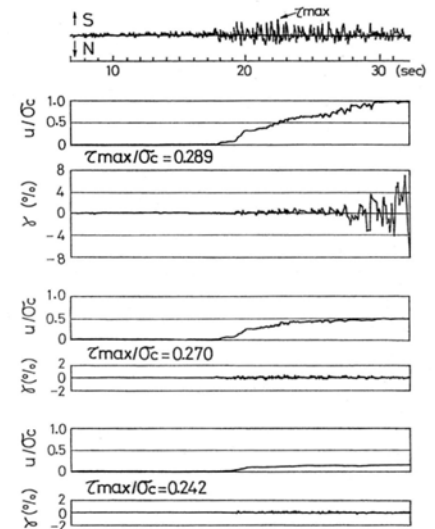
Shock type: only 0–2 cycles before occurrence of  $\tau_{max}$  have amplitudes greater than 60% of  $\tau_{max}$   $\rightarrow C_2=1/0.55$ .

Vibratory type: 3 or more than 3 cycles before occurrence of  $\tau_{max}$  have amplitudes greater than 60% of  $\tau_{max}$   $\rightarrow C_2 = 1/0.70$ .

Seed and Idriss (1971) proposed to use  $C_2 = 1/0.65$  by engineering judgment.

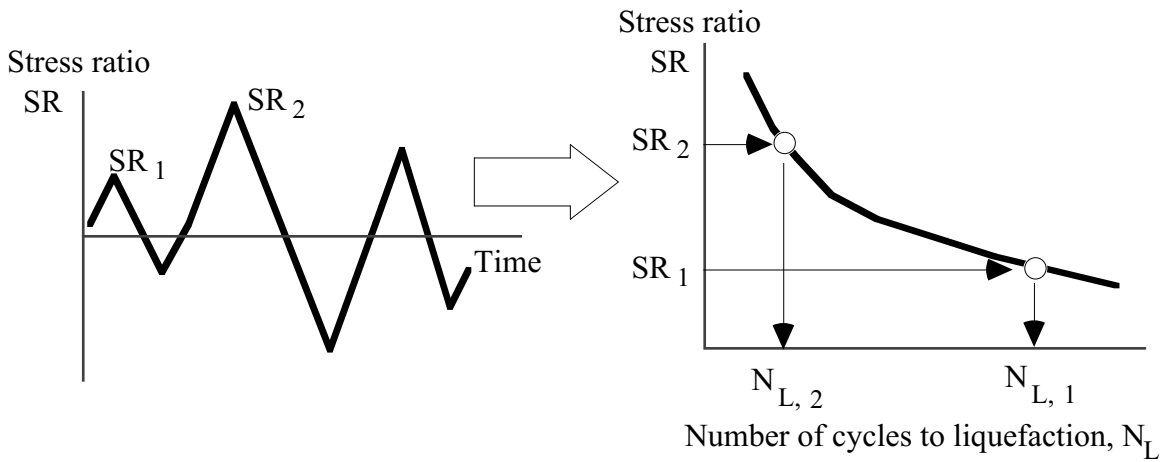


**Fig. 19.27** Liquefaction test with Hachinohe NS record (Ishihara and Yasuda, 1975)



**Fig. 19.29** Liquefaciton test with Aomori NS record (Ishihara and Yasuda, 1975)

Another approaches to assess the liquefaction potential under irregular stress time history is the use of accumulated damage concept (累積損傷). Originally developed in the field of fatigue failure of metals, this approach evaluates contribution to liquefaction of each stress cycle (Lee and Chan, 1972). For example in an irregular time history in Fig. 19.30, the first stress cycle has a stress ratio amplitude of  $SR_1$ . Since the liquefaction strength test implies that this stress ratio requires  $N_{L,1}$  cycles to liquefaction, this stress cycle makes  $(1/N_{L,1})$  contribution to the onset of liquefaction. Similarly, another cycle of  $SR_2$  makes a contribution of  $(1/N_{L,2})$ . Consequently, the entire stress ratio history makes a total contribution of  $\sum_i (1/N_{L,i})$ . If this total contribution exceeds 1.0, liquefaction is quite likely to occur. Considering anisotropic nature of soil and different magnitudes of stress between positive and negative directions, Annaki and Lee (1977) proposed to do the above calculation for each half cycle. Note that this idea does not consider the elastoplastic nature of soil in which the order of lower and higher stress affects elastic and plastic behavior of soils.



**Fig. 19.30** Contribution to liquefaction of individual stress cycle

**19.11 Correction of Stress Ratio with Depth**

When one calculates the factor of safety against liquefaction, the amplitude of cyclic shear stress is approximately assessed by

$$\tau_{cy} = \frac{A_{max}}{g} (\text{weight of soil}) \times r_d \quad (19.12)$$

in which the idea of rigid soil column is employed (Fig. 19.31) together with correction for deformation of real soil;  $r_d$ . The factor,  $r_d$ , is a function of depth,  $z$  (meter), (Figs. 19.4 and 19.32) and many response analysis by complex-modulus models found it approximated by

$$r_d = 1 - 0.015z \quad \text{or} \quad r_d = 1 - 0.025z \quad (19.13)$$

Consequently, the cyclic stress ratio in subsoil is given by

$$\frac{\tau_{cy}}{\sigma'_{vo}} = \frac{\frac{A_{max} (\text{weight of soil})}{g} \times r_d}{\text{weight of soil} - \text{buoyancy}} = \frac{A_{max} \sigma_{vo} r_d}{g \sigma'_{vo}} \quad (19.14)$$

Equation (19.13) is going to be examined here against a theoretical model in which the displacement amplitude is given by

$$u = 2E \cos \frac{\omega z}{V_s} \cos \omega t \quad (19.15)$$

(see Sect. 4.4 and Exercise 1). The amplitude of cyclic shear stress

$$\tau_{cy} = G \left| \frac{\partial u}{\partial z} \right|_{\text{amplitude}} = G \frac{2E\omega}{V_s} \sin \frac{\omega z}{V_s} \quad (19.16)$$

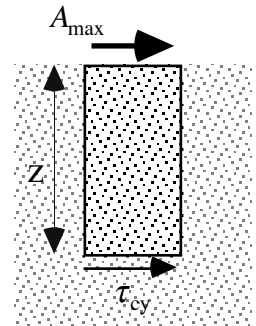
while the acceleration amplitude at the surface,  $A_{max}$ , and the weight of soil above  $z$  are derived as

$$A_{max} = 2\omega^2 E \quad \text{and} \quad \text{weight of soil} = \rho g z \quad (19.17)$$

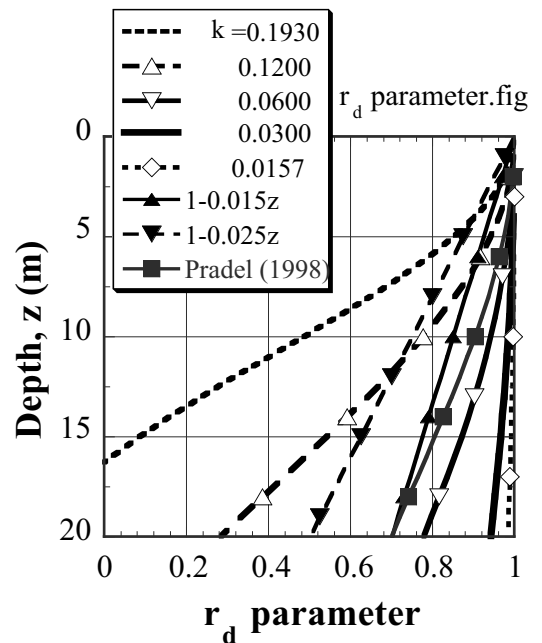
Consequently,  $r_d$  in (19.31) is expressed as

$$r_d = \frac{\tau_{cy} g}{A_{max} \sigma_{vo}} = \frac{G \frac{2E\omega}{V_s} \sin \frac{\omega z}{V_s} \times g}{2\omega^2 E \rho g z} = \frac{\sin \frac{\omega z}{V_s}}{\frac{\omega z}{V_s}} \quad (19.18)$$

Equations (19.13) and (19.18) are compared for cases below;



**Fig. 19.31** Shear stress derived by rigid column idealization



**Fig. 19.32** Comparison between empirical “ $r_d$ ” functions with harmonic response analyses

Low frequency and dense sand:  $0.5 \text{ Hz} \rightarrow \omega = \pi$  and  $\text{SPT-}N=15 \rightarrow V_s = 80 N^{1/3} = 200 \text{ m/s}$ . Hence,

$$k \equiv \omega/V_s = 0.0157.$$

Higher frequency at liquefaction and loose sand:  $4 \text{ Hz} \rightarrow \omega = 8\pi$  and  $N = 4 \rightarrow V_s = 130 \text{ m/s}$ . Hence,  
 $k = 0.193$ .

Figure 19.32 illustrates the  $r_d$  parameters when  $k$  varies between these two extreme values. How do you feel about this figure? Pradel (1998) proposed  $r_d = 1/\left\{1 + (z/30.5)^2\right\}$ .

### 19.12 Effects of Multi-Directional Shear on Liquefaction Resistance

Real earthquake motions in the horizontal direction consist always of EW and NS components, which exert subsils two components of cyclic shear stress. It seems, therefore, that real earthquake conditions are more likely to induce liquefaction than laboratory idealization that exerts only one component of shear stress.

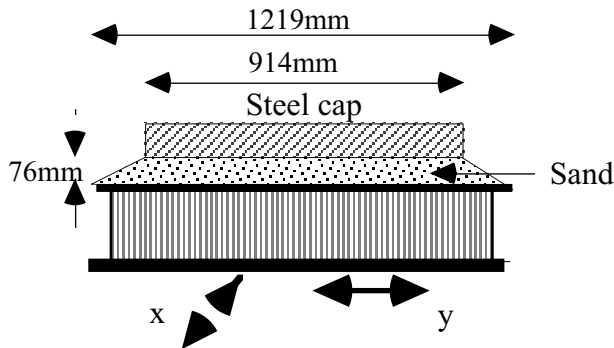


Fig. 19.33 Simple shear shaking table test (after Pyke et al. 1975)

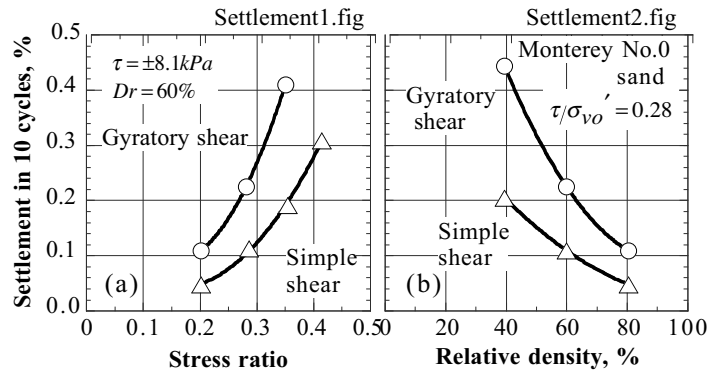


Fig. 19.34 Volume contraction of dry sand subjected to two-directional gyratory shear and one-directional simple shear (Pyke et al. 1975)

Pyke et al. (1975) carried out large simple shear tests on a two-directional shaking table (Fig. 19.33, see Sect. 19.7). The combination of EW and NS motions induced a greater volume contraction of dry tested sand than individual components did (Fig. 19.34) and, hence, it was expected that the two-directional shaking can induce liquefaction more easily than shaking in only one direction (Seed et al. 1978).

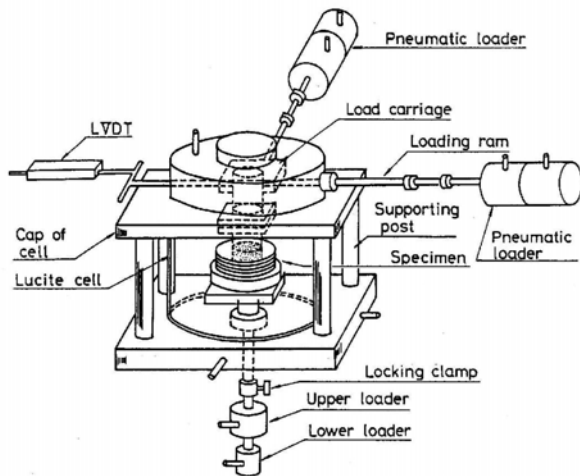


Fig. 19.35 Two-directional simple shear device (Ishihara and Yamazaki, 1980)

Ishihara and Yamazaki (1980) conducted two-directional undrained simple shear tests (Fig. 19.35). Figure 19.36 indicates that the stress ratio needed to cause 3% shear strain decreases as the magnitude of the second component of shear stress,  $\tau_s$ , increases. Consequently, Fig. 19.37 manifests that the correction factor,  $C_5$  in Sect. 19.4, for the multidirectional shaking becomes more important as the ratio of the minor and the major shear stresses,  $\tau_s/\tau_1$ , approaches one.

Experimental studies have so far shown that, in case that there is no initial static shear, the two-

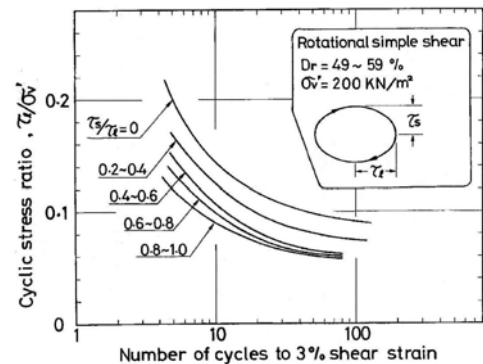


Fig. 19.36 Effects of multi-directional shear on liquefaction resistance of sand (Ishihara and Yamazaki, 1980)

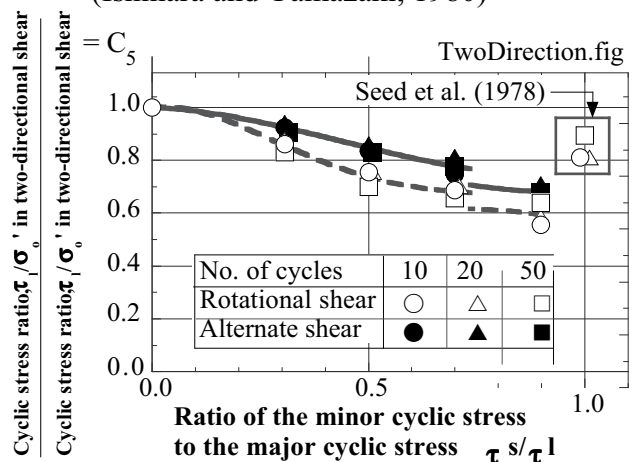
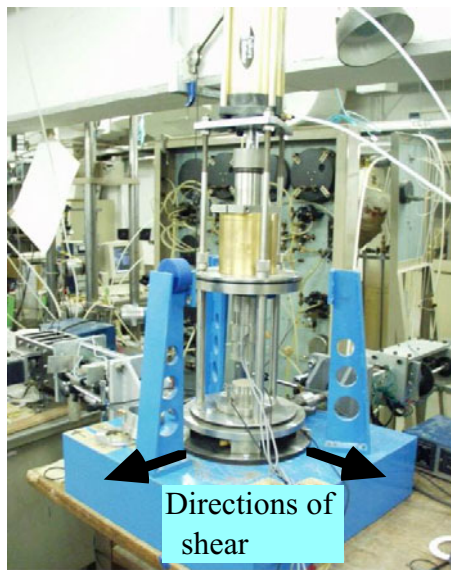


Fig. 19.37 Correction of liquefaction resistance of sand in terms of multi-directional shaking (Ishihara and Yamazaki, 1980)

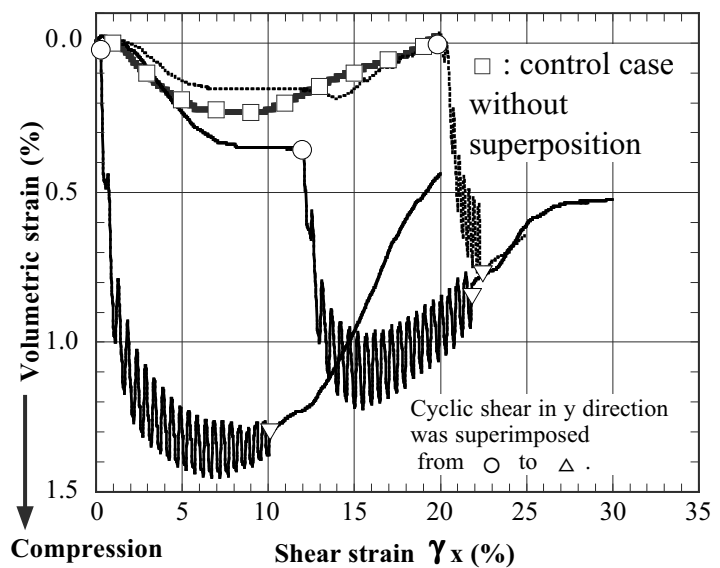
dimensional loading induces volume contraction or triggers liquefaction more easily than conventional one-dimensional loading (Pyke et al. 1975; Seed et al. 1978; Ishihara and Yamazaki, 1980; Kammerer et al. 2004). This certainly implies that negative dilatancy (volume contraction due to shear) is increased by two-dimensional loading. This issue was further indicated experimentally by running drained two-dimensional shear. Figure 19.38 illustrates an experimental device, which generates two-directional simple shear loading on sand.

Tests were performed on dense sand that normally exhibits volume expansion during shear. Figure 19.39 shows the volume change during shear. Since the relative density of the specimens exceeded 100%, volume expansion or positive dilatancy was going to start in the phase of monotonic shear in the  $x$  direction (between the origin and  $\circ$ ). When superposition of the cyclic loading in the  $y$  direction was initiated at the points of  $\circ$ , however, a significant extent of volume contraction (positive volumetric strain) started. This transition from positive dilatancy to negative one (volume contraction) is equivalent in undrained shear with higher pore water pressure and greater deformation. Thus, although positive dilatancy in conventional one-dimensional loading exhibited the development of rigidity and shear strength in undrained conditions (Sect. 18.7), two-dimensional loading may drastically change this situation.



**Fig. 19.38** Two-directional simple shear apparatus (Horie, 2000)

Volumetric compression induced by superimposed cyclic shear ( $\gamma_y$ ) on monotonic  $\gamma_x$ . Multi-directional shear.fig  
Yurakucho sand,  $D_r=100\%$ , 294 kPa.



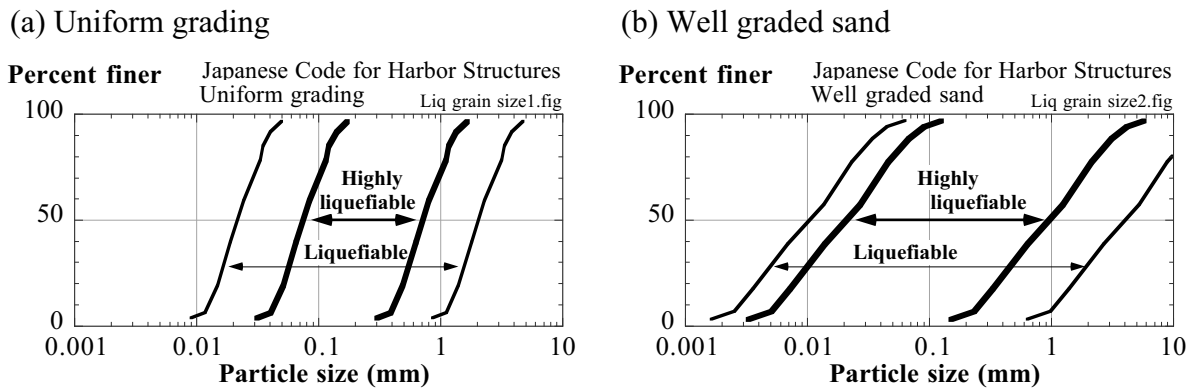
**Fig. 19.39** Volume change of dense sand specimen undergoing multidirectional simple shear (Horie, 2000)

**19.13 Grain Size Distribution of Liquefaction-Prone Sand**

It has been conventionally considered that fine sand with uniform grain size (clean sand) is highly susceptible to liquefaction. In contrast, gravelly soil and silty materials have been regarded as less liquefiable (see Sects. 20.2, 20.4, and 20.5). The ideas behind this have been as what follows:

1. Gravelly soil has high permeability. Therefore, the excess pore water pressure would dissipate quickly so that no time would be available for large ground deformation to occur.
2. Upon water sedimentation of soil, small sand grains sink more slowly than gravels due to viscous resistance of water (Stokes law). Slow velocity of sedimentation leads to loose grain packing (Kolbuszewski, 1948a, b).
3. Cohesion in silty soil prevents development of large deformation during strong shaking (Sect. 20.4).

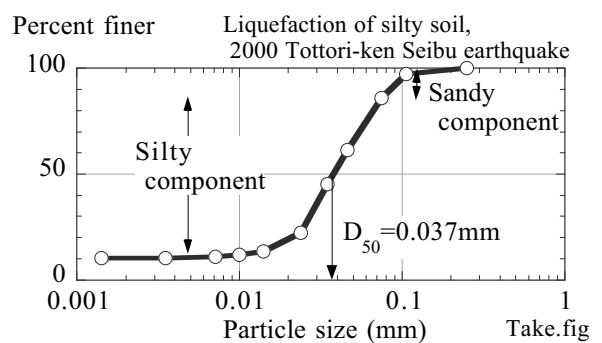
These remarks suggest the high liquefaction risk of fine loose sand in which permeability is low due to its small grain size and there is no cohesion. Accordingly, Fig. 19.40 has been widely accepted as the range of grain size distribution of potentially liquefiable sand. Compare Fig. 19.40 with Fig.19.41, which was obtained from silty sand that liquefied during the 2000 Tottoriken Seibu earthquake (Sect. 17.10).



**Fig. 19.40** Example of grain size distribution of liquefaction-prone sand (Japanese Seismic Code for Harbor Structures)

The three issues stated earlier are not the case under the following situations.

1. A loose and water-saturated gravelly deposit is covered by an impervious silty layer, which prevents seepage and dissipation of excess pore water pressure (Kokusho et al. 1995). Surface pavement has similar effects (Fig. 20.9).
2. Void space among gravel particles is filled with loose and water-saturated sand.
3. Fine silty material has no cohesion. This is the case of tailing materials that are made of crushed stones (Sect. 20.5). Since the grain size is very small, permeability is low as well and pore pressure dissipation is made very difficult within a limited time.



**Fig. 19.41** Grain size distribution of liquefied silty sand

Under such circumstances, liquefaction risk has to be taken into account. Since such materials are not common targets of study, it is desirable to investigate their liquefaction resistance by means of laboratory tests on undisturbed samples in place of using any empirical formula.



**List of References in Chapter 19**

- Annaki, M. and Lee, K.L. (1977) Equivalent uniform cycle concept for soil dynamics, Proc. of ASCE, Vol. 10, GT6, pp. 549–564.
- Arango, I. (1996) Magnitude scaling factors for soil liquefaction evaluations, J. Geotech. Geoenviron. Eng., ASCE, Vol. 122, No. 11, pp. 929–936.
- Cole, E.R.L. (1967) The behaviour of soils in the simple-shear apparatus, Ph.D. Thesis, Cambridge University.
- De Alba, P., Seed, H.B. and Chan, C.K. (1976) Sand liquefaction in large-scale simple shear tests, Proc. ASCE, Vol. 102, GT9, pp. 909–927.
- Federal Highway Administration (1997) Design Guidance: Geotechnical Earthquake Engineering for Highways, Vol. 1, Design Principles, p. 123.
- Finn, W.D.L., Bransby, P.L. and Pickering, D.J. (1971) Sand liquefaction in triaxial and simple shear tests, Proc. ASCE, Vol. 97, SM4, pp. 639–659.
- Horie, Y. (2002) Study on behavior of soil subjected to cyclic loading by simple shear test and site investigation, Master thesis, University of Tokyo.
- Ishihara, K. and Li, S. (1972) Liquefaction of saturated sand in triaxial torsion shear test, Soils Found., Vol. 12, No. 2, pp. 19–39.
- Ishihara, K. and Takatsu, H. (1979) Effects of overconsolidation and  $K_0$  conditions on the liquefaction characteristics of sands, Soils Found., Vol. 19, No. 4, pp. 59–68.
- Ishihara, K. and Yamazaki, F. (1980) Cyclic simple shear tests on saturated sand in multi-directional loading, Soils Found., Vol. 20, No. 1, pp. 45–59.
- Ishihara, K. and Yasuda, S. (1975) Sand liquefaction in hollow cylinder torsion under irregular excitation, Soils Found., Vol. 15, No. 1, pp. 45–59.
- Ishihara, K. and Yamazaki, F. (1980) Cyclic simple shear tests on saturated sand in multi-directional loading, Soils Found., Vol. 20, No. 1, pp. 45–59.
- Japanese Society of Soil Mechanics and Foundation Engineering (Former name of Japanese Geotechnical Society) (1988) Proc. Symp. Undrained Cyclic Tests on Soils, Committee Report, p. 23 (in Japanese).
- Kammerer, A.M., Seed, R.B., Wu, J., Riemer, M.F. and Pestana, J.M. (2004) Pore pressure development in liquefiable soils under bi-directional loading conditions, Proc. 11th Int. Conf. Soil Dynamics and Earthquake Engineering and the 3rd Int. Conf. Earthq. Geotech. Eng., Berkeley, Ed. T. Nogami and R.B. Seed, Vol. 2, pp. 697–704.
- Kokusho, T., Tanaka, Y., Kawai, T., Kudo, K., Suzuki, K., Tohda, S. and Abe, S. (1995) Case Study of rock debris avalanche gravel liquefied during 1993 Hokkaido-Nansei-Oki Earthquake, Soils Found., Vol. 35, No. 3, pp. 83–95.
- Kolbuszewski, J.J. (1948a) General investigation of the fundamental factors controlling loose packing of sands, Proc. 2nd Int. Conf. Soil Mech. Found. Eng, Vol. 1, pp. 47–49.
- Kolbuszewski, J.J. (1948b) An experimental study of the maximum and minimum porosities of sands, Proc. 2nd Int. Conf. Soil Mech. Found. Eng, Vol. 1, pp. 158–165.
- Lee, K.L. and Chan, K. (1972) Number of equivalent significant cycles in strong motion earthquakes, Proc. Int. Conf. Microzonation for Safer Construction Research and Application, pp. 609–627.
- Lee, K.L. and Seed, H.B. (1967) Cyclic stress conditions causing liquefaction of sand, Proc. ASCE, Vol. 93, SM1, pp. 47–70.
- Lee, K.L. and Seed, H.B. (1967) Dynamic strength of anisotropically consolidated sand, Proc. ASCE, Vol. 93, SM5, pp. 169–190.
- Pradel, D. (1998) Procedure to evaluate earthquake-induced settlements in dry sandy soils, J. Geotech. Geoenviron. Eng., ASCE, Vol. 124, No. 4, pp. 364–368.
- Pyke, R., Seed, H.B. and Chan, C.K. (1975) Settlement of sands under multidirectional shaking, Proc. ASCE, Vol. 101, GT4, pp. 379–398.

- Seed, H. B., Idriss, I. M. and Arango, I. (1983) Evaluation of liquefaction potential using field performance data. Proc. ASCE, Vol. 109, GT3, pp. 458–482.
- Seed, H.B. and Idriss, I.M. (1971) Simplified procedure for evaluating soil liquefaction potential, Proc. ASCE, Vol. 97, SM9, pp. 1249–1273.
- Seed, H.B. and Idriss, I.M. (1982) Ground motions and soil liquefaction during earthquakes, Earthq. Eng. Res. Inst., ISBN 0-943198-24-0, p. 110.
- Seed, H.B., Pyke, R.M. and Martin, G.R. (1978) Effect of multidirectional shaking on pore pressure, Proc. ASCE, Vol. 104, GT1, pp. 27–44.
- Vaid, Y.P. and Chern, J.C. (1985) Confining pressure, grain angularity, and liquefaction, J. Geotech. Eng., ASCE, Vol. 111, No. 10, pp. 1229–1235.
- Vaid, Y.P. and Finn, W.D.L. (1979) Static shear and liquefaction potential, Proc. ASCE, Vol. 105, GT10, pp. 1233–1246.
- Yokouchi, N. (1997) Undrained torsion shear on dense sand subjected to strong earthquake loading, Bachelor thesis, University of Tokyo.

# Chapter 20

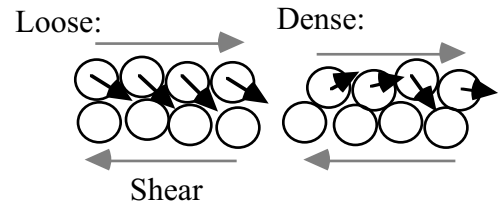
## Behavior of Soil Undergoing Cyclic Undrained Loading



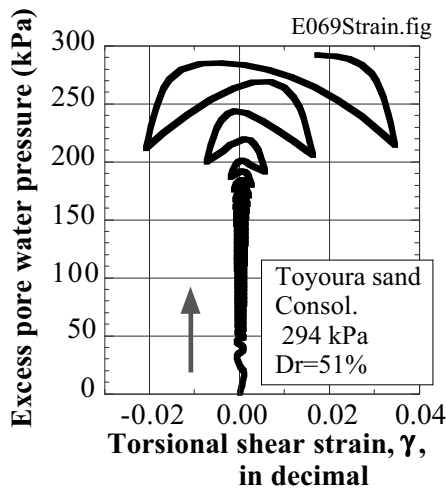
Ancient Buddhism stupa in Anuradhapura, Sri Lanka. Its long age and rain water have caused weathering and deterioration in this masonry structure. Restoration is now going on.

**20.1 Liquefaction Resistance of Dense Sand**

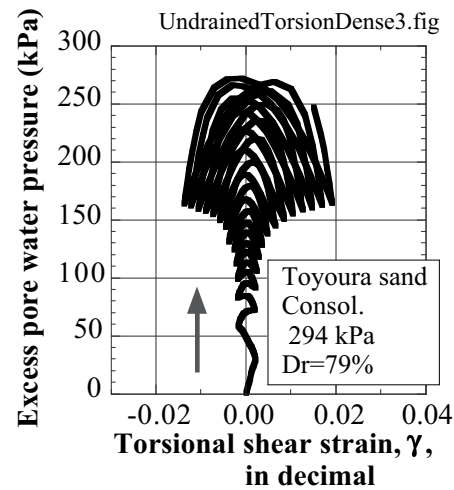
Dense sand has an increased resistance against liquefaction. Therefore, such densification as sand compaction pile, vibroflotation, and rod compaction are reliable mitigation measures against liquefaction. Densification is good also because its effects are permanently valid without maintenance efforts. Figure 20.1 compares the dilatancy of loose and dense sands schematically. Dense sand has a reduced possibility of volume contraction upon shear. Hence, it is less likely to liquefy. For experimental data on dense sand, see Figs. 18.18 and 18.19.



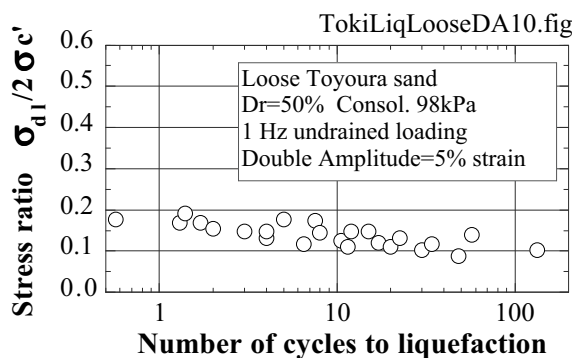
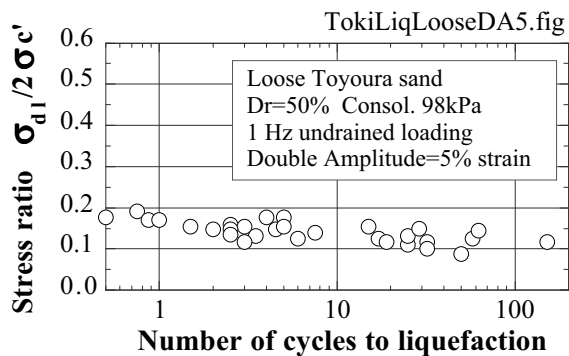
**Fig. 20.1** Effects of density on dilatancy



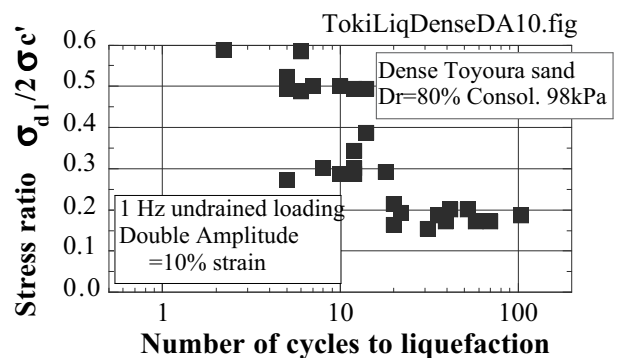
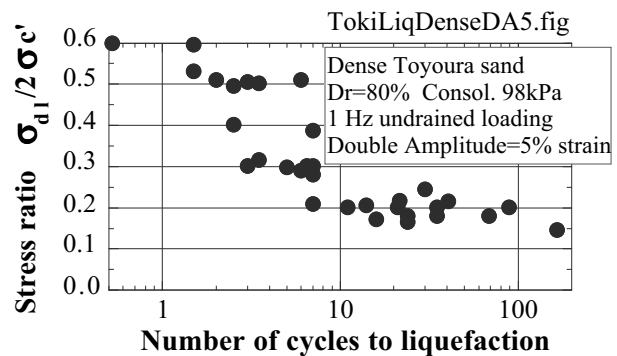
**Fig. 20.2** Strain path of loose sand



**Fig. 20.3** Strain path of dense sand



**Fig. 20.4** Resistance against liquefaction of loose Toyoura sand (after Toki et al. 1986)



**Fig. 20.5** Resistance against liquefaction of dense Toyoura sand (after Toki et al. 1986)

Further study is made here on the relationship between development of excess pore water pressure and that of shear strain amplitude. Figure 20.2 illustrates the data from loose sand, while Fig. 20.3 indicates

the behavior of dense sand. It is evident that loose sand quickly develops large strain and excess pore water pressure after the pressure exceeds 200 kPa. In contrast, dense sand maintains some resistance against large strain or high excess pore water pressure. Thus, dense sand has greater resistance against catastrophic failure due to earthquake loading.

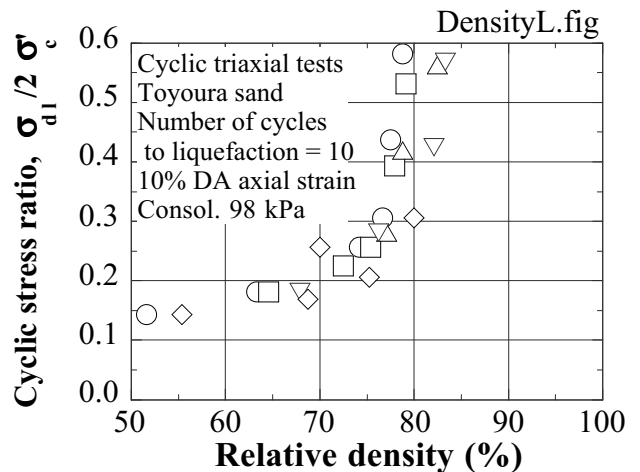
Figure 20.4 indicates the liquefaction curves of loose Toyoura sand (relative density;  $D_r = 50\%$ ); the criteria of liquefaction was the double amplitude of strain (DA: peak-to-peak) equal to 5 and 10%. Two diagrams do not have much difference, showing that 5% and 10% strain occurred almost simultaneously (sudden development of strain). In contrast, Fig. 20.5 shows that liquefaction curves of denser sand ( $D_r = 80\%$ ) vary with the DA value employed. This is particularly the case when the number of cycles to liquefaction is small.

Tanimoto (1971) carried out cyclic triaxial tests on Niigata Bandai-jima sand. Both axial and radial pressures were controlled at 1 Hz to vary with  $180^\circ$  out of phase so that the mean stress was held constant. It was found that resistance to liquefaction increases in proportion to relative density ( $D_r$  in %) of sand up to 100%;

$$\frac{\sigma_d}{2\sigma'_c} = 4.6 \times 10^{-3} D_r \quad (20.1)$$

This finding is different from later findings in Fig. 20.6 where the proportionality does not hold true for  $D_r > 75\%$ . This is probably because liquefaction in this early study was defined by the initiation of quick pore pressure increase at which the excess pore water pressure was still around 50% of the consolidation stress. As seen in Fig. 20.3, dense sand has significant resistance against large deformation.

Figure 20.6 examines the relationship between relative density and stress ratio that induces liquefaction at 10 cycles. Although a proportionality has been reported under lower densities, sand denser than 70% relative density drastically increases its liquefaction resistance.



**Fig. 20.6** Increase of liquefaction resistance with sand density (drawn after Tatsuoka et al., 1986)

20.2 Cyclic Undrained Shear of Gravel

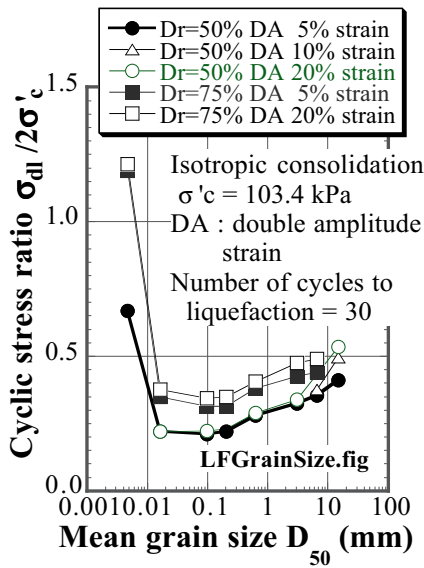


Fig. 20.7 Effects of grain size on stress ratio to cause liquefaction in 30 cycles (Lee and Fitton, 1969)

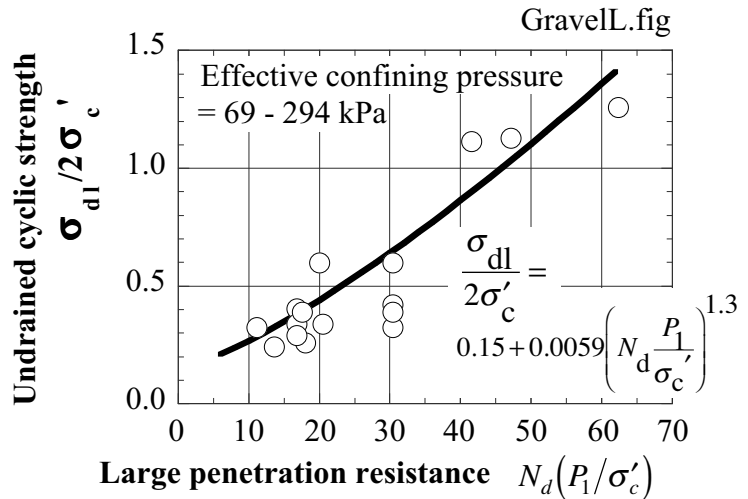


Fig. 20.8 Liquefaction resistance of gravel and sand (drawn after Tanaka et al., 1992)

Gravel has long been believed to be hardly liquefiable. Since gravel is highly permeable, any excess pore water pressure that develops in gravel dissipates quickly (Sect. 18.3) and prevents the onset of liquefaction. There are also cyclic triaxial tests showing that materials of coarse grain size have sufficient liquefaction resistance (Fig. 20.7). However, laboratory testing on gravel has been subjected to serious error called membrane penetration (Sect. 1.10). When excess pore pressure increased, the rubber membrane around the specimen was pushed outward; similar to partial drainage. Thus liquefaction resistance was overestimated.



Fig. 20.9 Liquefaction of gravelly ground

Case history studies (e.g., Youd et al. 1985; Andrus and Youd, 1987) suggest liquefaction in gravelly layers. Figure 20.9 was obtained at the surface of Port Island, 1995, where a large amount of gravels was seen after liquefaction near a sea wall. Sangawa (1992) excavated an ancient liquefaction where sand boil started in a gravelly layer, but gravels could not reach the surface during boiling.

Tanaka et al. (1992) conducted undrained tests on gravel. The specimen was frozen and its surface was trimmed smooth so that no membrane problem occurred. Figure 20.8, where  $P_1$  is 98 kPa, shows that liquefaction strength (stress ratio for DA = 2–2.5% in 20 cycles) of sand and gravel is similar when the large penetration blow counts ( $N_d$ ) is similar as well. Thus, gravel should be considered liquefiable today when it is not very stiff and has limited drainage.

*Note: Diameter of large penetration device is about 40% greater than standard penetration.*

20.3 Cyclic Undrained Shear of Clay

It is thought widely that clay does not liquefy. However, Ohara and Matsuda (1988) conducted cyclic simple shear tests with a constant strain amplitude on clay and observed pore pressure rise. Figure 20.10 is a data on NC (normally consolidated 正規圧密) clay. Excess pore water pressure increased with loading cycles. They finally obtained a relationship between strain amplitude and pore pressure rise after “n=200” cycles (Fig. 20.11). It appears that cyclic behavior of clay is similar to sand. However, there is no evidence of liquefaction in clay during past earthquakes such as floating of embedded structures and substantial shear distortion of ground; failure of clayey slope is a matter of shear failure in the classic sense of soil mechanics (Chap. 15).

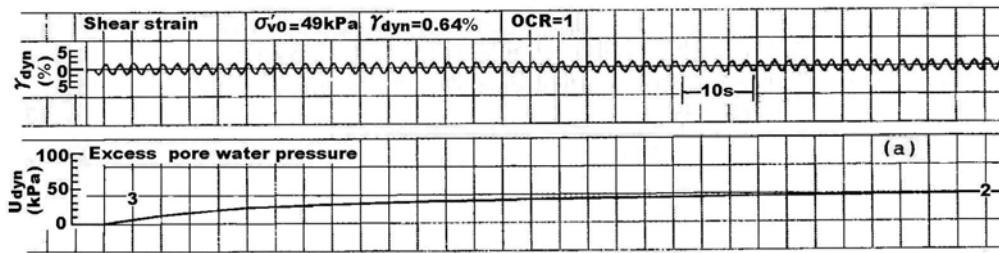


Fig. 20.10 Cyclic undrained shear of normally consolidated clay ( $\sigma'_c = 49$  kPa) (Ohara and Matsuda, 1988)

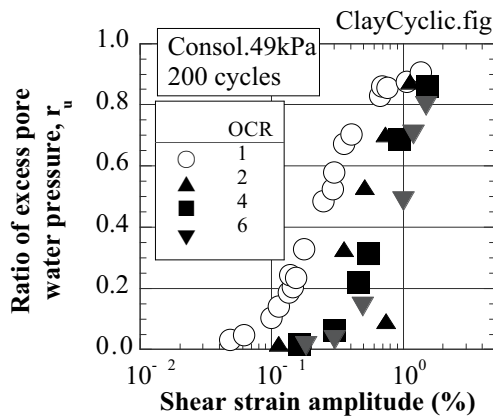


Fig. 20.11 Pore pressure rise and cyclic shear strain (Ohara and Matsuda, 1988)

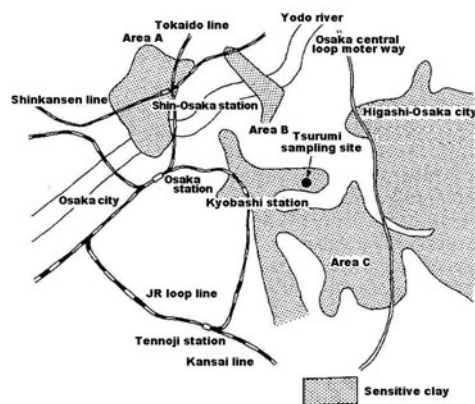


Fig. 20.12 Area of Eastern Osaka soft clay (Adachi et al., 1995)

Elevation (m)	Description of soil	Standard penetration test (N value)
0.73	fill	Standard penetration test (N value)
0.23	fine sand	
-0.68	fine sand	
-1.67	silt with silt	
-2.27	fine sand	
-3.77	fine sand with silt	
-5.77	sandy silt	
-10.27	silt	
-16.67	silty clay	
-17.57	gravel, silty sand	
-20.42	sand with gravel	
-28.77	silty clay	

Fig. 20.13 Typical soil profile (Adachi et al., 1995)

Adachi et al. (1995) carried out undrained cyclic loading tests on clay. The tested material was undisturbed samples of Eastern Osaka clay, which has a sensitivity of 10–15 and is widely distributed in the area shown in Fig. 20.12. This clay deposited in an ancient inland sea, which was gradually filled by river

action in the historical period. This process is similar to the one in formation of Norwegian quick clay. Figure 20.13 illustrates a typical soil profile. Major properties of this clay are: *natural water content* = 65–72%, *liquid limit* = 69–75%, *plasticity limit* = 25–27%, *silt and clay fractions* = 44 and 49%.

Figure 20.14 demonstrates the undrained test results in which  $\sigma'_{mo}$  stands for the atmospheric pressure (大気圧, 98 kPa). It can be noted in this figure that the amplitude of strain increases with the number of loading cycles, while the effective stress decreases gradually. When the effective-stress state comes close to the failure line in the later cycles of loading, the stress–strain curve exhibits an S shape. These features are similar to those found in dense sand (Fig. 18.18). Therefore, it is concluded that such large deformation as occurs in loose sandy deposit is unlikely in clayey subsoil.

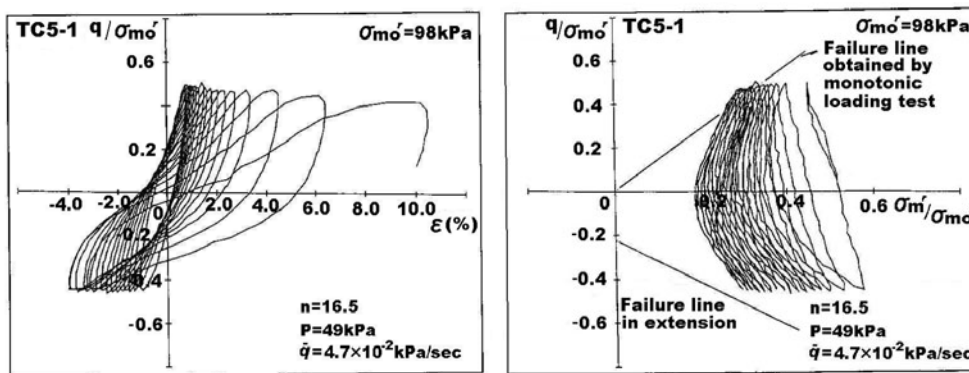


Fig. 20.14 Undrained test results of Eastern Osaka clay (Adachi et al. 1995)

Recently, Osipov et al. (2005) reported electronic microscope photographs of clayey sand. They demonstrated clay bridges connecting sand grains when the clay content was relatively low, while clay filled the intergranular void when the clay content was higher. They state that this different formation of clay content affects the dynamic behavior of clayey sand. When the amount of clay is less, the cyclic loading destroys the clay bridges and decreases the resistance of sand against liquefaction.



## 20.4 Does Clay Liquefy?

The softening of clay in the course of cyclic undrained loading in Sect. 20.3 is called degradation (see Sect. 10.14) and is not liquefaction. However, the fact that the amplitude of shear strain after some cycles exceeds 5 or 10% satisfies the criteria of liquefaction of sand. Therefore, “liquefaction hazard in clayey ground” attracted some concern in 1990s.

That idea was not suitable, however, because the behavior of clay in Fig. 20.14 is more similar to that of dense sand (Sect. 18.7) which hardly develops liquefaction hazard. It should be noted that the effective stress of clay was not reduced to zero, thus providing some stiffness to clay throughout the test.

One may claim that clayey slopes failed during earthquakes. This kind of events should be called shear failure of clay; not liquefaction.

Matsui et al. (1992) carried out cyclic triaxial undrained shear of clay, followed by monotonic loading. Figures 20.15 and 20.16 illustrate the stress–strain and stress–path diagrams during the monotonic loading that started after cyclic reduction of effective stress and pore pressure rise. The behavior of two clays shown there is similar to that of overconsolidated stable sand, without showing stress softening or loss of effective stress. This is in contrast with the postliquefaction behavior of loose sand that deforms to substantial strain without much resistance (Fig. 20.17).

Attempts have been made to study the variation of liquefaction resistance of clayey sand by changing the clay content. A common problem in this type of study is that it is impossible to maintain both void ratio and relative density constant simultaneously while changing the clay content. This is because  $e_{max}$  and  $e_{min}$  of clayey sand change with clay content. Moreover, when the clay content is low, sand grains are in contact with each other and the overall behavior is controlled by sand grain structure (sand matrix). In contrast when clay content is high, sand grains have no more contact with each other and the overall behavior is controlled by the nature of clay. It becomes thus difficult to directly compare liquefaction resistances that were obtained from different clay contents.

Kuwano et al. (1996) mixed Toyoura sand with Fujinomori clay whose plasticity index was 37.7%. Figure 20.18 illustrates the variation of liquefaction resistance with increasing clay content. Samples prepared by two methods consistently revealed that liquefaction resistance increases with the clay content. It is concluded, therefore, that *clay does not liquefy even if it develops some excess pore water pressure and degradation.*

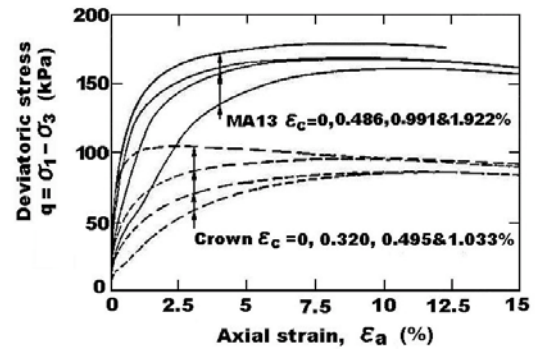


Fig. 20.15 Stress–strain behavior of clay after undrained cyclic loading (Matsui et al., 1992)

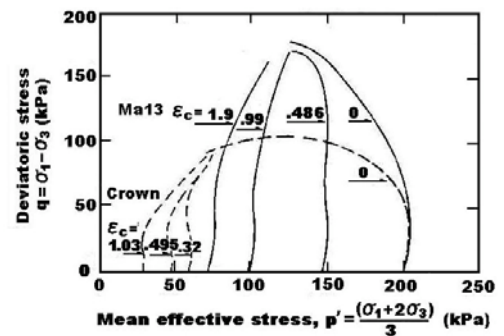


Fig. 20.16 Stress–path diagram of clay after undrained cyclic loading (Matsui et al., 1992)

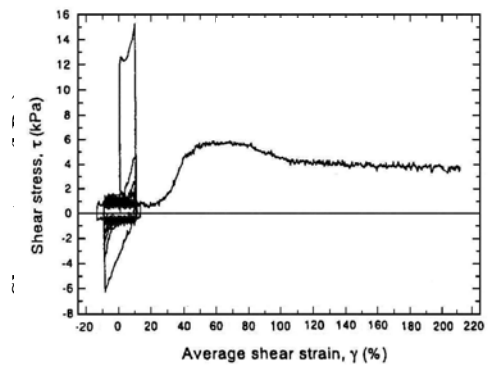


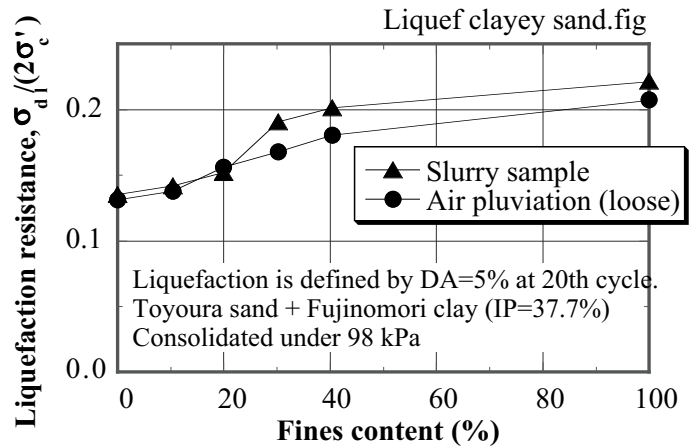
Fig. 20.17 Postliquefaction behavior of loose sand (ring shear test by W. Vargas)

The more important problem of clay occurs during the dissipation of excess pore water pressure. The volume reduction during consolidation induces ground subsidence. This can cause subsidence and leaning of surface structures. See examples in Sect. 17.11. Figure 20.19 shows the volume reduction as a function of cyclic shear strain and OCR (overconsolidation ratio; Sect. 1.4). This OCR effect is consistent with what was discussed in Sect. 19.7 for sand.

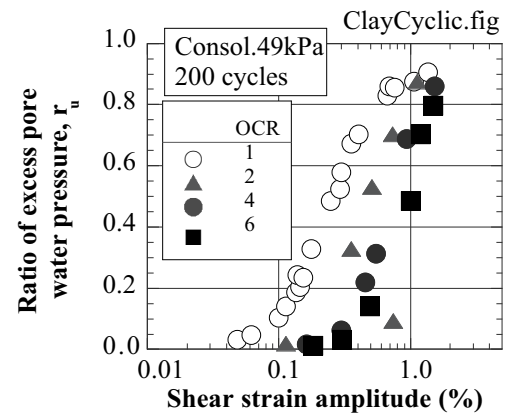
Concerning the liquefaction potential of sand-clay mixture (clayey sand), Seed and Idriss (1982) quoted what is called the Chinese criteria. According to them, clay is likely to liquefy when the following three conditions are satisfied at the same time:

1. Percent finer than 0.005 mm < 15%
2. Liquid limit < 35%
3. Water content > 0.9 times liquid limit

It should be pointed out that the earlier discussion on plastic clay content should not be applied to nonplastic fines. Cohesion in plastic clay content makes the behavior of clayey sand different from cyclic behavior of nonplastic and cohesionless fines. A typical example of the latter material is presented in Sect. 20.5.



**Fig. 20.18** Effects of clay content on resistance of sand to cyclic loading (Kuwano et al., 1996)



**Fig. 20.19** Volume change and cyclic shear strain (after Ōhara and Matsuda, 1988)

## 20.5 Liquefaction of Tailing Material

Former liquefaction tests on soils with fines ( $< 75 \mu$ ) revealed that they are more resistant against liquefaction (e.g., Figs. 20.7 and 20.18). It should be recalled here that fines as employed in former studies meant silts and clays that were of cohesive nature. In contrast, cohesionless fine materials are still vulnerable to liquefaction because

1. It does not have bonding between grains that would help reduce particle dislocation and negative dilatancy
2. Its small particle size reduces the permeability,  $k$ , and accordingly makes pore pressure dissipation slow. See Hazen's empirical relationship,  $k = 100D_{10}^2$  (cm/s) where  $D_{10}$  is the particle size (cm) at 10% passing
3. Velocity of particle deposition in water is very low because of viscosity of water (Stokes law). Consequently, the deposit becomes very loose

Tailing material 鉱滓こうさい is a typical fine material without cohesion. Being a crushed waste material of metal mines, tailing material is discharged into a water reservoir and deposits without densification.



**Fig. 20.20** Seismic failure of Mochikoshi tailing dam (Geotech. Engrg Lab., Univ. Tokyo)



**Fig. 20.21** Site of tailing dam failure in El Cobre, Chile



**Fig. 20.22** Discharging coarse material onto downstream slope of tailing dam (Lomeral in Chile)



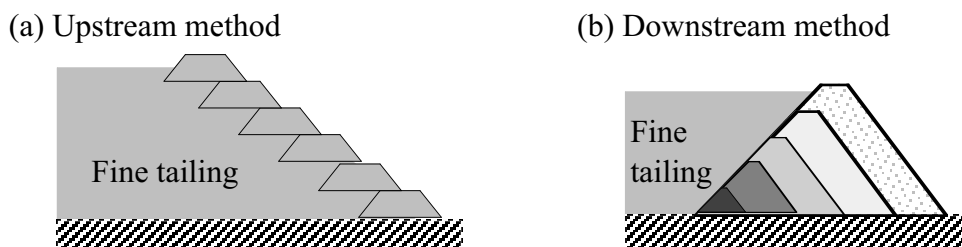
**Fig. 20.23** Discharging finer tailing materials into reservoir (Lomeral in Chile)

Consequently, it achieves a very loose state and is highly vulnerable to liquefaction. Figure 20.20 shows the failure of Mochikoshi tailing dam (伊豆の持越鉱山) during the 1978 Izu-Hanto-Kinkai-Oki earthquake. The liquefaction-induced collapse of El Cobre (copper en Español) Dam in Chile (1965) killed people (Fig. 20.21). Since tailings contains poisonous chemicals as mixed during processing, a failure of a tailing dam causes a serious environmental problem.

Figure 20.22 shows the practice of discharging relatively coarser components of tailing material to build up a dam body. The tailing material is mixed with water and sent to the site through pipes. This way of dam construction is called hydraulic filling. This practice is slightly different from semihydraulic filling of earth-fill dam construction in which soil is transported by trucks, unloaded on ground, and has water jetted so that segregation of materials may occur in the course of water flow. Semihydraulic filling of dam construction is seldom practiced today because dams constructed by this method caused liquefaction (Sect. 16.7).

Relatively finer components are discharged into reservoir water at the same time (Fig. 20.23). One of the key issues is the way of construction of a tailing dam that stores fine tailings in its reservoir.

Figure 20.24 compares two types of dam construction, which are called upstream and downstream methods, respectively. The upstream one is very dangerous during earthquakes. This is because the fine tailings in the reservoir, if they liquefy, exerts significant pressure to the surface crust of a dam and this thin crust cannot resist the earthquake pressure. Evidently, the dam constructed by the downstream method is more stable. Hence, the downstream method is more widely employed in the recent times irrespective of its higher construction cost.



**Fig. 20.24** Types of tailing dams

### 20.6 Empirical Relationship Between Excess Pore Water Pressure and Number of Loading Cycles

Excess pore water pressure increases with time in the course of undrained cyclic loading. It is possible to mitigate the excess pore water pressure by dissipating the pore pressure more quickly than its generation. This is the principle of the gravel drain: see Sect. 26.11.

Figure 20.25 illustrates the experimental relationship of loose Toyoura sand between pore pressure generation,  $r_u$ , and the number of loading cycles,  $N$ . Both coordinates are normalized by the initial isotropic consolidation pressure,  $\sigma'_c$ , and the number of cycles to the onset of liquefaction,  $N_L$ . There is a clear difference of the shape of curves because of the number of cycles to liquefaction (different stress amplitudes).

The design of gravel drain is facilitated by modeling the experimental relationship in Fig. 20.25 by an empirical equation (Seed and Booker, 1977);

$$r_u \equiv \frac{u_g}{\sigma'_c} = \frac{2}{\pi} \arcsin \left( \frac{N}{N_L} \right)^{1/(2\alpha)} \quad (20.2)$$

where  $\alpha$  is an empirical parameter, which accounts for different shape of curves; see Fig.20.26. The number of cycles to liquefaction,  $N_L$ , can be determined by the method shown in Sect. 19.3. The similarity can be found between curves in Fig. 20.25 and the experimental curve in Fig. 18.27.

Equation (20.2) can be converted to a relationship between pore pressure generation and time by assuming a reasonable period of earthquake shaking; for example, 9 s for 20 cycles of uniform stress application that is equivalent to a real irregular seismic loading. For more information, see Sect. 5.12. Thus, an equation of pore pressure rise,  $u$ , is derived, which takes into account both pore pressure generation and seepage/dissipation. In a one-dimensional form;

$$\frac{\partial u}{\partial t} = C_v \frac{\partial^2 u}{\partial z^2} + \frac{\partial u_g}{\partial t} \quad (20.3)$$

where  $z$  is the vertical coordinate and  $\partial u_g / \partial t$  is an input data given by (20.2). The practical design of a gravel drain is performed by using an axisymmetrically two-dimensional version of (20.3) (Seed and Booker, 1977). A typical value of  $\alpha$  is 0.7.

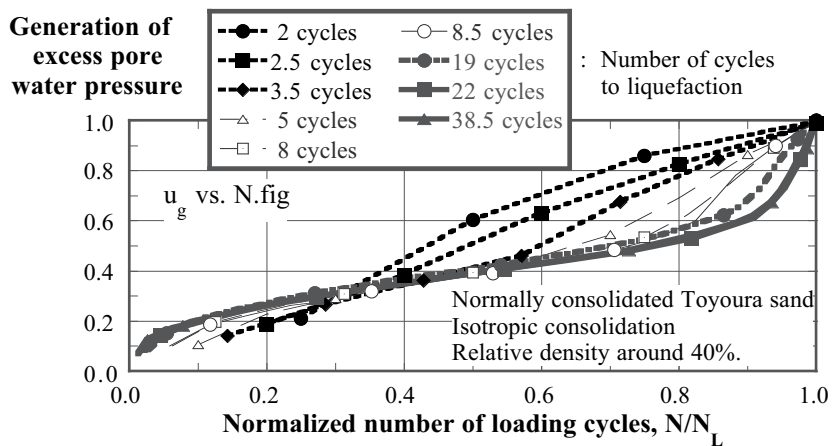


Fig. 20.25 Experimental relationship between pore pressure development and number of loading cycles (undrained torsion shear tests on Toyoura sand)

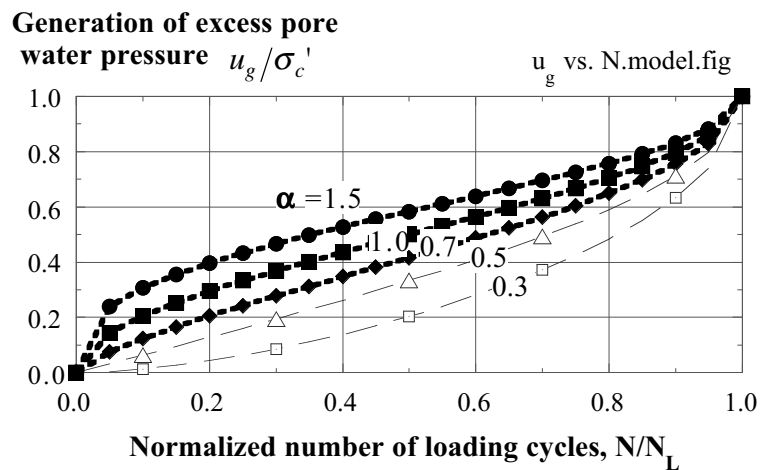


Fig. 20.26 Empirical formula for pore pressure generation with number of loading cycles (by Seed and Booker, 1977)

**20.7 Simple Assessment of Pore Pressure Rise**

It is often important in practice that the stability of slope or bearing capacity are assessed briefly even though liquefaction does not occur (the factor of safety against liquefaction  $F_L > 1$ ). This calculation is performed on the basis of  $F_L$  and evaluation of residual excess pore water pressure,  $\Delta u$ . Tokimatsu and Yoshimi (1983) combined (20.2) (relationship between pore pressure rise and number of loading cycles) with an empirical relationship between the constant stress amplitude,  $\tau$ , and the number of cycles to liquefaction,  $N_L$ ;  $(N_L)^\beta / \tau = \text{constant}$ ;

$$r_u \equiv \frac{\Delta u}{\sigma'_c} = 0.5 + \frac{\arcsin(2F_L^{1/\alpha\beta})}{\pi} \quad (20.4)$$

where  $1/(\alpha\beta)$  ranges between  $-2$  and  $-10$ . Later, Tokimatsu and Seed (1987) proposed a simpler equation;

$$r_u = F_L^{-n} \quad (20.5)$$

in which  $n$  is between 4 and 10 or typically equal to 7. Equations (20.4) and (20.5) are compared in Fig. 20.27.

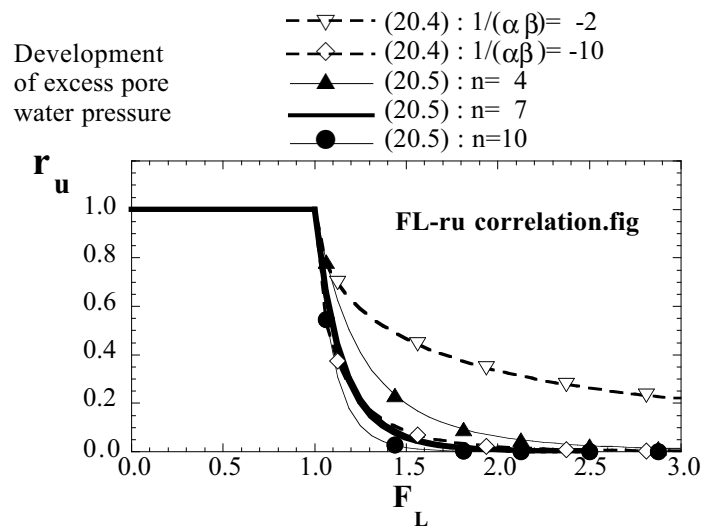
Another interesting approach was proposed by Dobry et al. (1982), who paid attention to the effects of strain amplitude (uniform strain amplitude,  $\gamma$ , equivalent to an irregular time history) on pore pressure rise,  $r_u$ . They used a secant stress-strain relationship;

$$\gamma = \frac{\tau}{G} = \frac{\tau}{G_{\max} \times (G/G_{\max})} \quad (20.6)$$

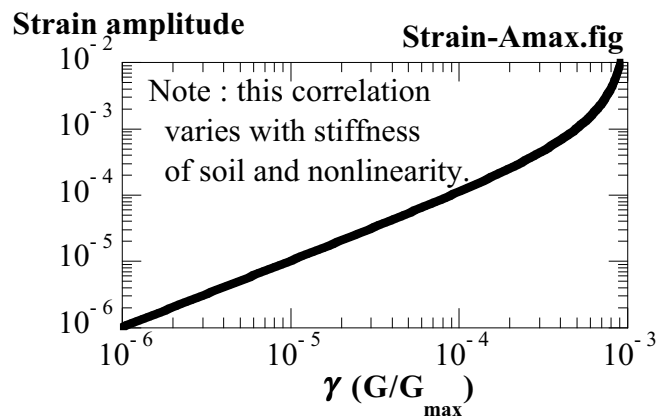
In (20.6),  $G_{\max}$  is the shear modulus at small strain amplitude. Since the shear stress amplitude is related to the maximum acceleration at the surface,  $A_{\max}$  (see Sect. 19.2),

$$\gamma \left( \frac{G}{G_{\max}} \right) = \frac{\tau}{G_{\max}} = \frac{0.65 A_{\max} \sigma_v r_d}{g G_{\max}} \quad (20.7)$$

where 0.65 accounts for the irregular time history,  $\sigma_v$  the total vertical stress,  $r_d$  the effects of depth, and  $g$  the gravity acceleration. By combining (20.7) with any  $G/G_{\max}$ -strain relationship, it becomes possible to determine  $\gamma(G/G_{\max})$  first and then the strain amplitude by using a design  $A_{\max}$ , which is substituted in the right-hand side of (20.7). In the example of Fig. 20.28, a hyperbolic model of  $G/G_{\max} = 1/(1 + \gamma/0.001)$  was employed. If the obtained strain is greater than the threshold strain of 0.0001 for example, pore pressure starts to rise. If it is as large as 0.01, liquefaction is possible.



**Fig. 20.27** Empirical correlation between factor of safety against liquefaction and development of pore water pressure



**Fig. 20.28** Example determination of strain amplitude from surface acceleration

## 20.8 Use of Strain Energy in Modelling of Soil Undergoing Cyclic Loading

Prediction of pore pressure generation under two-dimensional or three-dimensional loading conditions requires more complicated modeling of stress–strain behavior than what was described in Sect. 20.6. This is because the two-dimensional loading, for example, consists of two independent components of shear stress, which are namely  $(\sigma_v - \sigma_h)/2$  and  $\tau_{vh}$ ; see Fig. 20.29a. The former component stands for the triaxial-type shear, while the latter the simple-shear-type loading. The shear stress space in Fig. 20.29b is very convenient to illustrate the stress state as well as the orientation of major principal stress,  $\sigma_1$ .

Since the excess pore water pressure is a product of these two shear stress effects, its modeling is substantially complicated. One of the solutions for this problem is an energy correlation in which an empirical relationship between pore pressure generation and accumulated shear strain energy,  $W_s$ , is studied. The shear strain energy is defined by

$$W_s = \int \sigma_{ij} d\epsilon_{ij} \quad (20.8)$$

Since the soil volume is constant during undrained loading, (20.8) gives the strain energy due to shear deformation only. Although this idea was proposed by Nemat-Nasser (1979), experimental verification was not presented. Sect. 20.9 and 20.10 will show a detailed experimental findings obtained from combined loading of triaxial and torsional stresses.

From a theoretical viewpoint, the advantage of an energy correlation with excess pore water development in undrained condition is that

effects of a complicated stress/strain history on pore water pressure can be assembled into a single parameter that is the accumulated shear energy. Therefore, a modeling is simply made between energy and pore pressure.

This point is important when many shear stress components are superimposed as is the case in two- and three-dimensional stress conditions. Note, however, that this advantage is meaningless unless an energy correlation is verified by experimental data.

A similar advantage was expected from an endochronic model (Valanis, 1971) where a strain time history was assembled into a single parameter as well. In this model, a newly proposed parameter,  $z$ , is a function of the length of strain path. In the simplest form,

$$z = z\left(\int \left\{d\epsilon_{ij}d\epsilon_{ij}\right\}^{1/2}\right) \quad (20.9)$$

in which  $\int \left\{d\epsilon_{ij}d\epsilon_{ij}\right\}^{1/2}$  stands for the length of strain path in a strain space (Fig. 20.30). An experimental correlation of the length of strain path and excess pore water pressure was attempted by Finn and Bhatia (1979). A possible problem may be that two strain paths in Fig. 20.30 become physically identical when  $\Delta\epsilon \rightarrow 0$ , while, mathematically, their lengths are still substantially different.

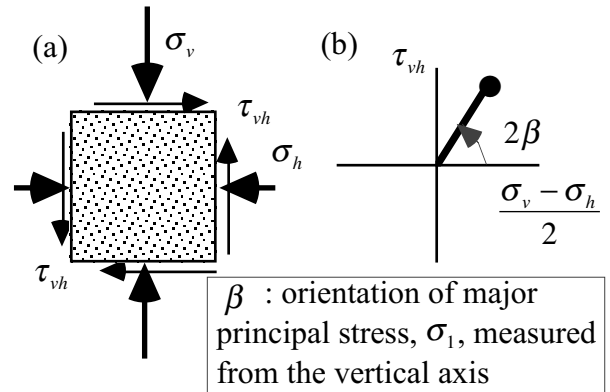


Fig. 20.29 Two components of shear stress in two-dimensional loading conditions

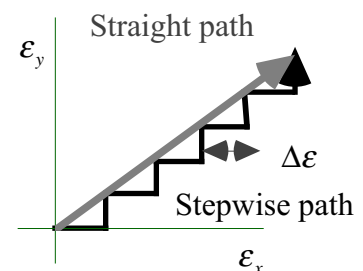


Fig. 20.30 Length of strain paths

20.9 Correlation Between Shear Strain Energy and Excess Pore Water Pressure

A series of undrained torsion shear tests were conducted on loose (40% relative density) Toyoura sand in a hollow cylindrical device (Sect. 18.8; Towhata and Ishihara, 1985a). Figure 20.31 illustrates three of the employed shear stress paths for cyclic loading after isotropic consolidation under 294 kPa. The path in Fig. 20.31a is

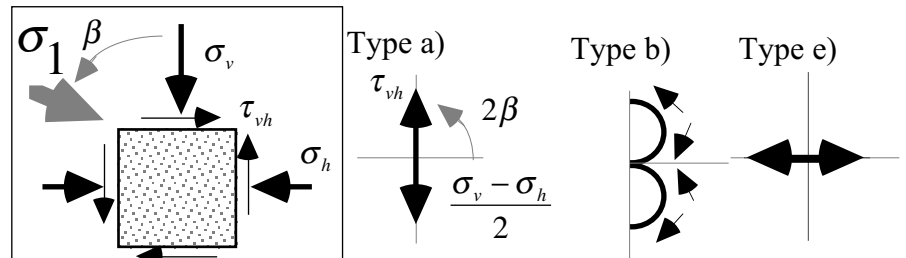


Fig. 20.31 Shear stress paths in torsion shear tests

cyclic torsion shear without vertical stress change, the one in Fig. 20.31b is a special one with continuous rotation of principal stress axes ( $\sigma_1$ : major principal stress), and Fig. 20.31e represents cyclic triaxial shear. See that the orientation of the principal stress,  $\sigma_1$ , which is designated by  $\beta$ , changes continuously for type b in Fig. 20.31.

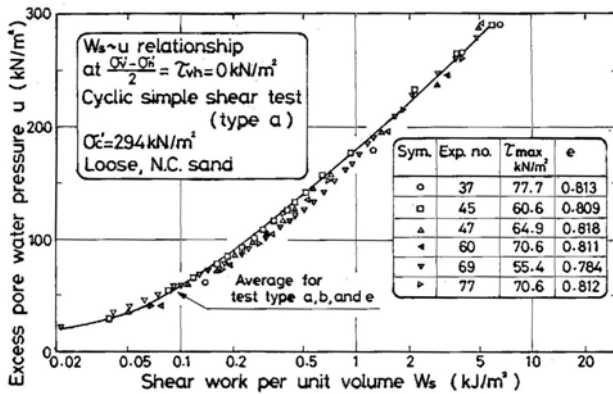


Fig. 20.32 Correlation in cyclic torsion shear (Type a) between excess pore water pressure and accumulated shear work at state of zero shear stress

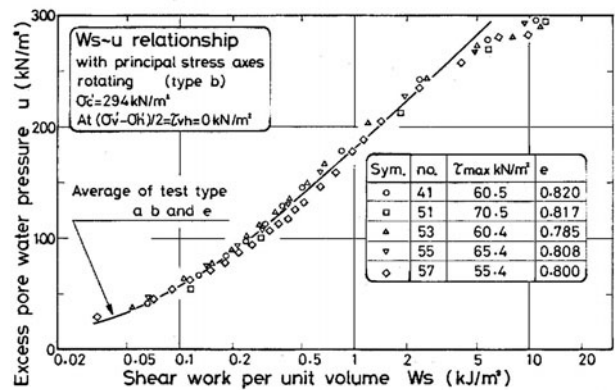


Fig. 20.33 Energy correlation of excess pore water pressure with cyclic rotation of principal stress axes (Type b)

A comprehensive study was made of possible correlation between excess pore water pressure and the accumulated shear strain energy that were recorded during undrained cyclic shear tests on loose Toyoura sand (Towhata and Ishihara, 1985b). The strain energy or shear work,  $W$ , was defined by

$$W = \int \sum_{i,j=1}^3 \sigma_{ij} d\epsilon_{ij} \quad (20.10)$$

in which summation was made for  $i$  and  $j$  from 1 to 3. By using the mean principal stress,  $\sigma_m$ , and the volumetric strain,  $\epsilon_{vol}$ , which is actually null in undrained tests,

$$W = \int \sum_{i,j=1}^3 (\sigma_{ij} - \delta_{ij}\sigma_m + \delta_{ij}\sigma_m) \left( d\epsilon_{ij} - \delta_{ij} \frac{d\epsilon_{vol}}{3} + \delta_{ij} \frac{d\epsilon_{vol}}{3} \right) \quad (20.11)$$

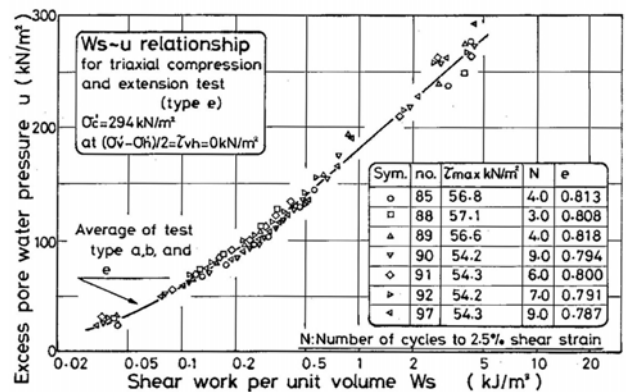


Fig. 20.34 Energy correlation of excess pore water pressure in cyclic triaxial shear (Type e)



in which Kronecker's delta,  $\delta_{ij}$ , = 1 if  $i = j$ , and equal to 0 if  $i \neq j$ , while  $\sigma_m = \frac{\sum_{i=1}^3 \sigma_{ii}}{3}$   
 =  $(\sigma_x + \sigma_y + \sigma_z)/3$ , and  $\epsilon_{vol} = \sum_{i=1}^3 \epsilon_{ii} = \sum_{i,j=1}^3 \delta_{ij} \epsilon_{ij} = \epsilon_x + \epsilon_y + \epsilon_z$ . Accordingly,

$$W = \int \sum_{i,j=1}^3 \left[ (\sigma_{ij} - \delta_{ij} \sigma_m) \left( d\epsilon_{ij} - \delta_{ij} \frac{d\epsilon_{vol}}{3} \right) + \delta_{ij} \sigma_m \left( d\epsilon_{ij} - \delta_{ij} \frac{d\epsilon_{vol}}{3} \right) + (\sigma_{ij} - \delta_{ij} \sigma_m + \delta_{ij} \sigma_m) \delta_{ij} \frac{d\epsilon_{vol}}{3} \right] \quad (20.12)$$

Since the second term is zero because of the definition of volumetric strain, and the third term is zero as well because of  $d\epsilon_{vol} = 0$  in undrained shear,

$$W = \int \sum_{i,j=1}^3 (\sigma_{ij} - \delta_{ij} \sigma_m) \left( d\epsilon_{ij} - \delta_{ij} \frac{d\epsilon_{vol}}{3} \right), \quad (20.13)$$

which implies that the calculated strain energy is equal to the accumulated shear strain energy in undrained shear.

The excess pore water pressure and the accumulated shear strain energy (shear work) were picked up every time when the stress state passed the origin in Fig. 20.31 (state of isotropic stress without shear stress). Figure 20.32 shows that there is a unique correlation in cyclic torsion shear. This relationship is independent of the stress amplitude under which the number of cycles to liquefaction varied from 2 to 40. Figures 20.33 and 20.34 illustrate similar correlation, independent of stress amplitude again, that were obtained from shear stress paths of type b (with stress axes rotation) and type e (cyclic triaxial shear) in Fig. 20.31. Note that all the data points in the three figures are consistent with a single average curve as shown in those figures.

It is further interesting that an alternate loading of  $\tau_{vh}$  and  $(\sigma_v - \sigma_h)/2$  (Fig. 20.35) exhibits the same correlation in Fig. 20.36.

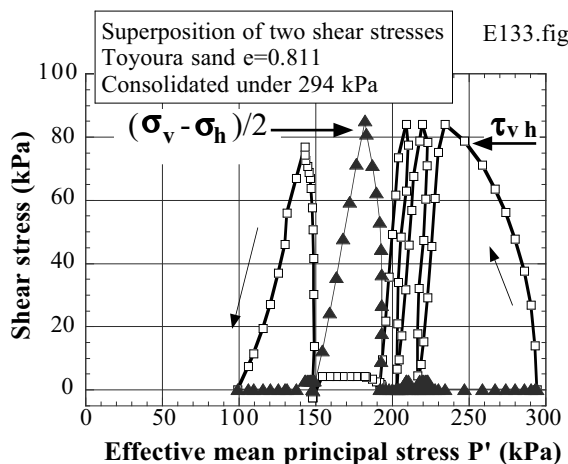


Fig. 20.35 Alternate loading of torsional shear stress and stress difference (Type I)

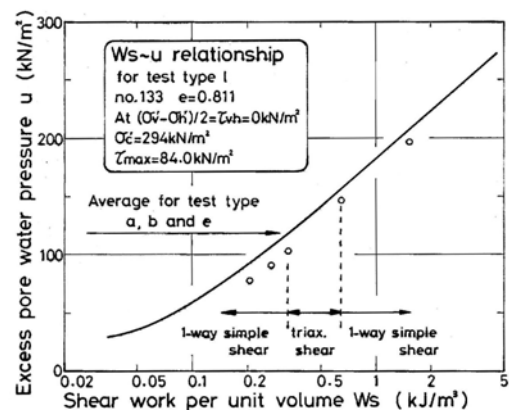


Fig. 20.36 Energy correlation of excess pore water pressure in alternate loading of two shear stress components

20.10 Energy Correlation of Pore Pressure at States of Shear Stress

In addition to the finding of energy correlation at zero shear stress in Sect. 20.9, a further examination was made at states of nonzero shear stress. Figure 20.37 shows that the state of torsion shear stress = ±60.4 kPa can be achieved by three kinds of paths: torsion shear (type a) and combination of axial and torsion shear (types b and d). The former type of loading maintains the principal stress axes fixed in  $\beta = \pm 45^\circ$ , while the latter includes continuous rotation of stress axes.

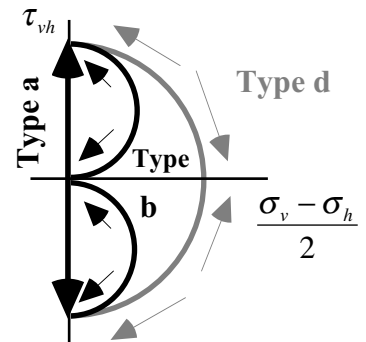


Fig. 20.37 Two shear stress paths reaching same torsional state of stress

Figure 20.38 reveals the energy correlation at ±60.4 kPa of torsional shear stress during cyclic torsion shear (type a). The shown correlation is independent of the stress amplitude as well as the state of stress; loading or unloading. The same state of stress was reached by shear stress paths of type b and d (see Fig. 20.31). Both have continuous rotation of principal stress axes. The test data in Fig. 20.39 indicates that the correlation is independent of the type of loading. Moreover, these data are consistent with the correlation in Fig. 20.38.

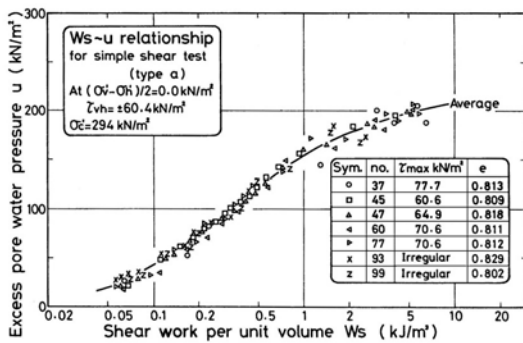


Fig. 20.38 Energy correlation of excess pore water pressure obtained at torsional state of shear (cyclic torsion shear tests)

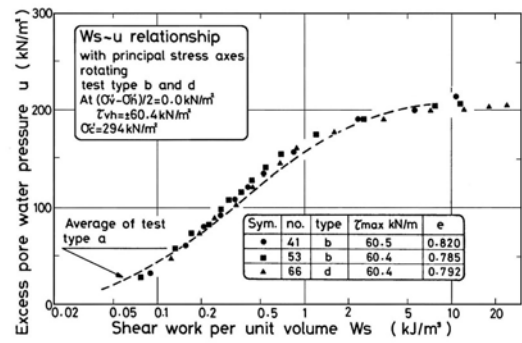


Fig. 20.39 Energy correlation of excess pore water pressure obtained at torsional state of shear (with continuous rotation of stress axes)

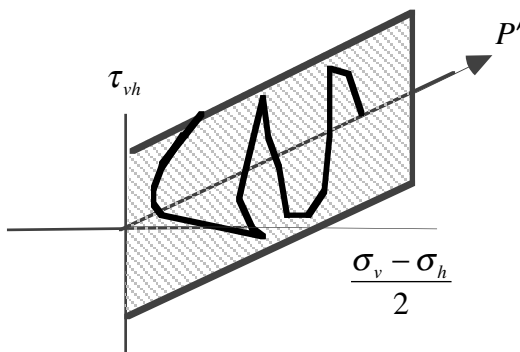


Fig. 20.40 State of torsion shear in three dimensional stress space

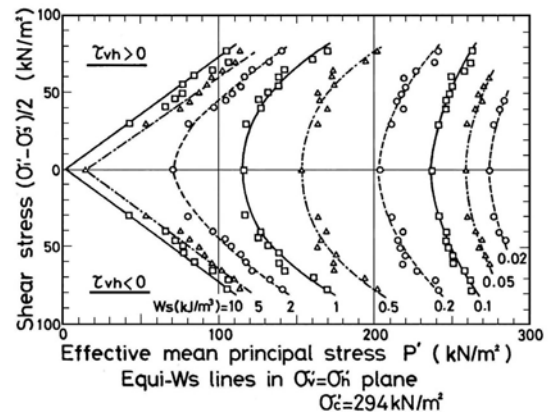


Fig. 20.41 Energy correlation in state of torsional shear stress ( $W_s$ : accumulated strain energy per volume)

The energy correlation means that any state of stress in a three-dimensional stress space of  $P' \sim (\sigma_v - \sigma_h)/2 \sim \tau_{vh}$  (Fig. 20.40) is associated with a unique value of accumulated strain energy (Fig. 20.41).  $P' = (\sigma_1' + \sigma_2' + \sigma_3')/3$  shows the reduction of mean effective stress from the initial isotropic consolidation of 294 kPa.

For example, the state of torsional shear stress of  $(\sigma_v - \sigma_h)/2 = 0$  is indicated in the plane illustrated in Fig. 20.41. When any stress path hits this plane, the energy correlation is given by the one in Figure 20.41. This correlation is valid even when the stress path includes cyclic loading of  $(\sigma_v - \sigma_h)/2$  out of the plane in Fig. 20.40. Accordingly, this figure implies that the development of excess pore pressure can be assessed for any complicated shear stress paths by simply knowing the accumulated shear strain energy during the undrained cyclic loading together with the current shear stress state. Thus, the accumulated strain energy is a state parameter (状態量) in the physico-chemical sense.

20.11 Stress–Strain Behavior Reproduced from Acceleration Records

Stress–strain behavior of insitu soil can be reproduced by using acceleration time history, which is obtained by a vertical array. Figure 20.42 shows the idea of linear interpolation of data along the vertical direction. This interpolated function is integrated along the vertical axis to derive shear stress at any depth by using the equation of motion of a vertical column in a horizontally layered ground.

$$\tau(z,t) = \int_{\zeta=0}^z \rho A(\zeta,t) d\zeta \tag{20.14}$$

in which  $\rho$  stands for the mass density of soil and  $A$  the acceleration at the depth of  $\zeta$  and time of  $t$ . Note that lateral earth pressures on left and right sides of the column (Fig. 20.43) cancel each other because the ground is infinite and level. Another integration along the time axis gives the displacement;

$$u(z,t) = \iint A(z,\tau) d\tau^2 \tag{20.15}$$

By obtaining displacements at two depths of  $z$  and  $z + \Delta z$ , the averaged shear strain between these two elevations is obtained;

$$\gamma(z,t) = \frac{u(z + \Delta z,t) - u(z,t)}{\Delta z} \tag{20.16}$$

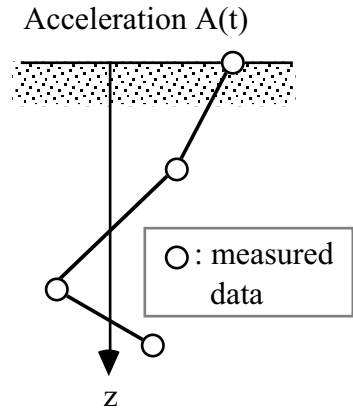


Fig. 20.42 Interpolation of acceleration recorded by vertical array

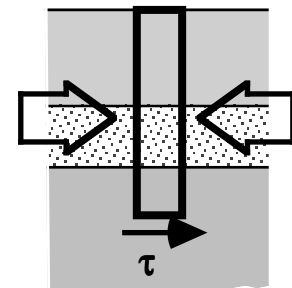


Fig. 20.43 Idea of equation of motion to soil column in horizontal ground

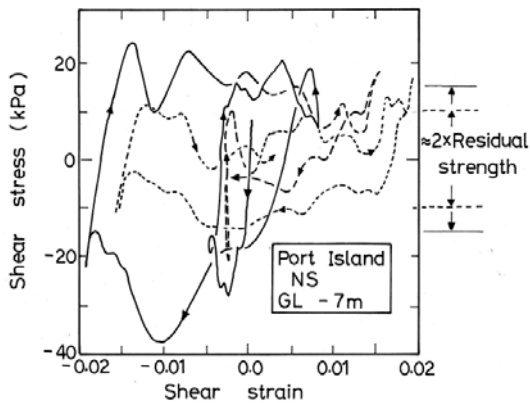


Fig. 20.44 Reproduced stress-strain behaviour of Port Island soil in Kobe undergoing liquefaction (Towhata et al., 1996)

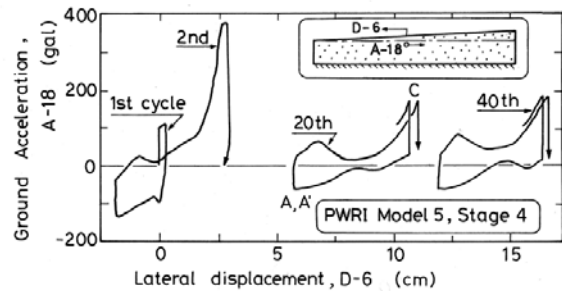


Fig. 20.45 Reproduced stress-strain behavior of model slope subjected to shaking and liquefaction (Sasaki et al., 1992)

This idea was applied to shaking model tests by Koga and Matsuo (1990). Zeghal and Elgamal (1994) analyzed a vertical array records to demonstrate the elongated continuation of dynamic displacement after the phase of strong acceleration has ceased at a site of subsoil liquefaction. Figure 20.44 illustrates an example stress–strain behavior of Kobe Port Island soil during liquefaction (Towhata et al. 1996). The difference of stress levels between the positive loading and negative loading gives the idea of soil strength during liquefaction and continued cyclic loading. Moreover, Fig. 20.45 shows a reproduced stress–strain diagram of liquefied sand in the course of a shaking model test (Sasaki et al. 1992). A peak strength followed by softening and residual strength prior to a second peak strength is noteworthy.

**List of References in Chapter 20**

- Adachi, T., Oka, F., Hirata, T., Hashimoto, T., Nagaya, J., Mimura, M. and Pradhan T., B.S. (1995) Stress–strain behavior and yielding characteristics of Eastern Osaka clay, *Soils Found.*, Vol. 35, No. 3, pp. 1–13.
- Andrus, R.D. and Youd, T.L. (1987) Subsurface investigation of a liquefaction-induced lateral spread Thousand Springs Valley, Idaho, Miscellaneous Paper (GL-87-8), US Army Corps of Engineers.
- Dobry, R., Ladd, R.S., Yokel, F.Y., Chung, R.M. and Powell, D. (1982) Prediction of pore water pressure buildup and liquefaction of sands during earthquakes by the cyclic strain method, National Bureau of Standards Building Science Series, No. 138.
- Finn, W.D.L. and Bhatia, S.K. (1981) Prediction of seismic pore water pressures, Proc. 10th Int. Conf. Soil Mech. Found. Eng., Vol. 3, Stockholm, pp. 201–206.
- Koga, Y. and Matsuo, O. (1990) Shaking table tests of embankments resting on liquefiable sandy ground, *Soils Found.*, Vol. 30, No. 4, pp. 162–174.
- Kuwano, K., Nakazawa, H., Sugihara, K. and Yabe, H. (1996) Undrained cyclic shear strength of sand containing fines, Proc. 11th Japan Nat. Conf. Geotech. Eng., Vol. 1, pp. 993–994 (in Japanese).
- Lee, K.L. and Fitton, J.A. (1969) Factors affecting the cyclic loading strength of soil, *Vibration Effects of Earthquakes on Soils and Foundations*, ASTM STP450, pp. 71–95.
- Matsui, T., Bahr, M.A. and Abe, N. (1992) Estimation of shear characteristics degradation and stress–strain relationship of saturated clays after cyclic loading, *Soils Found.*, Vol. 32, No. 1, pp. 161–172.
- Nemat-Nasser, S. and Shokooh, A. (1979) A unified approach to densification and liquefaction of cohesionless sand in cyclic shearing, *Canadian Geotechnical Journal*, Vol. 16, pp. 659–678.
- Ōhara, S. and Matsuda, H. (1988) Study on the settlement of saturated clay layer induced by cyclic shear, *Soils Found.*, Vol. 28, No. 3, pp. 103–113.
- Osipov, V.I., Gratchev, I.B. and Sassa, K. (2005) The mechanism of liquefaction of clayey soils (M124), Chapter 15, *Landslides: risk analysis and sustainable disaster management*, Springer, pp. 127–131.
- Sangawa, A. (1992) Evidence of earthquake in archaeological site, *Tsuchi-to-Kiso* Monthly magazine of Japanese Geotechnical Society, January, Frontispiece Photograph 10.
- Sasaki, Y., Towhata, I., Tokida, K., Yamada, K., Matsumoto, H., Tamari, Y. and Saya, S. (1992): Mechanism of permanent displacement of ground caused by seismic liquefaction, *Soils Found.*, Vol. 32, No. 3, pp. 79–96.
- Seed, H. B. and Idriss, I. M. (1982) Ground motions and soil liquefaction during earthquakes, *Earthquake Engineering research Institute, University of California, Berkeley, Monograph series*, p. 111.
- Seed, H.B. and Booker, J.R. (1977) Stabilization of potentially liquefiable sand deposits using gravel drains, *J. Geotech. Eng., ASCE*, Vol. 103, GT7, pp. 757–768.
- Tanaka, Y., Kudo, K., Yoshida, Y. and Kokusho, T. (1992) Undrained cyclic strength of gravelly soil and its evaluation by penetration resistance and shear modulus, *Soils Found.*, Vol. 32, No. 4, pp. 128–142.
- Tanimoto, K. (1971) Laboratory tests on liquefaction of water-saturated sand, Proc. 16th Soil Mechanics Symposium, Jpn. Soc. Soil Mech. Found. Eng., pp. 21–26 (in Japanese).
- Tatsuoka, F., Toki, S., Miura, S., Kato, H., Okamoto, M., Yamada, S., Yasuda, S. and Tanizawa, F. (1986) Some factors affecting cyclic undrained triaxial strength of sand, *Soils Found.*, Vol. 26, No. 3, pp. 99–116.
- Toki, S., Tatsuoka, F., Miura, S., Yoshimi, Y., Yasuda, S. and Makihara, Y. (1986) Cyclic undrained triaxial strength of sand by a cooperative test program, *Soils Found.*, Vol. 26, No. 3, pp. 117–128.
- Tokimatsu, K. and Seed, H.B. (1987) Evaluation of settlements in sands due to earthquake shaking, *J. Geotech. Eng., ASCE*, Vol. 113, No. 8, pp. 861–878.
- Tokimatsu, K. and Yoshimi, Y. (1983) Empirical correlation of soil liquefaction based on SPT N-value and fines content, *Soils Found.*, Vol. 23, No. 4, pp. 56–74.

- Towhata, I., Ghalandarzadeh, A., Sundarraj, K.P. and Vargas-Monge, W. (1996) Dynamic failures of subsoils observed in water-front areas, Special Issue on Geotechnical Aspects of the January 17 1995 Hyogoken-Nambu Earthquake, No. 1, Soils Found., pp. 149–160.
- Towhata, I. and Ishihara, K. (1985a) Undrained strength of sand undergoing cyclic rotation of principal stress axes, Soils Found., Vol. 25, No. 2, pp. 135–147.
- Towhata, I. and Ishihara, K. (1985b) Shear work and pore water pressure in undrained shear, Soils Found., Vol. 25, No. 3, pp. 73–84.
- Valanis, K.C. (1971) A theory of viscoplasticity without a yield surface Part I, Archives of Mechanics, Vol. 23, No. 4, pp. 517–533.
- Youd, T.L., Harp, E.L., Keefer, D.K. and Wilson, R.C. (1985) The Borah Peak, Idaho Earthquake of October 28, 1983 - Liquefaction, Earthquake Spectra, Vol. 2, No. 1, pp. 71–89.
- Zeghal, M. and Elgamal, A.-W. (1994) Analysis of site liquefaction using earthquake records, J. Geotech. Eng., ASCE, Vol. 120, DT6, pp. 996–1017.

# Chapter 21

## In-Situ Tests on Liquefaction Potential of Subsoils



唐高宗與武則天之乾陵



Grand entrance to the tomb of the third emperor of Tang Dynasty and his powerful empress, near Xi'an, China.

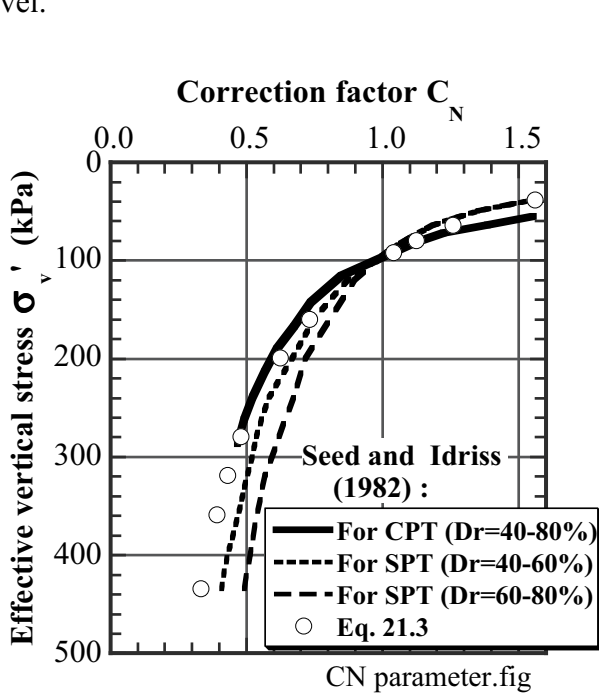
**21.1 Use of SPT for Assessing Liquefaction Potential**

The evaluation of  $F_L$  stated in Sect. 19.4 required laboratory tests on undisturbed soil specimens of loose sand. Undisturbed sampling of loose sand under the ground water table is not an easy job. The quality of samples might be poor unless an experienced engineer is engaged.

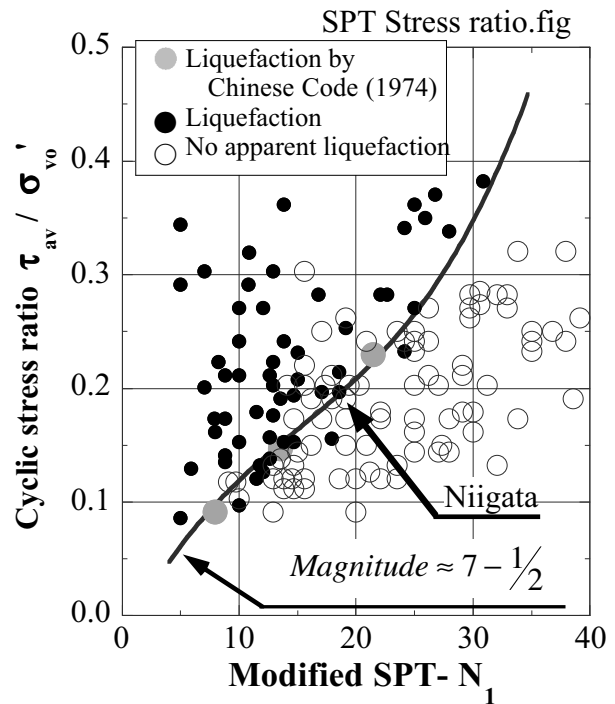
SPT- $N$  is a measure of sand density. Meyerhof (1957) proposed an empirical correlation between  $N$ ,  $\sigma'_v$  (effective vertical stress), and  $D_r$  (relative density in %);

$$D_r(\%) = 21 \sqrt{\frac{N}{\sigma'_v \text{ (kgf/cm}^2\text{)} + 0.7}} \quad (21.1)$$

Since liquefaction resistance of loose to medium loose sand has been said to be proportional to  $D_r$  (Fig. 20.4), an SPT-based assessment of in-situ liquefaction resistance seems possible. Although relative density ( $D_r$ ) and liquefaction resistance are essential characteristics of soil, SPT- $N$  is not. This is because  $N$  value is affected by the effective stress ( $\sigma'_v$ ); very loose sand may have high SPT- $N$  under high stress level.



**Fig. 21.1** Correction of SPT- $N$  for effective stress level (Seed and Idriss, 1982)



**Fig. 21.2** Seismic stress ratio produced by earthquakes of magnitude = 7.5 at sites with and without liquefaction (Seed and Idriss, 1982)

Equation (21.1) suggests a way to correct SPT- $N$  for the effects of stress level:

$$N_1 = C_N \times N \quad (21.2)$$

in which  $N_1$  stands for the SPT- $N$  at the effective stress level of  $1 \text{ t/m}^2$  (98 kPa), and  $C_N$  designates a correction factor. Among many correction factors, (21.1) leads to

$$C_N = \frac{1.7}{[\sigma'_v(\text{kPa})/98] + 0.7} \quad (21.3)$$



Seed and Idriss (2002) presented correction factors for both SPT (standard penetration tests) and CPT (cone penetration tests). Figure 21.1 compares those factors together with (21.3).

Seed and Idriss (1982) collected information about the earthquake-induced stress ratio and SPT- $N$  at sites of past liquefaction and sites without liquefaction. It was then attempted to study the relationship between onset of liquefaction and SPT- $N$ . To use the essential characteristics of sand, modified values of  $N_1$  was employed in place of  $N$ . Although not being very precise, their results in Fig. 21.2 shows the boundary between data from liquefied and unliquefied sites, which infers the liquefaction resistance of sand and can be correlated with  $N$ . It should be noted that this diagram is valid for earthquake magnitude of 7.5 for which the number of cycles is about 15 (Table 19.1). The use of SPT- $N$  for assessment of liquefaction resistance of soil (e.g., Sect. 21.4) is thus justified.

It is well known that fines content in sandy soil reduces the measured  $N$  value (Sect. 1.12). To account for this, there are several empirical corrections, and one of them is tabulated in Table 21.1. Another correction from the viewpoint of liquefaction is presented in Sect. 21.4.

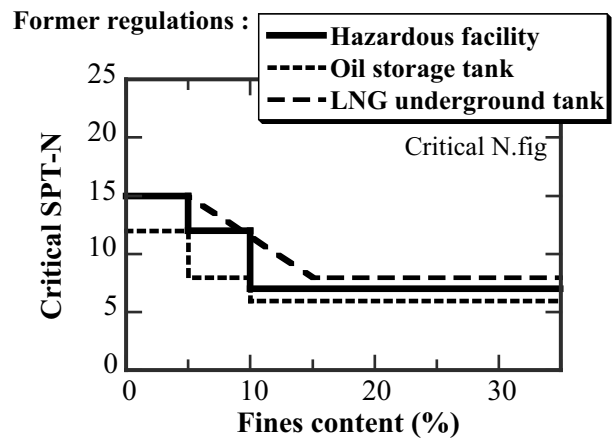
One of the early methods of assessment of liquefaction potential relied on SPT- $N$  as well. Figure 21.3 was employed previously by the Code for Design of Oil and LNG Storage Tanks. Remedial measures against liquefaction was required when  $N$  was less than the critical value ( $N_{cr}$ ) in this diagram. This early idea of  $N_{cr}$  came from the case studies in 1960s, which was conducted in Niigata city after extensive liquefaction (Sect. 21.2). As fines content (clay and silt, finer than  $75 \mu m$ ) increases in Fig. 21.3,  $N_{cr}$  decreases, because cohesive materials increase the liquefaction resistance and decreases the  $N$  value. Note that this early idea of critical  $N$  does not take into account the intensity of expected earthquakes and local earthquake activities. Actually, the seismic activity of Japanese Archipelago was intended by previous codes. Hence, the critical  $N$  value thus obtained is not valid in other parts of the world.

A similar assessment on liquefaction potential based on  $V_s$  does not yet work properly because  $V_s$  does not tell about type of soil (fines content).

**Table 21.1** Correction of  $N_1$  value of sandy soil in terms of fines content,  $F_c$  (Seed, 1987)

$F_c$ (%)	$\Delta N$
10	1
25	2
50	4
75	5

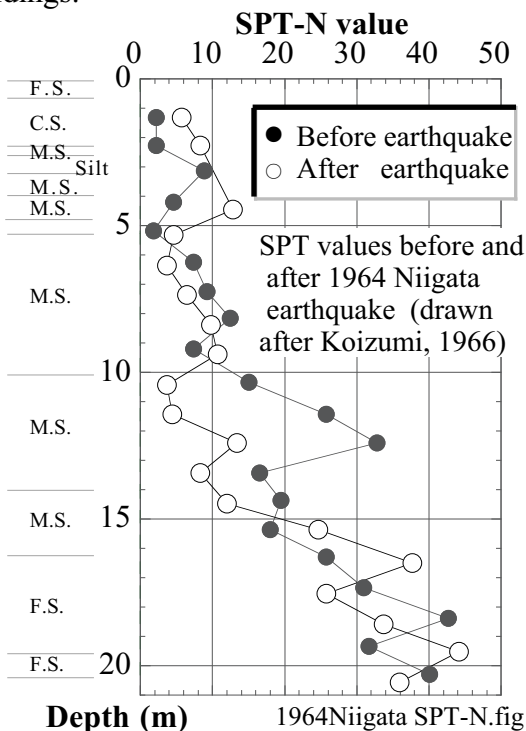
$$(N_1)_{effective} = (N_1)_{observed} + \Delta N$$



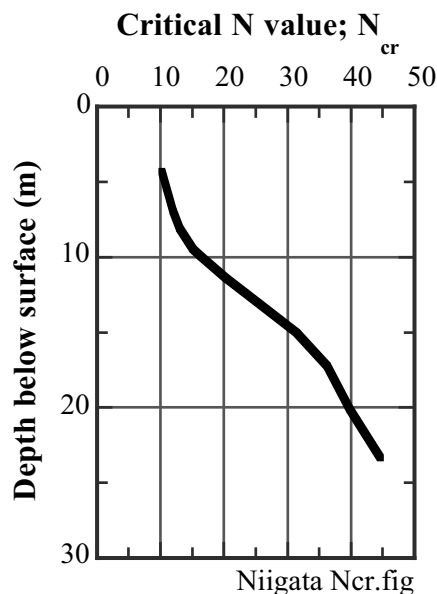
**Fig. 21.3** Minimum SPT- $N$  to resist against liquefaction in different codes

**21.2 SPT-N Observed in Niigata City**

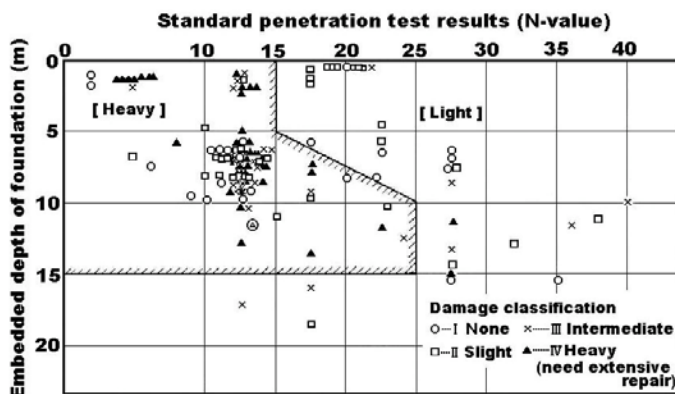
A great number of data were collected in Niigata City after the earthquake in 1964, making it possible to find a relationship between occurrence of liquefaction and SPT profile. Figure 21.4 shows a profile obtained before and after liquefaction. Liquefaction most probably occurred in layers where sand was densified and SPT-*N* value increased after the earthquake. This is due to densification after reconsolidation of liquefied loose sand. In contrast, SPT-*N* sometimes decreases after the quake probably due to dilatancy (volume expansion) of denser sand in consequence of shaking and disturbance. Hence, the boundary of the original *N* values that increased and decreased after the quake shows the largest *N* of liquefied sand. Koizumi (1966) presented this critical *N* as shown in Fig. 21.5. This finding led to a design criteria in Fig. 21.3. Figure 21.6 is a similar diagram on the critical *N* as a boundary of heavy and light damages in buildings.



**Fig. 21.4** SPT profile in Niigata before and after the earthquake (Koizumi 1966)



**Fig. 21.5** Maximum *N* in liquefied layers of Niigata City (Koizumi, 1966)



**Fig. 21.6** Boundary line between light and heavy damage as related to *N* (Kishida, 1966)

### 21.3 Assessment of Liquefaction Potential

The risk of liquefaction of a specified site during a future earthquake has been assessed by one of the three approaches in what follows. Each of them has a different way to evaluate the magnitude of seismic load as well as the resistance of soil against liquefaction.

**Table 21.2** Classification of practical assessments of liquefaction potential

Method	Seismic load	Resistance of soil	Concerned sections
1. Critical SPT- $N$	Out of scope	SPT- $N < 15$ for example is considered to mean high possibility of liquefaction	21.1 and 21.2
2. Factor of safety $F_L = \text{Resistance} / \text{Load}$	Shear stress amplitude = Surface acceleration ( $A_{\max}$ ) $\times$ (Mass of soil)	Obtained from cyclic undrained triaxial tests, or its empirical correlation with SPT- $N$ and fines content	19.3 and 21.4
2'. Modification of 2.	Put in time history of earthquake. Dynamic analysis is run to obtain maximum seismic shear stress  This is called total stress analysis	Ditto	
3. Effective stress analysis	Put in time history of earthquake. Information on nonlinear stress-strain behavior of soil is needed  Dynamic analysis is numerically run on the basis of the effective stress principle	Parameters for negative-dilatancy model (pore water pressure model) are needed; laboratory tests on undisturbed samples	22.3 and 22.4

#### Notes:

- Method 1 was obtained from SPT- $N$  values measured in Niigata city after the quake. Higher  $N$  values in sand mean greater density. This method is therefore meaningful to a certain extent. The problem is that the intensity of earthquake motion is out of scope. Regions of higher and lower seismic activities are treated equally, which is not a rational way. This method is being replaced by others in the recent times.
- The simplified calculation of load in Method 2 avoids dynamic analyses, which require additional soil investigations on  $V_s$  (shear wave velocity),  $G_{\max}$ , and nonlinear stress-strain behavior.
- Recent developments of dynamic analysis technique have allowed the improvement of method from 2 to 2'. This analysis is called *Total Stress Analysis* in which the degradation of soil modulus and shear strength due to development of excess pore water pressure (decrease in effective stress) is not taken into account. In this sense, this analysis is not so sophisticated as effective stress analysis in 3.
- Substantial researches on dilatancy and constitutive models of sand produced the effective stress analysis in 3. Shear stress and strain at every moment of time is combined with the dilatancy model and change of excess pore water pressure as well as effective stress is calculated. The effective stress is then put in the stress-strain model to update the shear modulus and shear strength. This interaction of two models is carried out in every time increment of analysis. It is also possible to perform a seepage/consolidation analysis to obtain more reasonable effective stress. Today, the effective stress analysis is widely used in many important construction projects.

**21.4 Assessment of Liquefaction Potential by SPT-N Before 1995**

The method of critical SPT-*N* value shown in Sects. 21.1 and 21.2 was very simple. It pays attention only to soil condition, and ignores the intensity of seismic load. Hence, this method cannot calculate  $F_L$  value. Most codes today calculate the resistance against liquefaction,  $R$ , by using SPT- $N$  and then compare it with the seismic stress ratio,  $L$ ;  $F_L = R/L$ . An example is taken of Highway Bridge Design Code, which has been influencing many other codes. This section is going to present a previous version of this code because it is easy to understand, is good for education, and will be used in the exercise of this book. A more recent version will be described later in Sects. 21.7 and 21.8.

In the use of SPT- $N$ , attention should be paid to possible errors or variation in practice in “standard” penetration procedure. Seed et al. (1985) mentioned the problems of insufficient impact energy, length of rod, and type of sampler (Sect. 1.12). Poor maintenance of the tip makes penetration more difficult. Noteworthy is that all these problems tend to increase the measured  $N$  value and consequently overestimate the soil strength.

In the Highway Bridge Design Code, liquefaction potential has to be examined when the ground water table is within 20 m from the surface and the mean grain size,  $D_{50}$ , is between 0.02 mm and 2.0 mm. No examination is required at depth more than 20 m, because soil at that depth is considered to be pleistocene or older, which is unlikely to liquefy.

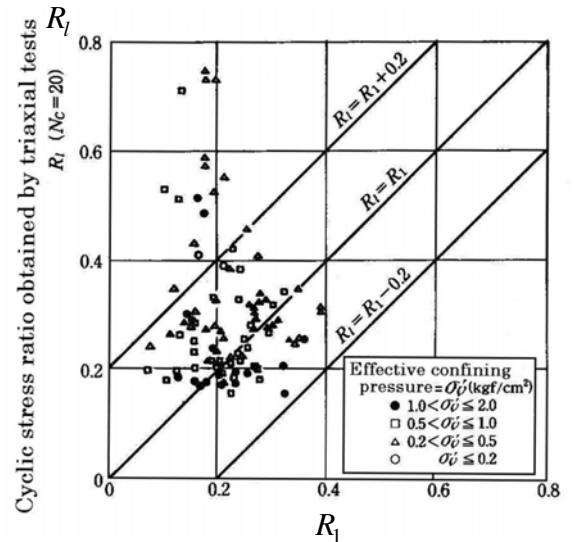
It is recently recognized that such cohesionless fine materials as mine tailings 鉱滓 can liquefy (Sect. 20.5). Liquefaction of gravelly materials was discussed in Sect. 20.2 as well. Some extent of rise in excess pore water pressure at depth more than 20 m was reported in Port Island of Kobe, 1995. Hence, details of the code are subjected to change.

The resistance,  $R$ , consists of three components

$$R = R_1 + R_2 + R_3,$$

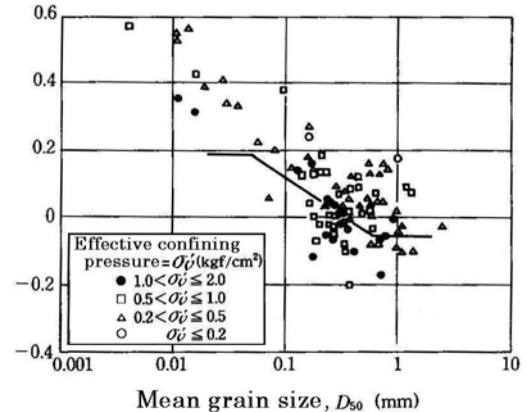
in which  $R_1$  stands for the effects of density (Fig. 21.7)

$$R_1 = 0.0042 \times (\text{assessed relative density, \%}) \\ = 0.0042 \times 21 \sqrt{\frac{N}{\sigma'_v \text{ (kgf/cm}^2\text{)} + 0.7}}.$$



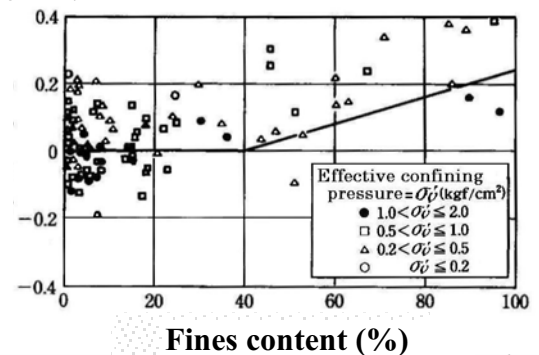
**Fig. 21.7** Cyclic stress ratio obtained by triaxial tests and assessed relative density (Former version of Highway Bridge Design Code)

$$R_2 = R_l - R_1$$



**Fig. 21.8** Correction of stress ratio by means of mean grain size (Former version of Highway Bridge Design Code)

$$R_3 = R_l - R_1 - R_2$$



**Fig. 21.9** Correction of stress ratio by means of fines content (Former version of Highway Bridge Design Code)

See (21.1). Since  $R_1$  above cannot precisely give the experimentally measured liquefaction resistance,  $R_f$ , a correction was made by using the mean grain size,  $D_{50}$ . When the grain size is small, soil is supposed to be clayey and has an increased resistance against liquefaction (Sect. 20.4). In calculation,  $N$  of clayey soil tends to be smaller and  $R_1$  may underestimate the resistance. Thus, the average curve in Fig. 21.8 was proposed for correction

$$\begin{aligned} R_2 &= 0.19 && \text{when } 0.02 \text{ mm} \leq D_{50} \leq 0.05 \text{ mm} \\ R_2 &= 0.225 \log_{10}(0.35/D_{50}) && \text{when } 0.05 \text{ mm} \leq D_{50} \leq 0.6 \text{ mm} \\ R_2 &= -0.05 && \text{when } 0.6 \text{ mm} \leq D_{50} \leq 2.0 \text{ mm.} \end{aligned}$$

Since  $R_2$  correction was found insufficient, a further correction has been made by  $R_3$ , which is based on fines content ( $F_c$ : silt and clay, finer than  $75 \mu$ ) (see Fig. 21.4);

$$R_3 = 0.0 \text{ when } 0\% \leq F_c \leq 40\%, \text{ and } R_3 = 0.004 F_c - 0.16 \text{ when } 40\% \leq F_c \leq 100\%.$$

In this code,  $r_d = 1 - 0.015 \times \text{depth (in meter)}$  is used for calculation of load ( $L$ ) (Sect. 19.2). Consequently, the safety factor (resistance against liquefaction) is determined by

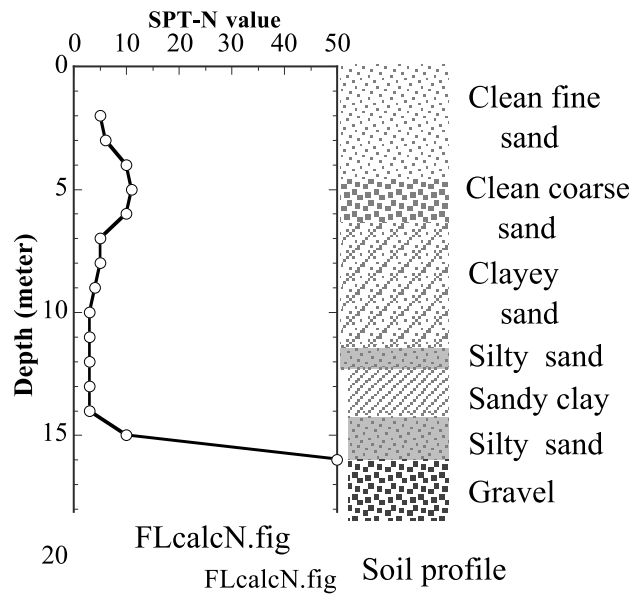
$$F_L = R/L.$$

**21.5 Exercise No. 6: Calculation of Factor of Safety Against Liquefaction**

This exercise employs the 1990 version of Highway Bridge Design Code. By learning this version, it becomes easy to understand the significance of its modification in 1995. Use  $r_d = 1 - 0.015z$ .

See Sect. 21.4 and calculate  $F_L$  by using the data as shown in the figure on the right and the table below:

- Depth of ground water table = 1.2 m
- Unit weight of soil above water table = 1.4 tf/m<sup>3</sup>
- Unit weight of soil below water table = 1.9 tf/m<sup>3</sup>
- Design  $A_{max}$  at the surface = 0.15 G



Depth (m)	SPT-N	Fines content $F_c$ (%)	$D_{50}$ (mm)	Type of soil
2	5	0.0	0.2	Clean fine sand
3	6	0.0	0.2	Ditto
4	10	0.0	0.3	Ditto
5	11	0.0	0.7	Clean coarse sand
6	10	0.0	0.7	Ditto
7	5	5.0	0.25	Clayey sand
8	5	5.0	0.25	Ditto
9	4	7.0	0.15	Ditto
10	3	10.0	0.15	Ditto
11	3	15.0	0.15	Ditto
12	3	41.0	0.06	Silty sand
13	3	80.0	0.02	Sandy clay
14	3	80.0	0.02	Ditto
15	10	5.0	0.4	Silty sand
16	50	1.0	2.0	Gravel

Remarks on ground water table: Evidently, the assessment of liquefaction risk is made of soils below the ground water table. The depth of ground water affects the effective stress in the subsoil. Thus, it is essentially important to determine precisely the elevation of ground water table, and many boring log (record) describes this information obtained from the water level in a bore hole. The problem is the uncertainty of the water table due to many reasons. For example, seasonal change is difficult to assess. Water leakage from a bore hole into gravelly layer may be significant. In an urban area, deep excavation of building foundation is often associated with pumping of ground water and lowering of the local water table. Hence, the judgment of water level should take into account the regional geological environment.

## 📁 21.6 Issue for Future Development of Code

The existing code is never considered to be good enough. Experiences obtained in real earthquakes have been continuously demanding its revision and correction. The major issues of modification in recent times are as follows:

### 1. Dense sand

When SPT- $N$  is large in dense sand, the true liquefaction resistance increases drastically (Fig. 20.4), whereas many existing codes assume a simple proportionality between resistance and relative density. The resistance is underestimated.

### 2. Equivalent number of loading cycles

Also, the equivalent number of cycles, equivalent to an irregular stress history, is assumed to be 20. Since the resistance is substantially larger at smaller number of loading cycles (Fig. 19.5), the resistance is underestimated when the number of cycles is small. In contrast, earthquakes of magnitude greater than 8 consist of a greater number of cycles.

### 3. Pleistocene soil

Being more than 10,000 years old, pleistocene sands have a high rigidity, a large SPT- $N$  value, and consequently a sufficient resistance against liquefaction. Hence, its liquefaction has been considered unlikely. The 1995 Hyogoken Nambu earthquake, however, induced some extent of excess pore water pressure in a pleistocene layer at the bottom of Port Island. Hence, it was learned that an earthquake with a short distance from the source may induce heavy shaking and pore pressure increase even in a relatively stable pleistocene soil.

### 4. Sand with fines

Nonplastic fine soil is prone to liquefaction. When a loose fabric structure of coarser sand grains is associated with loose nonplastic fine powder, the potential of liquefaction is high. Since existing design codes pay less attention to nature of fines, whether plastic or nonplastic, the assessment of liquefaction potential is incomplete.

### 5. Design $A_{\max}$ at surface

$A_{\max}$  is the surface acceleration specified for design and had been conventionally assumed to be around 15% of gravity acceleration. Since  $A_{\max}$  of as large as 340 Gal was recorded, however, at the ground surface of liquefied site in Port Island (Fig. 17.48),  $A_{\max}$  was increased in codes and may be reviewed again in future. It should be taken into account that the number of cycles in the Port Island shaking was small (Figs. 17.47 and 17.48).

### 6. Use of numerical tools in determining the field stress ratio

It is evident that the rigid-column evaluation of stress ratio caused by an earthquake (19.1) is nothing but a rough approximation, although it is easy to use. A use of such analytical and numerical methods as an equivalent linear analysis and finite element procedures are being considered.

### 7. Subsoil investigation which is more reliable than SPT- $N$

Although being popular and of a large background database, SPT is relatively approximate and is a time consuming tool. Also, SPT is not reliable in gravelly subsoil. A possible use of cone penetration and shear wave measurement has been studied. Both these methods are quick and economical, not requiring drilling of a bore hole. The use of these method that do not collect soil specimen, however, seems difficult, unless it is combined with other methods, because loose liquefiable sand and medium-stiff unliquefiable clay can exhibit a similar value of  $V_s$  (Sect. 22.5). Many CPT of  $V_s$  correlation with liquefaction relies on conversion to SPT- $N$  except the one by Shibata and Teparaksa (1988, Fig. 21.21).

**21.7 Revised Design Prediction of Liquefaction After 1995: Part 1, Design Load**

The lesson learned from liquefaction events during the 1995 Kobe earthquake was that liquefaction can be still fatal when the epicentral distance is very short (Sect. 5.10), the number of cycles is small, but the intensity of acceleration is substantial. After this earthquake, many design codes were revised and will be revised further in the near future. The revised code is described below by taking an example of the Highway Bridge Design Code.

**1. Design earthquakes**

Two kinds of design earthquakes are proposed; type I is the one that occurs in the tectonic subduction zone (Sect. 3.2) and has a greater earthquake magnitude; e.g., >7.5. With a longer duration time, the number of loading cycles is larger. In contrast, type II occurs inside a tectonic plate. Although its seismic magnitude is smaller and the duration time is shorter than those of type I, the short epicentral distance leads to a greater acceleration in an area of a limited size.

**2. Soil conditions susceptible to liquefaction**

Risk of liquefaction has to be studied for alluvial water-saturated sand when

- The sand lies within 20 m from the surface while the ground water table lies within 20 m from the surface,
- The fines content (<75  $\mu$ , silt and clay) is less than 35% or the plasticity index,  $I_p$ , is less than 15% (cohesion is small), and
- The mean grain size,  $D_{50}$ , is smaller than 10 mm while  $D_{10} < 1$  mm (excluding gravel, although gravelly sand is included).

**3. Judgement of liquefaction potential**

The possibility of liquefaction is judged by using a kind of factor of safety;  $F_L = R/L$ , in which  $R$  and  $L$  stand for resistance and load, respectively.

**4. Load**

A formula of  $L = (1 - 0.015z)(\sigma_v/\sigma'_v)(c_z k_{hc0})$  gives the loaded stress ratio (Fig. 19.3). The depth from the surface (meter) is designated by  $z$ , while  $\sigma_v$  and  $\sigma'_v$  denote the total and effective vertical stresses. Moreover,  $c_z k_{hc0}$  is the seismic coefficient for design as determined below

- (a) Classify the surface soil layer by using the natural period,  $T_G$

$$T_G = 4 \sum_{\text{layers}} \frac{\text{Layer thickness}}{V_s} \quad (21.4)$$

This calculation is made of shallow clayey layers with SPT- $N < 25$ , sandy layers of  $N < 50$ , or  $V_s < 300$  m/s. If in-situ  $V_s$  is not available, use formula in Sect. 8.4. For classification, see Table 21.3. Note that (21.4) is nothing more than an approximate calculation of the natural period.

- (b) The standard seismic coefficient,  $k_{hc0}$ , is determined according to the subsoil classification and the type of design earthquake (Table 21.4).

The values in Table 21.4 is much greater than the conventional value of 0.15. The “ $c_z$ ” parameter takes account of the regional seismic activity and ranges from 0.7 to 1.0. For example,  $c_z = 1$  in Tokyo and Kanto area together with Osaka. Only Okinawa has the lowest value of  $c_z = 0.7$ .

**Table 21.3** Classification of subsoil

Class I	$T_G < 0.2$ s	Hard
Class II	$0.2 \leq T_G < 0.6$	
Class III	$0.6 \leq T_G$	Soft

**Table 21.4** Standard seismic coefficient

Subsoil class	Design earthquake	
	Type I	Type II
I	0.30	0.80
II	0.35	0.70
III	0.40	0.60



## 21.8 Revised Design Prediction of Liquefaction After 1995: Part 2, Resistance Against Liquefaction

### 5. Resistance against liquefaction, $R$

The resistance stress ratio,  $R$ , is calculated as

$$R = C_w R_L, \quad (21.5)$$

in which  $R_L$  is the resistance as would be observed in cyclic undrained triaxial tests and  $C_w$  represents the effects of type of loading.

Although the triaxial resistance,  $R_L$ , should be determined by running laboratory tests on undisturbed good-quality specimens, this practice requires time-consuming and costly procedures. In most situations, therefore,  $R_L$  is determined by using SPT- $N$ .

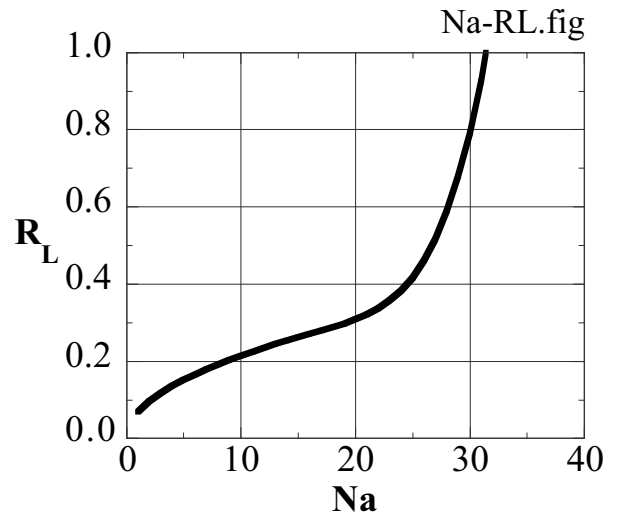


Fig. 21.10 Variation of design resistance of soil against liquefaction with SPT- $N$

(a) Adjusted  $N$  value,  $N_a$

$$N_a = c_1 \times \left( \frac{1.7N}{\sigma'_v + 0.7} \right) + c_2 \quad \text{for sand} \quad \text{and}$$

$$N_a = \left\{ 1 - 0.36 \log_{10} \left( \frac{D_{50}}{2} \right) \right\} N_1 \quad \text{for gravelly soil} \quad (21.6)$$

where

$$c_1 = \begin{cases} 1 & (0\% \leq F_c < 10\%) \\ (F_c + 40)/50 & (10\% \leq F_c < 60\%) \\ (F_c/20) - 1 & (60\% \leq F_c) \end{cases} \quad \text{and} \quad c_2 = \begin{cases} 0 & (0\% \leq F_c < 10\%) \\ (F_c - 10)/18 & (10\% \leq F_c) \end{cases},$$

where  $F_c$  stands for the fines content (finer than  $75 \mu$ ). Note that  $N_1 = \frac{1.7N}{\sigma'_v + 0.7}$  removes the influence of the effective vertical stress level,  $\sigma'_v$  ( $\text{kg}/\text{cm}^2$ ), from SPT- $N$  value and gives the penetration resistance under  $\sigma'_v = 1 \text{ kgf}/\text{cm}^2$  ( $=98 \text{ kN}/\text{m}^2$ ). Since  $c_1 = 1$  and  $c_2 = 0$  for  $F_c = 0\%$  (clean sand),  $N_a$  is understood to be the SPT- $N$  value for clear sand without fines.

(b) Determination of  $R_L$

Two formulae are used in accordance with the quality and density of soil

$$R_L = \begin{cases} 0.0882 \sqrt{N_a/1.7} & (N_a < 14) \\ 0.882 \sqrt{N_a/1.7} + 1.6 \times 10^{-6} (N_a - 14)^{4.5} & (14 \leq N_a) \end{cases} \quad (21.7)$$

The second formula above comes from the fact that dense sand of greater  $N$  has a liquefaction resistance dramatically greater than that of loose sand (Fig. 20.4). Figure 21.10 illustrates the variation of  $R_L$  with the increase in  $N_a$ . Note that this  $R_L$  is supposed implicitly to be the liquefaction resistance under 15–20 cycles of loading.

(c) Effects of type of loading

Conventionally, the irregular time history of earthquake loading has been converted to 20 uniform cycles of an equivalent amplitude by supposing a greater magnitude or type I earthquake. When the type II with

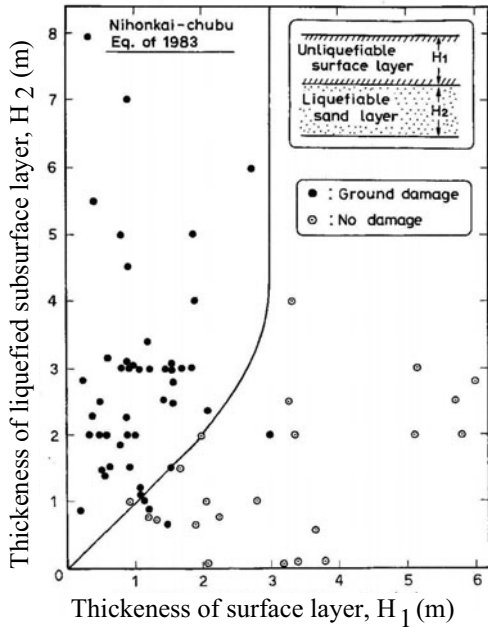
less number of cycles has to be taken into account from now on, the soil resistance against a smaller number of cycles should be employed. This goal is achieved by increasing the conventional strength by a factor of  $C_w$ . See that liquefaction resistance for less number of cycles is greater, in particular for dense sand (Fig. 20.2).

$$\text{For type I, } C_w = 1.0 \quad \text{and} \quad \text{for type II, } C_w = \begin{cases} 1.0 & (R_L \leq 0.1) \\ 3.3R_L + 0.67 & (0.1 < R_L \leq 0.4) \\ 2.0 & (0.4 < R_L) \end{cases} \quad (21.8)$$

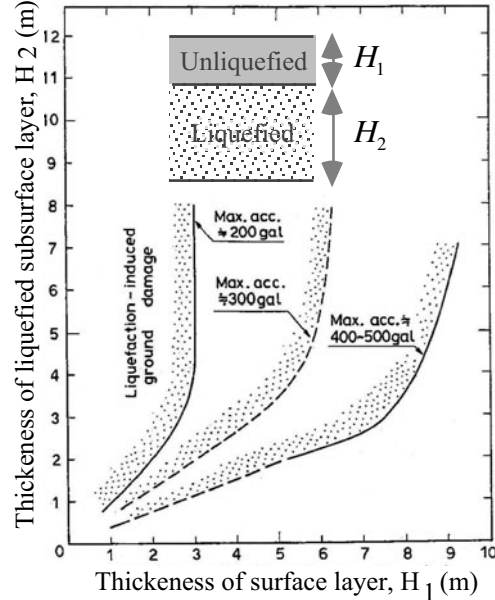
Note that dense sand with greater  $R_L$  receives a larger value of  $C_w$ . It seems interesting that this new version of code does not use the mean grain size ( $D_{50}$  of fine soil) any more.

**21.9 Factor of Safety Against Liquefaction and its Correlation With Extent of Damage**

When the factor of safety against liquefaction,  $F_L$ , is less than 1.0, the concerned soil layer is considered to liquefy under the design earthquake condition. It is noteworthy, however, that this small  $F_L$  value in a limited soil layer does not mean the overall liquefaction-induced disaster at the surface.



**Fig. 21.11** Empirical relationship between thickness of liquefied and unliquefied layers with and without surface damage (Ishihara, 1985)



**Fig. 21.12** Effects of thickness of unliquefied surfacelayer on mitigation of liquefaction-induced damage (Ishihara, 1985)

Figure 21.11 is a summary of damage report during the 1983 Nihonkai-Chubu earthquake in which liquefaction did or did not cause damage at the surface of a level ground (boiling of sand, surface cracks, floating of embedded objects, etc.); slope failure or subsidence of buildings are out of scope. When the thickness of surface unliquefied layer ( $H_1$ ) was relatively thick when compared with the thickness of liquefied subsoil ( $H_2$ ), no damage is likely at the surface. Similar studies on other earthquakes resulted in Fig. 21.12 in which curves for a family of surface acceleration are drawn.

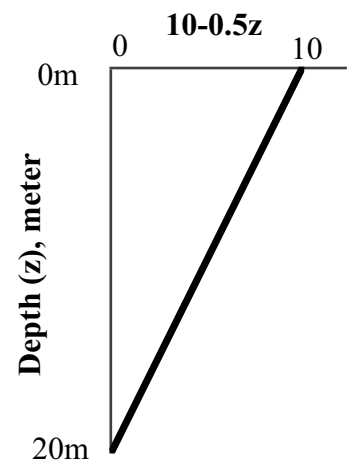
Generally speaking, the extent of damage is more substantial when

- $F_L$  is smaller
- The thickness of layer with  $F_L < 1$  is greater
- $F_L < 1$  occurs at shallower elevation

These viewpoints are assembled to a single parameter of  $P_L$  (Tatsuoka et al. 1980):

$$P_L = \int_0^{20} F(F_L)(10 - 0.5z) dz$$

where “z” is the depth in meter, while  $F(F_L) = 1 - F_L$  if  $F_L \leq 1.0$  and  $F(F_L) = 0$  if  $F_L > 1.0$ . Note that the function of depth,  $10 - 0.5z$ , puts more weights on liquefaction at shallower depth, see Fig. 21.13.



**Fig. 21.13** Variation of weight function with depth

Generally, the greater value of  $P_L$  occurs when  $F_L$  is less than 1.0 at shallow depth over a greater thickness of soil. It is suggested that  $P_L > 5$  corresponds to a limited extent of damage, while  $P_L > 15$  means a possibility of substantial damage.

There are more correlations between  $F_L$  and development of excess pore water pressure (Fig. 23.4) or post-liquefaction subsidence (Fig. 25.22).

## 21.10 Effects of Frequency on Liquefaction Resistance

Cyclic shear tests on liquefaction resistance of sand are conducted by using either a hydraulic actuator or a pneumatic loader. Although the former can generate cyclic force of higher frequency, which is comparable with a real earthquake loading, its installation is more expensive. The latter employs air pressure and is less expensive, but it is operated at frequency of not more than 0.1 Hz (there is a remarkable development recently to mitigate this technical limitation). Hence, it is frequently asked whether or not this low frequency affects the measured liquefaction resistance of sand.

A pneumatic system may work at a higher frequency as long as the strain of a tested specimen is small. This is because the motion of a loading ram is small and the volume of moving air is small (Fig. 21.14). When the specimen's deformation is large near the onset of liquefaction, a substantial volume of air has to flow through a tube into a cylinder within a limited time. This is difficult because of viscosity of air and other resistance against air flow.

Figure 21.15 shows the resistance of sand against liquefaction, which was measured by a ring shear apparatus (Yoshimi and Oh-oka, 1975) and cyclic triaxial tests (Wong et al. 1975). In both tests, liquefaction was defined as the first occurrence of 100% rise of excess pore water pressure (initial liquefaction). Despite the range of employed frequency, the difference in the measured liquefaction resistance is negligible. Yasuda and Soga (1984) conducted similar tests, defining liquefaction as the double amplitude of axial strain (peak-to-peak strain) exceeding 5%. Figure 21.16 again shows that loading frequency is not important.

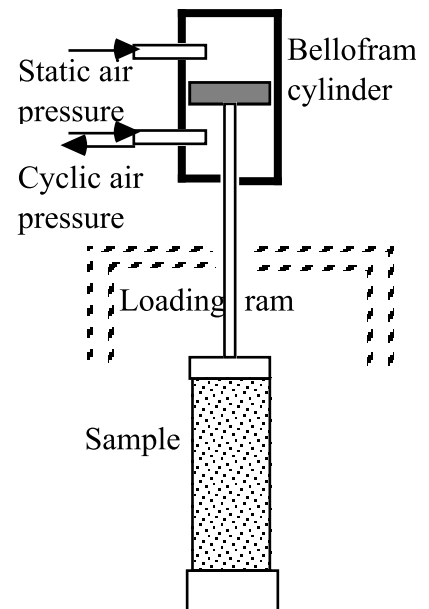


Fig. 21.14 Pneumatic loading system

The vertical coordinate in Fig. 21.15 stands for stress ratio of  $\tau_{\max}/\sigma'_{vc}$  in case of ring shear tests (similar to simple shear in mechanism) and  $\sigma_{dl}/(2\sigma'_c)$  for triaxial tests. The anisotropic stress state ( $K_0$  state) in the former test leads to the reduced stress ratio of  $(1+2K_0)/3$  times the latter tests (see  $C_1$  parameter in Sect. 19.4). The discussion in this section concerns sand behavior prior to liquefaction when effective stress does not yet diminish. Hence, there is no rate-dependent (viscous) behavior. In contrast, Sect. 25.17 will discuss post liquefaction behavior in which effective stress has disappeared and rate-dependent behavior becomes more significant.

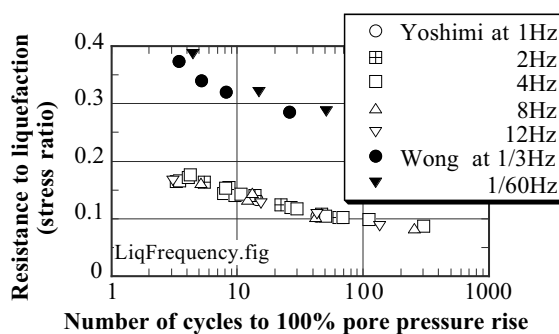


Fig. 21.15 Effects of loading frequency on liquefaction resistance curve of sand (data by Yoshimi and Oh-oka, 1975, and Wong et al. 1975)

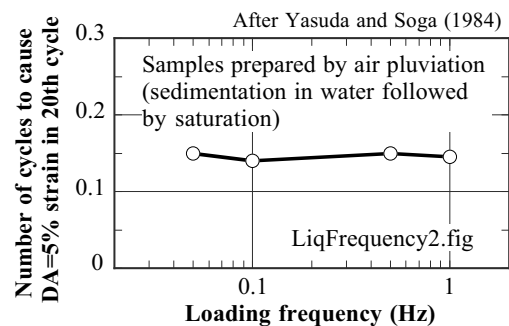
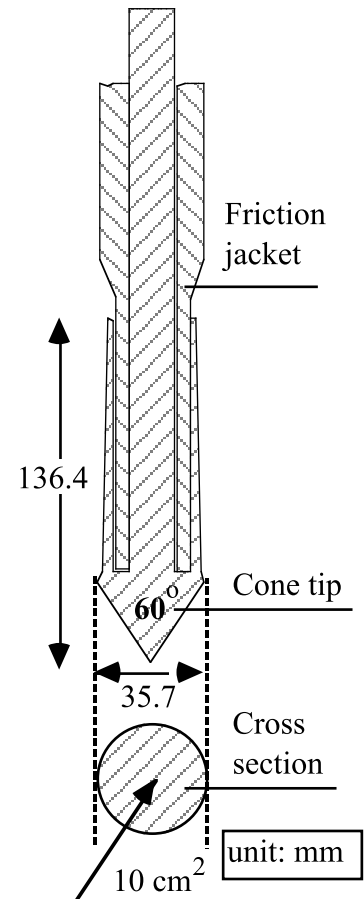


Fig. 21.16 Effects of loading frequency on stress ratio at 20 cycles (Yasuda and Soga, 1984)

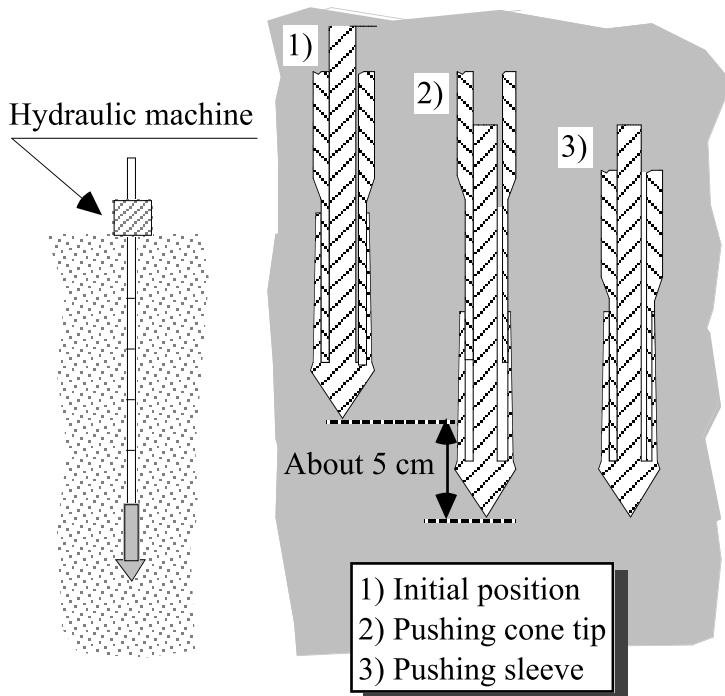
**21.11 Use of Cone Penetration Tests for Earthquake Geotechnical Survey**

Cone penetration test (CPT) is a popular in-situ investigation in which an equipment as in Fig. 21.17 is pushed by a hydraulic mechanism into subsoil at a specified velocity (for example, 1 cm/s); see conceptual Fig. 21.18. This device consists mainly of two parts, which are the cone tip where the tip resistance,  $q_c$ , is measured upon penetration and the friction jacket (Begemann, 1953) where skin friction,  $f_s$ , is recorded independent of the tip resistance. The order of penetration of these two parts is illustrated in Fig. 21.19. Firstly, the cone tip is pushed to measure the tip resistance, and then the friction jacket goes down to record the skin friction.

A portable cone penetrometer (Fig. 21.20) is a useful tool for field investigation as well. Its penetration capacity is, however, limited by human power and hence is applicable only to soft clay or similar soil. Its penetration in sandy ground is difficult.



**Fig. 21.17** CPT equipment



**Fig. 21.18** Penetration of CPT device into subsoil

**Fig. 21.19** Detailed procedure of CPT penetration



**Fig. 21.20** Portable cone penetrometer for soft clay (photo by S. Nishimura)

CPT has been used widely to assess the rigidity of soil, bearing capacity of foundation, and other subsoil properties by using their empirical correlations with cone tip resistance.

CPT has such advantages as

1. No need for drilling a bore hole
2. Being therefore economical and time-efficient
3. Data being less subject to personal difference

To make use of these advantages, there are recent technical developments such as

- Electric cone that records pore water pressure during penetration
- Seismic cone which measures S-wave propagation time and determines  $V_s$  (Campanella and Davies, 1994).

One shortcoming of CPT may be that no soil sample is collected, whether disturbed or undisturbed. Therefore, it is not easy to determine the type of soil, particle size, and plasticity. Although SPT-*N* value (standard penetration tests; Sects. 1.12, 8.4, 21.1) has the same problem, SPT allows eye inspection of collected disturbed samples (Fig. 1.37), while CPT does not. SPT further allows tests on physical properties such as gradation and plasticity index.

Attempts have been made to overcome this problem of CPT by developing empirical correlation between soil type and the ratio between skin friction,  $f_s$ , and tip resistance,  $q_c$ . For example, Begemann (1965) proposed a design chart in which a combination of cone tip resistance and the ratio of friction to tip resistance is employed for soil classification. For the same purpose, Robertson (1990) proposed to use the normalized cone tip resistance,  $(q_c - \sigma_{vo})/\sigma'_{vo}$  and friction,  $f_s/(q_c - \sigma_{vo})$ , where  $\sigma_{vo}$  and  $\sigma'_{vo}$  stand for the total and effective vertical stress at respective depth. In their idea, greater (normalized) tip resistance and lower (normalized) friction means sand and gravel, and in contrast, lower tip resistance and higher friction come from clayey soils.

Shibata and Teparaksa (1988) collected information on CPT tip resistance,  $q_c$ , from sites with and without liquefaction. Since the tip resistance is affected by the in-situ effective vertical stress ( $\sigma'_{vo}$ ), it was corrected by

$$q_{c1} = \left( \frac{0.17}{\sigma'_{vo} + 0.07} \right) q_c, \quad (21.9)$$

in which the unit of stress is MPa. Thus, the normalized cone resistance,  $q_{c1}$ , at the effective stress of 0.1 MPa (1 kgf/cm<sup>2</sup>) was obtained. Since fine grains in soil affect the cone resistance and liquefaction resistance of soil, the normalized cone resistance was further modified by introducing a factor of  $C_2$

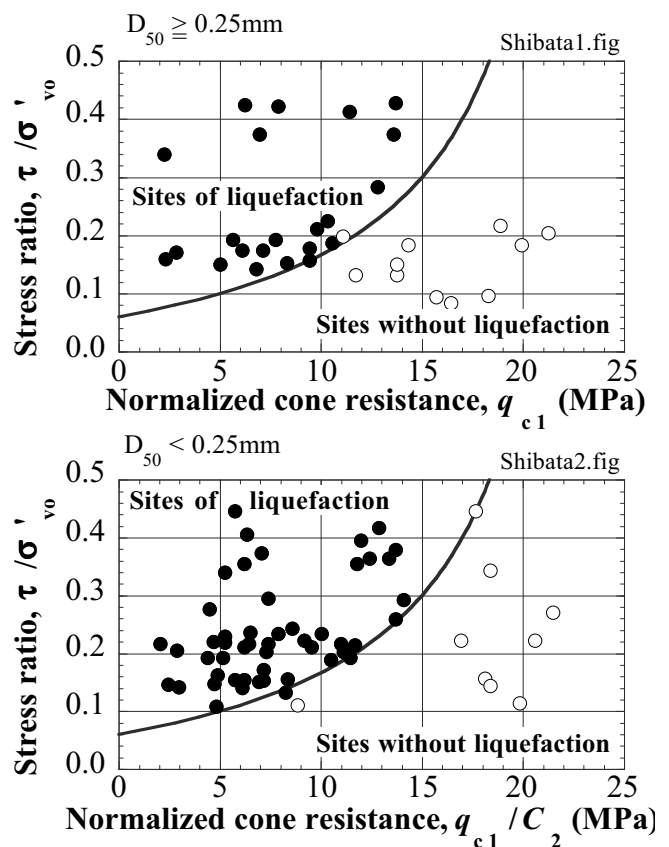
$C_2 = 1$  when the mean grain size ( $D_{50}$ , mm) is greater than 0.25 mm

$C_2 = D_{50}/0.25$  when  $D_{50} < 0.25$  mm.

Thus, the liquefaction potential was judged by using  $q_{c1}/C_2$ .

Figure 21.21 compares this new cone tip parameter and the field stress ratio,  $\tau/\sigma'_{vo}$ , which was assessed by using recorded motion during earthquakes. It is shown therein that there is a clear boundary between cases with and without liquefaction. Shibata and Teparaksa (1988) expressed this boundary curve by

$$\frac{q_{c1}}{C_2} = 5 + 20 \left( \frac{\frac{\tau}{\sigma'_{vo}} - 0.1}{\frac{\tau}{\sigma'_{vo}} + 0.1} \right). \quad (21.10)$$



**Fig. 21.21** Relationship between normalized cone tip resistance and stress ratio during earthquakes (after Shibata and Teparaksa, 1988)

Note that the more recent knowledge of fines content states that cohesive fines increases the liquefaction resistance of soils (Sect. 20.4), while cohesionless (non-plastic) fines does not (Sect. 20.5).

Robertson (1990) further proposed to classify soil type by using pore water pressure, which is measured beside the cone tip; generally, higher pore pressure implies finer soils.

Since CPT investigation is quick and economical, it is meaningful to apply this technology to detailed field investigation on liquefaction potential. "Detailed" means that the number of tests per unit area is so large that complicated geographical and geological conditions are accurately understood. In this respect, Robertson and Wride (1998) proposed to determine liquefaction resistance based on cone resistance. Note, however, that their data was based on conversion from SPT-*N* to CPT, which relied on many empirical knowledge of correlation.

Robertson et al. (1983) collected data of  $q_c / N$  from many literatures. Since this ratio had a wide range of variation, they further studied the correlation between  $q_c / N$  and the grain size. Figure 21.22 reveals a reasonable correlation which made it possible to convert the existing SPT-*N* correlation to a CPT correlation.

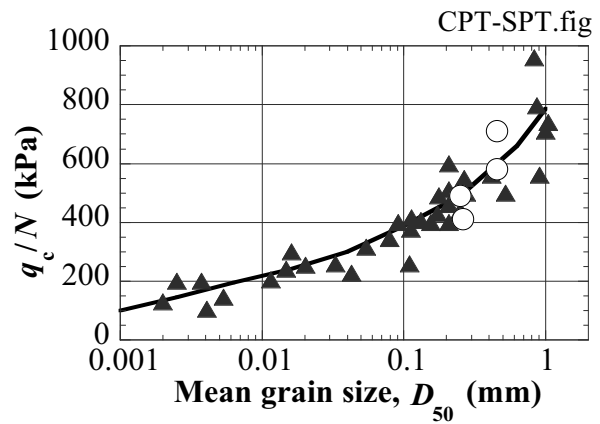
Noteworthy is that the cone tip resistance,  $q_c$ , is normalized in terms of the effective vertical stress,  $\sigma'_{vo}$ . This implies that the measured  $q_c$  leads to an overestimation of the sand density due to increased shear resistance under higher effective stress. The normalized cone resistance,  $q_{CIN}$ , is given by

$$q_{CIN} = \left( \frac{q_c}{P_a} \right) \left( \frac{P_a}{\sigma'_{vo}} \right)^n, \quad (21.11)$$

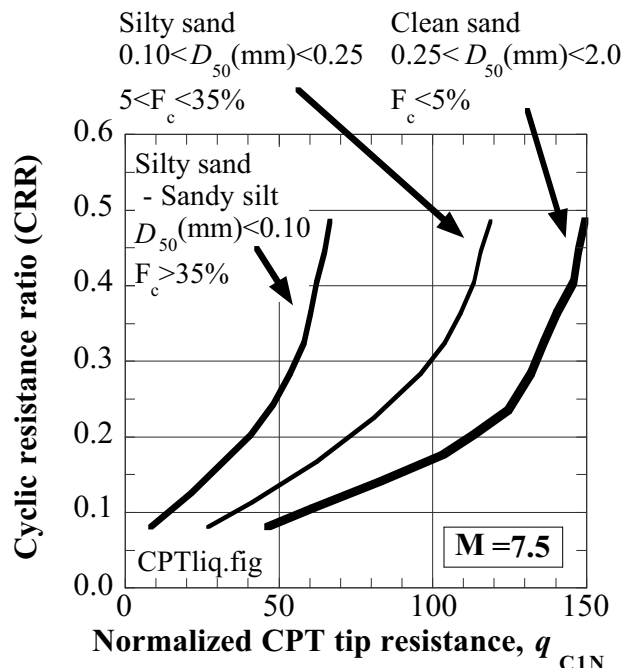
in which  $P_a$  designates the atmospheric pressure (= 98 kPa) and  $n = 0.5$  typically.

There are many data of SPT-*N* at sites with and without liquefaction (Fig. 21.2). Those SPT data were converted to CPT as mentioned above and the curves in Fig. 21.23 was obtained. In this diagram, liquefaction resistance or stress ratio CRR for soils of different fines content ( $F_c$ ) are illustrated as functions of the normalized cone resistance.

It should be noted that CPT cannot directly identify the soil type or fines content ( $F_c$ ) in Fig. 21.21. Soil types have to be identified separately. The fines in this figure seems to mean cohesive fine soils and therefore the cohesionless fine soil (for example, highly liquefiable tailing material in Sect. 20.5) is out of scope.



**Fig. 21.22** Empirical correlation between CPT/SPT ratio and mean grain size (drawn after Robertson et al., 1983)



**Fig. 21.23** Resistance of soil against liquefaction as assessed from cone penetration resistance (after Robertson and Wride, 1998)



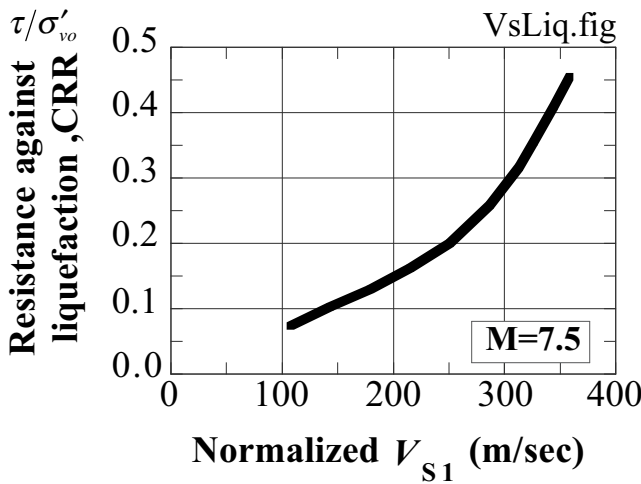
**21.12 Use of S-Wave Velocity for Liquefaction Investigation**

Denser sand has greater resistance against liquefaction. Denser sand has greater shear modulus,  $G_{max}$ , and S wave velocity,  $V_s = \sqrt{G_{max}/\rho}$ . Therefore, it is expected that  $V_s$  is a good index of liquefaction resistance of in-situ soils. This idea becomes more attractive because  $V_s$  can be economically measured by a seismic cone (Campanella and Davis, 1994) or surface wave monitoring (SASW in Sect. 8.11). Studies in this direction were conducted by Stokoe and Nazarian (1985) as well as Andrus and Stokoe (1996, 2000).

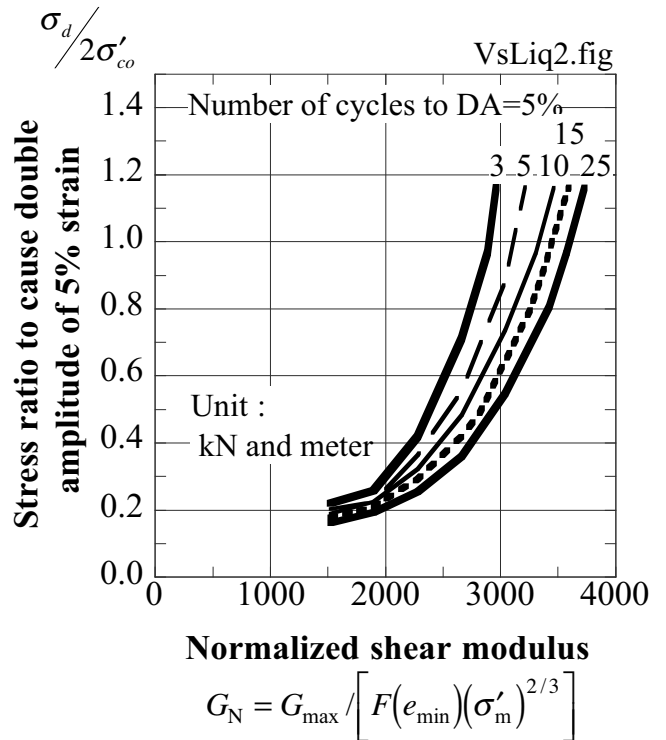
Robertson et al. (1992) collected  $V_s$  values from cases of several earthquakes. The boundary of liquefied and unliquefied sites results in Fig. 21.24. In this figure, the measured  $V_s$  value was corrected for the effect of overburden pressure by

$$V_{S1} = V_s \left( \frac{P_a}{\sigma'_{vo}} \right)^{0.25}, \quad (21.12)$$

where  $P_a$  stands for the atmospheric pressure.



**Fig. 21.24** Correlation between liquefaction resistance and S wave velocity (after Robertson et al., 1992)



**Fig. 21.25** Experimental relationship between normalized shear modulus and resistance against liquefaction (after Tokimatsu and Uchida, 1990)

Tokimatsu and Uchida (1990) demonstrated the use of  $V_s$  as what follows.

1. S wave velocity,  $V_s$ , is converted to shear modulus at small strain amplitude,  $G_{max} = \rho V_s^2$ .
2.  $G_{max}$  is normalized in terms of mean effective stress,  $\sigma'_m$ , and the minimum void ratio,  $e_{min}$

$$G_N = G_{max} / [F(e_{min})(\sigma'_m)^n], \quad (21.13)$$

where  $n$  is between 1/3 and 2/3, and the  $F$  function is defined by

$$F(e_{min}) = \frac{(2.17 - e_{min})^2}{1 + e_{min}}. \quad (21.14)$$

The mean effective stress is determined by using the effective vertical stress,  $\sigma'_{vo}$ , and an assessed value of earth pressure coefficient at rest ( $K_0$ )

$$\sigma'_m = \frac{1+2K_0}{3} \sigma'_{vo}. \quad (21.15)$$

3. Figure 21.25 illustrates a summary of experimental relationships between  $G_N$  and stress ratio (resistance to liquefaction), which is needed to trigger liquefaction after a variety of number of cycles. The number of cycles in design earthquakes can be determined by using Table 19.1. The minimum void ratio is evaluated without collecting soil samples ( $V_s$  survey) by using a Sakai-Yasuda (1977) empirical diagram (Fig. 21.26).

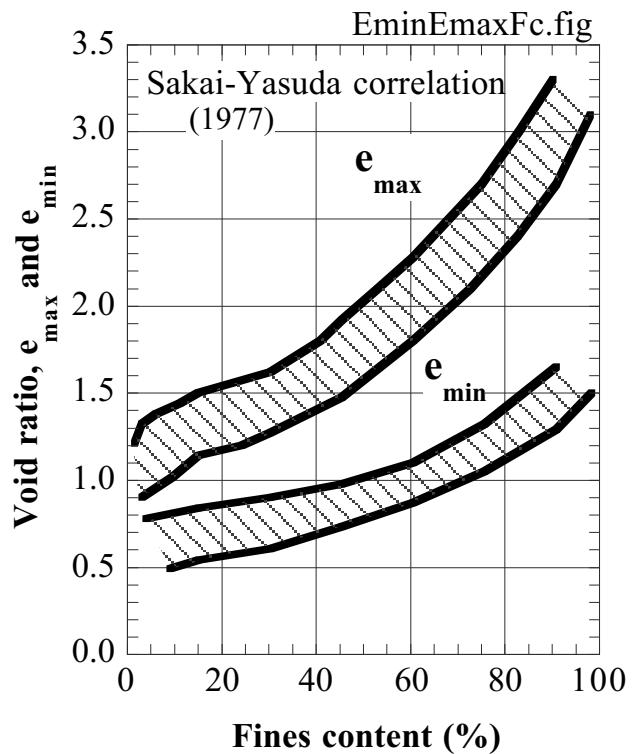
4. The field resistance against liquefaction is determined by

$$\frac{\tau}{\sigma'_{vo}} = \frac{1+2K_0}{3} \frac{\sigma_d}{2\sigma'_{co}}. \quad (21.16)$$

Noteworthy is that field investigation of  $V_s$  cannot identify directly the type of soil. Liquefiable sand and unliquefiable clay may have the same  $V_s$  but they cannot be discriminated without collecting soil samples. In this situation, it is advisable to combine  $V_s$  survey with other kind of soil investigation that can identify types of soil. For example, SPT soil profiles are interpolated by more economical  $V_s$  investigations (Sect. 22.5).

### List of References in Chapter 21

- Andrus, R.D. and Stokoe, II., K.H. (1996) Preliminary guidelines for liquefaction assessment using shear wave velocity, UJNR 28th Joint Meeting of United States-Japan Panel on Wind and Seismic Effects, Gaithersburg, Maryland:
- Andrus, R.D. and Stokoe II, K.H. (2000) Liquefaction resistance of soils from shear-wave velocity, Begemann, H.K.S.P. (1953) Improved method of determining resistance to adhesion by sounding through a loose sleeve placed behind the cone, Proc. 3rd Int. Conf. Soil Mech. Found. Eng., Vol. 1, pp. 213–217.
- Begemann, H.K.S.P. (1965) The friction jacket cone as an aid in determining the soil profile, Proc. 6th Int. Conf. Soil Mech. Found. Eng., Vol. 1, pp. 17–20.
- Campanella, R.G. and Davies, M.P. (1994) The seismic piezocone: a practical site investigation tool, Geophysical Characterization of Sites, Ed. R.D. Woods, Publication of Technical Committee No. 10 of Int. Soc. Soil Mech. Found. Eng., publ. Oxford & IBH Publishers, pp. 49–55.
- Highway Bridge Design Code (道路橋示方書) (1990) Japan Road Association, Part V, Seismic Design (this has been updated periodically later).
- Ishihara, K. (1985) Stability of natural deposits during earthquakes, Theme Lecture at 11th ICSMFE (Int. Conf. Soil Mech. Found. Eng.), San Francisco, Vol. 1, pp. 321–376.
- Kishida, H. (1966) Damage to reinforced concrete buildings in Niigata City with special reference to foundation engineering, Soil. Found., Vol. 6, No. 2, pp. 71–88.



**Fig. 21.26** Sakai-Yasuda relationship between fines content and minimum void ratio of sand

- Koizumi, Y. (1966) Change in density of sand subsoil caused by the Niigata Earthquake, *Soil. Found.*, Vol. 6, No. 2, pp. 38–44.
- Meyerhof, G.G. (1957) Discussion of Session 1, *Proc. 4th Int. Conf. Soil Mech. Found. Eng.*, Vol. 3, p. 110.
- Robertson, P.K. (1990) Soil classification using the cone penetration test, *Can. Geotech. J.*, Vol. 27, pp. 151–158.
- Robertson, P.K., Campanella, R.G. and Wightman, A. (1983) SPT-CPT correlations, *J. Geotech. Eng., ASCE*, Vol. 109, GT11, pp. 1449–1459.
- Robertson, P.K., Woeller, D.J. and Finn, W.D.L. (1992) Seismic cone penetration test for evaluating liquefaction potential under cyclic loading, *Can. Geotech. J.*, Vol. 29, pp. 686–695.
- Robertson, P.K. and Wride, C.E. (1998) Evaluating cyclic liquefaction potential using the cone penetration test, *Can. Geotech. J.*, Vol. 35, pp. 442–459.
- Sakai, Y. and Yasuda, S. (1977) Liquefaction characteristics of undisturbed sandy soils, *Proc. 12th Annual Conf. of JSSMFE*, pp. 389–392 (in Japanese).
- Seed, H.B. (1987) Design problems in soil liquefaction, *J. Geotech. Eng.*, Vol. 113, No. 8, pp. 827–845.
- Seed, H.B. and Idriss, I.M. (1982) Ground motions and soil liquefaction during earthquakes, *Earthq. Eng. Res. Inst.*, ISBN 0-943198-24-0, p. 107.
- Seed, H.B., Tokimatsu, K., Harder, L.F. and Chung, R.M. (1985) Influence of SPT procedures in soil liquefaction resistance evaluations, *Proc. ASCE*, Vol. 111, GT12, pp. 1425–1445.
- Shibata, T. and Teparaksa, W. (1988) Evaluation of liquefaction potential of soils using cone penetration tests, *Soil. Found.*, Vol. 28, No. 2, pp. 49–60.
- Stokoe, K.H. and Nazarian, S. (1985) Use of Rayleigh waves in liquefaction studies, *Measurement and use of shear wave velocity*, Ed. R.D. Woods, ASCE, pp. 1–17.
- Tatsuoka, F., Iwasaki, T., Tokida, K., Yasuda, S., Hirose, M., Imai, T. and Kon-no, M. (1980) Standard penetration tests and soil liquefaction potential evaluation, *Soil. Found.*, Vol. 20, No. 4, 95–111.
- Tokimatsu, K. and Uchida, A. (1990) Correlation between liquefaction resistance and shear wave velocity, *Soil. Found.*, Vol. 30, No. 2, pp. 33–42.
- Wong, R.T., Seed, H.B. and Chan, C.K. (1975) Cyclic loading liquefaction of gravelly soils, *Proc. ASCE*, Vol. 101, GT6, pp. 571–583.
- Yasuda, S. and Soga, M. (1984) Effect of frequency on undrained strength of sands, *Proc. 19th Nat. Conf. Soil Mech. Found. Eng.*, pp. 549–550 (in Japanese).
- Yoshimi, Y. and Oh-oka, H. (1975) Influence of degree of shear stress reversal on the liquefaction potential of saturated sand, *Soil. Found.*, Vol. 15, No. 3, pp. 27–40.

# Chapter 22

## Postliquefaction Behavior of Sandy Ground

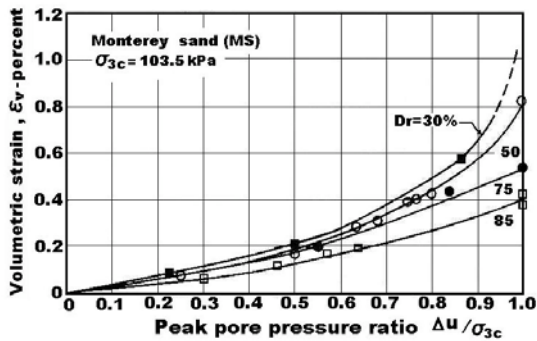


Persepolis (top) and Susa (bottom; present name is Sush) were two important capitals of the Persian empire and were destroyed by Alexander of Macedonia.

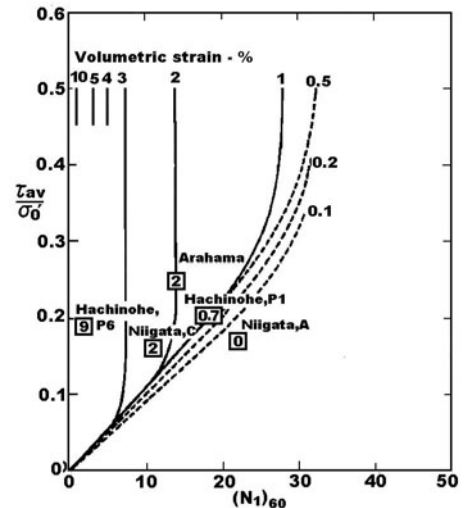
## 22.1 Ground Subsidence After Liquefaction

Subsidence of level ground that remains after liquefaction is a consequence of consolidation. Subsidence is also possible to occur near the top of a liquefied slope (Sect. 24.1) as well as in a foundation of a building. They are, however, due to lateral soil displacement and is out of scope in this section.

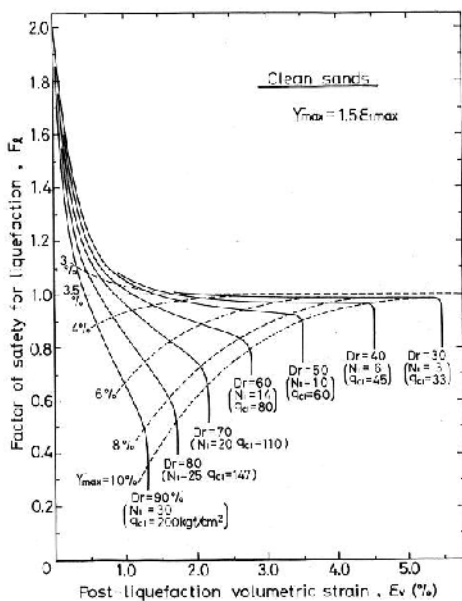
Lee and Albaisa (1974) summarized laboratory test results to obtain Fig. 22.1 that enables to predict the volume contraction of sand subjected to cyclic undrained loading. It is shown that looser sands develops greater subsidence. Their study, however, is concerned with unliquefied sand in which the excess pore pressure is less than 100%.



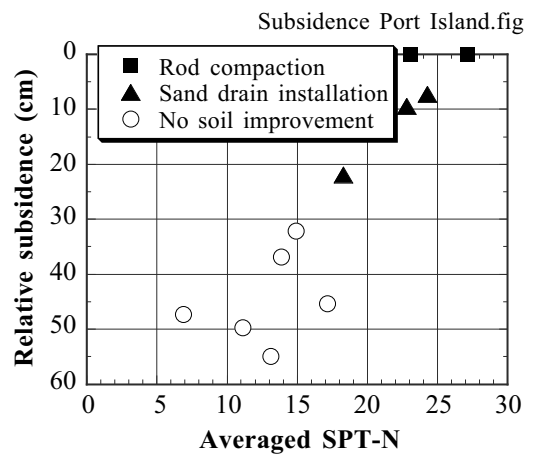
**Fig. 22.1** Volume contraction of sand subjected to cyclic loading (Lee and Albaisa, 1974)



**Fig. 22.2** Empirical prediction of liquefaction-induced volume contraction (Tokimatsu and Seed, 1987)



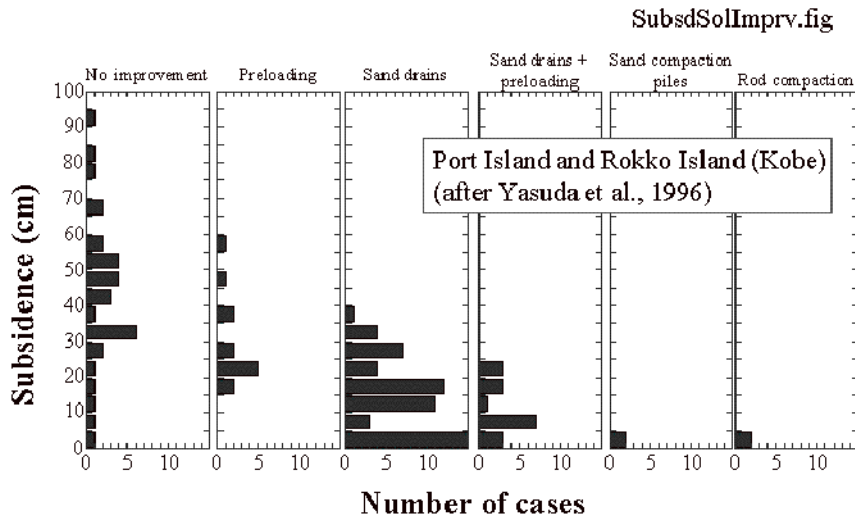
**Fig. 22.3** Experimental chart for prediction of liquefaction-induced volume contraction (Ishihara and Yoshimine, 1992)



**Fig. 22.4** Experience of ground subsidence in Port Island in 1995 (after Tsuboi et al., 1996)

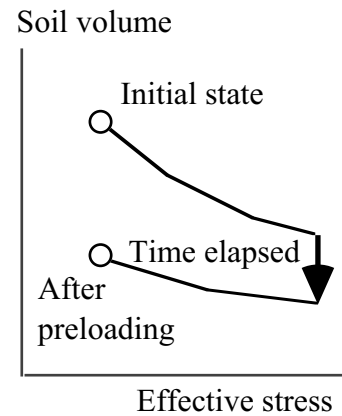
Tokimatsu and Seed (1987) summarized histories of liquefaction during past earthquakes (Fig. 22.2). This diagram compares the prediction with past experiences as shown in boxes. In this figure, the volume contraction is a function of SPT- $N$  and factor of safety.  $(N_1)_{60}$  is the SPT blow counts adjusted to the effective vertical stress of 1 kgf/cm<sup>2</sup> and the energy efficiency of 60% during impact.

Figure 22.3 shows an empirical correlation between extent of liquefaction,  $F_L$  (Sect. 19.4), and the volumetric strain of liquefied sand. Moreover, recent experiences in the Port Island of Kobe, 1995, shows that different extent of densification of sand results in different magnitude of ground subsidence. For details of rod compaction method of soil densification, refer to Sect. 26.4. Called relative subsidence, the elevation of the ground surface relative to pile-supported structures was assembled and Fig. 22.4 was obtained. Better soil improvement and consequently the greater SPT- $N$  value are associated with the less extent of subsidence after a strong earthquake. The same information is illustrated in a different way in Fig. 22.5. Details of sand compaction piles for densification of soil are available in Sects. 26.4 and 26.5.



**Fig. 22.5** Variation of earthquake-induced subsidence in Port Island affected by different methods of soil improvement (data by Yasuda et al., 1996)

Preloading and installation of sand drains were originally intended to improve soft marine clay underlying the land reclamation and improvement of the liquefaction resistance of the man-made island itself was not the aim. Preloading statically increases and then decreases the effective vertical stress so that the soft submarine clay may become overconsolidated (Fig. 22.6) and the future consolidation (Sect. 1.4) may be reduced. Sand drain also installs columns of sand from the ground surface down to the clayey subsoil. The installation of columns somehow densified the reclaimed part of Port Island.



**Fig. 22.6** Stress application in preloading of soil

## 22.2 Repeated Liquefaction

Sand becomes denser after liquefaction and dissipation of excess pore water pressure. Hence, it may be thought that liquefaction is unlikely at sites which liquefied during a previous earthquake (Fig. 18.8 and Sect. 20.1). However, there are examples of repeated liquefaction. Figure 22.7 shows the Tamanoike 玉の池 site in Oga Peninsula 男鹿半島 where liquefaction occurred in 1939 (Oga earthquake), 1964 (Niigata earthquake), and 1983 (Nihonkai Chubu earthquake). There used to be a pond here which was filled with sand later (Fig. 22.8); this is a typical situation vulnerable to liquefaction. This experience of repeated liquefaction appears to contradict with the idea that sand obtains resistance after dissipation of pore pressure and densification.

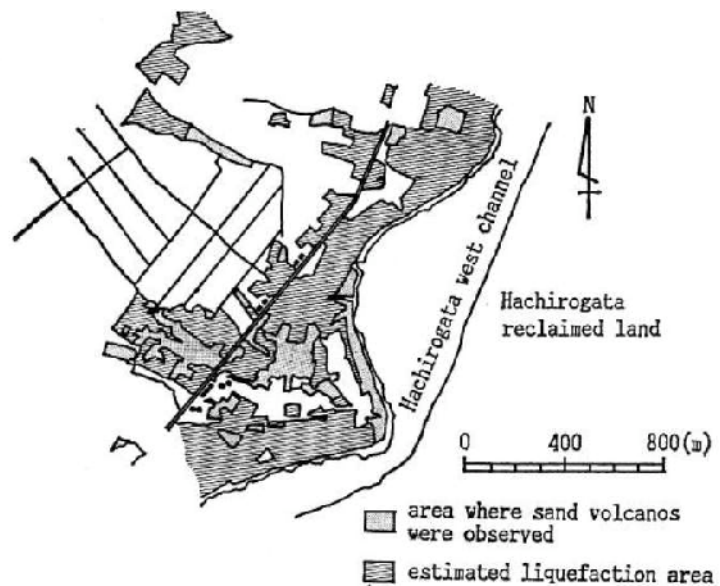


Fig. 22.7 Site of repeated liquefaction at Tamanoike (JSCE, 1986)

Finn et al. (1970) conducted simple shear tests on repeated liquefaction. Keeping the stress amplitude constant, they conducted the first liquefaction test until specified values of strain amplitude occurred. They then reconsolidated the specimen once more and carried out the second liquefaction test. The measured resistance against liquefaction in the second test decreased as the strain amplitude during the first test increased. Thus, the more significant history of previous liquefaction reduces the future liquefaction resistance.



Fig. 22.8 Present view of Tamanoike site (in 2003; by S. Fukui)

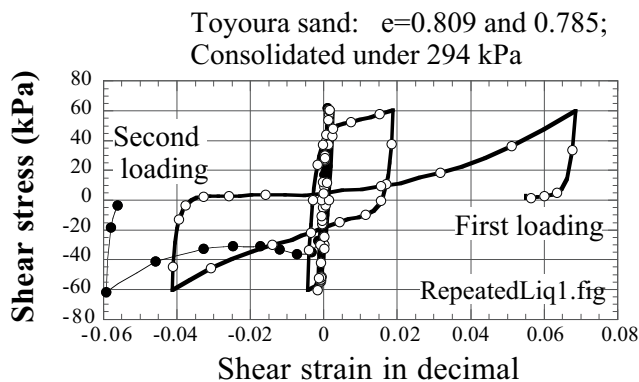


Fig. 22.9 Stress-strain behavior in repeated liquefaction test

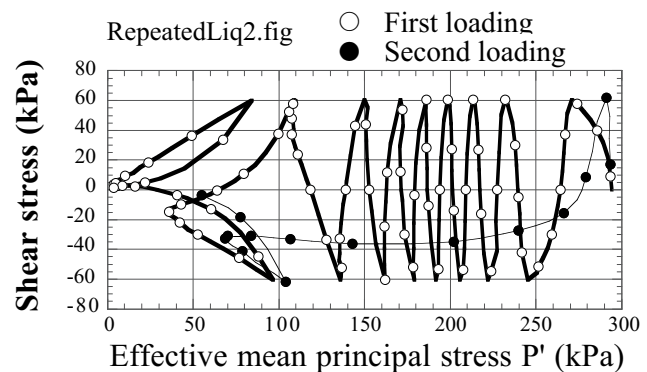


Fig. 22.10 Stress-path in repeated liquefaction test

Figures 22.9 and 22.10 illustrate an undrained torsion shear test in which a liquefied sand was consolidated again for a second undrained test. The first test (○) exhibited a symmetric behavior of sand between

positive and negative loadings of shear stress and ended with a positive residual deformation. Note that this residual deformation was preserved until the beginning of the second test. The sand behavior during the second test (●) was not symmetric at all, in the sense that the first half cycle in the positive direction encountered with an increased stiffness and resistance against pore pressure rise, while the second half cycle in the negative direction developed a drastic amount of excess pore water pressure. Consequently, the specimen in the second test liquefied easily during the first cycle.

The reduced resistance against liquefaction during the second test was induced by the anisotropic structure of sand fabrics that was developed at the end of the first test (Ishihara and Okada, 1978). The first test ended with a large positive strain which produced a fabric structure which is resistant against loading in the positive direction but weak against a negative loading. More in detail, the anisotropy is attributed to the predominant direction of contact planes between sand grains (Oda, 1972a–c).

Thus, repeated liquefaction is possible in young sandy deposits. After many earthquakes, the sand will gain a sufficient density and resistance and no more liquefaction would be repeated (Aging in liquefaction resistance in Sect. 18.13).



### 22.3 Effective Stress Analysis with Hyperbolic Model

The hyperbolic model (11.1) has two material properties;  $G_{\max}$  and  $\gamma_r$ . It should not be thought that these parameters are constant during shaking.

$G_{\max}$ , the shear modulus at very small strain amplitude, varies remarkably with the effective stress. When the excess pore water pressure develops in loose sand,  $G_{\max}$  decreases. It is reasonable that  $G_{\max}$  changes in proportion to (effective vertical stress)<sup>0.4-0.5</sup> (Sect. 10.5, Fig. 10.19).

The skeleton curve of the hyperbolic model indicates that the shear stress is asymptote to  $G_{\max} \times \gamma_r$  when the strain is very large. Therefore,  $G_{\max} \times \gamma_r$  is a soil parameter which is similar to shear strength. Since the shear strength is generally proportional to the effective stress, the reference strain of  $\gamma_r$  can be considered to vary with a square root of the effective stress.

The effective stress analysis on earthquake response of subsoil and earth structures is an analysis in which:

1. the development of excess pore water pressure with time is predicted by using the time history of shear stress and/or strain (this is not an easy task)
2. the material properties are updated at every moment with respect to the current strain (nonlinearity) and the effective stress
3. Consequently, the calculation of amplification takes into account the increase of excess pore water pressure

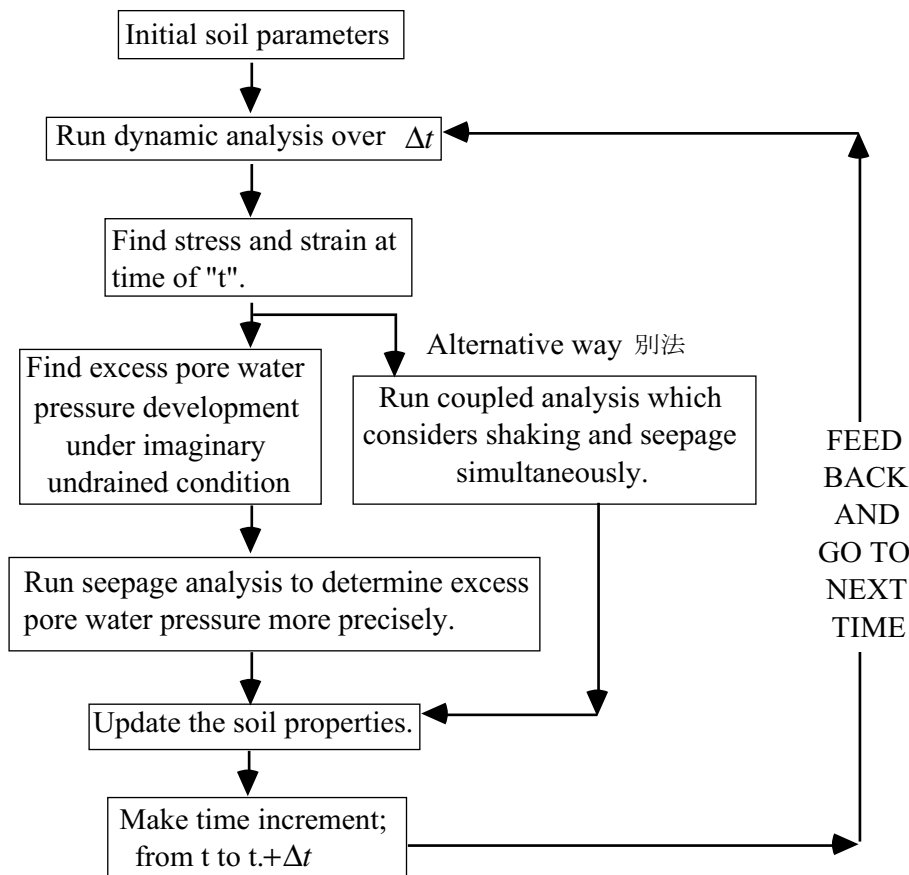


Fig. 22.11 Flow chart of dynamic response analysis based on effective stress principle

When the step (2) above does not include the correction in terms of effective stress, the analysis is called the total stress analysis.

Figure 22.11 illustrates the concept of the effective stress analysis. It should be noted that linear and nonlinear deformation characteristics of soil are *updated* periodically in terms of a “feedback” from the stress and strain. This feedback system requires that the analysis should be done along the time axis. The type of analysis which uses a harmonic motion and Fast Fourier Transformation does not suit an effective stress analysis.

It is also possible to consider the effects of void ratio change on  $G_{\max}$  and  $\gamma_r$ . It is generally not very necessary, however, because the change in void ratio during shaking is small and does not cause a substantial change in the soil parameters.

22.4 Example of Effective Stress Analysis

An effective stress analysis on one-dimensional level layered ground is shown here. Figure 22.12 is an idealized stratification of soil layers which are of different material properties. Figure 22.13 illustrates a one-dimensional model of ground (lumped mass model) in which the mass of soil is represented by points of mass, and they are connected with each other by nonlinear springs. The dashpot at the bottom connecting the model and the base represents an infinite viscous boundary (Fig. 6.41).

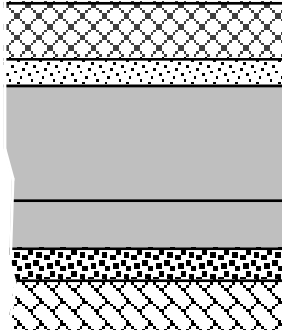


Fig. 22.12 Idealization as horizontally layered ground

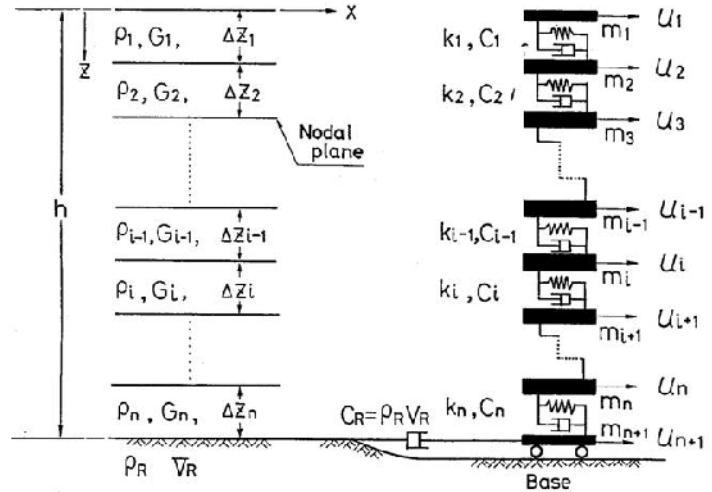


Fig. 22.13 Lumped mass model of one-dimensional horizontal ground

The stress-strain behavior is modeled by hyperbolic curves (Fig. 22.14 and Sect. 11.1). Since the effective stress changes with time, the parameters of  $G_{max}$  and  $\gamma_r$  vary with time as well. Hence, the complex-modulus analysis which assumes constant material properties do not work here. As an alternative, the equation of motion (wave propagation equation) is directly integrated in the time domain. Therefore, the hysteresis loop has to be explicitly specified by, for instance, the Masing rule (Masing, 1926);

$$\frac{\tau - \tau_a}{2} = \frac{G_{max} \frac{\gamma - \gamma_a}{2}}{1 + \left| \frac{\gamma - \gamma_a}{2\gamma_r} \right|}, \tag{22.1}$$

which is of a double-size of the hyperbolic skeleton curve (Fig. 22.14). Note that Masing rule overestimates the damping ratio at large strains;  $h \rightarrow 2/\pi$  when strain is infinitely large.  $G_{max}$  is updated repeatedly in proportion to varying  $\sqrt{\sigma'_v}$  and  $\gamma_r \propto \sqrt{\sigma'_v}$  which is more rational than the conventional complex-modulus analysis. This updating of parameters makes the calculated acceleration more reliable.

The decrease of effective stress with time is governed by dilatancy (excess pore water pressure development,  $u_g$ ) and seepage (consolidation which reduces the pore water pressure). In the present method, dilatancy under undrained conditions is modeled by an idealized stress-path (Fig. 22.15). Not only decreasing effective stress (pore pressure increase) but also phase transformation near failure line (Sect. 18.7) is reproduced herein. Seepage is taken into account by running conventional consolidation analysis in parallel;

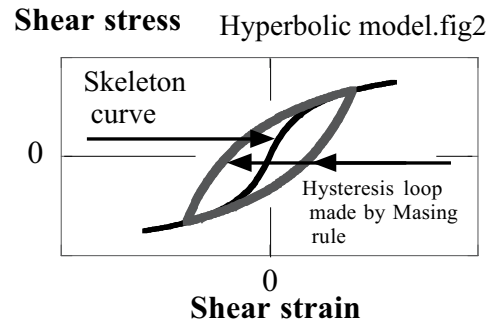


Fig. 22.14 Stress-strain loop constructed by Masing rule

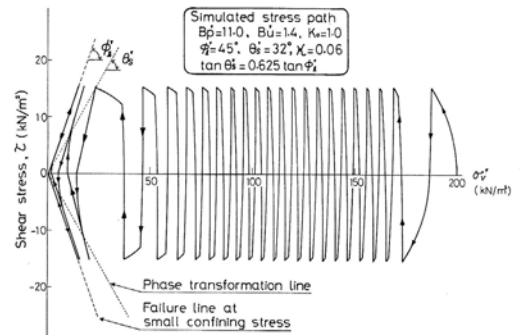


Fig. 22.15 Stress-path model of dilatancy

$$\frac{k}{m_v \gamma_w} \frac{\partial^2 u}{\partial z^2} = \frac{\partial u}{\partial t} - \frac{\partial u_g}{\partial t}, \quad (22.2)$$

in which  $u$  stands for the excess pore water pressure and this differential equation is different from that of conventional consolidation equation in additional consideration of  $u_g$ .

The structure of the entire analysis is shown in Fig. 22.16.

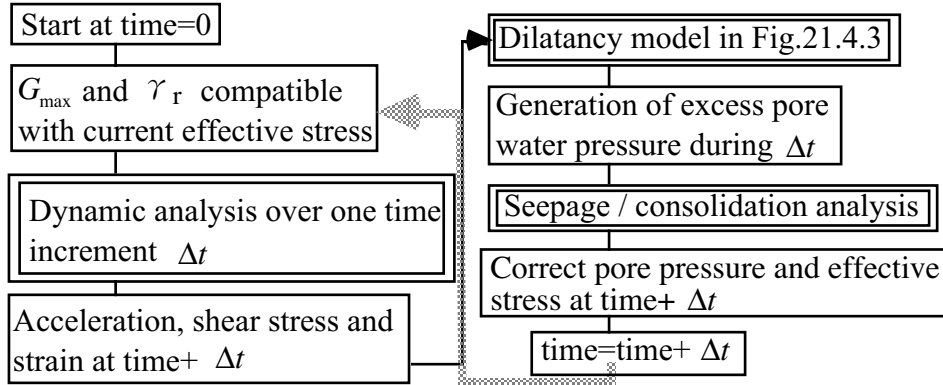


Fig. 22.16 Flow of effective stress analysis

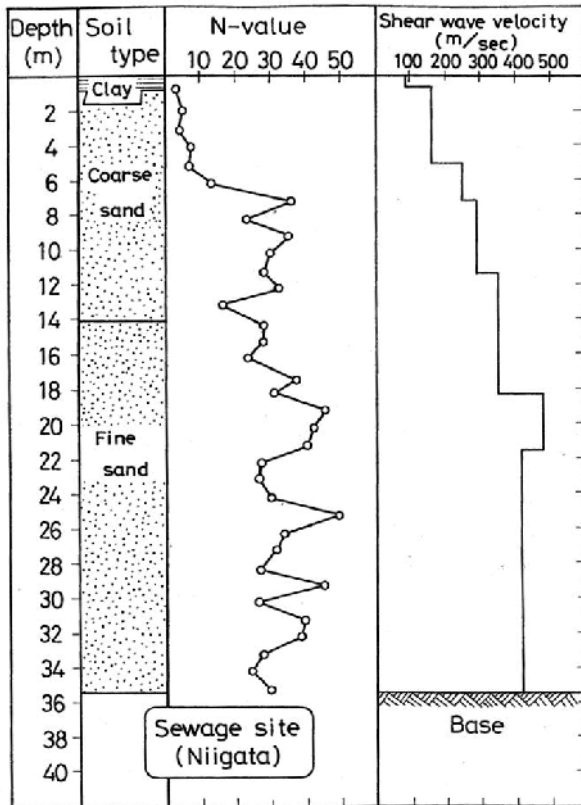


Fig. 22.17 Soil profile of analyzed subsoil in Niigata

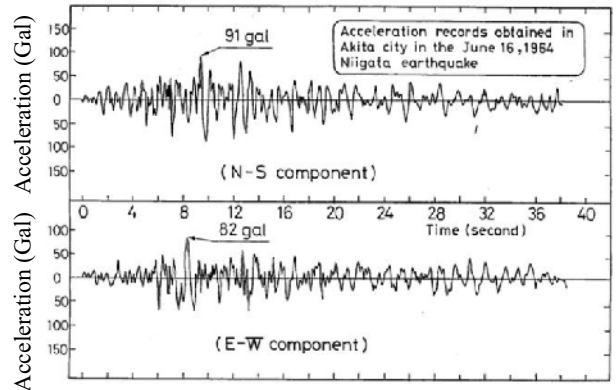


Fig. 22.18 Earthquake motion which was put in at a viscous boundary

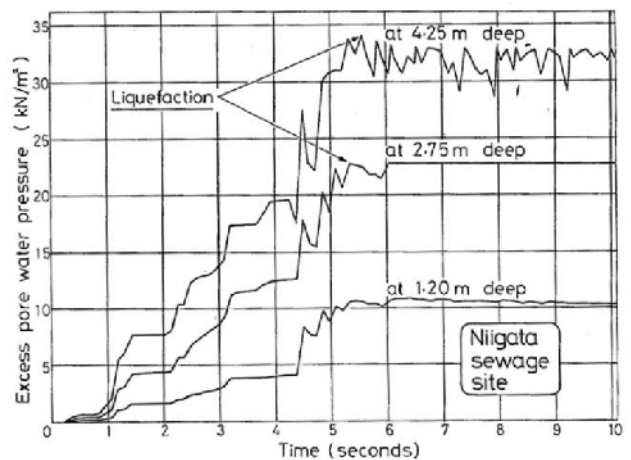


Fig. 22.19 Time history of excess pore water pressure

Example analysis on Niigata subsoil is going to be presented (Computer Code YUSAYUSA; Ishihara and Towhata, 1982). Figure 22.17 shows a soil profile, and the base earthquake excitation was the record obtained in Akita City during the same earthquake (1964 Niigata earthquake; Fig. 22.18). Since Akita City was farther from the epicenter than Niigata City,

its amplitude and predominant period were adjusted in order to take into account the different epicentral distance. Then the motion was considered to be an outcrop motion and employed as an incident motion (earthquake motion travelling upward in an elastic base; Fig. 6.41).

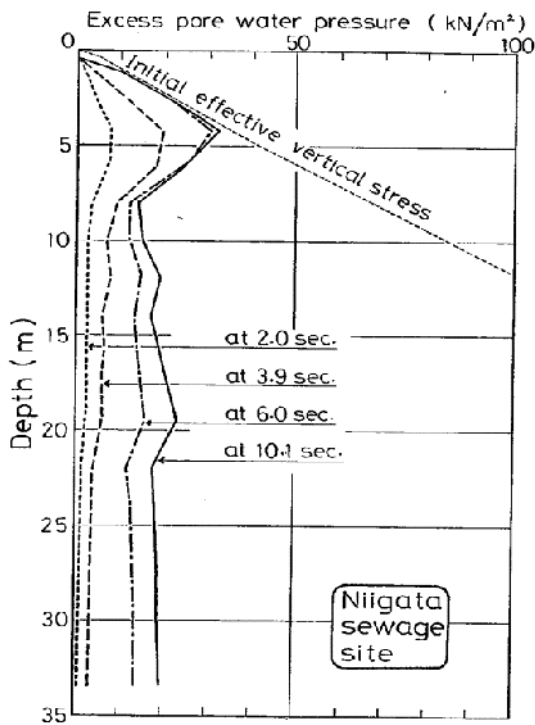


Fig. 22.20 Distribution of highest excess pore water pressure

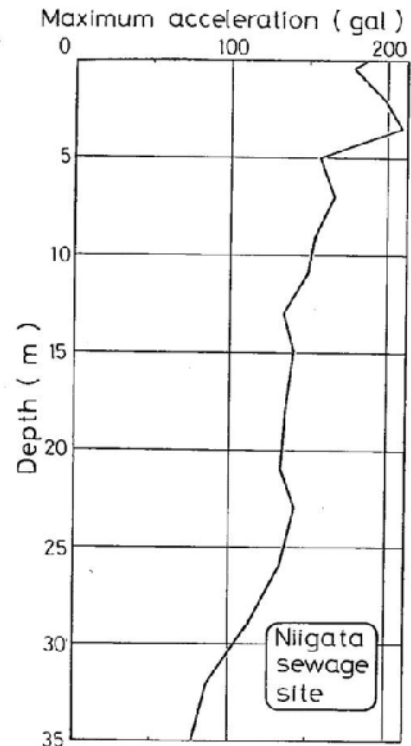


Fig. 22.21 Distribution of maximum acceleration in subsoil

Figure 22.19 indicates the time history of excess pore water pressure at three elevations. Since sand was loose at those elevations, excess pore water pressure developed 100 % and liquefaction occurred. Figure 22.20 reveals the distribution of excess pore water pressure in the vertical direction. The excess pore water pressure reached the initial effective vertical stress (effective overburden pressure) only in the shallow subsoil because SPT-*N* was very low therein (Fig. 22.17).

The distribution of maximum acceleration is shown in Fig. 22.21. In general, the maximum acceleration increased from the bottom toward the surface. However, there is some decrease within top 5 m because soil liquefied there and its rigidity was lost. The equation of motion for the surface soil is expressed as

$$\text{Shear stress in soil} = (\text{Soil mass}) \times (\text{Maximum acceleration.}) \quad (22.3)$$

Since the magnitude of shear stress in liquefied soil is limited, the maximum acceleration is reduced. The time histories of acceleration are shown in Fig. 22.22. The surface acceleration was reduced to very small values after 5 s at which excess pore water

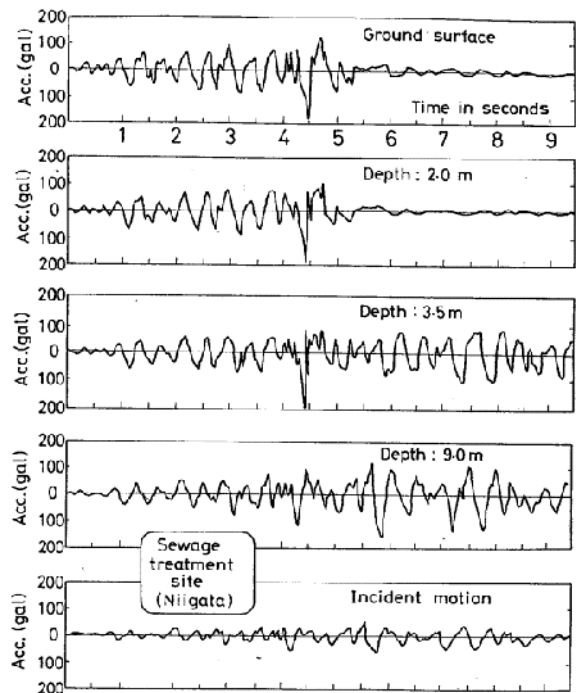


Fig. 22.22 Time history of acceleration at several elevations

pressure reached 100% liquefaction (Fig. 22.19). Note, moreover, that the predominant period of surface motion was elongated after liquefaction because the natural period of surface soil was elongated due to significant softening of liquefied soil and resonance occurred in long-period components of motion. This feature is similar to what was seen in real acceleration records in Sect. 17.12.

A computer code, DESRA, by Finn et al. (1976 and 1977) employs (11.14) to evaluate cyclically generated volume contraction and then converts it to development of excess pore water pressure. This excess pore water pressure is determined by (Volume Compressibility of Soil Skeleton)  $\times$  (Volumetric Strain in Drained Conditions) which are the pressure that would occur under undrained conditions. Since seepage and consolidation is taken into account furthermore, the real excess pore water pressure is different from the above-mentioned pore water pressure.

**22.5 Assessment of Liquefaction Resistance by Measuring Shear Wave Velocity**

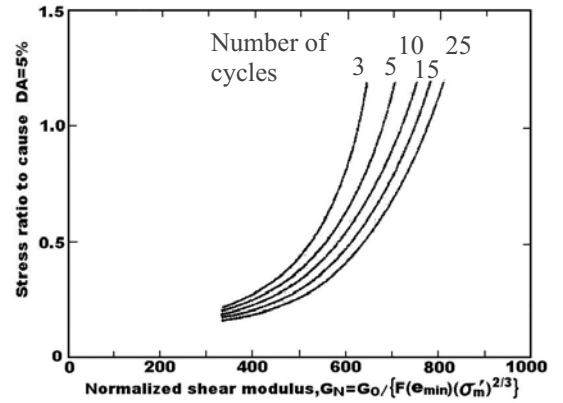
It is an attractive idea to assess the insitu liquefaction resistance of sand by measuring the shear wave velocity,  $V_s = \sqrt{G/\rho}$ .  $V_s$  values can be obtained economically without drilling a bore hole; e.g., surface wave measurement (Tokimatsu et al. 1991) and a seismic downhole survey method (Sect. 8.1).

The problem is that the  $V_s$ -liquefaction resistance correlation is affected by types of soil as well as the effective stress level. Hence, Tokimatsu and Uchida (1990) proposed to normalize the measured  $G_{max}$  ( $= \rho V_s^2$ ) by using the effective mean stress level,  $\sigma'_m = (\sigma'_1 + \sigma'_2 + \sigma'_3)/3$ , and a function of minimum void ratio,  $e_{emin}$ , of respective sand. The use of  $e_{emin}$  requires (disturbed) soil samples to be collected by drilling holes. Figure 22.23 illustrates their correlation between the normalized  $G_{max}$  and the liquefaction resistance, where the normalized modulus,  $G_N$ , is defined by

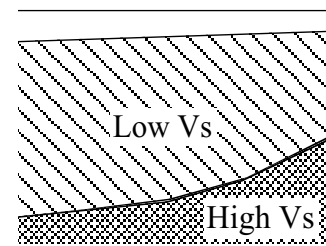
$$G_N = G_{max} / \left\{ \frac{(2.17 - e_{min})^2}{(1 + e_{min})} (\sigma'_m)^{2/3} \right\}. \quad (22.4)$$

One important problem is that liquefaction-vulnerable sand and unliquefiable clay may exhibit similar values of  $V_s$ . Measurement of  $V_s$  by seismic method, seismic cone penetrometer (e.g., Robertson et al. 1986) and other method cannot clearly show soil types, although tip resistance and skin friction in cone penetration tests can make some suggestion (Begemann, 1965). This problem is not solved by  $V_s$  correlations so far (Andrus and Stokoe, 1996), and the use of  $V_s$  is still difficult.

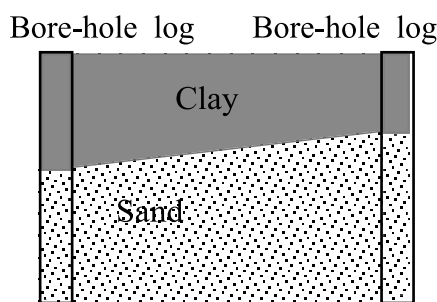
For a better use in practice,  $V_s$  measurement should be combined with boring profiles. Fig. 22.24 illustrates a two-dimensional  $V_s$  profile in which the area of low  $V_s$  may or may not be liquefiable, depending on types of soil. Figure 22.25 reveals an interpolation of soil types obtained from two boring logs. The location of sandy soil is somehow identified here. Combining Figs. 22.24 and 22.25 leads to identification of sandy soils (Fig. 22.26) with low  $V_s$  which has low resistance against liquefaction.



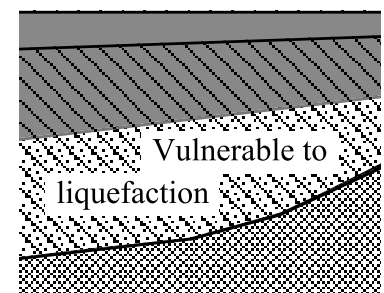
**Fig. 22.23** Correlation between normalized shear modulus at small strain and liquefaction resistance (Tokimatsu and Uchida, 1990)



**Fig. 22.24**  $V_s$  profile without information on soil type



**Fig. 22.25** Soil type profile made by boring logs



**Fig. 22.26** Location of liquefaction-prone deposits assessed by  $V_s$  and boring logs

**List of References in Chapter 22**

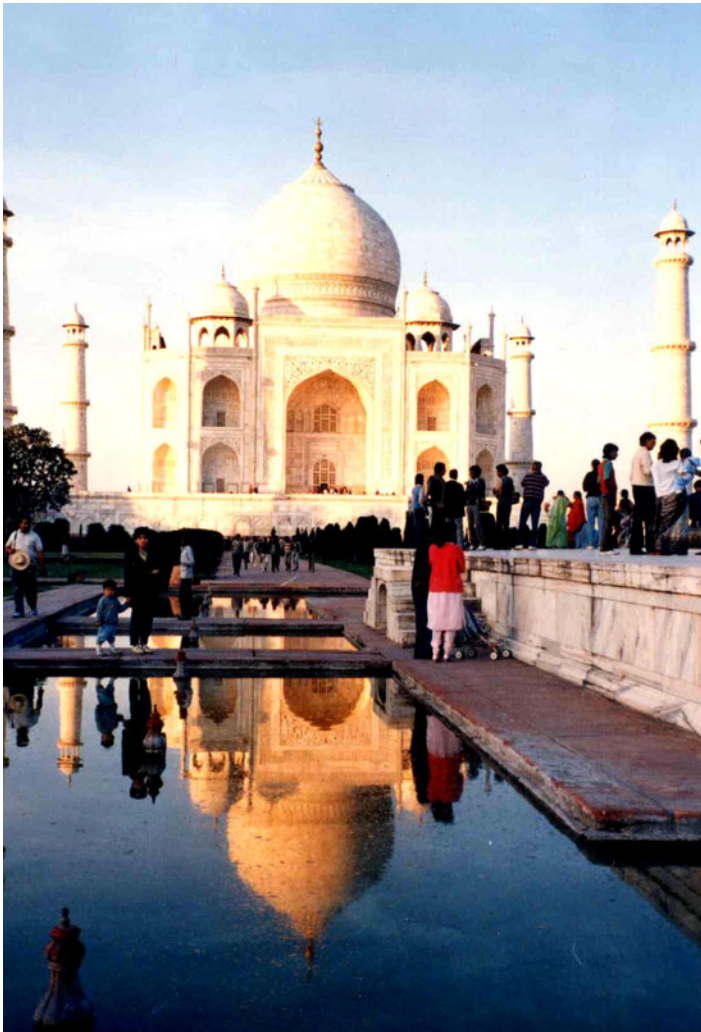
Andrus, R.D. and Stokoe, K.H. (1996) Preliminary guidelines for liquefaction assessment using shear wave velocity, Proc. UJNR 28th Joint Meeting of United States-Japan Panel on Wind and Seismic Effects, Gaithersburg, Maryland.

- Begemann, H.K.P. (1965) The friction jacket cone as an aid in determining the soil profile, Proc. 6th Int. Conf. Soil Mech. Found. Eng., Vol. 1, pp. 17–20.
- Finn, W.D.L., Bransby, P.L. and Pickering, D.J. (1970) Effect of strain history on liquefaction of sand, Proc. ASCE, Vol. 96, SM6, pp. 1917–1934.
- Finn, W.D.L., Byrne, D.M. and Martin, G.R. (1976) Seismic response and liquefaction of sands, Proc. ASCE, Vol. 102, GT8, pp. 841–856.
- Finn, W.D.L., Lee, K.W. and Martin, G.R. (1977) An effective stress model for liquefaction, Proc. ASCE, Vol. 103, GT6, pp. 517–533.
- Ishihara, K. and Okada, S. (1978) Effects of stress history on cyclic behavior of sand, Soil. Found., Vol. 18, No. 4, pp. 31–45.
- Ishihara, K. and Towhata, I. (1982) Dynamic response analysis of level ground based on the effective stress method, Soil Mechanics - Transient and Cyclic Loads, John Wiley and Sons, pp. 133–172.
- Ishihara, K. and Yoshi-mine, M. (1992) Evaluation of settlements in sand deposits following liquefaction during earthquakes, Soil. Found., Vol. 32, No. 1, pp. 173–188.
- JSCE (1986) Damage Report of the 1983 Nihonkai-Chubu earthquake, p. 204.
- Lee, K.L. and Albaisa, A. (1974) Earthquake induced settlements in saturated sands, J Geotech. Eng., ASCE, Vol. 100, No. 4, pp. 387–406.
- Masing, G. (1926) Eigenspannungen und Verfestigung beim Messing, Proc. 2nd Int. Cong. Applied Mech., pp. 332–335.
- Oda, M. (1972a) Initial fabrics and their relations to mechanical properties of granular materials, Soil. Found., Vol. 12, No. 1, pp. 17–36.
- Oda, M. (1972b) The mechanism of fabric changes during compressional deformation of sand, Soil. Found., Vol. 12, No. 2, pp. 1–18.
- Oda, M. (1972c) Deformation mechanism of sand in triaxial compression tests, Soil. Found., Vol. 12, No. 4, pp. 45–63.
- Robertson, P.K., Campanella, R.G., Gillespie, D. and Rice (1986) Seismic CPT to measure in situ shear wave velocity, Proc. ASCE, Vol. 112, GT8, pp. 791–803.
- Tokimatsu, K. and Seed, H.B. (1987) Evaluation of settlements in sands due to earthquake shaking, J. Geotech. Eng., ASCE, Vol. 113, No. 8, pp. 861–878.
- Tokimatsu, K., Kuwayama, S., Tamura, S. and Miyadera, Y. (1991) Vs determination from steady state Rayleigh wave method, Soil. Found., Vol. 31, No. 2, pp. 153–163.
- Tokimatsu, K. and Uchida, A. (1990) Correlation between liquefaction resistance and shear wave velocity, Soil. Found., Vol. 30, No. 2, pp. 33–42.
- Tsuboi, H., Takahashi, Y., Harada, K., Shin-kawa, N., Ishihara, K. and Yasuda, S. (1996) Damage by liquefaction and effect of soil improvement methods on the Hyogoken-Nanbu earthquake, JSCE 阪神・淡路大震災に関する学術講演会論文集, pp. 217–220 (in Japanese).
- Yasuda, S., Ishihara, K., Harada, K. and Shinkawa, N. (1996) Effect of soil improvement on ground subsidence due to liquefaction, Soil. Found., Special Issue on Geotechnical Aspects of the January 17 1995 Hyogoken-Nambu Earthquake, No. 1, pp. 99–107.



# Chapter 23

## Immediate Detection of Liquefaction Damage and Emergency Action



The emperors of Mughal tried to take their father's power. Shah Jehan, the fifth emperor, took it from Jehangir, while Aurangzeb, his son, from Shah Jehan himself. Shah Jehan spent a huge amount of money on the tomb of his empress, Mumtaz Mahal, which is known today as Taj Mahar (see left). Later, Aurangzeb tried to repeat it for his empress, Bibi-ka-Maqbara (see right). However, the budget was not sufficient any more to use expensive materials abundantly. This was because the Mughal had wasted much money on endless wars against local lords.

### 23.1 Response Spectrum

In spite of the idea of seismic coefficient, the maximum acceleration, which is equivalent to the seismic coefficient, is not a direct and only one parameter that accounts for the effects of earthquake shaking on a variety of structures. This is because, for instance, the period of shaking and number of cycles as well as the duration time can induce different extents of response in structures.

Response spectrum is one of the alternative ideas which can more explicitly account for the various nature of both earthquake shaking and structures of interest. Figure 23.1 illustrates a single-degree-of-freedom model employed for calculation of response spectrum. A given irregular seismic motion,  $u_b$ , is put in at the base, and the response of the mass,  $m$ , is calculated by solving an equation of motion;

$$m \frac{d^2u}{dt^2} + 2h\sqrt{mk} \frac{du}{dt} + ku = -m \frac{d^2u_b}{dt^2}, \quad (23.1)$$

in which “ $u$ ” stands for the relative displacement between the mass and the base. In other words, “ $u$ ” indicates the deformation of structure which is shaken by the base motion. Similarly,  $du/dt$  and  $d^2u/dt^2$  designate the first and second time derivatives of  $u$ , respectively; consequently velocity and acceleration. Furthermore, the effects of dashpot is represented by the critical damping ratio,  $h$ . The maximum values of  $u$ ,  $du/dt$ ,  $d^2(u+u_b)/dt^2$ , and others during an irregular shaking are calculated while varying the natural period,  $T=2\pi\sqrt{m/k}$  of the single-degree-of-freedom model.

Response spectra are relationships between the maximum values of response as mentioned above and the natural period. The critical damping ratio,  $h$ , is held constant while changing the natural period,  $T$ . Typical values of  $h$  are 0.05, 0.10, and 0.20 in accordance with the extent of nonlinearity of studied structure. The relationship between  $du/dt$  and  $T$  is called response (relative) velocity spectrum, while  $d^2(u+u_b)/dt^2$  vs.  $T$  is called response (acceleration) spectrum. The particular value of  $T$  at which the response spectrum value takes the maximum value is a good approximation of the dominant period (卓越周期; particular period at which the Fourier spectrum is maximum) of the input motion.

Figures 23.2 and 23.3 compare the (relative) velocity spectra of earthquake records obtained at the surface of unliquefied (Kaihoku 開北) and liquefied (Port Island, Kobe) sites. Both records consist of a linear increase at shorter period, the maximum value, and the more or less constant values at longer periods. The constant value at the longest period is approximately equal to the maximum velocity,  $du_b/dt$ , of the input motion. Note that the maximum spectrum value of the Port Island motion occurs at a longer period than the Kaihoku motion due to the subsoil liquefaction and the elongated natural period of the ground. The elongated natural period amplified the motion with longer periods of shaking, making the dominant period at surface longer.

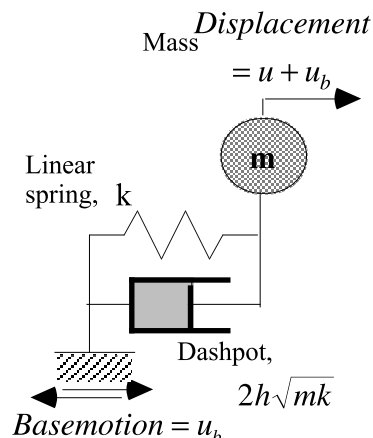


Fig. 23.1 Single-degree-of-freedom model for calculation of response spectrum

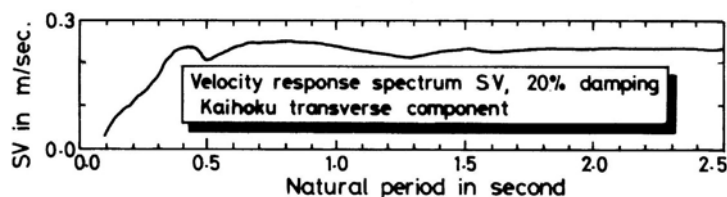


Fig. 23.2 Velocity spectrum of Kaihoku trasverse motion

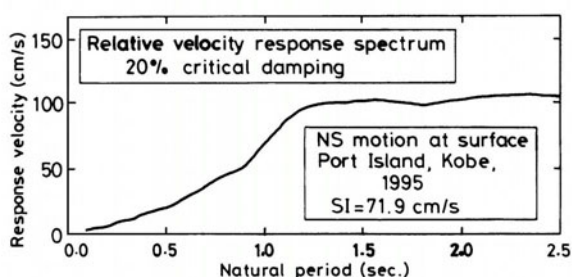


Fig. 23.3 Velocity spectrum on Port Island surface NS motion

### 23.2 Spectrum Intensity

Spectrum intensity, which is abbreviated as SI, is obtained by calculating the average value of the (relative) velocity response spectrum over the range of  $T = 0.1-2.5$  s (Housner, 1961). A typical value of critical damping ratio is  $h = 0.20$ :

$$SI = \frac{1}{2.4} \int_{0.1}^{2.5} (\text{velocity response spectrum})_{h=0.20} dT. \tag{23.2}$$

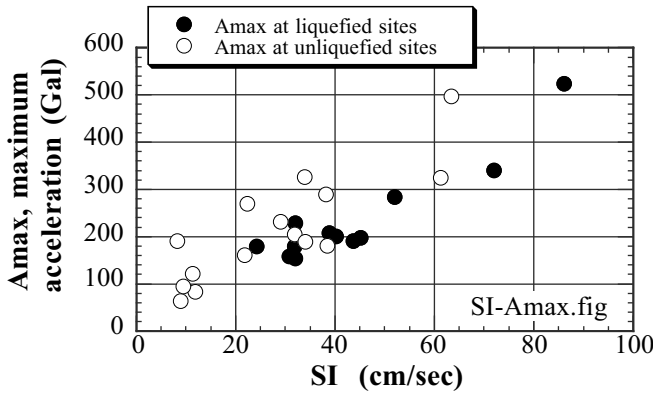


Fig. 23.4 SI and maximum acceleration of horizontal earthquake motion records

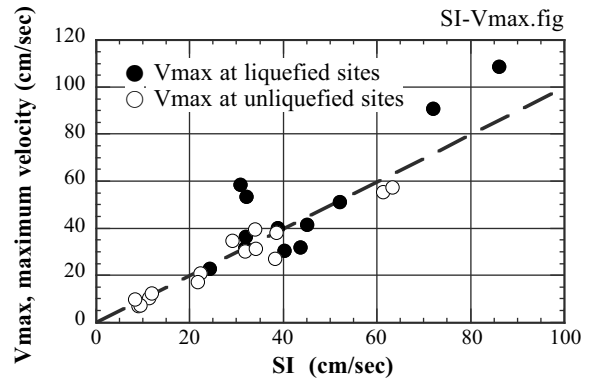


Fig. 23.5 Comparison of SI with maximum velocity of earthquake motion (Towhata et al. 1996)

Note that Housner’s original SI did not divide the integrated response spectrum by 2.4 s. Figure 23.4 plots SI in (23.2) against maximum acceleration,  $A_{max}$ , of many earthquake records. It is found therein that liquefied and unliquefied sites have a threshold SI of around 30–40 cm/s (=kine) while  $A_{max}$  does not discriminate cases with liquefaction and without liquefaction. Moreover, SI is approximately equal to the maximum velocity of the ground motion (Fig. 23.5);

$$SI \approx V_{max}. \tag{23.3}$$

It is somehow possible to theoretically verify (23.3). First, the equation of motion (23.1) of a single-degree-of-freedom model in Fig. 23.1 is rewritten as

$$\frac{d^2u}{dt^2} + 2h\omega_0 \frac{du}{dt} + \omega_0^2 u = -A(t), \tag{23.4}$$

in which  $\omega_0$  stands for the natural circular frequency that is related with the natural period,  $T$ , by  $T = 2\pi/\omega_0$ . Furthermore,  $A(t)$  designates the ground acceleration. It should be recalled that the maximal value (maximum of absolute value of velocity,  $|du/dt|$ ) gives the response (relative) velocity (SV; Sect. 23.1) and the averaging of SV from  $T = 0.1-2.5$  s gives the SI value. When the velocity achieves the maximal value of SV, time derivative of velocity (i.e., acceleration) is equal to zero. Accordingly, (23.4) is modified as

$$2h\omega_0 SV + \omega_0^2 u = -A \left( \text{when } \frac{du}{dt} = SV \right) \leq A_{max}.$$

When the natural period,  $T$ , is very short,  $\omega_0$  is large. Furthermore, it is reasonable that the maximum velocity and the maximum kinetic energy occur when the strain energy is fully released ( $u = 0$ ).

Accordingly,

$$2h\omega_0 SV \leq A_{\max}$$

and, by taking the maximum value,

$$SV = \frac{A_{\max}}{2h\omega_0} = \frac{A_{\max}}{4\pi h} T \quad (23.5)$$

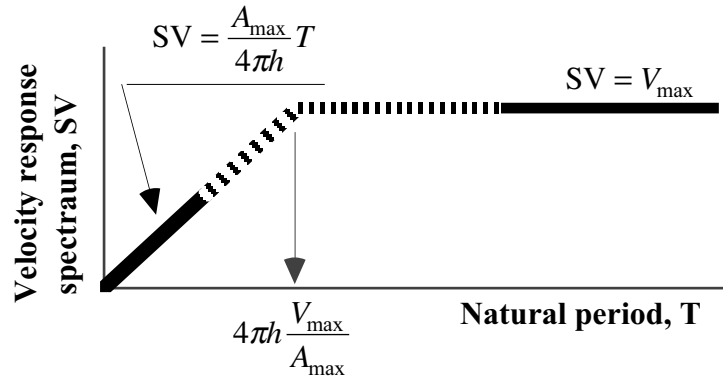


Fig. 23.6 Analytically derived velocity response spectrum

When  $T$  is very long on the contrary,  $\omega_0$  is small. Hence,  $2h\omega_0(du/dt)$  and  $\omega_0^2 u$  are relatively less important than  $d^2u/dt^2$ . Accordingly,

$$\frac{d^2u}{dt^2} \approx -A(t) \text{ and}$$

$$SV = \max\left(\frac{du}{dt}\right) = \max\left(\int \frac{d^2u}{dt^2} dt\right) \approx \max\left(\int A dt\right) = \max(\text{ground velocity}) = V_{\max} \quad (23.6)$$

It is thus possible to state by combining (23.5) and (23.6) that the variation of SV with the natural period (velocity response spectrum) is approximated by a trapezoidal function. This idea is schematically illustrated in Fig. 23.6 which is very similar to the velocity response spectrum of a real earthquake motion (Figs. 23.2 and 23.3). The dashed line in Fig. 23.6 shows a portion for which  $T$  lies in the intermediate range and neither (23.5) nor (23.6) are valid.

The theoretical value of SI is obtained by integrating the line in Fig. 23.6 from  $T = 0.1$  to  $2.5$  s and then taking the average value. Accordingly,

$$\text{when } V_{\max} < \frac{0.125}{\pi} A_{\max}, \quad SI = V_{\max} \quad (23.7a)$$

$$\text{when } \frac{0.125}{\pi} A_{\max} < V_{\max} < \frac{3.125}{\pi} A_{\max}, \quad SI = \frac{1}{2.4} \left( 2.5V_{\max} - \frac{A_{\max}}{160\pi} - 0.4\pi \frac{V_{\max}^2}{A_{\max}} \right) \quad (23.7b)$$

$$\text{and when } \frac{3.125}{\pi} A_{\max} < V_{\max}, \quad SI = 0.517A_{\max} \quad (23.7c)$$

Among three equations above, only the first one is consistent with the desired  $SI = V_{\max}$ . Thus, it appears still difficult to theoretically verify (23.3).

To further cast lights on the real values of  $A_{\max}$  and  $V_{\max}$ , Fig. 23.7 was drawn. The values of  $V_{\max}$  (maximum ground velocity) lies in the range of (23.7b), and among three terms in the parenthesis of (23.7b), the first term of  $2.5V_{\max}$  is significantly greater than others. Thus, it can be reasonably said that SI is approximately equal to  $V_{\max}$ . This is confirmed in Fig. 23.8 where SI is compared with three theoretical values in (23.7a)–(23.7c). The agreement between  $V_{\max}$  (23.7a) and (23.7b) are remarkable for all the cases. Thus, SI is approximately equal to  $V_{\max}$ .

There is a situation in which SI has a good correlation with the extent of damage. For example, Fig. 23.9 reveals a correlation of the rate of damage of embedded pipe line. It is seen therein that the greater value of SI is associated with the greater damage rate (number of damage per 1 km of pipe). In the past experience, the maximum acceleration,  $A_{\max}$ , does not give such a good correlation.

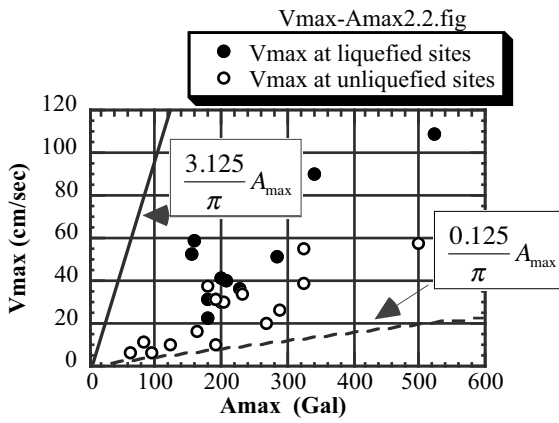


Fig. 23.7 Range of  $V_{max}$  and  $A_{max}$  in real earthquake motion records

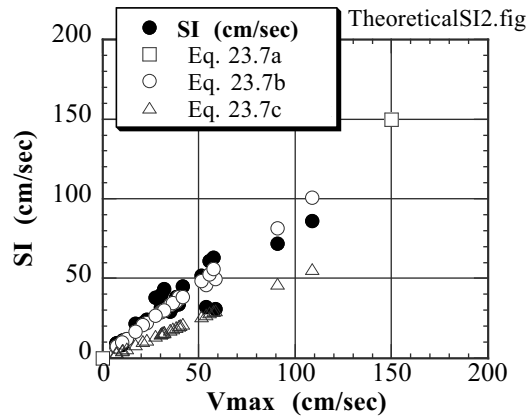


Fig. 23.8 Comparison of theoretical and real SI values

Tokyo Gas Company has deployed 3,700 SI sensors in its service area in order to immediately detect a strong earthquake motion that breaks embedded pipelines (Shimizu et al. 2006). SI sensors are able to record SI as well as the maximum acceleration during earthquakes and transmit them to the headquarter within a few minutes. This quick communication from so many stations would not be possible if the entire time history of ground motion were to be transmitted. The past experiences have shown that there is a correlation between magnitude of measured SI and the damage rate (number of damage per km) of embedded pipe lines. In Fig. 23.4,  $SI = 30$  (or  $40$ ) cm/s is the threshold value above which the possibility of subsoil liquefaction is high; see Fig. 23.5 as well. It seems appropriate that  $SI > 30$  cm/s triggers an emergency safety action of the pipeline system such as shutting down the gas supply.

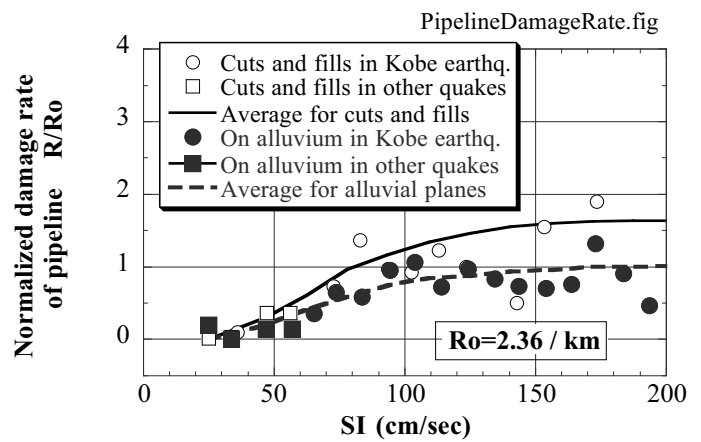


Fig. 23.9 Correlation between SI and seismic damage rate of pipeline (after Hosokawa et al., 2001; Shimizu et al., 2006)

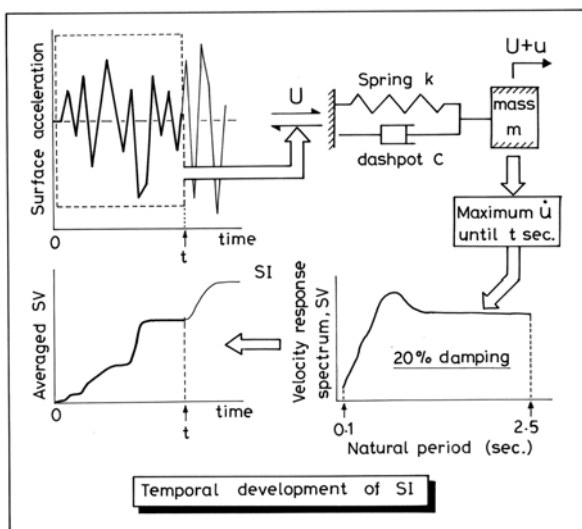


Fig. 23.10 Calculation of time history of SI (Towhata et al. 1996)

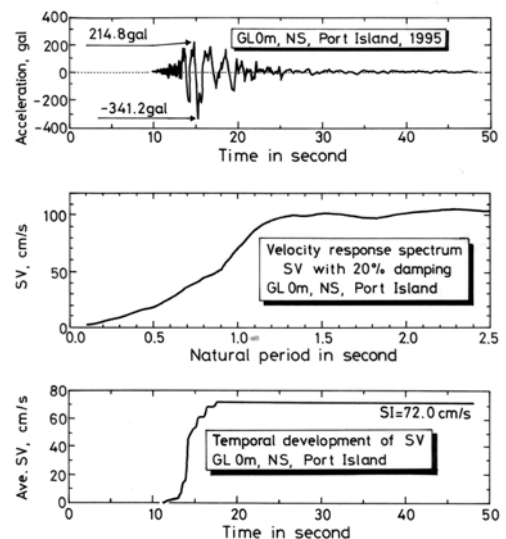
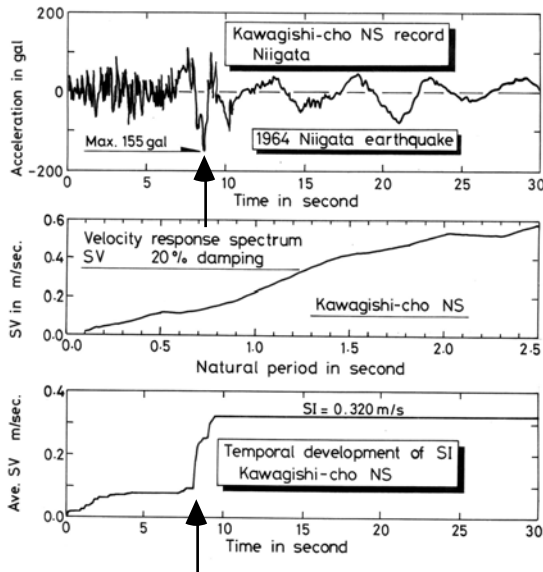
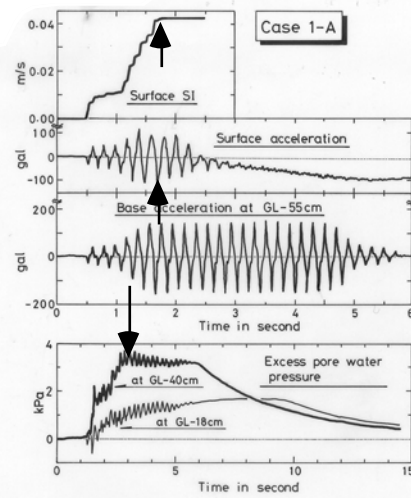


Fig. 23.11 Time history of SI in Kobe Port Island record

To further understand the nature of SI, the idea of time history of SI was developed. In line with the original idea in Sect. 23.1, a response spectrum, SV, is calculated by using a time history of acceleration up to an intermediate time,  $t$  (Fig. 23.10). Since the response spectrum stands for the maximum value (of velocity) up to the time of  $t$ , the obtained SV and consequently the SI value increases with time.



**Fig. 23.12** Time history of SI in Niigata Kawagishi-cho NS record



**Fig. 23.13** 1G shaking test on time history of SI .

Figure 23.11 illustrates an example of Port Island record in Kobe. It is therein seen that the SI value increases with time and achieves the ultimate value at around 16 s at which the maximum acceleration occurs as well (shown by arrows). The simultaneous occurrence of the ultimate value of SI and the maximum acceleration is found in the Niigata Kawagishi-cho record (Fig. 23.12) as well. It is further noteworthy that after the occurrence of the maximum acceleration, the period of the acceleration increased due to softening of ground and liquefaction. Thus, it seems that very small but still positive effective stress at those times made the shear modulus small as well which then turned to resonance and maximum acceleration. After this stage, the effective stress further decreased toward zero and the surface motion vanished. This idea is verified in shaking model tests. Figure 23.13 indicates that the maximum acceleration and the ultimate SI occur at 1.8 s, while the excess pore water pressure reaches 100% development after 2 s (the time scale in the pore pressure diagram is different from others). Thus, the SI value in liquefied ground is a product of resonance which occurs slightly prior to the onset of liquefaction. It is therefore reasonable to state that the subsurface displacement at the occurrence of SI follows a natural mode of the ground.

### ☛ 23.3 Immediate Detection of Subsoil Liquefaction by Using Spectrum Intensity (SI) – Principle

It is attempted by lifeline industries to detect occurrence of significant liquefaction in their service area immediately after a strong earthquake. It is intended to start an emergency action if liquefaction does occur and its magnitude is significant. Evidently a quick start of this emergency action is more efficient in damage mitigation; imagine leakage of gas from broken pipes.

First, SI greater than 30 or 40 cm/s is a good index of onset of liquefaction (Sect. 23.2). However, it cannot tell the extent of liquefaction-induced damage at all. It is therefore possible that the extent of damage is overestimated, leading to overreaction against minor liquefaction. Section 21.9 showed that the extent of damage is closely related to the thickness of liquefied and unliquefied layers. With this in mind, an attempt was made (Towhata et al. 1996) to assess the thickness of liquefied layers by using SI and  $A_{\max}$  which are recorded during a strong shaking.

Figure 23.14 illustrates the basic principle that the mode of displacement,  $u$ , of liquefied layer is similar to the fundamental mode of resonance (Sect. 23.2) which is a sinusoidal curve along the vertical axis. This mode is reasonable in particular at the moment when  $A_{\max}$  and SI are achieved immediately prior to the perfect loss of soil rigidity:

$$u = D_{\max} \sin \frac{\pi z}{2H}, \quad (23.8)$$

where  $D_{\max}$  denotes the amplitude of displacement at the surface, and  $H$  the unknown thickness of liquefied layer. Accordingly, the shear strain at the bottom ( $z = 0$ ) is given by

$$\gamma_{\text{liq}} = \left. \frac{\partial u}{\partial t} \right|_{z=0} = \frac{\pi D_{\max}}{2H}. \quad (23.9)$$

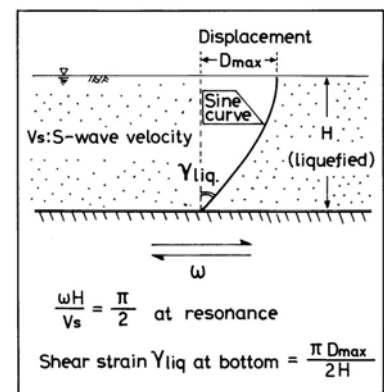
Since soil is liquefied, this strain is not very small. The present study chooses  $\gamma_{\text{liq}} = 0.01875$  as an evidence of liquefaction. Note that  $\gamma_{\text{liq}} = 0.01875$  is equivalent with the double amplitude (peak-to-peak) of axial strain of 0.025 (2.5%) in cyclic triaxial tests which is widely employed as the evidence of the onset of liquefaction. Hence, (23.9) gives the value of the thickness of liquefied layer,  $H$ ;

$$H = \frac{\pi D_{\max}}{2 \times 0.01875}. \quad (23.10)$$

It is important that the amplitude of displacement ( $D_{\max}$ ) is approximately given by

$$D_{\max} = \frac{2 \times \text{SI}^2}{A_{\max}}, \quad (23.11)$$

as shown in Fig. 23.15. By further considering the effects of surface unliquefied crust, Fig. 23.16 was obtained so that the thickness of liquefied layer can be easily assessed from the observed SI and  $A_{\max}$ .



**Fig. 23.14** Mode of displacement of liquefied layer without surface unliquefied crust

Figures 23.17 and 23.18 indicate a container of SI transducer which carries out the above-described procedure and a communication tower which sends the data to the head quarter.

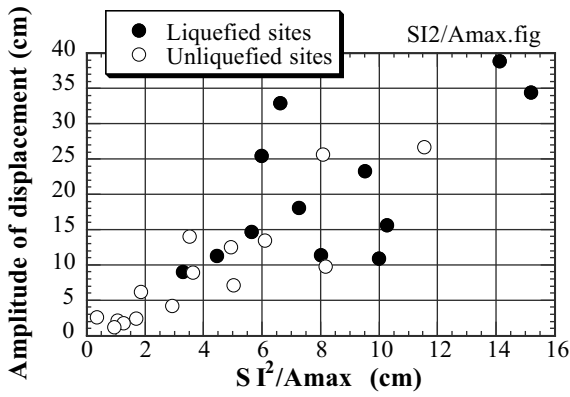


Fig. 23.15 Assessing displacement amplitude by using SI and  $A_{max}$

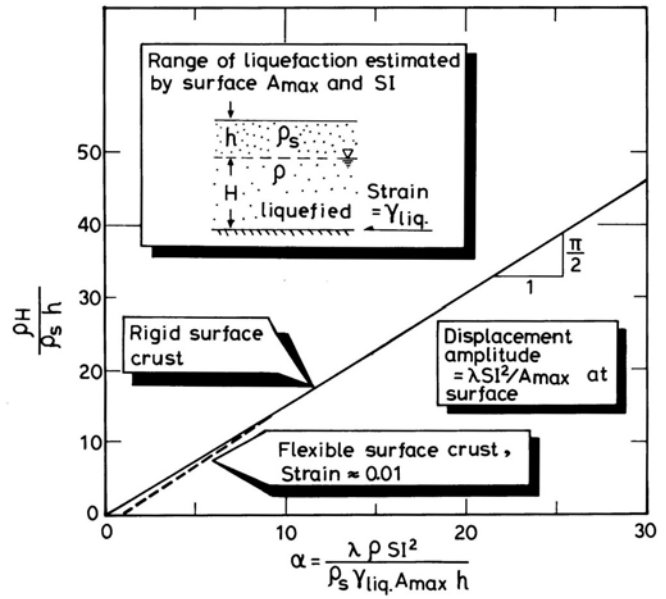


Fig. 23.16 Assessment of thickness of liquefied layer by using surface earthquake data

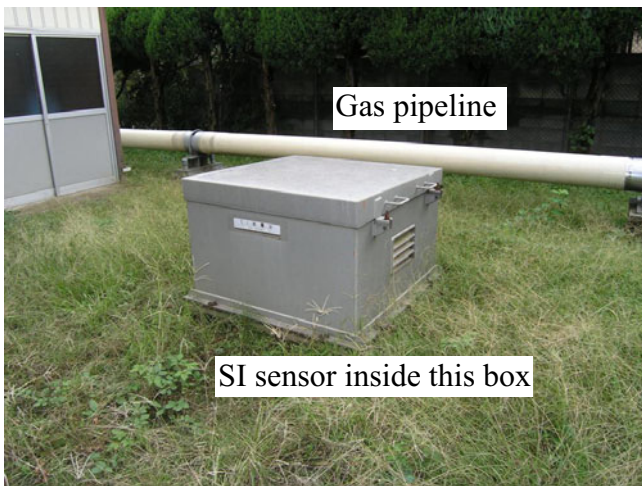


Fig. 23.17 Container of SI sensor

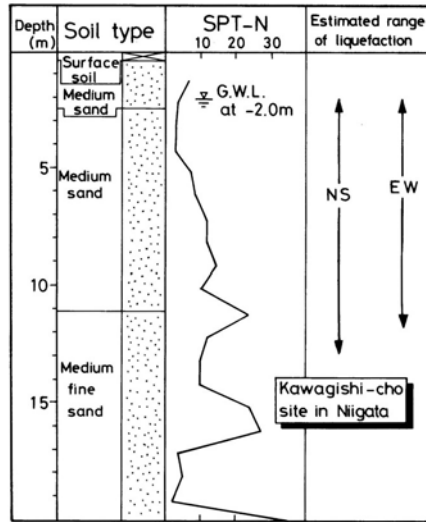


Fig. 23.18 Data transmission tower in Kodaira, Tokyo

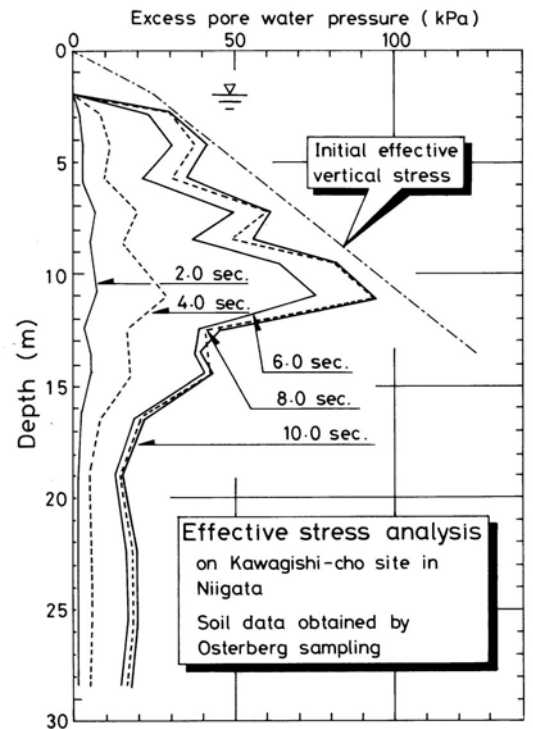


**23.4 Immediate Detection of Subsoil Liquefaction by Using Spectrum Intensity (SI) – Example**

The method for real-time detection of the extent of liquefaction (thickness of liquefied layer) is applied in this section to several case histories. Figure 23.19 shows an example of Kawagishi-Cho record in Niigata, 1964. Analyses of both NS and EW surface records suggest that liquefaction occurred from the ground water table down to the depth of 12 or 13 m. This assessment is compared with the results of effective stress analysis (YUS-AYUSA; Sect. 22.4) which was conducted by using data obtained from undisturbed soil samples. The calculated variation of maximum excess pore water pressure in Fig. 23.20 suggests that liquefaction occurred over the assessed range of depth.



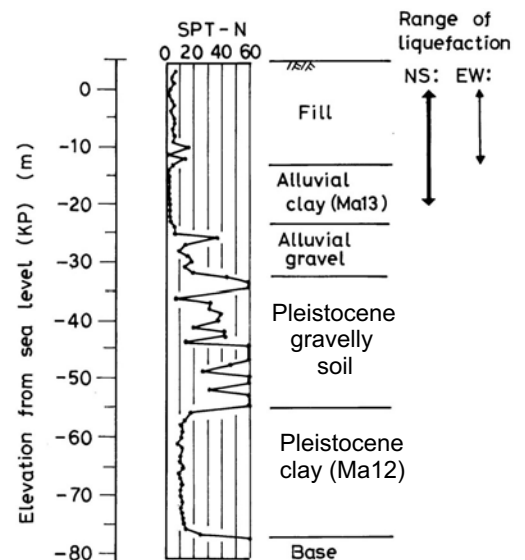
**Fig. 23.19** Assessed range of liquefaction at Niigata Kawagishi-Cho site



**Fig. 23.20** Excess pore water pressure distribution in Kawagishi-Cho deposit calculated by effective stress analysis

A more direct examination of the proposed method is made of the Port-Island record in Kobe. Figure 23.21 indicates the ranges of liquefaction from NS and EW records, respectively. EW record implies that only the artificial masa-soil deposit (decomposed granite) liquefied. In contrast, the liquefied range obtained by NS motion includes the Ma-13 alluvial clay deposit which is unlikely to liquefy. This overestimated extent of liquefaction has an important implication:

- In case that the real extent of liquefaction is substantial, the real strain,  $\gamma_{liq}$ , is greater than 0.01875. This greater strain reduces the thickness of liquefied layer to a more reasonable extent.
- Therefore, a necessary caution is that the assessed thickness of liquefied layer should be reduced to that of loose sandy deposit, at maximum, if the thickness includes such unliquefiable soils as clay, dense sand, and pleistocene gravel.
- The modification of the assessed thickness is possible if the soil profile is available. Therefore, the present method should be accompanied by boring data (subsoil investigation).



**Fig. 23.21** Initial assessment of thickness of liquefied layer at Port Island site in Kobe, 1995

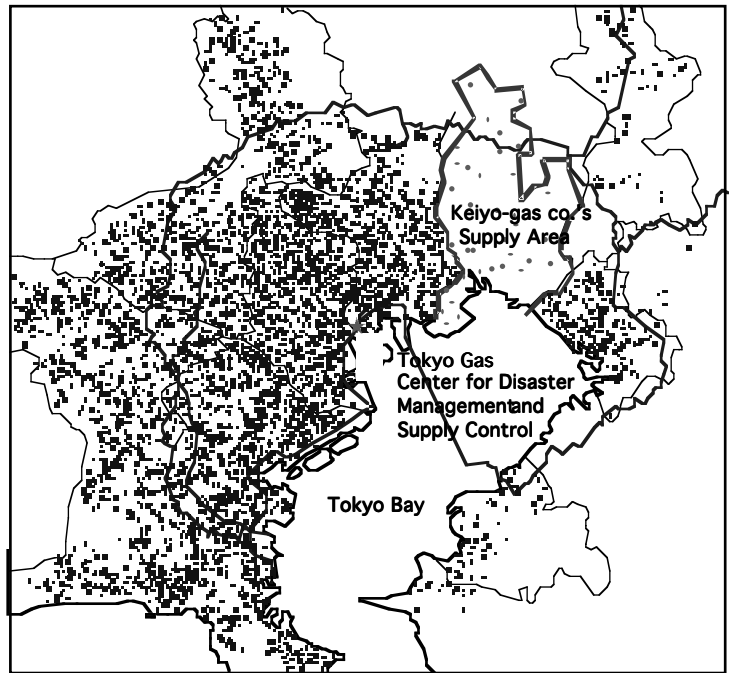
There are attempts by other people to detect liquefaction by using the elongation of predominant frequency of earthquake motion due to softening of subsoil. At best, they can detect the onset of

liquefaction. It is unlikely, however, that they can assess the extent of liquefaction which is very important in practice. This poor situation occurs because they are watching digital records only through a computer, without working in soil laboratory.

The SUPREME system for seismic safety of urban gas supply network (Shimizu et al. 2006) has deployed 3,700 stations for immediate detection of pipeline damage and liquefaction. Their locations are illustrated in Fig. 23.22. The thickness of liquefied soil,  $H$ , is assessed immediately by using a formula which is a minor modification of (23.10):

$$H = \frac{\pi(D_{\max} - 5 \text{ cm})}{2 \times \sqrt{0.01875^2 - 0.01^2}}. \quad (23.12)$$

A quick decision is made based on the record whether or not gas supply is stopped to areas where significant damage in embedded pipelines is likely.



**Fig. 23.22** Locations of 3,700 earthquake observation stations of SUPREME system in and around Tokyo (Shimizu et al., 2006)

### List of References in Chapter 23

- Hosokawa, N., Watanabe, T., Shimizu, Y., Koganemaru, K., Ogawa, Y., Kitano, T. and Isoyama, R. (2001) A study on damage estimation formula considering ground conditions for low-pressure screw-joint pipes in great earthquakes, Proc. 26th JSCE Earthq. Eng. Symp., Vol. 2, pp. 1333–1336 (in Japanese).
- Housner, G.W. (1961) Vibration of structures induced by seismic waves Part I. Earthquakes, *Shock and Vibration Handbook*, ed. C.M. Harris and C.E. Crede, McGraw-Hill, pp. 50-1–50-32.
- Shimizu, Y., Yamazaki, Y., Yasuda, S., Towhata, I., Suzuki, T., Isoyama, R., Ishida, E., Suetomi, I., Koganemaru, K. and Nakayama, W. (2006) Development of real-time safety control system for urban gas supply network, *J. Geotech. and Geoenv. Eng.*, ASCE, Vol. 132, No. 2, pp. 237–249.
- Towhata, I., Park, J.K., Orense, R.P. and Kano, H. (1996) Use of spectrum intensity in immediate detection of subsoil liquefaction, *Soil. Found.*, Vol. 36, No. 2, pp. 29–44.

# Chapter 24

## Permanent Displacement and Deformation of Liquefied Subsoil



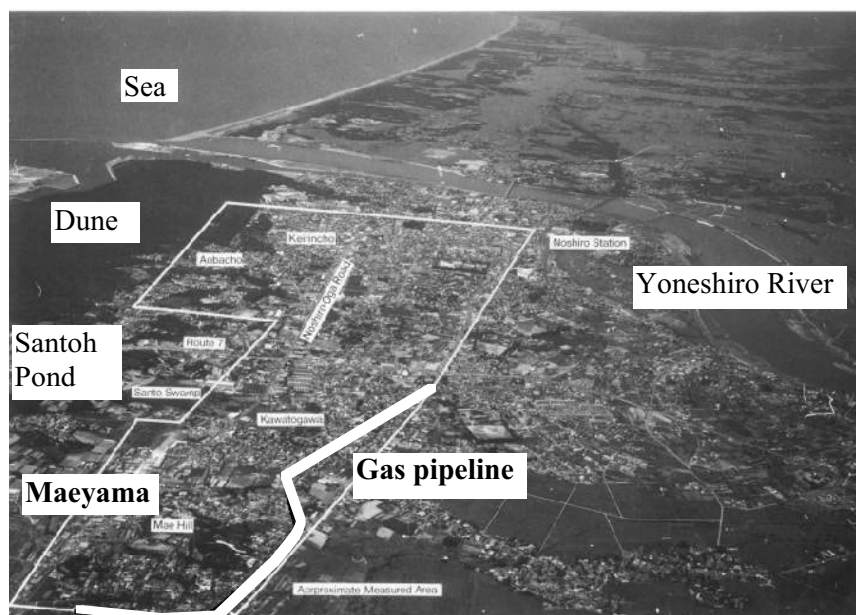
Phra Prang Sam Yot, Lopburi, Thailand.

This masonry Hindu shrine was made of laterite blocks and is subjected to weathering and disintegration today due to differential settlement of foundation which is made of a timber raft.

### 24.1 Lateral Displacement of Liquefied Subsoil

In 1984 a permanent lateral displacement was detected in a gentle slope in Noshiro City where a substantial liquefaction developed at the time of the 1983 Nihonkai Chubu earthquake (Hamada et al. 1986). Since the displacement was significant, exceeding 4 m at maximum, gas pipelines embedded in the area were broken in such manners as separation at connection and bending at curved portions. Figure 24.1 demonstrates an air photo of Noshiro City where liquefaction and lateral displacement occurred. Higher places in this photograph are sand dunes, including Maeyama. Liquefaction occurred in low places which used to be swamps. Dune sand fell into water and formed liquefaction-prone young loose water-saturated deposits. Liquefaction and lateral displacement occurred in dune hill slopes as well where the gradient was only a few percent and had never been a target of slope instability.

Prediction and mitigation of lateral displacement have attracted engineering concerns since then because of the fact that it strongly affects the function of buried lifeline networks which bear essential importance in the society of recent times.



**Fig. 24.1** Air photo of Noshiro City where liquefaction-induced ground displacement occurred (Association for Development of Earthquake Prediction, Tokyo)

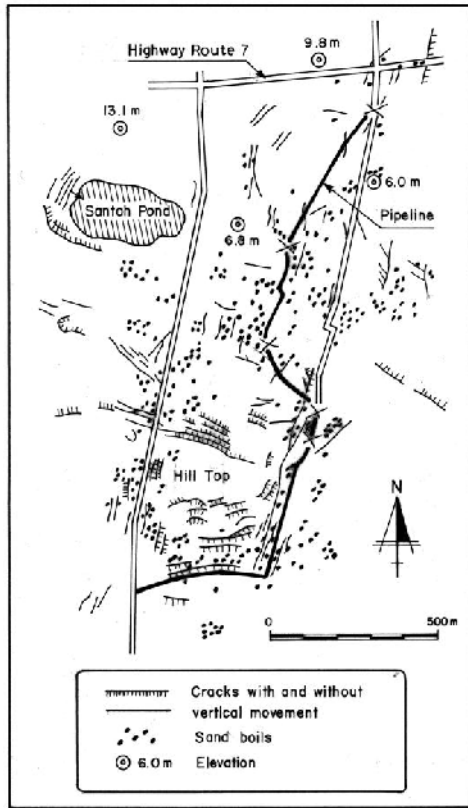
Figure 24.2a shows the location of sand boiling and surface cracks in the Maeyama area (bottom left in Fig. 24.1). Many sand boiling occurred in the low land where there was a liquefaction-prone deposit. Tension cracks on the contrary occurred at high places where ground water table was deep. Figure 24.2b indicates the distribution of the permanent displacement in Noshiro City which was detected by comparing two air photos taken a few years before and immediately after the earthquake (Hamada et al. 1986). The difference of locations of many objects before and after the quake is the displacement induced by liquefaction. The maximum displacement was detected around the top of Maeyama Hill where tension cracks were predominant. Note that the directions of displacement and cracks are perpendicular to each other. In contrast, the displacement was null at the lower place (Nagasaki in Fig. 24.2b) because two downward displacement from the north (Tagomukai) and the south (Maeyama) collided with each other.

Figure 24.3 was drawn by using the same data to show the permanent displacement in several cross sections in Noshiro City. Note that the vertical component of displacement as detected from two air photos is less accurate than the horizontal component. Major findings in these figures are as following.

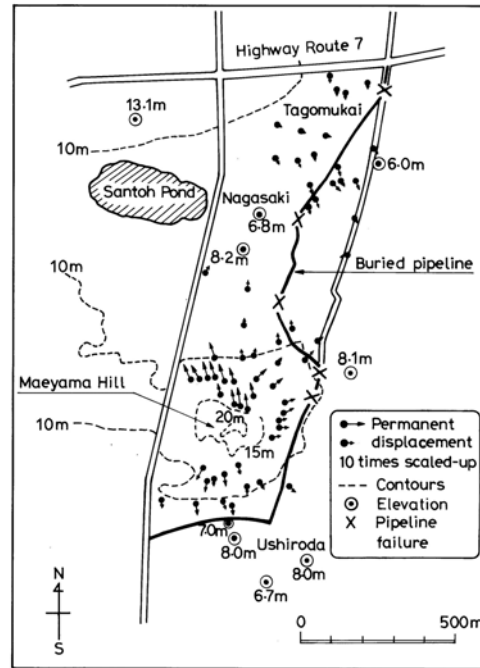
- (Obs. 1)** Many tension cracks are detected near the top of the liquefied slope. They are perpendicular to the direction of ground displacement.
- (Obs. 2)** The permanent displacement is oriented downwards along the slope, suggesting the important influence of gravity.

- (Obs. 3) Displacement is maximum at the top of the slope.
- (Obs. 4) Conversely, the displacement is negligible at the bottom of the slope.
- (Obs. 5) Subsidence is predominant near the top of the slope, while uplift is important in the lower portion of the slope. Note that the vertical displacement is much smaller than the horizontal component.

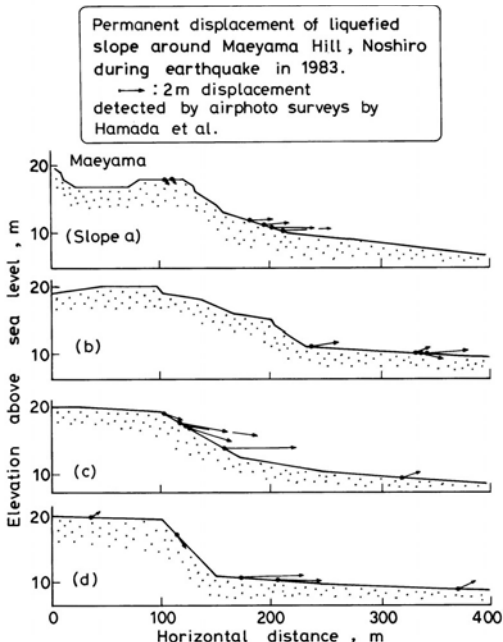
(a) Location of sand boils and cracks.



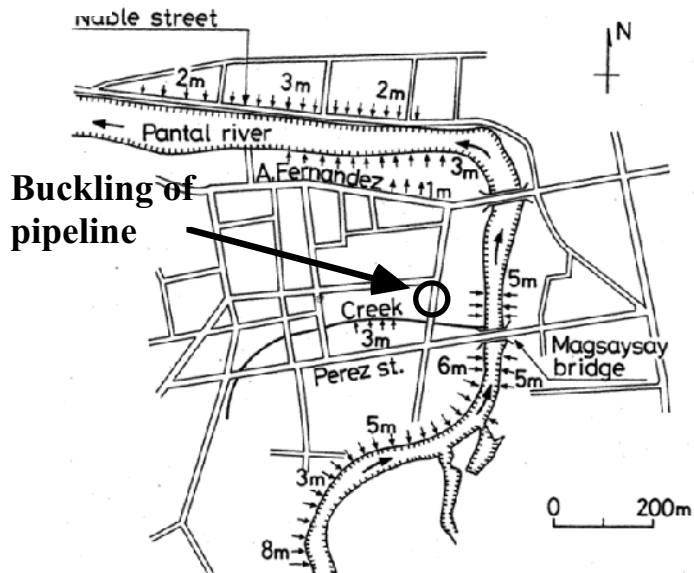
(b) Permanent displacement vectors.



**Fig. 24.2** Permanent displacement around Maeyama hill in Noshiro City (data by Hamada et al., 1986)



**Fig. 24.3** Permanent displacement in vertical cross sections of subsoil



**Fig. 24.4** Lateral displacement of ground in Dagupan City (drawn based on Wakamatsu et al., Hamada et al., 1991; Wakamatsu et al., 1991)

Another example of liquefaction-induced lateral displacement occurred in Dagupan City of the Philippines. Figure 24.4 reveals the lateral displacement of ground in Dagupan City (Wakamatsu et al. 1991; Hamada et al. 1991). The lateral displacement occurred toward the Pantal River where the ground surface was lowest. The site of pipeline buckling (Fig. 17.24) is situated within the area of lateral displacement.

24.2 Lateral Displacement of Quay Wall Induced by Subsurface Liquefaction

Liquefaction induces lateral displacement in a variety of situations. Figure 24.5 illustrates a distortion of a gravity-type quay wall (重力式護岸). A heavy concrete caisson box filled with sand was pushed toward the sea over a distance of several meters. The pore water pressure development in the backfill increased the seismic earth pressure, while the shear resistance in the foundation decreased, leading to this significant wall distortion. It is important in Fig. 24.5, however, that there is no boiled sand immediately behind the wall, which suggests that pore pressure did not fully develop to liquefaction near the wall. Such a wall movement can cause tensile deformation in the backfill area (Fig. 24.6). Many cracks at the ground surface implies that significant tensile deformation may affect underground structures such as piles (Fig. 24.7) and pipelines. The significant lateral displacement around the Port Island in Kobe is shown in Fig. 24.34.



Fig. 24.5 Lateral displacement of caisson quay wall in Port Island, Kobe, in 1995



Fig. 24.6 Tensile deformation at surface of backfill soil (Nishinomiya Harbor in 1995)



Fig. 24.7 Damage of piles caused by lateral soil flow (by Prof. K. Tokimatsu)

A similar damage occurred to a sheet-pile quay wall. Fig. 24.8 shows a distorted shape of a wall in Akita Harbor (Nihonkai Chubu earthquake in 1983). Since the top of the wall was connected by tie rods (鋼棒) to an anchorage (アンカー、控え工とも; see Fig. 24.9), it did not move laterally, and the bottom did not either, because the bottom penetrated into unliquefied bearing layer. Consequently, the middle of the wall deformed substantially outwards. This wall distortion led to the movement of the backfill soil and consequently the ground surface subsided tremendously. This wall was repaired after the quake by installing a new wall in front of the damaged one.



Fig. 24.8 Substantial damage of sheet-pile wall at Akita Harbor in 1983 (by Dr. K. Wakamatsu)

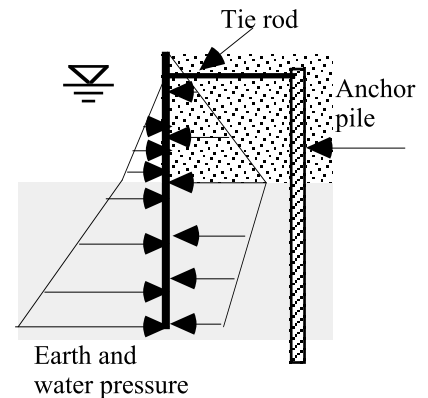


Fig. 24.9 Schematic diagram of sheet-pile wall supported by anchorage

Ishihara et al. (1996) studied the variation of horizontal ground displacement behind quay walls (Fig. 24.10). It was found by them that the displacement was maximal immediately behind the walls, decreasing gradually with the distance from the walls. The area of lateral displacement, however, ranged over 100 m. It should be hence understood that underground structures resting inside this unstable area are

somehow affected by this soil movement, although the extent of influence decreases as the distance from the quay wall increases.

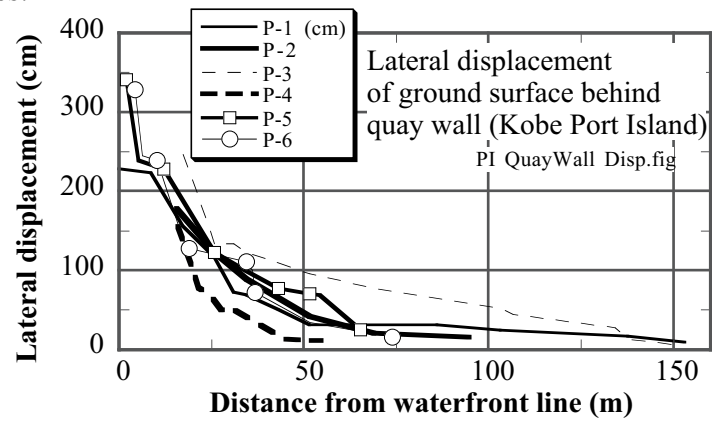


Fig. 24.10 Variation of lateral displacement with distance from unstable gravity quay wall in Kobe Harbor (Ishihara et al. 1996)

24.3 Steady State and Static Liquefaction

Cyclic loading induced by earthquakes is not the only one agent to cause liquefaction. A static load is also able to generate liquefaction of loose sand. Figure 24.11 illustrates the stress-strain and stress-path behaviors of very loose Toyoura sand under undrained conditions. Being different from cyclic behavior (Sect. 18.7), this sand exhibits softening after the peak shear stress is attained. Hence, it is possible that a small stress increment in situ which exceeds the peak stress state leads suddenly to an extremely large deformation. This phenomenon is called static liquefaction or flow failure.

Offshore land filling is sometimes vulnerable to static liquefaction because deposition of sand in water makes very loose packing of sand grains which is represented by relative density around 40% or less. Figure 24.12 manifests an example of this phenomenon which occurred in an artificial island in the Beaufort Sea off the Canadian arctic region, where a newly constructed sandy island started to collapse uniformly in all the directions without the effect of earthquake or storm. Similar failure frequently occurs in the seabed slope off a big river mouth where the rate of sedimentary deposition is so rapid that the rate of consolidation and development of shear strength cannot catch up with the increase of shear stress; for example, Bohai Bay off the Yellow River 黄河河口沖の渤海湾 (Keller et al. 1990), Mediterranean Sea slope off Var River near Nice, France (Seed et al. 1988), Fraser River mouth, British Columbia of Canada (McKenna et al. 1992), and the Mexico Bay off the Mississippi river mouth (Prior and Coleman, 1982). Cyclic stress induced by wave action during storms helps develop this type of disaster.

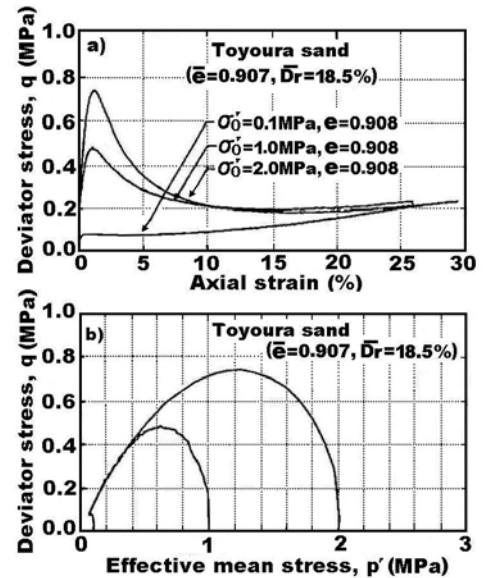


Fig. 24.11 Undrained softening of very loose Toyoura sand (Verdugo and Ishihara, 1996)

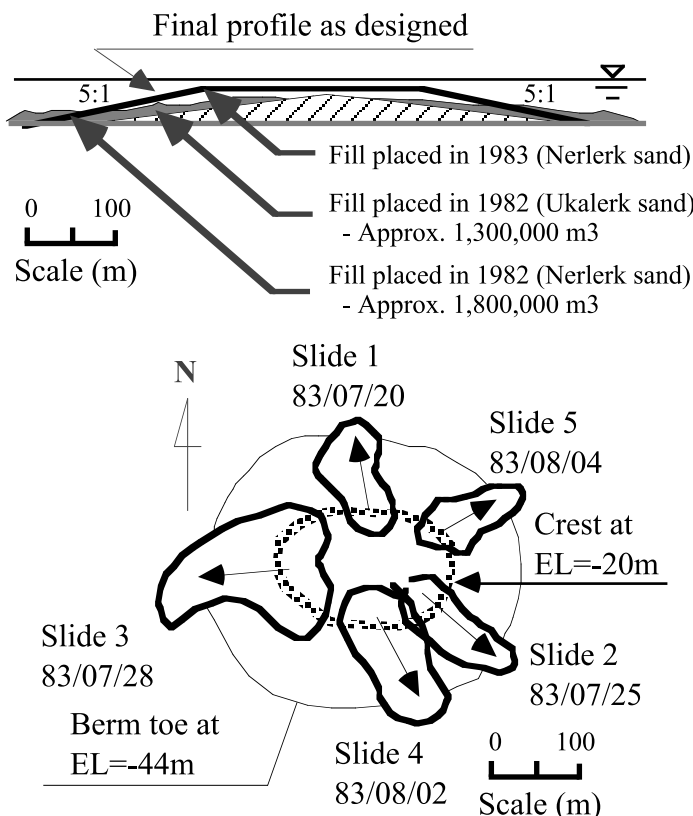


Fig. 24.12 Failed shape of Nerlerk Berm (after Sladen et al. 1985)

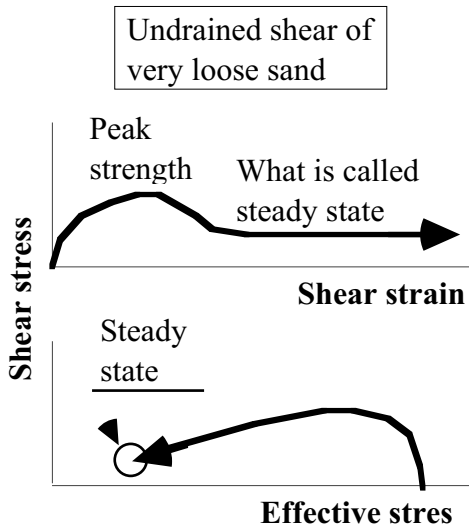
Figure 24.13 shows a consequence of liquefaction of backfill sand that was made for an underground fuel tank. Probably the backfill sand was not well compacted. When ground water came into the backfill, this sand became saturated and highly vulnerable to static liquefaction. When one engineer came to inspect this site alone, liquefaction did occur without earthquake, the embedded tank floated upward, and the backfill sand flowed into the base of the tank (回り込み).



Fig. 24.13 Static liquefaction of backfill and flotation of underground fuel-storage tank



One of the approaches to interpret and predict the large deformation of loose sandy ground is the one based on “steady state.” When sand is sheared in undrained manners, large slip deformation can occur without increase or decrease of shear stress level (Fig. 1.23). Since no drainage occurs, the volume of sand is constant. This state is called “residual” or “steady-state.” A conceptual sketch in Fig. 24.14 illustrates that softening of stress after the peak strength is associated with very rapid decrease in the effective stress (increase in excess pore water pressure).

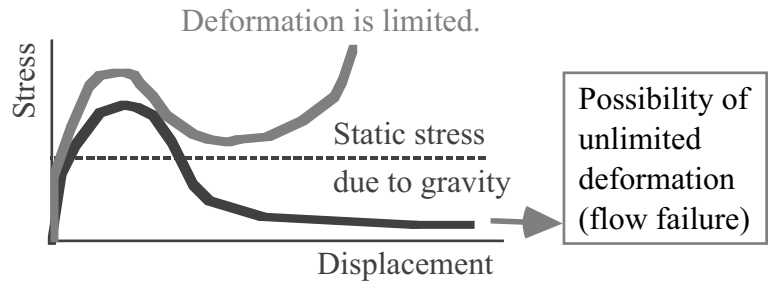


**Fig. 24.14** Conceptual illustration of stress softening toward large strain in undrained shear

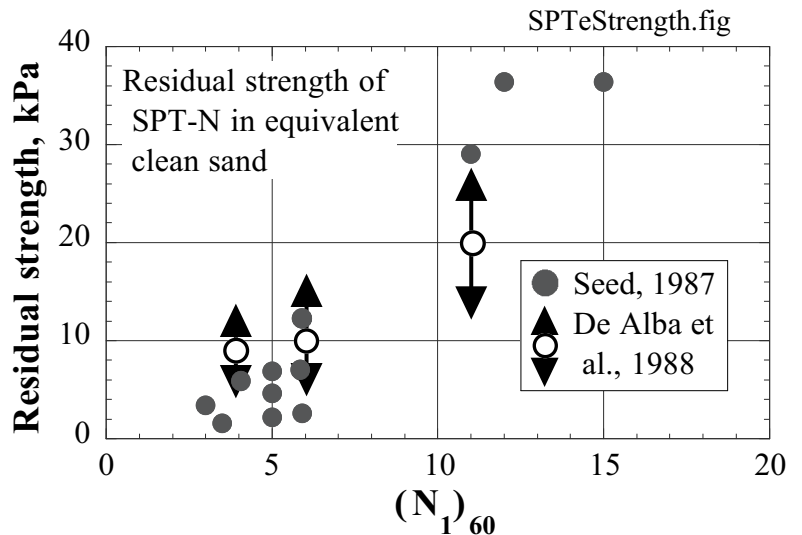
Figure 1.23 presented an example of undrained shear data in which the residual (steady state) strength decreased as the sand became looser. Figure 24.11 showed that the residual strength is similar when the initial confining stress is different but the soil density is identical. Thus, the magnitude of the steady state strength depends on density, but is independent of the initial confining pressure.

The theory of steady state supposes that an extremely large deformation (flow-type failure) is possible to occur when the static stress due to gravity is greater than the steady-state strength (Poulos et al. 1984; Whitman, 1985). As illustrated in Fig. 24.15, in contrast, the deformation is limited when the static stress is lower than the residual strength (Ishihara, 1993). In such a situation, deformation is induced only by cyclic application of stress during an earthquake.

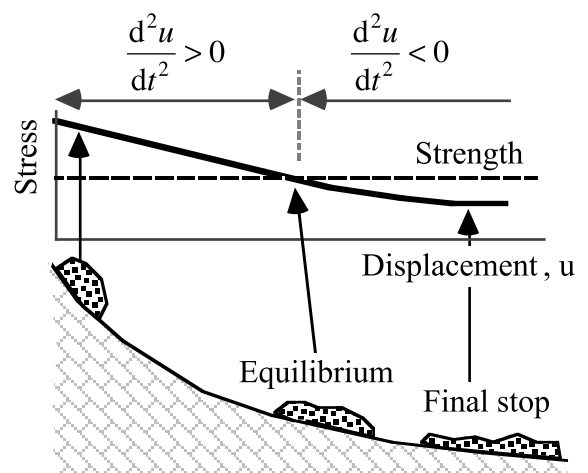
Seed (1987) together with De Alba et al. (1988) analyzed past case histories of flow failure of soil mass (for example, see dam failure in Fig. 17.26). They determined the residual strength of soil by assuming force equilibrium in the final configuration. Their results in Fig. 24.16 show that the strength increases with SPT-*N* values. There are, however, substantial uncertainty. Wride et al. (1999) reviewed the data originally used by Seed and his colleagues. Although



**Fig. 24.15** Use of steady-state strength for undrained stability analysis of loose sandy ground



**Fig. 24.16** Empirical correlation between SPT-*N* and residual strength of sand (after De Alba et al., 1988)



**Fig. 24.17** Variation of gravity-induced stress with displacement

they finally obtained similar results, it was found that there are still much uncertainty about determining the residual strength. It may be stated that the determination of the steady-state strength from the configuration of final stop of movement (Fig. 24.17) may be an underestimation. As illustrated in Fig. 24.17, the gravity-induced stress varies with flow displacement. The equilibrium of stress and strength is achieved at an intermediate point, after which the strength is greater than the stress. Hence, the stress is lower than the true strength. This point may not be very important, however, as compared with the complicated and uncertain nature of the problem.

Olson et al. (2000) reanalyzed therefore a dam failure which was triggered by static forces without seismic effects. By conducting Newmark-type sliding analysis (Sect. 12.1) to take into account the dynamic issues as mentioned above, it was found that the assessed shear strength of the dam body was consistent with Fig. 24.16.

There is a big discussion about the significance of steady-state strength in liquefaction problems. Major controversial points are (1) significant variation of steady-state strength for a minor change in density (Yoshimine et al. 1998a and b), (2) reduction of soil strength by on-going shaking, and (3) anisotropy of steady-state strength (Yoshimine et al. 1998a and b).

Concerning the on-going shaking, Meneses et al. (1998 and 2000) carried out torsion shear tests in which one of the shear stresses (torsional stress or stress difference,  $\sigma_v - \sigma_h$ ) was increased monotonically (strain-controlled shear) and the other was varied cyclically. An example of test results (Fig. 24.18) shows that the effective stress decreased during the stress superposition, leading to very low shear stress level. This situation stopped when the stress superposition was ceased, and more dilatant behavior (increase of effective stress) started.

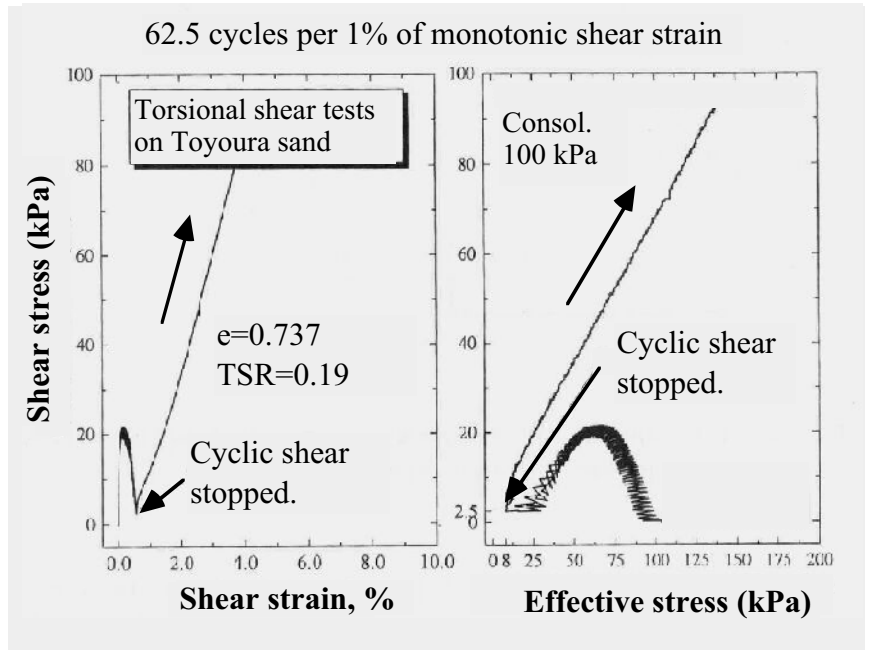


Fig. 24.18 Effects of complementary shear stress on undrained monotonic behavior of sand (Meneses et al., 1998)

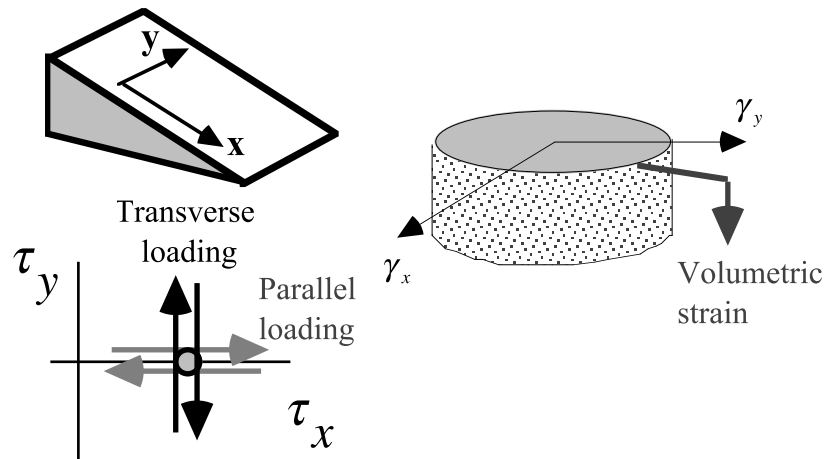


Fig. 24.19 Significance of superimposing two shear stress components

Since the above finding was subject to discussion, a more convincing test was conducted by using a two-directional shear device (Fig. 19.38). The stress condition produced by this device is illustrated in Fig. 24.19. The results of drained shear on even very dense sand (Fig. 19.39) clearly indicates that sand volume contracted due to stress superposition. This is equivalent with higher pore water pressure and lower shear strength in undrained shear. Thus, the idealization of stress condition by monotonic shear, while ignoring the continuous cyclic shear, in the steady-state theory is an oversimplification.

## 24.4 Small Shaking Table Tests on Lateral Displacement

One of the limitations lying in case history studies in Sect. 24.1 is that the subsurface deformation cannot be observed. This problem is solved by running shaking table tests on model sandy deposits. The employed sand density has been typically 40–60%. Figure 24.20 illustrates one of the earliest attempts in which the length of the soil container was only one meter. For details, see Sasaki et al. (1992) and Towhata et al. (1992).

In Fig. 24.20, a model of liquefied deposit overlain by an embankment was shaken laterally. The shaking continued until the permanent lateral displacement stopped, indicating the maximum possible displacement. The top of the fill sank, while its toe uplifted. This nature of displacement is identical with the experience in Noshiro City (Fig. 24.2). Consequently,

the ground surface became level. Since the soil movement was ultimately stabilized with a shape of level surface, there seems to be no shear resistance in the liquefied sand. It is reasonable, therefore, to say that the liquefied sand behaves similar to liquid without shear strength.

The deformation and displacement of liquefied sand were visualized by employing a grid of dyed (colored) sand 染料で色付けした砂. The use of colored sand is good because the colored sand has no rigidity and is of approximately the same density as the surrounding sand. These features enabled the colored sand to move together with the liquefied ground without disturbing the ground deformation. Embedding noodle may be useful for the same purpose. After several tests, however, the organic materials of noodle decay and start to produce bad smell.

The extent of shear distortion was substantial. It is important that the lateral displacement is maximum at the surface, while it is negligible at the base.

The model fill in Fig. 24.20 liquefied because it absorbed water by meniscus action and became nearly water saturated. A dry fill, in contrast, was prepared in Fig. 24.21 by placing a layer of gravel at the base of the fill and preventing water absorption. Upon shaking, the dry fill maintained its rigidity at least to some extent. After liquefaction, the top of the fill was still seen above the ground surface. This situation is similar to a ship floating in water. The unit weight of the dry fill was lighter than that of the liquefied sand. Hence, the fill was able to float in the liquefied layer. This accounts for the empirical finding that the subsidence of river dikes during past earthquakes does not exceed 75% of the original height (Figs. 17.36 and 17.37).

In addition to the findings in case history studies (Sect. 24.1), the knowledge learned from Figs. 24.20 and 24.21 are summarized as what follows:

**(Obs. 6)** Liquefied sand behaves similar to liquid.

**(Obs. 7)** The lateral displacement in liquefied layer is maximum at the surface, while negligible at the base.

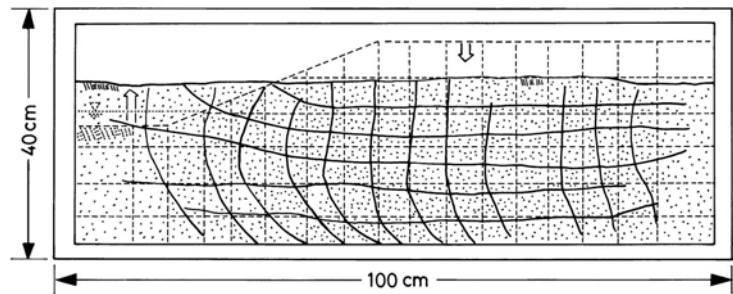


Fig. 24.20 Deformation of model with liquefied fill

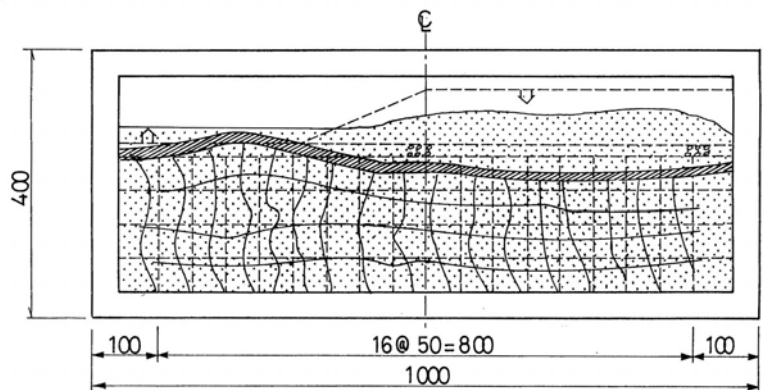


Fig. 24.21 Deformation of model with dry fill

**24.5 Role Played by Gravity**

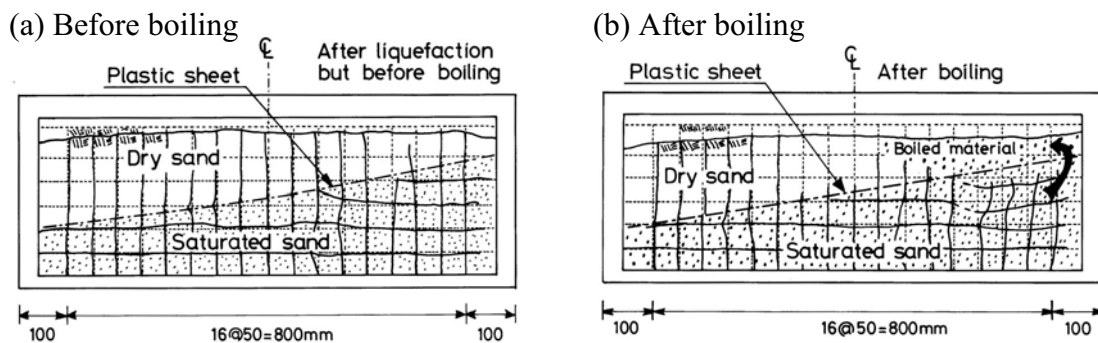
Sections 24.1–24.3 already illustrated that a liquefied slope moves downward. In that context, the effects of gravity are apparent. It is intended in this section to show more precisely the role of gravity.

The model in Fig. 24.22 consists of a loose water-saturated sand at the bottom and a dry layer at the top. A plastic sheet was placed at their interface in order to prevent water migration into the dry layer. Although the top of the saturated sublayer was inclined, the ground surface was level.

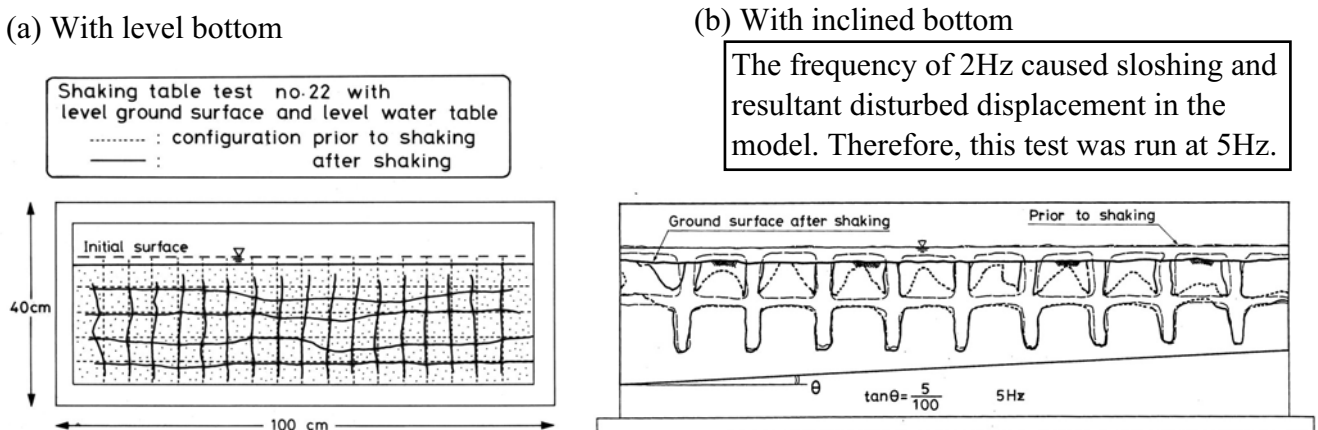
At the onset of liquefaction (Fig. 24.22), the lower layer developed a significant strain amplitude. The residual deformation, however, was negligible. This is because the ground surface was level, making the total overburden pressure approximately uniform in the horizontal direction (different unit weights of dry and saturated sands are neglected in this discussion). Accordingly, there was no static shear stress that could induce lateral displacement. Similar to Darcy’s law, more precisely, the soil movement seems to be controlled by (the total head) = (elevation head) + (total overburden pressure head), which is constant in the horizontal direction in Fig. 24.22.

After a while, the plastic sheet at the interface suddenly got punctured at the top of the inclined interface. The pore water started to boil through this puncture and the excess pore water pressure dropped, thereby decreasing the total stress as well. Consequently, both water and sand in the sublayer moved toward this place and permanent displacement was generated (Fig. 24.22b). Thus, the soil flow is governed by the gradient of the total head.

Figure 24.23 shows test results on level ground models. Whether or not the bottom was inclined, there was no permanent displacement; a level ground does not move laterally, although it shakes. Note that the hydraulic gradient is null in a level deposit. Thus, a liquefied layer behaves similar to liquid (Obs. 6).



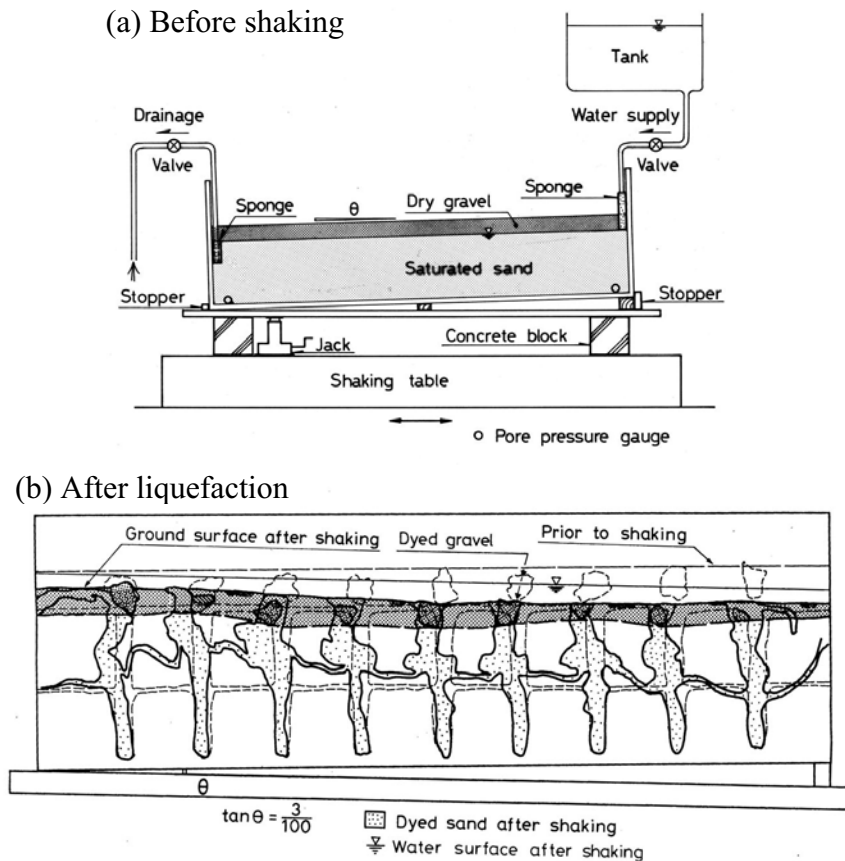
**Fig. 24.22** Deformation of liquefied subsoil overlain by dry layer



**Fig. 24.23** Displacement of level subsoil after liquefaction

**24.6 Behavior of Surface Dry Crust**

There is always a dry and unliquefiable layer at the surface above the ground water table. Its role played in permanent lateral displacement is going to be studied here.



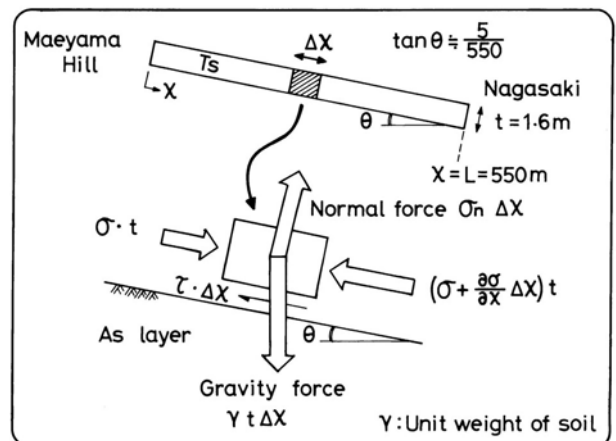
**Fig. 24.24** Deformation of subsoil with gravelly surface crust

Figure 24.24a indicates a model ground which is inclined and has a gravelly unliquefiable crust at the surface. The surface gravel was colored. Water was supplied at the upper lateral boundary and drained out from the lower end, causing a realistic seepage flow in the lateral direction. Upon liquefaction, colored gravel at the surface indicated that both liquefied sand and surface gravel layer moved together without slip at their interface (Fig. 24.24b). Moreover, the gravelly layer was compressed in the lateral direction. Since this layer did not liquefy, it maintained some rigidity, resisting against its lateral compression. Hence, the liquefied subsoil could not flow so freely as in the case without a surface crust. This is a constraint to lateral displacement made by the surface crust.

**(Obs. 8)** The unsaturated layer at the surface does not liquefy. It moves together with the liquefied subsoil without slip surface at the interface.

Since the liquefied subsoil has no significant shear resistance, the force equilibrium of the surface layer is studied approximately without paying attention to the shear stress exerted by the subsoil. In Fig. 24.25, the force equilibrium in the lateral “x” direction is given by

$$\frac{d\sigma}{dx} = \frac{d}{dx} \left( -E \frac{dU}{dx} \right) = \gamma \sin \theta, \quad (24.1)$$



**Fig. 24.25** Model of deformation in surface dry crust

in which  $U$  denotes the lateral displacement,  $\sigma$  the lateral normal stress,  $E$  the elastic modulus,  $\gamma$  the unit weight, and  $\theta$  the slope angle. By considering boundary conditions of zero displacement at the bottom of a slope ( $x = L$ ) and zero stress (open crack,  $E dU/dx = 0$ , see Fig. 25.14) at the top of a slope ( $x = 0$ ), (24.1) is integrated to derive

$$U = \frac{\gamma \sin \theta}{2E} (L^2 - x^2), \quad (24.2)$$

which is a very simple prediction of permanent lateral displacement. This idea has been extended to a three-dimensional prediction of permanent displacement (Towhata, 1986).

Although the subsoil is considered free of shear resistance after liquefaction, actually there is small shear strength in it. This strength is able to make the displacement continuous (no slip) between the surface crust and the sublayer.

In the early stage of studies on liquefaction-induced ground displacement, several empirical formulae were proposed based on regression analysis on the field-measured displacement and local soil conditions as well as topography and earthquake intensity. For example, Hamada et al. (1986) proposed

$$\text{Displacement (m)} = 0.75 H^{0.25} \theta^{0.33}, \quad (24.3)$$

in which  $H$  is the thickness of liquefied subsoil (m) and  $\theta$  (%) the greater gradient (%) of surface or bottom of liquefied layer. More elaborate formulae have been proposed by Youd and Perkins (1987), Bartlett and Youd (1995), and Youd and Perkins (1987) and Youd et al. (2002). Those formulae are convenient and equivalent with (24.2). Note, however, that they cannot take into account the two- or three-dimensional topography (Sect. 24.4). Hence a level ground adjacent to a liquefied slope is considered to have null displacement in spite of a clear evidence of displacement in Fig. 24.20. Furthermore, those formulae cannot take into account the human efforts to mitigate the displacement by compacting soil or construction of underground walls (Sect. 26.3).

## 24.7 Shaking Table Tests on Lateral Soil Displacement

Since the aforementioned model tests were conducted in a very small container, its validity was not clear. In this respect, a series of model tests were carried out at the Public Works Research Institute with the maximum size of 6 m in length (Sasaki et al. 1992).

Among eight tests, Fig. 24.26 indicates a test conducted on an axisymmetric 軸対称 model (more precisely, half of an axisymmetry). A circular and unliquefiable fill of a cone shape was constructed upon a loose water-saturated layer and was subjected to shaking in the designated direction. Except near the diameter of the circular fill, where a friction with the side wall prevented soil movement, the lateral displacement occurred in an approximately radial direction. Thus, the effects of gravity is more important than the inertia force which occurred only in the shaking direction. This findings is consistent with the radial displacement around the top of Maeyama Hill (Sect. 24.1).

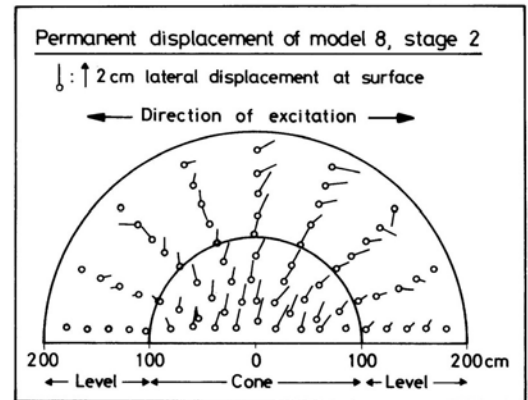


Fig. 24.26 Permanent displacement of axisymmetric model

(Obs. 9) The permanent displacement is caused by the gravity force. The cyclic inertia force triggers liquefaction but does not affect the displacement significantly.

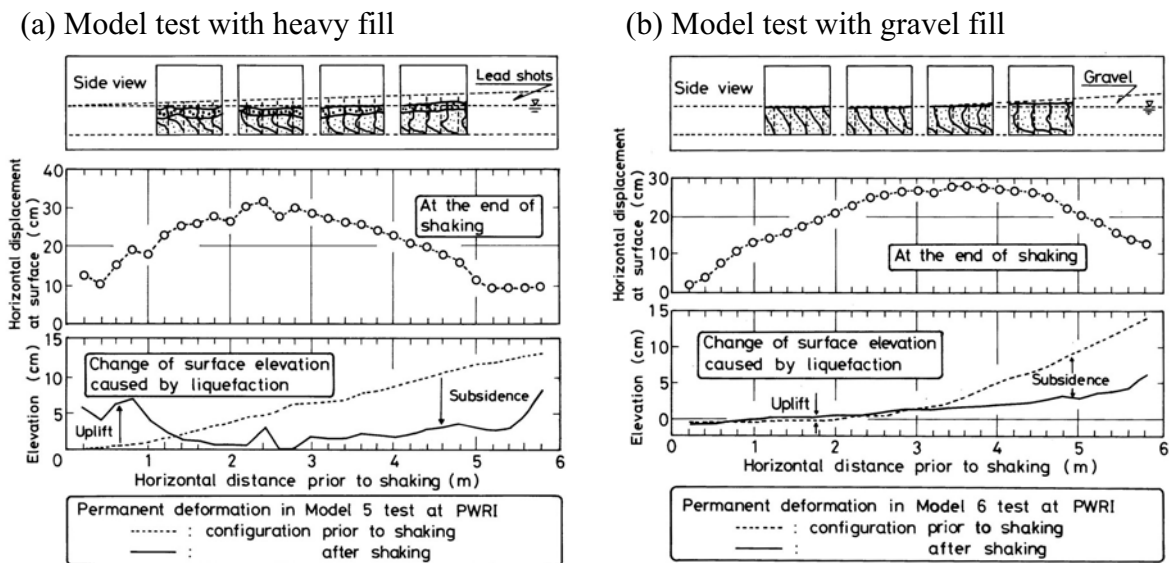


Fig. 24.27 Permanent displacement of model slope of big size (Sasaki et al. 1992)

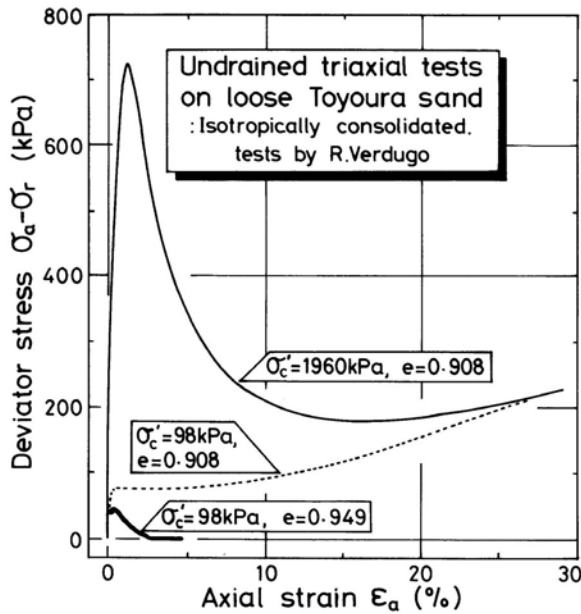
The models in Fig. 24.27 measure 6 m in length. The deformed shape in the figures validates the knowledge obtained by small shaking table tests. The lateral displacement increases toward the surface, displacement is continuous between the fill and the subsoil, and the liquefied soil moves from beneath the slope toward the toe, in accordance with the total head gradient.

It is important in Fig. 24.27b that the left half of the liquefied layer moved laterally as well, although its surface was level. This fact does not conflict against Fig. 24.23 in which a level deposit did not move. In the present case, a nearby fill sank and pushed subsoil laterally.

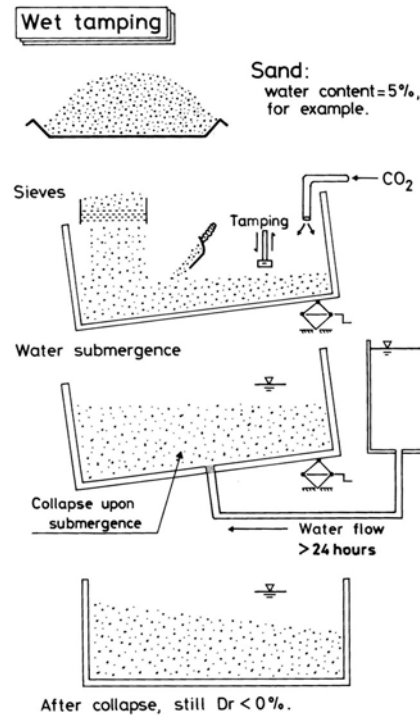
(Obs. 10) The lateral displacement depends not only on the local soil conditions and topography at the concerned point but on the global conditions in the surrounding area.

**24.8 Need for Tests on Extremely Loose Sandy Deposits**

Loose sandy deposits insitu 原位置 has normally a relative density ranging from possibly 35% up to 60%. The relative density around 35% is the minimum density achieved by water sedimentation in which sand grains fall slowly in water and their speed is limited by viscosity of water (Stokes law). From the viewpoint of similitude 相似則, it has been believed that shaking table tests should be conducted on models of the same density as insitu. When the liquefaction and large deformation are concerned, however, this convention is not suitable.



**Fig. 24.28** Triaxial undrained tests with varying density and confining pressure (Data by Verdugo and Ishihara, 1996)



**Fig. 24.29** Wet tamping method of model preparation

Three undrained triaxial compression tests on Toyoura sand in Fig. 24.28 indicate the effects of confining pressure and density of sand on the stress–strain behavior.

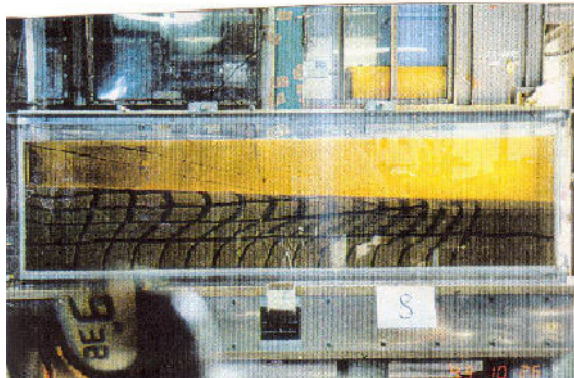
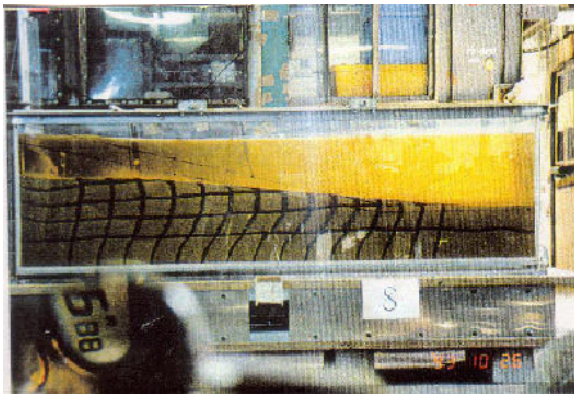
1. When the pressure was high, equal to 1,960 kPa ( $=20 \text{ kgf/cm}^2$ ), and the void ratio was  $e = 0.908$ , this loose sand revealed a peak strength followed by a drastic softening. This softening easily leads to a catastrophic flow failure of sand because the shear resistance decreases so substantially that it can be less than the acting gravity load. This phenomenon should be reproduced in model tests.
2. Shaking table model tests in a gravity field cannot produce such a high confining pressure as insitu. Hence, model tests have been conducted under reduced pressure but still with the same density as insitu. This is somehow represented by the second test in Fig. 24.28 with the confining pressure of 98 kPa and  $e = 0.908$ . Although the sand density is similar, the behavior in this test is remarkably different from the first test. The deviator stress of  $\sigma_1 - \sigma_3$  increased monotonically, not showing softening after a peak strength. This behavior does not lead to a catastrophe. Note that this residual strength is close to the aforementioned strength, irrespective of the different initial confining pressures.
3. A better similarity was obtained by employing looser sand. In the third test under the lower pressure of 98 kPa, the void ratio was 0.949. This reduced density of sand changed the shape of the stress–strain curve from the monotonic type of the second test to a softening type which is vulnerable to flow failure.



Thus, dilatancy of sand, development of excess pore water pressure, and the consequent softening are governed by a combined effect of density and initial effective stress level. This is consistent with the discussion in Sect. 1.5.

With these findings, it was considered necessary to employ in shaking table tests extremely loose sand which is much looser than the insitu sand so that the effect of reduced stress would be compensated for by reduced density. Since the water sedimentation method of preparation of model ground cannot produce the relative density of lower than, for instance, 30%, a new method which is called wet tamping or moist compaction was used. See Fig. 24.29. This method is characterized by placing wet sand in a container. Since the wet sand has an apparent cohesion, it can sustain its weight at an extremely low density. Upon careful water submergence, the apparent cohesion disappears, and collapse and minor densification occur. The relative density of sand is, however, still as low as  $\sim 20\%$  in the author's experience. Figure 24.60 will present the relative density of sand in model tests which is equivalent with the field density from the viewpoint of Fig. 24.28.

24.9 Shaking Table Tests on Extremely Loose Deposit



A model that was composed of very loose sand was excited by a single impact given in a direction perpendicular to the direction of flow. This direction of impact made soil flow independent of inertial force. The model was 2 m long. When the relative density was  $-20\%$  (minus twenty percent), the sandy slope flowed laterally under the gravity force (Fig. 24.30). This situation was similar to the event of Showa Bridge in Niigata, 1964, which is said to have fell down due to subsoil liquefaction and the collapse of foundation after the strong phase of shaking had ceased (Horii, 1968) (Fig. 24.31).

Figure 24.32 compares the time history of measured lateral displacement during flow. The looser deposit of sand developed the greater displacement. In the loosest case (Fig. 24.30), the ground surface ultimately became level. Probably there was no shear resistance at all in this loosest sand. In contrast, models of higher density stopped its flow when the surface was still inclined. There was some residual strength in those materials.



Fig. 24.30 Free flow of liquefied extremely loose sand (Toyota et al. 2004)

Fig. 24.31 Falling of Showa Bridge in Niigata (Department of Civil Engineering, University of Tokyo)

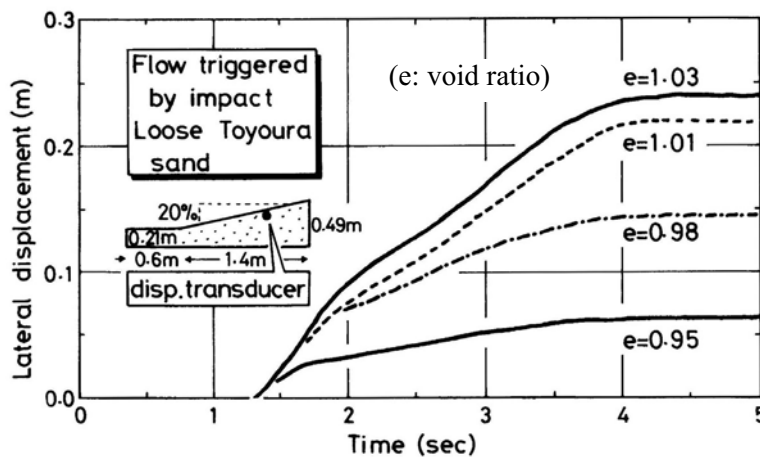


Fig. 24.32 Time history of lateral flow (Toyota et al. 2004)

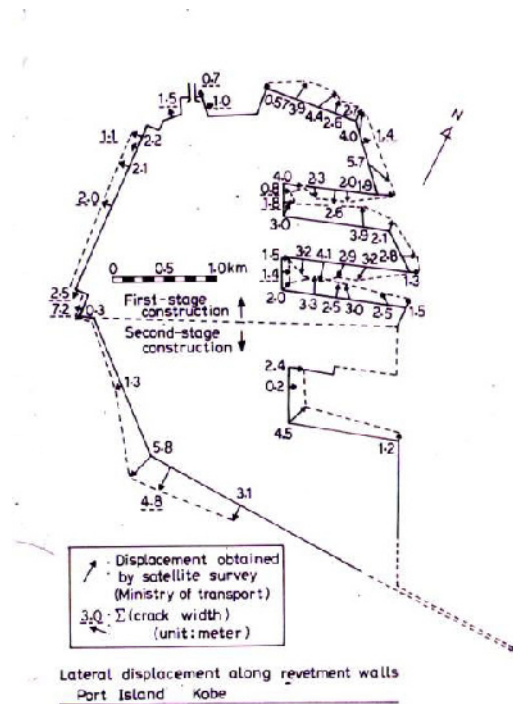
## 24.10 Shaking Table Tests on Distribution of Caisson Quay wall During Earthquakes



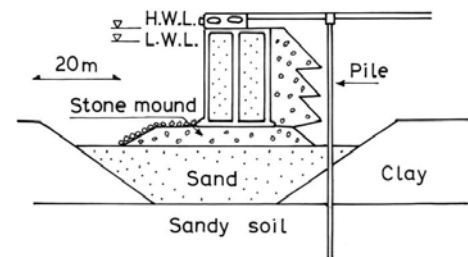
**Fig. 24.33** Distortion of caisson quay wall in Kobe

The earthquake in 1995 caused a remarkable damage to gravity-type caisson quay walls in Kobe harbor. Figure 24.33 shows that a quay wall translated and tilted toward the water. It was controversial what was the cause of the quay wall distortion, strong seismic inertia force or subsoil liquefaction. The idea of strong motion came from the fact that quay wall displacement was more significant in the North–South direction than in the East–West direction (Fig. 24.34), which was consistent with the stronger acceleration in the North–South direction (Fig. 16.17). Another possibility was certainly the subsurface liquefaction. To investigate this problem, shaking table model tests were conducted (Ghalandarzadeh et al. 1998). The cross section of the model was determined by referring to a typical cross section of a gravity-type wall around Port Island (Fig. 24.35). Since the seabed in Kobe Harbor is made of soft marine clay which is subjected to settlement under the heavy weight of quay walls, the clay was excavated, removed, and replaced by sandy soil. Note that earthquake was not of a major concern in Kobe area in 1960s and 1970s when the construction of Port Island was planned; subsidence of soft marine clay was considered more important.

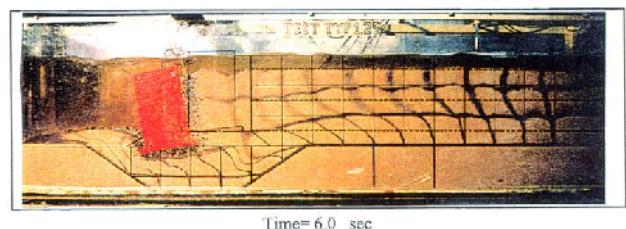
The shaking table tests were characterized by the use of very loose Toyoura sand;  $e = 1.01$  or  $1.02$  while  $e_{\max}$  is  $0.977$ . The extremely loose state makes the dilatancy negative as occurs insitu under higher stress level. Figure 24.36 indicates the deformation of the model. It is found that large deformation of sand is the cause of quay wall distortion; no slip plane (discontinuity of displacement) occurred. Figure 24.37 shows the distribution of pore pressure ratio; 100% means the excess pore pressure equal to the initial overburden pressure. The low percentage of pore pressure rise just behind the caisson wall is



**Fig. 24.34** Earthquake-induced displacement of quay walls around Port Island (Satellite survey data by Inagaki et al, 1996, and measurement of cracks by Towhata et al., 1996)



**Fig. 24.35** Typical cross section of quay wall around Port Island (after Development Bureau of Kobe Municipal Government)



**Fig. 24.36** Deformed shape of model caisson quay wall

Figure 24.37 shows the distribution of pore pressure ratio; 100% means the excess pore pressure equal to the initial overburden pressure. The low percentage of pore pressure rise just behind the caisson wall is

consistent with the fact that sand boiling did not occur near the real quay wall (Figs. 24.5 and 24.33). The cause of this is the large distortion of backfill sand which was induced by the quay wall movement and led to positive dilatancy (volume expansion) in spite of the low density.

A special attempt was made to reproduce the stress-strain (Fig. 24.38) and stress-path (Fig. 24.39) behaviors of the foundation sand. By using the measured acceleration, displacement, water pressure, and earth pressure, time histories of stress and strain were obtained. It revealed that the permanent displacement of a model caisson wall was caused by the repeated loading of shear stress and the accumulation of residual strain. The elevated pore water pressure made this accumulation easier as suggested by the stress path near the failure locus in Fig. 24.39.

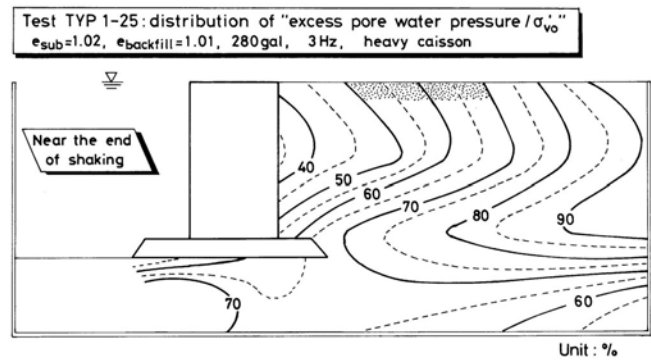


Fig. 24.37 Distribution of excess pore water pressure ratio in %

Finally, it was concluded that the significant deformation of walls was a consequence of the combined effects of shaking and development of pore water pressure in sand under the wall. The Ministry of Transport restored the significant distortion of quay walls by first removing sand inside the caisson, making the caisson float, removing it, restoring the rubble (stone) mound and foundation, and bringing back the caisson again.

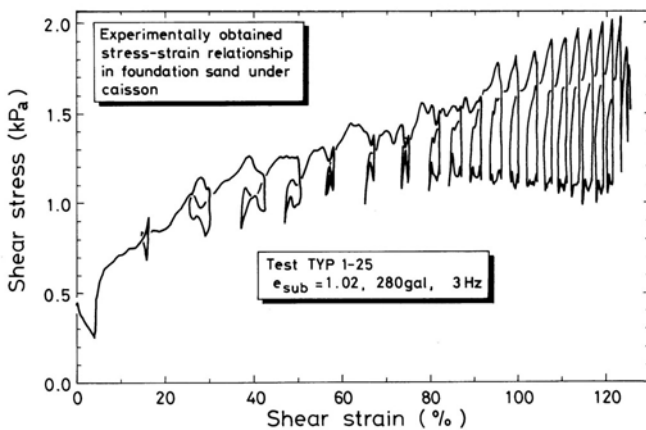


Fig. 24.38 Reproduced stress-strain behavior of foundation sand under caisson

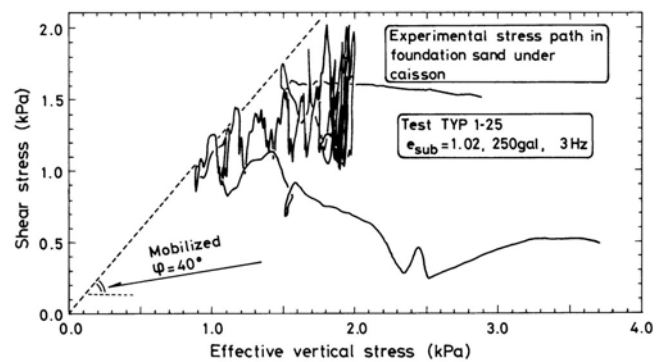
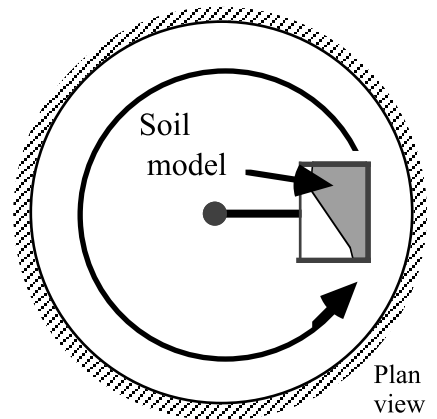


Fig. 24.39 Reproduced stress-path behavior of foundation sand under caisson

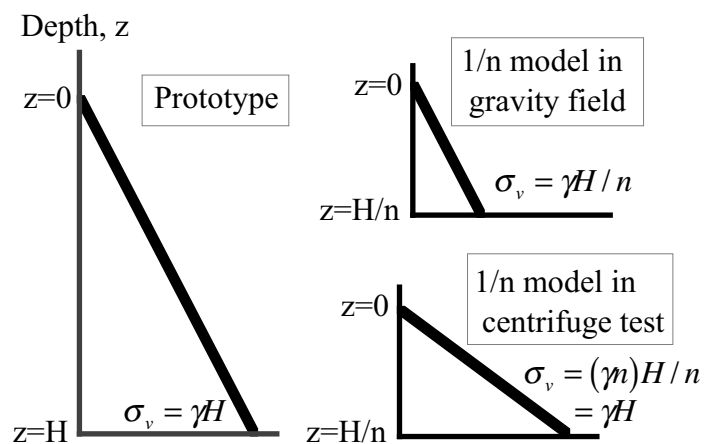
**24.11 Geotechnical Centrifuge Model Tests**

Model testing is a popular way to investigate the behavior of earth structures in both static and dynamic conditions. The centrifugal model testing (遠心力載荷実験) in particular is highly acknowledged. A centrifugal device rotates a model container around the central axis and the generated centrifugal effect makes the unit weight of materials (apparent gravity)  $n$  ( $= 30$  for example) times greater. Hence, a small model of  $1/n$  size of the field prototype can develop the same stress level as in the field. Since the stress–strain–strength behavior of soil depends on the effective stress, it is expected that a centrifugal machine can reproduce the insitu level of stress and thus the same stress–strain behavior as in the field.



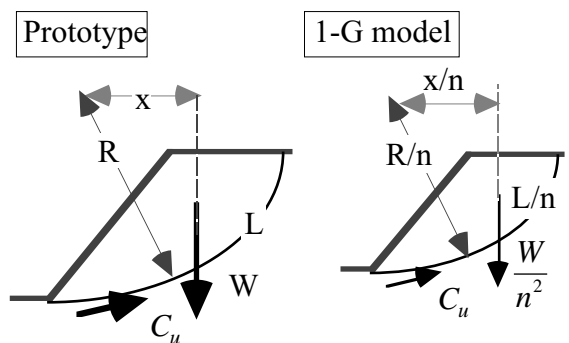
**Fig. 24.40** Schematic idea of geotechnical centrifuge tests

Figure 24.40 illustrates the idea of centrifuge model tests in which a container of a model rotates in the horizontal plane around the axis and exerts a centrifugal force on the soil. This centrifugal test is used to increase the weight of soil to  $n$  times that of the natural unit weight. Thus, it becomes possible to achieve the same stress level as in the field, although the size of the soil deposit is only  $1/n$  of the reality. This is a very important point because the material property of soil is highly dependent on the effective stress level.



**Fig. 24.41** Reproduction of vertical stress by centrifugal technique

Figure 24.41 compares the variation of vertical stress in the field (prototype), and models undergoing 1-G gravity and  $n$ -G centrifugal force. Although a small model in 1-G field can produce only low stress level, the centrifugal effects increase the unit weight to  $n$  times and brings back the stress to the prototype level.



**Fig. 24.42** Slope stability in prototype and 1-G model

Figure 24.42 compares the slope stability problems in the prototype and the 1-G model. Since the same clayey material is assumed, the undrained shear strength ( $C_u$ ) is common. The factor of safety,  $F_s$ , of the prototype is given by

$$F_s = \frac{C_u RL}{Wx},$$

where  $L$  is the length of the slip plane and  $W$  the weight of soil. In the 1-G model, second,

$$F_s = \frac{C_u (R/n) (L/n)}{(W/n^2) (x/n)} = \frac{C_u RL}{Wx} \times n.$$

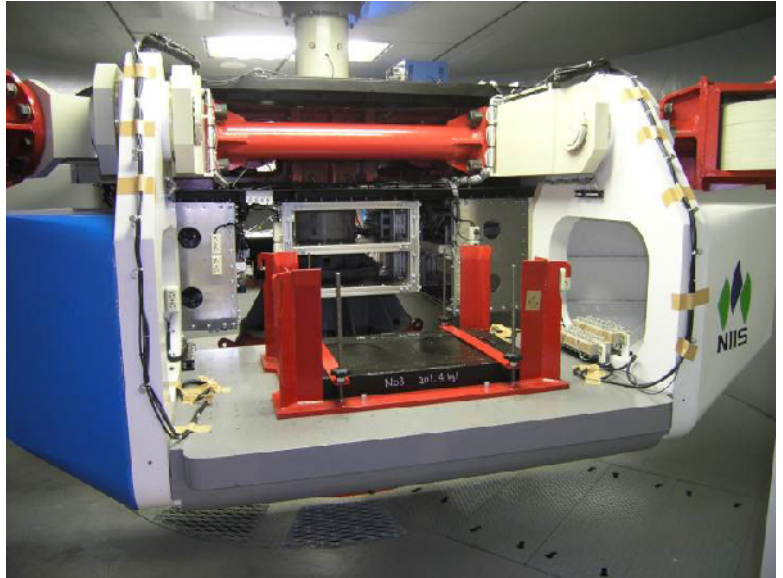
Thus, a model test in the gravity field overestimates the stability unless  $C_u$  is properly reduced. This problem is solved in a centrifuge test by increasing the weight of soil  $n$  times.

$$F_s = \frac{C_u(R/n)(L/n)}{(nW/n^2)(x/n)} = \frac{C_u RL}{Wx}.$$

Thus, a centrifuge test is able to reproduce the prototype factor of safety. Figure 24.43 shows a platform of a centrifuge apparatus in which a ground model is placed. Being still a model test, however, centrifuge tests do not take into account the geological history and aging effects.

The earliest centrifugal tests concerned (e.g., Pokrovsky and Fedorov, 1936) concerned static geotechnical problems such as earth pressure. One of the advantages was the accelerated rate of consolidation settlement. Since the consolidation time changes in proportion to  $SIZE^2$ , a model of 1/50 of the prototype size completes consolidation in 1/2,500 time of the prototype. Nonlinear stress–strain ( $e$ - $\log P'$ ) behavior (Sect. 1.4) is supposed to be identical in both model and prototype, because soil is subjected to the same level of stress. Actually, however, this may not be true because the behavior of field soil includes the effects of geological history which a model ground as produced in laboratory does not have.

Another drawback of centrifugal model tests lies in grain size. Because model tests employ the same soil as in the prototype, the grain size in model is  $n$ -times greater than the desired size. This point is particularly important in shear failure in which shear strain is localized in a shear band of width of 10–20 times grain size. Its high maintenance cost is possibly another practical problem.

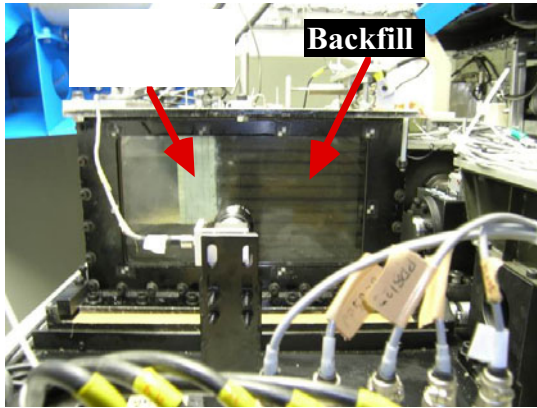


**Fig. 24.43** Testing platform of centrifugal machine in National Institute of Industrial Safety, Tokyo

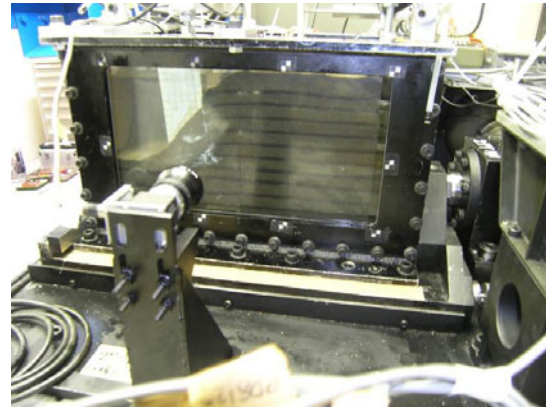
## 24.12 Law of Similitude in Dynamic Centrifuge Tests

It is possible to run shaking tests by installing dynamic actuators in a platform of a centrifugal device. Unless the platform is tightly fixed in position during the rotation of the centrifugal device, actuators are not supported in a reasonable way and the desired level of shaking may not be produced. Figure 24.44 demonstrates details of a model on liquefaction-induced deformation of gravity quay wall and its backfill.

(a) Prior to shaking



(b) After liquefaction and large distortion



**Fig. 24.44** Centrifugal model test on liquefaction-induced deformation of gravity-type quay wall (Alam et al, 2004; test conducted at National Institute of Industrial Safety)

**Table 24.1** Similitude law in dynamic centrifugal model test.

Parameters	Prototype	Model	Parameters	Prototype	Model
Size	$n$	1	Displacement	$n$	1
Mass density	1	1	Velocity	1	1
Gravity	1	$n$	Acceleration	1	$n$
Unit weight	1	$n$	Time (shaking)	$n$	1
Stress	1	1	Consolidation time		
Strain	1	1	for pore water	$n^2$	1
Modulus	1	1	$n$ -Times more viscous		
Damping ratio	1	1	liquid in model	$n^2$	$n$

The rule of correlation between parameters in prototype and model grounds is called the law of similitude. Following early studies on static phenomena (Rocha, 1957; Roscoe, 1968), there is a similitude law for dynamic tests today. When the same soil with the same density is involved in both prototype and model, the extent of effective stress is similar and consequently the stress–strain behavior is expected to be identical. Hence, shear modulus, nonlinearity, shear strength, dilatancy, and other mechanical properties are expected to be identical. Table 24.1 shows the similitude law in which a prototype is supposed to be  $n$  times greater than a model.

Since  $S$  wave velocity,  $V_s = \sqrt{G_{\max}/\rho}$ , is a soil property, it is identical in both prototype and model. Then, the natural period of soil layer, which is an example of time concerning shaking, is given by  $4H/V_s$  (Sect. 6.8;  $H$  is the thickness of layer), and the natural period changes with the ratio of  $H$  (ratio =  $n$ ; see Sect. 24.11). This time ratio is different from the ratio of consolidation time ( $n^2$ ) when pore liquid is water in a model test. This means that liquefaction test with water in the soil pore is subject to very quick rate of consolidation and dissipation of excess pore water pressure, leading to underestimation of excess pore water pressure and liquefaction-induced damage.

To overcome this problem, it is desired to reduce the permeability in model test to  $1/n$ ; finer sand has lower permeability. This goal is achieved by either employing viscous liquid or using finer cohesionless soil which has lower permeability (Fig. 26.22 and Alam et al. 2004). Although the former technique is more popular, it may be difficult to achieve perfect saturation. Furthermore, the recent trend for environmental protection requires careful treatment of such viscous liquid as glycerine after testing. The use of cellulose solution is rather easy because it can be discharged directly into sewage system (this is a rule in Tokyo). Noteworthy finding by Ellis et al. (2000) is that damping ratio of sand is increased by a few % when pore water is replaced by more viscous fluid. This may imply that the use of viscous fluid violates the similitude requirement. On the other hand, the use of finer sand may sound strange. However, it should be recalled that Table 24.1 requires all the sizes in a model to be reduced to  $1/n$ , and particle size of soil is not an exception. Use of finer sand or cohesionless sand satisfies both size requirement and time requirement. One problem therein is the elongated time of consolidation prior to shaking (this is a problem in viscous pore liquid as well) and the achievement of saturation. Introduction of water into silty ground is a time-consuming business.

Theoretically, centrifugal tests satisfy all the similarity requirements and can reproduce the field behavior in the laboratory. There are, however, problems in reality. First, sand grains in centrifugal tests correspond to bigger gravel particles in prototype. It should be recalled, however, that the behavior of real ground is affected by the geological history, former seismic shaking, age, packing of soil grains, etc. which are difficult to be reproduced in laboratory-prepared model ground. To overcome this difficulty, Fujiwara et al. (2005) collected big undisturbed block samples without disturbance (Fig. 10.58) and conducted centrifugal tests on them.

Centrifugal model tests often employ models of piles and sheet pile walls which are subjected to lateral force and earth pressure. The similitude requirements for bending stiffness,  $EI$ , of these structures are discussed in what follows.

The similitude is studied by running a simple structural analysis, calculating the displacement, and satisfying similitude requirement for displacement by adjusting  $EI$ . The first analysis on a pile is carried out by using that of a vertical beam for simplicity. Figure 24.45 shows a simple loading condition of a vertical beam. Horizontal force ( $F$ ) is loaded at the top, while the bottom is fixed without displacement and rotation. The elastic theory of a beam gives a solution for displacement,  $u$ , as

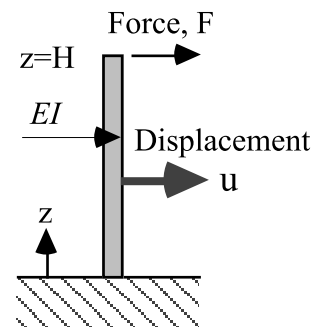
$$u = \frac{F}{6EI}(-z^3 + 3Hz^2). \quad (24.4)$$

Hence, the displacement at the top of the beam is

$$u(z = H) = \frac{FH^3}{3EI}. \quad (24.5)$$

The ratio of prototype displacement ( $u_p$ ) and model displacement ( $u_m$ ) has to satisfy the following requirement for similitude (see Table 24.1);

$$u_p : u_m = n : 1. \quad (24.6)$$



**Fig. 24.45** Vertical beam subjected to horizontal force at top



The ratio of force is equal to the ratio of  $Stress \times Area = Stress \times Size$  ,

$$F_p : F_m = n^2 : 1. \quad (24.7)$$

By substituting (24.5) and (24.7) in (24.6),

$$(EI)_p : (EI)_m = n^4 : 1. \quad (24.8)$$

This means that a model pile can be made of a material which is softer and different from the prototype pile; there is no need to simply use the same material and reduce the diameter of a pile to an extremely small size of  $1/n^4$ .

In case of a sheet pile wall, the bending stiffness per unit width, which is denoted by  $EI/B$ , is important. Figure 24.46 illustrates a loading condition in which the earth pressure is given by  $K\rho g(H-z)$ . In this expression,  $K$  stands for the earth pressure coefficient at relevant conditions and is independent of the centrifugal acceleration. The unit weight of soil is designated by  $\rho g$  and

$$(\rho g)_p : (\rho g)_m = 1 : n. \quad (24.9)$$

The lateral displacement of the sheet pile wall is given by

$$u = \frac{K\rho g H^5}{24(EI/B)} \left\{ \left( \frac{z}{H} - 1 \right) - \frac{1}{5} \left( \frac{z}{H} - 1 \right)^5 + \frac{4}{5} \right\}. \quad (24.10)$$

Since the displacement has to satisfy (24.6) for similitude, the similitude requirement for bending stiffness per unit width of sheet pile wall is derived;

$$\left( \frac{EI}{B} \right)_p : \left( \frac{EI}{B} \right)_m = n^3 : 1. \quad (24.11)$$

Apart from such displacement as above, a different discussion is made from the viewpoint of time. Fig. 24.47 shows a beam of bending stiffness  $EI$  supporting a mass of  $M$ . The free vibration of this system is expressed by

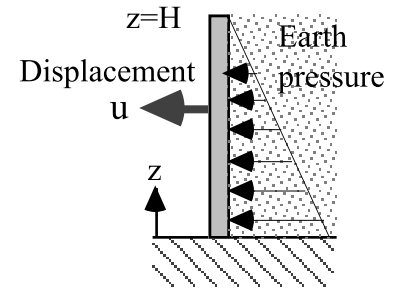
$$\text{Deflection } U(z, t) = u(z) \sin \omega t. \quad (24.12)$$

Since the beam has neither lateral force nor mass for  $0 < z < H$ , while  $u$  and  $du/dz$  are zero at  $z = 0$ ,

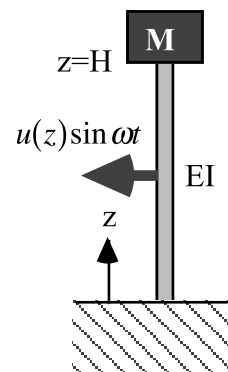
$$u(z) = C_1 z^2 + C_2 z^3.$$

Moreover, bending moment = 0 and shear force =  $-EI \partial^2 U / \partial z^2$  at  $z = H$ . Hence,

$$\omega^2 = \frac{3EI}{MH^3}. \quad (24.13)$$



**Fig. 24.46** Sheet pile wall subjected to earth pressure from backfill



**Fig. 24.47** Free vibration of beam-mass system

Accordingly, the natural period,  $T_n$ , of this system is given by

$$T_n = \frac{2\pi}{\omega} = 2\pi \sqrt{\frac{MH^3}{3EI}}. \quad (24.14)$$

Because the natural period should satisfy the similitude requirement for shaking time in Table 24.1,

$$\frac{T_{n,p}}{T_{n,m}} = \frac{n}{1} = \sqrt{\frac{M_p H_p^3 (EI)_m}{M_m H_m^3 (EI)_p}}. \quad (24.15)$$

Since the same material is used in the top mass in both prototype and model, the ratio of the mass is equal to the cube of the size (mass density  $\times$  size<sup>3</sup>);  $M_p/M_m = n^3$ . Since  $H_p/H_m = n$ , moreover,

$$(EI)_p : (EI)_m = n^4 : 1, \quad (24.16)$$

which is consistent with (24.8). Thus, the same similitude rule is obtained for EI from both displacement and time viewpoints.

Similarly, the similitude law for a column subjected to vertical static force is studied in what follows. By denoting the rigidity of the column by EA in which A stands for the cross section of the column (Fig. 24.48),

The vertical displacement,  $u$ , is given by

$$u(z) = \frac{Fz}{EA}. \quad (24.17)$$

Since  $u_p : u_m = n : 1$  (24.6),  $F_p : F_m = n^2 : 1$  (24.7), and  $z_p : z_m = n : 1$ ,

$$(EA)_p : (EA)_m = n^2 : 1. \quad (24.18)$$

For a unit width of a column, accordingly,

$$\left(\frac{EA}{B}\right)_p : \left(\frac{EA}{B}\right)_m = n : 1. \quad (24.19)$$

By further calculating the natural period of a column-mass system (Fig. 24.49),

$$T_n = 2\pi \sqrt{\frac{MH}{EA}}. \quad (24.20)$$

Note that the column has no mass in this calculation. To satisfy the similitude law for time,

$$(EA)_p : (EA)_m = n^2 : 1. \quad (24.21)$$

Thus, again, the requirements of similitude for displacement and time give the identical similitude rules for EA.

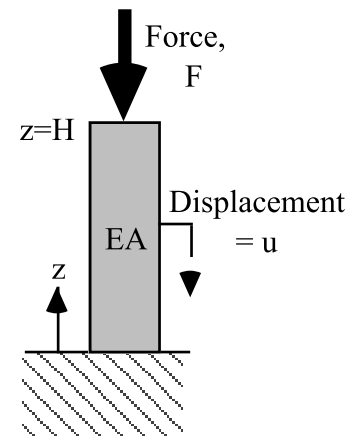


Fig. 24.48 Vertical column subjected to axial load

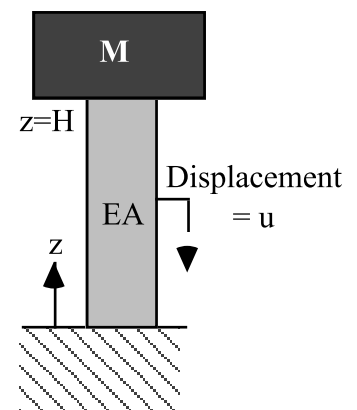
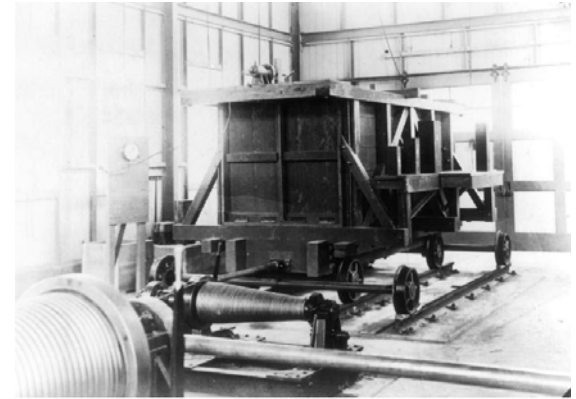


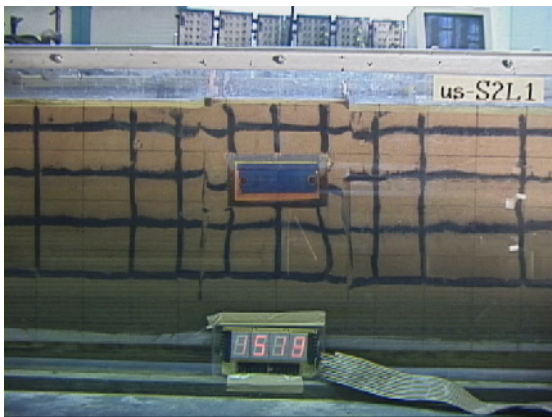
Fig. 24.49 Free vertical vibration of column-mass system

### 24.13 1-G Shaking Table Tests

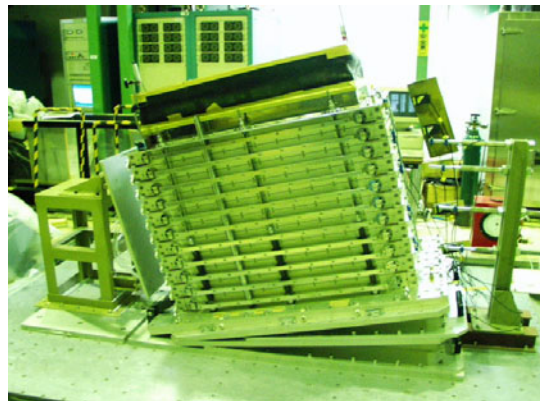
Since the importance of model tests have been understood widely from early days, there is a long history of 1-G shaking tests. Figure 24.50 illustrates one of the pioneering works in which a big soil container moves back and force along a track. This innovation shows that fabrication of 1-G shaking device is much simpler than that of a centrifugal device. The advantage of 1-G shaking table test is that preparation of a model is easier than a centrifugal model due to its reasonably bigger size. Maintenance cost is lower as well. Figure 24.51 shows a 1-G test on mitigation of floating of an embedded structure by installing sheet pile walls. Figure 24.52 shows a laminar box which consists of many thin frames with smooth ball bearings between them so that each horizontal frame can move freely without much friction. There is a rubber membrane inside the laminar box in order to avoid water leakage. The aim of a laminar box is to reproduce dynamic behavior of a level ground in a limited size. It is sometimes felt, however, that the displacement of the external laminar frame and that of the soil inside are not exactly equal to each other.



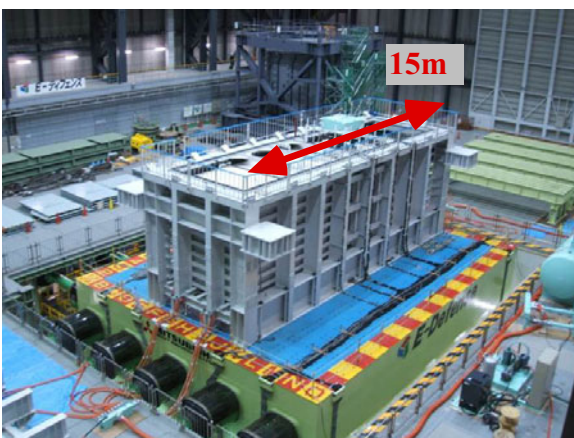
**Fig. 24.50** Early generation of shaking table device (Public Works Research Institute)



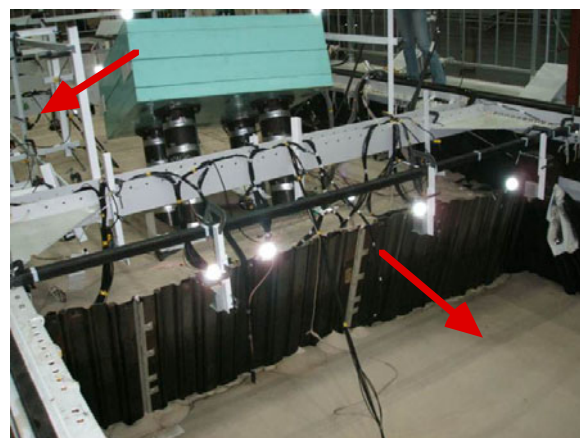
**Fig. 24.51** Mitigation of liquefaction-induced floating of underground structure by installing sheet pile walls



**Fig. 24.52** Laminar soil box placed on sloping shaking foundation



**Fig. 24.53** Huge shaking facility at E-defense (Miki, Hyogo) (photograph by R. Motamed)



**Fig. 24.54** Large distortion of sheet pile quay wall and backward tilting of pile foundation after shaking (E defense)(photograph by R. Motamed)

There is a long discussion on the significance of 1-G model tests which cannot reproduce the field stress level and accordingly the stress-strain behavior of tested soil under low-effective stress is different from

that of the prototype. On the other hand, it has often been discussed that centrifuge tests are not perfect because the employed sand grain in a reduced scale is equivalent to gravels and cobbles in the supposed prototype. It seems that people recently understand shortcomings of model tests. Consequently, nobody claims that any kind of model testing facility is a perfect reproduction of a prototype phenomenon. One big attempt is a 1-G model test of a prototype size. Figure 24.53 shows a soil container for liquefaction tests. This container measures 16 m in length and the soil deposit in the container has 4.5 m in thickness. This thickness seems sufficient to claim that the facility reproduces the prototype stress level. The model in the container concerned failure of cantilever sheet pile quay wall due to liquefaction of backfill sand. The consequence of shaking in Fig. 24.54 illustrates that the quay wall collapsed completely and a pile foundation in the backfill tilted significantly.

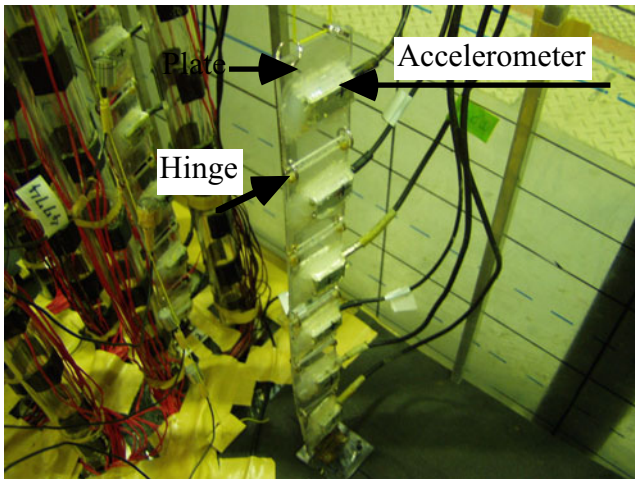


Fig. 24.55 Inclinometer in soil container prior to filling with liquefiable sand (Photo by R. Motamed)



Fig. 24.56 Inclinometer upon excavation after liquefaction test (Photo by R. Motamed)

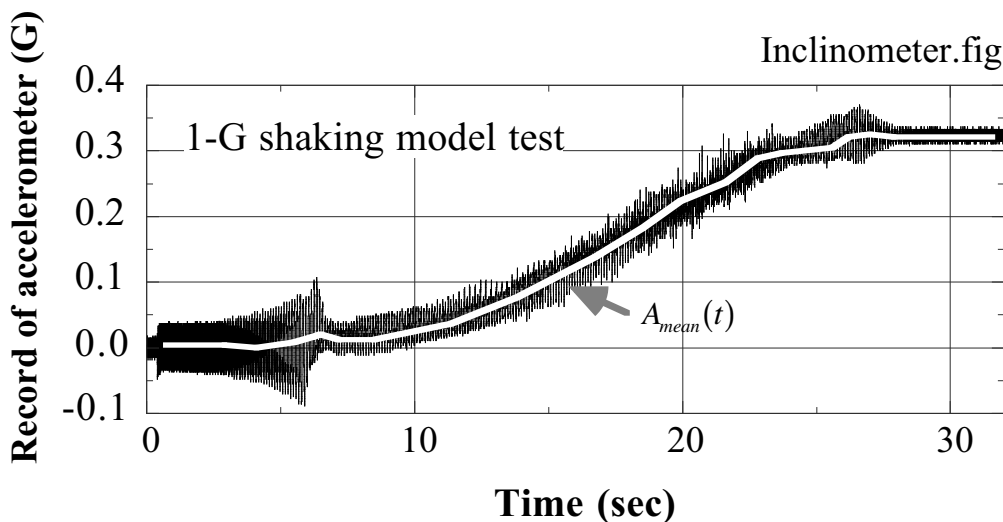


Fig. 24.57 Example of acceleration record

The permanent horizontal displacement in a liquefied model ground is measured efficiently by using an inclinometer (Figs. 24.55 and 24.56). This inclinometer was originally developed by Sasaki et al. (1991). This equipment consists of many small plates which are connected to each other by a smooth hinge. Each plate has an accelerometer of strain-gage type attached to its surface. This accelerometer is able to record the DC (static) component of acceleration,  $A_{mean}(t)$ , as well as the dynamic component (Fig. 24.57). Moreover, the average mass density of each plate is made equal to that of surrounding water-saturated sand by attaching light objects so that both sand and inclinometer move together without sinking or floating. A series of plate is fixed to the bottom of the model ground, and hence any lateral displacement of the ground causes tilting of the plates (Fig. 24.58).

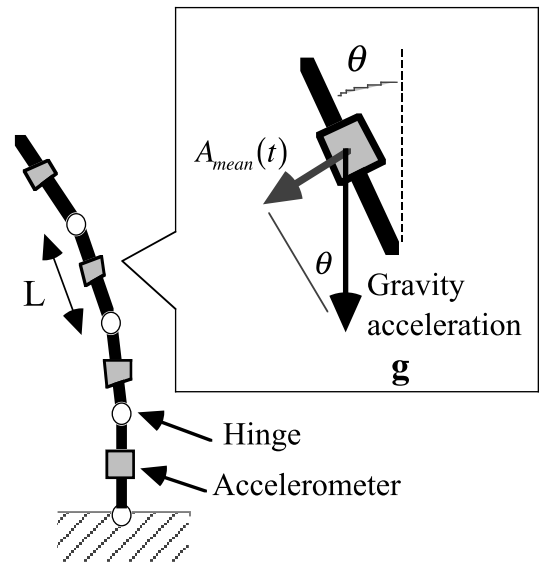
An example time history of measured acceleration is illustrated in Fig. 24.57. By numerically removing the high-frequency components from this, the mean acceleration,  $A_{\text{mean}}(t)$ , is obtained. Since this mean value is produced by tilting of the plate (Fig. 24.58), the tilting angle of  $\theta$  is obtained;

$$\theta = \arcsin \frac{A_{\text{mean}}(t)}{g}$$

By using the geometric relationship as illustrated in Fig. 24.58, the time history of lateral displacement of the inclinometer (= soil displacement) is obtained;

$$u(t) = \sum_{\text{bottom}}^{\text{top}} L \sin \theta = \frac{L}{g} \sum_{\text{bottom}}^{\text{top}} A_{\text{mean}}(t), \quad (24.22)$$

in which  $L$  stands for the length of a plate.



**Fig. 24.58** Operation mechanism of displacement transducer

### ☛ 24.14 Law of Similitude for 1-G Shaking Tests

Many shaking model tests have been undertaken in 1-G gravity field. Since the stress level in 1-G tests is lower than in the prototype (real ground), except for a full-scale shaking test (Figs .24.53 and 24.54), engineering concern has been addressed to develop any law of similitude. The similitude law has been expected to indicate for any model test a corresponding prototype whose dynamic behavior the model is trying to reproduce.

Before presenting detailed theories, it is good to address basic concepts. When the prototype ground is  $n$  times greater than a model, the stress (effective stress) in the prototype is greater by  $n$  times as well. Consequently, the shear strength,  $\tau_f$ , is greater by  $n$  times, while shear modulus at small strain,  $G_{\max}$ , changes in proportion to  $\sqrt{\sigma'}$  or varies by  $\sqrt{n}$  times (Fig. 10.19). When the nonlinear stress–strain relationship is expressed by a hyperbolic model (see (11.1)),

$$\tau = \frac{G_{\max}\gamma}{1 + |\gamma/\gamma_r|} \quad (24.23)$$

and the shear strength is derived by making the shear strain infinite;

$$\tau_f = \lim_{\gamma \rightarrow \infty} \frac{G_{\max}\gamma}{1 + |\gamma/\gamma_r|} = G_{\max}\gamma_r. \quad (24.24)$$

Hence, the reference strain varies with the size ( $n$ ) by

$$\gamma_r \equiv \tau_f / G_{\max} \propto \sqrt{n}. \quad (24.25)$$

Thus, a law of similitude correlates the prototype and model strains by  $\sqrt{n}$ . Since the strain level affects dynamic properties of soil, there may be discrepancy between a prototype and its 1-G model tests.

Moreover,  $V_s = \sqrt{G_{\max}/\rho} \propto \sigma'^{1/4}$  because the mass density of  $\rho$  cannot be changed substantially. Therefore, S wave propagation velocity ( $V_s$ ) varies with size by  $n^{1/4}$ . Accordingly, the natural period (time) of a horizontal ground, which is given by  $(4 \times \text{Thickness}) / (V_s)$ , changes with size by  $n^{3/4}$ . More generally, the time which is related with vibration phenomena varies with  $n^{3/4}$ .

1-G model tests cannot satisfy all the possible requirements from similitude. Accordingly, past studies picked up only essential parameters and tried to satisfy a limited number of requirements. In any theory, so far proposed, only dynamic issues such as shaking and cyclic stress have been interested in. Slope failure or flow of liquefied slope have never been studied therein from the viewpoint of similitude.

Kokusho (1979) picked up the ground thickness ( $H$ ), mass density of soil ( $\rho$ ), shear modulus,  $G_{\max}$ , the damping ratio at large strain ( $h_{\max}$ ), circular frequency of shaking ( $\omega$ ), acceleration ( $A$ ), cyclic displacement ( $u$ ), shear strain ( $\gamma$ ), and reference strain ( $\gamma_r$ ) as nine important parameters. Among them,  $H$  varies with  $n$ , while the reference strain is a parameter which controls the nonlinearity of soil. On the other hand, four independent factors such as the vertical size, the horizontal size, mass, and time were chosen as governing the phenomenon of shaking. In accordance with the Buckingham  $\pi$  theorem,  $9 - 4 = 5$  nondimensional numbers are constructed out of nine parameters. For example,

$$\pi_1 = h_{\max}, \pi_2 = \gamma/\gamma_r, \pi_3 = u/(\gamma H), \pi_4 = (\rho u^2 \omega^2)/(G_{\max} \gamma^2), \text{ and } \pi_5 = A/(u \omega^2).$$

To maintain their values unchanged in both model and prototype,  $h_{\max}$  has to be identical,  $\gamma_r$  and cyclic shear strain ( $\gamma$ ) should follow the same similitude law ( $\gamma \propto \sqrt{n}$ ), the horizontal displacement ( $u$ ) changes with  $\gamma \times H \propto n^{3/2}$ , the circular frequency (inverse of time) changes with  $\sqrt{(G_{\max}\gamma^2)/(\rho u^2)} \propto n^{-3/4}$ , hence the time change with  $n^{3/4}$ , and the acceleration changes with  $u\omega^2 = \text{constant}$ . Therefore, when the model scale is 1/50 ( $n = 50$ ), the model acceleration = 300 Gal, model strain = 0.01 (1%), shaking period = 0.25 s, and model displacement amplitude is 0.1 cm, their equivalent values in the prototype are 300 Gal, 0.071 (7.1% strain), 4.7 s, and 35.4 cm, respectively. The law of similitude obtained by Kokusho is summarized in Table 24.2.

Kagawa (1978) picked up important forces in shaking phenomena, and tried to make their prototype-model ratio constant. In other words, when the gravity force changes by  $n^3$  times, the inertia force should change by  $n^3$  times as well. The derived similitude law is identical with Kokusho’s one except for the horizontal size. Note that these theories studied horizontal ground and did not concern such two-dimensional configuration as embankments and slopes.

Iai (1989) presented governing equations of ground motion and attempted to maintain constant the ratio of corresponding terms in prototype and model scales. Examples of the governing equations are the equation of motion and the mass conservation equation as well as the displacement–strain relationships, seepage law, and others. This theory is characterized by additional consideration of pile foundations. However, the scope is still limited to ground shaking, and failure and soil flow are out of scope.

Table 24.2 compares three similitude theories. It is found that they are quite similar to each other. In particular, the similitude laws for EI of pile and EA of column are obtained by using

ratio of mass:  $M_p : M_m = n^3 : 1$ ,

ratio of force:  $F_p : F_m = M_p \times \text{Acceleration} : M_m \times \text{Acceleration} = n^3 : 1$ , and

displacement ratio ((24.10) and (24.17)) as well as time ratio ((24.14) and (24.20)).

It is interesting that both similitudes for time and displacement result in identical similitude laws.

**Table 24.2** Summary of three similitude studies for 1-G shaking model tests

Ratio of	Kokusho <sup>a</sup>	Kagawa	Iai	Remarks
Vertical length	$n$	$n$	$n$	
Horizontal length	$n^{3/2}$	$n$	$n$	
Mass density	1	1	1	
Stress and pressure	$n$	$n$	$n$	
Shear modulus, $G_{\max}$	$\sqrt{n}$	$\sqrt{n}$	$\sqrt{n}$	
Shear strain	$\sqrt{n}$	$\sqrt{n}$	$\sqrt{n}$	
Horizontal displacement	$n^{3/2}$	$n^{3/2}$	$n^{3/2}$	
Shaking time	$n^{3/4}$	$n^{3/4}$	$n^{3/4}$	
Strain rate	$n^{-1/4}$	$n^{-1/4}$	$n^{-1/4}$	
Velocity	$n^{3/4}$	$n^{3/4}$	$n^{3/4}$	
Acceleration	1	1	1	Reduction of permeability in model is difficult
Permeability	-	-	$n^{3/4}$	
Bulk modulus of water	-	-	$\sqrt{n}$	Air is too soft to reduce modulus in model to this extent
EI of pile/width	-	-	$n^{7/2}$	This rule is applicable to sheet pile wall
EA of column/width	-	-	$n^{3/2}$	

a: Kokusho’s theory for nonlinear soil is used here

Large displacement and deformation caused by liquefaction (Sect. 24.9) is one of the important issues which cannot be fully considered by the similitude theories. One way to overcome this is to run a big model test (Fig. 24.53). This is, however, extremely expensive. In the author’s opinion, it is important to design the configuration and materials in models so that reasonably large deformation may occur as in the real natural hazards. The observed facts in model tests should be examined against case history studies. This idea is particularly important in EI/width of sheet pile wall. A reasonably soft wall should be prepared for model tests, without being too strict with the law of similitude, so that significant distortion may occur upon liquefaction and studies can be made of the mechanism of significant damage.

It was stated in Sect. 24.8 that very loose sand should be used in 1-G tests on liquefaction-induced ground deformation. This changing of material property (density) from the prototype in mind is special because traditionally model testing people believed that they should employ the same density of sand as in the field. The new idea puts more emphasis on producing similar shape of stress–strain curve and dilatancy in model tests under low-effective stress.

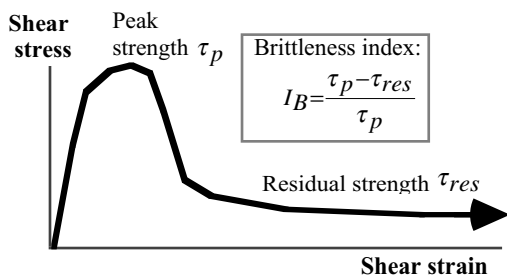


Fig. 24.59 Conceptual sketch of brittleness index

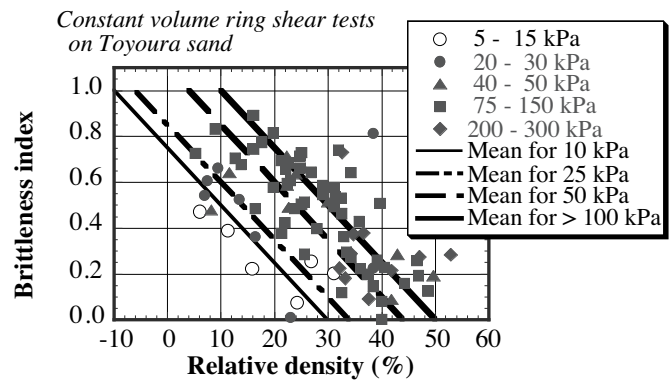


Fig. 24.60 Combination of relative density and effective stress level which keeps brittleness index constant (data by Vargas-Monge, 1998)

Vargas-Monge (1998) conducted ring shear tests under constant-volume condition to study this issue in a more quantitative manner. It was intended therein to achieve similar extent of stress softening under different stress levels by changing the sand density as well. The stress softening was focused on because the extent of softening controls the vulnerability of sand to large deformation and flow failure. It should be recalled further that softening is a consequence of pore pressure development (loss of effective stress) due to dilatancy and that dilatancy is affected by both stress levels and density (Figs. 1.15 and 1.16). Thus, by changing density it is possible to cancel the effects of different stress level under different size of ground.

The extent of softening toward the residual state was quantified by the brittleness index proposed by Bishop et al. (1971). For its definition, see Fig. 24.59. Figure 24.60 demonstrates the test results which illustrate relative density and effective stress level (prior to shear) that make the same extent of brittleness index. It can be seen in this figure that, when the effective stress level decreases to 1/10, the relative density ( $D_r$ ) should be reduced by approximately 20%; for example from  $D_r = 50\%$  in the prototype to  $D_r = 30\%$  in a 1-G shaking model. This is an experimental solution to achieve similitude in vulnerability of liquefied sand to flow and large deformation.

In addition to the effects of stress level which affects deformation characteristics of soils, the effects of shaking frequency (similitude in time scale) is an important issue. For example, most shaking tests are conducted at a frequency of less than 10 Hz, while the natural frequency of a model ground is typically 40 Hz or higher. Thus, the loading frequency is substantially lower than the resonance frequency, which may not be the case in the prototype.

To cope with this problem, study is herein made of the similitude of the residual displacement. As case studies of seismic damage in geotechnical structures show, the damage extent is fully governed by the



magnitude of residual displacement. The intensity of amplification and the onset of liquefaction are less important because they are nothing more than the triggering mechanisms of large displacement. By using the Newmark analogy, Figure 12.4 revealed that the development of residual displacement per loading cycle,  $U_1$ , is a function of  $K_{\max}/K_{\text{cr}}$ ,

$$\frac{\omega^2 U_1}{gK_{\text{cr}}} = F\left(\frac{K_{\max}}{K_{\text{cr}}}\right),$$

in which  $K_{\max}$ , multiplied by the weight of soil, stands for the magnitude of inertial force. By adjusting the input of model shaking so that the response acceleration is identical between model and prototype, it is possible to make  $K_{\max}$  identical as well. Equation (12.1) showed that  $K_{\text{cr}}$  is determined by the configuration of ground (slope angle  $\alpha$  in Fig. 12.1) and the magnitude of frictional parameter,  $\mu$ . Although Chap. 12 assumed drained shear without excess pore water pressure, it is also possible in practice to consider undrained shear and development of excess pore water pressure by employing reduced frictional parameter. This idea has been called total stress approach in soil mechanics. Note that the extent of excess pore water pressure can be made identical by employing looser sand in model tests (Sect. 24.8 and Fig. 24.60). Consequently, the similitude of residual displacement is achieved by satisfying the following condition,

$$\frac{U_{1,m}}{H_m} = \frac{U_{1,p}}{H_p}$$

where  $H$  stands for the size of ground. By using  $K_{\max}$  and  $K_{\text{cr}}$  that are made identical between model and prototype,

$$\frac{gK_{\text{cr}}}{H_m \omega_m^2} \left\{ F\left(\frac{K_{\max}}{K_{\text{cr}}}\right) \right\}_m = \frac{gK_{\text{cr}}}{H_p \omega_p^2} \left\{ F\left(\frac{K_{\max}}{K_{\text{cr}}}\right) \right\}_p$$

Because  $g$ ,  $K_{\text{cr}}$ , and the function,  $F$ , are identical in model and prototype,

$$\frac{\omega_m}{\omega_p} = \sqrt{\frac{H_p}{H_m}}$$

By substituting the period of shaking,  $T = 2\pi/\omega$ ,

$$\frac{T_m}{T_p} = \sqrt{\frac{H_m}{H_p}}$$

This implies that the time scale in shaking tests in 1-G field should be reduced in proportion to the square root of the size. This is different from the time scale in Table 24.2 which concerns only shaking problems.

In summary, the similitude of residual displacement in 1-G model tests is achieved by

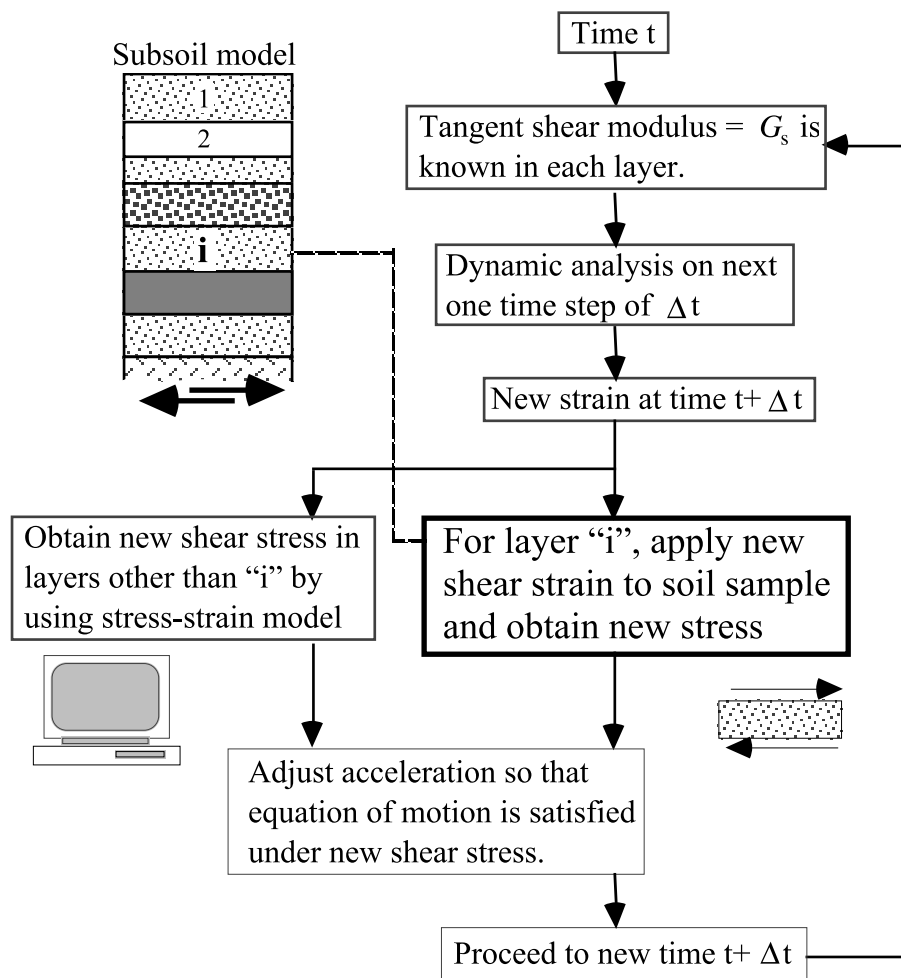
- The use of reduced soil density (Fig. 24.60)
- Shaking a model so that surface acceleration may be identical in model and prototype
- Reducing the time scale in proportion to square root of size

**24.15 Online Tests**

Laboratory shear tests and numerical analyses have been combined in a more advanced manner in online experiments. Being otherwise called hybrid tests, the online experiments replace complicated stress–strain model of soils by a soil testing machine. In a schematic illustration of Fig. 24.61, a seismic response of a horizontally layered ground is employed. Suppose that the layer “i” has a highly nonlinear and complicated stress–strain behaviour, and that its numerical modeling is difficult. In this situation, the stress–strain behavior of this particular soil is determined by running a shear test which is run in parallel with the dynamic analysis. It is certainly possible to employ two or more testing machines.

The online experiment was first conducted by Hakuno et al. (1969) on dynamic behavior of steel structure. In this pioneering attempt, a nonlinear behavior of a steel member was replaced by a structural model for which an actuator was combined with an analog computer. Structural dynamics have been running online tests; e.g., Toki et al. (1990).

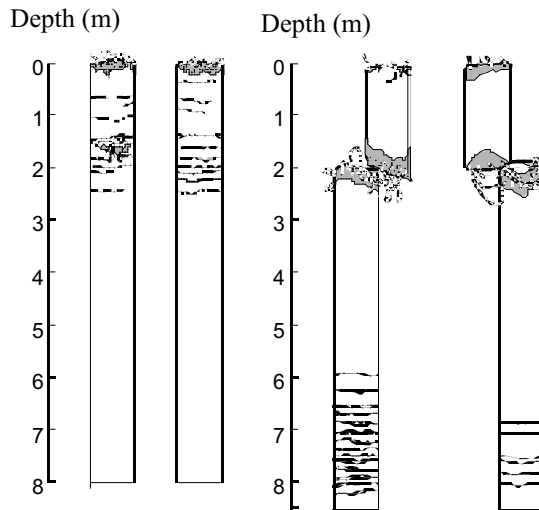
In the recent times, it has been extended to geotechnical problems and, in particular, liquefaction problems in which stress–strain behavior is difficult to model numerically. Fujii et al. (2000) used three simple shear devices for experiments with the dynamic response of horizontally layered ground in mind; they intended to study a slope as well by applying the initial shear stress to a soil specimen as well. Its more advanced stage is found in Orense et al. (2006). Kusakabe and Morio (1995) used six torsion shear machines which controlled triaxial and torsional shear stresses,  $(\sigma_v - \sigma_h)/2$  and  $\tau_{vh}$ , and reproduced nonlinear soil behavior of six different soil layers.



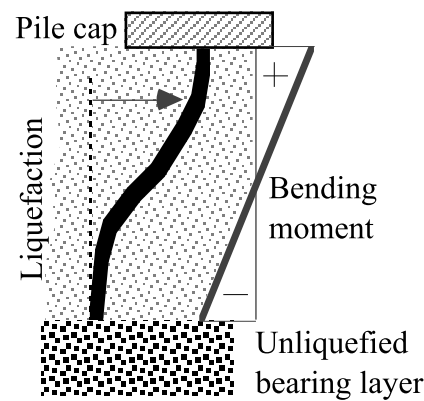
**Fig. 24.61** Schematic illustration of online experiment

## 24.16 Interaction Between Pile and Lateral Flow of Liquefied Sand

Lateral displacement of liquefied ground causes significant effects on a pile foundation. One of the most famous examples is the one in Fig. 17.25 where all the piles were subjected to bending failure in the same direction. This case was detected 20 years after the 1964 Niigata earthquake when the building was demolished for renewal (Kawamura et al. 1985). This earthquake affected piles of other buildings as well. Figure 24.62 illustrates the location of cracks along excavated concrete piles (Yoshida and Hamada, 1991). Since cracks occurred near the top and the bottom of the piles, it is reasonable to state that the piles were similar to a beam which was fixed (no rotation) at both top and bottom and was subjected to forced displacement at the top (Fig. 24.63). This mode of deformation produced the maximum bending moment at top and bottom, leading to bending failure at those elevations as occurred in reality.



**Fig. 24.62** Extent of damage in piles due to lateral displacement of liquefied subsoil (sketch by Prof. Nozomu Yoshida)



**Fig. 24.63** Inferred mode of deformation along damaged pile

To prevent the bending failure, it is good to increase the number of piles. For example, Fig. 24.64 indicates the failed shape of Showa Bridge (also see Fig. 24.31) which was destroyed by the 1964 Niigata earthquake. This bridge was probably destroyed by the lateral earth pressure which was exerted on piles by the lateral flow of liquefied river bed. Note, however, that this idea does not fully account for the fact that the bridge collapse started at the center of the river where the lateral displacement was minimal. In this regard, Yoshida et al. (2007) carried out very detailed inquiry studies to eyewitnesses and suggested that the failure was possibly caused by decreased subgrade reaction in softened liquefied subsoil and large displacement amplitude of piles. Figure 24.64 clearly shows that each bridge pier was composed of one row of piles. After reconstruction, the bending stiffness of the bridge foundation was increased by constructing two rows of piles (Fig. 24.65). Increasing the number of piles under expanded pile cap is popular in the recent times as well (Fig. 24.66).



**Fig. 24.64** Fallen Showa Bridge crossing Shinano River (Department of Civil Engineering, University of Tokyo)

Because pile foundation is supposed to bear vertical load, it does not suit horizontal load, resulting frequently in bending or shear failure. To mitigate this problem, Kimura et al. (2002) proposed to use

battered pile that is inclined to some extent so that the applied horizontal load is transferred in the axial direction. By running centrifuge tests on four consequent piles (two of them being inclined), they showed that the lateral loading capacity increased by 50–100 %.

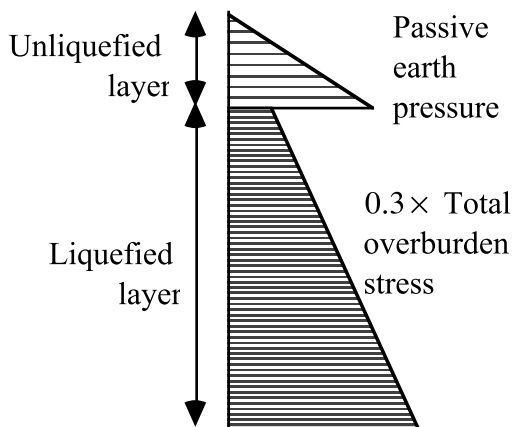


**Fig. 24.65** Present foundation of Showa Bridge after reconstruction

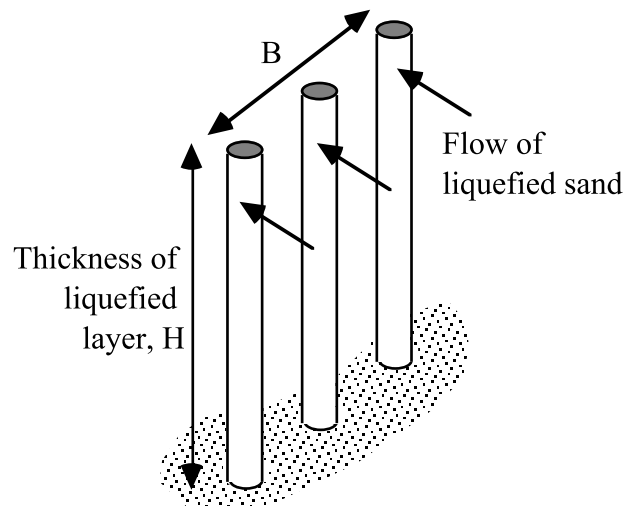


**Fig. 24.66** Increasing lateral resistance of pile foundation by enlargement of pile cap and increasing number of piles (in the center of Sunnomiya, Kobe)

The effect of lateral displacement on foundation due to subsurface liquefaction consists of two components; the unliquefied surface layer exerts passive pressure and the liquefied soil generates additional pressure which is a very important point of dispute. As shown in Fig. 24.67, the Highway Bridge Design Code after the 1995 Kobe earthquake urgently investigated damaged piles and specified the magnitude of lateral load for design. While the Coulomb passive earth pressure is easy to evaluate, the earth pressure in liquefied subsoil is assessed as 30% of the total overburden pressure (total stress). Since this pressure is calculated over the entire width of a group pile ( $B$  in Fig. 24.68), the total load becomes significant or possibly overestimation when, in particular, the pile spacing is large. The calculated lateral load is uniformly distributed among all individual piles.



**Fig. 24.67** Example of lateral earth pressure for design due to lateral displacement of liquefied subsoil



**Fig. 24.68** Range of calculation of lateral flow pressure

In model tests usually, the variation of bending moment,  $M$ , along a pile axis ( $z$  coordinate) is measured by pasting strain gauges at many elevations. Then the lateral pressure on a pile,  $p(z)$ , is determined by the second derivative of bending moment;  $p = -\partial^2 M / \partial z^2$ . It is noteworthy that the second derivative is subject to a significant error due even to minor difference in  $M$ . Hence, there are many unfortunate

examples in which the derived  $p$  is totally nonsense. One should understand that only fortunate and good examples have been published.

An alternative idea to avoid such a problem is to assume a realistic variation of  $p$  in the vertical direction. For example, employ a simple function of  $z$ ;

$$p(z) = az^2 + bz + c, \tag{24.26}$$

in which parameters,  $a$ ,  $b$ , and  $c$ , are unknown. This equation is integrated twice to obtain bending moment;

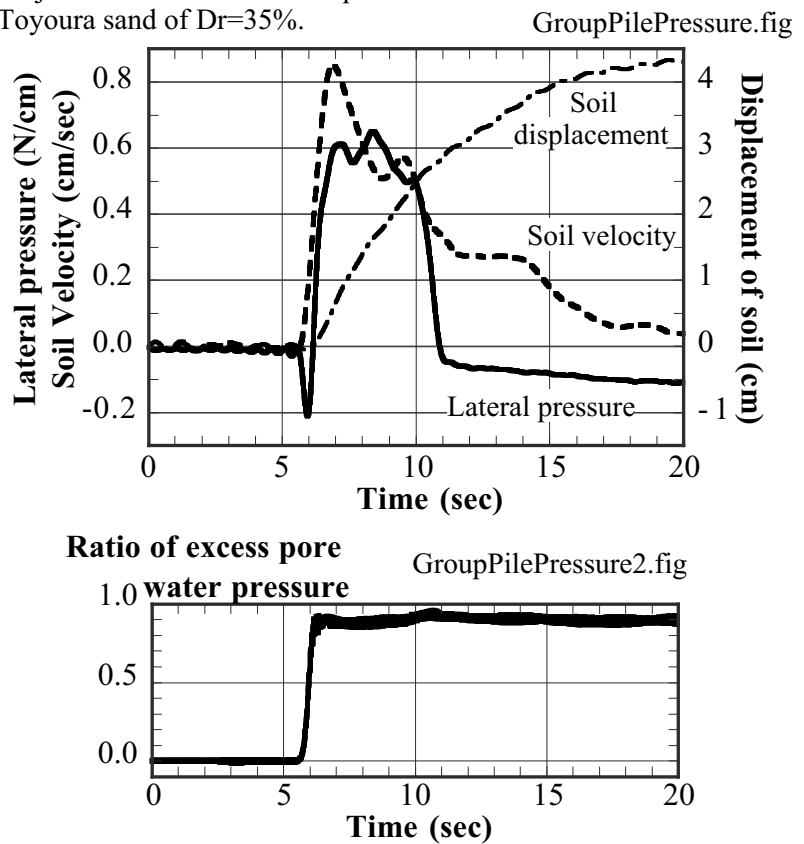
$$M = -\left( \frac{az^4}{12} + \frac{bz^3}{6} + \frac{cz^2}{2} + dz + e \right) \tag{24.27}$$

and five parameters ( $a$ ,  $b$ ,  $c$ ,  $d$ , and  $e$ ) are determined by relevant boundary conditions and curve fitting with the measured bending moment.

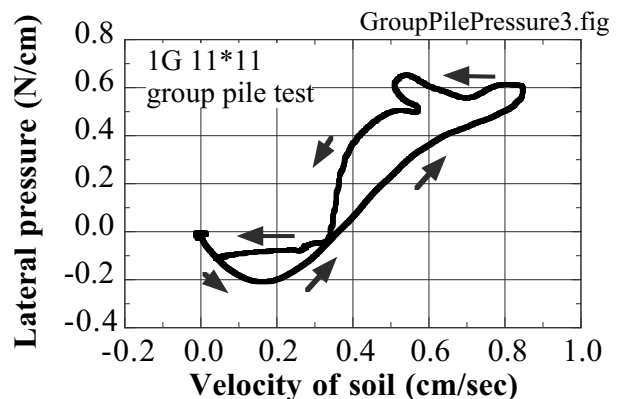
Figure 24.69 illustrates a typical time-variation of earth pressure on a model pile,  $p$ , in liquefied subsoil (Motamed et al. 2007). Liquefaction (high pore water pressure) occurred after 6 s and the ground started to move laterally. Simultaneously, the lateral earth pressure increased. It is important that the time history of earth pressure is better correlated with the velocity of soil movement than soil displacement. Figure 24.70 shows a positive correlation between the velocity and the lateral earth pressure. Similar correlation was reported from model tests by Ohtomo (1998). This velocity dependency implies that liquefied subsoil behaves similar to viscous liquid. This is consistent with finding in laboratory shear tests (Sect. 25.17). Similar finding on lateral drag force is stated in Sect. 25.13.

There is an opinion against the idea of rate dependent drag force on pile (Fig. 24.70). The opinion says that the excess pore water pressure in front of a pile is higher due to compressional deformation, while it is lower behind a pile due to dilation (Fig. 24.71). The measured drag force is generated by this pore pressure difference and, when the rate of soil flow is higher, seepage cannot equalize the two pressures. Therefore, the higher flow produces the greater drag force.

1G shaking table test on 11\*11 group piles subjected to lateral flow of liquefied sand. Toyoura sand of  $Dr=35\%$ .



**Fig. 24.69** Velocity dependency of interaction between pile and lateral flow of liquefied subsoil

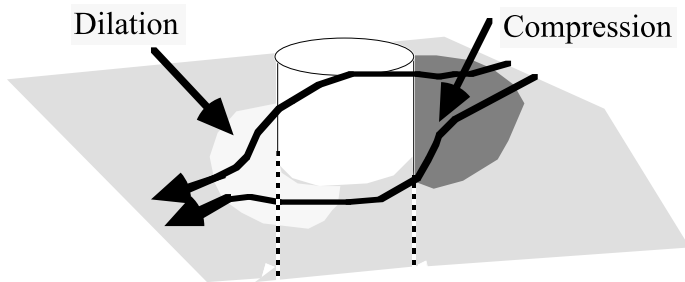


**Fig. 24.70** Relationship between flow velocity of soil and lateral force on pile

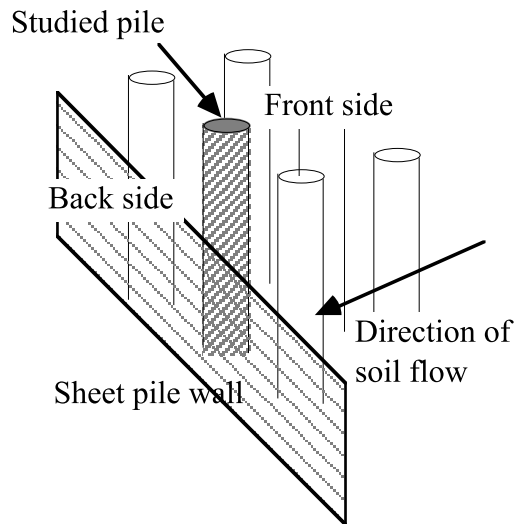
This idea was examined in one of the E-Defense full scale test (Figs. 24.48 and 24.49). Out of six model piles, the middle one in the back row near an unstable sheet pile wall was studied (Fig. 24.72). The measured pore water pressures in front and back of the pile are plotted in Fig. 24.73. There is evidently a pressure difference. Figure 24.74 demonstrates the lateral force (per 1 m of pile length) due to this pressure difference; the lateral force was calculated by

$$[(\text{Pore water pressure in front of a pile}) - (\text{Pore water pressure in back of a pile})] \times (\text{pile diameter}).$$

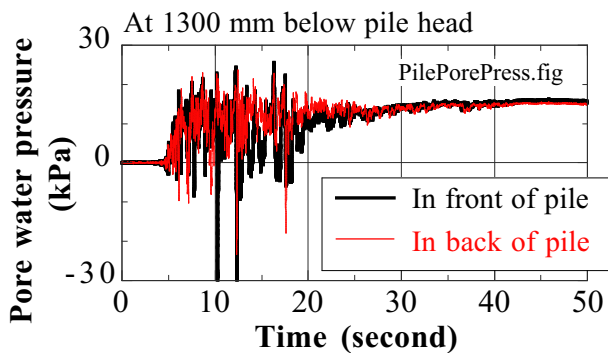
The pressure difference thus calculated is much lower than the measured lateral force (Fig. 24.74). Thus, the idea of pressure difference is declined. See also Fig. 25.41.



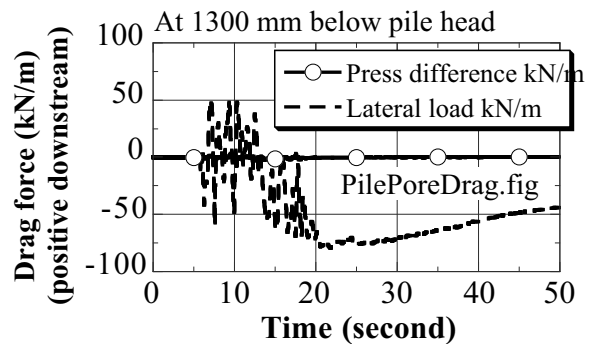
**Fig. 24.71** Possible mechanism accounting for rate dependency of lateral pile load



**Fig. 24.72** Location of studied pile in E-Defense project on lateral flow of liquefied subsoil behind sheet pile wall



**Fig. 24.73** Time history of pore pressure difference in front and back of a pile



**Fig. 24.74** Pore pressure difference in front and behind a pile

A detailed study was conducted on the behavior of a group pile undergoing lateral soil flow (Sesov et al. 2005; Towhata et al. 2006). The employed models were characterized by the number of piles which is realistic in building foundations. One type of model was composed of  $6 \times 6 = 36$  piles with the spacing of five times pile diameter, while the other had  $11 \times 11 = 121$  piles with the spacing of 2.5 times diameter (Fig. 24.75).

Figure 24.76 indicates the situation before shaking and lateral flow. There are therein straight lines on the surface made of colored sand. Being perpendicular to the direction of soil flow, these lines were intended to demonstrate the soil displacement around a pile. According to Fig. 24.77, the effects of pile on soil displacement are limited to a very narrow area that is 1.5–2 times the pile diameter.

The lateral load induced by soil flow is not uniformly distributed among piles. Figure 24.78 illustrates the variation of load from the upstream row towards the downstream row. It is interesting that both upstream and downstream rows are subject to greater load, while the internal piles undergo lower load due to protection by upstream ones (shadow effect).

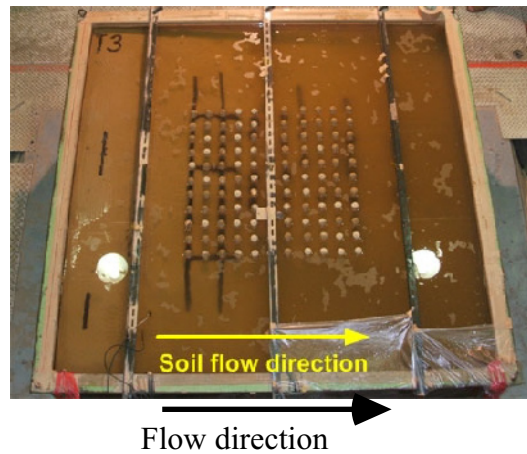
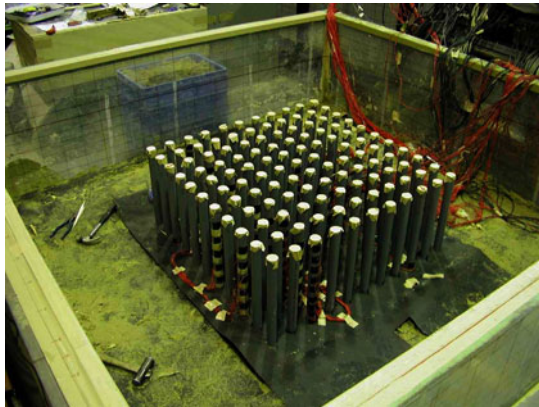


Fig. 24.75 Model of 121 piles prior to filling of soil

Fig. 24.76 Model of 121 piles prior to shaking

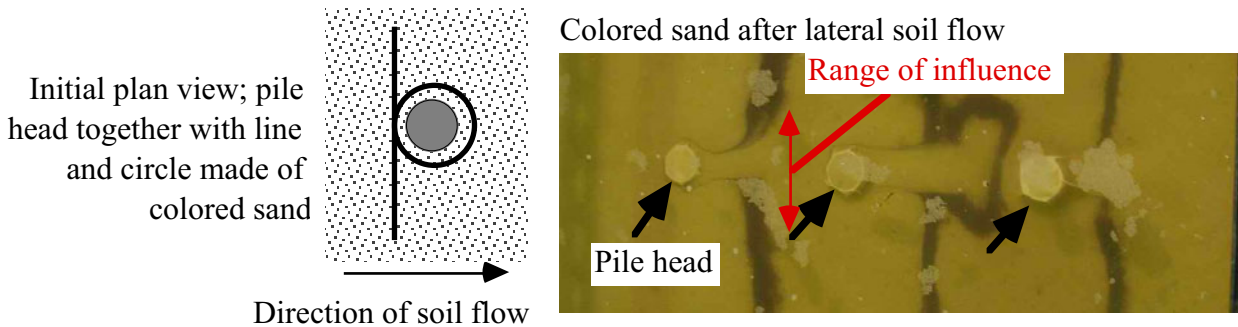


Fig. 24.77 Local soil displacement around pile heads during flow

The shadow effects in Fig. 24.78 implies that existing pile foundation of a building may be protected from the lateral flow of liquefied ground by installing new rows of piles in front and behind it. Since the extra rows of piles thus installed do not bear building load, their distortion during liquefaction does not affect the function of the superstructure.

The shadow effect (mitigation of lateral earth pressure on piles due to other piles) has been studied from the viewpoint of static lateral resistance of a group pile. For example, Rollins et al. (1998) reported from their field tests that the front row of piles receives greater lateral load than middle and trailing rows. McVay et al. (1995) showed that the shadow effect is increased when pile spacing is smaller. Ilyas et al. (2004) demonstrated that side piles receive greater load than central piles. It was also found that the shadow effect is insignificant when pile spacing is greater than five times pile diameter. While Rollins et al. (2006) revealed the greatest load on front piles, they additionally showed minor increase of earth pressure in rear piles as well. This is consistent with the finding in Fig. 24.78.

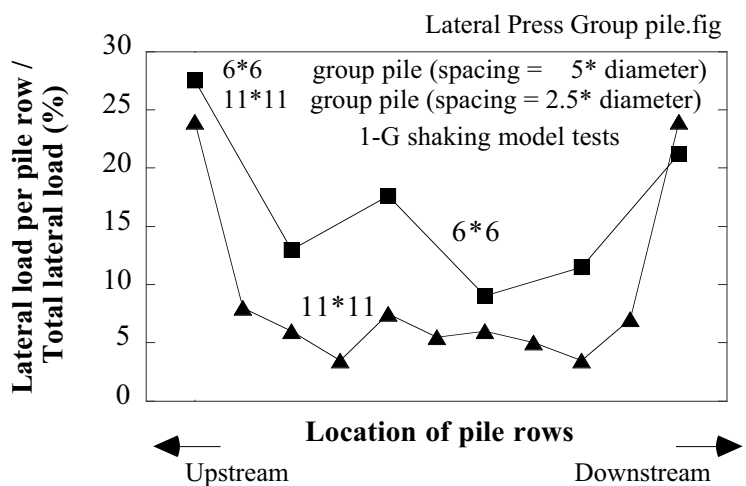


Fig. 24.78 Distribution of lateral force among rows of piles

Similarly, Kimura et al. (2002) demonstrated shadow effects in centrifugal model tests. In Fig. 24.79, the percentage of lateral load decreases in the downstream direction. While both monotonic and cyclic loadings were carried out, the monotonic load shows that the pile No. 4 at the downstream edge receives greater load than the pile No. 3. This is again consistent with Fig. 24.78.

Consequently, Suda et al. (2005) conducted large shaking model tests and proposed design formulae for lateral load exerted on group piles. Firstly when the extent of soil displacement is small, the subgrade reaction modulus controls the pile deformation. In liquefied soil in particular, the subgrade reaction modulus should be reduced to approximately 1% of the original value.

When liquefied layer translates over meters, the lateral earth pressure is important. This lateral load on an individual pile is divided into two components. Hence, the lateral load per unit length of a pile,  $p$ , at a depth of  $z$  (Fig. 24.80) is given by

$$\text{for pile body above ground water table, } p(z) = \alpha\beta^{j-1}K_pD\sigma'_z(z) \quad (24.28)$$

$$\text{for part of pile in liquefied subsoil, } p(z) = \alpha\beta^{j-1}KD\sigma_v(z), \quad (24.29)$$

in which  $\sigma'_z(z)$  stands for the effective vertical stress, and  $\sigma_v(z)$  in (24.29) is the total vertical stress. Moreover,  $j$  stands for the number of rows counted from the upstream side (Fig. 24.80),  $\beta^{j-1}$  the shadow effects (Fig. 24.80) with typically  $\beta = 0.8$  reducing the magnitude of load in the downstream direction,  $K_p = \tan^2(45^\circ + \phi/2)$  which is the passive earth pressure coefficient, and  $D$  the pile diameter. The  $\alpha$  parameter in the unliquefied surface layer is determined by

$$\alpha = \frac{0.877(1-\eta)}{0.877\eta + 0.123} \times f\left(\frac{H_1}{D}\right) + 1.0, \quad (24.30)$$

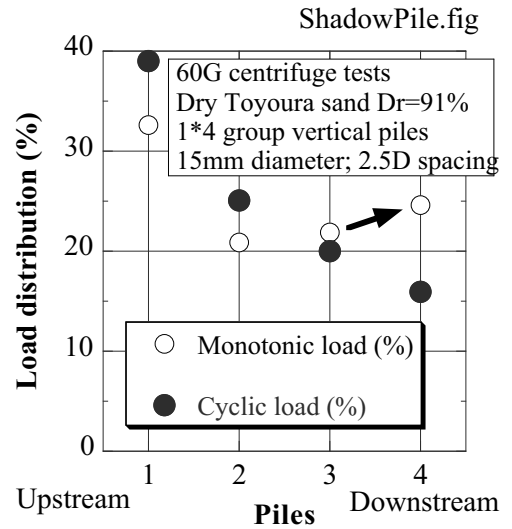
in which  $H_1$  designates the thickness of surface unliquefied layer (Fig. 24.81), the pile spacing (center-to-center) is designated by  $d$ , and  $\eta$  the ratio of pile spacing ( $D/d$  in Fig. 24.81); if the pile spacing is very large,  $\eta = 0$ . The function  $f$  is specified as

$$f\left(\frac{H_1}{D}\right) = 1.0 \text{ when } H_1/D \leq 3.8, \text{ and}$$

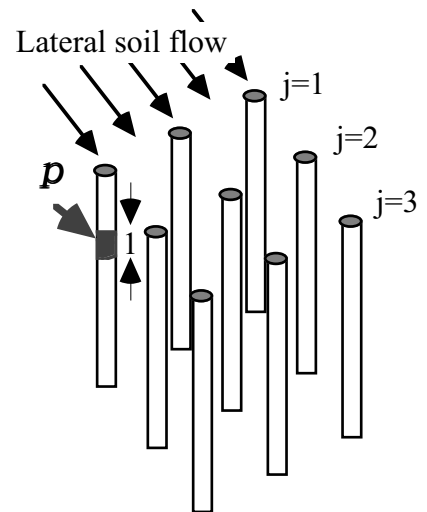
$$f\left(\frac{H_1}{D}\right) = 14\left(\frac{1}{H_1/D}\right)^2 + 0.03 \text{ when } H_1/D > 3.8. \quad (24.31)$$

In the liquefied subsoil, moreover,

$$\alpha = \frac{1}{0.599\eta + 0.401} \text{ and } \beta = 0.8. \quad (24.32)$$



**Fig. 24.79** Shadow effects in centrifugal pile tests (Kimura et al., 2002)



**Fig. 24.80** Notations in assessment of parameters in design calculation of lateral load on group pile



The variation of  $\alpha$  with the pile spacing ratio,  $\eta$ , is illustrated in Figs. 24.81 and 24.82 for different ratios of  $H_1/D$ . Evidently,  $\alpha$  decreases as the pile spacing decreases ( $\eta = D/d \rightarrow 1$ ).

In design practice, the dynamic earth pressure (Fig. 24.84) which is exerted by liquefied subsoil on embedded walls is assessed by using the Westergaard formula (Sect. 13.5). It is, however, reasonable to state that the magnitude of the dynamic pressure may be reduced if the wall is flexible and is subject to distortion. This point was verified experimentally by Tamari and Towhata (2003).

Doi and Hamada (1992) reported the undamaged pile foundation of H Building in Niigata. It is noteworthy that this building was next to the building in Fig. 17.25 where significant damage occurred in piles due to subsoil liquefaction and soil flow. It is important that the foundation of H Building was surrounded by sheet pile walls that were constructed for safe excavation of the foundation and,

during the 1964 Niigata earthquake, probably protected the piles from the effects of lateral soil flow. Note that another building in Kobe was protected by underground walls as well (Fig. 24.83). For more information, refer to Sect. 25.11.

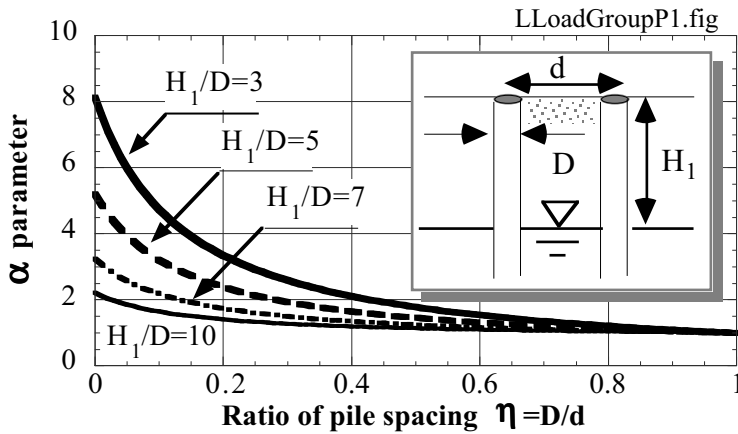


Fig. 24.81 Design diagram for pile above ground water table

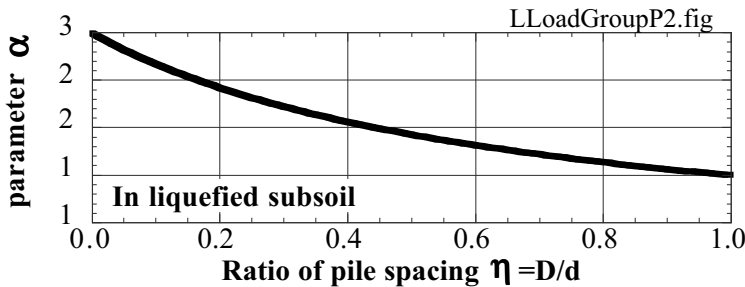


Fig. 24.82 Design diagram for pile lying in liquefied subsoil



Fig. 24.83 Building foundation which was protected by underground walls from effects of lateral soil flow (Shimagami Pumping Station, Kobe; Photograph by Prof. Koseki)

24.17 Earth Pressure Exerted on Wall by Liquefied Subsoil

The earth pressure exerted by liquefied subsoil on an underground structure is always an important design issue. Generally, the development of excess pore water pressure is divided into the mean pressure and the cyclic component as illustrated in Fig. 24.84. Hence, the simplest approach may be to determine the mean pressure as increasing from the initial hydrostatic pressure toward the total overburden pressure at 100% liquefaction, while the cyclic component is modeled by the Westergaard (1931) theory (Sect. 13.5) on hydrodynamic pressure acting on a rigid vertical wall. Note that the application of Westergaard theory to liquefied sand uses the unit weight of liquefied sand in place of that of water in the original theory.

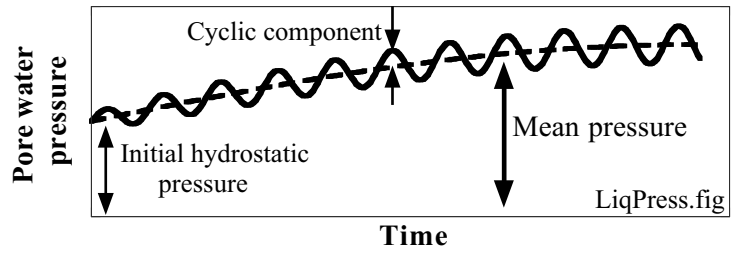


Fig. 24.84 Development of excess pore water pressure as combination of mean and cyclic components

As was shown experimentally by Tamari and Towhata (2003), the magnitude of cyclic pressure is reduced when a wall is flexible. Therefore, it is economical to avoid the Westergaard modeling of a rigid and stable wall that may overestimate the cyclic pressure on a flexible sheet pile wall.

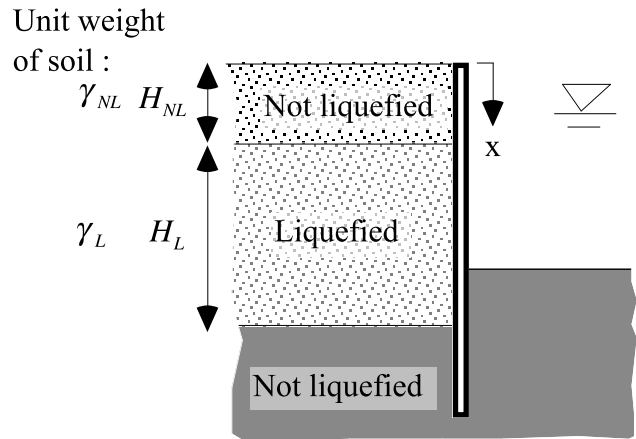


Fig. 24.85 Model of sheet pile wall with liquefied backfill

Based on large 1-G model tests (Okamura et al. 1999), (flexible) sheet-pile quay walls along a river channel is designed with due consideration of the wall flexibility (PWRI, 1998) as what follows. Figure 24.85 illustrates a model of sheet pile wall with a level backfill.

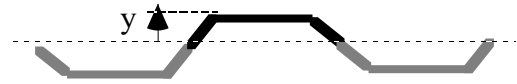


Fig. 24.86 Cross section of sheet pile wall as assembly of individual sheet piles

The amplitude of the cyclic earth pressure,  $p_d$ , in the liquefied subsoil is calculated as

$$p_d = \alpha_d \gamma_L K_h \sqrt{\left( H_{NL} \frac{\gamma_{NL}}{\gamma_L} + H_L \right) \left\{ x - \left( 1 - \frac{\gamma_{NL}}{\gamma_L} \right) H_{NL} \right\}}, \quad (24.33)$$

in which  $\alpha_d$  takes into account the flexibility of a sheet pile wall and  $K_h$  is the seismic coefficient,

$$\alpha_d = 0.40 \log_{10} \left[ \frac{EI/B}{y \gamma_L (H_{NL} + H_L)^3} \right] - 0.40, \quad (24.34)$$

where  $EI$  is the bending stiffness of an entire sheet pile wall,  $B$  is its width, and  $y$  stands for the size of its plane cross section (Fig. 24.86). Hence,  $EI/B$  designates the bending stiffness per unit length of a wall. Do not use  $EI$  and  $y$  of an individual sheet pile but use those of an assembled sheet-pile wall (Fig. 24.86). The  $\alpha_d$  parameter should be between 0 and 1. Practitioners sometimes designate  $I/(By)$  by  $Z$ .

In an very simple case where liquefaction occurs up to the ground surface ( $H_{NL} = 0$ ), (24.33) and (24.34) are reduced to

$$p_d = \alpha_d \gamma_L K_h \sqrt{H_L x} \tag{24.35}$$

$$\alpha_d = 0.40 \log_{10} \left[ \frac{EI}{By \gamma_L H_L^3} \right] - 0.40. \tag{24.36}$$

Accordingly, the entire cyclic earth pressure in a liquefied layer is given by

$$P_d = \int_0^{H_L} p_d dx = \frac{2}{3} \alpha_d \gamma_L K_h H_L^2. \tag{24.37}$$

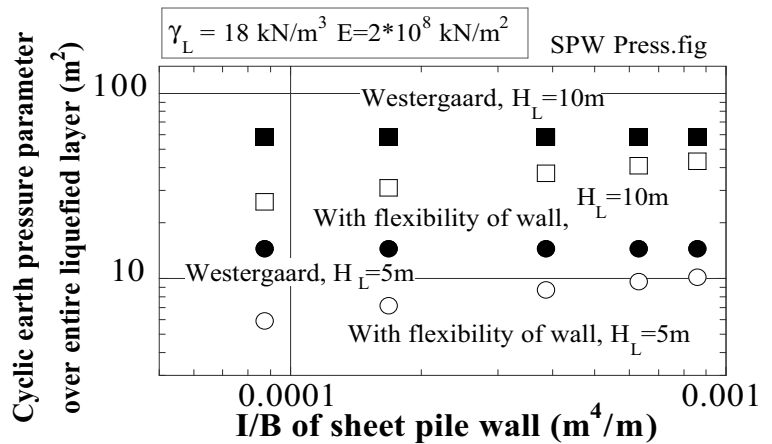
This formula is compared with Westergaard theory for liquefied subsoil (unit weight =  $\gamma_L$ );

$$p_d = \frac{7}{8} \gamma_L K_h \sqrt{H_L x}. \tag{24.38}$$

Note that this theory assumes a rigid wall. The Westergaard overall earth pressure in a liquefied layer is derived as

$$P_d = \int_0^{H_L} p_d dx = \frac{7}{12} \gamma_L K_h H_L^2. \tag{24.39}$$

Figure 24.87 compares  $(2/3)\alpha_d H_L^2$  in (24.37) and  $(7/12)H_L^2$  in (24.39) for two values of  $H_L$ . The employed rigidity of sheet pile walls is shown in Table 24.3. It is evident in this figure that the consideration of the flexibility of a wall reduces the design cyclic earth pressure to half over a realistic range of wall properties ( $I/B$ ).



**Fig. 24.87** Reduction of design cyclic earth pressure in liquefied layer by considering wall flexibility

In liquefiable subsoil, it is customary to calculate the mean pressure in Fig. 24.84 as being equal to the total overburden pressure when subsoil completely liquefies.

**Table 24.3** Parameters of sheet pile walls for earth pressure calculation

Type	SKSP-II	SKSP-III	SKSP-IV	SKSP-VL	SKSP-VIL
$I$ per meter ( $m^4/m$ )	$8.84 \times 10^{-5}$	$1.68 \times 10^{-4}$	$3.86 \times 10^{-4}$	$6.30 \times 10^{-4}$	$8.60 \times 10^{-4}$
$Z=I$ /meter / $y$ ( $m^3/m$ )	$8.74 \times 10^{-4}$	$1.34 \times 10^{-3}$	$2.27 \times 10^{-3}$	$3.15 \times 10^{-3}$	$3.82 \times 10^{-3}$

$$E = 2 \times 10^8 \text{ kN/m}^2$$

**List of References in Chapter 24**

Alam, M.J., Fukui, S., Towhata, I., Honda, T., Tamate, S., Tanaka, T., Uchiyama, J. and Yasuda, A. (2004) Centrifuge model tests on mitigation effects of underground walls on liquefaction-induced subsidence of embankment, Proc. 11th Int. Conf Soil Dynam. Earthq. Eng. and the 3rd Int. Conf. Earthq. Geotech. Eng., Berkeley, Vol. 2, pp. 537–544.

Bartlett, S.F. and Youd, T.L. (1995) Empirical prediction of liquefaction-induced lateral spread, J. Geotech. Eng., ASCE, Vol. 121, No. 4, pp. 316–329.

Bishop, A.W., Green, G.E., Garga, V.K., Andresen, A. and Brown, J.D. (1971) A new ring shear apparatus and its application to the measurement of residual strength, Geotech., Vol. 21, No. 4, pp. 273–328.

- De Alba, P.A., Seed, H.B., Retamal, E. and Seed, R.B. (1988) Analyses of dam failure in 1985 Chilean earthquake, *J. Geotech. Eng.*, Vol. 114, No. 12, pp. 1414–1434.
- Doi, M. and Hamada, M. (1992). A summary of case studies on liquefaction-induced ground displacements, *Proc. 4th Japan-US Workshop Liquefaction*, Hawaii, pp. 1–6.
- Ellis, E.A., Soga, K., Bransby, M.F. and Sato, M. (2000) Resonant column testing of sands with different viscosity pore fluids, *J. Geotech. Geoenv. Eng.*, ASCE, Vol. 126, No. 4, pp. 10–17.
- Fujii, T., Hyodo, M., Kusakabe, S. and Fukuda, K. (2000) On-line seismic response tests on embankments founded on saturated sandy deposits, *Proc. JSCE*, Vol. 652/III-51, pp. 229–243 (in Japanese).
- Fujiwara, T., Horikoshi, K. and Sakai, K. (2005) Development of a sampler designed for laminar box and its application to dynamic centrifuge modeling of footing settlement due to liquefaction, *Proc. 16th Int. Conf. Soil Mech. Geotech. Eng.*, Vol. 4, pp. 2645–2648.
- Ghalandarzadeh, A., Orita, T., Towhata, I. and Fang, Y. (1998) Shaking table tests on seismic deformation of gravity quay walls, *Special Issue on Geotechnical Aspects of the January 17 1995 Hyogoken-Nambu Earthquake*, No. 2, *Soils Found.*, pp. 115–132.
- Hakuno, M., Shidawara, M. and Hara, T. (1969) Dynamic destructive test of a cantilever beam, controlled by an analog-computer, *Proc. JSCE*, No. 171, pp. 1–9 (in Japanese).
- Hamada, M., Wakamatsu, K., Tazoh, T. and Yoshida, N. (1991) Soil liquefaction and resulting damage to structures during the July 16, 1990, Philippines earthquake, *Tsuchi-to-Kiso*, the monthly magazine of Jpn Geotech. Soc, Vol. 39, No. 2, pp. 51–56.
- Hamada, M., Yasuda, S., Isoyama, R. and Emoto, K. (1986) Observation of permanent displacements induced by soil liquefaction, *Proc. JSCE*, 376/III-6, pp. 211–220 (in Japanese).
- Hamada, M., Yasuda, S., Isoyama, R. and Emoto, K. (1986) Study on liquefaction-induced permanent ground displacements and earthquake damage, *Proc. JSCE*, No. 376/III-6, pp. 221–229.
- Horii, K. (1968) chapter on Highway Bridges, *General Report on the Niigata, Earthquake*, ed. Kawasumi, H., Tokyo Denki University Press, pp. 431–450.
- Iai, S. (1989) Similitude for shaking table tests on soil-structure-fluid model in 1g gravitational field, *Soils Found.*, Vol. 29, No. 1, pp. 105–118.
- Ilyas, T., Leung, C. F., Chow, Y. K. and Budi, S. S. (2004) Centrifuge model study of laterally loaded pile groups in clay, *J. Geotech. Geoenv. Eng.*, ASCE, Vol. 130, No. 3, pp. 274–283.
- Inagaki, H., Iai, S., Sugano, T., Yamazaki, H. and Inatomi, T. (1996) Performance of caisson type quay walls at Kobe Port, *Soils Found.*, *Special Issue on Geotechnical Aspects of the January 17 1995 Hyogoken-Nambu Earthquake*, No. 1, pp. 119–136.
- Ishihara, K. (1993) Liquefaction and flow failure during earthquakes, *Geotech.*, Vol. 43, No. 3, pp. 351–415.
- Ishihara, K. (1996) The steady state of sandy soils, *Soils Found.*, Vol. 36, No. 2, pp. 81–91.
- Ishihara, K., Yasuda, S. and Nagase, H. (1996) Soil characteristics and ground damage, *Soils Found.*, *Special Issue on Geotechnical Aspects of the January 17 1995 Hyogoken-Nambu earthquake*, pp. 109–118.
- Kagawa, T. (1978) On the similitude in model vibration tests of earth-structures. *Proc. JSCE*, Vol. 275, pp. 69–77 (in Japanese).
- Kawamura, S., Nishizawa, T. and Wada, K. (1985) Detection of damaged pile 20 years after earthquake, *Nikkei Architecture*, 29th of July, pp. 130–134 (in Japanese).
- Keller, G.H., Zhen, J., Yang, Z.-S., Bornhold, B.D., Prior, D.B., Suhayda, J.N., Wiseman Jr., W.J. and Wright, L.D. (1990) Mass physical properties of Huanghe Delta and Southern Bohai Sea near-surface deposits, *China, Marine Geotech.*, Vol. 9, pp. 207–225.
- Kimura, M., Makino, H., Okawa, K., Kamei, H. and Zhang, F. (2002) The bearing capacity of a group-pile foundation with inclined piles under lateral loading, *Proc. JSCE*, 722/III-61, pp. 97–107 (in Japanese).
- Kokusho, T. and Iwatate, T. (1979) Scaled model tests and numerical analyses on nonlinear dynamic response of soft grounds, *Proc. JSCE*, Vol. 285, pp. 57–67 (in Japanese).
- Kusakabe, S. and Morio, S. (1995) The development of a substructure on-line testing system for seismic response analysis of a geotechnical system, *Soils Found.*, Vol. 35, No. 2, pp. 117–125.

- McKenna, G.T., Luternauer, J.L. and Kostaschuk, R.A. (1992) Large-scale mass-wasting events on the Fraser River Delta front near Sand Heads, British Columbia, *Can. Geotech. J.*, Vol. 29, pp. 151-156.
- McVay, M., Casper, R. and Shang, T.-I. (1995) Lateral response of three-row groups in loose to dense sands at 3D and 5D pile spacing, *J. Geotech. Eng.*, Vol. 121, No. 5, pp. 436-441.
- Meneses, J., Ishihara, K. and Towhata, I. (1998) Effects of superimposing shear stress on the undrained behavior of saturated sand under monotonic loading, *Soils Found.*, Vol. 38, No. 4, pp. 115-127.
- Meneses-Loja, J., Ishihara, K. and Towhata, I. (2000) Flow failure of saturated sand under simultaneous monotonic and cyclic stresses, *J. Geotech. Geoenv. Eng., ASCE*, Vol. 126, No. 2, pp. 131-138.
- Motamed, R., Towhata, I. and Sesov, V. (2007) Study on p-y curve for piles subjected to lateral flow of liquefied ground, *Proc. 4th Int. Conf. Earthq. Geotech. Eng.*, Thessaloniki, Greece.
- Ohtomo, K. (1998) Load characteristics of ground lateral flow on in-ground structures, *Proc. JSCE*, No. 591/I-43, pp. 283-297 (in Japanese).
- Okamura, M., Matsuo, O. and Koga, Y. (1999) Effect of sheet piling as a measure against liquefaction-induced embankment failure, *Proc. 2nd Int. Conf. Earthq. Geotech. Eng.*, Portugal, Vol. 2, pp. 731-736.
- Olson, S.M., Stark, T.D., Walton, W.H. and Castro, G. (2000) 1907 static liquefaction flow failure of the north dike of Wachusett dam, *J. Geotech. Geoenv. Eng., ASCE*, Vol. 126, No. 12, pp. 1184-1193.
- Orense, R., Hyodo, M., Takahashi, S., Yoshimoto, N. (2006) Laboratory experiments on the cyclic shear behavior of partially saturated slopes, *Proc. New Zealand Workshop on Geotech. Earthq. Eng.*, pp. 231-240.
- Pokrovsky, G.I. and Fedorov, I.S. (1936) Studies of soil pressures and deformation by means of a centrifuge, *Proc. 1st Int. Conf. Soil Mech. Found. Eng.*, Vol. 1, pp. 70-76.
- Poulos, S.J., Castro, G. and France, J.W. (1984) Liquefaction evaluation procedure, *Proc. ASCE*, Vol. 111, GT6, pp. 772-792.
- Prior, D.B. and Coleman, J.M. (1982) Active slides and flows in underconsolidated marine sediments on the slopes of the Mississippi Delta, *Marine Slides and Other Mass Movements*, Putnam Press, pp. 21-55.
- PWRI (Public Works Research Institute) (1998) Design and construction manual of liquefaction-mitigation measures for river dikes (draft), pp. 7-14.
- Rocha, M. (1957) The possibility of solving soil mechanics problems by the use of models, *Proc. 4th Int. Conf. Soil Mech. Found. Eng.*, Vol. 1, pp. 183-188.
- Rollins, K.M., Olsen, R.J., Egbert, J.J., Jensen, D.H., Olsen, K.G. and Garrett, B.H. (2006) Pile spacing effects on lateral pile group behavior: load tests, *J. Geotech. Geoenv. Eng., ASCE*, Vol. 132, No. 10, pp. 1262-1271.
- Rollins, K.M., Peterson, K.T. and Weaver, T.J. (1998) Lateral load behavior of full-scale pile group in clay, *J. Geotech. Geoenv. Eng., ASCE*, Vol. 124, No. 6, pp. 468-478.
- Roscoe, K.H. (1968) Soils and model tests, *Journal of Strain Analysis*, Vol. 3, No. 1, pp. 57-64.
- Sasaki, Y., Tokida, K., Matsumoto, H., Saya, S. and Mori, T. (1991) Deformation characteristics of eccentrically loaded ground induced by soil liquefaction, *Technical Memorandum of PWRI 土木研究所資料*, No. 3000, p. 6.
- Sasaki, Y., Towhata, I., Tokida, K., Yamada, K., Matsumoto, H., Tamari, Y. and Saya, S. (1992) Mechanism of permanent displacement of ground caused by seismic liquefaction, *Soils Found.*, Vol. 32, No. 3, pp. 79-96.
- Seed, H.B. (1987) Design problems in soil liquefaction, *Proc. ASCE*, Vol. 113, GT8, pp. 827-845.
- Seed, H.B., Seed, R.B., Schlosser, F., Blondeau, F. and Juran, I. (1988) The Landslide at the Port of Nice on October 16 1979, *EERC Report -88/10*, Univ. California, Berkeley.
- Sesov, V., Towhata, I., Gonzalez, M., Ball, R. and Ishimatsu, S. (2005) Experimental study on large pile group response subjected to lateral flow of liquefied ground, *Proc. Int. Conf. Soil Mech. Geotech. Eng.*, Osaka, Vol. 4, pp. 2183-2186.
- Kusakabe, S. and Morio, S. (1995) The development of a substructure on-line testing system for seismic response analysis of a geotechnical system, *Soils Found.*, Vol. 35, No. 2, pp. 117-125.

- Sladen, J.A., D'Hollander, R.D. and Krahn, J. (1985) Back analysis of the Nerlerk Berm liquefaction slides, *Can. Geotech. J.*, Vol. 22, pp. 579–588.
- Suda, Y., Sato, M., Tamari, Y. and Kokusho, T. (2007) Design method for pile foundation subjected to liquefaction-induced lateral spread, accepted for publication by *Proc. JSCE-C* (in Japanese).
- Tamari, Y. and Towhata, I. (2003) Seismic soil-structure interaction of cross sections of flexible underground structures subjected to soil liquefaction, *Soils Found.*, Vol. 43, No. 2, pp. 69–87.
- Toki, K., Sato, T., Kiyono, J., Garmroudi, N.K., Emi, S. and Yoshikawa, M. (1990) Hybrid experiments on non-linear earthquake-induced soil-structure interaction, *Earthq. Eng. Struct. Dynam.*, Vol. 19, pp. 709–723.
- Towhata, I. (1986) Finite element model to predict permanent displacement of ground induced by liquefaction, *Proc. 2nd Int. Conf. Num. Models Geomech.*, Ghent, Belgium, pp. 689–697.
- Towhata, I., Sasaki, Y., Tokida, K., Yamada, K., Matsumoto, H., Tamari, Y. and Saya, S. (1992) Mechanism of permanent displacement of ground caused by seismic liquefaction, *Soils Found.*, Vol. 32, No. 3, pp. 79–96.
- Towhata, I., Ghalandarzadeh, A., Sundarraj, K.P. and Vargas-Monge, W. (1996) Dynamic failures of subsoils observed in water-front areas, *Special Issue on Geotechnical Aspects of the January 17 1995 Hyogoken-Nambu Earthquake*, No. 1, *Soils Found.*, pp. 149–160.
- Towhata, I., Sesov, V., Motamed, R. and Gonzales, M. (2006) Model tests on lateral earth pressure on large group pile exerted by horizontal displacement of liquefied sandy ground, *Proc. 8th US Nat. Conf. Earthq. Eng.*, CD ROM Proceedings, Paper Number 8, NCEE-001227, San Francisco.
- Toyota, H., Towhata, I., Imamura, S. and Kudo, K. (2004) Shaking table tests on flow dynamics in liquefied slope, *Soils Found.*, Vol. 44, No. 5, pp. 67–84.
- Vargas-Monge, W. (1998) Ring shear tests on large deformation of sand, Ph.D. Thesis, University of Tokyo.
- Verdugo, R. and Ishihara, K. (1996) The steady state of sandy soils, *Soils Found.*, Vol. 36, No. 2, pp. 81–91.
- Wakamatsu, K., Hamada, M., Tazoh, T., Yoshida, N. and Ando, T. (1991) Liquefaction and Landsliding from the July 16, 1990 Luzon, Philippine earthquake, *Proc. 3rd US-Japan Workshop on Earthquake Resistant Design of Lifeline Facilities and Countermeasures for Soil Liquefaction (NCEER-91-0001)*, pp. 23–38.
- Westergaard, H.M. (1931) Water pressure on dams during earthquakes, *Trans. ASCE*, Paper No. 1835, pp. 418–433.
- Whitman, R.V. (1985) On Liquefaction, *Proc. 11th Int. Conf. Soil Mech. Found. Eng.*, Vol. 4, pp. 1923–1926.
- Wride, C.E., Roberts, E.C. and Robertson, P.K. (1999) Reconsideration of case histories for estimating undrained shear strength in sandy soils, *Can. Geotech. J.*, Vol. 36, pp. 907–933.
- Yoshida, N. and Hamada, M. (1991) Damage to foundation piles and deformation pattern of ground due to liquefaction-induced permanent ground deformation, *Proc. 3rd Japan-U.S. Workshop on Earthquake Resistant Design of Lifeline Facilities and Counter Measures for Soil Liquefaction, NCEER-91-0001*, pp. 147–161.
- Yoshida, N., Tazo, T., Wakamatsu, K., Yasuda, S., Towhata, I., Nakazawa, H. and Kiku, H. (2007) Causes of Showa Bridge collapse in the 1964 Niigata Earthquake based on eyewitness testimony, *Soils Found.*, Vol. 47, No. 6, pp. 1075–1087.
- Yoshimine, M., Ishihara, K. and Vargas, W. (1998a) Effects of principal stress direction and intermediate principal stress on undrained shear behavior of sand, *Soils Found.*, Vol. 38, No. 3, 179–188.
- Yoshimine, M. and Ishihara, K. (1998b) Flow potential of sand during liquefaction, *Soils Found.*, Vol. 38, No. 3, pp. 189–198.
- Youd, T.L. and Perkins, D.M. (1987) Mapping of liquefaction severity index, *J. Geotech. Eng. ASCE*, 113, GT11, pp. 1374–1392.
- Youd, T.L., Hansen, C.M. and Bartlett, S.V. (2002) Revised multilinear regression equations for prediction of lateral spread displacement, *J. Geotech. Geoenv. Eng.*, ASCE, Vol. 128, No. 12, pp. 1007–1017.

# Chapter 25

## Prediction of Permanent Displacement Due to Liquefaction



西安 漢之未央宮前殿遺址

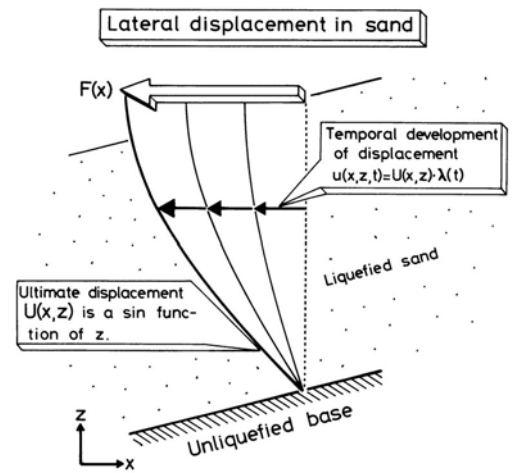
This is a foundation of an ancient palace. This palace of Han dynasty in present Xi'an of China was built in late third century, B.C. after a long war period. When the first emperor of Han Dynasty saw his gigantic palace for the first time, he blamed his minister for wasting money and labor at the time of governmental and people's poverty. The minister replied, however, that a magnificent palace would make people trust the new government and would contribute to peace. The emperor was pleased to hear this 高祖乃說.

**25.1 Mode of Displacement**

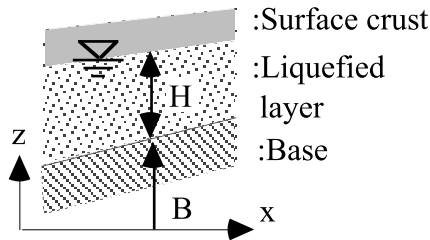
The observed shape of subsoil displacement (Sect. 24.4 and 24.7) indicated that the lateral displacement changes in a harmonic manner in the vertical direction, while the surface crust moves together with the liquefied subsoil (Sect. 24.7). Hence, it is possible to express the lateral displacement “*u*” as a sin function of elevation, *z* (Fig. 25.1);

$$U(x,z) = F(x) \sin \frac{\pi(z - B)}{2H} \tag{25.1}$$

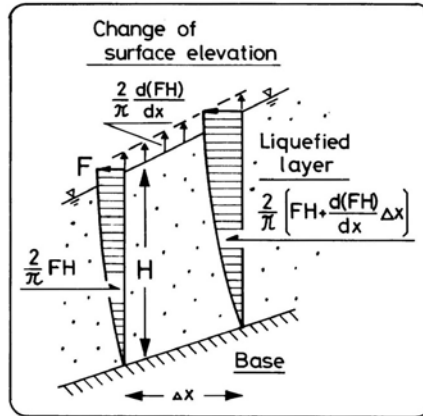
where *F* is “the amplitude of *sin* function,” *B* is the elevation of the bottom of the liquefied layer, and *H* is its thickness. Both *B* and *H* are functions of *x* (see Fig. 25.2). Note that there are many practical methods to assess the thickness of liquefied layer, *H*, by using for example SPT-*N* and others (Sect. 21.3).



**Fig. 25.1** Idealized mode of lateral displacement



**Fig. 25.2** Simplified configuration of liquefied subsoil



**Fig. 25.3** Increase of surface elevation

The nonlinear idealization as (25.1) allows one to avoid using many nodal points in the vertical direction. Hence, the computation load is drastically reduced.

By assuming an undrained (constant volume) deformation, the vertical displacement, *W*, which is positive downward in Fig. 25.3, can be expressed in terms of *F* by substituting (25.1) in a constant-volume condition;

$$\frac{\partial U}{\partial x} + \frac{\partial W}{\partial z} = 0. \tag{25.2}$$

Equation (25.2) is then integrated with *z* and a boundary condition of *W* = 0 at the bottom (*z* = *B*) is imposed;

$$W = -\frac{2}{\pi} \left\{ 1 - \cos \frac{\pi(z - B)}{2H} \right\} \frac{d(HF)}{dx} + \left\{ \frac{dB}{dx} H + \frac{dH}{dx} (z - B) \right\} \frac{F}{H} \sin \frac{\pi(z - B)}{2H}. \tag{25.3}$$

At the surface of liquefied layer (*z* = *B*+*H*) and consequently at the ground surface in particular,



$$W_{\text{surface}} = -\frac{2}{\pi} \frac{d(HF)}{dx} + \frac{d(B+H)}{dx} F. \quad (25.4)$$

This is the vertical displacement of a soil particle at the surface.

In case a consolidation subsidence is interested in as well, it is predicted separately (Sect. 22.1) and later added to (25.4).

On the other hand, the volume flux of the liquefied layer across a vertical cross section at  $x$  is derived as

$$\text{Volume of flow} = \int_B^{B+H} F \sin \frac{\pi(z-B)}{2H} dz = \frac{2}{\pi} (FH) \quad (25.5)$$

Figure 25.3 illustrates that the difference of this volume flux between two vertical cross sections results in the increase/decrease of the elevation of the ground surface. At a fixed  $x$  coordinate, the surface elevation increases by

$$\delta H = \frac{d}{dx} \left\{ \frac{2}{\pi} (FH) \right\} \quad (25.6)$$

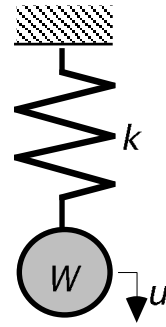
Thus, the change of elevation is different from the particle movement in (25.4).

**25.2 Principle of Minimum Potential Energy**

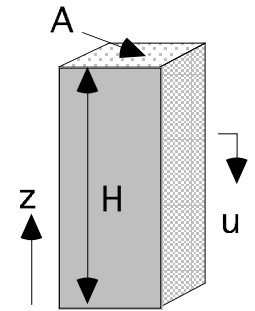
Any mechanical phenomenon tries to reduce the total potential energy for stabilization. Figure 25.4 is a simple example of a spring with a weight. When the weight moves by “ $u$ ” due to the action of gravity, the change of the potential energy,  $Q$ , is given by

$$Q = \frac{ku^2}{2} - Wu \tag{25.7}$$

in which the first term is the strain energy of the spring, while the second is the decrease in gravity potential energy. The potential energy,  $Q$ , is minimized when  $dQ/du = 0$  is satisfied. Consequently,  $u = W/k$  is derived. A minor change of displacement from this “ $u$ ” does not change  $Q$  because  $dQ/du = 0$ . This solution is well-known in elementary mechanics.



**Fig. 25.4** Spring-weight model



**Fig. 25.5** Simple model of column

The second example is a column under gravity action (Fig. 25.5). The elasticity modulus of the column is designated by  $E$ , the unit weight by  $\gamma$ , the cross section  $A$ , and the height  $H$ . The bottom of the column is fixed, while its top is free. When the vertical displacement of the column is denoted by  $u(x)$ , the change of the potential energy,  $Q$ , is given by

$$Q = \int_0^H A \left\{ \frac{E}{2} \left( \frac{du}{dz} \right)^2 - \gamma u \right\} dz \tag{25.8}$$

When “ $u(x)$ ” is the exact solution of displacement,  $Q$  takes the minimum value, and a minor arbitrary increment from this  $u$ , denoted by  $\delta u$ , does not change the value of  $Q$ . Hence,

$$\delta Q = A \int_0^H \left[ \frac{E}{2} \left\{ \left( \frac{d(u + \delta u)}{dz} \right)^2 - \left( \frac{du}{dz} \right)^2 \right\} - \gamma(u + \delta u - u) \right] dz = 0 \tag{25.9}$$

Because  $\delta u$  is very small for any value of  $z$ ,  $(\delta u)^2$  is negligible. Therefore,

$$\delta Q = A \int_0^H \left( E \frac{du}{dz} \frac{d\delta u}{dz} - \gamma \delta u \right) dz = \left[ \left[ AE \frac{du}{dz} \delta u \right]_0^H - \int_0^H A \left( E \frac{d^2u}{dz^2} + \gamma \right) \delta u dz \right] = 0 \tag{25.10}$$

Since (25.10) holds true for an arbitrary function of  $\delta u$ , the integrand in the second term has to be zero at any  $z$ ,

$$E \frac{d^2u}{dz^2} + \gamma = 0. \tag{25.11}$$

Equation (25.11) means that the  $z$ -derivative of stress,  $E(du/dz)$ , is balanced by the gravity force. Equation (25.9) represents the overall energy principle, i.e., minimization of potential energy, and (25.11) is a local expression of the same principle. Thus, the variational principle in (25.9) and a differential equation of (25.11) are equivalent with each other. Consequently, (25.11) is called the Euler’s equation of the variational principle (25.9).

The first term of (25.10) has to be zero for an arbitrary  $\delta u$  as well. By choosing a special  $\delta u$ , which is equal to zero at the bottom of the column (: fundamental boundary condition), the remaining requirement is  $AE(du/dz) = 0$  at  $z = H$ . This means a free boundary (stress = 0) and is mathematically called the natural boundary condition.

A closed form solution of a lateral flow of liquefied subsoil was derived by using the displacement functions in Sect. 25.1, obtaining the Euler's differential equation for  $F(x)$ , and solving it; Sect. 25.4.

### 25.3 Principle of Lagrangean Equation of Motion

The Lagrangean equation of motion is identical with the famous Newtonian equation of motion in principle. It, however, can deal with more complicated situations and is an extremely powerful tool of analysis.

The first example is taken of a dynamic response of a spring-weight model in Fig. 25.6. The kinetic energy,  $K$ , and the potential energy,  $Q$ , are described in terms of the displacement,  $u$ . Note that the potential energy consists of a gravity and a strain components;

$$K = \frac{W}{2g} \left( \frac{du}{dt} \right)^2 \quad \text{and} \quad Q = \frac{k}{2} u^2 - Wu. \quad (25.12)$$

The Lagrangean equation of motion is given by

$$\frac{d}{dt} \left[ \frac{\partial(K-Q)}{\partial(du/dt)} \right] - \frac{\partial(K-Q)}{\partial u} = 0 \quad (25.13)$$

when no viscous mechanism is involved. If a viscous mechanism dissipates energy of  $D$  per unit time, (25.13) is replaced by

$$\frac{d}{dt} \left[ \frac{\partial(K-Q)}{\partial(du/dt)} \right] - \frac{\partial(K-Q)}{\partial u} = -\frac{1}{2} \frac{\partial D}{\partial(du/dt)} \quad (25.14)$$

in which  $D = \mu(du/dt)^2$  and  $\mu$  is a dashpot coefficient.

By substituting (25.12) in (25.13), one derives

$$\frac{W}{g} \frac{d^2u}{dt^2} + ku = W \quad (25.15)$$

which is identical with a well-known equation of motion of a single-degree-of-freedom model as derived from the Newtonian theory.

The second example is taken of a two-degree-of-freedom model (Fig. 25.7). A rotational angle,  $\omega$ , is employed in order to show that the Lagrangean theory works with not only displacement but rotational angle and any other parameters that specify the kinetic and potential energies. In the present case,

$$K = \frac{I}{2} \left( \frac{d\omega}{dt} \right)^2 + \frac{W}{2g} \left( \frac{du}{dt} \right)^2 \quad \text{and}$$

$$Q = -Wu + \frac{j}{2} \omega^2 + \frac{k}{2} (u - R\omega)^2. \quad (25.16)$$

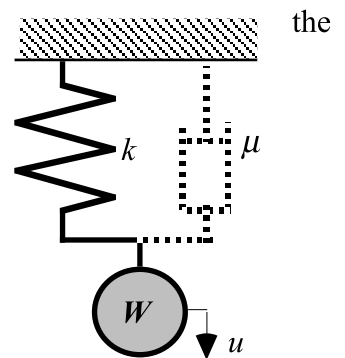


Fig. 25.6 Spring-weight model

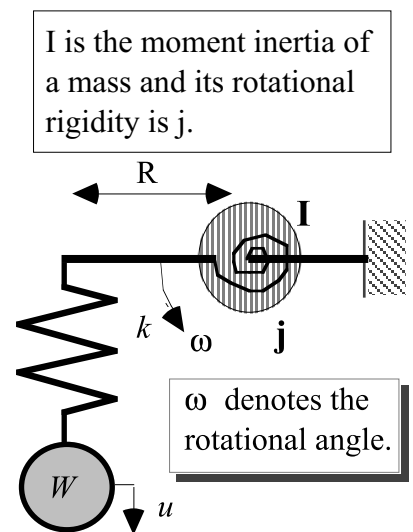


Fig. 25.7 Rotational spring model with two degrees of freedom

Note that  $u - R\omega$  stands for the extension of the spring. The Lagrangean equation of motion are consequently derived by

$$\frac{d}{dt} \left[ \frac{\partial(K-Q)}{\partial(d\theta/dt)} \right] - \frac{\partial(K-Q)}{\partial\theta} = 0 \quad (25.17)$$

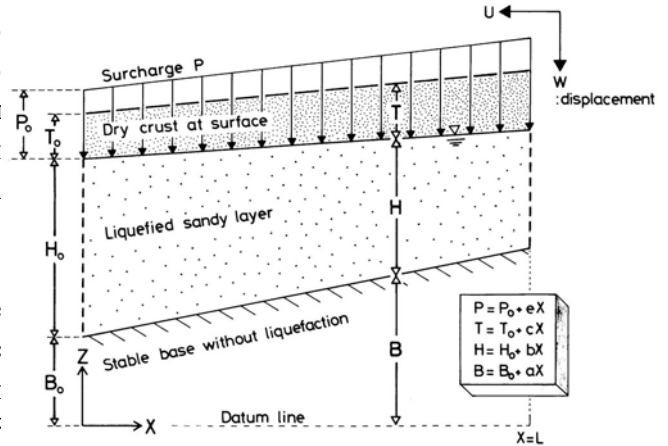
in which  $\theta$  is called a generalized displacement and is either  $u$  or  $\omega$  in the present case. Accordingly,

$$\begin{bmatrix} W/g & 0 \\ 0 & I \end{bmatrix} \begin{Bmatrix} d^2u/dt^2 \\ d^2\omega/dt^2 \end{Bmatrix} + \begin{bmatrix} k & -kR \\ -kR & j + kR^2 \end{bmatrix} \begin{Bmatrix} u \\ \omega \end{Bmatrix} = \begin{Bmatrix} 0 \\ 0 \end{Bmatrix} \quad (25.18)$$

**25.4 Energy Theory on Flow of Liquefied Subsoil**

It is possible to calculate strain energy components and gravity potential energy by using the horizontal and vertical displacement functions,  $U$  and  $W$ , as derived in Sect. 25.1. Since the “amplitude”  $F(x)$  of a sin function is unknown, it is attempted to determine it by using the principle of minimum potential energy.

A simplified model ground shown in Fig. 25.8 is used where a liquefied subsoil is overlain by a dry surface crust. The elevation of the bottom of the liquefied layer  $B$ , its thickness,  $H$ , the thickness ( $T$ ) and the weight ( $F$ ) of the crust vary linearly with  $x$ ;



**Fig. 25.8** Idealized model of liquefied ground

$$B = B_0 + ax \quad H = H_0 + bx \quad T = T_0 + cx \quad P = P_0 + ex \tag{25.19}$$

The components of the change of the potential energy upon lateral flow are as what follows. Note that all the energy components are integrated ones from  $x = 0$  to  $x = L$  in Fig. 25.8.

1. Increment of gravity energy of surface crust,  $P_s$

This component is derived by multiplying the weight of the soil crust by its vertical displacement (25.4). Hence

$$P_s = -\int_0^L P \times W dz = \int_0^L (P_0 + ex) \left[ \frac{2}{\pi} \frac{d}{dx} \{ (H_0 + bx)F \} - (a + b)F \right] dx \tag{25.20}$$

2. Increment of gravity energy of liquefied subsoil,  $P_1$

The present theory considers liquefied sand as liquid. Upon flow, the elevation of the surface is raised by  $\delta H$  ( see Fig. 25.3). Accordingly,

$$\begin{aligned} P_1 &= \int_0^L \left( \int_B^{B+H+\delta H} \gamma z dz - \int_B^{B+H} \gamma z dz \right) dx = \frac{\gamma}{2} \int_0^L \left\{ (B + H + \delta H)^2 - (B + H)^2 \right\} dx \\ &= \int_0^L \left[ \frac{2\gamma}{\pi^2} \left\{ (H_0 + bx) \frac{dF}{dx} + bF \right\}^2 + \frac{2\gamma}{\pi} \left\{ (H_0 + bx) \frac{dF}{dx} + bF \right\} (B_0 + H_0 + ax + bx) \right] dx \\ &\quad - \left[ \gamma \left( \frac{2HB}{\pi} + \frac{4H^2}{\pi^2} \right) F \right]_0^L \end{aligned} \tag{25.21}$$

3. Increment of strain energy in surface crust,  $E_s$

The lateral compression in the surface crust,  $\epsilon_x = dF/dx$ , mitigates the lateral flow of the subsoil (Sect. 24.6) and, hence, plays an essential role. Other strain components ( $\epsilon_x$  and  $\gamma_{xz}$ ) are smaller than  $\epsilon_x$  and are ignored. Therefore,

$$E_s \approx \int_0^L \frac{E \epsilon_x^2 T}{2} dx = \int_0^L \frac{E(T_0 + cx)}{2} \left( \frac{dF}{dx} \right)^2 dx \tag{25.22}$$

4. Increment of strain energy in liquefied subsoil,  $E_1$ 

The present study considers the liquefied sand as Bingham viscous liquid. Its shear strength is  $\tau_r$ ;

$$E_1 = \int_0^L \left\{ \int_B^{B+H} (\tau_r \times \text{strain}) dz \right\} dx = \int_0^L \left\{ \int_B^{B+H} \left( \tau_r \times \frac{dU}{dz} \right) dz \right\} dx = \int_0^L \tau_r F dx \quad (25.23)$$

In total, the increment of potential energy upon lateral flow,  $Q$ , is given by (Towhata et al. 1992)

$$Q = \int_0^L q(F, dF/dx, x) dx - \left[ \gamma \left( \frac{2HB}{\pi} + \frac{4H^2}{\pi^2} \right) F \right]_0^L \rightarrow \text{minimum} \quad (25.24)$$

where

$$q = (P_0 + ex) \left[ \frac{2}{\pi} \frac{d}{dx} \left\{ (H_0 + bx)F \right\} - (a + b)F \right] + \frac{2\gamma}{\pi^2} \left\{ (H_0 + bx) \frac{dF}{dx} + bF \right\}^2 + \frac{2\gamma}{\pi} \left\{ (H_0 + bx) \frac{dF}{dx} + bF \right\} (B_0 + H_0 + ax + bx) + \frac{E(T_0 + cx)}{2} \left( \frac{dF}{dx} \right)^2 + \tau_r F \quad (25.25)$$

### 25.5 Variational Principle and Its Euler's Differential Equation

The requirement of minimizing the overall potential energy as stated in Sect. 25.4 is a typical problem of variational principle of mathematics (数学における変分原理). It is therein attempted to find a special  $F(x)$  that makes an integration minimum. In the present case, what should be minimized is given by

$$Q = \int_0^L q(F, dF/dx, x) dx + \left[ r(F) \right]_0^L \quad (25.26)$$

where “ $r$ ” in the second term is a function of  $F$ :

$$r(F) = -\gamma \left( \frac{2HB}{\pi} + \frac{4H^2}{\pi^2} \right) F. \quad (25.27)$$

The mathematical procedure in what follows is in line with what was presented in Sect. 25.3. Suppose that we have the exact solution of  $F(x)$  that makes  $Q$  minimum. Hence, a small arbitrary variation of  $F$  from the exact one, which is designated by  $\delta F$ , does not change  $Q$ ;

$$\delta Q \equiv \int_0^L \left\{ \frac{\partial q}{\partial F} \delta F + \frac{\partial q}{\partial (dF/dx)} \frac{d\delta F}{dx} \right\} dx + \left[ \frac{\partial r}{\partial F} \delta F \right]_0^L = 0.$$

By partially integrating the second term in the integrand,

$$\delta Q = \int_0^L \left[ \frac{\partial q}{\partial F} \delta F - \frac{d}{dx} \left\{ \frac{\partial q}{\partial (dF/dx)} \right\} \delta F \right] dx + \left[ \left\{ \frac{\partial q}{\partial (dF/dx)} + \frac{\partial r}{\partial F} \right\} \delta F \right]_0^L = 0. \quad (25.28)$$

Equation (25.28) has to be satisfied for any kind of  $\delta F$ . Therefore,

$$\frac{\partial q}{\partial F} \delta F - \frac{d}{dx} \left\{ \frac{\partial q}{\partial (dF/dx)} \right\} = 0. \quad (25.29)$$

This is the Euler's differential equation, which specifies  $F(x)$  that makes the potential energy,  $Q$ , minimum. By substituting an explicit expression of “ $q$ ” into (25.29),

$$\frac{dF}{dx} = \frac{C_4 x^2 + C_5 x + A}{C_1 x^2 + C_2 x + C_3} \quad (25.30)$$

where

$$C_1 = \frac{4\gamma b^2}{\pi^2}, \quad C_2 = \frac{8\gamma b H_0}{\pi^2} + Ec, \quad C_3 = \frac{4\gamma H_0^2}{\pi^2} + ET_0, \\ C_4 = -\frac{1}{2} \left\{ (a+b) \left( e + \frac{2\gamma b}{\pi} \right) + \frac{2be}{\pi} \right\}, \quad \text{and} \quad C_5 = \tau_r - (a+b) \left( P_0 + \frac{2\gamma H_0}{\pi} \right) - \frac{2eH_0}{\pi}. \quad (25.31)$$

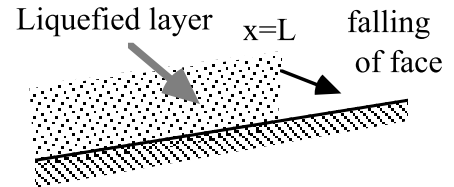


The second term on the right-hand side of (25.28) has to be zero for any  $\delta F$  as well. Therefore,

$$\frac{\partial q}{\partial(dF/dx)} + \frac{\partial r}{\partial F} = \frac{2PH}{\pi} + \frac{4\gamma H}{\pi^2} \left( H \frac{dF}{dx} + bF \right) + ET \frac{dF}{dx} - \frac{2\gamma H^2}{\pi^2} = 0 \quad (25.32)$$

at a boundary. This is a natural boundary condition and appears to be valid unless the value of  $F$  is directly specified (fixed or fundamental boundary condition).

Equation (25.32) gives a very strange result of calculation, however, in which the upper boundary of a slope moves further upwards. This happens because the mathematics in (25.32) assumes that there is an open space beyond this boundary. This situation is illustrated in Fig. 25.9 and it is very natural that the vertical face of a liquefied sand layer falls down to the right. In reality, there is a rigid wall at such a boundary (shaking table tests in a rigid box) or the unliquefied sand in the pstream side collapses toward the liquefied sand mass and pushes it downslope. This point will be discussed later in Sect. 25.8.



**Fig. 25.9** Inappropriate upper boundary as assumed by mathematics

### 25.6 Prediction of Lateral Displacement

The maximum possible displacement in the lateral direction,  $F$ , is the one at the surface of a liquefied subsoil of an idealized shape (Fig. 25.10). The basic hypotheses involved are:

1. Liquefied sand behaves similar to liquid with constant volume
2. The surface crust resists elastically against lateral compression
3. The maximum possible displacement is associated with the minimum potential energy

The required input data are

- a. Topography and thickness of liquefiable layer which is determined by SPT- $N$  etc.
- b. Total unit weights of liquefied sand,  $\gamma$ , and surface dry crust
- c. Residual strength of liquefied sand,  $\tau_r$
- d. Elastic modulus of surface crust, undergoing compression,  $E$

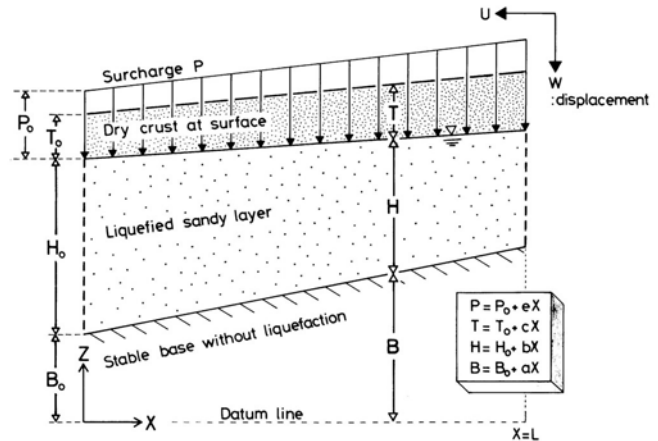
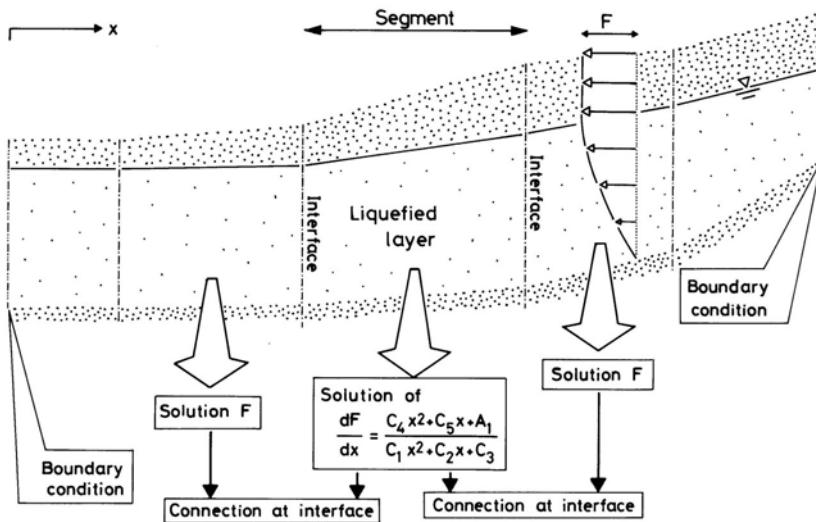


Fig. 25.10 Idealized model of liquefied ground



At interface, principle of minimum potential energy requires

$$\frac{4\gamma H}{\pi^2} \left( H \frac{dF}{dx} + bF \right) + \frac{2\gamma H^2}{\pi} + ET \frac{dF}{dx} + \frac{2PH}{\pi} - \frac{4\gamma H^2}{\pi^2}$$

to be continuous.

Fig. 25.11 Dividing an irregular cross section into regular segments

The solution for  $F$  is derived by solving a corresponding Euler's differential equation;

$$\frac{dF}{dx} = \frac{C_4 x^2 + C_5 x + A_1}{C_1 x^2 + C_2 x + C_3} \tag{25.33}$$

where

$$C_1 = \frac{4\gamma b^2}{\pi^2}, \quad C_2 = \frac{8\gamma b H_0}{\pi^2} + Ec, \quad C_3 = \frac{4\gamma H_0^2}{\pi^2} + ET_0, \quad C_4 = -\frac{1}{2} \left\{ (a+b) \left( e + \frac{2\gamma b}{\pi} \right) + \frac{2be}{\pi} \right\}, \quad \text{and}$$

$$C_5 = \tau_r - (a+b) \left( P_0 + \frac{2\gamma H_0}{\pi} \right) - \frac{2eH_0}{\pi} \tag{25.34}$$

See Fig. 25.10 for geometric parameters of  $a, b, c$  and  $e$ .  $A_1$  is determined from a boundary condition in terms of  $dF/dx$  ((25.36) for example), while  $P = P_0 + ex$  is the weight of the surface dry crust per unit area.

Once a solution of (25.33) is derived for a soil profile of a regular shape in Fig. 25.10, a cross section of an irregular shape (Fig. 25.11) can be solved easily. The lateral displacement changes in the vertical direction in a harmonic manner, and  $F$  is the amplitude of the harmonic function. This formulation reduces the computation load drastically. The cross section is divided into segments of a regular shape, segmentary solutions are derived as obtained earlier, and these solutions are connected with each other so that the displacement may become continuous and the overall potential energy may take the minimal value.

**25.7 Closed Form Solution of Maximum Possible Displacement**

For a cross section of a regular shape in Fig. 25.10, the following solution of displacement was developed. For its mathematical derivation, refer to Towhata et al. (1992 and 1996).

When  $b = 0$  and  $Ec = 0$ ,

$$F(x) = F_0 + \frac{F_L - F_0}{L}x + \frac{x(L-x)}{6\left(\frac{4\gamma H_0^2}{\pi^2} + ET_0\right)} \left[ ae(L+x) - 3\left\{ \tau_r - a\left(P_0 + \frac{2\gamma H_0}{\pi}\right) - \frac{2eH_0}{\pi} \right\} \right]$$

When  $b = 0$  and  $Ec \neq 0$ ,

$$F(x) = F_0 + \frac{C_4}{2Ec}x^2 + \frac{1}{Ec}\left(\frac{C_3C_4}{Ec} - C_5\right) \left( L \frac{\ln\left|\frac{Ecx}{C_3} + 1\right|}{\ln\left|\frac{EcL}{C_3} + 1\right|} - x \right) + \left(F_L - F_0 - \frac{C_4L^2}{2Ec}\right) \frac{\ln\left|\frac{Ecx}{C_3} + 1\right|}{\ln\left|\frac{EcL}{C_3} + 1\right|}$$

in which  $C_1, C_2, C_3, C_4$ , and  $C_5$  are parameters defined in (25.34).

When  $b \neq 0$  and  $D = C_2^2 - 4C_1C_3 > 0$ ,

$$F(x) = F_0 + \frac{C_4x}{C_1} + \frac{C_1C_5 - C_2C_4}{2C_1^2} \ln\left|\frac{C_1x^2 + C_2x + C_3}{C_3}\right| - \left\{ \frac{C_4L}{C_1} + \frac{C_1C_5 - C_2C_4}{2C_1^2} \right. \\ \left. \times \ln\left|\frac{C_1L^2 + C_2L + C_3}{C_3}\right| - (F_L - F_0) \right\} \frac{\ln\left|\frac{(C_1x^2 + C_2x + C_3)(C_2 + \sqrt{D})^2}{C_3(2C_1x + C_2 + \sqrt{D})^2}\right|}{\ln\left|\frac{(C_1L^2 + C_2L + C_3)(C_2 + \sqrt{D})^2}{C_3(2C_1L + C_2 + \sqrt{D})^2}\right|}$$

When  $b \neq 0$  and  $D = C_2^2 - 4C_1C_3 = 0$ ,

$$F(x) = F_0 + \frac{C_4x}{C_1} + \frac{C_1C_5 - C_2C_4}{2C_1^2} \ln\left|\frac{C_1x^2 + C_2x + C_3}{C_3}\right| + \frac{x(2C_1L + C_2)}{L(2C_1x + C_2)} \\ \times \left( F_L - F_0 - \frac{C_4L}{C_1} - \frac{C_1C_5 - C_2C_4}{2C_1^2} \ln\left|\frac{C_1L^2 + C_2L + C_3}{C_3}\right| \right)$$

When  $b \neq 0$  and  $D = C_2^2 - 4C_1C_3 < 0$ ,

$$F(x) = F_0 + \frac{C_4x}{C_1} + \frac{C_1C_5 - C_2C_4}{2C_1^2} \ln\left|\frac{C_1x^2 + C_2x + C_3}{C_3}\right| \\ - \left\{ \frac{C_4L}{C_1} + \frac{C_1C_5 - C_2C_4}{2C_1^2} \times \ln\left|\frac{C_1L^2 + C_2L + C_3}{C_3}\right| - (F_L - F_0) \right\} \frac{\arctan\frac{\sqrt{-D}x}{C_2x + 2C_3}}{\arctan\frac{\sqrt{-D}L}{C_2L + 2C_3}}$$

$F_0$  and  $F_L$  are displacements at boundaries of  $x = 0$  and  $x = L$ , respectively.

25.8 Boundary Conditions of Soil Mass Undergoing Lateral Flow

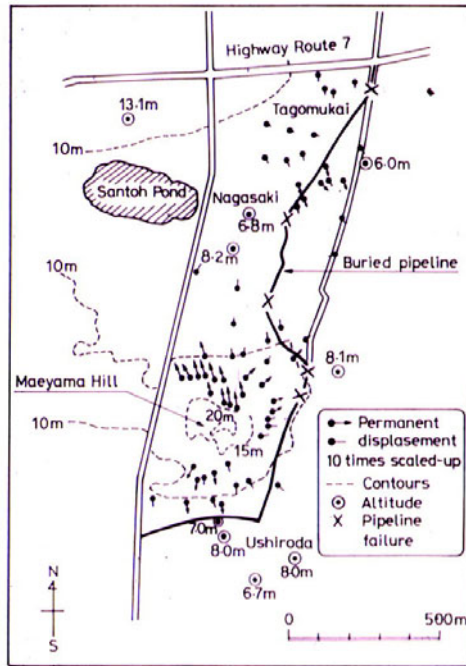


Fig. 25.12 Permanent displacement around Maeyama hill in Noshiro City (Hamada et al., 1986)

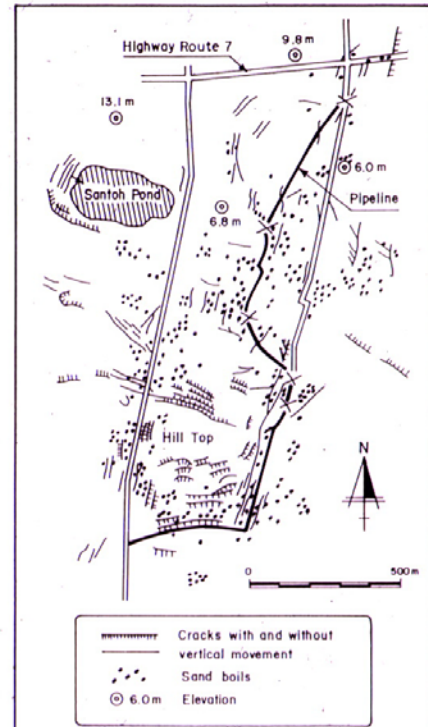


Fig. 25.13 Distortion at ground surface around Maeyama hill

Prediction of lateral flow requires boundary conditions to be clearly defined. In case of flow of a gentle liquefied slope, the past experience in Noshiro (Figs. 25.12 and 25.13) suggests

- Displacement = 0 at the bottom of a slope where a collision with a flow from an opposite slope prevents lateral displacement,

$$F = 0, \quad (25.35)$$

which is a fundamental boundary condition (基本境界条件) of the theory of variational principles

- Open crack at the top of a slope



Fig. 25.14 Pine tree split into two parts at upper boundary of flowing soil mass (courtesy of Noshiro Municipal Government)

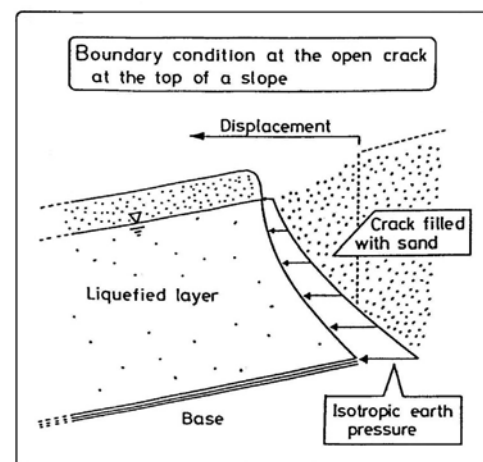


Fig. 25.15 Lateral earth pressure exerted by adjacent soil upon flowing soil mass

A mathematical expression of an open-crack boundary is derived as what follows.

One should not imagine a vertical opening at the top of a slope. Dry sand without cohesion cannot maintain a vertical face to stand without a retaining wall. Fig. 25.14 illustrates an open-crack boundary where a pine tree was split into two pieces, suggesting discontinuous displacement. Noteworthy is that the crack was filled with boiled sand.

The energy at an upper boundary should include loss of potential energy of soil mass that is pushed downward by the earth pressure exerted by collapsed sand mass (Fig. 25.15). Consequently, the principle of the minimum potential energy gives the following equation as the open-crack boundary condition.

$$ET \frac{dF}{dx} + \frac{4\gamma H}{\pi^2} \left( H \frac{dF}{dx} + bF \right) = 0, \quad (25.36)$$

which is the natural boundary condition (自然境界条件) as stated by the variational theory of mathematics.

The isotropic earth pressure as drawn in Fig. 25.16 occurs at a lower boundary of a slope, which is connected to a level infinite liquefied subsoil. Equation (25.36) is valid for such an infinite lower boundary as well.

Another boundary condition is necessary at an internal interface between two subsoil segments that are of regular shapes. As illustrated in Fig. 25.17, an irregular shape of a slope can be analyzed only by combining regular segments. Individual segments have their own analytical solutions as presented in Sect. 25.7, and those solutions are connected with each other so that the global minimum potential energy may be achieved. This requirement is satisfied by using

$$\left[ \frac{4\gamma H}{\pi^2} \left( H \frac{dF}{dx} + bF \right) + \frac{2\gamma H^2}{\pi} + ET \frac{dF}{dx} + \frac{2PH}{\pi} - \frac{4\gamma H^2}{\pi^2} \right]_{x^-}^{x^+} = 0 \quad (25.37)$$

at the interface. For mathematical details, refer to Towhata et al. (1992 and 1999). When there are embedded walls for mitigation of lateral displacement (Sect. 26.3), different internal boundary conditions are employed. For example calculation, see Sect. 26.3.

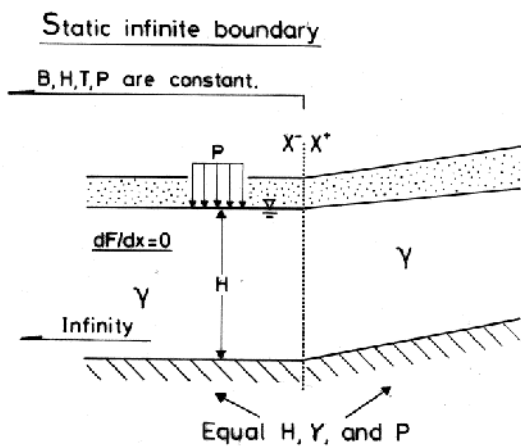


Fig. 25.16 Boundary condition at interface between liquefied slope and liquefied level ground

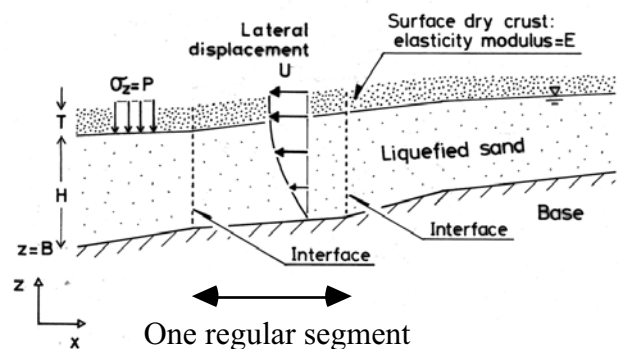


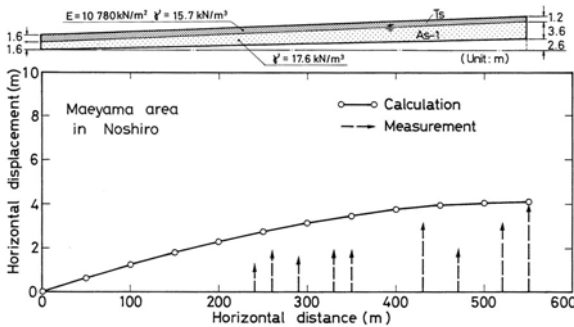
Fig. 25.17 Interface between two subsoil segments of regular shape

**25.9 Example Prediction of Lateral Displacement**

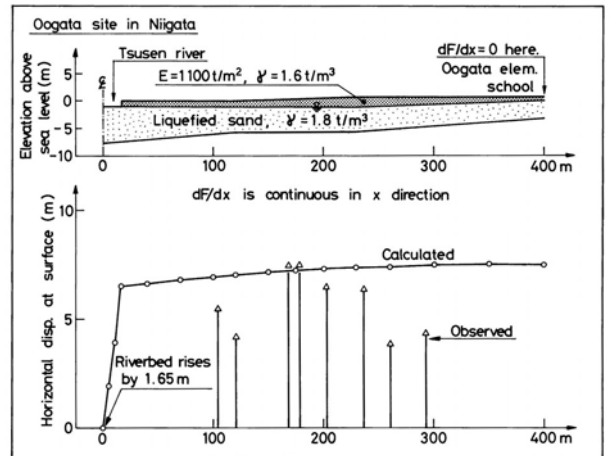
The solution of surface displacement “*F*” as derived in previous sections is going to be examined against observation. Note that the solution of “*F*” that makes the overall potential energy minimum is the maximum possible one and is not necessarily equal to the real displacement.

Figure 25.18 indicates the calculation in the Maeyama hill area in Noshiro City (Sect. 24.1). The author prefers to use the modulus of  $E = 10,780 \text{ kN/m}^2$  ( $=110 \text{ kgf/cm}^2$ ) in the surface dry crust. This value of modulus was derived by substituting  $SPT-N = 8$  into Shultze and Menzenbach’s (1961) empirical formula for fine sand:

$$E = 71 + 4.9N \quad (\text{kgf/cm}^2) \quad (25.38)$$



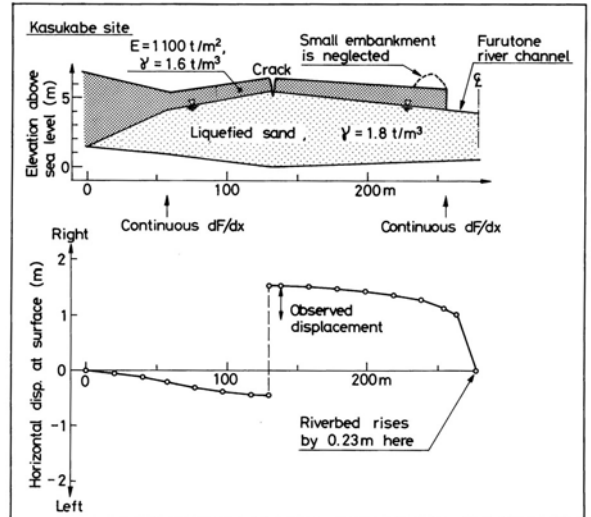
**Fig. 25.18** Calculated displacement vs. observation in north slope of Maeyama, Noshiro



**Fig. 25.19** Calculation vs. observation in Ohgata slope in Niigata



**Fig. 25.20** Distortion of trench in Kasukabe which is still visible today



**Fig. 25.21** Calculation vs. field assessment in Kasukabe site

It is seen in Fig. 25.18 that the calculated displacement is greater than the observation because the former is the maximum possible one. In reality, the state of ground flow ceased before the ultimate displacement was attained.

Figure 25.19 reveals the case of Ohgata (大形) area in Niigata where significant lateral flow and meandering of streets occurred in 1964 (Sect. 25.11). This site is characterized by its very small gradient of slope which is less than 1% (Fig. 25.32). The calculated displacement overestimates the reality again. Thus, it appears that the real displacement is approximately 60–70% of the calculated ones, and that the effects of time should be taken into account for a more precise prediction.

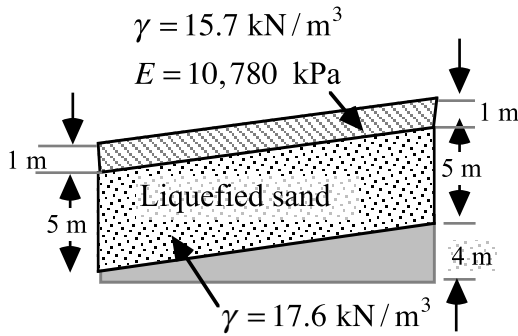
Kasukabe City (春日部) was subjected to lateral soil movement toward the channel of Furutone River (吉利根川) during the Kanto earthquake in 1923. Figure 25.20 shows the distortion of one of the trenches

that Wakamatsu et al. (1989) studied to assess the magnitude of lateral ground displacement to be 1.0–1.5 m. The displacement analysis in this area is indicated in Fig. 25.21. Since a tensile stress state occurred in the middle, a state of  $dF/dx = 0$  was imposed at the place of a “crack.” The analysis on displacement (Fig. 25.21) is again an overestimation.

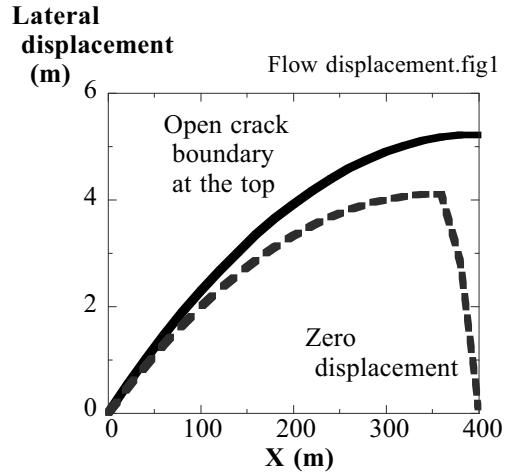


**25.10 Parametric Studies on Lateral Displacement**

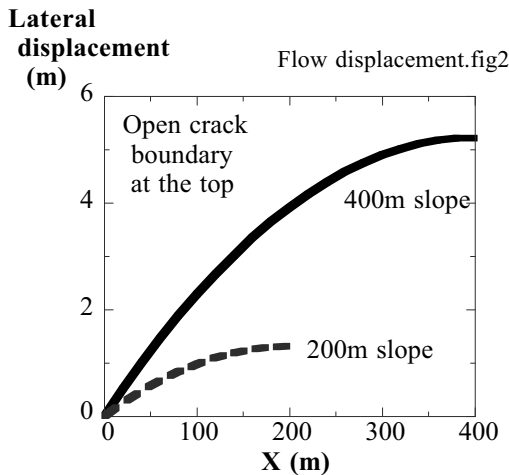
This section is going to study the effects on the magnitude of lateral displacement,  $F$ , exerted by various parameters. Figure 25.22 reveals a cross section of a liquefied slope, which is called the control case (標準). It measures  $L = 400$  m in length,  $H = 5$  m in the thickness of liquefied layer,  $T = 1$  m in the thickness of surface dry crust, and the slope gradient is 1%. The unit weight of soil is  $17.6 \text{ kN/m}^3$  in the liquefied layer and  $15.7 \text{ kN/m}^3$  in the surface crust. The modulus of deformation in the crust is  $10,780 \text{ kN/m}^2$ . Since sand cannot sustain tensile stress, the modulus,  $E$ , in the tensile portion of the crust is made zero by an iteration procedure.



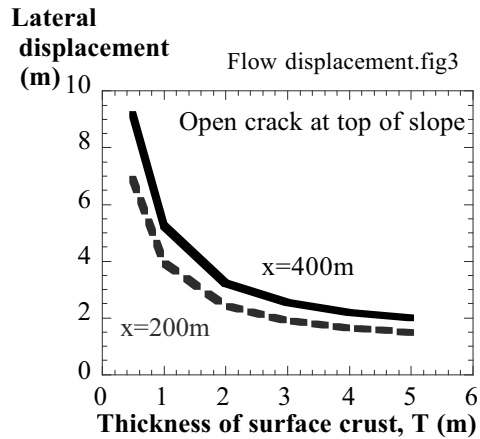
**Fig. 25.22** Shape of control case



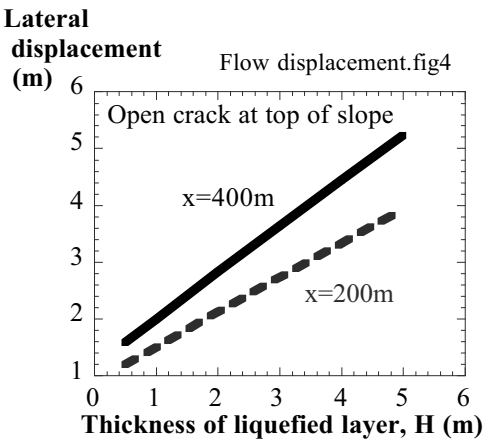
**Fig. 25.23** Effects of boundary condition at the top of slope



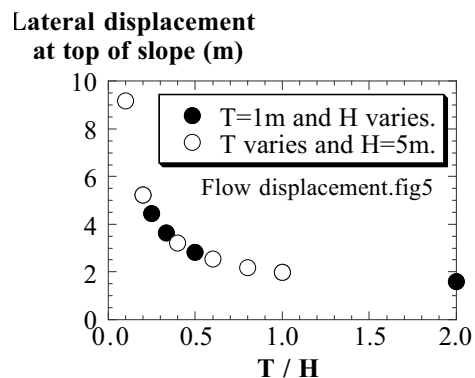
**Fig. 25.24** Effects of length of slope



**Fig. 25.25** Effects of thickness of surface crust



**Fig. 25.26** Effects of thickness of liquefied layer



**Fig. 25.27** Effects of T/H ratio

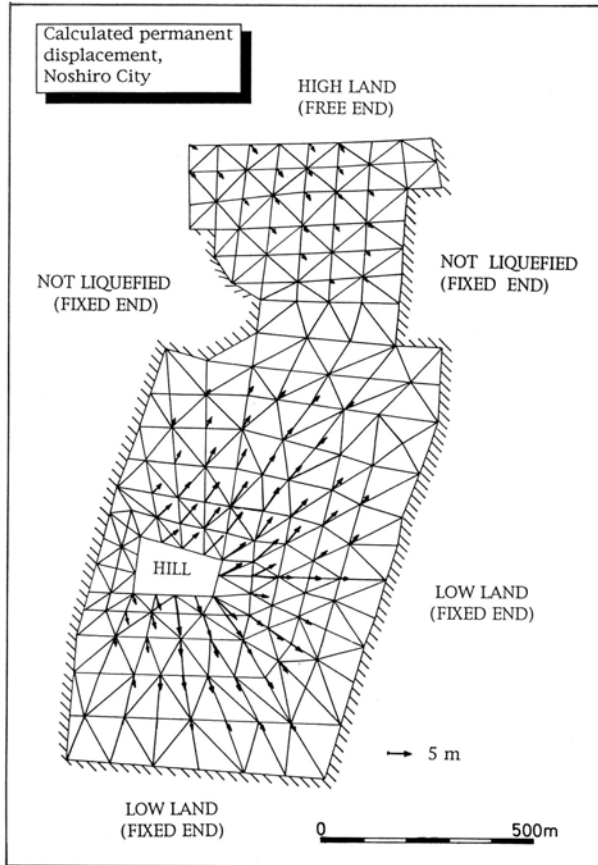
Figure 25.23 shows that an open-crack boundary at the top (Sect. 25.8) can produce a greater displacement than a fixed ( $F = 0$ ) one. The former is often the case in real earthquakes, while the latter occurs in shaking model tests inside a rigid box.

Figure 25.24 shows that a longer slope can generate a greater displacement. Hence, a short container in shaking table tests cannot generate as large displacement as insitu even though other conditions are held identical.

Figure 25.25 reveals that the thicker surface crust ( $T$ ) decreases the displacement both at the middle ( $x = 200$  m) and at the top ( $x = 400$  m) of a slope. In contrast, the greater thickness of liquefied layer ( $H$ ) increases the displacement (Fig. 25.26). Hence,  $T/H$  seems to play an essential role (Fig. 25.27). This significance of  $T/H$  ratio is consistent with the empirical finding on the significance of thickness ratio on the extent of damage (Fig. 21.12).

## 25.11 Three Dimensional Prediction of Lateral Displacement of Liquefied Deposit

The analytical method as described in preceding sections was extended to a three-dimensional analysis (Orense and Towhata, 1998). This section demonstrates the predicted surface displacement at the state of minimum potential energy. Hence, they are the maximum possible displacement and are probably greater than the real displacement.

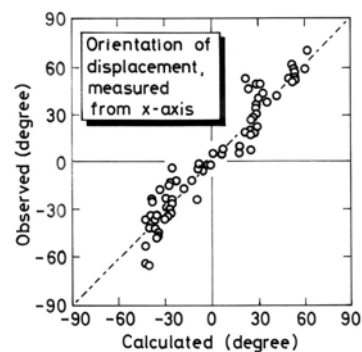
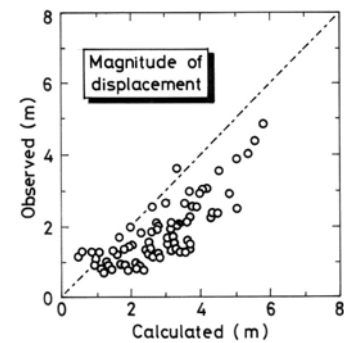


**Fig. 25.28** Predicted maximum possible displacement in Maeyama area of Noshiro city

Figure 25.28 illustrates the calculated displacement in the south area of Noshiro city where substantial liquefaction occurred during the 1983 Nihonkai-Chubu earthquake (Sect. 23.1). The consistency is found between this figure and observation in Fig. 25.12. Figure 25.29 compares the calculation and observation by Hamada et al. (1986) to show that the magnitude of observation is around 70% of the calculated maximum possible displacement, while the orientation is reasonably predicted. The reason for a good prediction of orientation is that the ground displacement is strongly affected by the gradient of slope that is precisely taken into account by the analysis.

A similar study was made of the Ohgata (大形) area in Niigata city. Figure 25.30 shows the dislocation of pine trees in Ohgata primary school. Although these trees were planted in a straight position, lateral ground displacement during the earthquake in 1964 changed their positions. Figure 25.31 shows the prediction, while Fig. 25.32 illustrates the observation in which the lateral soil flow occurred from the

Permanent displacement in south area of Noshiro  
Comparison: airphoto observation vs. 3-D calculation (max. possible value)



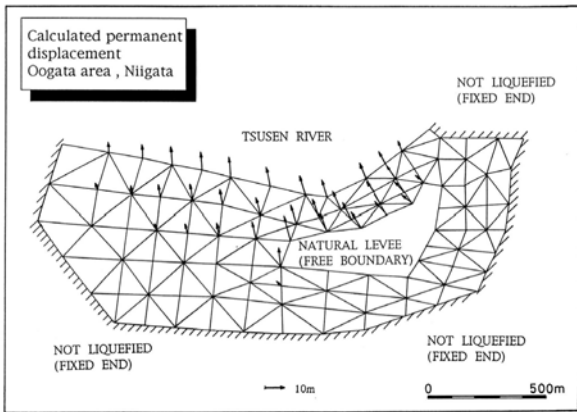
**Fig. 25.29** Comparison of predicted and observed displacement in Noshiro city



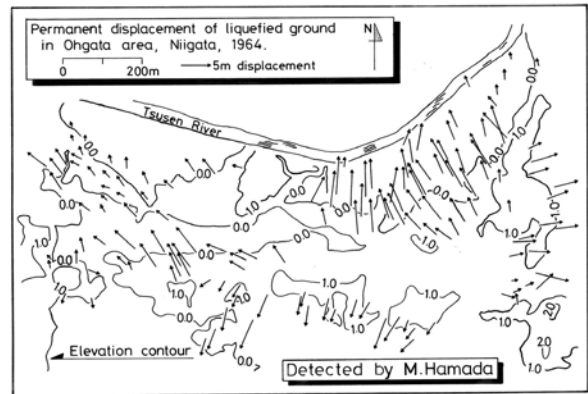
**Fig. 25.30** Dislocation of pine trees due to lateral ground displacement in Ohgata, Niigata

top of a natural levee toward the abandoned channel of the great Agano River (presently Tsusen River). In spite of the very gentle ground slope (about 1% gradient), the displacement was as large as 7 m or more. Figure 25.33 reveals again that observation is around 70% of calculation while the direction is in good agreement.

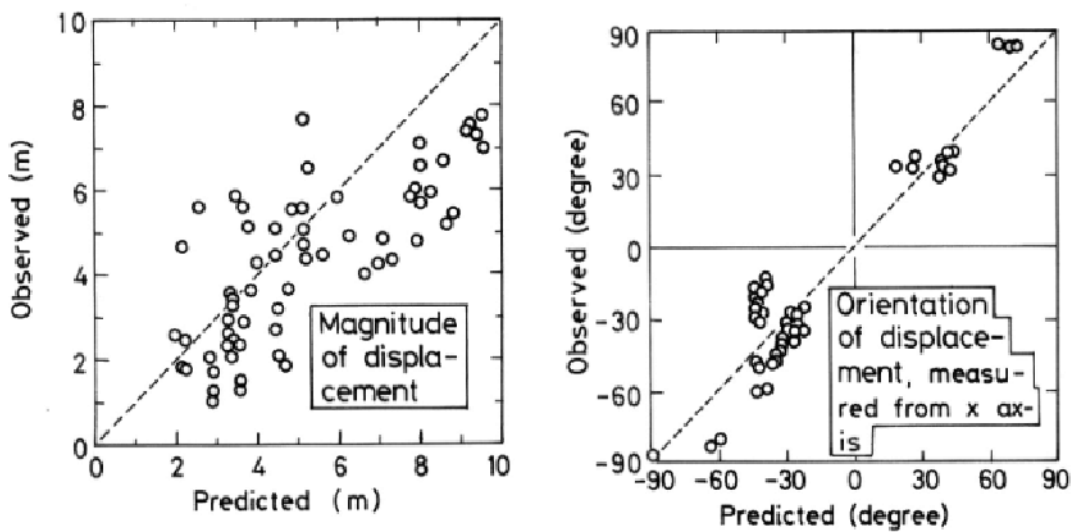
More recently, Kobayashi (2001) conducted three-dimensional dynamic analyses in which liquefied soil is modeled by a Bingham viscous liquid (Sect. 25.20).



**Fig. 25.31** Predicted maximum possible displacement in Niigata city



**Fig. 25.32** Observed displacement in Ohgata area of Niigata city (Hamada et al. 1992)



**Fig. 25.33** Comparison of predicted and observed displacement in Ohgata are in Niigata city

## ☛ 25.12 Glacier as Seen from Aircraft

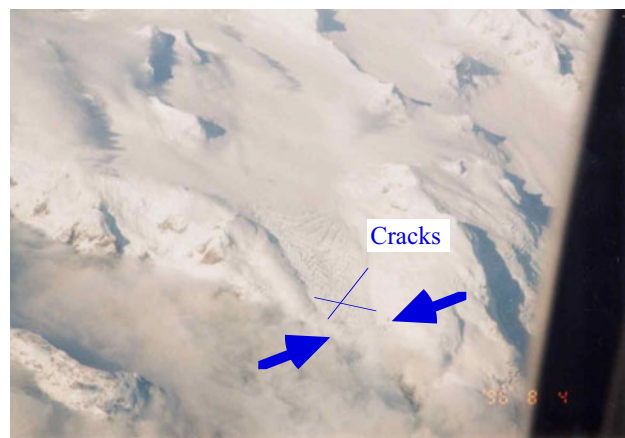
The lateral displacement of ground induced by subsurface liquefaction is a phenomenon in which a surface dry unliquefied crust moves laterally over liquefied subsoil. Although a predictive measure is being developed, the overall rationality of the predicted results has to be examined from time to time. One of the examination may be an inspection of a flow of glacier that is also a flow movement of a solid layer upon a lubricated floor.

Figures 25.34 and 25.35 are photographs of a glacier (*glaciar*) in Patagonia, which were taken from an airplane flying between Puerto Montt and Punta Arenas in Chile. Figure 25.34 indicates many cracks developing perpendicular to the direction of flow (shown by an arrow) at a place where a glacier is running down from a shoulder of a slope. This set of cracks was generated by tensile deformation at the surface of an ice mass. The present analysis of liquefaction-induced flow takes into account the tensile failure as well; namely the open-crack boundary and the iteration to make  $E = 0$  in tensile regions.

It is interesting in Fig. 25.35 that there are many conjugate cracks/distortions that are of two different orientations (shown by black lines). Since the glacier is flowing toward a narrow rock channel in this section (shown by black arrows:  $\rightarrow$ ), it is possible that the movement of the glacier is prevented by the decreased width of its path, and that a significant compressional state of stress is generated. If this idea is correct, the observed conjugate cracks are those generated by shear failure, which is generated in a frictional material to the direction of  $\pm(45^\circ - \phi/2)$  from the direction of major principal stress,  $\sigma_1$ . Triaxial tests on sand should be recalled.



**Fig. 25.34** Airphoto of a glacier in Patagonia



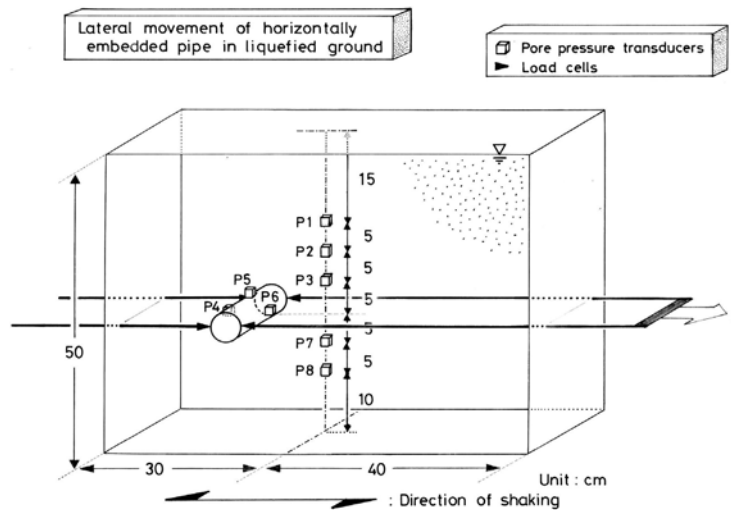
**Fig. 25.35** Crevasse or crack in Patagonia ice field

**25.13 Drag Force of Embedded Pipe in Liquefied Model Ground**

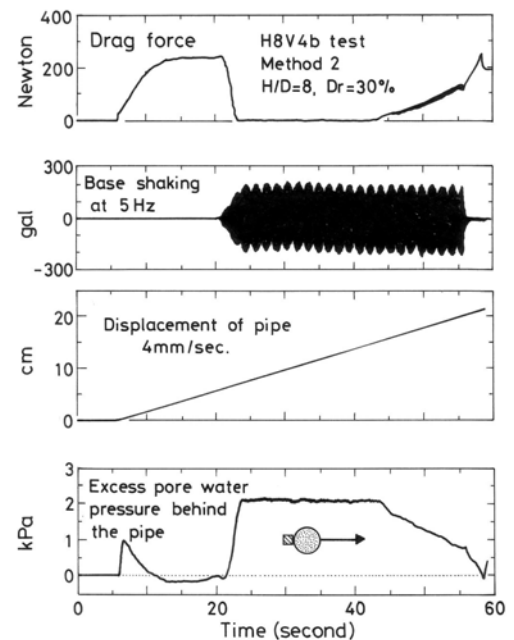
It is attempted from this section to discuss in detail the stress–strain behavior of liquefied sand undergoing lateral flow. Since the lateral displacement due to flow can exceed 5 m while the thickness of liquefied layer is 5–10 m, and not more than 20 m, the developed shear strain is most probably over 50%. The stress–strain behavior of liquefied sand under this large strain range is difficult to be studied by conventional triaxial and torsion shear devices. Another interest lies in the effects of continued shaking on liquefied sand. This topic is difficult to investigate because running laboratory shear tests on a shaking table is unreliable and even dangerous.

This research aim was achieved by running 1-G model tests on a shaking table. Density of sand was very loose (30% relative density) in order to cancel the bad effects of reduced confining pressure in 1-G model tests. Figure 25.36 illustrates the model sandy deposit in which a model pipe was embedded (Towhata et al. 1999). When the sandy deposit was shaken and liquefied, the pipe was pulled/pushed laterally. The force needed for this motion (drag force) was measured by four transducers. It was intended therein that the drag force was related to the shear stress in the surrounding liquefied sand, while the displacement of the pipe induced shear deformation in sand. Therefore, it was supposed that the measured force-displacement relationship can give information about the stress–strain behavior of liquefied sand.

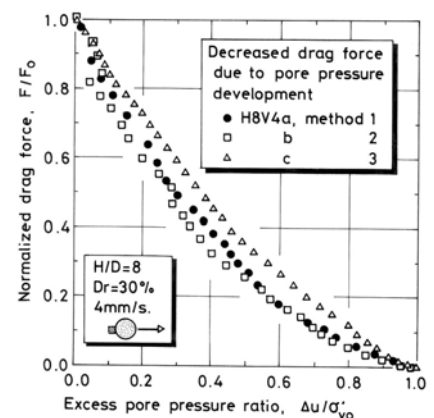
Figure 25.37 reveals time histories of measured records. Initially, the drag force increased together with the displacement. When shaking started, however, the excess pore water pressure increased and the drag force suddenly decreased. The discussion in the following pages will be focused on the drag force when excess pore water pressure is 100% high (state of liquefaction). Figure 25.38 shows the decrease of drag force with development of excess pore water pressure.



**Fig. 25.36** Model container with embedded pipe



**Fig. 25.37** Measured time history of drag force

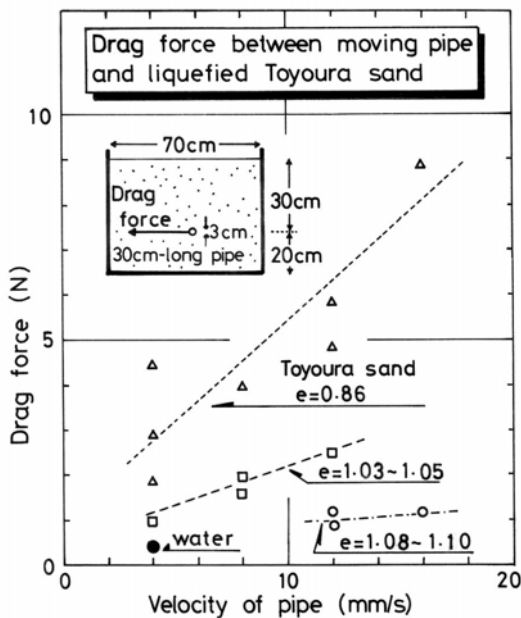


**Fig. 25.38** Relationship between drag force and pore water pressure rise

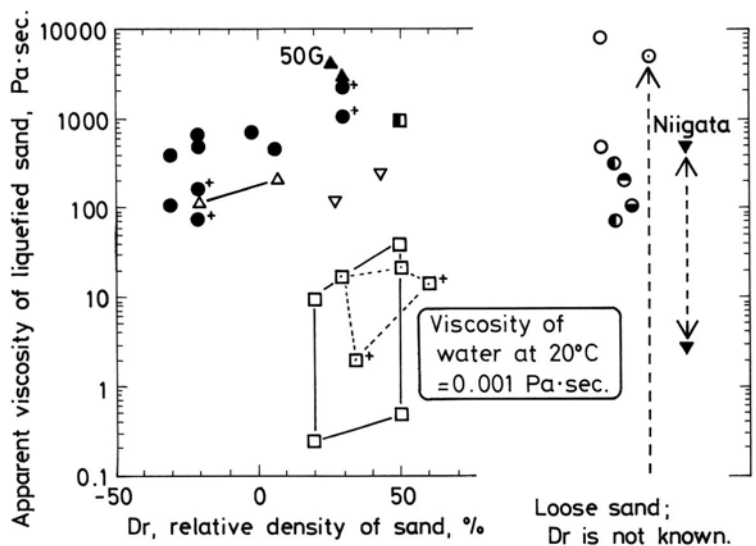
**25.14 Rate-Dependency of Liquefied Sand**

Lateral pulling of an embedded pipe in liquefied subsoil revealed that drag force is extremely small when pore pressure achieves liquefaction. Figure 25.39 shows the relationship between drag force at liquefaction and velocity of pipe movement. There is a velocity dependency in the measured drag force, and the denser sand upon liquefaction develops greater drag force. This rate-dependency is similar to the behavior of viscous liquid in fluid mechanics.

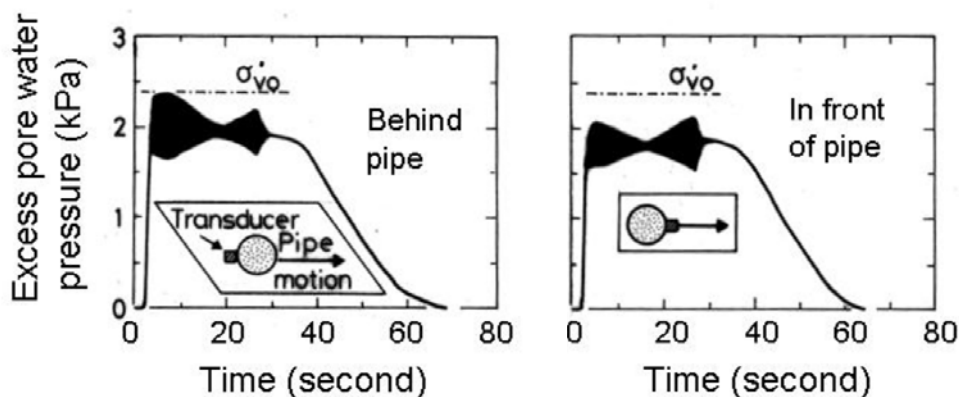
It is possible to use Fig. 25.39 to back-calculate the apparent viscosity of liquefied sand by using the theory of fluid mechanics. Figure 25.40 shows the results obtained from author's data as well as other literatures. Those literatures concern model tests in 1-G and centrifuge conditions. Moreover, the data from Niigata Airport were obtained by analyzing a motion picture by Mr. F. Yuminamochi (Figs. 25.58 and 25.59) in which the rate of subsidence of a terminal building was determined. Since the weight and size of the building were known, the apparent viscosity was determined. Noteworthy in Figure 25.40 is that the obtained apparent viscosity is significantly greater than the viscosity of pure water at 20°C. This is a controversial issue and needs to be investigated more in detail by element shear tests (Sect. 25.17).



**Fig. 25.39** Rate dependency of drag force upon liquefaction



**Fig. 25.40** Apparent viscosity coefficient of liquefied sand obtained from model tests (for legend, see Table 25.1)



**Fig. 25.41** Excess pore water pressure in front and behind pipe

There is an opinion that this velocity dependency is caused by pore pressure difference between front and back sides of a pipe. It is inferred that, since the back side of a pile produces negative pore water pressure due to cavity mechanism, the net effect of water pressure produces resistance against pipe movement. When the pipe velocity is greater, seepage and pore pressure equalization cannot catch up with the development of cavity effects and consequently the greater net pressure difference is generated. This opinion, however, does not have an experimental evidence. In the author's study in Fig. 25.41, pore pressures in front and behind an embedded pipe did not exhibit such a cavity-induced drag force, although the drag force was velocity dependent (Fig. 25.39). The seepage and pore pressure equalization occur very fast in a permeable sandy layer and the small size of a pipe does not allow pressure difference to remain for a significant time period.

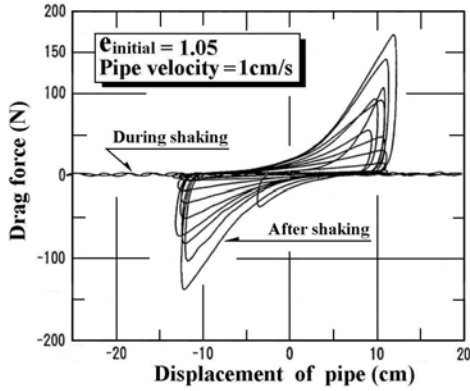
**Table 25.1** Literature list for Fig. 25.40

- 
- 1G pulling pipe; Towhata,I., Vargas-Monge,W., Orense,R.P. and Yao,M. (1999).
  - ▼ Prototype subsidence of building foundation in 1964 Niigata earthquake; Towhata,I. and Horikoshi,K. (1997).
  - Subsidence of sphere; Takada,S. and Nagai,J. (1987).
  - Pulling sphere; Ohtomo,K., Iwadate,T., Shimizu,M., Shumuta,Y. and Hamada,M. (1993).
  - Motion of sphere; Miyajima,M., Hasegawa,M., Kitaura,M., Koike,T. and Kitano,Y. (1994).
  - Motion of sphere; Miyajima,M., Kitaura,M. and Kitano,Y. (1994).
  - Motion of sphere; Miyajima,M., Kitaura,M., Koike,T. and Hasegawa,M. (1995).
  - ⊙ Pulling sphere and pipe; Sato,H., Hamada,M. and Doi,M. (1994).
  - ▲ Shaking in centrifuge; Sato,H., Doi,M, Ohbo,N., Honda,M. and Hamada,M. (1994).
  - 1G pulling sphere and 1G viscometer; Yuasa,A., Sato,H., Doi,T., Kawakami,T. and Hamada,M. (1994).
  - △ 1G flow of slope; Toyota,H. (1995).
  - ▽ 1G subsidence of foundation; Sasaki,Y., Udaka,K. and Miyamoto,Y. (1997).
-

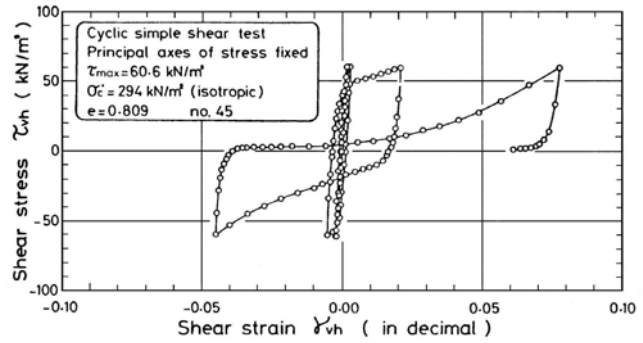


**25.15 Effects of Continued Shaking on Behavior of Liquefied Sand**

The idealization of liquefied sand as viscous liquid is contradictory to the theory of steady-state strength of sand (residual strength) at large shear deformation (Sect. 24.3). This contradiction is accounted for by different load conditions. Although the idea of viscosity was obtained from shaking model tests with 100% pore pressure rise, the steady-state modeling was developed by undrained monotonic shear on sand in which there was effective stress. Therefore, the lack of shaking-induced cyclic shear stress in monotonic shear tests deserves more attention.



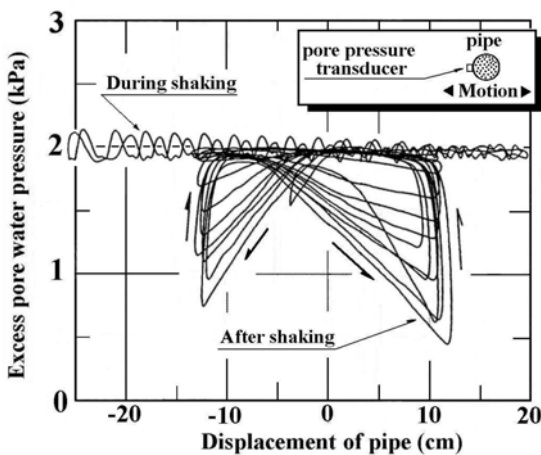
**Fig. 25.42** Experimental relationship between drag force and pipe displacement



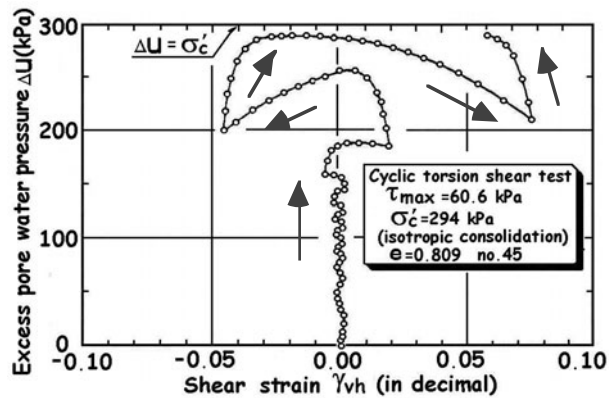
**Fig. 25.43** Shear stress–strain relationship of loose Toyoura sand in undrained torsion shear test

Figure 25.42 indicates the relationship between drag force for pulling pipe and the pipe displacement. As mentioned in Sect. 25.13, this relationship is equivalent with stress–strain behavior of liquefied sand. The large force–displacement loops in Fig. 25.42 have a similar shape as stress–strain loops of liquefied sand in Fig. 25.43, which were obtained by an undrained torsion shear test. This similarity supports the idea of equivalency between pipe pulling and undrained shear.

Figure 25.44 shows the variation of excess pore water pressure with the pipe displacement. Pore pressure decreased with the progress of pipe displacement, because shear deformation in sand resulted in positive dilatancy. When the direction of displacement was reversed, pore pressure increased suddenly and started to decrease again. This behavior is again similar to what was observed in cyclic torsion shear test (Fig. 25.45); see data after high pore pressure development.



**Fig. 25.44** Change of pore pressure in pipe pulling test



**Fig. 25.45** Relationship between pore pressure and shear strain in undrained torsion shear test

What is noteworthy is the data in Figs. 25.42 and 25.44 “during shaking.” The drag force was continuously small without dilatancy effects, and the pore pressure maintained the highest value. The lack of dilatancy and continued high pore pressure were probably because the shaking-induced cyclic shear stress prevented positively dilatant motion of grains, making more grains fall into big pores. Thus, liquefied subsoil maintains high pore pressure during strong shaking and can deform easily. The idea of steady state is valid only after the end of strong shaking when no more cyclic stress prevents dilatancy.

## 25.16 Attempt to Measure Viscosity of Liquefied Sand in Shear Tests

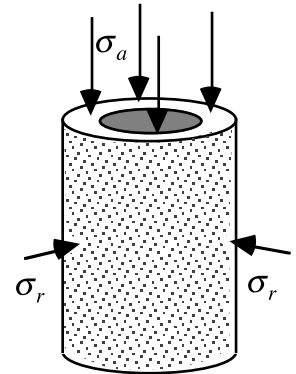
In the assessment of viscous coefficient of liquefied sand by means of model tests, which was discussed in Sect. 25.14, the state of stress and strain in model ground were neither measured directly nor uniform. Hence, the reliability of the obtained data was not satisfactory. To improve this situation, laboratory shear tests were undertaken to directly measure the possible viscosity of liquefied sand (Nishimura et al. 2001 and 2002). However, a conventional type of monotonic undrained shear tests encountered the following difficulties.

1. When shear stress is loaded on liquefied specimen in an undrained manner, positive dilatancy occurs and increases the effective stress. Hence, the measured shear stress consists of frictionally increasing component and a possibly viscous term. They cannot be easily separated.
2. The ideally zero state of effective stress is impossible in a sample. If the stress were zero, the sample would fail due to its own weight.
3. Superposition of cyclic loading that can reduce the dilatancy (Sect. 25.15) is missed.

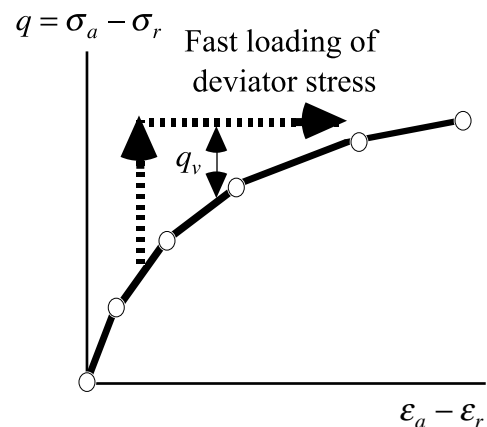
Consequently, it was decided to use a hollow cylindrical specimen in which monotonic axial loading and cyclic torsion shear can be superimposed (Nishimura et al. 2001). Moreover, it was attempted to maintain the effective stress level (lateral stress,  $\sigma'_r = \sigma'_3$ ) constant and positive by keeping the drainage valve open and supplying specified back pressure (pore water pressure controlled from outside) into the specimen. The influence of this positive effective stress (not zero) was examined by extrapolation of stress level toward zero (Sect. 25.17).

Figure 25.46 illustrates the testing scheme in which specimens of low isotropic effective stress (10–30 kPa) were axially compressed after isotropic consolidation under 100 kPa and reducing the effective stress by raising the back pressure. No cyclic loading was superimposed. In the meantime, the drainage valve was open so that the pore water pressure and the effective stress level ( $\sigma'_r$ ) were held constant: the effects of undesired dilatancy and pore pressure drop were avoided. Hollow circles in Fig. 25.47 stand for the results of a slow static shear test, while dashed arrows indicate the viscous response of a specimen to rapid increment of the deviator stress. Hence,  $q_v$ , which is the difference between the static stress–strain curve and the response to the rapid stress increment, is considered to be the viscous component of stress. The viscous coefficient,  $\eta$ , in the course of shear deformation was obtained by

$$\eta = \frac{\tau_{\text{viscous}}}{d\gamma/dt} = \frac{q_v}{2d(\epsilon_a - \epsilon_r)/dt} .$$



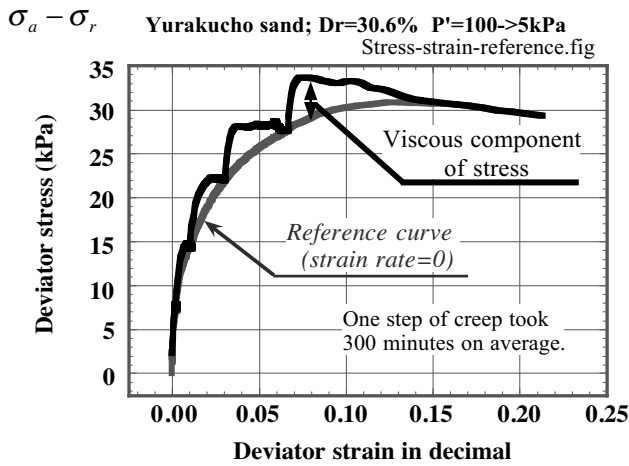
**Fig. 25.46** Axial compression of hollow cylindrical specimen



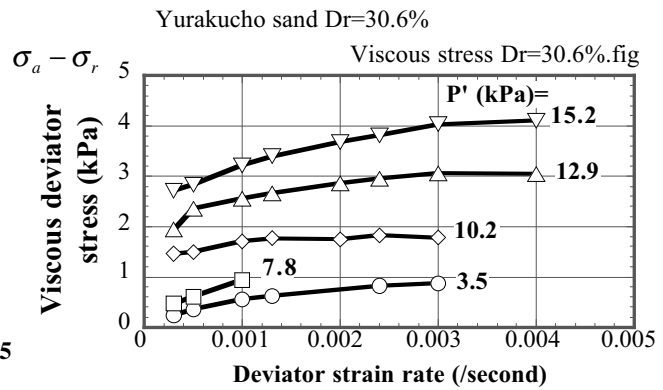
**Fig. 25.47** Measurement of rate dependent nature of specimen

**25.17 Viscosity of Liquefied Sand Measured in Laboratory Tests**

The methodology of testing on rate-dependent nature of sand under low effective stress was practiced by Gallage et al. (2005). Figure 25.48 shows the stress–strain behavior of Yurakucho sand, which is the alluvial sand in downtown Tokyo. It contains a few percent of plastic fines. After reducing the isotropic confining pressure from 100 kPa to 5 kPa, thus reproducing the effects of pore pressure increase during earthquake loading, the deviator stress was increased by steps in a drained manner. Each step loading was followed by 300 s of creep behavior from which the viscous (rate-dependent) nature of sand was measured. In the last stage of step loading, the creep deformation of the specimen was remarkable, the lateral deformation as well as the increase of cross section was substantial, and the decrease of the deviator stress (= constant axial force/increasing cross section) was significant. The reference curve that represents the behavior of sand without creep behavior was obtained by connecting the measured stress–strain points at the end of creep where the rate of strain became null and the viscous nature had ceased. The difference in the deviator stress between the measured stress–strain curve and the reference curve gives the viscous (rate-dependent) component of stress.

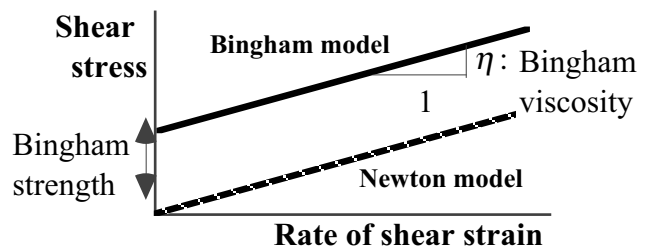


**Fig. 25.48** Stress–strain curve to examine creep behavior of sand



**Fig. 25.49** Variation of viscous component of shear stress with strain rate

The measured viscous stress,  $\sigma_a - \sigma_r$ , was plotted against the strain rate (increase of strain per second) to examine the nature of viscosity in sand. Figure 25.49 illustrates that the data vary in a linear manner with a certain vertical offset. The greater value of  $P'$  (mean effective stress) is associated with higher viscous stress, showing less importance of viscosity in deformation characteristics of sand under higher stress. The linear configuration of curves in this figure can be modeled reasonably by the Bingham viscous modeling in Fig. 25.50.



**Fig. 25.50** Conceptual diagram of Bingham viscous model

The Bingham model consists of two parameters, which are namely the Bingham strength and viscosity coefficient,  $\eta$  (Fig. 25.50). Their values were read from such diagrams as Fig. 25.49 and plotted in Figs. 25.51 and 25.52. Note that triaxial compression loading was conducted on not only Yurakucho sand but also 1-mm particles of styrofoam. This chemical material has a specific gravity of 1.03 and lost its effective stress when submerged in water. This feature was important in maintaining the stability of tested specimens under low effective stress. As illustrated in these figures, it became possible to reduce the effective stress toward zero. The effective stress is defined by the mean value of  $P' =$

$(\sigma'_1 + \sigma'_2 + \sigma'_3)/3 = (\sigma'_a + 2\sigma'_r)/3$  (see Fig. 25.46) in which  $\sigma'_a$  increased with triaxial compression while  $\sigma'_r$  was held constant at a low value. Another attempt to reduce the effective stress level was to conduct triaxial extension tests in which  $\sigma'_a$  decreased. These efforts helped extrapolate all the measured Bingham parameters toward zero effective stress, which corresponds to the fully liquefied state. The Bingham parameters decrease as the effective stress decreases toward zero, and, at the extreme state of zero effective stress, the Bingham viscosity would range between 0 and 100 kPa · s and the Bingham strength would vanish to zero. Thus, it is reasonable to state that liquefied sand with null effective stress behaves similar to Newton viscous liquid. Note that the state of zero effective stress cannot be reproduced in laboratory shear tests because gravity effects on particles cannot be eased (Sect. 25.16) and this extrapolation is useful.

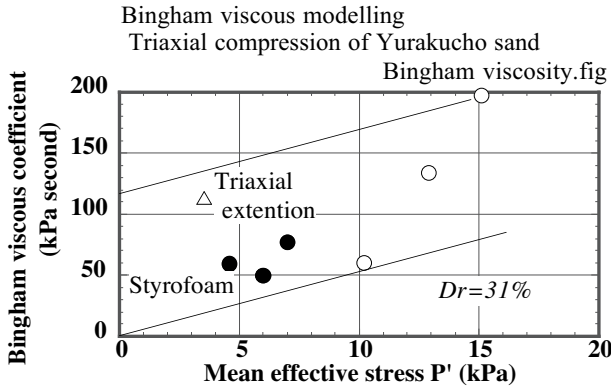


Fig. 25.51 Variation of Bingham viscous coefficient with effective stress level

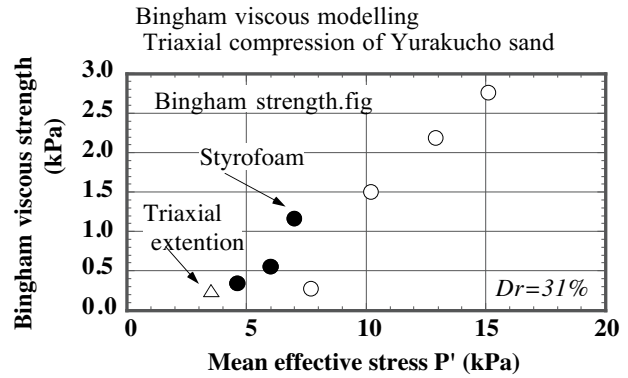


Fig. 25.52 Variation of Bingham viscous strength with effective stress level

A fundamental question is why sand under low effective stress exhibits viscous nature although its constituents (sand grain and pore water) have no (or very small) viscosity. To answer this question, additional tests were conducted on specimens in which pore was filled with air or pore was vacuum. For the vacuum specimen, the pore pressure was held near vacuum (-98 kPa) while the external pressure was varied so that the effective stress (external pressure - vacuum pore pressure) varied as intended. The measured viscosity in Fig. 25.53 indicates that the viscosity decreased from that of water specimen to vacuum specimen. Therefore, it seems that the viscous nature of pore fluid partly governs the overall viscous nature of liquefied sand. Probably the vortex in pore fluid develops significant viscosity when sand is subjected to large deformation. The viscosity of vacuum specimen is probably caused by collision between grains as is assumed in the analysis of debris flow (Egashira et al. 1997; Egashira and Miyamoto, 2000).

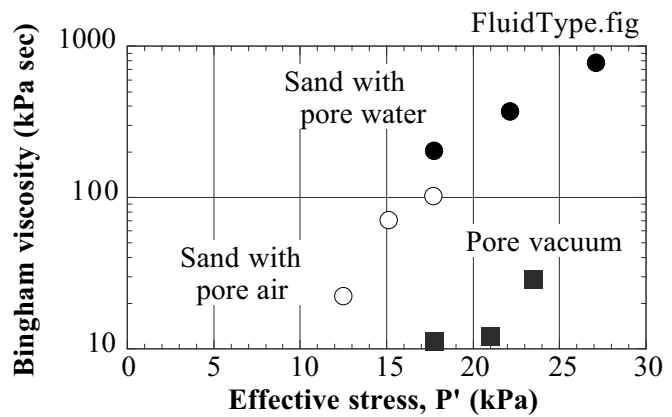


Fig. 25.53 Study on possible causative mechanism of rate-dependent nature in sand

The limitation in the present study in Fig. 25.53 is the gravity. It is attempted in 2007 by the authors to run triaxial shear tests under zero gravity environment (free fall in a vertical shaft) which is expected to further reduce the effective stress level.

Viscosity was investigated as well in model tests by focusing on the interaction between flow of liquefied sand and an embedded structure. A possible problem in this approach is that stress and strain

around a structure is not uniform. Hence, one should rely on fluid mechanic theory on viscous fluid too much. For example, the drag force,  $F$ , acting on a sphere in a viscous fluid is given by Stokes formula;

$$F = 6\pi\mu \frac{D}{2} V \tag{25.39}$$

in which  $\mu$  designates the viscosity coefficient of the fluid,  $D$  the diameter of a sphere, and  $V$  the flow velocity of the fluid. For a cylindrical object such as a pipe or a pile, Lamb's formula (Lamb, 1911) is available;

$$P = \frac{4\pi\mu V}{0.5 - \log_e \left( \frac{1.7811 \times DV\rho}{8\mu} \right)} \tag{25.40}$$

in which  $P$  is the lateral force per unit length of a cylinder,  $V$  the velocity of flow,  $D$  the diameter of a cylinder, and  $\rho$  the mass density of fluid. In a nondimensional form, Lamb's formula becomes

$$\frac{P}{4\pi\rho V^2 D} = \frac{\frac{\mu}{\rho DV}}{0.5 - \log_e \left( \frac{1.7811 \times \rho DV}{8\mu} \right)} \tag{25.41}$$

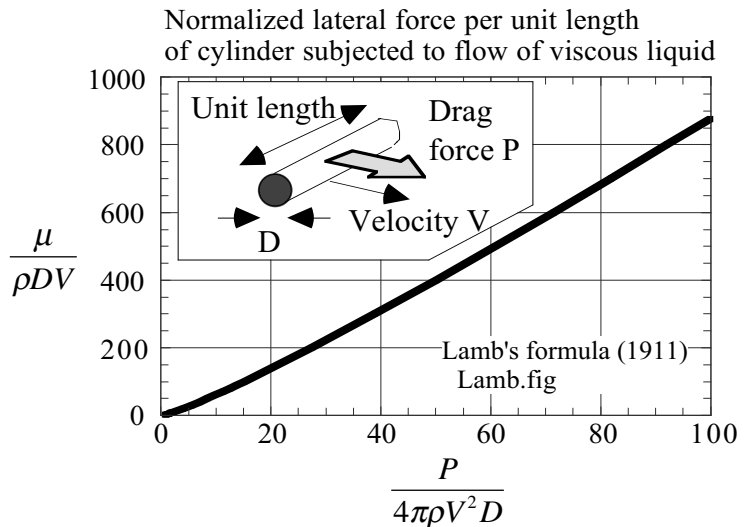


Fig. 25.54 Normalized illustration of Lamb's formula

This formula is illustrated in Fig. 25.54.

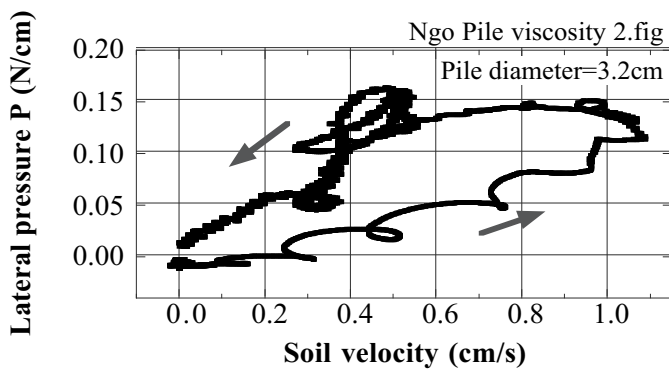


Fig. 25.55 Variation of lateral earth pressure on pile subjected to flow of liquefied subsoil (Ngo, 2007)

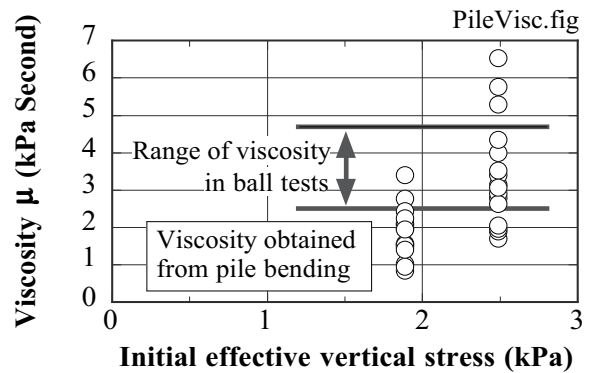


Fig. 25.56 Viscosity coefficient determined by 1-G shaking model tests (Ngo, 2007)

1-G shaking model tests were conducted on the interaction between pile and lateral flow of liquefied loose sand. The diameter of the pile was 3.2 cm. The drag force,  $P$ , per unit length of pile was determined by the second derivative of bending moment, while the lateral displacement and velocity of flow were determined by an embedded displacement transducer (Fig. 24.58). Strictly speaking,  $V$  in Lamb's formula is the velocity difference between soil flow and a pile. Since the displacement of pile is substantially smaller than that of soil flow, the measured  $V$  was substituted in (25.41) to determine the viscosity.

First, Fig. 25.55 shows the relationship between  $P$  and velocity ( $V$ ). Basically there is a positive relationship between  $P$  and  $V$ , which implies a rate-dependent nature of liquefied sand. On the basis of the measured force,  $P/(4\pi\rho V^2 D)$ ,  $\mu/(\rho VD)$ , and consequently the viscosity coefficient,  $\mu$ , was determined.

The viscosity coefficient was evaluated also by pulling up a ball (sphere) of 10 cm in diameter and substituting the drag force in the Stokes formula (25.39). The derived values are combined and plotted in Fig. 25.56. There is a consistency between two sets of viscosity coefficients. The data from pile test shows the dependency of viscosity on the initial effective stress. The ball test data were not interpreted in this manner because of the large size of the ball.

Moreover, Table 25.2 presents the viscosity determined from centrifuge pile tests (Hamada, 2005). The range of viscosity is similar to what is shown in Fig. 25.56. It was shown further by Hamada (2005) that viscosity changed with the flow velocity, suggesting Bingham viscosity modeling (Fig. 25.50).

It seems thus reasonable to consider liquefied sand as Bingham viscous material. On the basis of this idea, a method of dynamic analysis was developed by Towhata et al. (1999). This method avoided complicated dynamic analysis and employed a simplifying assumption in which the time development of horizontal and vertical displacement ( $u$  and  $v$ , respectively) vary with time with a single time function;

$$\begin{aligned} u(x, z, t) &= U(x, z)\lambda(t) \\ w(x, z, t) &= W(x, z)\lambda(t) \end{aligned} \tag{25.42}$$

in which  $U$  and  $W$  are displacement at the minimum potential energy. They are the maximum possible displacement and is derived by the method in Sect. 25.7. By using the theory of Lagrangean equation of motion (Sect. 25.3; Towhata et al. 1999) together with the solutions for  $U$  and  $W$ , an equation of motion for  $\lambda(t)$  is derived in such a form as

$$m \frac{d^2 \lambda}{dt^2} + \eta \times 2\sqrt{mk} \frac{d\lambda}{dt} + k\lambda = f \tag{25.43}$$

**Table 25.2** Viscosity of liquefied sand determined from centrifugal pile tests (after Hamada, 2005)

Centrifuge acceleration (G)	Viscosity (kPa.s)
10	3.1 – 4.41
20	5.16 – 7.3
30	4.39 – 12.56
40	10.21 – 34.85

in which  $\eta$  designates the critical damping ratio. Oscillation of motion occurs if this value is less than 1.0; oscillation has been hardly reported in model tests on lateral flow. Empirically, this critical damping ratio is 10–40 for reasonable prediction. Note that this range of critical damping ratio does not necessarily match the experimentally measured viscosity of sand. This point needs further investigation.

**25.18 Observed Rate of Strain During Liquefaction-Induced Ground Deformation**

Since the viscosity of liquefied sand was found to vary with the rate of strain in Sect. 25.17, a deformation analysis requires the real rate of strain to be determined prior to calculation. Although past earthquake experiences reported many examples of liquefaction-induced deformation of ground, they concern only the residual deformation and there is no information about the real rate of strain except one case.



**Fig. 25.57** Terminal building of Niigata Airport after liquefaction and subsidence (Department of Civil Engineering, University of Tokyo)

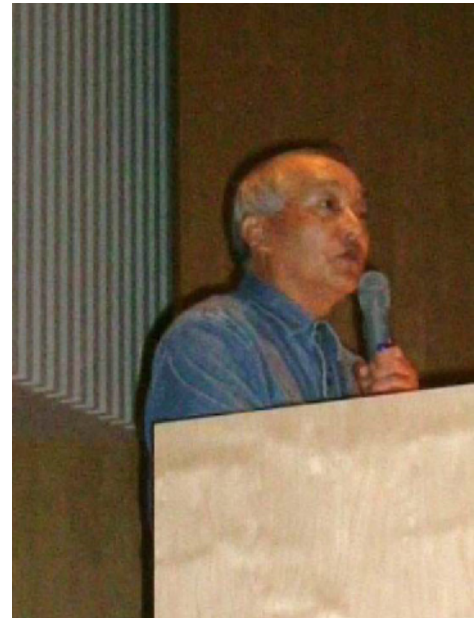
(a) Sinking building due to liquefaction



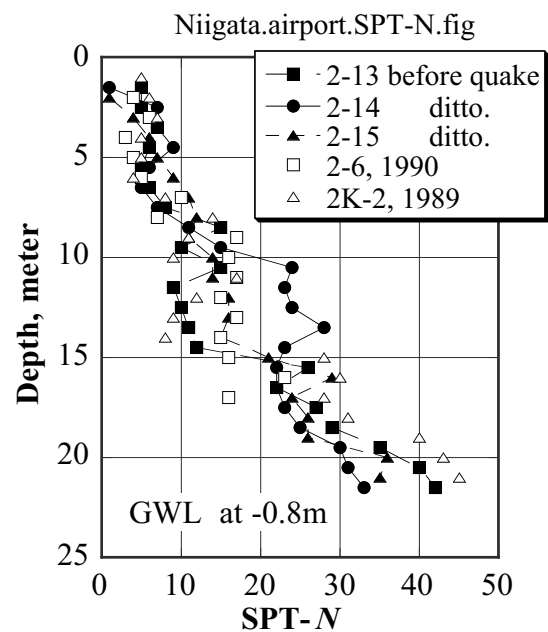
(b) Boiling of sand and water



**Fig. 25.59** Subsidence of Niigata Airport terminal building into liquefied subsoil (from motion picture by Mr. F. Yuminamochi)



**Fig. 25.58** Professional photographer, Mr. Fukuo Yuminamochi, who took the only one motion picture of ongoing liquefaction and boiling in Niigata, 1964 (this photo was taken in 2004)



**Fig. 25.60** SPT profile in foundation of Niigata Airport building (data by Ministry of Transport and Kiso-jiban Consultants Company)



The terminal building of the Niigata Airport subsided 1.2 m due to subsoil liquefaction in 1964 (Fig. 25.57), and was demolished later in 1965. A motion picture of this scene of subsidence was recorded by a professional photographer, Mr. F. Yuminamochi (Fig. 25.58), who was in the building with his cameras ready when the earthquake started (JGS, 1999 and 2004).

Mr. Yuminamochi was in the airport building when the Niigata earthquake occurred. His job was to take pictures of a new ferry ship from the sky, and an air plane was waiting for him in front of the terminal building. After taking photographs and motion pictures of liquefaction, Mr. Yuminamochi took off from the airport, and took air photographs of liquefaction and seismic damage of Niigata City from the sky. Later the Japanese Geotechnical society published his photographs. Since 1964, nobody else took motion photographs of ongoing liquefaction. It is unbelievable that such a miraculous combination of a professional photographer, cameras and films, air plane, strong earthquake, and liquefaction occurred in reality.

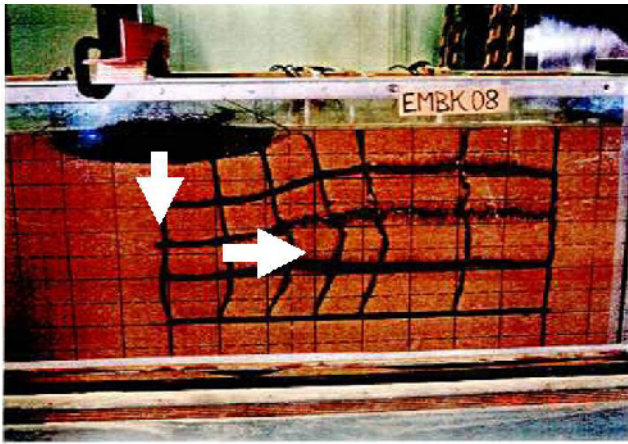
Mr. Yuminamochi's motion picture shows the time change of the building height that remained above the boiled water surface (Fig. 25.59). Consequently, the rate of subsidence was assessed to be not more than 1.1 cm/s (Towhata and Horikoshi, 1997). Note further that this building did not have significant structural damage. The essence of damage lay in the unacceptably large displacement (subsidence).

This study was made in the following manner:

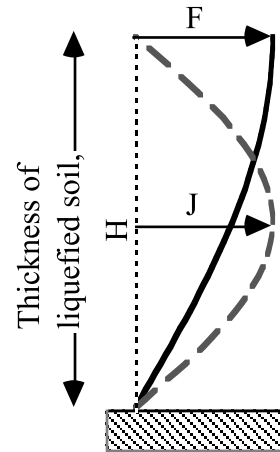
1. The building height above the water surface was compared between two shots of the motion picture with a certain time interval.
2. The remaining height of the building was assessed by using a design diagram of the building, which was supplied by the Ministry of Transport.
3. When the picture was taken, the surface of boiled water was located around the knee of the photographer. The rate of subsidence was determined by assuming that the water depth was more or less constant between two shots of picture.
4. The derived rate of subsidence (1.1 cm/s) is exact if the water depth was exactly unchanged. It is an overestimation, conversely, if the water surface was still rising slowly.

Figure 25.60 is a summary of standard-penetration-test profile (Sect. 1.11) of the building site. Although varying, large values of  $N$  starts at a depth of 8 or 14 m. By subtracting the thickness of the surface unliquefiable crust, the thickness of the liquefied deposit was 7–13 m. The rate of vertical strain of the liquefied soil was 1.1 cm/s divided by 7–13m. Thus, the rate of strain was of the order of 0.001/s.

**25.19 Three-Dimensional Dynamic Analysis on Liquefaction-Induced Permanent Deformation of Ground**



**Fig. 25.61** *J*-type mode of lateral displacement observed in 1-G test on subsidence of embankment (Mizutani et al., 2001)



**Fig. 25.62** Superposition of two modes of lateral displacement

Model tests demonstrated that there is a different displacement mode that develops under an embankment (Fig. 25.61). In this mode the maximum displacement occurs at the middle elevation, while null at both top and bottom. This mode is called the *J* mode, while the previous one (25.1) is called the *F* mode. In this context, the method of static analysis for a three-dimensional ground deformation induced by liquefaction was extended to a three-dimensional dynamic situation. Its major features are:

- Dynamic analysis makes it possible to calculate the time history of flow displacement, *F* and *J*. In contrast, static analysis cannot give the maximum possible displacement in terms of superposition of *F* and *J* modes. There is no unique solution for them (Orense and Towhata, 1998).
- The lateral displacement varies along the vertical axis in accordance with two modes in Fig. 25.62. *F* is important in slope displacement (Sect. 25.1), while *J* under embankments and shallow foundations. *F* and *J* in Fig. 25.62 stand for the amplitude of each mode.
- The mode superposition is made of two horizontal directions, which are namely *x* and *y*, or EW and NS. Hence,

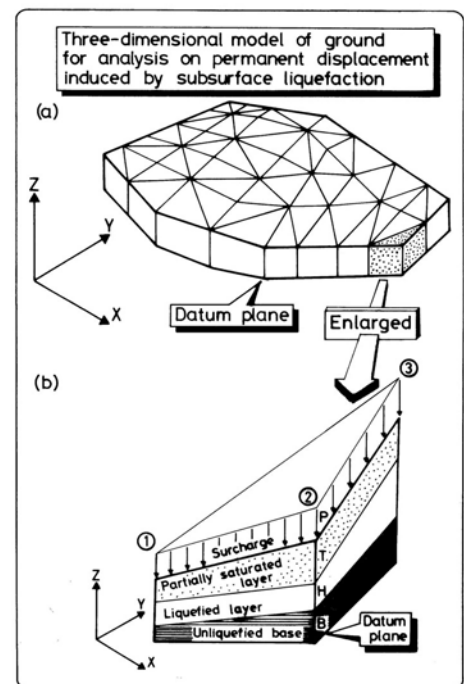
$$\begin{cases} u_x = F_x \sin \frac{\pi z}{2H} + J_x \sin \frac{\pi z}{H} \\ u_y = F_y \sin \frac{\pi z}{2H} + J_y \sin \frac{\pi z}{H} \end{cases} \quad (25.44)$$

in which  $F_x$ ,  $J_x$ ,  $F_y$ , and  $J_y$  are unknown. This superposition drastically reduces the amount of computation when compared with popular FE analyses.

- A constant volume (undrained) deformation is expressed by

$$\frac{\partial u_x}{\partial x} + \frac{\partial u_y}{\partial y} + \frac{\partial w}{\partial z} = 0. \quad (25.45)$$

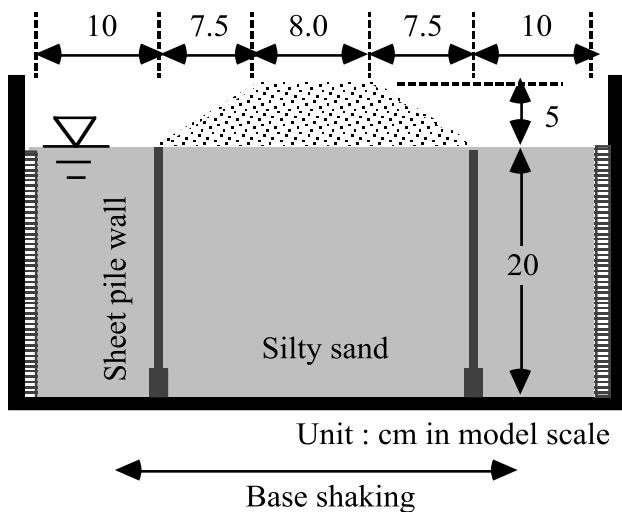
By substituting (25.44) in (25.45) and then integrating in terms of *z* with the boundary condition of  $w = 0$  at the bottom of liquefied layer, the vertical displacement of *w* is expressed by



**Fig. 25.63** Three-dimensional discretized model for liquefaction-induced ground displacement

$u_x$  and  $u_y$ . Consequently, all the components of three-dimensional displacement are expressed by  $F_x$ ,  $J_x$ ,  $F_y$ , and  $J_y$ . This is particularly important in a three-dimensional dynamic analysis.

- Liquefied sand is considered to be a viscous liquid.
- Displacement, velocity, and acceleration at any location are expressed by  $F_x$ ,  $J_x$ ,  $F_y$ , and  $J_y$  together with their time derivatives. Hence, the kinetic energy, the potential energy, and the energy dissipation due to viscosity of liquefied sand are expressed by  $F_x$ ,  $J_x$ ,  $F_y$ , and  $J_y$  together with their time derivatives.
- Discretization of  $F_x$ ,  $J_x$ ,  $F_y$ , and  $J_y$  in the  $x$ - $y$  plane makes it possible to obtain an equation of motion in terms of the discretized unknowns. In this procedure, the *Lagrangian* equation of motion (Sect. 25.3) plays an important role. Figure 25.63 illustrates a discretized model of a three-dimensional ground.
- The present analysis is a three-dimensional dynamic analysis of ground displacement. It further takes into account the fact that a slope finally ceases to flow when the surface becomes level or the potential energy achieves the minimal value (Sect. 24.6). Moreover, a shallow foundation stops to sink any more when the increased buoyancy becomes equal to the gravity. In this sense, the analysis is of a large-displacement formulation.

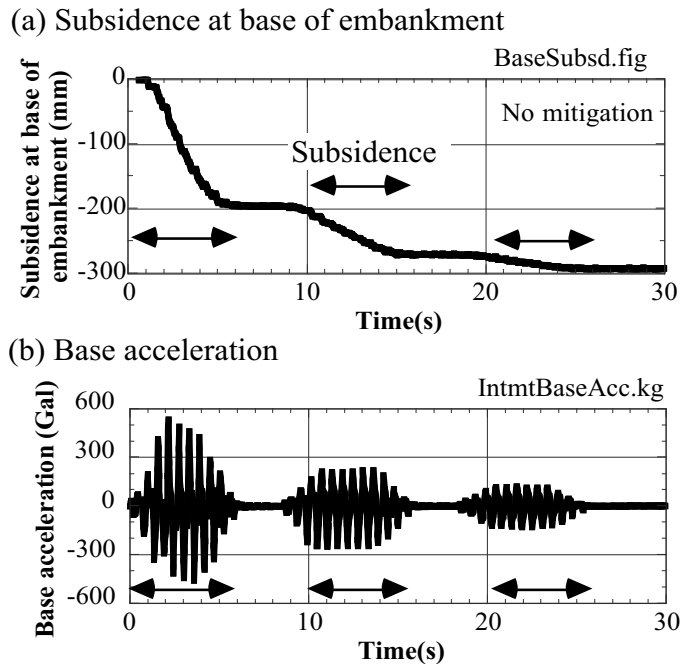


**Fig. 25.64** Configuration of centrifugal model of embankment resting on liquefiable subsoil

It is assumed that lateral flow develops during the strong shaking that is temporarily specified in Fig. 5.23. The idea that lateral flow occurs only during strong shaking is supported by model shaking tests.

For example, Alam et al. (2004a, b, c) conducted centrifugal model tests on an embankment model testing on liquefiable subsoil (Figure 25.64). The time history of subsidence of the embankment (without embedded sheet pile wall) is illustrated in Figure 25.65 where subsidence occurred intermittently only when base shaking was strong. Similar finding was made by centrifuge tests on lateral flow of slopes by Okamura et al. (2001).

The duration time of strong shaking was interested in by Housner (1965). However, no clear idea of “strong” shaking was specified. Later Lee and Chan (1972) stated that shaking greater than 50 Gal is the strong shaking. Similarly, the author considers the strong shaking to be greater than 50 Gal (Fig. 5.23).



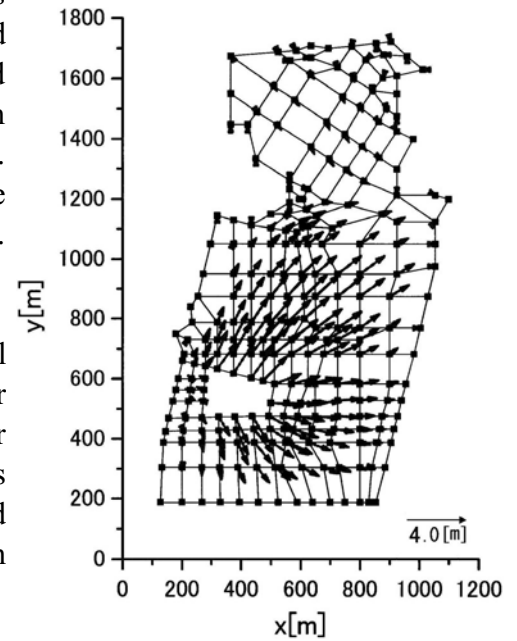
**Fig. 25.65** Intermittent development of embankment subsidence during strong excitation

**25.20 Example of Three-Dimensional Analysis on Liquefaction-Induced Permanent Deformation of Ground**

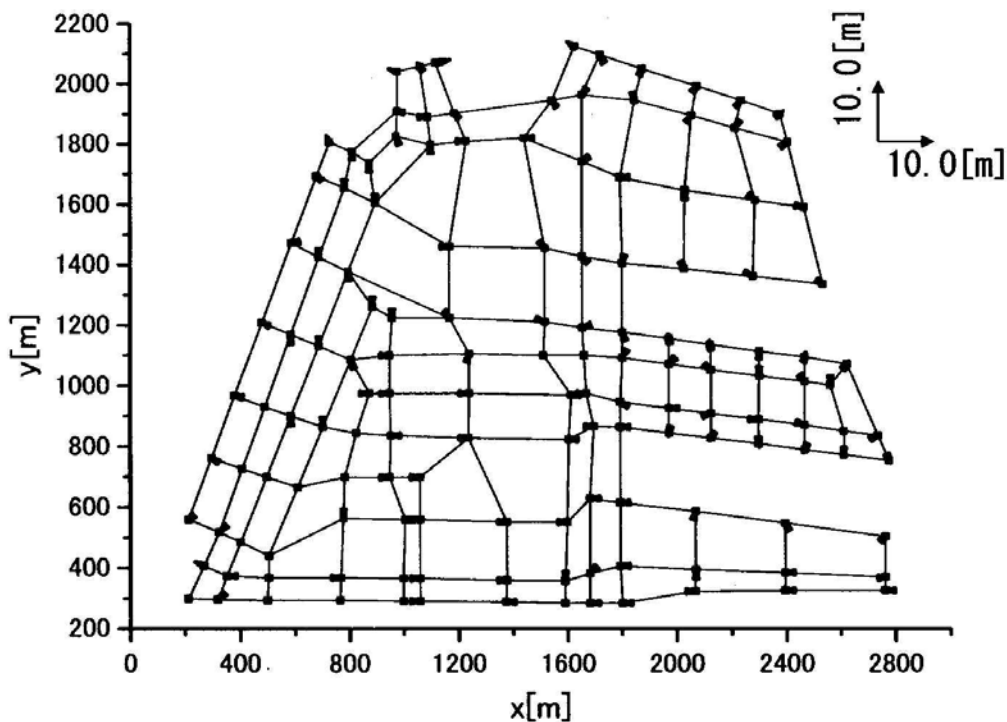
Figure 25.66 illustrates an example of three-dimensional analysis on the Maeyama area in Noshiro City. The thickness of liquefied soil was set equal to 5 m, while the surface unliquefied crust had 1 m of thickness. With the 1983 Nihonkai-Chubu earthquake in mind, the state of flow was considered to continue for 60 s (Fig. 5.23). The surface displacement,  $F_x$  and  $F_y$ , is oriented in the downslope direction that is consistent with the observation (Sect. 24.1).

Another example analysis is on the Port Island in Kobe. A special boundary condition was developed to take into account the behavior of gravity quay walls. Since the Kobe earthquake had a smaller earthquake magnitude, the duration time of flow deformation was set equal to only 10 s. The calculated displacement is outward from the land. Its magnitude is consistent with the observation in 1995 (Fig. 25.67).

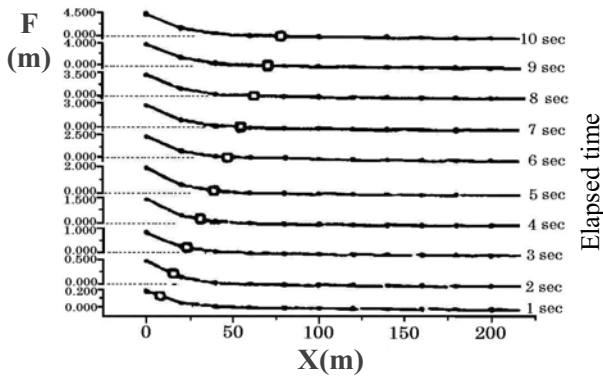
One of the important problems in lifeline earthquake engineering is the effects of quay wall movement on deformation of liquefied backfill area. The size of the affected area is evaluated by the distance from the quay wall. Figure 25.68 illustrates the calculated distribution of lateral displacement at surface ( $F$ ) that varies with the distance from the quay wall. The calculated size of a significant displacement increases with the elapsed time. Ground distortion behind a quay wall is, thus, generated by propagation of quay wall distortion toward the backfill. Noteworthy is that an analytical assessment of the size of the affected area ((25.46); indicated by  $\square$ ) is in good agreement with the numerically obtained size of influence.



**Fig. 25.66** Example analysis on Maeyama hill in Noshiro City



**Fig. 25.67** Example analysis on Port Island in Kobe



**Fig. 25.68** Analytical assessment of area of influence made by quay wall displacement ( $x = 0$  at quay wall)

The analytical assessment was obtained by

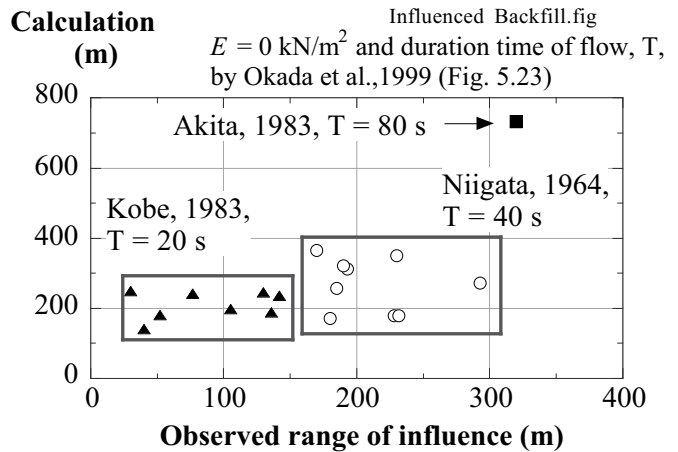
$$\text{Size of influence} = V_f \times \text{Elapsed time} \quad (25.46)$$

in which

$$V_f = \sqrt{\frac{2g(ET + 4\gamma H^2 / \pi^2)}{\gamma H + 2P}} \quad (25.47)$$

where  $g$  is the gravity acceleration,  $E$  the elastic modulus of surface dry crust,  $T$  the thickness of crust,  $\gamma$  the unit weight of liquefied subsoil,  $H$  the thickness of liquefied layer, and  $P$  the weight of surface crust per unit area (Towhata et al. 1996). Since the surface crust is subjected to tensile deformation in the backfill,  $E = 0$  is suitable.

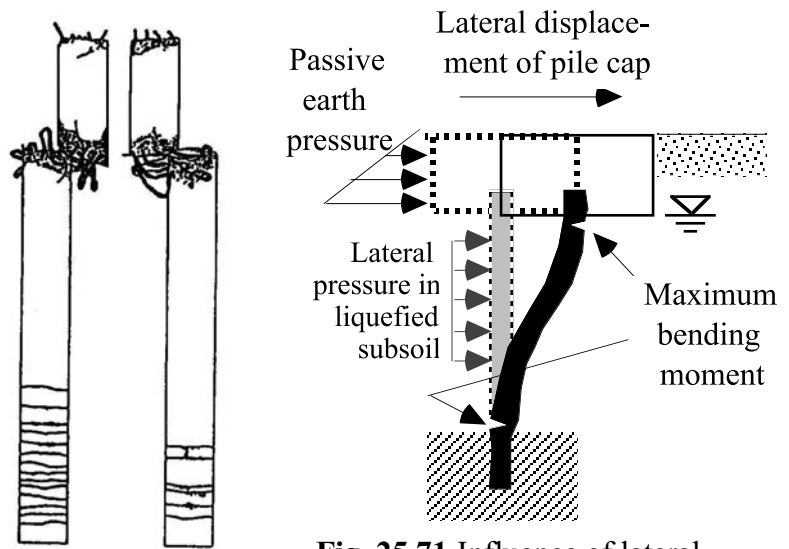
The value of  $V_f$  in (25.47) is around 10 m/s. Figure 25.69 compares calculated size of influence and the observed range (Yasuda et al. 1997). The elapsed time is the duration time of acceleration in past motion records from the maximum acceleration and the end of acceleration greater than 50 Gal (Fig. 5.23). The maximum acceleration finally determined the thickness of liquefaction ( $H$ ) and 50 Gal is considered to be the minimum intensity of motion to maintain the state of 100% excess pore water pressure. There is a good agreement between observation and calculation. Some difference in the case of Akita Harbor is probably due to the fact that the whole range of liquefaction was less than the calculation in this figure.



**Fig. 25.69** Comparison of size of ground displacement behind quay wall between calculation and observation

**25.21 Lateral Load on Pile Foundation Exerted by Lateral Displacement of Liquefied Ground**

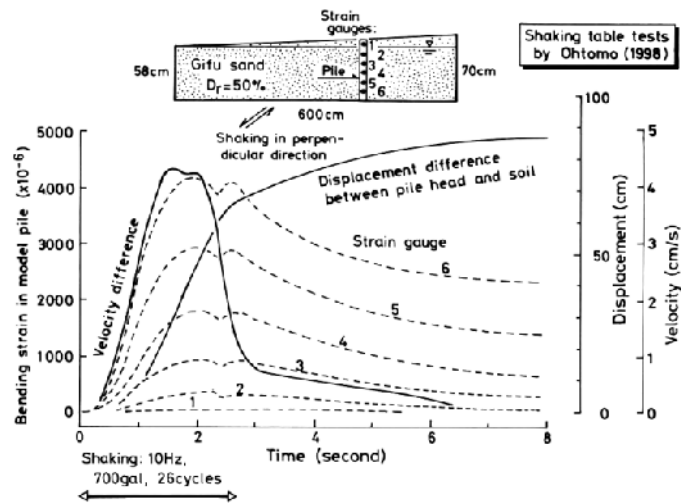
Section 24.16 described model tests on pile behavior subjected to lateral displacement of liquefied ground. As for real damage, the case in Fig. 17.25 was the first example in which a pile foundation was destroyed by lateral displacement of liquefied ground. Since then, several building foundations have been studied on the mechanism of failure of piles. Figure 25.70 is an example in which an excavated pile was seriously damaged at both top and bottom. The mechanism of failure is, accordingly, considered as illustrated in Fig. 25.71:



**Fig. 25.71** Influence of lateral displacement of liquefied ground on pile foundation

**Fig. 25.70** Damaged shape of excavated pile of “A” building in Niigata (Yoshida and Hamada, 1991)

- Lateral displacement of liquefied subsoil carries laterally the surface dry crust together.
- The surface crust hits a cap of a pile foundation and exerts passive earth pressure on it.
- The pile cap moves laterally together with the superstructure. Piles are tightly connected with cap and rotation is difficult.
- The bottom tip of a pile does not move laterally, because it penetrates into an unliquefied stable layer. Hence, rotation of pile is difficult.
- Thus, the pile behaves similar to a beam subjected to bending whose ends at top and bottom cannot rotate (fixed boundaries).
- The elastic beam theory states that the maximum bending moment occurs at those fixed ends.
- When the bending moment is significant, the pile is destroyed.



**Fig. 25.72** Viscous lateral pressure in liquefied soil on pile model (Ohtomo, 1998)

Note that the passive earth pressure within the unliquefied surface crust of soil is not necessarily equal to the conventional Rankine (Coulomb) passive pressure (Appendix 1), because those conventional theory assumes a two-dimensional plane-strain situation, while a real pile foundation is of a three-dimensional configuration.

The lateral pressure exerted by liquefied subsoil is less than the passive pressure mentioned earlier. Ohtomo (1998) demonstrated in a shaking table test that the bending strain of a pile is more closely related with the flow velocity of liquefied sand than the displacement (Fig. 25.72). This suggests that liquefied sand is similar to viscous liquid.

## 25.22 Passive Earth Pressure Exerted by Surface Unliquefied Soil on Foundation of Structures

The evidence of the passive state of lateral pressure on foundations and top of piles was reported by Keenan (1996) as well as Berrill et al. (2001) in New Zealand. They excavated a foundation of piers of Landing Road Bridge where the 1987 Edgecumbe earthquake triggered liquefaction and 1.5 m of lateral displacement occurred. Sand boilings were found on the south side of the pier, clearly indicating the liquefaction of subsoil.

A trench was excavated after the quake in order to examine the cross section of the surface unliquefied crust resting above the ground water table. Figure 25.73 illustrates the cross section. On the north side of Pier C, a slip surface was found as a consequence of passive earth pressure. The lateral displacement of the surface crust caused subduction of this crust near the pier. Heaving in front of the pier indicates the compressional deformation of the surface soil. This passive earth pressure was significantly greater than the lateral pressure exerted by liquefied subsoil as described in Sect. 25.21.

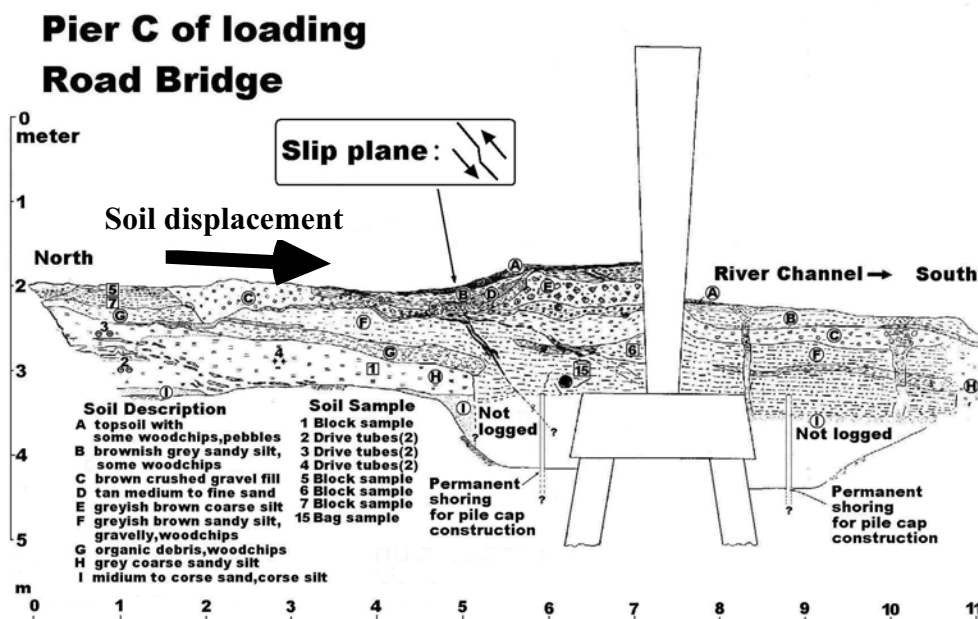


Fig. 25.73 Excavated cross section of surface unliquefied crust after lateral displacement (drawn after Keenan, 1996)

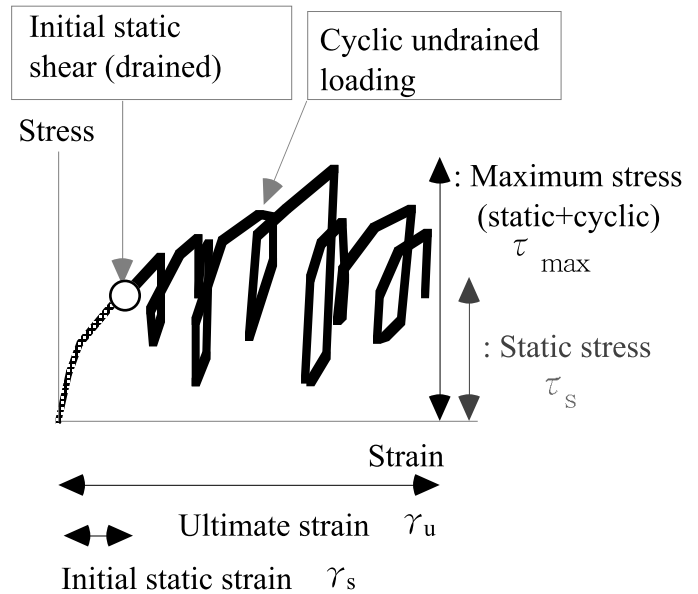
**25.23 Deformation Analysis Based on Strain Potential**

The predictive measures of earthquake-induced displacement so far described have limitations:

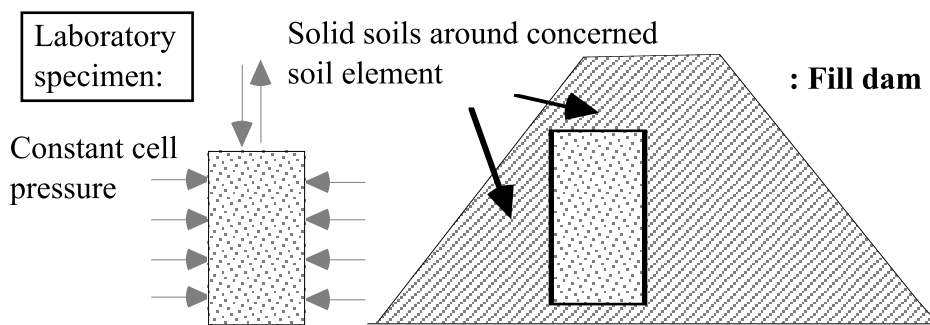
1. Newmark sliding block analogy (Sect. 12.1) is valid for sliding of a rigid soil block upon a specified slip plane; liquefaction and/or shear deformation is out of scope.
2. The energy principle in Sect. 25.1 supposes liquefied sand to be extremely soft; deformation of unliquefied compacted material is out of scope.

It is thus supposed that residual shear strain of, for example, a compacted earth-fill dam requires a different approach. Note that performance-based seismic design requires assessment of residual deformation (Sect. 14.7).

Lee (1974) proposed to run laboratory shear tests (Typically triaxial shear tests) on specimens that are subjected to consolidation stress state as well as cyclic undrained shear stress, both of which are assessed separately by some numerical method. The behavior of a tested sample is equivalent with that of the insitu soil.



**Fig. 25.74** Conceptual diagram of Lee’s method for assessment of seismic residual deformation



**Fig. 25.75** Different boundary conditions in triaxial-shear specimen and real soil element

Although a laboratory shear test in Fig. 25.74 suggests the cyclically-induced strain to be  $\gamma_u - \gamma_s$ , this strain does not occur in the real earth structure. This is because of different boundary conditions; a laboratory soil specimen (in a triaxial shear) is subject to pressure boundary condition in which displacement is free, while a soil element in a real dam is confined by adjacent soil (Fig. 25.75). Therefore, the strain measured in laboratory tests is called strain potential. Accordingly, the softening behavior in Fig. 25.74 is interpreted as reduction of modulus from the initial modulus of  $M_s \equiv \tau_s / \gamma_s$  to the reduced modulus of  $M_u = \tau_s / \gamma_u$ . Two static finite element analyses, one with  $M_s$  on preearthquake deformation and the other with  $M_u$  on postearthquake deformation are run and the difference of the pre- and postearthquake displacements gives the net earthquake-induced deformation.

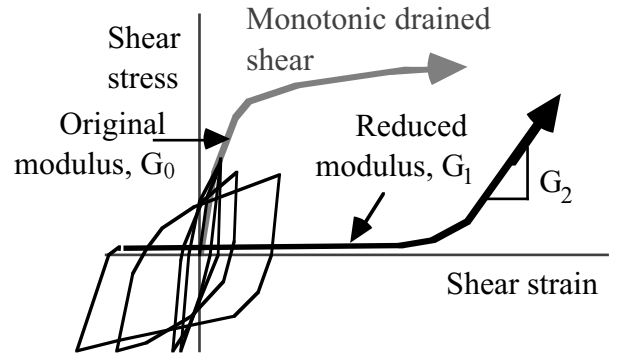
Since Lee (1974) did not specify details of the method, there are variations in the application of his idea. It is hence practiced also to use  $M_u = \tau_{max} / \gamma_u$  and run the second analysis with combined gravity and inertia forces.



A similar idea was applied to the prediction of liquefaction-induced ground deformation in the ALID analysis by Yasuda et al. (1992 and 1999). The stress–strain behavior of sand after liquefaction was reproduced by monotonic shear after cyclic shear tests on sand (Fig. 25.76). It is considered therein that shear rigidity of sand decreases from the original value of  $G_0$  to the postliquefaction value of  $G_1$ , thus producing large deformation under the static gravity-induced load. Hence, the liquefaction-induced deformation is obtained by

$$\frac{\text{static load}}{G_1} - \frac{\text{static load}}{G_0} \quad (25.48)$$

The extent of reduction in shear modulus,  $G_1/G_0$ , depends on the extent of liquefaction and the type of soil. The former factor is expressed by the factor of safety against liquefaction,  $F_L$  (Sect. 19.4), and the latter by the fines content,  $F_c$ . Generally, the reduction of modulus is more significant when  $F_L$  is smaller (more remarkable liquefaction; stronger shaking or longer duration of strong shaking) or fines content is smaller (clean sand). To date, there are experimental data only when  $F_L > 0.7$ , because laboratory shear tests cannot continue for a long time after the onset of liquefaction ( $F_L = 1.0$ ). After the onset of liquefaction, a tested specimen deforms significantly and sand grains and pore water are separated (segregation) inside a specimen: thus making continuation of shear test impossible. When  $F_L = 0.7$  and  $F_c = 0\%$ ,  $G_1/G_0$  is set equal to 0.00017.

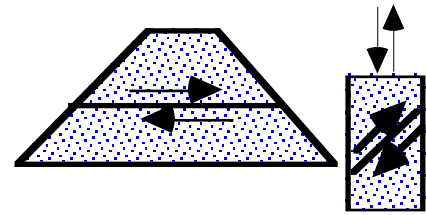


**Fig. 25.76** Monotonic undrained shear after liquefaction of sand

Since this method applies the undrained stress–strain behavior after liquefaction, the dilatancy becomes positive (volume expansion) after large deformation and the excess pore water pressure starts to decrease. Hence, the rigidity of sand starts to increase; compare  $G_2$  and  $G_1$  in Fig. 25.74. This feature is considered in the analysis by employing large-deformation formulation of finite element analysis.

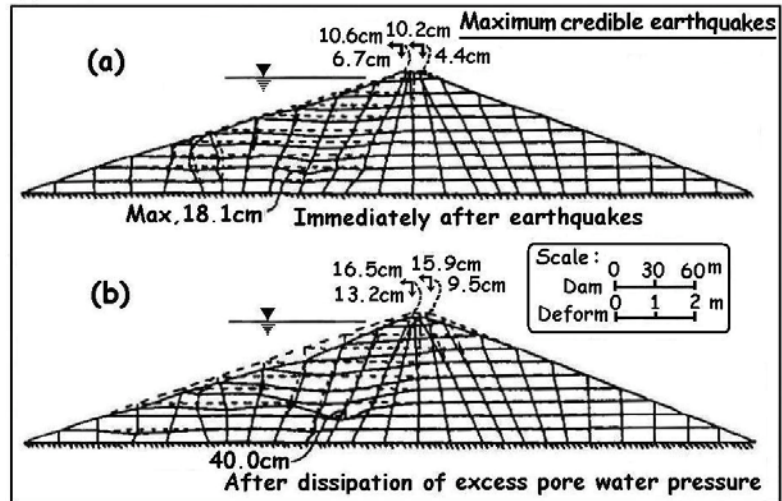
**25.24 Analysis on Seismic Deformation of Liyutan Dam in Taiwan**

Modification of the method by Lee (1974) in Sect. 25.23 was attempted by Kuwano and Ishihara (1988). It was proposed by them to use a torsion shear device in which two stress components can be controlled independently, and to generate stress histories that are equivalent to earthquake-induced complicated stress histories. Although this idea is elaborate, it is meaningful as well to employ a triaxial apparatus that can easily test undisturbed soil specimens.



**Fig. 25.77** Shear stresses in horizontal plane of dam and 45° plane of triaxial specimen

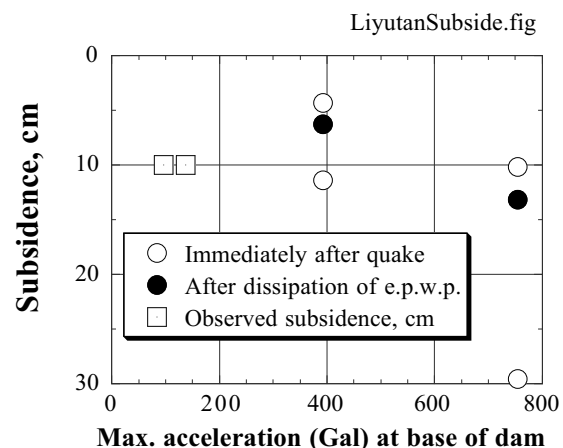
One of the shortcomings of a triaxial device is that only one component of shear stress (axial minus radial stress) can be controlled whereas a two-dimensional cross section of a dam is subject to two components; one in the horizontal plane,  $\tau_{xz}$ , and the stress difference between vertical and horizontal directions;  $(\sigma_z - \sigma_x)/2$ . Shi et al. (1989) decided to focus on the shear stress in the horizontal plane and produced an equivalent stress history in the 45° plane of a triaxial specimen (Fig. 25.77). Note that the stress state in the 45° plane is focused on in liquefaction studies as well (Fig. 19.7). They assessed the seismically-induced deformation of Liyutan Dam (鯉魚潭水庫), which was then being planned. Since the dam was not yet constructed, the material from the planned borrow area was compacted to the design density and was tested. The deformation at the end of the quake as well as after dissipation of excess pore water pressure was calculated. The latter in particular was assessed by reducing both bulk and shear moduli.



**Fig. 25.78** Calculated deformation of Liyutan dam under maximum credible earthquake (the largest predicted subsidence was obtained by assuming extreme extent of soil softening)



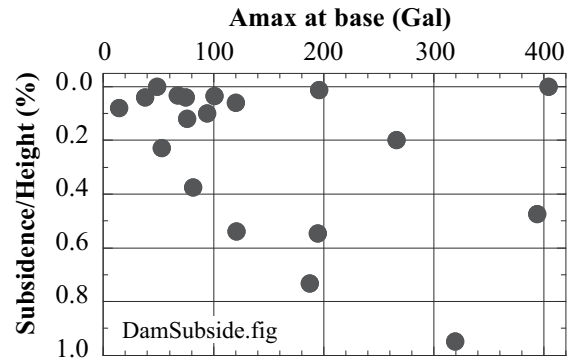
**Fig. 25.79** Liyutan Dam six months after ChiChi earthquake, Taiwan



**Fig. 25.80** Calculated and observed subsidence of Liyutan Dam

The calculated deformation induced by the maximum credible earthquake is illustrated in Fig. 25.78. For this calculation, the dynamic analysis put in an acceleration of 0.77 g (755 Gal) at the bottom of soil deposit 200 m below the dam body. The maximum subsidence at the dam crest was 30 cm. The completed Liyutan dam was shaken in 1999 by the ChiChi earthquake. When the author visited the dam

6 months after the quake, it was found that the dam developed merely 10 cm subsidence out of its 100-m height (Fig. 25.79). Thus, the ratio of the subsidence and the height was about 1%. Figure 25.80 compares the calculated subsidence and the real behavior. The horizontal coordinate for the observed subsidence is the acceleration measured at the base of the dam. This acceleration was the one reexamined in Taiwan and was supplied to the author by Prof. K. Konagai. Furthermore, the observed subsidence was supplied by the office of the dam (The Ministry of Economic Affairs, Water Conservancy Agency, Central Water Resources Bureau). It is found in Fig. 25.80 that the subsidence of the dam was negligible partly because the design and construction were satisfactory but also because the intensity of shaking was weak in the northern part of the causative fault. Compare the weak observed acceleration in Fig. 25.80 with 748 Gal (Sect. 15.4) in the southern part.



**Fig. 25.81** Seismic subsidence of rockfill dams in Japan (Okamoto, 2001)

Empirical information on subsidence of dam crest of Japanese rockfill dams due to earthquake is presented in Fig. 25.81. The subsidence has been less than 1% and the case of the Liyutan Dam is consistent with those of other dams. Note that these data are applicable to modern dams, which have been constructed under strict quality control and high safety margin. Those dams constructed by hydraulic filling is completely different (Figs. 17.26 and 17.27, and Sect. 20.5).

**25.25 Assessment of Subsidence of River Dikes Due to Subsurface Liquefaction by Using Limit Equilibrium Analysis**

One of the simplest methods for assessing liquefaction-induced subsidence of an embankment has been proposed in the field of river-dike engineering in Japan.

First, the factor of safety against liquefaction,  $F_L$ , is determined by any conventional methods. This  $F_L$  value is substituted in an empirical relationship between  $F_L$  and the development of excess pore water pressure in undrained tests,  $\Delta u$  (see Sect. 20.7);

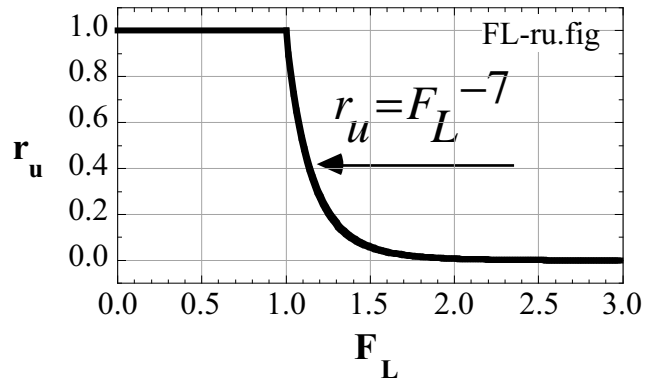
$$r_u \equiv \frac{\Delta u}{\sigma'_v} = \begin{cases} F_L^{-7} & \text{when } F_L > 1 \\ 1.0 & \text{when } F_L \leq 1 \end{cases} \quad (25.49)$$

This relationship is illustrated in Fig. 25.82.

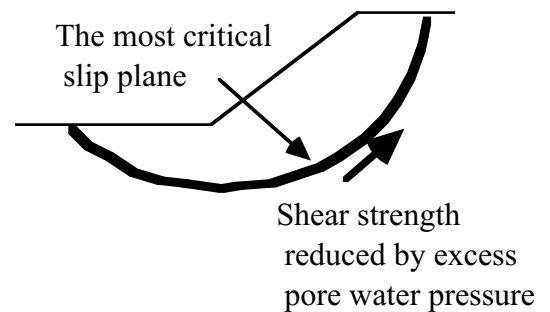
The second stage is a limit equilibrium analysis on stability of embankment slope in a static manner; see Fig. 25.83. Note that this stability analysis is a conventional one without taking account of any seismic force. This practice has been justified by the idea that significant parts of displacement of an embankment occur after strong shaking has ceased. The effects of earthquake are taken into account only by reducing the shear strength of soil in accordance with the development of excess pore water pressure: (25.49). In case the seismic force has to be considered, it is done by means of pseudostatic force (seismic coefficient method) but without considering pore pressure build-up. Consideration of both excess pore water pressure and seismic force is regarded over-conservatism.

The static factor of safety against slope failure,  $F_s$ , as calculated in Fig. 25.83 is substituted in an empirical relationship between  $F_s$  and the ratio of subsidence (subsidence/height). This is illustrated in Fig. 25.84. Readers should not confuse  $F_L$  and  $F_s$ . Note that Fig. 25.84 shows the upper bound of subsidence that occurred during past earthquakes.

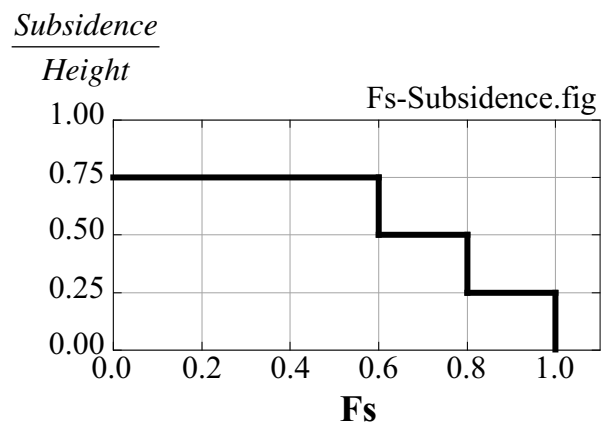
Figure 25.84 implies that the maximum possible subsidence is 75% of the original height of a fill. This is consistent with the experiences of earthquake disasters over 100 years (Fig. 17.36). This method is simple and easy to be used. Its shortcoming may be that deformation of the body of a fill cannot be calculated.



**Fig. 25.82** Empirical relationship between  $F_L$  and development of excess pore water pressure



**Fig. 25.83** Static slope stability analysis to obtain factor of safety by using circular slip plane

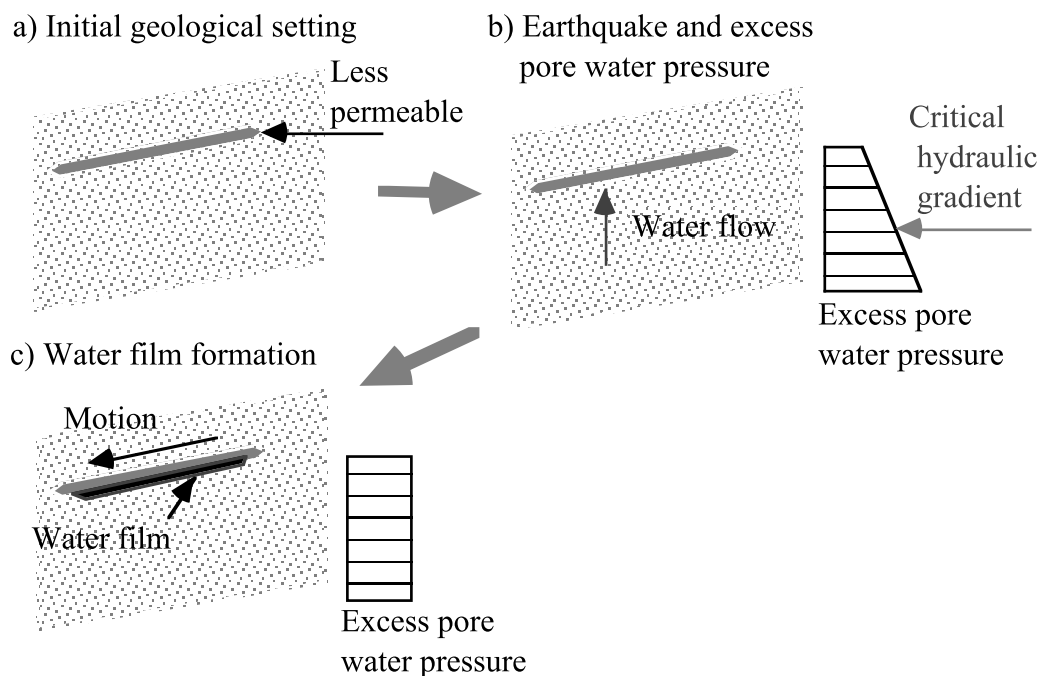


**Fig. 25.84** Empirical relationship between static factor of safety and ratio of subsidence

## 25.26 Water Film

Studies on mechanism of large deformation caused by liquefaction have been conducted from the viewpoint of softening in stress–strain behavior. A different idea, in contrast, pays attention to silty or clayey seams embedded in loose sandy deposits. According to recent ideas by Kokusho (1999 and 2000), the procedure occurs in the following manner.

1. There is a continuous thin layer of less pervious soils within a liquefiable sandy slope. The direction of the thin layer is approximately parallel to the slope direction (Fig. 25.85a).
2. Upon strong shaking, the underlying sandy soil develops high excess pore water pressure and the stress–strain behavior becomes soft (Fig. 25.85b). This situation, however, does not lead to large displacement because of the shear strength (steady-state strength in Sect. 24.3).
3. Pore water starts to migrate in accordance with the vertical hydraulic gradient (consolidation of sand). This stage takes some time. Since the thin layer has lower permeability, water cannot migrate immediately across it and stays beneath it. Thus, a thin film of water is formed (Fig. 25.85c).
4. Since the water film has no shear strength, the overlying layer moves downward significantly.
5. The excess pore water pressure dissipates later during or after large ground deformation.



**Fig. 25.85** Role in large ground deformation played by thin layer of less pervious soil

Since the water-film mechanism of large ground deformation is associated with consolidation process, ground motion starts some time after the end of strong shaking. Moreover, the void ratio changes in the subsoil; void ratio increases in the upper portion, and decreases in the lower part, which is called void redistribution.

The formation of water film was reported by centrifuge tests conducted by Arulanandan et al. (1988). It was described that water film or very loose sand (void redistribution) made easy the translation of upper soils. Fiegel and Kutter (1994) reported the displacement of ground caused by water film. In their tests, however, lateral ground displacement ceased at the end of shaking. Water film mechanism was reported by Boulanger and Truman (1996) as well.

The water-film approach is good because it can account for the delayed initiation of ground deformation. For example, Baranoha dam in Chile (1928) failed a few minutes after strong shaking, following some burst sound in the downstream slope of the dam body (Agüero, 1929; Dobry and Alvarez, 1967).

Moreover, Seed et al. (1975) suggested on the basis of the record of a seismoscope that the deformation of dam had occurred probably after the major part of earthquake motion. Kokusho and Fujita (2002) excavated the left bank area of Niigata City where substantial lateral displacement occurred in 1964. They found a continuous thin layer of clayey soils within liquefiable sandy deposits.

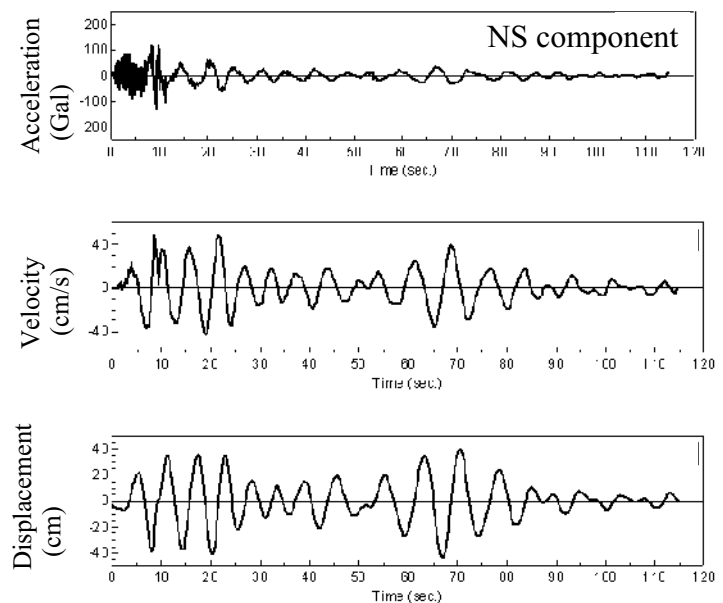
Horii and Miyahara (1966) together with Horii (1968) collected eyewitness reports to show that the Showa Bridge in Niigata City and revetment walls (Fig. 17.1) along the Shinano River collapsed after the strong shaking. It is, however, true that real earthquake shaking continues even after the phase of strong acceleration. For example, Zeghal and Elgamal (1994) integrated the vertical-array acceleration records to obtain the insitu displacement and stress–strain time histories. It was shown by them that large displacement amplitude continued even after strong acceleration was terminated because of subsoil liquefaction.

On the contrary, Yoshida (2005) integrated the acceleration records at the basement of Kawagishi-cho apartment building (Fig. 17.7) where significant liquefaction occurred during the 1964 Niigata earthquake. The original acceleration record was the one that was interpreted by Kudo et al. (2000) over the entire duration of shaking. The integration was conducted by FFT (Fast Fourier Transformation, Sect. 9.12) and its analytical integration. The results in Fig. 25.86 demonstrate that strong velocity and displacement continued for a longer time than acceleration. It is hence possible that many liquefaction damages were caused by significant velocity and/or displacement amplitudes. Yoshida et al. (2007) conducted very detailed studies on the falling of Showa Bridge in Niigata, 1964, including direct interview to eyewitnesses who were on the bridge at the time of the earthquake. It was concluded that the bridge fell down after strong acceleration but while displacement shaking was still going on.

One question addressing the water-film approach is whether or not there is a thin clayey layer in an artificial land reclamation. For example, Port Island of Kobe was constructed by using weathered granite whose grain size was that of sand or even coarser. It seems, therefore, that the water film is an important mechanism of ground deformation but is not the only one. This situation is similar to landslides that are caused by such many different mechanisms as rain fall, earthquake, human excavation, etc. For calculation of displacement, the water-film approach needs to develop a methodology by which the location and size of thin impervious layers are identified.

### List of References in Chapter 25

- Agüero, G. (1929) Formación de depósitos de relaves en el mineral del Teniente, Anales del Instituto de Ingenieros de Chile.
- Alam, M.J., Towhata, I., Honda, T. and Fukui, S. (2004a) Mechanism of liquefaction process under embankment without and with a mitigation measure studied by dynamic centrifuge testing, Proc. South East Asian Geotech.Conf., Bangkok, pp. 905–910.
- Alam, M.J., Fukui, S., Towhata, I., Honda, T., Tamate, S., Tanaka, T., Uchiyama, J. and Yasuda, S. (2004b) Centrifuge model tests on mitigation effects of underground walls on liquefaction-induced



**Fig. 25.86** Time history of Kawagishi-cho motion (Yoshida, 2005)

- subsidence of embankment, Proc. 11th Int. Conf Soil Dyn. Earthq. Eng. and the 3rd Int. Conf. Earthq. Geotech. Eng., Berkeley, Vol. 2, pp. 537–544.
- Alam, M.J., Honda, T., Towhata, T., Tamate, S., Fukui, S., Yasuda, S. and Tanaka, T. (2004c) Behavior of liquefaction mitigative measures of foundation soil under earth embankment, Proc. IS-Osaka, Eng. Practice Perform. Soft Deposits, pp. 343–348.
- Arulanandan, K., Yogachandran, C., Muraleetharan, K.K., Kutter, B.L. and Chang, G.S. (1988) Seismically induced flow slide on centrifuge, Journal of Geotechnical Engineering ASCE, Vol. 114, No. 12, pp. 1442–1449.
- Berrill, J.B., Christensen, S.A., Keenan, R.P., Okada, W. and Pettinga, J.R. (2001) Case study of lateral spreading forces on a piled foundation, Geotech., Vol. 51, No. 6, pp. 501–517.
- Boulanger, R.W. and Truman, S.P. (1996) Void redistribution in sand under post-earthquake loading, Can. Geotech. J., Vol. 33, pp. 829–834.
- Dobry, R. and Alvarez, L. (1967) Seismic failures of Chilean tailings dams, Proc. ASCE, Vol. 93, SM6, pp. 237–260.
- Egashira, S. and Miyamoto, K. (2000) Mechanism of debris flow, Tsuchi-to-Kiso, Monthly Magazine of Jpn. Geotech. Soc., Vol. 48, No. 8, pp. 46–52 (in Japanese).
- Egashira, S., Miyamoto, K. and Ito, T. (1997) Bed-load rate in view of two phase flow dynamics, Ann. J. Hydraulic Eng., JSCE, Vol. 41, pp. 789–794 (in Japanese).
- Fiegel, G.L. and Kutter, B.L. (1994) Liquefaction-induced lateral spreading of mildly sloping ground, J. Geotech. Eng., ASCE, Vol. 120, No. 12, pp. 2236–2243.
- Gallage, C.P.K., Towhata, I. and Nishimura, S. (2005) Laboratory investigation on rate-dependent properties of sand undergoing low confining effective stress, Soils Found., Vol. 45, No. 4, pp. 43–60.
- Hamada, M. (1992) Large ground deformations and their effects on lifelines; 1964 Niigata earthquakes, NCEER-92-0001: Case studies of liquefaction and lifeline performance during past earthquakes, pp. 3-1–3-123.
- Hamada, M. (2005) An experimental study on fluid properties for liquefied sand during its flow, Proc. JSCE, Vol. 792/III-71, pp. 13–25 (in Japanese).
- Hamada, M., Yasuda, S., Isoyama, R. and Emoto, K. (1986) Observation of permanent displacements induced by soil liquefaction, Proc. JSCE 376/III-6, pp. 211–220 (in Japanese).
- Horii, K. (1968) chapter on "Highway Bridges," General Report on the Niigata Earthquake, ed. H. Kawasumi, Tokyo Electrical Engineering College Press (present name is Tokyo Denki University Press), pp. 431–450.
- Horii, K. and Miyahara, F. (1966) Bridges spanning over the lower course of the River Shinano, Bull Science and Engineering Research Laboratory, Vol. 34 (special issue on Niigata earthquake), Waseda University.
- Housner, G.W. (1965) Intensity of earthquake ground shaking near the causative fault, Proc. 3rd World Conf. Earthq. Eng., New Zealand, Vol. 1, pp. III-94–III-115.
- JGS (Japanese Geotechnical Society) (1999 and 2004) Air photographs of the Niigata city immediately after the earthquake in 1964, ISBN4-88644-054-1.
- Keenan, R.P. (1996) Foundation loads due to lateral spreading at the landing road bridge, Whakatane, Research Report 96/10, Department of Civil Engineering, University of Canterbury.
- Kobayashi, Y. (2001) Numerical method for three-dimensional prediction of lateral flow in liquefied subsoil, Ph.D. Thesis, Department of Civil Eng., University of Tokyo.
- Kokusho, T. (1999) Water film in liquefied sand and its effect on lateral spread, J. Geotech. Geoenv. Eng., ASCE, Vol. 125, No. 10, pp. 817–826.
- Kokusho, T. (2000) Mechanism of water film generation and lateral flow in liquefied sand layer. Soils Found., Vol. 40, No. 5, pp. 99–111.
- Kokusho, T. and Fujita, K. (2002) Site investigation for involvement of water films in lateral flow in liquefied ground, J. Geotech. Geoenv. Eng., ASCE, Vol. 128, No. 11, pp. 917–925.

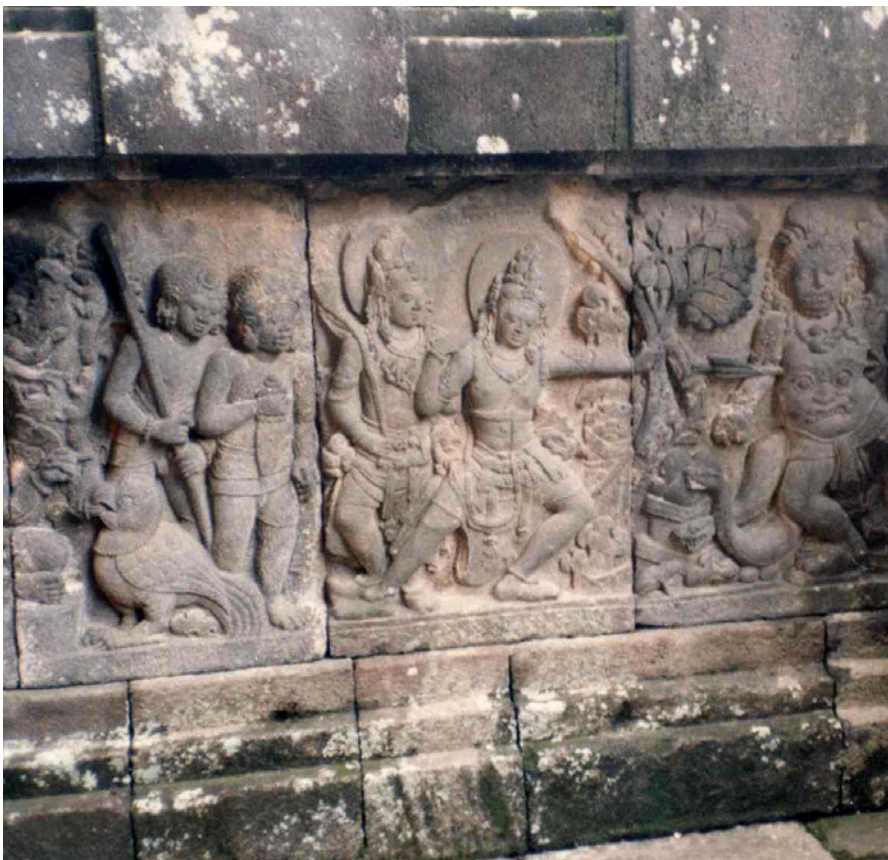
- Kudo, K., Uetake, T. and Kanno, T. (2000) Re-evaluation of nonlinear site response during the 1964 Niigata earthquake, using the strong motion records at Kawagishi-cho, Niigata City, Proc. 12th World Conf. Earthq. Eng., Auckland, New Zealand, Paper No. 0969.
- Kuwano, J. and Ishihara, K. (1988) Analysis of permanent deformation of earth dams due to earthquakes, Soils Found., Vol. 28, No. 1, pp. 41–55.
- Lamb, H. (1911) On the uniform motion of a sphere through a viscous fluid, Phil. Mag. J. Sci., Vol. 21, No. 121, pp. 112–121.
- Lee, K.L. (1974) Seismic permanent deformations in earth dams, Report to NSF, Project GI38521.
- Lee, K.L. and Chan, K. (1972) Number of equivalent significant cycles in strong motion earthquakes, Proc. Int. Conf. Microzonation for Safer Construction Research and Application, Seattle, pp. 609–627.
- Miyajima, M., Hasegawa, M., Kitaura, M., Koike, T. and Kitano, Y. (1994) Experimental study on effects of liquefaction-induced lateral spreading on buried structures, Proc. 9th Japan Earthq. Eng. Symp., Vol. 2, pp. 1363–1368.
- Miyajima, M., Kitaura, M. and Kitano, Y. (1994) Model tests on variation of soil properties with the extent of liquefaction, Proc. Annual Conf. JSCE, III, pp. 548–549.
- Miyajima, M., Kitaura, M., Koike, T. and Hasegawa, M. (1995) Experimental study on characteristics of liquefied ground flow, Proc. IS-Tokyo '95 First Int. Conf. Earthq. Geotech. Eng., Balkema, pp. 969–974.
- Mizutani, T., Towhata, I., Shinkawa, N., Ibi, S., Komatsu, T. and Nagai, T. (2001) Shaking table tests on mitigation of liquefaction-induced subsidence of river dikes, Proc. 16th ICSMGE, Istanbul, Vol. 2, pp. 1207–1210.
- Ngo, Anh Tuan (2007) Shaking table model tests on interaction between lateral flow of liquefied subsoil and embedded structure 振動台模型実験による液状化地盤の側方流動と埋設構造物との相互作用の研究, Bachelor thesis, University of Tokyo (in Japanese).
- Nishimura, S., Honda, T. and Towhata, I. (2001) Torsion shear tests on rate-dependent behavior of liquefied sand, 10th Int. Conf. Soil Dynam. Earthq. Eng., Philadelphia.
- Nishimura, S., Towhata, I. and Honda, T. (2002) Laboratory shear tests on viscous nature of liquefied sand, Soils Found., Vol. 42, No. 4, pp. 89–98.
- Ohtomo, K. (1998) Load characteristics of ground lateral flow on in-ground structures, Proc. JSCE, 591/I-43, pp. 283–297.
- Ohtomo, K., Iwadate, T., Shimizu, M., Shumuta, Y. and Hamada, M. (1993) Horizontal load exerted on pile foundation by lateral flow of liquefied sand, Proc. 22nd Earthq. Eng. Conf. of JSCE, pp. 95–98.
- Okamoto, T. (2001) Recent measurements of residual settlement of rockfill dams induced by earthquakes and some consideration of their influenced effects, 46th Geotechnical Engineering Symposium, Jpn. Geotech. Soc., pp. 65–70 (in Japanese).
- Okamura, M., Abdoun, T.H., Dobry, R., Sharp, M.K. and Taboada, V.M. (2001) Effects of sand permeability and weak aftershocks on earthquake-induced lateral spreading, Soils Found., Vol. 41, No. 6, pp. 63–77.
- Orense, R.P. and Towhata, I. (1998) Three dimensional analysis on lateral displacement of liquefied subsoil, Soils Found., Vol. 38, No. 4, pp. 1–15.
- Sasaki, Y., Udaka, K. and Miyamoto, Y. (1997) Prediction of subsidence of embankment resting on liquefied subsoil with consideration on duration of high pore pressure, Proc. Tech. Conf., Chugoku Chapter of JSCE.
- Sato, H., Doi, M., Ohbo, N., Honda, M. and Hamada, M. (1994) Dynamic centrifugal tests on lateral flow of sandy ground, Proc. 49th Ann. Conf. JSCE, 3A, pp. 520–521.
- Sato, H., Hamada, M. and Doi, M. (1994) An experimental study of effects of laterally flowing ground on in-ground structures, Proc. 5th Japan-US Workshop on Earthquake Resistant Design of Lifeline Facilities and Countermeasures against Soil Liquefaction, NCEER-94-0026, pp. 405–414.
- Seed, H.B., Lee, K.L., Idriss, I.M. and Makdisi, F. (1975) The slides in the San Fernando Dams during the earthquake of February 9, 1971, J. Geotech. Eng. Div., ASCE, Vol. 101, GT7, pp. 651–688.



- Shi, L.P., Towhata, I. and Wieland, M. (1989) Prediction of seismically induced deformation of Liyutan Dam, Taiwan, by means of cyclic triaxial testing and finite element analysis, *Computers and Geotechnics*, Vol. 7, No. 3, 205–222.
- Shultze, E. and Menzenbach, E. (1961) Standard penetration test and compressibility of soils, *Proc. 5th Int. Conf. Soil Mech. Found. Eng.*, Vol. 1, pp. 527–532.
- Takada, S. and Nagai, J. (1987) Dynamic stiffness and damping in liquefied ground, *The Construction Engineering Research Institute Foundation*, Rep. 29, pp. 53–98.
- Towhata, I. and Horikoshi, K. (1997) Analysis on subsidence of building resting on liquefied sandy ground, *Proc. 32nd Ann. Conv., Jpn. Geotech. Soc.*, 1997, Vol. 1, pp. 973–974.
- Towhata, I., Orense, R.P., Toyota, H. (1999) Mathematical principles in prediction of lateral ground displacement induced by seismic liquefaction, *Soils Found.*, Vol. 39, No. 2, pp. 1–19.
- Towhata, I., Sasaki, Y., Tokida, K., Matsumoto, H., Tamari, Y. and Yamada, K. (1992) Prediction of permanent displacement of liquefied ground by means of minimum energy principle, *Soils Found.*, Vol. 32, No. 3, pp. 97–116.
- Towhata, I., Vargas-Monge, W., Orense, R.P. and Yao, M. (1999) Shaking table tests on subgrade reaction of pipe embedded in sandy liquefied subsoil, *Soil Dynam. Earthq. Eng. J.*, Vol. 18, No. 5, pp. 347–361.
- Toyota, H. (1995) Shaking table tests and analytical prediction on lateral flow of liquefied ground, *Doctoral thesis, the University of Tokyo*, p. 380.
- Wakamatsu, K., Hamada, M., Yasuda, S. and Morimoto, I. (1989) Liquefaction induced ground displacement during the 1923 Kanto earthquake, *Proc. 2nd US-Japan Workshop on Liquefaction, Large Ground Deformation, and Their Effects on Lifelines*, Buffalo, pp. 36–49.
- Yasuda, S., Ishihara, K., Harada, K. and Nomura, H. (1997) Factors which affected the area of lateral flow that occurred in the ground behind quaywalls, *Proc. 2nd Conf. on Earthquake disasters in Hanshin-Awaji area, JSCE*, pp. 113–120 (in Japanese).
- Yasuda, S., Nagase, H., Kiku, H. and Uchida, Y. (1992) The mechanism and a simplified procedure for the analysis of permanent ground displacement due to liquefaction, *Soils Found.*, Vol. 32, No. 1, pp. 149–160.
- Yasuda, S., Yoshida, N., Adachi, K., Kiku, H., Gose, S. and Masuda, T. (1999) A simplified practical method for evaluating liquefaction-induced flow, *Proc. JSCE*, Vol. 638/III-49, pp. 71–89 (in Japanese).
- Yoshida, N. (2005) Time history of velocity and displacement in Kawagishi-cho apartment building site during 1964 Niigata earthquake and liquefaction, personal communication.
- Yoshida, N. and Hamada, M. (1991) Damage to foundation piles and deformation pattern of ground due to liquefaction-induced permanent ground deformation, *Proc. 3rd Japan-U.S. Workshop on Earthquake Resistant Design of Lifeline Facilities and Countermeasures for Soil Liquefaction (NCEER-91-0001)*, pp. 147–161.
- Yoshida, N., Tazo, T., Wakamatsu, K., Yasuda, S., Towhata, I., Nakazawa, H. and Kiku, H. (2007) Causes of Showa Bridge collapse in the 1964 Niigata Earthquake based on eyewitness testimony, *Soils Found.*, Vol. 47, No. 6, pp. 1075–1087.
- Yuasa, A., Sato, H., Doi, T., Kawakami, T. and Hamada, M. (1994) An experimental study on fluid properties of liquefied sand, *Proc. 9th Japan Earthq. Eng. Symp.*, 1994, 1, pp. 877–882.
- Zeghal, M. and Elgamal, A.-W. (1994) Analysis of site liquefaction using earthquake records, *J. Geotech. Eng., ASCE*, Vol. 120, DT6, pp. 996–1017.

# Chapter 26

## Mitigation of Liquefaction-Induced Damage

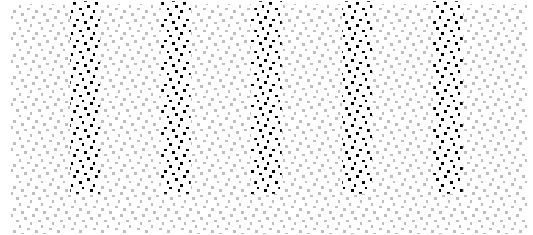


Borobudur was constructed as a Buddhism stupa in Java, Indonesia. After Islam came to the island, it was buried under earth until it was discovered once more in the recent times. This monument is decorated by elaborate Buddhism sculptures.

## 26.1 Principles in Mitigation of Liquefaction-Induced Damage

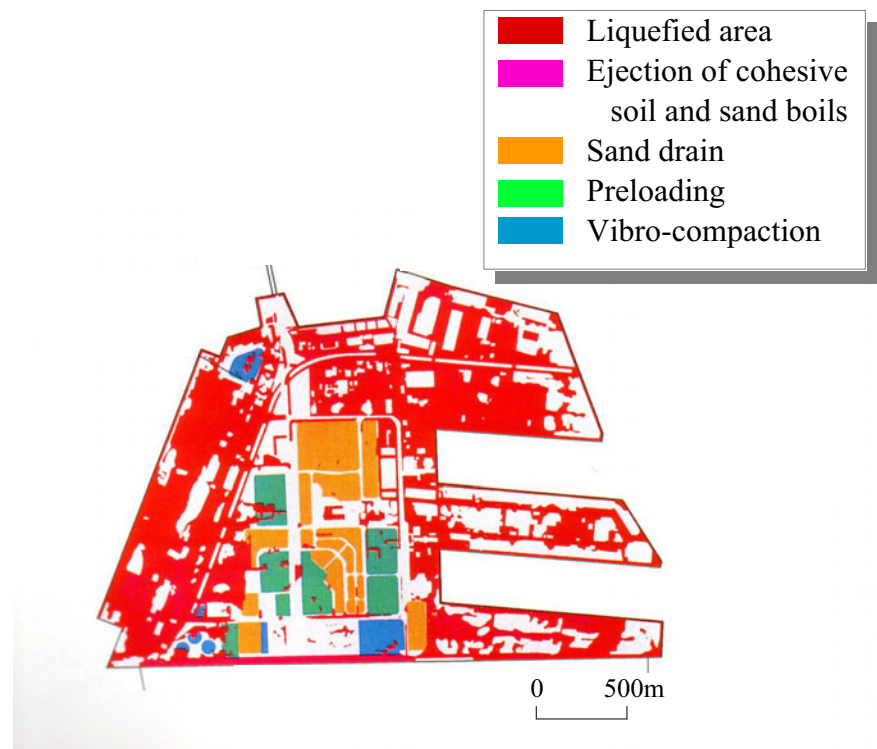
The traditional aim of mitigation of liquefaction-induced damages has been to prevent the 100% development of excess pore water pressure. When the factor of safety against liquefaction ( $F_L$ ) in the field is less than 1.0, several types of measures have been taken.

1. *Densification of liquefaction-prone sand.* Otherwise called compaction, densification of sand is the most fundamental type of mitigation. Since dense sand does not develop high excess pore water pressure as loose sand does and since dense sand does not deform so easily as loose sand (Sect. 18.7), densification by means of vibration has been carried out widely.



**Fig. 26.1** Loose sandy ground compacted by sand columns

Figure 26.1 illustrates a loose sandy deposit densified by installation of columns of dense sand. The original loose sand is made denser by (a) pushing extra volume of sand columns into loose subsoil, and (b) associating vibration. Consequently, the original sand is pushed outward in the lateral direction upon installation of sand columns. Figure 26.2 indicates that liquefaction did not occur in areas of the Port Island in Kobe where such densification as sand drains (limited densification upon installation), preloading (minor effects), and vibratory compaction were conducted. This is consistent with Figs. 22.4 and 22.5 which showed that different extent of soil densification achieved different extents of mitigation of subsidence. More details will be presented in Sect. 26.4.



**Fig. 26.2** Liquefied sites in Port Island (JGS, 1996)

2. *Gravel drains.* See Sect. 26.11 for more details. Briefly, columns of gravels are placed in holes that are drilled in liquefiable subsoil. Since this procedure does not cause lateral displacement of original soil, neither compaction of original soil nor damage in foundation of an adjacent structure occurs. The main aim of the gravel columns is the quick dissipation of excess pore water pressure by shortening the path of drainage from a vertical one toward the ground surface to a horizontal one to nearby gravel columns, thus keeping the development of excess pore water pressure less than 100% throughout an earthquake shaking. Even in the worst situation, the dangerous state of 100% excess pore water pressure is terminated quickly, and the subsoil cannot deform significantly. Since this measure does not prevent pore pressure rise, the dissipation of pore pressure results in consolidation settlement of loose sandy layers. In 1993, Kushiro Harbor with gravel piles avoided a large distortion, although minor settlement of 10 cm or so occurred (Fig. 26.89).

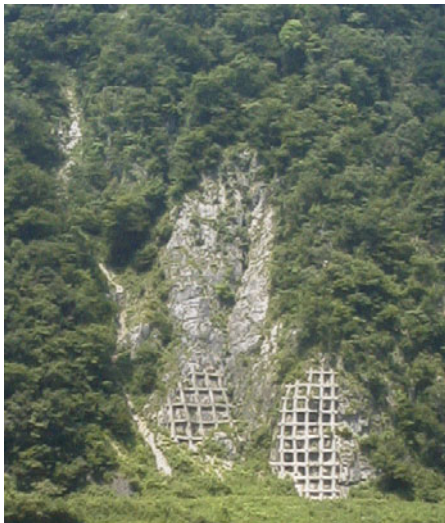
3. *Grouting and deep mixing.* These measures develop cohesion in sandy soils and prevent large shear strain. Hence, excess pore water pressure does not rise. Apparently, a large deformation is avoided. Details will be given after Sect. 26.13.

4. *Structural measures.* When a shallow foundation rests on a liquefiable layer, it should be replaced by such a deep foundation as piles. Care must be taken of the effects of lateral soil displacement which may occur in a sloping liquefied ground or ground behind a quay wall. This displacement exerts strong horizontal force on a pile foundation.



**Fig. 26.3** Minor distortion in Tokachi-river dike in 2004 caused by minor liquefaction

Since 1990s, the limitation of the above approach has been understood. For example, embedded pipelines are subjected to liquefaction-induced ground distortion (Fig. 17.24). Since the network area of the pipeline is so vast, it is financially impossible for a lifeline industry to improve the subsoil conditions completely. Moreover, the land is not owned by the industry, and the industry is not allowed to change the subsoil properties freely. Another example is a river dike in which liquefaction-induced deformation is allowed if its extent is minor (Fig. 26.3); quick restoration is more important (Sect. 14.5). This idea was called the performance-based design in Sect. 14.5.



**Fig. 26.4** Stabilization of unstable slope by reinforcement



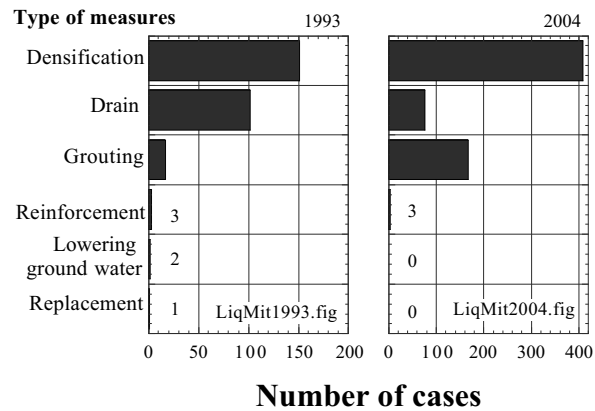
**Fig. 26.5** Dams of debris in river channel

A hint for strategy in mitigation of liquefaction-induced damage is found in erosion control (*sabo* 砂防) technology. In that field, a disaster is caused by debris which is produced in mountain slopes and is transported by river water upon flooding. Hence, the disaster-mitigation strategy consists of three stages which are (1) the mitigation at source (stabilization of mountain slopes; Fig. 26.4), (2) the mitigation on path (stopping of debris flow in river channel by construction of dams, Fig. 26.5), and (3) emergency action such as warning and evacuation if flooding is imminent. A debris dam is sometimes as large as the one in Fig. 26.6. Note that the second and the third mitigations allow the onset of slope failure but do not allow negative effects to human habitation.

Prevention of liquefaction as mentioned earlier is the mitigation at the source. The reduction of liquefaction-induced displacement and the emergency actions that were presented in Sect. 22 belong to the second and the third categories.



**Fig. 26.6** Debris dam near Medeo of Almaty in Kazakhstan (150 m high and 530 m long)



**Fig. 26.7** Histogram of liquefaction mitigation measures in construction practice

The Japanese Geotechnical Society studied the number of practices of liquefaction mitigation measures twice in 1993 and 2004 (JSSMFE 1993, and JGS 2004a). The results in Fig. 26.7 illustrates that densification has been the most popular measure, while the importance of drain decreased and grouting has become more important during the 10-year period. This situation may be related with the 1995 Kobe earthquake after which the preparedness against an extremely strong earthquake (Level 2 quake which may occur once every hundreds of years) has been in practice. It is therein feared that drains may not prevent liquefaction during such a very strong earthquake. It is, however, necessary to reevaluate gravel drains from the viewpoint of seismic performance, because gravel columns maintain rigidity during Level 2 shaking and would contribute to mitigation of ground distortion: this point is not considered in the current design framework. Although Fig. 26.7 implies that reinforcement (underground walls etc.), lowering of ground water, and replacement (with better materials) have decreased, this trend may change if any good measure is developed.

**26.2 Principles in Prevention of Liquefaction**

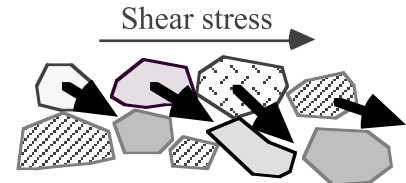
Section 18.1 described the basic mechanism of liquefaction. Fig. 26.8 illustrates that sand particles of loose density fall into big voids when subjected to shear (negative dilatancy). Since such a volume change cannot take place quickly in the real ground, void ratio of water-saturated sand is kept more or less unchanged and, consequently, the effective stress decreases; see “ $e$  vs.  $P'$ ” diagram (Sect. 1.4) in Fig. 26.9. It is seen in Fig 26.9 that the greater potential in volume contraction because of negative dilatancy induces more significant reduction in effective stress: leading to complete loss of effective stress in the extreme case.

This speculation suggests the following hints to practical soil improvement for preventing onset of liquefaction (prevention of high excess pore water pressure).

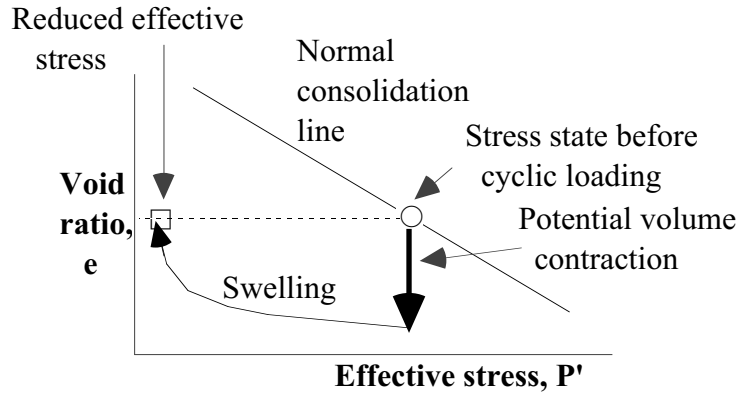
1. Do not allow sand grains to move during shear. Bonding of grains such as grouting (薬液注入) is developed.
2. Do not leave big voids among sand grains. Densification or compaction makes void size smaller.
3. Avoid the undrained conditions and allow pore water to be drained out of ground as quickly as possible. Gravel drains and other kinds of quick drainage are useful.
4. Reduce the degree of saturation so that pore air can be compressed, volume change is allowed, and swelling is not so substantial as shown in Fig. 26.9. Dewatering is the practical solution.

It should be borne in mind further that loss of effective stress as explained above is one of the mechanisms of ground failure during earthquakes. Therefore, loose sandy ground can also fail due to shear when effective stress is still positive. Partial reduction of effective stress leads to insufficient shear strength to maintain stability. Substantial distortion of quay walls in Sect 24.10 is an example.

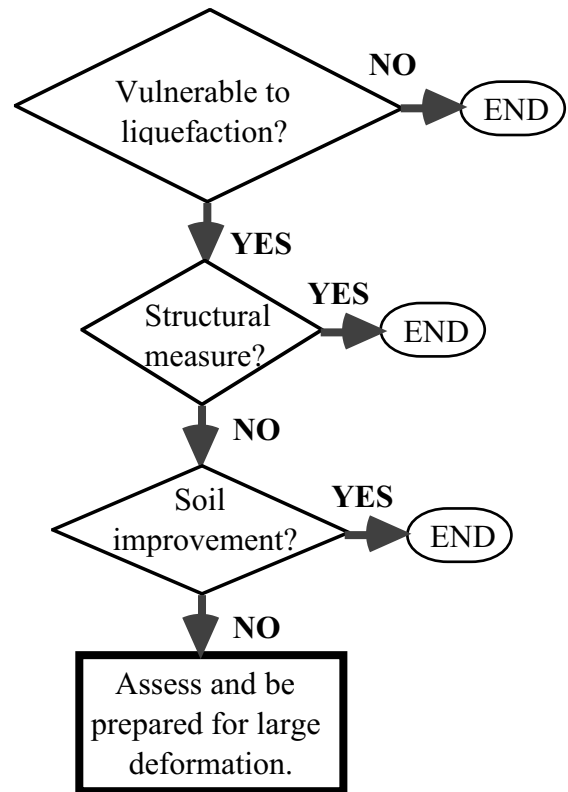
In case soil is not reliable after any kind of improvement, structural measures such as reinforcement of pile foundation are the solution. Recent ideas, however, focus on reduction of residual deformation of liquefied subsoil so that the function of concerned facilities is preserved or restored quickly (allowable displacement in Sect. 14.5). This approach allows onset of liquefaction during earthquakes but it tries to avoid negative effects to human society (Fig. 26.10).



**Fig. 26.8** Negative dilatancy of loose packing of sand grains



**Fig. 26.9** Decreased effective stress due to undrained condition



**Fig. 26.10** Flow of planning mitigation against liquefaction

### 26.3 Mitigation of Liquefaction-Induced Ground Displacement

Such linear structures 線状構造物 as lifelines, river dikes, and others are too long for economical practice of soil densification and other prevention of excess pore water pressure development which were discussed in Sect. 26.1. Those structures can, on the contrary, maintain their operation even when minor deformation occurs upon liquefaction. For this reason, mitigation (not prevention) of ground deformation/displacement in the lateral direction has been investigated.

Underground wall is a promising mitigation of liquefaction-induced damage in embankment and river dike. Its use is supported by experiences during earthquakes. Figure 26.11 shows a building near a damaged quay wall in Kobe. When the basement of this building was excavated upon construction, it was surrounded by a temporary retaining wall. After the completion of the building, the retaining wall remained in soil. When an earthquake hit the area in 1995, a quay wall in front of the building distorted significantly, but the building was protected from the ground movement by the embedded retaining wall.



**Fig. 26.11** Shimagami pumping station behind quay wall in Kobe (photograph by Prof. J. Koseki)

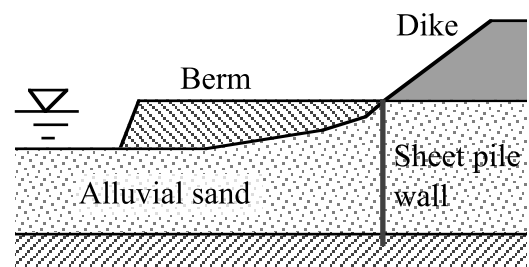


**Fig. 26.12** Undamaged dike of Yodo River at Takami site in Osaka (supplied by MLIT, Government of Japan)

It appears, therefore, that retaining walls for excavation should remain embedded after the end of construction and should be utilized as a mitigation against ground movement. This idea, however, encounters a practical difficulty because the current Japanese design regulation does not allow such a temporary wall to be considered as a permanent safety measure. Hence, the temporary wall which remains underground is supposed to be an extra safety measure that is not taken into account in a design analysis. As a consequence, budget is needed for installation of other permanent safety measure which is actually not very necessary.

A second example is found in Fig. 26.12 in which a dike of Yodo River was not damaged at Takami site during the 1995 Kobe earthquake. This good performance is in a clear contrast with the substantial damage in the Torishima site of the same river (Fig. 17.35). Probably there were three important issues that contributed to the good consequence of the Takami dike (Fig. 26.13):

1. More aged and less liquefiable alluvial soil
2. Existence of berm as a counter weight on the river side
3. Sheet pile walls which were located beneath the foot of the dike and reached the bottom of alluvial sandy deposits

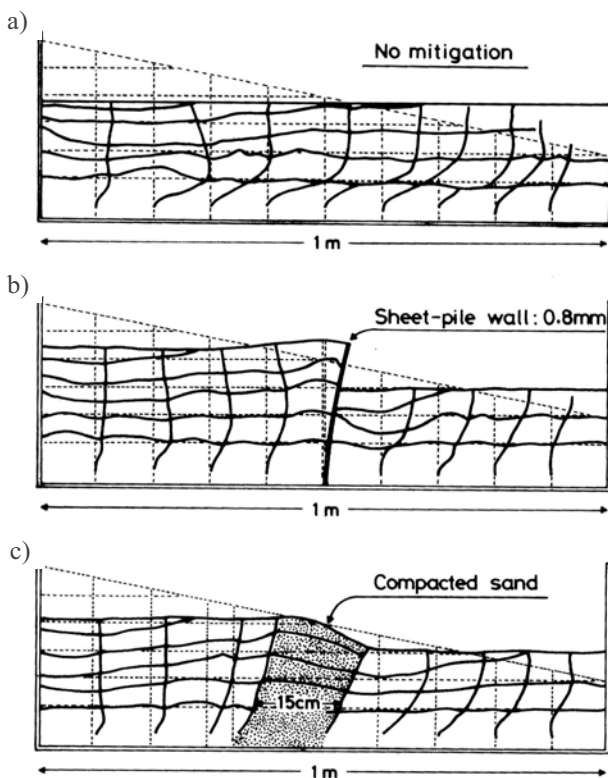


**Fig. 26.13** Three features that helped Takami river dike from liquefaction problem

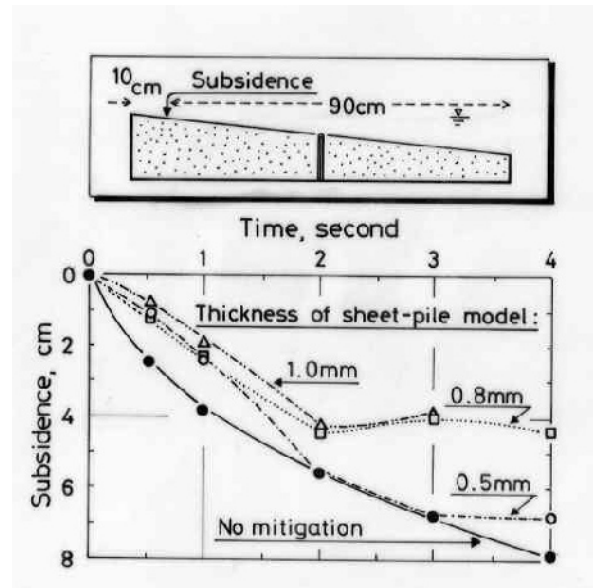
Probably there were three important issues that contributed to the good consequence of the Takami dike (Fig. 26.13):

Sheet pile walls in the Takami site prevented the lateral displacement of liquefiable subsoil. In contrast, they reached only an intermediate depth at the damaged Torishima site. At both sites, the wall was intended to prevent seepage flow of river water at the time of flooding and high water level; not being a seismic reinforcement. Most probably the wall unintentionally helped the dike at Takami site.

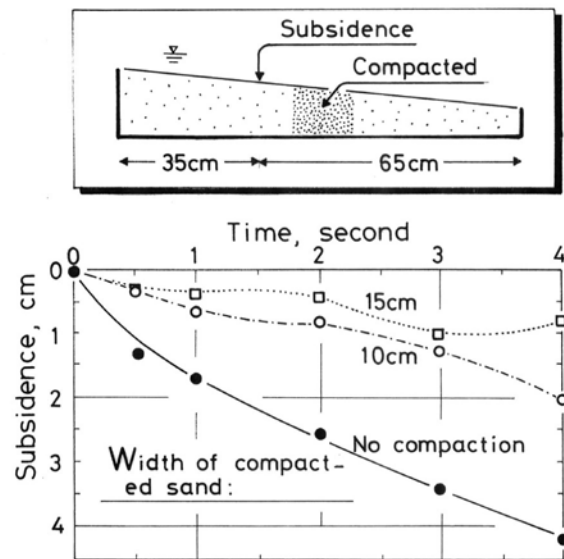
The mitigative effects of sheet pile walls have been studied by shaking models (Towhata, 2005). The first series of tests concerned liquefied slope. Fig. 26.14 presents results of small 1-G tests (Kogai et al. 2000; Towhata et al. 2000). The first model slope had no mitigation. After a sufficiently long time of shaking, the slope became completely level and the displacement ceased (Fig. 26.14a). The second and third models were reinforced by a sheet-pile wall and a compacted sand wall, respectively. It is seen in Figs. 26.14a-c that these walls behaved similar to a dam and reduced the displacement significantly.



**Fig. 26.14** Shaking table tests on effects of mitigative measures against lateral flow of ground (Kogai et al., 2000)



**Fig. 26.15** Effects of sheet-pile thickness on mitigation of lateral displacement (Kogai et al., 2000)



**Fig. 26.16** Effects of thickness of compacted soil wall on mitigation of lateral displacement (Kogai et al., 2000)

Sheet-pile wall models were made of aluminum plates. The thicker the plates were, the greater the bending stiffness ( $EI$ ) was; accordingly, the more mitigative effects were expected. Figures 26.15 illustrates the ultimate displacement decreasing as the plate became thicker. The thickness of a compacted wall improved the mitigative effects as well (Fig. 26.16). The idea of an underground wall was practiced to protect a bridge foundation by reducing lateral soil displacement (Fig. 26.17).

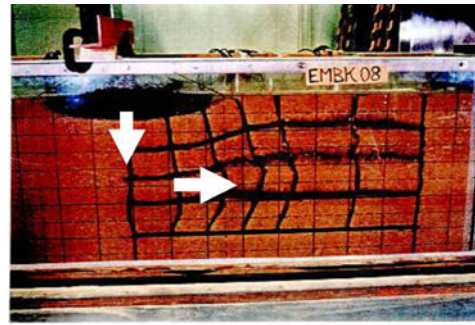
Subsidence of embankment resting on liquefiable subsoil was studied by 1-G model tests (Mizutani and Towhata, 2001; Mizutani et al. 2001). Figures 26.18 shows the distortion of soil under an embankment model. The subsidence of the embankment was accompanied by the lateral soil displacement. In other



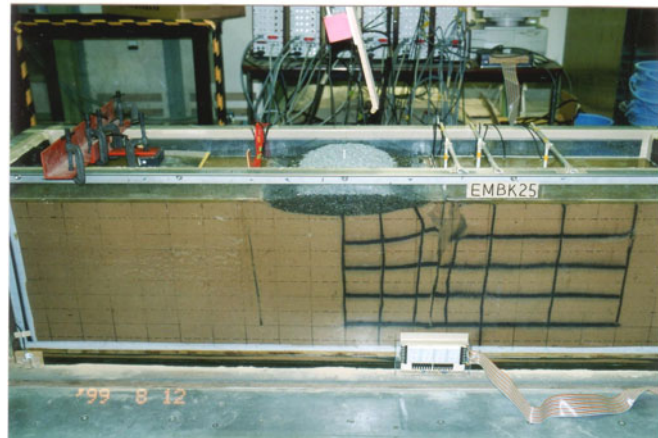
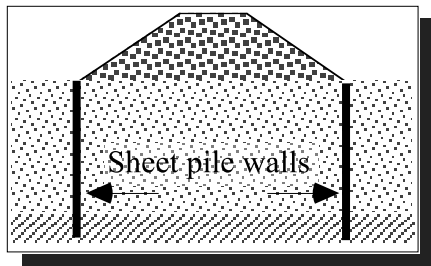
words (volume-flux viewpoint), the vertical compression of subsoil (and subsidence of the overlying embankment) was made possible by lateral movement of subsoil. Accordingly, it was attempted to reduce the subsidence by installing sheet pile walls beside the embankment and preventing lateral soil displacement (Fig. 26.19). As expected, the subsidence became significantly smaller (Fig. 26.20).



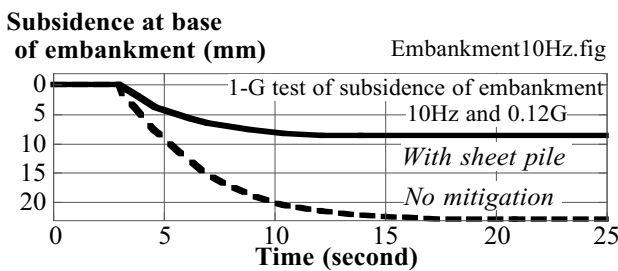
**Fig. 26.17** Installation of steel-pipe wall for protection of bridge foundation from lateral soil movement (Photo by Prof. S. Yasuda)



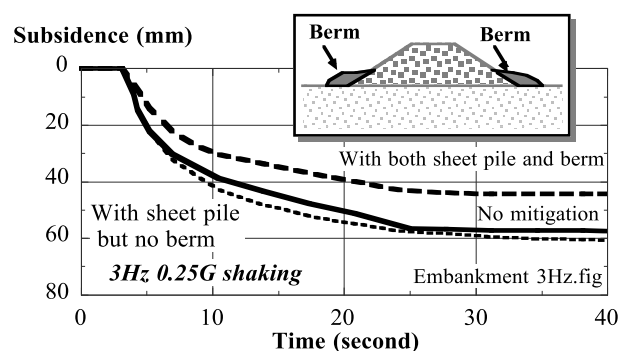
**Fig. 26.18** Distortion of liquefied sand after subsidence of surface embankment (Mizutani et al. 2001)



**Fig. 26.19** Mitigation of subsidence of embankment by sheet pile wall (Mizutani et al. 2001)



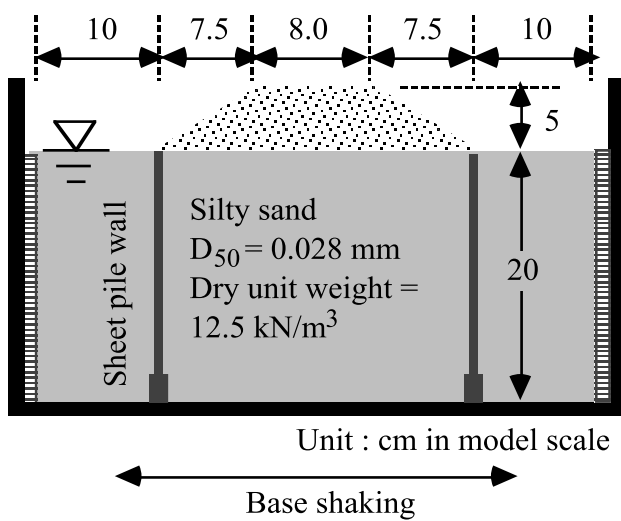
**Fig. 26.20** Mitigation of subsidence of surface embankment by sheet pile walls (Mizutani et al. 2001)



**Fig. 26.21** Subsidence of embankment in tests with lower frequency (Mizutani et al. 2001)

In the tests of Fig. 26.20, shaking was conducted with 10 Hz frequency. Although this value of shaking frequency seems reasonable for 1-G model tests (see similitude of time in Table 24.2), a special attention was paid to what would happen under a lower frequency. Figure 26.21 illustrates test results, which were run under 3 Hz excitation. Two models of “no mitigation” and “with sheet pile but no berm” developed similar subsidence. This unsatisfactory result occurred because sheet pile walls had significant displacement amplitude under the low frequency and a space opened between the wall and the embankment. Liquefied

subsoil was ejected through this space, leading to subsidence. Although it was not clear whether or not the same situation occurs in reality, a special provision was proposed in which soil berms were placed upon the top of the sheet pile walls. The berms were expected to behave as lids that prevent ejection of liquefied subsoil. Figure 26.21 shows that the third test “with both sheet pile and berm” developed less extent of subsidence.



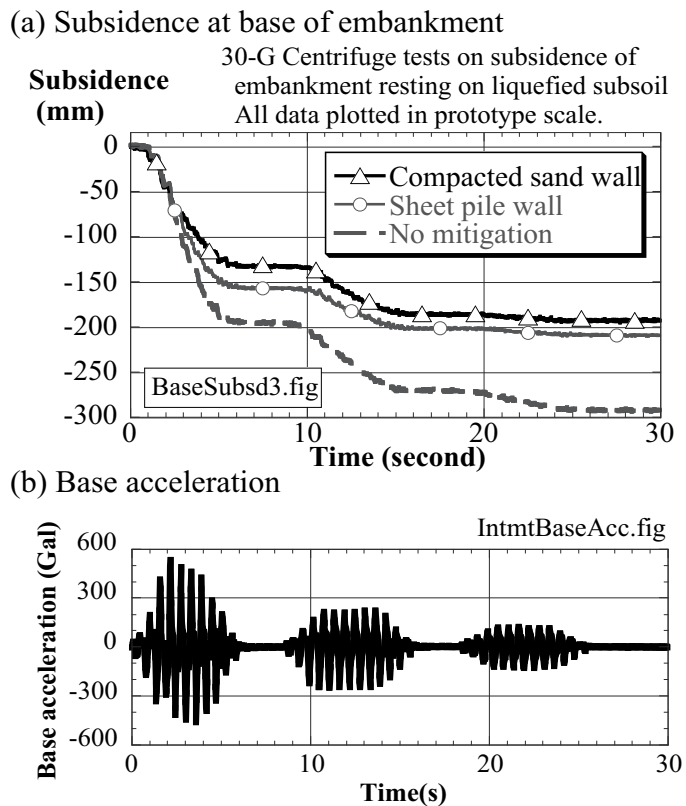
**Fig. 26.22** Configuration of centrifugal model of embankment resting on liquefiable subsoil

The mitigation of subsidence of embankment was studied by centrifugal tests as well (Alam et al. 2004). Figure 26.22 illustrates the configuration of a tested model (same as Fig. 25.64). Tests were run on loose silty sand under 30G centrifugal field. Since this sand had very fine grain size, the permeability of soil was automatically made very low so that the similitude of permeability was satisfied (refer to Table 24.1 and related remarks).

As shown in Fig. 26.23, the base was shaken in three stages, and the subsidence at the bottom of the embankment was recorded. The bottom subsidence was considered more meaningful for study of liquefaction problem than that at the top of the embankment, because the bottom displacement did not include the densification of the embankment. Both compacted sand walls and sheet pile walls reduced the subsidence by approximately 30%.

The next series of study was conducted on liquefaction problems of existing oil storage tanks. The seismic design code of tanks states that safety against liquefaction risk should be improved urgently. Figure 26.24 demonstrates a typical situation. Due to many tanks and pipes, big equipments for sand densification (Fig. 26.62) or gravel drain installation (Fig. 26.86) cannot come in and work. Moreover, industries do not like to remove existing tanks for improvement of the subsoil because their removal and reconstruction mean construction of new tanks and more strict rules for new tanks are applied; tank spacing has to be increased, and greater tank spacing means reduced number of tanks and less efficient business operation. Therefore, the soil under tanks has to be improved without touching the superstructure.

The bottom of a storage tank is made of a thin steel plate (Fig. 26.25). Since this plate is very thin as compared with the size of the tank, it is reasonably considered as a membrane which produces a uniform pressure distribution on the subsoil. Moreover, the bottom plate is subjected to breakage if the foundation



**Fig. 26.23** Effects of underground walls on mitigation of subsidence of embankment (Alam et al. 2004)

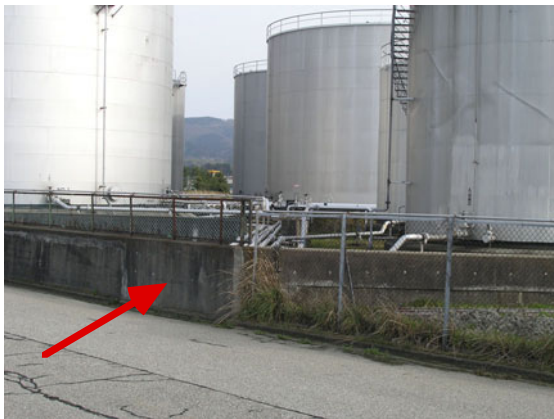
causes differential settlement. Since a consequent leakage of oil from the bottom would cause a fatal environmental pollution, a dike or a wall is constructed around a tank (Fig. 26.26).



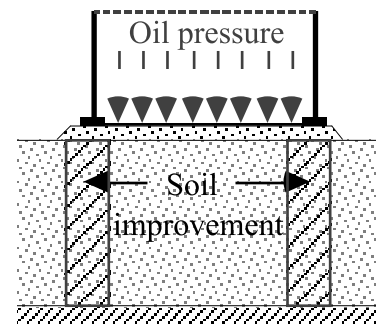
**Fig. 26.24** Narrow space in oil refinery plant



**Fig. 26.25** Bottom plate of a storage tank



**Fig. 26.26** Wall surrounding storage tanks  
(in Nanao Harbor)



**Fig. 26.27** Soil improvement intended  
by colloidal silica injection

Soil improvement without affecting the superstructure is conducted by injecting colloidal silica; see Figs. 26.116 and 26.119. This method of soil improvement does not require a big space for machine operation. Figure 26.27 illustrates the configuration of soil improvement by which the foundation soil is surrounded by a solidified soil wall and protected from lateral displacement. Model tests were conducted to verify this idea.

A construction of a two-dimensional model ground for a tank foundation is depicted in Fig. 26.28 (Isoda, 2002). A block of solidified sand was prepared by injecting colloidal silica into sand and then was placed in a trench excavated in sandy ground. Thereinafter, a tank model was placed upon the surface. The bottom of the tank model was made of a rubber membrane and a uniform pressure distribution was created by placing lead shots in the tank. Fluid was not used in order to avoid sloshing (Sect. 17.15) and its effects on test results. Figure 26.29 shows the time histories of input motion for tank tests.

Tests were run on four kinds of subsoil model; no improvement, 12.5-cm thickness of soil improvement (grouted by colloidal silica), 25-cm thickness, and the overall grouting. The overall grouting was chosen simply for comparison purposes. The interface between liquefiable sand and grouted sand was covered by plastic sheets in order to prevent quick propagation of excess pore water pressure and unrealistic softening of the grouted sand. The subsidence at the bottom of the tank model is plotted in Fig. 26.30. Apparently, the biggest subsidence occurred when no improvement was conducted. The subsidence decreased as the width of grouting increased, and ended with a very small value when subsoil was entirely improved.

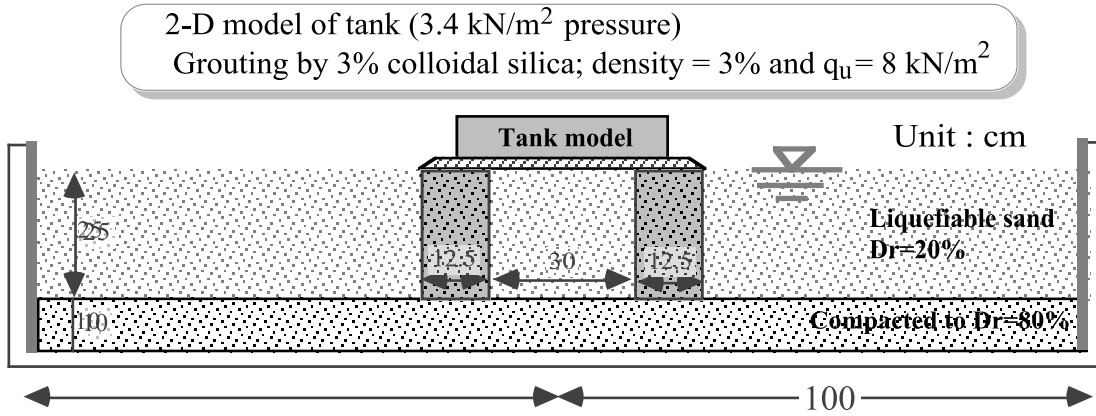


Fig. 26.28 Two-dimensional model of tank and underground wall for 1-G shaking tests

From a practical viewpoint, the damage extent is evaluated in terms of differential subsidence between the tank body and the surrounding free field. The subsidence of the free field is illustrated in Fig. 26.31, and the difference between Figs. 26.30 and 26.31 is presented in Fig. 26.32. In spite of the strong shaking, there were mitigative effects similar to what was found in Fig. 26.30. In brief, the differential subsidence was reduced by 30% by the installation of solidified sandy wall.

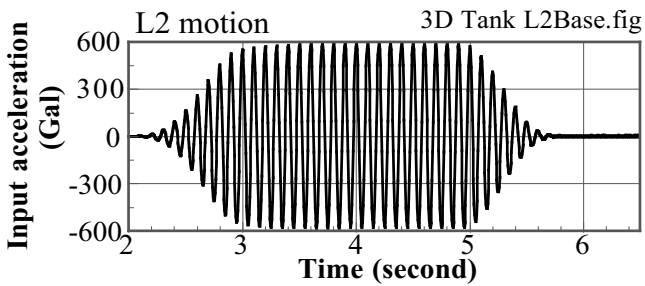


Fig. 26.29 Time history of input motion for tank tests

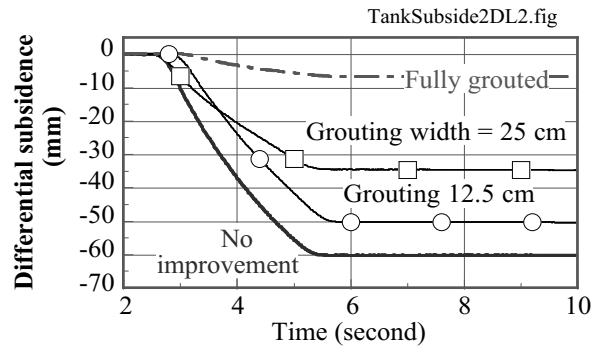


Fig. 26.30 Subsidence of 2-D tank model

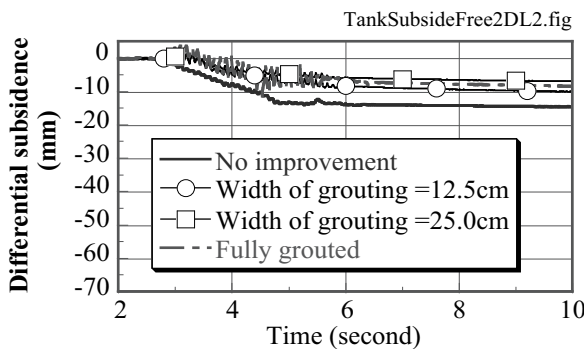


Fig. 26.31 Subsidence of free field in 2-D tank tests

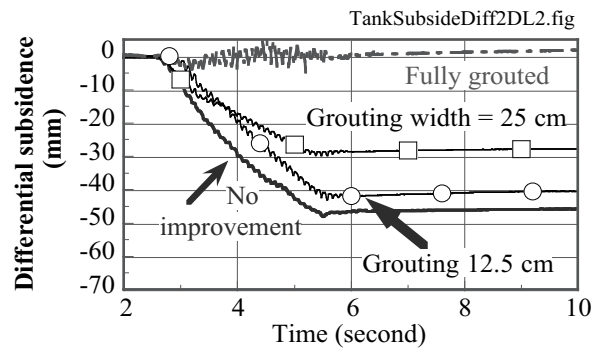


Fig. 26.32 Differential subsidence 2-D tank model and free field

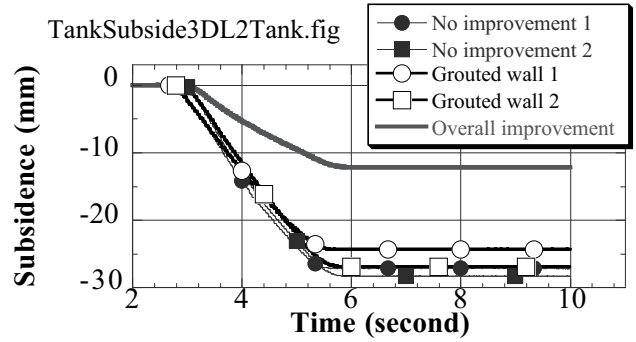
The study was continued to a three-dimensional tank model. Figure 26.33 shows an annular trench in which a grouted sand was placed and overlain by a circular tank model. To reproduce the three-dimensional (axisymmetric) feature as much as possible, the model was constructed in a square container of 2 m × 2 m in plan size. The base excitation was identical with the one in Fig. 26.29. The test results are presented in Figs. 26.34 and 26.35. Although there are mitigative effects of soil improvement, the extent of mitigation seems less significant than in the previous two-dimensional tests.

The use of underground sheet pile walls on mitigation of floating of embedded structures (Sect. 17.5) was investigated by Isoda et al. (2001) and Towhata et al. (2003). A conventional design practice of

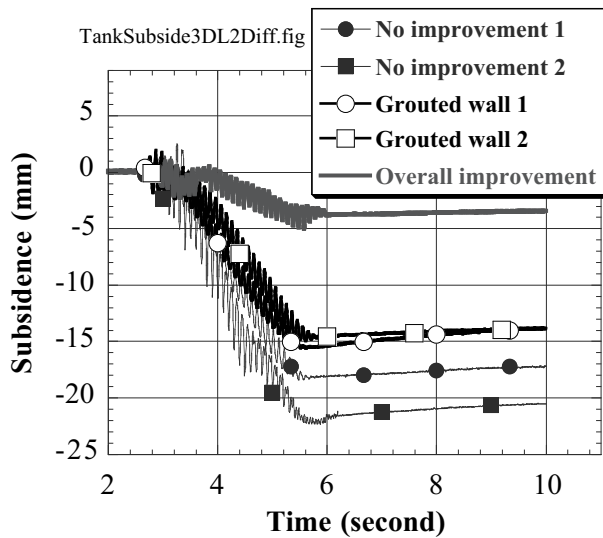
underground structures places them upon an unliquefiable soil (Fig. 26.36). It is expected therein that the unliquefiable subsoil does not deform as shown in Fig. 26.38 and, therefore, the embedded structure is not pushed upward. This idea does not work if the intensity of design earthquake is revised and the formerly unliquefiable soil becomes liquefiable. In such a situation, some remedial measure is required which does not affect existing underground structures. To achieve this goal, the use of underground sheet pile walls and walls of compacted sand was examined.



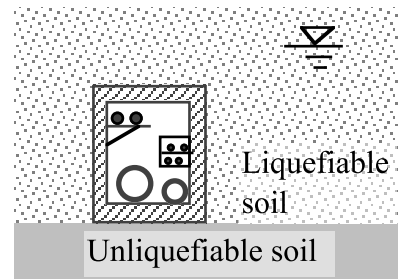
**Fig. 26.33** Modeling of tank foundation improved by colloidal silica injection



**Fig. 26.34** Subsidence of three-dimensional tank model



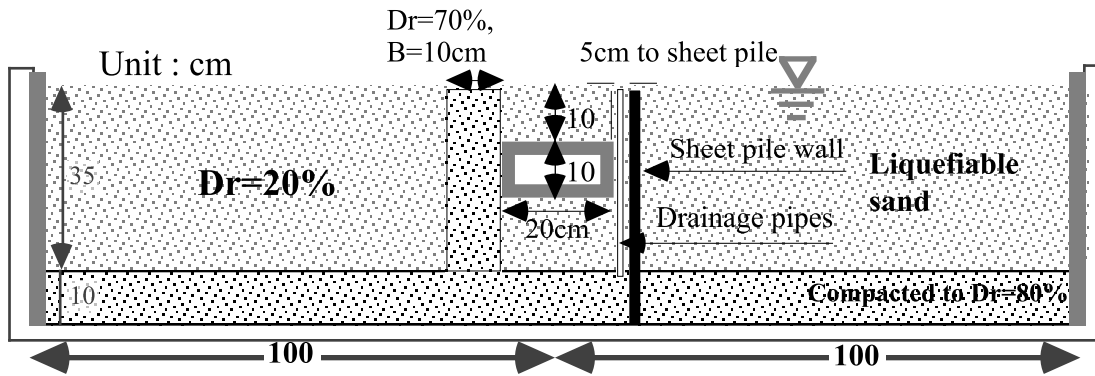
**Fig. 26.35** Differential subsidence between tank and free field in three-dimensional model tests



**Fig. 26.36** Underground structure resting on unliquefiable soil

Figure 26.37 illustrates a model ground for 1-G shaking tests. This model was shaken by base shaking of 180 Gal and 1 Hz for 12 s. Figure 26.38 illustrates the appearance of a model without any mitigation. Significant floating occurred due to the buoyancy force and lack of rigidity in liquefied subsoil. The floating was accompanied by the soil movement toward the bottom of the structure, and this soil pushed the structure upward. Accordingly, it was thought that the floating might be mitigated by preventing the soil displacement toward the bottom of the structure. This idea was examined by installing walls beside the structure. Models with compacted sandy wall or sheet piles with drainage (Fig. 26.90) exhibited reduced floating (Figs. 26.39 and 26.40).

To avoid softening of compacted sand due to migration of excess pore water pressure from the liquefied subsoil, the surface of the sandy wall was covered by impervious plastic sheets. Although the use of viscous fluid could similarly retard the pore pressure migration, such a fluid was not used because the viscosity of the fluid reduces the magnitude of ground deformation. The minor floating of the structure in Fig. 26.40 was probably induced by the upward motion of the sand under the structure; this volume flux (see Fig. 26.18) was balanced by the falling of sand between the walls and the structure.

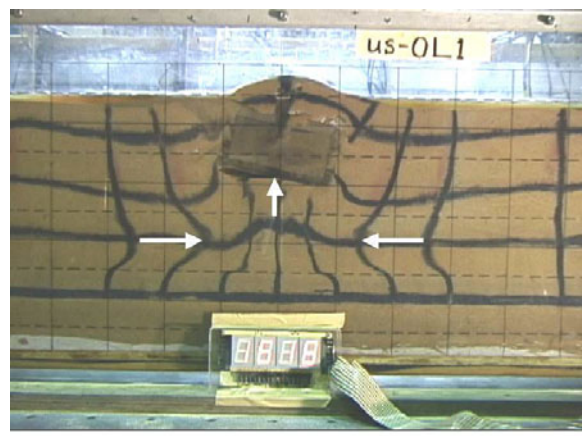


**Fig. 26.37** Shaking model for floating of embedded structure (as for mitigation, either compacted sandy walls or sheet piles were installed on both sides of the structure)

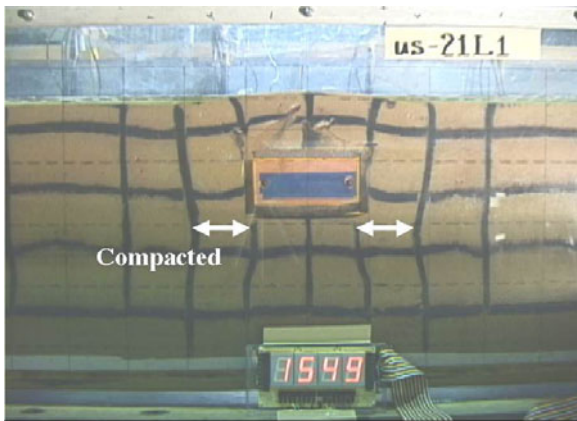
(a) Prior to shaking



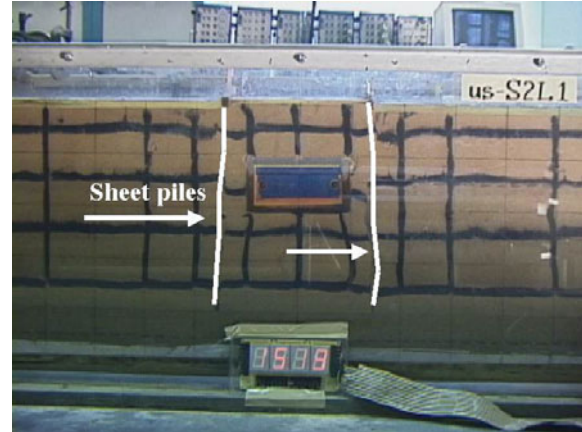
(b) After shaking and liquefaction



**Fig. 26.38** Floating test on model without mitigation



**Fig. 26.39** Reduced floating of model with compacted sandy walls



**Fig. 26.40** Reduced floating of model with sheet-pile walls with drainage

The mitigative effects in floating (Fig. 26.41) was particularly significant when compacted walls or sheet pile walls with drainage was employed. The reduction of the displacement was as much as 90%. Since this ratio of reduced floating is remarkably greater than the 30% mitigation of subsidence (Figs. 26.20, 26.32, and 26.35), a question arises; why the efficiency of underground walls is different between upward and downward displacements. The answer is illustrated in Fig. 26.42. When an underground structure starts to float upward, the surrounding liquefied sand flows in toward the base of the structure (Fig. 26.38). When there are walls, soil pushes the walls against the rigid underground structure, and the

walls are supported well by the rigidity of the structure. The rigidity of the wall-structure system is further improved by drainage which maintains the soil rigidity high. On the contrary when an embankment subsides downward, the walls are pushed outward, and there is no such a rigid subgrade reaction in liquefiable subsoil as an embedded structure. Thus, there is a significant difference in the mitigative effects of underground walls between subsidence and floating. Certainly, mitigation of floating is more efficient.

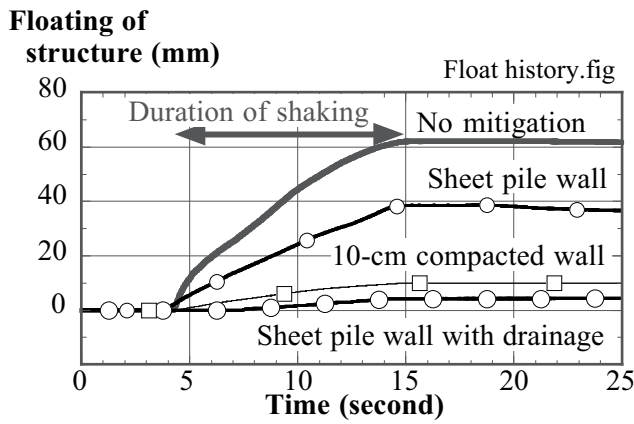


Fig. 26.41 Time history of floating mitigated by different measures

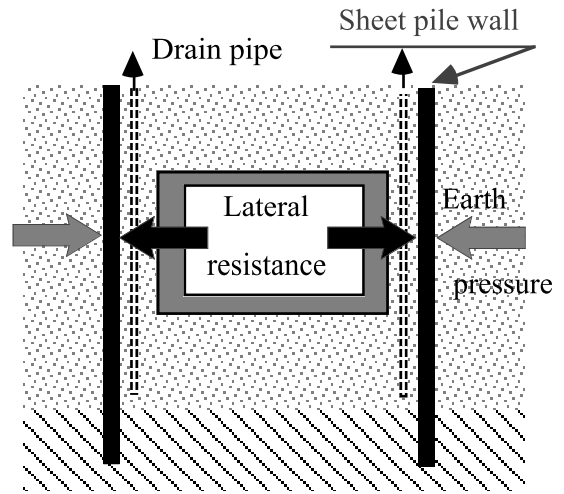


Fig. 26.42 Mitigative mechanism of floating as produced by underground walls

The analytical solution of ground displacement as presented in Sect. 25.8 can take into account the effects of underground walls. Figure 26.43 presents three kinds of walls which are an elastic sheet pile wall, elastically idealized wall of compacted sand, and compacted sand wall undergoing yield deformation.

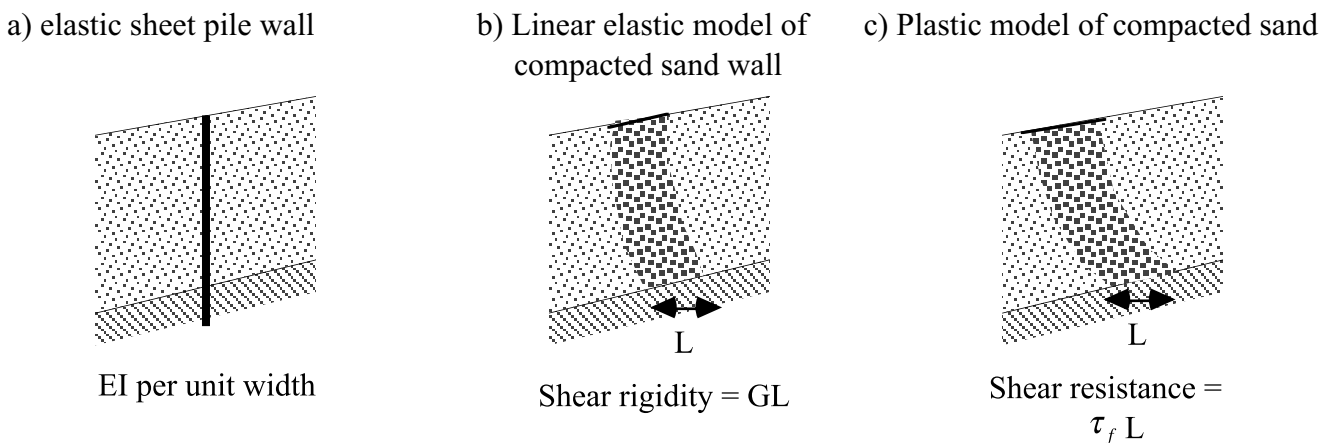


Fig. 26.43 Three models of underground walls

Equation 26.1 is the internal boundary conditions which connect analytical solutions of displacement in subsoil segments on the left and right sides of a wall:

$$\left[ ET \frac{dF}{dx} + \frac{2PH}{\pi} + \frac{2}{\pi} \left( 1 - \frac{2}{\pi} \right) \gamma H^2 + \frac{4\gamma H}{\pi^2} \left( H \frac{dF}{dx} + bF \right) \right]_{x^-}^{x^+} = \frac{80EI}{\pi^2 H^3} F \quad \text{for sheet pile wall}$$

$$\left[ ET \frac{dF}{dx} + \frac{2PH}{\pi} + \frac{2}{\pi} \left( 1 - \frac{2}{\pi} \right) \gamma H^2 + \frac{4\gamma H}{\pi^2} \left( H \frac{dF}{dx} + bF \right) \right]_{x^-}^{x^+} = \frac{12GL}{\pi^2 H} F \quad \text{for elastic sandy wall} \quad (26.1)$$

$$\left[ ET \frac{dF}{dx} + \frac{2PH}{\pi} + \frac{2}{\pi} \left( 1 - \frac{2}{\pi} \right) \gamma H^2 + \frac{4\gamma H}{\pi^2} \left( H \frac{dF}{dx} + bF \right) \right]_{x^-}^{x^+} = \tau_r L \text{ for sandy wall after yielding}$$

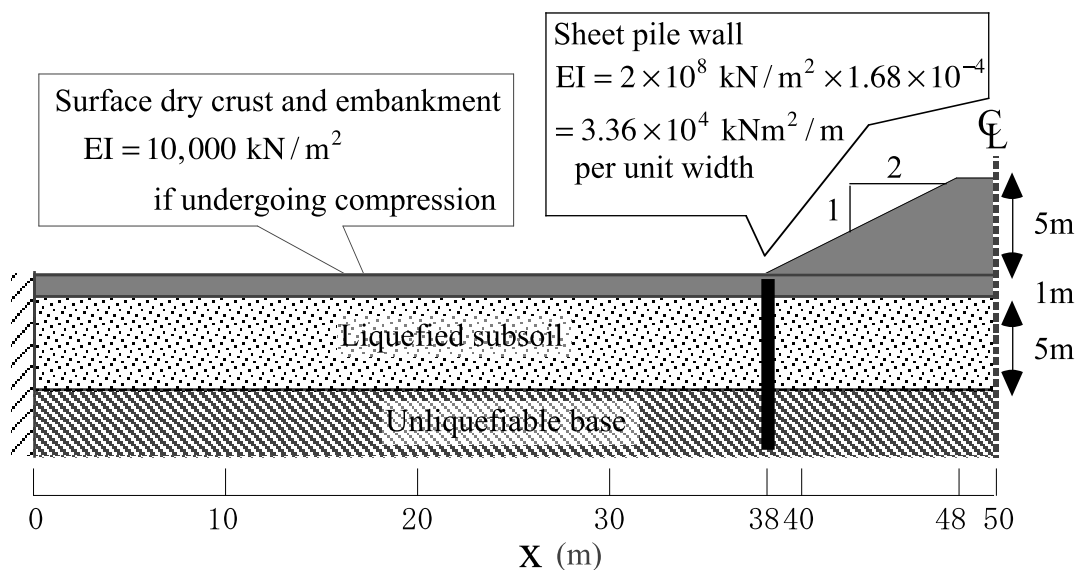
where  $F$  is the horizontal displacement at surface of the place of a wall,  $L$  the width of a sandy wall,  $G$  the shear modulus of elastic sand, and  $\tau_r$  the shear strength of compacted sandy wall. Compare these equations with the one for the case without any wall (25.36).

To show the mitigative effects of a sheet pile wall, numerical analyses were conducted by using the methods in Sect. 25.8 (static analysis for the maximum possible displacement) and (25.43) (dynamic analysis for displacement during 20 s of flow). Figure 26.44 shows the model of analysis in which an embankment rests on liquefiable subsoil and a sheet pile wall is installed beneath the slope in order to mitigate the subsidence of the embankment. Note that only half of the model is analyzed because of the symmetric geometry.

**Table 26.1** Material properties in flow analysis

	Unit weight (kN/m <sup>3</sup> )	Modulus ( $E$ ) (kN/m <sup>2</sup> )
Embankment and surface dry crust	15	10,000
Liquefied subsoil	20	0

The material properties are shown in Table 26.1. The boundary conditions are zero displacement at both  $x = 0$  m (far field) and  $x = 50$  m (axis of symmetry).



**Fig. 26.44** Model of flow analysis

The calculated results are presented in what follows. Figure 26.45 illustrates the maximum possible values of horizontal displacement at the surface ( $F$ ) and the vertical (downward) displacement at the surface as well. Subsidence due to consolidation is not included. In this figure, no sheet pile is assumed. Because zero horizontal displacement is assumed at both  $x = 0$  m and  $x = 50$  m, the maximum value of  $F$  occurred at around  $x = 45$  m, which is within the slope of the embankment. On the other hand, the subsidence was maximum at the crest of the embankment, while heaving (upward movement) occurred in the free field. Figure 26.46 compares the shape of the ground before and after the flow. Subsidence in the embankment and uplift in the free field are seen.

Figure 26.47 exhibits the maximum possible displacement when there is a sheet pile wall. Evidently, the magnitude of displacement was reduced by the sheet pile wall. Compare this figure with Fig. 26.45. Of particular interest is the discontinuity of vertical displacements in front and in back of the sheet pile wall ( $x = 38$  m). This means that lateral soil displacement was stopped by the wall like a dam.



Dynamic analyses were carried out by using the theory of (25.43), in which the critical damping ratio of 10 was assumed. Figures 26.48 and 26.49 compare the time development of subsidence and lateral displacement. Evidently, the rate of despoilment was reduced by a sheet pile.

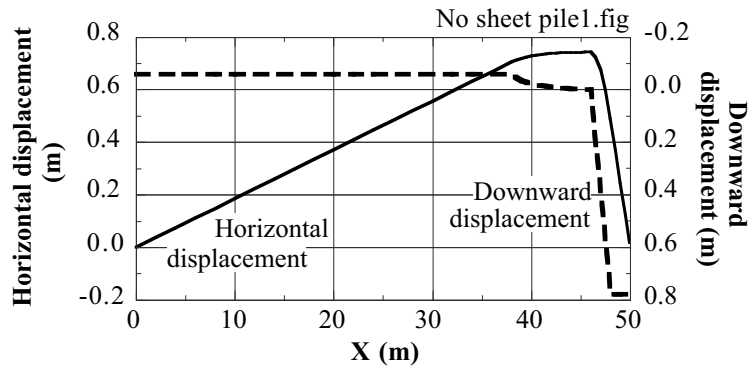


Fig. 26.45 Maximum possible values of horizontal displacement and subsidence at surface when there is no sheet pile wall

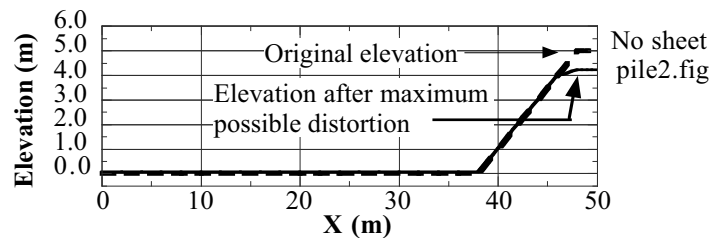


Fig. 26.46 Comparison of ground configuration before and after maximum possible distortion

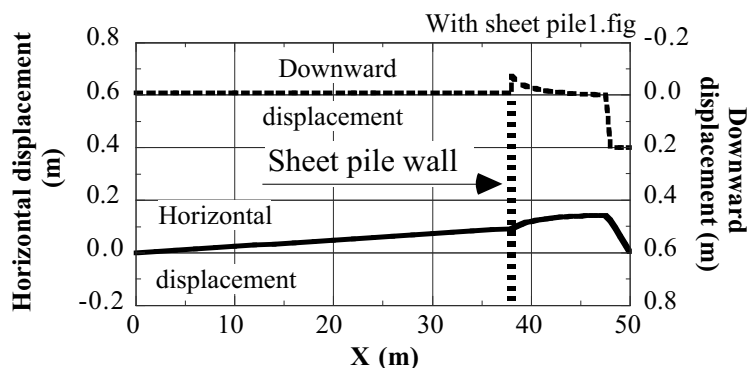


Fig. 26.47 Maximum possible values of horizontal displacement and subsidence at surface when there is a sheet pile wall

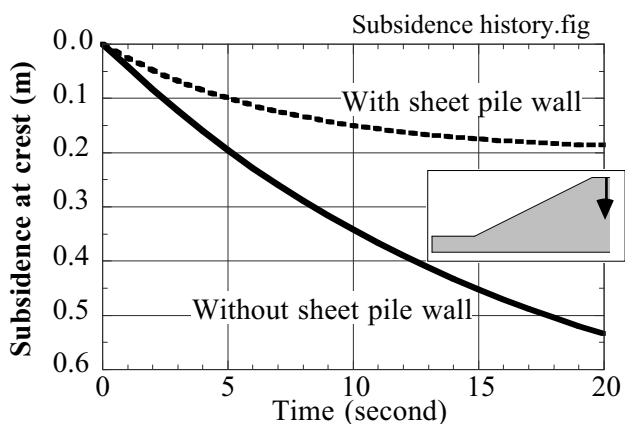


Fig. 26.48 Time history of subsidence at crest of dike

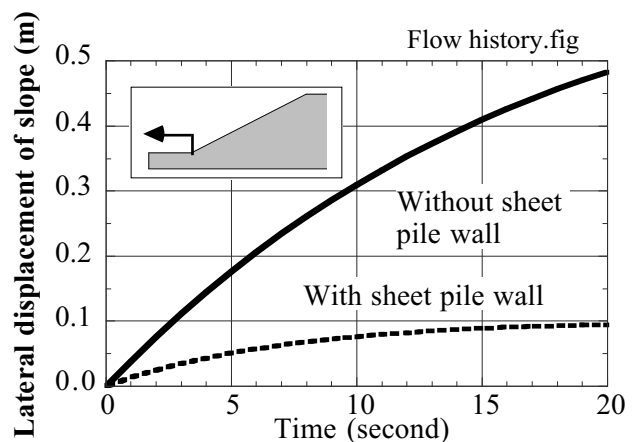
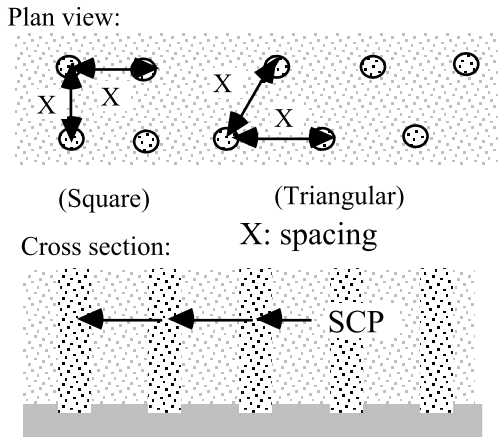


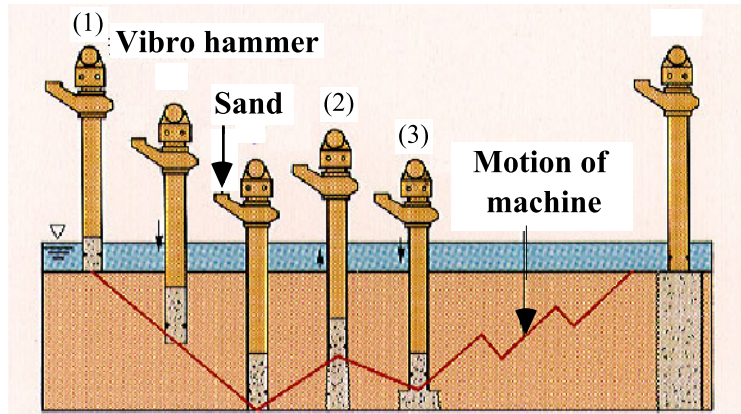
Fig. 26.49 Time history of lateral displacement at bottom of dike slope

**26.4 Sand Compaction Pipe for Densification of Loose Sand**

Vibration and tamping of loose sandy deposits can densify the sand. Densification makes sand highly resistant against large deformation, even when high excess pore pressure develops (Fig. 18.18). Note that the effects of densification are permanent without maintenance efforts. There are two kinds of densification technique; vibration caused by embedded device and tamping at the surface.



**Fig. 26.50** Configuration of ground improved by sand compaction piles



**Fig. 26.51** Procedure of producing sand compaction pile (after Dr. K. Harada of Fudo Tetra Company)



**Fig. 26.52** Machine for construction of sand compaction pile



**Fig. 26.53** Bottom of casing

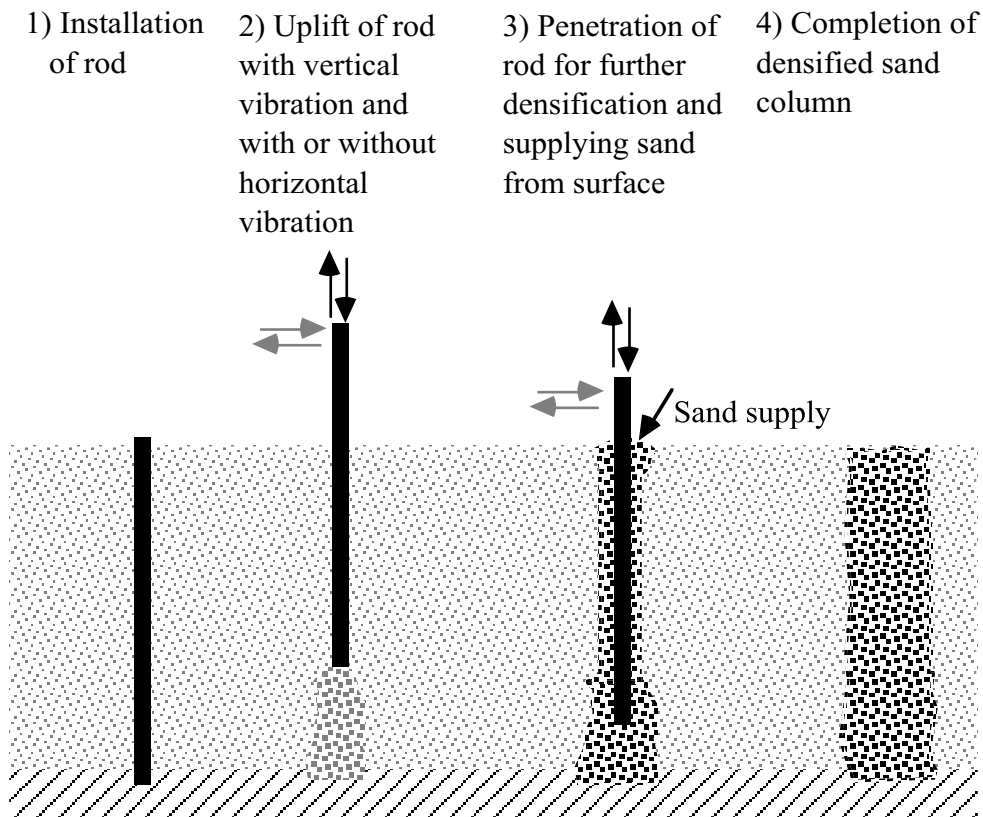
Sand compaction pile (SCP) is one of the measures of subsurface vibration. A number of densified sand columns are made as illustrated in Fig. 26.50. Its sequential procedure for construction is illustrated in Fig. 26.51 in which (1) a machine is pushed by vertical vibration into ground, (2) it is pulled up so that a column of sand is left behind while vibration continues, and (3) the vibrating machine is pushed again downward in order to make the diameter of sand column greater. The procedures of (2) and (3) are repeated many times.

Figure 26.52 indicates the machine and Fig. 26.53 shows the bottom of the casing for pile installation. The bottom is closed when the casing goes down.

SCP has two mechanisms of ground improvement. First, the generated sand piles is substantially dense with SPT-*N* ranging from 20 to 40. This dense sand does not liquefy and, hence, resists against ground deformation. Second, the original sandy deposit is compacted by vibration as well. Its volume decreases

by the same amount as the volume of the installed sand piles. Accordingly, the original sand becomes more resistant against liquefaction.

SCP machine pushes pressurized air (500 kPa for example) into ground through the casing in order to help migration of sand into ground. This air reduces the degree of saturation in the surrounding ground and may improve the liquefaction resistance further (Sect. 18.1) in addition to the effects of densification. Okamura and Teraoka (2005) and Okamura et al. (2006) studied the long-term variation of the degree of saturation in an improved ground and showed that reduced saturation improves liquefaction resistance of sand. This issue, however, requires further investigation.



**Fig. 26.54** Densification sequence of sandy ground by rod compaction

A very powerful densification is achieved by rod compaction. Figure 26.54 illustrates its principle; vertical vibration of a rod densifies the existing sandy ground. This method produces ground vibration and noise; similar to early version of SCP. There is no need, on the other hand, to prepare good sand for densification material in such a way as in the case of SCP.

One of the problems associating such a powerful densification is the development of excess pore water pressure during soil improvement. Since the effective stress is lost during heavy shaking, the efficiency of vibratory compaction is reduced. To mitigate this problem, Ishiguro et al. (1994) applied vacuum to sand around the vibratory rod so that pore water was absorbed and the effective stress was maintained high. Consequently, higher cone penetration resistance was achieved and higher resistance against liquefaction was verified. In their model ground, however, the relative density of sand (Sect. 1.2) was not improved by application of vacuum. Ishiguro et al. (1994) made microscopic studies of sand grain orientation and stated that densification under some extent of effective stress produces better orientation of sand grains that achieves greater resistance against liquefaction.

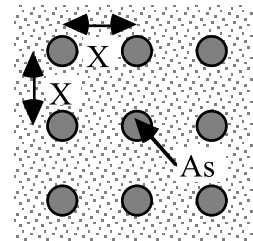
An interesting example of soil densification was practiced for seismic retrofitting (increasing liquefaction resistance of an existing structure) of Sardis Dam (Finn et al. 1998). In more details, an enormous number of piles were driven into the upstream slope of the dam for densification.

**26.5 Ground Improvement by Compaction**

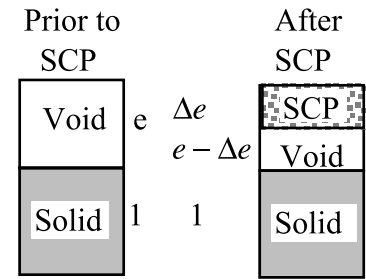
The spacing,  $X$ , between SCPs (Fig. 26.55) is determined in accordance with the desired extent of soil improvement. Since the diameter of SCP is determined by the method of construction, being typically 0.7 m, the cross section of the pile is derived as

$$A_s = 0.7^2 \times \pi / 4 = 0.38 \text{ m}^2.$$

Figure 26.56 illustrates the decrease in volume of the original sandy ground from “ $e$ ” to “ $e - \Delta e$ ” due to the installed volume,  $\Delta e$ , of SCP. Note that the volume of SCP in Fig. 26.56 consists of both compacted sand grains and the void therein. By calculating the ratio of the installed piles and the original sandy deposits in Figs. 26.55 and 26.56,



**Fig. 26.55** Square configuration of SCP



**Fig. 26.56** Decrease of void ratio upon installation of sand columns

$$A_s : X^2 = \Delta e : 1 + e.$$

Thus, the desired spacing,  $X$ , is determined by using the desired decrease of void ratio.

$$X = \sqrt{\frac{1 + e}{\Delta e}} A_s \tag{26.2}$$

The extent of improvement is often designated by  $a_s$ :

$$a_s = A_s / X^2 \quad (\text{改良率, 置換率}) = \Delta e / (1 + e), \tag{26.3}$$

which ranges typically from 0.05 to 0.20.

*Example* Calculate  $X$  when the relative density of sand is required to increase from  $D_r = 40\%$  to  $90\%$  (change of relative density). Use  $e_{\max} = 0.98$  and  $e_{\min} = 0.60$  (Toyoura sand).

$$\text{Since } D_r = 100 \times \frac{e_{\max} - e}{e_{\max} - e_{\min}} = 263(0.98 - e) (\%),$$

the initial void ratio,  $e = 0.828$  and the improved void ratio = 0.638. Therefore,  $\Delta e = 0.190$ . By substituting  $A_s = 0.38 \text{ m}^2$  in (26.2) and (26.3),  $X = 1.91 \text{ m}$  and  $a_s$  is found to be equal to 0.10 (10%).

The design procedure in practice is described in what follows (Mizuno et al. 1987; JGS, 2004a). Since fines content (silt and clay) always reduces the SPT- $N$  value, a special consideration is necessary.

1. The initial SPT- $N$  value prior to densification is designated by  $N_0$ . Being a measured value, this  $N$  value includes the effects of fines content. Decide then the target  $N$  value,  $N_1$ , after densification by assuming the fines content to be zero (clean sand).
2. Briefly assess the maximum and minimum void ratios of sand by running tests or use, for example, an empirical formula by HIRAMA (1981)

$$e_{\max} = 0.02F_c + 1.0 \quad \text{and} \quad e_{\min} = 0.008F_c + 0.6. \tag{26.4}$$

where  $F_c$  stands for the fines content (% weight of grains finer than  $75 \mu$ ).

3. Correction of SPT- $N$  for fines content,  $\Delta N_f$ , is determined by using an empirical formula (Fig. 1.38).
4. The initial relative density,  $D_{r0}$ , prior to densification is assessed by using an empirical formula (Sect. 1.12);

$$D_{r0}(\%) = 21 \sqrt{\frac{N_0}{0.7 + \sigma'_v/98} + \frac{\Delta N_f}{1.7}} \quad (26.5)$$

This makes it possible to assess the initial void ratio of ground;

$$e_0 = e_{\max} - \frac{D_{r0}}{100} (e_{\max} - e_{\min}) \quad (26.6)$$

5. Determine the void ratio after densification by using  $N_1$  of imaginary clean sand;

$$D_{r1}(\%) = 21 \sqrt{\frac{N_1}{0.7 + \sigma'_v/98}} \quad \text{and}$$

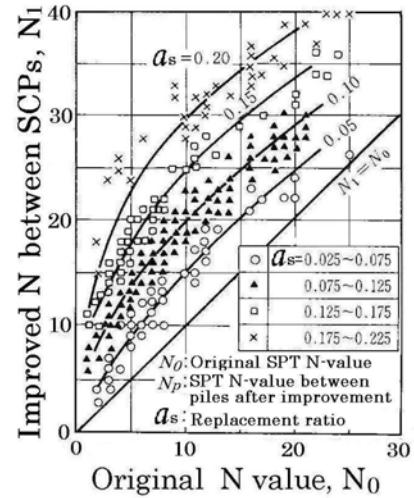
$$e_1 = e_{\max} - \frac{D_{r1}}{100} (e_{\max} - e_{\min}) \quad (26.7)$$

6. Although the extent of improvement,  $a_s$ , can be determined now by using (26.3), the effects of fines on the efficiency of densification have to be taken into account. Figure 26.56 supposes that the volume of SCP fully contributes to the densification of existing ground. When permeability is reduced by fines, however, the densification cannot fully take place and the ground surface heaves. This phenomenon is considered in a modified equation;

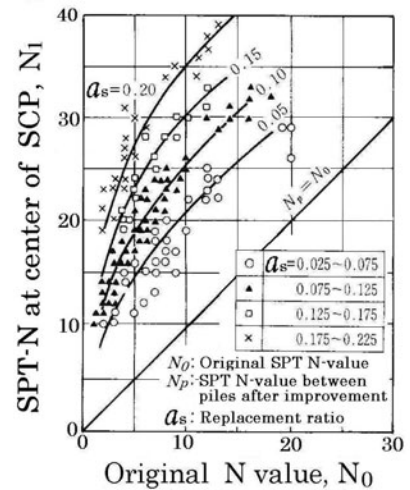
$$a_s = \frac{e_0 - e_1}{(1.05 - 0.46 \log_{10} F_c)(1 + e_0)} \quad (26.8)$$

7. Consequently, the spacing of SCP is determined;

$$X = \sqrt{A_s/a_s} \quad (26.9)$$



**Fig. 26.57** Empirical relationship between SPT- $N$  before and after densification (JGS, 2004a, p. 238)



**Fig. 26.58** Empirical relationship between SPT- $N$  of original deposit and SPT- $N$  of SCP (JGS, 2004a, p. 238)

Figures 26.57 and 26.58 illustrate the improved SPT- $N$  values in the original ground and at the center of newly constructed sand piles.

Due to inevitable uncertainty in the field, it is always important to examine the improvement by running site investigation after completing the densification. Practitioners sometimes suppose that SPT- $N$  increases in some weeks after densification due to unknown reasons. This is consistent with Mitchell and Solymar (1984) who pointed out the gradual increase in cone penetration resistance in densified sand. This delay is most probably because of thin layers of fine-grained soils which did not allow quick dissipation of excess pore water pressure that developed during densification. In this respect, it is reasonable to carry out SPT- $N$  one month after the densification when the effective stress has recovered to the original level. This idea is noteworthy in other kinds of densification measures as well. Moreover, Skempton (1986) mentioned this ageing effects but no evidence was presented. Figure 26.59 was drawn by using Skempton's idea on increasing of  $N_{1,60}/D_r^2$  with age, where  $N_{1,60}$  stands for the SPT- $N$  value corrected to the effective

stress level of 1 kgf/cm<sup>2</sup> (98 kPa) (Sect. 1.12, Fig. 21.1) and modified to 60% energy efficiency of impact (Sect. 1.12). The relative density,  $D_r$ , in Skempton's study was expressed not in terms of % but in decimal.

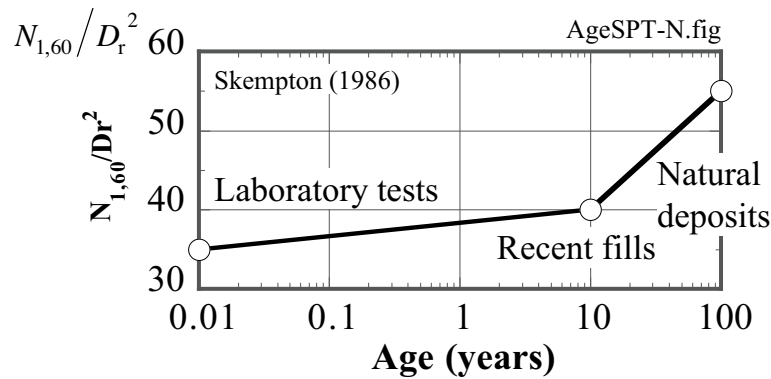


Fig. 26.59 Skempton's suggestion on increase in SPT-N with age ( $D_r$  in decimal)

Stone column is widely used for soil improvement as well. For its installation, a steel casing with its bottom closed is driven into ground by vertical vibration (Andrew, 2006). In this stage, the original ground is densified and pushed laterally so that installation may be allowed. Thereinafter, stone is placed and compacted, thus forming a rigid underground column. After removal of the casing, the stone column is expected to make a drainage channel of excess pore water pressure during an earthquake. It is possible that vibration upon installation causes liquefaction in the surrounding soil, which may flow into the stone column. Therefore, a possible problem in a stone column as a mitigation of liquefaction is the clogging of the column due to fines included in the liquefied sand.

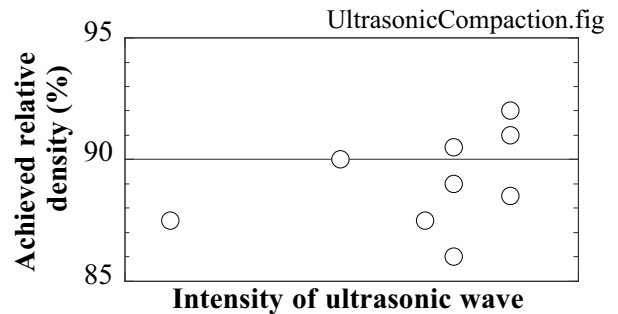


Fig. 26.60 Densification of sand by ultrasonic wave (Oh-uchi and Murakami, 2006)

There is a recent attempt to densify sand by means of ultrasonic wave. Since this wave has 20,000 Hz of frequency, no noise is detected by human sense. Figure 26.60 illustrates the results of laboratory validation in which a various intensity of ultrasonic wave hit a deposit of Toyoura sand prepared by water-sedimentation. Most probably the initial relative density was 40% or less and it was increased by the ultrasonic action to about 90%. Figure 26.61 shows an equipment for field validation which is operated by 300-W electric power resources. The author could not obtain data from field tests. It is thought by the manufacturer (Imori Kogyo Company) that minor shaking is induced in sand grains by the ultrasonic action and the intergranular friction is reduced, resulting in easy densification. More precisely, the intergranular friction is activated in the direction of high-frequency motion (relative displacement) and the resistance against the gravity-induced contact force is reduced. This mechanism is similar to the effects of stress superposition in Figs. 19.39, 24.18, and 24.19. Thus, particles are packed more densely under their weight.



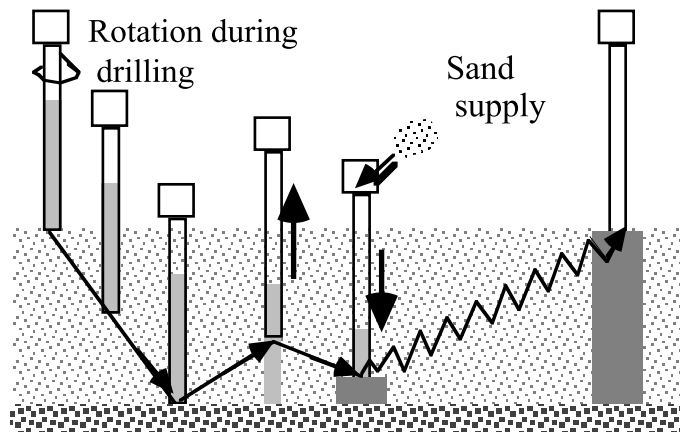
Fig. 26.61 Machine for insitu ultrasonic compaction of sand (Oh-uchi and Murakami, 2006)

**26.6 Static Installation of Sand Compaction Piles**

The conventional method for construction of sand compaction pile (SCP) had an environmental problem; significant noise and ground vibration. It was, hence, difficult to practice this method in the vicinity of existing structures and human activities. The recent development (Ohbayashi et al. 2006) has overcome this problem remarkably by employing static cyclic loading in place of vibratory compaction (Fig. 26.62). Figure 26.63 illustrates the methodology in which a machine moves up and down cyclically in a static manner by which columns of compacted sand (or gravel or recycled waste) are formed. Figures 26.64 and 26.65 illustrate the extent of reduction in ground vibration and noise. The intensity of ground vibration is expressed by the following formula;

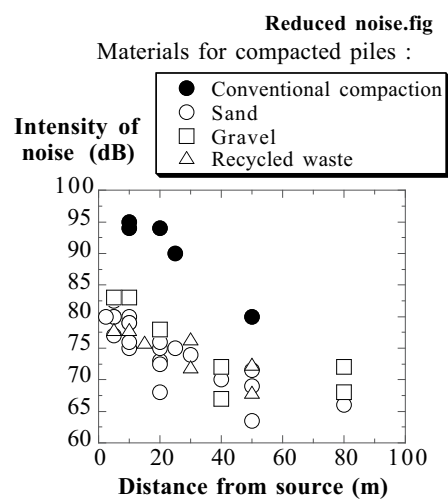
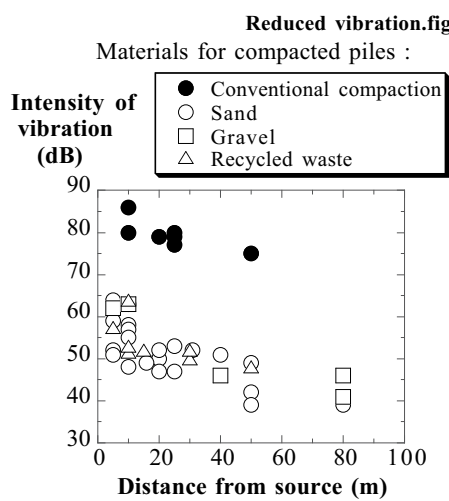
$$\text{intensity of ground vibration (dB: decibel)} = 20 \log_{10}(A/A_0) \tag{26.10}$$

where  $A$  is the measured level of acceleration (effective value, being 65% of amplitude in case of harmonic signal) and  $A_0$  the standard value of  $10^{-5} \text{ m/s}^2$ .



**Fig. 26.62** Machine for silent construction of sand compaction piles

**Fig. 26.63** Formation of compacted sand column by static compaction method (after Fudo Tetra Company)

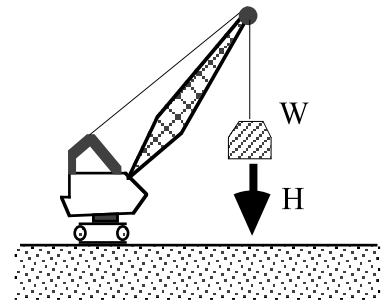


**Fig. 26.64** Reduced level of ground vibration during installation of compaction piles (data by Fudo Tetra Company)

**Fig. 26.65** Reduced level of noise during installation of compaction piles (data by Fudo Tetra Company)

**26.7 Dynamic Consolidation**

Dynamic consolidation method of soil improvement, which was proposed by Menard, lifts a weight of  $W = 50\text{--}300\text{ kN}$  ( $5\text{--}30\text{ tf}$ ) made of steel or concrete to the height of  $H = 20\text{--}30\text{ m}$  (Fig. 26.66). Then the weight falls freely to the ground surface. The impact made by this falling weight densifies the soil (Fig. 26.67). The effects of densification is maximum near the surface, decreasing at deeper elevation. The holes in Fig. 26.68 was made by the hitting impact and was later filled by new sand.



**Fig. 26.66** Basic concept of dynamic consolidation method

The procedure of free fall is repeated many times until the specified free fall energy is supplied to the ground and the desired density of sand is achieved. It is important to do soil investigation after dynamic consolidation in order to make sure the satisfactory improvement. It is possible to densify municipal waste landfill as well.



**Fig. 26.67** Impact on ground surface made by free fall of weight (at Mizushima)

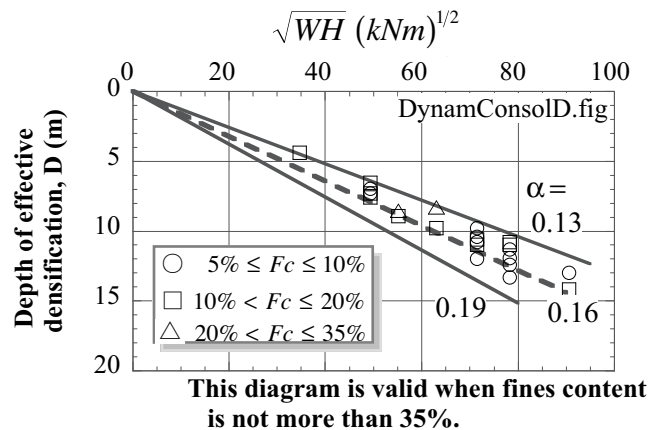


**Fig. 26.68** Big hole made by impact energy of free fall (at Mizushima)

The design procedure is summarized below. Firstly, the depth of effective compaction,  $D$  (m), is assessed by the following empirical formula;

$$D = \alpha \sqrt{WH}, \quad (26.11)$$

in which  $\alpha$  is an empirical parameter which varies with the gradation of soil, the expected extent of densification, and the supplied free-fall energy. Moreover, the unit for  $W$  in (26.11) is kN, while that for  $H$  is meter. Figure 26.69 illustrates examples of  $D$ .



**Fig. 26.69** Example calculation of expected depth of soil densification (after JGS, 2004a, p.259)

When the points of impact are located in a square configuration, the spacing between points,  $L$  (m), is determined as



$$L \approx D. \tag{26.12}$$

The required impact energy per unit area of ground surface,  $E$  (kNm/m<sup>2</sup>), is determined by

$$E = E_v D, \tag{26.13}$$

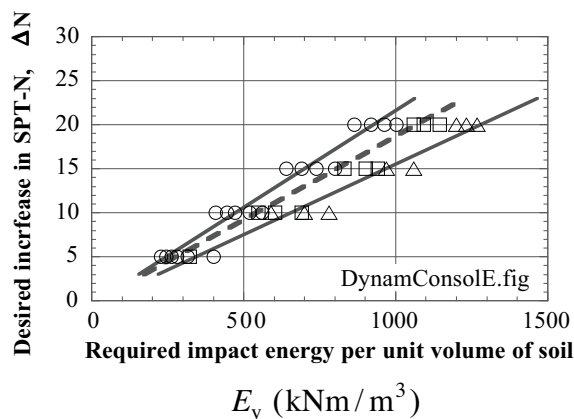
in which  $E_v$  (kNm/m<sup>3</sup>) designates the energy per unit volume of soil which is required to achieve the desired increase in SPT- $N$  value ( $\Delta N$ ) (Fig. 26.70).

Finally, the required number of impacts is determined;

$$\text{number of impacts} = \frac{EL^2}{WH}. \tag{26.14}$$

This number of impacts is executed by several stages in practice. Note that time has to be spent between stages in case of compacting less pervious soils. This is because impact is ineffective when excess pore water pressure, which was produced by previous impacts, remains high.

○	$5\% < F_c < 10\%$	$E_v = (\Delta N + 0.4) / 0.022$
□	$10\% < F_c < 20\%$	$E_v = (\Delta N + 0.3) / 0.019$
△	$20\% < F_c < 35\%$	$E_v = (\Delta N + 0.5) / 0.016$



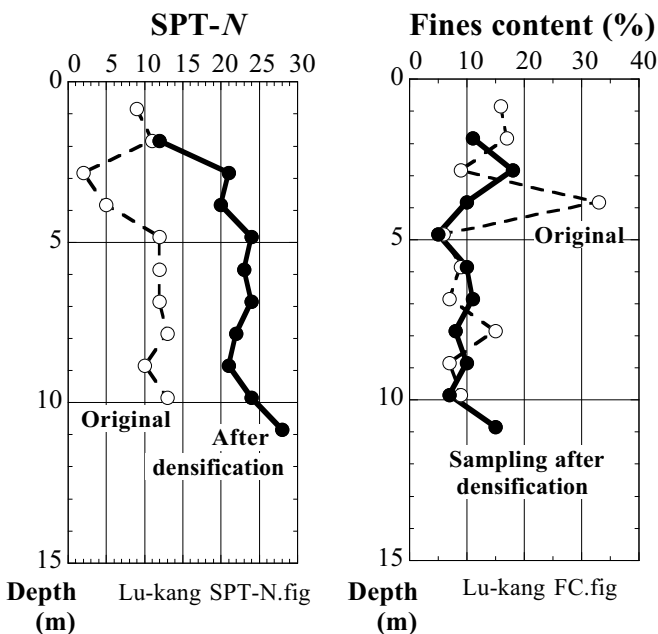
**Fig. 26.70** Empirical relationship between desired increase in SPT- $N$  and required energy per unit volume of soil (after JGS 2004a, p. 260)

**26.8 Verification of Effects of Dynamic Consolidation**

Soil improvement by using the dynamic consolidation method was going on in Lu-kang (鹿港) in the central part of Taiwan when the 1999 ChiChi (集集) earthquake occurred. The target SPT-*N* in this project was 20 for sand with fines content (*F<sub>c</sub>*) less than 15%. Although the work was incomplete, the improved part of the site was not affected by the earthquake (Fig. 26.71) (Lee et al. 2001; Hwang et al. 2003). In contrast, the unimproved ground developed liquefaction (Fig. 26.72). Fig. 26.73 compares the SPT-*N* values and fines content before and after the densification. It seems apparent that the target increment of *N* value was achieved.



**Fig. 26.71** Satisfactory effects of sand densification by dynamic consolidation in Lu-kang, Taiwan (Kaiyo Kogyo Company)



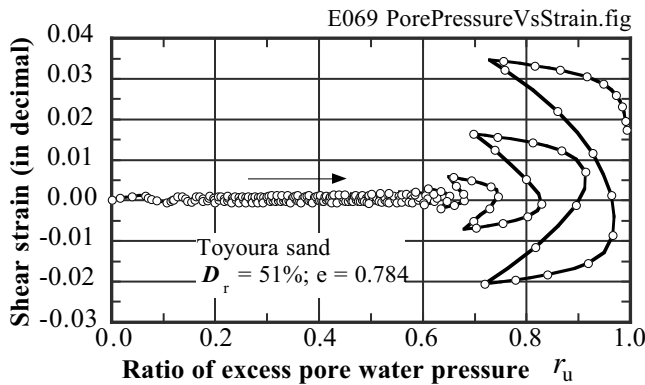
**Fig. 26.73** Improvement of SPT-*N* after dynamic consolidation in Lu-kang, Taiwan (Kaiyo-Kogyo Company)



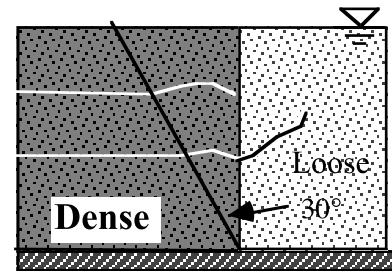
**Fig. 26.72** Liquefaction in unimproved sandy ground in Lu-kang, Taiwan (Kaiyo Kogyo Company)

**26.9 Range of Sand Densification**

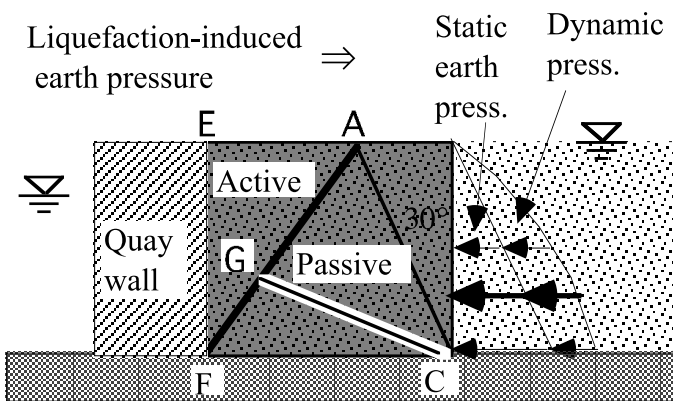
Study has been made on the appropriate size of soil-improvement area in order to prevent large deformation of subsoil and foundation. Figure 26.74 shows that loose sand maintains reasonable stiffness until the excess pore water pressure,  $\Delta u$ , exceeds 60% of the effective vertical stress. Iai et al. (1991) pointed out the importance of pore pressure increase due to pressure propagation from loose part of subsoil into densified part. Their shaking table test on the behavior of an interface between dense and loose sand deposits revealed that a certain extent of softening occurs due to propagation within the densified part as illustrated in Fig. 26.75.



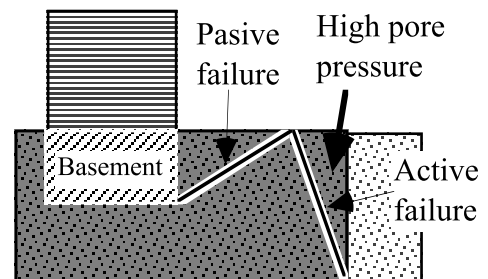
**Fig. 26.74** Development of shear strain amplitude with increase of excess pore water pressure (torsion shear test)



**Fig. 26.75** Increased deformation in densified sand due to pore pressure propagation (Iai et al. 1991)



**Fig. 26.76** Force equilibrium in densified backfill of gravity quay wall (after Iai et al. 1991)



**Fig. 26.77** Area of densification around building foundation (after Tsuchida et al. 1976)

Iai et al. (1991) further noticed the importance of stability analysis. Figure 26.76 illustrates the static and dynamic earth pressures acting on densified part of backfill soil behind a caisson quay wall. To avoid influence of the earth pressures on the quay wall, the passive shear plane (CG in Fig. 26.76) within the densified soil needs to be large enough to mobilize resistance against the static and dynamic earth pressures exerted by liquefied loose sand. The static pressure is equal to the total overburden pressure and the dynamic component is assessed by the Westergaard formula (Sect. 13.5). Note that the soil wedge of active failure mechanism (AEF) should not include the required size of CG. This is because AEF has to resist another active type of shear failure behind the wall, independent of the failure on the liquefaction side.

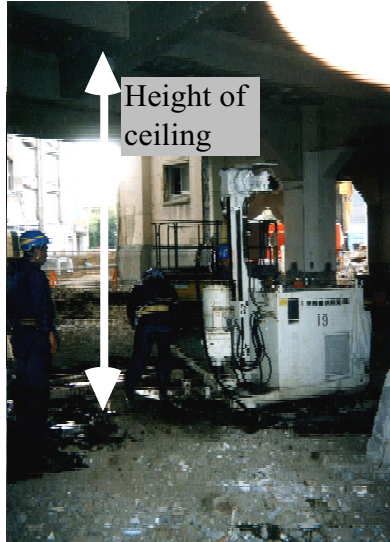
Figure 26.77 briefly illustrates another idea by Tsuchida et al. (1976) on densification of foundation of a building. The inertia force of a building is resisted by the passive resistance of the densified sand which is not affected by liquefaction.

**26.10 Compaction Grouting**

Compaction grouting pushes highly pressurized grout into soft ground and compresses the surrounding soil in the lateral direction. This procedure is static and does not cause bad noise or vibration. After some time, the grout is solidified and further increases the improvement effects.

Figure 26.78 indicates the boring procedure which installs a vertical steel pipe of 5 cm in diameter into the ground. Grout as a mixture of water, cement, and aggregates is pressurized and pushed into the steel pipe. The grout comes out of the bottom end of the pipe and opens a cavity filled with grout (cavity expansion). The principle of this method is illustrated in Fig. 26.79.

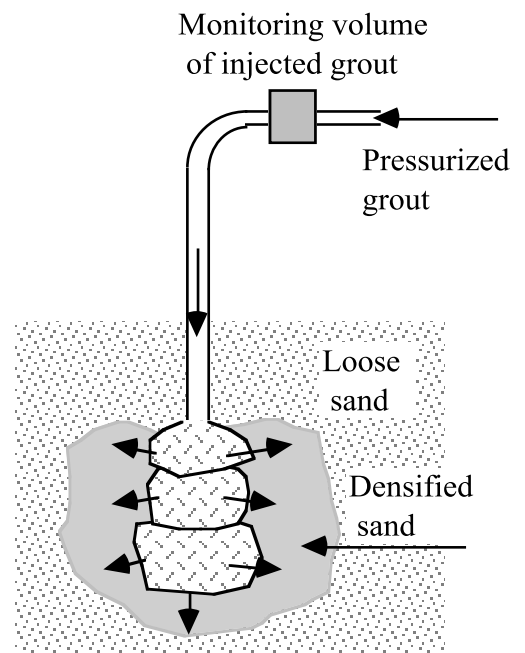
The typical composition of grout is 426 kg of water, 160 kg of cement, and 1,360 kg of aggregate (60% of sand, 20% of silt, and 20% of gravel finer than 10 mm); slump = 4.8 cm; and the compressional strength after 4 weeks = 3 MPa. The pressure of at maximum 6 MPa for example helps grout expand laterally into the ground. When a specified volume of grout has been pushed into ground, the injection procedure is stopped and the steel pipe is lifted up to the next elevation.



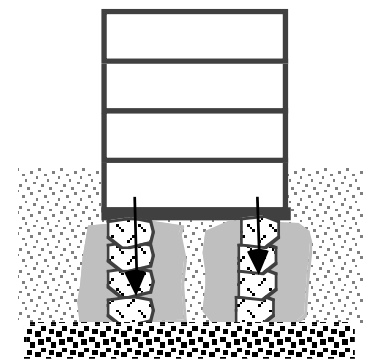
**Fig. 26.78** Drilling hole for installation of pipe



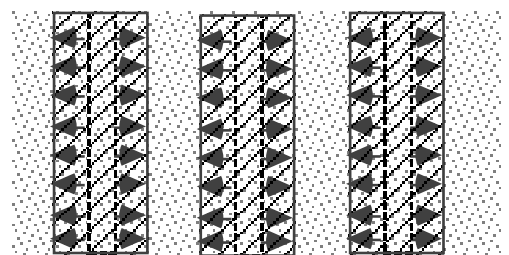
**Fig. 26.80** Ongoing injection



**Fig. 26.79** Schematic illustration of compaction grouting



**Fig. 26.81** Soil improvement under existing building



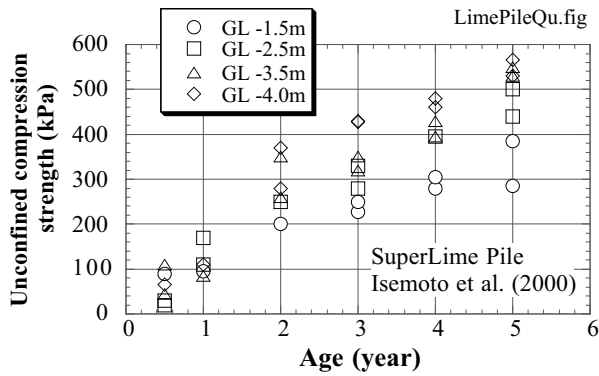
**Fig. 26.82** Conceptual sketch of soil densification by static swelling

Figure 26.80 indicates the ongoing injection. The installation of compaction grouting is a static procedure and very calm. The employed device is short in height and can be used in the basement of a building. Thus, the soil improvement under an existing building is possible (Fig. 26.81).

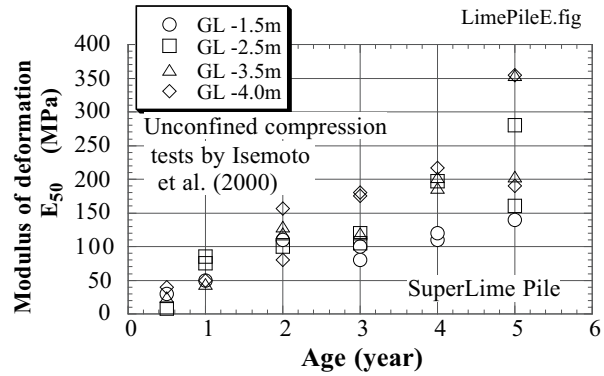
Static densification (Fig. 26.82) is possible by making use of water-absorption and swelling of lime which is embedded in ground (superlime pile) (Horikoshi et al. 2000). Since no ground vibration or noise is made, it can be executed in a busy urban area. The raw material consists of burnt lime and gypsum together with hard granulated slag and sand. A bored pile filled with these materials swells 140 % in volume and compresses the surrounding ground. At the same time, the lateral earth pressure increases. This increase of  $K_0$  value (earth pressure coefficient at rest) leads to further improvement of

liquefaction resistance (Table 19.2 and Sect. 19.7). It is important that the rate of swelling is controlled by a special recipe so that the entire body of the pile swells efficiently.

Isemoto et al. (2000) conducted long-term model tests on the material properties of 24 superlime piles. Full-scale piles were constructed in a big model container and their unconfined compression strength as well as the modulus of deformation (secant modulus,  $E_{50}$ , at 50% of the peak strength) was measured over five years. Figures 26.83 and 26.84 demonstrate that the properties continued to increase over five years. The diameter of the piles was maintained constant around 60 cm without significant change.



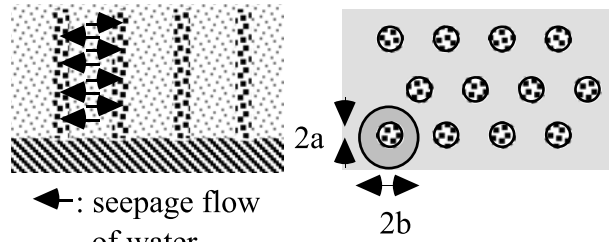
**Fig. 26.83** Development of unconfined compression strength of superlime pile material with time (after Isemoto et al. 2000)



**Fig. 26.84** Development of modulus of deformation in unconfined compression tests on superlime pile material with time (after Isemoto et al. 2000)

**26.11 Dissipation of Excess Pore Water Pressure**

A less expensive way of ground improvement is the use of gravel drains in which vertical columns of gravel are installed in holes that are drilled in loose sandy deposit. Since gravel is substantially more pervious than sand, the excess pore water pressure in loose sand around a gravel column quickly dissipates (decreases) so that the liquefied ground may not have time to deform significantly. The interval among holes are, for example, 1.5 m (Fig. 26.85). A typical diameter of a gravel drain is 0.5 m. Since no significant effort is made to cause vibration and compaction in either original sand or installed gravel, pore pressure does increase in sand.



**Fig. 26.85** Schematic view of gravel drain

(a) Overall view

(b) Screw mechanism for penetration

Figure 26.86 illustrates a machine which is installing a gravel drain under an existing river dike. Since the dike was close to wooden houses, no ground vibration or noise was allowed. Moreover, the short distance from houses did not allow lateral ground displacement which sand compaction pile would cause upon installation.



**Fig. 26.86** Construction machine for gravel drain

Since a gravel drain machine has a spiral outside the pipe (Fig. 26.86b), the existing soil is removed out of ground and is not pushed laterally. Thus, nearby structures are not affected by installation of gravel drains. Therefore, gravel drains were chosen and were constructed after removing half of the dike; the other half remained as a provision against possible flooding. Since the machine in Fig. 26.86 is screwed into subsoil, no ground vibration occurs. This is a significant difference from sand compaction pile and makes gravel drain construction possible near existing structures. Fig. 26.87 shows the employed gravel which achieved high permeability in the drain.



**Fig. 26.87** Gravel particles employed for drain (see a ball point pen on gravel)

Highly pervious gravel drains make the drainage path in loose sand shorter (Fig. 26.85). The water in sand flows horizontally only 1 m or less to reach the gravel drainage path, which is in contrast with the distance of several meters to the ground surface when no gravel drain is available. Therefore, the rate of dissipation of excess pore water pressure is accelerated so that the effective stress does not decrease very much or, even in the worst case of 100% pore pressure rise, the effective stress recovers quickly before ground fails substantially.

Design of gravel drains assumes that one drain collects water from a cylindrical area of radius equal to “b” (see Fig. 26.85). The radius of a gravel column is determined by a construction machine; e.g.,  $a = 0.25$  m. The required spacing,  $b$ , to avoid liquefaction disaster is determined by running a seepage analysis;

$$\frac{k_h}{\gamma_w m_v} \left( \frac{\partial^2 u}{\partial r^2} + \frac{1}{r} \frac{\partial u}{\partial r} \right) + \frac{k_v}{\gamma_w m_v} \frac{\partial^2 u}{\partial z^2} = \frac{\partial u}{\partial t} - \frac{\partial u_g}{\partial t} \quad (26.15)$$

in which  $k_h$  and  $k_v$  are permeability in the radial ( $r$ ) and vertical ( $z$ ) directions, respectively,  $\gamma_w$  the unit weight of water,  $m_v$  the volume compressibility of sand,  $u$  the excess pore water pressure, and  $u_g$  the excess pore water pressure generated by shaking. When subsoil is undrained,  $u = u_g$ . Equation (26.15) ignores the resistance of gravel drain against water flow (well resistance = 0). Onoue et al. (1987) made more detailed studies on the effects of well resistance.

Figure 26.88 illustrates the results of analysis and helps determine the “ $b$ ” value. It is assumed therein that cyclic shear is repeated  $N_{eq}$  cycles with a constant stress amplitude of  $\tau_{cy}$  ( $= 0.65 \tau_{max}$ ) and the sand would liquefy when  $\tau_{cy}$  is repeated  $N_1$  cycles. The development of pore water pressure,  $u_g$ , with time is calculated separately by, for example, (20.2).

As the allowable maximum pore pressure ratio,  $u_{max} / \sigma'_{vo}$ , decreases (conservatism safer side), the interval of drains,  $b$ , decreases. In Fig. 26.88 isotropic permeability of  $k_v = k_h = k$  is assumed, and a nondimensional time factor,  $T_d$ , is related to the real time “ $t$ ” by  $T_d = (kt) / (m_v \gamma_w a^2)$ .

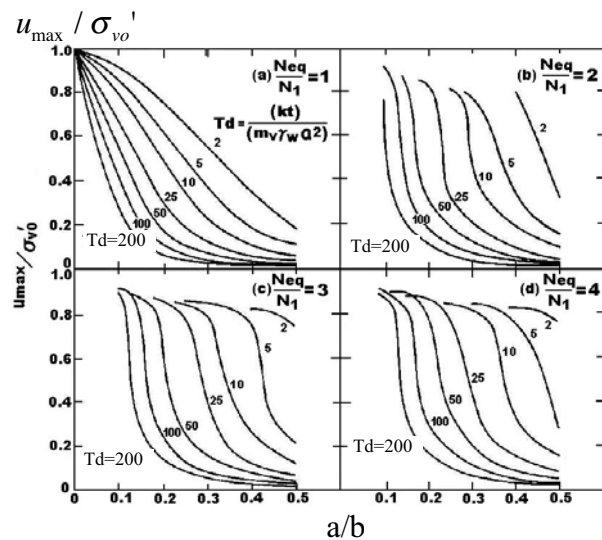


Fig. 26.88 Diagram for design of gravel drain (Seed and Booker, 1977)

Gravel drains functioned properly in Kushiro Harbor in 1993. Since it helps drainage, ground subsidence occurred to some extent after pore pressure dissipation; see an arrow in Fig. 26.89.

Recently, the number of construction of gravel drains is decreasing in Japan (Ohbayashi et al. 2006 and Fig. 26.7). This is because the major aim of liquefaction mitigation work has become preventing liquefaction during a very rare but strong earthquake (L2 design earthquake which would occur once every 500 or more years). Under this extremely strong earthquake, gravel drain cannot always maintain the excess pore water pressure less than 100%. This situation needs to be reexamined by taking into account the reinforcing effects of gravel piles that do not liquefy and maintain rigidity during shaking.

Stone column in Sect. 26.5 creates a similar column of gravel. Its difference from the gravel drain lies in ground vibration upon its installation.

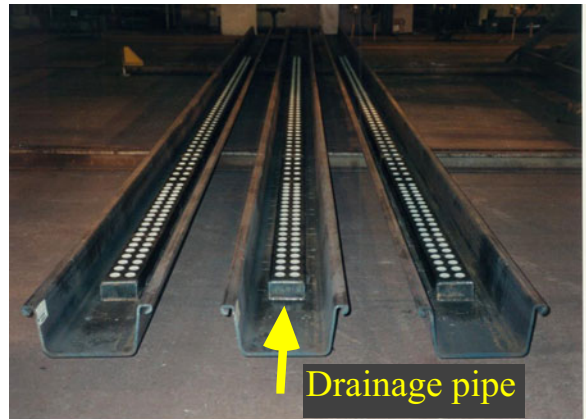
Drainage is achieved by installing pipes as well. Figure 26.90 shows a sheet pile wall to which a drainage pipe is attached. It is aimed to dissipate the excess pore water pressure around an embedded



Fig. 26.89 Subsidence of ground with gravel drains relative to stable quay wall (Kushiro Harbor, 1993)

sheet pile wall or in backfill behind a sheet-pile quay wall. This drain pipe can be combined with a steel pile as well.

A sheet pile equipped with drain is installed statically into ground as shown in Fig. 26.91. An embedded wall thus constructed is illustrated in Fig. 26.92. The advantage of a steel pile with drain was validated by field liquefaction test in which ground was shaken mechanically (Fig. 26.93) and excess pore water pressure was recorded near piles. Figure 26.94 indicates that excess pore water pressure near a drain pile was lower than the pressure near an ordinary pile without drain. In the second series of tests, piles were subjected to lateral load of 30 kN at the top (Fig. 26.93). It is seen in Fig. 26.95 that the lateral displacement of piles with drains was smaller than that of ordinary piles. It is thus concluded that drain reduces the excess pore water pressure around a pile and increases the lateral resistance in the subsoil.



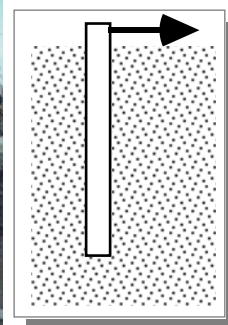
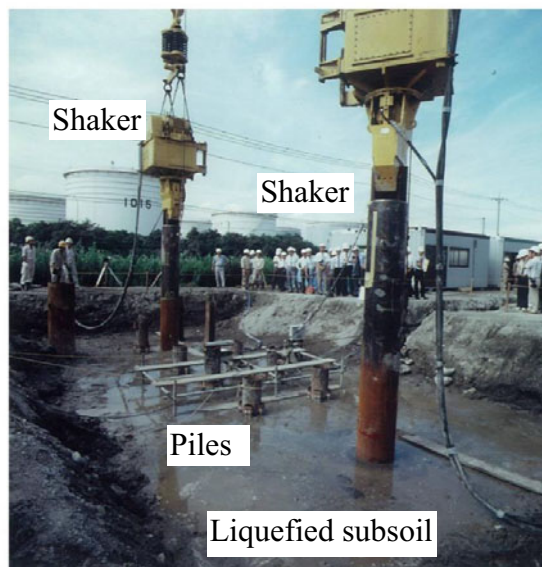
**Fig. 26.90** Sheet pile with attached drainage pipe (Sumitomo Metal Industries)



**Fig. 26.91** Installation of sheet pile wall with drain (Sumitomo Metal Industries)

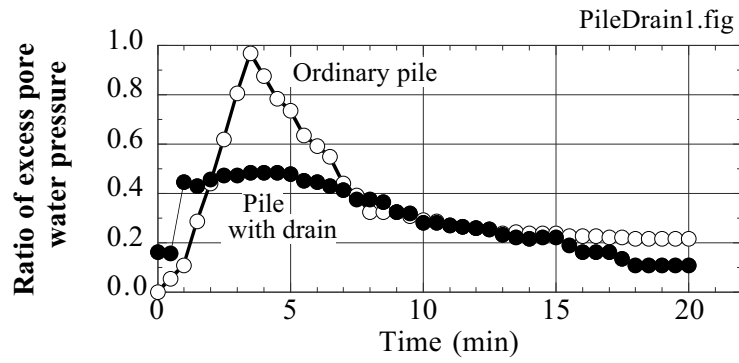


**Fig. 26.92** Appearance of sheet pile wall with drains (Sumitomo Metal Industries)

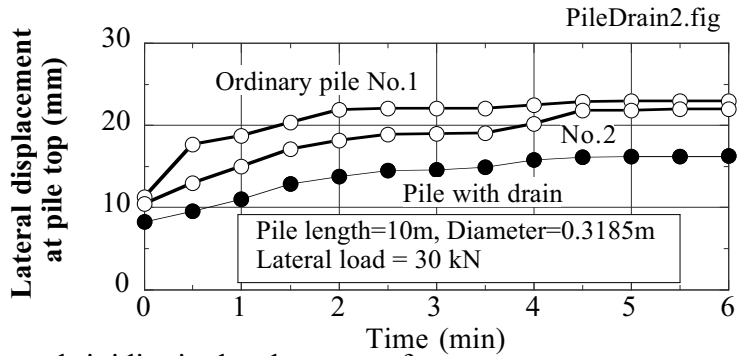


**Fig. 26.93** Field liquefaction test on lateral rigidity of piles (Sumitomo Metal Industries)

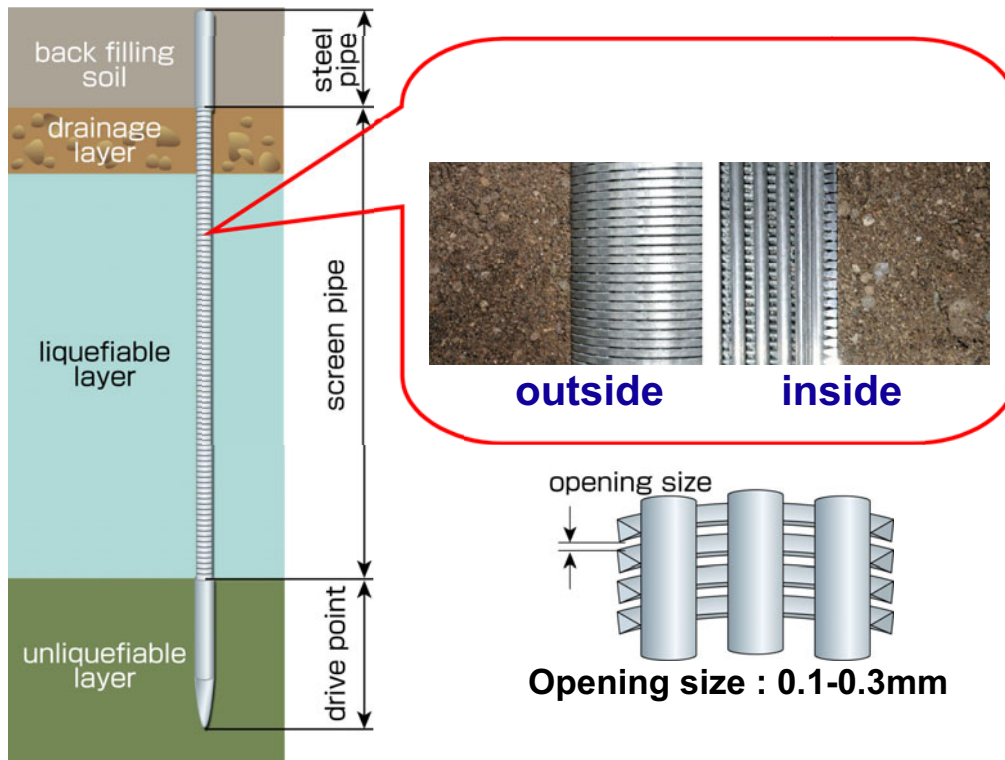




**Fig. 26.94** Difference in development of excess pore water pressure near piles with and without drain (Nishitani et al. 1992)



**Fig. 26.95** Different lateral rigidity in development of excess pore water pressure near piles with and without drain (Saimura et al. 1992)



**Fig. 26.96** Screen pipe (Zenitaka Corporation; Harada et al. 2006)

Figure 26.96 illustrates what is called a screen pipe. It is composed of slender rods in the axial direction combined with circular rings. The spacing of 0.1–0.3 mm between rings allows ground water to be drained into the hollow pipe. This pipe is dynamically penetrated into loose sand, and hence a relatively small equipment is good enough to install the pipe into liquefiable ground (Fig. 26.97). This implies that

a screen pipe can be installed from a basement of a building where the allowable height of installation machine is limited.

The effects of screen pipes were validated by shaking model tests (Sesov et al. 2001; Harada et al. 2006). In addition, field shaking tests were carried out by generating liquefaction artificially by a pile driver (Fig. 26.98). Figure 26.99 indicates the effects of screen-pipe spacing on the ratio of excess pore water pressure and the initial effective overburden stress: 1.0 means complete liquefaction. It is seen that screen pipes made excess pore water pressure lower within 5 m from the source than what was measured without pipes. This is particular the case when the spacing of pipes was 0.5 m. Moreover, the shorter the pipe spacing, the lower the excess pore water pressure. After tests, the screen pipes were excavated to show that ring spacing was not clogged by soil.

(a) By manual operation of pneumatic equipment



(b) By small boring machine



Fig. 26.97 Installation of screen pipe (Zenitaka Corporation)



Fig. 26.98 Artificial vibration by pile driver (Zenitaka Corp.)

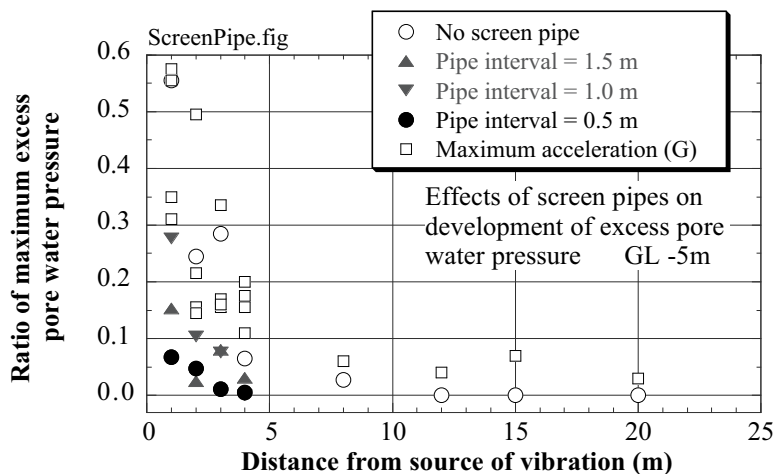


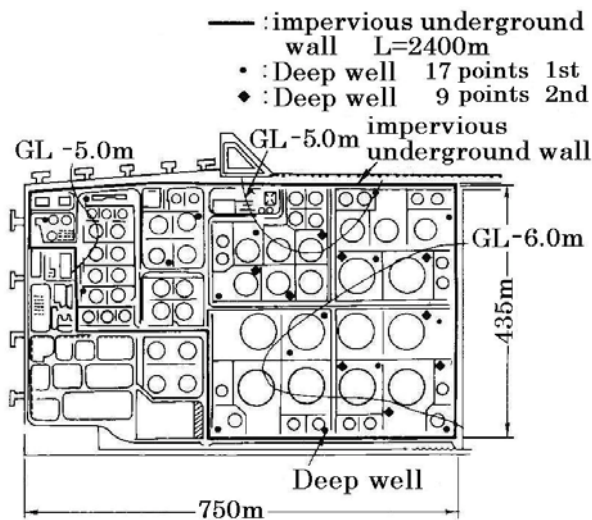
Fig. 26.99 Excess pore water pressure with and without screen pipe (field test by Zenitaka Corporation, Harada et al. 2006)

## 26.12 Lowering of Ground Water Table

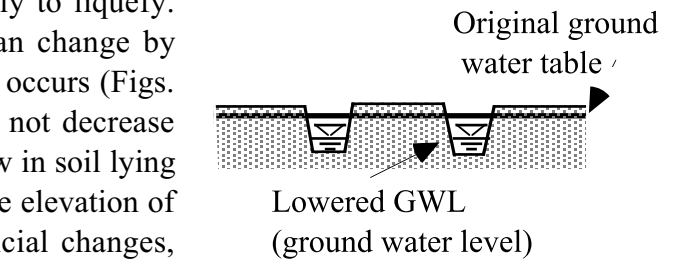
When sand is not saturated with water, it is unlikely to liquefy. This is because the volume of unsaturated sand can change by compressing the volume of pore gas when dilatancy occurs (Figs. 18.2 and 26.9). Therefore, the effective stress does not decrease significantly and the liquefaction potential is very low in soil lying above the ground water table. Note, however, that the elevation of ground water table is subject to seasonal and artificial changes, and the information described in a bore hole log may not be reliable.

One of the mitigation measures against liquefaction is, therefore, dewatering that makes sand unsaturated. The simplest way of dewatering is the use of a trench (Fig. 26.100). This method is feasible along dikes which is too long to practice more expensive methods but has to be protected from liquefaction.

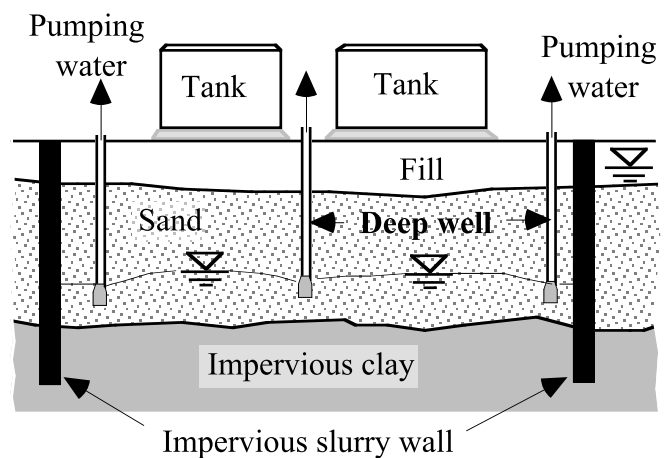
A more powerful dewatering was carried out in a reclaimed land in Kawasaki (川崎) City. A site of an oil refinery plant had a liquefaction-prone sandy subsoil. Many existing facilities in the plant, such as tanks and pipes, made vibratory compaction impossible. Since this sandy layer was underlain by an impervious clayey layer, it was decided to surround the site by an impervious underground wall (止水壁), prevent inflow of water from the outside and from the bottom, and remove water inside by using deep wells (Figs. 26.101 and 26.102).



**Fig. 26.101** Plan view of site of dewatering by means of deep well (JGS, 2004b, p. 351)



**Fig. 26.100** Lowering of ground water table by a trench



**Fig. 26.102** Cross section of dewatering

The impervious wall was made of locally available soil mixed with bentonite, and had a permeability of  $10^{-7}$  cm/s. Being flexible, this wall was expected to follow the deformation of the surrounding ground without cracking. Note that the dewatering and consequent increase in effective stress may trigger ground subsidence which may be hazardous to existing facilities.

Okamura and Teraoka (2005) conducted model tests in which air bubbles were pushed into sandy ground model that was initially saturated with water. It was shown by this desaturation that air bubbles reduced the development of excess pore water pressure and, more remarkably, the subsidence of foundation which was placed on the ground surface. There is a fear that the global warming would raise the sea water level and, consequently, the ground water table. The higher ground water level may increase the thickness of liquefied soil and cause more significant damage.

### 26.13 Grouting and Deep Mixing

Grouting develops stiff bonding among sand grains and prevents negative dilatancy of particle displacement (Fig. 18.3). Consequently the liquefaction resistance of sand is improved drastically. This effect is obtained by mixing sand with cement-like materials which are either dry or wet; choice which depends upon availability of water in ground. While liquefiable ground has ample water, grouting is practiced for such nonseismic purposes as construction of underground walls and others as well. The grouted sand has an unconfined compression strength of, typically,  $q_u = 300\text{--}500$  kPa.



**Fig. 26.103** Deep mixing of liquefiable sand for reinforcement of river dike



**Fig. 26.104** Construction machine for deep mixing method



**Fig. 26.105** Mixing tip of deep mixing machine under water flushing for cleaning



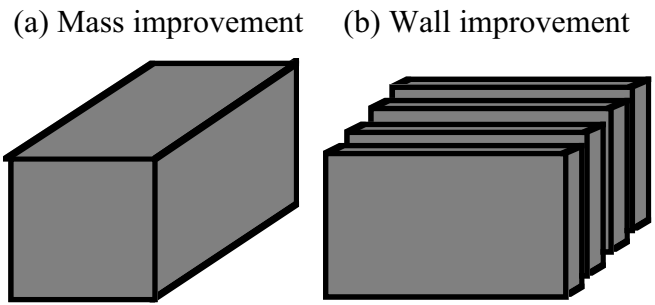
**Fig. 26.106** Tip of deep mixing machine



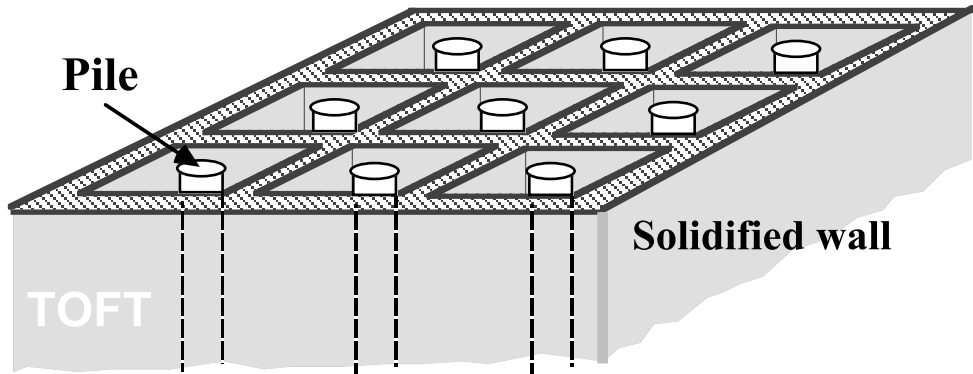
**Fig. 26.107** Reconstructed shape of Yodo River dike in Osaka

Deep mixing is a name of grouting which is carried out by mixing soil with a cement-like material either by jetting or by mechanical mixing. Deep jet mixing (DJM) mixes cement powder with soil, and ground water is used to start solidification. Apparently, this technology is not useful in dry soil. On the other hand, CDM (cement deep mixing) mixes cement slurry (water/cement ratio = 0.8–1.2). This technology may not be good in such soil of very high water content as peat, because the additional water in slurry

may make the soil even softer. Figure 26.103 indicates an example of mechanical mixing. The machine in Fig. 26.104 is equipped with two or three mixing rods which rotate in ground in different directions and mix soil with cement. Figs. 26.105 and 26.106 demonstrate the details. The deep mixing method was employed in reconstruction of the Yodo River dike (Fig. 17.35) which was destroyed by subsoil liquefaction during the 1995 Kobe earthquake (Fig. 26.107).



**Fig. 26.108** Configuration of ground improved by deep mixing



**Fig. 26.109** Square lattice configuration of grouted wall

Deep mixing was originally practiced to create a mass of grouted soil (Fig. 26.108a). As is well known in construction of slurry wall or diaphragm wall, it is also possible to construct a solidified wall (Fig. 26.108b) which is more economical than mass construction.

An interesting example of wall improvement has a square lattice configuration. In Fig. 26.109, pile foundation was installed inside the square space, thus liquefaction was prevented by the constraining effects of the grouted walls, while the bearing capacity and inertia force of the super structure were borne by piles. This idea worked remarkably during the 1995 Kobe earthquake.



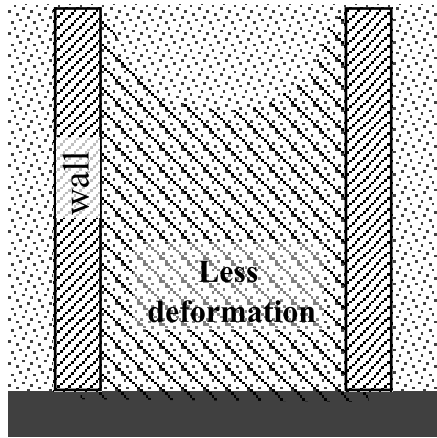
**Fig. 26.110** Hotel building which survived the 1995 Kobe earthquake (photograph by Takenaka Corporation)



**Fig. 26.111** Appearance of lattice structure immediately after installation (photograph by Takenaka Corporation)

Figure 26.110 shows a hotel building in Kobe Harbor in 1995. Although significant damage occurred in the water front ground upon the earthquake and liquefaction, the structure of this building did not suffer much damage. Figure 26.111 shows the appearance of the top of the lattice wall. It is seen that the wall consists of cylindrical columns of solidified soil.

The mitigative effects of the lattice wall come from the constraint of shear deformation of soils. As shown in Sect. 18.1 and Sect. 18.7, the onset of liquefaction is associated with substantial shear deformation (Fig. 20.2). Since the lattice wall does not deform during shaking, the soils inside the wall cannot distort significantly except near the ground surface (Fig. 26.112). Figure 26.113 is an evidence that no liquefaction occurred inside the lattice structure.



**Fig. 26.112** Constraint of shear deformation by embedded wall



**Fig. 26.113** Ground surface without sand boiling after Kobe earthquake inside lattice wall (timber columns are temporary supports during excavation (photograph by Takenaka Corporation))

## 26.14 Solidification by Colloidal Silica Grout

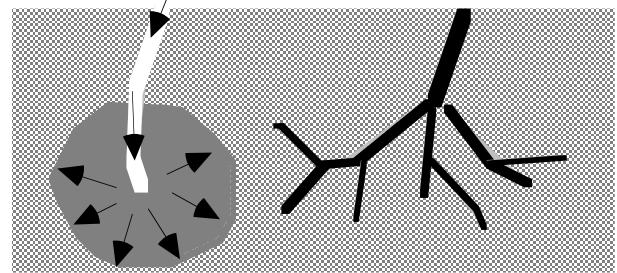
The use of liquid grout is popular in many aspects of soil improvement in geotechnical engineering. However, its use has been mostly limited to such temporary purposes as prevention of water seepage, generation of bearing capacity during construction, and rock stabilization in tunnel excavation. Permanent effects of soil improvement were not expected in the use of liquid grout because the following requirements were not satisfied:

1. No deterioration in mechanical strength (no weathering)
2. Uniform seeping of liquid
3. Not being harmful to human health

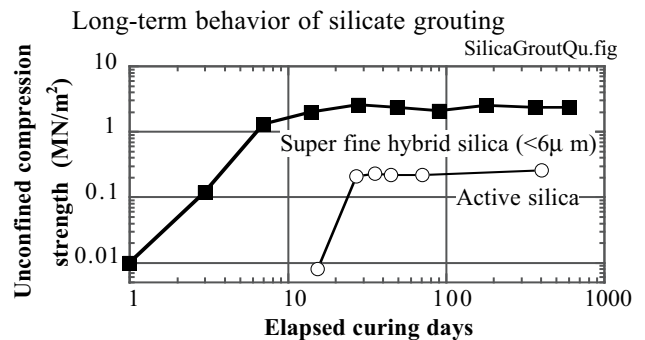
Among them, the second issue means that concerned soil has to be improved uniformly (Fig. 26.114). Improvement only in cracks is not accepted, which is opposite from the practice in rock mechanics and tunneling. A recent technical development has achieved a new grouting material (colloidal silica) that satisfies those three requirements mentioned above. Thus, the use of permanent grout is now in practice.

Yonekura and Shimada (1992) conducted tests on specimens of as long as 1,000 days of age. Figure 26.115 illustrates the temporal variation of unconfined compression strength of improved sand. It is shown therein that the strength was maintained constant without deterioration for 2 years. Furthermore, sandy ground that was grouted 16 years and 10 month ago was studied (Yonekura and Shimada, 2006). The unconfined compression strength of 11 undisturbed samples with active silica ranged between 0.28 and 0.47 MN/m<sup>2</sup> with the average of 0.38 MN/m<sup>2</sup>. To obtain the strength at very young age, the same sand was collected and treated by the same grout (active silica sol). The unconfined compression strength of this young grouted sand was 0.65 and 0.34 MN/m<sup>2</sup>. Thus, it was concluded that the strength of grouted sand did not deteriorate over 16 years.

(a) uniform seeping (b) improvement only along cracks



**Fig. 26.114** Configuration of ground improvement by injection of liquid grout



**Fig. 26.115** Long-term stability in unconfined compression strength of sand improved by silicate grout (Miwa et al. 2001; Yonekura et al. 2001).

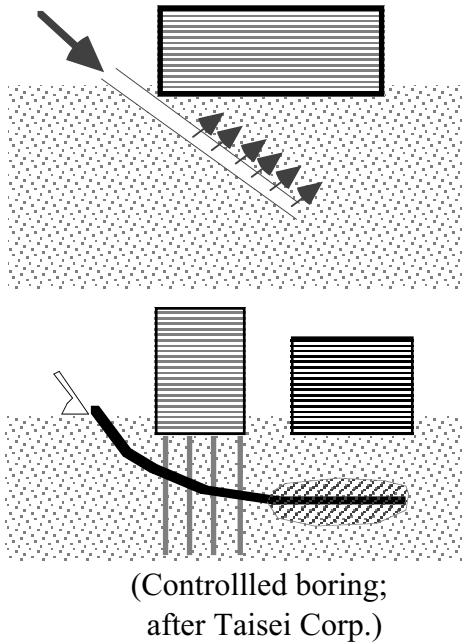


**Fig. 26.116** Injection of silica liquid through multiple tubes into sandy ground



**Fig. 26.117** Excavation of soil mass solidified by silica grouting

Liquid of colloidal silica is injected into ground through tubes or pipes under relatively low pressure. Figure 26.116 shows the ongoing injection through multiple tubes, and a good size of solidified mass of soil is formed. The very small size of colloidal silica particles (typically 10 nm) makes it possible for the silicate grout to seep into fine and silty sand. Figure 26.117 manifests an excavated mass, which is an evidence of uniform seeping due to very low viscosity and very fine size of silica grains in the liquid. The liquid solidifies within 1 h or a few days, depending upon its chemical composition.



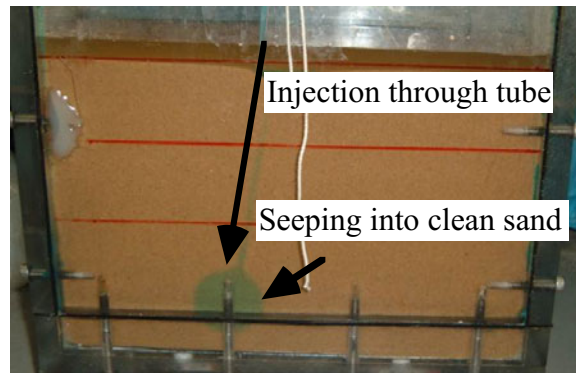
**Fig. 26.118** Soil improvement under existing structure



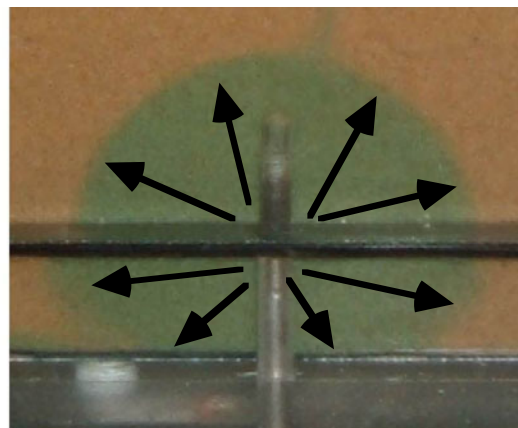
**Fig. 26.119** Inclined drilling of bore hole for grouting under existing structure (Toa Corporation)



**Fig. 26.120** Example of nozzle for injection of liquid (Pentaocean Inc.)



**Fig. 26.121** Uniform seeping test in sandy model ground

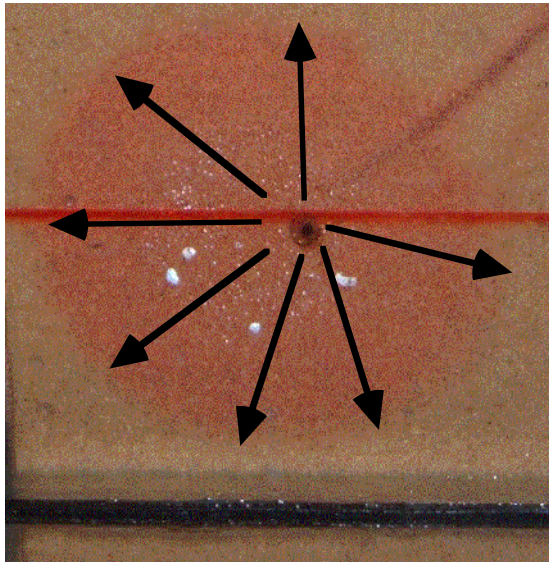


**Fig. 26.122** Detailed photograph of uniform seeping

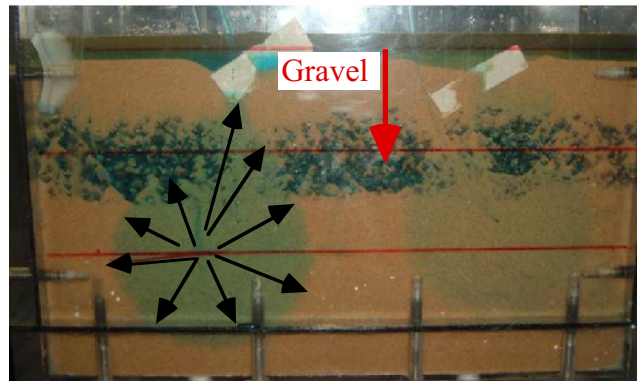
One of the advantages of the injection of colloidal silica liquid is its capability to improve soils under existing structures (Fig. 26.118). This is important because most of other soil improvement methods cannot do this job except compaction grouting (Sect. 26.10). Soil under an existing structure is improved by drilling a hole in an inclined direction (Fig. 26.119) and installing an injection nozzle (Fig. 26.120).



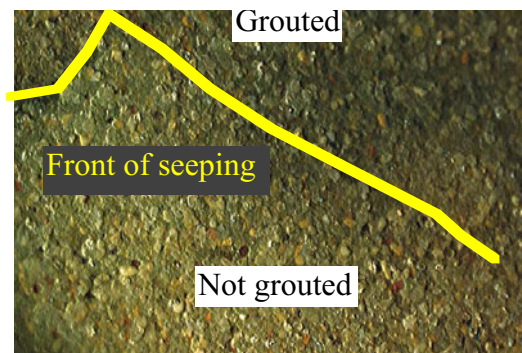
The extent of uniform seeping was examined by reproducing the process in a laboratory model ground (C. Conlee of Drexel University during her internship at University of Tokyo). Liquid of colloidal silica was injected under low pressure into sandy ground, and the observation of seeping was made easy by dyeing the liquid with green color (Fig. 26.121). The detail shown in Fig. 26.122 verifies the idea of uniform seeping. This extent of uniform seeping is equivalent with that of water, which is demonstrated by red color in Fig. 26.123. Finally, Fig. 26.124 indicates that the colloidal silica liquid can seep uniformly even into sandy ground with gravel layer in spite of the permeability contrast. Figure 26.125 is a microscopic photograph of the seeping front, which confirms that seeping of colloidal silica proceeds uniformly.



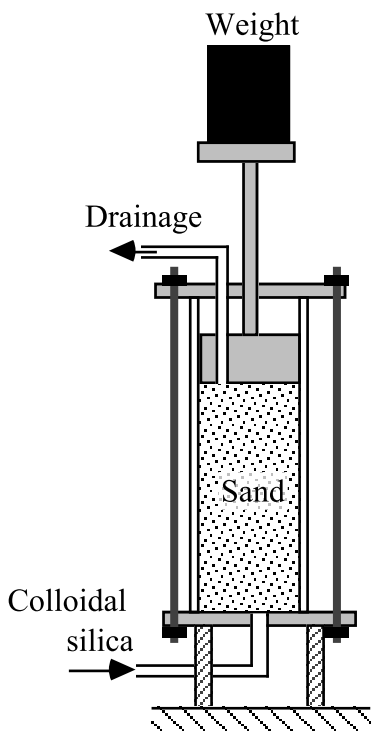
**Fig. 26.123** Seeping of dyed water into clean sand



**Fig. 26.124** Uniform seeping of colloidal silica liquid into nonuniform model ground

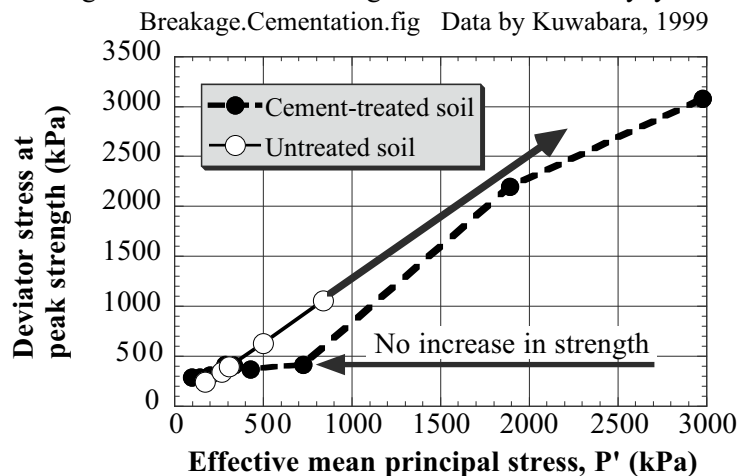


**Fig. 26.125** Microscopic photograph of uniform seeping of colloidal silica

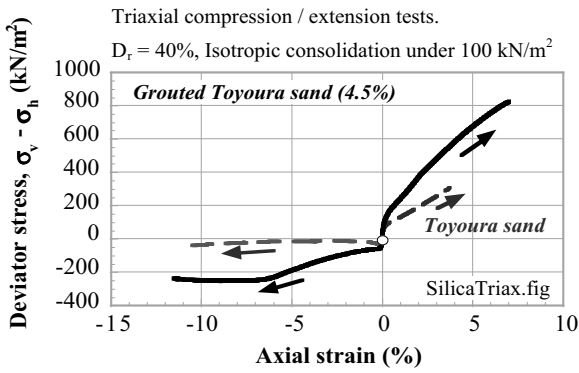


**Fig. 26.126** Curing of sand treated by colloidal silica liquid

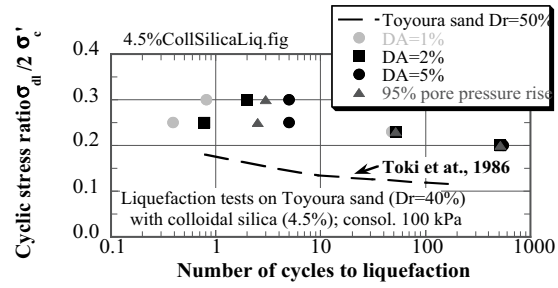
Breakage of cementation during consolidation of clayey soil



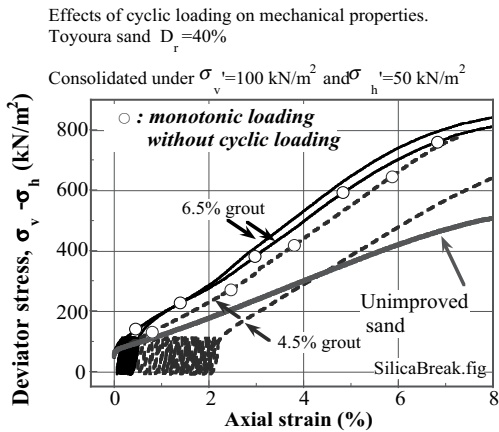
**Fig. 26.127** Example of destroyed cementation due to consolidation volume change in clayey soil mixed with cement



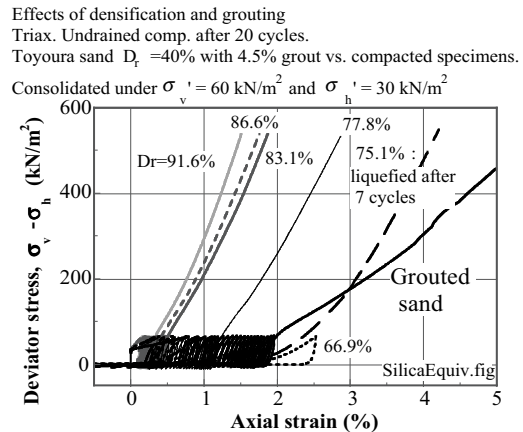
**Fig. 26.128** Comparison of sand improved by colloidal silica and untreated sand by means of monotonic undrained triaxial tests



**Fig. 26.129** Resistance of sand against liquefaction increased by colloidal silica



**Fig. 26.130** Effects of cyclic loading on subsequent rigidity of grouted sand



**Fig. 26.131** Densification of sand equivalent to grouting



**Fig. 26.132** Appearance of pure colloidal silica after curing

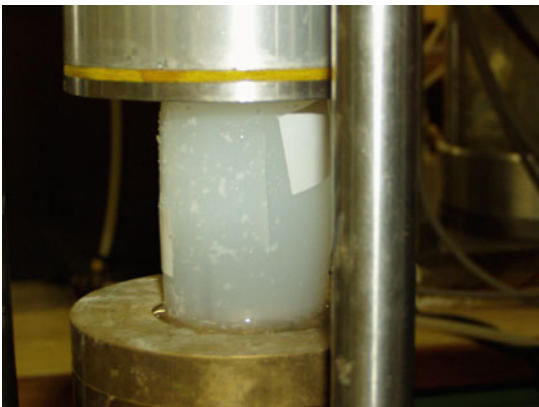
Laboratory shear tests were carried out on the effects of colloidal silica on mitigation of liquefaction resistance of loose sand (Kabashima and Towhata, 2000; Towhata and Kabashima, 2001). Tested specimens were prepared by reproducing the in-situ stress history as much as possible; loose water-saturated sand was consolidated in a  $K_0$  manner (Fig. 26.126), silicate liquid seeped into sand under the anisotropic consolidation pressure, and then the sand was cured for five weeks under pressure. Curing under pressure was considered important because of the possibility that consolidation and deformation of

sand after curing might destroy bonding that was developed by solidified silica. An example of broken bonding is illustrated in Fig. 26.127 in which cement mixed clay did not develop further shear strength until cementation was destroyed by consolidation volume change; after breakage the frictional strength increased together with the consolidation stress. Specimens thus prepared were first tested by undrained triaxial monotonic tests: both compression and extension tests. In Fig. 26.128, sand that was improved by silica shows better behavior than untreated sand. Liquefaction resistance was improved by colloidal silica as well (Fig. 26.129).

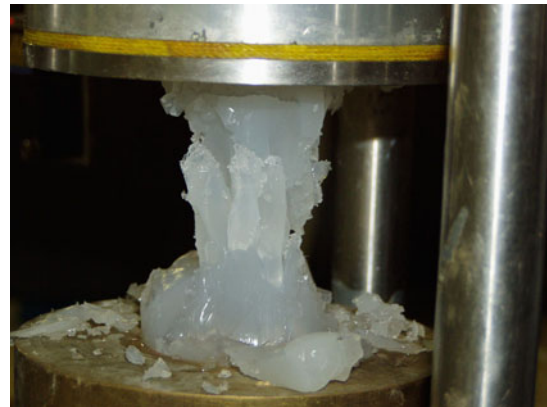
One of the study concerns lay in the possible breakage of bonding and grouting effects due to cyclic loading. It was feared that the first strong earthquake may be well resisted by bonding but that future earthquakes might not be. This issue was investigated in Fig. 26.130 where sand improved by colloidal silica was subjected to cyclic loading until a certain magnitude of strain occurred and then was sheared in a monotonic undrained manner. It can be found in this figure that stiffness of the improved sand (tangent of stress–strain curve) after cyclic loading is still similar to that of sand without cyclic loading and is certainly better than that of unimproved sand. Thus, no fear is needed of breaching of grouting effects.

In Fig. 26.131, sand of 40% relative density was improved and was compared with densified sand without grouting. This comparison was made in terms of the residual deformation after 30 cycles of triaxial compression as well as the monotonic behavior after this cyclic undrained loading. It may be found that the behavior of grouted sand is equivalent with densification to 80% relative density.

Figure 26.132 shows the appearance of solidified colloidal silica. It is substantially soft and, hence, it is difficult to understand why such a soft material improves the mechanical behavior of sand. One possible answer to this question may be the volume compressibility of this material (Di Benedetto, 2001). Being soft, this material decreases its volume upon compression and allows less excess pore water pressure to develop than water which is practically incompressible. Note that excess pore water pressure is generated in consequence of incompressibility of pore water upon negative dilatancy of sand (Fig. 18.3).



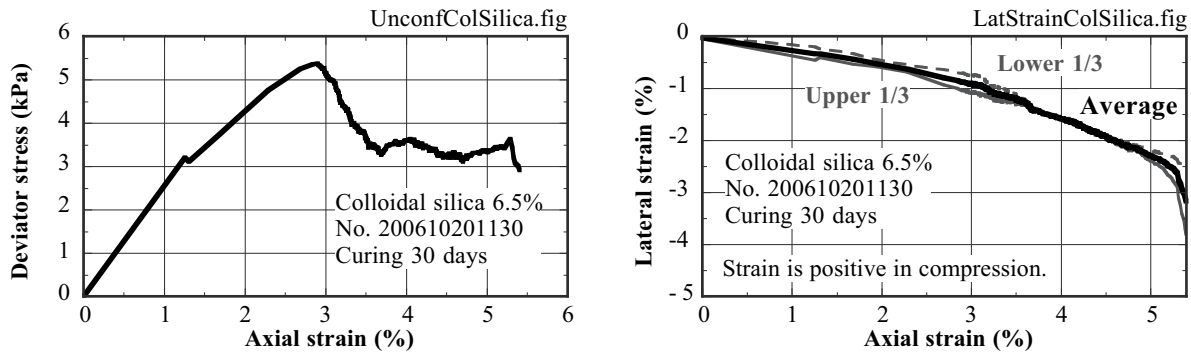
**Fig. 26.133** Unconfined compression test on solidified colloidal silica material



**Fig. 26.134** Ultimate shape of colloidal silica sample after failure in unconfined compression test

To understand the mechanical behavior of solidified colloidal silica, a series of unconfined compression tests were carried out on the solidified colloidal silica. Fig. 26.133 shows a specimen prior to test; the sample measured 7.0 cm in height, 4.7 cm in diameter, and 129 g in weight. The tested material was cured for 30 days in water so that drying might be avoided. Figure 26.134 illustrates the shape of the sample after failure. Due probably to some heterogeneity, the central part remained after large deformation.

The test results are presented in Fig. 26.135. The special interest lay in the measurement of lateral strain. Hence two sets of laser displacement transducers were placed at 1/3 and 2/3 of the sample height in order to monitor the lateral displacement at the sample surface. As seen in Fig. 26.133, sheets of white paper were attached to the surface so that reflection of laser beam was facilitated. The test results in Fig. 26.135 indicates that the ratio of axial and lateral strains, which is namely the Poisson ratio  $\nu$ , is around 0.3. Thus, the material has a volume compressibility; if  $\nu = 0.5$ , volume does not change during shear. It is therefore possible that the liquefaction resistance of sand is improved by volume compressibility of solidified colloidal silica. It should be recalled that constant volume of pore water is the important cause of high excess pore water pressure during undrained shear (Sect. 18.1). On the contrary, unsaturated soil is less likely to liquefy because volume of pore air can change (Okamura and Soga, 2006).



**Fig. 26.135** Result of unconfined compression test on solidified colloidal silica sample

Gallagher and Mitchell (2002) made use of the low cohesion of the colloidal silicate liquid for simple soil improvement. In their attempt, the liquid simply seeped into subsoil under gravity and liquefaction resistance of solidified sand was improved. It is noteworthy that solidification did not occur under alkaline environment ( $\text{pH} > 7$ ) due to electric nature of colloid particles. Another important point is that the mechanical properties of solidified sand such as CPT resistance and S-wave velocity do not increase in spite of the apparently improved resistance against liquefaction (Gallagher et al. 2007). This is probably because the colloidal silica even after curing is not such a rigid material as cement (Fig. 26.132). The improved liquefaction resistance comes from a different mechanism (Fig. 26.135).

### 26.15 Premixing Method

Most soil improvement methods intend to treat subsoil that already exists under the ground surface. It seems to be a good and efficient idea, in contrast, to create a good subsoil condition at the time of reclamation in place of making liquefaction-prone ground and improving it afterwards. This idea has been realized by the premixing method in which soil and a few percent of cement are mixed prior to reclamation. Premixing is expected to form a cemented contact between grains.

Saxena et al. (1988) mixed sand with a few percent weight of cement to show that liquefaction resistance increased substantially. Moreover, curing for 35 days increased the liquefaction resistance and made it equal to the ultimate value. Zen (1990) conducted a comprehensive study on the application of this idea to land reclamation technology. His drained triaxial compression tests revealed that premixing of sand with cement increased the cohesion while the frictional angle was more or less unchanged (Fig. 26.136). It was thus found that premixing of 5.5% of cement was equivalent to SPT-*N* of 15–20, while the equivalent unconfined compression strength was around 100 kPa. The premixed sand exhibited reduced permeability (*k*) of  $10^{-4}$  to  $10^{-6}$  m/sec. This value was 10% of the permeability of untreated sand. Since the volume compressibility, *m<sub>v</sub>*, decreased to 10% as well, the consolidation time was considered unchanged; Terzaghi consolidation theory (Sect. 1.4) states that consolidation time is governed by  $C_v = k / (m_v \gamma_w)$ . Thus, premixing of 5% cement content appears good to prevent the onset of liquefaction.

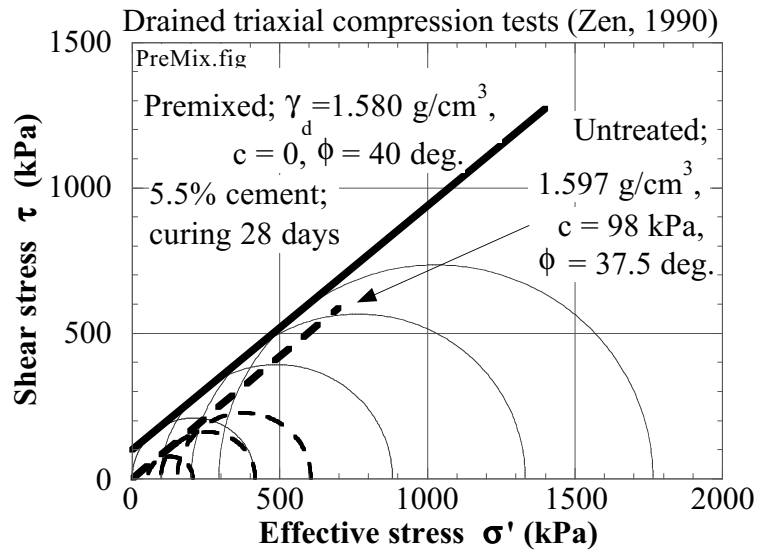


Fig. 26.136 Drained shear strength of premixed sand (drawn after Zen, 1990)

Having been employed in many land reclamation projects in water-front areas, the premixing method have such advantages as the following:

1. Time saving because soil improvement is not necessary after reclamation
2. Applicability to deep-water area

Possible disadvantages may be the variation of soil strength depending on soil type, and possibility of water contamination. Evidently, premixing is not possible in existing ground.

A technology that is somewhat similar to premixing is available for liquefaction-countermeasure against floating of sewage pipeline. Floating of an embedded sewage pipeline together with man holes is one of the important problems due to liquefaction (Fig. 26.137 together with Figs 17.17 and 17.18). Since sewage water flows under gravity, any change of pipeline slope due to floating affects its operation. A schematic

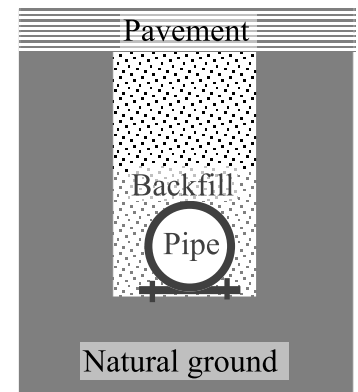


Fig. 26.137 Uplift of sewage manhole and boiled sand as evidence of backfill liquefaction (Ojiya City, 2004 Niigata Chuetsu earthquake)

Since sewage water flows under gravity, any change of pipeline slope due to floating affects its operation. A schematic

illustration of an embedded pipeline is presented in Fig. 26.138. Floating is caused by liquefaction in the backfill sand in areas where the ground water table is high. Figure 24.13 indicated similar floating caused by a nonseismic mechanism.

To avoid floating, it is required to densify or compact the backfill soil in the trench. This is, however, difficult in many cases because it is worried to damage a pipe upon compaction. Compaction of backfill soil under the pipe is certainly difficult. An alternative measure is the use of pervious gravelly soil in place of sand as a backfill material. This is not practical, however, when gravel is not available at a reasonable cost. A second alternative is mixing sand with cement. Yasuda and Kiku (2006) reported mixing cement with backfill sand at a rate of 20 kg of cement with 1 m<sup>3</sup> of dry sand. They also pointed out that liquefaction risk in backfill soil is higher if the natural ground is made of clayey soil, whose low permeability does not allow dissipation of excess pore water pressure in the backfill soil.



**Fig. 26.138** Schematic cross section of embedded pipeline

It is a promising idea to recycle waste soil generated by such geotechnical projects as excavation of basement, subway, and sewage pipeline trenches. The waste soil is mixed with cement, gravel, and water in a special factory (Fig. 26.139 流動化处理土), and is sent to filling projects. Before solidification, this soil has a reasonable fluidability (Fig. 26.140) and is easy to transport. After curing and solidification, this soil has good resistance against liquefaction. Another attempt of recycling waste car tires for liquefaction resistant backfill will be presented in Sect. 26.17.



**Fig. 26.139** Production factory for mixing waste soil with cement, gravel, and water



**Fig. 26.140** Fluid nature of fluidized soil

**26.16 Soil Densification by Blasting**

Figure 18.14 showed the ongoing blasting of liquefiable sand in Tokachi Harbor of Japan. Densification of loose sand by blasting is an attractive idea in the sense that it is economical and time saving. Its disadvantage is evidently the noise and ground vibration, and hence it is not feasible in populated areas.

Sato Kogyo Company in Tokyo carried out experimental blasting tests in Toyohashi Harbor in 2004. Many bore holes were drilled in the experimental site and several explosives were installed in each hole. Blasting was conducted in a controlled manner with short time intervals between individual explosions so that the interpretation of ground shaking data could count the number of explosions and detect any incomplete blasting. Figs 26.141 and 26.142 illustrate the ongoing blasting. Gas leaked out of the drilled holes and sand boiling occurred as an evidence of liquefaction and volume contraction.



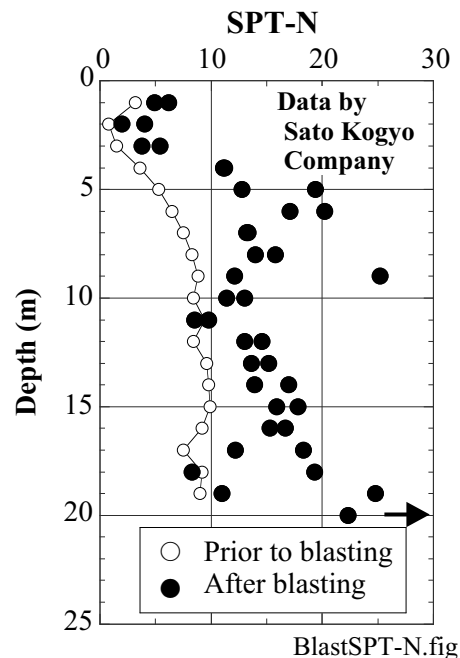
**Fig. 26.141** Blasting and leaking gas from bore hole



**Fig. 26.142** Liquefaction caused by blasting



**Fig. 26.143** Embedded sheet pile wall for insulation of ground from vibration



**Fig. 26.144** SPT-*N* values before and after blasting

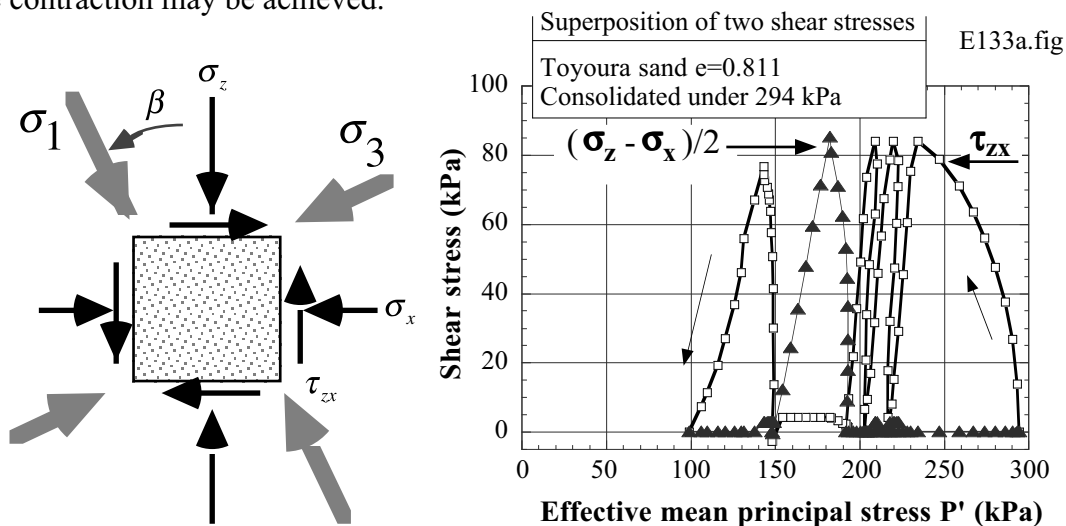
Figure 26.143 shows an attempt to mitigate the problem of ground vibration outside the test area. A sheet pile wall was embedded outside the area and propagation of ground vibration was mitigated. This kind of technical development is very important.

Figure 26.144 indicates SPT-*N* before and after blasting. It is seen that SPT-*N* increased substantially, validating the efficiency of blasting. However, under such circumstances as the design earthquake is

intended to be a very rare and strong one,  $SPT-N > 20$  is desired. To achieve this goal, more technological development is needed. There are several reports from sites of blasting in which cone penetration resistance increased with time after blasting over such a long time period as more than ten months (Charlie et al. 1992, Gohl et al. 2000; Ashford et al. 2004). Similar to this,  $SPT-N$  may increase further after several weeks (Fig. 26.59), since the post-blasting data was measured within one week after blasting when the subsoil may still have excess pore water pressure.

The current practice of blasting ignites dynamites from one side of a site towards the other. The order of blasting is not well investigated. This is in a clear contrast with the tradition of blasting in tunneling where the order and intensity of blasting have been studied elaborately so that the best efficiency may be achieved.

One shot of blasting generates one cycle of loading of compressional stress (major principal stress,  $\sigma_1$ ) in the direction of P-wave propagation. When the location of blasting changes, the direction of wave propagation and the orientation of  $\sigma_1$  stress change. According to the knowledge of soil mechanics on induced anisotropy of sand (Oda, 1972; Arthur et al. 1977; Yamada and Ishihara, 1981 and 1983), change of  $\sigma_1$  direction has a significant effect on development of excess pore water pressure and consequent volume contraction; stress-induced anisotropy. It is therefore proposed to make a special arrangement in the order of blasting (Wassan et al. 2006) so that the best efficiency of  $\sigma_1$  rotation and volume contraction may be achieved.



**Fig. 26.145** Effects of changing orientation of principal stress on development of excess pore water pressure in undrained shear on loose sand

A special consideration was made of the stress-induced anisotropy for better efficiency in blasting. According to Oda (1972), loading of stress to large deformation changes the statistic distribution in orientation of grain-to-grain contact planes, thus increasing the rigidity of sand in the same direction of loading (major principal stress,  $\sigma_1$ ) as in the previous loading, while the rigidity in the perpendicular direction is reduced. In line with rigidity, volume contraction due to dilatancy is reduced in the same direction of loading, while more contraction occurs upon perpendicular direction of loading. In the undrained repeated loading in Fig. 26.145, the first three cycles of loading were made by means of  $\tau_{zx}$ . The orientation of the major principal stress ( $\sigma_1$ ) was  $\beta = 45^\circ$ . Although the first cycle therein produced significant excess pore water pressure (decrease in effective mean principal stress,  $P'$ ), the second and the third cycles did not do so due to elasto-plastic nature of sand. The fourth cycle was conducted by  $(\sigma_z - \sigma_x)/2$  with  $\beta = 0^\circ$ , and the pore pressure developed significantly. This is a good example of stress-induced anisotropy. When the fifth cycle was carried out by  $\tau_{zx}$  again ( $\beta = 45^\circ$ ), the pore pressure developed remarkably as well. It is learned from this that changing the direction of  $\sigma_1$  helps develop higher excess pore water pressure, which results in more volume contraction after dissipation.



A study was made on effects of blasting sequence on efficiency in soil densification. In practice, blasting is fired with a time interval of, for example, 0.1 s so that any unsuccessful firing may be detected easily from a record of ground shaking. Hence, it is practical and possible to seek for a more efficient order of blasting. Figure 26.146 illustrates four investigated sequences of explosions. Note that the situation is idealized in a two-dimensional planar manner, while the reality is three-dimensional. Sequence 1 conducts blasting from one end of site towards the other, running always from left to right. This seems to be the current practice. In contrast, Sequence 2 changes the direction of blasting alternately. Sequence 3 was proposed to make more changes in principal stress orientation and more efficiency. Sequence 4 is basically similar to Sequence 1 except that the direction of sequence is oblique. Figure 26.147 illustrates P wave propagation from the source of blasting. The stress time history as produced by this P wave at the point of concern (Fig. 26.146) was reproduced in a torsion shear apparatus and the stress histories due to many consecutive blastings were superimposed on a sand specimen in an undrained manner. For more details, refer to Wassan et al. (2006), Sendir et al. (2006) and Towhata (2007).

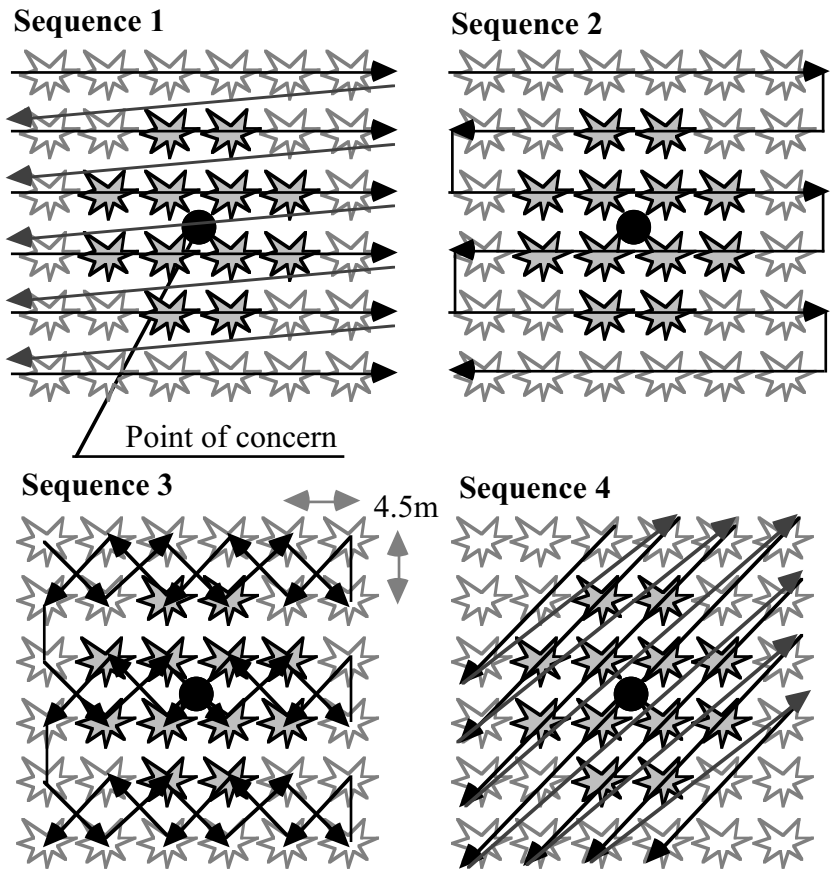


Fig. 26.146 Four sequences of blasting employed in study

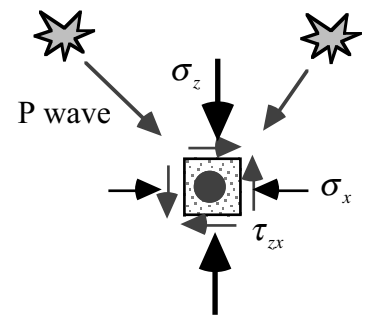


Fig. 26.147 P wave propagation generated by blasting

Figure 26.147 illustrates P wave propagation from the source of blasting. The stress time history as produced by this P wave at the point of concern (Fig. 26.146) was reproduced in a torsion shear apparatus and the stress histories due to many consecutive blastings were superimposed on a sand specimen in an undrained manner. For more details, refer to Wassan et al. (2006), Sendir et al. (2006) and Towhata (2007).

Figure 26.148 illustrates the shear stress–strain relationship as obtained from a laboratory reproduction of Sequence 1. The amount of explosive in a single blasting was assumed to be 2.5 kg. Both stress–strain curves (torsional and deviatoric stress–strain relationships) reveal that the maximum shear strain was less than 0.003 (0.3%). This is consistent with the stress-path diagram (Fig. 26.149) in which  $P'$  decreased from 50 kPa to 20 kPa, being still far from complete liquefaction.

Sequence 3, in contrast, produced greater deformation (Fig. 26.150) and higher excess pore water pressure (Fig. 26.151), although the same amount of explosive was assumed. Finally, the volumetric contraction after dissipation of the developed excess pore water pressure was summarized in Fig. 26.152. Data from two groups of test with consolidation pressure of 50 and 100 kPa is illustrated. Generally, Sequence 3 achieved the greatest volume contraction and densification than other sequences. It is therefore promising to seek for a better sequence that achieves more extent of change in principal stress orientation. It is important as well, however, that complicated order of blasting may cause trouble in practical setting of firing order.

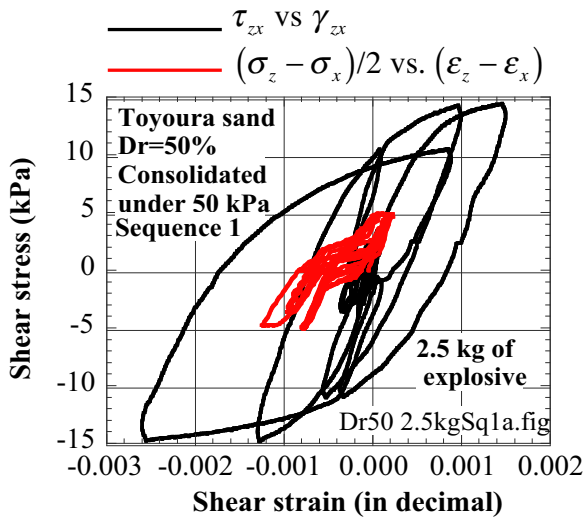


Fig. 26.148 Shear stress–strain relationships in laboratory reproduction of Sequence 1

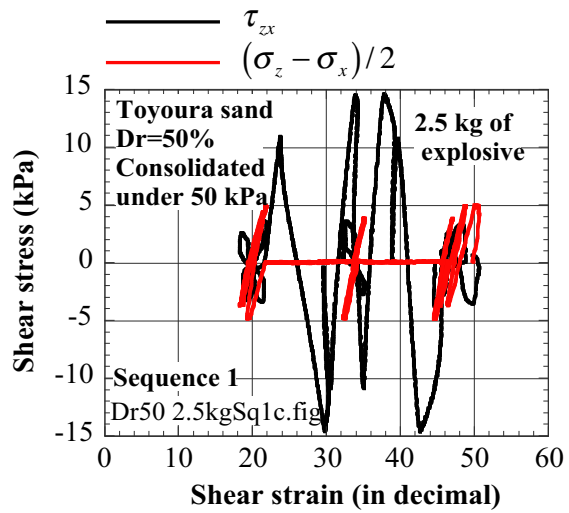


Fig. 26.149 Stress-path diagram in laboratory reproduction of Sequence 1

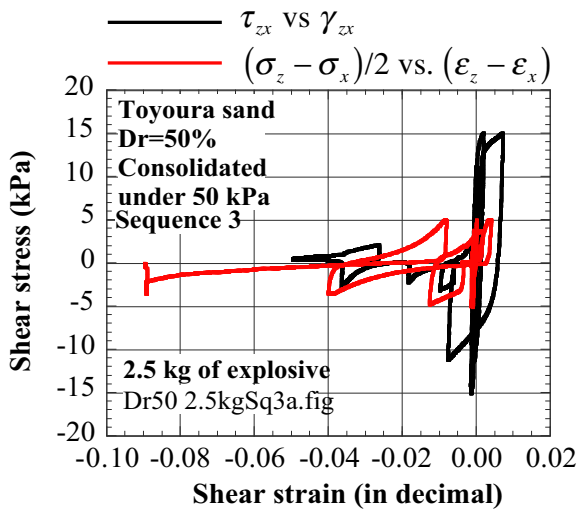


Fig. 26.150 Shear stress–strain relationships in laboratory reproduction of Sequence 3

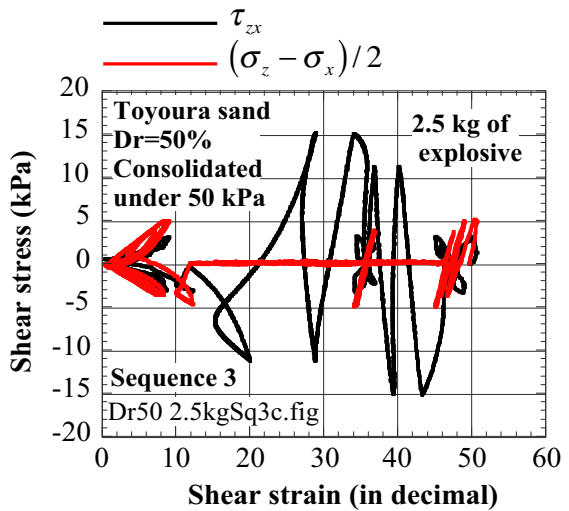


Fig. 26.151 Stress-path diagram in laboratory reproduction of Sequence 3

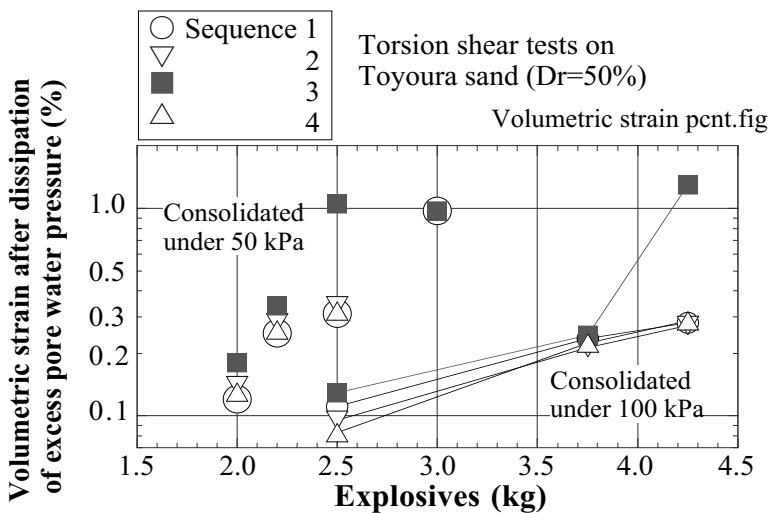


Fig. 26.152 Comparison of volume contraction after dissipation of excess pore water pressure

When liquefaction occurred during loading, test was terminated before completion of the entire stress history. This means that the true volume change would be greater than shown in this figure as inferred by arrows.

## 26.17 Backfilling by Shredded Tire Chips

There is a huge amount of waste car tires. Although most of them are used as fuel, there are still surplus waste whose recycling is an urgent issue. This section addresses the use of shredded tire chips for backfilling of pipelines, which achieves good resistance against liquefaction. Being recycling of waste, this idea appears to be more economical than mixing of sand and cement as described in Fig. 26.138.

Tire chips are produced by shredding the rubber part of a tire into small pieces (Fig. 26.153). Figures 26.154 and 26.155 compare cyclic undrained behavior of loose Toyoura sand (relative density,  $D_r = 30\%$ ) and mixture of Toyoura sand ( $D_r = 30\%$ ) with tire chips. The mixing ratio was 70% sand and 30% tire chips by weight. Evidently, mixture of tire chips improves the liquefaction resistance.



Fig. 26.153 Tire chips (Nguyen, 2007)

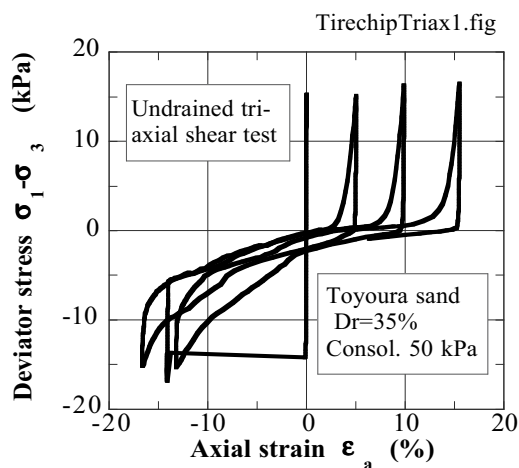


Fig. 26.154 Cyclic undrained triaxial test on loose Toyoura sand (Nirmalan, 2006)

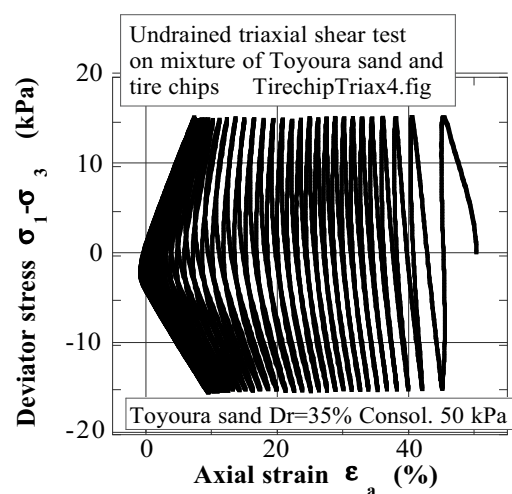
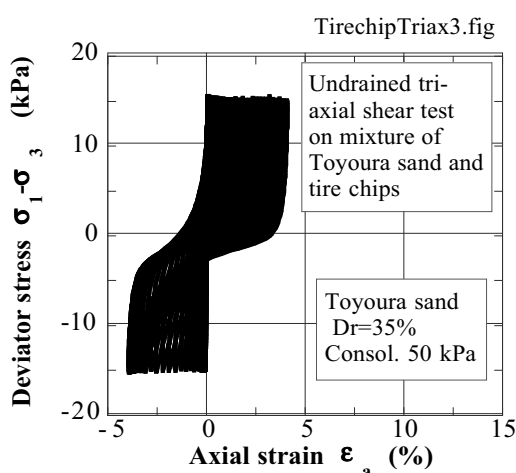
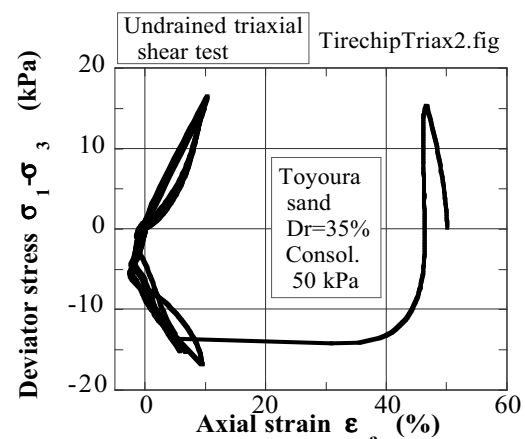


Fig. 26.155 Cyclic undrained triaxial test on mixture of loose Toyoura sand and tire chips (Nirmalan, 2006)

Based on the above finding, a shaking model test was conducted in 1-G field in which a pipe was embedded in two kinds of backfill materials. The backfill was made of Toyoura sand or its mixture with tire chips. To study the extreme situation, no compaction was made of the backfill. The base shaking had

400 Gal in amplitude and 5 Hz in frequency, lasting for 60 s. The excess pore water pressure in the tire-chip mixture was lower than that in sandy backfill, and, consequently, the floating of the embedded pipe was reduced as shown in Fig. 26.156. It is again evident that floating was reduced by mixing with tire chips.

The reason for the increased liquefaction resistance of tire chip mixture is probably that the rigidity of tire chip particles is lower than that of sand grains, allowing some volume compression under developed excess pore water pressure. Thus, the volume compression of tire chip produces a situation similar to drainage or dewatering which decrease the extent of excess pore water pressure.

Another advantage of tire chip backfill lies in its softness. Even when the surrounding ground (or road embankment) develops some lateral displacement, the soft tire-chip backfill does not produce such high earth pressure on a pipe as rigid sandy backfill. To support this, Fig. 26.157 compares drained stress-strain behavior of Toyoura sand and Toyoura sand mixed with tire chips. In the strain range less than 3%, the tire-chip mixture is softer than sand.

One possible problem in tire-chip backfilling is the long-term subsidence of the backfill undergoing daily traffic load. This issue was investigated by applying cyclic traffic load on a backfill model (Figs. 26.158 and 26.159). Note therein that the tire-chip backfill was made only in the lower part because the upper sandy backfill was expected to form an arch to support more efficiently the surface traffic load.

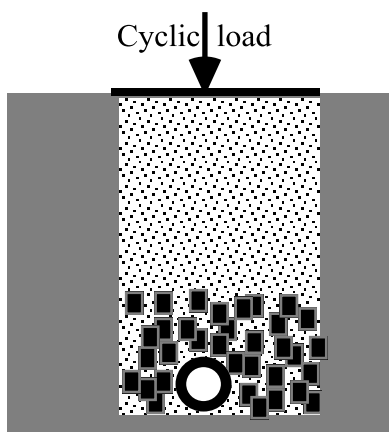


Fig. 26.158 Model of tire-chip backfilling

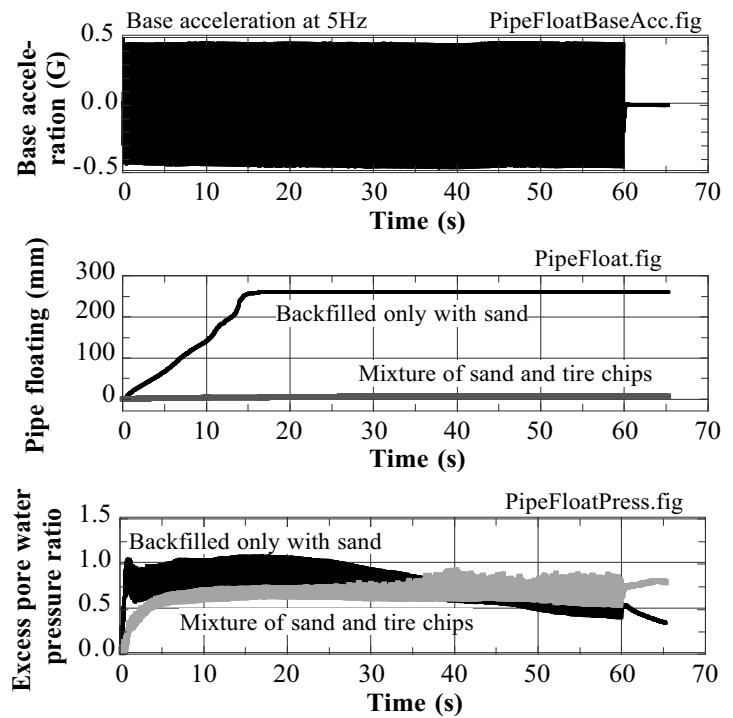


Fig. 26.156 Comparison of floating of embedded pipe in backfill made of sand only or sand mixed with tire chips (Nguyen, 2007)

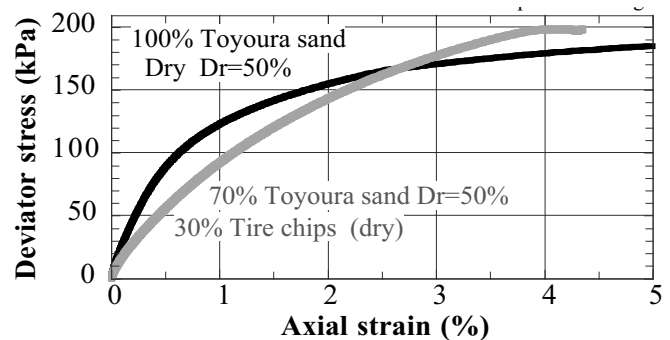


Fig. 26.157 Drained triaxial compression tests on Toyoura sand and Toyoura sand mixed with tire chips (Sato, 2007)

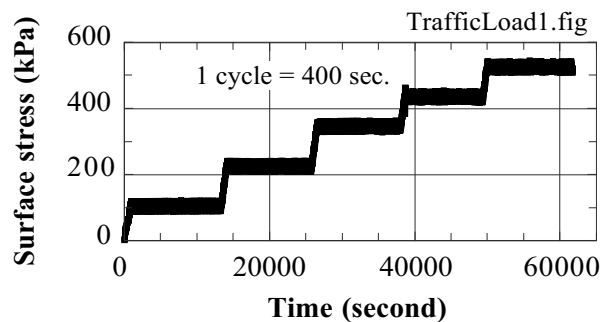
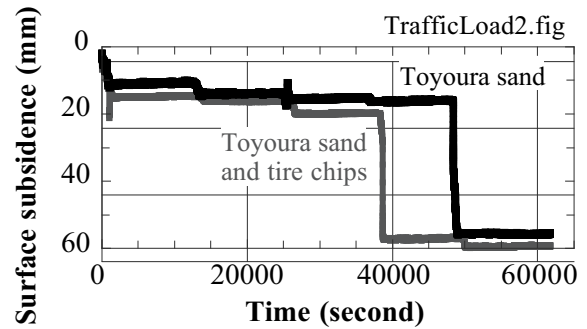


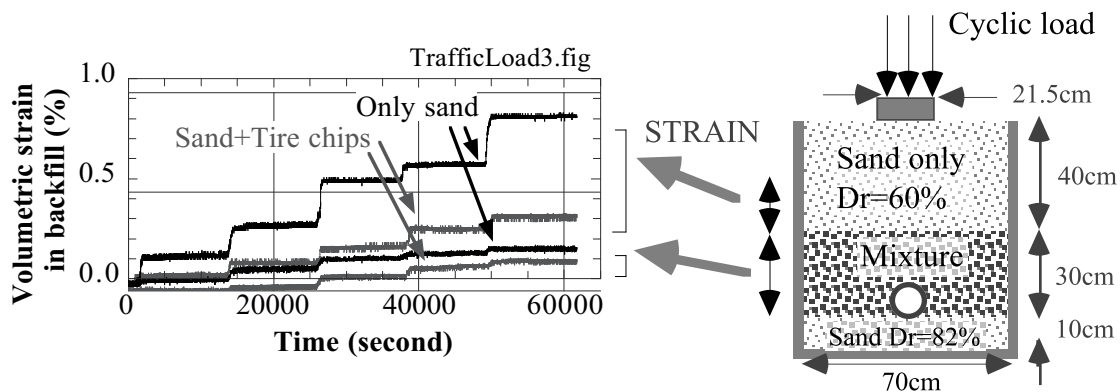
Fig. 26.159 Time history of surface cyclic load (Nguyen, 2007)

Figure 26.160 compares the time history of subsidence at the surface. Two types of backfill appear equivalent in the sense of surface subsidence.

More in detail, Fig. 26.161 demonstrates the time history of volumetric strain in sandy and tire-chip backfills. It may be seen that the use of tire chips reduced the volume contraction. Volume change near the surface, where arch was formed, was large in the tire-chip backfill test.



**Fig. 26.160** Time history of surface subsidence during cyclic surface load (Nguyen, 2007)



**Fig. 26.161** Time history of volumetric strain in backfill (Nguyen, 2007)

## List of References in Chapter 26

- Alam, M.J., Fukui, S., Towhata, I., Honda, T., Tamate, S., Tanaka, T., Uchiyama, J. and Yasuda, S. (2004) Centrifuge model tests on mitigation effects of underground walls on liquefaction-induced subsidence of embankment, Proc. 11th Int. Conf Soil Dynam. Earthq. Eng. 3rd Int. Conf. Earthq. Geotech. Eng., Berkeley, Vol. 2, pp. 537–544.
- Andrew, D.C.A. (2006) Design and construction of stone columns for the Blenheim Road deviation railway overbridge abutments, Christchurch, New Zealand, Proc. New Zealand Workshop Geotech. Earthq. Eng., Christchurch, pp. 160–167.
- Arthur, J.R.F., Chua, K.S. and Dunstan, T. (1977) Induced anisotropy in a sand, Geotech., Vol. 27, No. 1, pp. 13–30.
- Ashford, S.A., Rollins, K.M., and Lane, J.D. (2004) Blast-induced liquefaction for full-scale foundation testing, J. Geotech. Geoenv. Eng., ASCE, Vol. 130, No. 8, pp. 798–806.
- Charlie, W.A., Mutabihirwa, F.J.R., and Doehring, D.O. (1992) Time-dependent cone penetration resistance due to blasting, J. Geotech. Eng., ASCE, Vol.118, No. 8, pp. 1200–1215.
- Di Benedetto, H. (2001) Personal communication.
- Finn, W.D.L., Ledbetter, R.H., Fleming Jr., R.L., Forrest, T.W. and Stacy, S.T. (1998) Stabilization of an earth dam using driven prestressed concrete piles, J. Earthq. Eng., Vol. 2, No. 2, pp. 173–195.
- Gallagher, P.M. and Mitchell, J.K. (2002) Influence of colloidal silica grout on liquefaction potential and cyclic undrained behavior of loose sand, Soil Dynam. Earthq. Eng., 22, pp. 1017–1026.
- Gohl, W.B., Jefferies, M.G., Howie, J.A., and Diggle, D. (2000) Explosive compaction: design, implementation and effectiveness, Geotech., Vol. 50, No. 6, pp. 657–665.
- Gallagher, P.M., Conlee, C.M. and Rollins, K.M. (2007) Field testing of passive site stabilization. J. Geotech. Geoenv. Eng., ASCE, Vol. 133, No. 2, pp. 186–196.

- Harada, N., Towhata, I., Takatsu, T., Tsunoda, S. and Sesov, V. (2006) Development of drain method for protection of existing pile foundation from liquefaction effects, *Soil DynamEarthq. Eng. J.I.*, Vol. 26, No. 4, pp. 297–312.
- Hirama, K. (1981) Consideration on significance of relative density, *Proc. Symp. on relative density of sand and engineering properties*, Jpn. Geotech. Soc., pp. 53–56.
- Horikoshi, K., Tateishi, A., Higaki, K., Sueoka, T. and Goto, S. (2000) Soil improvement method with the use of granulated excavated-soil and expansive hardening materials (introduction), *Proc. 35th Ann. Conv. Jpn. Geotech. Soc.*, pp. 1421–1422 (in Japanese).
- Hwang, J.H., Yang, C.W. and Chen, C.H. (2003) Investigation on soil liquefaction during the Chi-Chi earthquake, *Soils Found.*, Vol. 43, No. 6, pp. 107-123.
- Iai, S., Koizumi, K. and Kurata, E. (1991) Area of ground compaction as a measure against liquefaction, *Monthly Magazine of Jpn. Soc. Soil Mech. Found. Eng. (Tsuchi-to-Kiso)*, Vol. 39, No. 2, pp. 35–40.
- Isemoto, N., Mitsunari, T., Kaneko, O., Shibata, Y. and Bessho, M. (2000) Long-term durability of super lime piles, *Proc. 35th Ann. Conv. Jpn. Geotech. Soc.*, pp. 1411–1412 (in Japanese).
- Ishiguro, T., Iijima, T., Sugai, M. and Shimada, S. (1994) A basic study on the vibrational compaction of saturated sands with elimination of excess pore-water pressure, *Proc. JSCE*, 505/III-29, pp. 79–88 (in Japanese).
- Isoda, S. (2002) Shaking table tests on mitigation of liquefaction-induced subsidence of structures, Master thesis, Department of Civil Engineering, University of Tokyo.
- Isoda, S., Nakai, N., Orense, R. and Towhata, I. (2001) Mitigation of liquefaction-induced uplift of underground structure by using sheet pile wall, *Proc. Soil Improvement Conf.*, Singapore, pp. 70–77.
- Japanese Geotechnical Society (2004) Mitigation measures against liquefaction, *Practices in Geotech. Eng.* No. 18, p. 198 (in Japanese).
- Japanese Geotechnical Society (1996) Report on Geotechnical Aspects of Hanshin Awaji Earthquake Disasters.
- Japan. Geotech. Soc. (2004a) Mitigation measures for liquefaction 液状化対策工法, ISBN 4-88644-917-4, pp. 238–240 (in Japanese).
- Japanese Geotechnical Society (2004b) Planning, design, and installation of mitigative measure for liquefaction (in Japanese).
- JSSMFE (1993) Site investigation, Design, and installation of liquefaction mitigation measures, *Soil and Foundation Engineering for Practitioners*, No. 20, p. 154 (in Japanese).
- Kabashima, Y. and Towhata, I. (2000) Improvement of dynamic strength of sand by means of infiltration grouting, *Proc. 3rd Int. Conf. Ground Improvement Techniques - 2000*, Singapore, pp. 203–208.
- Kogai, Y., Towhata, I., Amimoto, K. and Hendri Gusti Putra (2000) Use of embedded walls for mitigation of liquefaction-induced displacement in slopes and embankments, *Soils Found.*, Vol. 40, No. 4, pp. 75–93.
- Lee, D.-H., Juang, H. and Ku, C.-S. (2001) Liquefaction performance of soils at the site of a partially completed ground improvement project during the 1999 Chi-Chi earthquake in Taiwan, *Can. Geotech. Jo.*, Vol. 38, pp. 1241-1253.
- Mitchell, J.K. and Solymer, Z.V. (1984) Time-Dependent strength gain in freshly deposited or densified sand, *Proc. ASCE*, Vol. 110, GT11, pp. 1559–1576.
- Miwa, M., Yonekura, R., Nagoshi, T. and Shimada, S. (2001) Characteristics of active silica grout produced ion-exchange process (2), *Proc. 36th Japan National Conf. Geotech. Eng.*, Tokushima, pp. 1121–1122 (in Japanese).
- Mizuno, M., Suematsu, N. and Okuyama, K. (1987) Design method of sand compaction pile for sandy soils containing fines, *Tsuchi-to-Kiso Monthly Magazine*, Jpn. Geotech. Soc., May, pp. 21–26.
- Mizutani, T. and Towhata, I. (2001) Model tests on mitigation of liquefaction-induced subsidence of dike by using embedded sheet-pile walls, *CD-ROM Proc. 4th Int. Conf. Recent Advances in Geotech. Earthq. Eng. Soil Dyn.*, 2001, San Diego, Paper Number 5.24.

- Mizutani, T., Towhata, I., Shinkawa, N., Ibi, S., Komatsu, T. and Nagai, T. (2001) Shaking table tests on mitigation of liquefaction-induced subsidence of river dikes, Proc. 16th ICSMGE, Istanbul, Vol. 2, pp. 1207–1210.
- Nguyen, A.C. (2007) Mitigation of liquefaction-induced damages to buried pipes by backfilling with tire chips, Master thesis, University of Tokyo.
- Nirmalan, S. (2006) Strength and deformation characteristics of compacted scrap tire chips, Master thesis, University of Tokyo.
- Nishitani, M., Saimura, Y., Kita, H., Mizuta, M. and Ishihara, K. (1992) Field tests on effect of countermeasures against liquefaction by steel piles with drain (Part 1), Proc. 27th Nat. Conf. Jpn. Geotech. Soc., pp. 1167–1168 (in Japanese).
- Oda, M. (1972) The mechanism of fabric changes during compressional deformation of sand, Soils Found., Vol. 12, No. 2, pp. 1–18.
- Ohbayashi, J., Harada, K., Fukada, H. and Tsuboi, H. (2006) Trends and developments of countermeasure against liquefaction in Japan, Proc. 8th US Nat. Conf. Earthq. Eng., San Francisco, CD ROM Paper No. 1936.
- Oh-uchi, M. and Murakami, T. (2006) Sand compaction by means of ultrasonic wave, Poster presentation, Soil Mechanics Seminar, Chugoku Branch of Jpn. Geotech. Soc. (in Japanese).
- Okamura, M. and Soga, Y. (2006) Effects of pore fluid compressibility on liquefaction resistance of partially saturated sand, Soils Found., Vol. 46, No. 5, pp. 695–700.
- Okamura, M. and Teraoka, T. (2005) Shaking table tests to investigate soil desaturation as a liquefaction countermeasure, Geotech. Special Publication, ASCE, 145, pp. 282–293.
- Okamura, M., Ishihara, M. and Tamura, K. (2006) Degree of saturation and liquefaction resistance of sand improved with sand compaction pile, J. Geotech. Geoenviron. Eng., ASCE, Vol. 132, No. 2, pp. 258–264.
- Onoue, A., Mori, N. and Takano, J. (1987) In-situ experiment and analysis on well resistance of gravel drains, Soils Found., Vol. 27, No. 2, pp. 42–60.
- Saimura, Y., Iida, T., Kita, H., Nishitani, M. and Ishihara, K. (1992) Field tests on effect of countermeasures against liquefaction by steel piles with drain (Part 2), Proc. 27th Nat. Conf. Jpn. Geotech. Soc., pp. 1169–1170 (in Japanese).
- Sato, T. (2007) Liquefaction resistance and deformation characteristics of sand mixed with tire chips, Bachelor thesis, University of Tokyo.
- Saxena, S.K., Reddy, K.R. and Avramidis, A.S. (1988) Liquefaction resistance of artificially cemented sand, J. Geotech. Eng., ASCE, Vol. 114, No. 12, pp. 1395–1413.
- Seed, H.B. and Booker, J.R. (1977) Stabilization of potentially liquefiable sand deposits using gravel drains, Proc. ASCE, Vol. 103, GT7, pp. 757–768.
- Sendir, S., Wassan, T.H., Towhata, I. and Tsujino, S. (2006) Increasing effectiveness of explosive compression by changing the order of blasts, CD-ROM Proc. 12th Japan Earthq. Eng. Symp., Tokyo.
- Sesov, V., Talaganov, K., Harada, N. and Towhata, I. (2001) Mitigation of liquefaction potential by installing a new type of vertical drains, Proc. Earthq. Geotech. Eng. Satellite Conference, 15th Int. Conf. Soil Mech. Geotech. Eng., Istanbul, pp. 375–380.
- Skempton, A.W. (1986) Standard penetration test procedures and the effects in sands of overburden pressure, relative density, particle size, ageing and overconsolidation, Geotech., Vol. 36, No. 3, pp. 425–447.
- Toki, S., Tatsuoka, F., Miura, S., Yoshimi, Y., Yasuda, S. and Makihara, Y. (1986) Cyclic undrained triaxial strength of sand by a cooperative test program, Soils Found., Vol. 26, No. 3, 117–128.
- Towhata, I. (2005) Development of geotechnical earthquake engineering in Japan, Heritage Lecture, 16th Int. Conf. Soil Mech. Geotech. Eng., Osaka, Vol. 1, pp. 251–291.
- Towhata, I. (2007) Development of soil improvement technologies for mitigation of liquefaction risk, Theme Lecture, Proc. 4th Int. Conf. Earthq. Geotech. Eng., Thessaloniki, Greece.

- Towhata, I. and Kabashima, Y. (2001) Mitigation of seismically-induced deformation of loose sandy foundation by uniform permeation grouting, Proc. Earthq. Geotech. Eng. Satellite Conf., 15th Int. Conf. Soil Mech. Geotech. Eng., Istanbul, Turkey, pp. 313–318.
- Towhata, I., Kogai, Y. and Amimoto, K. (2000) Use of underground walls for mitigation of liquefaction-induced lateral flow, CD ROM Proceedings, GeoEng2000 Conf., Melbourne, Australia.
- Towhata, I., Nakai, N., Ishida, H., Isoda, S. and Shimomura, T. (2003) Mitigation of liquefaction-induced floating of embedded structures by using underground walls, Proc. 12th Asian Reg. Conf. Soil Mech. Geotech. Eng., Singapore, pp. 335–338.
- Tsuchida, H., Iai, S. and Kurata, E. (1976) Range of soil improvement for mitigation of liquefaction, Proc. 14th Earthq. Eng. Conf., JSCE, pp. 9–12 (in Japanese).
- Wassan, T.H., Towhata, I. and Tsujino, S. (2006) The effect of different firing sequences on plastic volumetric strains during blast-induced ground compression, Proc. 7th Int. Congress on Advances in Civil Eng., Istanbul, pp. 281–291.
- Yamada, Y. and Ishihara, K. (1981) Undrained deformation characteristics of loose sand under three-dimensional stress conditions, Soils Found., Vol. 21, No. 1, pp. 97–107.
- Yamada, Y. and Ishihara, K. (1982) Yielding of loose sand in three-dimensional stress conditions, Soils Found., Vol. 22, No. 3, pp. 15–31.
- Yamada, Y. and Ishihara, K. (1983) Undrained deformation characteristics of sand in multi-dimensional shear. Soils Found., Vol. 23, No. 1, pp. 61–79.
- Yasuda, S. and Kiku, H. (2006) Uplift of buried manholes and pipes due to liquefaction of replaced soils, Proc. 2nd Japan-Taiwan Joint Workshop, ATC 3 Committee of JGS, Nagaoka, pp. 146–149.
- Yonekura, R. and Shimada, S. (1992) Long term durability of chemical grouts, Monthly Magazine of Jpn. Geotech. Soc., Vol. 40, December, pp. 17–22.
- Yonekura, R. and Shimada, S. (2006) Durability of grouting -3-, Civil Eng. J. 土木施工, February, pp. 92–98 (in Japanese).
- Yonekura, R., Nagoshi, T., Shimada, S. and Mori, M. (2001) A durability experiment of suspension type hybrid silicas grout, Proc. 36th Japan Nat. Conf. Geotech. Eng., Tokushima, pp. 1117–1118 (in Japanese).
- Zen, K. (1990) Development of pre-mixing method as a measure to construct a liquefaction-free land, Tsuchi-to-Kiso, The Monthly Magazine, Jpn. Geotech. Soc., Vol. 38, No. 6, pp. 27–32 (in Japanese).



# Chapter 27

## Seismic Microzonation



大徳寺孤篷庵 忘筌

Koho-An of Daitoku-Ji Temple in Kyoto. This Zen temple invites people into a metaphysical world. The room and the garden in the photograph compose a symbolized sea as viewed from a boat; the paper screen at the top suggests the side board of a boat while the garden outside is the sea.

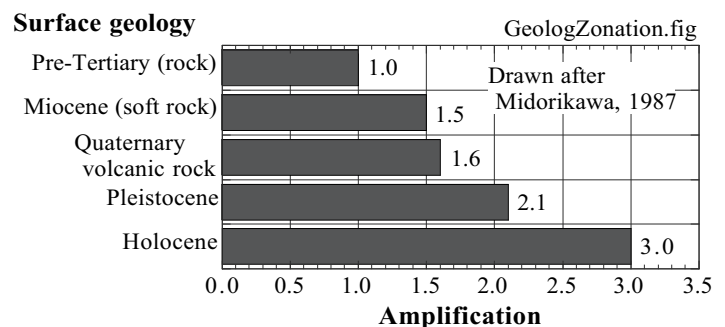
## 27.1 Microzonation for Intensity of Earthquake Motion

Seismic zonation or microzonation stands for assessing and classifying the extent of risk in localities by taking into account the expected nature of future earthquakes as well as topography, soil conditions, and other individual conditions. The name may or may not carry “micro”, depending upon the size of considered localities. This section concerns in particular the risk that is related to such earthquake problems as intensity of earthquake motion and liquefaction. Topics concerning landslide risk assessment were discussed in Sect. 15.46. Design requirements as well as emergency program after an earthquake disaster should take into account the microzonation so that relevant action may be taken for each localities. A good reference on this topic was published by the Technical Committee No. 4 for Earthquake Geotechnical Engineering under the auspices of International Society for Soil Mechanics and Geotechnical Engineering (ISSMGE) (1999). Most parts of this chapter rely on this report.

The quality and reliability of risk assessment depend on the amount of investigation and data interpretation. It is, therefore, very likely that high reliability is not achieved or even not necessary when there are time and financial limitations. Hence, the practice of (micro)zonation is classified into three grade groups; Grade 1 with least labor and Grade 3 that is most elaborate. The practice should choose the most appropriate grade, depending upon the situation and requirement. Differences among grades are described in what follows.

Microzonation begins with the assessment of regional seismic activity. Zoning is more important in tectonically more active region. The probability of an occurrence of a big earthquake in the studied region is assessed by historical records that are converted to, for example, the Gutenberg-Richter (1944) diagram. If historical record for a sufficiently long period of time is not available, an alternative approach may be trench excavation of a fault (Fig. 16.3) and paleoliquefaction (Sect. 18.4) for which the date is determined.

Zonation of grade 1 is carried out by using information and knowledge that are available in literatures. Hence, neither soil investigation nor numerical analysis is required. A typical important information is found in experiences during past earthquakes. For example, Fig. 5.32 illustrated the damage distribution in Tokyo during the 1923 Kanto earthquake. The area of heavy damage rate in this figure agreed with the area of soft and recent alluvial deposits. It is important that the magnitude of amplification in earthquake motion is somehow related with the surface geology. See the experience in California (Fig. 5.7). Figure 27.1, accordingly, illustrates a proposal by Midorikawa (1987), which was derived on the basis of calculated amplification (Sect. 6.8) of ground motion averaged over a certain frequency range. Note that the geological consideration of this type does not pay attention to the thickness of geomaterials. Moreover, since the amplification data were obtained from observation of frequent but weak ground motion, the amplification during a strong shaking may be different from the expectation because of the nonlinearity of soil (Fig. 9.13 and Chap. 10) that becomes significant during strong shaking.



**Fig. 27.1** Amplification of earthquake motion in different surface geology (drawn after Midorikawa, 1987)

Note: Amplification in this figure comes from TC4 committee report. Original paper by Midorikawa (1987) gave amplification 2.5 times bigger than those in this figure.

Zonation of grade 2 collects more subsurface data in addition to literature information. For example, SPT- $N$  values are converted to S-wave velocity,  $V_s = \sqrt{G_{\max}/\rho}$ , by using empirical correlations (Sect. 8.4–8.6). By using a  $V_s$  profile thus obtained above an engineering base layer, microzonation is carried

out. For example, Shima (1978) indicated that the greater ratio of ( $V_s$  in bedrock)/( $V_s$  in surface soil) leads to the greater amplification; softer surface soil generates greater amplification. Noteworthy is that the practical subsurface investigation is seldom conducted down to the real bedrock. It is a common practice to consider a soil layer with  $V_s \geq 600$  m/s as an engineering base (rock), although a real rock layer lies far below it. Few engineering soil investigation is conducted below a layer of SPT- $N > 50$  that is a good bearing layer for foundation of structures.

$T_G$  is one of the applications of the  $V_s$  profile which is defined by

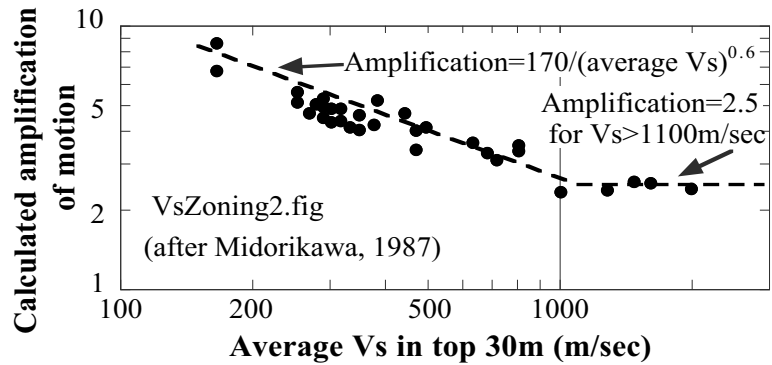
$$T_G \equiv 4 \sum_{\text{surface}}^{\text{base}} \frac{H_i}{V_{s_i}} \quad (27.1)$$

where  $H_i$  and  $V_{s_i}$  are thickness and  $V_s$  of the  $i$ th layer in the ground (see (21.4)). Being similar to the natural period of a uniform soil deposit,  $T_G$  is expected to help assess the magnitude of amplification (6.30). Table 21.3 in Sect. 21.7 gave an idea of ground classification (microzonation), based on this parameter.

Moreover, it is expected that the mean value of  $V_s$  in the surface deposit is approximately related with the amplification of motion averaged over a certain frequency range. Figure 27.2 demonstrates an example formula proposed by Midorikawa (1987).

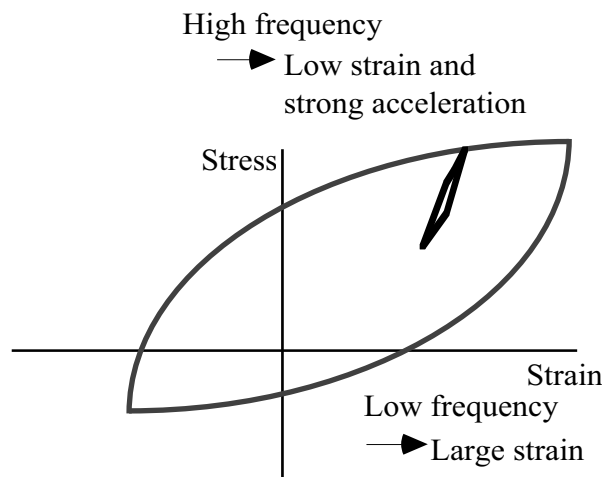
A different kind of grade-2 approach is the use of microtremor observation. Figures 8.35 and 8.36 illustrated two examples of microzonation, based on intensity and period of this weak ground vibration.

Zonation of grade 3 runs nonlinear dynamic analyses. For simplicity,  $V_s$  or  $G_{\max} = \rho V_s^2$  at small strain amplitude is determined by SPT- $N$ , while nonlinearity is considered by using literature information (Chap. 10). This implies that the equivalent linear analysis (Sect. 9.14) is most frequently employed. However, care is needed in analyses on very soft ground undergoing strong shaking. A commonly encountered problem is that the calculated motion at the surface is stronger upon hard soil than on such soft soil, which appears contradictory to knowledge of damage distribution (Fig. 5.32). The reason for this problem is that the existing computer codes (equivalent linear analysis with complex-modulus modelling) assume equal values of secant shear modulus ( $G$ ) and damping ratio to all the

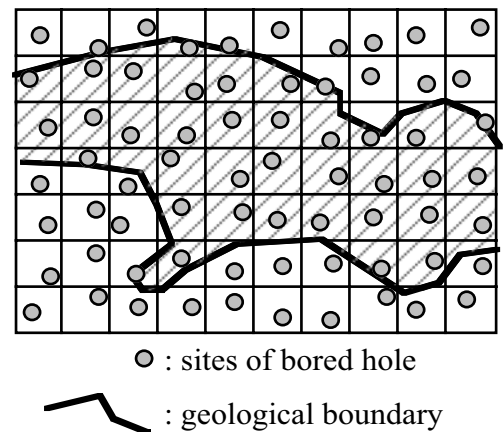


**Fig. 27.2** Assessment of amplification of ground motion by average  $V_s$  (Midorikawa, 1987)

Note: Amplification in this figure comes from the original paper by Midorikawa. Later, TC4 committee report reduced the amplification to 1/2.5.



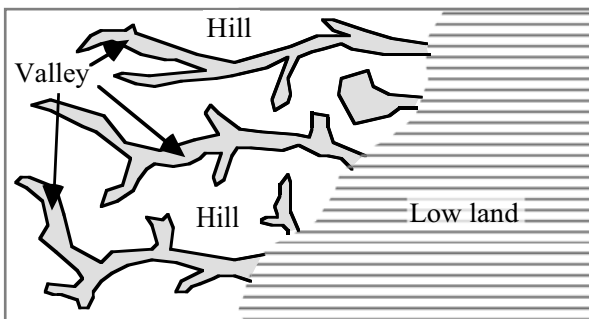
**Fig. 27.3** Appropriate rigidity and damping ratio for low- and high-frequency components



**Fig. 27.4** Square grids on more irregular geological conditions

frequency components. Since the strain amplitude is large under strong shaking, small  $G$  and large damping ratio are assumed. Although these values are reasonable for low-frequency components that generate large strain, they are not appropriate for high-frequency components whose strain amplitude is small but contribution to acceleration is significant (Figs. 9.46 and 27.3). These high-frequency components are unduly decayed by the overestimated damping ratio, and the acceleration at the ground surface is underestimated. Sugito et al. (1994) together with Sugito (1995) proposed to allocate different damping characteristics to different frequency components on the basis of the respective strain amplitudes. Note that some constitutive models that are employed in analyses in the time domain overestimate the energy damping at large strain amplitude as well.

Zoning may be made easy by constructing square grids (Fig. 27.4) in the studied region and determining a representative soil profile in each of them. By using the representative soil profile, one of the above procedures is practiced and the corresponding grid is classified. The problem lying in this procedure is that the geological and topographical boundaries do not necessarily match the boundary of square grids. It is better to determine the zone boundary on the basis of the geological and topographical boundaries.



**Fig. 27.5** Small valley in pleistocene hilly area



**Fig. 27.7** Peaty soil in small valley

Ohsaki (1983) issued a caution on the problem lying in the bottom of a small valley within a hilly area. Figure 27.5 illustrates such a geological condition. Figure 27.6 shows a site in such a small valley. When an excavation was planned in this site, a very soft deposit of peaty soil was encountered (Fig. 27.7). Being too soft for any construction machine to come in, this peat was grouted (Fig. 27.8) and thereafter a machine came in to excavate. This soft deposit was produced when this place was a small pond in such a valley.



**Fig. 27.6** Magome site of Tokyo in small valley



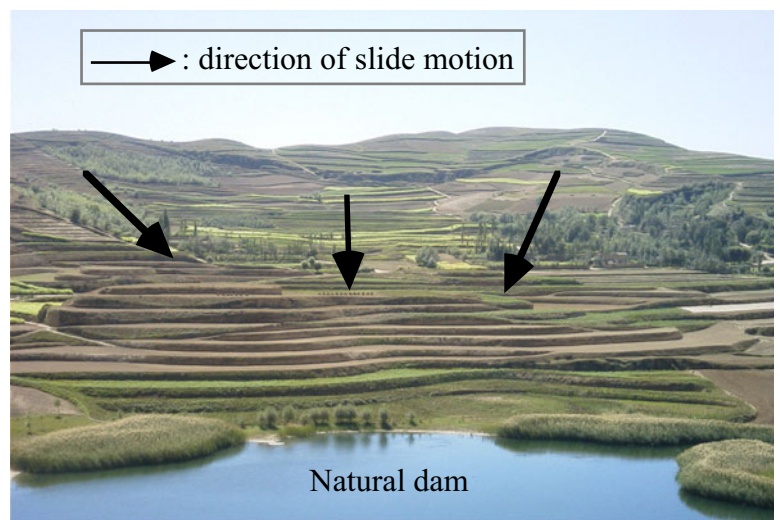
**Fig. 27.8** Soil improvement of peaty material by grouting special liquid

## 27.2 Microzonation for Liquefaction

This section continues the foregoing discussion with an emphasis on liquefaction hazard. There are again three grades in microzonation for liquefaction risk. Grade 1 uses literature and experiences. Therefore, it does not require field investigation.

Figure 18.38 demonstrated the distribution of liquefaction during the earthquake in 1923. It was therein shown that liquefaction-prone geology is the abandoned river channel and the deltaic deposit. Figure 17.34 showed as well the difference in liquefaction resistance between old and recent subsoils in Dagupan, the Philippines. The experience in Kobe in 1995 indicated that recent man-made islands are vulnerable to liquefaction as well (Fig. 18.43). Figure 27.9 illustrates a huge landslide, which was triggered by liquefaction of loess soil (aeolian deposit) during the 1920 earthquake ( $M=8.5$ , Wang et al. 2000 and 2001). Therefore, recent loose deposits of cohesionless soil lying under ground water table have high potential to liquefy. In contrast, cohesive soil would not liquefy (Sect. 20.4).

Microzonation of grade 2 relies on more efforts to collect information from unpublished literatures and interview to residents. Youd and Perkins (1978) presented a very elaborate information that is shown in Table 27.1. Liquefaction is unlikely in most dunes because the ground water table is low. It is, however, important that the secondary deposit of dune sand results in high liquefaction susceptibility. The secondary deposit means that dune sand is transported by wind and gravity into low and wet land adjacent to dune hill and develops loose and water-saturated layer.



**Fig. 27.9** Failure of very gentle loess slope due to earthquake (寧夏回族自治區西吉, Ningxia, China)

Ageing increases the liquefaction resistance (Sect. 18.13). It is, however, true that the rate of this increase varies from region to region, probably depending on the frequency of strong shaking in the particular region (local seismic activity; Sect. 18.13); densification of sand by repeated past earthquakes. Wakamatsu (1992) proposed a similar idea (Table 27.2) on liquefaction susceptibility for the JMA (Japanese Meteorological Agency) seismic intensity scale of  $V$ .

The grade-3 microzonation for liquefaction hazard is conducted by running subsoil investigation, such as SPT, and necessary calculation or analysis. The factor of safety against liquefaction,  $F_L$ , is obtained from SPT- $N$  and other bore hole data (Sect. 19.4), which is then converted to a single value (for example,  $P_L$  in Sect. 21.9) that represents the bore hole site (Sect. 21.9). Then, microzonation becomes possible. However, the ignorance of local topographical boundaries in a grid operation (Fig. 27.4) should be borne in mind. Attention should be paid to the reliability or details of SPT procedure, which may affect the quality of obtained  $N$  values.

It is further possible to take into account the risk of lateral displacement of liquefied sand in sloping ground as well as behind an unstable quay wall (Chap. 24). Youd and Perkins (1987) proposed an index of LSI (liquefaction severity index), which is a function of earthquake magnitude, distance from the seismic source, and local geological as well as topographical conditions. Standing for the maximum possible displacement in lateral directions, LSI can be an index to perform microzonation. Note that LSI cannot take into account human efforts to improve soil conditions and to mitigate liquefaction problems.

**Table 27.1** Liquefaction susceptibility in different surface geology (original table by Youd and Perkins, 1978, was modified and/or summarized by the author) (author's remarks are shown in the foot note)

Type of deposit	Susceptibility to liquefaction when saturated with water.			
	Age < 500 years	Holocene	Pleistocene	Older than Pleistocene
<i>Inland deposits</i>				
River channel	Very high	High	Low	Very low
Flood plain	High	Moderate	Low	Very low
Alluvial fan and plain <sup>a</sup>	N/A	Low	Very low	Very low
Marine terraces and plains	Moderate	Low	Low	Very low
Delta and fan delta	High	Moderate	Low	Very low
Lacustrine and playa	High	Moderate	Low	Very low
Colluvium	High	Moderate	Low	Very low
Talus	Low	Low	Very low	Very low
Dune <sup>b</sup>	High	Moderate	Low	Very low
Loess <sup>c</sup>	High	High	High	Very low
Glacial till	Low	Low	Very low	Very low
Tuff <sup>d</sup>	Low	Low	Very low	Very low
Tephra	High	High	?	?
Residual soil	Low	Low	Very low	Very low
<i>Coastal deposits</i>				
Delta	Very high	High	Low	Very low
Estuarine	High	Moderate	Low	Very low
Beach <sup>e</sup>				
high wave energy	Moderate	Low	Very low	Very low
low wave energy	High	Moderate	Low	Very low
Lagoon	High	Moderate	Low	Very low
Fore shore	High	Moderate	Low	Very low
<i>Artificial deposits or land reclamation</i>				
Not densified	Very high	N/A	N/A	N/A
Densified / compacted	Low	N/A	N/A	N/A

a: Be careful of small former river channel, etc.

b: Most dune sand lies above ground water and is unlikely to liquefy. However, be careful of low and wet low lands between dune hills.

c: Loess slope failed easily (Fig. 27.9).

d: Normally volcanic ash is hot upon deposition near the crater and develops bonding.

e: Beach sand is compacted by wave energy

**Table 27.2** Susceptibility of soil to liquefaction in a variety of geomorphological units undergoing JMA seismic intensity scale of V (Wakamatsu, 1992)

Geomorphological conditions		Possibility to
Classification	Specific condition	liquefy
Valley plain	Valley plain consisting of gravel or cobble	Not likely
Alluvial fan	Valley plain consisting of sandy soil	Possible
	Vertical gradient of more than 0.5%	Not likely
Natural levee	Vertical gradient of less than 0.5%	Possible
	Top of natural levee	Possible
Back marsh	Edge of natural levee <sup>a</sup>	Likely
	Abandoned river channel	Possible
Former pond		Likely
Marsh and swamp		Possible
Dry river bed	Dry river bed consisting of gravel	Not likely
	Dry river bed consisting of sandy soil	Likely
Delta		Possible
Bar	Sand bar	Possible
	Gravel bar	Not likely
Sand dune	Top of dune	Not likely
	Lower slope of dune	Likely
Beach	Beach	Not likely
	Artificial beach	Likely
Interlevee lowland		Likely
Land reclaimed by drainage		Possible
Reclaimed land		Likely
Spring		Likely
Fill	On boundary between sand and lowland	Likely
	Adjoining cliff	Likely
	On march or swamp	Likely
	On drained and reclaimed land	Likely
	Other type of fill	Possible

a: Figure 17.34 illustrated a boundary between natural levee and more recent deposit. Significant ground failure, probably due to liquefaction, occurred only in the latter geology. Figures 17.56 and 18.40 showed liquefaction in the area of young land reclamation in Dagupan, while Fig. 18.41 demonstrated that natural levee had more resistance against liquefaction.

### List of References in Chapter 27

- Gutenberg, B. and Richter, C.F. (1944) Frequency of earthquakes in California, Bull. Seism. Soc. Am., Vol. 34, pp. 185-188.
- Midorikawa, S. (1987) Prediction of isoseismal map in the Kanto Plain due to hypothetical earthquake, J. Struct. Eng., JSCE, Vol. 33B, pp. 43-48 (in Japanese).
- Ohsaki, Y. (1983) Earthquake and Building, Iwanami Shinsho Books, No. 240, p. 179 (in Japanese).
- Shima, E. (1978) Seismic microzoning map of Tokyo, Proc. 2nd Int. Conf. Microzonation, Vol. 1, pp. 433-443.

- Sugito, M. (1995) Frequency dependent equivalent strain for equi-linearized technique, Proc. First Int. Conf. Earthq. Geotech. Eng., Tokyo, Vol. 2, pp. 655-660.
- Sugito, M., Goda, H. and Masuda, T. (1994) Frequency dependent equi-linearized technique for seismic response analysis of multi-layered ground, Proc. JSCE, 493/III-27, pp. 49-58 (in Japanese).
- Technical Committee for Earthquake Geotechnical Engineering (TC4 of Int. Soc. Soil Mech. Geotech. Eng.) (1999) Manual for zonation on seismic geotechnical hazard, Revised version.
- Wakamatsu, K. (1992) Evaluation of liquefaction susceptibility based on detailed geomorphological classification, Proc. Ann Meet. Arch. Inst. Japan, Vol. B, pp. 1443-1444 (in Japanese).
- Wang, L.-M., Hwang, H., Lin, Y., Ryashenko, T.G. and Akulova, V.V. (2001) Comparison of liquefaction potential of loess in China, USA, and Russia, CD-ROM Proc. 4th Int. Conf. on Recent Advances in Geotech. Earthq. Eng. Soil Dynam., San Diego, Paper No. 4.04.
- Wang, L.-M., Yuan, Z.-X. and Wang, J.L.L. (2000) The effect to densify on seismic subsidence of loess, CD-ROM Proc. 12th WCEE, Auckland, Paper No. 1319.
- Youd, T.L. and Perkins, D.M. (1978) Mapping liquefaction-induced ground failure potential, J. Geotech. Eng., ASCE, Vol. 104, GT4, pp. 433-446.
- Youd, T.L. and Perkins, D.M. (1987) Mapping of liquefaction severity index, J. Geotech. Eng, ASCE, Vol. 113, No. 11, pp. 1374-1391.



# Appendix



Jiayuguan 嘉峪关 which was the western end of traditional China and the entrance to Central Asia.

## A.1 Derivation of Coulomb’s Active Earth Pressure Formula

### 1. Introduction

Coulomb’s theory on static active earth pressure is well known. However, its derivation is hardly described in detail in most textbooks, probably because of its extremely lengthy nature. Recently, Oka (1995) summarized the derivation of the formula for a case of level backfill slope. By referring to his solutions, the present text attempts to describe the derivation of Coulomb formula for a general situation.

Figure A.1 illustrates the situation to be analyzed. A retaining wall, which measures  $H$  in height, is subjected to earth pressure of  $P$  in its back face. Because of the forward tilting of the wall, the backfill soil subsides. The back face of the wall is inclined from the vertical direction by an angle of  $\alpha$ . The friction angle between the wall face and the backfill soil is denoted by  $\delta$ , which makes the direction of action of the earth pressure,  $P$ , inclined by  $\alpha + \delta$  from the horizontal direction. The slip plane is assumed to be a planar one that starts from the heel of the wall and is inclined by  $\theta$  angle from the horizontal direction. The failure condition of cohesion = 0 and friction angle =  $\phi$  is assumed to be fulfilled at the same time along the entire failure line; no progressive failure is taken into account. Therefore, the total force acting on the failure plane is inclined by  $\phi$  angle from the normal; inclination of  $\theta - \phi$  from the vertical. No cohesion is assumed in the backfill soil.

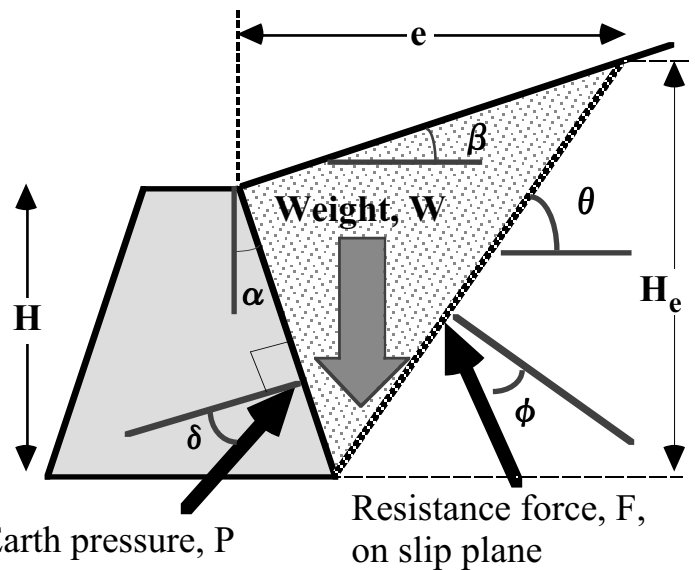


Fig. A.1 Situation of active failure of retaining wall

### 2. Method of Calculation

The limit equilibrium of a triangular soil wedge in the backfill is calculated. Firstly, the direction of the slip plane,  $\theta$ , is assumed. Then the weight of the soil wedge is calculated. By using the force equilibrium requirements in the vertical and horizontal directions on the soil wedge, the earth pressure,  $P$ , is derived. By changing the inclination of the slip plane,  $\theta$ , the maximum of the earth pressure,  $P$ , is searched. Although the idea is simple, the real calculation procedure is extremely complicated and lengthy.

### 3. Size and Weight of Soil Wedge

The size and the weight of the triangular soil wedge are calculated first. By using geometrical relationships in Fig. A.1,

$$e = H \tan \alpha + \frac{H_e}{\tan \theta} \tag{A.1}$$

$$e \tan \beta = H_e - H$$

By erasing  $e$  from (A.1).

$$H \tan \alpha \tan \beta + H_e \tan \beta / \tan \theta = H_e - H \tag{A.2}$$

$$H_e = \frac{1 + \tan \alpha \tan \beta}{1 - \tan \beta / \tan \theta} H = \frac{1 + \tan \alpha \tan \beta}{\tan \theta - \tan \beta} \tan \theta H$$

Consequently,  $e$  is determined;

$$e = \left( \tan \alpha + \frac{1 + \tan \alpha \tan \beta}{\tan \theta - \tan \beta} \right) H = \frac{1 + \tan \alpha \tan \theta}{\tan \theta - \tan \beta} H \quad (\text{A.3})$$

The weight of the soil wedge,  $W$ , is then calculated by using the unit weight of soil,  $\gamma$ ;

$$\begin{aligned} W &= \gamma \left\{ \frac{e}{2} (H + H_c) - \frac{H^2}{2} \tan \alpha - \frac{H_c^2}{2 \tan \theta} \right\} \\ &= \gamma \left\{ \frac{1 + \tan \alpha \tan \theta}{\tan \theta - \tan \beta} \cdot \frac{H}{2} \times \frac{\tan \theta - \tan \beta + \tan \theta + \tan \alpha \tan \beta \tan \theta}{\tan \theta - \tan \beta} H - \frac{H^2}{2} \tan \alpha \right. \\ &\quad \left. - \frac{1}{2 \tan \theta} \frac{(1 + \tan \alpha \tan \beta)^2 \tan^2 \theta}{(\tan \theta - \tan \beta)^2} H^2 \right\} \\ &= \frac{\gamma H^2}{2(\tan \theta - \tan \beta)^2} \left\{ (1 + \tan \alpha \tan \theta)(2 \tan \theta - \tan \beta + \tan \alpha \tan \beta \tan \theta) \right. \\ &\quad \left. - \tan \alpha (\tan \theta - \tan \beta)^2 - \frac{(1 + 2 \tan \alpha \tan \beta + \tan^2 \alpha \tan^2 \beta)}{\tan \theta} \tan^2 \theta \right\} \\ &= \frac{\gamma H^2}{2(\tan \theta - \tan \beta)^2} \left\{ (\tan \theta - \tan \beta) + \tan \alpha (\tan \theta + \tan \beta)(\tan \theta - \tan \beta) \right. \\ &\quad \left. + \tan^2 \alpha \tan \beta \tan \theta (\tan \theta - \tan \beta) \right\} \\ &= \frac{\gamma H^2}{2(\tan \theta - \tan \beta)} (1 + \tan \alpha \tan \beta)(1 + \tan \alpha \tan \theta) \end{aligned} \quad (\text{A.4})$$

When  $\beta = 0$  in particular, a simple expression is derived;

$$W = \frac{\gamma H^2}{2 \tan \theta} (1 + \tan \alpha \tan \theta) = \frac{\gamma H^2}{2} (\cot \theta + \tan \alpha) \quad (\text{A.5})$$

#### 4. Calculation of Limit Equilibrium

The force equilibrium is going to be analyzed in vertical and horizontal directions, by using three forces; gravity,  $W$ , earth pressure,  $P$ , and resistance along the assumed slip plane,  $F$ :

$$\begin{aligned} W &= F \cos(\theta - \phi) + P \sin(\alpha + \delta) \\ F \sin(\theta - \phi) &= P \cos(\alpha + \delta). \end{aligned} \quad (\text{A.6})$$

By eliminating  $F$ ,

$$\begin{aligned} W \sin(\theta - \phi) &= P \cos(\alpha + \delta) \cos(\theta - \phi) + P \sin(\alpha + \delta) \sin(\theta - \phi) = P \cos(\alpha + \delta - \theta + \phi) \\ P &= \frac{W \sin(\theta - \phi)}{\cos(\alpha + \delta - \theta + \phi)} \end{aligned} \quad (\text{A.7})$$

Substituting (A.4) in (A.7),

$$P = \frac{\gamma H^2}{2(\tan \theta - \tan \beta)} (1 + \tan \alpha \tan \beta)(1 + \tan \alpha \tan \theta) \frac{\sin(\theta - \phi)}{\cos(\alpha + \delta - \theta + \phi)}$$

$$= \frac{\gamma H^2 (1 + \tan \alpha \tan \beta)}{2} \times \frac{1 + \tan \alpha \tan \theta}{\tan \theta - \tan \beta} \times \frac{\sin(\theta - \phi)}{\cos(\alpha + \delta - \theta + \phi)}. \quad (\text{A.8})$$

Angles of  $\alpha$ ,  $\phi$ , and  $\theta$  are now replaced by new parameters such as

$$\alpha' \equiv \alpha - \beta, \quad \phi' \equiv \phi - \beta, \quad \text{and} \quad \theta' \equiv \theta - \beta \quad (\text{A.9})$$

Equation (A.8) is then modified as what follows;

$$\begin{aligned} \frac{1 + \tan \alpha \tan \theta}{\tan \theta - \tan \beta} &= \frac{1 + \tan(\alpha' + \beta) \tan(\theta' + \beta)}{\tan(\theta' + \beta) - \tan \beta} = \frac{1 + \frac{\tan \alpha' + \tan \beta}{1 - \tan \alpha' \tan \beta} \cdot \frac{\tan \theta' + \tan \beta}{1 - \tan \theta' \tan \beta}}{\frac{\tan \theta' + \tan \beta}{1 - \tan \theta' \tan \beta} - \tan \beta} \\ &= \frac{1 + \tan \alpha' \tan \theta'}{\tan \theta' (1 - \tan \alpha' \tan \beta)} \end{aligned} \quad (\text{A.10})$$

$$\begin{aligned} \frac{\sin(\theta - \phi)}{\cos(\alpha + \delta - \theta + \phi)} &= \frac{\sin(\theta' - \phi')}{\cos(\alpha' + \beta + \delta - \theta' + \phi')} = \frac{\sin(\theta' - \phi')}{\cos(-\theta' + \alpha' + \beta + \delta + \phi')} \\ &= \frac{\sin \theta' \cos \phi' - \cos \theta' \sin \phi'}{\cos \theta' \cos(\alpha' + \beta + \delta + \phi') + \sin \theta' \sin(\alpha' + \beta + \delta + \phi')} \end{aligned} \quad (\text{A.11})$$

$$\begin{aligned} P &= \frac{\gamma H^2 (1 + \tan \alpha \tan \beta)}{2} \times \frac{1 + \tan \alpha' \tan \theta'}{\tan \theta' (1 - \tan \alpha' \tan \beta)} \\ &\quad \times \frac{\sin \theta' \cos \phi' - \cos \theta' \sin \phi'}{\cos \theta' \cos(\alpha' + \beta + \delta + \phi') + \sin \theta' \sin(\alpha' + \beta + \delta + \phi')} \end{aligned} \quad (\text{A.12})$$

in which  $\alpha$  and  $\alpha'$  exist together. A function of  $\theta$  is picked up from (A.12) for simplification of derivative.

$$\begin{aligned} P' &\equiv \frac{2P(1 - \tan \alpha' \tan \beta)}{\gamma H^2 (1 + \tan \alpha \tan \beta)} \\ &= \frac{1 + \tan \alpha' \tan \theta'}{\tan \theta'} \times \frac{\sin \theta' \cos \phi' - \cos \theta' \sin \phi'}{\cos \theta' \cos(\alpha' + \beta + \delta + \phi') + \sin \theta' \sin(\alpha' + \beta + \delta + \phi')} \\ &= (\tan \alpha' + \cot \theta') \frac{\cos \phi' - \cot \theta' \sin \phi'}{\cot \theta' \cos(\alpha' + \beta + \delta + \phi') + \sin(\alpha' + \beta + \delta + \phi')} \end{aligned} \quad (\text{A.13})$$

By using for simplicity  $x \equiv \cot \theta'$  as well as  $\mu \equiv \alpha' + \beta + \delta + \phi' = \alpha - \beta + \delta + \phi$

$$P' = (\tan \alpha' + x) \frac{\cos \phi' - x \sin \phi'}{x \cos \mu + \sin \mu} \rightarrow \text{Max}. \quad (\text{A.14})$$

## 5. Detecting Direction of a Slip Plane

The direction of slip plane is determined by making the  $\chi$ -derivative of  $P'$  in (A.14) equal to zero;

$$\frac{dP'}{d\chi} = \frac{\cos \phi' - \chi \sin \phi'}{\chi \cos \mu + \sin \mu} - (\tan \alpha' + \chi) \frac{\sin \phi' (\chi \cos \mu + \sin \mu) + (\cos \phi' - \chi \sin \phi') \cos \mu}{(\chi \cos \mu + \sin \mu)^2} = 0$$

Accordingly,

$$\sin \phi' \cos \mu \chi^2 + 2 \sin \phi' \sin \mu \chi - (\cos \phi' \sin \mu - \sin \phi' \sin \mu \tan \alpha' - \cos \phi' \cos \mu \tan \alpha') = 0 \quad (\text{A.15})$$

By taking the positive root of this equation,

$$\begin{aligned} \chi &\equiv \cot \theta \\ &= \frac{-\sin \phi' \sin \mu + \sqrt{\sin^2 \phi' \sin^2 \mu + \sin \phi' \cos \mu (\cos \phi' \sin \mu - \sin \phi' \sin \mu \tan \alpha' - \cos \phi' \cos \mu \tan \alpha')}}{\sin \phi' \cos \mu} \\ &= -\tan \mu + \frac{\sqrt{\sin \phi' \{ \sin \phi' \sin^2 \mu + \cos \phi' \sin \mu \cos \mu - \sin \phi' \sin \mu \cos \mu \tan \alpha' - \cos \phi' \cos^2 \mu \tan \alpha' \}}}{\sin \phi' \cos \mu} \\ &= -\tan \mu + \frac{\sqrt{\cos \alpha' \sin \phi' \sin^2 \mu + (\cos \alpha' \cos \phi' - \sin \alpha' \sin \phi') \sin \mu \cos \mu - \sin \alpha' \cos \phi' \cos^2 \mu}}{\sin \phi' \cos \alpha'} \\ &= -\tan \mu + \frac{\sqrt{\cos \alpha' \sin \phi' \sin^2 \mu + \cos(\alpha' + \phi') \sin \mu \cos \mu - \sin \alpha' \cos \phi' \cos^2 \mu}}{\cos \mu} \end{aligned} \quad (\text{A.16})$$

in which

$$\begin{aligned} &\cos \alpha' \sin \phi' \sin^2 \mu + \cos(\alpha' + \phi') \sin \mu \cos \mu - \sin \alpha' \cos \phi' \cos^2 \mu \\ &= \frac{1}{2} \{ \cos \alpha' \sin \phi' (1 - \cos 2\mu) + \cos(\alpha' + \phi') \sin 2\mu - \sin \alpha' \cos \phi' (1 + \cos 2\mu) \} \\ &= \frac{1}{2} \{ -\sin(\alpha' - \phi') - \sin(\alpha' + \phi') \cos 2\mu + \cos(\alpha' + \phi') \sin 2\mu \} \\ &= \frac{1}{2} \{ -\sin(\alpha' - \phi') + \sin(2\mu - \alpha' - \phi') \} \\ &= \frac{1}{2} \{ -\sin(\alpha' - \phi') + \sin(\alpha' + \phi' + 2\beta + 2\delta) \} \\ &= \frac{1}{2} [ -\sin\{(\alpha' + \beta + \delta) - (\phi' + \beta + \delta)\} + \sin\{(\alpha' + \beta + \delta) + (\phi' + \beta + \delta)\} ] \\ &= \sin(\phi' + \beta + \delta) \cos(\alpha' + \beta + \delta) \\ &= \sin(\phi + \delta) \cos(\alpha + \delta) \end{aligned} \quad (\text{A.17})$$

because of definitions of  $\alpha'$  and  $\phi'$ .

$$\mu = \alpha - \beta + \delta + \phi$$

Substituting (A.17) in (A.16),

$$\begin{aligned} \chi &\equiv \cot \theta' = \cot(\theta - \beta) \\ &= -\tan \mu + \frac{1}{\cos \mu} \sqrt{\frac{\sin(\phi' + \beta + \delta) \cos(\alpha' + \beta + \delta)}{\cos \alpha' \sin \phi'}} \end{aligned} \quad (\text{A.18})$$

$$\cot(\theta - \beta) = -\tan \mu + \frac{1}{\cos \mu} \sqrt{\frac{\sin(\phi + \delta) \cos(\alpha + \delta)}{\cos(\alpha - \beta) \sin(\phi - \beta)}} \quad (\text{A.19})$$

Thus, the direction of slip plane is determined. When  $\beta = 0$  in particular,

$$\cot \theta = -\tan(\alpha + \delta + \phi) + \frac{1}{\cos(\alpha + \delta + \phi)} \sqrt{\frac{\sin(\phi + \delta) \cos(\alpha + \delta)}{\cos \alpha \sin \phi}} \quad (\text{A.20})$$

## 6. Calculation of active earth pressure

Now (A.19) is going to be substituted in (A.14) to calculate the active earth pressure. The earth pressure coefficient is given by

$$P' \equiv P'_a = (\tan \alpha' + \chi) \frac{\cos \phi' - \chi \sin \phi'}{\chi \cos \mu + \sin \mu} \rightarrow \text{Max.}$$

Here, two new parameters are introduced;

$$\chi' \equiv \chi \cos \mu = \sqrt{\frac{\sin(\phi' + \beta + \delta) \cos(\alpha' + \beta + \delta)}{\cos \alpha' \sin \phi'}} - \sin \mu \tag{A.21}$$

and

$$z \equiv \sqrt{\frac{\sin(\phi' + \beta + \delta) \cos(\alpha' + \beta + \delta)}{\cos \alpha' \sin \phi'}} \tag{A.22}$$

Because

$$z = \chi' + \sin \mu = \chi \cos \mu + \sin \mu \tag{A.23}$$

the following equation is derived;

$$\begin{aligned} P'_a &= \frac{(\tan \alpha' + \chi)(\cos \phi' - \chi \sin \phi')}{z} \quad P'_a = \frac{(\tan \alpha' + \chi)(\cos \phi' - \chi \sin \phi')}{z} \\ &= \frac{\cos \phi'}{z} (\tan \alpha' + \chi)(1 - \chi \tan \phi') \\ &= \frac{\cos \phi'}{z} \left( \tan \alpha' + \frac{z - \sin \mu}{\cos \mu} \right) \left( 1 - \frac{z - \sin \mu}{\cos \mu} \tan \phi' \right) \\ &= \frac{\cos \phi'}{z \cos^2 \mu} \{ z + (\tan \alpha' \cos \mu - \sin \mu) \} \{ -z \tan \phi' + (\cos \mu + \sin \mu \tan \phi') \} \\ &= \frac{\cos \phi'}{z \cos^2 \mu} \{ -\tan \phi' z^2 + (\cos \mu + \sin \mu \tan \phi' - \tan \alpha' \cos \mu \tan \phi' + \sin \mu \tan \phi') z \\ &\quad + (\tan \alpha' \cos^2 \mu - \sin \mu \cos \mu + \tan \alpha' \cos \mu \sin \mu \tan \phi' - \sin^2 \mu \tan \phi') \} \\ &= \frac{\cos \phi'}{z \cos^2 \mu} \{ -\tan \phi' (z^2 + \sin^2 \mu - 2 \sin \mu \cdot z) - \tan \alpha' \tan \phi' (\cos \mu \cdot z - \cos \mu \sin \mu) \\ &\quad + \cos \mu \cdot z - \cos \mu \sin \mu + \tan \alpha' \cos^2 \mu \} \\ &= \frac{\cos \phi'}{z \cos^2 \mu} \left[ \{ -\tan \phi' (z^2 - 2 \sin \mu \cdot z) - \tan \alpha' \tan \phi' \cos \mu \cdot z + \cos \mu \cdot z \} \right. \\ &\quad \left. + \{ -\sin^2 \mu \tan \phi' + \sin \mu \cos \mu \tan \alpha' \tan \phi' \} \right. \\ &\quad \left. + \{ -\cos \mu \sin \mu + \tan \alpha' \cos^2 \mu \} \right] \end{aligned} \tag{A.24}$$

:1. First term  
:2. Second term  
:3. Third term

The second term (:2.) is modified as

$$\begin{aligned} \text{Second term} &= -\sin \mu \tan \phi' (\sin \mu - \tan \alpha' \cos \mu) \\ &= -\frac{\sin \mu \tan \phi'}{\cos \alpha'} (\cos \alpha' \sin \mu - \sin \alpha' \cos \mu) = -\frac{\sin \mu}{\cos \alpha'} \tan \phi' \sin(\mu - \alpha') \\ &= -\frac{\sin \mu}{\cos \alpha'} \tan \phi' \sin(\beta + \delta + \phi') \end{aligned} \tag{A.25}$$

$\mu = \alpha' + \beta + \delta + \phi'$

Similarly, the third term (:3.) is modified as

$$\begin{aligned} \text{Third term} &= -\cos \mu \sin \mu + \tan \alpha' \cos^2 \mu \\ &= \frac{\cos \mu}{\cos \alpha'} (\sin \alpha' \cos \mu - \cos \alpha' \sin \mu) = \frac{\cos \mu}{\cos \alpha'} \sin(\alpha' - \mu) \end{aligned}$$

$\mu = \alpha - \beta + \delta + \phi$

$$= -\frac{\cos \mu}{\cos \alpha'} \sin(\beta + \delta + \phi') \quad (\text{A.26})$$

By adding (A.25) and (A.26),

$$\begin{aligned} \text{Second + third terms} &= -\frac{\tan \phi' \sin(\beta + \delta + \phi')}{\cos \alpha'} \left( \sin \mu + \frac{\cos \mu}{\tan \phi'} \right) \\ &= -\tan \phi' \frac{\sin(\beta + \delta + \phi')}{\cos \alpha' \sin \phi'} (\sin \phi' \sin \mu + \cos \phi' \cos \mu) \\ &= -\tan \phi' \frac{\sin(\beta + \delta + \phi') \cos(\mu - \phi')}{\cos \alpha' \sin \phi'} \\ &= -\tan \phi' \frac{\sin(\phi' + \beta + \delta) \cos(\alpha' + \beta + \delta)}{\cos \alpha' \sin \phi'} \\ &= -\tan \phi' \times z^2. \end{aligned} \quad (\text{A.27})$$

Equation (A.27) is substituted in (A.24):

$$\begin{aligned} P'_a &= \frac{\cos \phi'}{z \cos^2 \mu} \left( -\tan \phi' z^2 - \tan \phi' z^2 + 2 \tan \phi' \sin \mu z - \tan \alpha' \tan \phi' \cos \mu z + \cos \mu z \right) \\ &= \frac{\cos \phi'}{\cos^2 \mu} \left\{ -2 \tan \phi' z - \tan \phi' (\tan \alpha' \cos \mu - \sin \mu) + (\tan \phi' \sin \mu + \cos \mu) \right\} \\ &= \frac{\cos \phi'}{\cos^2 \mu} \left\{ -2 \tan \phi' z - \frac{\tan \phi'}{\cos \alpha'} (\sin \alpha' \cos \mu - \cos \alpha' \sin \mu) + \frac{1}{\cos \phi'} (\sin \phi' \sin \mu + \cos \phi' \cos \mu) \right\} \\ &= \frac{\cos \phi'}{\cos^2 \mu} \left\{ -2 \tan \phi' z + \frac{\tan \phi'}{\cos \alpha'} \sin(\mu - \alpha') + \frac{\cos(\mu - \phi')}{\cos \phi'} \right\} \\ &= \frac{\cos \phi'}{\cos^2 \mu} \left\{ -2 \tan \phi' z + \frac{\tan \phi'}{\cos \alpha'} \sin(\beta + \delta + \phi') + \frac{\cos(\alpha' + \beta + \delta)}{\cos \phi'} \right\} \end{aligned} \quad \boxed{\mu = \alpha - \beta + \delta + \phi}$$

By substituting (A.22) for  $z$  and changing the order of terms,

$$\begin{aligned} P'_a &= \frac{\cos \phi'}{\cos^2 \mu} \left\{ \frac{\cos(\alpha' + \beta + \delta)}{\cos \phi'} - 2 \tan \phi' \sqrt{\frac{\sin(\phi' + \beta + \delta) \cos(\alpha' + \beta + \delta)}{\cos \alpha' \sin \phi'}} + \frac{\sin \phi' \sin(\beta + \delta + \phi')}{\cos \alpha' \cos \phi'} \right\} \\ &= \frac{\cos \phi'}{\cos^2 \mu} \left\{ \frac{\cos(\alpha' + \beta + \delta)}{\cos \phi'} - 2 \sqrt{\frac{\sin \phi' \sin(\phi' + \beta + \delta) \cos(\alpha' + \beta + \delta)}{\cos \alpha' \cos^2 \phi'}} + \frac{\sin \phi' \sin(\beta + \delta + \phi')}{\cos \alpha' \cos \phi'} \right\} \\ &= \frac{\cos \phi'}{\cos^2 \mu} \left\{ \sqrt{\frac{\cos(\alpha' + \beta + \delta)}{\cos \phi'}} - \sqrt{\frac{\sin \phi' \sin(\beta + \delta + \phi')}{\cos \alpha' \cos \phi'}} \right\}^2 \\ &= \frac{\cos \phi'}{\cos^2 \mu} \times \frac{\left\{ \frac{\cos(\alpha' + \beta + \delta)}{\cos \phi'} - \frac{\sin \phi' \sin(\beta + \delta + \phi')}{\cos \alpha' \cos \phi'} \right\}^2}{\left\{ \sqrt{\frac{\cos(\alpha' + \beta + \delta)}{\cos \phi'}} + \sqrt{\frac{\sin \phi' \sin(\beta + \delta + \phi')}{\cos \alpha' \cos \phi'}} \right\}^2} \\ &= \frac{1}{\cos \phi' \cos^2 \alpha'} \left\{ \cos \alpha' \cos(\alpha' + \beta + \delta) - \sin \phi' \sin(\beta + \delta + \phi') \right\}^2 \\ &= \frac{\cos^2 \mu \cos(\alpha' + \beta + \delta)}{\cos \phi'} \left\{ 1 + \sqrt{\frac{\sin \phi' \sin(\beta + \delta + \phi')}{\cos \alpha' \cos(\alpha' + \beta + \delta)}} \right\}^2 \end{aligned} \quad (\text{A.28})$$

The terms in { } of the numerator is modified by considering

$$\begin{aligned}
 & \cos(\phi' - \alpha') \cos(\alpha' + \beta + \delta + \phi') - \{ \cos \alpha' \cos(\alpha' + \beta + \delta) - \sin \phi' \sin(\beta + \delta + \phi') \} \\
 &= \cos(\phi' - \alpha') \{ \cos(\phi' + \alpha') \cos(\beta + \delta) - \sin(\phi' + \alpha') \sin(\beta + \delta) \} \\
 & \quad - \{ \cos^2 \alpha' \cos(\beta + \delta) - \cos \alpha' \sin \alpha' \sin(\beta + \delta) - \sin^2 \phi' \cos(\beta + \delta) - \sin \phi' \cos \phi' \sin(\beta + \delta) \} \\
 &= \frac{1}{2} (\cos 2\phi' + \cos 2\alpha') \cos(\beta + \delta) - \frac{1}{2} (\sin 2\phi' + \sin 2\alpha') \sin(\beta + \delta) \\
 & \quad - (\cos^2 \alpha' - \sin^2 \phi') \cos(\beta + \delta) + (\cos \alpha' \sin \alpha' + \sin \phi' \cos \phi') \sin(\beta + \delta) \\
 &= \left( \frac{1}{2} - \sin^2 \phi' + \cos^2 \alpha' - \frac{1}{2} - \cos^2 \alpha' + \sin^2 \phi' \right) \cos(\beta + \delta) \\
 & \quad + (-\sin \phi' \cos \phi' - \sin \alpha' \cos \alpha' + \cos \alpha' \sin \alpha' + \sin \phi' \cos \phi') \sin(\beta + \delta) \\
 &= 0
 \end{aligned} \tag{A.29}$$

Thus, the terms in { } of numerator of (A.28) is replaced by the first term on the left-hand side of (A.29).

$$\begin{aligned}
 P'_a &= \frac{\{ \cos(\phi' - \alpha') \cos(\alpha' + \beta + \delta + \phi') \}^2}{\cos^2 \alpha' \cos^2(\alpha' + \beta + \delta + \phi') \cos(\alpha' + \beta + \delta) \left\{ 1 + \sqrt{\frac{\sin \phi' \sin(\beta + \delta + \phi')}{\cos \alpha' \cos(\alpha' + \beta + \delta)}} \right\}^2} \\
 &= \frac{\cos^2(\phi' - \alpha')}{\cos^2 \alpha' \cos(\alpha' + \beta + \delta) \left\{ 1 + \sqrt{\frac{\sin \phi' \sin(\beta + \delta + \phi')}{\cos \alpha' \cos(\alpha' + \beta + \delta)}} \right\}^2} \quad \boxed{\mu = \alpha' + \beta + \delta + \phi'}
 \end{aligned} \tag{A.30}$$

By substituting (A.30) in (A.13), the active earth pressure formula is derived.

$$\begin{aligned}
 P_a &= \frac{\gamma H^2}{2} \frac{1 + \tan \alpha \tan \beta}{1 - \tan \alpha' \tan \beta} \times \frac{\cos^2(\phi' - \alpha')}{\cos^2 \alpha' \cos(\alpha' + \beta + \delta) \left\{ 1 + \sqrt{\frac{\sin \phi' \sin(\beta + \delta + \phi')}{\cos \alpha' \cos(\alpha' + \beta + \delta)}} \right\}^2} \\
 &= \frac{\gamma H^2}{2} \frac{1 + \tan \alpha \tan \beta}{\{1 - \tan(\alpha - \beta) \tan \beta\} \cos^2(\alpha - \beta)} \times \frac{\cos^2(\phi - \alpha)}{\cos(\alpha + \delta) \left\{ 1 + \sqrt{\frac{\sin(\phi - \beta) \sin(\delta + \phi)}{\cos(\alpha - \beta) \cos(\alpha + \delta)}} \right\}^2}
 \end{aligned}$$

where

$$\begin{aligned}
 & \frac{1 + \tan \alpha \tan \beta}{\{1 - \tan(\alpha - \beta) \tan \beta\} \cos^2(\alpha - \beta)} = \frac{1 + \tan \alpha \tan \beta}{\{ \cos(\alpha - \beta) - \sin(\alpha - \beta) \tan \beta \} \cos(\alpha - \beta)} \\
 &= \frac{(1 + \tan \alpha \tan \beta) \cos \beta}{\{ \cos(\alpha - \beta) \cos \beta - \sin(\alpha - \beta) \sin \beta \} \cos(\alpha - \beta)} \\
 &= \frac{\cos \beta + \tan \alpha \sin \beta}{\cos \alpha \cos(\alpha - \beta)} \\
 &= \frac{\cos \alpha \cos \beta + \sin \alpha \sin \beta}{\cos^2 \alpha (\cos \alpha \cos \beta + \sin \alpha \sin \beta)} = \frac{1}{\cos^2 \alpha}
 \end{aligned} \tag{A.31}$$



Therefore,

$$\text{Active earth pressure } P_a = \frac{\gamma H^2}{2} \frac{1}{\cos^2 \alpha} \frac{\cos^2(\phi - \alpha)}{\cos(\alpha + \delta) \left\{ 1 + \sqrt{\frac{\sin(\phi - \beta) \sin(\delta + \phi)}{\cos(\alpha - \beta) \cos(\alpha + \delta)}} \right\}^2} \quad (\text{A.32})$$

Finally, the active earth pressure is expressed by

$$P_a = \frac{\gamma H^2}{2} K_a \quad (\text{A.33})$$

in which the active earth pressure coefficient is given by

$$K_a = \frac{\cos^2(\phi - \alpha)}{\cos^2 \alpha \cos(\alpha + \delta) \left\{ 1 + \sqrt{\frac{\sin(\phi - \beta) \sin(\delta + \phi)}{\cos(\alpha - \beta) \cos(\alpha + \delta)}} \right\}^2} \quad (\text{A.34})$$

The direction of slip plane,  $\theta$ , was already derived in (A.19).

In particular, when the back face of the wall is vertical and smooth ( $\alpha = \delta = 0$ ) and the surface of the backfill is level ( $\beta = 0$ ),

$$K_a = \left( \frac{\cos \phi}{1 + \sin \phi} \right)^2 = \tan^2 \left( \frac{\pi}{4} - \frac{\phi}{2} \right) \quad (\text{A.35})$$

The direction of slip plane as given by (A.20) is rewritten as

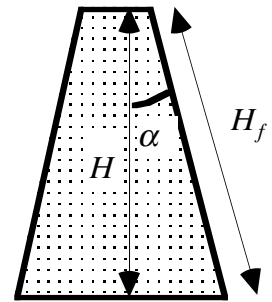
$$\begin{aligned} \cot(\theta - \beta) &= -\tan \mu + \frac{1}{\cos \mu} \frac{\sin(\phi + \delta) \cos(\alpha + \delta)}{\sqrt{\cos(\alpha - \beta) \sin(\phi - \beta)}} \\ &= -\tan(\alpha - \beta + \delta + \phi) + \frac{1}{\cos(\alpha - \beta + \delta + \phi)} \frac{\sin(\phi + \delta) \cos(\alpha + \delta)}{\sqrt{\cos(\alpha - \beta) \sin(\phi - \beta)}} \end{aligned} \quad (\text{A.36})$$

When  $\alpha = \beta = \delta = 0$ ,

$$\begin{aligned} \cot \theta &= -\tan \phi + \frac{1}{\cos \phi} = \frac{1 - \sin \phi}{\cos \phi} = \frac{\cos \frac{\phi}{2} - \sin \frac{\phi}{2}}{\cos \frac{\phi}{2} + \sin \frac{\phi}{2}} \\ \theta &= \arctan \frac{\cos \frac{\phi}{2} + \sin \frac{\phi}{2}}{\cos \frac{\phi}{2} - \sin \frac{\phi}{2}} = \arctan \frac{1 + \tan \frac{\phi}{2}}{1 - \tan \frac{\phi}{2}} = \frac{\pi}{4} + \frac{\phi}{2} \end{aligned} \quad (\text{A.37})$$

This is identical with the formula of Rankine active pressure. Thus, the Rankine theory concerns a special situation of  $\alpha = \beta = \delta = 0$  in the more general Coulomb theory.

It is sometimes the case that the height of a wall is expressed by the length of the face of the wall;  $H_f = H/\cos \alpha$ ; see Fig. A.2. In this situation,



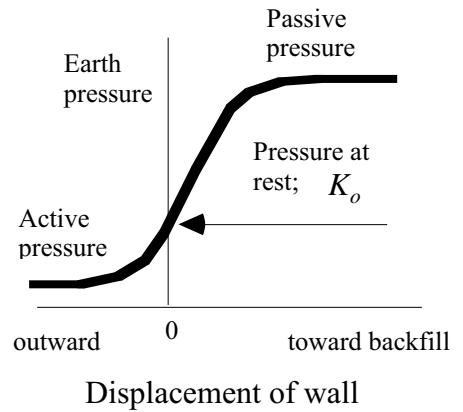
**Fig. A.2** Length of the back face of a wall

$$P_a = \frac{\gamma H_f^2}{2} K_{af} \tag{A.38}$$

$$K_{af} = \frac{\cos^2(\phi - \alpha)}{\cos(\alpha + \delta) \left\{ 1 + \sqrt{\frac{\sin(\phi - \beta) \sin(\delta + \phi)}{\cos(\alpha - \beta) \cos(\alpha + \delta)}} \right\}^2} \tag{A.39}$$

**7. Active vs. Passive and  $K_0$  Pressures**

Figure A.3 illustrates a conceptual relationship between earth pressure and the displacement of a retaining wall. The two extreme earth pressures are called active and passive pressures. The passive pressure, denoted by  $P_p$ , is much greater than the active one.



**Fig. A.3** Relationship between earth pressure and displacement of retaining wall

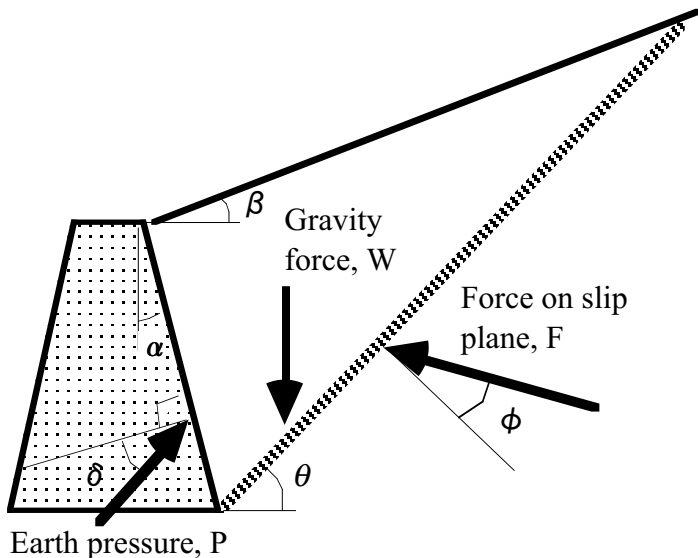
Figure A.4 presents a situation in which Coulomb’s passive pressure is calculated. A retaining wall is pushed toward the backfill soil, and, accordingly, the soil wedge is pushed up along the failure plane. Since the direction of movement is opposite from what was assumed in active failure, the inclinations of earth pressure and shear resistance,  $P$  and  $F$  respectively, from the normal direction are different as well. The passive pressure is given by

$$P_p = \frac{\gamma H^2}{2} K_p \tag{A.39}$$

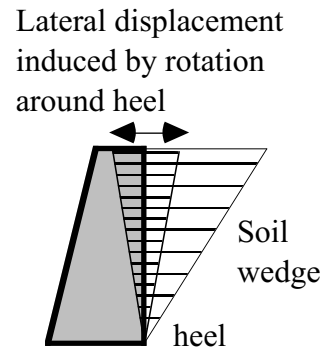
$$K_p = \frac{\cos^2(\phi + \alpha)}{\cos^2 \alpha \cos(\alpha - \delta) \left\{ 1 - \sqrt{\frac{\sin(\phi + \beta) \sin(\delta + \phi)}{\cos(\alpha - \beta) \cos(\alpha - \delta)}} \right\}^2} \tag{A.40}$$

The point of action of this earth pressure is one-third from the heel.

**8. Consistency of Wall Translation and Strain of Backfill Soil**



**Fig. A.4** State of passive earth pressure in Coulomb theory



**Fig. A.5** Distribution of strain in soil wedge

It is assumed in Coulomb theory that a retaining wall rotates around the heel in both active and passive situations. The rotation around the heel means that the displacement of the wall varies in proportion to the distance from the heel, while the width of the assumed triangular soil wedge varies with the same distance (Fig A.5). Hence, the horizontal strain in the soil wedge is constant, independent of the height from the heel. This uniformity suggested that the whole soil wedge reaches the yield condition simultaneously. In reality, however, effects of stress level and more complicated wall movement causes yielding at smaller strain at shallow depth as well as at larger strain at deeper elevation. Furthermore, rotation of a wall around the top and displacement of wall because of scouring at the foundation makes more complicated behavior of the wall and consequently the earth pressure distribution is made more complex. Such a situation is out of scope of the Coulomb theory.

## A.2 Convenient Expression in International Conversations

You may visit earthquake-affected countries for emergency aids, investigation, or retrofitting. In such situations, speaking a bit of local language improves the personal relationships. This section intends to facilitate your efforts in this direction. Note, however, that this section is neither sufficient due to page limitations nor accurate because of different styles of pronunciations. For a better skill, buy a conversation text book or go to a language school.

English	Spanish	Thai	Hindhi	Urdu (Pakistan)	Iran (Persian)
I	Yo	Phom <i>or</i> Dichan <sup>a</sup>	Maen	Main	Man
You	usted	Khun	aap	āp	Shoma
Thank you very much	Muchas gracias	Koopkhun maak kh <sup>b</sup>	Husti daniya-waad	Bahut sukiriya	Kheili (= <i>very much</i> ) motshakkeram
Hello	Hola	Sawadii kh <sup>b</sup>	Namaskar		Salaam
Nice to meet you	Mucho gusto	Sabaidii ruu kh <sup>b</sup>	Namaskar		Hoshbagtam
What	que/cual	arai	kya	kya	chi
What is your name?	¿Como se llama usted?	Chuu arai kh <sup>b</sup> ?	aap ka nam kya hai?		Esme shomaa chist?
My name is **	Me llamo **	Phom chuu ** : <i>male</i> . Dichan chuu ** : <i>female</i> .	mera nam ** hai.	mērā nām ** hai.	Esme man ** hast.
I am sorry	Lo siento	Khoothood kh <sup>b</sup>	maf kiziye	muaf kiziye	Moteassefan
Good bye	Hasta luego	Sawadii kh <sup>b</sup>	phir mileng	xudā hāfiz	Khoda hafez
This	esto <i>or</i> esta	Nii	ye	ye	Iin
Yes	Si	Kh <sup>b</sup>	jii haan	jī hān	Baale
No	No	Mai aw <sup>c</sup>	nahiin	nahīn	Nakheir
1	uno	nun	ek	ēk	yek
2	dos	son	do	dō	do
3	tres	saam	tiin	tin	se
4	cuatro	sii	char	car	chahar
5	cinco	haa	panji	panc	panj
6	seis	hog	che	che	shesh
7	siete	jet	saat	sāt	haft
8	ocho	pad	aat	āth	hasht
9	nueve	gaw	naw	nau	noh
10	dies	ship	das	das	dah
11	once	ship-ed	gyara	gyārā	yaz-dah
12	doce	ship-son	bara	bārā	davaz-dah
13	trece	ship-saam	tehra	terā	siz-dah
water	agua	nam	paanii	pānī	ab
earthquake	terremoto	pandīnwai	bhukampa	zalzala	zelzele

Find similarities among English, Spanish, Hindhi, Urdu, and Iran (Persian). They are similar because they come from a common ancient Indo-Eurasian language. Urdu is between Hindhi and Iran

a Thai language has different expressions for male (Phom) and female (Dichan) speakers

b *Kh* in Thai (meaning is polite ending of a spoken sentence) is “khrap” for men and “khaa” for women.

For politeness, *Kh* is put at the end of a sentence

c In Thai, no single expression is found for “No” in general. “Mai” means “not” and “aw” is “want”:  
 “Mai aw” actually means “I do not want” which is a convenient sentence during shopping

English	Indonesia	Philippines	Japanese	Turkish
I	Saya	Ako	Watashi	ben
You	Anda	Ikaw	Anata	sen (sngl), siz(pl)
Thank you very much	Terimakasih	Maraming salamat	Arigatou gozaimasu	teshekkür <sup>a</sup> ederim
Hello	Hai/Hello	Kumusta	Kon-nichi-wa	Merhaba
Nice to meet you	Senang bertemu anda	Nagagalak kitang makilala	Yoroshiku onegai shimasu	Nasılsınız <sup>b</sup>
What	apa	ano	nani	ne
What is your name?	Nama nya si apa?	Anong pangalan mo?	Anata no namae wa nani desu ka?	Adınız <sup>b</sup> nedir?
My name is **	Nama saya adalah **	Ang pangalan ko ay **	Watashino namae wa ** desu	Ben **.
I am sorry	Maaf	Ipagpaumanhin	Gomen nasai	Affedersiniz
Good bye.	Salamat ringgal <sup>c</sup> Selamat jalan <sup>d</sup>	Paalam	Sayonara	Hosça kalın
This	ini	Ito	Kore	bu
Yes	ya	Oo/Opo	Hai	evet
No	tidak	Hindi	iie	hayır
1	satu	isa	ichi	bir
2	dua	dalawa	ni	iki
3	tiga	tatlo	san	üç
4	unpat	apat	shi	dört
5	lima	lima	go	bes
6	nnam	anim	roku	altı
7	tujuf	pito	nana	yedi
8	durapan	walo	hachi	sekiz
9	sumbiran	siyam	ku	dokuz
10	supruf	sampu	juu	on
11	se-belas	labing isa	juu-ichi	on bir
12	dua-belas	labing dalawa	juu-ni	on iki
13	tiga-belas	labing tatlo	juu-san	on üç
water	ai r <sup>e</sup>	tubig	mizu	su
earthquake	gempa <sup>f</sup>	lindol	jishin	deprem

The author found that many Kazakhstan people understands Turkish spoken by engineers from Istanbul. This is because the ancient Turkish people moved from Mongolian area toward the west

a In Turkish writing, this “sh” is written by using a special character

b “ı” in Turkish language looks similar to “i” but has no point at its top. Its pronunciation is slightly similar to “u” but your mouth is pulled laterally

c Used when you are leaving

d Used when you are seeing somebody off

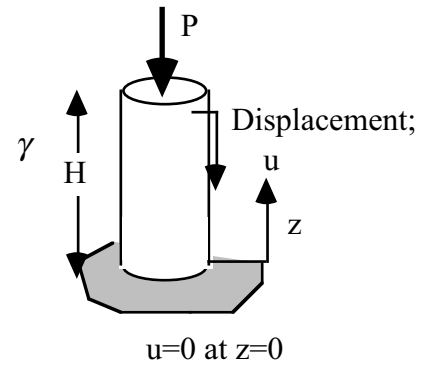
e Pronunciation is “ai - r”, and is different from that of English word for *air*

f For better pronunciation, this may be written as *gümpa*

**Excuse:** different languages use different alphabets. It is impossible to write them correctly in this page. In this respect, the table above is extremely primitive.

### A.3 Application of Variational Principle of Mathematics to Deformation Analysis

An example of application of variational principle of mathematics is presented in this appendix. A study is made of a vertical elastic column (Fig. A.6) that is subjected to the axial compression due to gravity (unit weight) as well as the top loading,  $P$ . The cross section of the column is taken equal to unity (1.00) for simplicity, while the elastic modulus is denoted by  $E$ .



**Fig. A.6** Elastic vertical column subjected to axial loading

#### 1. Classic Approach

In the classic method of analysis, first, the normal stress at the elevation of  $z$  is calculated;

$$\sigma(z) = P + \gamma(H - z) \quad (\text{A.42})$$

in which  $\gamma$  stands for the unit weight (gravity force per volume). Accordingly, the vertical strain and displacement are quickly calculated by using the fixed boundary condition of  $u = 0$  at  $z = 0$  (at the bottom):

$$\varepsilon = \frac{(P + \gamma H) - \gamma z}{E} \quad \text{and} \quad u = \int_0^z \varepsilon dz = \frac{P + \gamma H}{E} z - \frac{\gamma}{2E} z^2. \quad (\text{A.43})$$

#### 2. Approach Based on Energy Approach

By referring to (A.43), an assumption is made of a displacement solution such as

$$u = az + bz^2 \quad (\text{A.44})$$

in which  $a$  and  $b$  are unknown and are going to be determined by using the principle of minimum potential energy. Note that equilibrium of forces is equivalent with the minimum potential energy.

The potential energy,  $Q$ , of the model in Fig. A.6 consists of the strain energy and a gravity contribution,

$$\begin{aligned} Q &= \int_0^H \frac{E}{2} \varepsilon^2 dz - \int_0^H \gamma u dz - P u_{z=H} \\ &= \frac{E}{2} \int_0^H (z^2 + 4abz + 4b^2 z^2) dz - \gamma \int_0^H (az + bz^2) dz - P(aH + bH^2) \\ &= \frac{E}{2} \left( a^2 H + 2abH^2 + \frac{4b^2}{3} H^3 \right) - \gamma \left( \frac{a}{2} H^2 + \frac{b}{3} H^4 \right) - P(aH + bH^2). \end{aligned} \quad (\text{A.45})$$

Equation (A.45) is minimized by choosing suitable values of  $a$  and  $b$ ;

$$\begin{aligned} \frac{\partial Q}{\partial a} = \frac{\partial Q}{\partial b} &= 0 \\ EH(a + bH) &= \frac{\gamma H^2}{2} + PH \quad \text{and} \quad \frac{EH}{3}(3aH + 4H^2 b) = \frac{\gamma H^3}{3} + pH^2. \end{aligned} \quad (\text{A.46})$$

Consequently,

$$a = \frac{\gamma H + P}{E} \quad \text{and} \quad b = -\frac{\gamma}{2E}, \tag{A.47}$$

which agree with the classical solution in (A.45). Thus, an energy approach can provide a good solution as long as an assumed function is reasonable.

### 3. Simplification of Analysis by Energy Approach

An approximate solution is attempted by using a further simplified function;

$$u = c \sin \frac{\pi z}{2H} \quad \text{and} \quad \varepsilon = \frac{du}{dz} = \frac{\pi c}{2H} \cos \frac{\pi z}{2H} \tag{A.48}$$

in which  $c$  is unknown. The potential energy is calculated by using (A.48);

$$\begin{aligned} Q &= \int_0^H \frac{E}{2} \varepsilon^2 dz - \int_0^H \gamma u dz - P u_{z=H} \\ &= \frac{E\pi^2}{16H} c^2 - \left( \frac{2\gamma H}{\pi} + P \right) c \rightarrow \text{minimum.} \\ \frac{dQ}{dc} &= \frac{E\pi^2}{8H} c - \left( \frac{2\gamma H}{\pi} + P \right) = 0. \end{aligned} \tag{A.49}$$

Therefore,

$$u = c \sin \frac{\pi z}{2H} = \frac{8H}{E\pi^2} \left( \frac{2\gamma H}{\pi} + P \right) \sin \frac{\pi z}{2H}. \tag{A.50}$$

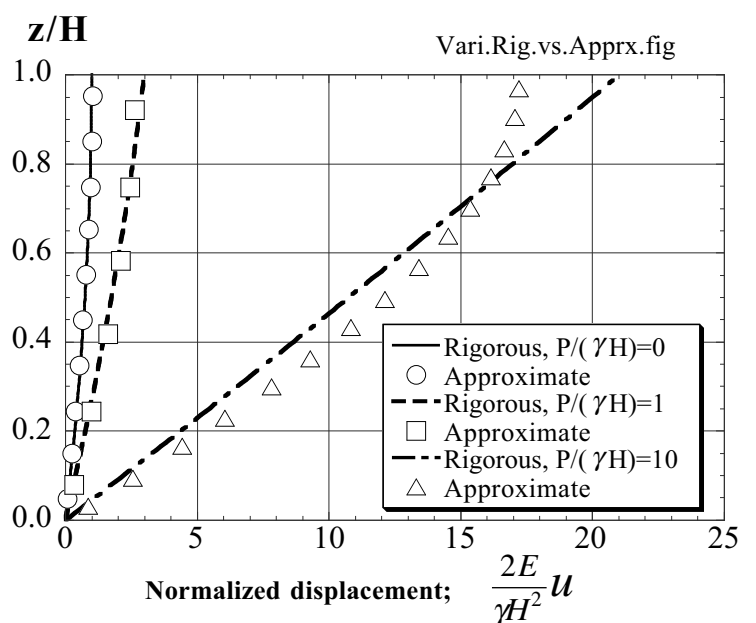
This approximate solution (A.50) is compared with the rigorous solution (A.43) in Fig. A.7. It can be therein found that the approximate solution is not bad generally. Even when the top load,  $P$ , is significantly greater than the weight of the column, the approximation is still reasonable.

### 4. Analysis Based on Variational Principle

Finally, it is intended to find the displacement solution,  $u$ , by combining the principle of minimum potential energy with the variational principle of mathematics. The problem to be solved is described as

*detecting a function,  $u(z)$ , which minimizes the integration;*

$$Q = \int_0^H \frac{E}{2} \varepsilon^2 dz - \int_0^H \gamma u dz - P u_{z=H} .$$



**Fig. A.7** Comparison of approximate and rigorous solutions

Similar to the idea of  $df/dx = 0$  when  $f(x)$  is minimum, the present problem is rewritten as

“ $Q$  does not change when function,  $u$ , changes slightly from the true solution of  $u$  to  $u(z) + \Delta u(z)$ .”

It is assumed that the incremental function,  $\Delta u$ , is arbitrary but satisfies the boundary condition at the base;

$$\Delta u = 0 \text{ at } z = 0. \quad (\text{A.51})$$

Accordingly,

$$\begin{aligned} \Delta Q &\equiv Q(u + \Delta u) - Q(u) = 0 \\ \int_0^H \left[ \frac{E}{2} \left\{ \left( \frac{du}{dz} + \frac{d\Delta u}{dz} \right)^2 - \left( \frac{du}{dz} \right)^2 \right\} - \gamma(u + \Delta u - u) \right] dz - P\Delta u_{z=H} &= 0 \\ \int_0^H \left[ \frac{E}{2} \left\{ 2 \frac{du}{dz} \frac{d\Delta u}{dz} + \left( \frac{d\Delta u}{dz} \right)^2 - \gamma\Delta u \right\} \right] dz - P\Delta u_{z=H} &= 0 \end{aligned}$$

Since the second-order term,  $(d\Delta u/dz)^2$ , is negligible,

$$\int_0^H \left[ \frac{E}{2} \left\{ 2 \frac{du}{dz} \frac{d\Delta u}{dz} - \gamma\Delta u \right\} \right] dz - P\Delta u_{z=H} = 0$$

By partial integration,

$$\begin{aligned} E \left[ \frac{du}{dz} \Delta u \right]_0^H - \int_0^H \left( E \frac{d^2 u}{dz^2} + \gamma \right) \Delta u dz - P\Delta u_{z=H} &= 0 \\ \left[ \left( E \frac{du}{dz} - P \right) \Delta u \right]_{z=H} - E \left[ \frac{du}{dz} \Delta u \right]_{z=0} - \int_0^H \left( E \frac{d^2 u}{dz^2} + \gamma \right) \Delta u dz &= 0 \end{aligned}$$

for an arbitrary function of  $\Delta u$ .

Since the boundary condition already specified  $\Delta u = 0$  at  $z = 0$ , the second term is already equal to zero. Therefore, this requirement is satisfied when

$$E \frac{d^2 u}{dz^2} + \gamma = 0 \quad (\text{A.52})$$

$$E \frac{du}{dz} = P \text{ at the top.} \quad (\text{A.53})$$

It is thus found that the energy principle (minimization of integration) is equivalent with a differential equation (A.52) together with a relevant boundary condition (A.53). Equation (A.52) is called *Euler's* differential equation of the original integration principle.

### List of References in Appendix

Oka, F. (1995) Exercises in Soil Mechanics, Morikita Publ., ISBN4-627-42660-7, pp. 215–222 (in Japanese).



# Answer to Exercises



Stone sculpture of Bhuddism, Kyoto.

**Exercise 1 in Sect. 4.6 on Amplification of Motion with Surface Mass**

1. Use (4.14). Suppose that real and imaginary parts of  $E$  and  $F$  are given by  $E = E_R + iE_I$  and  $F = F_R + iF_I$ . Taking only the real part of  $u$  and  $\partial u/\partial z$ ,

$$\text{Re}(u) = E_R \cos\omega\left(t + \frac{z}{V_s}\right) - E_I \sin\left(t + \frac{z}{V_s}\right) + F_R \cos\omega\left(t - \frac{z}{V_s}\right) - F_I \sin\left(t - \frac{z}{V_s}\right) \tag{E.1}$$

$$\text{Re}\left(\frac{\partial u}{\partial z}\right) = \frac{\omega}{V_s} \left\{ -E_R \sin\omega\left(t + \frac{z}{V_s}\right) - E_I \cos\left(t + \frac{z}{V_s}\right) + F_R \sin\omega\left(t - \frac{z}{V_s}\right) + F_I \cos\left(t - \frac{z}{V_s}\right) \right\} = 0 \tag{E.2}$$

at  $z=0$  at any time. Hence,

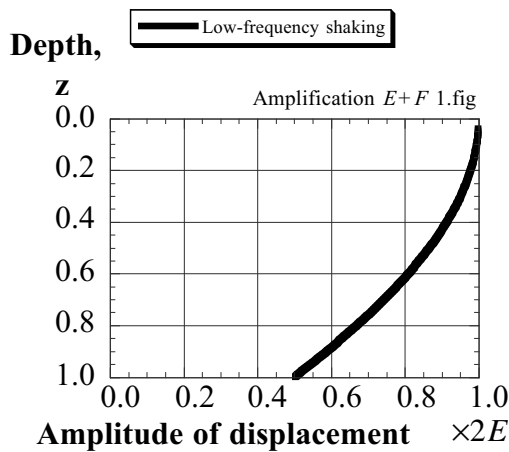
$$(-E_R + F_R)\sin\omega t + (-E_I + F_I)\cos\omega t = 0$$

at any  $t$ . Therefore,  $E_R = F_R$  and  $E_I = F_I$ . Hence,  $E = F$ .

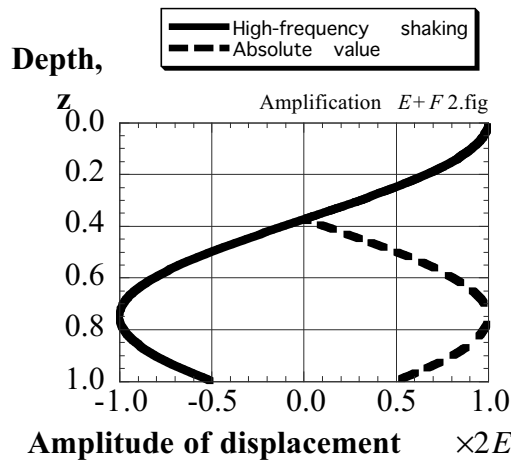
2. By using  $E = F$ ,

$$\text{Re}(u) = E \left[ \cos\left\{\omega\left(t + \frac{z}{V_s}\right)\right\} + \cos\left\{\omega\left(t - \frac{z}{V_s}\right)\right\} \right] = 2 \cos\frac{\omega z}{V_s} \cos\omega t$$

Therefore, the amplitude of displacement is given by  $2 \cos\frac{\omega z}{V_s}$ . See Figs. E.1 and E.2.



**Fig. E.1** Amplitude of motion for low frequency



**Fig. E.2** Amplitude of motion for high frequency

3. Amplification factor is given by

$$\frac{2E \cos\frac{\omega \times 0}{V_s}}{2E \cos\frac{\omega \times H}{V_s}} = \frac{1}{\cos\frac{\omega \times H}{V_s}}$$

See Fig. E.3 for plotting. Note that an infinite amplification (resonance) occurs at

$$\frac{\omega H}{V_s} = \frac{\pi}{2}, \frac{3\pi}{2}, \frac{5\pi}{2}, \dots \text{etc.}$$

In the fundamental mode,  $\frac{\omega H}{V_s} = \frac{\pi}{2}$  and the period of motion  $T = 2\pi/\omega = 4H/V_s$ . This is extremely important.

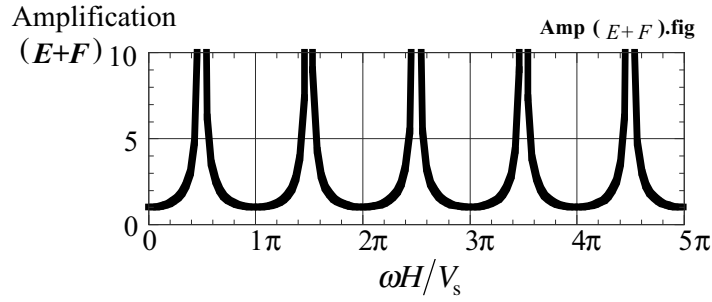


Fig. E.3 Amplification of motion in terms of  $E+F$

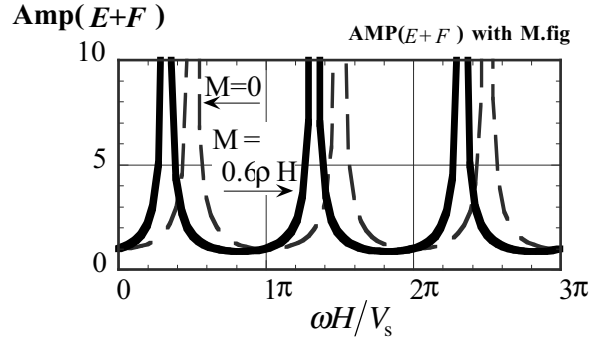


Fig. E.4 Amp( $E+F$ ) for surface mass of  $M$

4. The boundary condition at the surface where a rigid mass of  $M$  moves together with soil is given by the continuity of displacement and the equation of motion

$$M \frac{\partial^2 u}{\partial t^2} = \text{Shear stress} = G \frac{\partial u}{\partial z} \quad \text{at } z=0. \quad (\text{E.3})$$

By substituting (E.1) and (E.2) with  $z=0$ ,

$$-M\omega^2 \left\{ (E_R + F_R) \cos \omega t - (E_I + F_I) \sin \omega t \right\} = -\frac{\omega G}{V_s} \left\{ (E_I - F_I) \cos \omega t + (E_R - F_R) \sin \omega t \right\}.$$

Since this equation holds true at any time of  $t$ ,

$$M\omega(E_R + F_R) = \rho V_s (E_I - F_I) \quad \text{and} \quad M\omega(E_I + F_I) = -\rho V_s (E_R - F_R),$$

for which  $G = \rho V_s^2$  was used. Accordingly,

$$\begin{Bmatrix} F_R \\ F_I \end{Bmatrix} = \frac{1}{\rho^2 V_s^2 + M^2 \omega^2} \begin{bmatrix} \rho^2 V_s^2 - M^2 \omega^2 & \rho V_s M \omega \\ -\rho V_s M \omega & \rho^2 V_s^2 - M^2 \omega^2 \end{bmatrix} \begin{Bmatrix} E_R \\ E_I \end{Bmatrix}.$$

The calculation is made simpler by employing complex numbers. Start with

$$u = E \exp \left\{ i\omega \left( t + \frac{z}{V_s} \right) \right\} + F \exp \left\{ i\omega \left( t - \frac{z}{V_s} \right) \right\} \quad \text{and}$$

$$\tau = G \frac{\partial u}{\partial z} = \rho V_s^2 \frac{i\omega}{V_s} \left[ E \exp \left\{ i\omega \left( t + \frac{z}{V_s} \right) \right\} - F \exp \left\{ i\omega \left( t - \frac{z}{V_s} \right) \right\} \right].$$

Substituting these in (E.3) with  $z=0$ ,

$$-M\omega^2 (E + F) = i\rho V_s \omega (E - F) \quad \text{and} \quad F = -\frac{M\omega + i\rho V_s}{M\omega - i\rho V_s} E.$$

Consequently, the amplification is calculated as what follows and illustrated in Fig. E.4.

$$\text{Amp}(E + F) = \left| \frac{u(z=0)}{u(z=H)} \right| = \left| \frac{E + F}{E \exp \left( \frac{i\omega H}{V_s} \right) + F \exp \left( -\frac{i\omega H}{V_s} \right)} \right| = \left| \frac{\rho V_s}{\rho V_s \cos \frac{\omega H}{V_s} - M\omega \sin \frac{\omega H}{V_s}} \right|$$

$$= \frac{1}{\left| \cos \frac{\omega H}{V_s} - \frac{M\omega}{\rho V_s} \sin \frac{\omega H}{V_s} \right|}$$

**Exercise 2 on Response to Outcrop Motion**

Displacement is expressed as in Sect. 6.7:

$$\text{In the surface alluvium, } u_1 = E_1 \exp\left\{i\omega\left(t + \frac{z}{V_{s1}}\right)\right\} + F_1 \exp\left\{i\omega\left(t - \frac{z}{V_{s1}}\right)\right\} \quad (\text{E.4})$$

$$\text{and in the base rock and outcrop, } u_2 = E_2 \exp\left\{i\omega\left(t + \frac{z-H}{V_{s1}}\right)\right\} + F_2 \exp\left\{i\omega\left(t - \frac{z-H}{V_{s1}}\right)\right\}.$$

1. Since the ground surface is a free boundary (shear stress=0),

$$F_1 = E_1.$$

$$\text{Referring to Sect. 6.7, } \begin{Bmatrix} E_2 \\ F_2 \end{Bmatrix} = E_1 \begin{pmatrix} \cos \frac{\omega H}{V_{s1}} \pm i \frac{\rho_1 V_{s1}}{\rho_2 V_{s2}} \sin \frac{\omega H}{V_{s1}} \end{pmatrix}$$

Since the outcrop is a continuation of the elastic base,

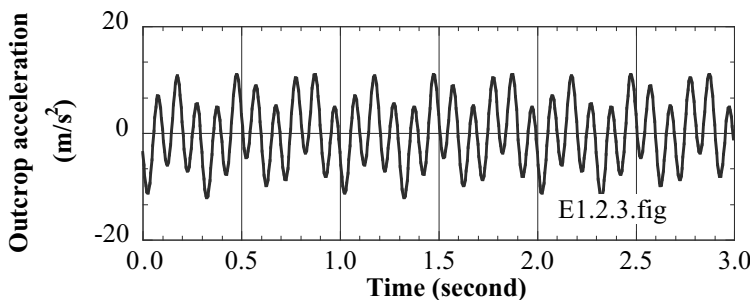
$$E'_1 = F'_1 = E_2 = E_1 \left( \cos \frac{\omega H}{V_{s1}} + i \frac{\rho_1 V_{s1}}{\rho_2 V_{s2}} \sin \frac{\omega H}{V_{s1}} \right) \text{ and } F'_1 = F_2^* \quad (\text{E.5})$$

$$2. \text{ Amp}(E + F) = \left| \frac{2E_1}{E_2 + F_2} \right| = \frac{1}{\left| \cos \frac{\omega H}{V_{s1}} \right|} \text{ and}$$

$$\text{Amp}(2E) = \left| \frac{2E_1}{2E'_2} \right| = \frac{1}{\sqrt{\left( \cos \frac{\omega H}{V_{s1}} \right)^2 + \left( \frac{\rho_1 V_{s1}}{\rho_2 V_{s2}} \sin \frac{\omega H}{V_{s1}} \right)^2}}$$

3. By differentiating the displacement time history twice,

$$\begin{aligned} \text{Accel}_{\text{outcrop}}(t) &= \frac{d^2 u_{\text{outcrop}}}{dt^2} \\ &= -(2\pi)^2 0.02 \sin 2\pi t - (6\pi)^2 0.01 \cos 6\pi t - (20\pi)^2 0.002 \sin 20\pi t. \end{aligned}$$



**Fig. E.5** Time history of outcrop acceleration

Note that the acceleration record is dominated by higher frequency components than the displacement time history.

4. As shown by (6.44), the outcrop displacement history consists of three harmonic components for which  $E'_1 = F'_1 = 0.02/2, 0.01/2,$  and  $0.002/2$  for  $\omega = 2\pi, 6\pi,$  and  $20\pi,$  respectively. By using (E.5) together with  $\rho_1 = \rho_2$  (this assumption is not very bad),

$$\begin{aligned}
 E_1 &= \frac{E_2}{\cos \frac{\omega H}{V_{s1}} + i \frac{\rho_1 V_{s1}}{\rho_2 V_{s2}} \sin \frac{\omega H}{V_{s1}}} = \frac{E'_1}{\cos \frac{\omega H}{V_{s1}} + i \frac{\rho_1 V_{s1}}{\rho_2 V_{s2}} \sin \frac{\omega H}{V_{s1}}} \\
 &= \frac{0.01}{\cos \frac{2\pi \times 12}{150} + i \frac{150}{800} \sin \frac{24\pi}{150}} \frac{0.005}{\cos \frac{6\pi \times 12}{150} + i \frac{150}{800} \sin \frac{72\pi}{150}} \frac{0.001}{\cos \frac{20\pi \times 12}{150} + i \frac{150}{800} \sin \frac{240\pi}{150}} \\
 &= \frac{0.01}{0.876 + 0.090i} \frac{0.005}{0.063 + 0.187i} \frac{0.001}{0.309 - 0.178i} \frac{150}{800}. \tag{E.6}
 \end{aligned}$$

Note that  $E_1 = F_1$ .

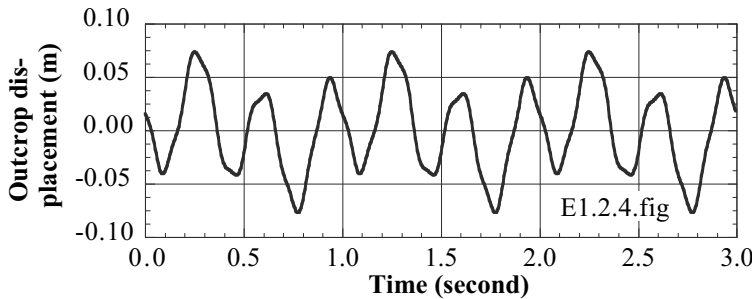
By substituting these values and  $z=0$  in (E.4),

$$u_1 = E_1 \exp\left\{i\omega\left(t + \frac{z}{V_{s1}}\right)\right\} + F_1 \exp\left\{i\omega\left(t - \frac{z}{V_{s1}}\right)\right\} = 2E_1 \exp(i\omega t) \tag{E.7}$$

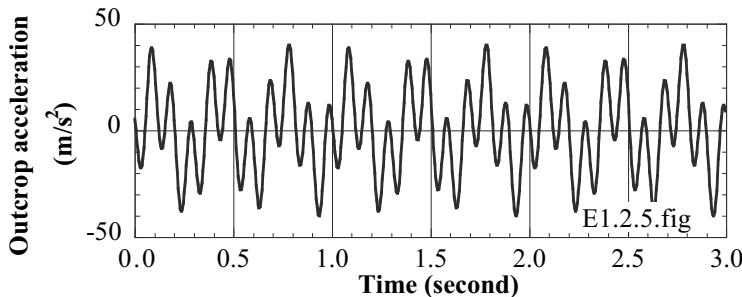
Also, (6.44) is converted to a complex function of time whose real part is equal to the original time history

$$u_{\text{outcrop}}(t) = -i \times 0.02 \exp(2\pi i t) + 0.01 \exp(6\pi i t) - i \times 0.002 \exp(20\pi i t) \tag{E.8}$$

The surface motion of alluvium is *not* obtained by multiplying *amplification* to the outcrop motion. The imaginary part of (E.6) has to be taken into account because they produces phase difference between the incident (outcrop) motion and the surface motion. By applying Eqs (E.5) or (E.6) to three frequency components of the outcrop record (6.44),



**Fig. E.6** Time history of displacement at surface of alluvium



**Fig. E.7** Time history of acceleration at surface of alluvium

$$\begin{aligned}
 u_{\text{outcrop}}(t) &= -i \times \frac{0.02}{0.876 + 0.090i} \exp(2\pi i t) + \frac{0.01}{\cos \frac{6\pi \times 12}{150} + i \frac{150}{800} \sin \frac{72\pi}{150}} \exp(6\pi i t) \\
 &\quad - i \times \frac{0.002}{\cos \frac{20\pi \times 12}{150} + i \frac{150}{800} \sin \frac{240\pi}{150}} \exp(20\pi i t), \text{ whose real part is plotted in Fig. E.6.}
 \end{aligned}$$

It is found therein that the surface displacement has stronger high frequency component than the outcrop motion (Fig. 6.48) because the natural period of the alluvium is  $4H/V_{s1}=0.32$  second and is close to the loading period of the second component (3 Hz, 0.33 s).

Finally, the acceleration time history is calculated by double differentiation of the displacement time history. The result is plotted in Fig. E.7.

### Exercise 3 on Calculation of Amplification Factor

The harmonic solutions for displacement and stress are as what follows.

In the first layer,

$$u_1 = E_1 \exp\left\{i\omega\left(t + \frac{z}{V_{s1}}\right)\right\} + F_1 \exp\left\{i\omega\left(t - \frac{z}{V_{s1}}\right)\right\} \text{ and}$$

$$\tau_1 = G_1 \frac{\partial u_1}{\partial z} = i\omega\rho_1 V_{s1} \left[ E_1 \exp\left\{i\omega\left(t + \frac{z}{V_{s1}}\right)\right\} - F_1 \exp\left\{i\omega\left(t - \frac{z}{V_{s1}}\right)\right\} \right].$$

In the second layer,

$$u_2 = E_2 \exp\left\{i\omega\left(t + \frac{z - H_1}{V_{s2}}\right)\right\} + F_2 \exp\left\{i\omega\left(t - \frac{z - H_1}{V_{s2}}\right)\right\}$$

$$\tau_2 = G_2 \frac{\partial u_2}{\partial z} = i\omega\rho_2 V_{s2} \left[ E_2 \exp\left\{i\omega\left(t + \frac{z - H_1}{V_{s2}}\right)\right\} - F_2 \exp\left\{i\omega\left(t - \frac{z - H_1}{V_{s2}}\right)\right\} \right].$$

Since the displacement and stress are continuous across the interface of these two layers,

$$E_1 \exp\left(\frac{i\omega H_1}{V_{s1}}\right) + F_1 \exp\left(-\frac{i\omega H_1}{V_{s1}}\right) = E_2 + F_2$$

$$\frac{\rho_1 V_{s1}}{\rho_2 V_{s2}} \left[ E_1 \exp\left(\frac{i\omega H_1}{V_{s1}}\right) - F_1 \exp\left(-\frac{i\omega H_1}{V_{s1}}\right) \right] = E_2 - F_2.$$

Therefore,

$$\begin{Bmatrix} E_2 \\ F_2 \end{Bmatrix} = \frac{1}{2} \begin{bmatrix} \left(1 + \frac{\rho_1 V_{s1}}{\rho_2 V_{s2}}\right) \exp\left(\frac{i\omega H_1}{V_{s1}}\right) & \left(1 - \frac{\rho_1 V_{s1}}{\rho_2 V_{s2}}\right) \exp\left(-\frac{i\omega H_1}{V_{s1}}\right) \\ \left(1 - \frac{\rho_1 V_{s1}}{\rho_2 V_{s2}}\right) \exp\left(\frac{i\omega H_1}{V_{s1}}\right) & \left(1 + \frac{\rho_1 V_{s1}}{\rho_2 V_{s2}}\right) \exp\left(-\frac{i\omega H_1}{V_{s1}}\right) \end{bmatrix} \begin{Bmatrix} E_1 \\ F_1 \end{Bmatrix}.$$

There is a similar relationship between  $(E_3, F_3)$  and  $(E_2, F_2)$ . Combining them and using  $\exp(ix) = \cos x + i \sin x$  and  $E_1 = F_1$  (shear stress = 0 at the surface),

$$\begin{Bmatrix} E_3 \\ F_3 \end{Bmatrix} = E_1 \begin{Bmatrix} \left( \cos \frac{\omega H_1}{V_{s1}} \cos \frac{\omega H_2}{V_{s2}} - \frac{\rho_1 V_{s1}}{\rho_2 V_{s2}} \sin \frac{\omega H_1}{V_{s1}} \sin \frac{\omega H_2}{V_{s2}} \right) + i \frac{\rho_2 V_{s2}}{\rho_3 V_{s3}} \left( \cos \frac{\omega H_1}{V_{s1}} \sin \frac{\omega H_2}{V_{s2}} + \frac{\rho_1 V_{s1}}{\rho_2 V_{s2}} \sin \frac{\omega H_1}{V_{s1}} \cos \frac{\omega H_2}{V_{s2}} \right) \\ \left( \cos \frac{\omega H_1}{V_{s1}} \cos \frac{\omega H_2}{V_{s2}} - \frac{\rho_1 V_{s1}}{\rho_2 V_{s2}} \sin \frac{\omega H_1}{V_{s1}} \sin \frac{\omega H_2}{V_{s2}} \right) - i \frac{\rho_2 V_{s2}}{\rho_3 V_{s3}} \left( \cos \frac{\omega H_1}{V_{s1}} \sin \frac{\omega H_2}{V_{s2}} + \frac{\rho_1 V_{s1}}{\rho_2 V_{s2}} \sin \frac{\omega H_1}{V_{s1}} \cos \frac{\omega H_2}{V_{s2}} \right) \end{Bmatrix}$$

The two types of amplification are given by

$$\text{Amp}(2E) = \frac{|2E_1|}{|2E_3|} = \frac{1}{\sqrt{\left(\cos\frac{\omega H_1}{V_{s1}}\cos\frac{\omega H_2}{V_{s2}} - \frac{\rho_1 V_{s1}}{\rho_2 V_{s2}}\sin\frac{\omega H_1}{V_{s1}}\sin\frac{\omega H_2}{V_{s2}}\right)^2 + \left(\frac{\rho_2 V_{s2}}{\rho_3 V_{s3}}\right)^2 \left(\cos\frac{\omega H_1}{V_{s1}}\sin\frac{\omega H_2}{V_{s2}} + \frac{\rho_1 V_{s1}}{\rho_2 V_{s2}}\sin\frac{\omega H_1}{V_{s1}}\cos\frac{\omega H_2}{V_{s2}}\right)^2}}$$

$$\text{Amp}(E+F) = \frac{|2E_1|}{|E_3 + F_3|} = \frac{1}{\left|\cos\frac{\omega H_1}{V_{s1}}\cos\frac{\omega H_2}{V_{s2}} - \frac{\rho_1 V_{s1}}{\rho_2 V_{s2}}\sin\frac{\omega H_1}{V_{s1}}\sin\frac{\omega H_2}{V_{s2}}\right|}$$

When  $\rho_1 = \rho_2 = \rho_3$ ,  $V_{s1} = 100$  m/s,  $V_{s2} = 200$  m/s,  $V_{s3} = 500$  m/s,  $H_1 = 5$  m,  $H_2 = 15$  m, for example, the amplification was illustrated below. The outcrop motion is identical with  $(E_3, F_3)$ , because the rock medium reaches the surface. Therefore,  $\text{Amp}(2E)$  is the ratio of surface motion and rock-outcrop motion.

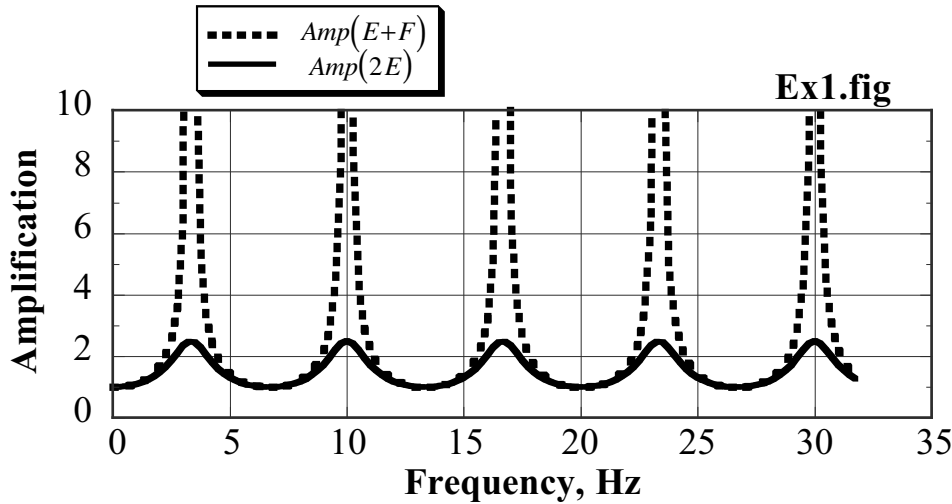


Fig. E.8 Different amplification factors for  $\text{Amp}(E+F)$  and  $\text{Amp}(2E)$

#### Exercise 4 on Amplification of complex-Modulus Ground

By referring to Sect. 9.7, displacement and shear stress in three layers are derived

$$u_1 = E_1 \left[ \exp\left\{i\omega\left(t + \frac{z_1}{V_{s1}^*}\right)\right\} + \exp\left\{i\omega\left(t - \frac{z_1}{V_{s1}^*}\right)\right\} \right]$$

$$\tau_1 = G_1(1 + 2ih_1) \frac{i\omega}{V_{s1}^*} E_1 \left[ \exp\left\{i\omega\left(t + \frac{z_1}{V_{s1}^*}\right)\right\} - \exp\left\{i\omega\left(t - \frac{z_1}{V_{s1}^*}\right)\right\} \right]$$

$$= \rho_1 V_{s1}^* i\omega E_1 \left[ \exp\left\{i\omega\left(t + \frac{z_1}{V_{s1}^*}\right)\right\} - \exp\left\{i\omega\left(t - \frac{z_1}{V_{s1}^*}\right)\right\} \right]$$

$$u_2 = E_2 \exp\left\{i\omega\left(t + \frac{z_2}{V_{s2}^*}\right)\right\} + F_2 \exp\left\{i\omega\left(t - \frac{z_2}{V_{s2}^*}\right)\right\}$$

$$\tau_2 = \rho_2 V_{s2}^* i\omega \left[ E_2 \exp\left\{i\omega\left(t + \frac{z_2}{V_{s2}^*}\right)\right\} - F_2 \exp\left\{i\omega\left(t - \frac{z_2}{V_{s2}^*}\right)\right\} \right]$$

$$u_b = E_b \exp\left\{i\omega\left(t + \frac{z_b}{V_{sb}^*}\right)\right\} + F_b \exp\left\{i\omega\left(t - \frac{z_b}{V_{sb}^*}\right)\right\}$$

$$\tau_b = \rho_b V_{sb}^* i\omega \left[ E_b \exp\left\{i\omega \left(t + \frac{z_b}{V_{sb}^*}\right)\right\} - F_b \exp\left\{i\omega \left(t - \frac{z_b}{V_{sb}^*}\right)\right\} \right],$$

in which  $V_s^* = V_s(1+4h^2)^{1/4} \exp(i\delta/2)$  and  $V_s = \sqrt{G/\rho}$  in each layer.

The requirement for continuity of displacement and shear stress between the first and the second layers ( $z_1=H_1$  or  $z_2=0$ ) leads to

$$\begin{bmatrix} 1 & 1 \\ \left(\frac{\rho_2 V_{s2}^*}{\rho_1 V_{s1}^*}\right) & -\left(\frac{\rho_2 V_{s2}^*}{\rho_1 V_{s1}^*}\right) \end{bmatrix} \begin{Bmatrix} E_2 \\ F_2 \end{Bmatrix} = \begin{Bmatrix} \exp\left(\frac{i\omega H_1}{V_{s1}^*}\right) + \exp\left(-\frac{i\omega H_1}{V_{s1}^*}\right) \\ \exp\left(\frac{i\omega H_1}{V_{s1}^*}\right) - \exp\left(-\frac{i\omega H_1}{V_{s1}^*}\right) \end{Bmatrix} E_1$$

The requirement for continuity between the second layer and the base ( $x_2=H_2$  or  $z_b=0$ ) leads to

$$\begin{bmatrix} 1 & 1 \\ \left(\frac{\rho_b V_{sb}^*}{\rho_2 V_{s2}^*}\right) & -\left(\frac{\rho_b V_{sb}^*}{\rho_2 V_{s2}^*}\right) \end{bmatrix} \begin{Bmatrix} E_b \\ F_b \end{Bmatrix} = \begin{Bmatrix} \exp\left(\frac{i\omega H_2}{V_{s2}^*}\right) & \exp\left(-\frac{i\omega H_2}{V_{s2}^*}\right) \\ \exp\left(\frac{i\omega H_2}{V_{s2}^*}\right) & -\exp\left(-\frac{i\omega H_2}{V_{s2}^*}\right) \end{Bmatrix} \begin{Bmatrix} E_2 \\ F_2 \end{Bmatrix}.$$

By starting with  $E_1=1.0$ , two sets of linear equations above give  $E_b$  and  $F_b$ , both of which are complex numbers. Consequently,

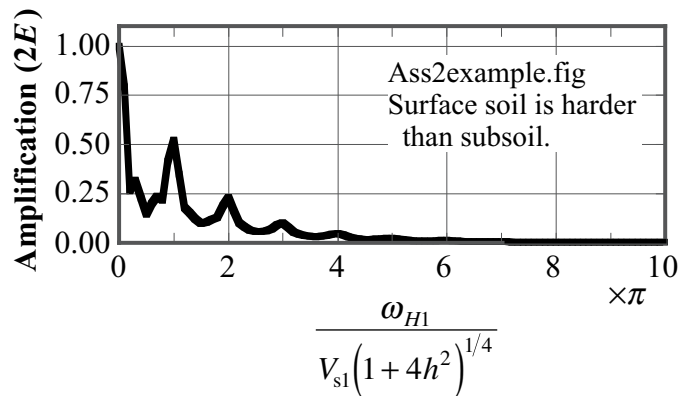
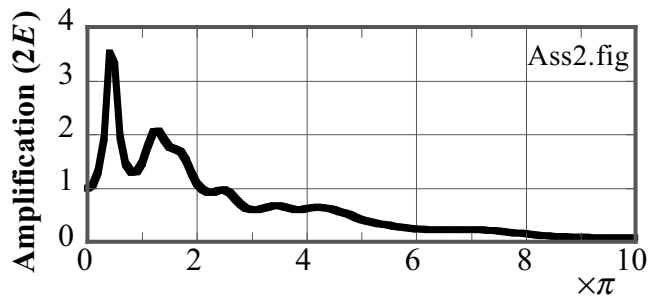
$$\text{Amp}(2E) = \frac{|2E_1|}{|2E_b|},$$

which is plotted in the figure.

More example calculation is made under the following conditions:

- Constant  $\rho$  of soils from the surface to the base
- $V_{s1}/V_{s2} = 6/1$  and,  $V_{s2}/V_{sb} = 1/3$
- Damping ratio :  $h_1=0.03$  and  $h_2=0.06$
- $H_1:H_2=2:1$ .

See that the amplification is less than unity. Thus, the surface motion is reduced when the top layer is harder than the underlying ones.



$$\frac{\omega_{H1}}{V_{s1}(1+4h^2)^{1/4}}$$



**Exercise 5 on Equivalent Linear Method of Analysis**

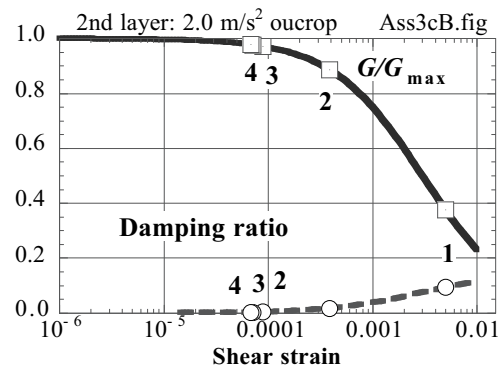
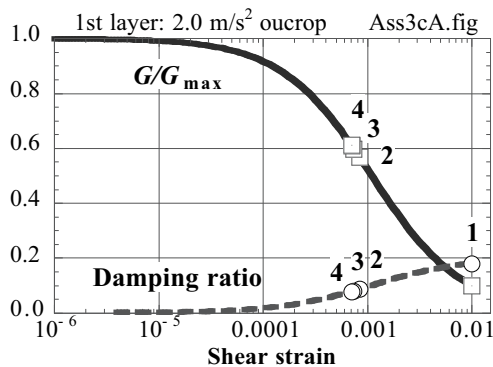
1. For the case of the outcrop motion = 0.2 m/s<sup>2</sup> and 5 Hz, the iteration proceeded as shown in the table below.

Iteration	Layer 1				Layer 2				Surface accel.
	Estimated strain	Shear modulus	Damping ratio	Obtained strain	Estimated strain	Shear modulus	Damping ratio	Obtained strain	
1	0.0100	4,460	0.180	8.4×10 <sup>-5</sup>	0.0050	91,900	0.094	3.8×10 <sup>-5</sup>	0.218
2	8.4×10 <sup>-5</sup>	41,800	0.014	6.1×10 <sup>-5</sup>	3.8×10 <sup>-5</sup>	242,000	0.002	1.9×10 <sup>-6</sup>	0.316
3	6.1×10 <sup>-5</sup>	42,600	0.011	6.1×10 <sup>-5</sup>	1.9×10 <sup>-6</sup>	245,000	0.000	2.3×10 <sup>-6</sup>	0.320
4	6.1×10 <sup>-5</sup>	42,600	0.011	6.1×10 <sup>-5</sup>	2.3×10 <sup>-6</sup>	245,000	0.000	2.3×10 <sup>-6</sup>	0.320
end	6.1×10 <sup>-5</sup>	42,600	0.011	6.1×10 <sup>-5</sup>	2.3×10 <sup>-6</sup>	245,000	0.000	2.3×10 <sup>-6</sup>	

Unit : strain in decimal, modulus in kN/m<sup>2</sup>, and acceleration in m/s<sup>2</sup>

2. For the case of the outcrop motion = 2.0 m/s<sup>2</sup> and 5 Hz, the iteration proceeded as shown in the table below. For the variation of modulus and damping with the number of iteration, see the figures below. Note that the developed strain for this outcrop motion = 2 m/s<sup>2</sup> is greater than that for 0.2 m/s<sup>2</sup>. Moreover, the strain in the upper layer is greater than in the second layer because of the different magnitudes of modulus.

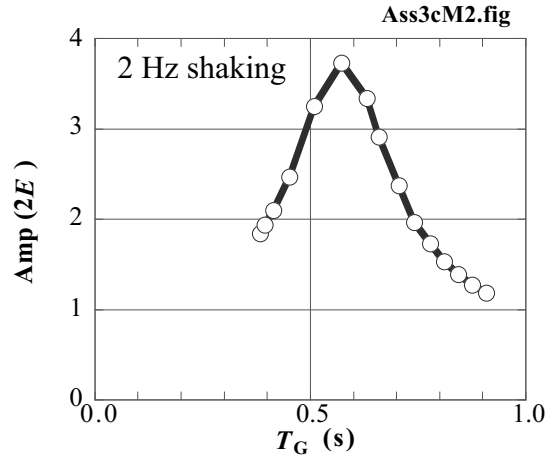
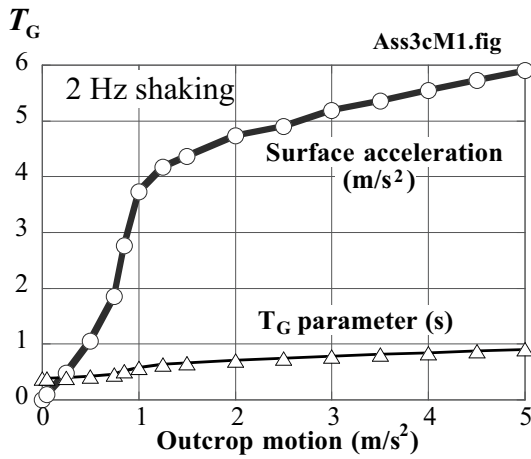
Iteration	Layer 1				Layer 2				Surface accel.
	Estimated strain	Shear modulus	Damping ratio	Obtained strain	Estimated strain	Shear modulus	Damping ratio	Obtained strain	
1	0.0100	4,460	0.180	8.35×10 <sup>-4</sup>	0.0050	91,900	0.094	3.8×10 <sup>-4</sup>	2.183
2	8.35×10 <sup>-4</sup>	25,600	0.086	7.41×10 <sup>-4</sup>	3.8×10 <sup>-4</sup>	217,000	0.017	8.9×10 <sup>-5</sup>	2.684
3	7.41×10 <sup>-4</sup>	26,900	0.080	7.07×10 <sup>-4</sup>	8.9×10 <sup>-5</sup>	238,000	0.004	7.2×10 <sup>-5</sup>	2.646
4	7.07×10 <sup>-4</sup>	27,400	0.078	7.01×10 <sup>-4</sup>	7.2×10 <sup>-5</sup>	239,000	0.003	6.8×10 <sup>-5</sup>	2.653
end	7.01×10 <sup>-4</sup>	27,500	0.078	7.01×10 <sup>-4</sup>	6.8×10 <sup>-5</sup>	240,000	0.003	6.8×10 <sup>-5</sup>	



(Analysis by ASS3c.f and Numbers in the figure indicate the sequence of iteration.)

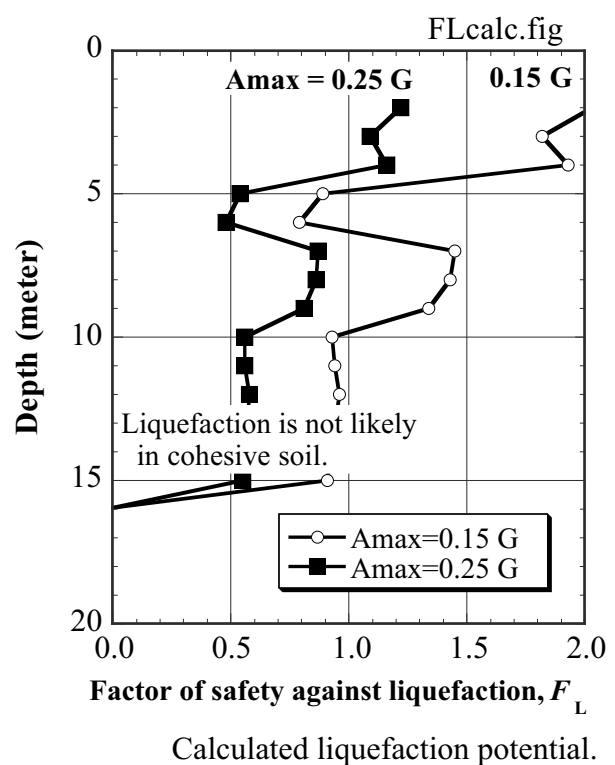
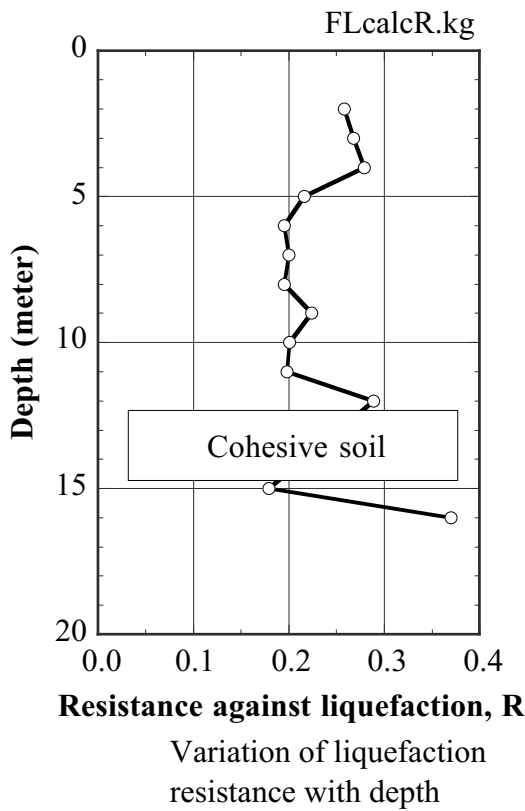
For more information, the figure to the right compares the magnitude of the 2 Hz outcrop motion against the motion at the surface of the soft alluvium. It is seen that the amplification (ratio of surface motion and the outcrop motion) decreases as the intensity of outcrop motion increases. This is mainly because of the nonlinearity of soil in which the stronger shaking makes strain greater and modulus smaller, and,

consequently, the natural period of subsoil longer. Eventually, the hyperbolic model becomes unable to transfer shear stress greater than  $G_{max} \times \gamma_{rr}$ . Note that the maximum amplification occurred around  $1 \text{ m/s}^2$  input at which  $T_G \approx 0.5 \text{ s}$ ; the input motion period. This point is more clearly shown in the figure at the bottom. Idriss (1990) used real earthquake motion records to show the same point. For the significance of  $T_G$ , refer to (6.30).



**Exercise No.6 on Liquefaction Potential**

The calculation was made of two cases with  $A_{max} = 0.15$  and  $0.25 \text{ G}$ . See Figure below. No calculation is necessary in the clayey layer at 13 and 14 m of depth.



**List of Reference in Answer to Exercise**

Idriss, I.M. (1990) Response of soft soil sites during earthquakes, H.B.Seed Memorial Symposium, publ. Bi Tech in Canada, Vol.2, pp. 273-289

## ACKNOWLEDGMENTS

This book is a product of a long-term teaching in the Asian Institute of Technology in Bangkok, Thailand, and at the Civil Engineering Department, University of Tokyo. Although this teaching was not continuous throughout the period, it gave the author an important opportunity to collect lots of materials.

This book presents many outputs from the author's research activities at the University of Tokyo and elsewhere. The names of those who made significant contribution are shown as much as possible in what follows:

Prof. R. Verdugo, Dr. W. Vargas-Monge, Dr. R. Orense, Dr. M. Yoshimine, Mr. K. Yamada, Mr. Y. Kawano, Dr. Y. Tamari, Dr. H. Toyota, Dr. T. Uchimura, Mr. Y. Kogai, Mr. K. Amimoto, Mr. J. Kohchi, Mr. T. Maeda, Mr. K. Furumoto, Prof. K. Tokida, Mr. K. Watanabe, Prof. H. Di Benedetto, Dr. A. Ghalandarzadeh, Dr. T. Mizutani, Dr. S. Shimada, Mr. N. Shinkawa, Dr. T. Iwasaki, Mr. T. Nasu, Dr. S. Nakamura, Mr. H. Tanaka, Mr. Y. Kabashima, Prof. W.D.L. Finn, Dr. A. Tateishi, Dr. K. Wakamatsu, Dr. S. Tsujino, Dr. F. Kölsch, Mr. S. Imamura, Dr. J. Meneses, Dr. T. Tazo, Mr. K. Horie, Mr. Bach Thai Thuan, Mr. A. Shimokawa, Dr. S. Sendir, Mr. T. Itoh, Prof. I. Yoshida, Mr. H. Matsumoto, Dr. R. Isoyama, Mr. T. Orita, Prof. J. Koseki, Dr. S. Nakamura, Dr. N. Suzuki, Mr. N. Harada, Mr. Z. Athanasios, Prof. Y. Sasaki, Mr. Talib Wassan, Mr. H. Isoda, Prof. N. Yoshida, Miss M. Kameda, Dr. S. Tamate, Mr. C.EF. Lin, Dr. T. Namikawa, Dr. Y. Kobayashi, Ms. M. Nakamura, Mr. S. Kokeyuchi, Prof. S. Yasuda, Mr. N. Nakai, Mr. H. Ishida, Dr. H. Shahnazari, Mr. H. Matsumoto, Mr. M. Tatsuta, Mr. A. Yoshida, Mr. T. Sannomiya, Dr. M. Mohajeri, Mr. S. Nishimura, Mr. C. Gallage, Dr. T. Honda, Dr. V. Sesov, Dr. Alam Jahangir, Prof. K. Ishihara, Mr. R. Motamed, Mr. H. Sato, Mr. A. Hayakawa, Mr. C. Nguyen, Miss M. Nakamura, Dr. K. Watanabe, Mr. K. Kawano, Mr. A.T. Ngo, Dr. S. Kawamura, and Mr. T. Sato among many others.

The author is grateful for permissions to use figures in other publications. Those permissions were given by Japanese Geotechnical Society, Japan Society of Civil Engineers, BiTech Publishers, Soil Dynamics and Earthquake Engineering Journal, Geotechnique, Canadian Geotechnical Journal, Landslides Journal, Yama-to-Keikoku Publ., Aoba Publ, Kaiyo Kogyo Company, Nikkei Architecture Magazine, Niigata Nippo News, Akita Sakigake Shimpo, National Archives, Earthquake Engineering Research Institute, American Society of Testing and Materials, US Geological Survey, Bulletin of the Seismological Society of America, International Society for Soil Mechanics and Geotechnical Engineering, Ministry of Land, Infrastructure, and Transport, Public Works Research Institute, National Center for Earthquake Engineering Research, Kohchi Prefectural Government, Noshiro Municipal Government, Central Research Institute of Electric Power Industries, Kaiyo Kogyo, Okumura Gumi Corporation, Port and Airport Research Institute, Prof. R. Dobry, Mr. F. Yuminamochi, Mr. Y. Takeuchi, Mr. G. Soto Melo, and many other institutes as well as individuals. Furthermore, a sincere gratitude to the American Society of Civil Engineers has to be expressed by stating that the following figures are used with permission from ASCE: 4.21, 6.1, 6.2, 10.8, 10.9, 10.30, 10.31, 11.20, 11.21, 19.1, 19.2, 19.14, 19.15, 19.16, 19.17, 19.18, 19.19, 19.20, 19.33, 19.34, 21.22, 22.1, 22.2, 23.22, 24.16, and 26.88.



Qutb Minar in Delhi,

The construction of this religious tower was initiated by Qutub-ud-din Aybak who was the first Islamic monarch of Delhi in late twelfth century.

The author was supplied with many information on practical developments in earthquake geotechnical engineering. Those information came, for example, from Fudo-Tetra Corporation, Zenitaka Corporation, Sumitomo Metal Industries, Public Works Research Institute, Tokyo Gas, Tokyo Electric Power Company, and Mr. Junichi Ikeda at Association for Development of Earthquake Prediction among many others.

During the preparation of manuscript, assistance was made by Mr. N. Kohmoto, Miss M. Matsumoto, Mr. K. Sugo, Miss S. Kagawa, and Ms. A. Hirano. Very elaborate draft reading by a Springer personnel is deeply appreciated.

It is essential to appreciate financial aids for publication supplied by Japan Society of Promotion of Science (JSPS) and Grant-in-Aid for Scientific Research and Academic Publication of this book by the Ministry of Education, Culture, Sports, Science and Technology (MEXT). MEXT has been supporting the author's many research activities in the field of geotechnical earthquake engineering, including activities on large shaking table tests (Special Project for Earthquake Disaster Mitigation in Urban Area and E-Defense Project). The Japan Iron and Steel Federation supported the research on the use of sheet pile walls for mitigation of liquefaction-induced displacement. Moreover, studies on submarine slope stability was supported by Kajima Foundation, and that on ground vibration by the Nissan Science Foundation. Studies on performance based design and life cycle cost principle were supported by the New Energy and Industrial technology Development Organization (NEDO).

The author expresses his sincere thanks to all the collaboration and assistance that were supplied to the author in the past decades.

# INDEX

(numbers show section.)

## - 1 -

1-G shaking table test 24.13

## - A -

abandoned channel 18.11

accumulated damage  
concept 19.10

active fault 16.1

adobe 5.14

age  
10.12,10.16,10.18.11,18.13

ageing 1.14,18.13,25.5

air pluviation 18.18

air bag 4.12

Akita Harbor 24.2

Alaska 16.11

Alaska pipeline 16.5

ALID analysis 25.23

allowable deformation 14.5

allowable displacement  
14.6,14.7

allowable restoration time  
14.7

alluvial deposit 5.6

alluvial soils 8.4

amplification 4.11

amplification in soft soil 9.7

Amp(2E) 6.8

Amp(E+F) 6.8,9.6

anisotropic consolidation  
10.3,19.7,19.8

anisotropy 22.2

apparent friction angle  
15.8,15.9

arch 26.17

archaeological site 18.2

area of densification 26.9

Arias intensity 5.9

ash 10.24

associated flow rule 11.3

attenuation 5.11

Awaji Island 16.4

anchorage 24.2

axial stress 1,9

## - B -

backfill 17.5,26.15,26.17

backfill soil 24.2

Balakot 6.14

Bam 5.14

base rock 6.9

basin 5.8

bender element 10.5

bending moment 24.16

bending stiffness 24.17

bentonite 10.23

berm 14.8

Bessel functions 6.12,6.15

Bingham viscosity 25.17

blasting 26.16

block sampling 10.19

body wave 4.1

boiling 1.13,25.18

bonding 26.14

boundary condition 4.5,25.8

bowl model 11.5

breaching of grout 26.14

brittle behavior 7.1

brittleness index 24.14

buoyancy 17.3

## - C -

caisson 24.10

catfish 3.1

CDM 26.13

cellulose 24.12

centrifuge machine 24.11

centrifuge model 24.11

Chan Dam 14.3

Chi Chi earthquake  
15.5,25.24

Chinese criteria 20.4

Chuetsu earthquake 15.6

circular frequency 1.11

classification of subsoil 21.7

clay liquefaction 20.3,20.4

clay bridge 20.3

coaxiality 11.3

coda 5.13

colloidal silica 26.3,26.14

colored sand 24.4

compaction 26.4

compaction grouting 26.10

complex modulus 6.2

complex stress-strain model  
9.1,9.3

complex-modulus ground

9.7

complex-modulus medium  
9.5

conditionally stable 6.5

cone penetration 21.11

confining pressure 19.9

consolidation 1.4,18.10

consolidation settlement  
18.1

consolidation time  
10.4,10.16,18.13

constant-volume condition  
25.1

constant-volume shear 1.7

constraint of deformation  
26.13

contact 11.6

continued shaking 25.15

convergence 9.14

Coulomb's earth pressure  
theory 12.5,Appendix 1

Coulomb's failure criterion  
1.5,Appendix 1

counter weight 26.3

CPT 21.11

critical damping ratio  
9.2,25.17

critical hydraulic gradient  
1.13

critical SPT-N 21.1,21.3

cross-hole survey 8.3

CRR 19.1

crushing of grains 15.4

CSR 19.2

culvert 14.1

cyclic mobility 18.7

cyclic resistance ratio 19.1

cyclic stress ratio 19.2

cyclic triaxial test 18.15

## - D -

Dagupan  
17.3,17.5,17.13,18.13

Daikai subway station 13.1

d'Alembert's principle  
5.5,7.1

dam 6.14

dam subsidence 25.24

damping ratio 6.1,10.8

damping ratio of clay 10.15

damping ratio of sand 10.8

Darcy's law 1.13

deaired water 18.18

debris flow 15.2

- decay 4.7,4.9,5.11  
 deconvolution 9.15  
 deep mixing 26.1,26.13  
 degradation 10.10,10.14  
 degree of saturation  
     1.2,18.17,18.18  
 DEM 11.6  
 dense sand 18.7,20.1,21.6  
 densification 26.1  
 density 10.11,21.4  
 design earthquake motion  
     5.13  
 deterioration 14.8  
 detour 14.5  
 deviator stress 1.9  
 dewatering 26.12  
 differential settlement 17.8  
 dilatancy  
     1.6,1.7,11.2,11.4,20.1  
 direct damage cost 14.7  
 direct integration 6.5  
 direct shear 1.5,15.4  
 directivity 16.4  
 Dirichlet boundary  
     condition 6.16  
 discrete element analysis  
     11.6  
 distinct element analysis  
     11.6  
 discreteness 10.2  
 displacement 12.1  
 displacement amplitude 19.9  
 displacement behind quay  
     wall 24.2  
 displacement transducer  
     24.13  
 dissipation 18.3,18.10  
 DJM 26.13  
 double amplitude  
     10.6,19.1,19.3  
 downhole survey 8.1  
 downstream method 20.5  
 drag force 25.13  
 drain 26.11  
 drain pipe 18.6  
 drainage 1.5  
 dry crust 25.6  
 ductile behavior 7.1  
 dune sand 18.11  
 duration time 5.12  
 duration of lateral flow  
     5.12,25.19  
 dynamic consolidation  
     26.7,26.8  
 dynamic modulus 10.5  
 dynamite 26.16  
  
     - E -  
 earth fill dam 17.7,25.24  
 earth pressure 12.5,24.17  
 earthquake magnitude 5.4  
 earthquake moment 5.4  
 E-defense 24.13,24.16  
 effective stress  
     1.3,10.3,10.4,10.7  
 effective stress analysis  
     21.3,22.3,22.4  
 El Centro 5.7  
 El Cobre 20.5  
 elastoplasticity 11.3  
 electric cone 21.11  
 embankment  
     14.1,14.2,14.3,14.4,25.3  
 emergency action 23.3  
 EMS scale 5.1  
 energy correlation of excess  
     pore water pressure  
     20.8,20.9,20.10  
 endochronic model 20.8  
 energy absorbing boundary  
     6.16  
 energy theory 25.4  
 energy transmitting  
     boundary 6.16  
 envelope 5.13  
 environmental noise 4.12  
 epicenter 3.1,5.10  
 epicentral distance  
     5.10,5.11,15.6,18.12  
 equation of wave  
     propagation 4.4  
 equivalent linear analysis  
     9.13,9.14  
 equivalent linear model  
     9.10,9.16  
 equivalent number of cycles  
     19.3  
 equivalent spring-mass  
     model 13.4  
 erosion 15.1  
 Euler's equation 25.2  
 excavation 16.1  
 excess pore water pressure  
     1.8,18.1,18.16,20.6,20.7  
 explosion 18.6  
 extremely loose deposit 24.9  
  
     - F -  
 factor of safety 19.4,25.25  
 Fast Fourier Transformation  
     9.12  
 fault 16.8  
 fault 16.1  
 fault 3.1  
 FFT 9.12  
 fines content 21.4  
 fire 17.13  
 $F_L$  19.4  
 flexible joint 17.8  
 floating 17.5,23.13,26.3  
 flower structure 16.8  
 flow failure 24.3  
 flow rule 11.3  
 flux 1.13  
 foot wall 16.2  
 forced oscillation 9.4  
 Fourier series 6.4,9.11,9.12  
 free-field stress 13.1  
 freezing 10.20,10.21  
 frequency 1.11,10.9,21.10  
 frequency domain 6.4,6.16  
 friction angle 12.8  
 friction jacket 21.11  
 fundamental boundary  
     condition 25.2,25.8  
  
     - G -  
 gas pipeline 24.1  
 Gamma function 6.15  
 gas cushion 4.12  
 Gaussian elimination  
     Exercise 2  
 Genoa Fault 16.3,16.5,16.6  
 $G/G_{max}$  10.6  
 Gilan 5.14  
 $G_{max}$  10.5  
 Gomyoko 17.4  
 GPS 5.15  
 graben 16.3  
 Grand Banks 15.7  
 Green's function 5.13  
 glacier 25.12  
 grain movement 1.14  
 grain size 18.13,21.4  
 gravel 8.5,10.8,20.2,21.6

- gravel drain 26.1,26.11  
 gravity 24.5,24.7  
 ground vibration 26.6  
 ground water table 21.5  
 group pile 24.16  
 group velocity 4.8  
 grouting 26.1,26.13  
 Gujarat earthquake 14.3  
 Gutenberg and Richter 3.1
- H -**
- Hachinohe record 5.7  
 Haguro Tunnel 13.7  
 hanging wall 16.2  
 Hamming Window 9.12  
 Hanning Window 9.12  
 hardening function 11.3  
 Hardin and Drnevich 11.1, Exercise 3  
 hill 6.11  
 hill-induced amplification 6.12  
 Hokkaido-Toho-Oki earthquake 6.11  
 house 5.14,17.14  
 Hope Fault 16.6  
 hot liquefaction 18.6  
 Huascaran 15.2  
 human life 14.7  
 H/V spectrum 8.10  
 hybrid test 24.15  
 hydraulic filling 17.7,20.5  
 hydraulic gradient 1.13  
 hydrodynamic pressure 13.5  
 hyperbolic model 11.1,22.3, Exercise 3  
 hypocenter 3.1,5.10
- I -**
- Iida, K., Prof. 10.1  
 impact energy 26.7  
 impedance 4.10,6.8,9.7  
 incident wave 4.10,22.4  
 incinerated ash 10.24  
 inclinometer 24.13  
 indirect damage cost 14.7  
 inertia force 7.4  
 inertial interaction 13.1  
 infinite boundary 6.16  
 initial condition 1.11  
 instrumental seismic
- intensity 5.3  
 insulation 4.12  
 internal friction 1.5  
 irregular loading 19.10  
 iteration 9.14  
 Itoizawa 14.8  
 Izmit Bay 16.9
- J -**
- jacking up 17.14  
 JMA magnitude 5.4  
 JMA scale 5.1,5.2,5.3
- K -**
- Kaihoku motion 5.7  
 Kanagawa Prefecture 15.6  
 Kanto earthquake 5.14,18.11  
 Kasukabe 25.9  
 Kawagishi-Cho 17.3,17.12,23.4  
 Kawasaki City 18.11  
 Kawasumi magnitude 5.4  
 Kayanuma 14.2  
 Kerman 5.14  
 kinetic interaction 13.1  
 Kinoura Tunnel 13.7  
 Kisagata 16.11  
 Ko condition 19.7,19.8  
 Kobe 5.14  
 Kobe Harbor 24.10  
 Kohchi 16.10  
 Kolbuszewski 18.18  
 Koyna Dam 3.3  
 Kronecker's delta 16.3,20.9  
 Kushiro Harbor 26.11  
 Kushiro-Oki earthquake 6.11
- L -**
- Lagrangean equation of motion 13.3,25.3  
 Lamb's formula 25.17  
 Lamb's problem 4.9  
 laminar box 24.13  
 landfill 10.24  
 landslide 15.1  
 landslide risk 15.6  
 large penetration 20.2  
 lateral displacement 17.6,24.4,24.7
- lateral earth pressure 17.5  
 lateral earth pressure on pile 24.16  
 law of similitude 24.12  
 LCC, life cycle cost 14.7  
 LDT 10.1  
 Leuwigajah 10.24  
 lime column 26.10  
 limit equilibrium 7.1  
 liquefaction curve 19.3  
 liquefaction of clay 20.4  
 liquefaction-induced displacement 24.6  
 liquefied slope 17.7  
 liquid limit 1.1  
 Lituya Bay 16.12  
 Liyutan Dam 25.24  
 loam 8.4  
 local magnitude 5.4  
 local soil condition 5.6  
 local soil effect 4.4  
 logarithmic decrement 9.4  
 Loma Prieta earthquake 5.6  
 Lommel's formula 6.15  
 Love wave 4.8  
 LSI 27.2
- M -**
- Maeyama 24.1,25.8,25.9  
 magnitude 5.4,18.12  
 magnitude correction factor 19.3  
 man hole 26.15  
 Masing rule 11.1  
 masonry 5.14  
 maximum acceleration 12.3,18.9  
 maximum possible displacement 25.7  
 maximum velocity 18.9  
 Maxwell model 6.2  
 mean grain size 1.1  
 membrane penetration 1.10  
 method of seismic displacement 13.1,13.2  
 Mexico City Clay 10.10  
 microscope 1.14  
 microtremor 8.10  
 microzonation 8.10,27.1,27.2  
 minimum SPT-*N* 21.1

- minimum potential energy 25.2  
 MM scale 5.1  
 Mochikoshi 20.5  
 modified method of seismic coefficient 7.2  
 Mohr stress circle 1.3  
 Mononobe-Okabe theory 12.5,12.8  
 Modified Mononobe-Okabe theory 12.8  
 MSK scale 5.1  
 mudstone 14.8  
 multi nonlinear spring model 11.5  
 multi-directional shear 19.12  
 multi-layered ground 6.10, Exercise 2  
 multiple sieve method 18.18  
 municipal waste 10.24  
 Muzaffarabad 15.1
- N -
- N* value 1.12,6.7  
 $N_1$  21.8  
 Narbakan 16.11,18.14  
 Naruto 15.8  
 natural boundary condition 25.8  
 natural dam 15.3  
 natural frequency 1.11,9.12  
 natural levee 18.11  
 natural period 1.11,9.12  
 natural period of building 5.14  
 natural period of ground 6.8  
 Navrakhi Harbor 13.8,17.4  
 negative dilatancy 18.1  
 negative effects to public 14.6  
 Neodani 16.1  
 Nerlerk Berm 24.3  
 Neumann boundary condition 6.16  
 Newmark's analogy of rigid block 12.1  
 Newmark's  $\beta$  method 9.9  
 Nihonkai-Chubu earthquake 17.4,17.7  
 Niigata 17.13  
 Niigata Airport 25.18
- Nobl Plane 16.11  
 nodular pile 13.8,17.10  
 noise 26.6  
 nonassociated flow rule 11.3  
 non-plastic silt 17.10  
 nonlinearity 9.10,10.2,10.6  
 normal fault 16.1,16.3  
 normality 11.3  
 normalized cone resistance 21.11  
 normally consolidated 1.4  
 Noshiro 17.7,24.1,25.8  
 number of cycles 19.4  
 numerical damping 6.6  
 Nyquist frequency 9.11
- O -
- objectivity 11.3  
 OCR 1.4,19.8,20.4  
 Ohya slide 15.1  
 Ohgata 25.9,25.11  
 Okabe, S., Dr. 12.5  
 one-way loading 19.5,19.6  
 on-line experiment 24.15  
 Ontake Mountain 15.1  
 open-crack boundary 25.8  
 organic soil 8.4  
 Orléansville 15.7  
 outcrop amplification 9.7  
 outcrop motion 6.8,6.9  
 overconsolidation 1.4,10.4,19.8,20.4
- P -
- paleoliquefaction 18.4  
 paraxial boundary 6.16  
 participation factor 13.3  
 particle size 18.2,18.3,21.4  
 passive earth pressure 25.22  
 peak strength 1.9  
 performance 14.5  
 performance matrix 14.7  
 performance-based design 7.1,14.7,26.1  
 period 1.11,4.4  
 permanent displacement 17.7,24.1,25.23  
 permanent grout 26.14  
 permeability 1.13  
 phase transformation 18.7  
 pile 24.1,24.16,25.21
- pile with drain 26.11  
 pipeline 13.2,16.8,26.15,26.17  
 $P_L$  21.9  
 plastic limit 1.1  
 plasticity 10.6,11.3  
 plasticity index 1.1,10.2,10.13  
 plastic potential 11.3  
 plastic waste 10.24  
 plate tectonics 3.2  
 Pleistocene soil 8.6,21.6  
 plume tectonics 3.2  
 pneumatic loading 21.10  
 pore water pressure 1.3  
 Port Island 17.12,18.9,20.2,23.4,24.10  
 Port Island acceleration 17.12  
 portable cone penetrometer 21.11  
 Portage of Alaska 16.11  
 power 5.9  
 predominant frequency 9.12  
 prediction of lateral displacement 25.6  
 preloading 10.24,19.8,22.1  
 premixing 26.15  
 prestraining 10.4  
 prevention of liquefaction 26.2  
 primary consolidation 1.4  
 principal stress 1.3,18.8  
 pseudo static method 7.1  
 pull-apart action 16.9  
 P wave 4.1,4.2
- Q -
- quasi static method 7.1  
 quay wall 24.2,24.10  
 quick construction 14.5  
 quick restoration 14.1,14.5
- R -
- radial stress 1.9  
 Ramberg-Osgood model 11.1  
 rapid sedimentation 15.8  
 rate dependency 6.1,10.9,25.14  
 Rayleigh wave 4.7,4.12,8.11



- $r_d$  19.11  
 rebound 3.2  
 reconnaissance 5.15  
 reference strain 11.1  
 reflection 4.2,4.10  
 refraction 4.2,4.3  
 relative density 1.2  
 repeated liquefaction 22.2  
 reservoir-triggered seismicity 3.3  
 residual displacement 12.2,12.4  
 residual strength 1.9,12.8,23.3  
 resonance 1.11,9.3,23.2  
 resonant column 10.1  
 response spectra 5.13,23.1  
 return period 5.13  
 reverse fault 16.1,16.2  
 Richter scale 5.4  
 ring shear 15.4  
 river dike 14.1,17.4,17.9  
 $R_L$  21.8  
 rockfill dam 25.24  
 rod compaction 26.4  
 rupture 3.1
- S -
- sample disturbance 10.21,19.4  
 sample preparation method 18.18  
 sand boiling 17.10,18.2,18.5  
 sand compaction pile 22.1,26.4,26.5  
 sand drain 22.1  
 sand with fines 21.6  
 San Fernando Dam 17.7  
 San Francisco earthquake 7.1  
 San-no-kai Dam 6.14  
 Sano, T., Prof. 7.1  
 Sardis Dam 26.4  
 SASW 8.11  
 saturation 18.1,18.16,26.4,26.12  
 SAVE 26.6  
 scale 24.12  
 scour 15.1  
 screen pipe 26.11  
 secondary compression 1.4  
 Seed-Whitman approximation 12.7  
 seepage force 1.13  
 Seimareh 15.9  
 seismic coefficient 7.1,12.3,12.4  
 seismic cone 21.11  
 seismic earth pressure 12.5,12.6  
 seismic intensity 5.1  
 seismic performance 14.7  
 seismic refraction 8.7  
 self curing 10.24  
 semi-hydraulic filling 17.7,20.5  
 sensitivity 10.4  
 sequence of blasting 26.16  
 sewage pipeline 26.15  
 sewage tank 17.5  
 Seward 15.7  
 shadow effect 24.16  
 shaking table 19.7,24.13  
 shallow foundation 17.13  
 shear band 1.14  
 shear modulus of clay 10.13  
 shear strain path 11.5  
 shear wave velocity 10.5,22.5  
 shear window 4.9  
 shear work 20.9  
 sheet pile 24.17,26.3  
 sheet pile with drain 26.3,26.11  
 shock type 19.10  
 Showa Bridge 17.1,24.9,24.16,25.26  
 shredded tire 26.17  
 SH wave 4.2  
 SI 23.2,23.3  
 silent boundary 6.16  
 silent earthquake 3.1  
 silty soil 17.10  
 similitude 24.12,24.14  
 single amplitude 10.6  
 single-degree-of-freedom 1.11  
 Skempton 26.5  
 Skempton's B value 18.16  
 skin friction 13.8,21.11  
 slaking 14.8  
 sliding surface liquefaction 15.4  
 sloshing 17.15  
 slow earthquake 3.1  
 slow slip event 3.1  
 slug 10.24  
 Smith boundary 6.16  
 smoothing of spectrum 9.12  
 Snell's law 4.3,8.7  
 softening 1.9  
 specific gravity 1.2  
 spectrum analysis 9.12  
 spectrum intensity 23.2  
 SPT 1.12,21.1,26.5  
 SPT in Niigata 21.2  
 SPT- $V_s$  correlation 8.4  
 stacking 8.8  
 standard penetration 1.12  
 Static densification 26.10  
 static liquefaction 24.3  
 static modulus 10.5  
 statistic shear stress 19.5  
 steady state 24.3  
 Stokes formula 25.17  
 stone column 26.5  
 Storegga submarine landslide 16.12  
 strain 10.22,19.1  
 strain amplitude 10.2,10.3,10.4  
 strain compatible modulus 9.13  
 strain energy 20.8,20.9,20.10  
 strain localization 1.14  
 strain path 20.8  
 strain potential 25.22  
 strain-controlled 1.9  
 stress 11.1  
 stress axes 19.4  
 stress axes rotation 11.3,20.9,20.10  
 stress-induced anisotropy 26.16  
 stress path 1.8,18.7  
 stress ratio 18.15,19.1,19.2,19.4  
 stress reversal 19.6  
 stress-controlled 1.9  
 stress-dilatancy 1.6,11.2,11.3,11.4,18.7  
 stress-strain of in-situ soil 20.11  
 stress superposition 24.3

- strike slip 3.1,16.1,16.4  
strip foundation 17.14  
strong shaking 5.12,25.19  
submarine landslide  
15.7,15.8  
subsidence  
14.4,16.9,16.10,16.11,17.4,  
17.8,17.11,17.13,22.1,25.25  
subsidence of building  
17.13  
Sumatra 16.11,16.12  
superlime pile 26.10  
super riverdike 7.2  
surface dry crust 24.6,25.10  
surface geology  
5.14,18.11,27.2  
surface rupture 16.5  
surface wave 4.7  
suspension-type downhole  
survey 8.2  
Suzaki Bay 16.10  
SV 4.2,23.2  
S wave 4.1,27.1  
S-wave propagation 4.5  
Swedish weight sounding  
5.15,8.9  
swelling 15.6
- T -**
- Tachikawa fault 16.1  
tailing material 20.5  
Tamanoike 22.2  
tank 17.15,26.3  
Tanna Tunnel 16.7  
tectonic plate 3.2  
tensor 11.3  
 $T_G$  6.8,10.1,21.7,27.1  
thickness of liquefied layer  
25.10  
thin-wall sampler 10.19  
three dimensional prediction  
25.11  
three-dimensional analysis  
25.19,25.20  
time domain 6.4  
time envelope 5.13  
tip resistance 21.11  
tire chip 26.17  
Tohya Lake 15.7  
Tokachi Riverdike 14.3,17.4  
topographic effects 6.14  
topography 6.12,6.13
- torsion shear 18.8  
total head 24.5  
total stress analysis 21.3  
Tottoriken Seibu earthquake  
17.10  
traditional house 5.14  
traffic 4.12  
transient response 6.3  
travel insurance 14.7  
trench 4.12,16.1  
triaxial shear device 1.9  
triple-tube sampler 10.19  
Tsaoling landslide 15.3,15.4  
tsunami 15.7,15.8,16.12  
tsunami intensity scale  
6.12  
tube sampler 10.21  
tunnel 13.7,16.7  
two-way loading 19.5,19.6
- U -**
- ultrasonic wave 26.5  
unconditionally stable 6.6  
unconfined compression  
10.9  
unconformity 9.9  
undercompaction 18.18  
underground wall 26.3  
undisturbed sample  
1.9,10.17,10.19,10.20  
undrained shear 1.7,18.7  
undrained softening 24.3  
unliquefied surface 21.9  
unsaturated sand 18.1  
upstream method 20.5
- V -**
- Valdez 15.7  
Valdivia 16.11  
variational principle of  
mathematics  
25.2,25.5,Appendix 3  
Vajont Dam 16.12  
vertical motion 7.3  
vibratory type 19.10  
viscosity 25.14,25.16,25.17  
viscous boundary 6.16  
void ratio 1.2  
void redistribution 25.26  
Voigt model 6.2,9.2  
volcanic slope 15.1,15.8  
volume compressibility 1.4
- volume contraction 22.1  
 $V_p$  4.2,8.1  
 $V_s$   
4.1,8.2,8.4,10.5,21.12,27.1  
 $V_{30}$  5.11
- W -**
- wall 26.3  
water content 1.2,10.4  
water film 25.26  
water pressure 13.5  
water saturated backfill 13.6  
water sedimentation 24.8  
water table 14.2  
wave action 15.8  
wave energy 4.11  
wave length 4.4  
wave number 4.4  
wave propagation velocity  
4.1  
weathering of grout 26.14  
weathering of rock 15.1  
well resistance 26.11  
Westergaard 13.5,24.17  
wet tamping 18.18,24.8  
wet vibration 18.18  
white noise 5.13  
Winkler foundation  
13.1,13.2
- Y -**
- yield function 11.3  
Yodo River 17.9,26.13  
Yuminamochi, F., Mr. 25.18  
Yungay 15.2
- Z -**
- zonation 27.1,27.2
- Symbols -**
- $\phi$  1.5